MASSOUD KAVIANY

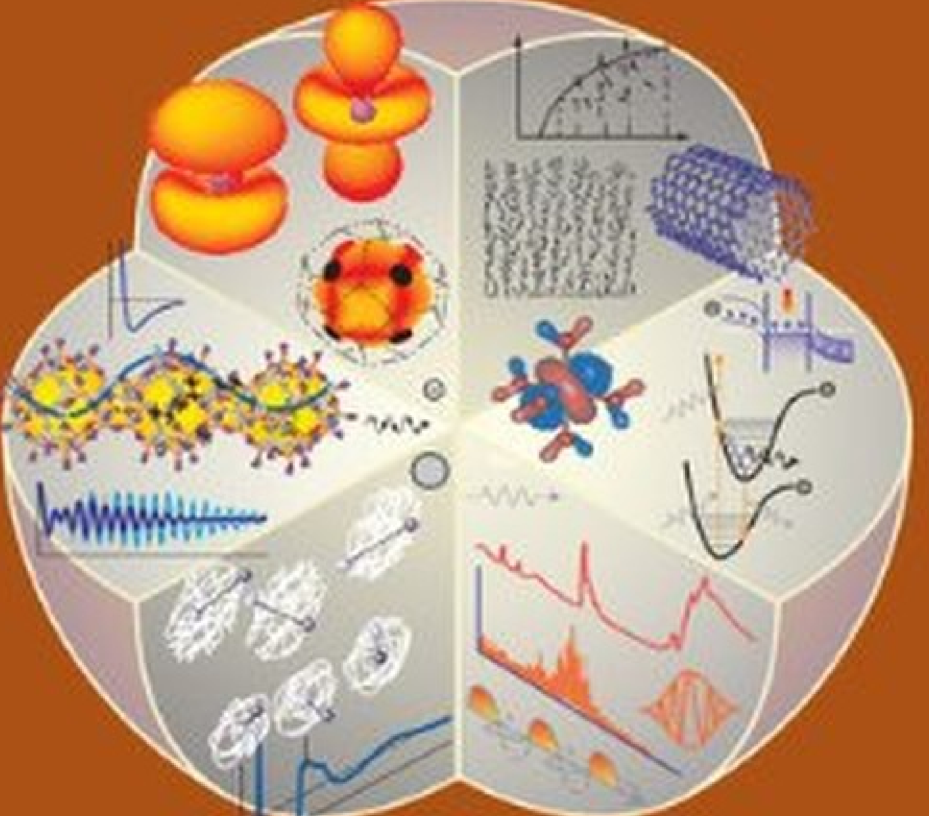

HEAT TRANSFER PHYSICS

SECOND EDITION

CAMBRIDGE

HEAT TRANSFER PHYSICS, SECOND EDITION

This graduate textbook describes atomic-level kinetics (mechanisms and rates) of thermal energy storage, transport (conduction, convection, and radiation), and transformation (various energy conversions) by principal energy carriers. The approach combines the fundamentals of molecular orbitals-potentials, statistical thermodynamics, computational molecular dynamics, quantum energy states, transport theories, solid-state and fluid-state physics, and quantum optics. The textbook presents a unified theory, over fine-structure/molecular-dynamics/Boltzmann/macroscopic length and time scales, of heat transfer kinetics in terms of transition rates and relaxation times, and its modern applications, including nano- and microscale size effects. Numerous examples, illustrations, and homework problems with answers to enhance learning are included. This new edition includes applications in energy conversion (including chemical bond, nuclear, and solar), expanded examples of size effects, inclusion of junction quantum transport, and discussion of graphene and its phonon and electronic conductances. New appendix coverage of phonon contributions to the Seebeck coefficient, Monte Carlo methods and ladder operators is also included.

Massoud Kaviany is a Professor in the Department of Mechanical Engineering and in the Applied Physics Program at the University of Michigan, where he has been since 1986. His area of teaching and research is heat transfer physics, with a particular interest in porous media. His current projects include atomic structural metrics in high-performance thermoelectric materials (both electron and phonon transport) and in laser cooling of solids (including ab initio calculations of photon-electron and electron-phonon couplings), and the effect of pore water in polymer electrolyte transport and fuel cell performance. His integration of research into education is currently focused on heat transfer physics, treating the atomic-level kinetics of transport and interaction of phonon, electron, fluid particle, and photon in a unified manner. It combines ab initio (fine structure), molecular dynamics, Boltzmann transport, and macroscopic treatments, but on increasing length and times scales. He is author of the monographs *Principles of Heat Transfer in Porous Media* (2nd Ed.) and *Principles of Convective Heat Transfer* (2nd Ed.), and the undergraduate textbooks *Principles of Heat Transfer* and *Essentials of Heat Transfer*. He received the College of Engineering's Education Excellence Award in 2003. He is an editor of the *Journal of Nanoscale and Microscale Thermophysical Engineering* and is on the editorial board of the *International Journal of Heat and Mass Transfer* and several other international journals. He is an ASME Fellow (since 1992) and an APS Fellow (since 2011), was Chair of the Committee on Theory and Fundamental Research in Heat Transfer (1995–98), and is the recipient of the 2002 ASME Heat Transfer Memorial Award (Science) and the 2010 Harry Potter Gold Medal (Thermodynamics Science).

Heat Transfer Physics

Second Edition

Massoud Kaviany
University of Michigan

CAMBRIDGE
UNIVERSITY PRESS

CAMBRIDGE
UNIVERSITY PRESS

32 Avenue of the Americas, New York, NY 10013-2473, USA

Cambridge University Press is part of the University of Cambridge.

It furthers the University's mission by disseminating knowledge in the pursuit of education, learning, and research at the highest international levels of excellence.

www.cambridge.org
Information on this title: www.cambridge.org/9781107041783

© Massoud Kaviany 2014

This publication is in copyright. Subject to statutory exception
and to the provisions of relevant collective licensing agreements,
no reproduction of any part may take place without the written
permission of Cambridge University Press.

First published 2014

Printed in the United States of America

A catalog record for this publication is available from the British Library.

Library of Congress Cataloging in Publication Data
Kaviany, M. (Massoud), author.
Heat transfer physics / Massoud Kaviany. – Second edition.
  pages cm
Includes bibliographical references and index.
ISBN 978-1-107-04178-3 (hardback)
1. Nuclear reactor kinetics. 2. Change of state (Physics) 3. Heat storage. 4. Heat – Transmission.
I. Title.
QC787.N8K39 2013
536′.2–dc23 2013032185

ISBN 978-1-107-04178-3 Hardback

Cambridge University Press has no responsibility for the persistence or accuracy of URLs for external or third-party Internet Web sites referred to in this publication and does not guarantee that any content on such Web sites is, or will remain, accurate or appropriate.

To curiosity, reason, doubt,

dialogue, understanding, tolerance,

and humility.

Contents

Preface *page* xvii

Acknowledgments xxi

1 **Introduction and Preliminaries** **1**

- 1.1 Principal Carriers: Phonon, Electron, Fluid Particle, and Photon 3
  - 1.1.1 Phonon 4
  - 1.1.2 Electron (and Hole) 7
  - 1.1.3 Fluid Particle 8
  - 1.1.4 Photon 9
- 1.2 Equilibrium and Nonequilibrium Energy Occupancy Distributions 10
  - 1.2.1 Nonequilibrium Energy Carrier Occupancy by Energy Conversion 10
  - 1.2.2 Transport Phenomena Related to Energy Occupancy Distributions 14
- 1.3 Particles, Waves, Wave Packets and Quasi-Particles and Density of States 16
- 1.4 A History of Contributions Toward Heat Transfer Physics 17
- 1.5 Fundamental Constants and Fine-Structure Scales 20
  - 1.5.1 Boltzmann and Planck Constants 20
  - 1.5.2 Atomic Units and Fine-Structure Scales 21
- 1.6 Principal Carriers: Concentration, Energy, Kinetics, and Speed 23
  - 1.6.1 Principal-Energy Carriers Concentration 24
  - 1.6.2 Principal-Carrier Energy 25
  - 1.6.3 Principal-Carrier Energy Transport/Transformation Kinetics 26
  - 1.6.4 Principal-Carrier Speed 28
- 1.7 Periodic Table of Elements 28

1.8 Heat Transfer Physics: Atomic-Level Energy Kinetics 32
  1.8.1 Thermal Energy Storage 32
  1.8.2 Thermal Energy Transport 33
  1.8.3 Thermal Energy Transformation 35
1.9 Density of States and Carrier Density 40
1.10 *Ab Initio*/MD/BTE/Macroscopic Treatments 42
1.11 Scope 44
1.12 Problems 46

2 Molecular Orbitals/Potentials/Dynamics, and Quantum Energy States 50

2.1 Interatomic Forces and Potential Wells 50
  2.1.1 Interatomic Forces 52
  2.1.2 Intermolecular Forces 52
  2.1.3 Kinetic and Potential Energies and Potential Wells 53
2.2 Orbitals and Interatomic Potential Models 58
  2.2.1 Atomic and Molecular Electron Orbitals 58
  2.2.2 *Ab Initio* Computation of Interatomic Potentials 61
  2.2.3 Potential Models and Phases 65
  2.2.4 Examples of Atomic Bond Length and Energy 72
  2.2.5 Radial Distribution of Atoms in Dense Phase 73
2.3 Molecular Ensembles, Temperature, and Thermodynamic Relations 75
  2.3.1 Ensembles and Computational Molecular Dynamics 75
  2.3.2 Energy Equipartition 75
  2.3.3 Thermodynamic Relations 76
2.4 Hamiltonian Mechanics 77
  2.4.1 Classical and Quantum Hamiltonians 77
  2.4.2 Probability and Partition Function 79
  2.4.3 Ergodic Hypothesis in Theoretical Statistical Mechanics 81
2.5 Molecular Dynamics Simulations 81
  2.5.1 Ensemble and Discretization of Governing Equations 81
  2.5.2 A Molecular Dynamics Simulation Case Study: L–J Ar FCC 86
  2.5.3 L–J FCC MD Scales in Classical Harmonic Oscillator 88
  2.5.4 L–J Potential Phase Transformations 92
  2.5.5 Atomic Displacement in Solids and Quantum Effects 93
  2.5.6 Specific Heat Capacity 94
  2.5.7 Heat Flux Vector 95
2.6 Schrödinger Equation and Quantum Energy States 96
  2.6.1 Time-Dependent Schrödinger Equation and Wave Vector 97
  2.6.2 Bloch Wave Form 99

2.6.3 Quantum-Mechanics Formalism, Bra–Ket and Matrix Element 100
2.6.4 Quantum Mechanical, Harmonic Oscillator 101
2.6.5 Periodic, Free Electron (Gas) Model for Metals 105
2.6.6 Electron Orbitals in Hydrogenlike Atoms 109
2.6.7 Perturbation and Numerical Solutions to Schrödinger Equation 111
2.7 Problems 115

3 Carrier Energy Transport and Transformation Theories 119

3.1 Boltzmann Transport Equation 120
3.1.1 Particle Probability Distribution (Occupancy) Function 120
3.1.2 A Simple Derivation of BTE 120
3.1.3 In- and Out-Scattering 123
3.1.4 Relaxation-Time Approximation of Scattering and Transport Properties 124
3.1.5 Boltzmann Transport Scales 128
3.1.6 Momentum, Energy, and Average Relaxation Times 129
3.1.7 Moments of BTE 130
3.1.8 Numerical Solution to BTE 131
3.2 Energy Transition Kinetics and Fermi Golden Rule 131
3.2.1 Elastic and Inelastic Scattering 132
3.2.2 Phonon Interaction and Transition Rates 133
3.2.3 Electron (and Hole) Interaction and Transition Rates 134
3.2.4 Fluid Particle Interaction and Transition Rates 138
3.2.5 Photon Interaction and Transition Rates 138
3.3 Maxwell Equations and Electromagnetic Waves 138
3.3.1 Maxwell Equations 138
3.3.2 Electromagnetic Wave Propagation Equation 142
3.3.3 EM Wave and Photon Energy 144
3.3.4 Electric Dipole and Emission, Absorption, and Scattering of EM Waves 145
3.3.5 Dielectric Function and Dielectric Heating 147
3.3.6 Electrical Resistivity and Mobility and Joule Heating 151
3.4 Onsager Coupled Transport Coefficients 152
3.5 Stochastic Particle Dynamics and Transport 154
3.5.1 Langevin Particle Dynamics Equation and Brownian Motion 154
3.5.2 Fokker–Planck Particle Conservation Equation 155
3.5.3 Mean-Field Theory 155
3.6 Equilibrium Fluctuation–Dissipation and Green–Kubo Transport Theory 156
3.7 Macroscopic Fluid Dynamics Equations 159
3.8 Macroscopic Elastic Mechanics Equations 159

3.9 Macroscopic Scales 161
3.10 Problems 163

4 **Phonon Energy Storage, Transport and Transformation Kinetics 173**

4.1 Phonon Dispersion in One-Dimensional Classical Lattice Vibration 174
4.2 Phonon Density of States and Debye Model 181
4.2.1 Phonon DOS for One-Dimensional Lattice and van Hove Singularities 182
4.2.2 Debye and Other Phonon DOS Models 184
4.3 Reciprocal Lattice, Brillouin Zone, and Primitive Cell and Its Basis 186
4.3.1 Reciprocal Lattice 187
4.3.2 Brillouin Zone 189
4.3.3 Primitive Cell and Its Basis: Number of Phonon Branches 190
4.4 Normal Modes and Dynamical Matrix 191
4.5 Quantum Theory of Lattice Vibration 196
4.6 Examples of Phonon Dispersion and DOS 198
4.7 Phonon Specific Heat Capacity and Debye Average Acoustic Speed 201
4.7.1 Acoustic Phonon Specific Heat Capacity 201
4.7.2 Estimate of Directional Acoustic Velocity 206
4.8 Atomic Displacement in Lattice Vibration 208
4.9 Phonon BTE and Callaway Conductivity Model 211
4.9.1 Single-Mode Relaxation Time 211
4.9.2 Callaway Phonon Conductivity Model from BTE 212
4.9.3 Callaway–Holland Phonon Conductivity Model 215
4.9.4 Phonon Scattering Relaxation Time Models 215
4.9.5 Phonon Dispersion Models: Ge As Example 223
4.9.6 Comparison of Dispersion Models 226
4.9.7 Lattice Thermal Conductivity Prediction 228
4.10 Einstein and Cahill–Pohl Minimum Phonon Conductivities 231
4.11 Material Metrics of Phonon Conductivity: Slack Relation 233
4.11.1 Derivation of Slack Relation 234
4.11.2 Force-Constant Combinative Rule for Arbitrary Pair-Bond 235
4.11.3 Evaluation of Sound Velocity and Debye Temperature 241
4.11.4 Prediction of Grüneisen Parameter 244
4.11.5 Prediction of Thermal Conductivity 249
4.12 Phonon Conductivity Decomposition: Acoustic Phonons 254
4.12.1 Heat Current Autocorrelation Function 255
4.12.2 Phonon Conductivity Decomposition 258
4.12.3 Comparison with Experiment 260

4.13 Phonon Conductivity Decomposition: Optical Phonons 261
4.14 Quantum Corrections to MD/G-K Predictions 262
4.15 Phonon Conductivity from BTE: Variational Method 267
4.16 Experimental Data on Phonon Conductivity 269
4.17 Phonon Boundary Resistance 271
4.18 Absorption of Ultrasound Waves in Solids 275
4.19 Size Effects 276
  4.19.1 Finite-Size Effect on Phonon Conductivity 276
  4.19.2 Superlattice Phonon Conductivity 278
  4.19.3 Phonon Density of States of Nanoparticles 280
  4.19.4 Phonon Conductivity Rectification in Anisotropic, One-Dimensional Systems 286
  4.19.5 Heat Flow in Molecular Wire 287
  4.19.6 Quantum Vibrational Energy Flow in Nanostructures 288
  4.19.7 Nanocone Conductivity 289
4.20 Problems 289

5 Electron Energy Storage, Transport and Transformation Kinetics . . . 306

5.1 Schrödinger Equation for Periodic-Potential Electronic Band Structure 309
5.2 Electronic Band Structure in One-Dimensional Ionic Lattice 311
5.3 Three-Dimensional Bands Using Tight-Binding Approximation 314
  5.3.1 General LCAO 315
  5.3.2 Example of Tight-Binding Approximation: FCC, Single s-Band 317
5.4 *Ab Initio* Computation of Electron Band Structure 319
5.5 Electron Band Structure for Semiconductors and Effective Mass 321
5.6 Periodic Electron Gas Model for Metals 325
5.7 Electron/Hole Density of Carrier and States for Semiconductors 327
5.8 Specific Heat Capacity of Conduction Electrons 331
5.9 Electron BTE for Semiconductors: Thermoelectric Force 334
5.10 Electron Relaxation Time and Fermi Golden Rule 335
5.11 Average Relaxation Time $\langle\langle\tau_e\rangle\rangle$ for Power-Law τ_e (Momentum) (E_e) 338
5.12 Thermoelectric Transport Property Tensors for Power-Law $\tau_e(E_e)$ 344
5.13 TE Transport Coefficients for Cubic Semiconductors 347
  5.13.1 Seebeck, Peltier, and Thomson Coefficients, and Electrical and Thermal Conductivities 347
  5.13.2 Electron Mean Free Path for Metals 349
5.14 Magnetic Field and Hall Factor and Coefficient 350

5.15 Electron–Phonon Relaxation Times in Semiconductors 351
  5.15.1 Electron–Phonon Wave Function 352
  5.15.2 Rate of Acoustic-Phonon Scattering of Electrons 354
  5.15.3 Rate of Optical-Phonon Scattering of Electrons 355
  5.15.4 Summary of Electron-Scattering Mechanisms and Relaxation-Time Relations 359
5.16 TE Transport Coefficients Data for Metals and Semiconductors 359
  5.16.1 Structural Defects in Crystalline Solids 359
  5.16.2 Metals 360
  5.16.3 Semiconductors 366
  5.16.4 TE Figure of Merit Z_e 372
5.17 *Ab Initio* Computation of TE Transport Property Tensors 377
  5.17.1 TE Transport Tensors and Variable Chemical Potential 377
  5.17.2 Introduction to BoltzTraP 379
  5.17.3 Relaxation Times Based on Kane Band Model 380
  5.17.4 Predicted Seebeck Coefficient and Electrical Conductivity 385
  5.17.5 Electric and Phonon Thermal Conductivities 388
5.18 Electron and Phonon Transport Under Local Thermal Nonequilibrium 393
  5.18.1 Derivations 393
  5.18.2 Phonon Modal Energy Equations 395
  5.18.3 Summary of Conservation (Electrohydrodynamic) Equations 396
5.19 Cooling Length in Electron–Phonon Local Thermal Nonequilibrium 397
5.20 Electronic Energy States of Ions in Crystals 400
5.21 Electronic Energy States of Gases 404
5.22 Size Effects 407
  5.22.1 Quantum Well for Improved TE Z_eT 408
  5.22.2 Reduced Electron–Phonon Scattering Rate in Quantum Wells 411
  5.22.3 Electronic and Phonon Thermal Conductance of Graphene–Flake Junctions 413
  5.22.4 Heterobarrier for Converting Hot–Phonon Energy to Electric Potential 418
5.23 Problems 422

6 Fluid Particle Energy Storage, Transport, and Transformation Kinetics 434

6.1 Fluid Particle Quantum Energy States and Partition Functions 436
  6.1.1 Translational Energy and Partition Function 436
  6.1.2 Vibrational Energy and Partition Function 438

- 6.1.3 Rotational Energy and Partition Function 439
- 6.1.4 Electronic Energy and Partition Function 440
- 6.1.5 *Ab Initio* Computation of Vibrational and Rotational Energy States 441

6.2 Ideal-Gas Specific Heat Capacity 443

6.3 Dense-Fluid Specific Heat Capacity: van der Waals Model 447

6.4 Gas BTE, f_f^o and Thermal Velocities 451
- 6.4.1 Interparticle Collisions 451
- 6.4.2 Equilibrium Distribution Function for Translational Energy 453
- 6.4.3 Inclusion of Gravitational Potential Energy 456

6.5 Ideal-Gas Binary Collision Rate and Relaxation Time 456

6.6 Ideal-Gas Mean Free Path and Viscosity 459

6.7 Kinetic-Limit Evaporation/Condensation Heat Transfer Rate 461

6.8 Ideal-Gas Thermal Conductivity from BTE 462
- 6.8.1 Nonequilibrium BTE and Relaxation-Time Approximation 462
- 6.8.2 Thermal Conductivity 463

6.9 Liquid Thermal Conductivity from Mean Free Path and Molecular Dynamics 469

6.10 Effective Conductivity with Dispersed Particles in Thermal Motion 470
- 6.10.1 Langevin Derivation of Brownian Diffusion 471
- 6.10.2 Thermal Relaxation Time and Effective Fluid Thermal Conductivity 472

6.11 Interaction of Moving Fluid Particle and Surface 474
- 6.11.1 Fluid Flow Regimes 474
- 6.11.2 Knudson-Flow-Regime Surface Accommodation and Slip Coefficients 476
- 6.11.3 Slip Coefficients in Transitional-Flow Regime 480
- 6.11.4 Solid Particle Thermophoresis in Gases 481
- 6.11.5 Physical Adsorption and Desorption 482
- 6.11.6 Disjoining Pressure in Ultrathin-Liquid Films 486

6.12 Turbulent-Flow Structure and Boundary-Layer Transport 487
- 6.12.1 Turbulent Kinetic Energy Spectrum for Homogeneous Turbulence 489
- 6.12.2 Boundary-Layer Turbulent Heat Flux 491
- 6.12.3 Turbulent Mixing Length and Turbulent Thermal Conductivity 492
- 6.12.4 Spatial Variation of Boundary-Layer Turbulent Mixing Length 493
- 6.12.5 Turbulent Mixing Using Lagrangian Langevin Equation 494

6.13 Thermal Plasmas: Plasma Thermal Conductivity 494
6.13.1 Free Electron Density and Plasma Thermal Conductivity 496
6.13.2 Thermal Nonequilibrium Plasma Energy Equation 500
6.13.3 Species Concentrations for Two-Temperature Plasmas 501
6.13.4 Kinetics of Energy Exchange Between Electrons and Heavier Species 501
6.14 Size Effects 502
6.14.1 Effective Thermal Conductivity in Gas-Filled Narrow Gaps 502
6.14.2 Thermal Creep (Slip) Flow in Narrow Gaps 508
6.15 Problems 511

7 Photon Energy Storage, Transport, and Transformation Kinetics 519

7.1 Quantum-Particle Treatment: Photon Gas and Blackbody Emission 523
7.2 Lasers and Near-Field (EM Wave) Thermal Emission 527
7.2.1 Lasers and Narrow-Band Emissions 527
7.2.2 Classical EM Wave Near-Field Thermal Emission 528
7.3 Quantum and Semiclassical Treatments of Photon–Matter Interaction 529
7.3.1 Hamiltonians of Radiation Field 530
7.3.2 Photon-Matter Interactions 533
7.4 Photon Absorption and Emission in Two-Level Electronic Systems 534
7.4.1 Einstein Excited-State Population Rate Equation 535
7.4.2 Einstein Coefficients for Equilibrium Electronic Population 537
7.4.3 Spontaneous Versus Stimulated Emissions in Equilibrium Thermal Cavity f_{ph}^{o} 538
7.4.4 Spectral Absorption Coefficient and Cross–Section Area 539
7.5 Particle Treatment: Photon BTE with Absorption, Emission, and Scattering 541
7.5.1 Combining Absorption and Emission 543
7.5.2 Photon–Free Electron Elastic Scattering Rate and Cross–Section Area 544
7.6 Photon Intensity: Equation of Radiative Transfer 547
7.6.1 General Form of ERT 547
7.6.2 Optically Thick Limit, Mean Free Path, and Radiant Conductivity 549
7.7 Wave Treatment: Field Enhancement and Photon Localization 552
7.7.1 Photon Localization in One-Dimensional Multilayer 552

7.7.2 Coherence and Electric Field Enhancement 556
7.7.3 Comparison with Particle Treatment (ERT) 558
7.8 Continuous and Band Photon Absorption 562
7.8.1 Photon Absorption Coefficient for Solids 562
7.8.2 Photon Absorption Coefficient for Gases 567
7.9 Continuous and Band Photon Emission 571
7.9.1 Emission Mechanisms 571
7.9.2 Absorption and Emission Reciprocity (Kirchhoff Law) 572
7.10 Spectral Surface Emissivity 574
7.11 Radiative and Nonradiative Decays and Quantum Efficiency 577
7.12 Anti-Stokes Fluorescence: Photon–Electron–Phonon Couplings 582
7.12.1 Anti-Stokes Laser Cooling (Phonon Absorption) of Ion-Doped Solids 582
7.12.2 Laser Cooling Efficiency 584
7.12.3 Photon–Electron–Phonon Transition Rate Using Weak Coupling Approximation 587
7.12.4 Time Scales for Laser Cooling of Solids (Weak Couplings) 592
7.12.5 Optimal Host Material 596
7.12.6 Photon–Electron and Electron–Phonon Transition Rates Using Strong Couplings (Ab Initio Computation) 598
7.13 Gas Lasers and Laser Cooling of Gases 608
7.13.1 Molecular-Gas Lasers 608
7.13.2 Laser Doppler Cooling of Atomic Gases and Doppler Temperature 627
7.14 Photovoltaic Solar Cell: Reducing Phonon Emission 631
7.14.1 Single-Bandgap Ideal Solar PV Efficiency 633
7.14.2 Multiple-Bandgap Ideal Solar PV Efficiency 636
7.14.3 Semiempirical Solar PV Efficiency 639
7.15 Size Effects 642
7.15.1 Enhanced Near-Field Radiative Heat Transfer 642
7.15.2 Photon Energy Confinement by Near-Field Optical Microscopy 645
7.15.3 Hot Phonon Recycling in Photonics 646
7.16 Problems 650

APPENDIX A: Tables of Properties and Universal Constants 661

APPENDIX B: Derivation of Green–Kubo Relation 668

APPENDIX C: Derivation of Minimum Phonon Conductivity Relations . . . 676

APPENDIX D: Derivation of Phonon Boundary Resistance 683

APPENDIX E: Derivation of Fermi Golden Rule 689

APPENDIX F: Derivation of Equilibrium, Particle Probability Distribution Functions 696

APPENDIX G: Phonon Contributions to the Seebeck Coefficient 701

APPENDIX H: Monte Carlo Method for Carrier Transport 709

APPENDIX I: Ladder Operators 713

Nomenclature 719

Abbreviations 725

Glossary 727

Bibliography 741

Index 765

Preface

Heat is atomic motion of matter, and temperature indicates the equilibrium distribution of this motion. Nonequilibrium atomic motions, created for example by a temperature gradient, result in heat transfer. Heat transfer physics describes the thermodynamics and kinetics (mechanisms and rates) of energy storage, transport, and transformation by means of principal energy carriers. Heat is energy that is stored in the temperature-dependent motion and within the various particles that make up all matter in all of its phases, including electrons, atomic nuclei, individual atoms, and molecules. Heat can be transferred to and from matter by one or more of the principal energy carriers: electrons[†] (either as classical or quantum entities), fluid particles (classical particles or quantum particles), phonons (lattice-vibration quantum waves, i.e., quasi-particles), and photons[‡] (quantum particles). The state of the energy stored within matter or transported by the carriers can be described by a combination of classical and quantum statistical mechanics. The energy is also transformed (converted) between the various carriers. All processes that act on this energy are ultimately governed by the rates at which various physical phenomena occur, such as the rate of particle collisions in classical mechanics. It is the combination of these various processes (and their governing rates) within a particular system that determines the overall system behavior, such as the net rate of energy storage or transport. Controlling every process, from the atomic level (studied here) to the macroscale (covered in an introductory heat transfer course), are the laws of thermodynamics, including conservation of energy.

The focus of this text is on the heat transfer behavior (the storage, transport, and transformation of thermal energy) of the aforementioned principal energy carriers at the atomic scale. The specific mechanisms are described in detail, including elastic–inelastic collisions–scattering among particles, quasi-particles, and waves. Particular attention is given to the time scales over which energy transport or transformation processes occur, so that the reader gains some sense of how they compare with one another, as well as how they combine to produce overall system energy storage–transport–transformation rates. The approach taken here begins with a survey of fundamental concepts of atomic-level physics. This survey includes a look at the energy within the electronic states of atoms, as well as interatomic forces and potentials. Various theories of molecular dynamics and transport are also described. After this overview, in-depth, quantitative analyses are performed for each of the principal energy carriers, including analysis of how they interact with each other. This combination should allow for the teaching of a thorough introduction of heat transfer physics within one semester, without prolonged preparation or significant prerequisites. In general, several areas of physics are relevant to the study of heat transfer: (a) atomic–molecular dynamics, (b) solid state (condensed matter), (c) electromagnetism, and (d) quantum optics. No prior knowledge of these areas is necessary to appreciate the material of this text (a knowledge of introductory heat transfer is assumed).

[†] For semiconductors, the holes are included as energy carriers. For electrolytes, ion transport is treated similarly.

[‡] Here, *photon* refers to both the classical (Maxwell) and the quantum (quasi-particle, Schrödinger) descriptions of the electromagnetic waves.

Crystalline solids and their vibrational and electronic energies are treated first. This discussion is followed by an examination of energies of fluid particles and their interactions with solid surfaces. Then the interactions of photons with matter are posed with photons as EM waves, as particles, or as quasi-particles.

The text is divided into seven chapters, starting with the introduction and preliminaries of Chapter 1, in which the microscale carriers are introduced and the scope of the heat transfer physics is defined. Chapter 2 is on molecular electronic orbitals, interatomic and intermolecular potentials, molecular dynamics, and an introduction to quantum energy states. Chapter 3 is on microscale energy transport and transition kinetics theories, including the Boltzmann transport equation, the Maxwell equations, the Langevin stochastic transport equation, the Onsager coupled transport relation, and the Green–Kubo fluctuation–dissipation transport coefficients and relations. Chapters 4, 5, 6, and 7 cover the transport and interactions of phonons, electrons, fluid particles, and photons, respectively.

The size effects (where the system size affects the atomic-level behavior) on transport and energy conversion, for each principal carrier, are considered at the ends of Chapters 4 to 7. This allows for reference to applications in nanostructured and microstructured systems.

Some of the essential derivations are given as appendices. Appendix B gives the Green–Kubo relation, Appendix C gives the minimum phonon conductivity relations, Appendix D gives the phonon boundary resistance, Appendix E gives the Fermi golden rule, and Appendix F gives the particle energy distribution (occupancy) functions for bosons (phonons and photons), fermions (electrons), and Maxwell–Boltzmann (fluid) particles. Appendix G is on contributions to the Seebeck coefficient from various charge-carrier interactions, including with phonons. Appendix H is on the Monte Carlo method used for the simulation of energy carrier transport. Appendix I is on the ladder operators used for the carrier state transition by creation (raising) and annihilation (lowering).

Some end-of-chapter problems are provided to enhance understanding and familiarity and to allow for specific calculations. When needed, computer programs are also used. A full, digital solutions manual is available.

In general, vectors (lowercase) and tensors (uppercase) are in bold symbols. A nomenclature, an abbreviation list, and a glossary of relevant terms are given at the end of the text. Numbers in parenthesis indicate equation numbers. The periodic table of elements, with the macroscopic (bulk) and atomic properties, is given in Appendix A (in Tables A.1 and A.2), along with the tables of the universal and derived constants and unit prefixes.

It is hoped that this treatment provides an idea of the scope and some of the fundamentals of heat transfer physics, along with some of the most recent findings in the field.

Massoud Kaviany
Ann Arbor
kaviany@umich.edu

Acknowledgments

Many doctoral students and postdoctoral fellows working with me have contributed to this book. Among them are Jae Dong Chung, Luciana da Silva, Baoling Huang, Gi Suk Hwang, Dan Johnson, Ankur Kapoor, Hyoungchul Kim, Jedo Kim, Scott Gayton Liter, Alan McGaughey, Corey Melnick, Da Hye Min, Brendan O'Connor, Xiulin Ruan, Seungha Shin, and Xiangchun Zhang. Alan, Baoling, Corey, Gayton, Gi Suk, Hyoungchul, Seungha, and Xiulin have provided many ideas and have been constant sources of inspiration. I am indebted to all of them; without them this task could not have been completed. I would also like to thank the National Science Foundation (Thermal Transport and Processes) and the Department of Energy (Basic Energy Sciences) for sponsoring the research leading to some of the materials presented here.

1

Introduction and Preliminaries

The macroscopic heat transfer rates use thermal-energy related properties, such as the thermal conductivity, and in turn these properties are related to the atomic-level properties and processes. Heat transfer physics addresses these atomic-level processes (e.g., kinetics). We begin with the macroscopic energy equation used in heat transfer analysis to describe the rates of thermal energy storage, transport (by means of conduction k, convection u, and radiation r), and conversion to and from other forms of energy. The volumetric macroscopic energy conservation (rate) equation is listed in Table 1.1.[†] The sensible heat storage is the product of density and specific heat capacity ρc_p, and the time rate of change of local temperature $\partial T/\partial t$. The heat flux vector $\boldsymbol{q}$ is the sum of the conductive, convective, and radiative heat flux vectors. The conductive heat flux vector $\boldsymbol{q}_k$ is the negative of the product of the thermal conductivity k, and the gradient of temperature ∇T, i.e., the Fourier law of conduction. The convective heat flux vector[‡] $\boldsymbol{q}_u$ (assuming net local motion) is the product of ρc_p, the local velocity vector $\boldsymbol{u}$, and temperature. For laminar flow, in contrast to turbulent flow that contains chaotic velocity fluctuations, molecular conduction of the fluid is unaltered, whereas in turbulent flow this is augmented (phenomenologically) by turbulent mixing transport (turbulent eddy conductivity). The radiative heat flux vector $\boldsymbol{q}_r = \boldsymbol{q}_{ph}$ (ph stands for photon) is the spatial (angular) and spectral integrals of the product of the unit vector $\boldsymbol{s}$ and the electromagnetic (EM), spectral (frequency dependent), directional radiation intensity $I_{ph,\omega}$, where ω is the angular frequency of EM radiation (made up of photons). When the spherical, (solid angle) integral of $I_{ph,\omega}$ is nonzero, there is a net photon flux in the medium (matter). This intensity is influenced by the spectral emission, absorption, and scattering of photons by matter, i.e., its radiative properties (Table 7.1). Among these properties are the photon spectral, absorption coefficient $\sigma_{ph,\omega}$, which results from the interaction

---

[†] In deriving this equation, it is assumed that c_p is constant. The more general form is also given in [232].

[‡] The surface-convection heat flux vector $\boldsymbol{q}_{ku}$ is the special case of conduction occurring on an interface separating a moving fluid from a generally stationary solid. Then, assuming no fluid slip on this interface, the heat transfer through the fluid is only by conduction, but the interface temperature gradient is influenced by the fluid motion [232].

Table 1.1. *Macroscopic energy conservation equation and the heat flux vector [232].*

Energy equation

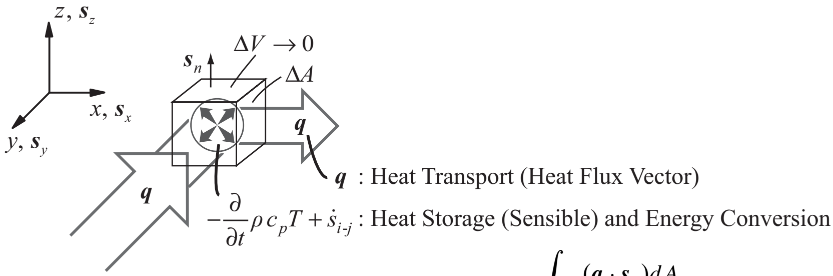
z, $\boldsymbol{s}_z$
x, $\boldsymbol{s}_x$
y, $\boldsymbol{s}_y$
$\boldsymbol{s}_n$
$\Delta V \rightarrow 0$
ΔA
$\boldsymbol{q}$
$\boldsymbol{q}$
$\boldsymbol{q}$: Heat Transport (Heat Flux Vector)
$-\frac{\partial}{\partial t}\rho c_p T + \dot{s}_{i\text{-}j}$: Heat Storage (Sensible) and Energy Conversion

$$\nabla \cdot \boldsymbol{q} = -\frac{\partial}{\partial t}\rho c_p T + \sum_{i,j} \dot{s}_{i\text{-}j}, \qquad \nabla \cdot \boldsymbol{q} = \frac{\int_{\Delta A} (\boldsymbol{q} \cdot \boldsymbol{s}_n) dA}{\Delta V \rightarrow 0}$$

Heat flux vector

$$\boldsymbol{q} = \boldsymbol{q}_k + \boldsymbol{q}_u + \boldsymbol{q}_r = -k\nabla T + \rho c_p \boldsymbol{u} T + 2\pi \int_0^\infty \int_{-1}^1 \boldsymbol{s} I_{ph,\omega} d\mu d\omega$$

A	area, m^2
$I_{ph,\omega}$	spectral, directional radiation intensity, $\mathrm{W/(m^2\text{-}sr\text{-}rad/s)}$
c_p	specific heat capacity, J/kg-K
k	thermal conductivity, W/m-K
$\boldsymbol{q}$	heat flux vector, $\mathrm{W/m^2}$
$\boldsymbol{s}_n$	surface normal, unit vector
$\boldsymbol{s}$	unit vector
$\dot{s}_{i\text{-}j}$	energy conversion rate between principal carrier i and carrier j, $\mathrm{W/m^3}$
T	temperature, K
$\boldsymbol{u}$	velocity, m/s
V	volume, $\mathrm{m^3}$
ρ	density, $\mathrm{kg/m^3}$
μ	$\cos\theta$, θ is polar angle
ω	angular frequency, rad/s

of an EM waves with electric entities in its travelling medium (e.g., vibrating electric dipoles, free electrons, electronic bandgap).

In Table 1.1, it is noted that the divergence of $\boldsymbol{q}$ is integral to its surface normal component on the differential surface area ΔA of a vanishing deferential volume ΔV. The rate of energy conversion to and from thermal energy $\dot{s}_{i\text{-}j}$ is determined by the nature and frequency of the interactions between the principal energy carriers i and j. This rate describes various bond (chemical, nuclear and physical), electromagnetic, and mechanical energy conversions. The rate is related to the available energy transitions as well as the contributions from promoting/limiting mechanisms (e.g., energy distribution probabilities, kinetics, transport, and temperature). It is this interplay among storage, transport, and transformation rates that allows for the behaviors exhibited by energy conversion phenomena and devices.

As mentioned, heat is atomic motion of matter and temperature represents equilibrium distribution of this motion [represented by the equilibrium energy distribution function $f^{\circ}(T)$]. Heat transfer results from nonequilibrium distribution function $f(T)$ which in turn is caused by spatial and/or temporal variation of temperature or presence of related force fields, and/or thermal energy conversion. In particular, thermal energy conversion creates spectral heat transfer at the atomic level. Here spectral refers to a selected atomic motion mode (e.g., a vibration frequency). The rate of heat transfer is the kinetics of return to equilibrium. The motion of atoms, because of vibration, rotation, and translation, creates kinetic energy within matter and this defines its temperature or sensible heat. Electrons (valence electrons as they orbit the nuclei or conduction electrons as they move among atoms) are also central to the energy contained within matter. Electronic energies (including bond energy between atoms), kinetic energy (created by the motion of atoms), and even the annihilation/creation of mass (i.e., relativistic effects), can all be converted to electromagnetic energy (photons). The energy contained in photons can then, in turn, interact with other matter (through electric entities such as dipole moments) resulting in energy conversion.

The state of an electron (which defines its energy level), as well as its coupling with atomic nuclei (in a free atom, or in molecules), is central to the energy of a system, its interactions (including conversion to other forms of energy), and its transport (both within the system and across its boundaries), especially when the energy per unit mass is much larger than $k_\mathrm{B}T$ (which is 0.026 eV for $T = 300$ K), where k_B is the Boltzmann constant. $k_\mathrm{B}T$ is the energy of thermal fluctuations (Section 2.3.3). In ideal electrical insulators, no conduction (free) electrons exist, metals have a large number (over 10^{21} cm^{-3}), and intrinsic (undoped) semiconductors have a small, temperature-dependent number (less than 10^{15} cm^{-3}) of conduction electrons. Mobile and stationary ions, as intrinsic constituents or as dopants, also have their own particular electronic energy states.

Thus the microscopic model of thermal energy storage, transport, and interactions is assembled through the study of each of the principal energy carriers, namely: phonons (p), electrons (e), fluid particles (f), and photons (ph).[†]

This introduction–preliminaries chapter continues with attributes of the four principal heat carries, including their combinatorial energy-state occupational probabilities and their wave, particle, and quasi-particle treatments. Then we present a brief history of contributions to heat transfer physics, and introduce the universal constants and atomic-level (fine-structure) time, length, and energy scales. Then we give examples of atomic-level kinetics controlling energy storage, transport, and conversion, and define the scope of heat transfer physics and this text.

1.1 Principal Carriers: Phonon, Electron, Fluid Particle, and Photon

The energy of matter can be divided into potential and kinetic energies E_p and E_k. Each of the principal energy carriers can have potential and kinetic energy (for photon it is electric and magnetic field energies). Here we discuss the energy attributes of carriers, including their equilibrium occupancy probabilities, which allow for inclusion of these attributes into statistical presentation of energy of matter.

[†] The suffix "on" indicates having properties of particles.

1.1.1 Phonon

Heat as atomic motion is stored in atomic vibration in solids. A phonon is a quantized mode of vibration occurring in rigid atomic lattices, such as those in crystalline solids.[†] The properties of long-wavelength phonons give rise to sound in solids (hence the name phonon). Phonons participate in many of the physical properties of materials, including heat capacity and thermal/electrical conductivities (the propagation of phonons is responsible for the conduction of heat in electrical insulators).

In classical mechanics, any vibration of a lattice can be decomposed into a superposition of nonlocalized normal modes of vibration. When these modes are analyzed by use of quantum mechanics, they are found to possess some quantum particlelike properties (quasi-particles). Thus a phonon is an indistinguishable quasi-particle (see Glossary). When treated as particles, phonons are called bosons (see Table 1.2, and the derivation given in Appendix F) and are said to possess zero spin. The thermal equilibrium particle probability distribution (occupation) function $f_p^{\rm o}$ indicates, that at thermal equilibrium (the superscript $^{\rm o}$ indicates equilibrium), phonons are distributed based on their scaled energy $E_p/k_{\rm B}T$. This is also shown in Figure 1.1, which shows the phonon energy is the sum of its potential and kinetic energy. Here, $E_p = \hbar\omega_p$ is the phonon energy, and $\hbar = h_{\rm P}/2\pi$, where $h_{\rm P}$ is the Planck[‡] constant (fundamental constants are discussed in Section 1.5.1).

The equilibrium, energy-occupation probability (or distribution) function $f_i^{\rm o}$ is based on principles of (a) equal *a priori* probability applied to all energy states of the system (equipartition of the energy states), and (b) ensemble averaging which gives the macroscopic properties of the system and constrains this probability in favor of lower probability of highest energy states (in general). This second principle introduces the system temperature and results in increased occupancy of the higher energy states at higher temperatures. Spin is one of the properties of elementary particles, which can be thought of as rotating tops. Based on spin, the particles are either fermions or bosons. The spin (quantum angular momentum) of a particle is given by $S = \hbar[s(s+1)]^{1/2}$ (Section 2.6.6), where s is 0, 1/2, 3/2, 2, ... If s is 1, 2, ..., then the particle is called a boson, and if s is 1/2, 3/2, ..., then it is called a fermion. No two fermions can be found in the same quantum state (because of the Pauli exclusion principle), whereas bosons tend to accumulate in certain favored states.

There are two types of phonons: acoustic phonons, denoted with the subscript A, and optical phonons, denoted with the subscript O. Acoustic phonons have frequencies that become small for long wavelengths and correspond to sound waves in the lattice (this is a property of phonon dispersion relation). These long wavelengths correspond to bulk translations. Longitudinal- and transverse-acoustic phonons are often abbreviated as LA and TA phonons, respectively. Optical phonons, which

---

[†] In lattice dynamics, there are a finite number of vibrational modes, and the energy of each mode is quantized. So, phonons are also these normal modes. Also, although phonons are exclusively a property of periodic media, vibrations exist in all solids.

[‡] The subscript P is for consistency with other fundamental constants (Table 1.4 and also listed in Table A.3) and also is used to avoid confusion with the specific enthalpy h.

Table 1.2. *Thermal equilibrium particle (energy occupancy) distribution (statistical) function* $f_i^{\rm o}(E_i)$, $i = p,\ e,\ f,\ ph$ *and its temperature dependence for principal energy carriers.*

Attributes	Phonon	Electron and Hole[a]	Fluid Particle	Photon
Iconic presentation	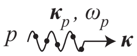	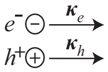	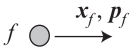	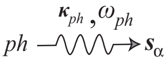
Energy presentation	wave vector $\boldsymbol{\kappa}_p$, dispersion $\boldsymbol{\kappa}_p(\omega_p)$, and polarization in reciprocal lattice space $\boldsymbol{g}$	wave vector $\boldsymbol{\kappa}_e$, band structure (conduction and valence bands), and spins	momentum $\boldsymbol{p}_f$, kinetic, potential, and electronic energy states	frequency ω_{ph}, dispersion $\boldsymbol{\kappa}_{ph}(\omega_{ph})$, and polarization in real space $\boldsymbol{s}_\alpha$
Particle type	Bose–Einstein (boson)	Fermi–Dirac (fermion)	Maxwell-Boltzmann (M–B)	Bose–Einstein (boson)
Nature of particle	particles are indistinguishable, integer spin (angular momentum), and any number of particles may occupy a given eigenstate	particles are indistinguishable, odd, half-integer spin (angular momentum) and obey the Pauli exclusion principle (only one particle may be found in a given quantum state)	particles are distinguishable, and any number of particles may occupy a given eigenstate (classical particle or nondegenerate limit)	particles are indistinguishable, integer spin (angular momentum), and any number of particles may occupy a given eigenstate
Equilibrium distribution (occupancy) function, $f_i^{\rm o}(E_i)$	$\dfrac{1}{\exp(\dfrac{E_p}{k_{\rm B}T})-1}$	$\dfrac{1}{\exp(\dfrac{E_e-\mu}{k_{\rm B}T})+1}$	$\dfrac{1}{\exp(\dfrac{E_f}{k_{\rm B}T})}$	$\dfrac{1}{\exp(\dfrac{E_{ph}}{k_{\rm B}T})-1}$
Energy	$E_p = E_{p,p} + E_{p,k}$ $= \hbar\omega_p$	$E_e = E_{e,p} + E_{e,k}$ $E_{e,k} = \dfrac{\hbar\kappa_e^2}{2m_e}$ μ is chemical potential $\mu = E_{\rm F}[1 - \dfrac{1}{3}(\dfrac{\pi k_{\rm B}T}{2E_{\rm F}})^2]$	$E_f = E_{f,t} + E_{f,v} + E_{f,r} + E_{f,e} + E_{f,p}$ $E_{f,t} = \dfrac{p_f^2}{2m_f}$, $E_{f,v} = (l+\frac{1}{2})\hbar\omega_f$	$E_{ph} = E_{ph,e} + E_{ph,m}$ $E_{ph} = \hbar\omega_{ph}$

$\hbar = h_{\rm P}/2\pi$ and $k_{\rm B}$ are the reduced Planck and the Boltzmann constants

$k_{\rm B}T = 0.02585$ eV for $T = 300$ K

[a] Holes are represented by h^+

A general relation can be used for all particles as $f_i^{\rm o} = \dfrac{1}{e^{(E_i-\mu)/k_{\rm B}T}+\gamma}$, where $\gamma = 1$ (fermion), 0 (M–B), -1 (boson).

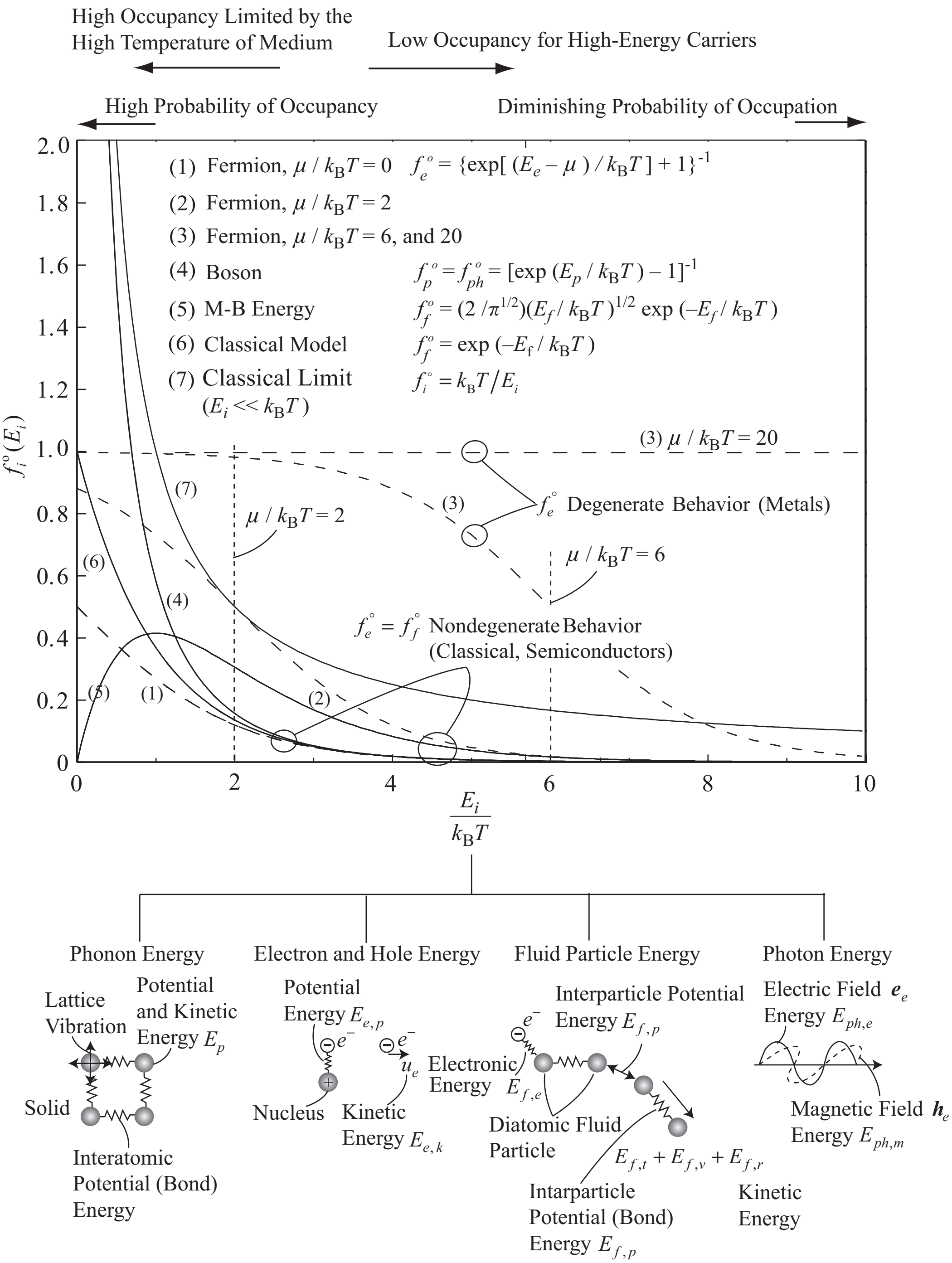

Figure 1.1. Variation of equilibrium particle (energy-state occupation) distribution function with respect to energy (scaled with respect to thermal fluctuation energy k_BT) for different energy carriers. For fermions, three different reduced chemical potentials $\mu/k_BT = E_F/k_BT$ (Fermi energy) are used. Conduction electrons in metals have a highly degenerate behavior. The high-energy (low population) approximation (nondegenerate behavior) for electrons and holes in semiconductors is also shown (discussed in Section F.5 in Appendix F). The classical limit distribution function is also shown. Various contributions (e.g., kinetic and potential) to the total energy of each principal carrier, are also shown. The photon energy is divided between electric and magnetic energies.

arise in lattices with more than one atom per unit cell, always have some minimum frequency of vibration, even when their wavelength is infinite. They are called optical, because in ionic crystals (such as NaCl) they are excited very easily by light (such as infrared radiation). This is because they correspond to a mode of vibration where positive and negative ions at adjacent lattice sites move, thus creating a time-varying electric dipole moment. Optical phonons that interact in this way with light are called infrared active. Optical phonons, which are known as Raman active, can also interact indirectly with light, through Raman scattering (an inelastic scattering of a photon that creates or annihilates an optical phonon). Optical phonons are often abbreviated as LO and TO for the longitudinal and transverse varieties, respectively (although they are readily distinguishable for low-symmetry crystals).

1.1.2 Electron (and Hole)

Electrons store heat and potential energy and here are divided into conduction and bound electrons. The electron e^- is a charged subatomic particle. In an atom, electrons surround the nucleus, made of protons and neutrons, in a manner termed the electronic configuration (or structure). The electron is among a class of subatomic particles called leptons, believed to be fundamental particles (i.e., they cannot be divided into smaller constituents). The electron has a spin of 1/2 (which makes it a fermion), and follows the Fermi–Dirac statistical energy distribution $f_i^{\rm o}$ (Table 1.2; derivation is given in Appendix F). These distributions are based on the equipartition of energy and the partition function, and are dictated by the statistical mechanics–thermodynamics laws and relations).

Electrons can exhibit properties of both particles and waves, and thus can be treated as quasi-particles. An electron bound to a nucleus behaves as a standing wave (due to the periodic boundary condition).

For matter in the solid state, electrons are responsible for bonding within crystals; they hold the nuclei together. These bonds belong to one of four types: van der Waals, ionic, covalent, or metallic. The Fermi surface is the set of loci in electron momentum space with zero excitation energy. The topology of the Fermi surface is important in understanding the electronic properties of materials. Electrons in solids are divided into core and outer electrons. Core electrons do not participate in bonding and are assumed to move with the nucleus at all times. Outer electrons reside farther away from the nucleus, and are in turn divided into conduction (or free) electrons and valence electrons.

In quantum mechanics, the electron is described by the Dirac equation. In the Standard Model of particle physics, it forms a doublet in SU(2) with the electron neutrino, as they interact through the weak force.[†] The electron has two variations with the same charge but different masses: the muon and the tauon. The antimatter counterpart of the electron, its antiparticle, is the positron. The positron has the same amount of electrical charge, mass and spin as the electron, except that the charge is positive.

[†] The Standard Model is a quantum field theory and is the union of quantum chromodynamics and the electroweak theory. In the Standard Model, there are 16 fundamental particles: 12 particles of matter (fermions of spin 1/2) and 4 force carrier particles. The fermions are six quarks (up, down, charm, strange, top, bottom) and six leptons (electron, electron neutrino, muon, muon neutrino, tau, tau neutrino). The gauge bosons or force carriers mediate the strong, weak, and electromagnetic

The variation of the three equilibrium distribution functions [boson, fermion, and Maxwell–Boltzman (M–B)] with respect to dimensionless (scaled) energy are shown in Figure 1.1. For electrons, the chemical potential μ is the datum of energy, and the results for a few values of the scaled (also called reduced) electron chemical potentials $\mu/k_{\rm B}T$ are also shown. All distributions become similar to the classical distributions for large energies (for electrons also in the case of small μ). As will be discussed in Section 2.6.5 (metals) and 5.7 (semiconductors), the number density of conduction electrons is related to the chemical potential (Fermi energy), and because semiconductors have smaller conduction electron density, their chemical potential is smaller than that of metals. As shown in Figure 1.1, whereas the occupation probability of conduction electrons in metals is high and subject to exclusion principle (degenerate), that of semiconductors is low and is generally treated with the nondegenerate, classical distribution.

For a general treatment, the energy of electron (and hole h^+) are divided into potential (representing its bond energy) and kinetic (representing its velocity) energy. Electron (or hole) is a charge particle (single charge), other charge particles (e.g., ions) also transport heat (as current). For example in proton transport, this particle is much larger and heavier than an electron, and therefore, has a much smaller velocity and requires vacancy or surface to travel (hop).

1.1.3 Fluid Particle

Fluid particles temperature is due to their kinetic energy (thermal motion). Gases and liquids are composed of single atoms or molecules (here broadly termed fluid particles), which can be neutral or charged, in motion. The fluid particle (see Glossary) energy is divided into potential (among atoms), electronic, and kinetic energy. The fluid specific volume is fixed under constant temperature and pressure, and its shape may be determined by the container it fills or through cohesive forces such as surface tension. The moving particles constantly collide with each other (and, possibly, with the container wall). In ideal gas behavior, the collisions between the gas particles are elastic (energy is conserved among colliding particles) and the forces of attraction between the particles are negligible. For ideal gases, the M–B distribution $f_f^{\rm o}$ (Table 1.2 and Figure 1.1; derivation is given in Appendix F) can be derived

fundamental interactions. An additional particle, known as the Higgs boson, must also be included to explain why the other 16 have mass. It is also proposed that particles acquire their mass through interactions with an all-pervading field, called the Higgs field, which is carried by the Higgs boson. It is accepted that the Standard Model cannot be a fundamental theory of nature because it does not embrace gravity and only makes sense if viewed as a low-energy approximation. The quantum group theory deals with noncommutative algebra with additional structure, and the special unitary group of degree n, denoted by SU(n), which is the group of $n \times n$ unitary matrices with determinant 1 [[176]].

by use of statistical mechanics (and the concepts of energy partitioning and symmetry). In polyatomic-gas lasers, e.g., CO_2, the population distribution deviates from equilibrium (population inversion is created). So, in both the energy transport and conversion involving fluid particles, nonequilibrium distribution occurs. Figure 1.1 also shows various contributions to the total energy of the fluid particle (translational, vibrational, rotational, electronic, intraatomic, and interatomic potential). For these ideal, noninteracting particles in the ground state, all energy is only in the form of kinetic energy, and (by use of the equipartition energy principle) each mode has a kinetic energy equal to $k_{\rm B}T/2$. This corresponds to the most probable energy distribution, in a collision-dominated system consisting of a large number of noninteracting particles with no net motion, but with a nonzero root-mean-square (RMS) thermal fluctuation velocity $\langle u_f^2 \rangle^{1/2}$. This velocity is related to the speed of sound in fluids a_s, and is temperature dependent. So, the probability of occurrence of very-high velocity fluid particles decreases as the temperature decreases.

A liquid is considered to be a substance that's particles have enough kinetic energy to stretch the intermolecular forces of attraction, but not completely overcome them (so their densities are close to solids). Collisions thus occur between the particles more often than in gases (ideal or otherwise). As the temperature of a liquid is raised, the velocity of the particles increases. The kinetic energy eventually becomes so great that the particles overcome all intermolecular forces and move freely, thus becoming a gas.

1.1.4 Photon

Photons are emitted from matter according to its temperature and also by other excitations. A photon (Greek for light) is a quantum of excitation of an electromagnetic field, and is also an elementary particle in quantum electrodynamics (QED), which is part of the Standard Model of particle physics. Photons are thus the building blocks of EM radiation, some of which we observe as light. According to quantum mechanics, all particles, including the photon, have some of the properties of a wave. Photons have zero invariant mass, but a definite, finite energy. Because they have energy, the theory of general relativity states that they are affected by gravity, something that has been confirmed by experiment.

Photons have a spin of 1, which makes them bosons ($f_{ph}^{\rm o}$ in Table 1.2). This is the equilibrium distribution, as in blackbody radiation. However, lasers have highly nonequilibrium distributions (amplified, stimulated emission). Photons act as mediators to the EM spectrum; they are the particles that enable other particles to interact with each other electromagnetically and with an electromagnetic field. Individual photons are circularly polarized (as compared to electrons that have a spin up or spin down) because of their unit spin. They travel at the speed of light, u_{ph} (or c), and their lifetime is infinite, although they can be created and destroyed.

In general, an EM field consists of plane, monochromatic waves, of frequency f (angular frequency $\omega = 2\pi f$), wavelength λ, and speed u_{ph}, with $\omega_{ph} = 2\pi u_{ph}/\lambda$.

The quantum property of an EM waves is given by its energy $E_{ph} = \hbar\omega$. The photon also has a quantum momentum $\boldsymbol{p} = \hbar\boldsymbol{\kappa}$, where $\boldsymbol{\kappa}$ is the wave vector and the wave number $\kappa = 2\pi/\lambda$. Note that for a classical particle, the energy is $p^2/2m$, i.e., it is proportional to p^2.

In a vacuum, the dispersion relation of photons (the relation between angular frequency or energy and wave vector or momentum) is linear, and the constant of this proportionality is the Planck constant.

In matter, photons couple to the excitations (polarizing vibration, electric and magnetic) of the material. These excitations can often be described as quasi-particles (such as phonons and excitons defined in Glossary) with quantized wave-like or particlelike entities propagating through the material. Photons can transform into these excitations (that is, a photon is absorbed and the medium is excited, creating a quasi-particle) and vice versa (the quasi-particle transforms back into a photon, i.e., the medium relaxes by re-emitting the energy as a photon). These transformations are subject to probability rates and are presented as a polariton (Glossary). This is a quantum-mechanical superposition of the energy quantum being a photon as well as being one of the quasi-particle, matter excitations (such as photons). According to the rules of quantum mechanics, a measurement breaks this superposition; that is, the quantum is either absorbed into the medium and stays there, or it reemerges as a photon.

Matter excitations (photon emissions) have a nonlinear dispersion relation, and their momentum is not proportional to their energy. Hence, these particles propagate more slowly than the speed of light in vacuum (Section 3.3.1). The propagation speed is the derivative of the dispersion relation with respect to momentum (angular frequency with respect to wave vector). A photon, by coupling with the excitation of matter and forming a polariton, acquires an effective mass, which means that it cannot travel at speed of light in vacuum.

1.2 Equilibrium and Nonequilibrium Energy Occupancy Distributions

1.2.1 Nonequilibrium Energy Carrier Occupancy by Energy Conversion

Nonequilibrium atomic motion (mostly as vibration in solids and in polyatomic fluids) is formed in the initial states of the energy conversions. As examples, in Figures 1.2(a) to (c), the time (and entropy) evolution of the energy in solar, chemical bond, and nuclear fission conversion are shown. Initially the energy is not converted to atomic motion (e.g., phonon in solids), and this period is called the pre-phonon period. In these examples we also show how nonequilibrium atomic motions can be harvested, with early interventions (e.g., prior to thermalization, which creates equilibrium population distributions for these atomic motions, or by the recycling of equilibrium phonons).

When solar energy is absorbed in semiconductors, electron and hole pairs are created and experience various processes of energy conversion as shown in Fig. 1.2(a). Overpopulated electron-hole pairs decay by three recombination mechanisms (radiative, Auger, and Schockley-Read-Hall). The electrons are also relaxed

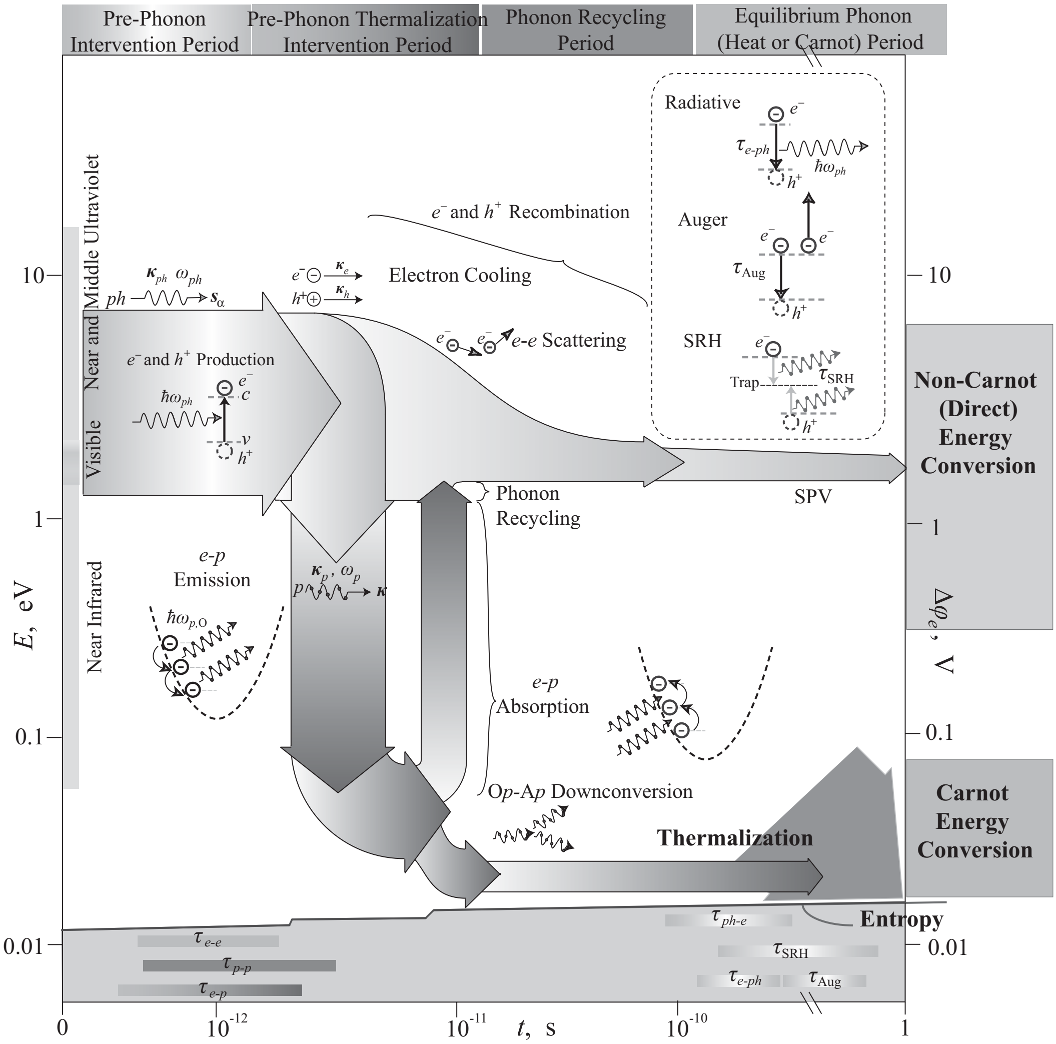

Figure 1.2. (a) Time-energy diagram for solar energy conversion. Solar photon irradiation creates an electron-hole pair in semiconductors. These photogenerated electron and hole pairs can recombine, relax and emit phonons, or be extracted as electric energy. The emitted phonons relax to lower energy phonons or are converted to electric energy. Typical interaction rates for the solar energy conversion are shown. The increase of entropy with time is also shown and indicates a reduction in the quality of energy. Once equilibrium atomic motion is reached, the heat content can be used in the Carnot cycle energy conversion.

by electron-phonon or electron-electron interactions. These are designated with interaction or relaxation times τ_{i-j} between energy carriers i and j. The remainder of the electron energy is extracted in the solar photovoltaic cell. The high-energy phonon overpopulation is caused by electron relaxation (thus forming hot phonons).

Figure 1.2(b) shows surface-mediated chemical-bond energy conversion processes. Chemical-bond energy in methane oxidation is converted to adsorbed molecules vibrational energy, as well as rotational and translational energy. Since the vibration temperatures of the molecules are very high (Table 6.2), the vibration

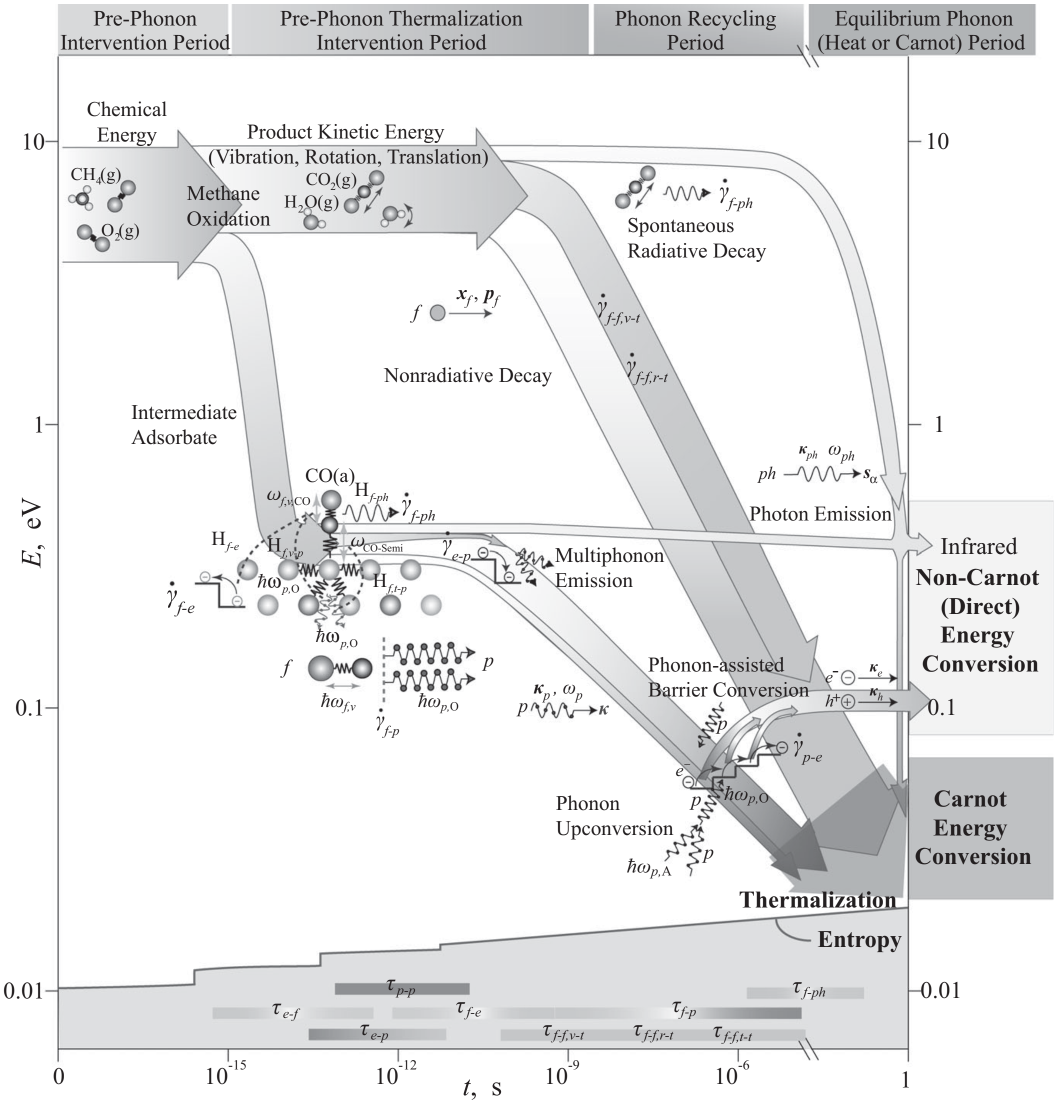

Figure 1.2. (*continued*) (b) Time-energy diagram for surface-mediated chemical energy conversion (from a catalytic methane oxidation process). In addition to the relaxation of product molecules through radiative and nonradiative processes, the relaxation and energy conversion of the frustrated vibration of the chemisorbed molecules can be harvested. Typical interaction rates for this energy conversion are also shown.

modes are relaxed to low kinetic energy. Once the molecules are adsorbed on the substrate surface, the vibrational modes are frustrated, and this frustrated vibrational mode is relaxed by photon emission, electron-hole pair creation (in metal), and multiple phonon generation within the substrate (semiconductor or insulator). The emitted phonons can be converted to electric energy by barrier structures.

Uranium 235 undergoes scission shortly (within τ_{sc}) after absorbing a neutron and releases a tremendous amount of energy, as shown in Figure 1.2(c).

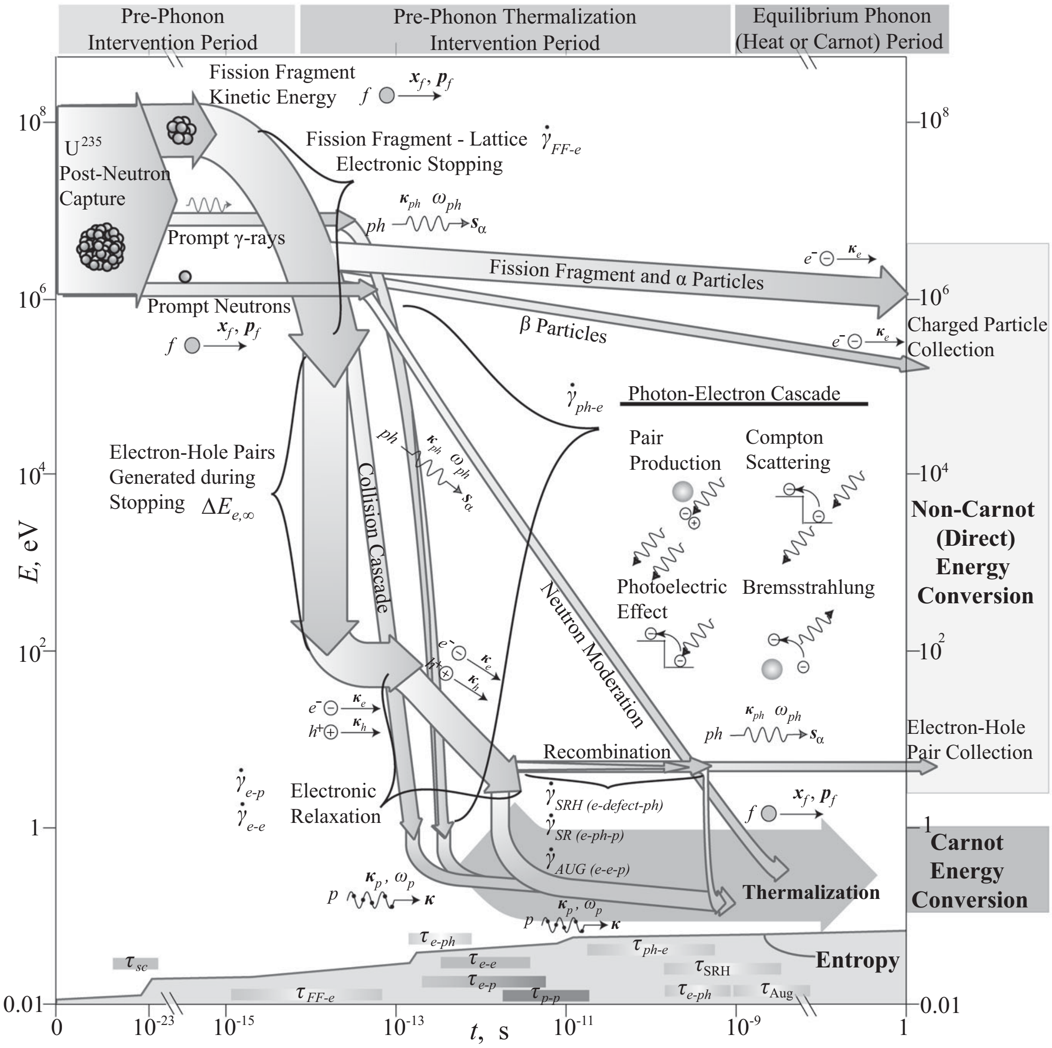

Figure 1.2. (*continued*) (c) Time-energy diagram for nuclear energy conversion. Nuclear fission releases energetic particles (neutrons and fission fragments) and photons (γ-rays). Some of these carriers can be extracted as energy directly or after they have created numerous electron-hole pairs, which relax to the band edge by emitting hot phonons. Otherwise, the electron-hole pairs will recombine, and the particles will thermalize with the surroundings. Typical interaction rates for these energy conversions are also shown.

This fission (mass loss) energy is concentrated in a few carriers, e.g., 160 MeV in the kinetic energy of two fission fragments, 8 MeV in a few high-energy photons (γ-rays), 2 MeV in neutrons, and 10 MeV in delayed electrons (β particles) and helium ion (α particles) emissions. In thermonuclear reactors, these carriers are allowed to relax until they thermalize via the relaxation pathways. These include fission fragment electronic stopping (which generates electron-hole pairs), the electron-photon cascade (which creates tertiary electrons and photons from primary γ and β-rays through electron-photon interactions), collision cascade caused by relatively low-energy fission fragments and α-particle collisions, and electron-phonon and phonon-phonon interactions that bring the electron and phonon distributions toward equilibrium.

1.2.2 Transport Phenomena Related to Energy Occupancy Distributions

Starting with the four principal energy carriers first discussed, we note that our measurements and observations are at relatively large length scales, which include many such principal particles in each observation. Also, it is possible for each observed macrostate to correspond to many microstates, which is addressed by the use of statistical mechanics [156]. We are interested in both the microstates and what governs them individually and in their collective behavior.

In Chapter 3, we will discuss the Boltzmann transport equation that governs the dynamics of the probability distribution function $f_i(i = p, e, f, ph)$ under applied forces. In turn, the dynamics involved in the deviation of f_i from the equilibrium value $f_i^{\rm o}$, influences the transport properties. As will be shown, the function f_i is central to principal transport phenomena.

In a system made of a number of particles, the observed macrostate (ensemble averaged over all particles in the system) is related to the microstate of each particle (i.e., the position and momentum of each particle) by the probability of existence of each microstate, as described by the probability distribution function f_j, where j denotes the microstate. As shown in Figure 1.1, the higher energy states, in general, have lower probabilities of existence at a given temperature. As the temperature increases, the higher-energy states are more probable (because the energy is scaled with $k_{\rm B}T$).

An ensemble averaged quantity, denoted by the angle brackets $\langle\ \rangle$, is related to a corresponding microstate quantity, which we denote here as ϕ_j, through

$$\langle\phi\rangle = \sum_j \phi_j f_j. \tag{1.1}$$

The summation can be changed to an integral when the probability can be given as a continuous function (as is given in Table 1.2).

The probability distribution (or occupancy) function is used in determining the carrier energy and its transport properties. For example, the conduction electron density, its current density vector, and its energy density are related to the moments of $f_e(\boldsymbol{x}, \boldsymbol{\kappa}, t)$, where $\boldsymbol{\kappa}$ is the wave vector, as

$$n_{e,c} = \langle n_{e,c}\rangle = \sum_{\boldsymbol{\kappa}} f_e(\boldsymbol{x}, \boldsymbol{\kappa}, t) \qquad \text{carrier density} \tag{1.2}$$

$$\boldsymbol{j}_e = \langle \boldsymbol{j}_e\rangle = -e_c \sum_{\boldsymbol{\kappa}} \nabla_{\boldsymbol{\kappa}} E_e(\boldsymbol{\kappa}) f_e(\boldsymbol{x}, \boldsymbol{\kappa}, t) \qquad \text{carrier current density vector} \tag{1.3}$$

$$\frac{E_e}{V} = \langle\frac{E_e}{V}\rangle = \sum_{\boldsymbol{\kappa}} E_e(\boldsymbol{\kappa}) f_e(\boldsymbol{x}, \boldsymbol{\kappa}, t) \qquad \text{carrier energy density,} \tag{1.4}$$

where e_c is charge of an electron. The derivations are given in Section 5.18.1. The summations are then written as integrals, for example over the energy as in (5.61). These short-hand summation presentations include integrations involving the particle density of states (1.19).

For conduction electrons, these relations will be derived in Sections 5.7, 5.11, and 5.18. Each principal energy carrier has its own particular features. For example, the energy (or velocity) distribution of fluid particles in a dilute-gas phase may be described using classical mechanics with symmetry constraints. Electrons, by contrast, are treated with quantum mechanics, which includes an antisymmetry constraint (regarding electron spin).

The equilibrium probability distribution function $f_i^{\rm o}$ gives the most probable distribution of microstates under zero disturbing force or potential [including zero-temperature gradient, i.e., for constant (time invariant) uniform (space-invariant) temperature]. This would mean allowing sufficient elapsed time for the particles to thermalize, meaning they reach the equilibrium distributions given in Table 1.2. The thermalization time is actually rather small, generally of the order of 10^{-12} s, or 1 picosecond (ps), (see Table A.4 in Appendix A for unit prefixes) for most of the principal carriers.

These particle probability distributions functions enable us to describe the temperature dependence of the lattice (phonon) and electron specific heat capacities, the relation between the temperature and the kinetic energy of gases, and the blackbody thermal emission of photons. Many other principal heat carrier behaviors and properties can also be described and predicted by use of f_i.

Table 1.2 and Figure 1.1 summarize some of the characteristics of the four principal heat carriers and their equilibrium distribution functions. The derivations of $f_p^{\rm o}$ and $f_{ph}^{\rm o}$ are given in Appendix F and are also given in [12]. The derivation of $f_e^{\rm o}$ is given in [245] and that of $f_f^{\rm o}$ is given in [73]. For $E_i/k_{\rm B}T \gg 1$, all particles follow the classical (M–B) distribution.

The deviation from the equilibrium distribution f_i' is used in the particle treatment of the transport of these carriers (i.e., Boltzmann transport theory). Also, population inversion (a steady-state nonequilibrium distribution) is central to the lasers (Section 7.13.1 for $\rm CO_2$ lasers). For example, the heat conduction in a solid by phonons is given by

$$\boldsymbol{q}_{k,p} = \sum_{\alpha} \frac{1}{8\pi^3} \int E_p \boldsymbol{u}_p f_p' {\rm d}\boldsymbol{\kappa}_\alpha, \tag{1.5}$$

where α is the polarization in the phonon dispersion relation (Section 4.1), $\boldsymbol{u}_p$ is the phonon velocity, and $\boldsymbol{\kappa}$ is the wave vector. A general treatment is given in Chapter 3, and then specifics are given for each of the carriers in the subsequent chapters. A derivation of the Bose–Einstein (boson) distribution function is given in Section 2.6.4 (for a harmonic, quantum oscillator). The classical distribution function (M–B) is presented in Section 6.4.2. Appendix F gives a feneral treatement for all carriers.

So both the equilibrium energy occupancy $f_i^{\rm o}$ and its deviation under an external force f_i' are central in atomic-energy storage, transport, and transformation.

Additionally, their atomic-structure property is presented by the particle density of states D_i, which also indicates what range of energy is possible for the carrier.

1.3 Particles, Waves, Wave Packets and Quasi-Particles and Density of States

Quantum-particles (including phonons, electrons, and photons) have properties of both particles and waves, and can be described by use of wave packets, i.e., localizations of energy that are due to the superposition of many plane waves of different wavelengths. These are, in a sense, both a particle and a wave at the same time, a concept termed particle–wave duality. Below, we discuss particle, wave, and particle–wave behaviors.

Particles, which are sometimes called corpuscles, are discrete; their energy is concentrated into what appears to be a finite space with definite boundaries, and its contents are considered to be homogeneous (the same at any point within the particle). Particles exist at a specific location and can never exist in more than one place at once. To travel to a different point in space, a particle must move according to the laws of kinematics. Interactions between particles follow simple laws, such as the laws of conservation of energy and momentum in the case of elastic collisions. Such laws are fundamental to Newtonian mechanics and provide relatively simple, yet powerful, tools for predicting particle behavior. When there is no hindering interaction, the particle is said to be ballistic.

Waves, unlike particles, cannot be considered finite entities. Their energy is distributed in space and in time. Unlike a particle, a wave can propagate until it exists in all locations and at all times. Like particles, a part (or phase) of the wave can be analyzed to determine its velocity in space. Waves are specified by frequency and wavelength. An EM wave is a propagating oscillation of a perpendicular electric field and a magnetic field in space.

For wave/particle, the classical distinctions between particles and waves can become blurred. They behave partly according to wave theory and partly according to particle theory. For example, in blackbody thermal radiation, by analysis of the spectral intensity of the EM radiation for various temperatures, it is noted that the total radiation intensity (integrated over the entire spectrum) is a function of temperature to the fourth power. Also, a wavelength corresponding to a maximum radiant intensity is observed for a given temperature. As the temperature of the body increases, the wavelength of maximum intensity decreases. The wave treatment of a blackbody cavity shows that the cavity is full of EM standing waves with nodes at the walls, and the number of these standing waves can be determined as function of the size of the cavity. Each wave contributes $k_B T$ joules of energy to the system, giving the classical Rayleigh–Jeans formula. Compared with the measured blackbody spectral intensity (which is quantum-particle treatment, Section 7.1), this relation, based on wave treatment, overestimates significantly the intensity at short wavelengths (an error called the UV catastrophe).

The concept of wave packets addresses the overestimation problem by allowing us to almost determine the location of a wave. This in turn allows us to measure energy, location, and momentum at a specific time. A wave packet is a quasi-particle because it exhibits some particle-like behavior. The principle of superposition describes the addition of waves, in which the overlapping of two pure sine waves of similar amplitude and frequency produces areas of constructive and destructive interference. This produces a beat phenomenon, which can be shown by two waves ($\sin \kappa x$) with slightly different wavelengths ($2\pi/\kappa$) which when superimposed, leads to a wavepacket. The energy of the waves is located in an area that is approximated with a distance Δx. By adding together many waves of slightly different amplitudes and frequencies (with a range of wave numbers $\Delta\kappa$) it is possible to create a beat of any shape. Increasing the number of waves used (and thus $\Delta\kappa$), decreases Δx. This means the range of wave numbers and the size of the beats are inversely proportional, i.e., $\Delta x \Delta\kappa \simeq 1$. The smaller the wave packet (the more localized), the larger the spread of wavelengths needed to construct the packet.

Using the quasi-particle concept of a wave packet, the Planck distribution (Section 7.1) can be developed that describes the thermal equilibrium distribution of these packets of energy (photons). We will then compare this with the wave treatement in Section 7.7, and show the need for the appropriate treatement depending on the application.

In addition to the energy probability distribution function $f_i(E_i, T, \text{etc.})$ (probability of occupation based on temperature, and in nonequilibtrium also depends on the applied disturbing field), the structure of the matter limits the number of states at each energy level which are available to be occupied. This structural limit is the density of states $D_i(E_i)$. For example, the phonon energy $\hbar\omega$ is limited by the maximum frequency (cut-off frequency) allowed in the lattice vibration and this depends on the constituent atoms and their arrangement. Or, in semiconductors the energy in the bandgap is forbidden. The density of states of phonon and electron includes these limitations and features. Then the product $f_i(E_i, T, \text{etc.})D_i(E_i)$ is number of allowed occupied states. The size effect is also included in the density of states. For electrons this leads to density of states for quantum wires, wells, and dots, and for photon to photonic crystals (allowing only selective photon transmission through bandgap, etc.). We will discuss this further in Section 1.9.

1.4 A History of Contributions Toward Heat Transfer Physics

Heat is a form of energy that manifests itself as the motion of the molecules of a substance and is capable of being transmitted from one body to another by conduction (by means of phonons, electrons, and fluid particles), convection (by means of fluid particles), and radiation (by means of photons). It can also be transformed into other forms of energy, e.g., EM energy.

The areas of physics most relevant to heat transfer physics are (a) atomic/molecular dynamics, (b) solid-state (condensed-matter) and fluid-state physics, (c) electromagnetism, and (d) quantum optics.

Table 1.3 gives a chronological overview of the contributions to the physics of energy and its transport, as related to heat transfer. These include thermoelectricity,

Table 1.3. *A chronological list of historical contributions to the physics (atomic-level description) of energy storage, transport, and transformation.*

1773	Coulomb's and Navier's (1820) theory of elasticity (mechanics of solids) [489]
1811	Avagadro's number and Fourier's law of heat conduction [32]
1821	Seebeck's discovery of electromotive force of heated junctions of two conductors [163]
1827	Navier's and Stoke's (1845) fluid momentum conservation [32]
1828	Brown's observation of pollen grains' motion in water [32]
1834	Peltier's thermoelectric cooling/heating at junction of two current-carrying conductors [163]
1845	Waterston's suggestion of what later became the kinetic theory of gases [32]
1859	Kirchhoff's law of equality of spectral, directional absorptivity and emissivity [428]
1865	Loschmidt's estimation of the diameter of gases [285], also Clausius' introduction of entropy [285]
1866	Maxwell's dynamical theory of gases [285], also Boltzmann's first attempt to relate entropy with average property of gas in thermal motion [285]
1872	Boltzmann's minimum (or H-) theorem and M–B distribution function [285]
1873	Gibb's first publication of thermodynamic properties and their relations [285], van der Waals' equation of state for liquids (and dense gases) including the attractive intermolecular forces [209]
1877	Boltzmann's introduction of his proportionality constant [285]
1879	Stefan's empirical relation for total emissive power of blackbody [32, 359]
1897	Thomson's discovery of electrons [12]
1900	Drude's theory of electron and phonon thermal conductivity [12]
1901	Planck's spectral distribution of blackbody emissive power [428]
1905	Einstein's molecular theory of heat capacity of solids [32, 359]
1908	Langevin's stochastic particle dynamics equation [93]
1909	Knudsen's experiment on viscous, transitional, and molecular-flow regimes [32]
1911	Eucken's T^{-1} relation for thermal conductivity of dielectrics [12]
1912	Debye's theory of crystal specific heat capacity based on lattice vibration [109]
1914	Millikan's verification of photoelectric effect (quantization of energy and Planck constant)
1916	Chapman–Enskog's expansion of distribution using the Knudsen number in derivation of Navier–Stokes equations from Boltzmann transport equation [479]
1917	Einetein's stimulated emission [429]
1918	Langmuir's theory of adsorbed monolayers and isotherms [277]
1924	de Broglie wave–matter theory [32, 359], Güneisen's lattice dynamics-based solid equation of states [173]
1925	Heisenberg's and Schrödinger's wave function-equation for matter wave [463], Pauli's exclusion principle [32, 359], Prandtl's phenomenological turbulent mixing-length theory [195]
1926	Schrödinger's equation using de Broglie's hypothesis that each particle has a wavelength [32], Fermi's quantum state exclusion principle for ideal gas [32, 359], Dirac's similar treatment [32, 359]
1928	Bloch's theory of electron energy surfaces in crystals [463]
1929	Peierl's inclusion of lattice anharmonicity and introduction of phonons as wave packets and U–processes [363], Pringsheim's radiation cooling by anti-Stokes fluorescence [367]
1931	Onsager's reciprocal relations for coupled irreversible thermoelectric processes [354]
1932	Sommerfeld's model of electron gas in solids [32, 359], Dirac's positron experimentally confirmed [32, 359]
1934	Fermi's (contributions from Dirac) golden rule for electronic transition probability rate [359]
1935	Taylor's introduction of velocity correlation and statistical theory of turbulence [25]
1937	Wheeler's quantum-mechanical description of particle scattering [32, 359]
1938	Kapitsa's (also by Allen and Misener) discovery of superfluid liquid helium [32, 359]

1939	Landau's theory on superthermal conductor liquid helium II [32, 359]
1949	Feynman's quantum electrodynamics diagram for charged-particle scattering [32, 359]
1954	Green's and Kubo's (1957) transport coefficient determined from current autocorrelation integral [187], Bhatagar–Gross–Krook's model for restoration of equilibrium distribution due to particle collision [479]
1954	Townes and Schawlow's maser [429]
1956	Barden/Brattain/Schockley recognition for semiconductors and transistor effect [32]
1959	Ziman's variational treatment of nonequilibrium phonon in transport properties [516], Callaway's inclusion of N– and U–processes in the relaxation-time model of lattice thermal conductivity [163]
1960	Maiman's ruby laser [429]
1967	Tien's radiation tunneling analysis [102] and contribution to photon (infrared) gaseous absorption [459], Slack's high-temperature phonon conductivity relation T^{-1} [437]
1981	Djeu and Whitney's anti-Stokes laser cooling of CO_2 gas mixtures [114]
1985	Discovery of C_{60}: Buckminsterfullerene [259]
1997	Chu/Cohen–Tannoudji/Phillips's Bose-Eienstein condensate experiment using laser cooling of atomic gasses [367]
1998	Tien *et al.* book on Microscale Energy Transport [461]
1999	Goznell's anti-Stokes laser cooling of ion-doped solids [164]

the theory of thermal motion (fluctuation), the theory of harmonic oscillation and photon emission, and the theory of phonons and phonon thermal conductivity. We will encounter and discuss these principles and contributions in the following chapters. A review of recent advances in heat transfer physics is given in [74].

Kelvin helped in the creation of a new kind of mathematical and experimental physics based on the concept of energy. In describing rules for the conservation of energy, he introduced the term energy dissipation/degradation (in terms of the kinetic and potential energy). These rules later became the first and second laws of thermodynamics.

Boltzmann developed the idea that heat content, entropy (a measure of the disorder of a system), and other thermodynamic properties were the result of the behavior of large numbers of atoms, and could be treated by use of mechanics and statistics. He introduced the equation for the relation of entropy to probability, not to mention the Boltzmann constant k_B. He made important contributions to the kinetic theory of gases and developed the law of equipartition of energy with Maxwell (the M–B law), stating that the total energy of an atom or molecule is, on average, equally distributed over the degrees of freedom.

Maxwell created the EM theory of light. He formulated a group of equations summarizing the relation of electric and magnetic fields to the charges and currents producing them. He also contributed to the kinetic theory of gases (the M–B law just mentioned), molecular physics, and thermodynamics.

Planck discovered that energy exists in discrete units, which came to be called quanta, a Latin word translated as how much? He assumed that nature was being selective in the amount of energy it would allow a body to accept or emit, allowing only amounts (or quanta) that were multiples of $h_P f$, i.e., quanta, where f is the photon frequency.

Bohr laid the foundations for one of the most important scientific achievements of the time: the model of the atom. While considering the simplest atom, hydrogen, and studying its atomic line spectrum, he postulated that its electron radiated energy only when it dropped from one allowed level to a lower energy level. The atom can absorb and emit energy only in quanta, which correspond to the energy differences between allowed levels. The electrons in the atom begin to occupy the orbit nearest the nucleus, but not all the electrons can fill the lowest orbit.

Pauli articulated a rule for atomic structure (commonly known as the Pauli exclusion principle) in which the state of each electron in an atom is defined by a unique set of four quantum numbers, and no two electrons in a single atom may have the same set of quantum numbers or the same energy state.

Schrödinger introduced the equation that describes the form of the probability waves (or wave functions) that govern the motion of small particles and that specify how these waves are altered by external influence. These functions, and the idea that particles have wavelike properties, are the foundation of quantum wave mechanics.

Fermi devised a method for calculating the behavior of particle systems obeying the Pauli exclusion principle (i.e., having nonequal quantum numbers), later termed Fermi statistics. Dirac independently developed an equivalent theory. Fermi also developed a method for calculating the quantum electron transition probability rates.

Green and Kubo developed the fluctuation–dissipation theory of transport coefficients, and Callaway and Holland formulated (and solved) the single-mode relaxation-time model (Boltzmann transport) of lattice thermal conductivity.

Chu/Cohen–Tannoudj/Phillips laser cooled Na gas atoms to very close to 0 K to form the quantum, Bose–Einstein condensate. The laser cooling of molecular gasses and of solids continues to be pursued.

In the history of mathematical physics the most notable milestone between Newton and Einstein is the work of Hamilton, who brought the theory of classical mechanics to a level of great sophistication. Relatively recent developments in semiconductos, lasers, and nanostructures have led to further discoveries and applications related to heat transfer.

1.5 Fundamental Constants and Fine-Structure Scales

1.5.1 Boltzmann and Planck Constants

The Boltzmann constant is $k_{\rm B} = 1.3806503(24) \times 10^{-23}$ J/K and is defined in the relation between the average thermal energy (related to the potential and kinetic energy) of a principal energy carrier (phonon, electron, photon, or fluid particle) to its absolute temperature T (The digits in parentheses correspond to uncertainty in the last two digits.[†]). This thermal energy $k_{\rm B}T$ is used to scale (normalize) the energy of principal energy carriers when they are treated as particles. In the classical systems, thermal energy is assumed to vary continuously with temperature (in contrast to quantum systems).

[†] In this text, we use four significant figures, for consistency. Whenever appropriate, more significant figures are shown. Also, when accuracy is limited, only the available significant digits are given.

The Boltzmann constant is a classical quantity. In statistical mechanics, the entropy S (a macroscopic property) of a system of N distinguished particles is defined as [†] [323]

$$S = k_{\rm B} N \ln Z + \frac{E}{T}, \tag{1.6}$$

Here, Z is called the partition function, which is the probability function describing the distribution of energy states available to a system given its macroscopic constraints (such as a fixed total energy E). This will be further discussed in Section 2.4.1 and in Chapter 6. In principle, the Boltzmann constant is a derived physical constant, as its value is determined by other physical constants. Its independent derivation has yet to be completed due to its complexity.

In kinetic theory, from the equipartition of energy, for each degree of motion an energy equal $k_{\rm B}T/2$ is assigned (Section 2.3.1).

The Planck constant h or $h_{\rm P} = 6.62606896(33) \times 10^{-34}$ J-s arises in quantum mechanics, such that the energy within a body obeying quantum mechanics is the product of its frequency f and $h_{\rm P}$. The reduced Planck constant (also called the Dirac constant) is $\hbar = h_{\rm P}/2\pi$.

The Planck constant is used to describe quantization, a phenomenon for principal energy carriers, in which certain physical properties occur in fixed amounts rather than a continuous range of possible values.

The Planck constant also occurs in statements of the Heisenberg uncertainty principle, in which the uncertainty (the standard deviation) in any position measurement Δx and the uncertainty in a momentum measurement along the same direction Δp_x, obeys (and also energy/time) the relations (Chapter 2 problem)

$$\Delta p_x \Delta x \geq \frac{\hbar}{2}, \quad \Delta E \Delta t \geq \frac{\hbar}{2}. \tag{1.7}$$

Table 1.4 lists the fundamental physical constants used in the text. This table is also repeated as Table A.3 in Appendix A, for easy reference. The electron charge e_c, the Newton gravitational constant G_N, electron and nuclear particle masses, and EM constants are also listed. Some derived constants, such as the Bohr radius $r_{\rm B}$, the universal gas constant R_g, and the Stefan–Boltzmann constant $\sigma_{\rm SB}$ are also listed.

1.5.2 Atomic Units and Fine-Structure Scales

Four fundamental constants, the reduced Planck constant $\hbar$, the electron mass m_e, the Coulomb (electrostatic) constant $1/4\pi\epsilon_{\rm o}$ (where $\epsilon_{\rm o}$ is the free-space electric permittivity), and the electron charge e_c, are used to define atomic units. Based on these, the atomic length unit (the Bohr radius for electron in hydrogen atom) is $4\pi\epsilon_{\rm o}\hbar^2/m_e e_c^2 = 5.2917725 \times 10^{-11}$ m $= 0.52917725$ Å, the atomic energy unit

---

[†] For indistinguishable particles (Appendix F)

$$S = k_B (N \ln Z - \ln N!) + \frac{E}{T}.$$

Table 1.4. *Fundamental constants, derived quantities, and units conversions [282, 283].*

Symbol	Magnitude and units
Fundamental constants:	
c_o	speed of light in vacuum, 2.99792458×10^8 m/s
e_c	electron charge, 1.602×10^{-19} C (1 eV = 1.602×10^{-19} J, where V = J/C)
G_N	Newton (gravitational) constant, 6.673×10^{-11} m^3/kg-s^2
h_P	Planck constant, 6.626×10^{-34} J-s = 4.136×10^{-15} eV-s
$\hbar$	$h_P/2\pi = 1.055 \times 10^{-34}$ J-s = 6.583×10^{-16} eV-s
k_B	Boltzmann constant, 1.381×10^{-23} J/K = 8.618×10^{-5} eV/K
m_e	electron mass, 9.109×10^{-31} kg
m_n	neutron mass, 1.675×10^{-27} kg = 1.675 yg
m_p	proton mass, 1.673×10^{-27} kg = 1.673 yg
N_A	Avogadro number, 6.022×10^{23} molecule/mole = 6.022×10^{26} molecule/kmole
μ_o	free-space magnetic permeability, $4\pi \times 10^{-7} = 1.257 \times 10^{-6}$ N-s^2/C^2
Derived quantities:	
$\epsilon_o = \dfrac{1}{c_o^2 \mu_o} = 8.854 \times 10^{-12}$ C^2/N-m^2	free-space electric permittivity
$D = e_c r_B/2.54 = 3.3356 \times 10^{-30}$ C-m	Debye (atomic dielectric dipole moment)
$N_{L,o} = \dfrac{\pi^2}{3}\dfrac{k_B T^2}{e_c^2} = 2.442 \times 10^{-8}$ W-Ω/K^2	Lorenz number
$r_C = \dfrac{e_c^2}{4\pi\epsilon_o m_e c_o^2} = 2.8179 \times 10^{-15}$ m	classical (Compton) electron radius
$r_B = \dfrac{4\pi\epsilon_o \hbar^2}{m_e e_c^2} = 5.292 \times 10^{-11}$ m	Bohr radius (atomic length unit)
$\dfrac{e_c^2}{4\pi\epsilon_o r_B} = 27.2114$ eV $= 4.35975 \times 10^{-18}$ J	hartree (atomic energy unit)
$\dfrac{e_c^2}{4\pi\epsilon_o r_B^2} = 8.2378 \times 10^{-8}$ N	atomic force unit
$R_g \equiv k_B N_A = 8.3145 \times 10^3$ J/kmole-K	universal gas constant
$\mathrm{Ry} = \dfrac{m_e e_c^4}{8\epsilon_o^2 c_o \hbar^3} = 13.606$ eV $= 1.0974 \times 10^5$ cm^{-1}	Rydberg ground-state energy of H
$\dfrac{1}{4\pi\epsilon_o} = 8.9876 \times 10^9$ Nm^2/C^2	Coulomb constant
$\alpha = \dfrac{e_c^2}{4\pi\epsilon_o \hbar c_o} = 7.29735 \times 10^{-3}$	fine-structure constant
$\sigma_{SB} \equiv \dfrac{\pi^2 k_B^4}{60\hbar^3 c_o^2} = 5.670 \times 10^{-8}$ W/m^2-K^4	Stefan–Boltzmann constant
Units conversions:	
1 eV = 8.0655×10^3 cm^{-1} = 2.418×10^{14} Hz = 11,600 K = 1.602×10^{-19} J = 96.485 kJ/mole	
1 cm^{-1} = 0.12398 meV = 2.998×10^{10} Hz	
1 Trad/s = 0.6582 meV = 5.309 cm^{-1}	

(1 hartree = $e_c^2/4\pi\epsilon_o r_B$) is $e_c^4 m_e/(4\pi\epsilon_o\hbar)^2 = 4.3597482 \times 10^{-18}$ J = 27.211396 eV, the atomic time unit $\tau_a = m_e r_B^2/\hbar$ is $2.4188843 \times 10^{-17}$ s, the atomic (electron) velocity $u_e = r_B/\tau_a = \hbar/m_e r_B$ is 2.1876914×10^6 m/s, and the atomic electric dipole moment $e_c r_B$ is $8.4783579 \times 10^{-30}$ C-m = 2.54 D, where D = 3.3356×10^{-30} C-m is one Debye. The atomic (*ab initio*) scales are summarized in Table 1.5. The unit prefixes (e.g., y, z, f, p, n) are defined in Table A.4 in Appendix A.

Table 1.5. *Atomic scales (*ab initio *or fine-structure), based on hydrogen atom.*

Scale	Relation
Mass	$m_e = 9.109 \times 10^{-31}$ kg $= 9.109 \times 10^{-4}$ yg
Length	$r_B = \dfrac{4\pi\epsilon_o\hbar^2}{m_e e_c^2} = 5.2918 \times 10^{-11}$ m $= 52.918$ pm
Time	$\tau_a = \dfrac{m_e r_B^2}{\hbar} = 2.4189 \times 10^{-17}$ s $= 2.14189 \times 10^{-2}$ fs
Energy	$\dfrac{e_c^2}{4\pi\epsilon_o r_B} = 4.3597 \times 10^{-18}$ J $= 27.211$ eV
Velocity	$\dfrac{r_B}{\tau_a} = 2.1877 \times 10^6$ m/s
Dipole moment	$e_c r_B = 8.4783 \times 10^{-30}$ C-m= 2.54 D
Fine-structure constant	$\alpha = \dfrac{e_c^2}{4\pi\epsilon_o\hbar c_o} = 7.29735 \times 10^{-3}$

More commonly, the electron-volt (eV) is used as the unit of atomic-level energy and is defined as the amount of kinetic energy gained by a single unbound electron (of charge e_c) when it passes through an electrostatic potential difference $\triangle\varphi_e$ of one volt (V) in vacuum.

Note that from the Einstein relation $E = mc^2$, E/m_e in atomic mass units is 931.5 MeV/m_e

The fine-structure constant

$$\alpha = \frac{e_c^2}{4\pi\epsilon_o\hbar c_o} = 7.29735 \times 10^{-3} \tag{1.8}$$

is the ratio of electron velocity in the Bohr model of an atom to the speed of light. It is also an indicative of scaled EM interaction (energy needed to bring two electrons from infinity to a close distance, divided by the energy of a photon having a wavelength equal to the same separation distance). We will discuss this electrostatic force in Section 2.1.

The hyperfine structure is a small perturbation in the energy levels of atoms and molecules that is due to the magnetic dipole–dipole interactions (nuclear–electron magnetic moment interactions). The hyperfine energies are not in the optical regime, but in the radio waves and microwaves regimes.

1.6 Principal Carriers: Concentration, Energy, Kinetics, and Speed

The energy storage, transport, and transformation involving the four principal carriers are related to their concentration n_i, energy E_i, kinetics (represented by time constants, relaxation times, and rates) τ_i and speed u_i.

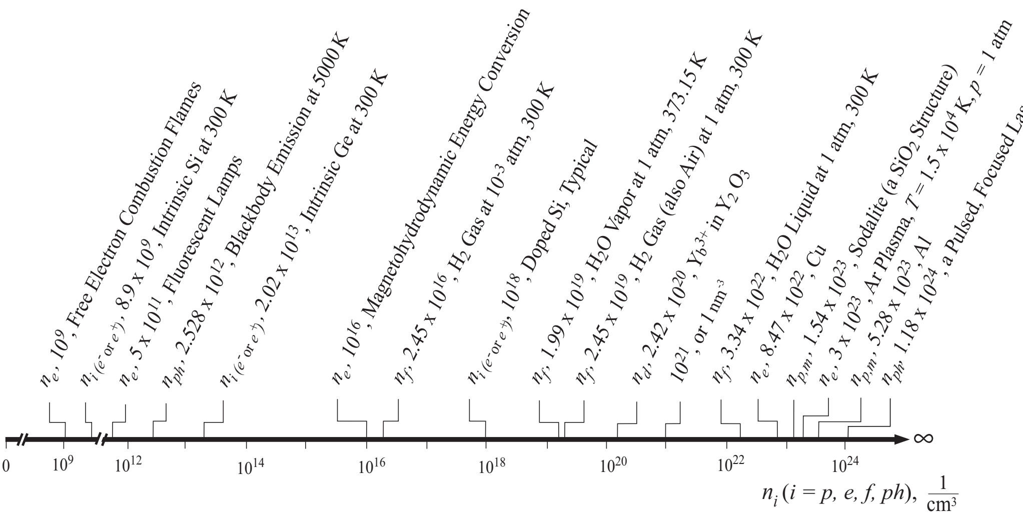

Figure 1.3. Typical number densities for phonon modes, electrons (conduction), fluid particles, and photons. For Yb^{+3} in Y_2O_3, n_d is the optimum ion dopant concentration for the laser cooling of an Y_2O_3 crystal. The $n = 1/\text{nm}^3$ is also marked.

In this section these properties of the principal carriers are briefly examined, and examples of their magnitudes are given. Full treatments are given in Chapters 4 to 7.

1.6.1 Principal-Energy Carriers Concentration

Figure 1.3 lists several typical carrier densities, in units of carriers per cubic centimeter. A convenient reference is 10^{21} 1/cm^3 = 1 1/nm^3, which is marked there, In the Debye model of the lattice specific heat of monotonic crystals, the number of phonon modes is three times (for dimension of motion) the number density of the atoms. For Al [face-centered-cubic (FCC) structure] this phonon mode density is found from

$$n_{p,m} = 3n = 3\frac{\rho}{m} = 3\frac{\rho N_\text{A}}{M} \quad \text{monatomic FCC crystals,} \tag{1.9}$$

where n is atomic number density, ρ is density and M is molecular weight, and gives 5.28×10^{23} 1/cm^3 (shown in Figure 1.3). The mass of elements m are generally given in yoctogram (yg), which is 10^{-24} g (prefixes are listed in Table A.4). For the polyatomic crystalline sodalite, a silica (SiO_2) structure, the number of phonon modes is 1.54×10^{23} 1/cm^3. The actual phonon density n_p depends on temperature.

We concentrate on free (conduction) electrons, because of their role in transport, with metals having one or more conduction electrons per atom, such as Cu having one (found from the outermost electron orbital). The number density of free (conduction) electrons in metals is given by

$$n_{e,c} = \frac{\rho N_A}{M} z_e \quad \text{metals,} \tag{1.10}$$

where M is the molecular weight, ρ is the density, and z_e is the number of free electrons per atom. (Table 5.2 gives listing of n_e for other metals.) There are no conduction electrons in semiconductors at $T = 0$ K, and the number of conduction electrons per unit volume increases as the temperature increases. Semiconductors can also have electron-donating dopants, which add to their overall electron density. Typical conduction electron densities for metals are of the same order as that for Cu, 8.47×10^{22} 1/cm^3. For semiconductors, the value for intrinsic Ge at 300 K of 2.5×10^{13} 1/cm^3 is typical. These are listed in Figure 1.3. For semiconductors, the density value reported includes both electrons and holes. Intrinsic (not doped) Si, for example, at $T = 300$ K has equal concentrations of electrons and holes of 8.72×10^9 1/cm^3 each. An ion dopant (Yb^{3+}) in the Y_2O_3 crystal, with applications in laser cooling of solids, is also shown ($n_d = 2.42 \times 10^{20}$ 1/cm^3). The number of free electrons in a typical combustion flame and in an Ar plasma ($T = 1.5 \times 10^4$ K) is also shown in Figure 1.3. Thermal plasmas reach the free-electron density of metals.

The atomic and molecular gases and liquids, which we call fluids for simplicity, have carrier densities n_f that depend on their pressures and temperatures. The molecular number density of H_2 (gas) at 10^{-3} atm and 300 K is found from

$$n_f = \frac{\rho_f N_{\rm A}}{M} = \frac{p}{k_{\rm B} T} \quad \text{ideal gas,} \tag{1.11}$$

and is 2.45×10^{16} 1/cm^3. As an example of liquids, H_2O liquid at 1 atm and 300 K has $n_f = 3.34 \times 10^{22}$ 1/cm^3.

In the blackbody emission of photons, the number of photons per unit volume is given by (Chapter 7 problem)

$$n_{ph} = 2.404 \times 8\pi (\frac{k_{\rm B}}{h_{\rm P} u_{ph,\rm o}})^3 T^3 \quad \text{blackbody emission.} \tag{1.12}$$

From the constants in Table 1.4, this gives 2.023×10^{10} photons/cm^3 for $T =$ 1000 K. For $T = 5000$ K this is 2.528×10^{12} 1/cm^3 and is marked in Figure 1.3. In lasers and other amplified, pulsed, and focused radiation, the number of photons per unit volume can be extremely large. For example, a 10^{-3} J laser pulse at a wavelength of 5×10^{-7} m = 0.5 μm (green light) released over a period of 10^{-15} s (femtoseconds, fs) with a beam cross-sectional area of 10^{-10} m^2, and using $\dot{s}_{ph} = \hbar \omega_{ph} n_{ph} u_{ph} A$, gives $n_{ph} = 1.18 \times 10^{22}$ 1/cm^3. (Table 1.4 is repeated in Appendix A, along with a table of unit prefixes.)

1.6.2 Principal-Carrier Energy

As was listed in Table 1.2, wave or particle characteristics are used in presenting the carrier energy. The energy of a phonon is generally given in terms of its wave vector $\boldsymbol{\kappa}_p$, and by use of the phase velocity, it can also be given in terms of its angular frequency ω_p and direction $\boldsymbol{s}_\alpha$. The energy of an electron is also given in terms of $\boldsymbol{\kappa}_e$. For fluid particles (and classical particles in general), the particle momentum $\boldsymbol{p}_f$ in its kinetic energy is used. For photons, generally the frequency ω_{ph} (or wavelength λ) is used. Regardless of their specific presentations, these carriers contain continuous and discrete energies and exchange these energies through various interactions.

Figure 1.4 shows examples of typical energies for phonons, fluid particles, electrons, and photons. As depicted in the figure, these energies are atomic-level kinetic energy (translational, rotational, and vibrational motion which define the temperature), and potential energy (interatomic potential or in the bound electron), the EM waves (photons) can be emitted or absorbed due to charge non-uniformity (δ_+, δ_-) and their motion. As an example, the quantized electronic energy in a two-level system, with phonon absorption/emission is also shown in the figure. Such interactions among the carriers results in energy conversion. Carrier energies larger than 10 eV (of the order of 1 hartree = 27.21 eV) are considered high energy here, as most of the phonon, electron, fluid particle, and photon energies in heat transfer phenomena are less than 1 hartree. As shown, the very high energies (10^8 eV) are associated with nuclear forces (strong and weak nuclear electronic energy) and associated with γ-rays (made up of photons). The corresponding thermal (or mechanical) energy represented by the product of the Boltzmann constant and absolute temperature is exceptionally high. For fluid particles, high-temperature thermal plasmas may have ionized atoms with energies of the order of 10 eV. Phonon energies are limited by the temperature of the crystalline solid they travel through, which is limited to around 4000 K. The lattice vibrations with the highest energies are associated with optical phonons, which typically contain less than 1 eV. The highest electron energies are associated with accelerated electrons and some electron emissions. We have included the nuclear energy in the electron, just because here we are not addressing this energy directly. The energies released during radioactive decay, fission, and fusion, are very large. The highest photon energies are in the γ-rays and cosmic radiation ranges.

In Figure 1.4, the symbol R stands for a resonance phenomenon, and indicates an electronic transition energy, or bond energy, or mechanical vibration energy. Resonance phenomena require atomic-level energy-matching metrics and allow for atomic-level design of energy conversion devices.

Although these carrier energies are available for use in thermal energy storage, transport and conversion, the rate of such processes, which is central to heat transfer physics, is controlled by the atomic-level kinetics. These are addressed below.

1.6.3 Principal-Carrier Energy Transport/Transformation Kinetics

The smallest time unit typically used is the Planck time $\tau_{\rm P} = (h_{\rm P} G_{\rm N}/c_{\rm o}^5)^{1/2}$, where $G_{\rm N}$ is the Newton gravitational constant (Table 1.4), yielding an atomic time unit equal to 2.42×10^{-17} s (Table 1.5). Figure 1.5 shows typical times for various microscale energy interactions (transitions) $\tau_{i\text{-}j}$. The inverse of $\tau_{i\text{-}j}$ is the interaction (transition) rate $\dot{\gamma}_{i\text{-}j}$, which signifies the rate of hindering or enabling atomic-level energy transfers, i.e., microscale energy kinetics. The examples in Figure 1.5 are for T = 300 K. As shown in Figure 1.5, the fastest processes are associated with photons and their interactions with electrons (or electric fields). An electron orbiting a hydrogen

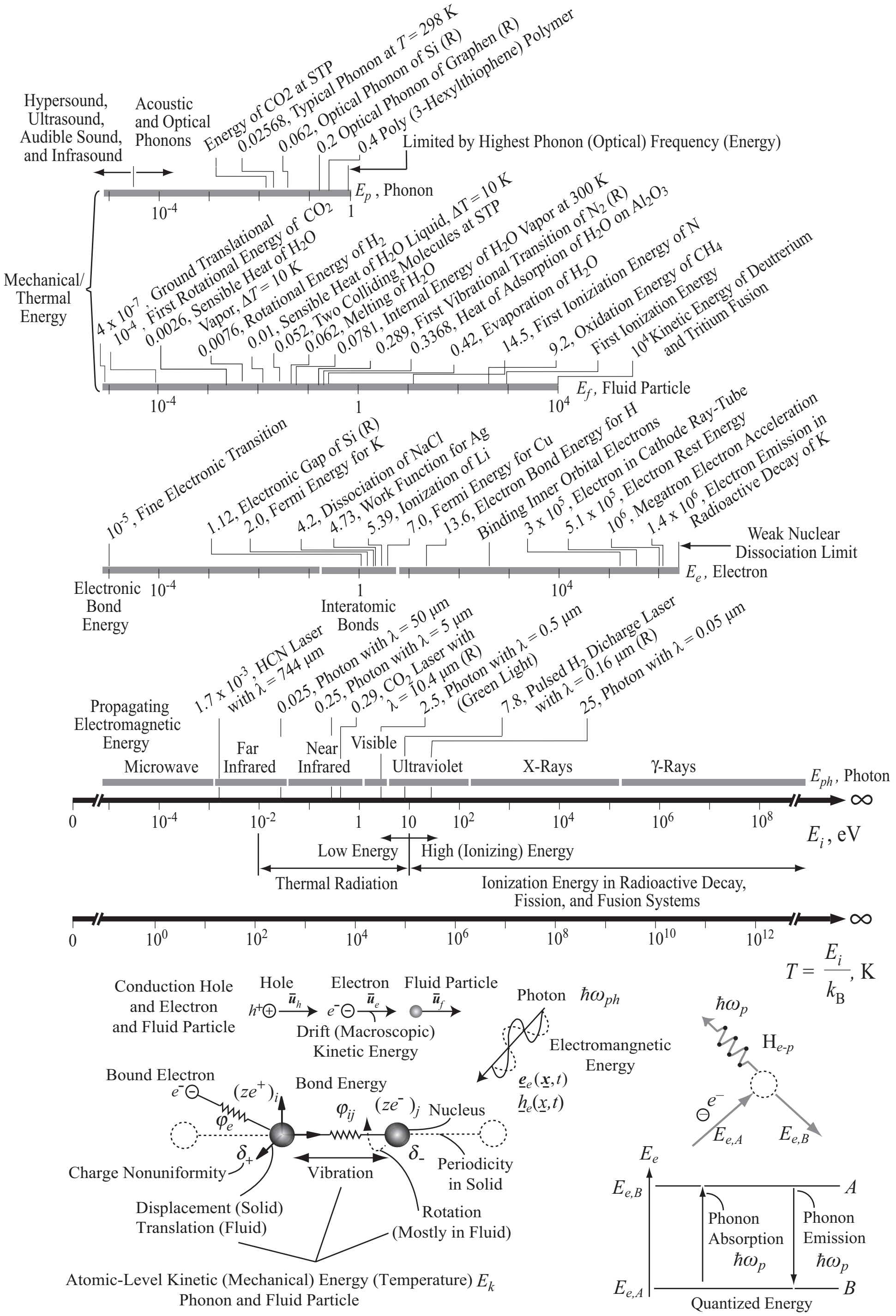
Hypersound, Ultrasound, Audible Sound, and Infrasound
Acoustic and Optical Phonons
Energy of CO2 at STP
0.02568, Typical Phonon at $T = 298$ K
0.062, Optical Phonon of Si (R)
0.2 Optical Phonon of Graphen (R)
0.4 Poly (3-Hexylthiophene) Polymer
Limited by Highest Phonon (Optical) Frequency (Energy)
E_p, Phonon
10^{-4}
1
Mechanical/ Thermal Energy
4×10^{-7}, Ground Translational
10^{-4}, First Rotational Energy of CO_2
0.0026, Sensible Heat of H_2O Vapor, $\Delta T = 10$ K
0.0076, Rotational Energy of H_2
0.01, Sensible Heat of H_2O Liquid, $\Delta T = 10$ K
0.052, Two Colliding Molecules at STP
0.062, Melting of H_2O
0.0781, Internal Energy of H_2O Vapor at 300 K
0.289, First Vibrational Transition of N_2 (R)
0.3368, Heat of Adsorption of H_2O on Al_2O_3
0.42, Evaporation of H_2O
14.5, First Ionizition Energy of N
9.2, Oxidation Energy of CH_4
First Ionization Energy
10^4 Kinetic Energy of Deutrerium and Tritium Fusion
E_f, Fluid Particle
10^{-4}
1
10^4
10^{-5}, Fine Electronic Transition
1.12, Electronic Gap of Si (R)
2.0, Fermi Energy for K
4.2, Dissociation of NaCl
4.73, Work Function for Ag
5.39, Ionization of Li
7.0, Fermi Energy for Cu
13.6, Electron Bond Energy for H
Binding Inner Orbital Electrons
3×10^5, Electron in Cathode Ray-Tube
5.1×10^5, Electron Rest Energy
10^6, Megatron Electron Acceleration
1.4×10^6, Electron Emission in Radioactive Decay of K
Weak Nuclear Dissociation Limit
E_e, Electron
Electronic Bond Energy
10^{-4}
1
10^4
Interatomic Bonds
Propagating Electromagnetic Energy
1.7×10^{-3}, HCN Laser with $\lambda = 744$ μm
0.025, Photon with $\lambda = 50$ μm
0.25, Photon with $\lambda = 5$ μm
0.29, CO_2 Laser with $\lambda = 10.4$ μm (R)
2.5, Photon with $\lambda = 0.5$ μm (Green Light)
7.8, Pulsed H_2 Dicharge Laser with $\lambda = 0.16$ μm (R)
25, Photon with $\lambda = 0.05$ μm
Microwave
Far Infrared
Near Infrared
Visible
Ultraviolet
X-Rays
γ-Rays
E_{ph}, Photon
0
10^{-4}
10^{-2}
1
10
10^2
10^4
10^6
10^8
∞
E_i, eV
Low Energy
High (Ionizing) Energy
Thermal Radiation
Ionization Energy in Radioactive Decay, Fission, and Fusion Systems
0
10^0
10^2
10^4
10^6
10^8
10^{10}
10^{12}
∞
$T = \frac{E_i}{k_B}$, K
Conduction Hole and Electron and Fluid Particle
Hole
Electron
Fluid Particle
h^+
$\overline{u}_h$
e^-
$\overline{u}_e$
$\overline{u}_f$
Drift (Macroscopic) Kinetic Energy
Photon $\hbar\omega_{ph}$
Electromangnetic Energy
$\underline{e}_e(\underline{x}, t)$
$\underline{h}_e(\underline{x}, t)$
$\hbar\omega_p$
H_{e-p}
e^-
$E_{e,A}$
$E_{e,B}$
Bound Electron
e^-
$(ze^+)_i$
φ_e
Bond Energy
φ_{ij}
$(ze^-)_j$
Nucleus
δ_+
δ_-
Charge Nonuniformity
Vibration
Periodicity in Solid
Displacement (Solid) Translation (Fluid)
Rotation (Mostly in Fluid)
Atomic-Level Kinetic (Mechanical) Energy (Temperature) E_k Phonon and Fluid Particle
E_e
$E_{e,B}$
A
Phonon Absorption $\hbar\omega_p$
Phonon Emission $\hbar\omega_p$
$E_{e,A}$
B
Quantized Energy

Figure 1.4. Examples of typical energies for the four principal energy carriers. The highest phonon energies are in the optical phonons, the highest fluid particle energies are the electronic energy, the highest electron energies are in electron emissions and in accelerated electrons, and the highest photon energies are in γ-rays and cosmic radiations. Symbol R stands for a resonance phenomenon.

atom, for example, has an orbital period of about 2.42×10^{-17} s. The time it takes for particles to thermalize to their equilibrium distribution is around 10^{-12} s, which also corresponds to phonon–phonon interaction relaxation times. Collision time intervals (relaxation times) for gas molecules are around 10^{-10} s. There are also much slower times, such as the lifetime of excited electronic states of Yb^{+3} (a typical rare-earth ion in dielectric crystals), which is about 10^{-6} s.

As also emphasized in Figure 1.5, in transport, the process (scattering) rate that is the fastest (with the smallest $\tau_{i\text{-}j}$) dominates, because the resistances are additive [for independent scattering mechanisms as will be shown by the Matthiessen rule (4.111)]. There are also cases in which the conductances are additive, in which the slowest process dominates. For example, in solids both phonons and free electrons contribute to thermal conductivity and the transport with least scattering (as well as other desired attributes such as number density) dominates. Also, for energy conversions (transitions) involving multiple processes, the slowest process dominates [such as the absorption time τ_{ph-e-p} in the laser cooling of ion doped solids (7.198)]. Also shown in Figure 1.5 is the process of energy absorption emission in a three level energy system, under nonequilibrium occupancy of the energy states occurs. This process of energy conversion involves four time constants with some relations among them (similar to the laser cooling of solids and gases in Sections 7.12 and 7.13).

As an example, in the thermoelectric material $\mathrm{Bi_2Te_3}$ (a semiconductor of the p-type, described in Section 5.17), electrons are scattered most rapidly by the polar optical phonons ($\tau_{e\text{-}p} = 5\times10^{-14}$ s), and least rapidly by Coulombic scattering from the nucleus ($\tau_{e\text{-}\mathrm{C}} = 8\times10^{-13}$ s).

1.6.4 Principal-Carrier Speed

Three of the four carriers have speeds associated with the motion of atoms and free (conduction) electrons. For electrons, quantum effects persist to high temperatures, whereas for fluid particles and phonons, room temperature classical descriptions generally suffice. The speed of light in vacuum c_o is a physical constant, although it decreases during interactions with matter. Figure 1.6 gives examples of thermal speeds, starting with the Brownian motion of copper particles in water (with a dependence on the mass of the particle, Section 6.10), which is rather low. The lighter particles in thermal motion have higher thermal speeds. Electrons, travelling at the Fermi speed, have the highest speed of such particles. The highest speed achievable is the speed of light in a vacuum $u_{ph,\mathrm{o}} = c_\mathrm{o}$, which is reached by photons (quasi-particles).

1.7 Periodic Table of Elements

The periodic table of elements, with their bulk and atomic properties, is given in Appendix A, Tables A.1 and A.2. The principal carrier energies and interactions determine their energy-storage and energy-transport properties, and some of these properties for elements are also listed in Tables A.1 and A.2. The properties listed

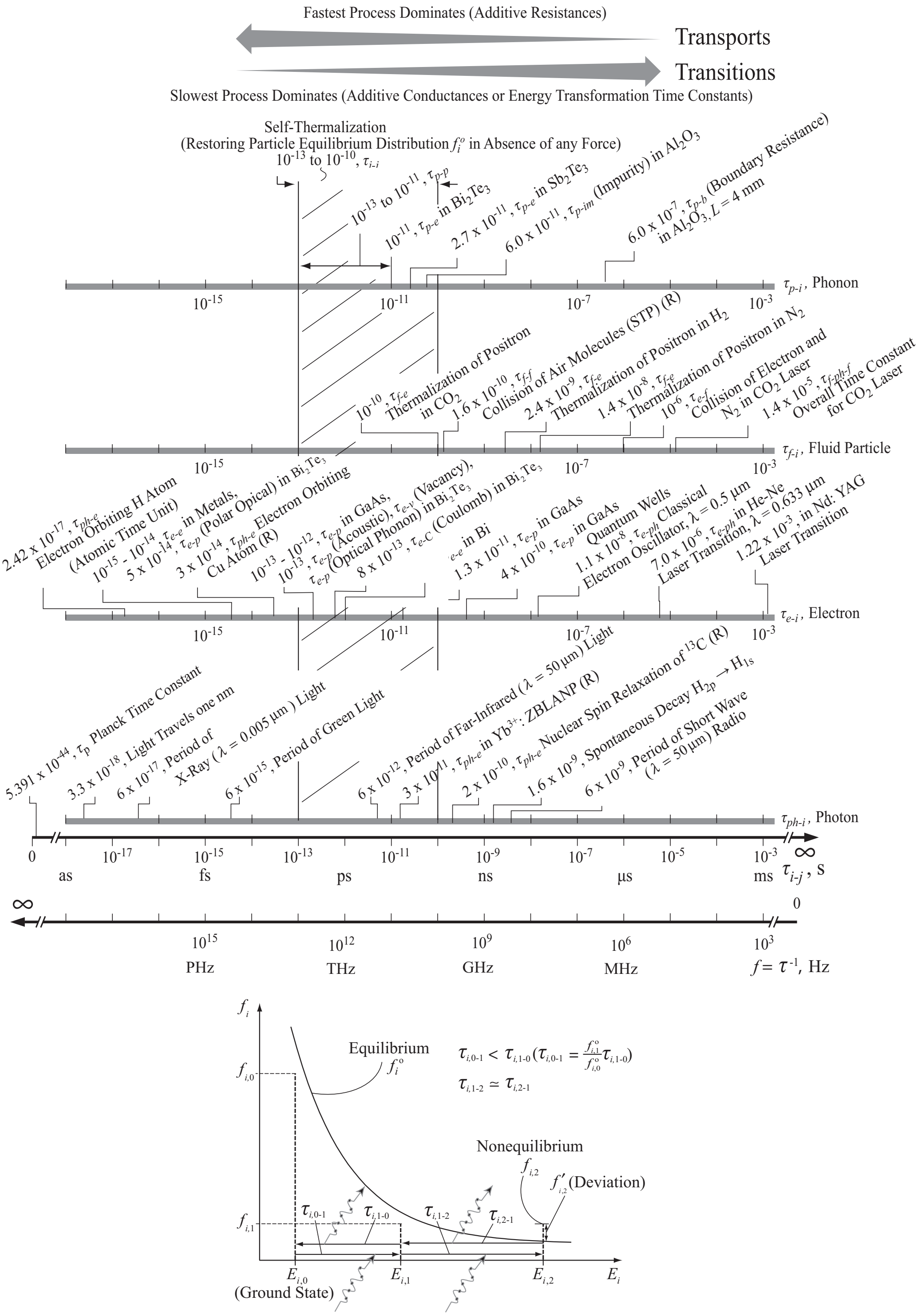
Fastest Process Dominates (Additive Resistances)
Transports
Transitions
Slowest Process Dominates (Additive Conductances or Energy Transformation Time Constants)
Self-Thermalization
(Restoring Particle Equilibrium Distribution f_i^o in Absence of any Force)
10^{-13} to 10^{-10}, τ_{i-i}
10^{-13} to 10^{-11}, τ_{p-p}
10^{-11}, τ_{p-e} in Bi_2Te_3
2.7×10^{-11}, τ_{p-e} in Sb_2Te_3
6.0×10^{-11}, τ_{p-im} (Impurity) in Al_2O_3
6.0×10^{-7}, τ_{p-b} (Boundary Resistance) in Al_2O_3, $L = 4$ mm
10^{-15}
10^{-11}
10^{-7}
10^{-3}
τ_{p-i}, Phonon
10^{-10}, τ_{f-e} Thermalization of Positron in CO_2
1.6×10^{-10}, τ_{f-f} Collision of Air Molecules (STP) (R)
2.4×10^{-9}, τ_{f-e} Thermalization of Positron in H_2
1.4×10^{-8}, τ_{f-e} Thermalization of Positron in N_2
10^{-6}, τ_{e-f} Collision of Electron and N_2 in CO_2 Laser
1.4×10^{-5}, τ_{f-ph-f} Overall Time Constant for CO_2 Laser
10^{-15}
10^{-7}
10^{-3}
τ_{f-i}, Fluid Particle
2.42×10^{-17}, τ_{ph-e} Electron Orbiting H Atom (Atomic Time Unit)
10^{-15} - 10^{-14}, τ_{e-e} in Metals,
5×10^{-14}, τ_{e-p} (Polar Opical) in Bi_2Te_3
3×10^{-14}, τ_{ph-e} Electron Orbiting Cu Atom (R)
10^{-13} - 10^{-12}, τ_{e-p} in GaAs,
10^{-13}, τ_{e-p} (Acoustic), τ_{e-v} (Vacancy), τ_{e-p} (Optical Phonon) in Bi_2Te_3
8×10^{-13}, τ_{e-C} (Coulomb) in Bi_2Te_3
τ_{e-e} in Bi
1.3×10^{-11}, τ_{e-p} in GaAs
4×10^{-10}, τ_{e-p} in GaAs Quantum Wells
1.1×10^{-8}, τ_{e-ph} Classical Electron Oscillator, $\lambda = 0.5$ μm
7.0×10^{-6}, τ_{e-ph} in He-Ne Laser Transition, $\lambda = 0.633$ μm
1.22×10^{-3}, in Nd: YAG Laser Transition
10^{-15}
10^{-11}
10^{-7}
10^{-3}
τ_{e-i}, Electron
5.391×10^{-44}, τ_p Planck Time Constant
3.3×10^{-18}, Light Travels one nm
6×10^{-17}, Period of X-Ray ($\lambda = 0.005$ μm) Light
6×10^{-15}, Period of Green Light
6×10^{-12}, Period of Far-Infrared ($\lambda = 50$ μm) Light
3×10^{-11}, τ_{ph-e} in Yb^{3+}: ZBLANP (R)
2×10^{-10}, τ_{ph-e} Nuclear Spin Relaxation of ^{13}C (R)
1.6×10^{-9}, Spontaneous Decay $H_{2p} \rightarrow H_{1s}$
6×10^{-9}, Period of Short Wave ($\lambda = 50$ μm) Radio
τ_{ph-i}, Photon
0
10^{-17}
10^{-15}
10^{-13}
10^{-11}
10^{-9}
10^{-7}
10^{-5}
10^{-3}
∞
as
fs
ps
ns
μs
ms
τ_{i-j}, s
∞
0
10^{15}
PHz
10^{12}
THz
10^{9}
GHz
10^{6}
MHz
10^{3}
$f = \tau^{-1}$, Hz
f_i
$f_{i,0}$
$f_{i,1}$
Equilibrium
f_i^o
$\tau_{i,0\text{-}1} < \tau_{i,1\text{-}0} (\tau_{i,0\text{-}1} = \frac{f_{i,1}^o}{f_{i,0}^o} \tau_{i,1\text{-}0})$
$\tau_{i,1\text{-}2} \simeq \tau_{i,2\text{-}1}$
Nonequilibrium
$f_{i,2}$
$f'_{i,2}$ (Deviation)
$\tau_{i,0\text{-}1}$
$\tau_{i,1\text{-}0}$
$\tau_{i,1\text{-}2}$
$\tau_{i,2\text{-}1}$
$E_{i,0}$
(Ground State)
$E_{i,1}$
$E_{i,2}$
E_i

Figure 1.5. Kinetics of atomic-level energy transport and transition interaction. Examples of typical energy interaction (transition) times for various principal energy carrier pairs. The frequency (here defined as $1/\tau$) is also shown. Unless specified, $T = 300$ K. Symbol R indicates resonance. Energy kinetics represented by time constants create nonequilibrium energy occupancy of carriers, and in order to proceed the kinetics should favor the increase/decrease in population.

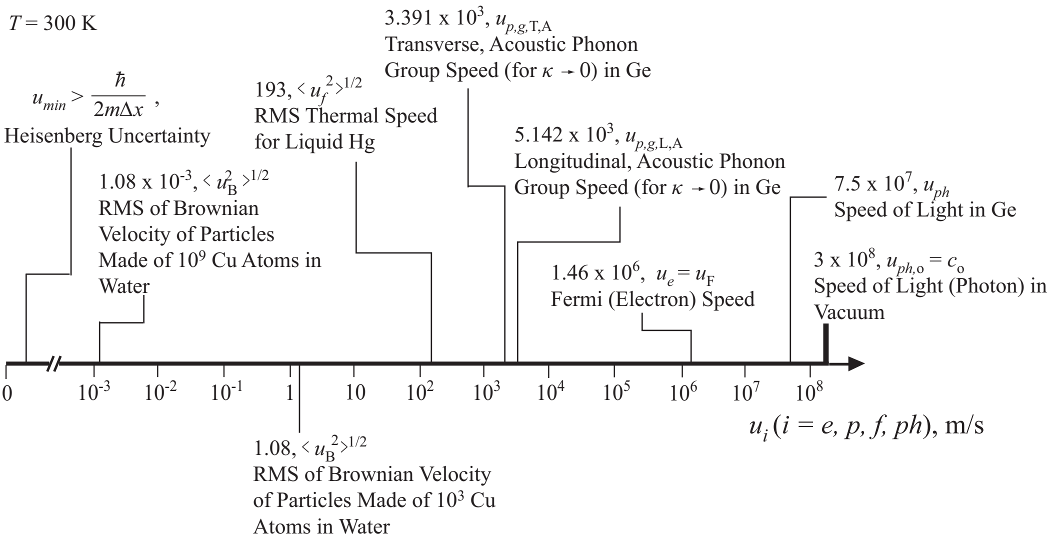
$T = 300$ K
$u_{min} > \frac{\hbar}{2m\Delta x}$,
Heisenberg Uncertainty
1.08×10^{-3}, $\langle u_B^2 \rangle^{1/2}$
RMS of Brownian Velocity of Particles Made of 10^9 Cu Atoms in Water
193, $\langle u_f^2 \rangle^{1/2}$
RMS Thermal Speed for Liquid Hg
3.391×10^3, $u_{p,g,T,A}$
Transverse, Acoustic Phonon Group Speed (for $\kappa \rightarrow 0$) in Ge
5.142×10^3, $u_{p,g,L,A}$
Longitudinal, Acoustic Phonon Group Speed (for $\kappa \rightarrow 0$) in Ge
1.46×10^6, $u_e = u_F$
Fermi (Electron) Speed
7.5×10^7, u_{ph}
Speed of Light in Ge
3×10^8, $u_{ph,o} = c_o$
Speed of Light (Photon) in Vacuum
0
10^{-3}
10^{-2}
10^{-1}
1
10
10^2
10^3
10^4
10^5
10^6
10^7
10^8
$u_i (i = e, p, f, ph)$, m/s
1.08, $\langle u_B^2 \rangle^{1/2}$
RMS of Brownian Velocity of Particles Made of 10^3 Cu Atoms in Water

Figure 1.6. Typical principal carrier speeds (when applicable, $T = 300$ K). For the electrons, the Fermi speed is used, whereas for the phonon and fluid particles, the thermal speed is used. For the photons, the speed of light is used.

are for the state at $T = 300$ K and $p = 1$ atm, with the most common phase or a stated phase (the diamond phase of carbon, for example). An example is given in Figure 1.7, where the thermal conductivity of elements (Table A.1) is plotted versus the atomic number. Among the high thermal conductivity elemental solids, the thermal conductivity of diamond (a crystalline solid phase of C) is almost entirely due to phonon transport k_p, while those of metals such as Cu, Ag, and Au are dominated by electron transport k_e. They are marked in Figure 1.7. Those elements in the gaseous phase have the lowest thermal conductivities k_f.

The transport of thermal energy in various phases and by various principal heat carriers is discussed in Chapters 3 to 7. The bulk properties of elements (Table A.1) include the molecular weight, specific heat capacity, density, thermal conductivity, melting temperature, phase state, electrical conductivity, heat of fusion, heat of evaporation, and melting temperature. The atomic properties (Table A.2) include the electronic orbital structure, first ionization energy, crystal structure, electronegativity, cohesive energy, atomic radius, oxidation states, isotopes, lattice constant, and mean Debye temperature. Electronegativity is the potential of an atom to attract electrons to itself (fluorine is the most electronegative). The electronegativity ranges from 0.7 for Fr to 3.98 for F. The first ionization energy (the energy required to remove the outermost orbital electron from an atom) varies from 3.98 eV for C to 24.58 eV for He.

The group number (1 through 18) is the number assigned to the vertical columns of the periodic table, and elements within the same group all have the same number of electrons in their outer electron shells (Table A.2), as well as similar chemical properties. The group 18 elements have a full outer electronic shell and no tendency

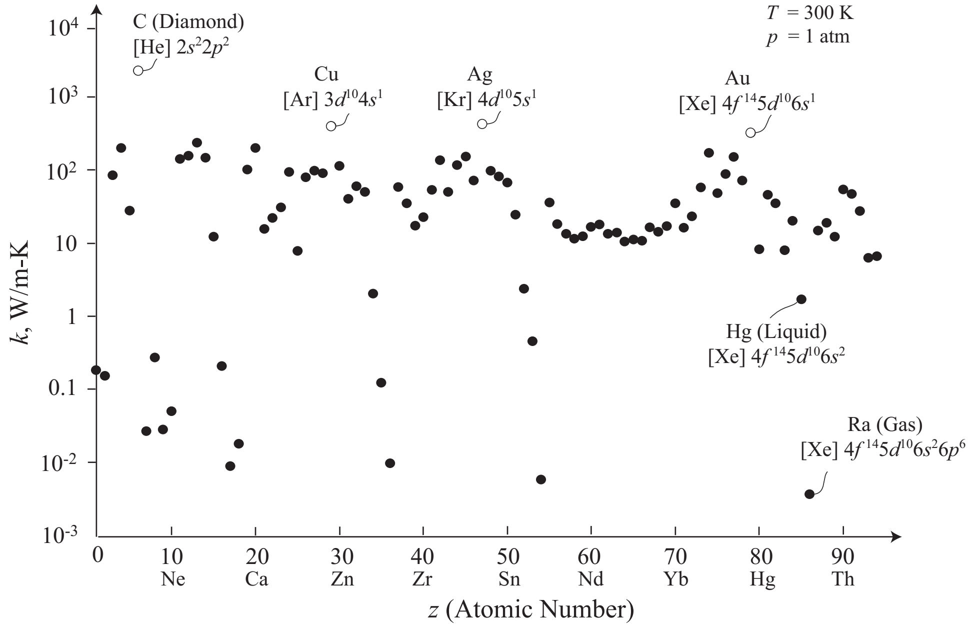

Figure 1.7. Variation of thermal conductivity k of elements (Appendix A, and Table A.1) with respected to atomic number z. The experimental results are for $T = 300$ K (and $p = 1$ atm, when relevant). Most elements are in the crystalline phase, but a few are in the gas phase and Hg is in the liquid phase. High k solids are also marked along with their electronic orbitals.

to lose, gain, or share electrons. The elements in that group are thus chemically inert and gaseous under atmospheric conditions (0.1013 MPa and 288.15 K), leading to their being termed the noble gases.

Group 1 alkali metals (highly active) on the left-hand side are followed by a column of group 2 alkaline-earth metals (known for their oxides). These columns are followed by a block of 40 elements divided into ten columns of four elements each. This group collectively called the transition metals (have or can rise to an incomplete d sub-shell). Groups 13 through 18 make up the right-hand side of the table. A diagonal dividing line separates the nonmetals in the upper-right-hand portion of this block, such as oxygen, carbon, and nitrogen, from the metals such as tin and lead in the lower-left portion.

There is an additional block of 28 elements, divided into two rows of 14 elements each, that is usually placed beneath the main table. These are the rare-earth metal elements, whose properties are all remarkably similar. This additional block belongs between the first block, consisting of groups 1 and 2, and the transition-metals-block. The chemical properties of the lanthanides (elements 57–71) and the actinides (elements 89–103) are also very similar to each other.

Semiconductors are defined in the Glossary and have no conduction electrons at $T = 0$ K, but at higher temperatures become conductors. The elemental and compound semiconductors are made from elements in groups 12-16. Elemental semiconductors (group 12) have increasing room-temperature electrical conductivity σ_e with increasing atomic weight.

Group 17 consists of halogens, which are nonmetals, and are highly reactive. Noble elements, group 18, are highly nonreactive (outer shell is full).

The filling order of the quantum states (wave functions) of electrons, commonly known as orbitals, is [s, p, d, and f are designations of the first four azimuthal quantum numbers (Section 2.6.6)]

$$\begin{array}{llll}
1s & & & \\
2s & 2p & & \\
3s & 3p & 3d & \\
4s & 4p & 4d & 4f \\
5s & 5p & 5d & 5f \\
6s & 6p & 6d & \\
7s. & & &
\end{array}$$

The s orbitals have up to 2 electrons, p up to 6, d up to 10, and f up to 14. For example, Xe ($1s^2 2s^2 2p^6 3s^2 3p^6 3d^{10} 4s^2 4p^6 4d^{10} 5s^2 5p^6$) has 54 electrons (atomic number 54). Note that the next element Cs has its 6s orbital occupied before 5d, and La is $[\mathrm{Xe}]5d^1 6s^2$ and Hf is $[\mathrm{Xe}]4f^{14} 5d^2 6s^2$.

We will discuss quantum numbers and electron wave functions in connection to the solution of the Schrödinger equation in Section 2.6. In the periodic table of the elements we also use the letter and number of the highest energy orbital to designate a group of elements, as shown in Table A.2. The f block is divided into a lanthanide (La) series and an actinide (Ac) series.

As the nuclear charge and the number of electrons increase, the electrons are pulled closer to the nucleus and the atomic diameter decreases. There is a screening effect by the inner electrons, so the outer electrons experience an effective nuclear charge.

We will examine various chemical compounds (natural or synthesized) and in various phases, for their desired thermal energy storage, transport, and conversion. These are done by examination of their bonds and thermal motions (defining their temperature), their quantum energy states, and their interaction kinetics.

1.8 Heat Transfer Physics: Atomic-Level Energy Kinetics

Heat transfer physics describes the transport, storage, and transitions of principal energy carriers appearing in the macroscopic energy equation (Table 1.1), which is central to heat transfer analysis.

1.8.1 Thermal Energy Storage

Energy is stored in principal carriers both as kinetic (translational, rotational, and vibrational) and potential (positions of nuclei and electrons) energy. Depending on the degrees of freedom of motion and the extent of influence of other carriers (or other entities in the system), these energies vary among the different carriers. Table 1.6 shows how the specific heat capacity (at constant volume or pressure) describes energy storage (sensible heat) in each carrier.

Internal motion enters into the carrier specific heat capacity through, for example, the frequency of vibration of atoms in a crystal (lattice). In the Debye model of solid specific heat capacity, the maximum frequency of vibration is designated as ω_D, called the Debye cut-off frequency or Debye frequency (a filtering parameter). We will show that, for monatomic crystals, ω_D is close to the maximum frequency obtained from the interatomic force constant and the atomic mass (Section 2.5.3). The temperature-dependent specific heat capacity of monatomic, crystalline solids is related to this frequency through (Section 4.7)

$$c_{v,p}(T) = 9\frac{k_\mathrm{B}T}{m}\left(\frac{k_\mathrm{B}T}{\hbar\omega_\mathrm{D}}\right)^3 n\int_0^{\hbar\omega_\mathrm{D}/k_\mathrm{B}T}\frac{x^4e^x}{e^x-1}\,\mathrm{d}x,\quad \frac{\hbar\omega_\mathrm{D}}{k_\mathrm{B}T}\equiv\frac{T_\mathrm{D}}{T}$$

$$\text{phonon specific heat of monatomic, crystalline solids,} \qquad (1.13)$$

where m is the mass of atom, n is the number of atoms per unit volume, ω is the phonon angular frequency, and the scaled energy $x = \hbar\omega/k_\mathrm{B}T$ is integrated up to the Debye energy $\hbar\omega_\mathrm{D}/k_\mathrm{B}T \equiv T_\mathrm{D}/T$, which defines the Debye temperature T_D. The higher the cut-off frequency, the higher the temperature needed to reach a constant specific heat (or the more temperature sensitive the heat capacity is at moderate temperatures). Here, the kinetics of phonon energy storage are contained in ω_D.

In (1.13),[†] the Debye frequency is related to the Debye temperature T_D, and for $T \gg T_\mathrm{D}$ we will show that per atom and per mass $c_{v,p}$ is equal to $3k_\mathrm{B}$, which represents 3 degrees of freedom for both the kinetic and potential energies.

1.8.2 Thermal Energy Transport

Transport of thermal energy by phonons and electrons is presented by the Fourier law and phonon and electron conductivities k_p and k_e. The magnitude of these conductivities is limited by carrier scattering (the diffusion limit), and when these resistances are not present, ballistic transport occurs. Fluid particles experiencing thermal motion while under an external force (i.e., pressure gradient) undergo a net motion. The thermal motion of fluid particles results in a similar Fourier conduction and conductivity k_f.

The microscopic (Boltzmann transport) heat transfer rate by carrier i having velocity $\boldsymbol{u}_i$, energy E_i and energy occupancy deviation from equilibrium f_i', is given by (1.23) where α is the polarization, μ is the chemical potential and κ_i is the wave vector.. For the case of conduction this is set to the Fourier law, thus defining the thermal conductivity k_i (assuming isotropy).

The simplified form of the Boltzmann transport theory based on the relaxation time (Section 4.9.2), and also the kinetic theory of gases (Section 6.8.2) leads to the

---

[†] (x.y) denotes it means Chapter x and Equation number y.

Table 1.6. *Thermal energy storage (kinetic and potential) in principal carriers. The specific heat capacities are defined as,* $\partial e/\partial T|_v \equiv c_v$, $\partial h/\partial T|_p \equiv c_p$, $c_p - c_v = T\beta^2/\rho\boldsymbol{\kappa}$, *where the volumetric thermal expansion coefficient and isothermal compressibility are* $\beta \equiv \partial v/\partial T|_p/v$, *and* $\boldsymbol{\kappa} \equiv -\partial v/\partial p|_T/v$.

Carrier	Kinetic energy	Potential energy storage	Temperature dependence of energy occupancy	Quantum effects
Phonon (lattice vibration)	atoms vibrate about their equilibrium position, governed by interatomic potential; motion is anharmonic and three dimensional	weak and strong interatomic forces, and potentials, for harmonic motion the kinetic and potential energies are equal	boson	at high temperatures (marked by the Debye temperature), anharmonic classical behavior is reached, but at low temperatures quantum effects and harmonic behavior are dominant
Electron (free or bound)	electrons move around nuclei in three-dimensional motion and depending on their orbits are divided into core, valence, and conduction electrons	electric charge potential between electrons and nuclei	fermion	strong quantum behavior at all temperatures; heat capacity per electron is small at moderate temperatures
Fluid particle (gas or liquid phase)	nucleus–electron collective translational, vibrational and rotational motions (polyatomic) as well as electron motion around nuclei	for gases the potential energy vanishes for ideal gas and increases as the thermodynamic critical point is approached (dense gas); for liquids the potential energy can reach the kinetic energy	in additional to M–B distribution, vibrational and rotational energies are activated at certain transition temperatures	strong quantum behavior, at high temperatures (above transition temperatures) heat capacity of polyatomic gas approaches the classical behavior
Photon	under diffusive photon transport (Table 1.7), specific heat capacity can be assigned to photons	photon trapping	boson	significant quantum characteristics, although classical treatment (EM wave) is also used

following relation for the thermal conductivity, and we generalize it for all carriers as

$$\begin{aligned} k_i &= \frac{1}{3} n_i c_{v,i} u_i \lambda_i \\ &= \frac{1}{3} n_i c_{v,i} u_i^2 \tau_i, \end{aligned} \tag{1.14}$$

where n_i is the number of carriers per unit volume, u_i is the carrier-average speed, λ_i is the carrier-average mean free path, and τ_i is the carrier-average scattering relaxation time ($\tau_i = \lambda_i / u_i$).

In general, the carrier population will have a range of transport properties and here averages are used. For a carrier travelling in a medium of linear dimension L, ballistic motion refers to $\lambda_i \gg L$ and localization refers to $\lambda_i \ll L$. When fluid particle collisions are not present, collisions with the bounding surface determine energy transport (this happens in the molecular-flow regime, or Knudsen regime). The Knudsen number $\mathrm{Kn}_L = \lambda_i / L$, defines the molecular-flow regimes as $\mathrm{Kn}_L \gg 1$. In the viscous-flow regime ($\mathrm{Kn}_L \ll 1$, where the molecular collisions dominate), the net (macroscopic) motion can be laminar (ordered) or turbulent (chaotic fluctuations). Heat transfer by net motion is referred to here as convective heat transfer.

Photons carry energy without any resistance in a vacuum and experience scattering, absorption, and emission when interacting with matter. When the absorption is rather large, such that distant effects are negligible, the system exhibits the diffuse limit of photon transport. Table 1.7 summarizes some of these attributes of microscale transport. The radiative properties of matter include its spectral (wavelength-dependent) absorption and emission, which depend on its fine electronic structure and their motions/displacements.

Similar to the phonon specific heat capacity previously given, the Callaway model (single-mode relaxation time) of the phonon thermal conductivity of crystalline solids is (Section 4.9.2)

$$k_p = \left(48\pi^2\right)^{1/3} \frac{1}{a} \frac{k_\mathrm{B}^3}{h_\mathrm{P}^2} \frac{T^3}{T_\mathrm{D}} \int_0^{T_\mathrm{D}/T} \tau_p(x) \frac{x^4 e^x}{(e^x - 1)^2} \mathrm{d}x \quad \text{phonon thermal conductivity,} \tag{1.15}$$

where a is the lattice constant. Here τ_p is the effective phonon relaxation time. The longer the relaxation time, the larger the phonon thermal conductivity. The relaxation time is related to the mean free path, through the carrier speed as, $\lambda_i = u_i \tau_i$. The kinetics of phonon transport is represented in τ_p and ω_D.

1.8.3 Thermal Energy Transformation

From the macroscopic energy equation of Table 1.1, Thermal energy (which is related to the kinetic energy or motion) of systems is directly controlled in the

Table 1.7. *Transport kinetics of thermal energy by principal carriers (e.g., k_i thermal conductivity, $i = p, e, f, ph$).*

Carrier	Transport regimes	Transport mechanism	Controlling kinetics
Phonon	diffusive ($\lambda_p \ll L$, controlled by scattering) or ballistic ($\lambda_p \gg L$, no resistance, except at boundaries)	phonons of energy $\hbar\omega_p$ (or bulk heat capacity $\rho c_{v,p}$) travel at speed u_p and encounter resistance (as represented by mean free path λ_p) by conduction electrons, other phonons, impurities, and grain boundaries	interphonon scattering rate, phonon-impurity, and phonon-grain boundary scattering rates
Electron	diffusive (controlled by scattering), tunnelling, or by electric field (drift)	electrons of heat capacity $n_e c_{v,e}$ travel at Fermi speed $\langle u_{\rm F} \rangle$ and encounter resistance (mean free path λ_e) by phonons and impurities	electron–phonon and electron–impurity scattering rates
Fluid particle	convective	fluid particle transit, fluid flows with a net speed $\overline{u}_f$ and travels distance L in time $\tau_f = L/\overline{u}_f$, in single-phase flow the fluid particle will have change in its sensible heat during this transit	in laminar flow the fluid thermal conductivity is not altered, but in turbulent flow (containing chaotic velocity fluctuations) it is augmented by turbulent mixing (eddy) conductivity
	diffusive/viscous (controlled by collision), ballistic (molecular flow), transitional (moderate Knudsen number $\mathrm{Kn}_L = \lambda_f/L$), and net (bulk) motion called convection	fluid particles of energy $\rho_f c_{v,f}$ travel at thermal speed $\langle u_f \rangle$ and collide (mean free path λ_f) with each other or with surfaces, when there is no collision the transport is ballistic	interfluid particle collisions or fluid particle surface scattering rates
Photon	transparent (vacuum, no absorption or emission), semi-transparent, or diffusive (dominated by strong absorption/scattering, also called optically thick)	photons of energy $\hbar\omega_{ph}$ travel at speed u_{ph} and are absorbed, scattered, and emitted (mean free path λ_{ph}); the interaction is mostly through coupling of the photon as an electromagnetic wave with electric entities such as dipoles	photon scattering and absorption (EM wave–electric entity interactions) rates, photon emission rate

intended heating/cooling, or is altered as a result of the heat loss in energy conversion. So, the kinetics of absorption or addition of carrier kinetic energy relates to spectral excitation or de-excitation of phonons, electrons, and fluid particles.

For example, the transport of photon through media involves absorption and for the case of a medium allowing for absorption of photons/excitation of free electrons

Table 1.8. *Examples of volumetric* $\dot{S}_{i\text{-}j}/V$ *and surface* $\dot{S}_{i\text{-}j}/A$ *thermal energy conversions (resulting in heating/cooling) and their kinetics relations. R stands for a resonance phenomenon.*

Thermal energy conversion	Relation
Phonon Ultrasonic heating (Section 4.18)	$\frac{\dot{S}_{p\text{-}p}}{V} = 2\sigma_p I_{ac} = 2\gamma_G^2 \frac{c_{v,p}}{2u_{p,\mathrm{A}}^2} \frac{\omega\tau_p}{1+2\omega^2\tau_p^2} I_{ac}$
Laser cooling of solids (R) (Section 7.12)	$\frac{\dot{S}_{ph,e,p}}{A} = N_d \frac{\tau_{ph,tr}}{\tau_{ph\text{-}e\text{-}p}} (1 - \frac{\omega_{ph,e}}{\omega_{ph,i}} \frac{\tau_{e\text{-}ph}^{-1}}{\tau_{e\text{-}ph}^{-1} + \tau_{e\text{-}p}^{-1}}) q_{ph,i}$
Electron Joule heating (Section 5.13)	$\frac{\dot{S}_{e\text{-}p,\mathrm{J}}}{V} = \frac{j_e^2}{\sigma_e} = \frac{j_e^2}{n_{e,c} e_c \mu_e}$ $\sigma_e = \frac{8\pi}{3} (\frac{1}{2\pi^2\hbar^2})^{3/2} e_c^2 m_e^{1/2} \tau_{e,o} (\frac{E_\mathrm{F}}{k_\mathrm{B} T})^{s+3/2}$ metals
Peltier cooling/heating (Section 5.16)	$\frac{\dot{S}_{e\text{-}p,\mathrm{P}}}{A} = \mp\alpha_S T j_e,\ \alpha_S = \mp\frac{\pi^3}{3}\frac{k_\mathrm{B}}{3}\frac{s+3/2}{E_\mathrm{F}/k_\mathrm{B}T}$ metals
Fluid particle Exothermic or endothermic reaction (Section 6.5)	$\frac{\dot{S}_{f\text{-}f,r}}{V} = -\rho_\mathrm{F} \Delta h_{r,\mathrm{F}} \frac{n_{f,\mathrm{F}}}{\tau_{f\text{-}f}} e^{-\Delta E_a/k_\mathrm{B}T}$
Surface evaporation (R) (condensation) (Section 6.8.1)	$\frac{\dot{S}_{f\text{-}f,lg}}{A} = -\Delta h_{lg} \dot{m}_{f,lg},\ \ \dot{m}_{f,lg,max} = \frac{1}{4} m n_f (\frac{8k_\mathrm{B}T}{\pi m})^{1/2}$
Photon Laser cooling of atomic gases (R) (Section 7.13.2)	$\frac{\dot{S}_{ph,e,p}}{V} = -\dot{n}_{ph}\hbar\Delta\omega_o\dot{\gamma}_{ph\text{-}t\text{-}ph}$
Dielectric heating (Section 3.4)	$\frac{\dot{S}_{ph,e,p}}{V} = \epsilon_\mathrm{o}\epsilon_{e,c}\omega\, \overline{\boldsymbol{e}_e \cdot \boldsymbol{e}_e}$

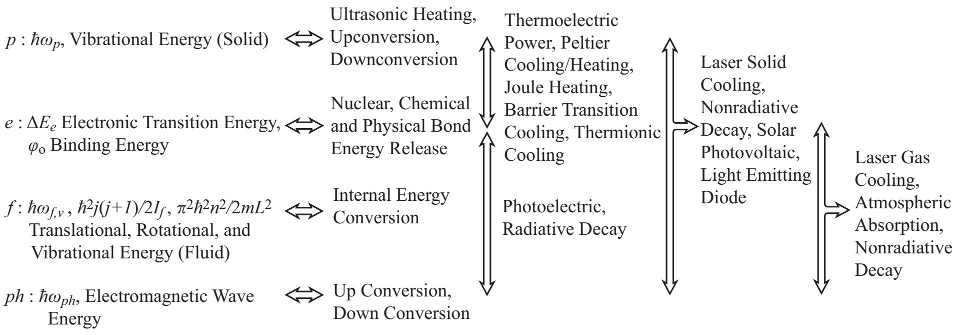
$p : \hbar\omega_p$, Vibrational Energy (Solid)
$e : \Delta E_e$ Electronic Transition Energy, φ_o Binding Energy
$f : \hbar\omega_{f,v}$, $\hbar^2 j(j+1)/2I_f$, $\pi^2\hbar^2 n^2/2mL^2$ Translational, Rotational, and Vibrational Energy (Fluid)
$ph : \hbar\omega_{ph}$, Electromagnetic Wave Energy
Ultrasonic Heating, Upconversion, Downconversion
Nuclear, Chemical and Physical Bond Energy Release
Internal Energy Conversion
Up Conversion, Down Conversion
Thermoelectric Power, Peltier Cooling/Heating, Joule Heating, Barrier Transition Cooling, Thermionic Cooling
Photoelectric, Radiative Decay
Laser Solid Cooling, Nonradiative Decay, Solar Photovoltaic, Light Emitting Diode
Laser Gas Cooling, Atmospheric Absorption, Nonradiative Decay

(metals), we have (Section 7.8)

$$\sigma_{ph,\omega} = \frac{1}{\lambda_{ph,\omega}} = \frac{1}{u_{ph}\tau_{ph,a,\omega}} = (\frac{2n_{e,c}e_c^2\langle\langle\tau_e\rangle\rangle\omega}{\epsilon_\mathrm{o} m_e u_{ph}^2})^{1/2}, \qquad (1.16)$$

where $\sigma_{ph,\omega}$(1/m) is the spectral photon absorption coefficient (and is related to $\dot{s}_{ph\text{-}e}$, as listed in Table 1.8), $\tau_{ph,a,\omega}$ is the spectral photon relaxation (absorption) time, $\langle\langle\tau_e\rangle\rangle$ is the energy-averaged electron relaxation time (Section 5.7), and ω is the angular frequency of the photon. This energy in turn adds to the kinetic energy (i.e., temperature) of the carrier(s) of the medium. The natural and engineered transformation of energy among principal energy carriers continues to be an important subject of study. In microscopic heat transfer there are many complex heating and cooling processes, and as our understanding of phenomena occurring at the atomic scale increases, we expand the possibilities for energy conversion. Table 1.8 lists some relations of energy transformation rates involving the four principal carriers as well as their heating or cooling effects. Table 1.9 gives examples of mechanisms of energy conversion with explanations of the kinetics.

Some of the more novel energy-conversion methods being studied include the absorption of ultrasound in solids (which involves the interaction of forced external vibrations with phonons), thermoelectric cooling/heating, dielectric and Joule heating, endothermic/exothermic phase changes and chemical reactions, laser cooling of gases, and various other photon–electron interaction-mediated heating–cooling processes in solids and fluids.

In thermoelectricity, the thermoelectric figure of merit Z_e is defined as

$$Z_e T = \frac{\alpha_S^2 \sigma_e T}{k_e + k_p}, \tag{1.17}$$

where α_S is the junction Seebeck coefficient (Section 5.13.2), σ_e is the electrical conductivity, and $k_e + k_p$ is the total (sum of phonon and electric) thermal conductivity. In thermoelectric power generation and cooling, large $Z_e T$ is sought through reduced total thermal conductivity and enhanced α_S and σ_e, using atomic and nanostructure optimizations (Section 5.16.4).

Cooperative processes (Glossary) are those in which more than one carrier assists in promotion (and decay) of an energy transition. This involves couplings among various carriers, these coupling kinetics are critical in such energy conversions. R stands for resonance, indicating an electronic for mechanical resonance energy match is needed or involved. For example, an electronic bandgap, or a bond energy, or a mechanical vibration frequency.

The expressions given in Table 1.8, will be described in the related sections noted, and various variables will be discussed, and the relations developed.

For example, similar to the preceding phonon specific heat and thermal conductivity examples, the acoustic absorption rate of ultrasound in crystals can be described as a volumetric heat source $\dot{s}_p$(W/m^3) as (Section 4.18)

$$\frac{\dot{S}_{p\text{-}p}}{V} = \dot{s}_{p\text{-}p} = 2\sigma_p I_{ac} = 2\gamma_{\mathrm{G}}^2 \frac{c_{v,p}}{2u_{p,\mathrm{A}}^2} \frac{\omega\tau_p}{1 + 2\omega^2\tau_p^2} I_{ac}$$

$$\text{acoustic wave absorption rate}, \tag{1.18}$$

where γ_{G} is the Grüneisen parameter (see Glossary), $u_{p,\mathrm{A}}$ is the average acoustic-phonon speed, ω is the frequency of the external ultrasound wave, and I_{ac} is the ultrasonic intensity of this wave. Again, the kinetics of the energy conversion rate involves the phonon relaxation time τ_p and frequency ω. This energy excites the medium phonons (kinetic energy) and temperature (after phonon thermalization, i.e., equilibrium).

Table 1.9. *Examples of microscale energy transformation (conversion) kinetics (from/to thermal energy), involving principal carriers, $\dot{s}_{ij}$.*

Carrier	Energy conversion mechanism	Cooling/heating	Controlling kinetics
Phonon	phonon-assisted fluorescence emission in electronic transitions (R), $\dot{s}_{ph\text{-}f\text{-}p}$	phonon emission or absorption	relaxation rate of thermal phonons, coupling between photon (electromagnetic wave) and electric entity, coupling between electron and phonon, number density of these three carriers
	ultrasonic heating, $\dot{s}_{p\text{-}p}$	absorption of ultrasound waves	rate of inelastic relaxation of external sound waves by thermal phonons and inter-phonon relaxation
Electron	electrical resistivity (conduction electron), $\dot{s}_{e-p}$	Joule resistive heating	scattering of conduction electrons by phonons and impurities
	dielectrics: coupling of photon (electromagnetic wave) with electric dipoles (R) $\dot{s}_{ph-e-p}$	dielectric (microwave) heating	dielectric loss factor (imaginary part of electric permittivity) and frequency of EM wave
	semiconductors: thermoelectric coupling (R) $\dot{s}_{e-p}$	Peltier cooling/heating	bandgap, Fermi energy, electron relaxation rate, and temperature
Fluid particle	interparticle collision rate in gases, $\dot{s}_{f-f}$	endothermic and exothermic thermal reactions	collision rate, particle concentration, and temperature
	physical adsorption and desorption of gas molecules on solid surfaces with or without photo-assist (R), $\dot{s}_{f-f}$, $\dot{s}_{f-p}$, $\dot{s}_{f-e}$, $\dot{s}_{ph-f-f-p}$	heating (e.g., physical adsorption) and cooling (e.g., physical desorption), chemisorbed vibrational energy transfer to a substrate	attraction force between the gas and surface atoms, number of adsorbed atomic layers, temperature
Photon	conversion of valence electrons in semiconductors to conduction electrons by absorbed photon (R), $\dot{s}_{ph-e}$	heating when some photon absorption leads to high kinetic energy (hot electrons)	absorption rate of photon, lack of multiple-bandgap semiconductors, electron–phonon coupling
	photon emission by conversion of kinetic energy of excited gases (mixture of molecules in translational, vibrational, and rotational motion) (R), $\dot{s}_{f-ph}$	heating by nonradiative decays	rate of collision between species, relaxation time for radiative and nonradiative decays

Heat transfer physics (the kinetics of microscale energy storage, transport, and transitions) addresses energy dynamics at the atomic scale. Examples of the time scales of these atomic-level dynamic interactions are given in Figure 1.5. In general, although shorter time scales are desirable in energy-storage and conversion rates, longer time scales are desirable for high transport rates. When multiple mechanisms are involved in the kinetics, the mechanism with the longest response time dominates the conversion rate, whereas the mechanism with the shortest response (scattering) time dominates the transport. This is evident in the acoustic wave absorption rate in (1.18) and in the phonon thermal conductivity in (1.15). We discuss the evaluation of the various interaction rates, time constants, and relaxation times throughout the text. These are the central governors of the atomic-level heat transfer.

We also discuss recycling of the kinetic energy generated otherwise as losses in energy conversion (e.g., excitation of phonons or vibrational modes of fluid particles), before they are thermalized (turned into heat by collision/scattering with other phonons and fluid particles). This allows for atomic-level energy recycling for higher energy conversion efficiencies.

1.9 Density of States and Carrier Density

The energy state occupancy probability is given by f_i and its equilibrium distribution by f_i^o. However, the structure of matter limits and controls (determines) the energy states it can have. This property of atomic structure is the density of states D_i and is given such that the carrier density n_i is related to f_i and D_i through [an extended form of (1.2)]

$$n_i = \int_0^\infty f_i(E_i) D_i(E_i) \mathrm{d}E_i \qquad i = p, e, ph, \tag{1.19}$$

so D_i is given in the units of inverse of the product of energy and volume.

Similarly the specific entropy (1.6) of carriers is given in terms of f_i as [403]

$$s = k_B \int D_i(E_i)[(f_i \pm 1)\ln(f_i \pm 1) - f_i \ln(f_i)]\mathrm{d}E_i, \ + \text{ for } p \text{ and } ph, - \text{ for } e. \tag{1.20}$$

Since fluids form to the volume of their container, D_i is not used for fluid particles.

The kinetics are associated with some atomic-level energy resonances, which allow for the creation of desired spectral energy behavior in materials and devices. For example, crystalline Si has a relatively narrow optical-phonon bandwidth, as shown in Figure 1.8(a). The phonon density of states D_p is the number of phonon energy states per unit volume and energy $\mathrm{d}E_p$. This material also has an electronic energy bandgap, which is shown in Figure 1.8(b) for its electron density of states D_e.

The photon density of states of Si, $D_{ph}(E_{ph})$, is shown in Figure 1.81(c). This is based on emission (Section 7.10) and is a rough presentation. D_{ph} has a peak near the electron bandgap energy (1.1 eV), which is in the near infrared regime. There is also a peak near the optical-phonon (R) regime. The blackbody emission density of states (called the Debye density of states, which is also used as a model for acoustic

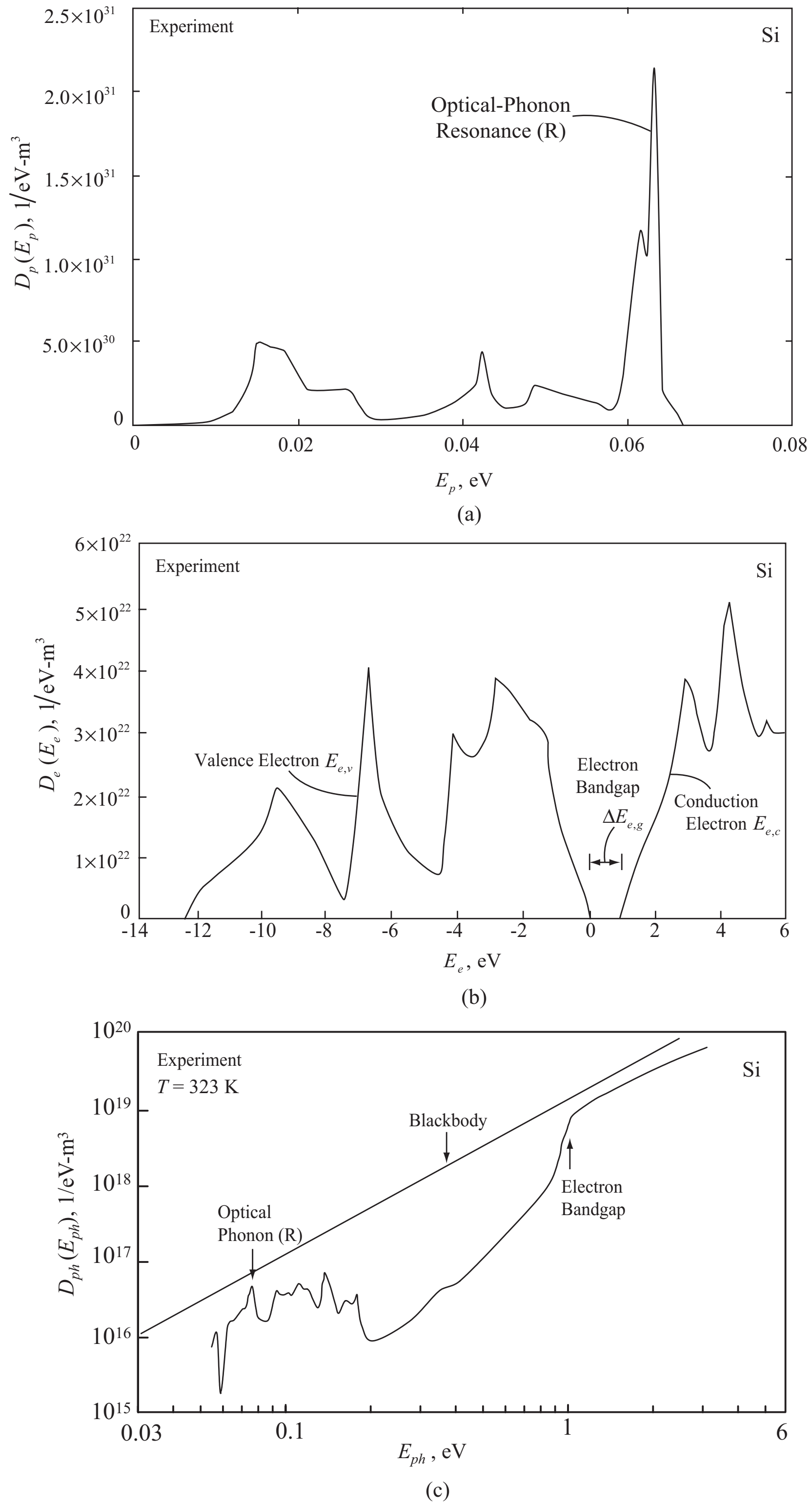

Figure 1.8. (a) Phonon density of states for Si (described in Section 4.6), (b) electron density of states for Si (described in Section 5.7), and (c) photon density of states for Si. Here R stands for resonance. $E_{e,c}$ and $E_{e,v}$ indicate conduction and valence electrons, respectively.

phonons) is also shown and has no resonance features. The total number of carriers is the integral of $D_i f_i \mathrm{d}E_i$, over all polarizations (and spins).

The densities of states are atomic-structure properties (Sections 4.2 and 5.7). The resonant optical phonon (marked with R) has an energy much less than the electron bandgap energy, but does play a role in the absorption and emission of photons from Si (doping can charge the electronic bandgap). Heat transfer physics examines and exploits resonances in these and other carrier interactions. In Figures 1.4 and 1.5, some carrier kinetics resonances are marked with (R).

1.10 *Ab Initio*/MD/BTE/Macroscopic Treatments

Figure 1.9 shows the regimes of application of the Schrödinger equation (Table 2.8), computational molecular dynamics (MD) simulations (this classical treatment is given in Table 2.5), the Boltzmann transport equation (BTE) (Table 3.1), and the macroscopic energy equation (including all carriers) (Table 1.1).

The Schrödinger equation uses the atomic scale units of Table 1.5, in Section 1.5.2 (r_B for length and $\tau_a = m_e r_\mathrm{B}^2/\hbar$ for time). The time-independent Schrödinger equation provides the quantum energy states E_i of each carrier in a field (Hamiltonian), and the time-dependent Schrödinger equation gives the kinetics of transition between these states (transition or relaxation time $\tau_{i\text{-}j}$). The heat flux vector for a molecular chain or wire connecting two photon reservoirs (L and R) is from the master equation of quantum mechanics (Section 4.19.5),

$$\boldsymbol{q}_k = \frac{1}{2A}\sum_{n,m}(E_m - E_n)|S_{n,m}|^2 f_n(\frac{1}{\tau_{n\rightarrow m,L}} - \frac{1}{\tau_{n\rightarrow m,R}})\boldsymbol{s}_{lr}, \quad \text{quantum}, \qquad (1.21)$$

where $E_m - E_n = \hbar\omega_{mn}$ is the transition energy, A is area, $\boldsymbol{s}_{lr}$ is the unit vector connecting L and R, f_n is the normalized population, $S_{n,m}$ is a quantum operator, and $1/\tau_{n\rightarrow m,L}$ and $1/\tau_{n\rightarrow m,R}$ are the interaction rates with the reservoirs. For molecular junctions, the Landauer quantum transport based on the junction scattering is discussed in Section 4.19.6.

The MD uses interatomic interaction units that are r_{nn} the distance between the nearest neighbor atoms, and $\tau_n = \pi/\omega_n$ where ω_n is the natural frequency of atomic vibration (Section 2.5.3 and Table 2.7). The conduction heat flux vector in the classical MD is determined from the relative position and energies of the particles (in a multibody dynamic system) and is given as (Table 3.9)

$$\boldsymbol{q}_k = \frac{1}{V}\frac{\mathrm{d}}{\mathrm{d}t}\sum_i^N (E_{k,i} + E_{p.i})\boldsymbol{x}_i, \qquad (1.22)$$

where N is the number of particles, V is the volume, and E_k and E_p are the particle kinetic and potential energy. For the two-body interaction force $\boldsymbol{F}_{ij}$ this becomes

$$\boldsymbol{q}_k = \frac{1}{V}[\sum_i^N E_i\boldsymbol{u}_i + \frac{1}{2}\sum_{i,j}^N(\boldsymbol{F}_{i,j}\cdot\boldsymbol{u}_i)\boldsymbol{x}_{ij}, \quad \text{MD}, \qquad (1.23)$$

where E_i is the total energy and $\boldsymbol{u}_i$ is the particle (atom) velocity.

The BTE uses the many (N-) atoms length scale $N^{1/3}r_{nn}$ and the particle collision (scattering) relaxation time $\tau_{i\text{-}j}$ (Figure 1.5). The Boltzmann transport scales (Table 3.2) are discussed in Section 3.1.6. The heat flux vector in Boltzmann transport is given by (1.5) and is discussed in Section 3.1.4. A more general form of it is repeated here:

$$\boldsymbol{q}_k = \sum_j \sum_\alpha \frac{1}{2\pi^3} \int (E_j - \mu)\boldsymbol{u}_j f'_j d\boldsymbol{\kappa}_\alpha, \quad \text{Boltzmann (or meso)}, \tag{1.24}$$

where f' is the population deviation from equilibrium, $\boldsymbol{\kappa}$ is the wave vector, μ is chemical potential, $\boldsymbol{u}$ is velocity, and α designates polarization. The summation j is over the carrier (phonon, etc.). The wavevector and momentum vector are related through the de Broglie momentum $\boldsymbol{p} = \hbar\boldsymbol{\kappa}$.

The macroscopic energy equation (Table 1.1) and macroscopic fluid and elastic-solid mechanics (Tables 3.10 and 3.11) assume that the system dimension and time resolutions are large enough that local and temporal variations in density, temperature, velocity, etc., can be represented by smooth (continuous) functions. This is marked by $L \gg \lambda_i$, where λ_i is the mean free path of carrier i. The mean free path signifies how far a carrier travels before it undergoes an encounter with another carrier that significantly alters its momentum (Section 3.1.3). Similarly, the macroscopic time scale is $t \gg \tau_{i\text{-}j}$. The macroscopic length and time scales are given in Table 3.12.

The heat flux vector in macroscopic transport (Table 1.1) is

$$\boldsymbol{q} = \boldsymbol{q}_k + \boldsymbol{q}_u + \boldsymbol{q}_r = -k\nabla T + \rho c_p \boldsymbol{u} T + 2\pi \int_0^\infty \int_{-1}^1 \boldsymbol{s} I_{ph,\omega} \mathrm{d}\mu \mathrm{d}\omega, \quad \text{macro}, \tag{1.25}$$

where $\mu = cos\theta$, θ is the polar angle, and $\boldsymbol{s}$ is the unit vector (Table 7.1).

Note that the t axis in Figure 1.9 can be further marked by other kinetic times listed in Figure 1.5 for each of the carriers. For photons treated as EM waves, the Maxwell equations (Table 3.5) are used at length scales for which quantum effects are not important. The Maxwell equations are also used for describing electric and magnetic quantities and continue to be valid down to the atomic length scale. The Schrödinger-equation-based calculations are called *ab initio* (Latin for from the beginning) calculations and describe what is referred to as the fine structure of matter. The *ab initio* calculations require the least amount of empiricism.

The Schrödinger, Maxwell, Newton, Hamilton, Boltzmann, and macroscopic-energy (and a few other equations; e.g., Langevin, Navier-Stokes (fluid), Navier (elastic solid), Einstein (population rate)) equations are conservation expressions (also called the equations of change) in differential form (e.g., time, space, momentum), along with their related constitutive relations. These equations are specialized for particular length scales and physical phenomena (e.g., classical particles, quasi-particles, fields, waves, continua, probabilities). They describe states or deviation/return to equilibria under various internal and external factors. The constitutive relations include the kinetics (rates), and among them is the Fermi golden rule for interaction rates involving quasi-particles.

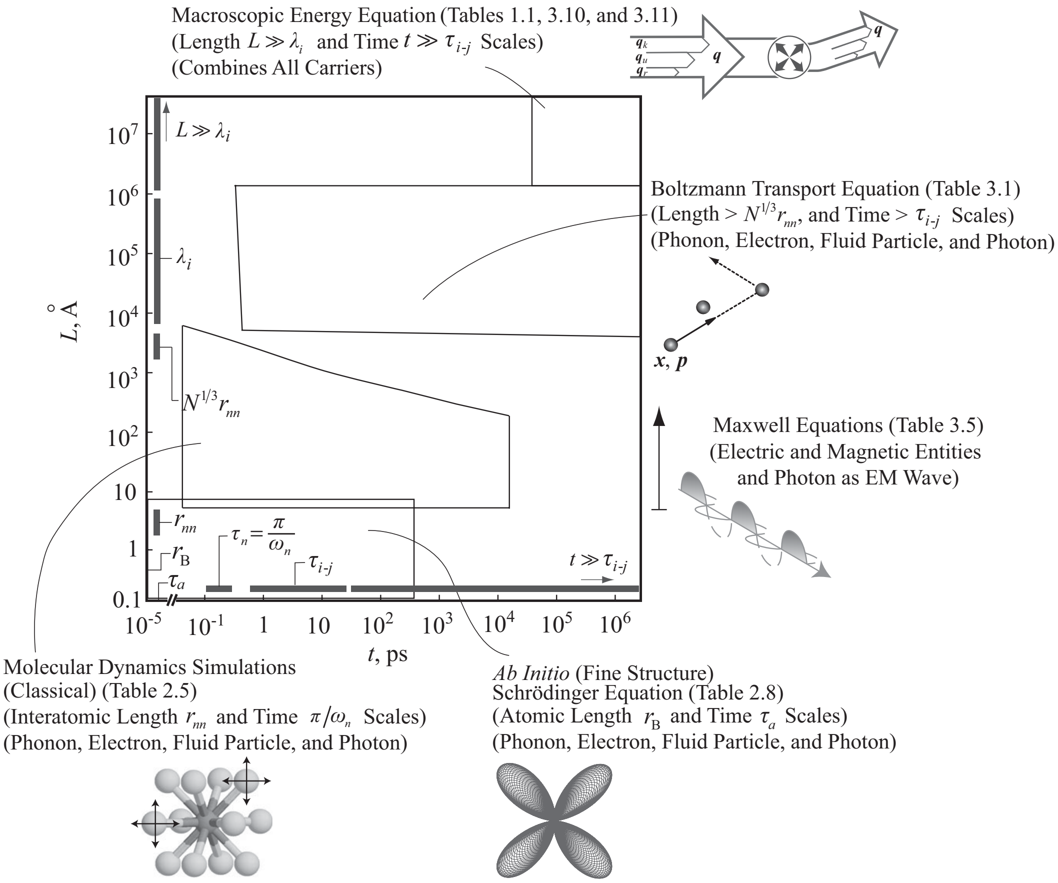
Macroscopic Energy Equation (Tables 1.1, 3.10, and 3.11)
(Length $L \gg \lambda_i$ and Time $t \gg \tau_{i\text{-}j}$ Scales)
(Combines All Carriers)
q_k
q_u
q_r
q
q
10^7
$L \gg \lambda_i$
10^6
10^5
λ_i
10^4
L, Å
10^3
$N^{1/3} r_{nn}$
10^2
10
1
0.1
r_{nn}
r_{B}
τ_a
$\tau_n = \dfrac{\pi}{\omega_n}$
$\tau_{i\text{-}j}$
$t \gg \tau_{i\text{-}j}$
10^{-5}
10^{-1}
1
10
10^2
10^3
10^4
10^5
10^6
t, ps
Boltzmann Transport Equation (Table 3.1)
(Length > $N^{1/3} r_{nn}$, and Time > $\tau_{i\text{-}j}$ Scales)
(Phonon, Electron, Fluid Particle, and Photon)
$\boldsymbol{x}$, $\boldsymbol{p}$
Maxwell Equations (Table 3.5)
(Electric and Magnetic Entities
and Photon as EM Wave)
Molecular Dynamics Simulations
(Classical) (Table 2.5)
(Interatomic Length r_{nn} and Time π/ω_n Scales)
(Phonon, Electron, Fluid Particle, and Photon)
Ab Initio (Fine Structure)
Schrödinger Equation (Table 2.8)
(Atomic Length r_{B} and Time τ_a Scales)
(Phonon, Electron, Fluid Particle, and Photon)

Figure 1.9. Length–time scale regimes for *ab initio*, MD, Boltzmann transport, and macroscopic treatments of heat transfer.

The Schrödinger equation is a continuum (allowing for smooth, spatial variation) equation at the atomic scale, the BTE is a continuum equation at the mesoscale, and the macroscopic momentum and energy equations are continuum equations at larger scales. MD uses the Newton equations to treat multibody dynamics of atomic motion by tracking individual, interacting (through interatomic potential) particles (atoms or molecules).

1.11 Scope

The transport and transitions of principal thermal energy carriers are rendered in Figure 1.10, and are discussed in the following chapters. As shown in Figure 1.10, size effects and the inclusion of various phonon, electron, fluid particle, and photon energy transport/transition kinetics in the macroscopic energy equation, connect heat transfer physics to its applications at various length scales.

In Chapter 2, atoms, their interactions (such as forming bonds), and their collective properties lead to the definition of temperature and other properties. The

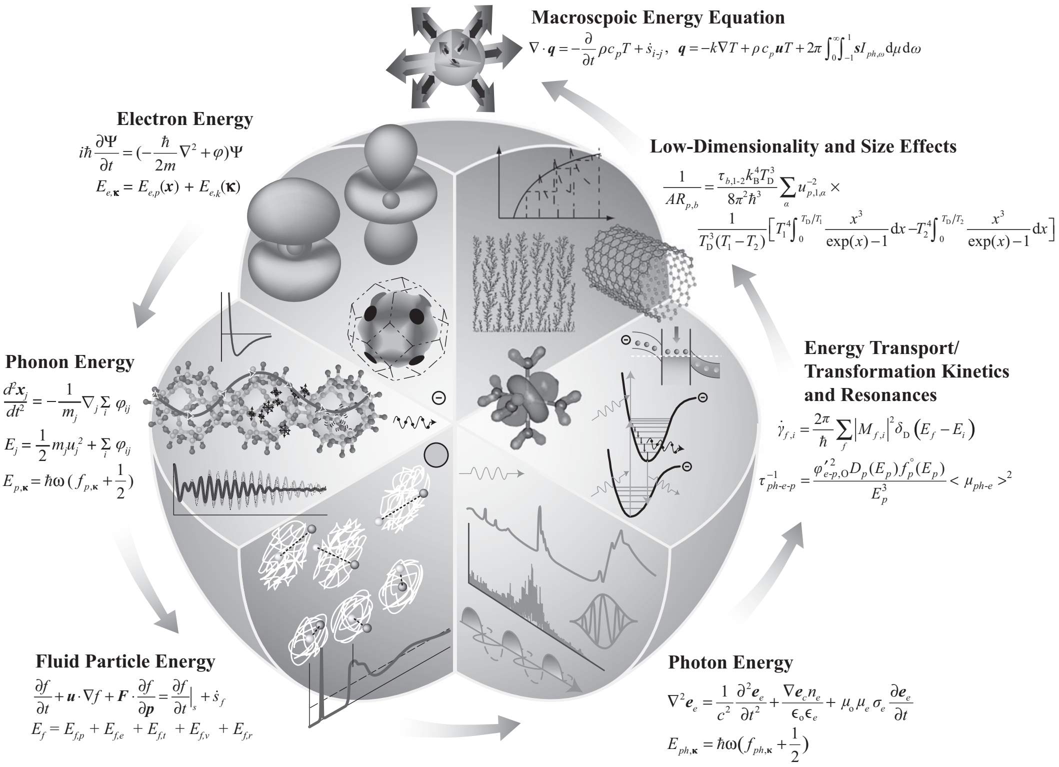
Macroscpoic Energy Equation
$\nabla\cdot\boldsymbol{q}=-\frac{\partial}{\partial t}\rho c_pT+\dot{s}_{i\text{-}j},\quad \boldsymbol{q}=-k\nabla T+\rho c_p\boldsymbol{u}T+2\pi\int_0^\infty\int_{-1}^1\boldsymbol{s}I_{ph,\omega}\mathrm{d}\mu\,\mathrm{d}\omega$
Low-Dimensionality and Size Effects
$\frac{1}{AR_{p,b}}=\frac{\tau_{b,1\text{-}2}k_{\mathrm{B}}^4T_{\mathrm{D}}^3}{8\pi^2\hbar^3}\sum_\alpha u_{p,1,\alpha}^{-2}\times \frac{1}{T_{\mathrm{D}}^3(T_1-T_2)}\left[T_1^4\int_0^{T_{\mathrm{D}}/T_1}\frac{x^3}{\exp(x)-1}\mathrm{d}x-T_2^4\int_0^{T_{\mathrm{D}}/T_2}\frac{x^3}{\exp(x)-1}\mathrm{d}x\right]$
Energy Transport/
Transformation Kinetics
and Resonances
$\dot{\gamma}_{f,i}=\frac{2\pi}{\hbar}\sum_f\left|M_{f,i}\right|^2\delta_{\mathrm{D}}\left(E_f-E_i\right)$
$\tau_{ph\text{-}e\text{-}p}^{-1}=\frac{\varphi_{e\text{-}p,\mathrm{O}}'^2D_p(E_p)f_p^\circ(E_p)}{E_p^3}<\mu_{ph\text{-}e}>^2$
Photon Energy
$\nabla^2\boldsymbol{e}_e=\frac{1}{c^2}\frac{\partial^2\boldsymbol{e}_e}{\partial t^2}+\frac{\nabla\boldsymbol{e}_c n_e}{\epsilon_{\mathrm{o}}\epsilon_e}+\mu_{\mathrm{o}}\mu_e\sigma_e\frac{\partial\boldsymbol{e}_e}{\partial t}$
$E_{ph,\boldsymbol{\kappa}}=\hbar\omega(f_{ph,\boldsymbol{\kappa}}+\frac{1}{2})$
Fluid Particle Energy
$\frac{\partial f}{\partial t}+\boldsymbol{u}\cdot\nabla f+\boldsymbol{F}\cdot\frac{\partial f}{\partial\boldsymbol{p}}=\frac{\partial f}{\partial t}\Big|_s+\dot{s}_f$
$E_f=E_{f,p}+E_{f,e}+E_{f,t}+E_{f,v}+E_{f,r}$
Phonon Energy
$\frac{d^2\boldsymbol{x}_j}{dt^2}=-\frac{1}{m_j}\nabla_j\sum_i\varphi_{ij}$
$E_j=\frac{1}{2}m_ju_j^2+\sum_i\varphi_{ij}$
$E_{p,\boldsymbol{\kappa}}=\hbar\omega(f_{p,\boldsymbol{\kappa}}+\frac{1}{2})$
Electron Energy
$i\hbar\frac{\partial\Psi}{\partial t}=(-\frac{\hbar}{2m}\nabla^2+\varphi)\Psi$
$E_{e,\boldsymbol{\kappa}}=E_{e,p}(\boldsymbol{x})+E_{e,k}(\boldsymbol{\kappa})$

Figure 1.10. A summary rendering of the four principal thermal energy carriers and their transport and interaction. Also shown are the size effects and the macroscopic energy equation.

Schrödinger equation Newtonian and Hamiltonian mechanics (and energy relations) are discussed in relation to molecular interactions and molecular dynamics.

In Chapter 3, the principal energy carrier transport and kinetics theories are reviewed. These form the foundations for the treatments of each carrier in the subsequent four chapters. The Boltzmann transport equation used here for all principal carriers (phonons, electrons, fluid particles, and photons), the probability distribution functions f_i, the stochastic transport equation, and the G–K autocorrelation equation are reviewed. There are also equations that are derived from these, such as the macroscopic energy equation, the equation of radiative transport, the Navier–Stokes equations, and the macroscopic elastic fluid mechanics equation. The unified treatment of transport phenomena by fluid particles, electrons, and phonons has been made in [440], and for all four principal carriers in [85].

Chapter 4 describes phonons, Chapter 5 covers electrons, Chapter 6 details fluid particles, and Chapter 7 explains photons. The unique energy transport (including various inter- and intra-carrier interactions) and storage characteristics of each carrier are described in each of these chapters. The common element unifying the coverage of all of these carriers is the use of the Boltzmann transport equation.

1.12 Problems

Problem 1.1

(a) Express the conductive heat flux vector as $|\boldsymbol{q}_k| = k_s dT_s/dx = k_s \Delta T/\Delta x$. Determine $|\boldsymbol{q}_k|$ for (i) a high-conductivity elemental solid (Table A.1) along with $\Delta T = T_s - T_{ls}$, where T_{ls} is the melting temperature, and $\Delta x = l$, where l is the thickness along which $T_s - T_{lg}$ is applied (this is an approximation for a thin slab as part of a structure). (ii) Repeat using a high-melting-temperature elemental solid (Table A.1). Use $T_s = 300$ K.

(b) For the convective heat flux vector, determine $|\boldsymbol{q}_u| = (\rho c_p)_f u_f T_f$, using (i) a gas, and (ii) a liquid, moving at velocities equal to the speeds of sound and at $T_f = 300$ K. (iii) For the surface-convection heat flux vector, $|\boldsymbol{q}_{ku}| = \langle \mathrm{Nu}\rangle_D k_f (T_s - T_{f,\infty})/D$, for Nusselt number $\langle \mathrm{Nu}\rangle_D = 100$, $D = 10^{-2}$ m, $T_s - T_{f,\infty} = 100$ K, and k_f of nitrogen at $T_f = 300$ K, at 1 atm pressure (Table A.1).

(c) Determine the radiative heat flux vector, $|\boldsymbol{q}_r| = n_{ph} u_{ph,o} \hbar\omega_{ph}$, for a typical (i) continuous laser and (ii) pulsed laser, for $\lambda = 0.5$ μm. (iii) Also use the blackbody (thermal) radiation $|\boldsymbol{q}_r| = \sigma_{\mathrm{SB}} T^4$, for $T = 300$ K, where σ_{SB} is the Stefan–Boltzmann constant (Table 1.4).

Problem 1.2

(a) Show that M–B energy probability distribution function (6.65), given by

$$f_f^{\mathrm{o}}(E_f^*) = \frac{2}{\pi^{1/2}} E_f^{*\,1/2} \exp(-E_f^*), \quad E_f^* = \frac{E_f}{k_{\mathrm{B}} T},$$

satisfies

$$\int_0^\infty f_f^{\mathrm{o}}(E_f^*) \mathrm{d}E_f^* = 1.$$

Superscript * indicates dimensionless quantity.

(b) Show that the classical distribution

$$f_f^{\mathrm{o}}(E_f^*) = \exp(-E_f^*),$$

also satisfies the preceding integration.

(c) Show that

$$\langle E_f \rangle = \int_0^\infty f_f^{\mathrm{o}}(E_f^*) E_f^* \mathrm{d}E_f^* = \frac{3}{2} k_{\mathrm{B}} T,$$

i.e., the average energy (in a M–B system) is equal to $3k_{\mathrm{B}}T/2$. Use gamma functions given by (5.114).

The integral of the other equilibrium probability distribution functions are also physically meaningful. For the bosons and fermions, the integral of f_p^{o} (f_e^{o} and f_{ph}^{o})

leads to the number densities, i.e.,

$$
\begin{aligned}
n_i &= \int_0^\infty f_i D_i(E_i)\mathrm{d}E_i \\
&= \int_0^\infty \frac{D_i(E_i)\mathrm{d}E_i}{\exp(\frac{E_i}{k_\mathrm{B}T} - \mu) \pm 1}, \qquad i = \begin{cases} +\ e\ (\mu \neq 0) \\ -\ p, ph\ (\mu = 0) \end{cases} .
\end{aligned}
$$

This is the same as (1.19).

Problem 1.3

(a) Plot f_e^o listed in Table 1.2, versus E_e for copper (E_F listed in Table 5.2). Use (i) $T = 0$, (ii) $T = 300$ K, (iii) $T = 1000$ K, and (iv) $T = 10{,}000$ K, and use $0 \leq E_e \leq 1.5E_\mathrm{F}$. Note the rather abrupt change in f_o^e for metals.

(b) Indicate in the graph the region $\Delta E_e = k_\mathrm{B}T$ on both sides of $E_e = E_\mathrm{F}$, where f_e^o changes the most.

(c) For metals a constant Fermi energy is used, and the $T = 0$ K approximations of f_e^o, i.e., $f_e^\mathrm{o} = 1$ for $E_e \leq E_\mathrm{F}$, and $f_e^\mathrm{o} = 0$ for $E_e > E_\mathrm{F}$, are used. Based on the results of parts (a) and (b), is this a good approximation?

Problem 1.4

(a) For Si, typical maximum E_p for acoustic and optical phonons are 0.019 and 0.062 eV, respectively. Using $T = 300$ and 1000 K, determine f_p^o (boson) for these two energies.

(b) Consider a conduction electron in Cu and use $\mu = E_\mathrm{F}$ (Table 5.2), and for $T = 300$ and 1000 K, determine f_e^o (fermion) for $E_e = 1$ and 10 eV.

(c) For an Ar gas, with the average thermal speed given by (6.63), determine the M–B energy distribution f_f^o, given in Figure 1.1, for $T = 300$ K.

(d) For a photon of energy $E_{ph} = \hbar\omega_{ph}$, and for (i) $\lambda = 20\ \mu$m (near infrared), (ii) $\lambda = 0.63\ \mu$m (red), (iii) $\lambda = 0.50\ \mu$m (blue), (iv) $\lambda = 0.30\ \mu$m (ultraviolet), and (v) $\lambda = 0.001\ \mu$m (X-rays), determine f_{ph}^o (boson) at $T = 300$ K.

(e) Compare the results of part (a) with those of part (d).

Note that these are equilibrium (thermalized or allowed to reach thermal equilibrium) distributions. For lasers, for example, a selective amplification of a narrow band of energy is used, so the photon distribution does not follow the equilibrium boson. The Fermi energy of semiconductors is temperature dependent.

Problem 1.5

Complete and unified derivation of f_i^o is given in Appendix F, while a shorter derivation of f_{ph}^o (or f_p^o) i.e., B–E distribution, is possible and is outlined here for a quasi-particle having energy $E_n = n\hbar\omega$.

(a) Start with the classical probability (expected to be valid for large n, i.e., curves 4 and 6 in Figure 1.1 become the same)

$$P_n = \frac{e^{-n\hbar\omega/k_{\rm B}T}}{\sum\limits_{n=0} e^{-n\hbar\omega/k_{\rm B}T}}.$$

Then use the expansion

$$\frac{1}{1-x} = \sum_{i=0}^{\infty} x^i,$$

and show

$$P_n = e^{-n\hbar\omega/k_{\rm B}T}(1 - e^{-n\hbar\omega/k_{\rm B}T}).$$

(b) Show that the mean energy is

$$\langle E\rangle = \sum_{n=0}^{\infty} E_n P_n = (1 - e^{\hbar\omega/k_{\rm B}T}) \sum_{n=0}^{\infty} e^{-n\hbar\omega/k_{\rm B}T}$$

$$= \hbar\omega(1 - e^{-\hbar\omega/k_{\rm B}T}) \sum_{n=0}^{\infty} n e^{-n\hbar\omega/k_{\rm B}T}.$$

(c) Then show that

$$\sum_{n=0}^{\infty} n e^{\alpha x} = -\frac{\mathrm{d}}{\mathrm{d}\alpha} \sum_{n=0}^{\infty} e^{-\alpha x}$$

$$= -\frac{\mathrm{d}}{\mathrm{d}x} \frac{1}{1 - e^{-\alpha}} = \frac{e^{-\alpha}}{(1 - e^{-\alpha})^2}.$$

(d) Then using this show that

$$\langle E\rangle = \frac{\hbar\omega e^{-\hbar\omega/k_{\rm B}T}}{1 - e^{-\hbar\omega/k_{\rm B}T}} = \frac{\hbar\omega}{e^{\hbar\omega/k_{\rm B}T} - 1} = \hbar\omega f_{ph}^{\rm o},$$

or

$$f_{ph}^{\rm o} = \frac{1}{e^{\hbar\omega/k_{\rm B}T} - 1}, \quad \text{B–E distribution.}$$

Problem 1.6

(a) Verify the magnitude and unit of the atomic length, time, velocity, energy, and dipole moment given in Table 1.5.

(b) Show that the atomic unit of energy is the product of the electron mass (at rest) and the square of the atomic velocity.

(c) Compare the atomic energy unit with $k_{\rm B}T$ ($T = 300$, 10^3 and 10^5 K), in eV.

Problem 1.7

Similar to Figure 1.7, plot electronegativity of elements versus the atomic number. Electronegativity is a measure of atom attracting electrons (forming bonds). What trends are observed?

Problem 1.8

(a) Using Table A.1, plot the scaled specific heat capacity ($c_v m/k_\mathrm{B}$) versus atomic number z for the elements (at 300 K), where m is the mass of the atom (M/N_A). Note that here c_v is per atom or molecule. Also, note that for a monatomic solid $c_v m/k_\mathrm{B} = 3$ (Section 4.7), and for monatomic ideal gas $c_v m/k_\mathrm{B} = 3/2$ (Section 6.2).

(b) Similarly, plot the scaled specific heat of phase change, $\Delta h_{sl} m/k_\mathrm{B} T_{sl}$ and $\Delta h_{lg} m/k_\mathrm{B} T_{lg}$, versus z, where T_{sl} is the saturation solid–liquid temperature and T_{lg} is the saturation liquid–gas (vapor) temperature at $p = 1$ atm.

(c) Comment on the trends (Figure 1.7 displays similar results for the thermal conductivity k). Note that Δh_{ij} is scaled with respect to the specific energy $k_\mathrm{B} T_{ij}$, which represents the kinetic energy.

2

Molecular Orbitals/Potentials/Dynamics, and Quantum Energy States

Energy is stored within atoms (electrons and relativistic effects) and in the bonds among them when they form molecules, and also between these molecules when they form clusters and bulk materials. In this chapter we review the intraatomic and interatomic forces and energies (potentials). We examine electron orbitals of atoms and molecules and review *ab initio* computations of interatomic potentials and potential models. Then we discuss the dynamics (and scales) of molecular (or particle) interactions in classical (Newtonian and Hamiltonian) treatments of multibody dynamics and the relationship between the microscopic and macroscopic states (particle ensembles). We also begin examining the quantum energy states of the simple harmonic oscillator, free-electron gas, and electrons in hydrogen atom orbitals, by seeking exact solutions to the Schrödinger equation.

2.1 Interatomic Forces and Potential Wells

Atoms and molecules, at sufficiently low temperatures, can aggregate into linked structures that form what we know as the condensed phases of matter. What causes this aggregation behavior are the attractive forces generated by the opposite electrical charges of each particle (be it individual atom, ion, or polar molecule) in the system. These forces are in turn caused by the innate charges of the constituent subatomic particles of each atom, ion, or molecule. All physical and chemical bonding is the result of such molecular forces that are electrical in origin (the Coulomb forces). Intramolecular (or interatomic) forces keep atoms in a molecule (a compound of atoms) together, such as the H–O bond in a H_2O molecule, whereas intermolecular forces keep neighboring molecules together, such as H_2O molecules in the gas, liquid, or solid phase. The intramolecular forces are stronger than the intermolecular forces. The difference among solids, liquids, and gases is the degree to which the thermal energy of the particles k_BT in the system can overcome the attractive forces holding them together. At a given temperature, substances that contain strong interatomic bonding are more likely to be solids (or liquids), whereas those that contain weak or no bonding will be gases. The interatomic potential φ, a form of energy

Interatomic and Intermolecular Forces

Force	**Structure**	**Electric Force**	φ_e, **eV**/Bond	**Example**	r_e, Å
Interatomic (**δ Denotes Charge Fraction**)					
Ionic bond	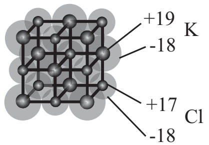	Opposite charges	4 to 40	K–Cl	2.36
Covalent bond	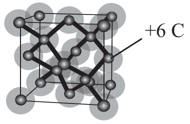	Nuclei shared electron pair	1.5 to 30	C–C (Diamond)	1.54
Metallic bond	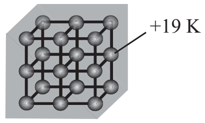	Metal cations and delocalized electrons	0.75 to 10	K–K	4.54
London dispersion (weak) bond	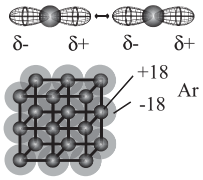	Induced dipoles of polarizable molecules	0.005 to 0.4	Ar–Ar	3.76
Intermolecular (**δ Denotes Charge Fraction**)					
Ion-dipole bond	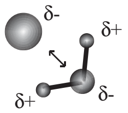	Ion and polar molecule	0.4 to 6	Na^+–H_2O	2.93
Dipole-dipole bond	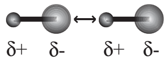	Partial charges of polar molecules	0.05 to 0.25	HCl–HCl	2.45
Hydrogen bond	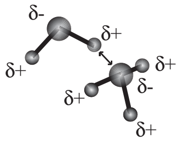	H bonded to N, O, or F, and another N, O, or F	0.1 to 0.4	NH_3–H_2O	3.09

Figure 2.1. A classification of the interatomic and intermolecular forces, atomic structures, electric forces, ranges of their bond energy (potential), examples, and interatomic bond lengths.

(which explains/describes interatomic and intermolecular integrations) and a measure of bond strength, is generally expressed in electron volts (eV), which is the work required to displace an electron through an electric potential of 1 volt (1 V is 1 J/C). Figure 2.1 gives a summary of the interatomic and intermolecular forces and bond length r_e, and they are subsequently described.

2.1.1 Interatomic Forces

These forces include ionic bonding forces, covalent bonding forces, and metallic bonding forces, and London dispersion (van der Waals) bonding forces. Ionic bonding forces are generated between oppositely charged ions. Ions themselves can arise from electron transfer that can occur when atoms of elements that have a large difference in electronegativity (the tendency of an atom to draw electrons in a bond toward itself) come in close proximity to one another. Such bonding is frequently seen between a metal and a nonmetal (cation and anion), i.e., NaCl, MgF_2. In ionic crystals, an array of ions are arranged at regular positions in a crystal lattice.

Covalent bonding forces are formed by two atoms coming together and sharing one or more electrons. Neither atom is able to overcome the attractive forces of the nucleus of the other and completely take its electron(s) for itself. This results in a balance between the forces of attraction and repulsion that act between the nuclei and electrons of the atoms. In many cases, this electron sharing enables each atom to reach a noble gas configuration (i.e., a filled outer electron shell).

Metallic bonding forces arise when metallic atoms (typically with two valence electrons each, Table 5.2) bond to one another. In the free-electron model of this type of bonding, the valence electrons of each atom are no longer restricted to a single atom but are delocalized, forming a sea of electrons that hold the positively charged nuclei together. Metals are easily deformed, due to the layers of positive ions (the nuclei) being able to slide over one another without disrupting the sea of electrons between them. It is also due to the delocalized behavior of the electrons in these bonds that metals are good electrical conductors. The greater the number of valence electrons (and the larger the positive charge of the nuclei), the stronger the metallic bonding forces.

2.1.2 Intermolecular Forces

The attractive forces between neutral molecules are usually ion–dipole forces, dipole–dipole forces, London dispersion forces, or hydrogen bonding forces. The dipole–dipole and dispersion varieties are grouped together and termed van der Waals forces (sometimes hydrogen bonding is also included with this group). The attractive forces between neutral and charged (ionic) molecules are called the ion–dipole forces.

Ion–dipole forces arise between charged ions and polar molecules (molecules with an asymmetric charge distribution), where cations are attracted to the negative end of a dipole, and anions are attracted to the positive end. The magnitude of the interaction potential (with the force being the negative gradient of the potential) is directly proportional to the charge of the ion and the dipole moment of the molecule, and inversely proportional to the distance from the center of the ion to the midpoint of the dipole. Ion–dipole forces are important in solutions of ionic substances in polar solvents (e.g. a salt in an aqueous solvent).

Dipole–dipole forces exist between neutral or polar molecules and polar molecules. They attract one another when the partial positive charge (δ_+ in Figure 2.1) on one molecule is near the partial negative charge (δ_-) on the other. The molecules must be in relatively close proximity (a few Å) for dipole–dipole forces to be significant. These forces are characteristically weaker than ion–dipole forces, and increase with an increase in the polarity of the molecules.

Hydrogen bonds are special dipole–dipole forces between electronegative atoms and hydrogen atoms bonded to adjacent electronegative atoms. Their bond strength is weak covalent. The intermolecular hydrogen bond results in relatively high boiling temperature of H_2O.

2.1.3 Kinetic and Potential Energies and Potential Wells

A system in which intramolecular and intermolecular forces act can possess two types of energy: kinetic energy E_k and potential energy $E_p = \varphi$. The magnitude of the kinetic energy is a function of temperature only. Potential energy arises from the action of the Coulombic forces previously mentioned. Although there are differences among the various forces, they all give rise to potential energy between the interacting particles. It is the relative difference between the kinetic and potential energies of a system of particles that determines many of the properties of the substance.

Kinetic energy is energy of motion. A body of mass m, moving with velocity u, has kinetic energy given by

$$E_k = \frac{mu^2}{2}. \tag{2.1}$$

The kinetic energy of atoms and molecules has a thermal origin and, from equipartition of energy [156], is related to the absolute temperature as follows:

$$E_k = \frac{\alpha k_B T}{2}, \tag{2.2}$$

where k_B is the Boltzmann constant and α is related to the degrees of freedom of the atomic motion of the system. Potential energy φ is the energy of position. When a particle begins to move, potential energy is converted to kinetic energy. The opposite happens as a moving particle is affected by forces generated as it approaches another body. The total energy of any mechanical system is the sum of its kinetic and potential energies, and on a per-atom/molecule basis we have

$$E = e = E_k + E_p \equiv E_k + \varphi, \tag{2.3}$$

where e is the specific (per-atom/molecule) internal energy. In addition to the gravitational potential, there are three other potentials: the strong nuclear, electrostatic (or Coulombic), and weak nuclear potentials. As discussed, the Coulombic force is the force by which electrons are attracted to and held by the nucleus of an atom, and this force is responsible for all interactions between atoms and molecules. It is far stronger than the gravitational force, which may be neglected in discussing atomic and molecular interactions (the electromagnetic force of repulsion between two electrons is 10^{42} times stronger than the gravitational force of attraction between them). The magnitude of the electrical force is given by the Coulomb law [289]

$$F_{12} = \frac{1}{4\pi\epsilon_o}\frac{q_1 q_2}{r^2} \quad \text{Coulomb law,} \tag{2.4}$$

where q_1 and q_2 are the sign-magnitudes of the two interacting electric charges (given in electron charge e_c), in coulombs (C), r is the distance between them, in meters and ϵ_o is the free-space electric permittivity and has a value of 8.854×10^{-12} C^2/N-m^2 = C^2/J-m (also listed in Table 1.4). Here $1/4\pi\epsilon_o = 8.9876 \times 10^9$ N-m^2/C^2 = J-m/C^2 is called the Coulomb constant. The potential energy associated with the Coulombic force is called the Coulomb potential energy. Because force is the negative derivative of potential energy with respect to distance ($F_{12} = -\partial\varphi_{12}/\partial r_{12}$), the Coulombic potential energy can be obtained by the integration of the Coulomb law

$$\varphi_{12} = -\frac{1}{4\pi\epsilon_o}\frac{q_1 q_2}{r}, \quad \boldsymbol{F}_{12} = -\frac{\partial\varphi}{\partial r}\boldsymbol{s}_{12} \quad \text{force–potential relation,} \tag{2.5}$$

where $\boldsymbol{s}_{12}$ is the unit vector along $\boldsymbol{r}$, connecting 1 and 2. Bold characters signify vectors (lowercase) or tensors (uppercase).[†] When one of the charges is positive and the other negative, the potential energy is negative at all finite values of r.[‡]

For a system of two or more particles (atoms, molecules, and/or ions), we assume that the interparticle forces are electrical and are attractive, except at very close distances, and described by the Coulomb law. The magnitude (strength) of the force between two particles varies with their distance of separation. The force is zero for an infinite separation, increases as the particles get closer, reaches a maximum when the particles just touch, and becomes strongly repulsive when the centers of the particles are separated by less than one particle diameter because of interpenetration and repulsion of electron clouds (Pauli exclusion principle). The force has two components, one repulsive and dominant at only very small distances, and the other attractive and acting at all distances. The sum of these forces between

---

[†] The screened Coulomb potential is

$$\varphi = -\frac{q_1 q_2}{4\pi\epsilon_o r}e^{-r/r_o},$$

where r_o is the screening distance.

[‡] In the Bohr model of a hydrogen atom, the single electron is in the ground state has $r_B = 4\pi\epsilon_o\hbar^2/m_e e_c^2 = 5.292 \times 10^{-11}$ m (Bohr radius, Table 1.4), and the potential energy [for charge of unity on proton and electron, using (2.5)] is twice the kinetic energy $m_c u_e^2/2$ (but negative), and this gives the total energy as

$$\begin{aligned} E_k + \varphi &= \frac{1}{2}\frac{1}{4\pi\epsilon_o}\frac{e_c^2}{r_B} - \frac{1}{4\pi\epsilon_o}\frac{e_c^2}{r_B} \\ &= -\frac{1}{2}\frac{1}{4\pi\epsilon_o}\frac{e_c^2}{r_B} = -13.606 \ \text{eV} \quad \text{ground state for hydrogen atom.} \end{aligned}$$

Thus, to remove the electron from hydrogen, an ionization energy of 13.606 eV is needed. Note that this is for $n = 1$ (the ground state). For other principal quantum numbers, we have $r_B n^2$ in place of r_B.

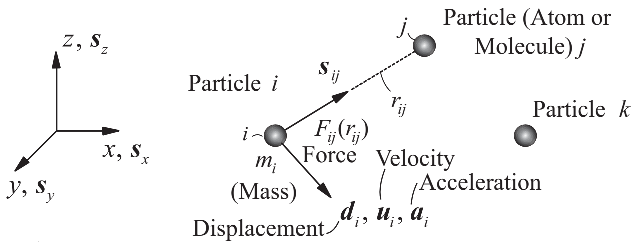

$$m_i \frac{\mathrm{d}\boldsymbol{u}_i}{\mathrm{d}t} = m_i \boldsymbol{a}_i = \sum_j F_{ij} \boldsymbol{s}_{ij} = -\sum_j \Gamma_{ij} \boldsymbol{d}_i \quad \text{Newton Law}$$

$$F_{ij}(r_{ij}) = -\frac{\partial \varphi_{ij}}{\partial r_{ij}} \quad \text{Interatomic Force and Potential}$$

$$\Gamma_{ij} = \left. \frac{\partial^2 \varphi_{ij}}{\partial r_{ij}^2} \right|_e \quad \text{Spring Force Constant (Harmonic Approximation),} \quad F_{ij} = -\Gamma_{ij} d_{ij}$$

$$\frac{d^2 \boldsymbol{x}_i}{dt^2} = -\frac{1}{m_i} \sum_j \nabla \varphi_{ij} \quad \text{Position-Potential Relation}$$

φ_{ij} Interatomic Potential from Solution to Schrödinger Equation
(*ab initio* Calculations) or from Potential Models

$$N\langle \varphi \rangle = \frac{1}{2} \sum_{i,j} \varphi_{ij} \quad \text{Total Potential Energy}$$

Figure 2.2. Interatomic forces F_{ij} acting on particle (atom or molecule) i and presentation of these forces by the interatomic potentials. The net effect of these forces determines the classical (Newton) dynamics of the particle i, while the electronic structure of atom i and its neighbors determine the interatomic potential (fine-structures from the Schrödinger equation). $\langle \varphi \rangle$ is the effective potential and $N\langle \varphi \rangle$ is the total potential energy.

two particles is thus

$$F_{12} = \frac{1}{4\pi \epsilon_o} \frac{q_1 q_2}{r_{12}^2} + b \quad \text{attractive and repulsive forces,} \tag{2.6}$$

where b is a positive, repulsive force that noticeably acts at only very small distances.

At distances greater than one particle diameter, intermolecular forces draw particles together as part of the natural tendency for the system to seek the lowest potential energy state possible for the pair (or collection) of particles. As mentioned, the attractive force becomes stronger until the particles nearly touch, which means the potential energy also keeps decreasing until this point. Figure 2.2 shows the interatomic forces acting on atom i and the resulting motion from the net force on this atom (particle). When the distance between atom/particle i and atom/particle j, r_{ij} [called the normal coordinate (Glossary)], is less than one particle diameter, the force becomes repulsive and the potential energy begins to increase, meaning the system is again deviating from its ideal, lowest energy state. The interatomic potential is determined by solving the Schrödinger equation (Section 2.2.2). The force (spring) constant is related to the second derivative of the interatomic potential along the normal coordinate (at equilibrium location), and the interatomic force is related to the first derivative.

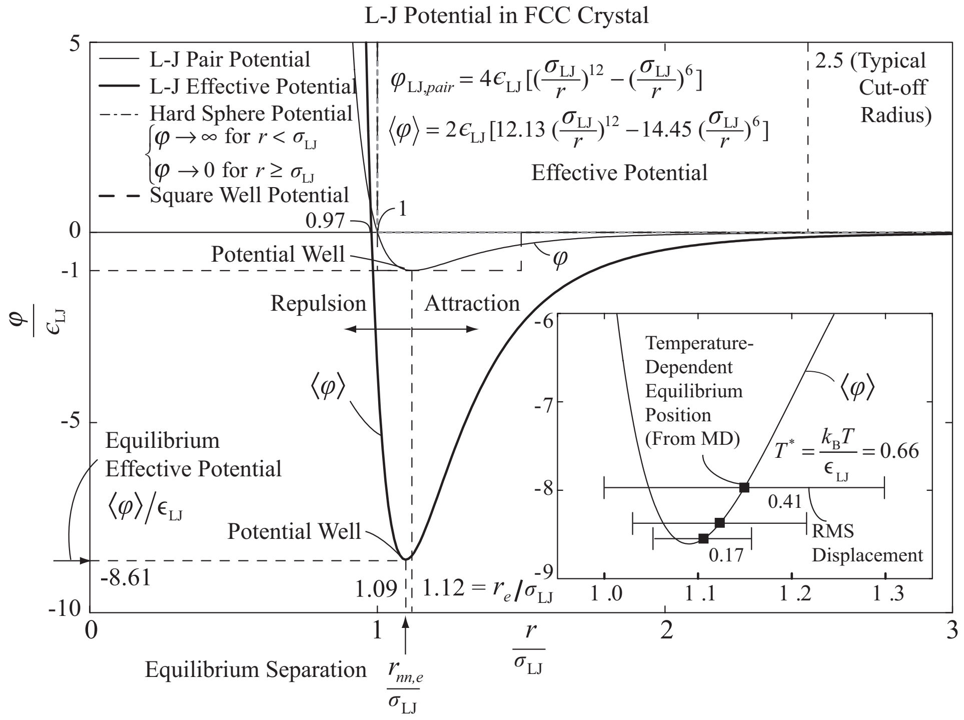

Figure 2.3. Variation of the scaled L–J interatomic potential with respect to scaled separation distance for Ar. The effective $\langle\varphi\rangle$ (per atom) potential indicating the cumulative potential that is due to presence of all neighboring atoms (FCC arrangement) is also shown. The hard-sphere and square-well approximations are also shown. The RMS displacement of each atom in the crystalline solid phase, at three different reduced temperatures $T^* = k_B T/\epsilon_{LJ}$ (scaled with $\epsilon_{LJ}/k_B = 120.7$ K for Ar), are shown around the equilibrium (e) nearest-neighbor spacing $r_{nn,e}$, for solid Ar [320]. The constants ϵ_{LJ} and σ_{LJ} for noble gases are listed in Table 2.2 in Section 2.2.

For all types of interatomic forces, the potential energy varies with distance between the interacting bodies r. An example of a typical potential energy $\varphi(r)$ curve (often called the potential energy well) is shown in Figure 2.3 for a FCC crystal, using the Lennard–Jones (L–J) potential model. The depth of the well is the energy that must be added to increase the distance of separation between particles until the force between them is nearly zero. Most interatomic potentials are characterized by a potential well of similar shape. However, the depth of the well increases with the strength of the force. We discuss interatomic potentials in Section 2.2.3. The effective, or net, potential $\langle\varphi\rangle$ that a particle experiences when surrounded by many others is discussed in Section 2.5.3. Because the potential is shared by adjacent particles, $\langle\varphi\rangle$ is the sum of the potentials between all interacting pairs divided by the total number of particles in the system N.

The hard sphere model (potential) does not contain any field (potential) outside the radius σ. This is used in ideal-gas kinetics (Secion 6.5).

For a system in which there is a very large separation between atoms, molecules, or ions, there is a state of deaggregation. The gas phase of a pure substance is an example of a deaggregated state. At the minimum level of separation distance, the particles nearly touch, and the attractive forces are maximized while potential energy is at a minimum. This is an aggregated state (e.g., the solid phase of a pure substance). In an ionic compound, such as KBr, this corresponds to a situation in which positive ions are surrounded by equally spaced negative ions. In a covalent compound, such as H_2O, this state occurs when the hydrogen atoms are covalently bonded to the oxygen atom at a distance corresponding to the lowest point of the well and are separated from each other by an angle of 104°.

A collection of atoms or molecules seeks to minimize potential energy by aggregating in such a way that a particular atom/molecule nearly touches as many of its neighbors as possible. This organization is referred to as close packing, and characterizes the solid state of a pure substance (not all solids are close packed, there is also an amorphous phase that has no long-range order). Note that the potential energy increases when an aggregated state is converted to a deaggregated state. The phases (solid, liquid, and gas) of a pure substance fit the aggregation/deaggregation model very well. In the solid phase, the fundamental units of a substance are packed together in an orderly, often repeating, arrangement (or lattice) that minimizes potential energy. In the gaseous phase, the fundamental units are widely separated and experience only very weak forces from one another. The liquid phase has distances of molecular separation and potential energy only somewhat greater than those of the solid, but no long-range order.

The inset in Figure 2.3 shows equilibrium separation (interatomic) distance at three different dimensionless temperatures. Note that the equilibrium interatomic distance increases with temperature. Also note that in the limit of $T \rightarrow 0$, the displacement becomes nearly symmetric. This is the harmonic limit of the displacements. In many analytical treatments (Sections 2.5.3, 2.6.4, and 4.4) this harmonic approximation is used.

The fundamental forces are the strong and weak nuclear forces, the electromagnetic force and the gravity force. The nuclear forces act over one fm (10^{-5} Å) distance and hold the nucleus together (for < 0.7 fm the forces become repulsive).

Figure 2.4 gives examples of nuclear, intra-atomic and interatomic forces and distances. Referring to Figure 1.9, the L range here covers *Ab initio*, and MD treatments. For all cases shown, the gravitational force is less than 10^{-33} N. The quantum chromodynamics and electroweak theories were mentioned in the footnote of Section 1.1.2. For electron–proton interactions shown, the weak nuclear force is 10^{-37} N, and the strong nuclear force is also negligible compared with that. Note that the atomic force microscopy techniques generate forces smaller than those holding together some solids, allowing them to be used without damaging those materials. For interatomic interactions, the length given is the nearest neighbor distance. The data for quartz and argon are obtained from the MD simulations. The calculation of the potential energy as $\varphi = FL$ (force times separation) is a very rough approximation of the potential energy for a pair of particles [based on (2.5)]. A calculation exhibiting better accuracy would need to consider how the force changes nonlinearly as a function of the separation [such as (2.6)]. For example, the energy required to

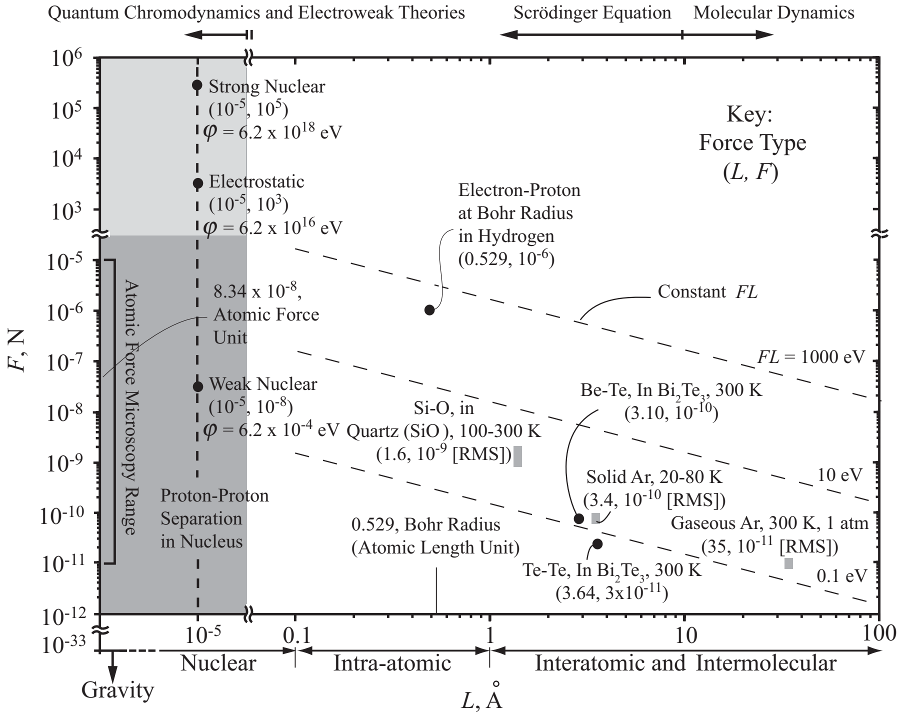

Figure 2.4. Forces at nuclear (strong and weak), intra-atomic, and interatomic and intermolecular (electromagnetic) at the related lengths. The gravity force is also shown. For demonstration of the potential energy, a linear relation FL is used to show equipotential lines.

remove the electron from a hydrogen atom is 13.6 eV, (compared with the value of FL, which is 312 eV.)

The interatomic and intermolecular forces (electromagnetic forces) lead to binding energies which are generally below 50 eV (Figure 2.1), while the nuclear forces lead to MeV binding energies. The nuclear binding energy is from the strong nuclear force holding protons and neutrons together in the nucleus. The electron binding energy for inner orbital electrons is as high as 1400 eV.

2.2 Orbitals and Interatomic Potential Models

2.2.1 Atomic and Molecular Electron Orbitals

The electronic orbitals are the wave-function solutions obtained from the Schrödinger equation (as will be discussed in Section 2.6.6) of the nucleus–electron electrodynamic (i.e., in motion) system. The arrangement of electrons in the orbitals of an atom (known as the electronic configuration) follows the Pauli exclusion principle. The configuration is specified by a combination of a letter and number for each sublevel, along with a superscript number to represent the number of electrons

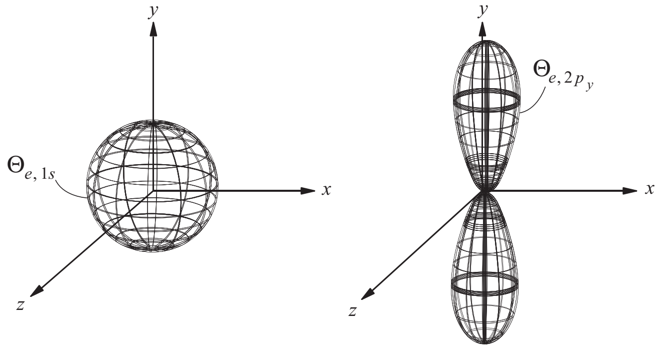

(a) $1s$ Orbital (b) $2p_y$ Orbital

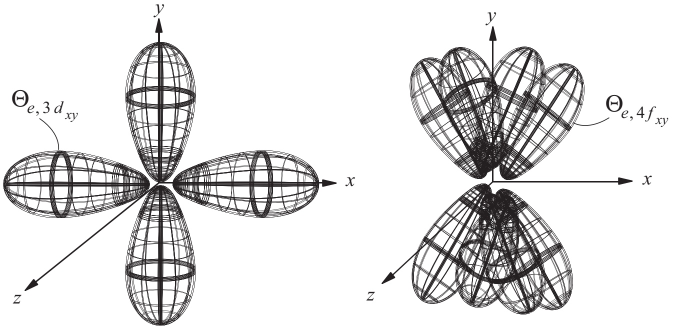

(c) $3d_{xy}$ Orbital (d) $4f_{xy}$ Orbital

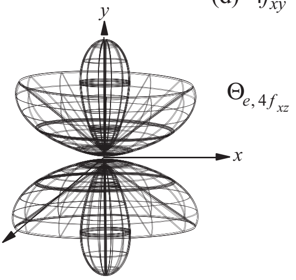

(e) $4f_{xz}$ Orbital

Figure 2.5. Three-dimensional angular part of probability (orbital) of the hydrogenlike atom electron wave function represented as $\psi_e = R_e(r)\Theta_e(\theta, \phi)$, for (a) $1s$-, (b) $2p$-, (c) $3d$-, and (d), and (e) $4f$- orbitals around the nucleus.

contained in the sublevel. The periodic table (Section 1.7 and Appendix A) is arranged based on these electronic configurations within orbitals. For example, $1s^1$ describes the state of the single electron in a hydrogen atom, which resides in the first s-orbital (a spherical shape). In geometric space, an orbital is the space having the highest probability of containing an electron.

Figures 2.5(a) to (e) show typical s, p, d, and f (two) orbitals for hydrogenlike atoms, for principal quantum numbers $n = 1, 2, 3,$ and 4. The four quantum numbers are defined in Section 2.6.6. Every energy level has an s-sublevel (momentum or azimuthal quantum number $l = 0$) containing one s orbital (magnetic quantum number $m = 0$). The fourth quantum number is the spin quantum number. The first energy level has a $1s$-orbital, the second a $2s$ orbital, etc. The geometry of s orbitals is spherical, and the higher the energy level, the larger the radius. The charge density of the electron cloud generally increases the closer it is to the nucleus. Above the first energy level, s orbitals have radial nodes (regions inside the orbital with zero charge density). A $2s$ orbital has one radial node, a $3s$ orbital has two, etc. Each orbital has one less radial node than the number of energy levels. The second energy level and higher have p sublevels (azimuthal quantum number $l = 1$), each containing three p orbitals. There are two lobes for each p orbital, separated from each other by a planar node passing through the nucleus. The three p orbitals are mutually perpendicular and are denoted as p_x, p_y, and p_z. The third and higher energy levels have d sublevels (quantum number $l = 2$), each containing five d orbitals ($m = 0, +1, -1, +2$, and -2), and four of the five d orbitals are identical in shape, having four lobes. These orbitals are designated as d_{xy}, d_{yz}, d_{xz}, and $d_{x^2-y^2}$. The fifth orbital consists of a torus with two lobes perpendicular to the plane of the torus. The fourth and higher energy level have f sublevels (magnetic quantum number $l = 3$), each containing seven f orbitals ($m = 0, +1, -1, +2, -2, +3$, and -3). The geometries of the f orbitals are more complex, as shown in Figures 2.5(d) and (e). These figures in general represent the angular part of the hydrogen wave function Θ_e, where $\psi_e = R_e(r)\Theta_e(\theta, \phi)$. They show a probability for the specific orbital. We will discuss this further in Section 2.6.6. Table A.2 (periodic table) in Appendix A gives the electron orbitals of the elements.

Molecular orbitals represent electron positions in molecules (which contain more than one nucleus). The probability function shows that the electron density is the highest in the space between adjacent nuclei.

When two atoms are brought close together, an electron can simultaneously experience a strong attraction to both nuclei, leading it to exist in a molecular orbital that is distributed between the two atoms, producing the chemical bond. A molecular orbital is modeled as a linear combination (overlap) of the wave functions for two (or more) atomic orbitals. If the two wave functions, $\psi_{e,1}$ and $\psi_{e,2}$, have the same sign in the region of overlap, a constructive interaction between the two wave functions occurs and a bonding orbital is produced. If the two wave functions have opposite signs in the region of overlap, a destructive interaction between the two wave functions occurs and an antibonding orbital is produced. For example, in H_2, the sigma bond (i.e., a single lobe of one electron orbital overlaps a single lobe of the other electron orbital) is formed by the overlap of two $1s$ orbitals. Pi bonds are formed where two lobes of one electron orbital overlap two lobes of the other electron orbital (for example, B_2H_2). Pi bonds are weaker than sigma bonds. A single bond is always a sigma bond. A double bond (e.g., C_2H_4) is made up of a sigma bond and a pi bond. A triple bond (e.g., HCN) contains a sigma bond and two pi bonds.

The C atom is versatile in the number of compounds it makes with single, double, and triple bonds, which involve hybridization. Bonding is with the valence shell electrons found in the incomplete, outermost shell. The ground carbon has four valence electrons, two in the $2s$ subshell and two in the $2p$ subshell, to hybridize from this ground state C forms two bonds by promoting one of its 2s electrons into its empty $2p$ orbital. By forming this excited state, carbon will be able to form four bonds. Since both the $2s$ and $2p$ subshells are half-filled, the excited state is relatively stable.

When four hybrid orbitals are formed for each C, i.e., four atomic orbitals are mixed, the s orbital and all three p are mixed, thus the hybridization is sp^3. The four sp^3 hybrid orbitals arrange themselves in three-dimensional space to be as far apart as possible (to minimize repulsion). The geometry that achieves this is tetrahedral geometry, with the bond angle 109.5°, as in CH_4 bonds, each hybrid orbital contains 1 electron and a hydrogen $1s$ overlaps with it forming a sigma bond (head-on overlap).

When three hybrid orbitals are formed for each C, i.e., three atomic orbitals are mixed, the s orbital and two of the p orbitals for each carbon have been mixed, thus the hybridization for each carbon is sp^2. The three sp^2 orbitals arrange themselves in trigonal plane geometry with the bond angle of 120°. The unmixed pure p orbital will be perpendicular to this plane. The head-on overlap of sp^2 orbitals forms a bond and the side-by-side overlap of pure p orbitals forms a pi bond between the carbon atoms, thus carbon-carbon double bond, as in C_2H_4.

When two hybrid orbitals are formed for each C, i.e., two atomic orbitals are mixed, the two sp hybrid orbitals arrange themselves in the linear geometry with the bond angle of 180°. The two pure p orbitals which were not mixed are perpendicular to each other. The triple bond consists of one sigma bond and two pi bonds, as in C_2H_4.

2.2.2 *Ab Initio* Computation of Interatomic Potentials

The interaction between electrons, as atoms are brought in close contact, is treated by use of various approximations of the potential force appearing in the Schrödinger equation (electronic structure theory) [12]. As will be discussed in Section 2.6.4, the Schrödinger equation contains a potential energy that here is the Coulombic repulsion/attraction (2.6). For an electron the charge is $-e_c$ and for the nucleus it is ze_c, where z is the atomic number.[†]

The *ab initio* calculations, such as those described in the Gaussian series of computational chemistry computer programs [144], determine the potential and electron cloud densities by using the Hartree–Fock self-consistent field algorithm.

[†] The system potential energy (N_e electrons and N_n nuclei) electron–nuclear attraction, the electron–electron repulsion, and the nuclear–nuclear repulsion are given by [144]

$$\varphi_{e\text{-}n} + \varphi_{e\text{-}e} + \varphi_{n\text{-}n} = \frac{e_c^2}{4\pi\epsilon_{\text{o}}}\Big(\underbrace{-\sum_i^{N_e}\sum_I^{N_n}\frac{z_I}{\Delta r_{iI}}}_{\text{electron–nuclear}} + \underbrace{\sum_i^{N_e}\sum_{j<i}^{N_e}\frac{1}{\Delta r_{ij}}}_{\text{electron–electron}} + \underbrace{\sum_I^{N_n}\sum_{J<I}^{N_n}\frac{z_I z_J}{\Delta r_{IJ}}}_{\text{nuclear–nuclear}}\Big),$$

where z is the atomic number and Δr is the absolute value of separation distance between the two charged entities.

The Hartree–Fock method is an approximation to the electronic Schrödinger equation. In this approximation, the exact Hamiltonian (the sum of kinetic and potential energies) is replaced with the Fock operator. This is an approximation describing the interaction of each electron with the average electronic field (rather than with every other electron separately). We will discuss the solutions to the Schrödinger equation, including the density functional theory (DFT), in relation to electronic band structures in Section 5.4.

The bond order is the number of pair electrons shared, i.e., single bond means one pair shared, double means share two pairs, etc. O=O shares two $2s$ and two $2p$ electrons (two pairs). Figure 2.6(a) shows an O=O bond (The double bond exists at the bottom of the well.) calculated with the Gaussian.[†] As the separation distance decreases, first a single and then a double bond is formed ($r < 1.25$Å). As discussed in Section 1.5.2, we use the atomic length unit, the Bohr radius $r_\mathrm{B} = h_\mathrm{P}^2/4\pi^2 m_e e_c^2 = 0.52917725$ Å, and energy unit e_c^2/r_B (a hartree), $27.2114\text{eV} = 4.35975 \times 10^{-18}$ J. Atomic oxygen has the electronic configuration $1s^2 2s^2 2p^4$ (Table A.2).

After obtaining the *ab initio*, results for $\varphi(r)$ are obtained by use of several existing potential models. These contain constants that are fitted by the use of least-square fit. The models (from Table 2.1) considered here are the Morse, expanded harmonic, and 12–6 L–J potentials, i.e.,

$$\begin{aligned}
\text{Morse potential} \quad & \varphi = \varphi_\mathrm{o}\{[1 - e^{-a_\mathrm{o}(r - r_\mathrm{o})}]^2 - 1\}, \\
\text{expanded harmonic potential} \quad & \varphi = \frac{1}{2}\Gamma_a (r - r_\mathrm{o})^2 + \frac{1}{6}k_1 (r - r_\mathrm{o})^3 + \frac{1}{12}k_2 (r - r_\mathrm{o})^4, \\
\text{12–6 L–J potential} \quad & \varphi = \frac{A}{r^{12}} - \frac{B}{r^6}.
\end{aligned} \tag{2.7}$$

Here we have used Γ instead of k as the spring constant. Note that, compared with the L–J model given in Figure 2.2, here $\sigma_\mathrm{LJ} = (B/A)^{1/6}$, and $\epsilon_\mathrm{LJ} = A^2/2B$.

[†] The input begins with the command line scan requested followed by a file title line. The third input line begins specification of particular species, beginning with the number of charge on the molecule (zero in this case) and then the spin multiplicity (one here). The fourth line sets oxygen as the first atom. In the fifth, the second atom is set as oxygen and is bonded to the first atom in the molecule "1" at a distance r from the first. This distance is variable as defined by the sixth (r as variable) and seventh (range of r starting from 0.8 Å, with 37 steps of size 0.03 Å) lines. The self energy is −150.12056 hartree (the inner-orbital electrons of O atoms have very large energy). Note that 1hartree = 27.2114eV. The input file ⟨⟩ to Gaussian is listed subsequently (no entry implies blank line).

```
1. ♯ T B3LYP/6-311+=g(3df,3pd) scan test
2.
3. OO scan
4.
5. 0 1
6. O
7. O 1 r
8. Variable
9. r 0.8 37 0.03
10. add a blank line
```

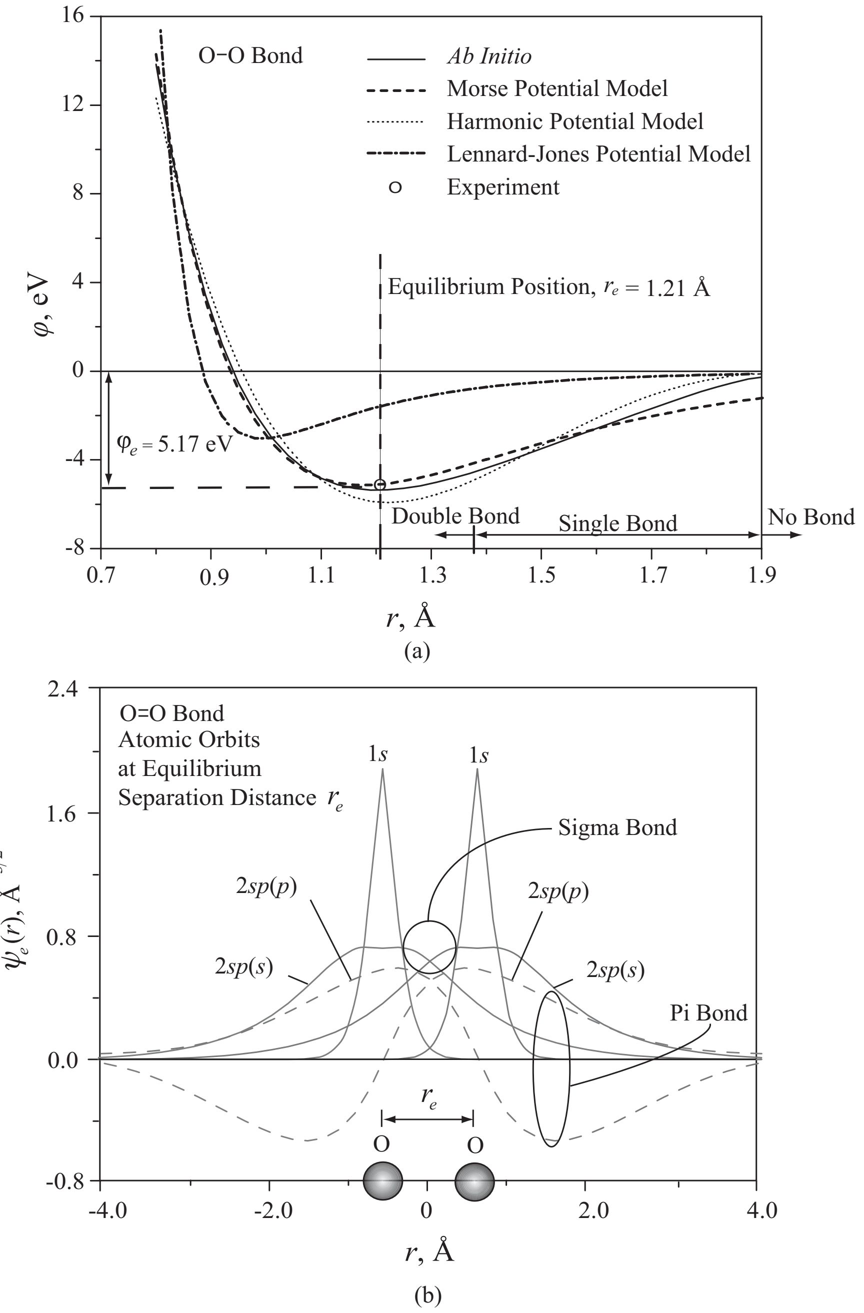

Figure 2.6. (a) *Ab initio* potential for dioxygen O=O covalent double (at well bottom) bond from Hartree-Fock approximation [144] and various potential models fitted to it. The experimental results for equilibrium potential and separation distance are also shown. (b) Wave function distribution along the O=O axis, for unchanged $1s$ orbitals, and s-type and p-type orbitals in the $2sp$ shell. Atomic O has the electronic structure $1s^2 2s^2 2p^4$. The sigma and pi bonds are also shown.

For the O=O bond considered here, we have

$$\begin{aligned}
\text{Morse potential } \varphi_o &= 5.14228\ \text{eV},\ a_o = 2.87104\ \text{Å}^{-1},\ r_o = 1.17618\ \text{Å},\\
\text{expanded harmonic potential } \Gamma_a &= -1.1695\times 10^{-6}\ \text{eV-Å}^{-2},\\
k_1 &= 276.678\ \text{eV-Å}^{-3},\\
k_2 &= 518.141\ \text{eV-Å}^{-4},\ r_o = 2.02355\ \text{Å},\\
\text{L–J potential } A &= 2.7602\ \text{eV-Å}^{-12},\ B = 5.79201\ \text{eV-Å}^{-6}.
\end{aligned} \tag{2.8}$$

Figure 2.6(a) also shows the results for the preceding models. The experimental result for the equilibrium bond length r_e (1.21 Å), and bond energy φ_e (5.17 eV) are also shown and are in good agreement with the *ab initio* results (some other bonds are listed in Table 2.3 and will be discussed in Section 2.2.4). The closest fit to the *ab initio* data, over the entire range, is the Morse potential. In addition, this potential matches the magnitude and location of the potential well.

Figure 2.6(b) shows the wave function distributions (Section 2.6) of the oxygen atomic orbits along the O–O axis.[†] The results are for the covalent, double-bond

---

[†] In molecular physics, the atomic orbits are often described by a set of Gaussian-type orbitals (GTOs) for fast calculations, i.e.,

$$\psi_\mu = \sum_i^N d_{\mu,i} g_i,$$

where the coefficients $d_{\mu,i}$ are called the contraction coefficients, and g_i is a GTO.
The GTO (also called the Cartesian Gaussian or Gaussian primitive function) is expressed as

$$g(\alpha, l, m, n, f; x, y, z) = c\, e^{-\alpha f^2 r^2} x^l y^m z^n.$$

Here α is called the exponent, f is a scale factor (determined by the basis), and c is a normalization constant determined by f and α. Also x, y, z are Cartesian coordinates, and the summation of their exponents $L = l + m + n$ is used to mark functions as s-type ($L = 0$), p-type ($L = 1$), d-type ($L = 2$), and so on. For example, the following GTOs are normally used

$$\begin{aligned}
1s &= c\, e^{-\alpha f^2 r^2}\\
2p_x &= c\, e^{-\alpha f^2 r^2} x\\
2p_y &= c\, e^{-\alpha f^2 r^2} y\\
2p_z &= c\, e^{-\alpha f^2 r^2} z.
\end{aligned}$$

Gaussian03 will output the components and contraction coefficients when the keyword “GFPrint” appears in the command line. The output of Gaussian with the basis of 6-31G is as follows

```
 1. Atom O1 Shell 1 S 6
 2.        0.5484671660D+04      0.1831074430D-02
 3.        0.8252349460D+03      0.1395017220D-01
 4.        0.1880469580D+03      0.6844507810D-01
 5.        0.5296450000D+02      0.2327143360D+00
 6.        0.1689757040D+02      0.4701928980D+00
 7.        0.5799635340D+01      0.3585208530D+00
 8. Atom O1 Shell 2 SP 3
 9.        0.1553961625D+02     -0.1107775495D+00      0.7087426823D-01
10.        0.3599933586D+01     -0.1480262627D+00      0.3397528391D+00
11.        0.1013761750D+01      0.1130767015D+01      0.7271585773D+00
12. Atom O1 Shell 3 SP 1
```

dioxygen equilibrium separation distance. The 1s orbital is a core orbital and the overlap between the two 1s orbitals is small. The 2s orbital has symmetry around the nucleus centers. However, the 2p has an anti-symmetry around the nucleus centers. Thus the possibility of having an electron located between the two nuclei is high.

The sigma (two) and pi (one) bonds and double bond O=O are also shown in Figure 2.6(b).

2.2.3 Potential Models and Phases

Table 2.1 lists some of the most commonly used interatomic potentials [152]. A review of various potentials is given in [90]. In addition to the motion along the bond axis shown in Figure 2.6, for a diatomic molecule, there are torsional and various other in-plane and out-of-plane motions. Figure 2.7 lists 11 such motions. These are bond stretching, angle, torsion, out-of-plane, bond–bond, angle–angle, bond–angle, electrostatic, angle–angle-torsion, out-of-plane–out-of-plane, and nonbonded. The complete interatomic potential (not the form always used) would contain the contribution from all of these motions, when applicable.

The L–J potential is an effective potential that describes the interaction between two uncharged molecules or atoms (Figure 2.4). This potential is mildly attractive as two uncharged molecules or atoms approach one another from a distance, but strongly repulsive when they come too close to each other. At equilibrium, the pair of atoms or molecules tends to go toward a separation distance corresponding to the minimum of the L–J potential.

The potential models represent the interatomic forces discussed in Section 2.1. The London dispersion forces exist between nonpolar molecules that would seem to have no basis for attractive interactions. However, gases of nonpolar molecules can be liquefied, indicating that, if the thermal (kinetic) energy is reduced to a sufficiently low level, an attractive force can dominate. The London forces arise from the motions of electrons within an atom or nonpolar molecule that can produce a fluctuating dipole moment. This causes neighboring atoms to be attracted to one another, but is significant only when the atoms are close together. The ease with which an external electric field can induce a dipole (alter the electron and charge distribution) within a molecule is referred to as the polarizability of that molecule. The greater the polarizability of a molecule, the easier it is to induce a momentary dipole and the stronger the dispersion forces. The larger molecules tend to have greater polarizability because their electrons are farther away from the nucleus (any asymmetric distribution produces a larger dipole due to larger charge separation), and their number of electrons is greater (higher probability of asymmetric distribution).

```
13.        0.2700058226D+00       0.1000000000D+01       0.1000000000D+01
```

Here, lines 1, 8, and 12 start with the atom index, followed by the index of the electronic shell, shell type, and the number of primitive functions. In the lines following them, the first column shows the exponents, the second column shows the contraction coefficients for s-type GTOs, and the third column shows the contraction coefficients for p-type GTOs. The shell type "SP" means that the s-type GTOs and p-type GTOs share the same exponents. The summation of the GTOs for an orbit gives the wave function of the orbit (note that the wave function should be normalized to make sure the integral of the square of it over the space is equal to 1.0)

Table 2.1. *Some interatomic potential models (two, three, and four-body, including bond angles) [152].*

Potential designation	Model	Units for parameters
Buckingham	$A\exp(-r/r_o) - Cr^{-6}$	A in eV, r_o in Å, C in eV-Å^6
L–J (combinative rule permitted, Section 4.11.2)	$Ar^{-m} - Br^{-n}$ or $\epsilon_{LJ}[c_1(\sigma/r)^m - c_2(\sigma_{LJ}/r)^n]$ $c_1 = [n/(m-n)](m/n)^{[m/(m-n)]}$ $c_2 = [m/(m-n)](m/n)^{[m/(m-n)]}$	A in eV-Å^m, B in eV-Å^n ϵ_{LJ} in eV, σ_{LJ} in Å
Expanded harmonic (k_3 and k_4 optional)	$(1/2)\Gamma_a(r-r_o)^2 + (1/6)k_1(r-r_o)^3 + (1/12)k_2(r-r_o)^4$	Γ_a in eV Å^{-2}, r_o in Å, k_1 in eV-Å^{-3}, k_2 in eV-Å^{-4}
Born harmonic	$(1/2)\Gamma(r-r_o)^2$	Γ in eV-Å^{-2}
Morse	$\varphi_o(\{1-\exp[-a_o(r-r_o)]\}^2 - 1)$	φ_o in eV, a_o in Å^{-1}, r_o in Å
Spring (core-shell)	$(1/2)\Gamma_a r^2 + (1/24)k_1 r^4$	Γ_a in eV-Å^{-2}, k_1 in eV-Å^{-4}
General	$A\exp(-r/r_o)r^{-m} - Cr^{-n}$	A in eV-Å^m, r_o in Å, C in eV-Å^n
Two-body Stillinger–Weber	$A\exp[r_o/(r-r_{max})](Br^4 - 1)$	A in eV-Å, r_o in Å, B in eV-Å^4
Three-body Stillinger–Weber	$\varphi_o\exp[r_o/(r_{12}-r_{max}) + r_o/(r_{13}-r_{max})][\cos(\theta_{213}) - \cos(\theta_o)]^2$	φ_o in eV, r_o in Å
Expanded three-body harmonic	$(1/2)k_1(\theta-\theta_o)^2 + (1/6)k_2(\theta-\theta_o)^3 + (1/12)k_3(\theta-\theta_o)^4$	k_1 in eV-rad^{-2}, θ_o in degrees, k_2 in eV-rad^{-3}, k_3 in eV-rad^{-4}
Expanded three-body harmonic + exponential	$(1/2)k_1(\theta_{213}-\theta_0)^2 \times \exp(-r_{12}/r_o)\exp(-r_{13}/r_o)$	k_1 in eV-rad^{-2}, θ_0 in degrees, r_o in Å
Axilrod–Teller	$k[1 + 3\cos(\theta_{213})\cos(\theta_{123})\cos(\theta_{132})]/(r_{12}r_{13}r_{23})^3$	k in eV-Å^9
Three-body exponential	$\varphi_o\exp(-r_{12}/r_o)\exp(-r_{13}/r_o)\exp(-r_{23}/r_o)$	φ_o in eV, r_o in Å
Urey–Bradley	$(1/2)\Gamma(r_{23}-r_0)^2$	Γ in eV-Å^{-2}, r_o in Å
Four-body	$\varphi_o[1 + \cos(n\theta - \theta_o)]$	φ_o eV, θ_o in degrees
Ryckaert–Bellemans	$\sum_{n=1}^{N} \varphi_n(\cos\phi)^n$	φ_n in eV

θ_{ijk} represents the angle between the two interatomic vectors i-j and j-k and ϕ_{ijk} is the torsional angle between the planes ijk and jkl. We will use Γ instead of k for the spring constant, since k is used for the thermal conductivity.

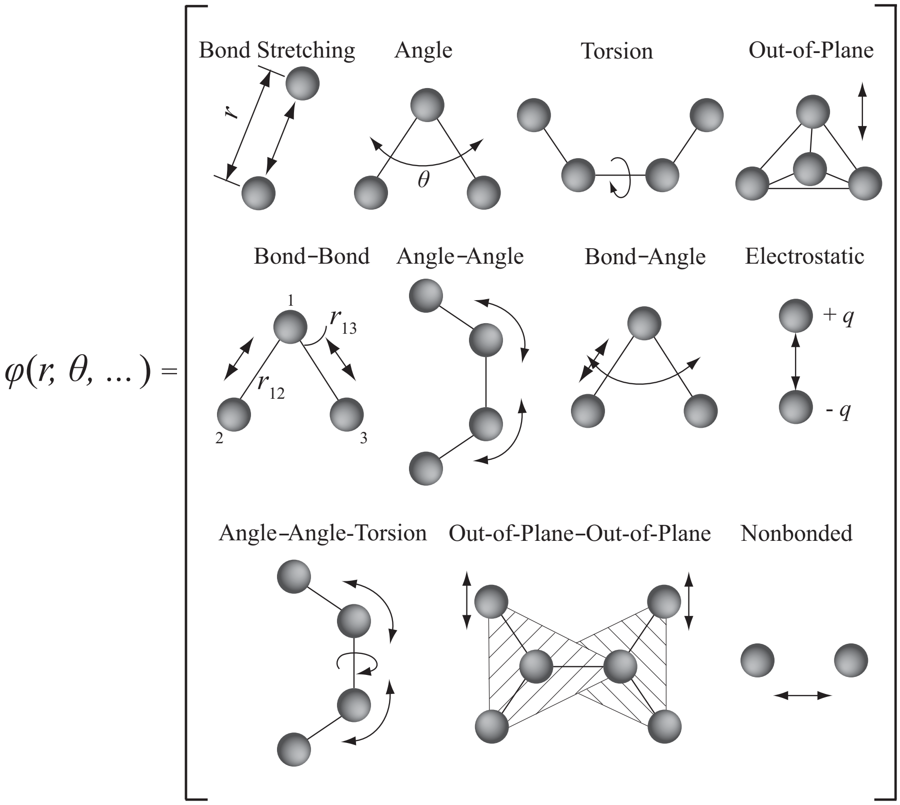

Figure 2.7. Various atomic motions contributing to the interatomic potential.

Hydrogen bonding forces arise when a hydrogen atom in a polar bond (e.g., H–F, H–O or H–N) experiences an attractive force with a neighboring electronegative molecule or ion that has an unshared pair of electrons (usually a F, O or N atom on another molecule). Hydrogen bonds are considered to be dipole–dipole-type interactions. The hydrogen atom has no inner core of electrons, so the side of the atom facing away from the bond represents a virtually naked nucleus (a proton). The positive charge of this electron-deficient side is attracted to the negative charge of an electronegative atom in a nearby molecule. Water is unusual in its ability to form an extensive hydrogen bonding network.

The simple interatomic potential (for van der Waals forces) of a pair of atoms/mole-cules following the 12–6 L–J potential model is given by [similar to that given in (2.7)]

$$\varphi_{\rm LJ} = 4\epsilon_{\rm LJ}[\underset{\text{repulsion}}{(\frac{\sigma_{\rm LJ}}{r})^{12}} - \underset{\text{attaction}}{(\frac{\sigma_{\rm LJ}}{r})^{6}}] \quad \text{L–J potential.} \tag{2.9}$$

In Figure 2.3, the effective L–J potential is that which results when interactions with all the atoms in a FCC lattice are taken into account. The inset of Figure 2.3 shows the equilibrium position and the RMS displacement obtained by MD simulations for three temperatures. The maximum temperature is close to the melting

Table 2.2. *L–J potential model constants for noble-gas element atomic pairs [12, 245].*

Noble-gas pair	$\epsilon_{\rm LJ}$, **eV**	$\sigma_{\rm LJ}$, **Å**	$r_{nn,e}$, **Å**
Ne–Ne	0.0031	2.74	3.13
Ar–Ar	0.0104	3.40	3.76
Kr–Kr	0.0140	3.65	4.01
Xe–Xe	0.0200	3.98	4.35

point (89.8 K for molecular dynamics). Note that, as the temperature increases, the solids generally expand (increasing the atomic spacing). The cutoff used is $r/\sigma_{\rm LJ} = 2.5$, as shown in the figure. Values of the L–J scales for some noble gas element pairs are given in Table 2.2. Note that for example for Ar, in Table A.2 the isolated atom has a radius of 1.88 A, and σ_{LJ} is 3.40 Å, or nearly twice the atomic radius. Ne has a smaller atomic radius and Kr has a larger one. The atomic radius is found from the electron orbital probability obtained from the Schrödinger equation (Section 2.6.6).

The temperature scale is $\epsilon_{\rm LJ}/k_{\rm B}$. More information on the L–J potential can be found in [12]. The hard-sphere and square-well potentials are not appropriate in MD simulations because they are not differentiable, as needed to calculate forces. They are more commonly used in Monte Carlo simulations, for which only energy calculations are required. The choice of the transition lengths in these potentials may depend on the system of interest. Here, they are chosen at $r/\sigma_{\rm LJ}$ values of 1 (hard sphere and square well) and 1.5 (square well). The distance to nearest neighbors in the FCC solid state is also listed.

As another example of interatomic potential, consider a polyatomic molecule such as SiO_2. The van Beest–Krammer–van Staten (B–K–S) interatomic potential between atom i and j separated by a distance r is [474]

$$\varphi_{\rm BKS} = \frac{q_i q_j}{r} + Ae^{-r/r_{\rm o}} - \frac{C}{r^6} \quad \text{B-K-S potential,} \tag{2.10}$$

shown in Figure 2.8. To match the dynamic behavior and potential of SiO_2 crystals, further refinement to this potential is made to arrive at [318]

$$\varphi_{\rm BKS} = \frac{q_i q_j}{r}{\rm erf}(\alpha r) + Ae^{-r/r_{\rm o}} - \frac{C}{r^6} + 4\epsilon[(\frac{\sigma}{r})^{24} - (\frac{\sigma}{r})^6] \quad \text{modified B-K-S potential.} \tag{2.11}$$

This is a combined Wolf [496] and modified 12–6 L–J (2.9). Only the two-body term is shown in Figure 2.8 for the Stillenger–Weber (S–W) model (Table 2.1) for silicon [450]. For the B–K–S silica curves [256, 474], the Wolf method [496] has been used to model the electrostatic interactions with an α value of 0.431 Å^{-1}. The cutoff radius used is 6.44 Å. The Si–O and O–O curves show nonphysical behavior below the minimum value of the distance plotted. However, this atomic separation falls below anything encountered in the solid state. If liquid silica is modeled, an L–J

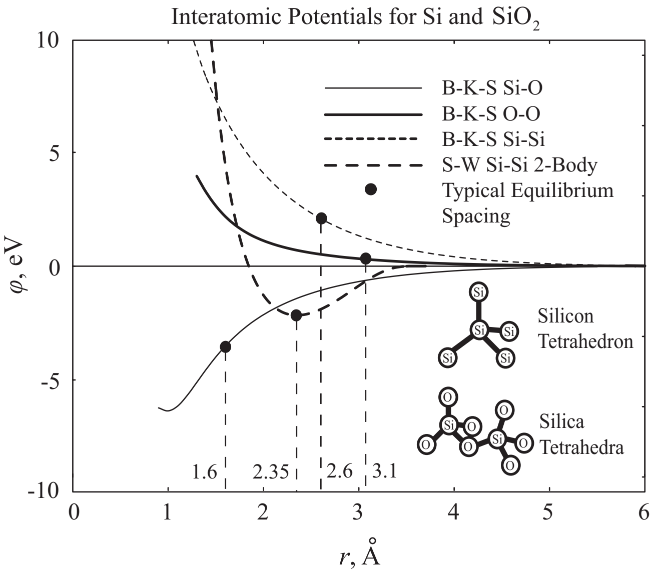

Figure 2.8. Variation of the interatomic potential for silicon and silica (SiO_2) with respect to separation distance.The B–K–S potential model for Si–O, O–O, Si–Si, and the S–W two-body Si–Si potential model are shown. Typical equilibrium spacings are also shown [318].

24–6 potential must be added to the B–K–S potential to prevent the system from blowing up [174]. Note the different behaviors of the Si–Si curves. This is because the Si–Si interactions in silicon are covalent, whereas in silica they are ionic. The energies associated with the silicon and silica potentials are on the order of 100 times greater than those encountered in the L–J potential. This is an indication of the large strength of covalent and ionic bonds compared with bonds that result from dipole fluctuations (i.e., London forces).

Various solid silica structures can be constructed from the preceding potentials, and Figure 2.9(a) shows some of these [318]. Each Si, [Ne]$3s^2 3p^2$, is linked to four O, [He]$2s^2 2p^4$, and each O is linked to two Si. All electrons are used in the covalent bonds (no delocalized electrons), so this makes for an electrically nonconducting solid. Quartz is an anisotropic crystal (a and c directions) and has an ordered tetrahedral building block. Amorphous silica (glass) has a random structure made of such tetrahedrons. Zeolites have cages (crystal pores), and some silica zeolites have sodalite (SOD) cage building blocks.

In Section 7.13.1, we list the Morse potential parameters for several bonds. No one potential can accurately represent arbitrary bonds, and in Section 4.11.2 we discuss a general bond strength estimation using a general form of the Lennard–Jones potential. A combination of the formation process (from gas, liquid, or solid phase), atomic stoichiometry of the ingredients temperature and pressure, as well a presence of mediating chemical and physical agents (e.g., catalysts), determines the particular atomic arrangement. For example, Figure 2.9(b) shows the various solid-state

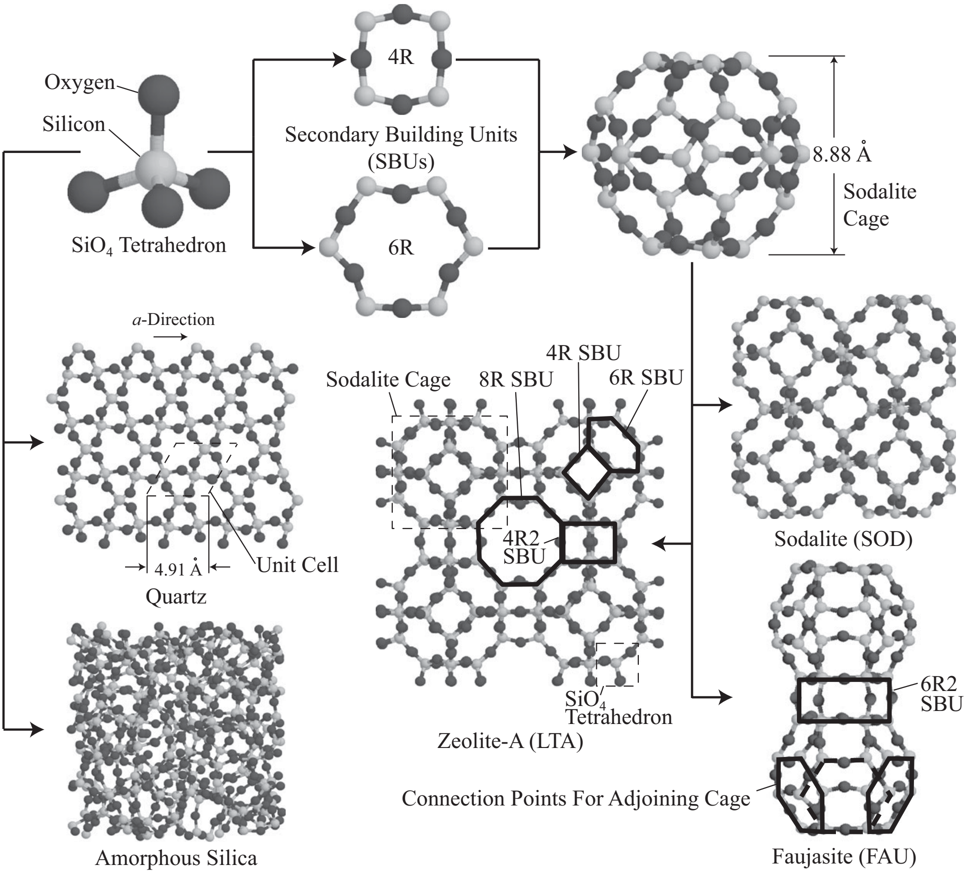

(a) Various SiO_2 (Silica) Structures

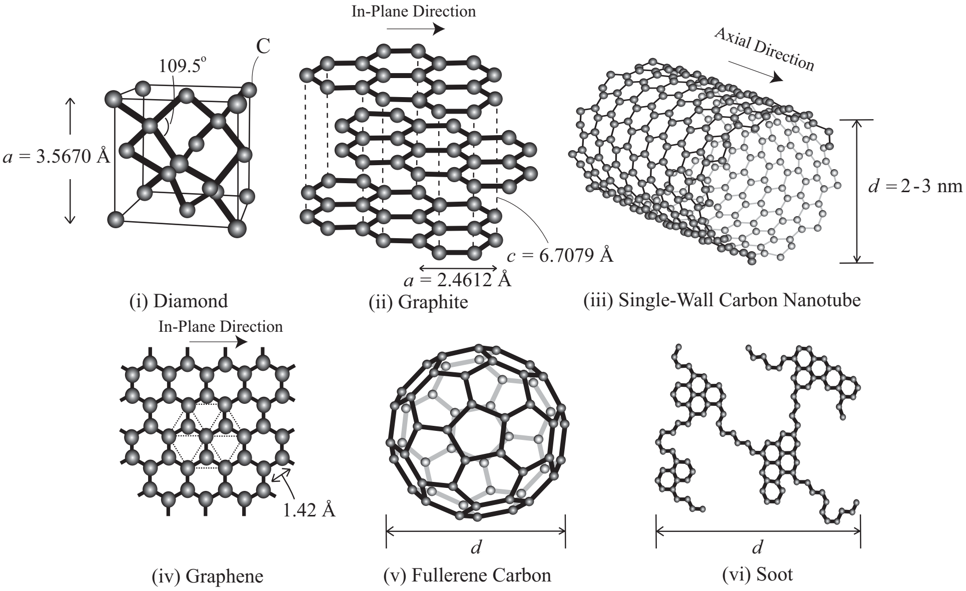

(b) Various C (Carbon) Structures

Figure 2.9. (a) Various solid-state phases (structures) of silica, and (b) various solid-state phases of carbon [320]. These include crystalline and amorphous phases.

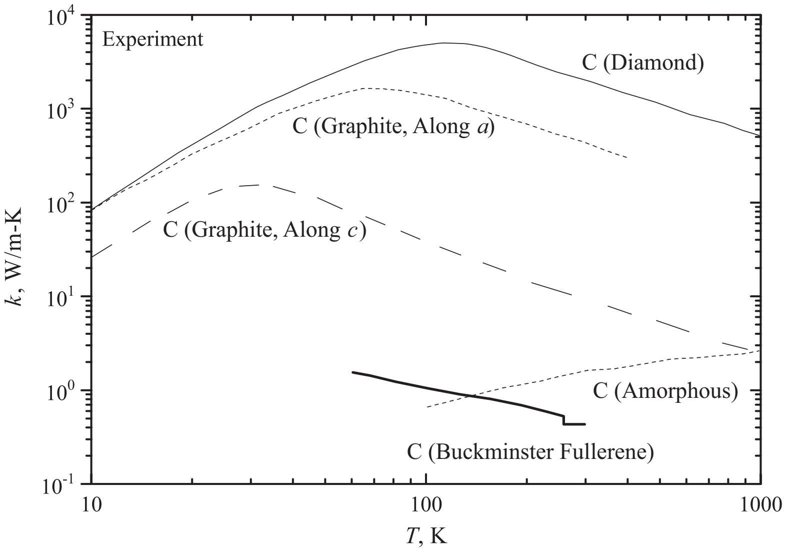

(c) k(T) for Solid Various Carbon Phases

Figure 2.9. (*continued*)(c) Variations of thermal conductivity of carbon solids with respect to temperature. The experimental results for diamond, graphite (anisotropic), fullerene, and amorphous phase are shown.

structures of carbon (e.g., diamond, graphite, carbon nanotube, graphene, fullerene carbon, and soot). With the [He]$2s^22p^2$ orbitals of C, single and double bonds are possible. In diamond the bonds are single and each C atom has four near neighbor C atoms (tetrahedral, bond angle 109.5°). In graphene there are three near neighbor C atoms, so the fourth electron is delocalized (conduction or free electron). Graphene C-C average bond length is 1.42 Å, and it is the basic structural element of graphite, carbon nanotubes and fullerenes. Due to the delocalized electron, these are all electrically conducting. The diameters d of a single-walled nanotube, Buckyball (e.g., carbon cage or fullerene carbon), and soot of the order of one nanometer conglomerates and become larger.

Figure 2.9(c) shows the variation of phonon (equal to the total thermal conductivity, i.e., no electron contribution) thermal conductivity of carbon in diamond, graphite (which is an anisotropic crystal), Buckminister fullerene solid, and amorphous solid phases, with respect to temperature [320]. Diamond has the overall tightest (smallest average interatomic spacing) packing among the crystalline phases shown, and has the highest thermal conductivity. These show the dominant role of molecular arrangement on the properties (including transport properties), and the ability to synthesize the desired structure (for function) from constituent atoms.

The properties of a nanotube depend on the wall (single-, double-, or multiple layer), chirality (Glossary), and diameter. We will discuss the temperature dependence of the crystalline and amorphous phase phonon conductivities and the crystalline atomic structures in Chapter 4.

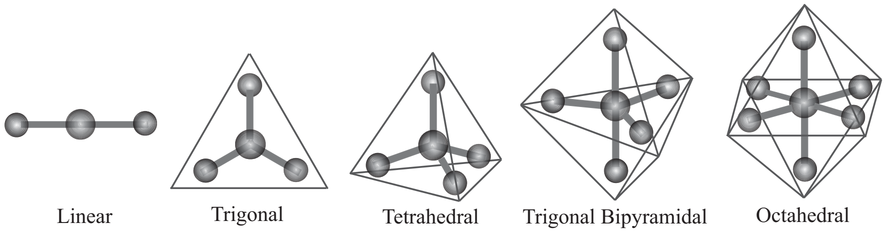

(a) Structure

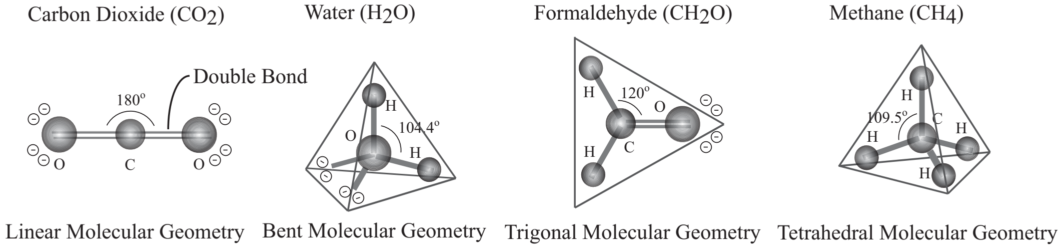

(b) Electron Pairings

Figure 2.10. (a) Examples of classifications of gaseous molecular structures, and (b) electron pairing and bond angles for the same gas molecules in (a).

Figures 2.10(a) and (b) show the atomic structure of some gases. Figure 2.10(a) shows the linear, trigonal, tetrahedral, trigonal bipyramidal and octahedral molecular geometries. Figure 2.10(b) shows the electron pairing and the bond angles for some gas molecules.

2.2.4 Examples of Atomic Bond Length and Energy

Table 2.3 lists the bond length r_e and energy φ_e for some atom pairs appearing in compounds of common chemical reactions of interest [409]. The bond lengths range from 1 to 3 Å, and the bond energies range from 1 to 10 eV. The nitrogen triple bond in N_2 is among the tightest and most energetic. Note that some of the bonds, for example C=C, can have different lengths and energy levels when they appear in different compounds. Examples of weaker bonds are the noble-gas elements, for which the pair bonding energies (same as ϵ_{LJ}) are listed in Table 2.2, such as 0.0031 eV for Ne–Ne.

From Table 2.3, the energy released/absorbed during reactions can be calculated. For example, the reaction of $2H_2$ and O_2 resulting in $2H_2O$ releases energy of 4.99 eV/O_2, and when this is divided by the charge of four electrons it produces, it gives 1.248 V as the ideal electric potential produced (see end-of-chapter problem). It can be shown that oxidation of methane (CH_4) results in release of 11.33 eV/CH_4 (end-of-chapter problem). There are also endothermic reactions (where net energy is absorbed), in that case more energy is needed to break the reactant bonds than is formed by the reactant bonds. For example, in photosynthesis of glucose ($6CO_2 + H_2O \rightarrow C_6H_{12}O_6 + 6O_2$) energy input is needed (provided by photon absorption).

Table 2.3. *Atomic pair bond length r_e and bond energy φ_e for some typical strong bonds and their compounds, as encountered in common chemical reactions [409].*

Atom pairs	Compound	r_e, **Å**	φ_e, **eV**	Atom pairs	Compound	r_e, **Å**	φ_e, **eV**
Al–F	AlF	1.65	6.86	K–Br	KBr	2.82	3.95
Al–H	AlH	1.65	2.95	K–Cl	KCl	2.95	4.41
Al–O	AlO	1.62	5.02	K–I	KI	3.29	3.37
As–F	AsF$_3$	1.71	5.04	Mg–Cl	MgCl	2.18	4.22
B=O	BOF	1.23	9.00	Mg–F	MgF	1.75	5.72
B–Br	BBr	1.87	4.32	N≡N	N$_2$	1.09	9.80
B–Cl	BCl	1.76	5.22	N=O	NO	1.15	6.55
B–I	BI	2.1	3.54	Na–Br	NaBr	2.68	3.85
Br–Cl	BrCl	2.14	2.22	Na–Cl	NaCl	2.53	4.29
Br–F	BrF	1.76	2.58	N–F	NF	1.37	2.99
C≡C	C2H2	1.2	8.20	N–F	NOF	1.52	2.61
C≡O	CO	1.13	11.34	N–S	NS	1.5	4.99
C=C	CH$_2$CO	1.31	6.11	O=O	O$_2$	1.21	5.17
C=C	C$_2$	1.31	6.53	O–F	OF	1.42	2.00
C=O	CO$_2$	1.16	8.34	P≡P	P2	1.89	5.42
Ca–F	CaF	2.02	5.51	Pb–F	PbF	2.11	3.24
Ca–O	CaO	1.82	4.03	P–Br	PBr	2.23	2.75
C–C	CCl$_3$CHO	1.52	3.11	P–Cl	PCl	2.04	3.26
Cl–F	ClF	1.63	2.60	P–F	PF	1.59	4.87
Cl–O	ClO	1.55	2.80	P–H	PH	1.42	3.14
Cs–I	CsI	3.32	3.25	P–O	PO	1.45	5.22
Ga–H	GaH	1.58	2.84	P–S	PS	1.92	5.36
Ge–Br	GeBr	2.3	2.62	Rb–Br	RbBr	2.95	3.92
Ge–Cl	GeCl	2.08	3.56	Rb–F	RbF	2.87	5.02
Ge–F	GeF	1.68	5.07	Sb–Cl	SbCl$_3$	2.33	9.76
H–As	AsH$_3$	1.51	3.07	Si≡S	SiS	1.93	6.66
H–C	CH$_2$CO	1.08	4.28	Si=Si	Si$_2$	2.25	3.29
H–H	H$_2$	0.74	4.52	Si–Cl	SiCl	2.0	4.02
H–O	H$_2$O	0.96	4.80	Si–Cl	SiC	1.65	4.48
H–O	OH	1.03	4.44	Si–F	SiF	1.6	5.72
H–S	HS	1.36	3.78	Si–N	SiN	1.57	4.58
I–Br	IBr	2.45	1.84	Sn–H	SnH	1.79	3.21
I–Cl	ICl	2.3	2.18	Te–Se	TeSe	2.5	2.30
I–F	IF	1.91	2.91	Tl–F	TlF	2.08	4.60
In–H	InH	1.84	1.99	Xe–O	XeO$_3$	1.76	1.31

2.2.5 Radial Distribution of Atoms in Dense Phase

The local density of a collection of particles (molecules) $\rho(r)$ is given in terms of the radial distribution (RDF) function $g(r)$ as

$$\rho(r) = \langle\rho\rangle g(r), \quad \langle g(r)\rangle = \frac{1}{V}\int_0^r g(r) 4\pi r^2 \mathrm{d}r, \quad \langle g(r)\rangle \to 1 \text{ for } r \to \infty. \quad (2.12)$$

Here the radial location r is measured from the center of a reference particle. For ideal gases, $g(r) = 1$, everywhere, whereas for nonideal gases, liquids, and solids $g(r)$ varies greatly over several intermolecular lengths (measured from the central particle).

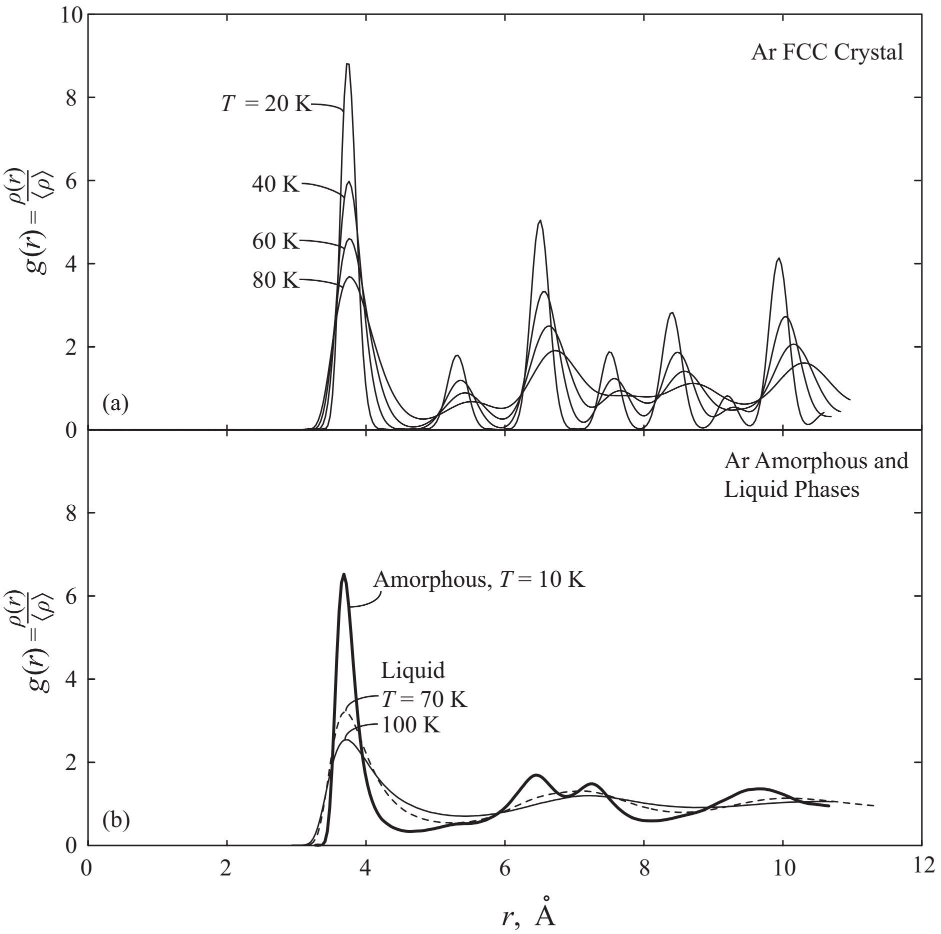

Figure 2.11. Ar L–J potential radial distribution functions for (a) the FCC crystal at $T = 20$, 40, 60, and 80 K, and (b) the amorphous phase at $T = 10$ K and the liquid phase at $T = 70$ and 100 K [315].

The RDF describes the distribution of the atoms in a system from the standpoint of a fixed, central atom. Its numerical value at a position r is the probability of finding an atom in the region $r - \mathrm{d}r/2 < r < r + \mathrm{d}r/2$. The Fourier transform of the RDF is called the structure factor, which can be determined from scattering experiments. The RDFs for the Ar FCC crystal from MD simulations at temperatures of 20, 40, 60, and 80 K, the amorphous phase at a temperature of 10 K, and the liquid phase at temperatures of 70 and 100 K are shown in Figure 2.11. The RDF can be determined only up to one half of the simulation cell size, which here is about 3.25 σ_{LJ} for the solid phases and slightly larger for the liquid.

The RDF of the Ar FCC crystal phase shows well-defined peaks that broaden as the temperature increases and the atomic displacements increase. Each peak can be associated with a particular set of nearest-neighbor atoms. The locations of the peaks shift to higher values of r as the temperature increases and the crystal expands. In the amorphous phase, the first peak is well-defined, but after that, the disordered nature of the system leads to a much flatter RDF. There is no order beyond a certain point. The splitting of the second peak is typical of amorphous phases, and consistent with the results for L–J Ar [280]. The presence of only short-range order is also seen in the liquid phase, in which only the first neighbor peak is well-defined. This is expected, because the physical size of the atoms defines the minimum distance over which they may be separated.

2.3 Molecular Ensembles, Temperature, and Thermodynamic Relations

2.3.1 Ensembles and Computational Molecular Dynamics

The ensemble-average behavior of a collection of particles is used in statistical mechanics (Section 1.3) and allows for the determination of macroscopic properties of the system. Each ensemble includes a collection of positions and velocities of a given number of particles at a given energy and volume (for *NVE* ensemble, discussed in Section 2.5.1). It is possible for these same particles to have different positions and velocities, but the same macroscopic properties. This means the particles are allowed to differ microscopically, while retaining the same macroscopic, independent properties when looked at as a whole.

Because of the way an ensemble is constructed, if snapshots of all the possible configurations (different particle positions and velocities) is taken at some instant in time, we will find that they differ in the instantaneous values of their bulk properties. This phenomenon is called fluctuation. Thus the true value of any particular bulk property must be calculated as an average over all the possible microscopic arrangements of the ensemble. This is what is meant by an ensemble average, and the instantaneous values are said to fluctuate about the average value.

MD proceeds by numerically integrating the equations of motion of these particles. Each time step generates a new arrangement (or configuration) of the atoms and new instantaneous values for macroscopic properties such as temperature, pressure, and energy. Determining the thermodynamic values of these variables requires an ensemble average. In MD, this is achieved by finding the average over successive configurations generated by the simulation. It is assumed that an ensemble average (which relates to many configurations of the system) is the same as an average over time of one configuration (the system simulated). This assumption is known as the ergodic hypothesis and is generally true, provided a long enough time behavior is included in the average. The specifics of this hypothesis are given in Section 2.3.3. Other examples of properties that can be calculated as ensemble averages include the elastic properties of solids and time correlations.

2.3.2 Energy Equipartition

The energy equipartition theorem relates the temperature of an ensemble of atoms or molecules (treated as classical particles) with its average energy. Under thermal equilibrium (where the particles energy follows the energy occupation probability f_i^{o}) this energy is shared equally among all of its various forms. This means the average kinetics energy per degree of freedom in the translational motion of particle should equal that of its rotational motion (we will use this in Section 4.7 for phonons and in Section 6.2 for fluid particles). This energy per degree of freedom of each type of motion is equal to $k_\mathrm{B}T/2$.

The equipartition theorem works well at relatively high temperatures, but at low temperatures the quantum effects become significant, since the thermal energy $k_\mathrm{B}T$ becomes smaller than the quantum energy increments in a particular degree of freedom. For example the phonon average specific heat capacity per degree of freedom becomes less than that predicted by the classical equipartition as the temperature becomes less than the Debye temperature (Section 4.7.1). Phonon (atomic vibration) represent both the kinetic and potential energy and the energy equipartition also applies to the potential energy (and for the harmonic oscillator, the average kinetic and potential energies are equal, Section 2.5.2).

2.3.3 Thermodynamic Relations

From the microscopic (statistical) perspective, temperature is the measure of the average kinetic energy of the molecules (or atoms) of a substance, i.e., the greater the translational kinetic energy, the higher the temperature. Note that this energy is solely due to thermal fluctuations of the constituent particles (the particular phase these particles assume is determined in part by their temperature). The absolute zero of temperature (0 K) is where the molecules have no motion in classical systems (there is a zero point motion in quantum mechanics). This definition of temperature, for a system of N particles, with individual particles having mass m_i and instantaneous translational speed u_i, as shown in Figure 2.2, is [460]

$$T \equiv \frac{\dfrac{1}{2}\langle \displaystyle\sum_{i=1}^{N} m_i u_i^2 \rangle}{\dfrac{1}{2} N_f k_\mathrm{B}}, \quad \text{each partitioned energy is } \frac{1}{2}k_\mathrm{B}T \ (\text{for } N \gg 1) \tag{2.13}$$

where $N_f = 3N$ is the number of translational degrees of freedom of the system of particles. We will discuss vibrational and rotational motions in Section 6.1. This kinetic definition of temperature is an integral part of its relation to the entropy S (a measure of multiplicity) of the system. For the vibrational and rotational energy, these kinetic energies (and their occupancies) are represented with similar average as in (2.13).

The equilibrium thermodynamic state of N particles in a volume V is given in terms of $E = E(S, V, N)$, and T is also related to the derivatives of these functions. We defined S in terms of the partition function Z in (1.6), and Z in turn is related to the energy (Table 2.4), so we have

$$S \equiv k_\mathrm{B}N \ln Z + \frac{E}{T} = k_\mathrm{B}N \ln \sum_{i=0}^{\infty} e^{E_i/k_\mathrm{B}T} + \frac{E}{T}, \tag{2.14}$$

where each E_i (includes translational, vibrational, rotational, and electronic energy, Figure 1.1) is an individual micro energy state of the system and E is the total internal energy. These are repeated in Table 2.4, along with the definition of N_f.

In fluctuation theory, allowance is made for the anharmonic motions, and then the temperature is defined in terms of the anharmonicity parameter $\alpha(T)$.

Thermal equilibrium in a system of particles corresponds to its maximum entropy, and the rate of approach to that state is proportional to the difference in temperature between parts of the system. The equilibrium state of a collection of particles then becomes the state of greatest multiplicity, and the temperature (and similarly pressure and chemical potential) defined in terms of this multiplicity (entropy) is [72]

$$T \equiv \frac{1}{\left.\frac{\partial S}{\partial E}\right|_{V,N}} = \left.\frac{\partial E}{\partial S}\right|_{V,N}, \quad p \equiv -\left.\frac{\partial E}{\partial V}\right|_{S,N}, \quad \mu \equiv \left.\frac{\partial E}{\partial N}\right|_{S,V}, \tag{2.15}$$

where we have also included the definitions of pressure and chemical potential μ. The macroscopic thermodynamic definition of temperature is expressed as the inverse of the rate of change of entropy with respect to internal energy, with the volume V and the number of particles N held constant. A few other useful thermodynamic relations are given in Table 2.4.

2.4 Hamiltonian Mechanics

2.4.1 Classical and Quantum Hamiltonians

In Newtonian mechanics, the equation of motion of particle k, in a multibody system (subject to two- and three-body forces) is

$$\frac{\mathrm{d}}{\mathrm{d}t}(m_k \boldsymbol{u}_k) = \frac{\mathrm{d}\boldsymbol{p}_k}{\mathrm{d}t} = \frac{\mathrm{d}^2 m_k \boldsymbol{x}_k}{\mathrm{d}t^2} = \boldsymbol{F}_k, \tag{2.16}$$

where m_k is the mass, $\boldsymbol{u}_k$ and $\boldsymbol{x}_k$ are the velocity and position vector of particle k, and $\boldsymbol{F}_k$ is the sum of all the external forces acting on it (Table 2.4). However, in statistical mechanics the equation of motion is not directly solved, and instead the total energy of the particle is tracked, i.e., the Hamiltonian (on its derivatives).

In classical mechanics, the Hamiltonian $\mathrm{H}(\boldsymbol{x}, \boldsymbol{p})$ is a function describing the total energy state of a mechanical system. The Hamiltonian equations of motion are the relations between H and its derivatives of $\boldsymbol{x}$, $\boldsymbol{p}$, and their time derivatives (i.e., a generalized coordinate $\boldsymbol{x}$ and a generalized momentum $\boldsymbol{p}$) are [323]†

$$\frac{\partial \boldsymbol{x}}{\partial t} = \frac{\partial \mathrm{H}}{\partial \boldsymbol{p}}, \quad \frac{\partial \boldsymbol{p}}{\partial t} = -\frac{\partial \mathrm{H}}{\partial \boldsymbol{x}}, \tag{2.17}$$

---

† The total derivative of H is [323]

$$\mathrm{dH} = \sum_k \frac{\partial \mathrm{H}}{\partial p_k} \mathrm{d}p_k + \sum_i \frac{\partial \mathrm{H}}{\partial x_i} \mathrm{d}x_i .$$

Then the equipartition of energy gives

$$\langle p_k \frac{\partial \mathrm{H}}{\partial p_k} \rangle = k_\mathrm{B} T, \quad \langle x_i \frac{\partial \mathrm{H}}{\partial x_i} \rangle = k_\mathrm{B} T,$$

where $\langle \quad \rangle$ indicates ensemble average.

Table 2.4. *Microscopic (statistical) and macroscopic thermodynamic relations [460, 72].*

Microscopic (statistical) thermodynamic relations include the following:

Temperature, pressure and potential, and kinetic energy are related to individual particle (atom or molecule in translational motion)

$$T = \frac{\frac{1}{2}\langle \sum_{i=1}^{N} m_i u_i^2 \rangle}{\frac{1}{2} N_f k_\mathrm{B}} = \frac{\sum_{i=1}^{N} \frac{|\boldsymbol{p}_i|^2}{m_i}}{3(N-1)k_\mathrm{B}} = \frac{2E_{k,T}}{3(N-1)k_\mathrm{B}} \quad \text{for translational (displacement) kinetic energy only}$$

$$p = \frac{N k_\mathrm{B} T}{V} + \frac{1}{3V}(\sum_{i=1}^{N}\sum_{j \neq i}^{N} \boldsymbol{x}_{ij} \cdot \boldsymbol{F}_{ij})$$

$$E = E_k + E_p$$

$$E_{k,t} = \sum_{i=1}^{N} \frac{1}{2} m_i u_i^2, \ E_p = \langle \varphi \rangle = \frac{1}{2} \sum_{i=1}^{N}\sum_{j \neq i}^{N} \varphi(\boldsymbol{x}_{ij}) \quad \text{for pair potentials}$$

where N_f is number of translational (displacement) degrees of freedom in the system [in translational or displacement-only MD, $N_f = 3(N-1)$, where N is the number of particles] for systems with $N \gg 1$, and $N-1$ is required for having zero momentum for the system.

Entropy, internal energy, and pressure are related to the partition function Z (and Hamiltonian H)

$$Z = \int\int \exp[\frac{-\mathrm{H}(\boldsymbol{x}, \boldsymbol{p})}{k_\mathrm{B} T}]\mathrm{d}\boldsymbol{x}\,\mathrm{d}\boldsymbol{p}, \ \ \mathrm{H} = \sum_l \mathrm{H}_l \quad \text{partition of energies and partition function}$$

$$Z = \frac{1}{h_\mathrm{P}^{3N} N!} \int \exp[\frac{-\mathrm{H}(1, ..., N)}{k_\mathrm{B} T}]\mathrm{d}^{3N}x\ \mathrm{d}^{3N}p \quad \text{integral grand (canonical) partition function}$$

$$S = k_\mathrm{B} N \ln Z + \frac{E}{T} = k_\mathrm{B} N \ln \sum_{i}^{\infty} e^{E_i/k_\mathrm{B}T} + \frac{E}{T}$$

$$E = \frac{\sum_i E_i e^{-E_i/k_\mathrm{B}T}}{Z} = k_\mathrm{B} T^2 N \frac{\partial \ln Z}{\partial T}|_{N,V}$$

$$p = k_\mathrm{B} T \frac{\partial \ln Z}{\partial V}|_{T,N}.$$

Thermal fluctuation theory uses energy deviations, and temperature is defined as

$$T = [\frac{\langle (E - \langle E \rangle)^2 \rangle}{k_\mathrm{B} c_v}]^{1/2}, \qquad c_v = \alpha(T) N_f k_\mathrm{B}$$

where $\alpha(T)$ represents anharmonicity in the system.

Macroscopic thermodynamic relations include:

$$\mathrm{d}E = T\mathrm{d}S + \mu \mathrm{d}N - p\mathrm{d}V, \ \ \mu - T\frac{\partial \mu}{\partial T}|_p = h, \ \ T = \frac{1}{\left.\frac{\partial S}{\partial E}\right|_{V,N}} = \left.\frac{\partial E}{\partial S}\right|_{V,N}, \ \ -\frac{\mu}{T} = \left.\frac{\partial S}{\partial N}\right|_{E,V}, \ \ c_v \equiv \left.\frac{\partial e}{\partial T}\right|_v$$

E	internal energy, J, e specific internal energy, J/kg
h	specific enthalpy, J/moleculae
H	Hamiltonian, J
S	entropy, J/K
V	volume (m^3), v specific volume, m^3/kg
Z	partition function
μ	chemical potential, J/molecule
φ	potential energy, J

The quantum mechanical expectation value of temperature (kinetic energy) is based on the quasi-particle momentum and is [171] (derivation left as Chapter 5 problem)

$$\langle E_k \rangle = -\frac{\hbar^2}{2m} \int \Psi^\dagger \nabla^2 \Psi \mathrm{d}\boldsymbol{x}.$$

which is a set of first-order differential equations. Also, $\partial \mathrm{H}/\partial t = 0$. The dynamical states of a system of N particles is completely determined by $2N$ vectors $\boldsymbol{x}$ and $\boldsymbol{p}$, and the energy of the system is given by the Hamiltonian function (for 3 degrees of freedom)

$$E = \mathrm{H}(\boldsymbol{x}, \boldsymbol{p}) = \sum_l \mathrm{H}_l = \sum_{k=1}^{3N} \frac{p_k^2}{2m} + \sum_{i=1}^{N} [\varphi_e(\boldsymbol{x}_i) + \sum_{i<j}^{N} \varphi_{ij}(\boldsymbol{x}_i - \boldsymbol{x}_j)] \quad \text{classical Hamiltonian,} \tag{2.18}$$

where φ_e is the external potential and φ is the interparticle pair potential (Section 2.2 and depends on particle position only). The Hamiltonian is the central function in the theory of statical mechanics. The preceding relations are also listed in Table 2.5.

As indicated in (2.18), the total Hamiltonian of a system contains the various energies (e.g., kinetic, electronic). Each of these can be further divided; the kinetic energy can be divided into translational, rotational, and vibrational, through the partition of energies.

In (2.18) we have partitioned the energy into kinetic and potential, and further partitioned each one. Now using (2.13) we can relate the kinetic energy and temperature, and also by defining the partition function Z we relate thermodynamics properties to Z. The partition function is used to define the probability of a system (equilibrium) of particles to be found in a particular energy state P_n, where n designates the energy eigenstate [156]. The grand canonical (for systems that can exchange both energy and particles with a much larger reservoir) partition function is also listed in Table 2.4.

In quantum mechanics, the Hamiltonian operator (or observable) of the system is the sum of its kinetic and potential energy φ, but in an operator form also (operating on a quantum wave function):

$$\mathrm{H} = -\frac{\hbar^2}{2m}\nabla^2 + \varphi(\boldsymbol{x}) \quad \text{quantum Hamiltonian operator.} \tag{2.19}$$

We discuss this in relation to the Schrödinger equation in Section 2.6.

2.4.2 Probability and Partition Function

The energy probability density of state n of the ensemble (assuming zero chemical potential, $\mu = 0$) is given by

$$P_n(\boldsymbol{x}, \boldsymbol{p}) = \frac{1}{Z}\exp[-\mathrm{H}_n(\boldsymbol{x}, \boldsymbol{p})/k_\mathrm{B}T], \qquad \sum_n P_n = 1, \tag{2.20}$$

where $\mathrm{H}_n(\boldsymbol{x}, \boldsymbol{p}) = E_n(\boldsymbol{x}, \boldsymbol{p})$ is the Hamiltonian of state n, and Z is the partition function (dimensionless), introduced in (1.6), and is defined in the general form as

$$Z \equiv \int\!\!\int \exp[\frac{-\mathrm{H}(\boldsymbol{x}, \boldsymbol{p})}{k_B T}]\mathrm{d}\boldsymbol{x}\mathrm{d}\boldsymbol{p} = \frac{1}{h_\mathrm{P}^{3N} N!}\int \exp[\frac{-\mathrm{H}(1, \dots, N)}{k_\mathrm{B} T}]\mathrm{d}^{3N}x\, \mathrm{d}^{3N}p, \tag{2.21}$$

Table 2.5. *Classical particle (molecular) dynamics equations (Newton and Hamiltonion equations).*

Newton particle momentum conservation equation:

$$\frac{\mathrm{d}}{\mathrm{d}t}(m_k \boldsymbol{u}_k) = \frac{\mathrm{d}}{\mathrm{d}t}(m_k \frac{\mathrm{d}\boldsymbol{x}_k}{\mathrm{d}t}) = \boldsymbol{F}_k \equiv \sum_j \boldsymbol{F}_{kj} + \sum_{i,j} \boldsymbol{F}_{kij} + \cdots$$

$$\boldsymbol{F}_{kj} = -\frac{\partial \varphi}{\partial \boldsymbol{x}_{kj}} = -\frac{\partial \varphi}{\partial r}\boldsymbol{s}_{kj} \quad \text{interatomic force}$$

$$\boldsymbol{F}_{kj} = -\Gamma_{kj}\boldsymbol{d}_{kj},\ \Gamma_{kj} = \left.\frac{\partial^2 \varphi_{kj}}{\partial r_{kj}^2}\right|_e \quad \text{harmonic approximation}$$

Γ_{kj} is force constant

In terms of displacement vector $\boldsymbol{d}$,

$$m_k \frac{\mathrm{d}^2 \boldsymbol{d}}{\mathrm{d}t^2} = \boldsymbol{F}_k$$

Hamiltonian (energy) function:

$$\mathrm{H} = \mathrm{H}(\boldsymbol{x}, \boldsymbol{p}) = \sum_l \mathrm{H}_l \quad \text{Hamiltonian, and partition of energies}$$

$$= \frac{1}{2}\frac{|\boldsymbol{p}|^2}{m} + \varphi(\boldsymbol{x}) = E_k + E_p = E(\boldsymbol{x}, \boldsymbol{p}) \quad \text{classical Hamiltonian}$$

Hamilton equations of motion:

$$\frac{\partial \boldsymbol{x}}{\partial t} = \frac{\partial \mathrm{H}(\boldsymbol{x}, \boldsymbol{p})}{\partial \boldsymbol{p}} = \frac{\partial E(\boldsymbol{x}, \boldsymbol{p})}{\partial \boldsymbol{p}}$$

$$\frac{\partial \boldsymbol{p}}{\partial t} = -\frac{\partial \mathrm{H}(\boldsymbol{x}, \boldsymbol{p})}{\partial \boldsymbol{x}} = -\frac{\partial E(\boldsymbol{x}, \boldsymbol{p})}{\partial \boldsymbol{x}}$$

Hamiltonian function for a system of N particles:

$$E = \mathrm{H} = \sum_{k=1}^{3N} \frac{p_k^2}{2m} + \sum_{i=1}^{N} [\varphi_e(\boldsymbol{x}_i) + \sum_{i<j}^{N} \varphi_{ij}(\boldsymbol{x}_i - \boldsymbol{x}_j)] + \ldots$$

E	energy, J
$\boldsymbol{d}_{kj}$	displacement vector, m
$\boldsymbol{F}_k$	applied external force on particle k, N
H	Hamiltonian, J
$\boldsymbol{p}$	particle momentum, N-s
φ_e	external potential energy, J
φ_{ij}	interparticle potential energy, J
Γ_{kj}	spring (force) constant, N/m

where the grand canonical ensemble (Section 2.5.1) is a statistical ensemble in equilibrium with an external bath (particle and energy exchange) at fixed T, V, and μ. This integral is in turn represented as a summation, as given in Table 2.4, and is generally extremely difficult to calculate because one must calculate all possible states of the system. In MD simulation, the points in the ensemble are calculated sequentially in time, so to calculate an ensemble average; the MD simulations must pass through states corresponding to the particular thermodynamic constraints. To cover all possible states, simulations with different initial conditions are used. As shown in Appendix F, the energy occupancy distribution functions f_i^{o} $(i = p, e, f, ph)$ are derived based on the partition function (and the scaled energy $E_i/k_{\text{B}}T$).

From (2.21), we note that the contribution from each component of the Hamiltonian to the partition function is multiplicative, i.e., $Z = \Pi_i Z_i$, where each Z_i is for a Hamiltonian. We will use this in Chapter 6 for the fluid particles and its various energies.

2.4.3 Ergodic Hypothesis in Theoretical Statistical Mechanics

In statistical mechanics, average values are defined as ensemble averages. The ensemble average is given by

$$\langle \phi \rangle_{\boldsymbol{x},\boldsymbol{p}} = \int_{\boldsymbol{p}} \int_{\boldsymbol{x}} \phi(\boldsymbol{x}, \boldsymbol{p}) P(\boldsymbol{x}, \boldsymbol{p}) \mathrm{d}\boldsymbol{x}\, \mathrm{d}\boldsymbol{p}, \tag{2.22}$$

where ϕ is the observable of interest and it is expressed as a function of the positions $\boldsymbol{x}$ and momenta $\boldsymbol{p}$ (or velocity $\boldsymbol{u}$) of the system. The integration is over all possible values of $\boldsymbol{x}$ and $\boldsymbol{p}$.

Another way, as done in a MD simulations, is to determine a time average of ϕ, which is expressed as

$$\langle \phi \rangle_t = \lim_{\tau \to \infty} \frac{1}{\tau} \int_{t=0}^{\tau} \phi[\boldsymbol{x}(t), \boldsymbol{p}(t)] \mathrm{d}t \simeq \frac{1}{K} \sum_{t=1}^{K} \phi[\boldsymbol{x}(t), \boldsymbol{p}(t)], \tag{2.23}$$

where τ is the simulation time, K is the number of time steps in the simulation and $\phi[\boldsymbol{x}(t), \boldsymbol{p}(t)]$ is the instantaneous value of ϕ.

The ergodic hypothesis states that the phase-space $(\boldsymbol{x}, \boldsymbol{p})$ ensembles and time ensemble (t) are equal for ergodic systems, i.e., ergodic hypothesis:

$$\langle \phi \rangle_{\boldsymbol{x},\boldsymbol{p}} = \langle \phi \rangle_t \quad \text{ergodic hypothesis.} \tag{2.24}$$

In an ergodic system, all points in phase space $(\boldsymbol{x}, \boldsymbol{p})$ are accessible from any starting point.

2.5 Molecular Dynamics Simulations

In a MD simulation [3, 148], the position and momentum space trajectories of a system of classical particles are predicted by the Newtonian laws of motion and an appropriate interatomic potential. By use of the positions and momenta, it is possible to investigate a variety of thermal transport problems at the atomic level. Below, we summarize key aspects of MD simulations.

2.5.1 Ensemble and Discretization of Governing Equations

MD [148] is concerned with molecular motion, i.e., conformational transitions (fluids) and local vibrations (solids), which are represented by changes in the positions and velocities of molecules (or atoms/particles) with respect to time. The Newtonian equations of motion are used in the MD formalism to simulate these particle motions as classical, multibody systems. The particles are generally considered hard spheres, but elastic particles can also be studied. The rate and direction of motion (velocity) are governed by the forces that the particles of the system exert on each other as described by the Newtonian momentum conservation equation. In practice, the atoms are assigned initial velocities that conform to the total kinetic energy of the system (but this may not remain constant during simulation), which in turn is dictated by the desired simulation temperature. This can be carried out by slowly heating the system (initially at absolute zero) and then allowing the energy to equilibrate among the constituent particles. The basic elements of molecular dynamics are the calculation of the force on and (from that information) position of each particle throughout a specified period of time Δt (typically of the order of fs, 10^{-15} s). The force on a particle can be calculated from the change in potential energy between its current position and its position a small distance away. This can be recognized as the derivative of the potential energy with respect to the change in position (Figure 2.2).

The potential energies can be calculated by either molecular mechanics or quantum mechanical methods. Molecular-mechanic energies are limited to applications that do not involve drastic changes in electronic structure, such as bond making/breaking. Quantum-mechanical energies can be used to study dynamic processes involving chemical changes, but computation time becomes intensive. Knowledge of the atomic forces and masses can then be used to solve for the positions of each atom along a series of extremely small time steps Δt. The resulting series of snapshots of structural changes over time is called a trajectory.

These particle motions, which are microscopic, are used in ensemble averages (statistical mechanics) to calculate macroscopic observable properties, including both static (e.g., pressure, energy, heat capacity) and kinetic-transport (e.g., thermal conductivity) properties. The thermodynamic state of a system is usually defined by a small set of parameters, for example, the temperature T, the pressure p, and the number of particles N. Other thermodynamic properties may be derived from the equations of state and other fundamental thermodynamic relations.

(A) *Ensembles*

The mechanical or microscopic state of a system is defined by the particle positions $\boldsymbol{x}$ and momenta $\boldsymbol{p}$ (or velocities $\boldsymbol{u}$), and these can also be considered as coordinates in a multidimensional space called the phase space. For an N particle system, this space has $6N$ dimensions. A single point in the phase space describes the state of the system. An ensemble is a collection of points in phase space satisfying the conditions of a particular thermodynamic state. A MD simulation generates a sequence of points in phase space as a function of time. These points belong to the same ensemble, and they correspond to the different conformations of the system and their respective momenta.

Several different ensembles are used, including the microcanonical ensemble (NVE), where the thermodynamic state is characterized by a fixed number of particles N, a fixed volume V, and a fixed energy E, which corresponds to an isolated system. The canonical ensemble (NVT) is a collection of all systems whose thermodynamic state is characterized by a fixed N, a fixed V, and a fixed temperature T (the system can exchange heat with an ambient reservoir). The isobaric–isothermal ensemble (NpT) is characterized by a fixed N, a fixed pressure p, and a fixed T. The grand canonical ensemble (μVT) is characterized by a fixed chemical potential μ, a fixed V, and a fixed T (the system can exchange heat and particle with an ambient reservoir).

(B) *Ensemble-Averaged Energy*

The average potential energy is

$$\langle \varphi \rangle_K = \frac{1}{K} \sum_{i=1}^{K} \varphi_i, \tag{2.25}$$

where K is the number of configurations in the MD trajectory and φ_i is the potential energy of each configuration. The pair-potential version of this will be given in Section 2.5.3.

The average kinetic energy is

$$\langle E_k \rangle_K = \frac{1}{K} \sum_{j=1}^{K} (\sum_{i=1}^{N} \frac{m_i}{2} \boldsymbol{u}_i \cdot \boldsymbol{u}_i)_j, \tag{2.26}$$

where K is the number of configurations in the simulation, N is the number of atoms in the system, m_i is the mass of the particle i, and $\boldsymbol{u}_i$ is the velocity of particle i.

Using the degeneracy g_n (microstates having the same energy E_n), discrete canonical partition function (2.21) with $\mathrm{H}_n = E_n$ is defined as [73]

$$Z = \sum_{n=0}^{\infty} g_n \ \exp(-\frac{E_n}{k_\mathrm{B} T}) \quad \text{with } \mathrm{H}_n = E_n, \text{discrete canonical partition function}, \tag{2.27}$$

where the summation is over all the energy levels.

A degenerate state is that for which $g_n \geq 2$ for an energy state E_n. For the nondegenerate states, $g_n = 1$.

Here we first proceed with the computational MD simulations, and in the following chapters (in particular Chapters 4 and 6) we will make use of the preceding theoretical statistical mechanics (thermodynamics). A MD simulation must be performed over a sufficiently long elapsed time so sufficient representative configurations have been sampled (Section 2.4.3).

(C) *Computational Classical Particle Dynamics*

The MD simulation method is based on the Newton second law, $\boldsymbol{F} = m\boldsymbol{a}$, where $\boldsymbol{F}$ is the force exerted on the particle, m is its mass, and $\boldsymbol{a}$ is its acceleration. From a knowledge of the force on each atom/particle, it is possible to determine the acceleration of each atom/particle in the system. Integration of the equations of motion then yields a trajectory that describes the positions, velocities, and accelerations of the particles as they vary with time. From this trajectory, the average values of properties can be determined. The method is deterministic; once the positions and velocities of each atom/particle are known, the state of the system can be predicted at any time in the future or the past. MD simulations can become computationally extensive.

The Newton equation of motion is given by

$$\boldsymbol{F}_i = m\boldsymbol{a}_i, \tag{2.28}$$

where F_i is the force exerted on particle i, m_i is the mass of particle i and $\boldsymbol{a}_i$ is the acceleration of particle i. The force can also be expressed as the negative gradient of the potential energy φ, i.e.,

$$\boldsymbol{F}_i = -\nabla_i \varphi. \tag{2.29}$$

Combining the preceding two equations, and for a one-dimensional translation, we have

$$-\frac{\mathrm{d}\varphi}{\mathrm{d}x_i} = m_i \frac{\mathrm{d}^2 x_i}{\mathrm{d}t^2}. \tag{2.30}$$

Note that φ is the collective (or effective/average) potential energy that a particle experiences. The Newtonian equation of motion can then relate the derivative of the potential energy to changes in position as a function of time.

The Newton second law of motion is

$$F_i = m_i a_i = m_i \frac{\mathrm{d}u_i}{\mathrm{d}t} = m_i \frac{\mathrm{d}^2 x_i}{\mathrm{d}t^2}. \tag{2.31}$$

Taking the simple case in which the acceleration is constant, we have

$$a_i = \frac{\mathrm{d}u_i}{\mathrm{d}t}, \tag{2.32}$$

we obtain an expression for the velocity after integration,

$$u_i = a_i t + u_{i,o}, \tag{2.33}$$

and because

$$u_i = \frac{\mathrm{d}x_i}{\mathrm{d}t}, \tag{2.34}$$

we can once again integrate to obtain

$$x_i = u_i t + x_{i,o}. \tag{2.35}$$

Combining this equation with the expression for the velocity, we obtain the following relation that gives the value of x at time t as a function of the acceleration a, the initial position, x_o, and the initial velocity u_o:

$$x_i = a_i t^2 + u_{i,o} t + x_{i,o}. \tag{2.36}$$

The acceleration is given as the derivative of the potential energy with respect to the position x, i.e.,

$$a_i = -\frac{1}{m_i}\frac{\mathrm{d}\varphi_i}{\mathrm{d}x}. \tag{2.37}$$

Therefore, to calculate a trajectory, one needs only the initial positions of the atoms, an initial distribution of velocities and the acceleration, which is determined by the gradient of the potential energy function that is dependent on positions. The equations of motion are deterministic, e.g., the positions and the velocities at time zero determine the positions and velocities at all other times t. The initial positions can be obtained from experimental structures, such as the X-ray crystal structure of the protein or the solution structure determined by nuclear magnetic resonance (NMR) spectroscopy (or quantum calculations).

The initial distributions of velocities are usually determined from a random distribution with the magnitudes conforming to the required temperature and corrected so there is no overall momentum, i.e.,

$$\langle \boldsymbol{p} \rangle = \sum_{i=1}^{N} m_i \boldsymbol{u}_i = 0. \tag{2.38}$$

This operation removes 3 degrees of freedom from the system and leads to $3(N-1)$ degrees of freedom for the particles (Table 2.4).

(D) *Descretization Verlet Algorithm for MD Computation*

The potential energy of a system is a function of the positions of all of the particles in the system. Because of the complicated nature of this function, there is no analytical solution to the equations of motion; they must be solved numerically. Numerous numerical algorithms have been developed for integrating the equations of motion. Among them are the leap-frog, position-Verlet, velocity-Verlet, and Beeman algorithms [148]. These algorithms conserve energy and momentum, are computationally efficient, and permit a large time step for integration. All the integration algorithms assume the position, velocity, and acceleration are expandable in Taylor series as

$$x(t+\Delta t) = x(t) + u(t)\Delta t + \frac{1}{2}a(t)\Delta t^2 + \cdots \tag{2.39}$$

$$u(t+\Delta t) = u(t) + a(t)\Delta t + \cdots \tag{2.40}$$

$$a(t+\Delta t) = \frac{F(t+\Delta t)}{m} + \cdots \tag{2.41}$$

For example, to derive the position-Verlet algorithm, consider $t \pm \Delta t$, so we have

$$x(t+\Delta t) = x(t) + u(t)\Delta t + \frac{1}{2}a(t)\Delta t^2 \tag{2.42}$$

$$x(t-\Delta t) = x(t) - u(t)\Delta t + \frac{1}{2}a(t)\Delta t^2, \tag{2.43}$$

and by summing these two equations, we have

$$x(t+\Delta t) = 2x(t) - x(t-\Delta t) + a(t)\Delta t^2 \quad \text{position-Verlet algorithm.} \tag{2.44}$$

Then the velocity is $[x(t+\Delta t) - x(t-\Delta T)]/2\Delta t$. The position-Verlet algorithm uses position and acceleration at time t and the position from time $t-\Delta t$ to calculate the new position at time $t+\Delta t$. The Verlet algorithm uses no explicit velocities. The advantages of the position-Verlet algorithm are that it is straightforward and the storage requirements are modest. The disadvantage is that the algorithm is of only moderate precision.

Another approach is the velocity-Verlet algorithm, which yields position, velocity, and acceleration at time $t+\Delta t$, so there is no compromise on precision. This uses (2.39) and an average acceleration (force), i.e.,

$$x(t+\Delta t) = x(t) + u(t)\Delta t + \frac{1}{2m}F(t)\Delta t^2 \tag{2.45}$$

$$u(t+\Delta t) = u(t) + \frac{1}{2m}[F(t) + F(t+\Delta t)]\Delta t \quad \text{velocity-Verlet algorithm,} \tag{2.46}$$

where $a(t+\Delta t)$ uses $x(t+\Delta t)$. So, the new positions and forces (accelerations) are computed before the new velocities are calculated [148].

2.5.2 A Molecular Dynamics Simulation Case Study: L–J Ar FCC

Choosing a simple system allows for the elucidation of results that may be difficult to resolve in more complex materials, in which multi-atom unit cells (and thus optical phonons) can generate additional effects. The L–J atomic interactions are described by the pair potential (2.9), i.e.,

$$\varphi_{\mathrm{LJ},ij}(r_{ij}) = 4\epsilon_{\mathrm{LJ}}[(\frac{\sigma_{\mathrm{LJ}}}{r_{ij}})^{12} - (\frac{\sigma_{\mathrm{LJ}}}{r_{ij}})^6], \tag{2.47}$$

where $\varphi_{\mathrm{LJ},ij}(r_{ij})$ is the potential energy associated with particles i and j (i is not equal to j), which are separated by a distance r_{ij}. The depth of the potential energy well is ϵ_{LJ}, and corresponds to an equilibrium particle separation of $2^{1/6}\sigma_{\mathrm{LJ}}$.

The force acting between i and j is

$$F_{\mathrm{LJ},ij}(r_{ij}) = -\frac{\partial\varphi_{\mathrm{LJ},ij}}{\partial r_{ij}} = 24\epsilon_{\mathrm{LJ}}(2\frac{\sigma_{\mathrm{LJ}}^{12}}{r_{ij}^{13}} - \frac{\sigma_{\mathrm{LJ}}^{6}}{r_{ij}^{7}}). \tag{2.48}$$

Ar and its FCC crystal (Section 4.3 describes this crystal structure), amorphous, and liquid phases are considered. The 12 nearest neighbors of an atom in a FCC crystal and of a sample atom in an amorphous structure are shown in Figures 2.12(a) and 2.12(b). In the FCC crystal, all atoms are at equivalent positions, and the atomic displacements are isotropic. In the amorphous phase, each atom has a unique environment, with a range of neighbor orientations and bond lengths. The resulting atomic displacements are anisotropic. The plane formed by the [100] and [010] directions in the FCC crystal is shown in Figure 2.12(c). Both the lattice constant a and the size

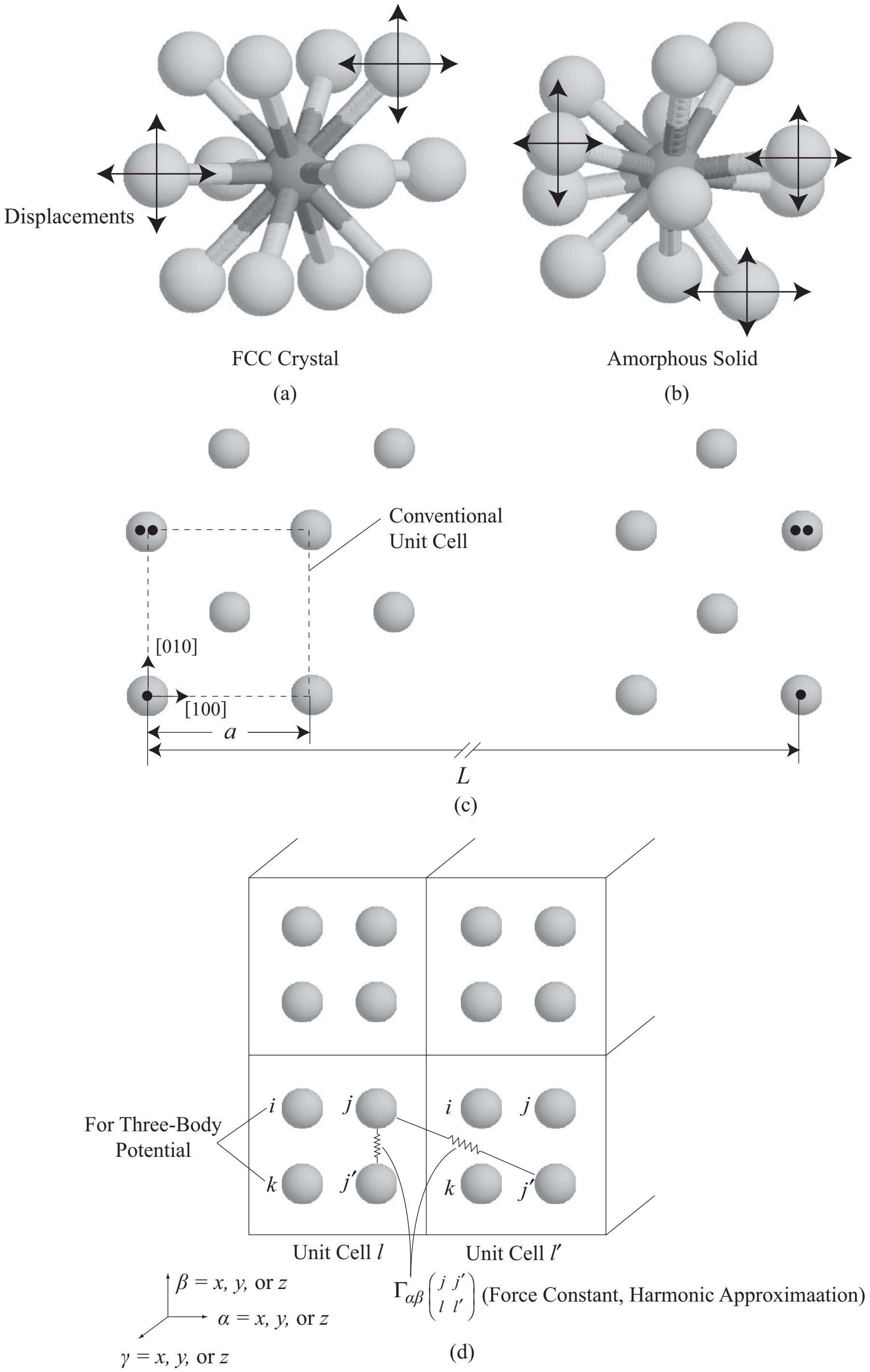

Figure 2.12. Local environment for an atom in (a) the FCC crystal, and (b) the amorphous structure. In the crystal, there are 12 nearest neighbors. For the amorphous phase, the 12 nearest atoms are shown. Although the color of the center atom is a darker gray than the neighbors, all the atoms are the same. Also shown are representative atomic displacements (not to scale) for some of the neighbor atoms for each case. The motions in the FCC crystal are isotropic and equivalent between atoms, whereas those in the amorphous structure are not. (c) Notations in the FCC crystal. The atoms with black dots are equivalent through the use of periodic boundary conditions [319]. (d) Shows coordinate and atom designations used in dynamical analysis of lattice vibration (will be further discussed in Section 4.4).

of the simulation cell L are indicated. Note that the conventional unit cell, which is cubic, contains four atoms. The true FCC unit cell, containing one atom, is rhombohedral, and not as suitable for analysis.

The simulations are run in the NVE ensemble at zero pressure with a time step $\Delta t = 4.285$ fs. The simulation cell is cubic and contains 256 atoms for the crystal and liquid phases, and 250 atoms for the amorphous phase. In similar simulations [226], good agreement has been found between the FCC crystal thermal conductivities predicted from cells containing 256 and 500 atoms [319]. This result indicates that 256 atoms are sufficient to eliminate size effects. Periodic boundary conditions are imposed in all directions. The equations of motion are integrated with a Verlet leapfrog algorithm described above. Atomic interactions are truncated and shifted at a cutoff radius equal to $2.5\sigma_{\rm LJ}$ (for computational economy).

For the FCC crystal, temperatures between 10 and 80 K are considered in 10 K increments. Melting occurs at a temperature of about 87 K at 1 atm [Figure 2.13(a)]. The amorphous phase is generated by starting with the desired number of atoms placed in a FCC lattice, running at a temperature of 300 K for 10^4 time steps to eliminate any memory of the initial configuration, and then quenching at 8.5×10^{11} K/s back to a temperature of 10 K. Table 2.6 lists the results of the simulations. The amorphous phase is stable up to a temperature of 20 K. Above this point, the equilibrium thermal fluctuations in the system are large enough to return the atoms to a FCC crystal structure. Temperatures of 10, 15, and 20 K are considered. Three different amorphous phases (each with 250 atoms) have been formed to check if the systems are truly disordered, and cells with 500 and 1000 atoms have been created to investigate size effects. The liquid phase is obtained by first heating the crystal phase to a temperature of 100 K to induce melting, then lowering the temperature. When this approach is used, a stable liquid is found to exist at temperatures as low as 70 K. As shown in Figure 2.13(a), the triple point of Ar is at 83.6 K, so this liquid state is not expected in experiments. Because of the small length and time scales used (necessary for reasonable computational times), the melting/solidifying temperature is not well-defined, and it is possible to have stable FCC crystal and liquid phases at the same temperature and pressure, although the densities differ. Temperatures of 70, 80, 90, and 100 K are considered for the liquid simulations. The time scale $\tau_{nn,e} = \pi/\omega_n$, where ω_n is the natural frequency evaluated at equilibrium interatomic distance (next section).

2.5.3 L–J FCC MD Scales in Classical Harmonic Oscillator

When relaxed to zero temperature, the MD FCC crystal unit-cell parameter, a (the lattice constant), is 5.2686 Å. The experimental value for Ar is 5.3033 Å [12].

The lattice constant can also be predicted from the analytical form of the L–J potential. To do this, one must consider the total potential energy associated with one atom $\langle\varphi\rangle$. If the energy in each pair interaction is assumed to be equally distributed between the two atoms, $\langle\varphi\rangle$ will be given by [245]

$$\langle\varphi\rangle = \langle\varphi_i\rangle = \frac{1}{2}\sum_{i\neq j}\varphi_{{\rm LJ},ij}. \tag{2.49}$$

Table 2.6. *Simulation cell parameters and equilibrium properties of the Ar FCC L–J phases. Note that the specific heat capacity is per atom and per degree of freedom [319].*

Structure	T, K	a, Å	ρ, kg/m^3	$\tau_{nn,e}$, ps	$\langle\varphi\rangle_e$, eV	$\langle\lvert\Delta_i\rvert^2\rangle^{1/2}$, Å	c_v/k_B
FCC crystal	0	5.269	1813	–	−0.0778	0	1
	10	5.290	1791	0.240	−0.0765	0.117	0.988
	20	5.315	1766	0.270	−0.0751	0.180	0.976
	30	5.341	1740	0.278	−0.0736	0.244	0.959
	40	5.370	1713	0.278	−0.0720	0.309	0.953
	50	5.401	1684	0.278	−0.0703	0.383	0.944
	60	5.436	1651	0.283	−0.0684	0.464	0.937
	70	5.476	1615	0.291	−0.0663	0.560	0.922
	80	5.527	1571	0.296	−0.0638	0.682	0.914
Amorphous	0	–	1717	–	−0.0719	0	1
	10	–	1694	0.291	−0.0706	–	0.976
	15	–	1682	0.291	−0.0699	–	0.979
	20	–	1669	0.283	−0.0691	–	0.970
Liquid	70	–	1432	–	−0.0562	–	0.857
	80	–	1363	–	−0.0527	–	0.826
	90	–	1287	–	−0.0491	–	0.803
	100	–	1202	–	−0.0453	–	0.758

The equilibrium position-effective potential (per atom) for the FCC crystal lattice can be expressed as

$$\langle\varphi\rangle_e = 2\epsilon_{\rm LJ}[A_{12}(\frac{\sigma_{\rm LJ}}{r_{nn,e}})^{12} - A_6(\frac{\sigma_{\rm LJ}}{r_{nn,e}})^6] = -8.607\epsilon_{\rm LJ} \quad \text{L–J FCC crystal}, \tag{2.50}$$

where $A_{12} = \sum(r_{nn}/\Delta r_i)^{12}n_i$, $A_6 = \sum(\Delta r_1/\Delta r_i)^6 n_i$, where n_i is the number of i-th nearest neighbors, and Δr_i is the distance to the nearest neighbor. Using these for large i, A_{12} and A_6 have values of 12.13 and 14.45, respectively (for FCC, other lattices are also reported in [12]), and r_{nn} is the nearest neighbor (nn) separation. This effective L–J potential is plotted in Figure 2.3 alongside the pair potential, given by (2.47). By setting

$$\frac{\partial\langle\varphi\rangle}{\partial r_{nn}}|_{r_{nn,e}} = 0, \tag{2.51}$$

the equilibrium value of $r_{nn,e}$ is found to be

$$r_{nn,e} = (\frac{2A_{12}}{A_6})^{1/6}\sigma_{\rm LJ} = 1.090\sigma_{\rm LJ} \quad \text{L–J FCC crystal}. \tag{2.52}$$

The location of the minimum is slightly shifted from that in the pair potential, and the energy well is deeper and steeper. The value of $r_{nn,e}$ for noble-gas elements are listed in Table 2.2. For Ar, the equilibrium separation (2.52) gives $r_{nn,e} = 3.706$ Å, and corresponds to a unit-cell parameter (lattice constant $a = 2^{1/2}r_{nn,e}$) of $a = 5.2411$ Å, which agrees with the zero-temperature MD result to within 0.6%.

In a simplified real-space model of atomic-level behavior, the energy transfer between neighboring atoms can be assumed to occur over one half of the period

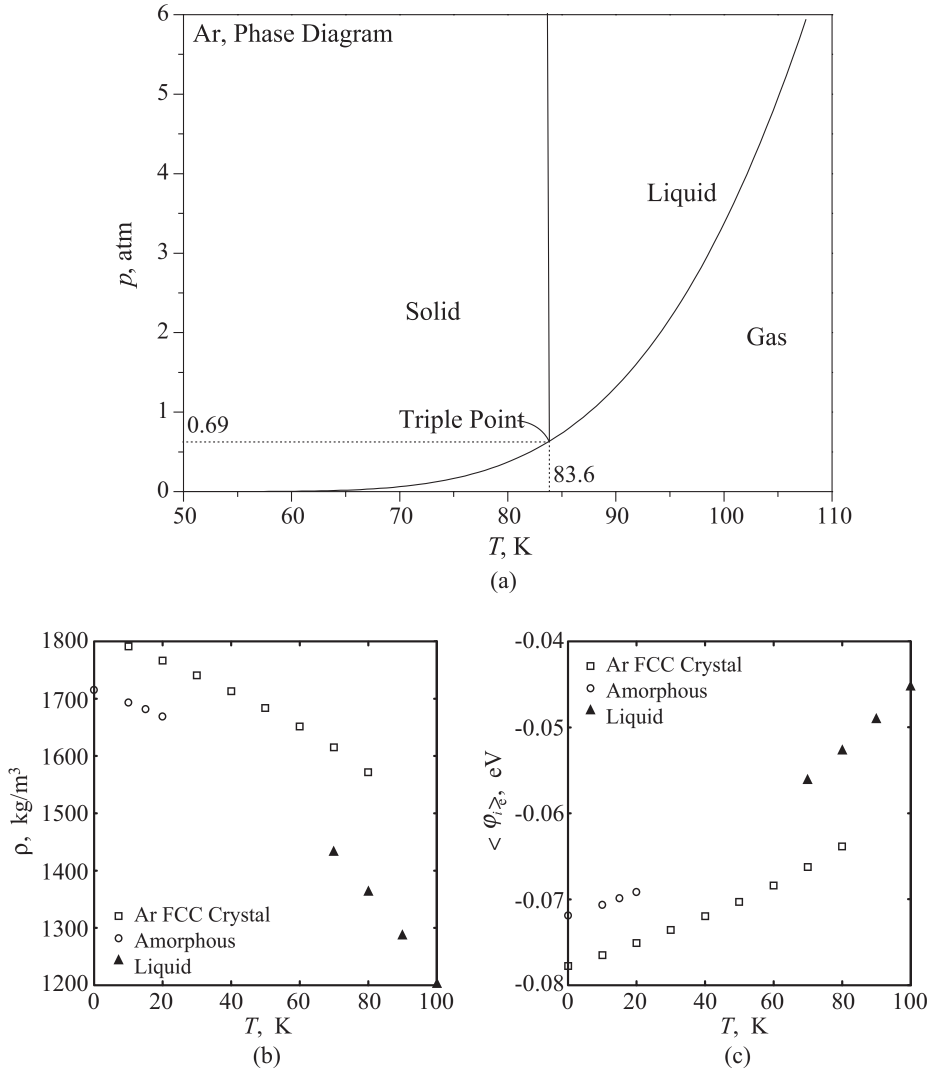

Figure 2.13. (a) Ar solid-liquid-gas phase equilibrium diagram [219]. Temperature dependencies of the Ar L–J phase: (b) densities, and (c) per particle potential energies [320].

of oscillation of an atom [68, 69, 126]. The associated time constant τ_D can be estimated from the Debye temperature (listed in Table A.2 for elements and discussed in Sections 4.2 and 4.7) τ_D as

$$\tau_D = \frac{2\pi\hbar}{2k_B T_D} . \tag{2.53}$$

The factor of 2 in the denominator is included because of the half period of oscillation that is used. By fitting the specific heat (as predicted by the MD zero-temperature phonon density of states) to the Debye model using a least squares method, the Debye temperature, is found to be 81.2 K. This compares well with the experimental value of 85 K [12] listed in Table A.2 (Appendix A). The MD result is used in subsequent calculations and gives τ_D = 0.296 ps ($\sim$ 69 time steps).

An estimate of this time constant can also be made with the L–J potential. The time constant is related to the curvature of the potential well that an atom experiences at its minimum energy. Assuming that the potential is harmonic at the minimum, then we can write the interatomic forces as $-\Gamma d_x$ (Table 2.5), where d_x is the displacement in a one-dimensional motion along x. The natural angular frequency (for sinusoidal motion) ω_n of the atom is given by [†]

$$\omega_n = \omega_{\rm LJ} = (\frac{1}{m}\frac{\partial^2 \langle\varphi\rangle}{\partial r_{nn}^2}|_{r_{nn}=r_{nn,e}})^{1/2} = (\frac{\Gamma}{m})^{1/2} = 22.88(\frac{\epsilon_{\rm LJ}}{m\sigma_{\rm LJ}^2})^{1/2},$$

$$\Gamma_{\rm LJ} = \left.\frac{\partial^2 \langle\varphi\rangle}{\partial r_{nn}^2}\right|_{r_{nn}=r_{nn,e}} = (22.88)^2\frac{\epsilon_{\rm LJ}}{\sigma_{\rm LJ}^2}, \quad \text{FCC structure,} \tag{2.54}$$

where m is the mass of one atom, which for Ar, m = 6.634×10^{-26} kg = 66.34 yg (yoctogram Table A.4), and $\langle\varphi\rangle$ and $r_{nn,e}$ are taken from (2.50) and (2.52). Note that the larger the spring (or force) constant Γ (which in turn requires larger $\epsilon_{\rm LJ}$) and the smaller the mass, the larger is ω_n. The value of Γ for some element pairs is given in Table 4.4, and for some compounds in Figure 4.29. For FCC Ar which $\Gamma = \Gamma_{\rm ArAr,FCC} = 7.545$ N/m, and $\omega_n = 1.068\times10^{13}$ rad/s or 10.68 Trad/s. In contrast, the covalent bond O–H has $\Gamma_{\rm OH} = 228$ N/m [Table 7.5 and (7.307)]. For heteronuclear pairs, the reduced mass $m_1m_2/(m_1+m_2)$ is used in $\omega_n = (\Gamma/m_{12})^{1/2}$. In Section 4.11.2, we will describe a general method for calculating Γ_{ij} for any atomic pair.

Note that for a paired atom (as in a molecule), the force constant is similarly found from (2.54) as is $\Gamma_{\rm LJ} = (7.735)^2\epsilon_{\rm LJ}/\sigma_{\rm LJ}^2$. We will list experimental Γ for atomic pairs in Table 4.4 and discuss the strength of their bonds.

The second derivative of the potential is designated as Γ and has the role of a spring constant in that it relates force to displacement in the mechanical system (Figure 2.2). For an isotropic, cubic lattice, the relation between the spring constant and the bulk modulus E_p (and the lattice constant a which is equal to $2^{1/2}r_e$ for FCC) is

$$\Gamma = E_p a = E_p(2^{1/2}r_{nn,e}),\ E_p = \frac{1}{\kappa_p},\ \kappa_p = \frac{1}{\rho}\frac{\partial\rho}{\partial p}|_T. \tag{2.55}$$

So, the stronger the force constant of a continuum, the larger the bulk modulus (and other moduli, Section 4.7.2), and the larger will be the bulk speed of sound $(\partial p/\partial\rho)_s^{1/2} \approx (E_p/\rho)^{1/2}$.

[†] In the simple classical harmonic oscillator $F = -\Gamma x$ (Table 2.5) and
$m\frac{{\rm d}^2x}{{\rm d}t^2} = -\Gamma x,\ x = x_{\rm o}\cos(\omega_n t+\phi), \omega_n = (\frac{\Gamma}{m})^{1/2}$.
The instantaneous kinetic and potential energies and their sum are
$E_k(t) = \frac{1}{2}\Gamma x_{\rm o}^2\sin^2(\omega_n t+\phi), E_p(t) = \varphi(t) = \frac{1}{2}\Gamma x_{\rm o}^2\cos^2(\omega_n t+\phi),\ E_k+\varphi = \frac{1}{2}\Gamma x_{\rm o}^2$.
Also, in harmonic lattice vibration, $\langle E_k\rangle = \langle\varphi\rangle = 3k_{\rm B}T/2$, which is the expectation value in kinetic and potential energy here. The lattice energy for a linear chain of atoms is discussed in Section 4.1.

Table 2.7. *MD scales, for L–J potential and for effective potential in gas and in FCC crystal [12].*

Scale	Relation (Gas)	Relation (FCC)
Length	$L_{\mathrm{LJ}} = \sigma_{\mathrm{LJ}}$	$L_{\mathrm{LJ}} = r_{nn,e} = 1.09\sigma_{\mathrm{LJ}}$
Mass	m	m
Time	$\tau_{\mathrm{LJ}} = (\frac{\sigma_{\mathrm{LJ}}^2 m}{\epsilon_{\mathrm{LJ}}})^{1/2}$	$\tau_{\mathrm{LJ}} = \frac{\pi}{\omega_n} = 0.137(\frac{\sigma_{\mathrm{LJ}}^2 m}{\epsilon_{\mathrm{LJ}}})^{1/2} = 0.137(\frac{m}{\Gamma_{\mathrm{LJ}}})^{1/2}$
Temperature	$T_{\mathrm{LJ}} = \frac{\epsilon_{\mathrm{LJ}}}{k_{\mathrm{B}}}$	$T_{\mathrm{LJ}} = \frac{\epsilon_{\mathrm{LJ}}}{k_{\mathrm{B}}}$
Potential Energy	ϵ_{LJ}	$\langle\varphi\rangle_{e,\mathrm{LJ}} = \langle\varphi\rangle_{\mathrm{LJ}} = 2\epsilon_{\mathrm{LJ}}[12.13(\frac{\sigma_{\mathrm{LJ}}}{r_{nn,e}})^{12}$ $-14.45(\frac{\sigma_{\mathrm{LJ}}}{r_{nn,e}})^6] = -8.61\epsilon_{\mathrm{LJ}}$
Natural frequency	$\omega_{\mathrm{LJ}} = (\frac{\epsilon_{\mathrm{LJ}}}{\sigma_{\mathrm{LJ}}^2 m})^{1/2}$	$\omega_{\mathrm{LJ}} = \omega_n = 22.88(\frac{\epsilon_{\mathrm{LJ}}}{\sigma_{\mathrm{LJ}}^2 m})^{1/2} = (\frac{\Gamma_{\mathrm{LJ}}}{m})^{1/2}$
Force constant	$\Gamma_{\mathrm{LJ}} = \frac{\epsilon_{\mathrm{LJ}}}{\sigma_{\mathrm{LJ}}^2}$	$\Gamma_{\mathrm{LJ}} = (22.88)^2 \frac{\epsilon_{\mathrm{LJ}}}{\sigma_{\mathrm{LJ}}^2}$

The bulk modulus in a L–J FCC crystal is $E_p = 75.14\epsilon_{\mathrm{LJ}}/\sigma_{\mathrm{LJ}}^3$ (end-of-chapter problem). We further discuss this in Section 4.7.2. One half of the period of oscillation is then

$$\tau_{\mathrm{LJ}} = \frac{1}{2}\frac{2\pi}{\omega_n} = 0.137(\frac{\epsilon_{\mathrm{LJ}}}{m\sigma_{\mathrm{LJ}}{}^2})^{-1/2}, \tag{2.56}$$

which gives $\tau_{\mathrm{LJ}} = 0.294$ ps, or within 1% of τ_D. The temperature scale here is $\epsilon_{\mathrm{LJ}}/k_{\mathrm{B}}T$ and for Ar crystal gives $T_{\mathrm{LJ}} = 120.7$ K. The mean Debye temperature for Ar FCC is (Table A.2) 85 K.

The physical significance of this time constant can be further investigated by considerations of the flow of energy between atoms in the MD simulation cell. As the atomic separation increases, it takes longer to transfer energy between two atoms. The time constants τ_{D}, τ_{LJ}, and τ_{nn} agree to within 10%, which supports the assumed link between the period of atomic oscillation and the time scale of the atom to atom energy transfer.

Table 2.7 list the various scales derived from the L–J potential for these FCC crystals. Other crystal geometries are explained in [12]. For gases for which the potential energy vanishes, ϵ_{LJ} and σ_{LJ} are used for scaling with similar results. It is also common to use m, σ_{LJ}, and ϵ_{LJ} to scale the quantities, then numerical constants appearing in Table 2.7 will be changed to unity.

2.5.4 L–J Potential Phase Transformations

The phase diagram for Ar is shown in Figure 2.13(a), along with its triple point [219]. The densities and potential energies per particle of the zero pressure L–J FCC crystal, liquid, and amorphous phases are plotted as functions of temperature in Figures 2.13(b) and 2.13(c), and are also given in Table 2.6. The energies correspond to the shifted potential that is used as a result of the application of the potential cutoff. As would be expected, the FCC phase has the lowest potential energy at a given temperature. Note the consistent trend between the amorphous and liquid phases in both density and potential energy. This is consistent with the idea of an amorphous phase being a fluid with a very high viscosity.

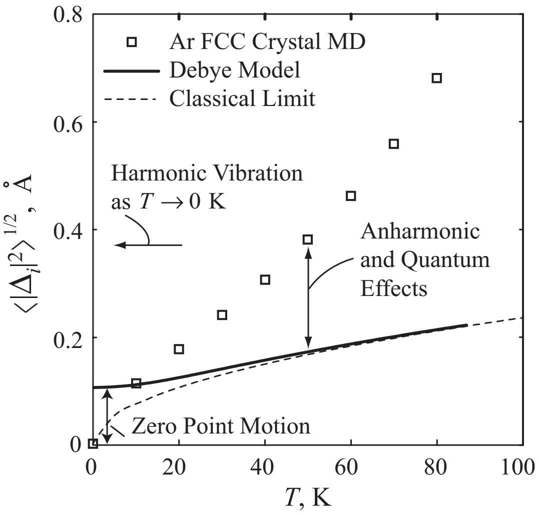

Figure 2.14. MD predicted RMS atomic mean-square directional displacement for Ar FCC and comparison with Debye model, a quantum-mechanical prediction. The zero-point RMS atomic displacement value is $(3\hbar/4m\omega_\mathrm{D})^{1/2}$ [320].

2.5.5 Atomic Displacement in Solids and Quantum Effects

The RMS displacement, $\langle|\boldsymbol{\Delta}_i|^2\rangle^{1/2}$ where $\boldsymbol{\Delta}_i$ is the displacement of atom in direction i from its equilibrium position, of the atoms in the FCC crystal is shown as a function of temperature in Figure 2.14. The numerical values are given in Table 2.6. The results presented are based on 10^5 time steps of NVE simulation, with data extracted every five time steps. The mean-square displacement (MSD) atomic displacement can be predicted from a quantum-mechanical description of the system under the Debye approximation (for isotropic lattice) in [29] (the more general Beni–Platzman–Debye model is derived in Section 4.8)

$$\langle|\boldsymbol{\Delta}_i|^2\rangle^{1/2} = (\boldsymbol{d}_j - \boldsymbol{d}_\mathrm{o}) \cdot \boldsymbol{s}_j = \{\frac{3\hbar}{m\omega_\mathrm{D}}[\frac{1}{4} + (\frac{T}{T_\mathrm{D}})^2 \int_0^{T_\mathrm{D}/T} \frac{x\mathrm{d}x}{e^x - 1}]\}^{1/2}$$

Debye model for mean-square directional displacement, (2.57)

where $\boldsymbol{d}_j$ and $\boldsymbol{d}_\mathrm{o}$ are the displacement vector of the atom j and the central atom, $\boldsymbol{s}_j$ is the equilibrium position unit vector of the atom j, T_D for elements for elements is given in Table A.2 (Appendix A), and $\omega_\mathrm{D} = \pi/\tau_\mathrm{D}$ and τ_D is given by (2.53).

This relation is also shown in Figure 2.14. Considering the minimal input required in the theoretical model (only the atomic mass and the Debye temperature), the agreement between the two curves is fair because the anharmonicity is not included in the model (the model uses the dynamical matrix, which assumes a harmonic behavior and is valid as $T \to 0$ K). Note that although the quantum model predicts the finite zero-point motion $(3\hbar/4m\omega_\mathrm{D})^{1/2}$, the MD results show a trend toward no motion at zero temperature. This is what one expects in a classical system, as the phase space approaches a single point when motion ceases. The results for the classical harmonic oscillator† is also shown in Figure 2.14.

Also, from the Heisenberg uncertainty principles (1.7), and using the de Broglie momentum, we have (end-of-chapter problem)

$$\Delta p_x \Delta x \geq \frac{\hbar}{2} \quad \text{or} \quad \Delta E \Delta t \geq \frac{\hbar}{2}, \quad \frac{\Delta x}{\Delta t} = u_g = \frac{\hbar \kappa}{m}, \tag{2.58}$$

where u_g is the group velocity. After substitutions (including $\Delta E = \hbar\omega$), we have

$$\Delta x_{min} = (\frac{\hbar}{2m\omega})^{1/2}, \tag{2.59}$$

where ω is the maximum frequency (here $\omega_{\rm D}$). As expected, this is slightly smaller than the zero-point motion displacement ($3\hbar/4m\omega_{\rm D}$) given in (2.57).

The displacement (2.59) is used in the definition of quantum normal coordinate (Glossary), for atomic displacement and in relation to phonons.

2.5.6 Specific Heat Capacity

The specific heat is defined thermodynamically as the rate of change of the total system energy (kinetic and potential) as a function of temperature at constant volume (Table 2.4) [12] Such a calculation can be explicitly performed by use of the results of the MD simulations. The predicted, scaled specific heats for the FCC crystal, amorphous, and liquid phases are plotted in Figure 2.15 and given in Table 2.6. The values given correspond to the specific heat per degree of freedom [there are $3(N-1)$, Table 2.4]. The calculation is performed by varying the temperature in 0.1 K increments over a ±0.2 K range around the temperature of interest.

The specific heat predicted from the MD simulations is a classical-anharmonic value. Also shown in Figure 2.15 are the classical-harmonic and the quantum-harmonic specific heats for the crystal phase. The classical-harmonic value, $k_{\rm B}$, is based on an assumption of equipartition of kinetic and potential energy between normal modes. The equipartition assumption is always valid for the kinetic energy (i.e., it contributes $k_{\rm B}/2$ to c_v, which has been verified). For the potential energy, however, it is true only under the harmonic approximation, which itself is valid only at zero temperature. The deviations of the classical-anharmonic results from the classical-harmonic model (the Dulong–Petit limit) are significant. The quantum-harmonic specific heat that is based on the zero-temperature phonon density of states is discussed in Section 4.7.1 (the Dulong–Petit limit) and is given by

$$c_{v,p} = \left.\frac{\partial \langle E \rangle}{\partial T}\right|_v = k_{\rm B} \sum_i^{N_p} \frac{x_i^2 e^{x_i}}{(e^{x_i}-1)^2} \quad \text{quantum harmonic}, \tag{2.60}$$

---

† The high-temperature (classical) limit of (2.57) is found from the simple, classical harmonic oscillator of Section 2.5.3, as is
$\langle |\boldsymbol{\Delta}_i|^2 \rangle^{1/2} = (\boldsymbol{d}_j - \boldsymbol{d}_{\rm o}) \cdot \boldsymbol{s}_j = x_{\rm o} = \left(3k_{\rm B}T/m\omega_n^2\right)^{1/2}$,
where $\boldsymbol{d}_j$ and $\boldsymbol{d}_{\rm o}$ are the j atom and the central atom displacements and $\boldsymbol{s}_j$ is the equilibrium position unit vector for atom j. $\langle |\boldsymbol{\Delta}_i|^2 \rangle$ shows a linear increase with temperature.

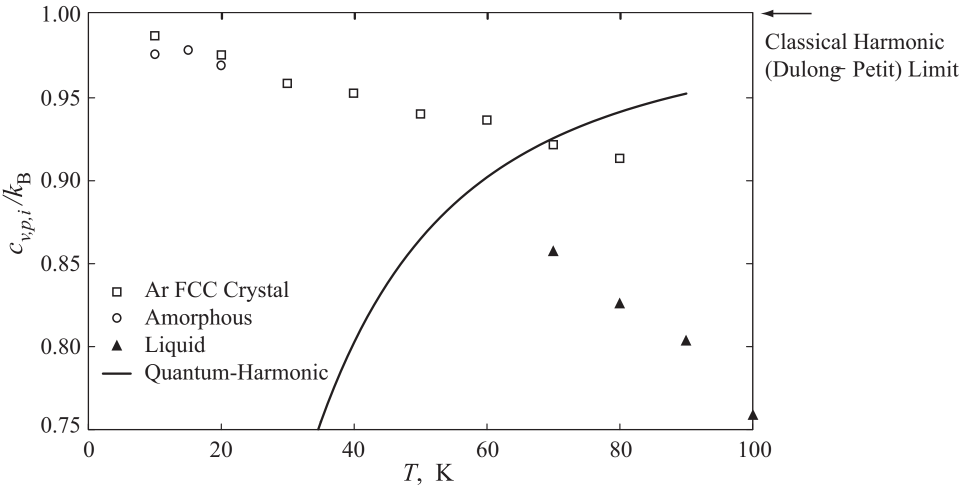

Figure 2.15. The classical-anharmonic specific heat per degree of freedom predicted from the MD simulations, and the classical-harmonic and quantum-harmonic curves for the crystal phase (all scaled by k_B), for Ar FCC. The theoretical predictions are stopped at $T = 87$ K, the melting point of the MD system [320].

where x_i is $\hbar\omega_i/k_BT$ and the summation is over the normal modes (N_p) of the system. As expected, the classical and harmonic specific heats are significantly different at low temperatures, where quantum effects are important. Prediction of the quantum-anharmonic specific heat (as would be measured experimentally) would require taking into account the temperature dependence and coupling of the normal modes. The results would be expected to converge with the classical-anharmonic value at high temperatures (i.e., of the order of the Debye temperature).

Not surprisingly, the FCC crystal and amorphous data are not significantly different. The crystal structure should not have a significant effect on the specific heat, especially at low temperatures for which the harmonic approximation is still reasonable. There is a definite drop in the liquid values, and the specific heat would continue to drop as the temperature is increased. The lower limit for the specific heat is $0.5k_B$, when potential energy effects have been completely eliminated (i.e., an ideal gas).

It should be noted that the MD simulations are clearly not harmonic in nature. It is sometimes assumed that the mode specific heat of solids in MD is equal to k_B, which is not the case and can lead to errors at high temperatures.

2.5.7 Heat Flux Vector

The heat flux vector in MD for two-body interatomic potentials (Appendix B) is

$$\boldsymbol{q} = \frac{1}{V}\sum_i \frac{\mathrm{d}}{\mathrm{d}t}(E_{k,i} + E_{p,i})\boldsymbol{x}_i = \frac{1}{V}\sum_i E_i\boldsymbol{u}_i + \frac{1}{2}\sum_{i,j}(\boldsymbol{F}_{ij}\cdot\boldsymbol{u}_i)\boldsymbol{x}_{ij}, \tag{2.61}$$

where E_i is the sum of kinetic and potential energy of particle i, and $\boldsymbol{F}_{ij}$ and $\boldsymbol{x}_{ij}$ are interparticle (interatomic) force and separation vector.

With this, in equilibrium and nonequilibrium MD [206] the heat flux through any place can be calculated. In equilibrium MD, $\boldsymbol{q} = 0$, while in nonequilibrium MD, $\boldsymbol{q}$ is nonzero and is either imposed (prescribed) or is a result of an imposed temperature difference across the computational domain.

2.6 Schrödinger Equation and Quantum Energy States

Referring to Figure 1.9, while MD applies to many-atom systems with their interactions modeled by empirical potential models, the Schrödinger equation allows for direct (*ab initio*) study of the mechanics-dynamics of the intra- and interatomic interactions. Experiments show that atomic particles are also wavelike in nature (e.g., electrons give diffraction patterns when passed through a double slit in a similar way to light waves). The Schrödinger equation is a wave equation that explains the behavior of atomic particles. We consider the electromagnetic wave in Section 3.3.1 and discuss some of its similarities and differences with the Schrödinger wave. The eigenvalues of the wave equation are the energy levels of the quantum mechanical system. This is used to find the energy levels of the hydrogen atom, and the energy levels are in good agreement with the Rydberg law.

In quantum mechanics, the Schrödinger equation plays the role of the Newton laws of motion and the energy conservation in classical mechanics. This is a wave equation in terms of the wave function that predicts analytically (although limited to a few cases) and precisely the probability of events or outcome. The detailed outcome is not strictly determined, but given a large number of events, the Schrödinger equation will predict the distribution of the results. In this equation, the kinetic and potential energies are transformed into the Hamiltonian H that acts upon the wave function Ψ to generate the evolution of the wave function in time and space.

In the Born–Oppenheimer approximation, the nuclear and electronic motions are separated (due to large mass for nuclear compared with electron). The electron distribution depends on the fixed positions of nuclei.[†]

The Schrödinger equation gives the quantized energies of the system and determines everything that can be known about the system. The wave function (or wavefunction) is a single-valued function of position and time, because that is sufficient to guarantee an unambiguous value of probability of finding the particle at a particular position and time. The wave function may be a complex function, because it is a product with its complex conjugate that specifies the real physical probability of finding the particle in a particular state. Also, the wave number ($\kappa = 2\pi/\lambda$, where λ is wavelength) is related to the wave momentum by equation $p = \hbar\kappa$. The Schrödinger equation and its variables are listed in Table 2.8. We will discuss this equation next. Then we solve this equation for the simple quantum-harmonic oscillator, the electron gas, and the electron in hydrogenlike atoms.

[†] The full Hamiltonian for the molecular system is (footnote of Section 2.2.2)

$$\mathrm{H} = \mathrm{H}_e + \varphi_{n\text{-}e} + \varphi_{e\text{-}e} + \varphi_{n\text{-}n},$$

where e and n stand for electron and nucleus.

Table 2.8. *Quantum (wave–particle) wave function dynamics equation (Schrödinger equation).*

$$i\hbar\frac{\partial\Psi}{\partial t} = (-\frac{\hbar^2}{2m}\nabla^2 + \varphi)\Psi \equiv \mathrm{H}\Psi \quad \text{time dependent}$$

$$\mathrm{H} = -\frac{\hbar^2}{2m}\nabla^2 + \varphi(\boldsymbol{x}) \quad \text{quantum Hamiltonian operator}$$

$$\mathrm{H}\psi = E\psi \quad \text{time independent}$$

$$\varphi = \varphi_a + \varphi_c + \varphi_s + \ldots \quad \text{various atomic-level potentials}$$

$$\int \Psi^\dagger\Psi \mathrm{d}V = \int |\Psi|^2 \mathrm{d}V = 1 \quad \text{normalization condition } (V \text{ contains the particle})$$

† indicates complex conjugate (or in general Hermitian conjugate)

$$P_V = \int_V |\Psi|^2 \mathrm{d}V \quad \text{probability of finding the particle in } V$$

$$\langle\phi\rangle = \int_V \Psi^\dagger\phi\Psi \mathrm{d}V \quad \text{expectation value of quantity } \phi \text{ in } V$$

$$\int \Psi_m^\dagger \mathrm{H}\Psi_n \mathrm{d}V = \langle\Psi_m|\mathrm{H}|\Psi_n\rangle \quad \text{matrix element}$$

E	energy eigenstates, J
H	quantum Hamiltonian operator, J
Ψ, ψ	wave function (for matter wave), 1/m$^{3/2}$
φ	total potential, J
φ_a	applied potential, J
φ_c	crystal potential, J
φ_s	scattering (interaction) potential between carriers, J

Note: The quantum electronic transition rates are determined based on a time-dependent perturbation theory as transition probabilities. This is referred to as the Fermi golden rule and is written as (derivation is given in Appendix E)

$$\dot{\gamma}_{1\text{-}2} = \frac{2\pi}{\hbar}|M_{1\text{-}2}|^2\delta_{\mathrm{D}}(E_1 - E_2 \pm \hbar\omega),$$

for transition between energy levels 1 and 2. Here $M_{1\text{-}2}$ is called the interaction matrix element and δ_{D} is the Dirac delta function (has units of J^{-1} as defined in Glossary). We use this for phonon absorption (–) and emission (+), in electron scattering (Section 5.10), and in photon absorption or emission in semiconductor (Section 7.8).

2.6.1 Time-Dependent Schrödinger Equation and Wave Vector

The time-dependent Schrödinger equation (also listed in Table 2.8) is

$$\begin{aligned} i\hbar\frac{\partial\Psi}{\partial t} &= (-\frac{\hbar^2}{2m}\nabla^2 + \varphi)\Psi \\ &\equiv \mathrm{H}\Psi, \quad \varphi = \varphi_a + \varphi_c + \varphi_s + \ldots, \end{aligned} \tag{2.62}$$

and describes the $\boldsymbol{x}$- and t-dependence of a quantum mechanical system described by H or φ. The Hamiltonian is the operator corresponding to total energy of the system, for each such system there is a set of possible outcomes (wave functions). The first part of H is the momentum (kinetic) operator $\hbar^2\nabla^2/2m$ and the second is the potential operator. Here the atomic-level potential energy φ has been decomposed to applied potential φ_a, crystal periodic potential φ_c, scattering (interaction) potential φ_s, etc. The applied potential can, for example, be an applied electric potential on free electrons. For example, in a periodic quantum harmonic oscillator (Section 2.6.4) $\varphi_a = \Gamma x^2/2$, while for electron orbiting H atom we will use (Section 2.6.6) the Coulomb potential (2.5). For electron scattered by phonon (lattice displacement), φ_s is given by (5.17). The quantum Hamiltonian operator was also defined in (2.19), but can have a more general form when multiple interactions (such as electronic-vibronic coupling) are considered.

In Chapter 7 (e.g., Section 7.12.4), we will consider multiple carrier interactions, and we decompose the Hamiltonian with terms for each carrier (i.e., H_i) and each interaction (H_{i-j}). So, the Hamiltonian not only determines the energy states, but also determines its energy-state transition rate (a form of time-dependent Schrödinger equation). So, the Hamiltonian is the cause of the states and its transition kinetics, as the applied forces are to Newtonian mechanics-dynamics.

Compared to the Helmholtz electromagnetic wave equation [given in Chapter 3, as (3.35)], the Schrödinger equation is first-order differential in time. Using the de Broglie quantum particle momentum and wave function, the quantum Hamiltonian can be derived.[†] Using the separation of variables technique, the wave function (a complex quantity) is written as a product of time-dependent and spatial-dependent parts as,

$$\Psi = \psi(\boldsymbol{x})\theta(t). \tag{2.63}$$

Then, inserting in (2.62) and separating variables, we have

$$i\hbar\frac{d\theta}{dt}\frac{1}{\theta} = E, \qquad \frac{1}{\psi}\left(-\frac{\hbar^2}{2m}\nabla^2 + \varphi\right)\psi = E, \tag{2.64}$$

[†] The de Broglie quantum wave function with momentum (and wave number) vector $\boldsymbol{p} = \hbar\boldsymbol{\kappa}$ and $E = \hbar\omega$, is

$$\Psi = A\exp[i(\boldsymbol{\kappa}\cdot\boldsymbol{x} - \omega t)] = A\exp[\frac{i}{\hbar}(\boldsymbol{p}\cdot\boldsymbol{x} - Et)].$$

Note that $\hbar\boldsymbol{\kappa}$ is based on $E = mu_{ph}^2 = \hbar\omega$ with m as mass at rest. Then $mu_{ph}^2 = \hbar u_{ph}\kappa$ or $p = mu_{ph} = \hbar\kappa$. Then the momentum is extracted from

$$\frac{\hbar}{i}\nabla\Psi = \boldsymbol{p}\Psi, \quad \frac{\hbar^2\nabla^2}{i^2} = -\hbar^2\nabla^2.$$

Similarly, the energy is extracted as

$$-\frac{\hbar}{i}\frac{\partial}{\partial t}\Psi = E\Psi.$$

Then, the classical Hamiltonian (Table 2.5) becomes the quantum Hamiltonian

$$\mathrm{H} = \frac{p^2}{2m} + \varphi = E, \quad -\frac{\hbar^2}{2m}\nabla^2\Psi + \varphi\Psi = i\hbar\frac{\partial\Psi}{\partial t},$$

which is (2.62).

where E is the eigenvalue. From the second and first equations, we have, respectively,

$$\mathrm{H}\psi = (-\frac{\hbar^2}{2m}\nabla^2 + \varphi)\psi = E\psi, \tag{2.65}$$

$$\theta(t) = \exp(-iEt/\hbar), \text{ exponential time dependence.} \tag{2.66}$$

Since there are n eigenvalues, a linear combination of the solutions gives [171]

$$\Psi = \sum_{n=1}^{\infty} a_n \psi_n(\boldsymbol{x}) \exp(-iE_n t/\hbar), \tag{2.67}$$

where E_n are the eigenvalues and ψ_n are the eigenstates.

The molecular Hamiltonian operator determines the dependence of the wave function on positions of electrons and the nuclei within the molecule. The potential energy φ portions of the Hamiltonian can for example be the Coulomb interaction between a pair of charged entities (2.5), where for electron $q = -e_c$ and for the nucleus it is ze_c, where z is the atomic number. In Section 2.2.2 (footnote), examples of electrons–electrons, electrons–nuclei, and nuclei–nuclei potential energies were given.[†]

2.6.2 Bloch Wave Form

Using the de Broglie momentum for quasi-particles $E = p^2/2m = \hbar^2\kappa^2/2m$, and the wave vector $\boldsymbol{\kappa}$, the spatial part of ψ is expressed as $\exp(i\boldsymbol{\kappa}\cdot\boldsymbol{x})$, where $\boldsymbol{\kappa}$ varies continuously [171], so we can use an integral presentation. Then the wave function of a continuous wave packet takes the form (called the Bloch wave form)

$$\Psi = \frac{1}{(2\pi)^{1/2}} \int_{-\infty}^{\infty} g(\boldsymbol{\kappa}) \exp[i(\boldsymbol{\kappa}\cdot\boldsymbol{x} - \frac{\hbar\kappa^2 t}{2m})] \mathrm{d}\boldsymbol{\kappa} \text{ Bloch wave form,} \tag{2.68}$$

where $(2\pi)^{-1/2} g(\boldsymbol{\kappa}) \mathrm{d}\boldsymbol{\kappa}$ normalizes the wave packet. Here $g(\boldsymbol{\kappa})$ is an inverse Fourier transform [171] that allows for a short-form presentation of (2.68). Using (2.68), time and spatial operators in the time-dependent Schrödinger equation (2.62),

---

[†] If we neglect the kinetic energy term for the nuclei, the electronic Hamiltonian in atomic units becomes (adding H_e to the Hamiltonian in footnote of Section 2.2.2)

$$\mathrm{H} = \mathrm{H}_e + \mathrm{H}_{e-n} + \mathrm{H}_{e-e} + \mathrm{H}_{n-n} = -\frac{\hbar^2}{2m}\sum_i \nabla_e^2 + \frac{e_c^2}{4\pi\epsilon_o}(-\sum_i^{N_e}\sum_I^{N_n} \frac{3z_I}{|\boldsymbol{R}_I - \boldsymbol{r}_i|}$$
$$+ \sum_i^{N_e}\sum_{j<i}^{N_e} \frac{1}{|\boldsymbol{r}_i - \boldsymbol{r}_j|} + \sum_I^{N_n}\sum_{J<I}^{N_n} \frac{z_I z_J}{|\boldsymbol{R}_I - \boldsymbol{R}_J|}),$$

where ∇_e^2 and $\boldsymbol{r}$ indicate position of electrons and $\boldsymbol{R}$ indicates the positions of nuclei.

become

$$\frac{\partial \Psi}{\partial t} = -i\frac{\hbar\kappa^2}{2m}\frac{1}{(2\pi)^{1/2}}\int_{-\infty}^{\infty} g(\boldsymbol{\kappa})\exp[i(\boldsymbol{\kappa}\cdot\boldsymbol{x} - \frac{\hbar\kappa^2 t}{2m})]\mathrm{d}\boldsymbol{\kappa}, \tag{2.69}$$

$$\nabla^2\Psi = -\kappa^2\frac{1}{(2\pi)^{1/2}}\int_{-\infty}^{\infty} g(\boldsymbol{\kappa})\exp[i(\boldsymbol{\kappa}\cdot\boldsymbol{x} - \frac{\hbar\kappa^2 t}{2m})]\mathrm{d}\boldsymbol{\kappa}. \tag{2.70}$$

We use the time-dependent Schroödinger for rate of transition of quantum states. This rate relation (called the Fermi golden rule) is derived in Appendix E. The time-independent Schrödinger equations is used to find the quantum energy states.

2.6.3 Quantum-Mechanics Formalism, Bra–Ket and Matrix Element

In quantum mechanics, the state of the physical system is identified with a vector designated by $|\phi\rangle$, in a Hilbert space H. Hilbert space is a (including all limits) inner product, complex vector space [171].[†] The inner product of two functions $\psi(\boldsymbol{x})$ and $\phi(\boldsymbol{x})$ is defined as $\langle\psi|\phi\rangle = \int \psi^*(\boldsymbol{x})\phi(\boldsymbol{x})\mathrm{d}\boldsymbol{x}$. The inner product of two vectors $|\psi\rangle$ and $|\phi\rangle$ is written as $\langle\psi|\phi\rangle$. Each vector is called a ket, and written as $|\psi\rangle$. The bra–ket inner product, $\langle\psi|\phi\rangle$ is a complex quantity.

Every ket has a dual bra, written as $\langle\psi|$, a continuous linear function on H defined as [along with its extension to include additional operator $A(\boldsymbol{x})$]

$$\langle\psi|\phi\rangle \equiv \int \psi^\dagger(\boldsymbol{x})\phi(\boldsymbol{x})\mathrm{d}\boldsymbol{x} \equiv (|\phi\rangle, |\psi\rangle),$$

$$\langle\psi|A|\phi\rangle = \int \psi^\dagger(\boldsymbol{x})A(\boldsymbol{x})\phi(\boldsymbol{x})\mathrm{d}\boldsymbol{x}. \tag{2.71}$$

The bra–ket (Dirac notation) is the standard notation for the quantum-mechanical state. The name comes from the linear product of two states denoted by a bracket $\langle\psi|\phi\rangle$ consisting of a left part $\langle\psi|$ bra and a right part $|\phi\rangle$ ket.

The commutator operator, operating on a function $f(\boldsymbol{x})$, is defined as

$$[A, B]f(\boldsymbol{x}) = (AB - BA)f(\boldsymbol{x}), \tag{2.72}$$

and if $[A, B] = 0$, then A and B commute, and otherwise they do not.

This is used in the uncertainty principle, for example,

$$[\boldsymbol{x}, \boldsymbol{p}] = i\hbar, \tag{2.73}$$

[†] For distinguishable (separable) particles we have for particles A and B, using the joint wave function Ψ^{AB} and individual states Ψ^{A} and Ψ^{B}

$$|\Psi\rangle^{\mathrm{A}} \in H^{\mathrm{A}}, \quad |\Psi\rangle^{\mathrm{B}} \in H^{\mathrm{B}},$$

$$|\Psi^{\mathrm{AB}}\rangle = |\Psi\rangle^{\mathrm{A}}|\Psi\rangle^{\mathrm{B}}.$$

For indistinguishable (tangled) particles, we have

$$|\Psi^{\mathrm{AB}}\rangle \neq |\Psi\rangle^{\mathrm{A}}|\Psi\rangle^{\mathrm{B}}.$$

Some properties of the Hilbert space are complex conjugate: $\langle y, x\rangle = \langle x, y\rangle^\dagger$, linearity: $\langle ax_1 + bx_2, y\rangle = a\langle x_1, y\rangle + b\langle x_2, y\rangle$, and inner product $\langle x, x\rangle \geq 0$. These will be further discussed in Appendix I.

(end-of-chapter problem), which states that position and momentum cannot be given precisely and simultaneously at a given time.

The matrix element i, f of the operator H (Hamiltonian) is defined as $\langle \psi_i | \mathrm{H} | \psi_f \rangle$. Here the operator represents the physical interaction that couples the initial and final states of the same carrier. This is a linear transformation and i and f are the matrix elements of operator H [171]. Examples are given in Sections 3.2.3, 4.9.4, 4.15, 5.10, 5.15, 7.8.1, and 7.12, and in Appendix E. In Section 2.2.2 we briefly discussed the numerical solution of the Schrödinger equation by Gaussian series, and we will use the numerical solvers again in Chapters 5, 6, and 7.

We now discuss solutions to (2.62) for the simple harmonic oscillator, electron gas, and electron in hydrogenlike atoms. We also discuss the perturbation and again the numerical techniques and for solving the Schrödinger equation.

2.6.4 Quantum Mechanical, Harmonic Oscillator

We begin with the quantum-harmonic oscillator to demonstrate the eigenvalue nature of quantum energy and the probability nature of the quantum-particle location. Consider a particle of mass m moving in one direction along x (taken to be the same as displacement d) and connected to a fixed point with a spring constant Γ, with its potential energy ($F = -\mathrm{d}\varphi/\mathrm{d}x = -\Gamma d = -\Gamma x$, when we place $x = 0$ at the equilibrium position) given by

$$\varphi = \frac{1}{2}\Gamma x^2 = \frac{1}{2}m\omega^2 x^2, \quad \mathrm{H} = \frac{p^2}{2m} + \frac{1}{2}m\omega^2 x^2, \tag{2.74}$$

where $\omega = (\Gamma/m)^{1/2}$ is its natural angular frequency given by (2.54).

In the classical treatment based on the Newton law described in Section 2.5.3, this oscillator experienced sinusoidal motion with natural frequency given by (2.54). For this simple (potential is proportional to displacement squared) harmonic system, the maximum kinetic and potential energies are equal and each is equal to $3k_{\mathrm{B}}T/2$.

The quantum-mechanical description of a simple harmonic oscillation begins with the Schrödinger equation giving the probability of finding the atom at a given location $\boldsymbol{x}$. The solution gives the eigenvalue E_n and $\psi_n(\boldsymbol{x})$ for the energy and the wave function, where n is the quantum number. Here we review the solution to the Schrödinger equation for this simple case.

Using the time-independent Schrödinger equation (Table 2.8), in one dimension, we have

$$(-\frac{\hbar^2}{2m}\frac{\mathrm{d}^2}{\mathrm{d}x^2} + \frac{1}{2}m\omega^2 x^2)\psi = E\psi \;\; \text{for } \varphi = \frac{1}{2}m\omega^2 x^2. \tag{2.75}$$

We write this in dimensionless form as

$$(-\frac{\mathrm{d}^2}{\mathrm{d}x^2} - \frac{m^2\omega^2}{\hbar^2}x^2)\psi = -\frac{2mE}{\hbar^2}\psi. \tag{2.76}$$

Two solution methods are available [171], the power-series expansion and the ladder operators.[†] The ladder operators are reviewed in Appendix I.

Here we use the power series solution, and begin by writing (2.76) as

$$\frac{\mathrm{d}^2\psi}{\mathrm{d}x^{*2}} + (E^* - x^{*2})\psi = 0, \tag{2.77}$$

where the dimensionless energy and coordinate are defined as

$$E^* = \frac{2E}{\hbar\omega}, \quad x^* = x(\frac{m\omega}{\hbar})^{1/2}. \tag{2.78}$$

Now, consider a solution to (2.77) in the form

$$\psi = X(x^*)\exp(-\frac{x^{*2}}{2}). \tag{2.79}$$

Substituting this solution into (2.77), we have

$$X'' + x^*X' + (E^* - 1)X = 0. \tag{2.80}$$

[†] The ladder operators ($a^\dagger$ is the raising or creation operator and a is the lowering or annihilation operator), are defined as (in one dimension x) and the Hamiltonian operator is related to these as

$$a^\dagger = \frac{1}{2^{1/2}m}(\frac{\hbar}{i}\frac{\mathrm{d}}{\mathrm{d}x} + im\omega x),$$

$$a = \frac{1}{2^{1/2}m}(\frac{\hbar}{i}\frac{\mathrm{d}}{\mathrm{d}x} - im\omega x)$$

$$\mathrm{H} = \hbar\omega(a^\dagger a + \frac{1}{2}).$$

The commentator operator (2.72) is used to find H from [171]

$$a^\dagger a = \mathrm{H} - \frac{1}{2}\hbar\omega, \quad \mathrm{H} = \frac{1}{2m}[(\frac{\hbar}{i}\frac{\mathrm{d}}{\mathrm{d}x})^2 + (m\omega^2 x)^2].$$

Using these, Schrödinger equation (2.75) becomes

$$\mathrm{H}\psi = \hbar\omega(a^\dagger a + \frac{1}{2})\psi = E\psi.$$

Using the ket notation, we have from the property of ladder operators,

$$a^\dagger|\psi_n\rangle \rightarrow |\psi_{n+1}\rangle$$

$$a|\psi_n\rangle \rightarrow |\psi_{n-1}\rangle.$$

Here we use $(a, a^\dagger)$ for electron, $(b, b^\dagger)$ for phonon, and $(c, c^\dagger)$ for photon.
The number of carriers is related to operators, for example

$$N_p = \sum_\alpha b_\alpha^\dagger b_\alpha,$$

α is the mode.
The action of operators are given by

$$b_\alpha^\dagger|f_{p,1}\cdots f_{p,\alpha-1}f_{p,\alpha}f_{p,\alpha+1}\cdots\rangle = f_{p,\alpha^\dagger}^{1/2}|f_{p,1}\ldots f_{p,\alpha-1}f_{p,\alpha+1}\cdots\rangle$$

$$b_\alpha|f_{p,1}\cdots f_{p,\alpha-1}f_{p,\alpha}f_{p,\alpha+1}\cdots\rangle = f_{p,\alpha}^{1/2}|f_{p,1}\cdots f_{p,\alpha-1}f_{p,\alpha+1}\cdots\rangle.$$

Note that Appendix I gives more details about these operators.

This is the harmonic differential equation and with $\lambda \equiv E^* - 1$, and the solution is

$$X(x^*) = A\ H_{\lambda/2}(x^*) + B\ {}_1F_1(-\frac{1}{4}\lambda;\ \frac{1}{2};\ x^{*2}), \tag{2.81}$$

where A and B are constants, $H_n(x^*)$ is a Hermite polynomial [1], and ${}_1F_1(-\lambda/4; 1/2; x^{*2})$ is a confluent hypergeometric function [1] of the first kind and is given as a series in x^* with the leading term being unity and the second term being $(-\lambda/4)x^*/(1/2)$. The first few terms of $H_n(x^*)$ are given in [1, 171] (for example, $H_0 = 1$, $H_1 = 2x^*$, $H_2 = 4x^* - 2$, $H_3 = 8x^{*3} - 12x^*$).

The solution to the original differential equation is

$$\psi(x^*) = e^{-x^{*2}/2}[A\ H_{\lambda/2}(x^*) + B\ {}_1F_1(-\frac{1}{4}\lambda;\ \frac{1}{2};\ x^{*2})]. \tag{2.82}$$

Because for $x^* \to \infty$ the wave function should diminish, the coefficient B should then be set to zero. Then we have

$$\psi(x^*) = Ae^{-x^{*2}/2}H_{\lambda/2}(x^*). \tag{2.83}$$

This solution always converges, but in order for the wave function to be square integrable, λ must be an even integer, i.e.,

$$\lambda_n = \frac{2E}{\hbar\omega} - 1 = 2n, \quad n = 0, 1, 2, \ldots, \tag{2.84}$$

which gives allowed energies as

$$E_n = \hbar\omega(n + \frac{1}{2}), \quad n = 0, 1, 2 \ldots \quad \text{fundamental quantization condition.} \tag{2.85}$$

The ground state is designated as $n = 0$ and is populated at $T = 0$ K. Then $\hbar\omega/2$ is called the zero-point energy (motion) and is a quantum-mechanical phenomenon [related to the Heisenberg uncertainty (2.58)]. Then from (2.83) the eigenfunctions (wave functions) are

$$\psi_n = CH_n(x^*)e^{-x^{*2}/2}. \tag{2.86}$$

Here, C is the normalization constant that is determined by the orthogonality of ψ_n and the final solution (dimensionless form by dividing by the first term or dimensional form) is

$$\begin{aligned}\psi_n &= (\frac{m\omega}{\pi\hbar})^{1/4}(\frac{1}{2^n n!})^{1/2}H_n(x^*)e^{-x^{*2}/2} \\ &= (\frac{m\omega}{\pi\hbar})^{1/4}(\frac{1}{2^n n!})^{1/2}H_n[(\frac{m\omega}{\hbar})^{1/2}x]\exp(-\frac{m\omega x^2}{2\hbar}).\end{aligned} \tag{2.87}$$

The first four dimensionless wave functions ψ_n^*, are listed in Table 2.9, where $\psi^* = \psi/(m\omega/\hbar)^{1/4}$.

These are plotted (qualitatively) in Figure 2.16. For higher quantum numbers, the wave function extends to higher values of x^*, which allow for the probability of the particles to be found outside of $|x^*| = 1$. From (2.78), this would be $x > (\hbar/m\omega)^{1/2} = [\hbar/(m\Gamma)^{1/2}]^{1/2}$, where Γ is the spring constant given in (2.54). The

Table 2.9. *The first four dimensionless wave functions for the quantum-harmonic oscillator,* $x^* = x(m\omega/\hbar)^{1/2}$ *[324].*

Quantum Number	Wave Function
0	$\psi_0^* = \pi^{-1/4}\exp(-x^{*2}/2)$
1	$\psi_1^* = (\frac{4}{\pi})^{1/4}x^*\exp(-x^{*2}/2)$
2	$\psi_2^* = (4\pi)^{-1/4}(2x^{*2}-1)\exp(-x^{*2}/2)$
3	$\psi_3^* = (9\pi)^{-1/4}(2x^{*3}-3x^*)\exp(-x^{*2}/2)$

dimensionless potential energy φ^* is also shown. Further graphical presentation of the wave function can be found in [58]. For the classical oscillator, $|x^*|$ is limited to ≤ 1 (end-of-chapter problem).

Although the calculation of $\psi_n(x)$ requires evaluation of H_n (examples given in [171]), a general result can be derived based on (2.87). The partition function (2.27) for this simple harmonic oscillator (with degeneracy $g_n = 1$) is

$$Z = \sum_{n=0}^{\infty}\exp[-\frac{(n+1/2)\hbar\omega}{k_{\rm B}T}] = \exp(-\frac{\hbar\omega}{2k_{\rm B}T})\sum_{n=0}^{\infty}[\exp(-\frac{\hbar\omega}{k_{\rm B}T})]^n$$
$$= \frac{\exp(-\frac{\hbar\omega}{2k_{\rm B}T})}{1-\exp(-\frac{\hbar\omega}{k_{\rm B}T})} = \frac{\exp(-\frac{\hbar\omega}{k_{\rm B}T})}{\exp(-\frac{\hbar\omega}{k_{\rm B}T})-1}, \tag{2.88}$$

so

$$\ln Z = -\frac{\hbar\omega}{2k_{\rm B}T} - \ln[1-\exp(-\frac{\hbar\omega}{k_{\rm B}T})]. \tag{2.89}$$

Relation (2.88) gives the Bose–Einstein (boson) distribution function given in Table 1.2 (a more detailed derivation of $f_p^{\rm o}$ is given in Appendix F). This is characteristic of phonons and photons. Finally, using Table 2.4, we have for the mean

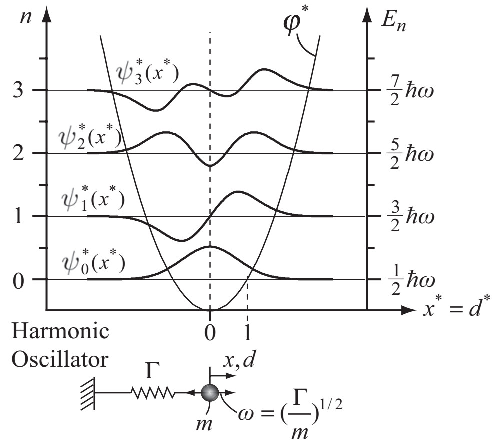

Figure 2.16. Qualitative distribution of the dimensionless harmonic-oscillator wave function with respect to the dimensionless distance along the force direction for the first four quantum numbers [324]. Also shown is the dimensionless potential energy.

energy

$$\frac{\langle E\rangle}{N} = k_{\rm B}T^2\frac{\partial \ln Z}{\partial T} = \hbar\omega[\frac{1}{2} + \frac{1}{\exp(\frac{\hbar\omega}{k_{\rm B}T}) - 1}] = \hbar\omega(f_p^{\rm o} + \frac{1}{2})$$

$$\text{mean energy of quantum oscillator.} \qquad (2.90)$$

Note that in comparison the mean energy of the classical oscillator (potential and kinetic energy) is $3k_{\rm B}T$.

2.6.5 Periodic, Free Electron (Gas) Model for Metals

The simplest electron system (structure) is the periodic, free (conduction) electron gas, where there is no potential, i.e., $\varphi = 0$. This is applicable to solid metals and is called the Drude–Sommerfeld electron gas model. If there are $n_{e,c}$ electrons per volume and the electrons do not interact (are prescribed within a periodic, three-dimensional space), then the ground state of the electron energy is found by examining a single electron in a volume V and the additional free electrons, while following the Pauli exclusion principle (two electrons per energy level). This volume is found from the number of free electrons per unit volume $n_{e,c}$, which in turn is found from the properties of metallic elements (valence electrons that are the outermost orbitals in Table A.2) and their densities in solid state. Then from the solution of the Schrödinger equation for a free electron in a box, we will also related this number density $n_{e,c}$ with the number of quantum states (and through this define the Fermi energy).

The wave function $\psi_e(\boldsymbol{x})$ with two possible spins and energy E_e satisfies the time-independent Schrödinger equation (Table 2.8), i.e.,

$$-\frac{\hbar^2}{2m_e}\nabla^2\psi_e(\boldsymbol{x}) = E_e\psi_e(\boldsymbol{x}) \text{ for } \varphi = 0. \qquad (2.91)$$

The periodic boundary conditions on a cube $L^3 = V$ is

$$\psi_e(x, y, z) = \psi_e(x, y, z + L), \qquad (2.92)$$

etc. The solution[†] is

$$\psi_{e,\boldsymbol{\kappa}}(\boldsymbol{x}) = L^{-3/2}e^{i(\boldsymbol{\kappa}\cdot\boldsymbol{x})} \quad \text{standing plane (Bloch) wave,} \qquad (2.93)$$

[†] Using (2.93) in (2.91), we have

$$-(\frac{\partial^2}{\partial x^2} + \frac{\partial^2}{\partial y^2} + \frac{\partial^2}{\partial z^2})\psi_\kappa(\boldsymbol{x}) = \kappa^2\psi_\kappa(\boldsymbol{x})$$

$$\kappa^2 = \kappa_x^2 + \kappa_y^2 + \kappa_z^2.$$

Then separating the variables, we have

$$\frac{\partial^2\psi_{\kappa,x}(x)}{\partial x^2} + \kappa_x^2\psi_{\kappa,x}(x) = 0, \text{ etc.}$$

The solution is $\psi_\kappa(\boldsymbol{x}) = A\exp[i(\kappa_x x + \kappa_y y + \kappa_z z)] = A\exp[i(\boldsymbol{\kappa}\cdot\boldsymbol{x})]$. Then A is determined from the normalization condition (Table 2.8), which gives $A = V^{-1/2} = L^{-3/2}$ (end-of-chapter problem).

with the electron energy (kinetic energy) given by

$$E_e = E_{e,k}(\boldsymbol{\kappa}) = \frac{\hbar^2\kappa^2}{2m_e}. \tag{2.94}$$

This relation between E_e and κ is called the dispersion relation and this κ^2 form is called the parabolic relation.

The electron wave function $\psi_{e,\boldsymbol{\kappa}}$ satisfies the normalization condition (Table 2.8). Applying the boundary condition (at L and at 0 for all three directions) gives (this is called the particle-in-box solution)

$$e^{i\kappa_x L} = e^{i\kappa_y L} = e^{i\kappa_z L} = e^0 = 1, \tag{2.95}$$

which shows that κ_i has discrete (quantized) values

$$\kappa_x = \frac{2\pi n_x}{L},\ \kappa_y = \frac{2\pi n_y}{L},\ \kappa_z = \frac{2\pi n_z}{L},\ n_i = 0, 1, 2, 3, \cdots. \tag{2.96}$$

Figure 2.17(a) shows the one-dimensional (x-direction) wave function (sine function) that satisfies $\psi_{e,n}(0) = \psi_{e,n}(L) = 0$ for $n = 1,\ 2$, and 3. The corresponding one-dimensional energy $E_{e,n}$ is also shown.

In these dimensions, we have $\kappa^2 = \kappa_x^2 + \kappa_y^2 + \kappa_z^2$. An electron in the level $\psi_{e,\boldsymbol{\kappa}}(\boldsymbol{x})$ has a momentum, velocity, and energy given by the de Broglie momentum relation for quasi-particles, i.e.,

$$\boldsymbol{p}_e = \hbar\boldsymbol{\kappa},\quad \boldsymbol{u}_e = \frac{\hbar\boldsymbol{\kappa}}{m_e},\quad E_e = \frac{\hbar^2\kappa^2}{2m_e} = \frac{p_e^2}{2m_e} = \frac{1}{2}m_e u_e^2 \text{ dispersion relation.} \tag{2.97}$$

Free electron dispersion relation $E_e(\kappa)$ is the parabolic dispersion. This constructs the $\boldsymbol{\kappa}$-space or wave-vector space, noting that the wave number is $2\pi/\lambda$, where λ is the wavelength. Figure 2.17(b) shows the two-dimensional Cartesian κ_x–κ_y space, with the coordinates $\kappa_x = 2\pi n_x/L$ and $\kappa_y = 2\pi n_y/L$. Then in the three-dimensional $\boldsymbol{\kappa}$-space of unit $(2\pi/L)^3$, the number of allowed $\boldsymbol{\kappa}$ values per unit $\boldsymbol{\kappa}$ space is $(L/2\pi)^3 = V/8\pi^3$. This also means that there is one distinct triplet quantum-numbers set $(\kappa_x, \kappa_y, \kappa_z)$ for volume $(2\pi/L^3)$ in the $\boldsymbol{\kappa}$-space. Now, for very large N_e, we can consider the volume to be spherical and referring to the radius of this sphere in the $\boldsymbol{\kappa}$-space as $\kappa_{\rm F}$ (having a volume $4\pi\kappa_{\rm F}^3/3$), the number of allowed values of κ (or orbitals) within this sphere is [Figure 2.17(b)]

$$\frac{4\pi\kappa_{\rm F}^3/3}{(2\pi/L^3)} = \frac{4\pi\kappa_{\rm F}^3}{3}\frac{V}{8\pi^3} = \frac{\kappa_{\rm F}^3}{6\pi^2}V \text{ number of allowed } \kappa \text{ points in } \kappa_{\rm F} \text{ volume.} \tag{2.98}$$

Below, we will show that V depends on the number of free electrons in metallic solids. The wave number and energy based electron density of states $D_e(x)$ and $D_e(E_e)$ (Glossary) are found based on Figure 2.17(b) as

$$D_e(\kappa)\mathrm{d}\kappa \equiv \frac{4\pi\kappa^2\mathrm{d}\kappa}{(2\pi)^3}, \text{ electron density of states,}$$

$$D_e(E_e)f_e^{\rm o}(E_e)\mathrm{d}E_e \equiv \mathrm{d}n_{e,c},\ D_e(E_e)\mathrm{d}E_e = 4\pi\kappa^2\frac{\mathrm{d}\kappa}{\mathrm{d}E_e}\mathrm{d}E_e = \frac{2^{1/2}m_e^{3/2}}{\pi^2\hbar^3}E_e^{1/2}\mathrm{d}E_e, \tag{2.99}$$

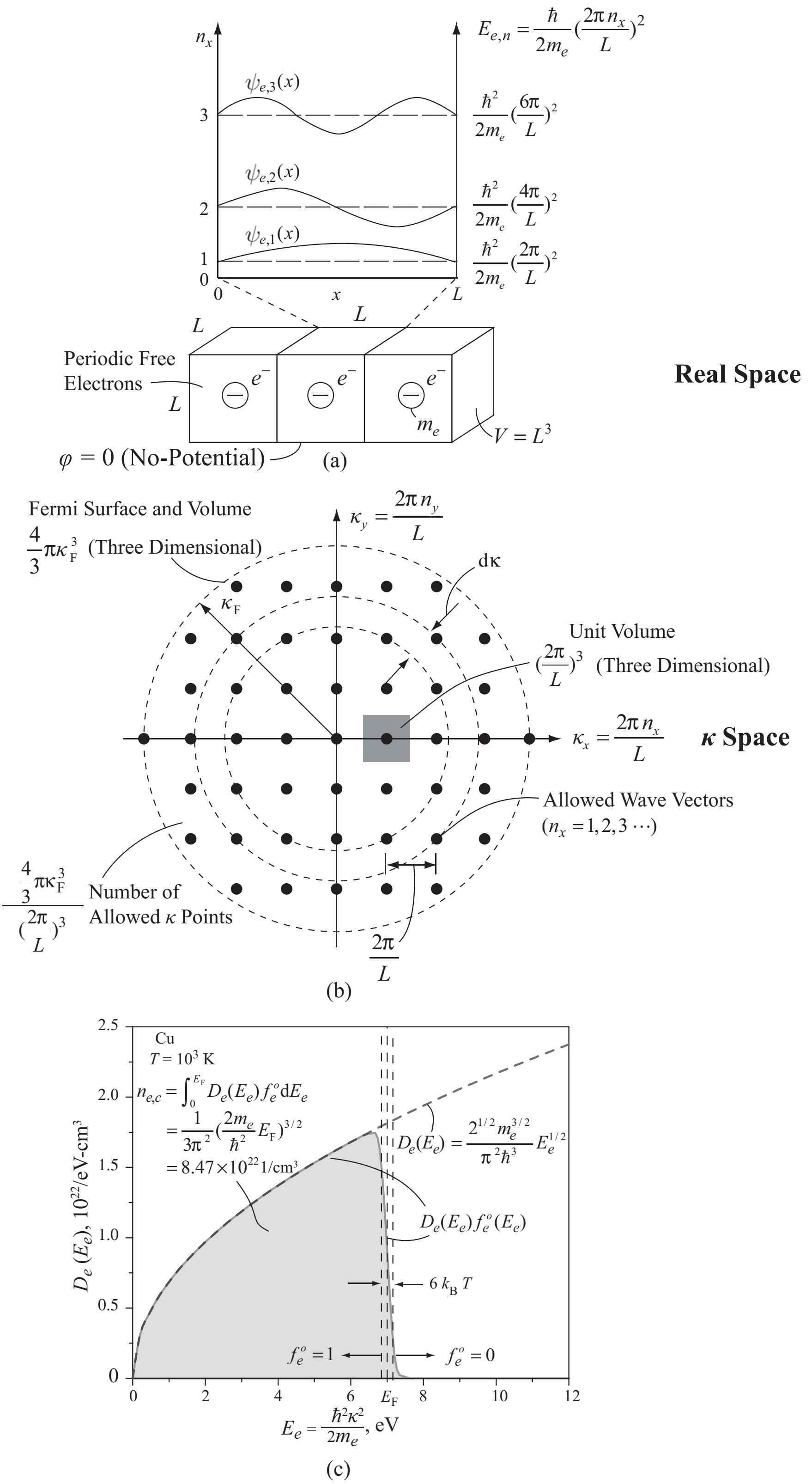
n_x
$E_{e,n} = \frac{\hbar}{2m_e}(\frac{2\pi n_x}{L})^2$
$\psi_{e,3}(x)$
3
$\frac{\hbar^2}{2m_e}(\frac{6\pi}{L})^2$
$\psi_{e,2}(x)$
2
$\frac{\hbar^2}{2m_e}(\frac{4\pi}{L})^2$
$\psi_{e,1}(x)$
1
0
$\frac{\hbar^2}{2m_e}(\frac{2\pi}{L})^2$
0
x
L
L
L
L
Periodic Free Electrons
e^-
e^-
e^-
m_e
$V = L^3$
Real Space
$\varphi = 0$ (No-Potential)
(a)
Fermi Surface and Volume
$\frac{4}{3}\pi\kappa_F^3$ (Three Dimensional)
$\kappa_y = \frac{2\pi n_y}{L}$
dκ
κ_F
Unit Volume
$(\frac{2\pi}{L})^3$ (Three Dimensional)
$\kappa_x = \frac{2\pi n_x}{L}$
κ Space
Allowed Wave Vectors
$(n_x = 1, 2, 3 \cdots)$
$\frac{\frac{4}{3}\pi\kappa_F^3}{(\frac{2\pi}{L})^3}$
Number of Allowed κ Points
$\frac{2\pi}{L}$
(b)
Cu
$T = 10^3$ K
$n_{e,c} = \int_0^{E_F} D_e(E_e) f_e^o \mathrm{d}E_e$
$= \frac{1}{3\pi^2}(\frac{2m_e}{\hbar^2}E_F)^{3/2}$
$= 8.47 \times 10^{22}$ 1/cm³
$D_e(E_e) = \frac{2^{1/2} m_e^{3/2}}{\pi^2 \hbar^3} E_e^{1/2}$
$D_e(E_e) f_e^o(E_e)$
$6\, k_B T$
$f_e^o = 1$
$f_e^o = 0$
$D_e\ (E_e)$, 10^{22}/eV-cm³
2.5
2.0
1.5
1.0
0.5
0
0
2
4
6
E_F
8
10
12
$E_e = \frac{\hbar^2\kappa^2}{2m_e}$, eV
(c)

Figure 2.17. (a) Real-space distribution of the one-dimensional (x direction) free-electron wave function $\psi_{e,\kappa_x}(x)$, standing waves, and its energy, for $n_x = 1,\ 2,$ and 3. (b) $\boldsymbol{\kappa}$-space shown in two dimensions, where each $\boldsymbol{\kappa}$ point occupies a space $(2\pi/L)^3 = 8\pi^3/V$ [12, 245]. (c) Variation of electron density of states, as a function of electron energy for Cu at $T = 10^3$ K.

and $D_e(\kappa)$ is the number of electronic states per unit volume (allowed $\boldsymbol{\kappa}$ values) in the increment $\mathrm{d}\kappa$ of a sphere of radius κ. Note that the spherical symmetry allows for using a spherical shell $\mathrm{d}\boldsymbol{\kappa} = 4\pi\kappa^2\mathrm{d}\kappa$. Figure 2.17(c) shows the variation of energy density of states $D_e(E_e)$ for Cu electron gas, at $T = 10^3$ K. As shown in the figure, it is common to assume that $f_e^{\mathrm{o}}(E_e) = 1$ for $E_e \le E_{\mathrm{F}}$, and zero beyond that.

The density of states represents the atomic structure of the matter influencing the carrier and in general can contain forbidden energy regimes (bandgaps) where the carrier of that energy range can not exist [e.g., Figures 1.8(a) and (b) for phonons and semiconductor conduction electrons]. Because each allowed κ is for two one-electron levels (for each spin), then using (2.98) or performing the integration over $\mathrm{d}E_e$ in (2.99), up to E_{F}, we have

$$N_{e,c} = 2V\int_0^{E_f} D_e(E_e) f_e^{\mathrm{o}}\mathrm{d}E_e = 2V\int_0^{E_f} D_e(E_e)\mathrm{d}E_e = 2\frac{\kappa_{\mathrm{F}}^3}{6\pi^2}V, \quad D_e(E_e) = \frac{\mathrm{d}n_{e,c}}{\mathrm{d}E_e} \tag{2.100}$$

$$n_{e,c} = \frac{N_e}{V} = \frac{\kappa_{\mathrm{F}}^3}{3\pi^2} = \frac{1}{3\pi^2}(\frac{2m_e}{\hbar^2}E_{\mathrm{F}})^{3/2}, \tag{2.101}$$

where the Fermi energy is found from (2.97) as

$$E_{\mathrm{F}} = \frac{\hbar^2\kappa_{\mathrm{F}}^2}{2m_e} = \frac{(3\pi^2 n_{e,c})^{2/3}\hbar^2}{2m_e}. \tag{2.102}$$

So, the Fermi energy is related to the number density of the free electrons. For conduction electrons, $n_{e,c}$ is also given by

$$n_{e,c} = \frac{N_{\mathrm{A}}}{M}\rho z_e, \tag{2.103}$$

where ρ is the density, and z_e is the number of free (conduction) electrons (i.e., valence electrons, outermost orbitals in Table A.2, in metallic bond) per atom. This is also listed as one of the oxidation states in Table A.2. These conduction (delocalized) electrons are due to the electronic band overlaps (Section 5.6). These leave the outermost orbital electrons to be free. For example, Cu has one $4s$ electron in its outermost orbital while Al has three, two in $3s$ and one in $3p$. Then

$$\kappa_{\mathrm{F}} = (3\pi^2\frac{N_{\mathrm{A}}}{M}\rho z_e)^{1/3}. \tag{2.104}$$

Equations (2.103) and (2.104) show that the Fermi energy and the number density of free electrons are related. The tabulated results for solid metals will be given in Table 5.2; for example, for copper, $z_e = 1$, $n_{e,c} = 8.47 \times 10^{22}$ 1/cm^3, and $E_{\mathrm{F}} = 7.00$ eV. For metals $n_{e,c}$ and E_{F} (which is also closely related to the chemical potential μ) are directly related and are independent of temperature, and $n_{e,c}$ in semiconductors is temperature dependent (zero at $T = 0$ K, and increasing with increase in T). We will discuss these in Sections 5.6 and 5.7.

By defining a radius r_s containing a conduction electron, i.e.,

$$\frac{1}{n_{e,c}} = \frac{4\pi r_s^3}{3}, \tag{2.105}$$

we have

$$\kappa_{\rm F} = \frac{(\dfrac{9\pi}{4})^{1/3}}{r_s} = \frac{1.92}{r_s}. \tag{2.106}$$

The Fermi velocity is found from the momentum, i.e.,

$$u_{\rm F} = \frac{\hbar}{m_e}\kappa_{\rm F}. \tag{2.107}$$

The energy density of the electron gas is (for two spins) [12]

$$\begin{aligned}\frac{\langle E_e\rangle}{V} &= \frac{2}{(2\pi)^3}\int E_e f_e^{\rm o} {\rm d}\boldsymbol{\kappa} \\ &= \frac{1}{4\pi^3}\int_0^{\kappa_{\rm F}} \frac{\hbar^2\kappa^2}{2m_e}{\rm d}\boldsymbol{\kappa} = \frac{1}{4\pi^3}\frac{\hbar^2}{2m_e}\int_0^{\kappa_{\rm F}} 4\pi\kappa^4 {\rm d}\kappa \\ &= \frac{1}{\pi^2}\frac{\hbar^2\kappa_{\rm F}^5}{10m_e}.\end{aligned} \tag{2.108}$$

We will further discuss this integral over ${\rm d}\boldsymbol{\kappa}$ in Chapters 3 and 4.

Using (2.101), $N_e/V = \kappa_{\rm F}^3/3\pi^2$, the energy per electron, in ground state, is

$$\frac{\langle E_e\rangle}{N_{e,c}} = \frac{3}{10}\frac{\hbar^2\kappa_{\rm F}^2}{2m_e} = \frac{3}{5}E_{\rm F} \equiv \frac{3}{5}k_{\rm B}T_{\rm F}, \quad T_{\rm F} = \frac{E_{\rm F}}{k_{\rm B}} \quad \text{Fermi temperature.} \tag{2.109}$$

This constant $\langle E_e\rangle$ is one of the limitations of the Drude–Sommerfeld model. We will further discuss the free-electron gas model for metals in Section 5.6. This simple model again allows for an analytical solution to the Schrödinger equation and the resulting discretization of energy. Note that the density of states is based on energy packets in $\boldsymbol{\kappa}$ space, while the electron density is in real space $\boldsymbol{x}$. We will now do another analytical solution.

2.6.6 Electron Orbitals in Hydrogenlike Atoms

In the hydrogen atom model, the electron interacts with a stationary proton (nucleus), through the Coulombic potential (2.5), i.e.,

$$\varphi_e = {\rm H}_{e-n} = -\frac{1}{4\pi\epsilon_{\rm o}}\frac{e_c^2}{r}. \tag{2.110}$$

Then, using the spherical coordinates (r, θ, ϕ), the time-independent Schrödinger equation (Table 2.8) becomes [324]

$$\begin{aligned}(-\frac{\hbar^2}{2m_e}\nabla^2 + \varphi_e)\psi_e &= -\frac{\hbar^2}{2m_e}[\frac{1}{r^2}\frac{\partial}{\partial r}(r^2\frac{\partial}{\partial r}) + \frac{1}{r^2\sin\theta}\frac{\partial}{\partial\theta}(\sin\theta\frac{\partial}{\partial\theta}) \\ &\quad + \frac{1}{r^2}\frac{1}{\sin^2\theta}\frac{\partial^2}{\partial\phi^2} - \frac{e_e^2}{4\pi\epsilon_{\rm o}r}]\psi_e \\ &= E_e\psi_e.\end{aligned} \tag{2.111}$$

Then variables are separated by use of

$$\psi_e(r,\theta,\phi) = R_e(r)\Theta_e(\theta,\phi) \text{ radial angular decomposition.} \tag{2.112}$$

Then when this is substituted, the equation for $R_e(r)$ is called the radial equation. The equation for P_e is called the angular equation. The general form of the wave function (in terms of the first three quantum numbers n, l, and m) is [solution to (2.111)] [171, 324]

$$\psi_{e,nlm} = \{(\frac{2}{nr_{\rm B}})^3 \frac{(n-l-1)!}{2n[(n+1)!]}\}^{1/2} e^{-r^*/n} (\frac{2r^*}{n})^l \mathrm{L}^{2l+1}_{n-l-1}(\frac{r^*}{n}) \mathrm{Y}_{l,m}(\theta,\phi), \tag{2.113}$$

where L is the associated Laguerre (orthogonal confluent hypergeometric) polynomial, and Y is a spherical harmonic function [1].

There are four quantum numbers, n, l, m, and s. The first one n, is called the principal quantum number and describes the electron shell such that (it does not include the fine-structure that is due to spin). So, the discrete (quantized) energy states are

$$E_{e,n} = -\frac{e_c^2}{8\pi\epsilon_{\rm o} r_{\rm B} n^2}, \quad n = 1,\ 2,\ 3, \ldots, \tag{2.114}$$

where $r_{\rm B}$ is the Bohr radius defined in Section 1.5.2 and Table 1.4. This is the kinetic energy given in Section 2.1.3 (footnote). The total energy (kinetic and potential, which is $-e_c^2/4\pi\epsilon_{\rm o} r_{\rm B} n^2$, is also given there.

The second one, l, is the azimuthal quantum number (angular momentum) and describes the subshell, and $l = 0,\ 1, \ldots,\ n-1$. Also,

$$\begin{aligned} l &= 0 \text{ is designated by } s, \\ l &= 1 \text{ is designated by } p, \\ l &= 2 \text{ is designated by } d, \\ l &= 3 \text{ is designated by } f, \end{aligned} \tag{2.115}$$

followed by g, h, i, etc. Here s stands for sharp, p for principal, d for diffuse, and f for fundamental. Then for $n = 1$ and $l = 0$, we have $1s$, and for $n = 2, l = 0$, we have $2s$, etc.

The third quantum number, m, is called the magnetic quantum number and describes the orbital (cloud) within a subshell, and it takes on values of $2l + 1$, i.e., $m = 0,\ \pm 1,\ \pm 2,\ \ldots, \pm l$.

The fourth quantum number is the spin quantum number, s, describing the direction of electron spin (Section 1.1.1). The first electron is designated $s = +1/2$ (spin) and the next are $-1/2$ (opposite spin), and then repeated.

The lowest energy state for H is $1s$ and the radial function is

$$R_{e,1s}(r) = \frac{2}{r_{\rm B}^{3/2}} e^{-r/r_{\rm B}}, \tag{2.116}$$

and the complete 1s wave function is

$$\psi_{e,1s}(r) = \frac{1}{\pi^{1/2} r_{\rm B}^{3/2}} e^{-r/r_{\rm B}}. \tag{2.117}$$

The local probability of having a 1s electron between r and r+dr is (Table 2.8)

$$P(r) = 4\pi \int_r^{r+{\rm d}r} \psi^2_{e,1s}(r) r^2 {\rm d}r = \frac{4}{r_{\rm B}^3} r^2 e^{-2r/r_{\rm B}} {\rm d}r \ \ \text{local probability}. \tag{2.118}$$

Then local probability $P(r = 0) = P(r \rightarrow \infty) = 0$, with a peak near $r/r_{\rm B} = 1.5$. Note that in Table 2.8 the probability P_V is integrated over the entire volume V.

The electron wave functions for $n = 1,\ 2$, and 3 for hydrogenlike atomic wave functions (where z is atomic number) and $r^* = zr/r_{\rm B}$, are listed in Table 2.10 [324].

The possibility distribution P_e of some of the hydrogen atom electron orbitals shown in Figures 2.5(a)–(e). Note that in Figure 2.5(c), the x–y plane is used showing 3d_{xy} instead of 3d_{xz} shown in Table 2.10 (the choice of plane is arbitrary).

Figures 2.18(a) and (b) show the variation of the projected angular function of the 3d_{xy} wave function and the electron orbital (probability). Figure 2.19 shows radial variation of angular integral of the $\psi^\dagger_{e,3d_{xy}} \psi_{e,3d_{xy}}$ with respect to r^*. For the latter, the probability P_V (Table 2.8) of finding the 3d_{xy} electron within some radial locations are also shown (the 99% probability is for $r^* = 21.9$).

In Sections 2.6.4, 2.6.5, and 2.6.6, we reviewed three exact, analytical solutions to the Schrödinger equation; we now proceed to discuss perturbation and numerical solution methods.

2.6.7 Perturbation and Numerical Solutions to Schrödinger Equation

In addition to the preceding three exact solutions, we review the exact solutions to the Schrödinger equation for the case of an electron in a one-dimensional, periodic, ionic potential in Section 5.1 and for the translational motion of an ideal gas in a box in Section 6.1. These are other exact (analytic) solutions as discussed in [58, 171]. Because the electron–nuclei interactions are strong and the practical ones are many-body systems, the exact solutions are not possible and practical. There are also approximate (including numerical) solutions, including the perturbation theory, the variational principle, quantum Monte Carlo, DFT, Wentzel–Kramers–Brillouin (W-K-B) approximation, discrete delta-potential method, pseudo-potential method, etc. [432].

The development of the DFT and the accuracy of the local density approximation (LDA) and generalized gradient approximation (GGA) have allowed for useful quantum mechanics calculations.

The perturbation theory approximates the solution to the Schrödinger equation assuming the external disturbance to be a small perturbation, then by using solutions to simpler systems (i.e., simpler or weaker Hamiltonians). In the time-independent perturbation theory, the perturbation Hamiltonian is static. The solution begins with an unperturbed Hamiltonian $\rm H_o$ giving a set of discrete energy levels $E_{{\rm o},n}$ from the

Table 2.10. *Hydrogenlike atom, electron wave functions for the principal quantum numbers, 1, 2, and 3, where* z *is the atomic number, and the dimensionless radial position is* $r^* = zr/r_\mathrm{B}$ *[324]. The spin number* s *is* $+1/2$ *for first electron and* $-1/2$ *for the next, and then repeated.*

Principal	Azimuthal	Magnetic	Wave function
$n = 1$	$l = 0$	$m = 0$	$\psi_{e,1s} = \frac{1}{\pi^{1/2}}(\frac{z}{r_\mathrm{B}})^{3/2} e^{-r^*}$
$n = 2$	$l = 0$	$m = 0$	$\psi_{e,2s} = \frac{1}{4(2\pi)^{1/2}}(\frac{z}{r_\mathrm{B}})^{3/2}(2 - r^*)e^{-r^*/2}$
	$l = 1$	$m = 0$	$\psi_{e,2p_z} = \frac{1}{4(2\pi)^{1/2}}(\frac{z}{r_\mathrm{B}})^{3/2} r^* e^{-r^*/2} \cos\theta$
	$l = 1$	$m \pm 1$	$\psi_{e,2p_x} = \frac{1}{4(2\pi)^{1/2}}(\frac{z}{r_\mathrm{B}})^{3/2} r^* e^{-r^*/2} \sin\theta \cos\phi$
			$\psi_{e,2p_y} = \frac{1}{4(2\pi)^{1/2}}(\frac{z}{r_\mathrm{B}})^{3/2} r^* e^{-r^*/2} \sin\theta \sin\phi$
$n = 3$	$l = 0$	$m = 0$	$\psi_{e,3s} = \frac{1}{81(3\pi)^{1/2}}(\frac{z}{r_\mathrm{B}})^{3/2}(27 - 18r^* + 2r^*)e^{-r^*/3}$
	$l = 1$	$m = 0$	$\psi_{e,3p_z} = \frac{2^{1/2}}{81(\pi)^{1/2}}(\frac{z}{r_\mathrm{B}})^{3/2} r^*(6 - r^*)e^{-r^*/3} \cos\theta$
	$l = 1$	$m = \pm 1$	$\psi_{e,3p_x} = \frac{2^{1/2}}{81(\pi)^{1/2}}(\frac{z}{r_\mathrm{B}})^{3/2} r^*(6 - r^*)e^{-r^*/3} \sin\theta \cos\theta$
			$\psi_{e,3p_y} = \frac{2^{1/2}}{81(\pi)^{1/2}}(\frac{z}{r_\mathrm{B}})^{3/2} r^*(6 - r^*)e^{-r^*/3} \sin\theta \sin\theta$
	$l = 2$	$m = 0$	$\psi_{e,3d_{z^2}} = \frac{1}{81(6\pi)^{1/2}}(\frac{z}{r_\mathrm{B}})^{3/2} r^{*2} e^{-r^*/3}(3\cos^2\theta - 1)$
	$l = 2$	$m = \pm 1$	$\psi_{e,3d_{xz}} = \frac{2^{1/2}}{81(\pi)^{1/2}}(\frac{z}{r_\mathrm{B}})^{3/2} r^{*2} e^{-r^*/3} \sin\theta \cos\theta \cos\phi$
			$\psi_{e,3d_{yz}} = \frac{2^{1/2}}{81(\pi)^{1/2}}(\frac{z}{r_\mathrm{B}})^{3/2} r^{*2} e^{-r^*/3} \sin\theta \cos\theta \sin\phi$
	$l = 2$	$m = \pm 2$	$\psi_{e,3d_{x^2-y^2}} = \frac{1}{81(2\pi)^{1/2}}(\frac{z}{r_\mathrm{B}})^{3/2} r^{*2} e^{-r^*/3} \sin^2\theta \cos 2\phi$
			$\psi_{e,3d_{xy}} = \frac{1}{81(2\pi)^{1/2}}(\frac{z}{r_\mathrm{B}})^{3/2} r^{*2} e^{-r^*/3} \sin^2\theta \sin 2\phi$

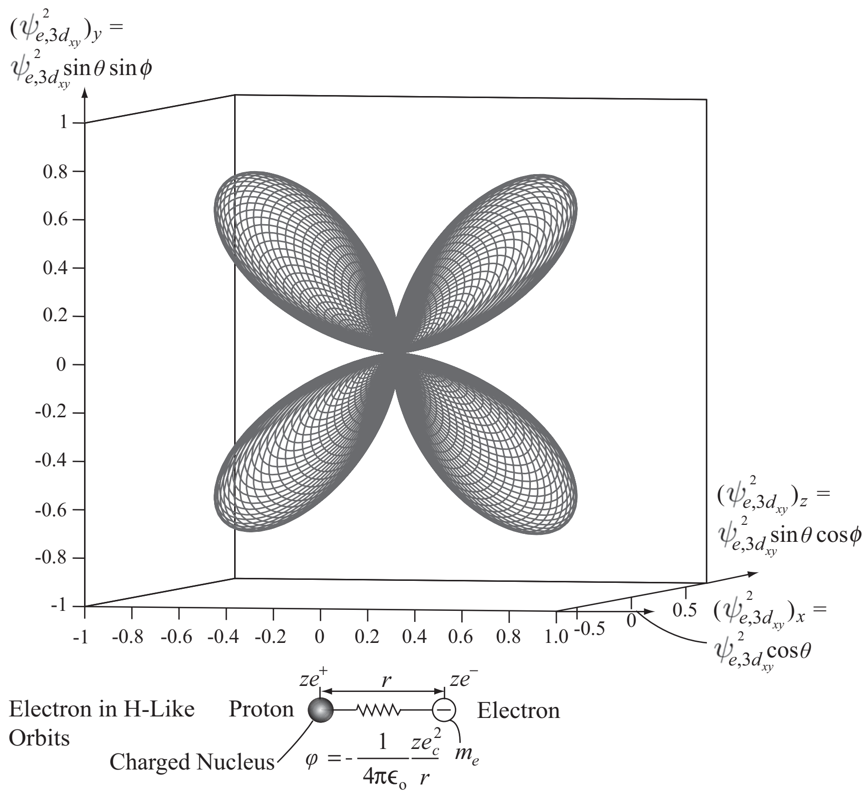

(a) Projected Variation of $3d_{xy}$ Wave Function: $\psi_e = \cos^2\theta\sin 2\phi$

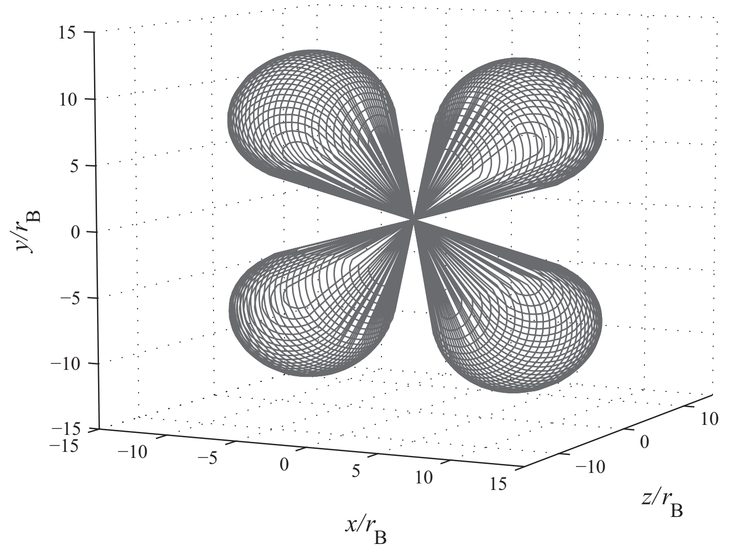

(b) Constant Probability Surface of $3d_{xy}$ Electron Orbital

Figure 2.18. (a) Projected, three-dimensional variation of $3d_{xy}$ wave function, and (b) three-dimensional electron orbital showing the surface of a constant probability.

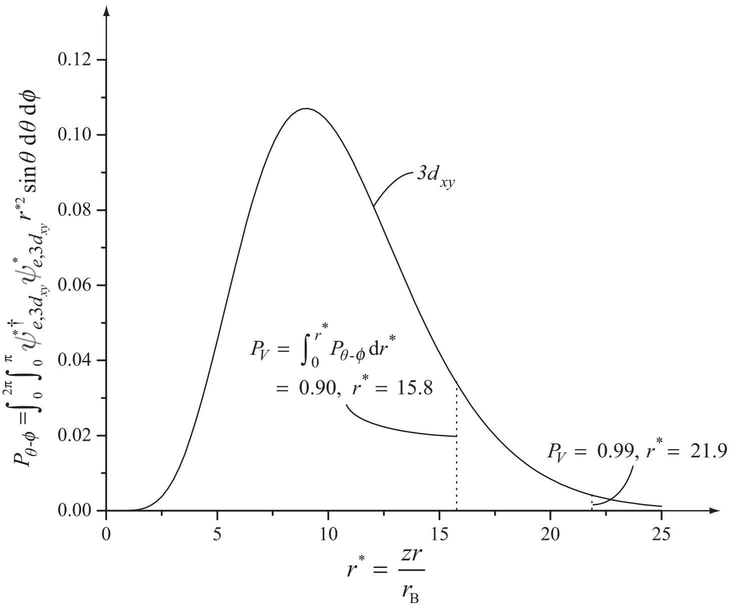

Figure 2.19. Distribution of the probability-related function with respect to dimensionless radial position for $3d_{xy}$ orbital. z is the atomic number.

Schrödinger equation written as

$$\mathrm{H_o}|n_\mathrm{o}\rangle = E_{\mathrm{o},n}|n_\mathrm{o}\rangle, \quad n = 1,\ 2,\ 3, \ldots. \tag{2.119}$$

Then the perturbation Hamiltonian H' is introduced, which represents a weak disturbance, along with a perturbation parameter ϵ $(0 \le \epsilon \le 1)$, such that

$$\mathrm{H} = \mathrm{H_o} + \mathrm{H}' = \mathrm{H_o} + \epsilon \mathrm{H}_1 + \epsilon^2 \mathrm{H}_2 + \cdots$$

$$(\mathrm{H_o} + \epsilon \mathrm{H}')|n\rangle = E_n|n\rangle, \quad \text{first-order perturbation in } \mathrm{H}_{1,n}. \tag{2.120}$$

In the perturbation approximation, instead of solving the preceding Schrödinger equation, a power-series solution is used for E_n, i.e.,

$$E_n = E_{\mathrm{o},n} + \epsilon \mathrm{H}_{1,n} + \epsilon^2 \mathrm{H}_{2,n} + \cdots,$$

$$|n\rangle = |n_\mathrm{o}\rangle + \epsilon|n_1\rangle + \epsilon^2|n_2\rangle + \cdots. \tag{2.121}$$

Now using these expansions in (2.119) and sorting the terms with the same power of ϵ, a series of equations emerges. The first one is the first-order energy shift:

$$E_{1,n} = \langle n_\mathrm{o}|\mathrm{H}_{1,n}|n_\mathrm{o}\rangle \quad \text{expectation value of } \mathrm{H}'. \tag{2.122}$$

The perturbation changes the average energy of the state by $E_{1,n}$. There are higher-order terms that can be indicated.

We have discussed and will discuss again numerical solutions to the Schrödinger equation in Section 2.2.2 (Hartree–Fock approximation), Section 5.3 (tight-binding approximation), Section 5.4 (DFT), and Section 7.12.6 (time-dependent DFT).

The time-dependent perturbation theory (given in Appendix E) includes $H'(t)$. This leads to the Fermi golden rule, which we use often (Sections 3.2.3, 4.9.4, 5.10, 5.15, 5.17.3, 7.8, and 7.12) in determining the various transition rates (atomic-level kinetics).

2.7 Problems

Problem 2.1

Using an available computer program for *ab initio* calculation of the interatomic potential (e.g., Gaussian), reproduce the O–O bond potential shown in Figure 2.6(a). After obtaining the *ab initio* potential, using a least-squares method, find the constants in the three interatomic potential models shown in Figure 2.6 and discussed in Section 2.2.2.

Problem 2.2

(a) In a polymer electrolyte membrane fuel cell (PEMFC), the interatomic bond energy from hydrogen fuel is converted to electric potential energy. The chemical reactions that occur throughout the membrane are

hydrogen is oxidized	$2H_2 \rightarrow 4H^+ + 4e^-$
oxygen is reduced	$O_2 + 4e^- \rightarrow 2O^{2-}$
net reaction	$2H_2 + O_2 \rightarrow 2H_2O$.

In this reaction, the oxidation of two hydrogen gas molecules releases four electrons, which later recombine to reduce the oxygen in the formation of two H_2O molecules. Use Table 2.3 for the bond energies and show that the maximum electric potential for this reaction is 1.248 V.

(b) Calculate the energy released per molecule of CH_4, in the one-step reaction

$$CH_4 + 2O_2 \rightarrow CO_2 + 2H_2O.$$

Compare this with the experimental value of 5.553×10^7 J/kg-CH_4. Note that we have not included any kinetic energy (temperature dependence), while the experiments include that. We will discuss the kinetic energy of solids in Chapter 4 and of fluids in Chapter 6.

Problem 2.3

(a) Show that the equilibrium separation distance is $r_{nn,e} = 1.090\sigma_{LJ}$, and the effective equilibrium potential for the L–J FCC atomic structure is $\langle\varphi\rangle_e = -8.6067\epsilon_{LJ}$. These are marked in Figure 2.1.3.

(b) Show that the isothermal bulk modulus $E_p = -v(\partial p/\partial v)_T = v\partial^2 e/\partial^2 v = v\partial/\partial v(\partial\langle\varphi\rangle/\partial v)$ [where $p = -(\partial e/\partial v)_{T=0}$ is used] is equal to $75.14\epsilon_{LJ}/\sigma_{LJ}^3$, for the L–J FCC atomic structure. Note that per particle, $v = a^3/4 = r^3/2^{1/2}$ (r is the interatomic spacing and a is the lattice constant) and use this to relate $\partial/\partial v$ to $\partial/\partial r$. Also note that at $r_{nn,e}$, $\partial\langle\varphi\rangle/\partial r = 0$.

Problem 2.4

(a) Energy broadening occurs in high scattering rates or atomic vibration phenomena. Calculate the energy uncertainty associated with vibration of Ar–Ar [use $\tau_{\rm LJ} = \Delta t$, in (2.58)].

(b) Using Ar again, determine Δx_{min} (2.59) for interatomic vibration displacement uncertainty and the associated uncertainty in x-direction momentum Δp_x. Use the natural frequency ω_n.

(c) Compare Δx_{min} in (b) with the zero-point atomic displacement, which is the leading term in (2.57).

Problem 2.5

Using the L–J potential given by (2.9), the L–J constants for Xe given in (Table 2.2), and the Debye temperature given in Table A.2, determine the equilibrium nearest-neighbor location $r_{nn,e}$, the total potential energy $\langle\varphi\rangle$ at $r_{nn,e}$, the natural angular frequency ω_n, the Debye time constant $\tau_{\rm D}$, and the L–J time constant $\tau_{\rm LJ}$. Note that MD scales are given in Table 2.7. Comment on their magnitudes. Compare with any similar length, energy, frequency, and time scales you have experience with. Use SI units.

Problem 2.6

Using the two-dimensional MD Matlab code, choose a simulation unit-cell size (dimension) and the number of particles in it. Use the dimensionless form of the variables as they are in the code. Since the L–J potential is used, it can apply to noble-gas elements (Table 2.2), but computation is done for dimensionless variable.

(a) Then plot, as a function of time, the variation in the kinetic energy, potential energy, total energy, temperature, and pressure by taking the proper ensemble averages over this simulation (Table 2.4, in dimensionless forms). Note that for this simulation volume is replaced with area. (Add code lines to compute these quantities.)

(b) Comment on your observations about fluctuations. Would these fluctuations disappear as the simulation size (both the dimension and the number of particles, but in the same proportion) is increased? (Try doubling these values a few times.) Note that using $m_{\rm o}$, $\epsilon_{\rm LJ}$, and $\sigma_{\rm LJ}$, the dimensionless quantities become, $x^* - x/\sigma_{\rm LJ}$, $m^* = m/m_{\rm o} = 1$, $E^* = E/\epsilon_{\rm LJ}$, $u^* = u/(\epsilon_{\rm LJ}/m_{\rm o})^{1/2}$, $t^* = t/(m_{\rm o}\sigma_{\rm LJ}^2/\epsilon_{\rm LJ})^{1/2}$, etc., similar to those in Table 2.7 (where we use the effective FCC potential).

Problem 2.7

(a) Plot the MSD atomic displacement $\langle|\mathbf{\Delta}_i|^2\rangle^{1/2}$ for Xe as a function of temperature for $0 < T < 150$ K. This is similar to Figure 2.14 given for Ar. Comment on the zero Kelvin motion predicted by the quantum mechanical treatment of the atomic motion.

(b) In the same graph, plot the classical atomic displacement $x_{\rm o} = (3k_{\rm B}T/m\omega_n^2)^{1/2}$, using ω_n given by (2.54).

Problem 2.8

Complete the steps in deriving the expression for $\Delta x_{\min}$ from the Heisenberg uncertainty principle (2.58).

Problem 2.9

Show that the wave function solution to the time-independent Schrödinger equation for free-electron gas in a volume $V = L^3$ is (Section 2.6.5 footnote)

$$\psi_{e,\kappa} = L^{-3/2} \exp[i(\boldsymbol{\kappa} \cdot \boldsymbol{x})].$$

This is for a free quasi-particle in a box. Show the separation of variables and the exponential solutions, and evaluate the single proportionality constant of integration (which becomes $L^{-3/2}$ when the normalization condition is used).

Problem 2.10

For the free-electron-gas model, determine the electron number density, equivalent radius, the Fermi wave number, Fermi energy, Fermi velocity, and Fermi temperature for Li, Cu, and Bi. Check with the values available in Table 5.2.

Problem 2.11

(a) Using the dimensionless form of the solution for the wave function of quantum harmonic oscillator (2.87), plot $\psi_n/(m\omega/\pi\hbar)^{1/4}$ versus x^* $(-5 \le x^* \le +5)$, for $n = 0,\ 1,\ 2$ and 3. Compare the results with those shown in Figure 2.16.

(b) Comment on the trend with increasing n.

(c) What does ψ_n indicate about the probability of finding the particle at a given location x^*?

Problem 2.12

Compare the behavior of the classical and quantum simple harmonic oscillators.

(a) Show that the classical harmonic oscillator (Section 2.5.3) extends to $x_{\rm o} = (\hbar/m\omega)^{1/2}$ only (use $m\omega^2 x_{\rm o}^2/2 = E_{\rm o} = \hbar\omega/2$).

(b) Using the definition for finding a particle in $x_{\rm o} \le x < \infty$ given in Table 2.8, show that this probability for a one-dimensional motion and for the ground state $(n = 0)$ is 0.157 (need to determine the error function for the interval 1 to ∞).

(c) Repeat (b) for $n = 1$.

Problem 2.13

For the quantum simple harmonic oscillator plot

(a) P_V versus x^*, and dimensionless potential energy φ_n^* versus dimensionless distance x^* (quantitative), for the first four quantum numbers.

(b) Comment on the trends and particle existance probability.

Problem 2.14

(a) For the $3d_{xy}$ orbital, reproduce the graph angular distribution of the wave function, Figure 2.18(a). Note that the 3 projections are $x = \psi_{3d_{xy}}^2 \sin\theta\cos\phi$, $y =$

$\psi^2_{3d_{xy}} \sin\theta \sin\phi$, and $z = \psi^2_{3d_{xy}} \cos\theta$, the standard transformation from spherical to Cartesian coordinate. Here $\psi_{3d_{xy}} = \sin^2\theta \sin 2\phi$.

(b) Also, reproduce Figure 2.19 showing the function related to the probability distribution (as a function of the dimensionless radial position) for finding the $3d_{xy}$ electron with the volume of radius r^*.

(c) What is the volume of r^* at which the probability $P_V = 0.5$?

(d) What is the energy of the hydrogen-like $3d_{xy}$ electron in eV?

Problem 2.15

The commutator operator $[A, B]$ has the property $[A, B] = AB - BA$.

Using momentum and Hamiltonian operators (footnote of Section 2.6.1), we have

$$\boldsymbol{p} \equiv \frac{\hbar}{i}\nabla \quad \text{and} \quad \mathrm{H} \equiv i\hbar\frac{\partial}{\partial t}.$$

Show that

(a) $[\boldsymbol{x},\ \boldsymbol{p}] = i\hbar$, and

(b) $[\boldsymbol{x},\ \mathrm{H}] = -\frac{i\hbar}{m_e}\boldsymbol{p}$.

3

Carrier Energy Transport and Transformation Theories

The Boltzmann transport equation (BTE) is based on classical Hamiltonian-statistical mechanics, as discussed in Section 6.10.1. This describes the state of a particle by its $\boldsymbol{x}$ and $\boldsymbol{p}$ and relates their time derivatives appearing in the equation of motion to their derivatives of the Hamiltonian H, through (2.17). The BTE also identifies the particle and its energy (in a system of particles) in terms of its position and momentum $(\boldsymbol{x}, \boldsymbol{p})$, and also allows for the determination of a nonequilibrium probability distribution of particles f_i under an applied force (on a return to equilibrium, after an initial nonequilibrium state). These distributions are used in determining transport coefficients under the influence of driving forces in cases of local nonequilibria.

The Maxwell equations describe the propagation of EM waves and their interactions with electronic entities. These are among the most useful fundamental equations (including the laws/relations of Gauss, Faraday, Ampere, and Ohm).

In treating carriers as particles, the fluctuation–dissipation transport theory associated with Green and Kubo [323] gives general expressions for the transport coefficients, valid at all times and densities, in terms of correlation or autocorrelation functions calculated from a system at equilibrium. The kinetic-theory-based transport coefficients require, as observed in experiments, imposition of an external gradient. These gradients lead to a breakdown of the correlation. Computer simulations (i.e., many-body problems, such as MD simulations) have provided equilibrium results, which are used in the G–K fluctuation dissipation theory, as well as in nonequilibrium theory. The nonequilibrium (imposed gradient) simulations require extrapolation to large systems, as well as having the complications of steep gradients and boundary conditions.

Stochastic transport processes can be described by stochastic particle dynamics equations, which are used for Brownian motion/diffusion and other transport phenomena.

In this chapter, these transport theories are reviewed to predict properties of the microscale carriers and their interaction rates. Macroscopic (continuum) equations for Newtonian fluid mechanics and elastic solid mechanics are also reviewed.

3.1 Boltzmann Transport Equation

3.1.1 Particle Probability Distribution (Occupancy) Function

In Sections 6.10.1 and 2.5 (also Appendix F) on classical particle dynamics, we discussed describing particles in a system by using particle position and momentum space (i.e., phase space). In a dilute gas, the fluid particles (atoms or molecules) are in free linear flight most of the time, and only in rare instances will their flight be interrupted by a collision with another particle. The result of such an event, which in general may be treated as a classical elastic collision, is a change in the speeds and directions of both particles. Boltzmann derived, in the kinetic theory of gases [49], a statistical treatment of such binary collisions, as well as predicting the macroscopic properties of gases. He defined a particle probability distribution (occupancy) function f_f that denotes the fraction of particles, at time t, are situated at a location $\boldsymbol{x}$ and have a given momentum $\boldsymbol{p}$ (in phase space). This BTE is also used for phonons, electrons, and photons, as well as their associated probability distribution functions f_p, f_e, and f_{ph}. Recall that the equilibrium occupancy can be expressed as (Table 1.2) $f_i^{\mathrm{o}} = [\exp(E_i - \mu)/k_{\mathrm{B}} + \gamma]^{-1}$, where $\gamma = +1$ for fermions, -1 for boson, and 0 for classical particles. We begin by noting that in classical mechanics (Section 6.10.1), particles are described by their position and momentum, to which we now add time. Thus we have $\boldsymbol{x}$, $\boldsymbol{p}$, and t as the independent variables (i.e., seven-dimensional space).

3.1.2 A Simple Derivation of BTE

The equation governing the evolution (nonequilibrium in time and space) of f is the BTE and its derivation starts with $f(\boldsymbol{x}, \boldsymbol{p}, t)$ being the fraction of particles whose positions and momenta are $\boldsymbol{x}$ and $\boldsymbol{p}$ at time t. If there were no collisions, then a short time Δt later, each particle would move from $\boldsymbol{x}$ to $\boldsymbol{x} + \boldsymbol{u}\Delta t$, and each particle momentum would change from $\boldsymbol{p}$ to $\boldsymbol{p} + \boldsymbol{F}\Delta t$, where $\boldsymbol{F}$ is the sum of the external forces on a particle at time t. Any difference between $f(\boldsymbol{x}, \boldsymbol{u}, t)$ and $f(\boldsymbol{x} + \boldsymbol{u}\Delta t, \boldsymbol{p} + \boldsymbol{F}\Delta t, t + \Delta t)$ is thus due to collisions. The collision term is set with respect to a collision rate $\partial f/\partial t|_s$ (this is not a formal derivative, but represents change) involving particles of positions $\boldsymbol{x}'$ and momenta $\boldsymbol{p}'$ over the time interval Δt entering $(\boldsymbol{x}, \boldsymbol{p})$. Figure 3.1(a) gives a one-dimensional presentation of the balance on f in the x–p_x space. Putting these terms together, we have [49, 291]

$$[f(\boldsymbol{x} + \boldsymbol{u}\Delta t, \boldsymbol{p} + \boldsymbol{F}\Delta t, t + \Delta t) - f(\boldsymbol{x}, \boldsymbol{p}, t)]\mathrm{d}\boldsymbol{x}\mathrm{d}\boldsymbol{p} = \frac{\partial f}{\partial t}|_s \mathrm{d}\boldsymbol{x}'\mathrm{d}\boldsymbol{p}'\Delta t, \tag{3.1}$$

where $\partial f/\partial t|_s$ is the time rate of change of f that is due to collisions (it does not create or remove particles, but changes their momentum). Expanding the first term

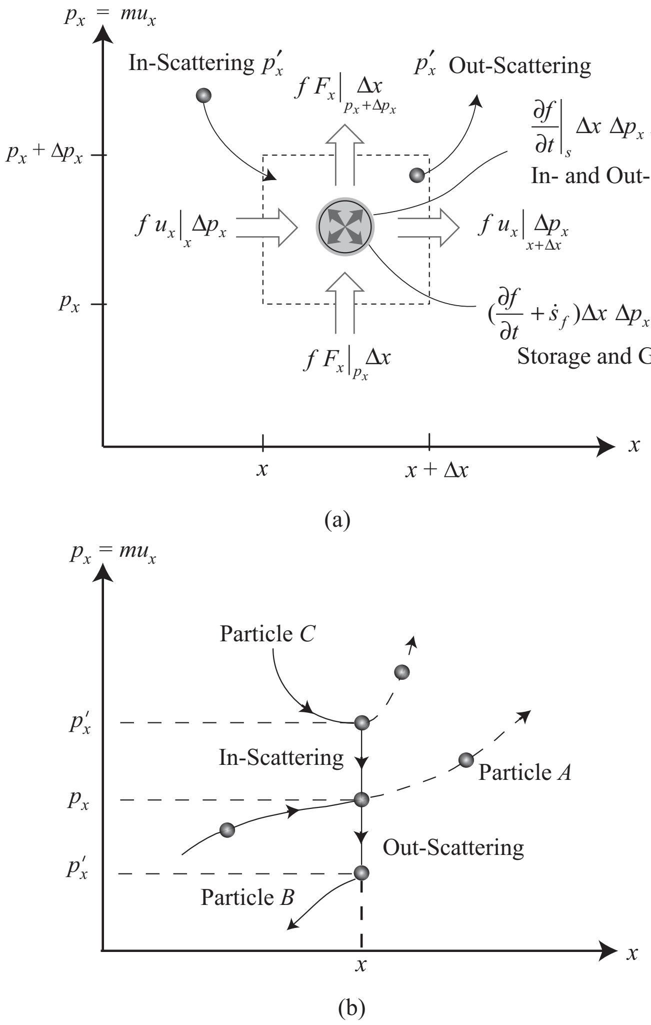
$p_x = mu_x$
In-Scattering p_x'
$f\,F_x\big|_{p_x+\Delta p_x} \Delta x$
p_x' Out-Scattering
$\left.\frac{\partial f}{\partial t}\right|_s \Delta x\,\Delta p_x\,\Delta t$
In- and Out-Scattering
$p_x + \Delta p_x$
$f\,u_x\big|_x \Delta p_x$
$f\,u_x\big|_{x+\Delta x} \Delta p_x$
p_x
$(\frac{\partial f}{\partial t} + \dot{s}_f)\Delta x\,\Delta p_x\,\Delta t$
Storage and Generation
$f\,F_x\big|_{p_x} \Delta x$
x
$x + \Delta x$
(a)
$p_x = mu_x$
Particle C
p_x'
In-Scattering
Particle A
p_x
Out-Scattering
p_x'
Particle B
x
(b)

Figure 3.1. (a) Simple, infinitesimal ($\Delta x \to 0$, $\Delta p_x \to 0$) balance on conserved property f, in single-space x and single-momentum p_x coordinates. The storage, scattering, and source terms are also shown. (b) Two-dimensional (x, p_x) rendering of particle scattering that results in a change in the particle momentum. In-scattering adds particles to state (x, p_x), whereas out-scattering removes particles from it.

on the left as a Taylor series about $f(\boldsymbol{x}, \boldsymbol{p}, t)$, we have

$$\begin{aligned} f(\boldsymbol{x} + \boldsymbol{u}\Delta t, \boldsymbol{p} + \boldsymbol{F}\Delta t, t + \Delta t) &= f(\boldsymbol{x}, \boldsymbol{p}, t) + (\frac{\partial f}{\partial x_j} u_j + \frac{\partial f}{\partial p_j} F_j + \frac{\partial f}{\partial t})\Delta t \\ &= f(\boldsymbol{x}, \boldsymbol{p}, t) + [(\nabla_{\boldsymbol{x}} f) \cdot \boldsymbol{u} + (\nabla_{\boldsymbol{p}} f) \cdot \boldsymbol{F} + \frac{\partial f}{\partial t}]\Delta t. \end{aligned} \tag{3.2}$$

Table 3.1. *Probability particle transport equation (BTE) for particle treatment of principal energy carrier i, i = p, e, f, ph [294].*

$$\frac{\partial f_i}{\partial t} + \boldsymbol{u}_i \cdot \nabla_{\boldsymbol{x}} f_i + \boldsymbol{F}_i \cdot \nabla_{\boldsymbol{p}} f_i = \frac{\partial f_i}{\partial t}|_s + \dot{s}_{f,i}, \quad i = p, e, f, ph$$

$\boldsymbol{F}_i$	applied force, N
f_i	i particle probability distribution function
$\dot{s}_{f,i}$	i carrier source rate, 1/s
$\nabla_{\boldsymbol{x}}$	spatial gradient, 1/m
$\nabla_{\boldsymbol{p}}$	momentum gradient, 1/N-s

Taking the limit as $\Delta t \rightarrow 0$, and by adding a sink/source term $\dot{s}_f$, we have

$$\frac{\partial f}{\partial t} + u_j \frac{\partial f}{\partial x_j} + F_j \frac{\partial f}{\partial p_j} = \frac{\partial f}{\partial t}|_s + \dot{s}_f$$

$$\frac{\partial f}{\partial t} + \boldsymbol{u} \cdot (\nabla_{\boldsymbol{x}} f) + \boldsymbol{F} \cdot (\nabla_{\boldsymbol{p}} f) = \frac{\partial f}{\partial t}|_s + \dot{s}_f \quad \text{BTE}. \tag{3.3}$$

The velocity term in BTE is the group velocity (the speed of propagation of the energy of the carrier), which is further defined in Section 4.1.

In (3.1), we have used unity for the determinant of the Jacobian matrix **J** for the transformation $\mathrm{d}\boldsymbol{x}'\mathrm{d}\boldsymbol{p}' = |\mathbf{J}|\mathrm{d}\boldsymbol{x}\mathrm{d}\boldsymbol{p}$, where **J** is the 6 × 6 matrix written as [49]

$$|\mathbf{J}| = \left| \frac{\partial(x, y, z, p_x, p_y, p_z)}{\partial(x', y', z', p_x', p_y', p_z')} \right| = 1, \tag{3.4}$$

to indicate no change in the coordinates. To extend (3.3) to phonons, electrons, and photons, we have also introduced a source/sink rate term $\dot{s}_f$, and (3.3) is also repeated in Table 3.1 for carrier i.

Examples of the force $\boldsymbol{F}$ include gravitational force $m\boldsymbol{g}$ for fluid particles, Coulombic force $\boldsymbol{e}_c\boldsymbol{e}_e$ for electrons, and thermoelectric coupling force $-\nabla E_f + T(E_e - E_f)\nabla T^{-1}$, where E_f is the Fermi Energy. Derivation of equilibrium distribution f_i^{o} include thermodynamics consideration and is given in Appendix E. For f_f^{o}, we will also use the equilibrium BTE discussed below, and use symmetry to arrive at the M–B distribution in Section 6.4.2.

The main feature of BTE is the return from nonequilibrium distribution f to equilibrium distribution f^{o}, through scattering $\partial f/\partial t|_s$. From Table 1.2, $f = f[E(\boldsymbol{x}, \boldsymbol{p}, t), T(\boldsymbol{x}, t)]$, so the derivatives $\partial f/\partial t$, $\partial f/\partial x_j$, $F_j \partial f/\partial p_j$ respond to scattering events (and source/sink or generation $\dot{s}_f$) in return to the equilibrium population. Also since the energy transport is related to $f - f^{\mathrm{o}}$, the slower the rate of scattering the more effective is the transport.

3.1.3 In- and Out-Scattering

The particles represented by a probability distribution (occupancy) function f_i (governed by the BTE) can have their positions and momenta ($\boldsymbol{x}$, $\boldsymbol{p}$) altered after collisions (scattering) with each other or with other microscale energy carriers. The instantaneous position of a colliding particle at time t_0 does not change, but its momentum does. This is shown in Figure 3.1(b).

For no scattering, where $\partial f_i/\partial t|_s = 0$, the particle continues on its trajectory (dashed curve) and the probability of occupying an energy state $f_i^{\rm o}$ does not change, i.e.,

$$\begin{aligned} f_i^{\rm o}(\boldsymbol{x}-\boldsymbol{u}\Delta t, \boldsymbol{p}-\boldsymbol{F}\Delta t, t-\Delta t) &= f_i^{\rm o}(\boldsymbol{x}, \boldsymbol{p}, t) \\ &= f_i^{\rm o}(\boldsymbol{x}+\boldsymbol{u}\Delta t, \boldsymbol{p}+\boldsymbol{F}\Delta t, t+\Delta t), \end{aligned} \tag{3.5}$$

or

$$\frac{{\rm D} f_i^{\rm o}}{{\rm D}t} = (\frac{\partial}{\partial t} + \boldsymbol{u}\cdot\nabla_{\boldsymbol{x}} + \boldsymbol{F}\cdot\nabla_{\boldsymbol{p}}) f_i^{\rm o} = 0 \quad \text{equlibrium distribution.} \tag{3.6}$$

This means that, if a given energy state is occupied, it remains occupied (and vice versa).

As shown in Figure 3.1(b) for particle B, as a result of collision (scattering), a particle can move out of its state ($\boldsymbol{x}$, $\boldsymbol{p}$) into ($\boldsymbol{x}$, $\boldsymbol{p}'$), thus decreasing the probability of occupation of this state. This is called out-scattering. Scattering can also cause a particle ($\boldsymbol{x}$, $\boldsymbol{p}'$) to enter a state ($\boldsymbol{x}$, $\boldsymbol{p}$), as shown in Figure 3.1(b) for particle C, a phenomenon called in-scattering (joining the state shared with particle A).

The right-hand side of the BTE allows for this change in f_i through

$$\frac{{\rm D} f_i}{{\rm D}t} = \frac{\partial f_i}{\partial t}|_s + \dot{s}_{f,i} \quad \text{nonequilibrium distribution,} \tag{3.7}$$

where $\dot{s}_{f,i}$ would account for any other source/sink not included in $\partial f_i/\partial t|_s$. Again, note that $\partial f_i/\partial t|_s$ is not a formal derivative, while $\partial f_i/\partial t$ is.

Deviation from equilibrium can be due to a force, a field, or a source. For example, an electric force on an electron for f_e, or a temperature field in a solid, fluid, or gas for f_p and f_f, or emission of photons for f_{ph}. The return to equilibrium is through collisions (scattering) $\dot{\gamma}_i$.

Let's represent the full occupancy of a state by unity. Then the sum of in- and out-scattering from ($\boldsymbol{p}'$ to $\boldsymbol{p}$ and from $\boldsymbol{p}$ to $\boldsymbol{p}'$) is represented in $\partial f/\partial t|_s$ as

$$\frac{\partial f_i}{\partial t}|_s = \underbrace{\sum_{\boldsymbol{p}'} f_i(\boldsymbol{p}')[1-f_i(\boldsymbol{p})]\dot{\gamma}_i(\boldsymbol{p}',\boldsymbol{p})}_{\text{in-scattering}} - \underbrace{\sum_{\boldsymbol{p}'} f_i(\boldsymbol{p})[1-f_i(\boldsymbol{p}')]\dot{\gamma}_i(\boldsymbol{p},\boldsymbol{p}')}_{\text{out-scattering}}, \tag{3.8}$$

where the first term is for in-scattering, $f_i(\boldsymbol{p}')$ gives the probability that $\boldsymbol{p}'$ is occupied, and $[1-f_i(\boldsymbol{p})]$ is the probability that $\boldsymbol{p}$ is empty (so it can be occupied). In the second term, $f_i(\boldsymbol{p})$ and $[1-f_i(\boldsymbol{p}')]$ are the probabilities that $\boldsymbol{p}$ is occupied and $\boldsymbol{p}'$ is empty, respectively.

Here $\dot{\gamma}_i(\boldsymbol{p}', \boldsymbol{p})$ is the transition-probability rate, or the probability of transition per unit time (1/s) that particle at state $\boldsymbol{p}'$ scatters to state $\boldsymbol{p}$. Note that we have also used $\dot{\gamma}_i$ as the scattering rate. This is the generalized symbol used throughout the book, which will be further discussed in Section 3.2.

For nondegenerate states (low occupancy, as shown in Figure 1.1) $f_i(\boldsymbol{p}) \ll 1$, and (3.8) becomes

$$\frac{\partial f_i}{\partial t}|_s = \sum_{\boldsymbol{p}'} f_i(\boldsymbol{p}')\dot{\gamma}_i(\boldsymbol{p}', \boldsymbol{p}) - \sum_{\boldsymbol{p}'} f_i(\boldsymbol{p})\dot{\gamma}_i(\boldsymbol{p}, \boldsymbol{p}'), \quad \text{nondegenerate particles.} \tag{3.9}$$

The sum of the collisions presented in $\partial f/\partial t|_s$ does not create or destroy carriers (particles), leading to

$$\sum_{\boldsymbol{p}} \frac{\partial f_i}{\partial t}|_s = 0 \quad \text{overall balance equation.} \tag{3.10}$$

This indicates that in-scattering originates from out-scattering of another state, and when adding all exchanges the net result is zero. The summation implies that integration for quasi-particles (including electrons) is taken over the momentum space (for isotropic behavior) by use of a spherical volume of radius $\boldsymbol{p}$.

Because we will apply the BTE to both classical and quantum-particles, here we make a preparation for making averages. We note that the integral (of any quantity φ) over momentum space $\mathrm{d}\boldsymbol{p}$ follows (2.108) we had for $\mathrm{d}\boldsymbol{\kappa}$, i.e., by using (2.97) $\boldsymbol{p} = \hbar\boldsymbol{\kappa}$ (the de Broglie relation, describing the parabolic energy dependence on κ, Glossary) and for isotropic behavior (spherical symmetry) noting that $\mathrm{d}\boldsymbol{p} = 4\pi p^2\mathrm{d}p$, we have the average of quantity ϕ per unit volume as

$$\langle\varphi\rangle = \sum_{\boldsymbol{\kappa}} \varphi = \frac{1}{8\pi^3}\int \varphi \mathrm{d}\boldsymbol{\kappa} = \frac{1}{8\pi^3\hbar^3}\int \varphi \mathrm{d}\boldsymbol{p} = \frac{1}{8\pi^3\hbar^3}\int_p \varphi\, 4\pi p^2\mathrm{d}p. \tag{3.11}$$

For electrons, allowing for two spins, we use $4\pi^3$ instead of $8\pi^3$. Thus, assuming isotropic behavior, the integral is over a radius p in momentum space.

Also, note that by allowing for the azimuthal angle ϕ and polar angle θ dependence (nonspherical symmetry), the integral (3.11) can be written as

$$\langle\varphi\rangle = \frac{1}{\hbar^3}\sum_{\boldsymbol{p}} \varphi = \frac{1}{8\pi^3\hbar^3}\int \varphi \mathrm{d}\boldsymbol{p} = \frac{1}{8\pi^3\hbar^3}\int_0^{\pi}\int_0^{2\pi}\int_p \varphi\, p^2\mathrm{d}p \sin\theta \mathrm{d}\phi \mathrm{d}\theta, \tag{3.12}$$

where for isotropic behavior the integral over the angles gives 4π.

3.1.4 Relaxation-Time Approximation of Scattering and Transport Properties

The scattering term in the BTE describes the elastic- (in which the energy of principal carrier groups is conserved) or inelastic- (energy exchange between principal carriers) scattering rate of particles as they collide with each other or different carriers. In Section 3.2, examples are given of such collisions involving phonons, electrons, fluid particles, and photons. These scattering events return the distribution to f_i^{o}.

The phonon scattering is mostly by other phonons. In a three-phonon-scattering event, a phonon of wave number $\boldsymbol{\kappa}_p$ can split its energy and create two other phonons (which keeps the energy and momentum conserved). These are generally inelastic scattering events.

The electron scattering is mostly by phonons, and again, it conserves total energy and momentum. Most electron collisions (scattering) are assumed to be elastic.

The fluid particle collision is mostly with other fluid particles, and while the total momentum and energy of the two particles are conserved (elastic collision), the particle trajectories undergo changes.

The inelastic photon interaction can for example be for a photon interacting with dipole moment of charge-unbalanced, vibrating atoms in a lattice. These can lead to absorption, emission, and/or elastic scattering of photons by lattice atoms.

Examples of expressions for the scattering rates is given in Section 3.2. These are generally in integral form, with the integral taken over the energy of the final (post-collision) state and the energy of the other participating particle. We will discuss these later in their appropriate chapters.

A more general treatment of f_i^{o} (the equilibrium distribution) uses symmetric and antisymmetric decomposition, both with respect to $\boldsymbol{p}$. The integrals of the $\boldsymbol{p}$-moments of the symmetric and antisymmetric portions of f_i and f_i/τ_i may then vanish, depending on the even or odd integrand [294].

As will be discussed in the following chapters, it is also customary to represent the collision rate by using a relaxation-time τ_i approximation, i.e.,[†]

$$f_i^{\text{o}} = f_i + \frac{\partial f_i}{\partial t}|_s \tau_i + \cdots$$

$$\frac{\partial f_i}{\partial t}|_s \approx -\frac{f_i - f_i^{\text{o}}}{\tau_i} = -\frac{f_i'}{\tau_i} = -\dot{\gamma}_i f_i'. \tag{3.13}$$

This is based on Taylor series expansion in τ_i and taking the leading term only (Section 6.8.1). It shows the smaller τ_i, the faster f_i returns to equilibrium. This approximation is generally valid for a small force field and under elastic or isotropic scattering (collisions).

Equation (3.13) represents a return to the equilibrium distribution f_i^{o} at a rate proportional to the deviation $f_i' = f_i - f_i^{\text{o}}$ and to the inverse of the collision rate τ_i (τ_i is in turn equal to $1/\dot{\gamma}_i$, where $\dot{\gamma}_i$ is the transition probability rate).

[†] Considering time dependence only, and with $\dot{s}_{f,i} = 0$, (3.7) and (3.13) give

$$\frac{\mathrm{d}f_i(t)}{\mathrm{d}t} = \frac{\partial f_i}{\partial t}|_s = -\frac{f_i(t) - f_i^{\text{o}}}{\tau_i}.$$

Using $f_i(t = 0) = f_i(0)$, the solution to this equation is

$$f_i(t) = f_i^{\text{o}} + [f_i(0) - f_i^{\text{o}}]e^{-t/\tau_i}.$$

This shows that within a few (say 4) time constants τ_i, the equilibrium distribution f_i^{o} is restored.

As an example consider the force electron mobility (transport property). For conduction electrons in semiconductors, under a steady-state and uniform electric field along the x direction $e_{e,x}$, we have $\partial f_e/\partial t = 0$ and $\nabla_{\boldsymbol{x}} f_e = 0$. Then, using the relaxation-time approximation ($F_x = -e_c e_{e,x}$), we find that (3.3) becomes

$$-e_c e_{e,x}\frac{\partial f_e}{\partial p_x} = -\frac{f_e - f_e^{\rm o}}{\tau_e} = -\frac{f_e'}{\tau_e}. \tag{3.14}$$

Furthermore, under the low-field approximation it is assumed that $\partial f_e/\partial p_x = \partial f_e^{\rm o}/\partial p_x$. Then

$$-\frac{e_c e_{e,x}}{\hbar}\frac{\partial f_e^{\rm o}}{\partial \kappa_x} = -\frac{f_e'}{\tau_e}, \tag{3.15}$$

where from (2.97) $p_x = \hbar\kappa_x$. Then

$$f_e' = \frac{e_c}{\hbar}e_{e,x}\tau_e\frac{\partial f_e^{\rm o}}{\partial \kappa_x} \quad \text{or} \quad f_e = f_e^{\rm o} + \frac{e_c}{\hbar}e_{e,x}\tau_e\frac{\partial f_e^{\rm o}}{\partial \kappa_x}, \tag{3.16}$$

where in general $\tau_e = \tau_e(\kappa)$. Then, with $f_e^{\rm o}(\kappa)$ from Table 1.1, f_e is determined, and $e_{e,x}$ is shown to cause departure from the equilibrium.

For example, consider a nondegenerate (so we can drop the unity from the denominator of $f_e^{\rm o}$) electron energy distribution, which is used for semiconductors. Assume a one-dimensional electron motion, in which the total energy (represented as $E_e - \mu$ in Table 1.1) can be divided into the potential and kinetic energy as

$$E_e = E_{e,p}(x) + E_{e,k}(p_x). \tag{3.17}$$

Then (this will be further explained in Section 5.7)

$$f_e^{\rm o} = \frac{1}{\exp(E_e - E_{\rm F} - 1)} \approx \exp[-\frac{E_{e,p}(x) - E_{\rm F}}{k_{\rm B}T}]\exp[-\frac{E_{e,k}(p_x)}{k_{\rm B}T}] \ \text{nondegenerate } f_e^{\rm o}. \tag{3.18}$$

The nondegenerate electrons do not obey the Pauli exclusion principle (low $n_{e,c}$ semiconductors). Using (2.97) again, $E_{e,k} = p_x^2/2m_e = \hbar^2\kappa_x^2/2m_e$, and we have

$$\frac{\partial f_e^{\rm o}}{\partial \kappa_x} = -\frac{\hbar^2\kappa_x}{m_e k_{\rm B}T}\exp[-\frac{E_{e,p}(x) - E_{\rm F}}{k_{\rm B}T}]\exp(-\frac{\hbar^2\kappa_x^2}{2m_e k_{\rm B}T}). \tag{3.19}$$

Finally,

$$\begin{aligned} f_e &= f_e^{\rm o}(1 - \frac{\hbar e_c e_{e,x}\tau_e}{m_e k_{\rm B}T}\kappa_x) \\ &= f_e^{\rm o}(1 - \frac{e_c e_{e,x}\tau_e}{m_e k_{\rm B}T}p_x) \\ &= f_e^{\rm o}(1 - \frac{2^{1/2}e_c e_{e,x}\tau_e}{m_e^{1/2}k_{\rm B}T}E_{e,k}^{1/2}). \end{aligned} \tag{3.20}$$

This shows that f_e is shifted on the $E_{e,k}$ axis when compared with the equilibrium distribution $f_e^{\rm o}$.

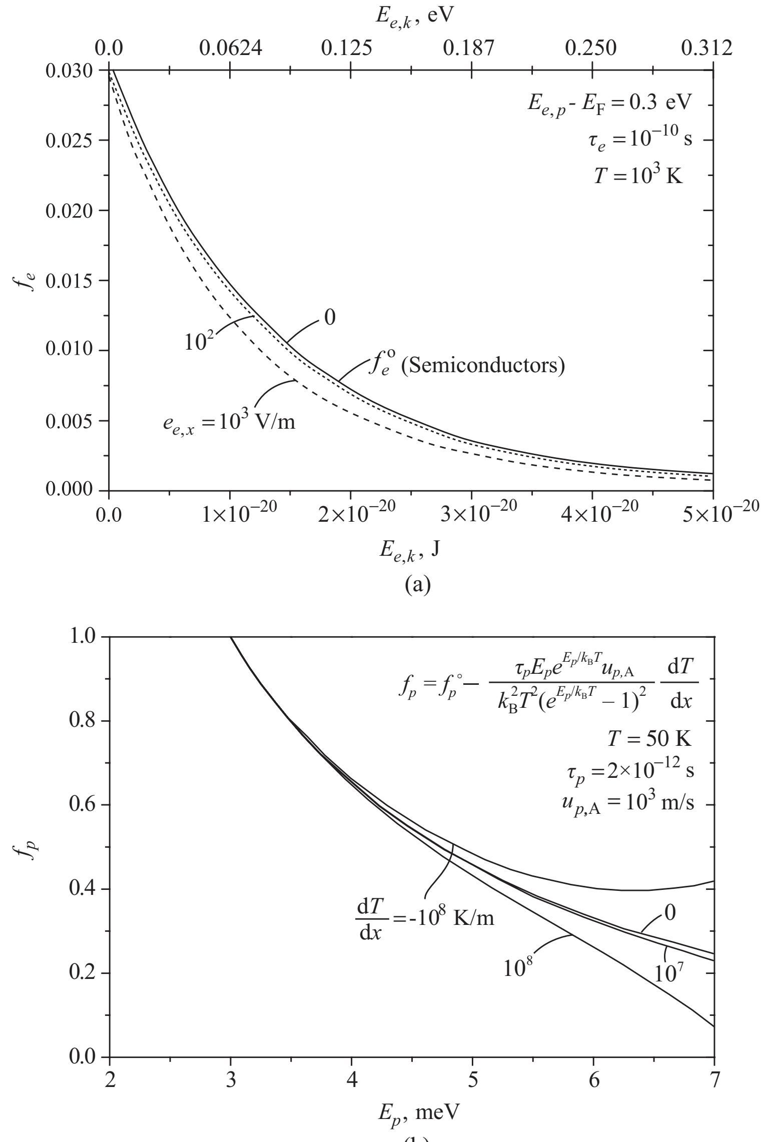

(a)

(b)

Figure 3.2. (a) Variations of f_e with respect to the kinetic energy for nondegenerate electrons in a one-dimensional electric field. (b) Variations of f_p for Ar FCC solid under a temperature gradient.

Figure 3.2(a) shows the variation f_e with respect to $E_{e,k}$ for $E_{e,p} - E_F = 0.3$ eV, $\tau_e = 10^{-10}$ s, $T = 1000$ K, and a range of e_e (0, 10^2, and 10^3 V/m). This is characteristic of high-temperature thermoelectric semiconductors. Note that for the smaller electric fields (e.g., $e_{e,x} = 0$), the deviation from equilibrium is not noticeable. This response to an electric field determines the transport properties. In Section 5.11 we use (3.20) to find the directional electron drift velocity $u_{e,x}$, the electron mobility $\mu_{e,x}$, and electrical conductivity $\sigma_{e,x}$, which are defined as

$$\mu_{e,x} = \frac{\langle u_{e,x} \rangle}{-e_{e,x}} \equiv \frac{1}{-e_{e,x}} \frac{\sum\limits_{p} u_{e,x} f_e}{\sum\limits_{p} f_e}, \quad \sigma_{e,x} = n_{e,c} e_c \mu_{e,x}, \tag{3.21}$$

where $n_{e,c}$ is the conduction electron density, and e_c is the electron charge. Through (3.20), τ_e and other properties enter into $\mu_{e,x}$.

The relaxation time τ_e represents the inverse of the transition rate $\dot{\gamma}_e$. This indicates that for a very large transition rate, in which the scattering drives the distribution toward equilibrium, the relaxation time tends to zero. This was also previously found for $\tau_e \rightarrow 0$.

Similarly, as is shown in Section 4.9.2, the thermal conductivity tensor $\boldsymbol{K}_i$ and the conduction heat flux $\boldsymbol{q}_{k,i}$ (diffusive as compared to convective transport) for carrier i are given by

$$\boldsymbol{q}_{k,i} = \sum_{\alpha} \frac{1}{8\pi^3} \int E_i \boldsymbol{u}_i f_i' \mathrm{d}\boldsymbol{\kappa}_\alpha \equiv -\boldsymbol{K}_i \cdot \nabla T, \quad \boldsymbol{K}_i = \sum_{\alpha} \frac{1}{8\pi^3} \int c_{v,i} \tau_i \boldsymbol{u}_i \boldsymbol{u}_i \mathrm{d}\boldsymbol{\kappa}_\alpha, \tag{3.22}$$

where α is the polarization of the carrier i (for electrons $8\pi^3$ is replaced with $4\pi^3$ to account for the two spins). Similar to (3.16), the deviation f_i' is related to the driving potential ∇T by use of BTE (as was previously done for electrons in an electric field). In Section 4.9, we will show that for phonons under a temperature gradient, $\mathrm{d}T/\mathrm{d}x$, where $f = f_\mathrm{o} - \tau_p E_p u_p \mathrm{d}T/\mathrm{d}x/[\exp(E_p/k_\mathrm{B}T) - 1]^{-2}$. This is plotted in Figure 3.2(b) for $\mathrm{d}T/\mathrm{d}x = -10^8, 0, 10^7, 10^8$ K/m, and for phonon properties of solid Ar at 50 K. The high-energy phonon population is most affected by the presence of a temperature gradient. Note that equation (3.22) can also be written in terms of $f_i^\mathrm{o} + f_i' = f_i$; however, the integral involving f_i^o is zero due to the symmetry.

As just demonstrated, the BTE is also used to determine macroscopic transport properties. We use it in Chapters 4 to 7 for all four microscale energy carriers.

3.1.5 Boltzmann Transport Scales

The relaxation time of principal carrier i, τ_i, signifies the time between encounter (scattering) events that alter the particle momentum $\boldsymbol{p}_i$. Examples are given in Figure 1.5, ranging from fs to ms. The particle momentum is in turn affected by the external force $\boldsymbol{F}_i$. The velocity of the particle $\boldsymbol{u}_i$ is related to its momentum. Then the time, length, and momentum scales of Boltzmann transport, τ_i, λ_i, and $\boldsymbol{p}_i$, respectively signify how long and how far the particle can retain its identity before the next scattering event. This length scale is the mean free path λ_i as introduced in (1.14).

Table 3.2 summarizes the Boltzmann transport scales. These can be compared with Table 1.5 which shows the *ab initio* (fine-structure) scales, and Table 2.7 which shows the MD scales. We also note that the macroscopic treatment scales are $L \gg \lambda_i$

Table 3.2. *Boltzmann transport scales (time, length, momentum, and force), based on relaxation time.*

Scale	Relation
Time (relaxation time)	τ_i
Length (mean free path)	$\lambda_i = u_i \tau_i$
Momentum	$\boldsymbol{p}_i = m\boldsymbol{u}_i = \boldsymbol{F}_i \tau_i$
Force	$\boldsymbol{F}_i$

and $t \gg \tau_i$, where the continuum theories are valid. The four levels of length and time scales were presented together in Figure 1.9. When λ_i is larger than the considered system length, i.e., $\lambda_i \gg L$, the transport is said to be ballistic (no momentum altering event during the transport).

3.1.6 Momentum, Energy, and Average Relaxation Times

Various approximations are used for the relaxation time. The simplest treatment assumes a constant τ_i. However, in most cases, this does not lead to accurate predictions.

The scattering rate $\dot{\gamma}(\boldsymbol{p}, \boldsymbol{p}')$ is the rate at which carriers with specific momentum $\boldsymbol{p}$ scatter to $\boldsymbol{p}'$. The relaxation time is the average time between such collisions, or the lifetime of state $\boldsymbol{p}$. Some scattering processes are not isotropic, such as small angle-momentum deflections, and using the angle θ between $\boldsymbol{p}$ and $\boldsymbol{p}'$, a momentum relaxation time τ_i(momentum) is defined as [294]

$$\tau_i^{-1}(\text{momentum}) = \sum_{\boldsymbol{p}} \dot{\gamma}_i(\boldsymbol{p}, \boldsymbol{p}') \frac{\Delta \boldsymbol{p}}{\boldsymbol{p}} = \sum_{\boldsymbol{p}'} \dot{\gamma}_i(\boldsymbol{p}, \boldsymbol{p}')(1 - \frac{|\boldsymbol{p}'|}{|\boldsymbol{p}|} \cos\theta), \ \boldsymbol{p} = \boldsymbol{p} \mp \boldsymbol{p}_i', \tag{3.23}$$

where $\pm \boldsymbol{p}_i$ indicates added/lost momentum, and θ is the polar angle between the incident and the scattered (initial and final) momenta. This shows the momentum relaxation time accounts for the change in direction of momentum. Only several relaxation times are needed to randomize the momentum. When the direction and magnitude of the particles do not change in the collision (scattering), then τ_i(momentum)$\rightarrow \infty$, as expected.

In Chapter 5, for electron–phonon scattering, we will also be interested in the rate of electron energy scattering by phonons. The energy relaxation time weighs each collision by the fractional change in the energy [294]

$$\tau_i^{-1}(\text{energy}) = \sum_{\boldsymbol{p}} \dot{\gamma}_i(\boldsymbol{p}, \boldsymbol{p}') \frac{\Delta E}{E} = \sum_{\boldsymbol{p}} \dot{\gamma}_i(\boldsymbol{p}, \boldsymbol{p}')[1 - \frac{E(\boldsymbol{p}')}{E(\boldsymbol{p})}], \ E_{\kappa'} = E_\kappa \mp E_i, \tag{3.24}$$

where $\pm E_i$ indicates added/lost energy (inelastic). This is the time required to dissipate or exchange carrier energy. For elastic scattering, $E(\boldsymbol{p}') = E(\boldsymbol{p})$, and τ_i(energy)$\rightarrow \infty$ (Section 5.10), as expected.

There are also simple models for energy-dependent relaxation times. Among them is the power-law energy-dependent relaxation time, which is used for electron scattering [294] and is given by

$$\tau_e(E_e) = \tau_{e,\mathrm{o}}(\frac{E_e}{k_\mathrm{B}T})^s \quad \text{energy-dependent electron relaxation time}, \tag{3.25}$$

where s is the power-law constant. For example, for electron–phonon (acoustic) scattering $s = -1/2$ (Table 5.3).

Using $\tau_e(E_e)$, the energy-averaged relaxation time, we find the energy-averaged $\langle\langle\tau_e\rangle\rangle$ (end-of-chapter problem). The double brackets indicates that the average is not a simple average, but actually a particularly weighted average (Section 5.11). We will apply this model to the electron scattering by phonons and impurities.

3.1.7 Moments of BTE

Within the particle treatment model, each microscale BTE can be used for deriving conservation equations involving the moments of f_i with respect to the power n of its momentum $\boldsymbol{p}_i^n$. This moment is then averaged over the entire momentum (or wave vector) space to arrive at the average conservation equations. When this procedure is applied to fluid particles, it gives the conservation of mass (continuity) equation for $\boldsymbol{p}_f^0$, the momentum conservation equation (the Navier–Stokes equations, Table 3.10, Section 3.7) for $\boldsymbol{p}_f^1$, and the mechanical energy equation for $|\boldsymbol{p}_f|^2 = p_f^2$. Similarly, we will arrive at the electron conservation (drift–diffusion) equation for $\boldsymbol{p}_e^\mathrm{o}$ and the energy conservation equation for $|\boldsymbol{p}_e|^2$. A similar set of equations can be developed for phonons. We will discuss the electron and phonon conservation equations in Section 5.18. For photons, the energy equation is developed from the BTE by use of the photon energy $\hbar\omega$, which is called the equation of radiative transfer (Section 7.6).

As an example, following (1.2) to (1.4), the nth moment $\boldsymbol{p}_e^n$ of the electron distribution function f_e averaged over the momentum space (allowing for two spins) (3.12) is

$$\begin{aligned}
\langle n_{e,c}\rangle &= \frac{1}{\hbar^3}\sum_{\boldsymbol{p}_e}\boldsymbol{p}_e^0 f_e = \frac{1}{\hbar^3}\sum_{\boldsymbol{p}_e} f_e \\
\langle n_{e,c}e_e\boldsymbol{u}_e\rangle &= \langle\boldsymbol{j}_e\rangle = \frac{e_c}{\hbar^3}\sum_{\boldsymbol{p}_e}\frac{\boldsymbol{p}_e f_e}{m_e} \\
\frac{\langle E_e\rangle}{V} &= \frac{1}{\hbar^3}\sum_{\boldsymbol{p}_e}\frac{1}{2m_e}\boldsymbol{p}_e^2 f_e = \frac{1}{\hbar^3}\sum_{\boldsymbol{p}_e}\frac{p_e^2}{2m_e}f_e,
\end{aligned} \tag{3.26}$$

where we have used $\boldsymbol{p}_e = \hbar\boldsymbol{\kappa}_e$ to turn summation that over $\boldsymbol{\kappa}_e$ to that over $\boldsymbol{p}_e$. The integral of the zeroth-moment gives the carrier density $\langle n_{e,c}\rangle$, that of the first-moment gives the drift current density vector $\boldsymbol{j}_e$, and that of the second-moment gives the average energy density $\langle E_e\rangle$ (these lead to the carrier continuity, momentum, and energy equations. An example is given in Section 5.18). Then, BTE (3.3) is accordingly multiplied by $\boldsymbol{p}_i^2$ and averaged. The wave number vector $\boldsymbol{\kappa}_i$ and momentum vector $\boldsymbol{p}_i$ are related through (2.98).

When the relaxation-time approximation is used, the momentum and energy equations will contain the moment-averaged relaxation times. As mentioned in Section 3.1.6, these are designated as τ_i(momentum) and τ_i(energy), and examples are given in Section 5.18.

3.1.8 Numerical Solution to BTE

There are two classes of computational techniques that are used to solve the BTE for energy carriers (p, e, f, ph): the deterministic method and the Monte Carlo method [428].[†] In the first method, the BTE is discretized by use of a variety of methods and then solved directly or iteratively. The discretization techniques include the discrete ordinates S_N, spherical harmonics P_N, collision probabilities, nodal methods, and others. In Section 7.7.3 we discuss an approximate discrete ordinate method using only two ordinates, one forward and one backward. This is called the two-flux method and is able to reveal much about the solution and the role of scattering.

The Monte Carlo method constructs a stochastic model in which the expected value of a certain random variable is equivalent to the value of a physical quantity to be determined. The expected value is estimated by the average of many independent samples representing the random variable. Random numbers, following the distributions of the variable to be estimated, are used to construct these independent samples. There are two different options to choose from in constructing a stochastic model for the Monte Carlo computations. In the first case, the physical process is stochastic and the Monte Carlo computation involves a simulation of the real physical process. In the other case, a stochastic model is constructed artificially, such as the solution of the deterministic equations, by the Monte Carlo method. Both the deterministic and the Monte Carlo methods have errors, but their source is different for each method. In the deterministic computational method, the computing errors are systematic. They arise from the discretization of the time–space–angle-energy phase space and the approximate geometry. The errors in the Monte Carlo method are from stochastic uncertainties. A review of Monte Carlo method used for phonon, electron, fluid particle, and photon is given in Appendix H.

3.2 Energy Transition Kinetics and Fermi Golden Rule

Central to heat transfer is the rate (time) of change of energy to and from thermal energy $\dot{s}_{i\text{-}j}$, as given in Table 1.1. These rates (energy transformation kinetics) are governed by the slowest of the processes involved (in a multiprocess energy conversion). For example, in laser cooling of solids, the photon-electron interactions

---

[†] Note that the equation of radiative transfer (for photon transport), given in Section 7.6.1, is derived from the BTE, and therefore, in its most general form is similar to the BTE. Many numerical methods used for the solution of the equation of radiative transfer, as described in [428], apply in general to solving the BTE.

(absorption), the electronic transition, the coupling of this transition with phonons (absorption of phonons), and luminescence (photon emission), are all encountered in the processes. Each of these processes, in which a carrier undergoes interaction with the same or different carrier, has an interaction/transition time.

Energy conversion is an inelastic carrier interaction. In Figure 1.5, examples of various interaction times $\tau_{i\text{-}j} = 1/\dot{\gamma}_{i\text{-}j}$ were listed. In semiconductors, for example, the presence of holes results in electron–hole radiative recombination, which depends strongly on dopant concentration.

We also consider the rate of return to equilibrium in particle interactions. An isolated, many-particle system will eventually reach equilibrium, irrespective of its initial state. The typical time for this is called the thermalization time, and depends on the nature of the interparticle interactions.

Because carrier energy distribution is temperature dependent (Table 1.2), all interaction and transition rates are temperature dependent. This gives rise to change in the dominant (slowest) process as temperature changes, in addition to a strong dependence of the rates.

A general qualitative discussion of the various interactions encountered by the carriers is given in subsequent sections. Then, in the following chapters, quantitative treatments of these rates are given while considering a central (e.g., source of energy) carrier.

3.2.1 Elastic and Inelastic Scattering

In classical particle collisions, an ideally elastic collision is one in which there is no loss of kinetic energy in the collisions; in an inelastic collision, part of the kinetic energy is changed to some other form of energy (e.g., internal energy). Collisions between hard spheres are considered elastic (the other extreme is that in which the colliding particles coalesce). In addition to energy, momentum conservation is also imposed in some treatments.

Therefore, an inelastic event is one in which part of the energy is “lost” in the scatter, giving rise to internal energy, and thus requiring additional independent variables.

In interaction among the same principal carriers (e.g., phonon–phonon), while energy (and momentum) is exchanged between them, such scattering is considered elastic. In scattering between different carriers (e.g., photons and electrons), although total energy (and in some analysis the momentum) conservation holds among them, the energy exchange between these carriers is considered inelastic. Table 3.3 gives examples of intracarrier and intercarrier scatterings. In many cases, idealized elastic scattering can be assumed.

In addition to energy, particle momentum conservation may also be included in the interaction analysis. In electron–phonon and phonon–phonon scattering events, this conservation is also imposed, with the added complexity of the analysis. In binary fluid particle collision, momentum conservation is readily imposed.

Table 3.3. *Some carrier scatterings of significance in heat transfer and thermal energy conversion.*

Carrier	Scattered by	Elastic or inelastic scattering
Phonon	phonon	elastic or inelastic
	impurity	elastic
	vacancy	elastic
	electron	elastic or inelastic
	grain boundary	elastic
Electron	phonon	elastic or inelastic
	ionized impurity	elastic
	piezoelectric	elastic
	photon	elastic or inelastic
Fluid particle	electron and ion	inelastic
	fluid particle	mostly elastic
	solid surface	inelastic
Photon	electron and ion	elastic or inelastic
	oscillating dipole	elastic or inelastic
	fluid particle	elastic or inelastic
	solid particles	elastic or inelastic
	gas plasma	inelastic

An example of elastic scattering is the Rayleigh scattering of light by air molecules resulting in the blue sky color. An example of inelastic scattering is the discriminate absorption of light by liquid water molecules (high absorption of infrared and red) resulting in blue water color. Another inelastic example is the Raman scattering where the kinetic energy of the solid or fluid medium changes the energy of the incoming photon (when the outgoing photon has higher energy it is called an anti-Stokes process).

3.2.2 Phonon Interaction and Transition Rates

Phonons interact with each other, electrons, impurity molecule sites, grain boundaries, and dislocations. A phonon's energy, manifested as lattice vibration, is proportional to k_BT, and its distribution also depends on temperature. This temperature dependence also creates a very strong temperature dependence for the specific heat capacity and interactions involving phonons. At high temperatures, inter-phonon interactions dominate others, whereas close to absolute zero, impurity and boundary interactions dominate. Also, as the melting temperature is reached and large atomic displacements occur, the ordered behavior of lattice vibration breaks down, leading to the disorder of the amorphous and liquid phases.

Liquid crystals are intermediates between liquids and crystals. The molecules are typically rod-shaped organic moieties (about 25 Å) and their order is temperature dependent. The nematic phase, for example, is characterized by the orientational order of the constituent molecules and can be controlled with an applied electric field. The smectic phases are found at lower temperatures and form well-defined layers that can slide over one another. Among such molecules are the chiral molecules that possess permanent polarizations, are ferroelectric, and whose time constant (relaxation time) in an applied field can be very small.

Figure 3.3 entry (a) and Table 3.4 entry (a), show interphonon scattering $\tau_{p\text{-}p}^{-1} = \partial f_p/\partial t|_s$ and these will be discussed in Chapter 4, including Section 4.13.

In some cases, the relaxation time is either directly or indirectly measured and is used as an empirical constant in the BTE. Examples of the magnitude of some time constant for each of the carriers are shown in Figure 1.5.

3.2.3 Electron (and Hole) Interaction and Transition Rates

Quantum theory gives an explanation for the probability of electronic transitions (interactions with other carriers, such as phonons and photons) in terms of the wave functions; this applies for transition probabilities (rates) that are time invariant, and it is generally expressed in a relationship referred to as the Fermi golden rule (FGR).

The transition rate depends on the strength of the coupling between the initial and the final state of a system and on the number of ways the transition may occur (i.e., the density of the final states). This transition probability is discussed in Section 5.10, and the derivation of the FGR is given in Appendix E. When the wave vector $\boldsymbol{\kappa}$ (which is more suitable for electrons) is used, the modal ($\boldsymbol{\kappa}'$) form of (E.24) is

$$\dot{\gamma}_{e\text{-}i}(\boldsymbol{\kappa}', \boldsymbol{\kappa}) = \frac{1}{\tau_{e\text{-}i}(\boldsymbol{\kappa}', \boldsymbol{\kappa})} = \frac{2\pi}{\hbar}|M_{\boldsymbol{\kappa}',\boldsymbol{\kappa}}|^2 \delta_{\mathrm{D}}(E_{\boldsymbol{\kappa}'} - E_{\boldsymbol{\kappa}} \mp \hbar\omega_i)$$

$$\text{FGR for transition probability rate,} \qquad (3.27)$$

where $\dot{\gamma}_{e\text{-}i}(\boldsymbol{\kappa}', \boldsymbol{\kappa})$ is transition probability rate, $M_{\boldsymbol{\kappa}',\boldsymbol{\kappa}}$ is the interaction matrix element for the interaction (for transition from state $\boldsymbol{\kappa}$ to state $\boldsymbol{\kappa}'$), and the energy Dirac delta function $\delta_{\mathrm{D}}(E)$ [291] (as compared to the Kronecker delta function) has a unit of J^{-1} (see Glossary). Here ω_i is the angular frequency of carrier i, which causes the transition. The integral of δ_{D} over $\boldsymbol{\kappa}'$-space (Section 5.7) gives the energy density of states, (5.65) as

$$D_e(E) = \sum_{\boldsymbol{\kappa}'} \delta_{\mathrm{D}}(E_{\boldsymbol{\kappa}'} - E_{\boldsymbol{\kappa}} \mp \hbar\omega_i) = \frac{1}{(2\pi)^3} \int_{\boldsymbol{\kappa}'} \delta_{\mathrm{D}}(E_{\boldsymbol{\kappa}'} - E_{\boldsymbol{\kappa}} \mp h\omega_i) \mathrm{d}\boldsymbol{\kappa}', \qquad (3.28)$$

where from (3.11), $\mathrm{d}\boldsymbol{\kappa}' = 4\pi\kappa'^2\mathrm{d}\kappa$ (bold designation indicate three-dimensional integration, or here a spherical volume).[†]

[†] Alternatively, (3.27) is written as

$$\dot{\gamma}_{e\text{-}i} = \frac{2\pi}{\hbar}|M_{\boldsymbol{\kappa}',\boldsymbol{\kappa}}|^2 D_e(E),$$

where $D_e(E)$ is per unit volume or per unit-cell volume. Since D_e represents the electronic structure of matter, it determines which interactions are physically allowed to occur.

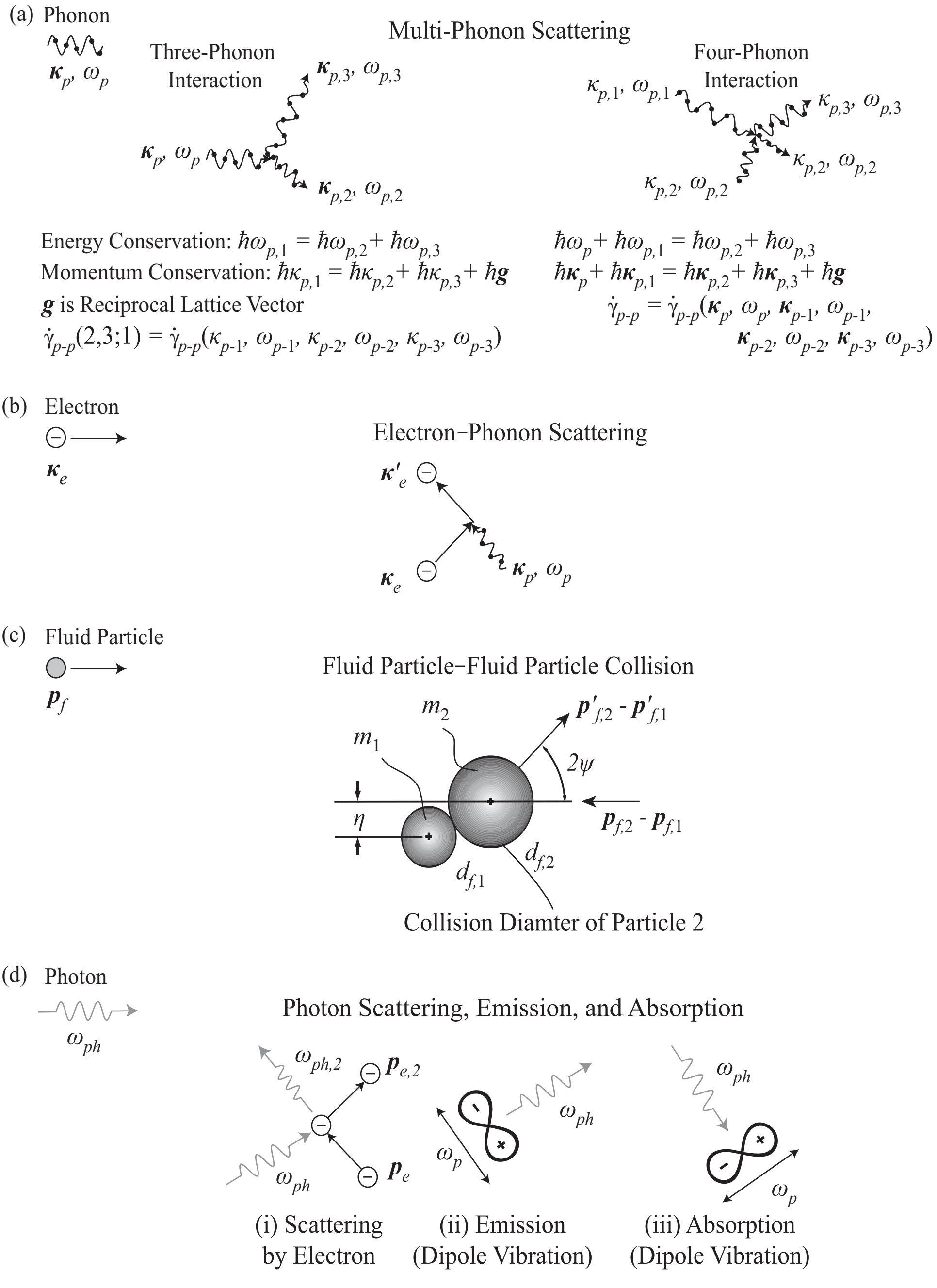
(a) Phonon
$\boldsymbol{\kappa}_p, \omega_p$
Multi-Phonon Scattering
Three-Phonon Interaction
$\boldsymbol{\kappa}_{p,3}, \omega_{p,3}$
$\boldsymbol{\kappa}_p, \omega_p$
$\boldsymbol{\kappa}_{p,2}, \omega_{p,2}$
Four-Phonon Interaction
$\kappa_{p,1}, \omega_{p,1}$
$\kappa_{p,3}, \omega_{p,3}$
$\kappa_{p,2}, \omega_{p,2}$
$\kappa_{p,2}, \omega_{p,2}$
Energy Conservation: $\hbar\omega_{p,1} = \hbar\omega_{p,2} + \hbar\omega_{p,3}$
Momentum Conservation: $\hbar\kappa_{p,1} = \hbar\kappa_{p,2} + \hbar\kappa_{p,3} + \hbar\boldsymbol{g}$
$\boldsymbol{g}$ is Reciprocal Lattice Vector
$\dot{\gamma}_{p\text{-}p}(2,3;1) = \dot{\gamma}_{p\text{-}p}(\kappa_{p\text{-}1}, \omega_{p\text{-}1}, \kappa_{p\text{-}2}, \omega_{p\text{-}2}, \kappa_{p\text{-}3}, \omega_{p\text{-}3})$
$\hbar\omega_p + \hbar\omega_{p,1} = \hbar\omega_{p,2} + \hbar\omega_{p,3}$
$\hbar\boldsymbol{\kappa}_p + \hbar\boldsymbol{\kappa}_{p,1} = \hbar\boldsymbol{\kappa}_{p,2} + \hbar\boldsymbol{\kappa}_{p,3} + \hbar\boldsymbol{g}$
$\dot{\gamma}_{p\text{-}p} = \dot{\gamma}_{p\text{-}p}(\boldsymbol{\kappa}_p, \omega_p, \boldsymbol{\kappa}_{p\text{-}1}, \omega_{p\text{-}1}, \boldsymbol{\kappa}_{p\text{-}2}, \omega_{p\text{-}2}, \boldsymbol{\kappa}_{p\text{-}3}, \omega_{p\text{-}3})$
(b) Electron
$\boldsymbol{\kappa}_e$
Electron−Phonon Scattering
$\boldsymbol{\kappa}'_e$
$\boldsymbol{\kappa}_e$
$\boldsymbol{\kappa}_p, \omega_p$
(c) Fluid Particle
$\boldsymbol{p}_f$
Fluid Particle−Fluid Particle Collision
m_2
m_1
$\boldsymbol{p}'_{f,2} - \boldsymbol{p}'_{f,1}$
2ψ
η
$\boldsymbol{p}_{f,2} - \boldsymbol{p}_{f,1}$
$d_{f,2}$
$d_{f,1}$
Collision Diamter of Particle 2
(d) Photon
ω_{ph}
Photon Scattering, Emission, and Absorption
$\omega_{ph,2}$
$\boldsymbol{p}_{e,2}$
ω_{ph}
$\boldsymbol{p}_e$
ω_p
ω_{ph}
ω_{ph}
ω_p
(i) Scattering by Electron
(ii) Emission (Dipole Vibration)
(iii) Absorption (Dipole Vibration)

Figure 3.3. Carrier presentation icons, and inter- and intraparticle (carrier) interactions. (a) Three- and four-phonon, (b) electron–phonon, (c) binary fluid particle, and (d) various photon interactions.

Table 3.4. *Examples of intercarrier and intracarrier scattering rates and relaxation times (in BTE) [408, 440, 445].*

(a) Phonon $\tau_{p\text{-}p}$:

$$\left.\frac{\partial\langle f_{p,1}\rangle}{\partial t}\right|_s = \sum_{\boldsymbol{\kappa}_2}\sum_{\alpha_2}[\sum_{\alpha_3}\dot{\gamma}_{\alpha_1,\alpha_2,\alpha_3}(\boldsymbol{\kappa}_1,\boldsymbol{\kappa}_2,-\boldsymbol{\kappa}_3)\langle f_{p,3}(f_{p,2}+1)(f_{p,1}+1)$$

$$-(f_{p,3}+1)f_{p,2}f_{p,1}\rangle\delta_{\mathrm{D}}(\omega_1+\omega_2-\omega_3)$$

$$+\frac{1}{2}\sum_{\alpha_3}\dot{\gamma}_{\alpha_1,\alpha_2,\alpha_3}(-\boldsymbol{\kappa}_1,\boldsymbol{\kappa}_2,\boldsymbol{\kappa}_3)\langle(f_{p,1}+1)f_{p,2}f_{p,3}-$$

$$f_{p,1}(f_{p,2}+1)(f_{p,3}+1)\rangle\delta_{\mathrm{D}}(\omega_1-\omega_2-\omega_3)]$$

(three-phonon scattering, Section 4.15)

(b) Electron $\tau_{e\text{-}p}$:

$$\left.\frac{\partial f_e(\boldsymbol{\kappa})}{\partial t}\right|_s = -\int\frac{\mathrm{d}\boldsymbol{\kappa}'}{4\pi^3}\{\dot{\gamma}_e(\boldsymbol{\kappa},\boldsymbol{\kappa})f_e(\boldsymbol{\kappa}')[1-f_e(\boldsymbol{\kappa})]-$$

$$\dot{\gamma}_e(\boldsymbol{\kappa},\boldsymbol{\kappa}')f_e(\boldsymbol{\kappa}')[1-f_e(\boldsymbol{\kappa}')]\}$$

(conduction-electron binary scattering, including electron-impurity and electron–phonon scattering, Section 5.11)

(c) Fluid particle

$\tau_{f\text{-}f}$:

$$\left.\frac{\partial f_f(\boldsymbol{p})}{\partial t}\right|_s = -\int\frac{\mathrm{d}\boldsymbol{p}'}{(2\pi\hbar)^3}[\dot{\gamma}_f(\boldsymbol{p}',\boldsymbol{p})f_f(\boldsymbol{p})-\dot{\gamma}_f(\boldsymbol{p},\boldsymbol{p}')f_f(\boldsymbol{p}')]$$

(fluid particle classical binary collision, Section 6.5)

(d) Photon

$\tau_{ph\text{-}e\,\mathrm{or}\,p}$:

$$\left.\frac{\partial f_{ph,\omega}(\boldsymbol{p},\boldsymbol{s})}{\partial t}\right|_s = -\sum_{i,j,k}\int\int\frac{u_{ph}\mathrm{d}\boldsymbol{p}_{i,j}}{(2\pi\hbar)^3}\mathrm{d}A_{ph,\omega}(\boldsymbol{p}_{i,j},\omega,\boldsymbol{s}\rightarrow\boldsymbol{p}_{i,k},\omega_2,\boldsymbol{s}_2)\times$$

$$f_{i,j}(\boldsymbol{p}_{i,j})[1\pm f_{i,k}(\boldsymbol{p}_{i,k})]\{f_{ph,\omega}(\boldsymbol{s})[1+f_{ph,\omega_2}(\boldsymbol{s}_2)]-$$

$$\{f_{ph,\omega}(\boldsymbol{s})[1+f_{ph,\omega}(\boldsymbol{s})]\times\frac{[1\pm f_{i,j}(\boldsymbol{p}_{i,j})]f_{i,k}(\boldsymbol{p}_{i,k})}{[1\pm f_{i,k}(\boldsymbol{p}_{i,k})]f_{i,j}(\boldsymbol{p}_{i,j})}\}$$

[photon binary scattering by boson (+) and fermion (-) carrier i, Section 7.5]

$A_{ph,\omega}$	phonon-scattering cross-section area with initial state j and final state k, m^2
$\boldsymbol{p}$	particle momentum, N-s
α_i	polarization of particle i
$\boldsymbol{\kappa}$	wave vector, 1/m
$\boldsymbol{s}$	unit vector
i	type of particle
j	initial state
f	final state
ω	angular frequency, rad/s
u_{ph}	speed of light, m/s
$\dot{\gamma}_i(\boldsymbol{p}',\boldsymbol{p})$	scattering transition rate from $\boldsymbol{p}'$ to $\boldsymbol{p}$, 1/s
$\tau_{i\text{-}j}$	relaxation time in scattering between carrier i and j, s

In some cases, (3.27) is expanded to include momentum conservation, and in that case, the right-hand side is also multiplied by $\delta_{\rm D}(\boldsymbol{\kappa}' - \boldsymbol{\kappa} \mp \boldsymbol{\kappa}_i)$. Because the FGR is a regular perturbation derivation, it applies to weak interactions. The transition-probability rate, also called the decay-probability rate, is related to the mean lifetime $\tau_{e\text{-}i}$ of the state by $\dot{\gamma}_{e\text{-}i} = 1/\tau_{e\text{-}i}$. The general form of the FGR can apply to atomic transitions, nuclear decay, scattering, and some other transitions.

A transition will proceed more rapidly if the coupling between the initial and the final states is stronger. The coupling term is the matrix element $M_{\boldsymbol{\kappa}',\boldsymbol{\kappa}}$ for the transition (emphasizing the formulation of quantum mechanics in terms of matrices rather than the differential equations of the Schrödinger equation). The matrix element is an integral, in which the interaction that causes the transition is expressed as an interaction Hamiltonian that operates on the initial-state wave function. (For example, the scattering of electrons by acoustic phonons is through the scattering Hamiltonian $\mathrm{H}' = \varphi_{d,\mathrm{A}} \nabla \cdot \boldsymbol{d}$, where $\varphi_{d,\mathrm{A}}$ is the scattering potential and $\boldsymbol{d}$ is the atomic displacement vector (Table E.1).) The transition-probability rate is proportional to the square of the integral of this interaction over all of the appropriate space, i.e.,

$$M_{\boldsymbol{\kappa}',\boldsymbol{\kappa}} = \int \psi^{\dagger}_{\boldsymbol{\kappa}'} \mathrm{H}' \psi_{\boldsymbol{\kappa}} \mathrm{d}V \quad \text{interaction matrix element,} \tag{3.29}$$

where $\psi^{\dagger}_{\boldsymbol{\kappa}'}$ is the conjugate wave function for the final state, $\psi_{\boldsymbol{\kappa}}$ is the wave function for the initial state, and H' is the scattering operator (perturbation Hamiltonian) for the physical interaction that couples the initial and final states of the system (for example, the scattering potential in electron-phonon interaction). Here $M_{\boldsymbol{\kappa}',\boldsymbol{\kappa}}$ has units of J, $D_e(E)$ has units of 1/J-m^3, and $\delta_{\rm D}$ has units of 1/J. In Section E.4 (Appendix E), we give examples of the perturbation Hamiltonian for some scatterings and couplings, involving the principal carriers.

The transition-probability rate is also proportional to the final density of states, which may be composed of several states with the same energy (i.e., degenerate states). This degeneracy is expressed as a statistical weight in the transition probability. For continuum final states, this final density of states is expressed as a function of energy.

Figure 3.3 entry (b) and Table 3.4 entry (b) show an electron–phonon scattering event, which will be discussed further in Chapter 5, including Sections 5.10, 5.11, and 5.15.

An example of nonradiative (no photon emission) coupling of transitions (decay) of excited electrons to the ground state and the vibrational/rotational (vibronic) energy of molecules is given in [181] and also in Chapter 7. These couplings (energy conversions) are referred to as internal conversions. The interaction matrix thus contains both the electronic and vibronic wave functions (from the Schrödinger equation). This involves the interaction Hamiltonian, as will be discussed in Appendix E.

A more general description of the FGR will be given in Section 5.7.

3.2.4 Fluid Particle Interaction and Transition Rates

Fluid particles in thermal motion constantly collide (in their translational motion) with each other and with their container wall, and this collision rate is central in gas kinetic theory. In addition, fluid particles can rotate and vibrate, and these have their own respective time constants. These are all temperature dependent.

Solids interact with fluid particles through surface forces, which cause physical phenomena such as gas adsorption (a thin layer of the condensed fluid phase) or physiochemical adsorption, as in surface-mediated (catalytic) reactions. These adsorbed fluid particles move about, and in and out of the adsorbed layer, because of thermal motion. Under equilibrium, these in and out flow rates balance, and as their kinetic energy (and temperature) increases beyond a threshold, they desorb.

Figure 3.3 entry (c) and Table 3.4 entry (c) show a binary, interfluid particle collision $\tau_{f\text{-}f}$. This will be further discussed in Section 6.5.

3.2.5 Photon Interaction and Transition Rates

As propagating electromagnetic waves, photons interact with electric fields (static and dynamic) in matter. This has been previously mentioned in regard to electron interactions with photons (radiation). Both classical (Maxwell) and quantum theory treatments of these interactions have been addressed. Photons can also participate in a mechanical interaction with fluid particles, as in photophoresis of nanoparticle and microparticles in rarefied gases.

Figure 3.3 entry (d) and Table 3.4 entry (d) show a phonon–electron scattering $\tau_{ph\text{-}e}$. This will be discussed in Chapter 7, including Sections 7.3, 7.4 and 7.10.

The photon interaction with electric entities (such as oscillating dipoles) can be assisted by phonons. The most fundamental approach uses the FGR (3.27). In general, photonic interactions with matter are the central phenomena in many energy-conversion processes (including photovoltaic, discussed in Chapter 7).

3.3 Maxwell Equations and Electromagnetic Waves

3.3.1 Maxwell Equations

Two of the microscale energy carriers, electrons (along with holes) and photons, can (in some cases) be treated by the Maxwell equations, which represent the fundamentals of classical electricity and magnetism. The heat transfer (energy equation in Table 1.1), includes the radiative heat flux vector $\boldsymbol{q}_r$ which is related to the photon (or EM wave) transport through the radiation intensity I_{ph}. Conduction includes electric thermal conductivity k_e, and the energy conversion term $\dot{s}_i$ contains many electron or photon related phenomena. The Maxwell equation play roles in all of these. In their dynamical form, the Maxwell equations describe the propagation of

EM waves in a medium, which is called the wave treatment of photons. Here, the differential (pointwise, as compared to integral) form of these equations is presented. These equations are compilations of various electrical and magnetic laws (including those of Ampere, Faraday, and Gauss, and here we add Ohm), and are listed in Table 3.5 [289].

The continuum properties of a medium that influence the propagation of electromagnetic waves are the electrical conductivity $\sigma_e = \sigma_{e,r} - i\sigma_{e,c}$, the relative complex electric permittivity (or relative dielectric function) $\epsilon_e = \epsilon_{e,r} - i\epsilon_{e,c}$, and the complex relative magnetic permeability $\mu_e = \mu_{e,r} - i\mu_{e,c}$ (which are wavelength λ and temperature dependent, and can be complex quantities).[†] The electric susceptivity is defined as $1 - \epsilon_e$, and we will discuss ϵ_e for different materials in Section 3.3.5. For vacuum, $\epsilon_e = \mu_e = 1$, and the electric susceptivity χ_e is zero. The speed of light is $c = (\mu_{\rm o}\mu_e\epsilon_{\rm o}\epsilon_e)^{-1/2}$, where $\epsilon_{\rm o}$ and $\mu_{\rm o}$ are the free-space permittivity and permeability (Table 1.4). For ideal insulators, $\sigma_e = 0$, and we will discuss σ_e for metals and semiconductors in Chapter 5 (experimental data in Section 5.16).

In the quantum treatment, these in turn depend on the molecular properties of the medium. In solids, for example, these depend on the electronic band structure, magnetism, the scattering rates (electron by phonon, etc.), the conduction electron density, etc. We will discuss these in Chapter 5.

Figure 3.4 shows the progression of representing EM-related properties of matter, starting from quantum mechanics, to the Maxwell equations, to optical properties, and finally the surface properties.

The optical properties presented by the spectral complex index of refraction m_λ and is introduced through the photon dispersion relation (for phase velocity) $u_{ph} = u_{ph,p} = \omega/\kappa = u_{ph,{\rm o}}/m_\lambda$. In turn m_λ is given in terms of these three fundamental, classical properties (σ_e, ϵ_e and μ_e), and has two components, i.e.,

$$m_\lambda = n_\lambda - i\kappa_\lambda = [\mu_{\rm o}\mu_e c_{\rm o}^2(\epsilon_{\rm o}\epsilon_e - i\frac{\sigma_e}{\omega})]^{1/2}, \quad \lambda f = c = u_{ph}, \quad \omega = 2\pi f,$$

$$\kappa = \kappa_{\rm o} m_\lambda = \frac{m_\lambda \omega}{c_{\rm o}} = \frac{(n_\lambda - i\kappa_\lambda)\omega}{c_{\rm o}} \quad \text{optical dispersion relation,} \tag{3.30}$$

where n_λ is the spectral index of refraction, κ_λ is the spectral index of extinction, and f is the frequency (ω is the angular frequency). Derivation of (3.30), from the Maxwell equations, is an end-of-chapter problem. For $\sigma_e/\omega\epsilon_{\rm o}\epsilon_e \gg 1$, we have a conductor and for $\sigma/\omega\epsilon_{\rm o}\epsilon_e \ll 1$, we have a dielectric. For non-magnetic ($\mu_e = 1$) dielectrics, from (3.30) we have $\epsilon_e = (n_\lambda - i\kappa_\lambda)^2$, which gives $\epsilon_{e,r} = n_\lambda^2 - \kappa_\lambda^2$, and $\epsilon_{e,c} = 2n_\lambda\kappa_\lambda$.

[†] The electric conductivity is in part related to the conduction electron density and the electronic band structure through the BTE (Section 5.12). The quantum-mechanics definition of the imaginary part of the dielectric function is [28]

$$\epsilon_{e,c} = \frac{4\pi^2}{\omega^2}\sum_f \langle \psi_f | \boldsymbol{s}_\alpha \cdot \boldsymbol{j}_e | \psi_i \rangle \delta_{\rm D}(E_f - E_i \mp \hbar\omega),$$

where $\boldsymbol{s}_\alpha$ is polarization direction unit vector and $\boldsymbol{j}_e$ is the macroscopic current density operator vector. The real part is related to an integral of $\epsilon_{e,c}$ [17].

Table 3.5. *Continuum (classical) Maxwell equations and the EM wave-propagation equation, in inhomogeneous, nonlinear anisotropic media, and some relationships with photons [289].*

$$\nabla \cdot \boldsymbol{e}_e = \frac{e_c n_e}{\epsilon_o \epsilon_e} \quad \text{Gauss law for electricity,} \ \boldsymbol{d}_e = \epsilon_o \epsilon_e \boldsymbol{e}_e$$

$$\nabla \cdot \boldsymbol{b}_e = 0 \quad \text{Gauss law for magnetism,} \ \boldsymbol{b}_e = \mu_o \mu_e \boldsymbol{h}_e$$

$$\nabla \times \boldsymbol{e}_e + \frac{\partial \boldsymbol{b}_e}{\partial t} = 0 \quad \text{Faraday law}$$

$$\nabla \times \boldsymbol{b}_e - \frac{1}{c^2}\frac{\partial \boldsymbol{e}_e}{\partial t} = \mu_o \mu_e \boldsymbol{j}_e \quad \text{Ampere law}$$

$$\boldsymbol{j}_e = \boldsymbol{j}_{e,f} + \boldsymbol{j}_{e,d} + \boldsymbol{j}_{e,m} = \sigma_e \boldsymbol{e}_e + \frac{\partial \boldsymbol{d}_e}{\partial t} + \nabla \times \boldsymbol{M} \quad \text{Ohm law, with displacement and magnetization currents}$$

$$n_e = n_{e,c} + n_{e,b} \quad \text{total (conduction and bound) electron density}$$

$$\boldsymbol{e}_e = e_{e,o} \boldsymbol{s}_\alpha e^{i(\omega t - \boldsymbol{\kappa} \cdot \boldsymbol{x})}$$

$$E_{ph,\omega} = E_{ph,e}(\omega) + E_{ph,m}(\omega) = \frac{1}{2}\int_V \epsilon_o \epsilon_e e_{e,o}^2 \mathrm{d}V \equiv V D_{ph,\omega}(f_{ph} + \frac{1}{2})\hbar\omega$$

quantum spectral energy of electromagnetic field [for harmonic (EM) field]

$$I_{ph,\omega} = |\boldsymbol{s}_e(\boldsymbol{x})|g(\omega) = |\boldsymbol{e}_e \times \boldsymbol{h}_e|g(\omega) = \frac{1}{2}|\mathrm{Re}(\boldsymbol{e}_e(\boldsymbol{x}) \times \boldsymbol{h}_e^\dagger(\boldsymbol{x}))|g(\omega) \quad \text{spectral intensity of radiation}$$

$$\int_{-\infty}^{\infty} g(\omega)\mathrm{d}\omega = 1, \ g(\omega) \quad \text{is line-shape function (broadening),} \quad g(\omega) = \frac{1}{\pi}\frac{\frac{1}{2}\Gamma}{(\omega - \omega_o)^2 + (\frac{1}{2}\Gamma)^2}$$

(Lorentzian function)

$$\nabla^2 \boldsymbol{e}_e = \frac{1}{c^2}\frac{\partial^2 \boldsymbol{e}_e}{\partial t^2} + \nabla \frac{e_c n_e}{\epsilon_o \epsilon_e} + \mu_o \mu_e \frac{\partial \boldsymbol{j}_{e,f}}{\partial t} \quad \text{electromagnetic wave equation for constant } \epsilon_e \text{ and } \mu_e$$

$$I_{ph} = I_{ph,o} e^{i(\boldsymbol{\kappa} \cdot \boldsymbol{x} - \omega t)}$$

$$m_\lambda = n_\lambda - i\kappa_\lambda = [\mu_o \mu_e c_o^2 (\epsilon_o \epsilon_e - \frac{i\sigma_e}{\omega})]^{1/2}, \quad c(\omega) = u_{ph}(\omega) = (\mu_o \mu_e \epsilon_o \epsilon_e)^{-1/2}$$

$$\kappa = \kappa_o m_\lambda = m_\lambda \frac{\omega}{c_o} \quad \text{optical dispersion relation,} \quad \sigma_{ph,\omega} = \frac{2\omega\kappa_\lambda}{c} = \frac{4\pi\kappa_\lambda}{\lambda} \quad \text{absorption coefficient}$$

Irrotational electric field, the scalar electric potential φ_e is defined through $\boldsymbol{e}_e = -\nabla\varphi_e$, replacing this in the Gauss law, gives the Poisson equation, $-\nabla^2\varphi_e = e_c n_e/\epsilon_o\epsilon_e$, also the magnetic induction vector is represented by magnetic vector potential $\boldsymbol{a}_e$ through $\boldsymbol{b}_e = \nabla \times \boldsymbol{a}_e$

Electromagnetic force (Lorentz) equation is $\boldsymbol{F}_e = e_c\boldsymbol{e}_e + e_c\boldsymbol{u} \times \boldsymbol{b}_e$

For optical fields, the spectral optical properties $m_\lambda = n_\lambda - i\kappa_\lambda$ are related to spectral ϵ_e, μ_e and σ_e, and the spectral absorption coefficient $\sigma_{ph,\omega}$

$\boldsymbol{a}_e$	vector potential, N/A-m^2
$\boldsymbol{b}_e$	magnetic induction vector, T = N/A-m = V-s/m^2
D_{ph}	photon density of states, 1/m^3-rad/s
$\boldsymbol{d}_e$	electric displacement vector, C/m^2
$\boldsymbol{e}_e$	electric field intensity vector, V/m
$\boldsymbol{h}_e$	magnetic field intensity, A/m, † indicates complex conjugate
$\boldsymbol{j}_e$	current density vector, A/m^2 = C/m^2-s
m_λ	spectral complex index of refraction, $m_\lambda = n_\lambda - i\kappa_\lambda$
$\boldsymbol{M}$	magnetization vector, A/m
n_e	total (free and bound) electron density, 1/m^3
n_λ	spectral index of refraction
$\boldsymbol{p}_e$	electric polarization vector (total dipole moment) per unit volume, C/m^2
$\boldsymbol{s}_e$	Poynting vector, W/m^2
ϵ_e	complex relative electric permittivity (or relative dielectric function)
ϵ_o	free-space permittivity, 8.854×10^{-12} C^2/N-m^2
κ_λ	spectral index of refraction and extinction
μ_e	complex relative magnetic permeability
μ_o	free-space permeability, $4\pi \times 10^{-7}$ N/A^2
σ_e	electrical conductivity, 1/Ω-m

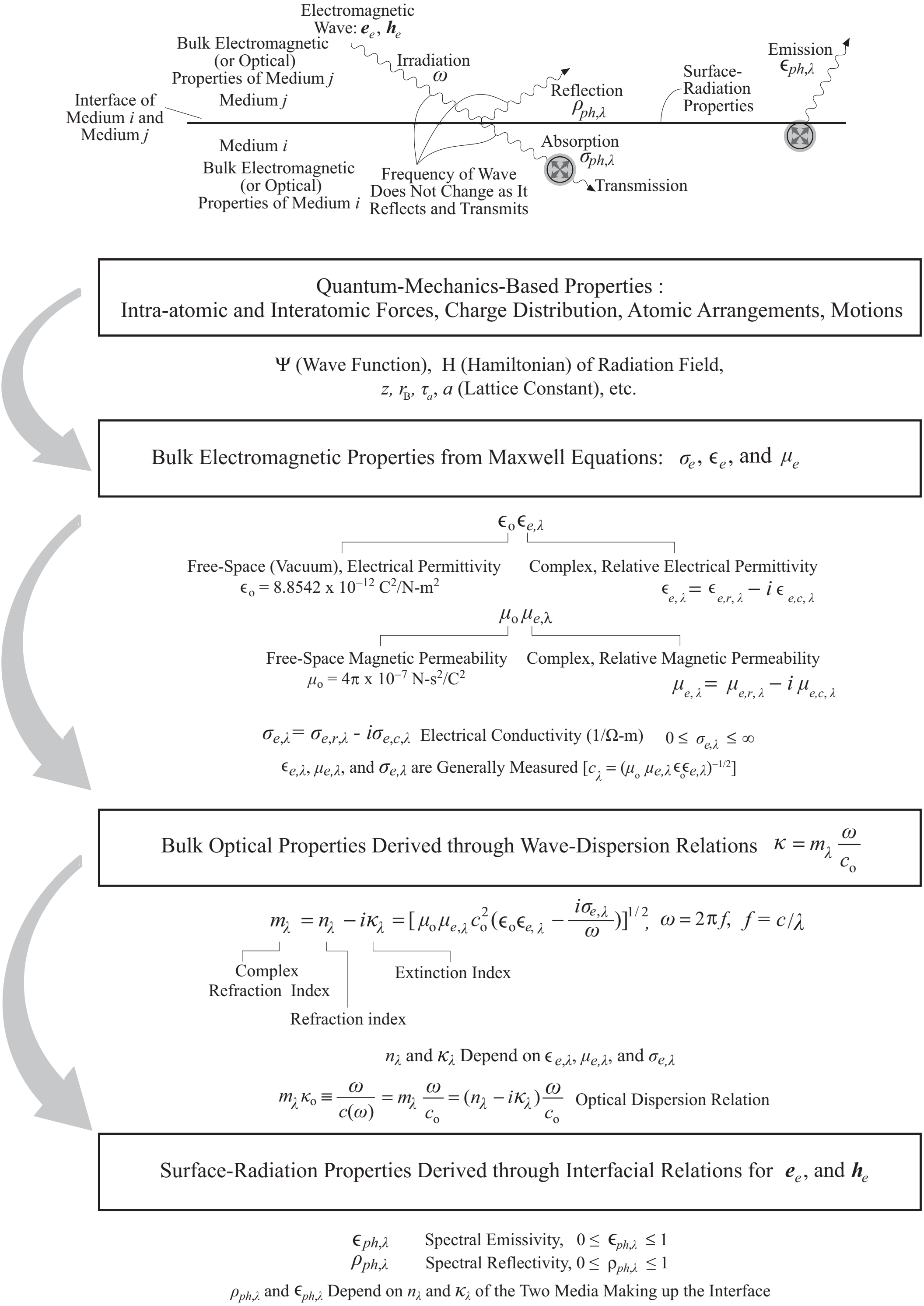
Electromagnetic Wave: $\boldsymbol{e}_e$, $\boldsymbol{h}_e$
Bulk Electromagnetic (or Optical) Properties of Medium j
Irradiation ω
Reflection $\rho_{ph,\lambda}$
Surface-Radiation Properties
Emission $\epsilon_{ph,\lambda}$
Interface of Medium i and Medium j
Medium j
Medium i
Absorption $\sigma_{ph,\lambda}$
Bulk Electromagnetic (or Optical) Properties of Medium i
Frequency of Wave Does Not Change as It Reflects and Transmits
Transmission
Quantum-Mechanics-Based Properties : Intra-atomic and Interatomic Forces, Charge Distribution, Atomic Arrangements, Motions
Ψ (Wave Function), H (Hamiltonian) of Radiation Field, z, r_B, τ_a, a (Lattice Constant), etc.
Bulk Electromagnetic Properties from Maxwell Equations: σ_e, ϵ_e, and μ_e
$\epsilon_o \epsilon_{e,\lambda}$
Free-Space (Vacuum), Electrical Permittivity $\epsilon_o = 8.8542 \times 10^{-12}$ C^2/N-m^2
Complex, Relative Electrical Permittivity $\epsilon_{e,\lambda} = \epsilon_{e,r,\lambda} - i\,\epsilon_{e,c,\lambda}$
$\mu_o \mu_{e,\lambda}$
Free-Space Magnetic Permeability $\mu_o = 4\pi \times 10^{-7}$ N-s^2/C^2
Complex, Relative Magnetic Permeability $\mu_{e,\lambda} = \mu_{e,r,\lambda} - i\,\mu_{e,c,\lambda}$
$\sigma_{e,\lambda} = \sigma_{e,r,\lambda} - i\sigma_{e,c,\lambda}$ Electrical Conductivity (1/Ω-m) $0 \le \sigma_{e,\lambda} \le \infty$
$\epsilon_{e,\lambda}$, $\mu_{e,\lambda}$, and $\sigma_{e,\lambda}$ are Generally Measured $[c_\lambda = (\mu_o \mu_{e,\lambda} \epsilon_o \epsilon_{e,\lambda})^{-1/2}]$
Bulk Optical Properties Derived through Wave-Dispersion Relations $\kappa = m_\lambda \dfrac{\omega}{c_o}$
$m_\lambda = n_\lambda - i\kappa_\lambda = [\mu_o \mu_{e,\lambda} c_o^2 (\epsilon_o \epsilon_{e,\lambda} - \dfrac{i\sigma_{e,\lambda}}{\omega})]^{1/2}$, $\omega = 2\pi f$, $f = c/\lambda$
Complex Refraction Index
Extinction Index
Refraction index
n_λ and κ_λ Depend on $\epsilon_{e,\lambda}$, $\mu_{e,\lambda}$, and $\sigma_{e,\lambda}$
$m_\lambda \kappa_o \equiv \dfrac{\omega}{c(\omega)} = m_\lambda \dfrac{\omega}{c_o} = (n_\lambda - i\kappa_\lambda)\dfrac{\omega}{c_o}$ Optical Dispersion Relation
Surface-Radiation Properties Derived through Interfacial Relations for $\boldsymbol{e}_e$, and $\boldsymbol{h}_e$
$\epsilon_{ph,\lambda}$ Spectral Emissivity, $0 \le \epsilon_{ph,\lambda} \le 1$
$\rho_{ph,\lambda}$ Spectral Reflectivity, $0 \le \rho_{ph,\lambda} \le 1$
$\rho_{ph,\lambda}$ and $\epsilon_{ph,\lambda}$ Depend on n_λ and κ_λ of the Two Media Making up the Interface

Figure 3.4. The classical (Maxwell) interaction of electromagnetic radiation with an interface marking a change in radiation properties. The quantum-mechanical, electromagnetic, optical (derived), and surface-radiation (derived) properties are also shown.

The surface-radiation properties are represented by the spectral reflectivity $\rho_{ph,\lambda}$, and spectral emissivity $\epsilon_{ph,\lambda}$, which can be related to EM or optical properties (Sections 7.10 and 7.15.1).

For semiconductors, the drift–diffusion equation is used for the electric current and is listed in Table 3.6. The electron (and hole) conservation (continuity) equation is also listed. These are derived and discussed in Section 5.18.

In addition to the electric potential φ_e ($\boldsymbol{e}_e \equiv -\nabla\varphi_e$), we will also use the magnetic vector potential $\boldsymbol{a}_e$ ($\boldsymbol{b}_e \equiv \nabla \times \boldsymbol{a}_e$), when treating the dipole radiation (end-of-chapter problem), and in quantization of EM wave in Section 7.3. The potentials are also listed in Table 3.5.

3.3.2 Electromagnetic Wave Propagation Equation

The EM wave equation for a constant property medium is obtained by taking the curl of the Faraday law, then substituting the Ampere law, followed by use of the Gauss laws (for constant ϵ_e and μ_e), i.e.,

$$\nabla \times \nabla \times \boldsymbol{e}_e = -\nabla^2 \boldsymbol{e}_e + \nabla(\nabla \cdot \boldsymbol{e}_e) \tag{3.31}$$

$$-\frac{\partial}{\partial t}\nabla \times \boldsymbol{b}_e = -\nabla^2 \boldsymbol{e}_e + \nabla(\nabla \cdot \boldsymbol{e}_e) \tag{3.32}$$

$$\nabla^2 \boldsymbol{e}_e - \nabla(\nabla \cdot \boldsymbol{e}_e) = \frac{\partial}{\partial t}(\frac{1}{c^2}\frac{\partial \boldsymbol{e}_e}{\partial t} + \mu_{\rm o}\mu_e \boldsymbol{j}_{e,f}), \quad c \equiv u_{ph} \tag{3.33}$$

$$\nabla^2 \boldsymbol{e}_e = \frac{1}{c^2}\frac{\partial^2 \boldsymbol{e}_e}{\partial t^2} + \nabla \frac{e_c n_e}{\epsilon_{\rm o}\epsilon_e} + \mu_{\rm o}\mu_e \frac{\partial \boldsymbol{j}_{e,f}}{\partial t}. \tag{3.34}$$

This EM wave propagation equation is used to derive (3.30) end-of-chapter problem,[†] using the optical dispersion relation $\kappa = m_\lambda \kappa_{\rm o} = m_\lambda \omega / c_{\rm o} = (n_\lambda - i\kappa_\lambda)$ $\omega/c_{\rm o}$, where $c_{\rm o}$ is the vacuum phase velocity (will be discussed in Section 4.2). When there is no charge gradient or current ($\sigma_e = 0$), then from (3.34) we have the simple wave (Helmholtz) equation

$$\nabla^2 \boldsymbol{e}_e = \frac{1}{c^2}\frac{\partial^2 \boldsymbol{e}_e}{\partial t^2} \quad \text{EM (classical) wave equation for } \nabla n_e = \boldsymbol{j}_{e,f} = 0. \tag{3.35}$$

The electric $\boldsymbol{e}_e$ and magnetic $\boldsymbol{h}_e$ field vectors are oriented perpendicular to each other, while propagating along the same direction. In Section 7.7.1, we discuss the continuity of the surface tangent components of these vectors as they cross interfaces with discontinuity in properties (e.g., change in m_λ). When compared with the time-dependent Schrödinger equation (2.62), which is first-order in the time derivative and has $i\hbar$ as the coefficient of this first derivative, we can expect similar solution

---

[†] This begins by introducing n_λ and κ_λ through (for propagation along x direction) and using the dispersion relation

$$e_{e,y} = e_{e,{\rm o}} \exp\{i[\omega t - \frac{(n_\lambda - i\kappa_\lambda)}{c_{\rm o}}\omega x]\} = e_{e,{\rm o}}\exp[i(\omega t - \kappa x)],$$

etc.

Table 3.6. *Electron (or hole) drift–diffusion equation, and continuity equation for semiconductors [294].*

Current is given by the drift–diffusion equation (for semiconductor heterostructures)

$$\boldsymbol{j}_e = \sigma_e \boldsymbol{e}_e + e_c D_e \nabla n_e + e_c \mathrm{S}_e \nabla T \quad \text{drift–diffusion equation}$$

where the drift is represented by conductivity and the diffusion is represented by the carrier density and temperature gradients, D_e is the electron diffusivity, and S_e is the Soret coefficient

For electrons

$$D_e = \frac{k_\mathrm{B} T}{e_c}\mu_e, \quad \mathrm{S}_e = n_e \mu_e \frac{k_\mathrm{B}}{e_c}$$

Carrier concentration is given by the electron (or hole) continuity equation (spatial variation of carrier distribution)

$$\frac{\partial n_e}{\partial t} = -\frac{1}{e_c}\nabla \cdot \boldsymbol{j}_e + \sum_i \dot{n}_{e,i} \quad \text{carrier continuity equation}$$

where $\dot{n}_{e,i}$ stands for various generations and recombinations.

D_e	carrier (electron or hole) diffusivity, m^2/s
n_e	carrier (electron or hole) density, 1/m^3
S_e	Soret coefficient, 1/K-m-s
σ_e	electrical conductivity, 1/Ω-m
μ_e	electron mobility, m^2/V-s

forms for Ψ and $\boldsymbol{e}_e$, although $\boldsymbol{e}_e$ is a vector. Also note that the quantum Hamiltonian has a Laplacian (kinetic energy) term as well as a potential term.

Using the optical dispersion relation (Figure 3.4) the classical (hyperbolic, linear), propagating EM wave equation (3.35) has a solution of the type [289][†]

$$\boldsymbol{e}_e = e_{e,\mathrm{o}} \boldsymbol{s}_\alpha e^{i(\omega t - \boldsymbol{\kappa} \cdot \boldsymbol{x})} = e_{e,\mathrm{o}} \boldsymbol{s}_\alpha e^{i(\omega t - \kappa_\mathrm{o} m_\lambda \cdot \boldsymbol{x})}, \qquad \kappa = \frac{\omega}{c_\mathrm{o}}(n_\lambda - i\kappa_\lambda), \tag{3.36}$$

where $\boldsymbol{s}_\alpha$ is the unit polarization vector, and $\boldsymbol{\kappa}$ is the wave vector. So, the Helmholtz equation (3.35) becomes $\nabla^2 \boldsymbol{e}_e = -\omega^2 \mu_e \epsilon_e \mu_\mathrm{o} \epsilon_\mathrm{o} \boldsymbol{e}_e = -\kappa_\mathrm{o}^2 m_\lambda^2 \boldsymbol{e}_e$.

Note the similarity to the time-dependent wave function (2.68) used for the Schrödinger equation in (2.69), and also note that $E = \hbar\omega$ or $E/\hbar = \hbar\kappa^2/2m$ in quantum mechanics. The Schrödinger equation has a first-order time derivative, but this term contains i.

We will use the Helmholtz equation (3.35) in treatment of radiation propagation in Section 7.7, where we show local interference of waves results in local electric field (photon energy) enhancement.

[†] Compared with de Broglie quantum wave, which is

$$\Psi = A e^{i(\boldsymbol{\kappa} \cdot \boldsymbol{x} - \omega t)},$$

where $\omega = E/\hbar = \hbar\kappa^2/2m$ as given in (2.68).

3.3.3 EM Wave and Photon Energy

The Poynting vector $\boldsymbol{s}_e$, when integrated over a closed surface, gives the total, outward flow of energy per unit time. The time-average magnitude (propagating in one direction) in a nonconducting (dielectric) medium[‡] is

$$|\bar{\boldsymbol{s}}_e| = |\overline{\boldsymbol{e}_e x \boldsymbol{h}_e}| = \frac{1}{2} c\, \epsilon_{\rm o}\epsilon_e e_{e,{\rm o}}^2 \quad \text{plane wave}, \tag{3.37}$$

and is equal to the phase velocity c (or u_{ph}) times the average energy density $E_{ph,\omega}/V$. This uses the cycle-averaged fields $\bar{\boldsymbol{e}}_e$ and $\bar{\boldsymbol{h}}_e$, in which electric and magnetic contributions to E_{ph} are equal. An alternate derivation of (3.37) will be given in Section 3.3.5.

Figure 3.5 shows the EM wave and photon presentations of energy contained in a volume V. The polarization $\boldsymbol{s}_\alpha$ is along the y direction, and the wave travels along the x direction.

The relation among energy density of EM wave with field intensity vector $\boldsymbol{e}_e$, i.e., (3.37), and frequency ω, the quantum occupancy number of photons with the same energy and frequency f_{ph}, and number of phonons of energy $\hbar\omega$ (Section 7.1) per volume (photon density of state) $D_{ph,\omega}$, using (2.85) for quantized photon energy density, is (Section 7.3)

$$\frac{E_{ph,\omega}}{V} = \frac{1}{2V}\int_V \epsilon_{\rm o}\epsilon_e e_{e,{\rm o}}^2 {\rm d}V \equiv D_{ph,\omega}(\omega)(f_{ph} + \frac{1}{2})\hbar\omega \quad \text{plane wave}, \tag{3.38}$$

where the 1/2 term is generally neglected.

For a plane wave, the radiative intensity $I_{ph,\omega}$ given as the average Poynting vector $|\bar{\boldsymbol{s}}_e|$ (3.37) becomes

$$I_{ph,\omega} = \frac{1}{2} c\, \epsilon_{\rm o}\epsilon_e e_{e,{\rm o}}^2 \quad \text{plane wave}. \tag{3.39}$$

In general, a line-shape function $g(\omega)$ is also added to (3.39), as shown in Table 3.5. These classical, electromagnetic waves can travel in vacuum ($\sigma_e = 0$, $\mu_e = 1$, and $\epsilon_e = 1$).

[‡] Plane-polarized electric field (using $\kappa = \omega/c$)

$$\boldsymbol{e}_e = e_{e,{\rm o}} e^{i\omega(t - \frac{x}{c})} \boldsymbol{s}_y,$$

has a counterpart magnetic induction field (from Faraday law in Table 3.5), given as

$$\boldsymbol{h}_e = \epsilon_{\rm o}\epsilon_e c_{\rm o} e_{e,{\rm o}} e^{i\omega(t - \frac{\omega x}{c})} \boldsymbol{s}_y,$$

so the Poynting vector is

$$\boldsymbol{s}_e = \boldsymbol{e}_e \times \boldsymbol{h}_e = \frac{1}{\mu_{\rm o}\mu_e c} e_{e,{\rm o}}^2 \boldsymbol{s}_z,$$

and its time average is (end-of-chapter problem) [289]

$$|\bar{\boldsymbol{s}}_e| = \frac{1}{2} c \epsilon_{\rm o}\epsilon_e e_{e,{\rm o}}^2,$$

which is half because of $\boldsymbol{e}_e$ and half because of $\boldsymbol{h}_e$.

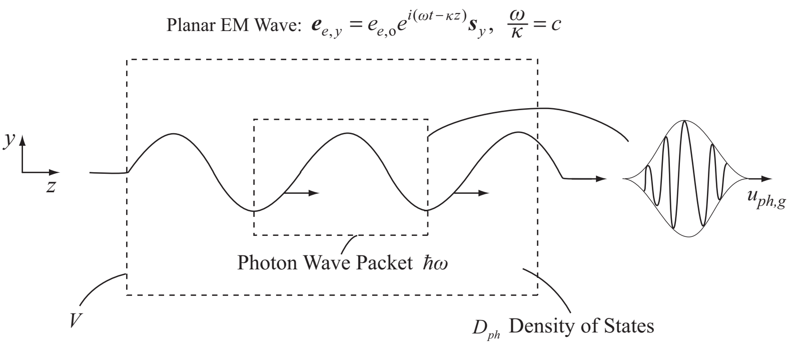
Planar EM Wave: $\boldsymbol{e}_{e,y} = e_{e,\text{o}} e^{i(\omega t - \kappa z)} \boldsymbol{s}_y$, $\frac{\omega}{\kappa} = c$
y
z
Photon Wave Packet $\hbar\omega$
$u_{ph,g}$
V
D_{ph} Density of States

Figure 3.5. The planar EM wave and its photon presentation (wave packet of energy $\hbar\omega$). The number of photons in the volume V is such that it matches the EM energy in the same volume.

The limits of the classical treatments are in the description of the electronic energy bandgaps, and in quasi-particle features of photons (including blackbody radiation). We will address these in Chapters 5 (electrons) and Chapter 7 (photons).

3.3.4 Electric Dipole and Emission, Absorption, and Scattering of EM Waves

Molecules with nonuniform charge distributions (Table 2.1) have permanent electric dipole moments. This strictly applies to two charges, one positive and one negative, of the same magnitude and separated by a distance x. Water vapor, for example, has a dipole moment of 6.20×10^{-30} C-m.[†] The presence of an electric field can also induce a dipole moment. The permanent dipole moment (vector) $\boldsymbol{p}_{e,\text{o}}$ is the product of the charge q and the separation distance and points toward the positive charge, i.e.,

$$\boldsymbol{p}_{e,\text{o}} = \frac{1}{V}\int \boldsymbol{x} q(\boldsymbol{x}) \mathrm{d}V \quad \text{electric dipole moment.} \tag{3.40}$$

These dipoles can be oscillating at the atomic frequencies related to their vibrations.

The Debye model of polar molecules is an electric dipole contained in a spherical molecule, free to rotate into alignment with the electric field, but subject to disorientation by collision with the neighboring molecules (by thermal motion). The net dipole moment (per molecule) is expressed as [289]

$$\boldsymbol{p}_e = N\alpha_e\left(\boldsymbol{e}_e + a\frac{\boldsymbol{p}_e}{\epsilon_\text{o}}\right) \quad \text{induced linear dipole}$$

$$\boldsymbol{p}_e = \frac{N\alpha_e}{1 - \dfrac{N\alpha_e a}{\epsilon_\text{o}}}\boldsymbol{e}_e = \epsilon_\text{o}\chi_\text{o}\boldsymbol{e}_e, \tag{3.41}$$

[†] One Debye D is 3.3356×10^{-30} C-m, Table 1.4. Then for water vapor, $p_{e,\text{o}} = 1.85$ D.

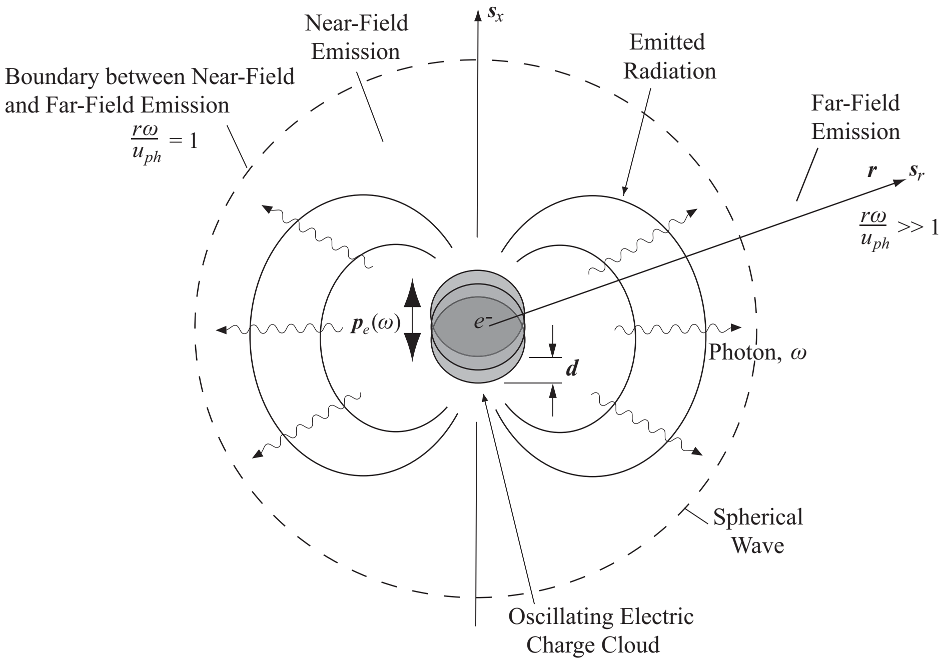
Near-Field Emission
s_x
Emitted Radiation
Boundary between Near-Field and Far-Field Emission
$\frac{r\omega}{u_{ph}} = 1$
Far-Field Emission
$\boldsymbol{r}$
s_r
$\frac{r\omega}{u_{ph}} >> 1$
$\boldsymbol{p}_e(\omega)$
e^-
$\boldsymbol{d}$
Photon, ω
Spherical Wave
Oscillating Electric Charge Cloud

Figure 3.6. Emission of EM radiation by sinusoidally oscillating electric charge [429], showing near- and far-field emitted EM waves.

where $\boldsymbol{p}_e$ is the induced dipole moment, α_e is the polarizibility (induced moment) produced by the applied field, a is a constant, N is the number of molecules per unit volume, and χ_e is electric susceptibility.

The emission of EM radiation by a sinusoidally oscillating charge $\boldsymbol{p}_{e,o} = e_c\boldsymbol{d}$ is shown in Figure 3.6. The purely radiative decay rate or spontaneous decay rate of a classical electron oscillator $\dot{\gamma}_{ph,e,sp,\text{o}}$ is determined from the classical electromagnetic theory [289] using the vector and scalar potentials and the poynting vector. For vacuum ($\epsilon_e = 1$), this is given as (end-of-chapter problem) [429]

$$\dot{\gamma}_{ph,e,sp,\text{o}} = \tau^{-1}_{e\text{-}p,\text{o}} = \frac{e_c^2\omega^2}{6\pi\epsilon_\text{o} m_e u_{ph}^3}$$

spontaneous emission (decay rate) by classical oscillating electron. (3.42)

The emission rate by transition dipole moment $\boldsymbol{\mu}_e$ (quantum-mechanics quantity) causing an energy transition $\hbar\omega_{e,g}$ in an excited electric entity (e.g., electron in an ion) is [194] (derivation based on FGR is Chapter 7 end-of-chapter problem)

$$\dot{\gamma}_{e\text{-}p}\ (\text{spontaneous}) = \dot{\gamma}_{ph,e,sp} = \frac{2\omega_{e,g}^3}{3\epsilon_\text{o} h_\text{P} u_{ph}^3}|\boldsymbol{\mu}_e|^2$$

spontaneous emission by transition dipole moment. (3.43)

In this relation it is assumed that $\dot{\gamma}_{e\text{-}p} \ll \omega_{e,g}/\pi$. This is the photon spontaneous emission and is part of the Einstein spontaneous and stimulated emission excited-state population rate equation (Section 7.4.1). The transition dipole moment (a quantum-electrodynamic quantity) will be discussed in Section 7.12.1. The energy generation $\dot{s}_{ph,e,sp}$ is $\hbar\omega_{e,g}\dot{\gamma}_{ph,e,sp}$, and in thermal radiation the thermal fluctuations in matter (including solids) results in thermal radiation emission (sum of stimulated and spontaneous emission, Section 7.4.3).

The far-field ($r\omega/u_{ph} \gg 1$), i.e., spherical-wave limit,[†] energy of interaction of EM with a molecular dipole is given by $\boldsymbol{p}_e \cdot \boldsymbol{e}_e$. EM waves are also absorbed by oscillating dipoles. There is also scattering of EM waves by dipoles, such as in Rayleigh scattering [52, 236, 329]. In Section 5.15.3(B) we will discuss the polarization (dipole moment created by polar optical-phonon lattice displacement). In quantum mechanics, the transition dipole moment is represented by an operator $\boldsymbol{\mu}_e$ (Section 7.12.1).

Similarly, EM waves are absorbed by dipoles, through electronic transitions, etc. EM wave scattering is generally referred to change in the direction (polarization), without a change in energy. We will discuss these emission, absorption, and scattering in Chapter 7.

3.3.5 Dielectric Function and Dielectric Heating

Dielectrics are materials with electrical conductivities much lower than those of metals (Section 5.16). Dielectric materials are generally categorized as materials having electrical resistivity larger than 10^4 Ω-m. These materials can absorb EM energy from an oscillating electric field $\boldsymbol{e}_e(t)$ by molecular rotation, especially at lower frequencies. This molecular rotation occurs in polar molecules. A material capable of being heated with radiowave or microwave energy is said to be polar or dipolar. An oscillating electric field is applied to the material, causing its molecules to rotate at the frequency of the field and line up their corresponding fields. The molecular friction generated by the molecules moving relative to each other generates heat. This method of generating heat within a material is termed dipole rotation and can be used to heat solids, liquids, or gases. Electric permittivity is a measure of ability of a material to resist the formation of an electric field within it. Dielectric materials have polar molecules (see Glossary) that can store charge and rotate under an applied alternating electric field of frequency f. The complex electric permittivity

---

[†] The far-field ($r \gg \lambda$) electric and magnetic field intensities are (Figure 3.6)

$$\boldsymbol{p}_e = \boldsymbol{p}_{e,\mathrm{o}} e^{i\omega t}$$

$$\boldsymbol{e}_e = \left(\frac{\mu_\mathrm{o}}{\epsilon_\mathrm{o}}\right)^{1/2} \boldsymbol{h}_e \times \boldsymbol{s}_r$$

$$\boldsymbol{h}_e = \frac{\omega^2}{4\pi u_{ph,\mathrm{o}}} (\boldsymbol{s}_r \times \boldsymbol{p}_e) \frac{e^{\frac{-i\omega r}{u_{ph,\mathrm{o}}}}}{r}.$$

More detail derivation is guided through end-of-chapter problem.

(also called the dielectric function) is defined as

$$\epsilon_e(\omega) = \epsilon_{e,r}(\omega) - i\epsilon_{e,c}(\omega) \quad \text{dielectric function (electric permittivity)}, \tag{3.44}$$

where $\epsilon_{e,r}$ is called the dielectric constant and $\epsilon_{e,c}$ is called the dielectric loss (or loss factor).

The dielectric constant $\epsilon_{e,r}$ is a measure of the capacitance of the material and the dielectric loss $\epsilon_{e,c}$ is a measure of the electrical energy dissipated as heat. Both $\epsilon_{e,r}$ and $\epsilon_{e,c}$ are functions of frequency and temperature.

Figures 3.7(a) and (b) show variations of $\epsilon_{e,r}$ and $\epsilon_{e,c}$ as functions of angular frequency, for five materials representing dielectrics (acrylic and quartz), semiconductors (GaAs), metals (Al), and liquids (H_2O), all at $T = 300$ K.

Although $\epsilon_{e,r}$ affects refraction and reflection, $\epsilon_{e,c}$ affects absorption and emission. It is possible for $\epsilon_{e,r}$ to have a negative value (shown for Al). H_2O as a liquid has strong absorption (large $\epsilon_{e,c}$) in the microwaves, far-infrared, and ultraviolet regimes. Acrylic has a small absorption coefficient (related to $\epsilon_{e,c}$), whereas GaAs has a strong absorption near its bandgap energy (1.42–1.90 eV, ultraviolet regime). Quartz (crystalline SiO_2) has a high absorption because of its lattice vibration in the near-infrared regime. The free electrons of Al are excited by photons over a large range of energy. The low and high-energy excitation regimes are also shown in Figure 3.7(a), starting from the ionic to electronic.

The Kramers–Kronig dispersion relation describes the interdependency of $\epsilon_{e,r}$ and $\epsilon_{e,c}$. The classical electron oscillator model for the dielectric function (the Drude model, Glossary) is based on the damping motion of the electron and an oscillating EM field. This is shown in Figure 3.8. For an electron as a particle (Table 2.5) the momentum conservation is

$$m_e \frac{\mathrm{d}^2 \boldsymbol{x}}{\mathrm{d}t^2} = -m_e \omega_{n,e}^2 \boldsymbol{x} - \frac{m_e}{\tau_e} \frac{\mathrm{d}\boldsymbol{x}}{\mathrm{d}t} - e_e \boldsymbol{e}_e$$

$$\omega_{n,e} = 0 \text{ for an unbound electron (Drude damped oscillator model)}, \tag{3.45}$$

where $\omega_{n,e}$ is the natural frequency related to the force constant through (2.54), and τ_e is the relaxation time for the damping mechanism (e.g., scattering by nuclei). For a time-periodic EM field $\boldsymbol{e}_e = \boldsymbol{e}_{e,\mathrm{o}} e^{i\omega t}$ (3.36), we have the form [512]

$$\frac{\mathrm{d}\boldsymbol{x}}{\mathrm{d}t} = \frac{e_c/m_e}{i\omega - 1/\tau_e} \boldsymbol{e}_{e,\mathrm{o}}, \tag{3.46}$$

which on using $\boldsymbol{j}_e = -n_{e,c} e_c \mathrm{d}\boldsymbol{x}/\mathrm{d}t = \sigma_e(\omega)\boldsymbol{e}_{e,\mathrm{o}}$, where $\sigma_e(\omega)$ is the complex electric conductivity (also called optical or dynamical electric conductivity), and $n_{e,c}$ is the free-electron density, gives

$$\sigma_e(\omega) = \frac{n_{e,c} e_e^2/m_e}{\tau_e - i/\omega} = \frac{\sigma_{e,\mathrm{o}}}{1 - i\omega\tau_e} \quad \text{Drude free-electron model}, \tag{3.47}$$

where $\sigma_{e,\mathrm{o}} = n_{e,c} e_c^2 \tau_e / m_e$ is the direct current (DC) ($\omega = 0$) electrical conductivity.

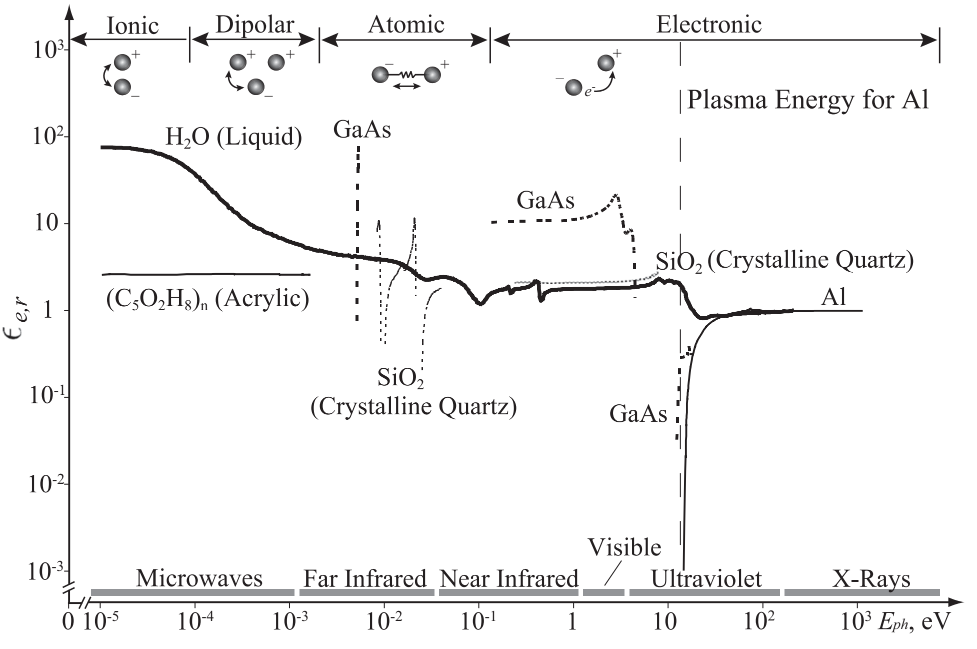

(a) Real Part of Relative Electric Permittivity (300 K)

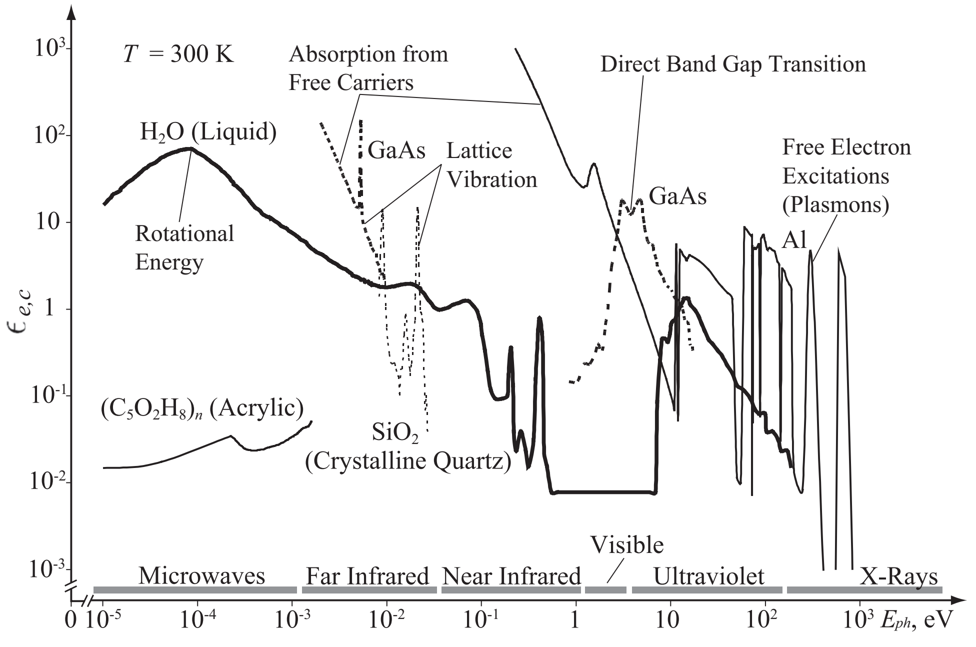

(b) Imaginary Part of Relative Electric Permittivity (300 K)

Figure 3.7. Variations of (a) the real and (b) imaginary parts of the electric permittivity (dielectric function) with respect to EM wave energy (angular frequency), for typical insulator (including an organic compound), conductor, and semiconductor solids and for liquid water. The data are for $T = 300$ K.

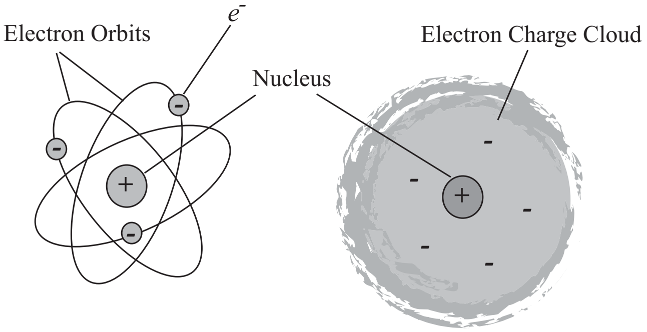

(a) Electron Cloud

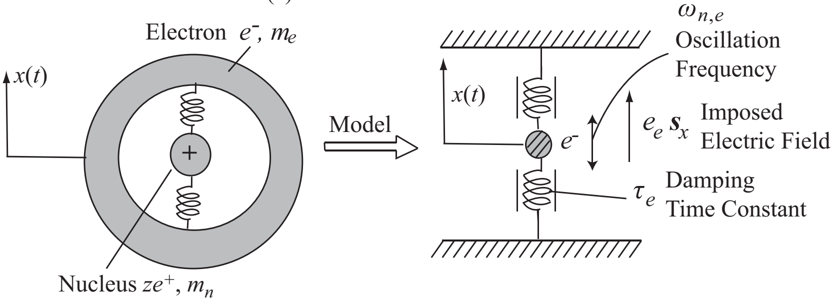

(b) Electron Damped-Oscillator Model

Figure 3.8. (a) Electronic models for an atom, and (b) the classical electron damped-oscillator model [429].

The real and imaginary components of the dielectric function are also related to $\sigma_e(\omega)$ [359, 512], e.g.,

$$\sigma_e(\omega) = -\epsilon_o \epsilon_{e,c} \omega, \quad \text{or} \quad \epsilon_{e,c} = \frac{\sigma_e(\omega)}{\omega \epsilon_o}, \tag{3.48}$$

and

$$\epsilon_e(\omega) = \epsilon_{e,\infty} - \frac{\sigma_{e,o}\tau_e}{\epsilon_o(\omega^2 + i\omega/\tau_e)} = \epsilon_{e,\infty} - \frac{\omega_{pl}^2}{\omega(\omega + i/\tau_e)}, \tag{3.49}$$

where $\epsilon_{e,\infty}$ is the high-frequency asymptote and ω_{pl} is the plasma frequency [quantum of plasma energy $\hbar\omega_{pl}$ is called plasmon, Figure 3.7(b) for Al] $\omega_{pl}(n_{e,c}e_c^2/\epsilon_o m_e)^{1/2}$. Generally, τ_e is the inverse of ω at which $\epsilon_{e,c}$ has a maximum.[†]

[†] In Debye model of a molecule of diameter d rotating in a viscous medium is,

$$\tau_e = \frac{4\pi(\frac{d}{2})^3 \mu_f}{k_B T},$$

where μ_f is the dynamic viscosity.

Using the low- and high-frequency limits, the modified Debye model is listed in Table 3.5, which is

$$\frac{\epsilon_e - \epsilon_{e,\infty}}{\epsilon_{e,s} - \epsilon_{e,\infty}} = \frac{1}{1 + i\omega\tau_e}, \tag{3.50}$$

where $\epsilon_{e,s}$ and $\epsilon_{e,\infty}$ are the low- and high-frequency emissions (real quantities). The Debye model is used in the electron-optical-phonon scattering (Section 5.15.3).

Similarly, the Lorentz model treats the oscillatory motion of a band carrier in an oscillating EM field [512], and is used for dielectrics (e.g., SiO_2).

For semiconductors (direct and indirect bands, Chapter 5), the Drude model is extended to include the bandgap (we will discuss this in Section 7.15.1).

In general, $\epsilon_e(\omega)$ is related to the electronic band structure and is given in terms of ω_{ij}, which is used along with the Brillouin zone average transition probability (between states i and j) and the joint density of states [377], so we have

$$\epsilon_e(\omega) = 1 + \frac{8\pi e_e^2}{m_{e,e}^2} \sum_{i,j} \int \omega_{ij}[g(\hbar\omega - E_e) - g(\hbar\omega + E_e)]\mathrm{d}\boldsymbol{x} \quad \text{optical dielectric}, \tag{3.51}$$

where $m_{e,e}$ is the effective electron (or hole) mass, g is the line-shape function, and E_e is the electronic energy difference $E_{e,ij}$. We will apply this to photon absorption by semiconductors in Section 7.8.1.

The Adachi model [2] for semiconductor ϵ_e is based on the Kramers–Kronig transformation and is a summation over active bands. Other models are discussed in [80]. The total field current in Table 3.5 is the sum due to free carrier and the displacement currents, $\boldsymbol{j}_e = \boldsymbol{j}_{e,f} + \boldsymbol{j}_{e,d} = \sigma_e \boldsymbol{e}_e + \omega\epsilon_o\epsilon_{e,c}\boldsymbol{e}_e$. So, for dielectrics we have only the second term.

The dielectric heating (commonly called he microwave heating) rate is

$$\dot{s}_{ph\text{-}p} = \sigma_e |\overline{\boldsymbol{e}_e}|^2 = \epsilon_{\text{o}}\epsilon_{e,c}\omega\overline{e_e^2} = \frac{1}{2}\epsilon_{\text{o}}\epsilon_{e,c}\omega e_{e,\text{o}}^2 \quad \text{volumetric dielectric heating}, \tag{3.52}$$

where the imaginary part of the electric conductivity σ_e is given by (3.48), and $\overline{e_e^2}$ is the time average of the square of the electric field (square of RMS). In general, $\epsilon_{e,c}(\omega, T)$ is found from absorption data.

Note the high magnitude of $\epsilon_{e,c}$ for H_2O in Figure 3.7(b) in the microwave regime making for high heating rates (thus the name microwave heating). Also, note that from (3.30) for $\mu_e = 1$ and $\sigma_e = 0$, we have $\kappa_\lambda = [(\epsilon_{e,r}^2 + \epsilon_{e,c}^2)^{1/2} - \epsilon_{e,r}]^{1/2}/2^{1/2}$, $n_\lambda = (\epsilon_{e,r})^{1/2}$, or $\epsilon_{e,c} = 2n_\lambda\kappa_\lambda$, and the spectral absorption coefficient of EM waves in a dielectric media is related to this through $\sigma_{ph,\lambda} = 4\pi\kappa_\lambda/\lambda = 2\pi\epsilon_{e,c}/n_\lambda\lambda$.

3.3.6 Electrical Resistivity and Mobility and Joule Heating

Electrical resistivity $\rho_e = 1/\sigma_e$ also measures the loss of electric power that is due to the inelastic scattering of electrons with the lattice (phonon), impurities, etc. These scattering mechanisms are temperature dependent and are discussed in Sections 5.13 and 5.15. According to the Matthiessen rule, the resistances that are due to various scattering mechanisms are additive in series [232], i.e.,

$$\rho_e = \sum_i \rho_{e,i} \quad \text{Matthiessen rule (series transport).} \tag{3.53}$$

For metals, $\rho_e(T)$ decreases with decreases in temperature, and nearly vanishes as $T \rightarrow 0$ (superconductivity). The electric mobility μ_e is related to the electric conductivity through $\sigma_e = n_{e,c} e_c \mu_e$. So, the mobility separates the electron transport kinetics from the electron density part of the conductivity.

Using this ρ_e, the volumetric Joule heating rate for conductors (metals) is

$$\dot{s}_{e\text{-}p} = \dot{s}_{e,\mathrm{J}} = \boldsymbol{j}_e \cdot \boldsymbol{e}_e = \sigma_e |\boldsymbol{e}_e|^2 = \rho_e j_e^2 \quad \text{volumetric Joule heating,} \tag{3.54}$$

where j_e is the free electron current density ($j_{e,f}$), and we have used the Ohm law (Table 3.5). For alternating current, $|\overline{\boldsymbol{e}_e}|^2 = e_{e,o}^2/2$ is used in (3.54). In Section 5.18 we will derive this, showing that the Joule heating represents relaxation of the electron kinetic energy.

Electron-lattice (phonon) scattering is dominant in inelastic scattering mechanisms. Joule heating results in phonon emission and, as governed by the energy equation (Table 1.1), may lead to sensible heating.

For semiconductors, Joule heating is given as [in addition to that due to net current of conduction electrons presented in (3.54)]

$$\dot{s}_{e\text{-}p} = \dot{s}_{e,\mathrm{J}} = \boldsymbol{j}_e \cdot \boldsymbol{e}_e + (\dot{n}_{e,rec} - \dot{n}_{e,gen})(\triangle E_{e,g} + 3k_\mathrm{B} T), \tag{3.55}$$

where $\boldsymbol{j}_e$ is given in Table 3.6, and $\dot{n}_{e,rec}$ and $\dot{n}_{e,gen}$ are volumetric, nonradiative recombination and generation rates (1/m^3-s). The electron–hole carrier energy equation will be derived in Section 5.18.

3.4 Onsager Coupled Transport Coefficients

The Gibbs fundamental thermodynamic relations hold between the state variables and involve derivatives of these variables. The entropy balance equation is derived from the continuity equation, with proper substitutions. From these, the first postulate of irreversible thermodynamics allows for defining the conjugated thermodynamic fluxes and forces. In the second postulate, a linear relation is assumed between the two and the phenomenological transport equations are introduced. Examples are $\boldsymbol{q} = -k\nabla T$ and $\boldsymbol{j}_e = -e c \sigma_e \nabla \varphi_e$, for isotropic materials.

The Onsager relationship for coupled transport, represented for flux j_i (where i can be e for electrical transport and t for thermal transport), is [354]

$$j_i = \sum L_{ik} F_j \quad \text{Onsager relation,} \tag{3.56}$$

where for each driving force F_i there is a corresponding conjugate primary flux j_i. Here L_{ik} is a phenomenological transport coefficient relating these two. These phenomena are called cross-coupling transport.

For example, for a system with two fluxes caused by two driving forces (i.e., two simultaneous irreversible processes), we have

$$j_1 = L_{11}F_1 + L_{12}F_2, \tag{3.57}$$

$$j_2 = L_{21}F_2 + L_{22}F_2, \tag{3.58}$$

where j_1 and j_2 denote the fluxes and F_1 and F_2 denote the forces causing these flows. The coefficients L_{ik} (with $i \neq k$) describe the interference (coupling) of the two irreversible processes i and k.

The Onsager reciprocity relation between the cross coefficients L_{ik} and L_{ki} is expressed as

$$L_{ik} = L_{ki}(i \neq k) \ \text{Onsager reciprocity relation.} \tag{3.59}$$

This Onsager reciprocity relations allows a reduction in the number of transport coefficients and provides for the following constraints

$$L_{11} \geq 0, \quad L_{22} \geq 0, \quad (L_{12} + L_{21})^2 < 4L_{11}L_{22}$$
$$\text{constraints on transport coefficients.} \tag{3.60}$$

The conjugate coefficients (L_{11} and L_{22}) must be positive, whereas the crossed (coupling or interference) coefficients (L_{12} and L_{21}) have no definite sign.

The last condition in (3.60) is based on the positive derivative of the entropy with respect to temperature [354]. We should note that the relations (3.59) and (3.60) are valid only when the fluxes and thermodynamic forces are suitably chosen.

As an example, consider the coupled electric and thermal current vectors $\boldsymbol{j}_e$ and $\boldsymbol{q}$ in solids. The choice of driving force is generally made by the examination of the transport equations, such as the BTE. As will be shown in Section 5.9, from the BTE the driving forces suitable for this analysis are $\nabla(E_\mathrm{F}/e_c)$ and $\nabla(1/T)$, where E_F is the Fermi energy. ∇E_F includes the carrier concentration and electric potential variations. Then, following (3.57) and (3.58), the general form of these coupled currents is

$$\boldsymbol{j}_e = \boldsymbol{L}_{ee} \cdot \nabla \frac{E_\mathrm{F}}{e_c} + \boldsymbol{L}_{et} \cdot \nabla \frac{1}{T} \tag{3.61}$$

$$\boldsymbol{q} = \boldsymbol{L}_{te} \cdot \nabla \frac{E_\mathrm{F}}{e_c} + \boldsymbol{L}_{tt} \cdot \nabla \frac{1}{T}. \tag{3.62}$$

The coupling tensors $\boldsymbol{L}_{ee}$, $\boldsymbol{L}_{et}$, $\boldsymbol{L}_{te}$, and $\boldsymbol{L}_{tt}$ are the electrothermal transport properties of the solid. The Onsager reciprocity relation (3.59) then requires that $L_{et,ij} = L_{te,ij}$, where ij designates the component of the tensor.

The more common form of the electrothermal transport equations (which are more suitable for experiments), and for the simple case of isotropic properties, is given in terms of the electric field intensity vector $\boldsymbol{e}_e$, i.e.,

$$\boldsymbol{e}_e = \rho_e \boldsymbol{j}_e + \alpha_\mathrm{S} \nabla T, \ \rho_e = \frac{1}{\sigma_e} \tag{3.63}$$

$$\boldsymbol{q} = \alpha_\mathrm{P} \boldsymbol{j}_e - k_e \nabla T, \ \alpha_\mathrm{P} = \alpha_\mathrm{S} T. \tag{3.64}$$

Here, $\rho_e(\Omega\text{-m})$ is the electrical resistivity (the inverse of electrical conductivity), $\alpha_S(\text{V/K})$ is the Seebeck coefficient, $\alpha_P(\text{V})$ is the Peltier coefficient, and k_e is the electric thermal conductivity. Here, the Onsager reciprocity relation leads to $\alpha_P = \alpha_S T$, as will be discussed in Section 5.13. Note that ρ_e and k_e have positive values.

3.5 Stochastic Particle Dynamics and Transport

3.5.1 Langevin Particle Dynamics Equation and Brownian Motion

The Langevin stochastic particle dynamics equation governs the motion of a particle through a medium by a combination of a mean force $\boldsymbol{F}_{k,s}$ and a time-dependent random (including form a Gaussian distribution) force $\boldsymbol{F}_k(t)$, with friction (e.g., viscous) from the medium $-\gamma \boldsymbol{u}_k$. This equation is listed in Table 3.7. The fluctuation-dissipation theorems also require some constraints on the random force, and these are also stated in the table. The brackets $\langle\ \rangle$ indicate integration over the volume. The Langevin equation is used in thermal bath simulations, where the time-dependent force is due to inter-particle interaction (e.g., harmonic potential) [206].

We will use the Langevin equation in Section 6.10 for Brownian motion of solid particles suspended in a liquid. In that case, the random force is from thermal fluctuations of the solid particles and the hindering force is the fluid viscous force on the particle. Here we summarize some of the results.

$\boldsymbol{F}_k(t)$ is a rapidly varying function, so correlation $\langle \boldsymbol{F}_k(0) \cdot \boldsymbol{F}_k(t)\rangle$ is only a function of t and its integral is related to the velocity squared. So, for $t \rightarrow \infty$ when the equipartition of energy is realized, the integral gives $6k_B T\gamma$ [323].

The ratio m_k/γ is called the collision (viscous or Langevin) relaxation time τ_μ and under no mean (steady) force $\boldsymbol{F}_{k,s} = 0$, the MSD $\langle [x(t) - x_o]^2\rangle$ is (note that from equipartition of energy $\langle m u_k^2/2\rangle = 3k_B T/2$, Section 6.10)

$$\langle x^2\rangle - \langle x_o^2\rangle = -\frac{6k_B T}{\gamma}[\tau_\mu(e^{-t/\tau_\mu} - 1) - t], \tag{3.65}$$

where x_o is the initial position. The short-time solution $t/\tau_\mu \ll 1$ gives the ballistic regime

$$\langle x^2\rangle - \langle x_o^2\rangle = \frac{3k_B T}{m_k} t^2. \tag{3.66}$$

This is the unresisted thermal motion. The long-time solution $t/\tau_\mu \gg 1$ gives the viscous regime

$$\langle x^2\rangle - \langle x_o^2\rangle = \frac{6k_B T}{\gamma} t = \frac{6k_B T}{m_k} t\tau_\mu, \quad \tau_\mu = \frac{m_k}{\gamma}. \tag{3.67}$$

This is the Brownian motion of particle in a viscous fluid. We will use these in derivation of the Brownian diffusion in Section 6.10.

The velocity distribution of the particles will equilibrate for $t \rightarrow \infty$, and becomes the M–B distribution (6.61).

Table 3.7. *Stochastic (Brownian) particle dynamics equation (Langevin stochastic equation) [93, 323], thermal motion in a viscous fluid.*

Langevin equation for particle k

$$\frac{\mathrm{d}}{\mathrm{d}t}(m_k \boldsymbol{u}_k) = \boldsymbol{F}_{k,s} - \gamma \boldsymbol{u}_k + \boldsymbol{F}_k(t)$$

Fluctuation-dissipation theorems

$$\langle \boldsymbol{F}_k(t) \rangle = 0 \quad \text{zero-mean } \overline{\boldsymbol{F}}_k(t) \text{ force}$$

$$\int_0^\infty \langle \boldsymbol{F}_k(t) \cdot \boldsymbol{F}_k(0) \rangle \mathrm{d}t = 6 k_\mathrm{B} T \gamma \quad \text{correlation of Gaussian distribution force (defines } T\text{)}$$

$$\frac{1}{2} m_k |\boldsymbol{u}_k|^2 = \frac{3}{2} k_\mathrm{B} T, \quad \text{equipartition of energy and temperature}$$

$\boldsymbol{F}_{k,s}$	steady, deterministic force on particle k, N
$\boldsymbol{F}_k(t)$	random (stochastic), time-dependent force on particle k, N
m_k/γ	Langevin relaxation time, s
$-\gamma \boldsymbol{u}_k$	frictional force on particle k, N

Note that the friction γ is a result of correlating the random force. It can also be viewed as how external forces dissipate into thermal energy by friction.

3.5.2 Fokker–Planck Particle Conservation Equation

The Fokker–Planck equation is a particle drift–diffusion equation and represents the probability of finding a particle in a drift vector field $\boldsymbol{u}$, and a diffusion tensor D is used in the probability density function (pdf) P. This time-evolution equation for stochastic processes [323] is listed in Table 3.8.

The Fokker–Planck equation is a powerful tool for solving stochastic problems. It usually appears for variables (represented by P) describing a macroscopic but small subsystem in the field of a stochastic force. The diffusion term is the result of the stochastic force [similar to $\boldsymbol{F}_k(t)$ in the Langevin equation], and contains the kinetics (or transition rates).

Note that the pdf must satisfy the normalization constraint (Table 3.8), as was the case for the other distribution functions and for the wave function in the Schrödinger equation (Table 2.8).

The Fokker-Planck equation describes evolution of a continuous pdf and is called a master equation (Glossary). There is also a quantum master equation [501].

3.5.3 Mean-Field Theory

In statistical mechanics, the interactions among the particles in a many-body system are generally very difficult to solve exactly without using those numerical approximations in MD, except for a few simple cases. The great difficulty in determining the partition function of the system results from the combining of the interaction terms in the Hamiltonian when summing over all states. The goal of mean-field theory

Table 3.8. *Stochastic differential equation for evolution of the pdf (Fokker–Planck stochastic equation) [323].*

$$\frac{\partial P}{\partial t} + \nabla \cdot \boldsymbol{u} P = \frac{1}{2} \sum_{i,j} \frac{\partial^2}{\partial x_i \partial x_j} D_{ij} P$$

$$\equiv L_{\mathrm{FP}} P$$

$$\int_{o}^{\infty} P \mathrm{d}V = 1 \text{ normalization constraint}$$

D_{ij}	diffusion tensor, m^2/s
L_{FP}	Fokker–Planck operator, 1/s
P	probability density function (pdf)
$\boldsymbol{u}$	drift coefficient vector

(also known as self-consistent field theory) is to resolve these combinatorial problems.

In mean-field theory, all interactions to any one body are replaced with an average (or effective) interaction. This reduces any multibody problem to an effective, one-body problem. This allows for predicting the behavior of the system without extensive inclusion of all interactions. In mean-field theory, the Hamiltonian may be expanded in terms of the magnitude of fluctuations around the mean of the field. In this context, mean-field theory can be viewed as the zeroth-order expansion of the Hamiltonian in fluctuations. Physically, this means a mean-field system has no fluctuations, but this coincides with the idea that one is replacing all interactions with a mean field. In the formalism of fluctuations, mean-field theory provides a convenient starting point for studying the first- or second-order fluctuations.

The stronger the role of the long-range forces, and the larger the dimensionality of the system (one versus two or three dimensional), the more appropriate the use of mean-field theory becomes. We will have an example of a mean-field potential in Section 6.11.6.

3.6 Equilibrium Fluctuation–Dissipation and Green–Kubo Transport Theory

The G–K relations state that the space–time integral of the flux–flux equilibrium correlation function divided by $k_{\mathrm{B}}T$ gives the corresponding steady-state transport coefficient. An example for thermal conductivity is shown in Table 3.9, and the derivation is given in Appendix B.

The complexity of many-particle systems is frequently the motivation for introducing mean-field approximations so as to simplify and solve the complicated equations of motion or the time-evolution equation for the pdf in configuration space. We are interested in the linear response of such a system to a small external influence, starting from the equilibrium situation. The usual procedure is to calculate the first-order deviation of the distribution function from its equilibrium form. This can be done if the statistical model equation is linear in the distribution function, as is the case, for example, in the Liouville equation (describes time evolution of phase space distribution function, i.e., conservation applied to evolution of ensemble in

Table 3.9. *G–K heat current autocorrelation decay relation for phonon or fluid particle thermal conductivity (linear response theory) [323].*

G–K autocorrelation for thermal conductivity (for cubic isotropy, derivation is given in Appendix B)

$$k = \frac{V}{3k_{\rm B}T^2}\int_0^\infty \langle \boldsymbol{q}(t)\cdot\boldsymbol{q}(0)\rangle^{\rm o}{\rm d}t$$

where the volume integral (over V) of the heat current autocorrelation function (based on equilibrium fluctuation) $\langle \boldsymbol{q}(t)\cdot\boldsymbol{q}(0)\rangle^{\rm o}$, and $\boldsymbol{q}$ defined as

$$\boldsymbol{q} = \frac{1}{V}\frac{\rm d}{{\rm d}t}\sum_i E_i\boldsymbol{x}_i = \frac{1}{V}\frac{\rm d}{{\rm d}t}\sum_i (E_{k,i}+E_{p,i})\boldsymbol{x}_i \quad \text{heat current vector}$$

where $E_{k,i}$ is the kinetic energy and $E_{p,i}$ is the potential energy of particle i (Table 2.4)

For a two-body potential, we have (end-of-chapter problem)

$$\boldsymbol{q} = \frac{1}{V}[\sum_i E_i\boldsymbol{u}_i + \frac{1}{2}\sum_{i,j}(\boldsymbol{F}_{ij}\cdot\boldsymbol{u}_i)\boldsymbol{x}_{ij}]$$

$$\langle \boldsymbol{q}(t)\rangle^{\rm o} = 0 \text{ no heat flow at equilibrium}$$

based on equilibrium distributions of $\boldsymbol{x}_i$ and $\boldsymbol{u}_i$ and $T = \sum_i m_i u_i^2/3(N-1)k_{\rm B}$

k	thermal conductivity, W/m-K
E	energy, J
$\boldsymbol{F}_{ij}$	force vector, N
$\boldsymbol{u}_i$	velocity vector, m/s
$\boldsymbol{q}$	heat current vector, W/m^2
$\boldsymbol{x}$	position vector, m

---

the phase space, $\boldsymbol{x}$, $\boldsymbol{p}$). The linear response to an external influence is around a distribution function and is valid for the Liouville equation with reversible dynamics and the dissipative Fokker–Planck equation.

Let H$_{\rm o}$ be the Hamiltonian of the given system when it is isolated. If we apply a weak disturbing field $\boldsymbol{F}(t)$ that couples to a property $\boldsymbol{b}(t)$, with $\langle\boldsymbol{b}\rangle = 0$, the Hamiltonian of the perturbed system is given by [478]

$$\text{H} = \text{H}_{\rm o} - \boldsymbol{b}\cdot\boldsymbol{F}(t). \tag{3.68}$$

Linear response theory then leads to the following first-order expression for the mean temporal change rate of $\boldsymbol{b}$, i.e., $\langle\dot{\boldsymbol{b}}(t)\rangle$ in terms of the autocorrelation of equilibrium

$$\langle\dot{\boldsymbol{b}}(t)\rangle\frac{1}{k_{\rm B}T}\int_{-\infty}^{t}\boldsymbol{F}(t')\langle\dot{\boldsymbol{b}}(t)\dot{\boldsymbol{b}}(t-t')\rangle_{\rm o}{\rm d}t'$$

$$\text{relation between mean rate and equilibrium autocorrelation,} \tag{3.69}$$

where the ensemble average of equilibrium function (no gradients present) $\langle\ \rangle^{\rm o}$ is for the unperturbed system.

Assuming a constant force field $\boldsymbol{F}$ starting at $t<0$, we have

$$\langle\dot{\boldsymbol{b}}\rangle = \frac{\boldsymbol{F}}{k_{\rm B}T}\int_{-\infty}^{t}\langle\dot{\boldsymbol{b}}(0)\dot{\boldsymbol{b}}(-t')\rangle^{\rm o}{\rm d}t'. \tag{3.70}$$

Independently, the fundamental G–K relation states that, for any conserved quantity $\boldsymbol{b}$, the appropriate isotropic Onsager transport coefficient $L_{ii} = L$ (3.56) is given by the equilibrium average

$$L_{ii} = L \equiv \int_0^\infty \langle \dot{\boldsymbol{b}}(0) \cdot \dot{\boldsymbol{b}}(t) \rangle^{\mathrm{o}} \mathrm{d}t. \tag{3.71}$$

The integral is over the equilibrium flux autocorrelation (also called self-correlation) function $\dot{\boldsymbol{b}}(0) \cdot \dot{\boldsymbol{b}}(t)$. At $t = 0$, the autocorrelation function is positive, as it is the mean-square value of the flux at equilibrium. At large t, $\dot{\boldsymbol{b}}(t)$ is uncorrelated with $\dot{\boldsymbol{b}}(0)$ and the autocorrelation decays to zero. This behavior is used in computational MD simulations (an example is given in Section 4.12).

Combining this with (3.70) and (3.71), we find that $\langle \dot{\boldsymbol{b}}(t) \rangle = \boldsymbol{F} L / k_{\mathrm{B}} T$, or

$$L_{ii} = L = \frac{k_{\mathrm{B}} T}{\boldsymbol{F}} \langle \dot{\boldsymbol{b}}(t) \rangle. \tag{3.72}$$

Thus we may determine the transport coefficient L either from an equilibrium simulation by using (3.71), or from a nonequilibrium simulation with applied field by using (3.72). Generally, the second method yields better statistics, but it is more prone to nonlinearity problems, such as large fields. Also, systems responding to an external field must be thermostated.

Consider a fluid sample of ions in an electric field $\boldsymbol{F}(t) = \boldsymbol{e}_e(t)$. The charge density is given by $\boldsymbol{b}(t) \equiv \sum_i q_i \boldsymbol{x}_i(t)$, where q_i is the charge of particle i. Then (3.68) becomes

$$\mathrm{H} - \mathrm{H}_{\mathrm{o}} = -\boldsymbol{b} \cdot \boldsymbol{F}(t) = -[\sum_i q_i \boldsymbol{x}_i(t)] \cdot \boldsymbol{e}_e(t). \tag{3.73}$$

The electric current density vector $\boldsymbol{j}_e$ is defined as

$$\dot{\boldsymbol{b}} = \sum_i q_i \dot{\boldsymbol{x}}_i(t) \equiv V \boldsymbol{j}_e(t), \tag{3.74}$$

where V is the volume.

Then the electrical conductivity σ_e is determined from an equilibrium simulation, using the isotropic G–K relation (3.71), i.e.,

$$\sigma_{e,xx} = \sigma_e = \frac{1}{k_{\mathrm{B}} T} \int_0^\infty \langle j_{e,x}(0) j_{e,x}(t) \rangle^{\mathrm{o}} \mathrm{d}t. \tag{3.75}$$

Alternatively, in a nonequilibrium simulation, using the measured response to an applied field $\boldsymbol{e}_e = \{e_{e,x}, 0, 0\} = -\{e_c \mathrm{d}\varphi_e / \mathrm{d}x, 0, 0\}$, we have from the Ohm law (Table 3.5)

$$\sigma_{e,xx} = \sigma_e = \frac{\langle j_{e,x} \rangle}{e_{e,x}} = -\frac{\langle j_{e,x} \rangle}{e_c \mathrm{d}\varphi_e / \mathrm{d}x}. \tag{3.76}$$

Table 3.9 gives a similar expression for the thermal conductivity k, with the corresponding nonequilibrium relation given by the Fourier law (Table 1.1)

$$k_{xx} = -\frac{\langle q_x \rangle}{\mathrm{d}T / \mathrm{d}x}, \tag{3.77}$$

for $\nabla T = \{\mathrm{d}T/\mathrm{d}x, 0, 0\}$, and for heat flux vector $\boldsymbol{q} = \{q_x, 0, 0\}$.

For cubic isotropy, the thermal conductivity (for phonons and fluid particles) is given in terms of the heat current vector (as in Section 2.5.7) or the correlation function (or vector) $\boldsymbol{q}(t)$, which replaces $\dot{\boldsymbol{b}}$ in (3.69), i.e.,

$$k_{xx} = k = \frac{V}{3k_{\rm B}T^2}\int_0^\infty \langle \boldsymbol{q}(t)\cdot\boldsymbol{q}(0)\rangle^{\rm o}{\rm d}t, \quad \boldsymbol{q} = \frac{1}{V}\frac{\rm d}{{\rm d}t}\sum_i (E_{k,i}+E_{p,i})\boldsymbol{x}_i. \tag{3.78}$$

The factor of 3 is due to using the three-dimension $\boldsymbol{q}$. Table 2.4 gives the relation for E_k and E_p.

The G–K relation derivation in Appendix B is for the thermal conductivity, and uses the Fourier transform of the energy equation in the absence of net motion but subject to thermal fluctuation.

Section 4.12 presents the results of using (3.78) along with MD to predict the phonon conductivity of some crystals. We will note there that the heat current autocorrelation decays in an exponential envelope (can have oscillations), and that the decay is presented by time constants indicating the strength of the thermal transport.

3.7 Macroscopic Fluid Dynamics Equations

In the energy equation (Table 1.1), the fluid velocity appearing in the convective heat flux $\boldsymbol{q}_u = \rho c_p \boldsymbol{u} T$ (and in the surface-convection heat flux $\boldsymbol{q}_{ku}$), is determined from the fluid mass and momentum conservations.

The Navier–Stokes equations are the macroscopic ($L \gg \lambda_f$), fundamental partial differential equations that describe the flow of incompressible fluids. Using the rate-of-stress and rate-of-strain tensors, the components of a viscous force in a nonrotating frame are derived. Table 3.10 gives the Navier–Stokes equations in vectorial form. Similar to thermal conductivity, the dynamic viscosity μ_f is a transport property related to atomic and dynamic behavior of the fluid. For gases, μ_f is related to the mean free path (Section 6.6). In Chapter 6, we will discuss various flow regimes, including molecular- and turbulent-flow regimes.

Also listed in Table 3.10 are the normal and tangential force balances at the liquid–gas interface with surface tension σ_{lg}, which is allowed to change along the interface.

A wave equation for a thermobuoyant disturbance (no mean velocity, $\overline{\boldsymbol{u}} = 0$) in a fluid layer with a mean temperature gradient $\overline{T} = \overline{T}(x)$ along the direction gravity acts is also listed. This wave can grow under favorable conditions to form a cellular motion with wave number κ [77, 220, 229, 231].

3.8 Macroscopic Elastic Mechanics Equations

Elastic solid mechanics describes the macroscopic ($L \gg r_{nn}$) elastic deformation of a solid that is caused by applied stress. For cubic (isotropic) crystals, there are only two independent elastic constants. The resistance to deformation is represented by the Young modulus $E_{\rm Y}$. The Hooke law relates the deformation (strain) to the stress (including thermal stress) through the Young modulus and the Poisson ratio $\nu_{\rm P}$.

Table 3.10. *Macroscopic Newtonian fluid mechanics (Navier–Stokes) equations (including thermomechanical wave propagation) [220, 231].*

$$\rho_f \frac{\partial \boldsymbol{u}}{\partial t} + \rho_f (\boldsymbol{u} \cdot \nabla)\boldsymbol{u} = -\nabla p + \nabla \cdot \boldsymbol{S}_\mu + \rho_f \boldsymbol{g} + \boldsymbol{f}_e \quad \text{Navier–Stokes momentum equation}$$

$$\tau_{ij} = \mu_f (\frac{\partial u_i}{\partial x_j} + \frac{\partial u_j}{\partial x_i}) + \delta_{ij} \lambda_\mu \frac{\partial u_k}{\partial x_k} \quad \text{Newtonian viscous fluid}$$

$$\frac{\partial \rho_f}{\partial t} + \nabla \cdot \rho_f \boldsymbol{u} = 0 \quad \text{continuity equation}$$

Liquid–gas (l–g) interfacial force balance:

$$\text{normal to interface: } p_e - p_g + \sigma_{lg}(\frac{1}{r_1} + \frac{1}{r_2}) = 2\mu_l \frac{\partial u_{l,n}}{\partial x_n} - 2\mu_l \frac{\mu_{g,n}}{\partial x_n} \quad \text{on } A_{lg}$$

$$\text{tangent to interface: } \mu_l (\frac{\partial u_{l,n}}{\partial x_t} + \frac{\partial u_{l,t}}{\partial x_n}) - \mu_g (\frac{\partial u_{g,n}}{\partial x_t} + \frac{\partial u_{g,t}}{\partial x_n}) = \frac{\partial \sigma_{lg}}{\partial x_t} \quad \text{on } A_{lg}$$

r_1 and r_2 are principal radii of interface curvature

The wave equation for a spatially sinusoidal disturbance $\boldsymbol{u}'$ in the mean velocity $\overline{\boldsymbol{u}}$, i.e., $\boldsymbol{u} = \overline{\boldsymbol{u}} + \boldsymbol{u}'$, of wave number $\kappa^2 = \kappa_y^2 + \kappa_z^2$ caused by thermobuoyancy ($\overline{\boldsymbol{u}} = 0$), $\rho_f = \rho_o[1 - \beta_f(T - T_o)]$, with the temperature field similarly given by $T = \overline{T}(x, t) + T'$, for the component u_x' along the gravity and the corresponding energy equations are

$$(\frac{\partial}{\partial t} + \mu_f \nabla^2) u_x' = -\rho_o \beta_f g (\frac{\partial^2}{\partial y^2} + \frac{\partial^2}{\partial z^2}) T', \quad \overline{\boldsymbol{u}} = 0$$

$$(\rho c_p)_f \frac{\partial T'}{\partial t} + (\rho c_p)_f u_x' \frac{\partial \overline{T}}{\partial x} - k_f \nabla^2 T' = 0$$

$$(\rho c_p)_f \frac{\partial \overline{T}}{\partial t} - k_f \frac{\partial^2 \overline{T}}{\partial x^2} = 0$$

or in terms of κ using $T' = T'(x, t) e^{i(\kappa_y y + \kappa_z z)}$, $\boldsymbol{u}' = u_x'(x, t) e^{i(\kappa_y y + \kappa_z z)}$, we have

$$[\frac{\partial}{\partial t} + \mu_f (\kappa^2 - \frac{\partial^2}{\partial x^2})](\frac{\partial^2}{\partial x^2} - \kappa^2) u_x' = \kappa^2 \rho_o \beta_f g T'$$

$$(\rho c_p)_f (\frac{\partial T'}{\partial t} + u_x' \frac{\partial \overline{T}}{\partial x}) - k_f (\frac{\partial^2}{\partial x^2} - \kappa^2) T' = 0$$

$$(\rho c_p)_f \frac{\partial \overline{T}}{\partial t} - k_f \frac{\partial^2 \overline{T}^2}{\partial x^2} = 0$$

$\boldsymbol{f}_e$	volumetric electromagnetic force vector, N/m^3
$\boldsymbol{g}$	gravitational acceleration vector, m/s^2
p	pressure, Pa
β_f	volumetric thermal expansion coefficient, 1/K
κ	wave vector, 1/m
ρ_f	fluid density, kg/m^3
σ_{lg}	liquid–gas surface tension, N/m
τ_{ij}	component of viscous shear stress tensor $\boldsymbol{S}_\mu$, Pa
μ_f	dynamic viscosity, Pa-s
λ_μ	second viscosity, Pa-s

Table 3.11 lists the macroscopic elastic solid mechanics equation. The Young modulus is related to the bulk modulus E_p (and in turn this is related to the isothermal compressibility κ_p). We discuss the relation between E_p and the atomic structure of the solid in Chapter 4, along with the speed of sound in solids.

Also listed in Table 3.11 is the displacement wave equation for the transverse wave (shear wave with no change in volume) [34]. There is also a longitudinal (compressional or density) wave. The shear waves are slower than the compressional waves.

The elastic constants in Table 3.11 are related to the interatomic potential φ in an N atom crystal occupying volume V. For a cubic lattice with lattice constant a, we have

$$c_{11} = \frac{Na^4}{2V} \sum_{j=2}^{N} x_j^4 (\frac{1}{r_j} \frac{\mathrm{d}}{\mathrm{d}r_j})^2 \varphi(r_j) \tag{3.79}$$

$$c_{12} = \frac{Na^4}{2V} \sum_{j=2}^{N} x_j^2 y_j^2 (\frac{1}{r_j} \frac{\mathrm{d}}{\mathrm{d}r_j}) \varphi(r_j), \tag{3.80}$$

$$r_j^2 \equiv x_j^2 + y_j^2 + z_j^2 \tag{3.81}$$

$$V = cNa^3, \quad c = 2 \text{ for FCC} \tag{3.82}$$

$$c = 4 \text{ for BCC,}$$

where r_j is the distance between the central atom (1) and atom j.

The isothermal compressibility is then

$$E_p = \frac{1}{\kappa_p} = \frac{c_{11} + 2c_{12}}{3}. \tag{3.83}$$

3.9 Macroscopic Scales

Similar to Table 1.5 for atomic scales, Table 2.7 for MD scales, and Table 3.2 for BTE scales, Table 3.12 lists the macroscopic scales for heat transfer. Here L is the system (macroscopic) length scale. Then depending on presence/dominance of conduction, convection, and radiation, the time scale is diffusion time ($\tau_\alpha = L^2/\alpha$, and thermal diffusivity $\alpha = k/\rho c_p$), transit time ($\tau_u = L/|\boldsymbol{u}_\mathrm{o}|$, $\boldsymbol{u}_\mathrm{o}$ is the characteristic velocity), or photon absorption time ($\tau_\sigma = 1/\sigma_{ph} u_{ph}$, σ_{ph} is the absorption coefficient). The temperature scale is generally absolute 0 K, or a characteristic temperature T_o such as the initial or undisturbed (far-field) temperature, or the phase change temperature T_{ij}.

In Figure 1.9, we marked possible ranges of the length and time scales for atomic, MD, BTE, and macroscopic treatments.

Table 3.11. *Macroscopic elastic solid-mechanics equations (including mechanical wave propagation) [34].*

$$\rho \frac{\partial^2 \boldsymbol{d}}{\partial t^2} = \frac{E_{\rm Y}}{2(1+\nu_{\rm P})}\nabla\cdot(\nabla\boldsymbol{d}) + \frac{E_{\rm Y}}{2(1+\nu_{\rm P})(1-\nu_{\rm P})}\nabla^2\boldsymbol{d}+\boldsymbol{f} \quad \text{Navier equation}$$

$$\epsilon_{ij} = \frac{1}{2}(\frac{\partial d_i}{\partial x_j}+\frac{\partial d_j}{\partial x_i}) \quad \text{strain-displacement, or compatibility equation}$$

$$\tau_{ij} = c_{ijkl}\epsilon_{kl} \quad \text{(stress-strain relation, generalized Hooke law)}$$

c_{ijkl} elastic stiffness constants (elastic constants)

$$\epsilon_{ij} = \frac{1+\nu_{\rm P}}{E_{\rm Y}}\tau_{ij} - \frac{\nu_{\rm P}\tau_{mm}\delta_{ij}}{E_{\rm Y}} + \beta_s(T-T_{\rm o}) \quad \text{Hooke law}$$

isotropic (cubic) crystal (only three independent elastic constants C_{11}, C_{12}, and C_{44}.)

The elastic wave equation is

$$\rho\frac{\partial^2 d_i}{\partial t^2} = c_{ijkl}\frac{\partial^2 d_l}{\partial x_j \partial x_k}$$

Shear (or isovoluminous) wave (also called S or secondary wave) for isotropic structure, in the [100] plane where the two transverse-mode speeds are the same, moves at the transverse wave speed, $u_{p,{\rm T}} = (\omega/\kappa)_{\rm T} = (c_{44}/\rho)^{1/2}$, which is the dispersionless (constant speed) relation (applies to long wavelength phonons)
Compression wave (also called P or primary wave) in the [100] plane moves at longitudinal wave speed, $u_{p,{\rm L}} = (\omega/\kappa)_{\rm L} = (c_{11}/\rho)^{1/2}$
Both $u_{p,{\rm L}}$ and $u_{p,{\rm T}}$ are independent of the frequency (no dispersion, large phonon wavelength limit)
The vectorial displacement plane wave is of the form

$$\boldsymbol{d} = d_{\rm o}\boldsymbol{s}_\alpha e^{i(\boldsymbol{\kappa}\cdot\boldsymbol{x}-\omega t)}$$

Relation between the isothermal compressibility κ_p, the bulk modulus E_p, the Young modulus $E_{\rm Y}$, and the shear modulus G, for cubic crystals, are

$$E_{\rm Y} = 3E_p(1-2\nu_{\rm P}),\quad G = \frac{E_{\rm Y}}{2(1+\nu_{\rm P})},\quad E_p = \kappa_p^{-1} = \rho\frac{\partial p}{\partial\rho}|_T = \frac{c_{11}+2c_{12}}{3}$$

c_{ijkl}	elastic constant, Pa
$\boldsymbol{d}$	displacement vector, m
E_p	isothermal bulk modulus, Pa
$E_{\rm Y}$	Young modulus, Pa
$\boldsymbol{f}$	volumetric external force vector, N/m^3
β_s	coefficient of linear thermal expansion, 1/K
ϵ_{ij}	strain tensor component
$\nu_{\rm P}$	Poisson ratio
G	shear modulus, Pa
κ_p	isothermal compressibility, Pa^{-1}
τ_{ij}	component of stress tensor $\boldsymbol{S}$, Pa

Table 3.12. *Macroscopic scales, based on thermal energy transport by conduction, convection, and radiation.*

Scale	Relation
Length	L
Time:	
conduction (diffusion time)	$\tau_\alpha = \frac{L^2}{\alpha^2}$, $\alpha = \frac{k}{\rho c_p}$ thermal diffusivity
convection (transit time)	$\tau_u = \frac{L}{\lvert \boldsymbol{u}_\mathrm{o} \rvert}$, $\boldsymbol{u}_\mathrm{o}$ characteristic net velocity
radiation (absorption time)	$\tau_\sigma = \frac{1}{\sigma_{ph} u_{ph}}$, σ_{ph} absorption coefficient $\sigma_{ph} L \gg 1$ optically thick media (radiation diffusion limit) $\sigma_{ph} L \ll 1$ optically thin media
Temperature:	
single phase	0 K, or T_o characteristic temperature
phase change	T_{lg}, and T_{sl} (phase-change temperatures), or T_c (critical-point temperature)

3.10 Problems

Problem 3.1

Show that when the in- and out-scattering presentation of $\partial f/\partial t|_s$ given by (3.8) is used, the summation over all $\boldsymbol{p}$ vanishes, i.e.,

$$\sum_{\boldsymbol{p}} \frac{\partial f}{\partial t}|_s = 0.$$

(Note to interchange the order of summations over $\boldsymbol{p}$ and $\boldsymbol{p}'$.)

Problem 3.2

Show that the equilibrium fermion

$$f_e^\mathrm{o} = \frac{1}{\exp[(\varphi_{e,\mathrm{o}} + E_{e,k} - E_\mathrm{F})/k_\mathrm{B}T] + 1}, \quad E_{e,k} = \frac{p_e^2}{2m_{e,e}},$$

satisfies the BTE (3.3).

Note that $\varphi_{e,\mathrm{o}}(\boldsymbol{x})$, $E_{e,k}(\boldsymbol{p}_e)$, E_F, and $T(\boldsymbol{x})$ are position dependent, and use

$$\boldsymbol{F}_e = -\nabla \varphi_{e,\mathrm{o}} \quad \text{built-in potential.}$$

However, at equilibrium, $\mathrm{D}f_e^\mathrm{o}/\mathrm{D}t = 0$, and we use

$$\nabla E_\mathrm{F} = \nabla T = \nabla |\boldsymbol{p}_e| = 0.$$

Problem 3.3

The conduction heat flux by a phonon can be written in terms of the nonequilibrium phonon population f_p' as

$$\boldsymbol{q}_{k,p} = \sum_\alpha \frac{1}{8\pi^3} \int E_p \boldsymbol{u}_p f_p' \mathrm{d}\boldsymbol{\kappa},$$

where α is for the different polarizations (longitudinal transverse).

Starting with the BTE, for steady-state condition and $\boldsymbol{F} = \dot{s}_f = 0$, use $\nabla f_p = \nabla f_p^{\text{o}}$, the spatial variation of temperature ∇T, and relaxation-time approximation (3.13)

(a) Show that

$$f_p' = -\tau_p \frac{\partial f_p^{\text{o}}}{\partial T} \boldsymbol{u}_p \cdot \nabla T.$$

(b) Show that

$$\begin{aligned} \boldsymbol{q}_{k,p} &= -(\frac{1}{8\pi^3} \sum_\alpha \int E_p \tau_p \frac{\partial f_p^{\text{o}}}{\partial T} \boldsymbol{u}_p \boldsymbol{u}_p \mathrm{d}\boldsymbol{\kappa}) \cdot \nabla T \\ &\equiv -\boldsymbol{K}_p \cdot \nabla T, \end{aligned}$$

where $\boldsymbol{K}_p$ is the phonon thermal conductivity tensor. Note that $\boldsymbol{u}_p \boldsymbol{u}_p$ is a tensor (diadic product).

Problem 3.4

Consider the power-law, energy-dependent relaxation time given by (3.25). The average relaxation time $\langle\langle \tau_e \rangle\rangle$ is defined as

$$\langle\langle \tau_e \rangle\rangle \equiv \frac{\langle E_e \tau_e \rangle}{\langle E_e \rangle} = \frac{\displaystyle\int E_e \tau_e f_e^{\text{o}} \mathrm{d}\boldsymbol{p}}{\displaystyle\int E_e f_e^{\text{o}} \mathrm{d}\boldsymbol{p}}.$$

Using the approximation

$$E_e = E_{e,k} = \frac{p^2}{2m_e} \quad \text{and} \quad f_e^{\text{o}} = \exp(\frac{-p^2}{2m_e k_{\text{B}} T}),$$

show that

$$\langle\langle \tau_e \rangle\rangle = \tau_{e,\text{o}} \frac{\Gamma(s + \frac{5}{2})}{\Gamma(\frac{5}{2})},$$

where Γ is the gamma function (5.114). This average relaxation time is related to the electron mobility and is a momentum relaxation time.

Problem 3.5

The collision rate term in BTE (3.8) is zero under the condition of detailed balance states in equilibrium, giving for the electron systems

$$\dot{\gamma}_{e,\text{o}}(\boldsymbol{p}', \boldsymbol{p}) f_e^{\text{o}}(\boldsymbol{p}')[1 - f_e^{\text{o}}(\boldsymbol{p})] = \dot{\gamma}_{e,\text{o}}(\boldsymbol{p}, \boldsymbol{p}') f_e^{\text{o}}(\boldsymbol{p})[1 - f_e^{\text{o}}(\boldsymbol{p}')].$$

Show that

$$\frac{\dot{\gamma}_{e,\text{o}}(\boldsymbol{p}', \boldsymbol{p})}{\dot{\gamma}_{e,\text{o}}(\boldsymbol{p}, \boldsymbol{p}')} = e^{[E_{e,k}(\boldsymbol{p}') - E_{e,k}(\boldsymbol{p})]/k_{\text{B}} T}.$$

Problem 3.6

(a) Using $\boldsymbol{F} = \partial \boldsymbol{p}/\partial t$, and for electrons $\boldsymbol{F}_e = -\nabla(\varphi_e + E_{e,k})$, show that the BTE becomes

$$\frac{\partial f_e}{\partial t} + \boldsymbol{u}_e \nabla f_e - \nabla\varphi_e \cdot \nabla_{\boldsymbol{p}} f_e - \nabla E_{e,k}(\boldsymbol{p}) \cdot \nabla_{\boldsymbol{p}} f_e = \frac{\partial f_e}{\partial t}|_s + \dot{s}_e.$$

(b) For $\nabla E_{e,k} = 0$, and $-\nabla\varphi_e = \boldsymbol{e}_e$, and using only the x component, show that (3.14) is obtained.

Problem 3.7

The nondegenerate behavior leads to classical distribution and simplifies the analysis when justified. The conduction electron density $n_{e,c}$ is temperature-dependent in the semiconductors.

(a) For electrons in semiconductors, the equilibrium probability distribution function is

$$\begin{aligned} f_e^{\mathrm{o}} &= \frac{1}{\exp\dfrac{E_{e,p} + E_{e,k} - E_{\mathrm{F}}}{k_{\mathrm{B}}T} + 1} \\ &= \frac{1}{\exp(-\eta_c + \dfrac{p^2}{2m_{e,e}k_{\mathrm{B}}T}) + 1} \quad \text{degenerate electrons} \end{aligned}$$

$$f_e^{\mathrm{o}} \simeq \exp(\eta_c - \frac{p^2}{2m_{e,e}k_{\mathrm{B}}T}) \text{ for nondegenerate electrons for } -\eta_c k_{\mathrm{B}}T + \frac{p^2}{2m_{e,e}} \gg k_{\mathrm{B}}T,$$

where $\eta_c = (E_{\mathrm{F}} - E_{e,p})/k_{\mathrm{B}}T$, and $m_{e,e}$ is the effective electron mass (5.45).

The equilibrium electron density is given by

$$\begin{aligned} n_{e,c} &= \frac{1}{4\pi^3\hbar^3}\int f_e^{\mathrm{o}}\mathrm{d}\boldsymbol{p} \\ &= \frac{1}{4\pi^3\hbar^3}\int_0^\infty \exp(-\frac{p^2}{2m_{e,e}k_{\mathrm{B}}T})e^{\eta_c}4\pi p^2\mathrm{d}p. \end{aligned}$$

Show that

$$n_{e,c} = 2(\frac{m_{e,e}k_{\mathrm{B}}T}{2\pi\hbar^2})^{3/2}e^{\eta_c}.$$

Note that the value of the definite integral can be found from mathematical tables, or from the gamma functions (5.114).

(b) Repeat (a) assuming degenerate electrons and show that

$$n_{e,c} = 2(\frac{m_{e,e}k_{\mathrm{B}}T}{2\pi\hbar^2})^{3/2}\mathrm{F}_{1/2}(\eta_c),$$

where $\mathrm{F}_{1/2}$ is the Fermi–Dirac integral of the order 1/2:

$$\mathrm{F}_{1/2}(\eta_c) = \frac{2}{\pi^{1/2}}\int_0^\infty \frac{x^{1/2}}{1 + \exp(x - \eta_c)}\mathrm{d}x.$$

The general form for Fermi–Dirac integral of the order of j is

$$\mathrm{F}_j(\eta_c) = \frac{1}{\Gamma(j+1)} \int_0^\infty \frac{x^j}{1+\exp(x-\eta_c)} \mathrm{d}x,$$

where $\Gamma(j+1)$ is the gamma function, given by (5.114). The Fermi–Dirac integral indicates a quantum behavior.

Problem 3.8

(a) Using (3.18), plot f_e^{o} versus $E_{e,k}$ (up to 0.3 eV) for $T = 10^3$ K, and $E_{e,p} = 0.2$.

(b) On the same graph, plot (3.20) for f_e versus $E_{e,k}$ for $T = 10^3$ K, $E_{e,p} = 0.2$ eV, $\tau_e = 10^{-11}$ s, $e_{e,x} = 10^3$ and 10^4 V/m, using the rest electron mass m_e.

(c) Comment on the shift from the equilibrium particle energy distribution, under applied external force.

Problem 3.9

(a) Using the definition of $\langle E_e \rangle$ is (3.26), and f_e^{o} and $n_{e,c}$ in Problem 3.2(a), show that

$$\langle E_e \rangle = \frac{3}{2} k_{\mathrm{B}} T n_{e,c},$$

which is the classical kinetic energy of conduction electrons.

(b) Using degenerate electrons, repeat part (a) and using f_e^{o} and $n_{e,c}^{\mathrm{o}}$ in Problem 3.2(b), to show that

$$\langle E_e \rangle = \frac{3}{2} n_{e,c} k_{\mathrm{B}} T \frac{\mathrm{F}_{3/2}(\eta_c)}{\mathrm{F}_{1/2}(\eta_c)}.$$

Problem 3.10

Use the current density $j_{e,x}$

$$j_{e,z} = \frac{e_c}{4\pi^3 \hbar^3} \sum_{p_z > 0} u_{e,z} f_e^{\mathrm{o}}, \quad m_{e,e} u_{e,z} = p_z \cos\theta,$$

[similar to (3.26)], where θ is the polar angle, and use (3.12) for the integration, along with $f_e^{\mathrm{o}}(\eta_c)$ in Problem 3.2(a), and show that

$$j_{e,z} = e_c \frac{m_{e,e}(k_{\mathrm{B}} T)^2}{2\pi^2 \hbar^3} e^{\eta_c} = e_c \left(\frac{k_{\mathrm{B}} T}{2\pi m_{e,e}}\right)^{1/2} n_{e,\mathrm{c}}.$$

Note that for $p_z = m_{e,e} u_{e,z} > 0$, the integral is over a hemisphere.

Problem 3.11

(a) In the derivation of the FGR, substitute (E.16) into (E.14), using zero for the constant of integration.

(b) Show that for a perturbation H′ applied from $t = 0$ to $t = t_{\rm o}$, the first order solution gives

$$a_{1,\kappa'}(t \geq t_{\rm o}) = -M_{{\rm o},\boldsymbol{\kappa}',\boldsymbol{\kappa}}\{\frac{\exp\{i\dfrac{[E(\boldsymbol{\kappa}') - E(\boldsymbol{\kappa}) + \hbar\omega]}{\hbar}t_{\rm o}\} - 1}{E(\boldsymbol{\kappa}') - E(\boldsymbol{\kappa}) + \hbar\omega} -$$

$$\frac{\exp\{i\dfrac{[E(\boldsymbol{\kappa}') - E(\boldsymbol{\kappa}) - \hbar\omega]}{\hbar}t_{\rm o}\} - 1}{E(\boldsymbol{\kappa}') - E(\boldsymbol{\kappa}) - \hbar\omega}\}.$$

(c) Show that for the case of $E(\boldsymbol{\kappa}') > E(\boldsymbol{\kappa})$, i.e., absorption, we have

$$|a_{1,\boldsymbol{\kappa}'}(t \geq t_{\rm o})|^2 = 4M^2_{{\rm o},\boldsymbol{\kappa}',\boldsymbol{\kappa}}\frac{\sin^2(\omega' t_{\rm o}/2)}{\hbar^2\omega'^2},$$

where ω' is defined by (E.18).

(d) Reproduce Figure E.1.

Problem 3.12

Consider electron scattering from a periodic potential (for example, scattering by acoustic phonons), along one dimension. The scattering potential and the confined wave function ($-L/2 \leq x \leq L/2$) are

$$\mathrm{H}' = \varphi_s = A_{\kappa_p}\boldsymbol{d}\cdot\boldsymbol{s} = A_{\kappa_p}e^{\pm i\kappa_p x},$$

$$\psi_e = L^{-1/2}e^{i\kappa x}.$$

(a) Write the expression for the matrix element (3.29), and show that the modal transition rate is

$$M_{\kappa',\kappa} = \int_{-L/2}^{L/2} L^{-1}A_{\kappa_p}e^{i(\kappa-\kappa'\pm\kappa_p)x}\mathrm{d}x.$$

(b) For $\kappa' = \kappa \pm \kappa_p$ (momentum conservation, $\hbar\kappa' = \hbar\kappa \pm \hbar\kappa_p$), show that

$$M_{\kappa',\kappa} = A_{\kappa_p}.$$

(c) Using (3.27), show that

$$\dot{\gamma}_{e\text{-}p}(\kappa',\kappa) = \frac{2\pi}{\hbar}A^2_{\kappa_p}\delta_{\rm D}[E_e(\kappa') - E_e(\kappa) \mp \hbar\omega_p],$$

where $E_e(\kappa') = E_e(\kappa) \pm \hbar\omega$ states energy conservation.

Note that the integrated $\dot{\gamma}_{e\text{-}p}$ over all κ' gives the overall transition rate. The integral of $\delta_{\rm D}(E_e)$ over all energy states ($\boldsymbol{\kappa}'$) leads to the density of states D_e, which is available in analytic form or as experimental data (e.g., Section 5.7). So $\dot{\gamma}_{e\text{-}p}$ integrated over all electron energy states ($\boldsymbol{\kappa}'$), becomes $2\pi A^2_{\kappa_p}D_e(E_e)/\hbar$.

Problem 3.13

As an example of the FGR, consider the spontaneous emission rate of hydrogen $2p$ state to ground state $1s$. There are three $2p$ states

$$(n, l, m) = (2, 1, 0),\ (2, 1, +1),\ (2, 1, -1),$$

so if we have one H atom, then the probability will be 1/3 of (3.43), i.e.,

$$\dot{\gamma}_{e,ph,sp} = \frac{2\omega_{e,g}^3}{9\epsilon_o \hbar u_p h^3}|\boldsymbol{\mu}_e|^2.$$

The electric transition dipole is given by (7.165), i.e.,

$$(\frac{|\boldsymbol{\mu}_e^2|}{e_c^2})^{1/2} = \int_0^\infty R_{e,1s}(R) r R_{e,2p}(r) r^2 \mathrm{d}r,$$

where

$$R_{e,1s} = \frac{2}{r_\mathrm{B}^{3/2}} e^{-r/r_\mathrm{B}}, \quad R_{e,2p} = \frac{r e^{-r/2r_\mathrm{B}}}{2(6)^{1/2} r_\mathrm{B}^{5/2}}.$$

(a) Show that

$$|\boldsymbol{\mu}_e^2| = \frac{2^{15}}{3^9} e_c^2 r_\mathrm{B}^2 = 1.665 e_c^2 r_\mathrm{B}^2.$$

(b) Then using the hudrogen transition energy (2.114)

$$\hbar\omega_{e,g} = \frac{e_c^2}{8\pi\epsilon_o r_\mathrm{B}}(\frac{1}{n_f^2} - \frac{1}{n_i^2}),$$

find

$$\dot{\gamma}_{e,ph,sp}(2p \to 1s) = 6.75 \times 10^8 \; 1/\mathrm{s}.$$

Problem 3.14

Starting from the Gauss, Faraday, and Ampere laws (Table 3.5) and using the magnetic vector potential and the electric potential

$$\boldsymbol{b}_e \equiv \nabla \times \boldsymbol{a}_e, \quad \boldsymbol{e}_e \equiv -\nabla\varphi_e - \frac{\partial}{\partial t}\boldsymbol{a}_e,$$

and also using the Coulomb gauge

$$\nabla \cdot \boldsymbol{a}_e = 0,$$

show that for vacuum, we have

$$\nabla^2 \boldsymbol{a}_e - \frac{1}{u_{ph,o}^2}\frac{\partial^2}{\partial t^2}\boldsymbol{a}_e = 0.$$

Problem 3.15

Consider plane EM wave in vacuum (free space), presented by

$$\boldsymbol{e}_e = e_{e,o} e^{i(\omega t - \omega \frac{z}{c_o})} \boldsymbol{s}_x.$$

(a) Show that

$$\boldsymbol{h}_e = c_o \epsilon_o e_{e,o} e^{i(\omega t - \omega \frac{z}{c_o})} \boldsymbol{s}_y.$$

So,

$$\frac{\boldsymbol{e}_e}{\boldsymbol{h}_e} = \frac{1}{\epsilon_{\rm o} c_{\rm o}}, \quad \frac{\frac{1}{2}\epsilon_{\rm o} e_e^2}{\frac{1}{2}\mu_{\rm o} h_e^2} = 1.$$

(b) Show that

$$\nabla \cdot (\boldsymbol{e}_e \times \boldsymbol{h}_e) = -\frac{\partial}{\partial t}(\frac{\epsilon_{\rm o} e_e^2}{2} + \frac{\mu_{\rm o} h_e^2}{2}).$$

This shows that energy lost per unit time and volume is equal to the outward flux of energy through the surface.

(c) Using the result of part (a), show that the integral of the Poynting vector is

$$\boldsymbol{s}_e = \boldsymbol{e}_e \times \boldsymbol{b}_e = \epsilon_{\rm o} c_{\rm o} e_e^2 \boldsymbol{s}_z.$$

(d) Show that the time-average energy flux can be decomposed as

$$|\bar{\boldsymbol{s}}_e| = \frac{1}{2} c_{\rm o} \epsilon_{\rm o} (\overline{e_e^2}) + \frac{1}{2} c_{\rm o} \mu_{\rm o} (\overline{h_e^2}) = c_{\rm o} \epsilon_{\rm o} (\overline{e_e^2}) = \frac{1}{2} c_{\rm o} \epsilon_{\rm o} e_{e,{\rm o}}^2,$$

where $(\overline{h_e^2})^{1/2}$ and $(\overline{e_e^2})^{1/2}$ are the RMS values.

Problem 3.16

The EM waves attenuate over a short distance in metals (good conductor, where $\omega \epsilon_{\rm o} \epsilon_e \leq \sigma_e / 50$).

(a) Use the Maxwell equations in Table 3.5 to arrive at expressions for $\nabla^2 \boldsymbol{e}_e$ (3.34) and $\nabla^2 \boldsymbol{h}_e$

$$\nabla^2 \boldsymbol{h}_e = \frac{1}{c^2} \frac{\partial \boldsymbol{h}_e}{\partial t^2} - \nabla \times \boldsymbol{j}_{e,f}.$$

(b) Start with a plane EM wave with $\boldsymbol{e}_e = e_{e,{\rm o}} e^{i(\omega t - \kappa z)} \boldsymbol{s}_x$, and show that

$$\boldsymbol{h}_e = e_{e,{\rm o}} \frac{\kappa}{\omega \mu_{\rm o} \mu_e} e^{i(\omega t - \kappa z)} \boldsymbol{s}_y,$$

and use this in the results of part (a) to show that

$$-\kappa^2 + \omega^2 \epsilon_{\rm o} \epsilon_e \mu_{\rm o} \mu_{\rm e} - i \omega \sigma_e \mu_{\rm o} \mu_e = 0,$$

where κ is in general complex ($\kappa = \kappa_r - i \kappa_c$). Use constant charge density n_e.

(c) Using the definition of a good conductor, show that spectral skin depth (penetration distance) δ_ω is

$$\delta_\omega = \frac{1}{\kappa_c} = (\frac{2}{\sigma_e \mu_{\rm o} \mu_e \omega})^{1/2}, \quad \text{or} \quad \frac{e_e(z)}{e_e(0)} = e^{-\kappa_c z} = e^{-z/\delta_\omega}.$$

Note that it should be shown that $\kappa_r = \kappa_c$.

(d) The absorption coefficient $\sigma_{ph,\omega}$ is related to the decay of intensity that is the square of the field (3.39). Then find $\sigma_{ph,\omega}$ as twice the inverse of penetration distance with the expression for $\sigma_{ph,\omega}$. This is generally expressed as

$$\frac{I_{ph}(z)}{I_{ph}(0)} = e^{-\sigma_{ph,\omega} z}.$$

Problem 3.17

(a) Using EM wave-propagation equation (3.34) and $\boldsymbol{j}_e = \sigma_e \boldsymbol{e}_e$, show that for uniform charge density and for free charge only, we have for a transverse EM field $e_{e,y}$,

$$\mu_o \mu_e \epsilon_o \epsilon_e \frac{\partial^2 e_{e,y}}{\partial t^2} = \frac{\partial^2 e_{e,y}}{\partial x^2} + \frac{\mu_o \mu_e}{\rho_e} \frac{\partial e_{e,y}}{\partial t}.$$

(b) Then using $m_\omega = n_\omega - i\kappa_\omega$, as the complex index of refraction, and the dispersion relation

$$\kappa = m_\lambda \frac{\omega}{c_o} = (n_\lambda - i\kappa_\lambda)\frac{\omega}{c_o}$$

or

$$e_{e,y} = e_{e,o} \exp\{i[\omega t + (n_\omega - i\kappa_\omega)\frac{\omega x}{c_o}]\},$$

show that

$$c_o^2 \epsilon_o \epsilon_e \mu_o \mu_e = \epsilon_e \mu_e = (n_\lambda - i\kappa_\lambda)^2 + \frac{i\mu_o \mu_e \lambda_o c_o}{2\pi \rho_e}.$$

(c) Separating the real and imaginary parts, show that

$$n_\lambda^2 - \kappa_\lambda^2 = \mu_o \mu_e \epsilon_o \epsilon_e c_o^2 = \epsilon_e \mu_e, \quad n_\lambda \kappa_\lambda = \frac{\mu \lambda_o c_o}{4\pi \rho_e}$$

or

$$\left\{\begin{matrix} n_\lambda^2 \\ \kappa_\lambda^2 \end{matrix}\right\} = \frac{\epsilon_e \mu_e}{2}\left\{\begin{matrix} + \\ - \end{matrix} 1 + [1 + (\frac{\lambda_o}{2\pi c_o \rho_e \epsilon_o \epsilon_e})^2]^{1/2}\right\}.$$

(d) Show that for metals (small ρ_e), and for long wavelengths, we have

$$n_\lambda = \kappa_\lambda = (\frac{\lambda_o \mu_o \mu_e c_o}{4\pi \rho_e})^{1/2}.$$

Problem 3.18

For an oscillating dipole moment $\boldsymbol{p}_{e,o} = q\boldsymbol{d}$ in vacuum with magnetic vector potential $\boldsymbol{a}_e$ and electric scalar potential φ_e [289],

$$\boldsymbol{a}_e = \frac{\mu_o}{4\pi r} I_o \exp[i\omega(t - \frac{r}{u_{ph}})]\boldsymbol{d},$$

$$\varphi_e = \frac{p_{e,o}}{2\epsilon_o r \lambda}(\frac{\lambda}{2\pi r} + i)\exp[i\omega(t - \frac{r}{u_{ph}})]\cos\theta,$$

where $\boldsymbol{d}$ is the separation distance between charges $+q$ and $-q$, $I_o d = i\omega p_{e,o}$.

(a) Write expressions $\boldsymbol{e}_e$ and $\boldsymbol{h}_e$ in terms of above parameters and variables.

(b) Show that

$$|\bar{\boldsymbol{s}}| = \frac{1}{2}\mathrm{Re}(\boldsymbol{e}_e \times \boldsymbol{h}_e^\dagger) = \frac{\mu_o u_{ph} I_o^2 d^2}{8 r^2 \lambda^2}\sin^2\theta \boldsymbol{s}_r.$$

(c) Show that the total irradiated power $|\bar{\boldsymbol{s}}|$ integrated over a sphere of radius r is

$$P_e = \frac{\omega^4 |p_{e,o}|^2}{12\pi \epsilon_o u_{ph}^3}.$$

(d) Using the energy of the classical electric dipole as

$$\Delta E_d = \frac{1}{2} m_e |p_{e,\mathrm{o}}|^2 \frac{\omega^2}{e_c^2},$$

derive (3.42) by using

$$\tau_{ph,e,sp,\mathrm{o}} = \frac{\Delta E_d}{P_e}.$$

Note that here $\boldsymbol{p}_{e,\mathrm{o}} = e_c \boldsymbol{d}$, so ΔE_d is the electric dipole energy.

Problem 3.19

Show that the heat current vector, in the G–K transport relation, i.e.,

$$\boldsymbol{q} = \frac{1}{V} \frac{\mathrm{d}}{\mathrm{d}t} \sum_i (E_{k,i} + E_{p,i}) \boldsymbol{x}_i,$$

can be written as

$$\boldsymbol{q} = \frac{1}{V} [\sum_i E_i \boldsymbol{u}_i + \frac{1}{2} \sum_{i,j} (\boldsymbol{F}_{ij} \cdot \boldsymbol{u}_i) \boldsymbol{x}_{ij}],$$

for two-body interatomic potentials.

Note that by using the Newton second law, we have

$$\frac{\mathrm{d}E_{k,i}}{\mathrm{d}t} = \sum_j \boldsymbol{F}_{ij} \cdot \boldsymbol{u}_i,$$

and also

$$\frac{\mathrm{d}E_{p,i}}{\mathrm{d}t} = \sum_j \frac{1}{2} \boldsymbol{F}_{ij} \cdot (\boldsymbol{u}_j - \boldsymbol{u}_i),$$

and that

$$\begin{aligned} \sum_i [\sum_j \frac{1}{2} \boldsymbol{F}_{ij} (\boldsymbol{u}_j + \boldsymbol{u}_i)] \boldsymbol{x}_i &= \frac{1}{2} \sum_{i,j} [\frac{1}{2} \boldsymbol{F}_{ij} (\boldsymbol{u}_i + \boldsymbol{u}_j) \boldsymbol{x}_i - \frac{1}{2} \boldsymbol{F}_{ij} (\boldsymbol{u}_i + \boldsymbol{u}_j) \boldsymbol{x}_j] \\ &= \frac{1}{2} \sum_{i,j} \frac{1}{2} \boldsymbol{F}_{ij} (\boldsymbol{u}_i + \boldsymbol{u}_j) \boldsymbol{x}_{ij}, \end{aligned}$$

because $\boldsymbol{F}_{ij} = -\boldsymbol{F}_{ji}$.

Problem 3.20

The EM wave equation follows from the Maxwell equations and for the electric field intensity the wave equation is given by (3.34) for nonconducting media ($\sigma_e = 0$) with zero gradient in the charge distribution. Consider a plane wave moving along the x direction.

(a) Show that (3.34), i.e., $e_{e,y} = e_{e,\mathrm{o}} \cos(\omega t - \kappa x)$ satisfies this equation, where $c = \omega/\kappa$ is the phase velocity.

(b) Show that the exponential notation presentation of this planar wave is $e_e = e_{e,\mathrm{o}} \exp[i(\omega t - \kappa x)]$.

(c) Explain that when this wave is attenuated, the decreasing amplitude can be shown by $e_{e,y} = e_{e,\mathrm{o}} \exp[i(\omega t - \kappa_r x) - \kappa_c x]$, where the real part of the wave vector κ_r remains as before, and κ_c is called the attenuation constant (has the unit of 1/m, and is related to the absorption coefficient σ_{ph}). Note that $\exp(-\kappa_c x)$ represents decay of the wave.

(d) Show that this can also be written as $e_{e,y} = e_{e,\mathrm{o}} \exp[i(\omega t - \kappa x)]$, where now $\kappa = \kappa_r - i\kappa_c$.

(e) Compare this solution with the de Broglie quantum wave (footnote, Section 2.6.1) for the Schrödinger equation.

Note that the time derivative term in Schrödinger equation (2.62) already has a coefficient $i = (-1)^{1/2}$, so the wave function for the Schrödinger equation has the similar form $\exp(-i\omega t)$ in (2.68), where the energy per particle is $E = \hbar\omega$.

The absorption coefficient, $\sigma_{ph} = 2\kappa_c$. The factor 2 is due to relation of radiation intensity to e_e^2, through (3.39).

Problem 3.21

(a) Show that (B.4) is the Fourier transform of (B.1). Note that the Fourier transform has the property $F(\nabla_1 E') = i\kappa_1 F(E')$. Assume isotropic, constant thermal conductivity i.e., $\nabla \cdot \boldsymbol{k} \cdot \nabla = k\nabla^2$.

(b) Show that (B.10) is the Taylor series expansion of the left-hand side of (B.9).

(c) Explain the transformation of the time integral to the difference in (B.31).

(d) Explain in words the steps in derivation of the right-hand side of (B.33).

Problem 3.22

(a) Use the Matlab solid-phase MD code (three-dimensional) set for Ar FCC and change the potential constants to that for Xe (Tables 2.2 and A.1 give potential and atomic properties). Then calculate the thermal conductivity of Xe FCC with the G–K autocorrelation relation in the code. The decay of the heat current autocorrelation function (HCACF), and the lattice thermal conductivity are shown in Figure 4.31 for Ar.

Note that only equilibrium MD results should be used. So, discard the initial portion of the MD results and set $t = 0$ in the correlation to when equilibrium is reached.

(b) Show the results in the forms of dimensionless autocorrelation function versus time. Use temperatures of 20 and 40 K (both are solid phases, for Xe, $T_{\mathrm{D}} = 55$ K in Table A.2).

(c) Comment on the autocorrelation function decay and any trends as the temperature increases.

Note that this simulation includes only the phonon–phonon interactions (the other interactions are discussed in Section 4.9.4, including the impurity, grain boundary, and electron scattering).

4

Phonon Energy Storage, Transport and Transformation Kinetics

Heat transfer by lattice (phonon) conduction is proportional to the lattice thermal conductivity tensor $\boldsymbol{K}_p$(W/m-K), i.e., $\boldsymbol{q}_k = -\boldsymbol{K}_p \cdot \nabla T$ (the Fourier law, Table 1.1), and sensible heat storage is determined by the phonon (lattice) specific heat capacity $c_{v,p}$(J/kg-K). The specific heat capacity is also given per unit volume(J/m^3-K), or per atom(J/K). Phonons participate in many thermal energy conversion phenomena, including laser cooling of solids, discussed in Chapter 7 [$\dot{s}_{i\text{-}j}$(W/m^3) in Table 1.1]. In this chapter, we examine how the atomic structure of a solid influences $c_{v,p}$, $\boldsymbol{K}_p$, and $\dot{s}_{i\text{-}j}$ involving phonons.

Phonons are lattice-thermal-vibration waves that propagate through a crystalline solid. Most lattice vibrations have higher frequencies than audible sound, ultrasound, and even hypersound. Figure 4.1 shows the various sound- and vibrational-wave regimes. A single, constant speed (dispersionless, i.e., having a linear frequency dependence on the wave number) of 10^3 m/s is used for the sake of illustration. In solids, the speed of sound is related to the moduli of elasticity and density and is as high as 18,350 m/s in diamond and as low as 818 m/s in thallium. As will be shown, the vibrational waves have different modes, and the propagation speed can be strongly frequency dependent. The phonon energy $\hbar\omega$ is general less than about 0.2 eV, with the high energy phonons being available more at higher temperatures.

In this chapter, we begin with lattice vibration and the relation between frequency and wave number (the dispersion relation) for a simple, harmonic, one-dimensional lattice. Then we discuss the quantization of phonons and a general three-dimensional treatment of dispersion. We discuss lattice specific heat capacity and thermal conductivity (from the BTE for phonons), including quantum effects, and discuss the atomic structural metrics of the thermal conductivity at high temperatures. Then we discuss the phonon boundary resistance (interface of dissimilar materials) and phonon absorption of external ultrasound. Finally we discuss the size effects.

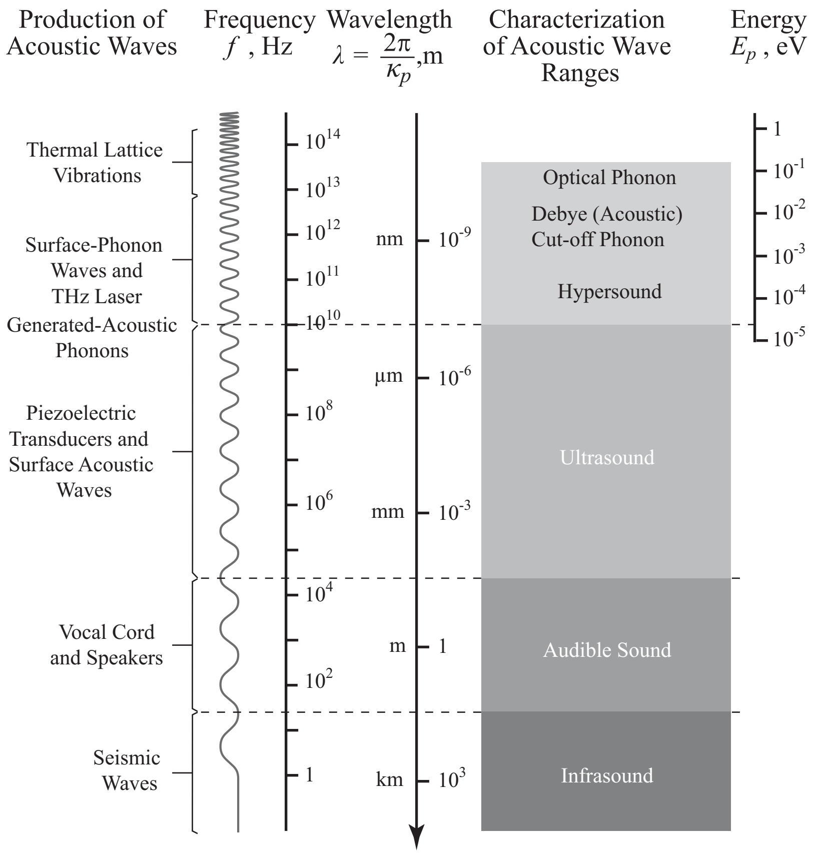

Figure 4.1. Spectra (wavelength and frequency) of acoustic- and vibrational- (mechanical- and thermal-) wave regimes. An average group speed of 10^3 m/s is used for the waves. The thermal lattice-vibration modes (phonons) have the highest frequency among the acoustic and vibrational waves.

4.1 Phonon Dispersion in One-Dimensional Classical Lattice Vibration

In this section we derive the phonon dispersion relation and the phonon velocities, for an idealized chain of atoms. In a crystalline solid, because of the temperature of this system of atoms, the constituent atoms vibrate about their equilibrium positions, and the extent of these thermal vibrations is determined by the intermolecular forces they exert on each other. These vibrations are quantized elastic waves (phonons) and persist even at $T = 0$ K (the zero-point motion, Section 2.5.3).

The quantized treatment of waves is done in the normal coordinates (through the Schrödinger equation), and this introduces $\hbar$ (discussed in Section 4.5). This is also termed the quantum harmonic-oscillator treatment of phonons. Here, to review some of the general features of these elastic waves, we begin with a classical dynamics (Newtonian) multibody equation of motion. The long wavelength (elastic) wave limit of this is given by the wave equation in Table 3.11. Here we are interested in all wavelengths allowed in the solid, so we will not assume a constant wave speed.

Consider two different atoms in a primitive basis (for example, having masses m_1 and m_2). We start with a linear (one-dimensional) lattice, as shown in Figure 4.2(a). A similar treatment is given in [117]. From Figure 2.2 and Table 2.5, and by expressing the external force with a spring force ($\boldsymbol{F}_{kj} = -\Gamma \boldsymbol{d}_{kj}$), where Γ is the force constant (2.54), we write a one-dimensional equation of motion. This is the harmonic approximation, as will be discussed in Section 4.4, and is valid near the bottom of the potential well as the zero-temperature asymptote (inset of Figure 2.3). We write the discretized form of this particle momentum (based on the nearest-neighbor interaction only) equation. We use the instantaneous locations of particle 1 and its relative position with respect to particle 2 to its left and right in a unit cell designated with index j, i.e.,

$$m_1 \frac{\mathrm{d}^2 d_1^j}{\mathrm{d}t^2} = -\Gamma(d_1^j - d_2^j) - [-\Gamma(d_2^{j-1} - d_1^j)] = \Gamma(d_2^j + d_2^{j-1} - 2d_1^j) \tag{4.1}$$

$$m_2 \frac{\mathrm{d}^2 d_2^j}{\mathrm{d}t^2} = \Gamma(d_1^{j+1} + d_1^j - 2d_2^j) \quad \text{harmonic motion of lattice atoms,} \tag{4.2}$$

where the movement to the right creates a restoring force to the left, and movement to the left creates a restoring force to the right. Here Γ represents the second derivative of the effective interatomic potential evaluated at the equilibrium separation distance, as given by (2.54) and further discussed in Section 4.4. The proceeding are wave equations and admit plane-wave solutions such as those discussed in Sections 2.6 and 3.3.2 for the Schröndinger and the Maxwell equations, respectively.

Noting that the equilibrium locations of atoms take discrete values, $x = ja$, where j is the unit-cell designation, the solutions are of the form in Table 3.11 for elastic waves and is also called the Bloch wave (for a periodic medium with period a)

$$d_1^j = d_{\mathrm{o},1} \exp[i(\kappa j a)] \exp[-i(\omega t)] \qquad \kappa = \frac{2\pi}{\lambda} \tag{4.3}$$

$$d_2^j = d_{\mathrm{o},2} \exp[i(\kappa j a)] \exp[-i(\omega t)], \tag{4.4}$$

where κ is the wave number, λ is the wavelength, and $\omega = 2\pi f$ (f is the frequency) is the angular frequency. In Section 4.4, we will write the general form of (4.1) and (4.2).

Substituting (4.3) and (4.4) into (4.1) and (4.2), and setting the determinant of $d_{\mathrm{o},1}$ and $d_{\mathrm{o},2}$ in the matrix given below equal to zero, we have the characteristic equation (dispersion relation), i.e.,

$$-m_1 d_{\mathrm{o},1}\omega^2 \exp[i(\kappa j a)] = \Gamma\{d_{\mathrm{o},2} \exp[i(\kappa j a)] + d_{\mathrm{o},2} \exp\{i[\kappa(j-1)a]\} - 2d_{\mathrm{o},1} \exp[i(\kappa j a)]\}$$

$$-m_2 d_{\mathrm{o},2}\omega^2 \exp[i(\kappa j a)] = \Gamma\{d_{\mathrm{o},1} \exp\{i[\kappa(j+1)a]\} + d_{\mathrm{o},1} \exp[i(\kappa j a)] - 2d_{\mathrm{o},2} \exp[i(\kappa j a)]\},$$

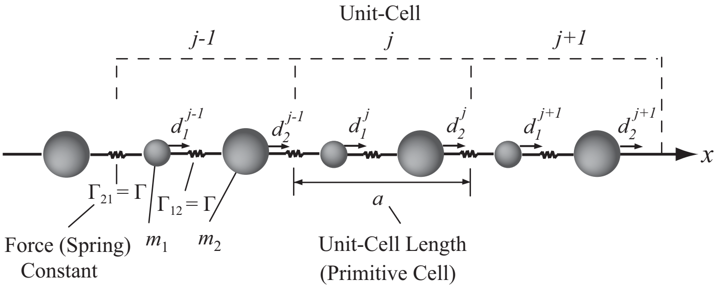

(a) Schematic of A Linear, Diatomic Chain

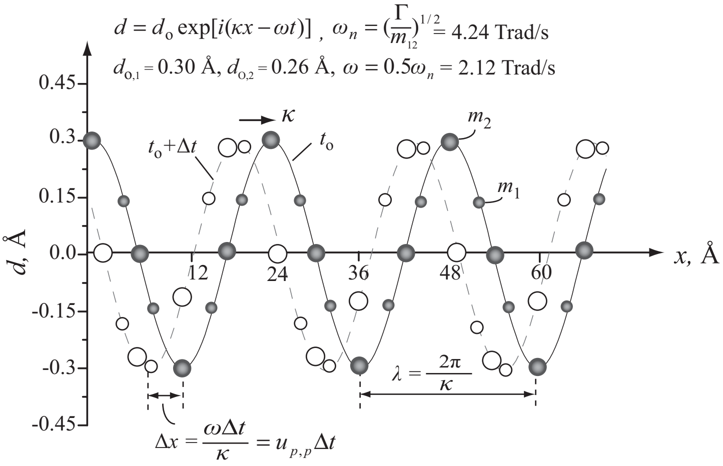

(b) Acoustic Phonon, $m_1 = 0.5m_2 = m_{Ar}$, $a = 6$ Å, $\Gamma = 0.8$ N/m

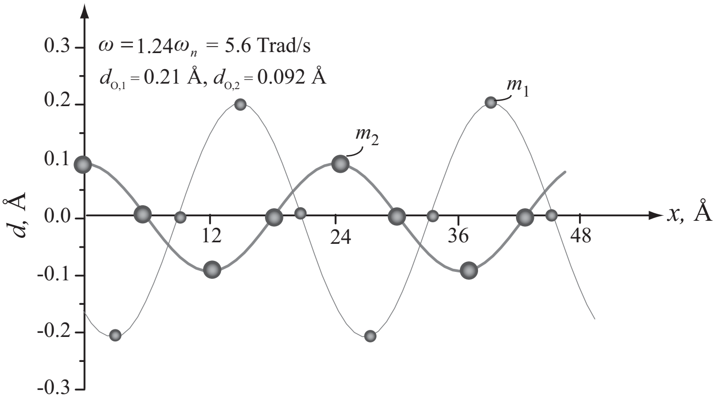

(c) Optical Phonon, $m_1 = 0.5m_2 = m_{Ar}$, $a = 6$ Å, $\Gamma = 0.8$ N/m

Figure 4.2. (a) Designation of a diatomic, linear chain solid (lattice), having the force constant Γ, and its displacements around equilibrium positions. (b) Displacement of a linear, diatomic chain of Ar atoms, but every other atom has a mass of $1/2m_{Ar}$. The values for Γ and a are discussed in Section 4.7.2. The acoustic phonon waves and their propagation is also shown. (c) Same as (b), but for the optical phonon.

or

$$-m_1 d_{\mathrm{o},1}\omega^2 = \Gamma d_{\mathrm{o},2}[1+\exp(-i\kappa a)] - 2\Gamma d_{\mathrm{o},1}$$
$$-m_2 d_{\mathrm{o},2}\omega^2 = \Gamma d_{\mathrm{o},1}[1+\exp(i\kappa a)] - 2\Gamma d_{\mathrm{o},2},$$

or

$$\begin{vmatrix} 2\Gamma - m_1\omega^2 & -\Gamma[1+\exp(-i\kappa a)] \\ -\Gamma[1+\exp(i\kappa a)] & 2\Gamma - m_2\omega^2 \end{vmatrix} = 0,$$

or[†]

$$m_1 m_2 \omega^4 - 2\Gamma(m_1+m_2)\omega^2 + 2\Gamma^2(1-\cos\kappa a) = 0 \quad \text{characteristic equation.} \qquad (4.5)$$

The roots of this quartic equation are

$$\omega^2(\kappa) = \frac{2\Gamma(m_1+m_2) \pm [4\Gamma^2(m_1+m_2)^2 - 8\Gamma^2 m_1 m_2(1-\cos\kappa a)]^{1/2}}{2m_1 m_2}$$
$$\text{dispersion relation for linear, diatomic lattice.} \qquad (4.6)$$

This phonon dispersion relation for a diatomic chain, shows that ratio ω/κ is not a constant and depends on κ (i.e., $2\pi/\lambda$) similar to that for photons in (3.36).

In general, the total number of branches (here two) is the number of modes per unit cell $n_{p,m}$ is equal to the number of dimensions of the motion (here one) times the number of atoms per primitive cell $N_\circ$ (here two over length a). We will discuss this further in Section 4.3.3.

The dimensionless form of this dispersion relation is

$$\omega^{*2} = \frac{1 \pm [1 - 2m_1^* m_2^*(1-\cos\pi\kappa^*)]^{1/2}}{2} \quad \text{dimensionless dispersion relation,} \qquad (4.7)$$

where the dimensionless quantities are

$$\omega^* = \frac{\omega}{\omega_\mathrm{o}} = \frac{\omega}{[2\Gamma(\dfrac{1}{m_1}+\dfrac{1}{m_2})]^{1/2}}, \qquad \kappa^* = \frac{\kappa a}{\pi}, \qquad m_i^* = \frac{m_i}{m_1+m_2},$$

$$\omega_\mathrm{o} = [2\Gamma(\frac{1}{m_1}+\frac{1}{m_2})]^{1/2}, \qquad \frac{1}{m_{12}} = \frac{1}{m_1}+\frac{1}{m_2} \quad \text{reduced mass,} \qquad (4.8)$$

where ω_o is twice the natural frequency ω_n (vibration of a pair of atoms) and for diatomic cell the reduced mass is $m_{12} = m_1 m_2/(m_1+m_2)$ and the natural frequency (2.54) is $\omega_n = (\Gamma/m_{12})^{1/2}$. Note that the dimensionless wave vector is $\kappa a/\pi$, but we

---

[†] This can be written as (Section 4.4)

$$\begin{bmatrix} \frac{1}{m_1} & 0 \\ 0 & \frac{1}{m_2} \end{bmatrix} \begin{bmatrix} 2\Gamma & -\Gamma[1+\exp(-i\kappa a)] \\ -\Gamma[1+\exp(i\kappa a)] & 2\Gamma \end{bmatrix} \equiv \boldsymbol{M}^{-1}\boldsymbol{D}(\kappa) = \omega^2 \boldsymbol{I},$$

where $\boldsymbol{I}$ is the identity matrix, $\boldsymbol{D}(\kappa)$ is the dynamical matrix and will be discussed in Section 4.4, and $\boldsymbol{M}$ is the mass matrix. For such harmonic displacements, the dynamical matrix facilitates the compact presentation of multidimensional, multiple-mass structures. The dimension of the dynamical matrix is the number of spatial dimensions times the number of atoms in a primitive cell, i.e., $3N_\circ$ for three-dimensional atomic structures.

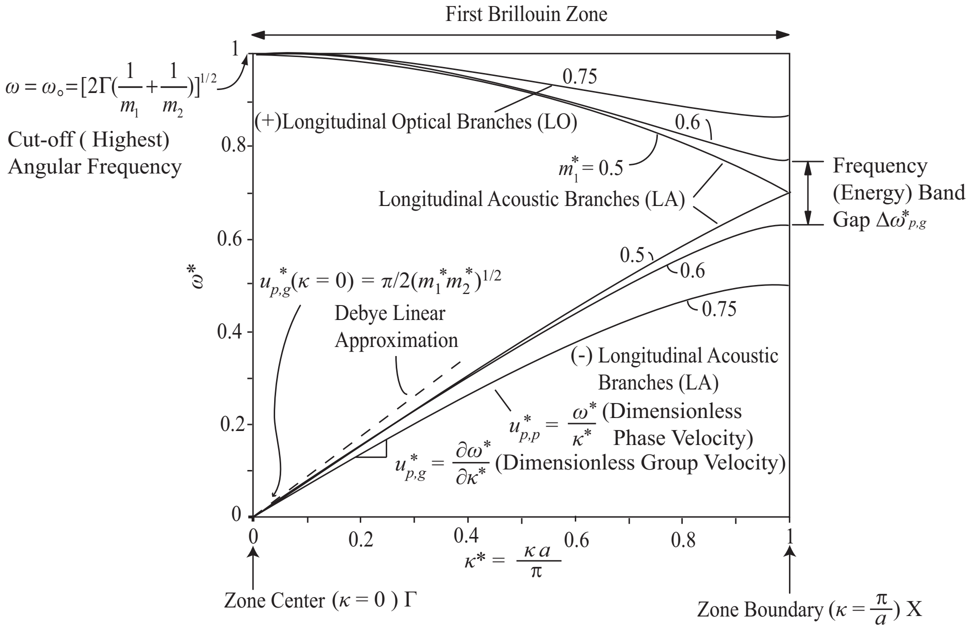

Figure 4.3. Dimensionless dispersion relation for a linear, diatomic chain. Both acoustic (–) and optical (+) branches are shown. The group velocity is also shown. Note that the maximum for ω^* is 1, and that for $m_1^* \neq 0.5$, at $\kappa = \pi/a$, there is a symmetry point referred to as the Brillouin-zone boundary. In the Debye approximation a linear dispersion relation (also called dispersionless, as the speed is independent of κ) is used.

could have also used $\kappa a/2\pi$, which is the more general usage. The (–) branch is acoustic (at $\kappa = 0$, $\omega = 0$ for the acoustic branch) and the (+) branch is optical.

As was mentioned in the last footnote, the dispersion relation (4.5) can be written in terms of the dynamical matrix $\boldsymbol{D}(\boldsymbol{\kappa})$ and this will be further discussed in Section 4.4.

Figure 4.3 shows the variation of scaled (dimensionless) angular frequency ω^* with respect to the scaled wave number κ^*, for $m_1^* = 0.75$ and 0.6, and 0.5 (same mass for all atoms). The solutions represent the two polarizations (branches of vibration modes). These are the acoustic (–) and optical (+) polarizations.

Some of the features of the dispersion relation can be explored for further insight. For $\kappa = 0$ (long-wavelength assumption, which is called the Brillouin zone center), we find by the expansion of $\cos\kappa a$, that

$$\kappa = 0: \qquad \omega_{\rm LO} = \omega_{\rm o} = [2\Gamma(\frac{1}{m_1} + \frac{1}{m_2})]^{1/2} = (\frac{2\Gamma}{m_{12}})^{1/2}$$

longitudinal-optical branch (LO) at Brillouin zone center, (4.9)

$$\omega_{\rm LA} = (\frac{1}{2}\frac{\Gamma}{m_1 + m_2})^{1/2}\kappa a = (\frac{\Gamma}{2m_{12}})^{1/2}\kappa a$$

longitudinal-acoustic branch (LA) at Brillouin zone center. (4.10)

The sound speed is found from (4.10).

The Brillouin zone center is designated as the Γ point (in the $\boldsymbol{\kappa}$ space), and the boundary is designated as X. For $\kappa = \pi/a$ (at the edge of the Brillouin zone), we have

$$\kappa = \frac{\pi}{a}: \qquad \omega_{\rm LO} = (\frac{2\Gamma}{m_1})^{1/2}$$

$$\text{LO at Brillouin zone edge (boundary X)}, \tag{4.11}$$

$$\omega_{\rm LA} = (\frac{2\Gamma}{m_2})^{1/2},$$

$$\text{LA at Brillouin zone edge (boundary X)}. \tag{4.12}$$

The difference between these is called the phonon energy gap $\Delta\omega_{p,g}$, i.e.,

$$\Delta\omega_{p,g} = \Delta\omega_{p,{\rm X}} = \omega_{\rm LO}(\kappa = \pi/a) - \omega_{\rm LA}(\kappa = \pi/a) \ \text{ at Brillouin zone boundary X}. \tag{4.13}$$

Also, note that $\kappa = \pi/a$ or $\lambda = 2\pi/\kappa = 2a$ is the shortest phonon wavelength allowed. Thus, while $2a \le \lambda \le \infty$, the wave number is bound as $0 \le \kappa \le \pi/a$ and then it is periodic at π/a or $2\pi/a$. The Brillouin zone that is in the space with coordinates that are in units of inverse of the lattice spacing or the wave vector (called the reciprocal lattice), will be discussed in Section 4.3. The Brillouin zone describes the symmetries of the dispersion relation (i.e., X-point which corresponds to π/a here).

The cut-off (highest) frequency is $\omega_{\rm o} = [2\Gamma(m_1^{-1} + m_2^{-1})]^{1/2} = 2^{1/2}\omega_n$ and is the largest frequency achievable. As an example, the spring constant Γ for the L–J potential in monatomic FCC, is given in Table 2.7 as

$$\Gamma_{\rm LJ} = \frac{\partial^2\langle\varphi\rangle}{\partial r_{nn}^2}|_{r_{nn,e}} = (22.88)^2\frac{\epsilon_{\rm LJ}}{\sigma_{\rm LJ}^2}. \tag{4.14}$$

For Ar FCC, we have $\Gamma = 7.545$ N/m and $\omega_n = 1.068 \times 10^{13}$ rad/s (10.68 Trad/s), which are much larger than the atomic-pair values (Section 2.5.3) used in Figure 4.2.

The phonon group velocity is defined as

$$u_{p,g} \equiv \frac{\partial\omega}{\partial\kappa}, \quad \text{in general } \boldsymbol{u}_{p,g} \equiv \nabla_{\boldsymbol{\kappa}}\omega \quad \text{phonon group velocity}. \tag{4.15}$$

The phase speed (velocity) is defined as

$$u_{p,p} \equiv \frac{\omega}{\kappa} \quad \text{phase speed (velocity)}, \tag{4.16}$$

and only for a nondispersive phonon are acoustic phonon the group and the phase speed the same and constant.

For this example, we have the dimensionless (and dimensional) group velocity at $\kappa = 0$ (called the characteristic velocity):

$$u^*_{p,g}(\kappa^* = 0) = u^*_{p,p}(\kappa = 0) = \frac{\pi}{2}(m^*_1 m^*_2)^{1/2},$$
$$u_{p,g}(\kappa = 0) = \frac{\omega_n a}{2} = (\frac{\Gamma}{m_{12}})^{1/2}\frac{a}{2}, \qquad (4.17)$$

and this is also shown in Figure 4.3. This is the long-wavelength, elastic, longitudinal wave (constant-sound-speed) asymptote (end-of-chapter problem) found from the macroscopic elastic wave (here the longitudinal wave) equation (Table 3.11).

Note that, for the optical branch at $\kappa = 0$, we have, by using (4.3) in (4.4),[†]

$$\frac{d_{o,1}}{d_{o,2}} = -\frac{m_2}{m_1}, \quad \kappa = 0 \quad \text{long-wavelength limit in optical branch,}$$
$$\frac{d_{o,1}}{d_{o,2}} = 1, \quad \kappa = 0 \quad \text{long-wavelength limit in acoustic branch,} \qquad (4.18)$$

i.e., the neighboring masses (atoms) move in the opposite directions for the optical branch, whereas for the acoustic branch. For the long-wavelength-acoustic branch, the neighboring atoms move together and with the same magnitude. These long-wavelength-acoustic phonons move at a constant speed of $a\omega_n(m^*_1 m^*_2)^{1/2}/2$. This is the elastic wave speed used in the macroscopic, elastic, solid mechanics (Navier) equation (Table 3.11).

For $m_1 = m_2$ ($m^*_1 = 0.5$), the dispersion spectrum becomes that of a monatomic chain. The gap disappears, and the top branch can be unfolded to cover the region $1 \leq \kappa^* \leq 2$. Then there is only the acoustic branch. This is shown in Figure 4.4, where four Brillouin zones (for atomic chain) are shown. Brillouin zone are periodic in $\boldsymbol{\kappa}$ space. Note that, for a monatomic chain, the interatomic distances are $a/2$. This is the reason that the first symmetry point X is at $\kappa a/\pi = 2$. If we scale κ with $2\pi/a$, then for a monatomic chain, X will be at $\kappa a/2\pi = 1$.

We generalize the result to three dimensions and introduce the dynamical matrix, which allows for a more general and compact analysis, in Section 4.4.

In the Debye approximation, a linear dispersion relation assumes $\kappa \rightarrow 0$ behavior, and this is shown in Figure 4.4.

The average lattice potential and kinetic energy are equal, and for a monatomic linear chain the total energy is $m\omega^2 a/2$ (end-of-chapter problem).

As an example, atomic displacements of a diatomic chain of Ar atoms (pair force constant in Table 4.4), with every other atom having a mass $0.5m_{\rm Ar}$, are shown in Figures 4.2(b) and (c). The acoustic wave propagation and phase velocity is shown in Figure 4.2(b). The wave at times $t_\circ$ and $t_\circ + \Delta t$ are shown, where the wave has

---

[†] The general relation for the ratio of displacements is

$$\frac{d_{o,1}}{d_{o,2}} = -\frac{m_1\omega^2 - 2\Gamma}{2\Gamma \cos\frac{a}{2}\kappa},$$

for $m_1 < m_2$, and ω is taken for the A or O branch for the same κ.

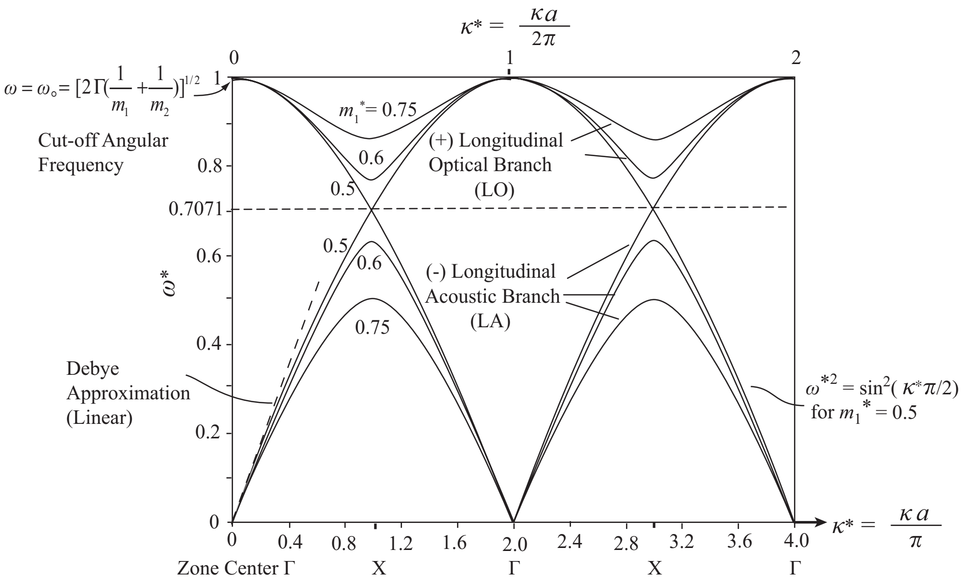

Figure 4.4. Dimensionless dispersion relation over four Brillouin zones. The results are for a linear, diatomic chain. The zone center is designated as Γ point (in the scaled $\boldsymbol{\kappa}$ space or Brillouin zone), and the first symmetry point as X. The conventional dimensionless wave vector uses $2\pi/a$ as a scale (shown on top).

travelled a distance $\omega\Delta t/\kappa$. Note that the displacement wave connects all adjacent atoms. In Figure 4.2(c), the optical waves are shown, with adjacent atoms moving in opposite directions. The results are frequencies near (but not at) the Γ point (Figure 4.3), so the amplitude ratio nearly follows (4.18). For both the acoustic and optical branches, κ is the same, while ω is taken along the appropriate branch ($\omega_A < \omega_\circ$). In crystals, $d_{\circ,1}$ is not a constant, but a function of frequency (Section 4.8).

This is a classical treatment of the lattice vibration based on a force constant (harmonic vibration), we will move to quasi-particle and quantum treatments in the following sections[†].

4.2 Phonon Density of States and Debye Model

Wave number density of states (DOS) $D_p(\kappa)$ is defined in the Glossary (and also in Section 2.6.5). The DOS of phonons is used in determining the total number of phonons N_p as well as the phonon-related properties. The frequency (in linear ω space) density of the normal modes or phonon DOS $D_p(\omega)$ is the total number

---

[†] The quantum lattice-dynamic properties are found from the Schrödinger equation

$$[-\sum_i \frac{\hbar^2}{2M_i}\frac{\partial^2}{\partial \boldsymbol{R}_i^2} + \varphi(\boldsymbol{R})]\psi_p(\boldsymbol{R}) = E_p\psi_p(\boldsymbol{R}),$$

where $\boldsymbol{R}_i$ is the coordinate of the nucleus, M_i its mass, $\varphi(\boldsymbol{R})$ is the clamped-ion energy of the system [20].

of modes in the frequency range ω to $\omega + \mathrm{d}\omega$, divided by volume V. In (2.99), the integral is taken to include all $\boldsymbol{\kappa}$ corresponding to ω in this range. Then we use the integral defined in Section 3.1.3 to make the integration over $\mathrm{d}\boldsymbol{\kappa}$, as in (3.11), using $\nabla_{\boldsymbol{\kappa}}\omega_\alpha$ to relate $\mathrm{d}\boldsymbol{\kappa}$ and $\mathrm{d}\omega_\alpha$, where α is the polarization (or branch) of the dispersion relation. The density of normal modes (Section 4.4) for three-dimensional, cubic lattices (of cubic volume L^3) is

$$D_p(\omega) \equiv \frac{1}{L^3}\left(\frac{L}{2\pi}\right)^3 \sum_\alpha \frac{1}{|\nabla_{\boldsymbol{\kappa}}\omega_\alpha|} = \left(\frac{1}{2\pi}\right)^3 \sum_\alpha 4\pi\kappa^2 \frac{\mathrm{d}\kappa}{\mathrm{d}\omega_\alpha}, \tag{4.19}$$

$$\alpha = \mathrm{A}, \mathrm{O} \quad \text{for acoustic and optical branches,}$$

where α is the branch index (the acoustic branches has 3 branches, two transverse, and one longitudinal). We have used integration (3.11) over the $\boldsymbol{\kappa}$-space [or the $\boldsymbol{p}$-space, because $\boldsymbol{p} = \hbar\boldsymbol{\kappa}$, de Broglie relation for parabolic energy distribution, (2.97)].

Note that in (4.19), when $\mathrm{d}\omega_\alpha/\mathrm{d}\kappa$ is zero, then D_p will have a singularity. This occurs at the X point for the acoustic and at the X and Γ points for the optical phonons in Figure 4.4.

The phonon DOS is used, similar to (2.99) to obtain integral of quantities which depend on the modes. For any quantity ϕ related to the modes, we have

$$\begin{aligned}\sum_\alpha\sum_{\boldsymbol{\kappa}} \phi[\omega_\alpha(\boldsymbol{\kappa})] &= \sum_\alpha \int_{\boldsymbol{\kappa}} \frac{1}{(2\pi)^3}\phi[\omega_\alpha(\boldsymbol{\kappa})]\mathrm{d}\boldsymbol{\kappa} \\ &\equiv \sum_\alpha \int_{\omega_\alpha} D_p(\omega_\alpha)\phi(\omega_\alpha)\mathrm{d}\omega_\alpha.\end{aligned} \tag{4.20}$$

Here again $D_p(\omega)\mathrm{d}\omega$ is the total number of modes in the interval ω to $\omega + \mathrm{d}\omega$, divided by volume V. So $D_p(\omega)$ has the units of 1/m^3-rad/s. Then DOS can be viewed as the degeneracy of states with energy $\hbar\omega$.

The total DOS for normal modes can also be written in terms of the Dirac delta function δ_D. Then, by use of (4.19), $D_p(\omega)$ also given by (2.99) or (3.28), for a particular frequency ω can be given as [294]

$$D_p(\omega) = \sum_\alpha \int_{\kappa'} \frac{\mathrm{d}\boldsymbol{\kappa}'}{(2\pi)^3}\delta_\mathrm{D}[\omega - \omega_\alpha(\boldsymbol{\kappa}')], \;\; \mathrm{d}\boldsymbol{\kappa}' = 4\pi\kappa'^2\mathrm{d}\kappa'. \tag{4.21}$$

The Dirac delta function $\delta_\mathrm{D}[\omega - \omega_\alpha(\boldsymbol{\kappa}')]$ is defined in the Glossary, where the energy Dirac delta function $\delta_\mathrm{D}[E - E_\alpha(\boldsymbol{\kappa}')]$ is used. This is an alternative presentation of (4.19). Note that $w_\alpha(\boldsymbol{\kappa})$ is the dispersion relation and the gradient (derivative) $|\nabla_{\boldsymbol{\kappa}}\omega_\alpha|$, has the same role in (4.19). DOS is generally scaled, such that its integral gives the number of modes.

4.2.1 Phonon DOS for One-Dimensional Lattice and van Hove Singularities

The phonon frequency density of states $D_p(\omega)$ converts the number of phonons of wave number κ [similar to (2.99)] to those of frequency ω, using the dispersion relation (Figure 4.3). The conversion leads to singularities in $D_p(\omega)$ at Brillouin zone centers and edges.

Note that for a 2-D lattice, in (4.19) instead of $4\pi\kappa^2$, we have $2\pi\kappa$, and for 1-D lattice it is 2. Then $D_p(\kappa)_{2-D} = 2\pi\kappa \mathrm{d}\kappa/(2\pi)^2$. Similarly $D_p(\kappa)_{1-D} = 2\mathrm{d}\kappa/2\pi$. As an example, for the one-dimensional (chain) lattice we have considered, using (4.19), $D_p(\omega)$ becomes

$$\begin{aligned} D_p(\omega) &= \frac{1}{a}\frac{a}{2\pi}\sum_\alpha \frac{2\mathrm{d}\kappa}{\mathrm{d}\omega_\alpha} \\ &= \frac{1}{a}\sum_\alpha \frac{1}{[2\Gamma(\dfrac{1}{m_1}+\dfrac{1}{m_2})]^{1/2}} \frac{1}{|\dfrac{\mathrm{d}\omega_\alpha^*}{\mathrm{d}\kappa^*}|}. \end{aligned} \tag{4.22}$$

Then using (4.7) for ω^*, we have

$$\begin{aligned} \frac{\mathrm{d}\omega^*}{\mathrm{d}\kappa^*} &= \frac{1}{2}\{\frac{1 \pm [1-2m_1^*m_2^*(1-\cos\pi\kappa^*)]^{1/2}}{2}\}^{-1/2} \\ &\quad \times \frac{1}{4}[1-2m_1^*m_2^*(1-\cos\pi\kappa^*)]^{-1/2}(-2m_1^*m_2^*\pi\sin\pi\kappa^*), \end{aligned} \tag{4.23}$$

and

$$\begin{aligned} D_p^*(\omega^*) &= \frac{D_p(\omega)}{a^{-1}[2\Gamma(\dfrac{1}{m_1}+\dfrac{1}{m_2})]^{-1/2}} = \sum_\alpha \frac{1}{u_{p,g}^*(\omega_\alpha)} \\ &= 8|\{\frac{1 \pm [1-2m_1^*m_2^*(1-\cos\pi\kappa^*)]^{1/2}}{2}\}^{1/2} \\ &\quad \times [1-2m_1^*m_2^*(1-\cos\pi\kappa^*)]^{1/2}(2m_1^*m_2^*\pi\sin\pi\kappa^*)^{-1}|. \end{aligned} \tag{4.24}$$

Now with dispersion relation (4.7) again used [which is inverse of $\omega^*(\kappa^*)$] for $\kappa^*(\omega^*)$, (4.24) is graphed with D_p^* as a function of ω^*, in Figure 4.5, for $m_1^* = 0.5$ and 0.75. Note the lack of the optical branch for the case of $m_1^* = m_2^* = 0.5$. Also note the singularities (where the group velocity is zero) at the Brillouin zone points corresponding to $\omega_{\mathrm{LA}}(\mathrm{X})$ and $\omega_{\mathrm{LO}}(\mathrm{X})$, given by (4.11) and (4.12), for $m_1^* = 0.75$. There is also a singularity at Γ for the optical phonons corresponding to $\omega_{\mathrm{LO}}(\mathrm{L}) = \omega_{\mathrm{o}}$ (or $\omega_{\mathrm{o}}^* = 1$).

The DOS can also be given as $D_p(E_p)\mathrm{d}E_p$, with quasi-particle energy $E_p = \hbar\omega = \hbar u_{p,g}\kappa$. Then the energy Dirac delta function $\delta_{\mathrm{D}}[E - E_\alpha(\kappa')]$ is used.

In addition to the longitudinal displacement and vibration just discussed for a linear array of atoms, in three-dimensional lattice vibrations there are transverse displacements and vibrations. The transverse vibrations are presented by two mutually perpendicular planes and these vibrations also travel along the lattice. For each phonon acoustic and optical branch, there are three polarizations (one longitudinal and two transverse). So, per atom, we have three phonon modes, and for more than one atom per unit cell we have the first three being acoustic and the rest being

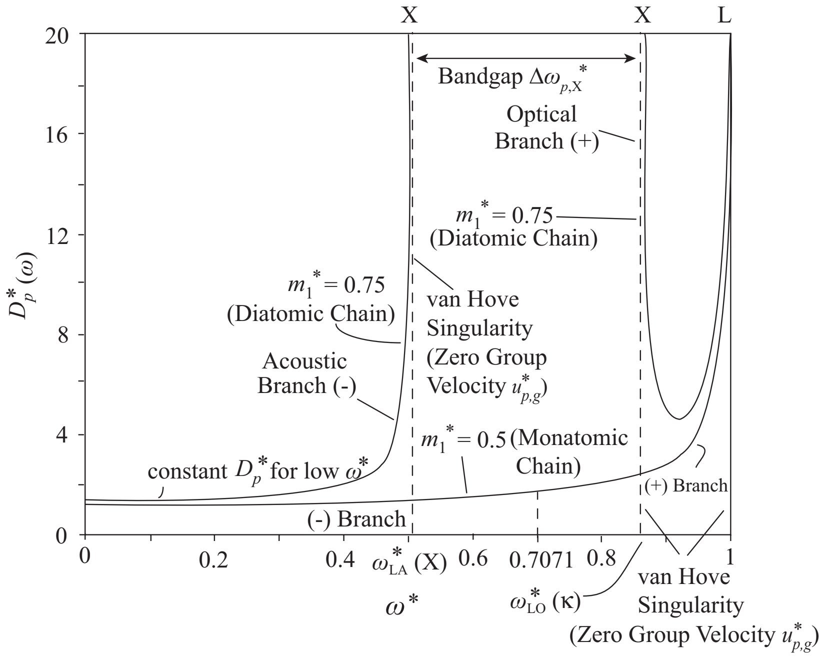

Figure 4.5. Dimensionless distribution of phonon DOS $D_p^*(\omega^*)$ as a function of dimensionless frequency for a linear, diatomic chain. Note that ω^* is the vertical axis in Figure 4.4 and the optical phonons are limited to high frequencies only.

optical phonons. Some of the characteristics of phonon modes are listed in Table 4.1. These include their external excitations. The total number of modes is three times the number of atoms per unit primitive cell. The number of optical modes is equal to this total minus 3 (for acoustic phonons).

4.2.2 Debye and Other Phonon DOS Models

For acoustic phonons, the case of linear dispersion relation at zone center ($\kappa \rightarrow 0$) corresponds to a constant phase velocity (which is also equal to the constant group velocity). This leads to the parabolic DOS (proportional to E_p^2), or the Debye model. In the simple Debye model, a constant phonon speed is used for each polarization (two transverse and one longitudinal), with a quantum-particle energy $E_p = \hbar\omega = \hbar u_{p,g}\kappa$.

From these, from (4.19) for three-dimensional $\boldsymbol{\kappa}$-space, we have the model form of the Debye DOS model

$$D_{p,\mathrm{D},\alpha}(\omega) = \frac{4\pi\kappa^2}{(2\pi)^3}\frac{1}{u_{p,g,\alpha}} = \frac{1}{2\pi^2}\frac{\omega^2}{u_{p,g,\alpha}^3}, \quad \frac{\mathrm{d}\omega}{\mathrm{d}\kappa} = u_{p,g,\alpha} = \frac{\omega}{\kappa} = u_{p,p,\alpha}$$

$$= \frac{1}{2\pi^2}\frac{E_p^2}{\hbar^2 u_{p,g,\alpha}^3}$$

polarized (modal), Debye DOS model with cut-off frequency ω_D. (4.25)

Table 4.1. *Characteristics of lattice-vibrational acoustic and optical polarizations.*

Characteristic	Acoustic polarization	Optical polarization
Group velocity	sound waves, constant for $\kappa \rightarrow 0$	smaller than acoustic mode
Displacement of adjacent atoms	in-phase	out-of-phase
Largest frequency	at the edge of Brillouin zone	higher than acoustic polarization
Density of states (per unit colume, per dω)	Debye model $D_{p,D,\alpha} = \frac{\omega^2}{2\pi^2 u^3_{p,g,\alpha}}$	Debye-Gaussian Model $D_{p,DG} = \mathrm{d}\omega^2 \exp[-(\frac{\omega - \omega_c}{\Delta\omega})^2]$
Phonon number density	$n_{p,\mathrm{A}} = \int f_p D_{p,\mathrm{A}}(\omega)\mathrm{d}\omega$	$n_{p,\mathrm{O}} = \int f_p D_{p,\mathrm{O}}(\omega)\mathrm{d}\omega$
Acoustic mode number density	$3n$ n is the atomic number density	$(3N_\mathrm{o} - 3)n$ N_o is number of atoms per primitive cell
Number of polarizations	two transverse and one longitudinal (per unit-cell lattice)	$3N_\mathrm{o} - 3$
f or ω versus λ or $1/\lambda = \kappa$ (dispersion relation)	longer-wavelength modes have smaller frequency, and for $\lambda \rightarrow \infty$ ($\kappa \rightarrow 0$), $\omega \rightarrow 0$	even long-wavelength modes have a finite frequency
External excitement	excited by microwave radiation	excited by infrared radiation (optical phonons cause time-varying electrical dipole moments)

Note that $E_p = \hbar\omega = \hbar u_{p,p,\alpha}\kappa$ in the Debye model represents a linear relation as compared to (2.94) for free electrons (parabolic relation).

Now assuming all modes (two transverse and one longitudinal-acoustic polarizations, Table 4.1) are the same, from the summation in (4.19), we have

$$D_{p,\mathrm{D}}(\omega) = \frac{3}{2\pi^2}\frac{\omega^2}{u^3_{p,\mathrm{A}}} \quad \text{simple Debye DOS model,} \tag{4.26}$$

where $u_{p,\mathrm{A}}$ is a single (average), modal acoustic-phonon speed. The units of D_p here are s/rad·m^3 and by adding $\hbar$ to the denominator it becomes 1/eV·m^3 or more commonly used 1/eV·Å^3

This is similar to the DOS for photons in vacuum (which also has a linear dispersion relation, with equal phase and group velocity, $u_{ph} = \omega/\kappa = \mathrm{d}\omega/\mathrm{d}\kappa$, Section 7.1), except there are only two transverse photon polarizations.

The Debye model $D_{p,\mathrm{D}}(\omega)$ is valid near the zone center, where the dispersion relation is linear (also called no dispersion) (because $\mathrm{d}\omega/\mathrm{d}\kappa$ is constant). It also assumes a cut-off angular frequency ω_D. This is generally from the experimentally determined Debye temperature T_D (using for example, variation of the average specific heat capacity of crystal with respect to temperature, as will be discussed in Section 4.7). The mean Debye temperature, for elemental crystals, is listed in Table A.2.

The polarized Debye temperature $T_{\mathrm{D},\alpha}$ for a monatomic crystal is related to the polarized cut-off frequency and in turn the polarized phonon group speed $u_{p,g,\alpha}$ (further discussed in Section 4.7.1) by

$$T_{\mathrm{D},\alpha} = \frac{\hbar\omega_{\mathrm{D},\alpha}}{k_\mathrm{B}} = \frac{\hbar}{k_\mathrm{B}} u_{p,g,\alpha}(6\pi^2 n)^{1/3} \text{ Debye polarization temperature,} \qquad (4.27)$$

where $u_{p,g,\alpha}$ is as previously defined and n is the atomic number density (1/m^3). The value of T_D for elements is listed in Table A.2. For some compounds, T_D is given in Figure 4.26. We will use the Debye DOS and temperature in Section 4.7, and where $u_{p,\mathrm{A}}$ is also defined. Debye temperature corresponds to activation of all phonons (including highest energy $\hbar\omega_\mathrm{D}$).

For the case of a simplified model of a single phonon speed, the Debye cut-off frequency is related to the average acoustic-phonon speed $u_{p,\mathrm{A}}$ through (as will be shown in Section 4.7.1)

$$\omega_\mathrm{D} = (6\pi^2 n u_{p,\mathrm{A}}^3)^{1/3} = (6\pi^2 n)^{1/3} u_{p,\mathrm{A}} \text{ Debye cut-off frequency.} \qquad (4.28)$$

In Section 2.5.3, we compared the Debye and natural frequency ω_n for Ar FCC and found a good agreement. Examples of the Debye DOS model, and comparison with experimental results, will be given in Figures 4.11 and 4.41(a).

Other phonon DOS models are also available, one example is the Debye–Gaussian model, i.e.,

$$D_p(E_p) = CE_p^2 \exp[-(\frac{E_p - E_{p,c}}{\Delta E_p})^2] \text{ Debye–Gaussian phonon DOS,} \qquad (4.29)$$

where C is a normalization constant, $E_{p,c}$ is energy at the center of the DOS, and ΔE_p is the width of the distribution. Note that $D_p(E_p) = D_p(\omega)\partial\omega/\partial E_p$. At low E_p, this behaves similarly to the Debye, and near the center behaves similarly to a Gaussian distribution. This also avoids the appearance of a cut-off frequency. This model preserves the optical phonons and is used in applications such as the anti-Stokes luminescence (Section 7.12) and in examining the size effects on $D_p(E_p)$ in Section 4.19.3. An example is given in Section 4.6.

Phonon dispersion models will be discussed in Sections 4.9.5. These include the so-called sine model.

4.3 Reciprocal Lattice, Brillouin Zone, and Primitive Cell and Its Basis

In the discussion of phonon energy $\hbar\omega$ and its dispersion relation $\omega(\boldsymbol{\kappa})$, we defined the lattice structure by using a lattice constant, and we noted that the dispersion relation exposed special symmetries in the $\boldsymbol{\kappa}$-space, which has a relation with the inverse (or reciprocal) of the lattice. We now proceed to generalize these symmetries to three-dimensional lattices.

An ideal crystal is constructed by the infinite repetition of identical structural units. In the simplest crystals the structural unit is a single atom. The structure of a crystal is defined in terms of a lattice with the structural unit or basis attached to each lattice point. The lattice points form a set such that the structure is the same as seen from each point. An ideal crystal is described by three fundamental translation vectors, $\boldsymbol{l}_1$, $\boldsymbol{l}_2$, and $\boldsymbol{l}_3$ (also called primitive vectors of the crystal lattice). If there is a lattice point represented by the position vector $\boldsymbol{x}$, there is then also a lattice point represented by the position vector $\boldsymbol{x}'$, i.e.,

$$\boldsymbol{x}' = \boldsymbol{x} + \boldsymbol{l} = \boldsymbol{x} + i\boldsymbol{l}_1 + j\boldsymbol{l}_2 + k\boldsymbol{l}_3 \quad \text{primitive lattice vectors,} \tag{4.30}$$

where i, j, and k are arbitrary integers. If all pairs of lattice points $\boldsymbol{x}'$ and $\boldsymbol{x}$ are given by (4.30), then the lattice is called primitive.

There are 14 possible Bravais lattices in three-dimensional space, arrived at by combining one of the seven lattice systems (or axial systems) with one of the lattice centerings. Each Bravais lattice refers to a distinct lattice type. The seven lattice systems are: triclinic, monoclinic, orthohombic, tetragonal, rhombohedral, hexagonal, and cubic.

Figures 4.6(a), (c) and (e) show the primitive lattice vectors $\boldsymbol{l}_1$, $\boldsymbol{l}_2$, and $\boldsymbol{l}_3$, for the three cubic lattice structures, simple cubic (SC), face-centered cubic (FCC), and body-centered cubic (BCC).

4.3.1 Reciprocal Lattice

As we noted from Figure 4.4, the periodicity of the dispersion relation (and other associated symmetries) is conveniently presented when the wave number is scaled with the inverse of the interatomic (or interplanar) spacing. For a cubic lattice of lattice constant a, this scale is $2\pi/a$ and is called the reciprocal lattice constant, and, when specified along a direction, it is the reciprocal lattice vector $\boldsymbol{g}$. The primitive (the actual atomic locations) and reciprocal (wave vector or momentum vector) space lattices are shown in Figure 4.6 for a two-atom lattice (SC, FCC, and BCC). Because a Fourier transform is used to convert the physical space results (i.e., MD simulations) to the reciprocal lattice space, the latter is also called the Fourier space. From the solution to the lattice atom displacement of (4.3), and noting the symmetries in the $\boldsymbol{\kappa}$-space, we note that the reciprocal lattice vectors satisfy $\exp[i(\boldsymbol{g}\cdot\boldsymbol{l})] = 1$, and is the Bravais lattice mentioned above. From solutions (4.3) and (4.4) to lattice displacement, we note how κ takes on discrete values of $\boldsymbol{g}$. For the translational vectors in (4.30), the three reciprocal lattice vectors $\boldsymbol{g}_1$, $\boldsymbol{g}_2$, and $\boldsymbol{g}_3$ are defined as $[\boldsymbol{g}_1\boldsymbol{g}_2\boldsymbol{g}_3]^T = 2\pi[\boldsymbol{l}_1\boldsymbol{l}_2\boldsymbol{l}_3]^{-1}$ [245]

$$\begin{aligned}
\boldsymbol{g}_1 &= 2\pi\frac{\boldsymbol{l}_2\times\boldsymbol{l}_3}{\boldsymbol{l}_1\cdot\boldsymbol{l}_2\times\boldsymbol{l}_3}, \quad e^{i\boldsymbol{g}_i\cdot\boldsymbol{l}_i} = 1\\
\boldsymbol{g}_2 &= 2\pi\frac{\boldsymbol{l}_3\times\boldsymbol{l}_1}{\boldsymbol{l}_1\cdot\boldsymbol{l}_2\times\boldsymbol{l}_3}\\
\boldsymbol{g}_3 &= 2\pi\frac{\boldsymbol{l}_1\times\boldsymbol{l}_2}{\boldsymbol{l}_1\cdot\boldsymbol{l}_2\times\boldsymbol{l}_3} \quad \text{primitive reciprocal-lattice vectors,}
\end{aligned} \tag{4.31}$$

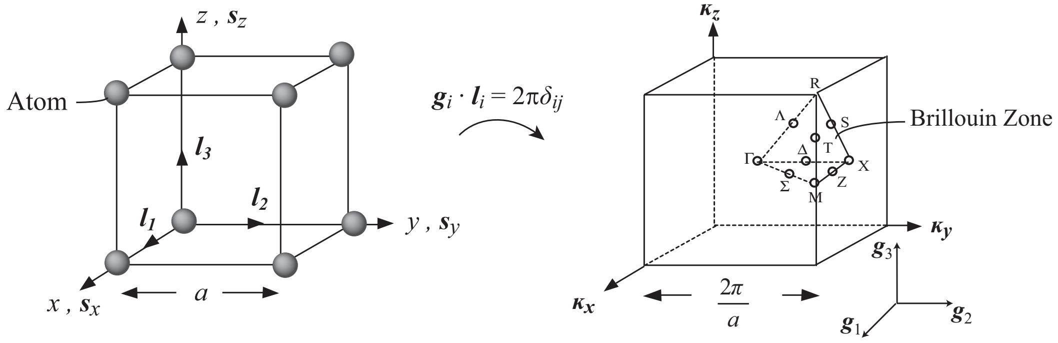

(a) Primitive Lattice Vectors in Simple Cubic (SC) Lattice

(b) Reciprocal Lattice Space and Brillouin Zones in SC

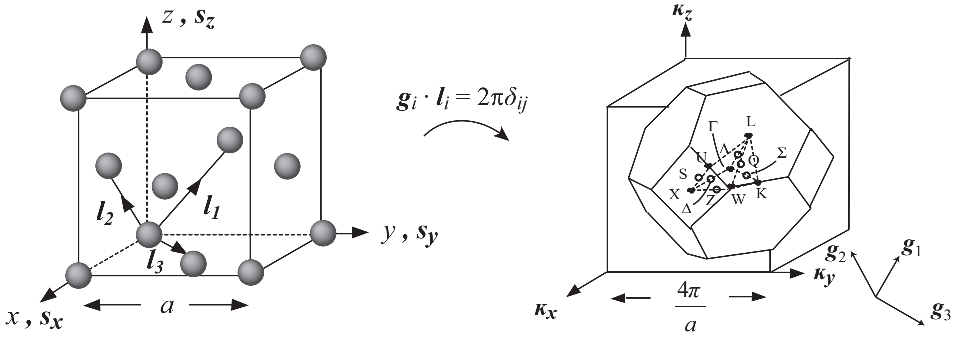

(c) Primitive Lattice Vectors in Face-Centered Cubic (FCC) Lattice

(d) Reciprocal Lattice Space and Brillouin Zones in FCC

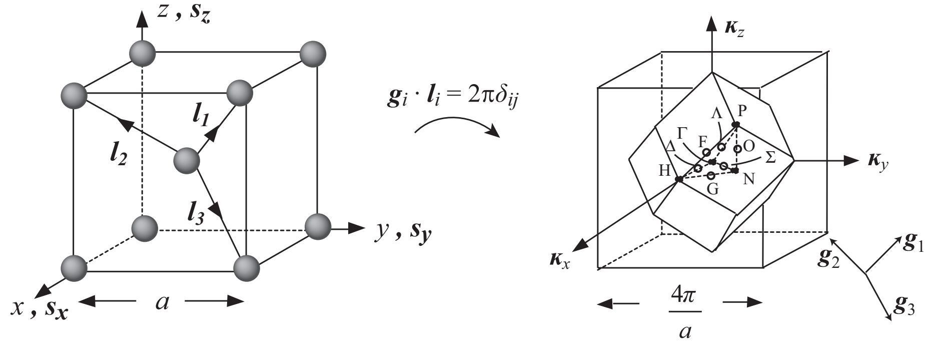

(e) Primitive Lattice Vectors in Body-Centered Cubic (BCC) Lattice

(f) Reciprocal Lattice Space and Brillouin Zones in BCC

Figure 4.6. The cubic lattices. (a) SC, (c) FCC, and (e) BCC The primitive translation vectors $\boldsymbol{l}_1, \boldsymbol{l}_2$, and $\boldsymbol{l}_3$ are also shown for each lattice. The Brillouin zone for cubic lattices are shown by (b) SC, (d) FCC, (f) BCC. The irreducible part of the zone is also shown. The Brillouin zone of BCC is identical to that for the diamond/zinc-blende structure crystals. $\boldsymbol{g}$ is the reciprocal lattice vector. δ_{ij} is the Kronecker delta.

in $\boldsymbol{g}$ space, the space defined by $\alpha \boldsymbol{g}_1 + \beta \boldsymbol{g}_2 + \gamma \boldsymbol{g}_3$, where α, β, and γ are arbitrary integers. The reciprocal lattice is a lattice in the Fourier space associated with the crystal. The diffraction pattern of a crystal maps the reciprocal lattice [245]. †

4.3.2 Brillouin Zone

Each of the $\boldsymbol{g}_i$ is orthogonal to two $\boldsymbol{l}_i$, such that $\boldsymbol{g}_i \cdot \boldsymbol{l}_i = 2\pi \delta_{ij}$, where δ_{ij} is the Kronecker delta. As noted in Section 4.1, in the propagation of lattice vibrations through a crystal lattice, the phonon frequency is a periodic function of the wave vector $\boldsymbol{\kappa}$, $\omega(\boldsymbol{\kappa}) = \omega(\boldsymbol{\kappa} + \boldsymbol{g})$, as shown in Figure 4.4. This function can be multivalued, i.e., it has more than one branch. Discontinuities may also occur. As we also noted, a zone in the $\boldsymbol{\kappa}$-space is defined that forms the fundamental periodic region, such that the frequency or energy for a $\boldsymbol{\kappa}$ outside this region may be determined based on those within it. This region is known as the Brillouin zone (Figure 4.3) (sometimes called the first or the central Brillouin zone). In general we consider only $\boldsymbol{\kappa}$ values inside the zone. Discontinuities occur only on its boundaries. If the zone is repeated indefinitely, all $\boldsymbol{\kappa}$-space will be filled. The first Brillouin zone is defined to be the primitive cell of the reciprocal lattice, and is the set of points in the $\boldsymbol{\kappa}$-space that can be reached from the origin without crossing any Bragg plane. A Bragg plane for two points in a lattice is the plane that is perpendicular to the line between the two points and passes through the bisector of that line. The second Brillouin zone is the set of points that can be reached from the first zone by crossing only one Bragg plane. For adjacent Brillouin zones, the numbered $(n+1)$th Brillouin zone is the set of points not in the $(n-1)$th zone that can be reached from the nth zone by crossing $n-1$ Bragg planes.

Figures 4.6(b), (d), and (f) show the reciprocal space lattices, and the Brillouin zone planes and points designations are shown for the three lattices.

For an SC lattice, the primitive lattice (transition) vectors are $\boldsymbol{l}_1 = a\boldsymbol{s}_x, \boldsymbol{l}_2 = a\boldsymbol{s}_y$, and $\boldsymbol{l}_3 = a\boldsymbol{s}_z$. The boundaries of the first Brillouin zones are the planes normal to the six reciprocal lattice vectors, $\pm\boldsymbol{g}_1$, $\pm\boldsymbol{g}_2$, and $\pm\boldsymbol{g}_3$, i.e.,

$$\pm\frac{1}{2}\boldsymbol{g}_1 = \pm\frac{\pi}{a}\boldsymbol{s}_x,\ \pm\frac{1}{2}\boldsymbol{g}_2 = \pm\frac{\pi}{a}\boldsymbol{s}_y,\ \pm\frac{1}{2}\boldsymbol{g}_3 = \pm\frac{\pi}{a}\boldsymbol{s}_z,$$

$$\boldsymbol{g}_1 = \frac{2\pi}{a}\boldsymbol{s}_x,\ \boldsymbol{g}_2 = \frac{2\pi}{a}\boldsymbol{s}_y,\ \boldsymbol{g}_3 = \frac{2\pi}{a}\boldsymbol{s}_z, \qquad (4.32)$$

where $\boldsymbol{s}_i$ are the Cartesian unit vectors. These six Brillouin zone planes bound a cube of volume $(2\pi/a)^3$, i.e., reciprocal lattice is also SC. This is shown in Figure 4.6(b).

---

† The geometrical structural factor $S_{\mathbf{g}}$ is a measure of order (lattice) and is defined as [245]

$$S_G = \sum_j e^{i\boldsymbol{g}\cdot\boldsymbol{x}_j},$$

where $\boldsymbol{x}_j$ is the equilibrium atomic position vector. It is a measure of the order (lattice), and expresses the extent of the interference of waves scattered from atoms (ions). For completely disorder structure, $S_{\mathbf{g}} = 0$, and for lattice $\boldsymbol{x}_j$ is given by (4.30), and $S_G = 1$.

For an FCC lattice, the primitive and reciprocal lattice vectors are

$$\begin{aligned}
&\boldsymbol{l}_1 = \frac{a}{2}(\boldsymbol{s}_y + \boldsymbol{s}_z),\ \boldsymbol{l}_2 = \frac{a}{2}(\boldsymbol{s}_x + \boldsymbol{s}_z),\ \boldsymbol{l}_3 = \frac{a}{2}(\boldsymbol{s}_x + \boldsymbol{s}_y)\\
&\boldsymbol{g}_1 = \frac{2\pi}{a}(-\boldsymbol{s}_x + \boldsymbol{s}_y + \boldsymbol{s}_z)\\
&\boldsymbol{g}_2 = \frac{2\pi}{a}(\boldsymbol{s}_x - \boldsymbol{s}_y + \boldsymbol{s}_z)\\
&\boldsymbol{g}_3 = \frac{2\pi}{a}(\boldsymbol{s}_x + \boldsymbol{s}_y - \boldsymbol{s}_z).
\end{aligned} \tag{4.33}$$

The volume of the reciprocal lattice cell is $4(2\pi/a)^3$. The FCC Brillouin zone is a truncated octahedron bounded by

$$\boldsymbol{g} = \frac{2\pi}{a}(\pm\boldsymbol{s}_x \pm \boldsymbol{s}_y \pm \boldsymbol{s}_z), \tag{4.34}$$

which for the octahedron and its corners, can be presented as having been cut with six planes given by

$$\frac{2\pi}{a}(\pm 2\boldsymbol{s}_x),\ \frac{2\pi}{a}(\pm 2\boldsymbol{s}_y),\ \frac{2\pi}{a}(\pm 2\boldsymbol{s}_z). \tag{4.35}$$

These planes are shown in Figure 4.6(d). Reciprocal lattice to FCC lattice is a BCC lattice.

The BCC lattice with cubic cell side a has an FCC reciprocal lattice with cubic cell side $4\pi/a$. This is shown in Figure 4.6(f).

The high symmetry points and lines in the $\boldsymbol{\kappa}$ space have been designated by symbols. Γ is the center of the Brillouin zone. In SC, M is center of an edge and R is a corner point. In FCC, K is in middle of an edge joining two hexagonal faces, U is the middle of an edge joining a hexagonal and a square face, and W is a corner point. In BCC, H is a corner point joining four edges, N is center of a face, and P is corner point joining three edges.

For example, the center Γ point is [0,0,0] in the $\boldsymbol{\kappa}$-space. The first Brillouin boundary point is designated by X (center of square face), and in an FCC crystal it is at $[2\pi/a,0,0]$ in the $\boldsymbol{\kappa}$-space and indicates cyclic permutation of the axes. Another symmetry point in FCC is L (center of hexagonal face) at $[\pm\pi/a, \pm\pi/a, \pm\pi/a]$, and this and X and Γ are shown in Figure 4.6(d). W is also a corner point. Δ, Λ and Σ are lines connecting Γ and X, Γ and L, and Γ and K. The points of symmetry in the $\boldsymbol{\kappa}$ space are also important for electrons in semiconductors, because similar to phonons having $E_p = \hbar\omega_p(\boldsymbol{\kappa})$, electrons are represented by $E_e = E_e(\boldsymbol{\kappa})$.

4.3.3 Primitive Cell and Its Basis: Number of Phonon Branches

The real-space primitive cell is a volume of real space that when translated fills all of the space without overlapping or leaving any voids. A primitive cell contains one lattice point and its atomic basis. So, basis is the congruent group of atoms located at each lattice point. The number of atoms in the basis determines the number of branches in the dispersion relation. The number of branches (three acoustic branches and the rest optical branches) are three times the number of atoms in the basis $N_\circ$, i.e., $3N_\circ$ branches. One of the properties of a lattice is that any lattice point is close to its nearest neighbor and has the same number of nearest neighbors, and this is the coordination number.

Monatomic SC, FCC, and BCC primitive cell structures [Figure 2.12(a)] such as Al (FCC) have only one atom in the primitive cell and this results in only three branches in the dispersion relation (acoustic only). Most metals form BCC (e.g., Li, Na, K, Ba, Cr, Mo), FCC (e.g., Pt, Cu, Ag, Au), or HCP (hexagonal close packed). The zinc-blende lattice [similar to diamond lattice, Figure 2.9(b)] such as C, Ge, Si and GaAs, InP, InAs have two atoms (in C, Ge, and Si, crystals, the two atoms are identical with four sp^3 bonds and it is called diamond lattice) in their basis, so there are total of six branches (three acoustic and three optical). SiO_2 crystal (quartz), shown in Figure 2.9(a), has nine atoms (Si_3O_6) in the tetrahedra-based anisotropic primitive cell, so it has 27 branches (3 acoustic and 24 optical).

Table A.2 gives the crystal structures of elements (e.g., FCC, tetrogonal, orthorhombic, rhombohedral, monoclinic), as well as the lattice constant(s).

4.4 Normal Modes and Dynamical Matrix

Along the lines developed in Section 4.1, in three-dimensional lattice-dynamics calculations, a frequency-space description is used for the motions of the atoms. Instead of the localized motions of individual atoms, the system is described by energy waves with given wave vector $\boldsymbol{\kappa}$, frequency ω, and polarization vector $\boldsymbol{e}_\alpha$. The formulation of lattice-dynamics theory is described in [12] and [516].

For an equilibrium potential energy, defined by (2.47), of a system with N atoms that is designated by $\langle\varphi\rangle_\mathrm{o}$, atom i is moved by an amount $\boldsymbol{d}_i$, and the resulting energy of the system, $\langle\varphi\rangle$, the total potential energy, is found by a Taylor series expression around the equilibrium state (small displacement of all atoms) as

$$\begin{aligned}\langle\varphi\rangle &= \langle\varphi\rangle_\mathrm{o} + \sum_i\sum_\alpha \frac{\partial\langle\varphi\rangle}{\partial d_{i\alpha}}|_\mathrm{o} d_{i\alpha} + \frac{1}{2}\sum_{i,j}\sum_{\alpha,\beta}\frac{\partial^2\langle\varphi\rangle}{\partial d_{i\alpha}\partial d_{j\beta}}|_\mathrm{o} d_{i\alpha}d_{j\beta} \\ &+ \frac{1}{6}\sum_{i,j,k}\sum_{\alpha,\beta,\gamma}\frac{\partial^3\langle\varphi\rangle}{\partial d_{i\alpha}\partial d_{j\beta}\partial d_{k\gamma}}|_\mathrm{o} d_{i\alpha}d_{j\beta}d_{k\gamma} + \cdots + \\ &\equiv \langle\varphi\rangle_\mathrm{o} + \frac{1}{2}\sum_{i,j}\sum_{\alpha,\beta}\Gamma_{\alpha\beta}d_{i\alpha}d_{j\beta} + \mathrm{O} \\ &\text{harmonic approximation and spring constant } \Gamma_{\alpha\beta}, \end{aligned} \tag{4.36}$$

where the i, j, and k sum over the atoms in the system (when including anharmonicity, for third-order interactions and for pair potentials, $i = j = k$ or $i = j$ or $j = k$), and the α, β, and γ sums are over the x, y, and z directions, as shown in Figure 2.12(d). Both $\langle\varphi\rangle$ and $\langle\varphi\rangle_{\mathrm{o}}$ are only functions of the atomic positions. The first derivative of the potential energy with respect to each of the atomic positions is the negative of the net force acting on that atom. Evaluated at equilibrium, this term is zero. The first nonnegligible term in the expansion is thus the second-order term. The harmonic approximation is made by truncating the Taylor series at the second-order term. For a given i and j, the nine elements of the form $\partial^2\langle\varphi\rangle/\partial d_{i\alpha}\partial d_{j\beta}$ make up the force-constant matrix. Γ was introduced in (2.54), when the natural frequency was defined.

The harmonic approximation is valid for small displacements ($d_{i\alpha} \ll r_{nn}$) about the zero-temperature minimum and corresponds to the well minimum (Figure 2.3). Raising the temperature will cause deviations, making it anharmonic.

Given the crystal structure of a material, the determination of the allowed wave vectors (whose extent in the wave vector-space makes up the first Brillouin zone) is now addressed.

Consider a general crystal with an n-atom unit cell, such that the displacement of the jth atom in the lth unit cell is denoted by $\boldsymbol{d}(jl,t)$. The force-constant matrix [made up of the second order derivatives in (4.36)] between the atom (jl) and the atom $(j'l')$ is denoted by $\boldsymbol{\Gamma}\binom{jj'}{ll'}$. The indices are shown in Figure 2.12(d). Note that this matrix is defined for all atom pairs, including the case of $j = j'$ and $l = l'$. Imagine that the atoms in the crystal are all joined by harmonic springs; the equation of motion (Table 2.5), written in terms of displacement, for the atom (jl) can be written as [the general form of (4.1)]

$$m_j \frac{\mathrm{d}^2\boldsymbol{d}(jl,t)}{\mathrm{d}t^2} = -\sum_{j'l'} \boldsymbol{\Gamma}\begin{pmatrix} jj' \\ ll' \end{pmatrix} \cdot \boldsymbol{d}(j'l',t) \text{ harmonic approximation,} \tag{4.37}$$

subject to a suitable cut-off radius (Figure 2.3)[†].

In (4.3), the modal displacement was given as a function of $\boldsymbol{\kappa}$, and to account for all modes (which are called the normal modes of vibration), we will use summation over $\boldsymbol{\kappa}$ space and also on the branches. For a system made of N atoms, there are $3N$ normal modes ($3N$ oscillator system) represented by $\boldsymbol{\kappa}$ and α.

[†] Similarly, the lattice potential energy is given as (Tables 2.4 and 2.5)

$$E_{p,p} = \langle\varphi\rangle = \frac{1}{2}\sum_{jj',ll'} \varphi\begin{pmatrix} jj' \\ ll' \end{pmatrix},$$

which is a form of writing $\varphi_{jl-j'l'}$, etc., (Figure 2.12).
The harmonic displacement (kinetic) energy is

$$E_{p,k} = \frac{1}{2}\sum_{jj',ll'}\sum_{\alpha,\beta} d_\alpha(jl)\Gamma_{\alpha\beta}d_\beta(j'l').$$

Now assume that the displacement of an atom can be written as a summation over the normal modes [using the form given by (4.3)] of the system, such that

$$\boldsymbol{d}(jl,t)=\sum_{\boldsymbol{\kappa},\alpha}\boldsymbol{s}_\alpha(j,\boldsymbol{\kappa},\alpha)\exp\{i[\boldsymbol{\kappa}\cdot\boldsymbol{l}(jl)]\}\exp[-i\omega(\boldsymbol{\kappa},\alpha)t] \quad \text{plane-wave displacement} \tag{4.38}$$

where $\boldsymbol{s}_\alpha(\boldsymbol{\kappa})$ is the unit normal coordinate vector [such that $\sum_{\alpha,\kappa}\boldsymbol{s}_\alpha(\boldsymbol{\kappa})\cdot\boldsymbol{s}_\alpha(\boldsymbol{\kappa})=N$], and $\boldsymbol{x}(jl)$ is the equilibrium location of atom jl. This equation expresses how this atom moves under the influence of $(\boldsymbol{\kappa},\alpha)$.

At this point, the wave vector is known, but the frequency and polarization vector are not (these are given by the dispersion relation). Note that the index k introduced in (4.36) has been replaced with $(\boldsymbol{\kappa},\alpha)$. The polarization vector and frequency are both functions of the wave vector and the dispersion branch, denoted by α. Substituting (4.38) and its second derivative into the equation of motion leads to the eigenvalue equation [similar to (4.5)]

$$\boldsymbol{M}\omega^2(\boldsymbol{\kappa},\alpha)\boldsymbol{s}_\alpha(\boldsymbol{\kappa})=\boldsymbol{D}(\boldsymbol{\kappa})\boldsymbol{s}_\alpha(\boldsymbol{\kappa})$$

$$\text{equation of motion for a plane wave using dynamical matrix,} \tag{4.39}$$

where $\boldsymbol{M}$ is the diagonal mass matrix $(m_1, m_2,\ldots)$, the mode frequencies are the square roots of the eigenvalues, and the polarization vectors are the eigenmodes. They are obtained by diagonalizing the matrix $\boldsymbol{D}(\boldsymbol{\kappa})$, which is known as the dynamical matrix, and has size $3n\times 3n$ (n is the number of atoms per unit cell). It can be broken down into 3×3 blocks (each for a given jj' pair), which will have elements [117]

$$D_{\alpha\beta}(jj',\boldsymbol{\kappa})=\sum_{l'}\Gamma_{\alpha\beta}\begin{pmatrix} jj' \\ ll'\end{pmatrix}\exp\{i\boldsymbol{\kappa}\cdot[\boldsymbol{l}(j'l')-\boldsymbol{l}(jl)]\} \quad \text{harmonic dynamical matrix,} \tag{4.40}$$

where we used the indices as in (4.36), and the sum is over the unit cells.

The dynamical matrix uses the dot product of the wave vector and the position vectors of the atoms in periodic primitive cells to express an infinite number of atoms by a set of linear, homogeneous equations. The nontrivial solution of the dispersion relation containing the dynamical matrix gives the eigenvalues. The dynamical matrix has the two symmetry properties discussed in [117], which ensure that its eigenvalues are real. The dynamical matrix is central to the lattice-dynamics analysis.

For the L–J monatomic crystal phase, the dynamical matrix has size 3×3. Each wave vector will therefore have three modes associated with it (Figure 4.7). Given the equilibrium atomic positions and the interatomic potential, the frequencies and polarization vectors can be found by substituting the wave vector into the dynamical matrix and diagonalizing. Although this calculation can be performed for any wave vector, it is important to remember that only certain values are relevant to the analysis of the MD simulation cell. The phonon dispersion curves are obtained by plotting the normal-mode frequencies as functions of the wave number in different directions.

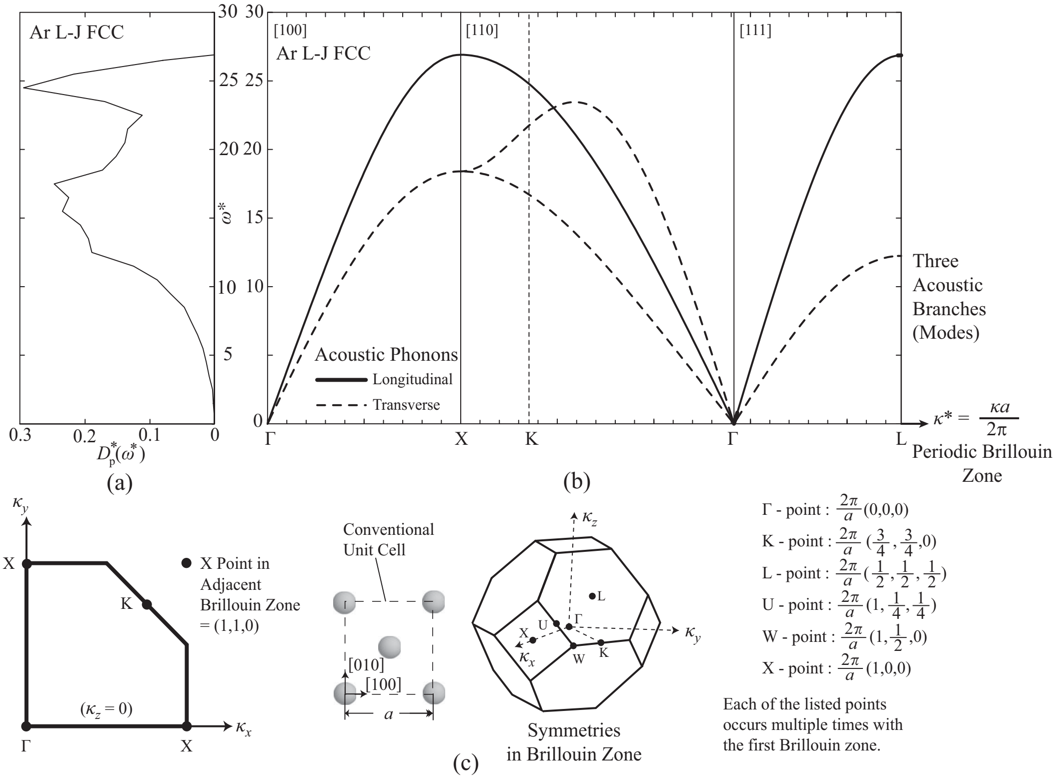

(a) (b) (c)

Figure 4.7. (a) DOS, (b) phonon dispersion for the Ar L–J FCC crystal [317], and (c) the directional designation and the Brillouin zone.

The Γ-point slope of the longitudinal branch is larger than the transverse polarization, because the Young modulus is larger than the shear modulus (Table 3.11). The dispersion relation is further developed because of some of the properties of $\boldsymbol{D}(\boldsymbol{\kappa})$ [12]. $\boldsymbol{D}(\boldsymbol{\kappa})$ is an even function of $\boldsymbol{\kappa}$, a real matrix, and is symmetric. Thus, it has three eigenvectors, $\boldsymbol{s}_1$, $\boldsymbol{s}_2$, and $\boldsymbol{s}_3$, which satisfy

$$\boldsymbol{D}(\boldsymbol{\kappa})\boldsymbol{s}_\alpha(\boldsymbol{\kappa}) = \lambda_\alpha(\boldsymbol{\kappa})\boldsymbol{s}_\alpha(\boldsymbol{\kappa}) \qquad \text{eigenvalues, } \alpha \text{ is polarization.} \tag{4.41}$$

The formulation of [12] does not include the mass matrix in $\boldsymbol{D}(\boldsymbol{\kappa})$, and the corresponding force-displacement equation will be discussed in Section 4.8. The three normal modes of wave-number vector $\boldsymbol{\kappa}$ will have polarization $\boldsymbol{s}_\alpha$ and frequency $\omega_\alpha(\boldsymbol{\kappa})$.

For a unit cell of $N_\circ$ atoms, the matrix $\boldsymbol{D}(\boldsymbol{\kappa})$ is $3N_\circ \times 3N_\circ$, and there are $3N_\text{o}$ frequencies for each discrete value of $\boldsymbol{\kappa}$. Then care must be made in distinction of the restricted phonon branches in the polyatomic lattices, such as SiO_2 in Figure 4.8.

Then the dispersion relation becomes [12]

$$\omega_\alpha(\boldsymbol{\kappa}) = [\frac{\lambda_\alpha(\boldsymbol{\kappa})}{M}]^{1/2} \text{ dispersion relation.} \tag{4.42}$$

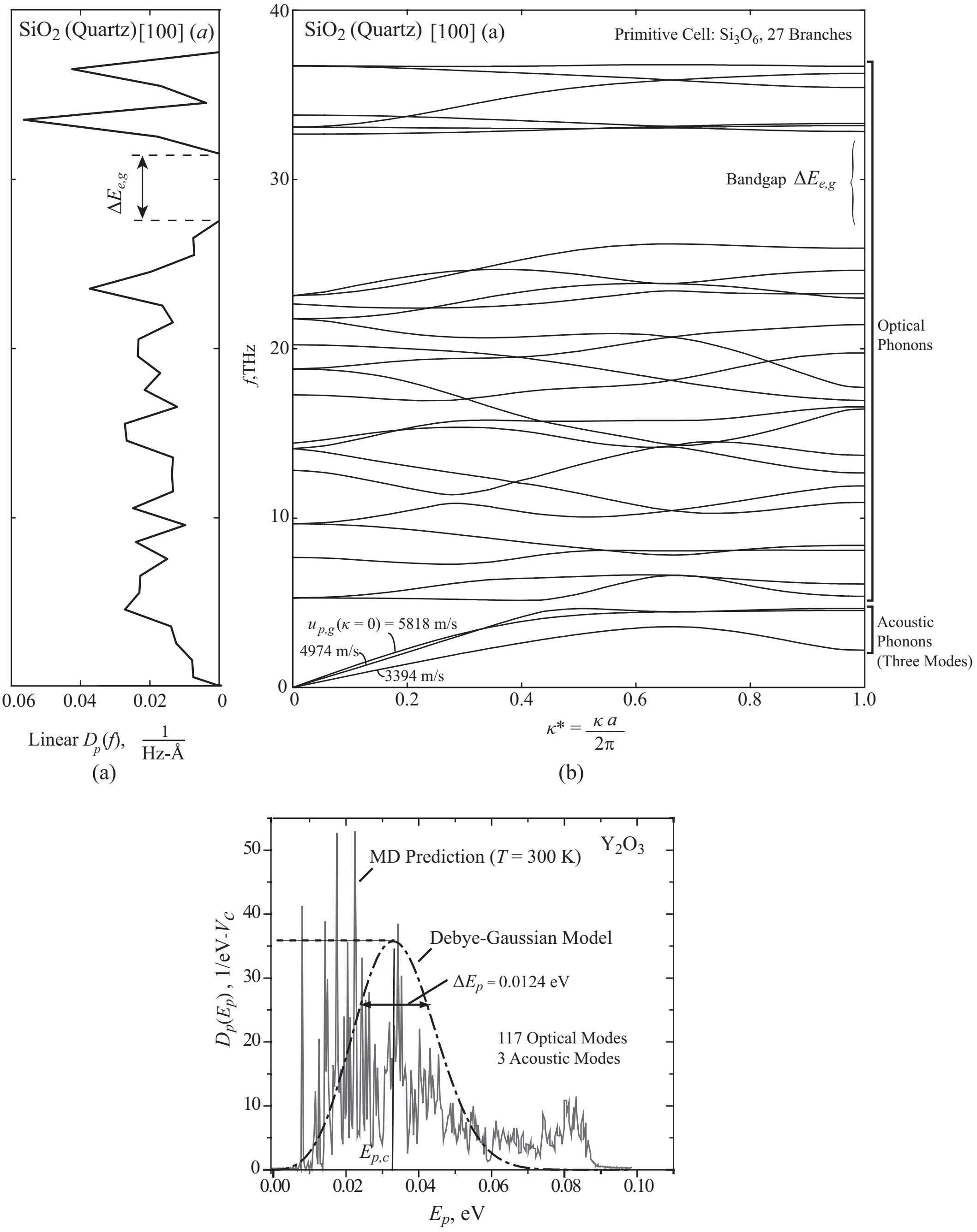

(a) (b)

(c)

Figure 4.8. (a) Phonon DOS, and (b) phonon dispersion for quartz (SiO_2) in the [100](a) direction at $T = 0$ K [315]. The anisotropic structure is given in Figure 2.9(a). The unit-cell structure of quartz is Si_3O_6 and there 27 phonon branches (modes). The phonon group velocity near the Brillouin zone center, for the three acoustic modes, are also shown. (c) Example of Debye–Gassian phonon DOS model used for Y_2O_3 crystal. V_c is the unit-cell volume [238].

In summary, in a monatomic $N_o = 1$ cubic lattice of lattice constant a, the discrete values that $\boldsymbol{\kappa}$ (normal modes) take on are (2.96)

$$|\boldsymbol{\kappa}| = \frac{2\pi i}{Na}, \quad i = 0, \pm 1, \pm 2, ..., \pm(N-1) \text{ normal modes}, \tag{4.43}$$

where N is the number of unit cells in the system. This leads to $3N$ total vibration modes (N longitudinal and $2N$ transversal), or $N_{p,m}$.

4.5 Quantum Theory of Lattice Vibration

It can be shown that the classical Hamiltonian of Table 2.5, which is applicable to each atom (center of mass) in a crystal lattice, has a general solution. This can be cast in terms of phonon annihilation and creation operators [12, 117, 167].

The Hamiltonian (Table 2.5) is given in terms of the dynamical matrix (4.40) as

$$\mathrm{H}_p = \sum_{\boldsymbol{x}} \frac{1}{2m} p^2(\boldsymbol{x}) + \frac{1}{2} \sum_{\boldsymbol{x},\boldsymbol{x}'} d_i(\boldsymbol{x}) D_{ij}(\boldsymbol{x} - \boldsymbol{x}') d_j(\boldsymbol{x}'). \tag{4.44}$$

Then with the solution to the dispersion relation, which gives $\omega_\alpha(\boldsymbol{\kappa})$, the phonon annihilation operator (footnote of Section 2.6.4 and the Glossary under creation and annihilation operators) is defined as

$$b_{\boldsymbol{\kappa},\alpha} = \frac{1}{N^{1/2}} \sum_{\boldsymbol{x}} e^{-i(\boldsymbol{\kappa}\cdot\boldsymbol{x})} \boldsymbol{s}_\alpha(\boldsymbol{\kappa}) \cdot [(\frac{m\omega_\alpha}{2\hbar})^{1/2} \boldsymbol{d}(\boldsymbol{x}) + i(\frac{1}{2\hbar m\omega_\alpha})^{1/2} \boldsymbol{p}(\boldsymbol{x})], \tag{4.45}$$

where N is the number of normal modes divided by α.

The annihilation operator is similar to the ladder operator defined in Section 2.6.5 footnote. Note that $\boldsymbol{s}_\alpha(\boldsymbol{\kappa})$ is the unit vector in the normal coordinates. One property of this is that $\sum_{\alpha,\boldsymbol{\kappa}} \boldsymbol{s}_\alpha(\boldsymbol{\kappa}) \cdot \boldsymbol{s}_\alpha(\boldsymbol{\kappa})$ is equal to N.

Similarly, the phonon creation operator is defined as

$$b^\dagger_{\boldsymbol{\kappa},\alpha} = \frac{1}{N^{1/2}} \sum_{\boldsymbol{x}} e^{i(\boldsymbol{\kappa}\cdot\boldsymbol{x})} \boldsymbol{s}_\alpha(\boldsymbol{\kappa}) \cdot [(\frac{m\omega_\alpha}{2\hbar})^{1/2} \boldsymbol{d}(\boldsymbol{x}) - i(\frac{1}{2\hbar m\omega_\alpha})^{1/2} \boldsymbol{p}(\boldsymbol{x})]. \tag{4.46}$$

Then the displacement $\boldsymbol{d}(\boldsymbol{x})$ and momentum $\boldsymbol{p}(\boldsymbol{x})$ are expressed by use of the properties of ladder operators $b_{\boldsymbol{\kappa},\alpha}$ and $b^\dagger_{\boldsymbol{\kappa},\alpha}$ (footnote of Section 2.6.4), as the new variables. This gives (the expression in terms of the normal coordinates will be given in Section 5.15.1)

$$\boldsymbol{d}(\boldsymbol{x}) = \frac{1}{N^{1/2}} \sum_{\boldsymbol{\kappa},\alpha} (\frac{\hbar}{2m\omega_\alpha})^{1/2} (b_{\boldsymbol{\kappa},\alpha} + b^\dagger_{\boldsymbol{\kappa},\alpha}) \boldsymbol{s}_\alpha(\boldsymbol{\kappa}) e^{i(\boldsymbol{\kappa}\cdot\boldsymbol{x})} \tag{4.47}$$

$$\boldsymbol{p}(\boldsymbol{x}) = -\frac{i^{1/2}}{N^{1/2}} \sum_{\boldsymbol{\kappa},\alpha} (\frac{\hbar m\omega_\alpha}{2})^{1/2} (b_{\boldsymbol{\kappa},\alpha} - b^\dagger_{\boldsymbol{\kappa},\alpha}) \boldsymbol{s}_\alpha(\boldsymbol{\kappa}) e^{i(\boldsymbol{\kappa}\cdot\boldsymbol{x})}. \tag{4.48}$$

Finally, the Hamiltonian (4.44) expressed in terms of these variables (i.e., for the momentum and potential energies) becomes[†]

$$\begin{aligned}
\mathrm{H}_p = & \frac{1}{4}\sum_{\kappa,\alpha}\hbar\omega_\alpha(b_{\kappa,\alpha} - b^\dagger_{\kappa,\alpha})(b^\dagger_{\kappa,\alpha} - b_{\kappa,\alpha}) + \\
& \frac{1}{4}\sum_{\kappa,\alpha}\hbar\omega_\alpha(b_{\kappa,\alpha} + b^\dagger_{\kappa,\alpha})(b^\dagger_{\kappa,\alpha} + b_{\kappa,\alpha}) \\
= & \frac{1}{2}\sum_{\kappa,\alpha}\hbar\omega_\alpha(b_{\kappa,\alpha}b^\dagger_{\kappa,\alpha} + b^\dagger_{\kappa,\alpha}b_{\kappa,\alpha}) \\
= & \sum_{\kappa,\alpha}\hbar\omega_\alpha(b^\dagger_{\kappa,\alpha}b_{\kappa,\alpha} + \frac{1}{2}),
\end{aligned} \tag{4.49}$$

where we have used the commutator operator (2.72) for the last step.

This is written in terms of energy (footnote of Section 2.6.4) by use of the probability distribution function $f_p(\boldsymbol{\kappa}, \alpha)$[‡] as [similar to (2.85) for the quantum-harmonic oscillator]

$$E_p = \sum_{\kappa,\alpha}[f_p(\boldsymbol{\kappa}, \alpha) + \frac{1}{2}]\hbar\omega_\alpha(\boldsymbol{\kappa}). \tag{4.50}$$

Therefore this is another solution path in arriving at the quantum energy of the harmonic oscillator (Section 2.6.4). The quanta of energy are $\hbar\omega$. We will make use of the quantum treatment of phonons in Sections 4.8, 5.15, and 7.12.

[†] The Hamiltonian is made of kinetic and potential energies that are

$$\begin{aligned}
\text{kinetic energy} &= \sum_{\boldsymbol{x}}\frac{1}{2m}p^2(\boldsymbol{x}) = \frac{1}{4}\sum_{\boldsymbol{\kappa},\boldsymbol{\alpha}}\hbar\omega_\alpha(\boldsymbol{\kappa})(b^\dagger_{\kappa,\alpha} - b_{\kappa,\alpha})(b^\dagger_{\kappa,\alpha} - b_{\kappa,\alpha}) \\
\text{potential energy} &= \frac{1}{2}\sum_{\boldsymbol{x},\boldsymbol{x}'}d_i(\boldsymbol{x})D_{ij}(\boldsymbol{x}-\boldsymbol{x}')d_j(\boldsymbol{x}') = \frac{1}{4}\sum_{\boldsymbol{\kappa},\boldsymbol{\alpha}}\hbar\omega_\alpha(\boldsymbol{\kappa})(b^\dagger_{\kappa,\alpha} + b_{\kappa,\alpha})(b^\dagger_{\kappa,\alpha} + b_{\kappa,\alpha}) \\
\text{Hamiltonian } \mathrm{H}_p &= \frac{1}{2}\sum_{\boldsymbol{\kappa},\boldsymbol{\alpha}}\hbar\omega_\alpha(\boldsymbol{\kappa})(b_{\kappa,\alpha}b^\dagger_{\kappa,\alpha} + b^\dagger_{\kappa,\alpha}b_{\kappa,\alpha}).
\end{aligned}$$

Using commutator operator (2.72), we have

$$\begin{aligned}
[b_{\kappa,\alpha}, b^\dagger_{\kappa,\alpha}] &= 1 = b_{\kappa,\alpha}b^\dagger_{\kappa,\alpha} - b^\dagger_{\kappa,\alpha}b_{\kappa,\alpha} \\
b_{\kappa,\alpha}b^\dagger_{\kappa,\alpha} &= b^\dagger_{\kappa,\alpha}b_{\kappa,\alpha} + 1 \\
\mathrm{H}_p &= \frac{1}{2}\sum_{\boldsymbol{\kappa},\boldsymbol{\alpha}}\hbar\omega_\alpha(\boldsymbol{\kappa})(b^\dagger_{\kappa,\alpha}b_{\kappa,\alpha} + 1 + b^\dagger_{\kappa,\alpha}b_{\kappa,\alpha}) \\
&= \sum_{\boldsymbol{\kappa},\boldsymbol{\alpha}}\hbar\omega_\alpha(\boldsymbol{\kappa})(b^\dagger_{\kappa,\alpha}b_{\kappa,\alpha} + \frac{1}{2}).
\end{aligned}$$

[‡] The temperature dependent total number of phonons summed over the normal modes and the polarizations as

$$N_p = \sum_{\kappa,\alpha} f_p.$$

4.6 Examples of Phonon Dispersion and DOS

Figure 4.7 shows the MD-computed dimensionless phonon dispersion and DOS for the Ar FCC crystal. The atomic coordinates used in the generation of the dispersion data were obtained from MD simulations as discussed in Section 2.5 [315]. A structure at finite temperature is slowly quenched to a temperature of 0 K. The cut-off used is $2.5\sigma_{\rm LJ}$. As the crystal structure is monatomic (number of atoms per primitive cell, $N_\circ = 1$, total number of modes is $3N_\circ$), all modes correspond to acoustic phonons.

The plotted angular frequency is dimensionless and has been normalized by the L–J time scale (Table 2.7, except for the constant), $(\sigma_{\rm LJ}^2 m/\epsilon_{\rm LJ})^{1/2}$. Note that from (2.54), ω_n is 22.88 time this ω scale, which is near the cut-off frequency in Figure 4.7(a). For Ar, the time scale has a value of 2.14 ps. The divisions on the horizontal axis (the wave number) are separated by $0.1 \times 2\pi/a$ (i.e., one-twentieth of the size of the first Brillouin zone in the [100] direction).

Note the degeneracies of the transverse branches in the [100] and [111] directions, but not in the [110] direction. Also, as seen in the [110] direction, the longitudinal branch does not always have the highest frequency of the three branches at a given point.

The volumetric density of states is based on a Brillouin zone with a grid spacing of $1/21 \times 2\pi/a$. This leads to 37,044 distinct points (each with three polarizations) covering the entire first Brillouin zone. The frequencies are sorted by a histogram with a bin size of 1, and the resulting data are plotted at the middle of each bin. The DOS axis is defined such that an integration over frequency gives $3(N-1)/V \simeq 12/a^3$ (for large V, where N is the number of atoms in volume V).

Figures 4.8(a) and (b) show the MD-computed phonon dispersion and DOS for silica (quartz). The predictions are made with the B-K-S potential (2.10). The Wolf method [496] is used to model the electrostatic interactions with an α value of 0.431 Å^{-1}. The cut-off radius used is 6.44 Å. The zero-temperature unit-cell parameters are a = 4.89 Å and c = 5.51 Å. The anisotropic structure of quartz is shown in Figure 2.9(a). The lattice-dynamics calculations are based on the description given in [117]. The dispersion results show reasonable agreement between experimental and theoretical predictions [21, 451]. The experiments use neutron inelastic scattering [242].[†]

The linear density of states is based on a grid spacing of $(1/1000) \times 2\pi/a$ in the [100] direction. This leads to 27,027 frequencies (there are $N_\circ = 9$ atoms per primitive cell and as discussed in Section 4.33, there are $3N_\circ = 27$ branches). The

---

[†] A neutron of mass m_n and wave vector $\boldsymbol{\kappa}_n$ is scattered to $\boldsymbol{\kappa}_n'$, and a phonon of wave vector $\boldsymbol{\kappa}_p$ is emitted or absorbed such that

$$\boldsymbol{\kappa}_n + \boldsymbol{g} = \boldsymbol{\kappa}_p' + \boldsymbol{\kappa}_n$$

$$\frac{\hbar^2\kappa_n^2}{2m_n} = \frac{\hbar^2\kappa_n'^2}{2m_n} \pm \hbar\omega_p.$$

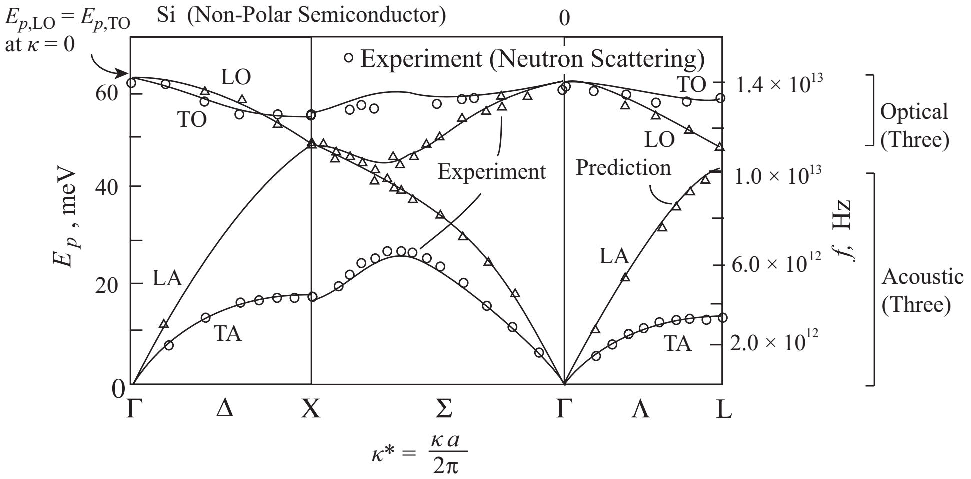

Figure 4.9. Predicted and measured phonon dispersion curves for Si (diamond structure). The solid curves represent the predicted results, and the open circles are experimental results [445]. The key Brillouin points are also shown. There are six branches, three acoustic and three optical; the transverse branches are degenerate.

frequencies are sorted by a histogram with a bin size of 1 THz, and the resulting data are plotted at the middle of each bin. The DOS axis is defined such that an integration over frequency gives $3(N_c - 1)/L \simeq 3/a$ (for large L, where N_c is the number of unit cells in a length L in the [100] direction).

Note that the Debye model for D_p represents the energy of acoustic phonons. To include the high-energy phonons, the dimensionless Debye–Gaussian distribution function (4.29) can be used instead of the Debye DOS, which has the form

$$D_p^*(E_p) = C E_p^2 \exp[-(\frac{E_p - E_{p,p}}{\Delta E_p})^2], \quad E_p = \hbar\omega, \tag{4.51}$$

where C is the normalization constant making D_p dimensionless, $E_{p,c}$ is the energy at the center of the distribution, and ΔE_p is the width (at $1/e$ from the peak) of the distribution. Note that this model has only one peak, i.e., the positive root of $E_p^2 - E_p E_{p,c} - \Delta E_p^2 = 0$. Figure 4.8(c) shows (4.51) applied to the Y_2O_3 crystal D_p (where D_p is dimensional) from MD results [398]. These MD results will be discussed in Section 4.19.3. The agreement near the peak is reasonable.

As further examples, typical dispersion relations are given in Figures 4.9 and 4.10, for Si and GaAs, respectively. Both predictions and measurements are shown and are in good agreement.

The phonon DOS for Si is shown in Figure 4.11. Note that the maximum phonon energy is that of $E_{p,\mathrm{LO}} = E_{p,\mathrm{TO}}$ at $\kappa = 0$ (Figure 4.9). The peaks are singularities (van Hove) at Γ, X, Σ and L points. The Debye energy (temperature) and Debye model of DOS are also shown. Note that the Debye model does not include the optical phonons.

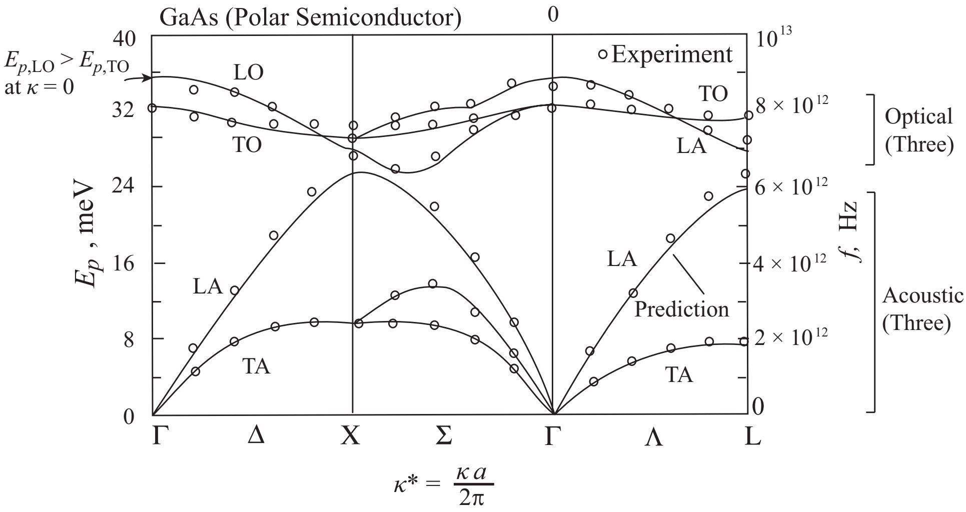

Figure 4.10. Predicted and measured phonon dispersion curves for GaAs (zinc-blende structure). The solid curves represent the predicted results, and the open circles are experimental results [445]. The key Brillouin points are also shown. There are six branches, three acoustic and three optical, the transverse branches are degenerate.

Figure 4.12 shows measured individual contributions from the transverse and longitudinal polarizations for $D_p(\omega)$ of Al (FCC) at $T = 80$ K [448]. Similar to Ar FCC, there is no optical phonon in this single-atom primitive cell (basis of one atom, Section 4.3).

The exact phonon dispersion curve varies depending on the existence of polar or nonpolar atoms in the primitive cell. In nonpolar semiconductors (Si and C),

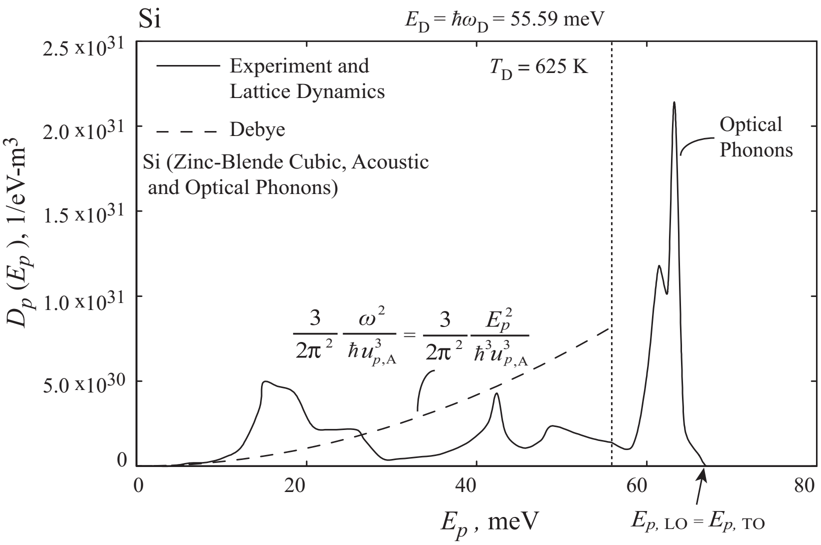

Figure 4.11. Measured and predicted phonon DOS for Si [492]. The Debye cut-off frequency (angular) is $\omega_\mathrm{D} = T_\mathrm{D} k_\mathrm{B}/\hbar = 8.443 \times 10^{13}$ rad/s $= 84.43$ Trad/s.

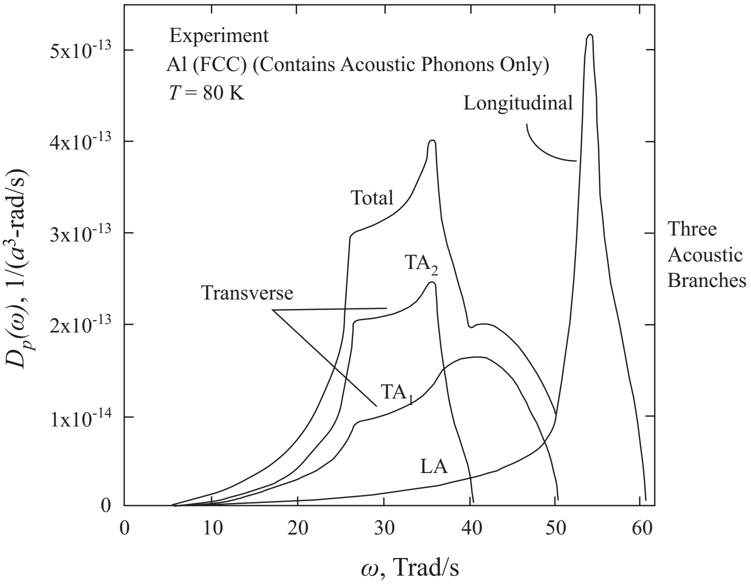

Figure 4.12. Measured phonon angular-frequency DOS for Al (FCC) at $T = 80$ K [448]. Also shown are the contributions from the three acoustic-phonon modes. The volume is a^3, and 1 Trad/s = 0.6582 meV.

the LO and TO branches of phonon dispersion have the same frequency at the zone center Γ (Figure 4.9). For polar semiconductors (like GaAs), the LO and TO frequencies split at the zone center Γ (Figure 4.10), because of the long-range dipolar interaction[†].

4.7 Phonon Specific Heat Capacity and Debye Average Acoustic Speed

4.7.1 Acoustic Phonon Specific Heat Capacity

The lattice (or phonon) specific heat capacity $c_{v,p}$, is the total value for all phonon modes. The specific heat capacity is given in J/kg-K, J/m^3-K, or J/K (per atom), depending on relevance. Using the Debye model of the phonon DOS, $c_{v,p}$ is derived for monatomic crystalline solids. It has a temperature dependence such that, as expected, it vanishes at 0 K, has a steep dependence as $T = 0$ K is approached, and the temperature dependence disappears at high temperatures (at high temperatures, it reaches a value of $3k_\mathrm{B}$ per atom, associated with 3 degrees of freedom, and equipartition of energy, which gives crystal kinetic and potential energies). Debye,

---

[†] The LO modes have an additional electric restoring force, such that [433]

$$\frac{\omega_{p,\mathrm{LO}}^2}{\omega_{p,\mathrm{TO}}^2} = \frac{\epsilon_{e,s}}{\epsilon_{e,\infty}},$$

where $\epsilon_{e,s}$ and $\epsilon_{e,\infty}$ are the static and high-frequency dielectric functions (Section 3.3.5).

noting these trends, suggested a cut-off frequency f_p^{o} beyond which the high-energy phonons do not contribute to the lattice specific heat capacity (Section 4.2.2). His formulation is subsequently given.

For a monatomic, isotropic crystal, the energy per unit volume, for N_p phonons, in a volume V, is

$$\begin{aligned}\langle E_p\rangle &= \int_0^\infty \hbar\omega f_p^{\text{o}} D_p(\omega)\mathrm{d}\omega\\ &= \int_0^\infty \hbar\omega \frac{1}{\exp(\frac{\hbar\omega}{k_\mathrm{B}T})-1} D_p(\omega)\mathrm{d}\omega.\end{aligned} \tag{4.52}$$

The number density of phonons n_p is found from (1.19), i.e., $\int_0^\infty f_p^{\text{o}} D_p(\omega)\mathrm{d}\omega$. Note that this is consistent with the result for the quantum oscillator (2.90), where the 1/2 is neglected there. Also, note the phonon DOS is in (1/m^3-rad/s). The lattice specific heat capacity of a solid at constant volume $c_{v,p}$ is found by differentiating e_p (4.52) with respect to temperature T (Table 2.4), i.e.,

$$nc_{v,p} = \frac{\partial\langle E_p\rangle}{\partial T}|_V = \int_0^\infty \hbar\omega \frac{\partial}{\partial T}[\exp(\frac{\hbar\omega}{k_\mathrm{B}T})-1]^{-1} D_p(\omega)\mathrm{d}\omega. \tag{4.53}$$

We simplify the differentiation on the right-hand side as

$$\frac{\partial}{\partial T}[\exp(\frac{\hbar\omega}{k_\mathrm{B}T})-1]^{-1} = \frac{\hbar\omega}{k_\mathrm{B}T^2}\frac{e^x}{(e^x-1)^2}, \quad x = \frac{\hbar\omega}{k_\mathrm{B}T}. \tag{4.54}$$

Substituting into (4.53), we have

$$nc_{v,p} \equiv k_\mathrm{B}\int_0^{\omega_\mathrm{D}} \frac{x^2e^x}{(e^x-1)^2} D_{p,\mathrm{D}}\mathrm{d}\omega, \quad x = \frac{\hbar\omega}{k_\mathrm{B}T}, \tag{4.55}$$

where we again used the integral over the DOS, along with the Debye cut-off angular frequency (Section 4.2.2). This Debye cut-off frequency $f_\mathrm{D} = \omega_\mathrm{D}/2\pi$ is the highest normal-mode frequency that the crystal can have (Glossary). As described in Section 4.3, there are $3n$ phonon modes (or three polarizations of acoustic phonons, two transversal and one longitudinal), for a monatomic, single-atom lattice crystal. Note that from (4.55), the specific heat capacity per phonon is $k_\mathrm{B}x^2e^x/[e^x-1]^2$.

In (2.99), we related the number of carriers to the density of states and the probability distribution function. Here we use the Debye DOS $D_{p,\mathrm{D}}$ (for three acoustic modes or polarizations per atom). We use the Debye oscillator conservation constraint which states that there are three modes per atom (one longitudinal and two transverse polarizations), i.e.,[†]

$$\frac{N_{p,m}}{V} = n_{p,m} = 3n = \int_0^\infty D_p(\omega)\mathrm{d}\omega \approx \int_0^{\omega_\mathrm{D}} D_{p,\mathrm{D}}\mathrm{d}\omega = \int_0^{\omega_\mathrm{D}} \frac{3\omega^2}{2\pi^2 u_{p,\mathrm{A}}^3}\mathrm{d}\omega$$

$$= \frac{3}{2\pi^3 u_{p,\mathrm{A}}^3}\int_0^{\omega_\mathrm{D}} \omega^2\mathrm{d}\omega,$$

$$D_{p,\mathrm{D}} = \frac{3\omega^2}{2\pi^2 u_{p,\mathrm{A}}^3} \quad \text{Debye acoustic-phonon relations.} \tag{4.56}$$

The total number density of phonons will use f_p^o and is temperature dependent (increasing with temperature). Note that we have used the frequency DOS, $D_p(\omega)$, and integration over frequency space (with cut-off), as compared with energy DOS in (2.99). Here $u_{p,\mathrm{A}}$ is the single, average phonon speed used to represent all polarizations and is generally defined as (4.15)

$$\frac{1}{u_{p,\mathrm{A}}} = \frac{1}{3}\left(\frac{1}{u_{p,g,\mathrm{L}}} + \frac{2}{u_{p,g,\mathrm{T}}}\right), \tag{4.57}$$

where L and T are the longitudinal and transverse polarizations. Using the inverse of speed originates from (4.22), when D_p is proportional to inverse of group phonon speed.

Evaluating the integral of (4.56) and solving for ω_D gives

$$3 = \frac{3}{2n\pi^2 u_{p,\mathrm{A}}^3}\frac{\omega_\mathrm{D}^3}{3} \tag{4.58}$$

$$\omega_\mathrm{D}^3 = 6\pi^2 n u_{p,\mathrm{A}}^3 \tag{4.59}$$

$$\omega_\mathrm{D} = (6\pi^2 n u_{p,\mathrm{A}}^3)^{1/3}, \tag{4.60}$$

which is the same as (4.28). The approximation in (4.56) has lead to a simple relation between ω_D and $u_{p,\mathrm{A}}$

Noting that, from the definition of the Debye temperature (Glossary), i.e., $\omega_\mathrm{D} = k_\mathrm{B}T_\mathrm{D}/\hbar$, and recalling that $x(T,\omega) = \hbar\omega/k_\mathrm{B}T$, we can write $x_\mathrm{D} = x(T, \omega = \omega_\mathrm{D})$ as

$$x_\mathrm{D} = \frac{\hbar\omega_\mathrm{D}}{k_\mathrm{B}T} = \frac{T_\mathrm{D}}{T} \quad \text{scaled, inverse temperature.} \tag{4.61}$$

In Section 4.11.3, we show how T_D relates to the atomic force constant and the atomic structure. For elemental solids, T_D is listed in Table A.2, and for some solid compounds in Figure 4.24. Substituting the expressions for f and $D_{p,D}(\omega)$ into the

---

[†] Note that similar to electron gas (2.100), the phonon κ-mode density is

$$n_{p,\kappa} \equiv \frac{\kappa_\mathrm{D}^3}{6\pi^2} = n, \quad \kappa_\mathrm{D} = \omega_\mathrm{D}/u_{p,\mathrm{A}}.$$

There are $3n_{p,\kappa} = n_{p,m}$ modes (one longitudinal and two transverse).

integral form of (4.55), using the Debye cut-off frequency, we have

$$\begin{aligned} nc_{v,p} &= k_{\rm B}\int_0^{\omega_{\rm D}} \frac{x^2e^x}{(e^x-1)^2}D_p(\omega)\mathrm{d}\omega \\ &= k_{\rm B}\int_0^{x_{\rm D}} \frac{x^2e^x}{(e^x-1)^2}\frac{3\omega^2}{2n\pi^2u_{p,{\rm A}}^3}\frac{k_{\rm B}T}{\hbar}\mathrm{d}x \\ &= k_{\rm B}\int_0^{T_{\rm D}/T} \frac{12\pi k_{\rm B}^3T^3}{nu_{p,{\rm A}}^3\hbar^3}\frac{x^4e^x}{(e^x-1)^2}\mathrm{d}x. \end{aligned} \tag{4.62}$$

Substituting $f_{\rm D}$ into the expression for $T_{\rm D}$ gives another form of (4.27), i.e.,

$$T_{\rm D} = \frac{\hbar\omega_{\rm D}}{k_{\rm B}} = \frac{\hbar}{k_{\rm B}}(6\pi^2nu_{p,{\rm A}}^3)^{1/3}, \tag{4.63}$$

which is the same as (4.27), written there for each polarization. We then have

$$\begin{aligned} nc_{v,p} &= k_{\rm B}12\pi T^3\frac{k_{\rm B}^3}{u_{p,{\rm A}}^3\hbar^3}\int_0^{T_{\rm D}/T}\frac{x^4e^x}{(e^x-1)^2}\mathrm{d}x \\ &= k_{\rm B}12\pi T^3\frac{1}{T_{\rm D}^3}\frac{6\pi^2n}{(2\pi)^3}\int_0^{T_{\rm D}/T}\frac{x^4e^x}{(e^x-1)^2}\mathrm{d}x \\ &= 9k_{\rm B}(\frac{T}{T_{\rm D}})^3n\int_0^{T_{\rm D}/T}\frac{x^4e^x}{(e^x-1)^2}\mathrm{d}x \end{aligned}$$

Debye model of lattice specific heat capacity. (4.64)

Therefore, to find $c_{v,p}$ per atom we divide the proceeding equation by n. Figure 4.13(a) shows variations of the predicted dimensionless specific heat capacity of a few elements, with respect to temperature. The asymptotic value of $nc_{v,p}/k_{\rm B} = 3$ (sum of kinetic and potential energy, each 3 degrees of freedom) is shown and reached for $T \gg T_{\rm D}$ (end-of-chapter problem). This is called the Dulong–Petit limit for solids and is derived from classical treatment of lattice vibration internal energy [11]. In Figure 2.15, it was shown that this limit is realized in classical MD at temperatures well below the melting temperature. However, in MD, $c_{v,p}$ decrease (can also increase) because of anharmonicity at higher temperatures, whereas the quantum effects cause lower $c_{v,p}$ at lower temperatures (Figure 2.15). Because of anharmonic vibrations, the high-temperature asymptotic value of $c_{v,p}$ may be less than $3k_{\rm B}$ (per atom), as shown in Figure 2.15, by as much as 10%.

The Debye temperature for elemental crystalline solids is listed in Table A.2. For some compounds, they can be found in [245].

For $T \ll T_D$ there is a $(T/T_{\rm D})^3$ trend (end-of-chapter problem), and this is also shown in Figure 4.13(a).

Figure 4.13(b) shows the variations of $f_p^{\rm o}$, and scaled $D_{p,{\rm D}}$, $D_{p,{\rm D}}f_p^{\rm o}$, and $\hbar\omega D_{p,{\rm D}}f_p^{\rm o}$ [appearing in integral (4.52)], with respect to ω, for Si at $T = 300$ K. Although $\hbar\omega D_{p,{\rm D}}f_p^{\rm o}$ does not peak at $\omega_{\rm D}$, its growth is not as large compared with

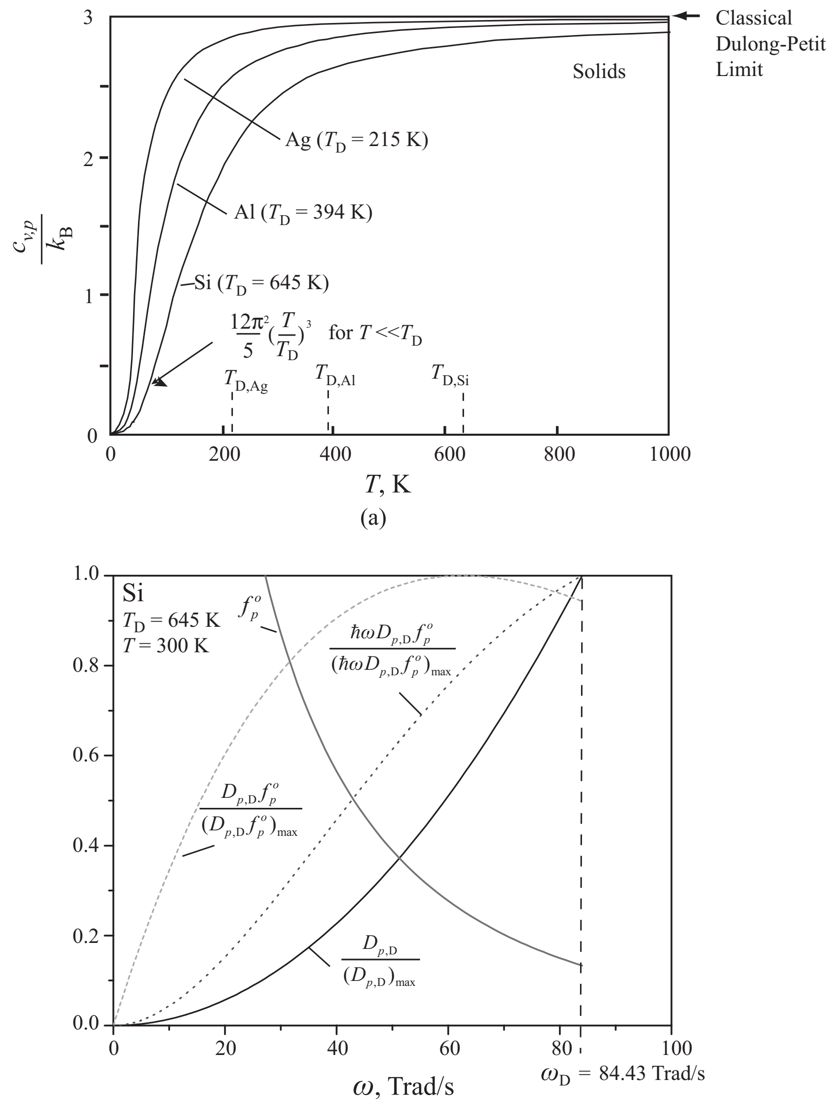

(a)

(b)

Figure 4.13. (a) Variation of the predicted dimensionless lattice (Debye acoustic phonon) specific heat capacity (per atom) with respect to temperature, for Ag, Al, and Si elements. Note that for Sn, the optical heat capacity is not included. The classical limit is also shown. (b) Variations of sealed $f_p^{\rm o}$, $D_{p,{\rm D}}$, $D_{p,{\rm D}} f_p^{\rm o}$, and $\hbar\omega D_{p,{\rm D}} f_p^o$ as functions of ω, for Si at $T =$ 300 K.

that at lower frequencies. As shown in Figure 4.11, the Debye DOS is not an accurate model for Si, especially when the role of optical phonons[†] becomes important

---

[†] The optical phonon contribution to heat capacity is approximated using the single-frequency model of Einstein discussed in Appendix C and given by (C.1). There the Einstein temperature is set equal to the cut-off phonon frequency, i.e., $\omega_{\rm o} = \omega_{p,{\rm O}}$, and $T_E = \hbar\omega_{p,{\rm O}}/k_{\rm B}$. Then $nc_{v,p}$ will be the sum of (4.64) and n times (C.1).

(e.g., in scattering of conduction electron by phonons, Section 5.15.3). However, for some applications, such as in total specific heat capacity, this model is easy to use and relatively accurate.

To write (4.64) $c_{v,p}$ per the molecular weight, we first use per atom using k_B/m and then use R_g/M $(R_g = k_B N_A)$.

For compounds, the average molecular weight $\langle M\rangle$ for x_i atomic fraction M_i

$$\langle M\rangle = \frac{\sum_i x_i M_i}{\sum_i M_i} \quad \text{average Molecular mass in polyatomic crystal.} \tag{4.65}$$

Again note that (4.64) does not include optical phonons present in polyatomic or multiatomic primitive cell crystals, which are discussed in [85].

Expressing the lattice volume by V_c and the number of atoms per lattice as N_c, the sensible heat content $\rho c_{v,p} T$ in the macroscopic energy equation (Table 1.1) for the lattice is

$$\rho c_p T = \frac{3\alpha(T) N_c k_B T}{V_c}, \tag{4.66}$$

where $\alpha(T)$ is dimensionless and expresses the temperature dependence. We note again that (4.64) is based on Debye model of acoustic phonons.

4.7.2 Estimate of Directional Acoustic Velocity

The long wavelength acoustic phonons are the elastic waves in the macroscopic elastic mechanics equation (Table 3.11). Here we discuss the relations among the group velocities of these waves, the elastic moduli, and the interatomic force constants.

(A) *Group Velocity from Directional Spring Constant*

The acoustic modes have all the atoms in the planes perpendicular to the transport direction moving in phase. For a lattice consisting of parallel planes, the transport perpendicular to the these planes is one dimensional, and similar to (4.17), by use of the harmonic potential, we have the sound speed as given by

$$u_{p,g,i} = l_i (\frac{\Gamma_i}{m_c})^{1/2}, \tag{4.67}$$

where l_i is the distance between the planes and m_c is the mass of the primitive cell. The spring constant is defined through (2.54) as

$$\Gamma = \sum_n \frac{\partial^2 \varphi_n}{\partial d_{i,n}^2}, \tag{4.68}$$

where $d_{i,n}$ is the displacement of the nth unit cell along the i direction and φ_n is the potential between the origin unit cell and the nth neighboring unit cell. Here, we consider the interactions only among the nearest neighbors.

(B) *Nearest-Neighbor FCC Structures*

Then, for an FCC structure (each atom has 12 nearest neighbors), along [111], we have $\Gamma_\mathrm{L} = 2\Gamma$, $\Gamma_\mathrm{T} = \Gamma/2$, where Γ is the effective spring constant of the pair potential and is defined as

$$\Gamma = (\frac{\partial^2 \varphi_\mathrm{LJ}}{\partial r^2})_{r_e} \quad r_e \text{ is the equilibrium separation distance.} \tag{4.69}$$

Then using projections, along [100] we have $\Gamma_\mathrm{L} = 2\Gamma$, $\Gamma_\mathrm{T} = \Gamma$. Value of Γ for some element pairs is given in Table 4.4 and for some compounds in Figure 4.29.

As an example, an Ar solid is an FCC crystal [Figure 4.6(c)] and each primitive cell contains only one atom. Then the distance between the nearest neighbors is $r_e = a/2^{1/2}$. For a L–J potential (2.9), and using the equilibrium condition, i.e., $\partial\varphi_\mathrm{LJ}/\partial r = 0$, we have $\sigma_\mathrm{LJ} = 2^{-2/3}a$. Then the effective spring constant becomes $\Gamma = 72\epsilon_\mathrm{LJ}/2^{1/3}\sigma_\mathrm{LJ}^2$. Note that $\Gamma_\mathrm{L} = 2\Gamma = 72 \times 2^{2/3}\epsilon_\mathrm{LJ}/\sigma_\mathrm{LJ}^2$, gives a result that is closer to the effective bulk value (2.54). The bulk modulus can also be derived and is (Chapter 2 problem) $E_p = 75\epsilon_\mathrm{LJ}/\sigma_\mathrm{LJ}^3$ and $a = 2^{1/2}r_e$, $r_e = 1.09\sigma_\mathrm{LJ}$. Also, note that the effective bulk (including long-range interactions) Γ given in Table 2.7 has a larger numerical value.

For Ar, from Table 2.2, we have $\sigma_\mathrm{LJ} = 3.40$ Å, $\epsilon_\mathrm{LJ} = 0.0104$ eV $= 1.67 \times 10^{-21}$ J, and then $\Gamma = 0.85$ N/m, $m_c = 6.634 \times 10^{-26}$ kg $= 66.34$ yg, and $a = 2^{2/3}\sigma_\mathrm{LJ} = 5.31$ Å.

Along the [100] direction, we have $l = 0.5a$, then $u_{p,g,\mathrm{L}} = 1362$ m/s and $u_{p,g,\mathrm{T}} = 963$ m/s, and the average speed is given by (4.57), so $u_{p,g,\mathrm{A}} = 1067$ m/s.

Along the [111] direction, we have $l = a/3^{1/2}$, then $u_{p,g,\mathrm{L}} = 1572$ m/s, $u_{p,g,\mathrm{T}} = 786$ m/s and $u_{p,g,\mathrm{A}} = 943$ m/s.

The Debye temperature of Ar is 89 K [317], and the corresponding average sound speed $u_{p,\mathrm{A}} = u_{p,g,\mathrm{A}}$ found from (4.63) is 999 m/s, which is close to the proceeding approximate prediction.

Note that the directional Debye frequency $\omega_{\mathrm{D},\alpha}$ and temperature $T_{\mathrm{D},\alpha}$ are related to the directional $u_{p,g,\alpha}$ through (4.60) and (4.61).

(C) *Nearest-Neighbor SC Structures*

For homogeneous deformation in SC structures, we have the relation for the isothermal bulk modulus $E_p = 1/\kappa_p$, $\kappa_p = -(\partial\rho/\partial p|_T)/\rho$ (Table 3.11), and the spring constant Γ_b through the lattice constant a, as

$$\frac{1}{E_p} = \kappa_p = -\frac{1}{v}\frac{\partial v}{\partial p}|_T = \frac{3a^2 d}{a^3\Gamma_b d/a^2} = \frac{3a}{\Gamma_b} \text{ along [111] \quad SC.} \tag{4.70}$$

where we have used the pressure relation $\mathrm{d}p = \Gamma_b d/a^2$. Then, using (4.67), we have

$$\begin{aligned} u_{p,b} &= l_b(\frac{\Gamma_b}{m_c})^{1/2} = l_b(\frac{3a}{\kappa_p m_c})^{1/2} \\ &= \frac{a}{3^{1/2}}(\frac{3a}{\kappa_p}m_c)^{1/2} = (\frac{a^3}{\kappa_p m_c})^{1/2} \\ &= (\frac{1}{\rho\kappa_p})^{1/2} = (\frac{E_p}{\rho})^{1/2}, \ \rho = \frac{m_c}{a^3}. \end{aligned} \tag{4.71}$$

This is the same as the bulk sound speed given next. Note that the results are slightly different from that for a FCC.

(D) *Bulk and Directional Velocities Using Moduli*

The bulk sound speed is found from (4.71)

$$u_{p,b} = (\frac{1}{n\langle m\rangle \kappa_p})^{1/2}, \tag{4.72}$$

where $\langle m\rangle$ is average atomic mass (4.65), n is the atomic number density, and $\rho = n\langle m\rangle$. The relation among the adiabatic compressibility κ_p $(= 1/E_p)$, the Young modulus $E_{\rm Y}$ and the shear modulus G is (Table 3.11)

$$\frac{1}{\kappa_p} = E_p = \frac{E_{\rm Y}}{3(1-2\nu_{\rm P})} = \frac{2G(1+\nu_{\rm P})}{3(1-2\nu_{\rm P})} \quad \nu_{\rm P} \text{ is Poisson ratio.} \tag{4.73}$$

The Poisson ratio for elements ranges from 0.15 (Eu) to 0.45 (Tl). Note the low speed of sound in Pb ($E_p = 46$ GPa, $\rho = 11,300$ kg/m^3) and high speeds in Si ($E_p = 102$ GPA, $\rho = 2330$ kg/m^3) and C (diamond) ($E_p = 442$ GPA, $\rho = 3510$ kg/m^3). The longitudinal and transverse sound speeds are

$$u_{p,\rm L} = (\frac{E_Y}{n\langle m\rangle})^{1/2} = (\frac{E_Y}{\rho})^{1/2} \quad \text{longitudinal sound speed} \tag{4.74}$$

$$u_{p,\rm T} = (\frac{G}{n\langle m\rangle})^{1/2} = (\frac{G}{\rho})^{1/2} \quad \text{transverse sound speed.} \tag{4.75}$$

When used in (4.60), the cut-off frequency (for each polarization) and when (4.63) is used, the Debye temperature, can be found from these velocities (thus relating them to the elastic constants).

4.8 Atomic Displacement in Lattice Vibration

In Section 2.5.3(B), the RMS displacement of lattice atoms was given by approximation (leading-order) relation (2.56). Here we derive a general expression, based on the treatment given in [29].

Consider a polyatomic molecule; based on the Newton law (Table 2.5) the force on atom i, $\boldsymbol{F}_i$, is

$$\boldsymbol{F}_i = -\sum_j \frac{\partial\varphi_{ij}}{\partial \boldsymbol{d}_i} = m_i\frac{{\rm d}^2\boldsymbol{d}_i}{{\rm d}t^2}. \tag{4.76}$$

With the harmonic approximation for the potentials and for small displacements, we have [similar to (4.37)]

$$\frac{\partial\varphi_{ij}}{\partial \boldsymbol{d}_i} = \frac{\partial^2\varphi_{ij}}{\partial \boldsymbol{d}_i\partial \boldsymbol{d}_j}\cdot(\boldsymbol{d}_i - \boldsymbol{d}_j). \tag{4.77}$$

Then equation of motion (4.39) is again

$$\boldsymbol{M}\omega^2\boldsymbol{s}_\alpha = \boldsymbol{D(\kappa)}\boldsymbol{s}_\alpha, \tag{4.78}$$

where $\boldsymbol{s}_\alpha$ is a polarization vector, $\boldsymbol{M}$ is the mass matrix, and $\boldsymbol{D(\kappa)}$ is the dynamical matrix (4.40)

$$D_{ij}(\boldsymbol{\kappa}) = \sum_i \left(\frac{\partial^2 \varphi_{ij}}{\partial d_i \partial d_j}\right) \exp[i\boldsymbol{\kappa} \cdot (\boldsymbol{l}_j - \boldsymbol{l}_i)]. \tag{4.79}$$

Rearranging (4.78), the eigenvalue equation becomes

$$[\boldsymbol{M}^{-1}\boldsymbol{D}(\boldsymbol{\kappa}) - \omega^2 \boldsymbol{I}] = 0, \tag{4.80}$$

where $\boldsymbol{I}$ is the identity matrix. Here $\boldsymbol{D}(\boldsymbol{\kappa})$ is specified by a complete set of internal displacement coordinates, including bond lengths and angle displacements. This set of coordinates can be represented by a column matrix $\boldsymbol{S}$ [29]. The mean-square relative displacement (MSRD) amplitude matrix $\boldsymbol{\Sigma}$ is defined as

$$\boldsymbol{\Sigma} = \langle \boldsymbol{S}\boldsymbol{S}^\dagger \rangle, \tag{4.81}$$

where $\boldsymbol{S}$ is chosen such that the diagonal elements of $\boldsymbol{\Sigma}$ of the MSRD of the atomic vibrations satisfy $\langle |\boldsymbol{\Delta}_j|^2 \rangle = \Sigma_{jj}$. The superscript † indicates complex conjugate. The coordinate $\boldsymbol{S}$ may be not normal, but we may find a matrix $\boldsymbol{L}$ to transform $\boldsymbol{S}$ to the normal coordinates $\boldsymbol{Q}$ (Glossary), i.e.,

$$\boldsymbol{S} = \boldsymbol{L}\boldsymbol{Q}. \tag{4.82}$$

Then we have

$$\boldsymbol{\Sigma} = \boldsymbol{L}\langle \boldsymbol{Q}\boldsymbol{Q}^\dagger \rangle \boldsymbol{L}^\dagger. \tag{4.83}$$

When $\boldsymbol{Q}$ satisfies

$$\langle \boldsymbol{Q}\boldsymbol{Q}^\dagger \rangle_{\alpha\alpha'} = \left[\frac{\hbar}{2\omega_\alpha} \coth\left(\frac{\hbar\omega_\alpha}{2k_\mathrm{B}T}\right)\right]\delta_{\alpha\alpha'}, \tag{4.84}$$

then we have the relations [104]

$$[\boldsymbol{L}^\dagger \boldsymbol{D}(\boldsymbol{\kappa})\boldsymbol{L}]_{\alpha\alpha'} = \omega_\alpha^2 \delta_{\alpha\alpha'}, \text{ and } \boldsymbol{L}\boldsymbol{L}^\dagger = \boldsymbol{M}^{-1}. \tag{4.85}$$

In the high-temperature regime (within harmonic approximation), we can derive a relationship between the MSRD amplitude matrix and the molecular force fields by using the relations (4.85), and then expanding the $\coth(x)$ term in (4.84) as

$$\coth\left(\frac{k_\mathrm{B}T}{2\hbar\omega_\alpha}\right) = \frac{2k_\mathrm{B}T}{\hbar\omega_\alpha} + \frac{\hbar\omega_\alpha}{8k_\mathrm{B}T} + \ldots + . \tag{4.86}$$

Then we have

$$\boldsymbol{\Sigma} = k_\mathrm{B}T\boldsymbol{D}(\boldsymbol{\kappa})^{-1} + \frac{\hbar^2}{16k_\mathrm{B}T}\boldsymbol{M}^{-1}, \tag{4.87}$$

or

$$\Sigma_{jj} = \langle |\boldsymbol{\Delta}_j|^2 \rangle = k_\mathrm{B}T F_{jj}^{-1} + \frac{\hbar^2}{16k_\mathrm{B}T} M_{jj}^{-1}. \tag{4.88}$$

Because $\boldsymbol{\Delta}_j = (\boldsymbol{d}_j - \boldsymbol{d}_\mathrm{o}) \cdot \boldsymbol{s}_j$, where $\boldsymbol{d}_j$ and $\boldsymbol{d}_\mathrm{o}$ are the j atom and the central atom displacements, the MSRD $\langle |\boldsymbol{\Delta}_j|^2 \rangle$ can be rewritten in terms of the

MSD $\langle(\boldsymbol{x}_j \cdot \boldsymbol{l}_j)^2\rangle$, $\langle(\boldsymbol{x}_\text{o} \cdot \boldsymbol{s}_j)^2\rangle$ and the displacement correlation function (DCF) $\langle(\boldsymbol{x}_0 \cdot \boldsymbol{s}_j)(\boldsymbol{x}_j \cdot \boldsymbol{s}_j)\rangle$ such that

$$\langle|\boldsymbol{\Delta}_j|^2\rangle = \langle(\boldsymbol{d}_j \cdot \boldsymbol{s}_j)^2\rangle + \langle(\boldsymbol{d}_\text{o} \cdot \boldsymbol{s}_j)^2\rangle - 2\langle(\boldsymbol{d}_\text{o} \cdot \boldsymbol{s}_j)(\boldsymbol{d}_j \cdot \boldsymbol{s}_j)\rangle, \tag{4.89}$$

where $\boldsymbol{s}_i$ is the equilibrium position unit vector of atom j ($\boldsymbol{l}_j$ is the equilibrium position vector of atom j).

In this form, the function can be divided into two parts (one composed of the MSD term and the other of the DCF term) so that the effect of each can be examined separately. For monoatomic crystals, this gives [173, 167]

$$\langle|\boldsymbol{\Delta}_j|^2\rangle = \frac{\hbar}{Nm}\sum_{\boldsymbol{\kappa},\alpha}(\boldsymbol{s}_{\boldsymbol{\kappa},\alpha} \cdot \boldsymbol{s}_j)^2 \frac{1}{\omega_{\boldsymbol{\kappa},\alpha}} \coth\left(\frac{\hbar\omega_{\boldsymbol{\kappa},\alpha}}{2k_\text{B}T}\right)[1 - \cos(\boldsymbol{\kappa} \cdot \boldsymbol{l}_i)]$$

$$\text{Beni–Platzman–Debye MSRD correlation,} \tag{4.90}$$

where N is the number of atoms of mass m, $\boldsymbol{s}_{\boldsymbol{\kappa},\alpha}$ is the polarization vector for phonons of momentum $\boldsymbol{\kappa}$, polarization α, and frequency $\omega_{\boldsymbol{\kappa},\alpha}$. The first term on the right-hand side of (4.90) is two times the MSD (which is independent of the central atom neighbor distance). The second term ensures that only the out-of-phase thermal motion of the atoms along $\boldsymbol{l}_i$ determines the decrease in extended X-ray absorption fine-structure. For a monoatomic cubic crystal, $(\boldsymbol{s}_{\boldsymbol{\kappa},\alpha} \cdot \boldsymbol{s}_j)^2$ can be replaced with (1/3). Then, by use of (4.56), the Debye approximation for the DOS (for monatomic, cubic crystals, $V\int_0^{\omega_\text{D}} D_p(\omega)\text{d}\omega = 3nV$ and $\omega = u_{p,\text{A}}\kappa$), we have

$$\langle|\boldsymbol{\Delta}_j|^2\rangle = \frac{3\hbar}{m\omega_\text{D}}\left[\frac{1}{4} + \left(\frac{T}{T_\text{D}}\right)^2 g_1\right] - \frac{3\hbar}{m\omega_\text{D}}\left\{\frac{1-\cos(\kappa_\text{D}l_j)}{2(\kappa_\text{D}l_j)^2} + \right.$$

$$\left.\left(\frac{T}{T_\text{D}}\right)^2\left[g_1 - \frac{1}{3!}\left(\kappa_\text{D}l_j\frac{T}{T_\text{D}}\right)^2 g_3 + \frac{1}{5!}\left(\kappa_\text{D}l_j\frac{T}{T_\text{D}}\right)^4 g_5 - ...\right]\right\}$$

$$\text{Beni–Platzman–Debye MSD model,} \tag{4.91}$$

where

$$g_n = \int_0^{T_\text{D}/T}\frac{x^n}{e^x - 1}\text{d}x, \text{ and } \omega_\text{D} = \frac{T_\text{D}k_\text{B}}{\hbar}. \tag{4.92}$$

In this expression, ω_D, T_D, and κ_D are the Debye frequency, temperature, and wave vector, respectively. The first term on the right-hand side is the MSD and the second term is the DCF. The MSRD is twice that given by (4.91). The leading term, MSD, was given by (2.57). Calculations show that the DCF has a relatively large contribution to the final value (temperature dependent, ranges from 15% to 40% of MSD for FCC and BCC crystals with respect to the first term).

Examination of (4.91) shows that $\langle|\boldsymbol{\Delta}_j|^2\rangle$ increases as T (e.g., Figure 2.14) and for high melting crystals with small T_D, this can lead to relatively large displacements at high temperatures. This relation can also be used for an isotropic crystal, for which the corresponding directional Debye temperatures are known. Note that this model is based on harmonic displacement of atoms and is expected to be valid for low temperatures.

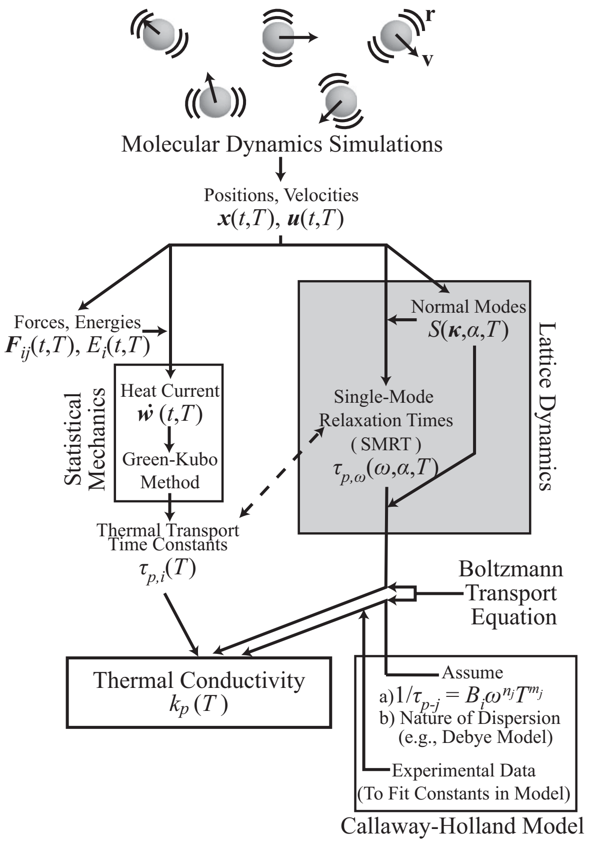
r
v
Molecular Dynamics Simulations
Positions, Velocities
$x(t,T)$, $u(t,T)$
Forces, Energies
$F_{ij}(t,T)$, $E_i(t,T)$
Statistical Mechanics
Heat Current
$\dot{w}(t,T)$
Green-Kubo Method
Thermal Transport Time Constants
$\tau_{p,i}(T)$
Normal Modes
$S(\kappa,\alpha,T)$
Single-Mode Relaxation Times (SMRT)
$\tau_{p,\omega}(\omega,\alpha,T)$
Lattice Dynamics
Boltzmann Transport Equation
Thermal Conductivity
$k_p(T)$
Assume
a) $1/\tau_{p\text{-}j} = B_j\omega^{n_j}T^{m_j}$
b) Nature of Dispersion (e.g., Debye Model)
Experimental Data (To Fit Constants in Model)
Callaway-Holland Model

Figure 4.14. The methods of prediction of phonon thermal conductivity, MD and BTE (Callaway–Holland) [316]. The relaxation time τ_{p-j} has a frequency dependence ω^{n_j} and temperature dependence T^{m_j}.

4.9 Phonon BTE and Callaway Conductivity Model

4.9.1 Single-Mode Relaxation Time

The single-mode relaxation time (SMRT) for a mode in a phonon system describes the temporal response of the system when that mode is excited and all other modes have their equilibrium populations. This is used in the BTE derivation of the phonon conductivity, as outlined in Figure 4.14. SMRT can be seen as being consistent with an exponential decay of the energy autocorrelations (Table 3.9) using the Green–Kubo theory for thermal conductivity (Section 3.6 and will also be discussed in Sections 4.12-4.13). The limitation of this approach is that the underlying assumption (one mode activated and others at equilibrium) is never realized. This is because the natural decay of the energy in a mode occurs in the presence of other modes that are excited or diminished.

In SMRT approximation, each phonon mode ω has a single, effective phonon relaxation time $\tau_p = \tau_p(\omega_p, \alpha, T)$ representing the various scattering mechanisms.

4.9.2 Callaway Phonon Conductivity Model from BTE

The derivation presented in this section is based on that given by Callaway [70] and Holland [199]. The method presented can be applied to either a quantum or classical system.

The heat flux generated by a change in the population of energy carriers can be expressed as the general form of (3.22), i.e.,

$$\boldsymbol{q} = \sum_{\alpha} \frac{1}{C\pi^3} \int [E_p(\boldsymbol{\kappa}) - \mu] \boldsymbol{u}_p(\boldsymbol{\kappa}) f_p'(\boldsymbol{\kappa}) \mathrm{d}\boldsymbol{\kappa} \quad \text{energy flux vector,} \tag{4.93}$$

where C is eight for phonons and four for electrons (because of spin degeneracy), the integral is over the first Brillouin zone, E_p is the carrier energy, μ is its chemical potential, $\boldsymbol{u}_p$ is the carrier velocity (group), and f_p' is the deviation of the mode population from the equilibrium distribution. For phonons, the sum is over the mode polarizations (three for a monatomic unit cell), the chemical potential is zero, and the carrier speed is the phonon group velocity. A form of (4.93) is sought that will allow for direct comparison with the Fourier law ($\boldsymbol{q} = -\boldsymbol{K}_p \cdot \nabla T$) and thus generate an expression for the thermal conductivity.

The steady-state BTE (with no external force and source) for a single-phonon mode (Table 3.1) is

$$\boldsymbol{u}_p \cdot \nabla f_p = \frac{\partial f_p}{\partial t}|_s \quad \text{phonon BTE.} \tag{4.94}$$

If the phonon population is only a function of temperature, then

$$\boldsymbol{u}_p \cdot \nabla f_p = \boldsymbol{u}_p \cdot \frac{\partial f_p}{\partial T} \nabla T = \boldsymbol{u}_p \cdot \nabla T \frac{\partial f_p}{\partial T} \quad \text{introducing temperature gradient.} \tag{4.95}$$

Let $f_p = f_p^\circ + f_p'$, where f_p° is the equilibrium phonon distribution. Assuming that the deviations from equilibrium f_p' are independent of temperature, we have

$$\frac{\partial f_p}{\partial T} \simeq \frac{\partial f_p^\circ}{\partial T}. \tag{4.96}$$

The relaxation-time approximation (3.13) is made for the collision term, whereby

$$\frac{\partial f_p}{\partial t}|_s = \frac{f_p^\circ - f_p}{\tau_p} = -\frac{f_p'}{\tau_p} \quad \text{SMRT approximation.} \tag{4.97}$$

The relaxation time τ_p describes the temporal response of the system when that particular phonon mode is activated (footnote of Section 3.1.4). Under these assumptions, (4.94) becomes

$$f_p' = -\tau_p \frac{\partial f_p^\circ}{\partial T} \boldsymbol{u}_p \cdot \nabla T. \tag{4.98}$$

As was shown in Figure 3.2(b), the presence of ∇T, changes mostly the population of high energy phonons (limited by the cut-off frequency). Inserting this expression into (4.93) leads to

$$\boldsymbol{q} = -(\frac{1}{8\pi^3}\sum_{\alpha}\int E_p\tau_p\frac{\partial f_p^\circ}{\partial T}\boldsymbol{u}_p\boldsymbol{u}_p\mathrm{d}\boldsymbol{\kappa})\cdot\nabla T. \tag{4.99}$$

Taking E_p to be independent of temperature, and using (2.107), we have

$$\int E_p f_p^\circ \mathrm{d}\boldsymbol{\kappa} = \frac{\langle E_p\rangle}{V}, \tag{4.100}$$

where $\langle E_p\rangle$ is the total system energy. The mode specific heat capacity is given by (4.53) as[†]

$$nc_{v,p} = \frac{\partial(E_p f_p^\circ)}{\partial T}|_V = E_p\frac{\partial f_p^\circ}{\partial T}. \tag{4.101}$$

Thus, for the heat flux

$$\boldsymbol{q} = -(\frac{1}{8\pi^3}\sum_{\alpha}\int c_{v,p}\tau_p\boldsymbol{u}_p\boldsymbol{u}_p\mathrm{d}\boldsymbol{\kappa})\cdot\nabla T, \tag{4.102}$$

where we will use the $c_{v,p}$ given by (4.64). Comparing this result with the Fourier law (Table 1.1, in tensor form) $\boldsymbol{q} = -\boldsymbol{K}_p\cdot\nabla T$ leads to an expression for the phonon thermal conductivity tensor,

$$\boldsymbol{K}_p = \frac{1}{8\pi^3}\sum_{\alpha}\int c_{v,p}\tau_p\boldsymbol{u}_p\boldsymbol{u}_p\mathrm{d}\boldsymbol{\kappa} \quad \text{phonon conductivity tensor}, \tag{4.103}$$

where the right hand side is a tensor as a result of the diadic product of $\boldsymbol{u}_p$ with itself. Noting that using $D_{p,\mathrm{D}}$ [same as (4.56), but not summed over modes] the atomic density is given by

$$\int \mathrm{d}\boldsymbol{\kappa} = 8\pi^3 n \quad \text{atomic density}, \tag{4.104}$$

over the volume of the first Brillouin zone. The expression for the thermal conductivity, if discretized, reduces to an expression similar to that found for gases (Section 6.8.2), $k_p = \sum_i n_i c_{v,p,i}u_{p,i}\lambda_{p,i}/3$, where $c_{v,p,i}$ is the heat capacity per carrier, following from the assumption of a SMRT.

To obtain the thermal conductivity in a direction with unit vector $\boldsymbol{s}$, the component of the group velocity in the desired direction is taken such that (4.103) becomes

$$k_{p,s} = \frac{1}{8\pi^3}\sum_{\alpha}\int c_{v,p}\tau_p(\boldsymbol{u}_{p,g}\cdot\boldsymbol{s})^2\mathrm{d}\boldsymbol{\kappa} = \frac{1}{8\pi^3}\sum_{\alpha}\int nc_{v,p}\tau_p u_{p,g}^2\cos^2\theta\,\mathrm{d}\boldsymbol{\kappa}, \tag{4.105}$$

where θ is the angle between the group velocity $\boldsymbol{u}_{p,g}$ and $\boldsymbol{s}$. It is convenient in some cases to assume that the medium is isotropic, so that the integration can be performed over the wave number as opposed to the wave vector. In this case,

---

[†] For a quantum-harmonic system, $E_p = \hbar\omega$, and the particles follow the Bose–Einstein distribution. For a classical system, the energy is not discretized, and the forms of E_p and f_p° are not obvious. These specifications are not critical, however, as E_p and f_p° fall out in the derivation, as long as they are defined as given in (4.100).

$d\boldsymbol{\kappa} = 4\pi\kappa^2 \mathrm{d}\kappa$, and the $\cos^2\theta$ term is replaced with 1/3, its average value over a unit spherical volume $\langle\cos^2\theta\rangle$ (Chapter 7 problem). This leads to

$$k_p = \frac{1}{6\pi^2}\sum_\alpha \int c_{v,p}\tau_p u_{p,g}^2 \kappa^2 \mathrm{d}\kappa. \qquad (4.106)$$

Furthermore, it can be convenient to change the variable of integration from the wave vector to the the angular frequency

$$k_p = \frac{1}{6\pi^2}\sum_\alpha \int c_{v,p}\tau_p u_{p,g}^2 \kappa^2 \frac{\mathrm{d}\kappa}{\mathrm{d}\omega}\mathrm{d}\omega = \frac{1}{6\pi^2}\sum_\alpha \int c_{v,p}\tau_p \frac{u_{p,g}}{u_{p,p}^2}\omega^2 \mathrm{d}\omega$$

isotropic phonon conductivity frequency integral, (4.107)

where the definitions of the phonon phase and group velocities given by (4.16) and (4.15) ($u_{p,p} = \omega/\kappa$ and $u_{p,g} = \mathrm{d}\omega/\mathrm{d}\kappa$,) have been used. Note that $\rho c_{v,p} = n c_{v,p}$, where n is the number of atoms per unit volume, and $c_{v,p}$ on the right-hand side is the heat capacity per atom as given by (4.64). One must take care when using this form of the thermal conductivity in cases in which the phonon frequency is not a monotonically increasing function of the wave number e.g., one of the transverse branches in the [110] direction in the FCC crystal, as shown in Figure 4.7(a). In such cases, the integral must be broken into appropriate parts.

Callaway [70] uses a single-phonon speed $u_{p,g}$ and the Debye specific heat capacity (4.64) (per atom), and for the three modes being treated the same, his expression for the phonon thermal conductivity is (end-of-chapter problem)

$$k_p = (48\pi^2)^{1/3}\frac{1}{a}\frac{k_\mathrm{B}^3}{h_\mathrm{P}^2}\frac{T^3}{T_\mathrm{D}}\int_0^{T_\mathrm{D}/T} \tau_p(x)\frac{x^4 e^x}{(e^x-1)^2}\mathrm{d}x \quad \text{Callaway phonon conductivity,} \qquad (4.108)$$

where $x = \hbar\omega/k_\mathrm{B}T$, a is the lattice constant $a = n^{-1/3}$ for a cubic lattice, and n is the atomic number density. Note that from (4.55) we have used $k_\mathrm{B}x^2e^x/(e^x-1)^2$ for $c_{v,p}$ in (4.107), since $c_{v,p}$ in (4.107) is per phonon.

Using the concept of the phonon mean free path (1.14) (derivation in Section 6.8.2), the phonon thermal conductivity is written as (note again that $c_{v,p}$ is in J/kg-K)

$$\begin{aligned} k_p &= \frac{1}{3}\rho\sum_\alpha c_{v,p,\alpha}u_{p,\alpha}\lambda_{p,\alpha} \\ &= \frac{1}{3}\rho\sum_\alpha c_{v,p,\alpha}u_{p,\alpha}^2\tau_{p,\alpha}, \end{aligned} \qquad (4.109)$$

where the sum is over $3N$ phonon normal modes for an N atom system (4.43) and $\lambda_{p,\alpha}$ is the modal mean free path.

In following a similar procedure, Callaway [70] developed a more comprehensive form for the thermal conductivity based on a refined expression for the collision term, the use of different relaxation times for the normal and resistive processes was considered and will be discussed in Sections 4.9.3(E) and 4.15 and is shown in Figure 4.37. (This is an end-of-chapter problem.) Equation (4.107) is the general form of these results.

4.9.3 Callaway–Holland Phonon Conductivity Model

Callaway single-mode relaxation-time model (4.109) successfully predicts (when using multiple fitting parameters) the low-temperature thermal conductivity using the Debye approximation (no phonon dispersion) and that there is no phonon dispersion and that the longitudinal and transverse polarizations behave identically. Holland [199] extended the work of Callaway by separating the contributions of LA and TA phonons, including some phonon dispersion, and using different forms of the relaxation times. Better high-temperature agreement is then found. This Callaway–Holland model has been refined to include further detail on the phonon dispersion and relaxation times [441, 464, 11]. The added complexities lead to more fitted parameters. One could argue that the resulting better fits with the experimental data are because of this increase in the number of fitted parameters and not to an improvement of the actual physical model.

The thermal conductivity of an isotropic crystal, with negligible contributions from optical phonons, is given by (4.107) written in Callaway–Holland form as

$$k_p = k_{p,\mathrm{L}} + k_{p,\mathrm{T}} = \frac{1}{6\pi^2}[\int_0^{\omega_{m\mathrm{L}}} c_{v,p}\frac{u_{p,g,\mathrm{L}}}{u^2_{p,p,\mathrm{L}}}\tau_{p,\mathrm{L}}\omega_\mathrm{L}^2 \mathrm{d}\omega_\mathrm{L}$$

$$+2(\int_0^{\omega_1} c_{v,p}\frac{u_{p,g,\mathrm{T}}}{u^2_{p,p,\mathrm{T}}}\tau_{p,\mathrm{T1}}\omega_\mathrm{T}^2 \mathrm{d}\omega_\mathrm{T} + \int_{\omega_1}^{\omega_{m\mathrm{T}}} c_{v,p}\frac{u_{p,g,\mathrm{T}}}{u^2_{p,p,\mathrm{T}}}\tau_{p,\mathrm{T2}}\omega_\mathrm{T}^2 \mathrm{d}\omega_\mathrm{T})]$$

Callaway–Holland phonon conductivity. (4.110)

The first term corresponds to longitudinal phonons, and the second and third terms to transverse phonons (two degenerate branches). Here, $c_{v,p}$ is the quantum-harmonic specific heat per normal mode and τ_p is a SMRT. The forms of τ_p are given in [199], and are discussed and summarized in Section 4.9.4. The upper limits of the first and third integrals are the angular frequencies of the phonon branches at the edge of the first Brillouin zone (marked by X in Figure 4.3), signified as $\omega_{m\mathrm{L}}$ and $\omega_{m\mathrm{T}}$. For the transverse phonons, the frequency ω_1 is that at the center of the first Brillouin zone. Also, two different relaxation times are used for the transverse wave in the first and second portions of the Brillouin zone, $\tau_{p,\mathrm{T1}}$ and $\tau_{p,\mathrm{T2}}$.

4.9.4 Phonon Scattering Relaxation Time Models

The approximation of adding resistivities to transport in series [Matthiessen rule, (3.53)] is used for combining the contribution from various scattering mechanisms[†].

This leads to

$$\frac{1}{\tau_p} = \sum_j \frac{1}{\tau_{p,j}} \quad \text{Matthiessen rule (resistivities in series),} \tag{4.111}$$

[†] Matthiessen rule is based on electric resistivity, where contributions of various scatterings are assumed to be additive and the resistivity is proportional to the inverse of the relaxation times, as given by (5.147). It has some requirements for its application, for example the independent scattering mechanisms should follow similar power-law energy dependence [294].

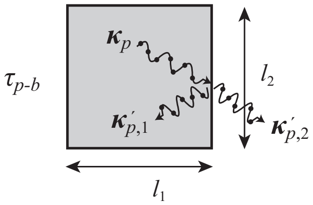

(a) Phonon-Crystalline (i.e., Grain or Casimir) Boundary Scattering

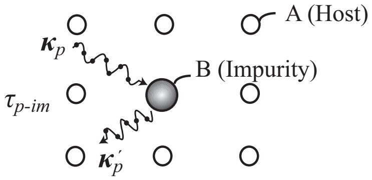

(b) Phonon-Impurity (B) Scattering

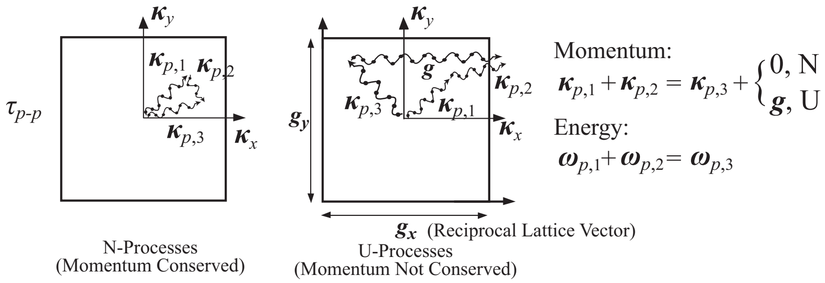

Momentum Conservation In Interphonon Scattering

(c) Three-Phonon Scattering

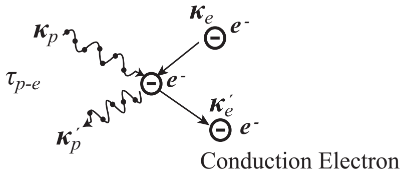

(d) Phonon-Electron Scattering

Figure 4.15. Phonon scattering by (a) crystalline (grain) boundary, (b) impurity, (c) other phonons (N–Processes, in which phonon momentum is conserved, and U–processes, in which the momentum balance allows for flipping into the adjacent Brillouin zone), and (d) electron.

where τ_p is the effective phonon relaxation time and $\tau_{p\text{-}j}$ is phonon scattering that is because of the j scattering mechanism.

Figure 4.15 shows phonon scattering by (a) crystalline (e.g. grain) boundary, (b) impurity, (c) other phonons (normal, or N–Processes, and Umklapp, or U–processes, will be discussed in Section 4.15), and (d) electrons.

Some of the common phonon relaxation-time models are listed in Table 4.2. These involve a frequency-dependent term, a temperature-dependent term, and some empirical constants. Typical constants used in these models are given in

Table 4.2. *Some phonon scattering relaxation times [30, 68, 199, 203].*

Scattering Source	Relaxation Time	Comment
Phonon–crystal boundaries	$\tau_{p\text{-}b}^{-1} = u_{p,\mathrm{A}}/L, \ L = \frac{2}{\pi^{1/2}}(l_1 l_2)^{1/2}$	l_1 and l_2 are crystal linear dimensions
Phonon–displacement	$\tau_{p\text{-}d} = \frac{\pi u_{p,\mathrm{A}}^3}{2nV_c^2}\frac{1}{a_{p\text{-}d}^2\gamma_G^2}(\frac{R}{\Delta R})^2\omega_p^{-4}$	R is radius of impurity atom, ΔR difference is radii of host and impurity, γ_{G} is Grüneisen constant, n is number density of impurity, V_c is unit-cell volume, and $a_{p\text{-}d}$ is impurity dependent
Phonon–impurity	$\tau_{p\text{-}im} = \frac{4\pi u_{p,\mathrm{A}}^3}{V_c \sum_i x_i(1-\frac{M_i}{M})^2}\omega_p^{-4}$	$V_c = Fa^3$ ($F = 1$ for cubic structures) is unit-cell volume, x_i is mass fraction of impurity atom i
Phonon–isotope impurity	$\tau_{p\text{-}is} = \frac{4\pi u_{p,\mathrm{A}}^3}{a_{p\text{-}is}V_{is}}\omega_p^{-4}, \ 3u_{p,\mathrm{A}}^{-1} = u_{p,\mathrm{L}}^{-1} + 2u_{p,\mathrm{T}}^{-1}$	$a_{p\text{-}is} = 2.1 \times 10^{-4}$ (for Si), V_{is} is isotope atom volume
Three phonons		
N-Processes		
Longitudinal	$\tau_{p\text{-}p,\mathrm{L,N}}^{-1} = B_{\mathrm{L}}\omega_p^2 T^3$	low T
Transverse	$\tau_{p\text{-}p,\mathrm{T,N}}^{-1} = B_{\mathrm{T}}\omega_p T^4$	low T
Longitudinal	$\tau_{p\text{-}p,\mathrm{L,N}}^{-1} = B'_{\mathrm{L}}\omega_p^2 T$	high T
Transverse	$\tau_{p\text{-}p,\mathrm{T,N}}^{-1} = B'_{\mathrm{T}}\omega_p T$	high T
U-Processes	(i) $\tau_{p\text{-}p,\mathrm{U}}^{-1} = B_{\mathrm{U}}\omega_p^2 T^3 \exp(-T_i/\alpha T)$	Klemens model
Dispersive	(ii) $\tau_{p\text{-}p,\mathrm{U}}^{-1} = B_{\mathrm{U}}\omega_p T^3 \exp(-T_i/\alpha T)$	Klemens model
Transverse	(iii) $\tau_{p\text{-}p,\mathrm{TU}}^{-1} = B_{\mathrm{TU}}\omega_p^2/\sinh x,$ $\omega_{p,1} \le \omega_p \le \omega_{p,2}, \ x = \hbar\omega_p/k_{\mathrm{B}}T$ $= 0, \ \omega_p < \omega_{p,1}$	
	(iv) $\tau_{p\text{-}p,\mathrm{U}}^{-1} = B_{\mathrm{U}}\omega_p^2 T^3$	Callaway model
	(v) $\tau_{p\text{-}p,\mathrm{U}}^{-1} = B_{\mathrm{U}}\omega_p^2 T$	high T
Roufosse [203]	$\tau_{p\text{-}p,\mathrm{R}}^{-1} = A(1 + B\omega_p^2)\omega_p^2 T, \ \omega < \omega_c$ $\tau_{p\text{-}p,\mathrm{R}} = \pi/\omega_p, \ \omega > \omega_c$	A, B, and ω_c are given in Section 4.11.1
Limit	$\tau_{p\text{-}p,\mathrm{C-P}} = \frac{\pi}{\omega_p},$	Cahill-Pohl [68]
Phonon–electron [491]	$\tau_{p\text{-}e}^{-1} = \frac{n_{e,c}^2 e_c^2 u_{p,\mathrm{A}}^2}{n_c k_{\mathrm{B}} T \sigma_e}\frac{1}{\alpha_1}(\frac{T_{\mathrm{D}}}{T})^{3/2}$ $= \frac{\sigma_e u_{p,\mathrm{A}}^2}{\mu_e^2 n_c k_{\mathrm{B}} T \alpha_1}(\frac{T_{\mathrm{D}}}{T})^{3/2},$ $\alpha_1 = 4^3(\frac{\pi V_a}{6})^{1/2}(\frac{m_{e,e}u_{p,\mathrm{A}}}{h_{\mathrm{P}}})^{3/2}$	V_a is volume per atom, n_c is number of unit cells per volume, σ_e and μ_e are the electron conductivity and mobility

Table 4.3. *Parameters used in phonon relaxation-time models, for Si and Ge [199].*

Parameter Symbol	Magnitude, Si	Magnitude, Ge
$u_{p,\mathrm{T}}$	5.86×10^3, m/s	3.55×10^3, m/s
$u_{p,\mathrm{L}}$	8.48×10^3	4.92×10^3
$u_{p,\mathrm{A}}$	6.4×10^3	3.9×10^3
$u_{p,\mathrm{TU}}(\omega < \omega_1)$	2.0×10^3	1.3×10^3
$u_{p,\mathrm{TU}}(\omega > \omega_1)$	4.24×10^3	2.46×10^3
F	~ 0.8	~ 0.8
T_T	180, K	101, K
T_TU	210	118
T_L	570	333
T_4	350	192
T_D	658	376
Γ	2.16×10^{-4}	5.72×10^{-4}
α	2	2
B_T	9.3×10^{-13} 1/K^4	1.0×10^{-11} 1/K^4
B_TU	5.5×10^{-18} s	5.0×10^{-13} s
B_L	2.0×10^{-24} s/K^3	6.9×10^{-24} s/K^3

Tables 4.2 and 4.3. These constants are typically found by fitting to experimental thermal conductivity results.

(A) *Crystal Boundary and Grain Scattering*

The crystal boundary scattering (crystal size effect) $\tau_{p\text{-}b}$ is based on diffuse boundary absorption/emission. It is referred to as Casimir boundary scattering and gives a mean free path for a phonon equal to the Casimir length L, which is the length of travel of the phonon before the boundary absorption/re-emission. For a rectangular path, l_1 and l_2, it is given as $L = (2/\pi^{1/2})(l_1 l_2)^{1/2}$ [199]. Then with a single phonon speed $u_{p,p} = u_{p,g} = u_{p,\mathrm{A}}$, the relaxation time is

$$\tau_{p\text{-}b}^{-1} = u_{p,\mathrm{A}}/L \quad \text{phonon boundary (Casimir) scattering.} \tag{4.112}$$

This represents ballistic transport within the crystal with the scattering bottleneck being the crystal boundary scattering. In microparticles and nanoparticles (crystalline), this boundary scattering dominates at very low temperatures [below the peak in $k_p(T)$].

(B) *Impurity Scattering*

Impurity (static imperfection) scattering is similar to the Rayleigh scattering of the transverse electromagnetic waves, which is proportional to ω_p^4.

The Klemens [247] derivation of scattering of low-frequency lattice waves by stationary imperfections is based on the quantum treatment of phonon. The general theory of transition probabilities is discussed by Ziman [515] and leads to the FGR. Starting from (4.47), the FGR (3.27) written for this transition rate (for elastic scattering, $\omega = \omega'$) is [247]

$$\frac{1}{\tau_{p\text{-}im}} = a^3 F \int 2|M_{\kappa,\kappa'}|^2 \frac{1}{M^2\omega^2}\frac{\pi}{(2\pi)^3}\frac{\mathrm{d}\kappa'}{\mathrm{d}\omega'}\mathrm{d}\boldsymbol{\kappa}'$$

$$|M_{\boldsymbol{\kappa}',\kappa}|^2 = x_i(1-\frac{M_i}{M})^2\frac{1}{6F}\omega^2\omega'^2, \qquad (4.113)$$

where $Fa^3 = V_c$ is the volume of crystal primitive cell and F allows for noncubic structures ($F = 1$ for cubic structures). Here M_i is the molecular weight of impurity species B in host A and x_i is its atomic fraction.

Based on this, Klemens [246] arrived at the phonon mean free path

$$\lambda_{p\text{-}im} = \frac{Fa}{\sum_i x_i(1-\frac{M_i}{M})^2}\frac{1}{(a\kappa)^4}, \qquad (4.114)$$

where $a\kappa = 2\pi a/\lambda$ is also called the size parameter, comparing the phonon wavelength with the interatomic spacing.[†] Then with $\lambda_{p\text{-}im} = u_{p,g}\tau_{p\text{-}im} = u_{p,\mathrm{A}}\tau_{p\text{-}im}$, this is written as

$$\tau_{p\text{-}im} = \frac{4\pi u_{p,\mathrm{A}}^3}{V_c\sum_i x_i(1-\frac{M_i}{M})^2}\omega^{-4} \quad \text{phonon impurity (static imperfection) scattering.} \qquad (4.115)$$

The form given in Table 4.2 also makes no distinction between the group and phase velocities, but it can be modified accordingly (Section 4.9.6).

(C) *Phonon–Phonon Scattering*

Interphonon scattering $\tau_{p\text{-}p}^{-1}$ shows a ω^1 and a ω^2, as ω increases. Also, unlike other mechanisms, interphonon scattering is highly temperature dependent. The MD/G-K prediction of $\tau_{p\text{-}p}$ for FCC Ar is reported in [316] and is in general agreement with these trends.

In general, the interphonon-scattering relaxation time is represented as

$$\frac{1}{\tau_{p\text{-}p}} = B\omega_p^n f(T), \qquad (4.116)$$

where n is a integer (1, 2, or 3) and $f(T)$ describes the temperature dependence. The temperature dependence is generally of the form T^m, although, as listed in Table 4.2, for three-phonon scattering, more complex relations are used.

[†] Here the impurity i has a molecular weight M_i and mass fraction x_i. The lattice constant is a, and the host molecular weight is M.

To be physically meaningful, the mean free path λ_p of a phonon should be longer than one-half of its wavelength, λ. Noting that $\lambda_p = u_{p,g}\tau_p$, $\lambda = 2\pi/\kappa$, and using the definition of $u_{p,p}$, this limit can alternatively be stated as

$$\frac{1}{\tau_{p\text{-}p}} \leq \frac{\omega u_{p,g}}{\pi u_{p,p}} \quad \text{limit on phonon–phonon-scattering relaxation time,} \tag{4.117}$$

and is also shown in Figure 4.16(a) for L–J FCC Ar. At a temperature of 50 K, the phonons at the edge of the first Brillouin zone ($\kappa^* = 1$) are outside of the allowed range for both polarizations. As the temperature increases, more of the phonon modes do not satisfy (4.117). At the highest temperature, 80 K, the transition occurs at κ^* values of 0.77 and 0.81 for the longitudinal and transverse polarizations, respectively.

The data for each polarization can be broken down into three distinct regions. The first two are fit with low-order polynomials. For the longitudinal polarization, the first region is fit with a second-order polynomial through the origin, and the second region with a second-order polynomial. For the transverse polarization, the first region is fit with a second-order polynomial through the origin, and the second region with a linear function. The resulting functions are also shown in Figure 4.16(a) and are considered satisfactory fits to the L–J FCC MD/G–K results for k_p. As the temperature increases, the behavior in the two regions becomes similar. For both polarizations at a temperature of 80 K, and for the longitudinal polarization at a temperature of 65 K, a single second order polynomial through the origin is used to fit the data. In the third region, the continuous relaxation-time functions are taken up to the maximum frequency ($\omega_{\mathrm{L},max}$ or $\omega_{\mathrm{T},max}$) by use of (4.117).

The raw data and continuous relaxation-time functions for all temperatures considered are shown in Figures 4.16(b) and (c). The parts of the relaxation-time curves are not forced to be continuous. For both the longitudinal and transverse polarizations, any resulting discontinuities are small and are purely a numerical effect.

The relaxation time functions do not contain the orders-of-magnitude discontinuities found in the Holland relaxation times (Table 4.2), which result from the assumed forms of the relaxation times and how the fitting parameters are determined.

Theoretical calculations predict that in the κ^* range of 0 to 0.2, the longitudinal and transverse curves should follow ω^2 and ω dependencies, respectively [190, 360]. This is not found in the relaxation times predicted by the MD/G–K simulations. The second-order fit found at the high temperatures is consistent with the high-temperature prediction of [445]. Of particular note is the turning over of the low-temperature transverse curves at higher frequencies. In general, it is clear that the extension of the low-frequency behavior to the entire frequency range, as is sometimes done, is not generally suitable. The effect of such an assumption on the thermal conductivity prediction will be considered.

As will be discussed in Section 4.13, the phonon–phonon scattering is divided into N (for normal) $\tau_{p\text{-}p,\mathrm{N}}$ and U (for Umklapp) $\tau_{p\text{-}p,\mathrm{U}}$ processes and the U–processes are dominant at high temperature. The derivation of the N- and

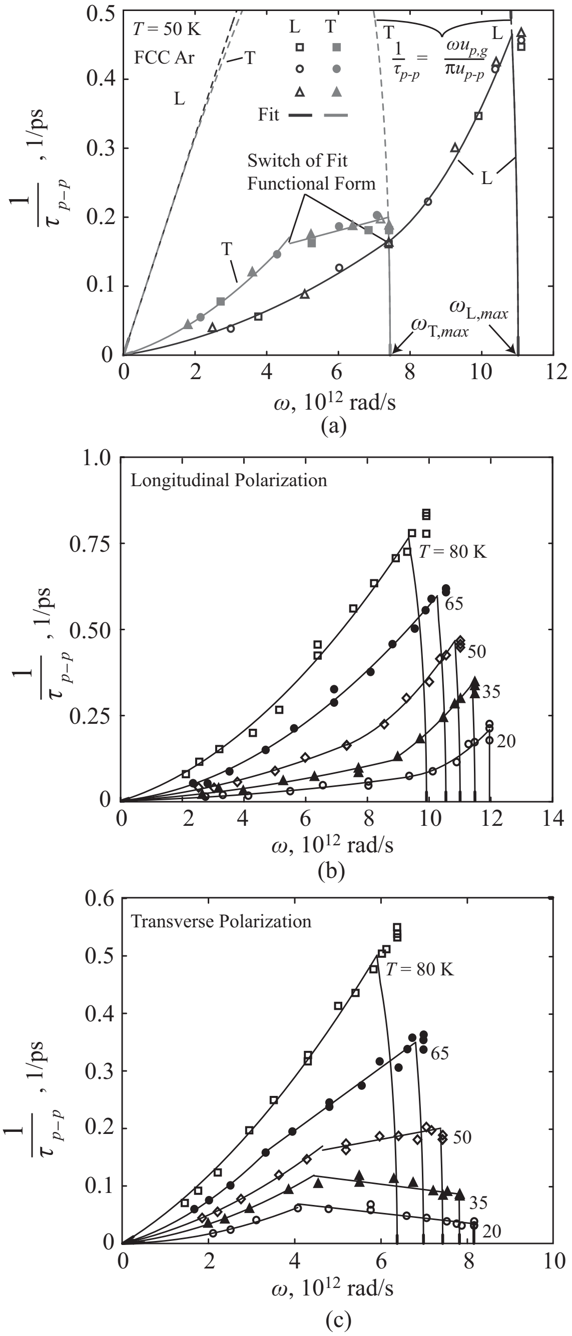

Figure 4.16. (a) Discrete phonon–phonon relaxation times and continuous curve fits $\tau_{p\text{-}p}$ at $T = 50$ K for FCC Ar. Also shown is the minimum physical value of the relaxation time, $\pi u_{p,p}/\omega u_{p,g}$. (b) MD/G-K results and continuous relaxation-time curve fits for the longitudinal polarization at all temperatures considered. (c) MD/G-K results and continuous relaxation-time curve fits for the transverse polarization at all temperatures considered [316].

U–Processes are based on quantum mechanics (FGR) [445], and some observations on the interphonon interaction rules based on MD results are presented in [316]. So, in tabulated relations, the phonon-phonon scattering relaxation times (4.116) are presented as $\tau_{p\text{-}p,i,j}$, where i = L, T, and j = N, U.

(D) *Electron Scattering*

The phonon–electron relaxation time is found from a momentum balance analysis based on maximum phonon frequency [490] as

$$\frac{1}{\tau_{p\text{-}e}} = \frac{3u_{p,\mathrm{A}}^2}{\mu_e^2}\frac{\sigma_e}{c_{v,p}T} \quad \text{phonon–electron scattering,} \tag{4.118}$$

where σ_e and μ_e are the electrical conductivity and mobility, and $c_{v,p}$ is the phonon specific heat of the phonons allowed to interact with conduction-band electrons. Using the Debye model for $c_{v,p}$ given in Section 4.7, an approximation for (4.118), in terms of the Debye temperature, is given in Table 4.2 [491]. We will discuss the phonon–electron coupling in Section 5.15, and for the case of acoustic phonons in elastic interaction with the conduction electrons, will use a coupling potential. In general, phonons affect conduction electron transport more than electrons affecting the phonon transport. The coupling potential is weaker for metals than semiconductors, but the conduction electron density is higher in metals (Chapter 5).

(E) *Displacement Scattering*

The impurities displace atoms and depending on the size mismatch in this replacement ΔR (difference in radius of host and impurity). Then they cause phonon scattering with $\tau_{p,d}$ proportional to ΔR^{-2}, as listed in Table 4.2. This relaxation time is temperature independent, and similar to impurity scattering (4.114), has a ω_p^{-4} dependence.

(F) *Normal and Resistive Relaxation Times*

Using (4.111) Callaway [70] divided the various scattering mechanisms into normal $\tau_{p\text{-}p,\mathrm{N}}$ and resistive $\tau_{p,r}$, i.e.,

$$\frac{1}{\tau_p} = \frac{1}{\tau_{p\text{-}p,\mathrm{N}}} + \frac{1}{\tau_{p,r}}, \tag{4.119}$$

where for N–Processes both energy and momentum of scattered phonons are conserved to be within a reciprocal space vector, whereas for U–Processes and other resistive processes the momentum is not conserved. The resistive scattering is further divided into displacement $\tau_{p\text{-}d}$, impurity $\tau_{p\text{-}im}$, Umklapp $\tau_{p\text{-}p,\mathrm{U}}$, crystal boundary $\tau_{p\text{-}b}$, and phonon–electron $\tau_{p\text{-}e}$, i.e.,

$$\frac{1}{\tau_{p,r}} = \frac{1}{\tau_{p\text{-}d}} + \frac{1}{\tau_{p\text{-}im}} + \frac{1}{\tau_{p\text{-}p,\mathrm{U}}} + \frac{1}{\tau_{p\text{-}b}} + \frac{1}{\tau_{p\text{-}e}}. \tag{4.120}$$

All of these are listed in Table 4.2.

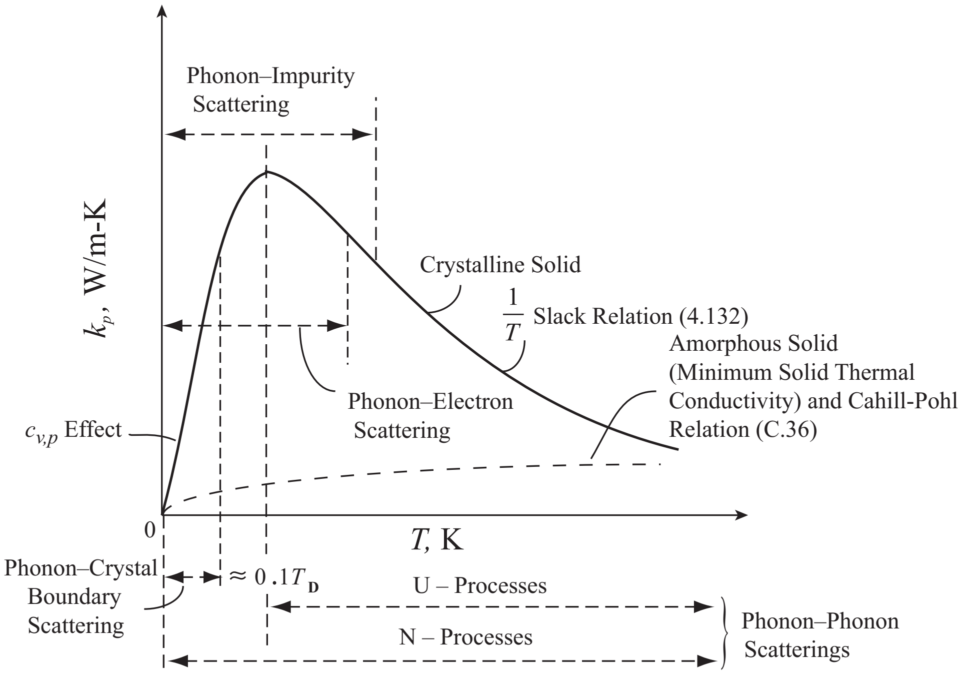

Figure 4.17. Regimes of important (or dominant) phonon-scattering mechanisms in variations of phonon conductivity with respect to temperature [30]. The behavior of an amorphous solid is also shown (the crystalline solid has a higher thermal conductivity) [244].

(G) *Temperature Dependence of Phonon Conductivity*

Figure 4.17, which shows the k_p-T behavior, summarizes the various phonon-scattering mechanisms and their regimes of importance (or dominance). Starting at $T = 0$, there is no atomic motion and $k_p = 0$. As the temperature increases, the initial increase in k_p is a specific heat effect [Figure 4.13(a)]. Then, first the phonon–grain boundary scattering dominates. As the temperature further increases, the impurity, electron, and finally the interphonon U–Processes dominate. The maximum in k_p occurs at a fraction of Debye temperature, around $0.1T_D$.

The high-temperature behavior is dominated by interphonon scattering and has a T^{-1} behavior (Slack relation). This will be discussed in Section 4.11. There it will be that the interatomic bond length controls the high-temperature behavior of k_p. The noncrystalline (amorphous) solids generally have a thermal conductivity that increases with temperature and is generally the lowest thermal conductivity for a solid phase [244]. We will discuss these in Section 4.10.

In the next section, we examine the predicted phonon conductivity of Ge, where phonon-electron scattering is negligible.

4.9.5 Phonon Dispersion Models: Ge As Example

Experimental results for the phonon dispersion of the acoustic modes of Ge in the [100] direction, at a temperature of 80 K, are shown in Figures 4.18(a) and (b) [349]. The horizontal axis is a dimensionless wave number, which is obtained by

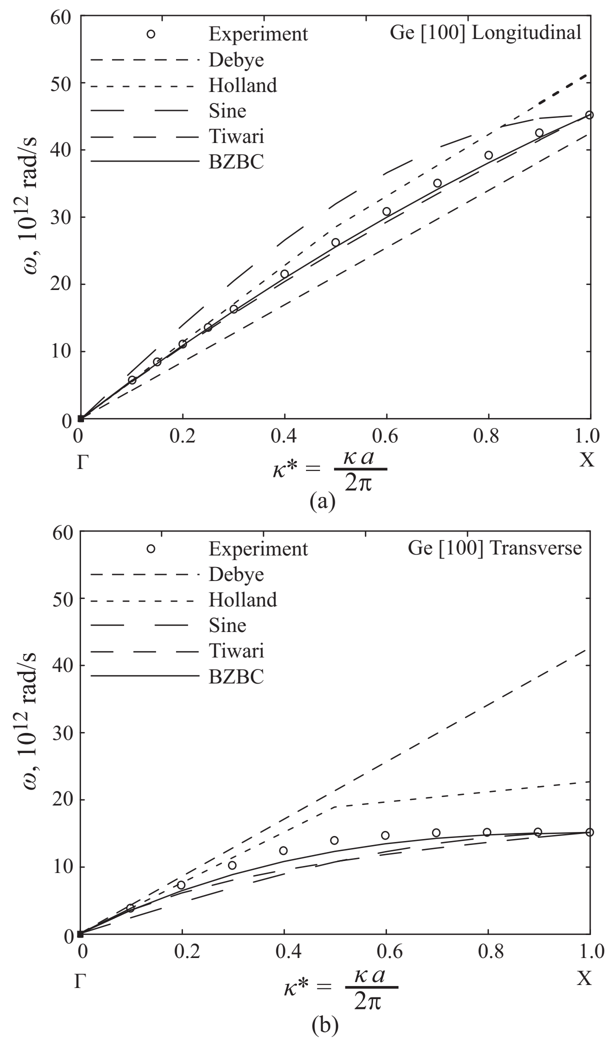

Figure 4.18. Germanium phonon dispersion in the [100] direction. Experimental data [349] and five models used in this study for (a) LA phonons and (b) TA phonons.

normalizing the wave number against its value at the edge of the first Brillouin zone, i.e., $\kappa^* = \kappa/\kappa_m = \kappa/(2\pi/a)$. For Ge at a temperature of 80 K, the value of a is 5.651 Å [349]. To allow for the use of (4.110), which assumes isotropic dispersion, this direction is used in the subsequent analysis. The temperature dependence of the dispersion [117] is not considered. The experimental data at a temperature of 80 K are used for all calculations. To assess the importance of accurately modeling the dispersion, five different models are examined.

(A) *Debye Model*

At low frequencies, the phonon frequency is proportional to its wave number, i.e., from (4.17) we have (Figure 4.3)

$$\omega = \kappa u_{p,g,0}, \tag{4.121}$$

where the subscript 0 refers to the low-frequency limit, i.e., $\kappa \rightarrow 0$, and $u_{p,g,0}$ is the low-frequency limit of the phonon group velocity. The Debye dispersion model uses (4.121) for all frequencies, and does not distinguish between the LA and TA phonons. Note that in this case $u_{p,p} = u_{p,g}$, so that in (4.110), $u_{p,g}/u_{p,p}^2$ becomes $1/u_{p,g}$. We write (4.57) as

$$\frac{1}{u_{p,g,0}} = \frac{1}{3}(\frac{1}{u_{p,g,\mathrm{L},0}} + \frac{2}{u_{p,g,\mathrm{T},0}}). \qquad (4.122)$$

With 5142 m/s and 3391 m/s used for $u_{p,g,\mathrm{L},0}$ and $u_{p,g,\mathrm{T},0}$, $u_{p,g,0} = 3825$ m/s for Ge [349].

(B) *Holland Model*

Holland [199] separated the contributions of LA and TA phonons, and included a partial effect of phonon dispersion by splitting each branch into two linear segments. The change in the slope (and thus the phonon velocities) is assumed to occur at a κ^* value of 0.5. As taken from the experimental data of [349], the phonon velocities $u_{p,g,\mathrm{L},0}$, $u_{p,g,\mathrm{T},0}$, $u_{p,g,\mathrm{L},0.5}$, and $u_{p,g,\mathrm{T},0.5}$ are 5142, 3391, 4152, and 678 m/s, where 0.5 refers to the segment between κ^* values of 0.5 and 1. Note that the change in slope implies that $u_{p,g}$ is not equal to $u_{p,p}$ in the second region. This effect was neglected by Holland, but is included in the current study.

(C) *Sine Function Model*

In the sine function model, the phonon dispersion relation for each polarization is approximated by that of a linear monatomic chain as in [245] [a special case of (4.7), end-of-chapter problem]

$$\omega_i = \omega_{mi} \sin(\frac{\pi \kappa_i^*}{2}), \qquad (4.123)$$

where the label i can be L or T (this notation holds for the rest of the dispersion models). The critical drawback of this model is the nonaccurate behavior at low frequencies ($\kappa \rightarrow 0$) where the asymptotic group velocities (4.15),

$$u_{p,g,i,0} = \frac{\partial \omega_i}{\partial \kappa_i}|_{\kappa_i \rightarrow 0} = \frac{\pi \omega_{mi}}{2\kappa_{mi}}, \qquad (4.124)$$

differ from the experimental results. For $u_{p,g,\mathrm{L},0}$ and $u_{p,g,\mathrm{T},0}$, we obtain 6400 and 2130 m/s, compared with the experimental values of 5142 and 3391 m/s.

(D) *Tiwari Model*

In the Tiwari model [464], the dispersion is assumed to be of the form

$$\kappa_\mathrm{L} = \frac{\omega_\mathrm{L}}{u_{p,g,\mathrm{L},0}}(1 + \alpha\omega_\mathrm{L}) \quad \text{and} \quad \kappa_\mathrm{T} = \frac{\omega_\mathrm{T}}{u_{p,g,\mathrm{T},0}}(1 + \beta\omega_\mathrm{T}^2), \qquad (4.125)$$

where α and β are constants, given in [464]. Note that these equations satisfy the Brillouin zone boundary conditions (BZBC) (4.17)

$$\kappa_i(\omega_i = 0) = 0 \quad \text{and} \quad \frac{\partial \kappa_i}{\partial \omega_i}|_{\omega_i=0} = \frac{1}{u_{p,g,i,0}}. \tag{4.126}$$

This model does not show the observed experimental behavior of

$$\frac{\partial \omega_{\mathrm{T}}}{\partial \kappa_{\mathrm{T}}}|_{\kappa_{\mathrm{T}}^* \to 1} = 0, \tag{4.127}$$

at the edge of the Brillouin zone X, as shown in Figures 4.3 and 4.18(b).

(E) *BZBC Model*

For the dispersion, a model referred to hereafter as the BZBC model has been introduced in [92]. A quadratic wave-number dependence for LA phonons and a cubic wave-number dependence for TA phonons are used. This model is a modification of the Tiwari model, in that the boundary conditions given by (4.126) and (4.127), and $\omega_i(\kappa_{mi}) = \omega_{mi}$, are applied. The resulting dispersion relations are

$$\begin{aligned}\omega_{\mathrm{L}} &= u_{p,g,\mathrm{L},0}\kappa_m\kappa^* + (\omega_{m\mathrm{L}} - u_{p,g,\mathrm{L},0}\kappa_m)\kappa^{*2}\\ \omega_{\mathrm{T}} &= u_{p,g,\mathrm{T},0}\kappa_m\kappa^* + (3\omega_{m\mathrm{T}} - 2u_{p,g,\mathrm{T},0}\kappa_m)\kappa^{*2} +\\ &\quad (u_{p,g,\mathrm{T},0}\kappa_m - 2\omega_{m\mathrm{T}})\kappa^{*3}.\end{aligned} \tag{4.128}$$

4.9.6 Comparison of Dispersion Models

A comparison of the five dispersion models, along with the experimental data for Ge [349], is shown in Figures 4.18(a) and (b). Here we neglect *p-e* scattering, since it is expected to be small[199]. For the both the longitudinal and transverse polarizations, both the Tiwari and BZBC models match the experimental data reasonably well over most of the first Brillouin zone. The agreement is not as good for the transverse polarization above κ^* values of 0.7 because of the plateau behavior, which is difficult to fit with a low-order polynomial. The other dispersion curves are unsatisfactory. Of the Tiwari and BZBC models, the BZBC curve gives the best agreement with the experimental data. We note than none of these dispersion relations will be consistent with the experimental phonon density of states because of the isotropic assumption. Additionally, the integral of the volumetric density of states will not go to the expected value of $3n$, where n is the volumetric density of unit cells. For this to occur, one would need to set the dispersion with this result in mind. For these calculations, we are more concerned with matching the experimental dispersion data.

Although the Tiwari and BZBC dispersion curves show some similarities, significant differences become apparent when the quantity they affect in the thermal conductivity expression, $u_{p,g}/u_{p,p}^2$, is considered. This is shown in Figures 4.19(a) and (b). The deviation is most significant for the TA phonons near the edge of the

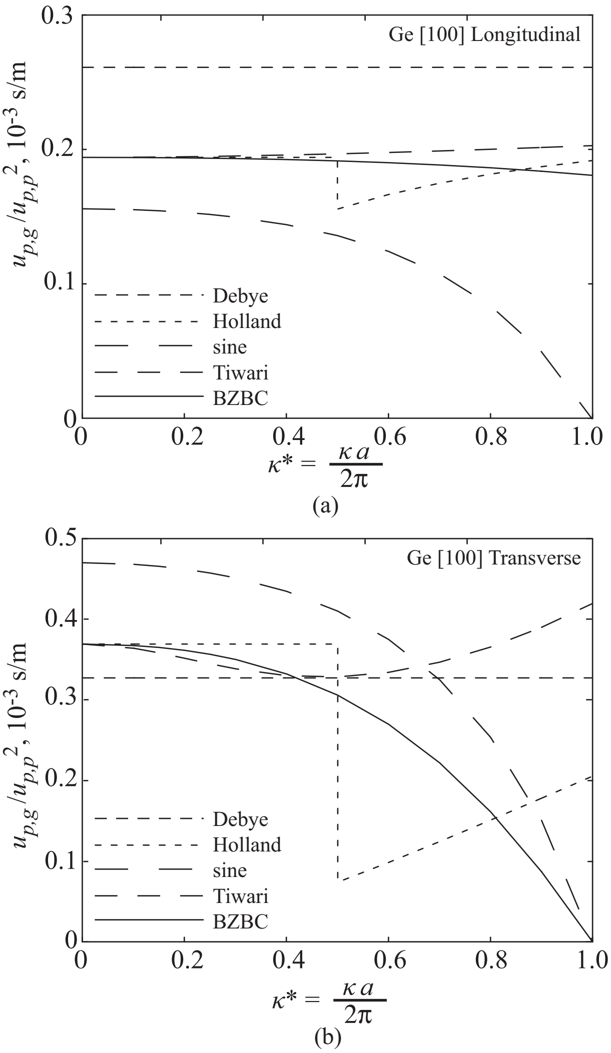

Figure 4.19. $u_{p,g}/u_{p,p}^2$ for the five Ge dispersion models plotted as a function of the normalized wave number for (a) LA phonons and (b) TA phonons [315].

Brillouin zone, and will result in an overprediction of the high frequency contribution to the thermal conductivity by the Tiwari model. This deviation occurs because the appropriate boundary condition at the edge of the Brillouin zone (4.127) has not been enforced in the Tiwari model.

The value of the thermal conductivity is sensitive to impurities, which include the isotopic content of an otherwise pure crystal [159]. The impurity relaxation time [248, 436], (4.115), should be written in terms of phonon phase velocity as,

$$\frac{1}{\tau_{p\text{-}im}} = \frac{V_c \sum_i x_i [1 - (M_i/M)]^2}{4\pi u_{p,g} u_{p,p}^2} \omega^4. \tag{4.129}$$

At low frequency, where $u_{p,g} = u_{p,p} = u_{p,g,0}$, the relaxation time displays an ω^{-4} dependence (similar to photon, Rayleigh scattering). Because of phonon dispersion, such an assumption will not be valid at higher frequencies and will lead to an overestimation of the thermal conductivity.

4.9.7 Lattice Thermal Conductivity Prediction

(A) *Role of Dispersion Model*

The accuracy of the thermal conductivity model described in Section 4.9.2 depends on the nature of the phonon dispersion and relaxation-time models. To isolate the effects of dispersion, the relaxation-time model used in the subsequent calculations is fixed to that of Holland [199].

In Figures 4.20(a) and (b), the effect of including the difference between the phonon group and phase velocities on the prediction of the thermal conductivity of Ge is shown. The experimental data are taken from Holland [199]. The predicted values in Figure 4.20(a) correspond to (i) the Holland model, that is, no distinction between $u_{p,g}$ and $u_{p,p}$ and a linear two-region treatment, (ii) no distinction between $u_{p,g}$ and $u_{p,p}$, but using the frequency dependence of the group velocity, (iii) different and frequency-dependent $u_{p,g}$ and $u_{p,p}$, and (iv) same as (iii), plus rigorous treatment of the impurity scattering by distinguishing between $u_{p,g}$ and $u_{p,p}$. In (ii)–(iv), the velocities are calculated with the BZBC dispersion model. In (i)–(iii) the impurity scattering is calculated with $u_{p,g} = u_{p,p} = u_{p,g,0}$ for each polarization.

In Figure 4.20(a), the relaxation-time model and fitting parameters originally obtained by Holland are used. In Figure 4.20(b), the curves have been refit to the experimental data. From Figure 4.20(a), it is evident that the fitting parameters are not universal and are strongly dependent on the dispersion model. Thus, to use the values obtained by Holland, one must also use that dispersion model. However, as shown in Figure 4.20(b), by refitting the relaxation time parameters, excellent agreement with the experimental data can be obtained in all cases, except when the impurity scattering is rigorously modeled. In this case, the predicted thermal conductivity becomes lower than the experimental data, especially at high temperatures. Under the Holland dispersion, the plateau in the TA dispersion curve is not properly addressed, and the TA phonons make a significant contribution to the thermal conductivity at high temperatures. Here, with the proper modeling of the TA phonons, this contribution is reduced, and, as such, the role of TA phonons should be reassessed. The effect is not seen at low temperatures, where it is the lower-frequency phonons that dominate the thermal transport.

(B) *Role of Relaxation-Time Model*

The use of a rigorous model for the phonon dispersion has led to an apparent failure of the Holland SMRT approach at high temperatures. The explanation for this must lie in the forms of the relaxation times used. Although exact expressions for

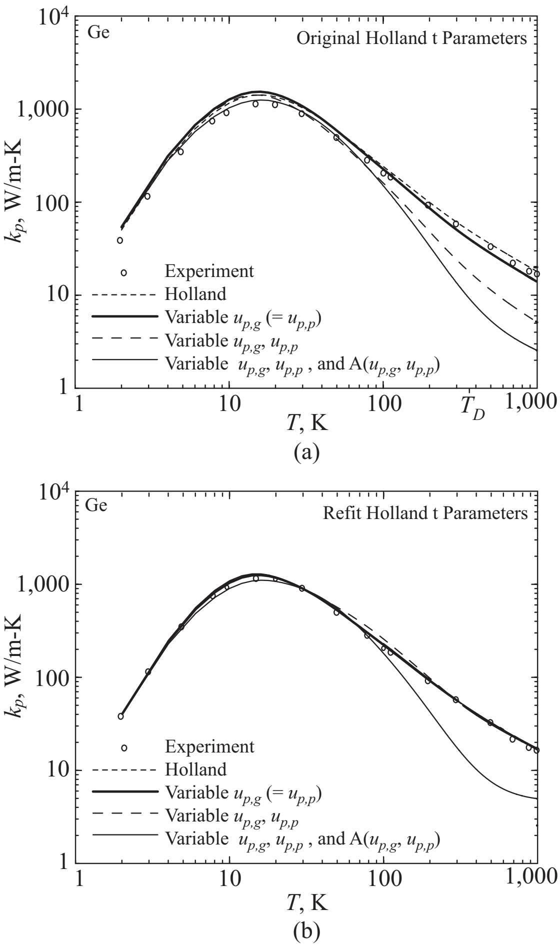

Figure 4.20. Effect of refining the treatment of the dispersion on the prediction of the thermal conductivity of Ge. (a) based on the original Holland fitting parameters, and (b) predictions refit to the experimental data [92].

the relaxation times can be developed [515], their evaluation is extremely difficult because of the required knowledge of the phonon dispersion and three-phonon interactions. Approximate expressions are generally based on low frequency asymptotes [70, 199] and yet are often applied over the entire temperature and frequency ranges.

Even with the observed disagreement, the importance of modeling the dispersion can still be shown. The Holland relaxation times are plotted in Figure 4.21(a) at temperatures of 80 K for the four cases shown in Figure 4.20(b). The most striking feature of these results is the large discontinuity in the TA relaxation time when κ^* is equal to 0.5, where the functional form is assumed to change [i.e., (4.110)]. As the temperature increases, the size of the discontinuity increases. For example, at a temperature of 900 K, the discontinuity covers four orders of magnitude. The size of the discontinuity decreases as the treatment of the dispersion is refined. This

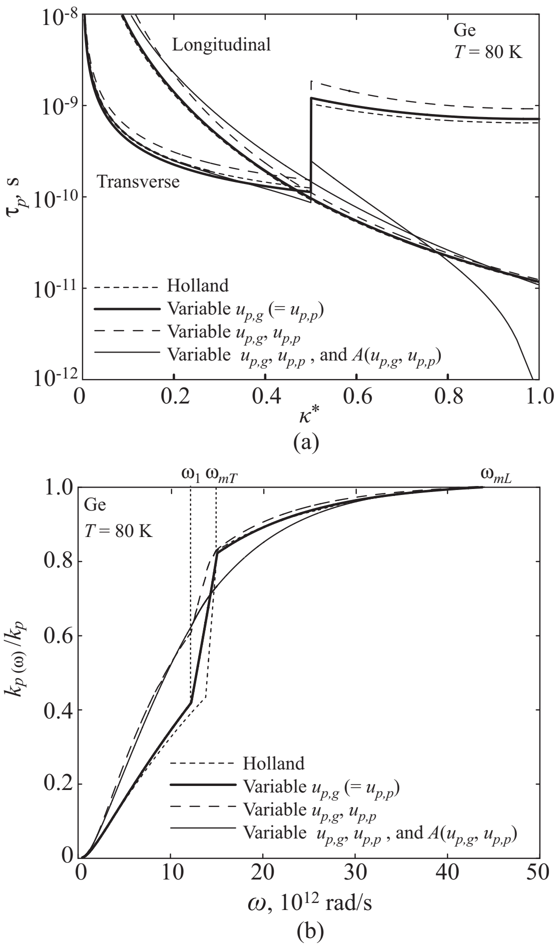

Figure 4.21. (a) Three-phonon relaxation times for refit data from Figure 4.20(b) at $T = 80$ K. (b) Cumulative frequency dependence of the thermal conductivity for refit data from Figure 4.20(b) at $T = 80$ K. The thermal conductivity is plotted as a percentage of the total value for each case. The curves show three distinct regions. The transition between the first and second regions takes place at ω_1, where the form of the TA relaxation time changes. The transition between the second and third regions occurs at $\omega_{m\mathrm{T}}$, after which there is no contribution from TA phonons [i.e., (4.110)] [92].

suggests that the observed behavior is more realistic. Such discontinuities are also found in other relaxation-time models [441, 464]. In theory, one would expect the relaxation-time curves to be continuous, and this has been found in MD simulations of the L–J FCC crystal [318].

The effect of the fitting parameters in the relaxation-time model can also be demonstrated by plotting the cumulative frequency dependence of the thermal conductivity. This is shown for the same four cases as Figures 4.21(a) and (b). Note that the thermal conductivity is normalized against the total value for each case. As the treatment of the dispersion is refined, the thermal conductivity curves become smoother.

(C) *Transverse and Longitudinal Phonon Contributions*

The relative contributions of LA and TA phonons to the total heat flow at high temperatures have not been fully resolved. As shown in Figure 4.22(a), the Holland model predicts that the TA phonons are the dominant heat carriers at high temperatures, even though they have lower group velocities than LA phonons. This result was supported in [177] by use of calculations based on a variational method, which does not involve the SMRT approximation. It has been ascertained that, above 100 K, TA phonons are the primary carriers of energy in Si (which has the same crystal structure as Ge) by use of the Monte Carlo simulations [314]. However, their calculations were based on the original Holland relaxation times, which may have contributed to this conclusion. In [11] it has been concluded that, although the heat flow in Ge at high temperatures is primarily because of TA phonons, the LA U–processes cannot be ignored (as they are in the Holland formulation). In [222] it has been suggested that LA phonons are the dominant heat carriers in Si near room temperature. In [441] it has been ascertained that LA phonons dominate heat transport in Ge at high temperatures.

In Figure 4.22(b), the relative contributions of LA and TA phonons to the thermal conductivity predicted by the BZBC dispersion model (with refit relaxation-time parameters) are shown. Compared with the results of Figure 4.22(a), the role of TA phonons is quite different when the dispersion and impurity scattering are rigorously modeled. We find a thermal conductivity of 5.2 W/m-K at a temperature of 1000 K, whereas the experimental value is 17 W/m-K. The high-frequency TA phonons cannot contribute much to the thermal conductivity of Ge because of their low group velocity, which appears directly in the thermal conductivity expression, and also results in a high impurity scattering rate. We note that the expected electronic contribution to the thermal conductivity of Ge at a temperature of 1000 K is 4 W/m-K [438], which is not sufficient to explain the predicted discrepancy.

4.10 Einstein and Cahill–Pohl Minimum Phonon Conductivities

In the Einstein solid thermal conductivity model, the atomic vibrational states are directly used (not related to phonon modes). The complete derivation of the Einstein thermal conductivity is given in Appendix C. He considers the interaction (through a spring constant) of the first, second, and third neighboring atoms with a central atom. He uses a quantum specific heat capacity and a single frequency and arrives at [30]

$$k_{p,\mathrm{E}} = \frac{n^{1/3}k_\mathrm{B}}{\tau_\mathrm{E}}\frac{x_\mathrm{E}^2 e^{x_\mathrm{E}}}{(e^{x_\mathrm{E}}-1)^2},\; x_\mathrm{E} = \frac{\hbar\omega_\mathrm{E}}{k_\mathrm{B}T} = \frac{T_\mathrm{E}}{T},\; \text{for } \tau_\mathrm{E} = \frac{T_\mathrm{E}k_\mathrm{B}}{\hbar\pi}$$

$$\text{Einstein model from (C.25) in Appendix C,} \qquad (4.130)$$

where n is the number density of atoms, and T_E is the Einstein temperature.

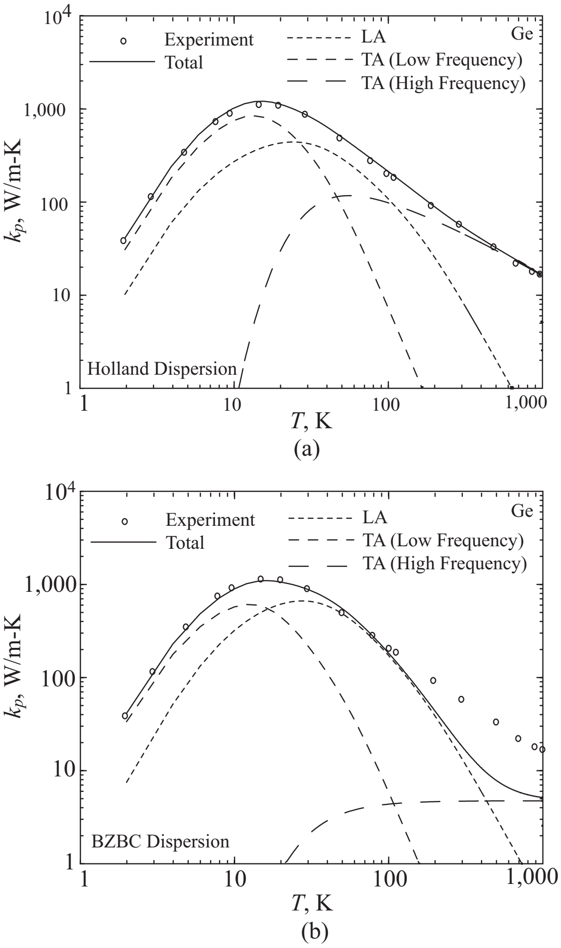

Figure 4.22. Contributions of LA and TA phonon branches to the thermal conductivity based on (a) Holland dispersion model and (b) BZBC dispersion model [92].

Cahill and Pohl [68] extend the proceeding equation to include a range of frequencies (details are given in Appendix C.2), and arrive at

$$k_{p,\text{C-P}} = (\frac{\pi}{6})^{1/3} k_{\text{B}} n^{2/3} \sum_{\alpha} u_{p,\alpha} (\frac{T}{T_\alpha})^2 \int_0^{T_\alpha/T} \frac{x^3 e^x}{(e^x-1)^2} \text{d}x, \ x = \frac{\hbar\omega}{k_{\text{B}}T}, \quad \text{for } \tau_{p,\alpha} = \frac{\omega}{\pi}$$

$$\text{Cahill–Pohl model from (C.36) in Appendix C,} \qquad (4.131)$$

where $u_{p,\alpha}$ and $T_{\text{D},\alpha}$ are the phonon (acoustic) speed and the Debye temperature for polarization α and are related through (4.27), by use of the Debye model.

It is generally accepted that $k_{p,\text{C-P}}$ is the lowest thermal conductivity for a solid, provided the proper values of $u_{p,\alpha}$ or $T_{\text{D},\alpha}$ [they can be related through (4.63)] are available. The phonon mean free path in (4.131) is $\lambda_p = \pi u_{p,\alpha}/\omega$, which unlike (4.116) is temperature independent. This is (C.32) in Appendix C. This mean free path is 1/2 of the wavelength $\lambda = 2\pi u_{p,p}/\omega$, using a constant phase velocity $u_{p,p} =$

$u_{p,\alpha}$. Based on this $k_{p,\text{C-P}}$ is used for thermal conductivity of amorphous solids and polymers. Figure 4.17 shows the variation of $k_{p,\text{C-P}}$ with respect to temperature. At low temperatures ($T < T_{\text{D},\alpha}$) it increases and for $T > T_{\text{D},\alpha}$ it reaches a plateau. We will have quantitative results for $k_{p,\text{C-P}}(T)$, for amorphous SiO_2, in Figure 4.34.

For $T > T_\text{D}$, (4.131) becomes independent of temperature and equal to $k_{p,\text{C-P}} = 0.40 k_\text{B} n^{2/3}\ (u_{p,\text{L}} + u_{p,\text{T}})$, and from Table 3.11, we can find $u_{p,\text{L}}$ and $u_{p,\text{T}}$ in terms of elastic contents.

4.11 Material Metrics of Phonon Conductivity: Slack Relation

Starting from the derivation in [224], in which the variational principle is used to obtain an analytical relaxation time for the rare-gas solids, Slack proposed that when heat is mainly carried by acoustic phonons scattered by means of the three-phonon process, the thermal conductivity of crystals with constant volume at high temperatures (normally above 1/4–1/5 of the Debye temperature) can be given by the Slack relation (based on BTE and SMRT, i.e. (4.107), and a $\tau_{p\text{-}p}$ relation) [30, 437]

$$k_{p,\text{S}} = \frac{3.1 \times 10^4 \langle M \rangle V_a^{1/3} T_{\text{D},\infty}^3}{T \langle \gamma_\text{G}^2 \rangle N_\circ^{2/3}}. \tag{4.132}$$

Here $\langle M \rangle$ is the mean atomic weight of the atoms in the primitive cell, $V_a = 1/n$ is the average volume per atom, $T_{\text{D},\infty}$ is the high-temperature Debye temperature, T is the temperature, $N_\circ$ (Section 4.3) is the number of atoms in the primitive cell, and $\langle \gamma_\text{G}^2 \rangle$ is the mode-averaged square of the dimensionless Grüneisen constant or parameter (Glossary)[†] at high temperatures. Note that 3.1×10^4 has units, and k_p is in W/m-K. The value of γ_G is listed in Table A.2 for crystalline elements. These values range from 0.5 for strong covalent bonds to 3.0 for weak van der Waals bonds (interactions). In Section 4.11.4, we will discuss the prediction of γ_G. Note that $T_{\text{D},\infty}$ is extracted from the phonon density of states D_p [437], i.e.,

$$T_{\text{D},\infty}^2 = \frac{5 h_\text{P}^2}{3 k_\text{B}^2} \frac{\int_0^\infty f^2 D_p(f) \text{d} f}{\int_0^\infty D_p(f) \text{d} f}, \tag{4.133}$$

where f is the phonon frequency. However, $T_{\text{D},\infty}$ cannot be conveniently determined, since it requires the information on DOS. Because the difference between $T_{\text{D},\infty}$ and the Debye temperature T_D (at 0 K), extracted from the elastic constant or the measurement of heat capacity, is normally small, and it is customary to use T_D instead of $T_{\text{D},\infty}$ in (4.132). Also, $\langle \gamma_\text{G}^2 \rangle$ is often replaced with $\langle \gamma_\text{G} \rangle^2$ (later, for simplicity we use γ_G to denote $\langle \gamma_\text{G} \rangle$), which can be determined from thermal expansion data (Glossary) at high temperatures.

[†] Grüneisen dimensionless parameter is related to the solid properties through (Glossary)

$$\gamma_\text{G} = \frac{3 \beta E_p}{\rho c_{v,p}},$$

where β is the linear expansion coefficient and E_p is the isothermal bulk modulus (4.70).

Equation (4.132) is widely tested with pure nonmetallic crystals, and the overall agreement is good, even for complex crystals [30, 437]. The Slack relation illuminates how the atomic structure affects the thermal transport and provides a useful guide to tailoring the thermal transport properties.

4.11.1 Derivation of Slack Relation

To understand the nature of the Slack relation, we can also derive a relation similar to the Slack relation. To be physically meaningful, the mean free path of a phonon mode should be longer than one half of its wavelength [69]. Therefore, a two-segment mean free path model can be constructed [203], i.e., when the phonon frequency is below a critical frequency, ω_c, its mean free path will vary according to the relaxation-time model of Roufosse for moderate and high temperatures (above T_D) [395]; when the phonon frequency is above the critical frequency, its mean free path (4.131) is set to one half of its wavelength [as in the Cahill-Pohl model, (C.32)]. This gives

$$\begin{aligned}\lambda_{p,\alpha}(\omega) &= u_{p,g,i}\tau_{p\text{-}p,\mathrm{R}} = \frac{u_{p,g,\alpha}}{A_i(1+B_i\omega^2)\omega^2 T},\ \ \omega<\omega_{c,\alpha},\\ &= \frac{\pi u_{p,g,\alpha}}{\omega},\ \ \omega_{c,\alpha}\le\omega\le\omega_{D,\alpha},\\ A_\alpha &= \frac{3\times 10^3 N_\mathrm{A}\pi V_a^{1/3}\gamma_\mathrm{G}^2 k_\mathrm{B}}{2^{1/2}\langle M\rangle u_{p,g,\alpha}^3},\ \ B_\alpha=\left(\frac{4\pi}{3}\right)^{2/3}\frac{5V_a^{2/3}}{12\pi^2 u_{p,g,\alpha}^2},\end{aligned} \tag{4.134}$$

where N_A is the Avogadro number. This $\tau_{p\text{-}p}$ is similar in form to (4.110), but covers a large range of ω (Figure 4.16 gives the change in power of ω for FCC Ar). To ensure a continuous $\lambda_{p,\alpha}(\omega)$, ω_c must satisfy

$$\omega_{c,\alpha}A_i(1+B_i\omega_{c,\alpha}^2)=\frac{1}{\pi T}. \tag{4.135}$$

For $B_\alpha \ll \pi^2 A_\alpha^2 T^2$, we have

$$\omega_{c,\alpha}\simeq\frac{1}{A_i\pi T}. \tag{4.136}$$

The critical frequency ω_c decreases with temperature. In other words, as the temperature increases, an increasing number of phonon modes reach the limiting mean free path of one half of their wavelength. Using (4.134), (4.107) can be rewritten as

$$\begin{aligned}k_{p,\mathrm{S}} &= \sum_{\alpha=1}^{3}\frac{k_\mathrm{B}}{2\pi^2 u_{p,g,\alpha}A_i T}\int_0^{\omega_{c,i}}\left[\left(\frac{4\pi}{3}\right)^{2/3}\frac{5\omega^2 V_a^{2/3}}{12\pi^2 u_{p,g,\alpha}^2}+1\right]^{-1}\mathrm{d}\omega\\ &+\left(\frac{\pi}{6}\right)^{1/3} n^{2/3}\sum_{\alpha=1}^{3}u_{p,g,\alpha}\frac{\hbar^4}{T_{\mathrm{D},\alpha}^2 k_\mathrm{B}^3 T^2}\int_{\omega_{c,i}}^{k_\mathrm{B}T_{\mathrm{D},i}/\hbar}\frac{\omega^3 e^{\frac{\hbar\omega}{k_\mathrm{B}T}}}{(e^{\frac{\hbar\omega}{k_\mathrm{B}T}}-1)^2}\mathrm{d}\omega.\end{aligned} \tag{4.137}$$

By setting ω_c equal to $\omega_{\rm D}$, $u_{p,g,\alpha}$ to the mean phonon speed $u_{p,g} = u_{p,{\rm A}}$, and using (4.60) $\omega_{\rm D} = u_{p,g}(6\pi^2 n/N_\circ)^{1/3}$, we have, from (4.137)

$$k_{p,{\rm S}} = \frac{4.48 \times 10^3 \langle M \rangle T_{\rm D}^3}{T n^{1/3} \gamma_{\rm G}^2 N_\circ^{2/3}}, \tag{4.138}$$

which is similar to Slack relation (4.132) except for the constant. The difference in the constants is because of the SMRT and a different Hamiltonian used in [395] for the three-phonon interactions.

As will be discussed in Section 4.13, the lattice thermal conductivity can be decomposed into three parts [318]

$$k_p = k_{p,lg,{\rm A}} + k_{p,sh,{\rm A}} + k_{p,{\rm O}}, \;\; k_{p,{\rm S}} = k_{p,lg,{\rm A}}. \tag{4.139}$$

Here $k_{p,lg,{\rm A}}$ is the contribution from long-range acoustic phonons, whose mean free path is larger than one-half of their wavelength; $k_{p,sh,{\rm A}}$ is the contribution from short-range acoustic phonons, whose mean free path is minimized to one-half of their wavelength; and $k_{p,{\rm O}}$ is the contribution from the optical phonons.

According to the proceeding derivation, the Slack relation corresponds to $k_{p,lg,{\rm A}}$ and is valid only when the short-range acoustic or optical phonons are not important. This condition is not always satisfied for crystals with low thermal conductivity, such as zeolites and metal–organic frameworks (MOFs). The Slack relation is valid only when ω_c is comparable with the Debye frequency $\omega_{\rm D}$ and long-range acoustic phonons dominate the thermal transport.

To use the Slack relation, $T_{\rm D}$ and $\gamma_{\rm G}$ must be known, which is the main difficulty in the estimation of the lattice conductivities of new materials. Because these two parameters directly relate the atomic structure to thermal transport, the knowledge of their relations provides more insightful information for the thermal design and allows for the estimation of thermal transport properties of new materials.

In [203] a simple microscopic model is presented for estimating these parameters. This model is based on a phenomenological combinative rule for force constants and a general L–J potential form for a bond.

4.11.2 Force-Constant Combinative Rule for Arbitrary Pair-Bond

The vibration energy is transferred in a crystal through interactions among the atoms, which can be theoretically calculated by quantum-mechanical methods. However, a quantum-mechanical method deals with the electron clouds of the atoms and is very cumbersome for a system involving many particles. Based on the Born-Oppenheimer approximation [269] described in the Glossary, the force-field method uses empirical potentials (fitted to experiments or quantum mechanic calculations), such as L–J and Buckingham potentials, to describe the interactions in the system. In most solids, when the temperature is well below the melting point, the particles only slightly oscillate around their equilibrium positions, and many of their behaviors (including the elastic behavior) can be well described in the framework of the harmonic approximation [12]. In this approximation, the energy of the system can normally be decomposed into four terms corresponding to the bond stretching, bending, torsion, and the nonbonded interactions [269], i.e.,

$$E = \sum_i \frac{\Gamma_i}{2}(\Delta r_i)^2 + \sum_j \frac{\Gamma_{\theta,j}}{2}(\Delta\theta_j)^2 + \sum_l \frac{\Gamma_{\phi,l}}{2}(\Delta\phi_l)^2 + \sum_n \frac{\Gamma_{m,n}}{2}(\Delta r_{m,n})^2, \qquad (4.140)$$

where Γ, Γ_θ, Γ_ϕ, and $\Gamma_{m,n}$ are the force constants of the bond length r, bond angle θ, torsion angle ϕ, and the distance between molecules r_m. Normally the stretching interaction is much stronger than the other interactions (by a factor of more than 10), so for a rigid structure, the elastic characteristics are mainly determined by the stretching force constants. The bending and torsion interactions are also important in molecular crystals and for structure stability and deformation.

Because atomic interaction is determined by the electronic structure, potentials and force constants are expected to be transferable if the bond type and surroundings are similar [191]. Here a phenomenological combinative rule is presented for the stretching and the van der Waals force constants.

The general form of two-body potentials can be written as

$$\varphi_{\mathrm{AB}}(r) = \varphi_{AB,rep}(r) - \varphi_{AB,att}(r), \qquad (4.141)$$

where φ_{AB} is the potential energy of the bond A–B, and the subscripts *rep* and *att* represent the repulsive and the attractive terms. The repulsive term is because of the Pauli exclusion principle and/or the electrostatic interactions. It has been shown that the exchange repulsive term for two different atoms can be given as the geometric mean of the corresponding terms for two pairs of equivalent atoms [35], i.e.,

$$\varphi_{\mathrm{AB},rep}(r) = [\varphi_{AA,rep}(r)\varphi_{BB,rep}(r)]^{1/2}. \qquad (4.142)$$

The attractive term is because of the interactions of dipoles, electrostatics, or a combination of them. The exchangeability of the dipolar and electrostatic interactions is apparent; thus a similar combinative rule is suggested for the attractive term, i.e.,

$$\varphi_{\mathrm{AB},att}(r) = [\varphi_{AA,att}(r)\varphi_{\mathrm{BB},att}(r)]^{1/2}. \qquad (4.143)$$

The potential near the equilibrium position can be described by the general L–J potential model (2.7)

$$\varphi(r) = \frac{A}{r^m} - \frac{B}{r^n}, \qquad (4.144)$$

where m and n (Table 2.1) depend on the interaction type; and their values will be discussed in Section 4.11.4. The force constant Γ (4.36) and the bond length r_e at the equilibrium position are given as

$$\Gamma = -\frac{mn\varphi_{\mathrm{o}}}{r_e^2} = \frac{m(m-n)A}{r_e^{m+2}} = n(m-n)B\left(\frac{Bn}{Am}\right)^{\frac{2+n}{m-n}}$$

$$r_e = \left(\frac{Am}{Bn}\right)^{\frac{1}{m-n}}, \qquad (4.145)$$

where $-\varphi_o$ is the potential energy at the equilibrium position. (4.145) shows that the force constant at the equilibrium position is proportional to φ_o when the bond type and the bond length are similar. Note that, at the equilibrium position, the ratio of the magnitudes of the contributions from the repulsive term and the attractive term is $(m+1)/(n+1)$. Therefore, for $m \gg n$ (e.g., for an ionic bond), the force constant is mainly determined by the repulsive term.

From (4.142), (4.143) and (4.145), if Γ_{AA} is defined as the force constant of the potential function $\varphi_{\mathrm{AA}}(r) = \varphi_{\mathrm{AA},rep}(r) - \varphi_{\mathrm{AA},att}(r)$, the force constant of A–B bond Γ_{AB} and its equilibrium bond length $r_{\mathrm{o,AB}}$ can be given as

$$\Gamma_{\mathrm{AB}} = (\Gamma_{\mathrm{AA}}\Gamma_{\mathrm{BB}})^{1/2}, \quad r_{e,\mathrm{AB}} = (r_{e,\mathrm{AA}}r_{e,\mathrm{BB}})^{1/2}. \tag{4.146}$$

Note that for ions, the A–A bond may not actually exist. However, because of the similarity of the electronic configuration of the ions in different compounds, we may assign a virtual potential φ_{AA} to the ions, e.g., keeping the interaction that is because of the Pauli exclusion principle as the repulsive term and setting the attractive term as $\varphi_{\mathrm{AA},att} = q^2/r$, where q is the ionic charge. The properties of the virtual potential (e.g., Γ_{AA}) can be extracted from the compounds. In this way, the combinative rule of (4.142) and (4.143) is still valid. Similar relations like (4.146) have been derived in [138] by a 12–6 L–J potential, but they did not consider the effects of bond order and the long-range electrostatic interactions. In addition, it is not appropriate to describe ionic bonds or covalent bonds by 12–6 L–J potential, as will be discussed later.

Note that this combinative rule is only applicable for the bonds with the same bond type (m and n are close) and bond order. In real compounds, a bond with the same atom configuration can have different bond orders. For example, C=O has the bond order of 2, and C–O has the bond order of 1. It is observed that the force constant is approximately proportional to the bond order [495], that is

$$\Gamma_{\mathrm{AB},s} = s\Gamma_{\mathrm{AB},1}, \tag{4.147}$$

where $\Gamma_{\mathrm{AB},s}$ is the force constant of the bond between A and B with the bond order of s. Thus (4.147) can be rewritten as

$$\Gamma_{\mathrm{AB},s} = s(\Gamma_{\mathrm{AA},1}\Gamma_{\mathrm{BB},1})^{1/2}. \tag{4.148}$$

Consequently, we have

$$\Gamma_{\mathrm{AC},s} = s\frac{(\Gamma_{\mathrm{AB},1}\Gamma_{\mathrm{BC},1})^{1/2}}{\Gamma_{\mathrm{BB},1}}. \tag{4.149}$$

According to (4.147), the potential energy φ can be assumed proportional to s, and r_e is expected to be independent of s. For ionic bonds, when this assumption is used, the resulting combinative rule for ionic bond length agrees well with the experiments (the error is less than 3%) [138]. However, this assumption is only moderately accurate for covalent bonds, because the L–J potential does not accurately describe the changes of electron clouds and the energy in the entire range of atomic distance. Generally, for covalent bonds, r_e will decreases slightly when s

increases. In [357] an empirical bond order–bond length relationship for covalent bonds is developed as

$$r_{e,s} = r_{e,1} - 0.78(s^{0.33} - 1), \tag{4.150}$$

where $r_{e,s}$ is the equilibrium bond length (in angstroms) with the bond order of s. (4.150) shows good agreements with the experimental results for many bonds [357] and can be used for the estimation of the bond length.

Table A.2 lists the electronegativity of elements. Table 4.4 lists the force constant $\Gamma_{\text{AA},1}$, electronegativity χ, and equilibrium bond length $r_{e,1}$ for most element paris. $\Gamma_{\text{AA},1}$ is extracted from the experimental spectra of diatomic molecules [192] according to (4.148) and (4.149) (the ionic $\Gamma_{\text{AA},1}$ of elements, e.g., O and S, is an average of the values extracted from their compounds). $r_{e,1}$ is extracted from the bond lengths of the diatomic molecules [192]. Table 4.4 shows that $\Gamma_{\text{AA},1}$ of ionic bonds for the elements with high electronegativity χ (e.g., O and Cl) are normally twice that of the corresponding covalent bond. This indicates that the virtual potential of ions is steeper than the covalent potential of the corresponding atoms near the equilibrium position. The electronegativity χ can be used to determine the bond type. Bonds between atoms with a large electronegativity difference (≥ 1.7), are usually considered to be ionic, whereas values between 1.7 and 0.4 are considered polar covalent and values below 0.4 are considered nonpolar covalent bonds [362]. For metallic elements, even though $\Delta\chi$ is small, their electron structures are similar to those in the ionic crystals, for the conduction electrons can move about [245].

Figure 4.23(a) shows that generally the ionic $\Gamma_{\text{AA},1}$ increases as the electronegativity increases. The alkali metals have the lowest $\Gamma_{\text{AA},1}$, whereas the halogen elements have the highest $\Gamma_{\text{AA},1}$. When $1.0 < \chi < 2.5$, most transition-metal elements and semiconducting elements have a $\Gamma_{\text{AA},1}$ around 50 N/m, which is a relatively low value. In general, $\Gamma_{\text{AA},1}$ decreases while the atomic radius increases. However, Figure 1(b) shows that, for covalent bonds, $\Gamma_{\text{AA},1}$ seems to relate to the ratio of χ/z (z is the atomic number) rather than χ. Nitrogen has the highest covalent $\Gamma_{\text{AA},1}$.

Figure 4.24 compares the experimental results of some bonds in diatomic molecules along with the calculated values. The mean-square error is less than 8%, and the overall agreement is good.

Note that the proceeding force constants and equilibrium bond lengths are derived from the data of gaseous diatomic molecules, for which the intermolecular effects are negligible. For crystal bonds, long-range interactions (mainly electrostatic interactions) from the surroundings may significantly affect the equilibrium bond length and force constant. For example, Na–Cl in a NaCl molecule has a force constant of 110 N/m and a bond length of 2.36 Å [192], while the distance between the nearest Na and Cl ions in a NaCl crystal at $T = 300$ K is 2.83 Å, and the effective force constant of each Na-Cl pair derived from the bulk modulus is only 20 N/m [435]. Thus, a relation between the force constant of a bond in a gaseous diatomic molecule and that in a crystal must be developed to account for the effects of long-range interactions. Here, only the effect of electrostatic interactions is considered. Our approach is to include long-range interactions in an effective bond potential

Table 4.4. *Electronegativity, equilibrium bond length, and force constants of element pairs (listed in order of atomic number) with the bond order of 1. The data are extracted from [192]. The symbols C and V represent covalent and van der Waals interactions, and the unlabeled are the values for ionic interactions.*

Atom	χ	$r_{e,1}$, Å	Γ, N/m	Atom	χ	$r_{e,1}$, Å	Γ, N/m
H	2.20	0.74[C]	575.67[C]	Br	2.96	2.28[C]	250.83[C], 539.78
He	–	1.04[C]	411.74[C]	Kr	3.00	4.03[V]	1.43[V]
Li	0.98	2.67	25.48	Rb	0.82	3.79	8.25
Be	1.57	1.39	120.62	Sr	0.95	3.05	26.57
B	2.04	1.76[C]	354.90[C]	Y	1.22	–	70.05
C	2.55	1.54[C]	510.5[C]	Zr	1.33	8.41	141.43
N	3.04	1.46[C]	771.20[C]	Nb	1.60	2.36	108.25
O	3.44	1.46[C]	593.57[C] 1305	Ru	1.02	2.17	56.53
F	3.98	1.41[C]	473.82[C] 1960	Ag	1.93	2.59	59.09
Ne	–	3.10[V]	0.12[V]	Cd	1.69	4.28	44.93
Na	0.93	3.08	17.28	In	1.78	2.86	34.41
Mg	1.31	3.89	41.60	Sn	1.96	2.80	58.34
Al	1.61	2.47	49.15	Sb	2.05	2.82[C]	70.64[C]
Si	1.90	2.34[C]	109.04[C]	Te	2.10	2.74[C]	119.46[C]
P	2.19	2.20[C]	201.50[C]	I	2.66	2.66[C]	172.73[C] 343.06
S	2.58	2.08[C]	250.65[C] 536.92	Xe	2.60	4.36[V]	1.74[V]
Cl	3.16	1.98[C]	330.42[C] 705.81	Cs	0.79	4.47	6.97
Ar	–	3.76[V]	0.80[V]	La	1.10	2.83	53.41
K	0.82	3.90	9.84	Ce	1.12	2.74	169.30
Ca	1.00	4.28	34.61	Pr	1.13	–	48.25
Sc	1.36	2.40	77.60	Eu	1.20	–	31.11
Ti	1.54	2.17	107.71	Tb	1.10	–	72.63
V	1.63	2.09	103.03	Ho	1.23	3.11	77.21
Cr	1.66	2.17	87.18	Yb	1.10	2.89	33.74
Mn	1.55	2.59	46.40	Lu	1.27	2.63	78.69
Fe	1.83	2.04	62.53	Hf	1.30	2.44	103.98
Co	1.88	3.20	116.61	Ta	1.50	2.36	179.07
Ni	1.91	2.96	130.00	W	2.36	–	202.54
Cu	1.90	2.22	65.82	Ir	2.20	2.36	110.01
Zn	1.65	3.41	81.15	Au	2.54	2.47	106.80
Ga	1.81	2.43	99.38	Hg	2.00	3.30	32.61
Ge	2.01	2.16	121.79	Tl	1.62	3.07	31.60
As	2.18	2.42	120.48	Pb	2.33	3.03	39.91
Se	2.55	2.34[C]	108.54[C]	Bi	2.02	3.07	49.08

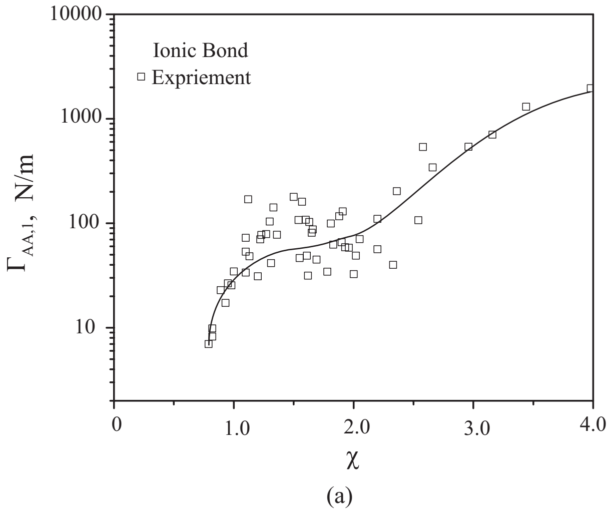

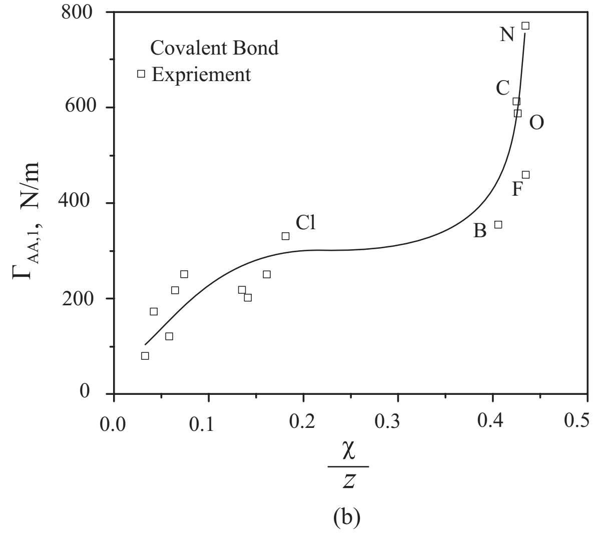

Figure 4.23. (a) Variation of calculated ionic force constant $\Gamma_{AA,1}$ with respect to the electronegativity. (b) Variation of the calculated covalent force constant $\Gamma_{AA,1}$ with respect to the ratio of the electronegativity and atomic number. The data are extracted from the spectra of diatomic molecules [192]. The curves are used to guide the eyes.

of the nearest-neighbor atoms. A bond (in a diatomic molecule) with a form in (4.144) is considered. Because the repulsive term is a very short-range interaction, we assume that only the long-range attractive term is affected by the surroundings. This effective bond in a crystal can then be represented as

$$\langle\varphi\rangle(r) = \frac{A}{r^m} - \eta\frac{B}{r^n}, \tag{4.151}$$

where η is the correction factor that is because of the long-range interactions (in simple ionic structures, it is related to the Madelung constant). However, η is difficult

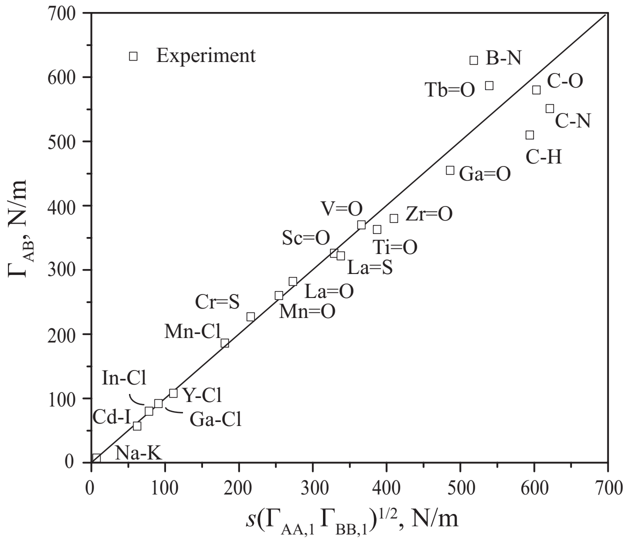

Figure 4.24. Comparison of calculated force constants and the corresponding values from the experimental spectra, for some atomic pairs [192].

to determine for complex crystal structures. In practice, according to this assumption and (4.145), the force constant of the bond in the crystal Γ'_{AB} can be simply calculated as

$$\Gamma'_{AB} = \Gamma_{AB}(\frac{r_o}{r'_o})^{m+2}, \tag{4.152}$$

where Γ_{AB} is the force constant of the bond in the diatomic molecule AB, and r'_o is the equilibrium bond length in the crystal. For example, for NaCl, by setting $m = 6.3$ [using approximation method (4.171)], and using the proceeding bond length data, we have $\Gamma'_{NaCl} = 110 \times (2.36/2.83)^{(6.3+2)} = 24$ N/m, which is very close to 20 N/m derived from the bulk modulus [435]. For ionic bonds, m is large, and (4.152) indicates that Γ'_{AB} is very sensitive to the values of r_o and r'_o, so the experimental values of r_o and r'_o will be preferred. When the experimental value of r_o is unavailable, combinative rule (4.146) can be used.

4.11.3 Evaluation of Sound Velocity and Debye Temperature

If the force constants between atoms are known, the dynamical matrix can be readily constructed to determine the sound velocity. However, for complex polyatomic crystals, the calculation is still very cumbersome, and it is difficult to explicitly relate the numerical results to the complex structure. For the purpose of estimation and design, a simple model that can directly relate the sound velocity and the Debye temperature to the crystal structure is needed.

A real crystal structure can always be considered as an underlying lattice, together with a basis describing the arrangement of the atoms, ions, and molecules

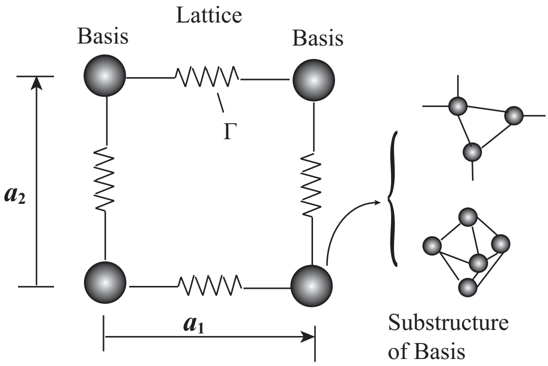

Figure 4.25. Decomposition of a complex crystal into lattice and bases, with equivalent bonds.

within a primitive cell [12]. The acoustic branches of the phonon dispersion correspond to the motion of the mass centers of the primitive cells [12]. Therefore, both the monatomic and polyatomic crystal structures can be modeled as a lattice with rigid bases connected by equivalent bonds with an equivalent force constant, as shown in Figure 4.25.

The elastic response of a solid can be divided into two parts, namely, (i) atomic vibrations at a fixed volume, and (ii) unit-cell volume fluctuations for a fixed atomic configuration (homogeneous deformation). The first part corresponds to the inhomogeneous deformation, in which the bending potentials and the torsion potentials may be important, especially in a flexible structure. The bending potential can also be converted into an equivalent stretching potential between the atoms at the two ends. Because the force constants of the bending potentials and the torsion potentials are normally small, the equivalent force constant will be much reduced by the inhomogeneous deformation. It is difficult to obtain a general simple analytical solution for such an inhomogeneous deformation, and a numerical calculation with a full dynamical matrix (including the bending potentials) is preferred for obtaining the equivalent force constant. However, for many solids, the crystallographic symmetries and the stability of a given phase with respect to small lattice deformations result in the diminishing effects from the first part [13], and the elastic behavior can be described by the equivalent force constants of the stretching potentials. In these cases, the bending potential and the torsion potential may contribute to the stability of the structure, but their contribution to the elastic response is negligible.

When only the bond stretching is considered, it is apparent that only the transport of stretching along the translational unit vector $\boldsymbol{a}$ can contribute to the energy transport in this direction. Thus we define the force constant of a bond along a given unit vector $\boldsymbol{a}$ as [117]

$$\Gamma_{\mu\nu,\boldsymbol{a}} = \frac{\partial^2 \varphi_{\mu\nu}}{\partial x_{\mathbf{a}}^2} = \frac{\partial^2 \varphi_{\mu\nu}}{\partial r_{\mu\nu}^2}\left(\frac{x_{\mathbf{a}}}{r_{\mu\nu}}\right)^2 = (\boldsymbol{a}\cdot\boldsymbol{s}_{\mu\nu})^2 \Gamma_{\mu\nu}, \tag{4.153}$$

where $x_{\mathbf{a}}$ is the projection of the bond length r along $\boldsymbol{a}$, and $\boldsymbol{s}_{\mu\nu}$ is the unit vector pointing from the particle μ to the particle ν. (4.153) shows that the projection of the force constant along $\boldsymbol{a}$ has a factor of $(\boldsymbol{a}\cdot\boldsymbol{s}_{\mu\nu})^2$.

The total deformation of the primitive cell is affected by all the bonds in it. Using (4.153), we may treat the bonds in a primitive cell as springs with the same $\Gamma_{\mu\nu,\boldsymbol{a}}$, and then convert the crystal primitive cell into a network composed of springs. This spring network can be simplified to obtain the equivalent force constant between two bases according to the following rules (we denote the force constants of two bonds as Γ_1 and Γ_2, and that of the equivalent bond of these two bonds as Γ_e)

(i) when the two bonds are in series

$$\Gamma_e^{-1} = \Gamma_1^{-1} + \Gamma_2^{-1}, \tag{4.154}$$

(ii) and when the two bonds are parallel

$$\Gamma_e = \Gamma_1 + \Gamma_2. \tag{4.155}$$

For a monatomic crystal, the primitive cell includes only one atom, and the equivalent force constant is just the force constant of the bond between the atoms.

From the lattice dynamics (Section 4.8), the sound velocities of acoustic branches at the long-wavelength limit are the square roots of the eigenvalues of the matrix [12]

$$-\frac{1}{2M}\sum_{\boldsymbol{l}}(\boldsymbol{s}_\kappa \cdot \boldsymbol{l})^2 \boldsymbol{D}(\boldsymbol{l}), \quad D_{i,j}(\boldsymbol{l}) = \frac{\partial^2 \varphi}{\partial d_i^\circ \partial d_j^{\boldsymbol{l}}}, \tag{4.156}$$

where $\boldsymbol{s}_\kappa$ is the unit wave vector, $\boldsymbol{D}(\boldsymbol{l})$ is the dynamical matrix, $\boldsymbol{l}$ is the position vector of the neighbor, d_i is the displacement of the mass center of the primitive cell from the equilibrium position ($\circ$ represents the origin), and M is the mass of the primitive cell.

Using the proceeding simplified model for crystal structures, if only the stretching energy is considered, we can rewrite (4.140) as

$$\varphi = \sum_{\boldsymbol{l}} \frac{\Gamma_{\boldsymbol{l}}}{2}[\boldsymbol{s}_{\boldsymbol{l}} \cdot (\boldsymbol{d}^{\boldsymbol{l}} - \boldsymbol{d}^\circ)]^2, \quad \boldsymbol{s}_{\boldsymbol{l}} = \frac{\boldsymbol{l}}{|\boldsymbol{l}|}, \tag{4.157}$$

where $\Gamma_{\boldsymbol{l}}$ is the equivalent force constant between the two bases. Thus $D_{i,j}(\boldsymbol{l}) = \eta_{i,j}\Gamma_{\boldsymbol{l}}$. Note that $\boldsymbol{l}$ is a linear function of the lattice constants, so the acoustic (sound) velocity (Section 4.7.2) will have the form (4.67)

$$u_{p,g,i} = l(\boldsymbol{s}_{k,i}, \{\boldsymbol{a}_i\})(\frac{\Gamma_s}{m})^{1/2}, \quad \Gamma_s = \sum_{\boldsymbol{l}}[\eta(\boldsymbol{l}, \boldsymbol{s}_{k,i})\Gamma_{\boldsymbol{l}}], \tag{4.158}$$

where $\{\boldsymbol{a}_i\}$ is the set of the translational vectors of the lattice. Note that (4.158) has the same form as the formula for the one-dimensional chain [117]. It is instructive to consider a plane wave traveling in a crystal, wherein the lattice consists of parallel planes perpendicular to the wave vector and the atoms in a plane will move in phase. The transportation along the wave vector is essentially one dimensional. From the comparison with the formula of the one-dimensional chain [117], l is indeed the equivalent distance between the planes and normally is the linear function of the lattice constants. The effective force constant Γ_s is the summation of the projections of the equivalent force constant in the polarization $\boldsymbol{s}_{\kappa,i}$, that is, $\eta(\boldsymbol{l}, \boldsymbol{s}_{\kappa,i}) = (\boldsymbol{s}_{\boldsymbol{l}} \cdot \boldsymbol{s}_{\kappa,i})^2$.

The average sound velocity $u_{p,g,\mathrm{A}}$ can be found from (4.57), i.e.,

$$u_{p,g,\mathrm{A}} = (\sum_{\alpha=1}^{3} \frac{1}{3u_{p,g,\alpha}^{3}})^{-1/3}. \tag{4.159}$$

For cubic structures, the average sound velocity is given by (4.71)

$$u_{p,g,\mathrm{A}} = \frac{1}{3^{1/2}} a (\frac{\Gamma}{m})^{1/2}, \tag{4.160}$$

where a is the lattice constant.

From the longitudinal and transversal sound velocities, we can obtain the polarization-dependent Debye temperature $T_{D,i}$ and the average Debye temperature T_{D} [12]:

$$\begin{aligned} T_{\mathrm{D},\alpha} &= u_{p,g,\alpha} \frac{\hbar}{k_B}(6\pi^2 n)^{1/3} \\ &= \frac{l_\alpha}{V_c^{1/3}}(\frac{\Gamma_\alpha}{m})^{1/2} \frac{\hbar}{k_B}(6\pi^2 N_\circ)^{1/3} \\ T_{\mathrm{D}} &= u_{p,g,A} \frac{\hbar}{k_B}(6\pi^2 n)^{1/3} = (\sum_{\alpha=1}^{3} \frac{1}{3T_{\mathrm{D},\alpha}^{3}})^{-1/3}, \end{aligned} \tag{4.161}$$

where n is the number density of atoms, $N_\circ$ is the number of atoms in a primitive cell, and V_c is the volume of a primitive cell. Here $l_\alpha / V_c^{1/3}$ is only a function of the ratio of lattice constants and the polarization, and the Debye temperature relates to the ratio of the lattice constants rather than their absolute values. It is apparent that if the lattice constant and other parameters are the same except the lattice type, the order of magnitude of T_{D} is $T_{\mathrm{D}}(\mathrm{FCC}) > T_{\mathrm{D}}(\mathrm{BCC}) > T_{\mathrm{D}}(\mathrm{SC})$.

Figure 4.26 compares the calculated and experimental Debye temperatures [437] (determined from elastic constants or specific heat capacity measurements) of some crystals. The force constants used in the calculation are from the combinative rule and Table 4.4. The overall agreement is good. The force constants for metals are calculated according to (4.152). It is found that $m = 8$ gives good agreement with experimental values. Again, it is found that, for metallic crystals, the force constants can be reduced significantly by the long-range electrostatic interaction (by a factor of about 5), which results in a low Debye temperature.

4.11.4 Prediction of Grüneisen Parameter

The Grüneisen parameter has been used to represent the volume dependence of the normal-mode frequencies. The overall Grüneisen parameter γ_{G} (Glossary) is defined as [12]

$$\gamma_{\mathrm{G}} = \frac{\sum_{\kappa,\alpha} \gamma_{\mathrm{G},\kappa,\alpha} c_{v,\rho,\alpha}(\kappa)}{\sum_{\kappa,\alpha} c_{v,\rho,\alpha}(\kappa)}, \quad \gamma_{\mathrm{G},\kappa,\alpha} = -\frac{V}{\omega_{\kappa,\alpha}} \frac{\partial \omega_{\kappa,\alpha}}{\partial V} = -\frac{\partial \ln \omega_{\kappa,\alpha}}{\partial \ln V}, \tag{4.162}$$

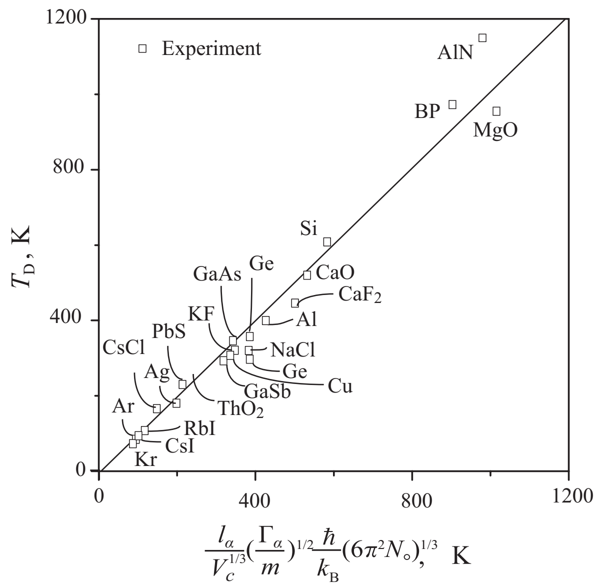

Figure 4.26. Comparison of the predicted and measured Debye temperature for some crystals. The force constants for metallic crystals are calculated according to (4.152) (m is chosen as 8). The experimental values are from [437].

where the subscript α denotes the branch of a normal mode, $c_{v,\rho,\alpha}$ is the heat capacity per normal mode, and V is the volume. In the Debye approximation, all the normal-mode frequencies scale linearly with the Debye temperature T_D, and therefore [12]

$$\gamma_G = \gamma_{G,\kappa,\alpha} = -\frac{\partial \ln \omega_D}{\partial \ln V}. \tag{4.163}$$

That is, γ_G represents the relative shift of the Debye angular frequency with respect to the volume.

We consider a crystal containing only one bond type. According to (4.158) and (4.163), because the Debye frequency $\omega_D \propto \Gamma^{1/2}$ [from (4.158) and (4.161)] and the volume $V \sim r_e^3$, we have

$$\gamma_G = -\frac{\mathrm{d} \ln \Gamma}{6 \mathrm{d} \ln r_e}. \tag{4.164}$$

Note that γ_G relates only to the bond. In [508] there is defined a “bonding-scaling parameter” γ'_G as

$$\gamma'_{G,i} = -\frac{\mathrm{d} \ln \Gamma'_i}{6 \mathrm{d} \ln r'_i}, \tag{4.165}$$

where Γ'_i and r'_i are the force constant and the equilibrium length of the bond i. For the crystals containing only one bond type, the Grüneisen parameter γ_G is equal to the bonding-scaling parameter γ'_G.

We can rewrite (4.165) in terms of a a small relative deviation fraction ϵ

$$\Gamma_i'(\epsilon) \simeq \Gamma_{\rm o}'(1-6\gamma_{\rm G}'\epsilon), \tag{4.166}$$

where $\Gamma_{\rm o}'$ is the initial equivalent force constant. It is apparent that $\gamma_{\rm G}'$ represents the intrinsic anharmonicity of a bond, i.e., the relative shift of the force constant with respect to the bond length. It seems reasonable that the $\gamma_{\rm G}'$ of each bond is independent of other bonds.

We again consider the crystal containing one bond type to obtain the bond-scaling parameter $\gamma_{\rm G}'$. In [405] a thermodynamic description of Morse oscillators using a statistical treatment is developed. Here a similar approach is applied for the L–J oscillators representing the interatomic potentials. Consider an assembly of independent oscillators with the interatomic potential of (4.144), of which the natural angular frequency (2.54) $\omega_n = \omega = (\Gamma/m_r)^{1/2}$ (m_r is the reduced mass of the oscillator). If (4.144) is expanded in a Taylor series, the vibrational energy $E_{p,l}$ and the mean atomic separation $\langle r_l\rangle$ of the motion with the principle quantum number l of this oscillator can be expressed as [311]

$$\begin{aligned} E_{p,l} &= \hbar\omega(l+\frac{1}{2}) - C_e\hbar^2\omega^2(l+\frac{1}{2})^2, \quad C_e = \frac{5(m+n+3)^2}{48\varphi_{\rm o}mn} \\ \langle r_l\rangle &= r_{\rm o} + C_r r_{\rm o}\hbar\omega(l+\frac{1}{2}), \quad C_r = \frac{3(m+n+3)}{2\varphi_{\rm o}mn}. \end{aligned} \tag{4.167}$$

Then, we have (a similar derivation is given in [405])

$$\begin{aligned} \gamma_{\rm G}' &\simeq \gamma_{\rm G,o}'[1+C_e k_{\rm B}T\frac{g_1(x_{\rm D})}{g(x_{\rm D})}], \quad \gamma_{\rm G,o}' = \frac{m+n+3}{6} \\ g(x_{\rm D}) &= \int_0^{x_{\rm D}} \frac{x^3{\rm d}x}{e^x-1}, \quad x_{\rm D} = T_{\rm D}/T \\ g_1(x_{\rm D}) &= \int_0^{x_{\rm D}} \frac{x^4(1+e^x){\rm d}x}{(e^x-1)^2}. \end{aligned} \tag{4.168}$$

Typically, the vibration energy is much smaller than the dissociation energy and $C_e k_{\rm B}T$ is small, so the temperature dependence of $\gamma_{\rm G}'$ is weak. At high temperatures, $\gamma_{\rm G}'$ will reach $\gamma_{\rm G,o}'$. It is very interesting to note that $\gamma_{\rm G,o}'$ depends only on m and n, or on the bond type.

(i) *Ideal Ionic Bonds*. The attractive potential is dominated by the electrostatic potential, and the lattice summation of the long-range electrostatic interactions does not change n (the Madelung term); thus $n = 1$. The repulsive term arises from the full-filled shells and the Pauli exclusion principle. The measurements for typical ionic bonds show $m = 6$–10 [12]. The midpoint $m = 8$ is a reasonable choice for the estimation; therefore $\gamma_{\rm o}' = 2.0$. In fact, $\gamma_{\rm G,o}' = 2.0$ agrees well with the high-temperature $\gamma_{\rm G}$ values of many typical ionic crystals with one bond type [117, 437].

(ii) *van der Waals Interactions*. The attractive term arises from the interaction between dipoles and varies as $1/r^6$, that is, $n = 6$. The widely used 12–6 L–J potential chooses $m = 12$ for the repulsive term. However, it is found that $m = 12$ makes the repulsive term very steep [269]. $m = 12$ gives $\gamma'_{\mathrm{G,o}} = 3.5$, a much higher value than the measured results. For example, at high temperatures, γ_{G} of Ne, Ar, Kr, and Xe are 2.76, 2.73, 2.84, and 2.65 [437], respectively. Considering the repulsive term of van der Waals interaction arises from the same mechanism (i.e., the filled outer shell) as in an ionic bond, it is reasonable to choose the same value 8 for m. This choice gives $\gamma'_{\mathrm{G,o}} = 2.83$, which agrees much better with the proceeding experimental results.

(iii) *Nonpolarized Covalent Bonds*. The attractive term is because of the electrostatic interaction, therefore $n = 1$. For m, the case is more complicated, because the distribution of valence electrons differs substantially from that in isolated atoms or ions. The repulsive term includes the electrostatic term because of the Pauli exclusion principle. In fact, the covalent bond is more appropriately described by the Morse potential (Table 2.1) [269]

$$\varphi = \varphi_{\mathrm{o}}[e^{-2a_{\mathrm{o}}(r-r_{\mathrm{o}})} - 2e^{-a_{\mathrm{o}}(r-r_{\mathrm{o}})}]. \tag{4.169}$$

In [405] an empirical relation is suggested, i.e., $a_{\mathrm{o}}r_{\mathrm{o}} = (m+4)/5$. For typical covalent bonds, $a_{\mathrm{o}}r_{\mathrm{o}} \simeq 1.0$–$1.2$, thus $m = 1$–2. Because $m > n$, we choose $m = 2$ and obtain $\gamma'_{\mathrm{G,o}} = 1.0$. This value is also in accord with the the relation Γr^6 = constant for covalent bonds, as suggested in [191].

The covalent bond between atoms with different electronegativities is partially polarized (ionic bonds can also be considered highly polarized covalent bonds). Using the relation of the percentage of the ionic character c proposed in [362], γ'_{G} of a polarized bond can be given as

$$\gamma'_{\mathrm{G}} = \gamma'_{\mathrm{G,AB}} = (1-c)\gamma'_{\mathrm{G},cov} + c\gamma'_{\mathrm{G},ion}, \; c = 1 - e^{-(\chi_{\mathrm{A}}-\chi_{\mathrm{B}})^2/4}, \tag{4.170}$$

where $\gamma'_{\mathrm{G},cov}$ and $\gamma'_{\mathrm{G},ion}$ represent the bond-scaling parameters of a nonpolarized covalent bond and the ideal ionic bond, respectively. Equation (4.170) together with (4.168) can also be used for the rough estimation of m in an interatomic potential

$$m \simeq 8 - 6e^{-(\chi_{\mathrm{A}}-\chi_{\mathrm{B}})^2/4}. \tag{4.171}$$

(iv) *Metallic Bonds*. Although metallic crystals also include ions, they are very different from ionic crystals. The metals can be treated as ions immersed in a sea of free electrons [12]. Thus the interactions between ions can be treated as the summation of the bare interactions between ions and the electron–ion interactions. Both the repulsive term and attractive term include the long-range electrostatic interactions. However, because of the screening effects of free electrons, the interaction between ions decays faster than the pure Coulomb interactions, thus $m > 1$ and $n \geq 1$ (because of the attractions of ions to free electrons, the repulsive term decays faster than the attractive term). The derivation of γ'_{G} for metallic bonds is complicated. To compare it with experimental results, one also needs

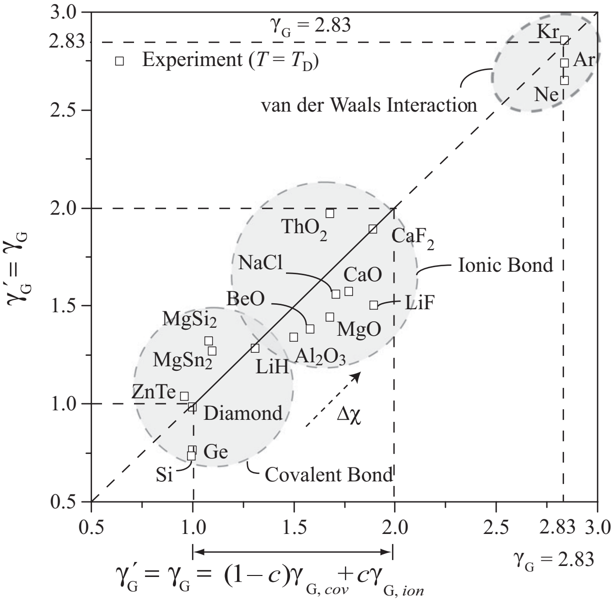

Figure 4.27. Comparison of predicted high-temperature Grüneisen parameters with the experimental results at the Debye temperatures for some crystals [437]. The Grüneisen parameter increases with an increase in the difference of electronegativity [201, 204]. Only for single-bond crystals, $\gamma_G = \gamma'_G$.

to include the contribution from the free electrons (it may be small at high temperatures). However, because the screening effects increase with the increasing electron number density [12], we would expect that, in the metals with high electron number densities, $m \simeq 8$ and $1 \le n \le 6$. For simplicity, in this work we set $m = 8$ and $n = 1$ (the same values for ionic bonds). The resulting $\gamma_G = 2.0$ is close to the experimental results of many metals (the alkali metals have a γ_G close to 1.2 because of the poor screening effects).

(v) *Other Interactions*. Some other interactions, e.g., the ion–dipole interaction, may exist in some crystals. These interactions may be considered as the cross terms of the above interactions. Using the combinative rule for potentials [(4.143) and (4.142)], we can have

$$m = \frac{(m_1 + m_2)}{2}, \; n = \frac{(n_1 + n_2)}{2}, \; \gamma'_G = \frac{(\gamma'_{G,1} + \gamma'_{G,2})}{2}, \tag{4.172}$$

where the subscripts 1 and 2 denote the individual interactions.

It can be seen that the order of magnitude of γ'_G for bonds is γ'_G(van der Waals bond) > γ'_G(ionic bond) > γ'_G(polarized covalent bond) > γ'_G(nonpolarized covalent bond). Figure 4.27 compares the calculated high-temperature Grüneisen parameters of crystals containing only one bond type with the experimental results (at the Debye temperature) [437], and the overall agreement is good. Note that, for ionic crystals, Grüneisen parameters are slightly overestimated. One reason is that the temperature at which the measurements are performed is not high enough. For example, γ_G of NaCl at the Debye temperature is 1.57, but at 800 K, its value is 1.76 [419], compared with 1.71 given by (4.170). Another possible reason is that c in (4.170) determined by Pauling is not very accurate.

Note that (4.165) is valid for the equivalent force constant Γ, so the Grüneisen parameter γ_G of a crystal can be obtained by evaluation of the equivalent γ'_G of the equivalent bond.

For two parallel bonds, (4.155) and (4.166) lead to

$$\gamma'_G = \frac{\Gamma_{10}}{\Gamma_{10}+\Gamma_{20}}\gamma'_{G,1} + \frac{\Gamma_{20}}{\Gamma_{10}+\Gamma_{20}}\gamma'_{G,2}, \tag{4.173}$$

where Γ_{10} and Γ_{20} represent the equilibrium force constants of bond 1 and 2. That is, the equivalent γ'_G of the parallel bonds is the summation of the $\gamma'_{G,i}$ of the bonds weighted by the fraction of force constants.

Similarly, for two bonds in series, the equilibrium requirement gives

$$\epsilon_1 = \frac{\Gamma_{20}(r_1+r_2)}{(\Gamma_{10}+\Gamma_{20})r_1}\epsilon, \ \epsilon_2 = \frac{\Gamma_{10}(r_1+r_2)}{(\Gamma_{10}+\Gamma_{20})r_2}\epsilon, \tag{4.174}$$

and (4.154) and (4.166) lead to

$$\gamma'_G = (\frac{\Gamma_{20}}{\Gamma_{10}+\Gamma_{20}})^2\frac{r_1+r_2}{r_1}\gamma'_{G,1} + (\frac{\Gamma_{10}}{\Gamma_{20}+\Gamma_{10}})^2\frac{r_1+r_2}{r_2}\gamma'_{G,2}. \tag{4.175}$$

Equation (4.175) shows the equivalent γ'_G is related not only to the force constants and $\gamma'_{G,i}$, but also to the bond lengths. Note when $\epsilon_1 = \epsilon_2 = \epsilon$ (homogeneous deformation), (4.175) can be reduced to

$$\gamma'_G = (\frac{\Gamma_{20}}{\Gamma_{10}+\Gamma_{20}})\gamma'_{G,1} + (\frac{\Gamma_{10}}{\Gamma_{20}+\Gamma_{10}})\gamma'_{G,2}, \tag{4.176}$$

which does not relate to the bond lengths. Note that $\gamma'_{G,i}$ is found from (4.168).

Assuming $r_1 \simeq r_2$ and $\gamma'_{G,2}$ is the smaller one, the dependence of $\gamma'_G/\gamma'_{G,2}$ on the ratio of force constants Γ_{10}/Γ_{20} is plotted in Figure 4.28.

Figure 4.28 shows that the equivalent γ'_G of both the parallel and serial arrangements is always higher than $\gamma'_{G,2}$. For the parallel arrangement, $\gamma'_{G,2} \le \gamma'_G \le \gamma'_{G,1}$, the stronger bond contributes more to the equivalent γ'_G; when $\gamma'_{G,1}/\gamma'_{G,2} = 1$, the equivalent γ'_G is independent of Γ_{10}/Γ_{20}. For the serial configuration, $\gamma'_{G,2} \le \gamma'_G \le 2\gamma'_{G,1}$, the weaker bond contributes more to γ'_G. For equivalent γ'_G, according to (4.175), the lowest value $2\gamma'_{G,1}\gamma'_{G,2}/(\gamma'_{G,1}+\gamma'_{G,2})$ is achieved when $\Gamma_{10}\gamma'_{G,1} = \Gamma_{20}\gamma'_{G,2}$, and the mismatch of $\Gamma_i\gamma'_{G,i}$ of neighboring bonds causes an increase in the anharmonicity. To increase anharmonicity and reduce the sound velocity, the serial arrangement is preferred.

4.11.5 Prediction of Thermal Conductivity

Using the relations for γ_G and T_D, when ω_c is comparable with ω_D, the thermal conductivity can be readily calculated with the Slack relation. The predicted thermal conductivities of some crystals at high temperatures are listed in Table 4.5 and

Table 4.5. *Predicted k_p and Slack model for parameters of some crystals, at listed temperatures. The experimental results [437, 12] are shown in the parentheses, and the calculated results by Slack are shown in the brackets. Slack used $T_{D,\infty}$ from the D_p, which is different from the experimental T_D. γ_G used by him are derived from experiments except for diamond, SiC, Ge, GaAs, and BP (0.7 was used for these crystals). m is found from (4.171).*

Crystals	T, K	T_D, K	$N_\circ$	γ_G	k_p, W/m-K
Ar	84	94 (85)	1	2.83 (2.73)	0.5 (0.4)[3.8]
Kr	66	87 (73)	1	2.83 (2.84)	1.1 (0.5)[0.4]
C(Diamond)	300	2183 (2230)	2	1.0 (0.9)	1292 (1350)
Ge	235	382 (360)	2	1.0 (0.76)	95 (83)[89]
Si	395	584 (625)	2	1.0 (0.56)	76.7 (115)[93]
Cu	300	339 (315)	1	2.0	14.4 (10^a)
Pt	300	194 (230)	1	2.0	9.1 (6^a)
GaAs	220	367 (346)	2	1.01 (0.75)	72 (81)[77]
CaF_2	345	453(510)	3	1.89 (1.89)	7.0 (8.5)[9.1]
MgO	600	1034 (945)	2	1.68 (1.44)	53 (25) [28]
NaCl	230	382(330)	2	1.71(1.57)	11.1 (8.6)[6.3]
c-BN	300	1614	2	1.22	733 (748)
SiC	300	1212 (1079)	2	1.11 (0.76)	463 (490)[461]
BP	670	891 (982)	2	1.0	97.46 (110)[166]

[a] The lattice conductivities are from reference [30]. They are obtained by subtracting the electrical thermal conductivity (derived from Wiedemann–Franz law) from the total thermal conductivity.

shown in Figure 4.29(a), and the measured values and the values calculated in [437] are also given. Note that Slack used $T_{D,\infty}$ calculated from the phonon DOS D_p, which is different from the measured T_D listed in Table 4.5. Table 4.5 shows that the thermal conductivities and the Debye temperatures estimated by our model

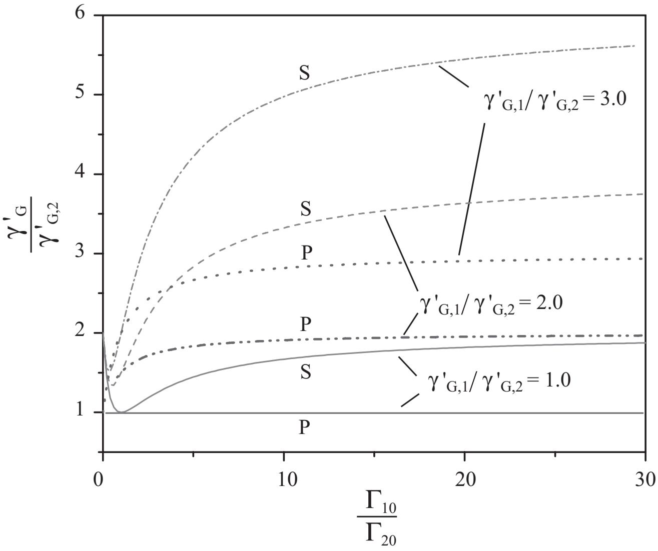

Figure 4.28. Variation of ratio of the equivalent bond-scaling parameter to the smaller bond-scaling parameter of the bonds $\gamma'_G/\gamma'_{G,2}$ with respect to the ratio of the force constants Γ_{10}/Γ_{20}. The symbols P and S denote the parallel and serial arrangements.

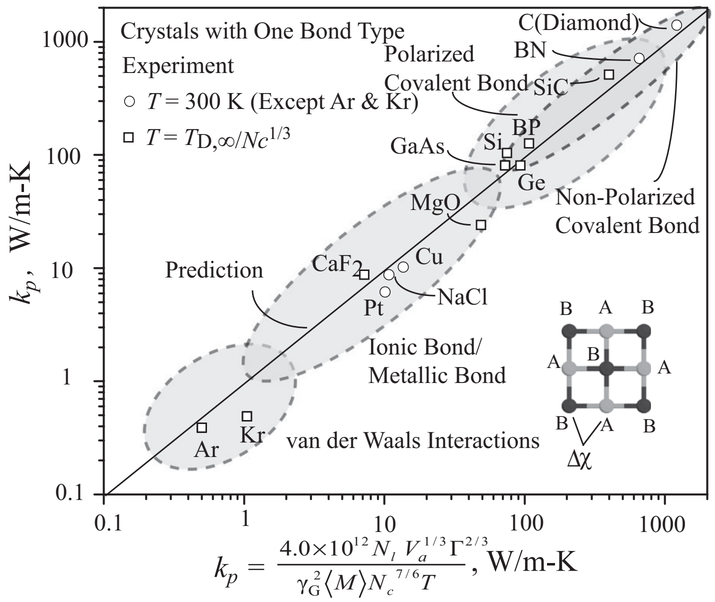

(a) $\omega_c \approx \omega_D$: Long-Range Acoustic Phonons Dominates

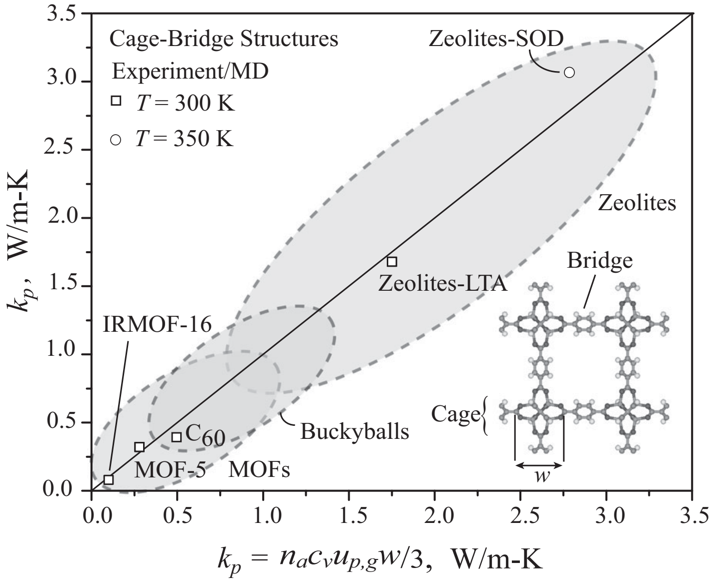

(b) $\omega_c \ll \omega_D$: Short-Range and Optical Phonons Are Important

Figure 4.29. Comparison of the predicted lattice thermal conductivity of some compact crystals with the experimental results. (b) Comparison of the calculated thermal conductivities of some cage-bridge crystals with the experimental or MD results [201, 204].

agree well with the experimental results and the Slack results, but the Grüneisen parameters are normally overestimated in our model, as discussed in Section 4.11.4. The average mean-square error between the estimated values and the experimental results is about 20%. Slack used $T_{D,\infty}$ along with the experimental γ_G (but 0.7 was used for Ge, Si, and SiC for better agreement with the experiments [437]), both of which are normally slightly lower than the values estimated in our model. Note that we also predict the lattice thermal conductivity of Al and Pt by considering only the phonon–phonon scattering. The crystalline metals normally have a low lattice thermal conductivity, not only because of the strong scattering of phonons by free electrons, but also because of their large Grüneisen parameters and small force constants (caused by long-range electrostatic interactions).

Also note that T_D and k_p used in Table 4.5 are different from those in Tables A.1 and A.2. This is because of the range of measured k_p reported for diamond.

When $\omega_c \ll \omega_D$, the thermal transport is dominated by the short-range acoustic phonons and optical phonons. Whereas the acoustic contribution can be calculated with a relation similar to the Cahill–Pohl (C–P) relation [69, 203], the optical part is difficult to determine and it is comparable to the acoustic contribution [203, 318]. However, for some special atomic structures, the phonon mean free path is limited by the crystal structure, and the thermal conductivities of such crystals often exhibit temperature-independence above the Debye temperature. From (4.109) and $k_p = nc_{v,p}u_{p,A}\lambda_p/3$ ($c_{v,p}$ is the heat capacity per atom), if the phonon mean free path λ can be determined from the characteristics of the structure, the thermal conductivity can also be easily calculated.

There exist many special structures that can limit the phonon mean free path at high temperatures. For example, in the filled skutterudite structures [473], the fillers act as scatterers and limit the phonon mean free path to be the distance between the scatterers. Here we discuss the cage-bridge structure, which is common for nanoporous crystals, e.g., zeolites, MOFs, and many molecular crystals.

The cage-bridge structure includes complex multiatomic cages connected by relatively simple bridges [see Figure 4.29(b)] (sometimes the cages may also be joined directly without bridges). In such a structure, the atoms in the cage are normally much more than the atoms acting as connectors. Zeolites and MOFs are good examples of such structures. Some siliceous zeolites, e.g., zeolite A (LTA), faujasite (FAU), and sodalite (SOD), contain the complex SOD cage built from SiO_4 tetrahedra [318]. MOF-5, the smallest cubic MOF structure, comprises Zn_4O clusters linked by 1,4-benzenedicarboxylate (BDC) [203].

Many molecular crystals consist of large, complex molecules held together by weak van der Waals interactions or hydrogen bonds. The intramolecular interactions are much stiffer than the intermolecular interactions. They can also be considered a special type of cage-bridge structure, and each complex molecule can be considered a cage.

When $T \geq T_D$, all the vibration modes will have the same contribution to the total vibration energy. Because most atoms lie in the cage, most vibration energy is located in the cage and a fraction of the vibration energy transports to the next cage

Table 4.6. *Comparison of predicted thermal conductivities of some cage-bridge structures calculated by (4.177) and the Slack relation, with the experimental and the MD results.*

Crystals	T, K	$u_{p,\mathrm{A}}$, m/s	w, Å	k_p, W/m-K (4.177)	$k_{p,\mathrm{S}}$	Experiment/MD
MOF-5[a]	300	1184	7.16	0.28	0.025	0.32
IRMOF-16[a]	300	600	7.16	0.10	0.01	0.08
SOD	350	4200[b]	8.88	2.79	1.58	3.09[c]
LTA	300	3200[b]	8.88	1.75	0.47	1.68[c]
C_{60}	260	2000[d]	7.00	0.52	0.007	0.4[e]

[a] values for MOF-5 are taken from [203]. The data for IRMOF-16 are calculated by MD using the same potentials

[b] values are derived from the bulk modulus [13], by setting the Poisson ratio as 0.3

[c] values are taken from MD results from [318]

[d] values are derived from the bulk modulus [119]

[e] values are from reference [507]

through connectors. However, the large coordination number difference or bond-stiffness difference makes the connector a bottleneck for the energy transport, and most phonon energy is localized in the cage or reflected at the connectors. In [318] it is shown that the Si–O–Si bonds contribute to the energy localization in FAU- and SOD-zeolites. The work for MOF-5 [203] also showed that the carbon connector limits the transport of phonon energy. An indicator of this phenomenon is the large difference between the phonon partial DOS, weighted by the concentration of atoms) of the cage and that of the connectors (as shown in [203]). Therefore the connectors will act as scatterers in the structure. If the cage is relatively rigid (phonons experience little scattering within the cage), the phonon mean free path will be limited by the distance between the connectors at the boundary of the cage, which is often the same as the cage size w. For molecular crystals, w is essentially the dimension of the molecule. Then we write (4.109) as

$$k_p = \frac{1}{3} n c_{v,p} u_{p,\mathrm{A}} w. \tag{4.177}$$

When the temperature is higher than the Debye temperature, c_v can be simply set as $3k_\mathrm{B}$.

This simple mean-free-path model for the cage-bridge structures leads to good agreement with the experimental values or the MD results, as shown in Table 4.6. The values calculated by the Slack relation ($k_{p,\mathrm{S}}$) are also shown, and it is apparent that $k_{p,\mathrm{S}}$ has a lower value.

When the temperature decreases, the high-frequency phonon modes caused by the internal vibrations of the cage will decrease much faster than the low-frequency modes, and the fraction of localized energy will decrease. When the temperature is much lower than the Debye temperature, the fraction of localized vibration energy will be small and the phonon mean free path will no longer be limited by the cage size.

This simple atomic-structure-based model can be used to quickly estimate the high-temperature thermal conductivity of crystals. On the other hand, some useful insights into the design of materials with desired properties can be extracted.

According to (4.132) and using (4.161), we have

$$k_{p,\mathrm{S}} = k_{p,lg,\mathrm{A}} = \frac{4.0 \times 10^{12} N_l \Gamma^{3/2} V_a^{1/3}}{\gamma_\mathrm{G}^2 \langle M \rangle^{1/2} N_\circ^{7/6} T}, \tag{4.178}$$

where N_l is a constant related only to lattice type. Therefore, to increase the thermal conductivity, one may increase the equivalent force constant Γ and lattice constant a, while reducing the mean atomic weight $\langle M \rangle$, $N_\circ$, and the Grüneisen parameter γ_G. Here FCC is expected to achieve a high thermal conductivity. The opposite approaches can be used to achieve a low lattice thermal conductivity.

Evidently molecular crystals will normally have a very low thermal conductivity because of the small Γ, large γ_G and $N_\circ$.

Table 4.4 and Figure 4.23(a) show that most metals have a low $\Gamma_{\mathrm{AA},1}$, around 50 N/m. Even when they bond with F (which has the highest $\Gamma_{\mathrm{AA},1}$), $\Gamma_{\mathrm{AB},1}$ is expected to be lower than 250 N/m. Also, metal elements normally have a heavy mass and ionic bonds have a relatively high $\Delta\chi$. In comparison, covalent bonds may have a higher $\Gamma_{\mathrm{AB},1}$, lower $\Delta\chi$, and those nonmetallic elements with a high $\Gamma_{\mathrm{AA},1}$ have a relatively light mass. Thus, for high thermal conductivity, covalent crystals are preferred. Among covalent crystals, the compounds of N and C are expected to have a high thermal conductivity, because N and C have the highest $\Gamma_{\mathrm{AA},1}$, moderate χ, light masses, and possibly high bond orders. In general, the sequence of lattice conductivity for crystals is k_p (nonpolarized covalent crystal) $>$ k_p (polarized covalent crystal) $>$ k_p (ionic crystal) $>$ k_p (molecular crystal), as shown in Figure 4.29(a). Furthermore, the oxidation states of the elements need to match and the mass difference should be small to achieve a small $N_\circ$. Materials satisfying these conditions are expected to have a high thermal conductivity, e.g., BN, AlN, BP, and SiC (listed in Table 4.5).

4.12 Phonon Conductivity Decomposition: Acoustic Phonons

Here we consider only the interphonon interactions (phonon–phonon scattering), which are dominant at high temperatures. Three main techniques have been developed to predict the thermal conductivity of a dielectric material by use of MD simulations. These are the G-K approach (an equilibrium method), a direct application of the Fourier law of conduction (a steady-state, nonequilibrium method, sometimes called the direct method), and unsteady methods. The G-K method was discussed in Section 3.6, and here we present some results for the Ar FCC crystal (acoustic phonons only, as there is one atom per primitive cell, Section 4.3) [317]. In Section 4.13, we discuss crystal, with optical phonons.

The net flow of heat in a solid, given by the heat current vector $\boldsymbol{q}$ (Table 3.9), fluctuates about zero at equilibrium. In the G–K method discussed in Section 3.5, the thermal conductivity is related to the elapsed time it takes these fluctuations to dissipate, and for an isotropic material is given by (3.78) as

$$k_p = k_{p,\text{G-K}} = k_{p,\text{MD}} = \frac{V}{k_\text{B}T^2}\int_0^\infty \frac{\langle \boldsymbol{q}(t)\cdot\boldsymbol{q}(0)\rangle}{3}\text{d}t, \tag{4.179}$$

where $\langle \boldsymbol{q}(t)\cdot\boldsymbol{q}(0)\rangle$ is the heat current autocorrelation function (HCACF) (Table 3.9). In materials for which the fluctuations are long lived (i.e., the mean phonon relaxation time is large), the HCACF decays slowly. The thermal conductivity is related to the integral of the HCACF and is accordingly large. In materials such as amorphous solids, for which the mean relaxation time of phonons is small, thermal fluctuations are quickly damped, leading to a small integral of the HCACF and a low thermal conductivity. The heat current vector is given by (3.78)

$$\boldsymbol{q} = \frac{1}{V}\frac{\text{d}}{\text{d}t}\sum_i \boldsymbol{x}_i E_i, \;\; E_i = E_{k,i} + E_{p,i}, \tag{4.180}$$

where the summation is over the particles in the system, and $\boldsymbol{x}_i$ and E_i are the position vector and energy (kinetic and potential) of a particle. A pair potential, such as the L–J potential, (4.180) can be recast (Table 3.9) as (Chapter 3 problem)

$$\boldsymbol{q} = \frac{1}{V}[\sum_i E_i\boldsymbol{u}_i + \frac{1}{2}\sum_{i,j}(\boldsymbol{F}_{ij}\cdot\boldsymbol{u}_i)\boldsymbol{x}_{ij}], \tag{4.181}$$

where $\boldsymbol{u}$ is the velocity vector of a particle, and $\boldsymbol{x}_{ij}$ and $\boldsymbol{F}_{ij}$ are the interparticle separation vector and force vector between particles i and j. This form of the heat current is readily implemented in MD simulation. A derivation of (4.179) and further discussion is given in Appendix B.

All simulations used in the thermal conductivity calculations consist of 10^6 time steps ($\Delta t = 4.205$ fs) beyond the standard initialization period over which the heat current vector is calculated every five time steps. A correlation length of 5×10^4 time steps starting after 2×10^5 time steps is used in the autocorrelation function. For all cases, five independent simulations (with random initial velocities) are performed and the HCACFs are averaged before finding the thermal conductivity. This ensures a proper sampling of phase space [281]. For the FCC crystal at a temperature of 10 K, where the correlation time is long, 10 independent simulations are performed.

4.12.1 Heat Current Autocorrelation Function

The decay of the HCACF for Ar is shown in Figure 4.30. The HCACF is normalized by its zero time value to allow for comparisons among the different temperatures. Longer time scales are shown for the Ar FCC crystal in Figures 4.31(a), 4.31(b), and 4.31(c) for temperatures of 10, 50, and 80 K, respectively. Note that, as the temperature increases, the HCACF decays of the three phases are approaching each other.

The Ar FCC crystal HCACF shows a two-stage behavior. There is an initial drop, similar for all cases, followed by a longer decay, whose extent decreases as the

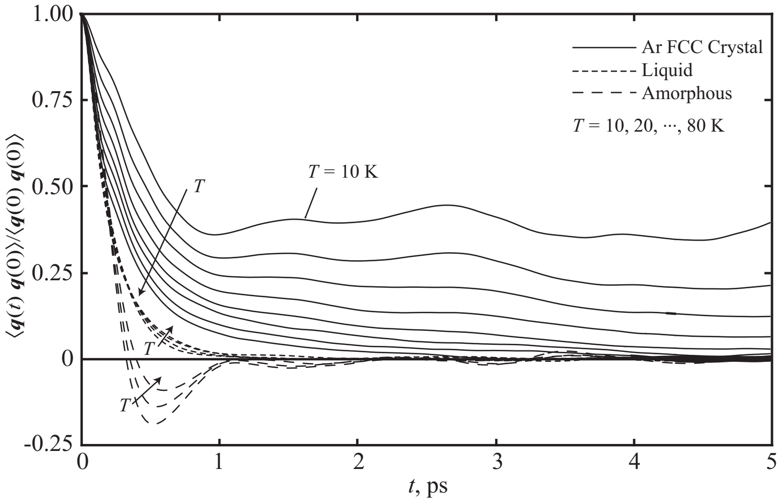

Figure 4.30. Time dependence (decay) of the HCACF for FCC, amorphous, and liquid Ar, for various temperatures [317].

temperature increases. The oscillations in the secondary decay are believed to be a result of the periodic boundary conditions.

For all cases considered, the integral of the HCACF converges well, and the thermal conductivity can be specified directly by averaging the integral over a suitable range. To remove the subjective judgment, in [281] two methods are proposed by which the thermal conductivity can be specified. In the first-dip (FD) method, the integral is evaluated at the first place where the HCACF goes negative. In the exponential fit (EF) method, an exponential function is fitted to the HCACF beyond a certain point (determined on a case-by-case basis), and this function is then used to calculate the contribution of the tail to the integral. Up to that point the integral is evaluated directly. In the investigation of β-SiC [281], no significant differences were found between the predictions of these two methods.

The liquid HCACF shows a single stage decay, with a time scale comparable with that of the initial drop in the FCC crystal HCACF. Both the FD and EF methods are suitable for specifying the thermal conductivity. The amorphous-phase HCACF shows a very different behavior. It drops below zero in the initial decay and oscillates between positive and negative as it converges to zero. The velocity autocorrelation function for amorphous L–J Ar shows a similar form [293]. This behavior is interpreted as follows. In the FCC crystal, each atom experiences the same local environment. By averaging over time, the same is true for the liquid. This is not the case for the amorphous solid, for which each atom has a distinct local environment. At short time scales, atoms near their equilibrium positions experience the free trajectory of a liquid atom. When the atom eventually feels the effects of the other atoms, the trajectory changes. Because the intended trajectory cannot be completed, the correlation goes negative.

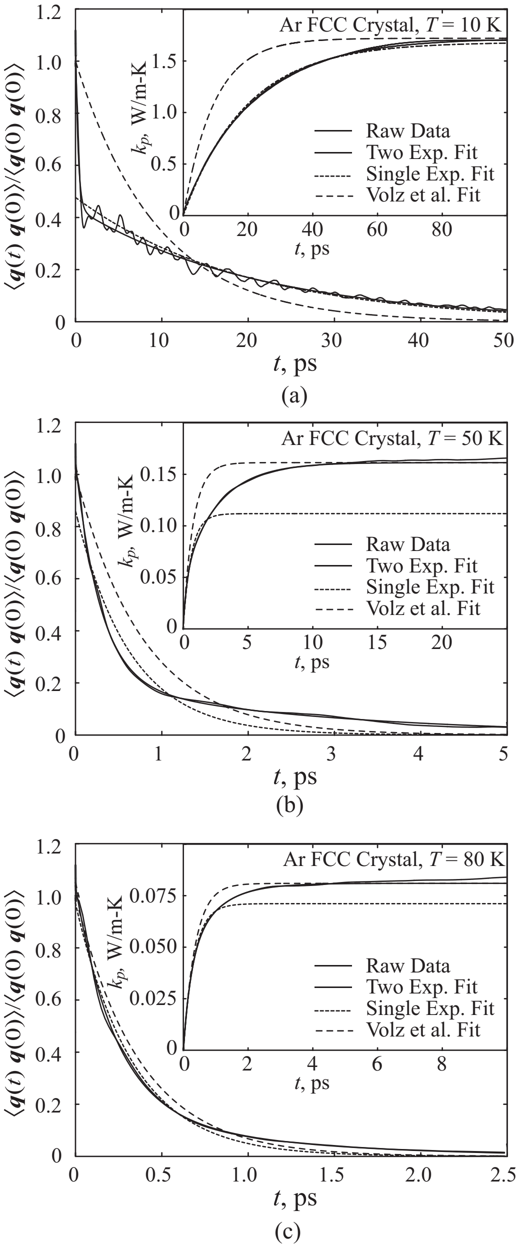

Figure 4.31. Time variation of the raw HCACF and thermal conductivity, and fits of one- and two-term exponential functions and the model of [482], for the FCC crystal at T = (a) 10 K, (b) 50 K, and (c) 80 K. Note the different time scales on the HCACF and thermal conductivity plots for each condition. For a number of cases, the raw data and the two-term exponential fits are indistinguishable [317].

The time scale for this behavior is comparable with that of the liquid HCACF. The FD and EF methods are not appropriate here, and the thermal conductivity must be found from a direct specification of the integral.

The low-temperature oscillations in the autocorrelation decay of Figure 4.30 are because of long-range phonons (the higher thermal conductivity). In this case the finite computational domain and the periodic boundary conditions influence the results (causing the oscillations)

4.12.2 Phonon Conductivity Decomposition

Based on the observed shape of the FCC crystal HCACF, it can be fitted to a sum of two exponential functions as

$$\frac{\langle \boldsymbol{q}(t)\cdot\boldsymbol{q}(0)\rangle}{3} = A_{sh,\mathrm{A}}\exp(-t/\tau_{p,sh,\mathrm{A}}) + A_{lg,\mathrm{A}}\exp(-t/\tau_{p,lg,\mathrm{A}}), \tag{4.182}$$

as suggested in [81]. The fitting procedure needs special care for large conductivities.

With (4.179), the thermal conductivity is then

$$\begin{aligned} k_p &= \frac{1}{k_\mathrm{B} V T^2}(A_{sh,\mathrm{A}}\tau_{p,sh,\mathrm{A}} + A_{lg,\mathrm{A}}\tau_{p,lg,\mathrm{A}}) \\ &\equiv k_{p,sh,\mathrm{A}} + k_{p,lg,\mathrm{A}}. \end{aligned} \tag{4.183}$$

In (4.182) and (4.183) the subscripts ac, sh, and lg refer to acoustic, short-range, and long-range. The two-stage decay in the HCACF was first observed in [262]. It is in contrast to the Peierls theory of thermal conductivity, which has been found to be consistent with a single-stage decay of the HCACF [262, 280]. In [226] it is suggested that the two stages in the HCACF represent contributions from local dynamics and the dynamics of phonon transport, each having a time constant τ_p and strength A. The use of the term "local" is questionable as, in a crystal, there are no localized vibrational modes. The fit curves for the HCACF and thermal conductivity obtained from (4.182) for temperatures of 10, 50, and 80 K are shown in Figs. 4.31(a), 4.31(b), and 4.31(c), respectively. The fit captures the two-stage decay very well at all temperatures. The fits of a single exponential function with time constant τ_p, according to

$$\frac{\langle \boldsymbol{q}(t)\cdot\boldsymbol{q}(0)\rangle}{3} = A_1\exp(-t/\tau_p), \tag{4.184}$$

are also shown in Figs. 4.31(a), 4.31(b), and 4.31(c). The agreement with the raw HCACF is reasonable at low and high temperatures, but poor at the intermediate temperatures.

The two-stage behavior of the FCC crystal HCACF and the resulting decomposition of the thermal conductivity into two distinct components are interpreted in the context of the phonon mean relaxation time. Although the relaxation time is generally taken to be an averaged quantity, it can be applied to an individual phonon. For a given phonon mode, there will thus be some continuous distribution of relaxation times. Physically, the lower bound on the relaxation time corresponds to a phonon with a mean free path equal to one-half of its wavelength. This is the C–P

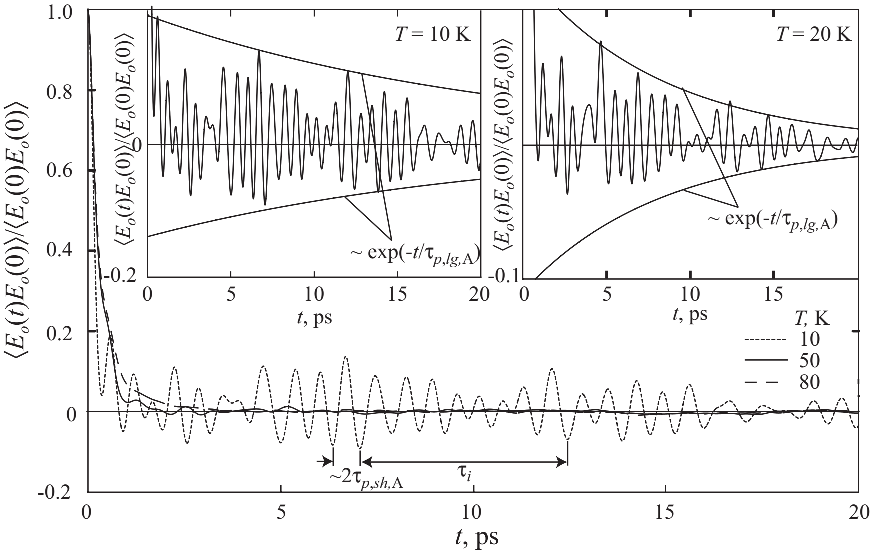

Figure 4.32. Particle energy autocorrelation functions for the Ar FCC crystal at $T = 10$, 50, and 80 K. The energy data correspond to deviations from the mean values. Note the diminishing long-time coherence as the temperature is increased. The inset plots show a smaller scale for the vertical axis for the temperatures of 10 and 20 K, along with curves representing the decay time associated with $k_{p,lg,\mathrm{A}}$ [317].

limit, a thermal conductivity model developed for amorphous materials (discussed in Section C.2 of Appendix C) [69, 126]. The first part of the thermal conductivity decomposition $k_{p,sh,\mathrm{A}}$ takes into account those phonons with this limiting value of relaxation time. Phonons with longer relaxation times are accounted for by the second term $k_{p,lg,\mathrm{A}}$, which has a longer decay time.

Self-energy correlations (i.e., an autocorrelation), similar to the nearest-neighbor correlations, are plotted in Figure 4.32 for temperatures of 10, 20, 50 K, and 80 K. Although there is coherent behavior over long time periods at the low temperatures, this effect diminishes as the temperature increases. This is consistent with the temperature trends in $\tau_{p,lg,\mathrm{A}}$ and $k_{p,lg,\mathrm{A}}$. For temperatures of 10 and 20 K (shown separately in the insets of Figure 4.32), exponentials with time constants equal to the appropriate $\tau_{p,lg,\mathrm{A}}$ from the thermal conductivity decomposition are superimposed. The trends in the energy correlation curves are well bounded by the exponentials. The manifestation of both $\tau_{p,sh,\mathrm{A}}$ and $\tau_{p,lg,\mathrm{A}}$ outside of the HCACF supports the use of energy correlation functions for understanding heat transfer in the real-space coordinates. The intermediate time scale in the long-time behavior at lower temperatures (shown as τ_i in Figure 4.32 for the 10 K curve) is thought to be associated with the periodic boundary conditions.

It is interesting to note that the long-time-scale behavior is made up of successive short-time-scale interactions ($\tau_{p,sh,\mathrm{A}}$, also shown in Figure 4.32). At the lower temperatures, the atom-to-atom interactions propagate step by step, leading to behavior with a period of $2\tau_{p,sh,\mathrm{A}}$ over the long time scale. At higher

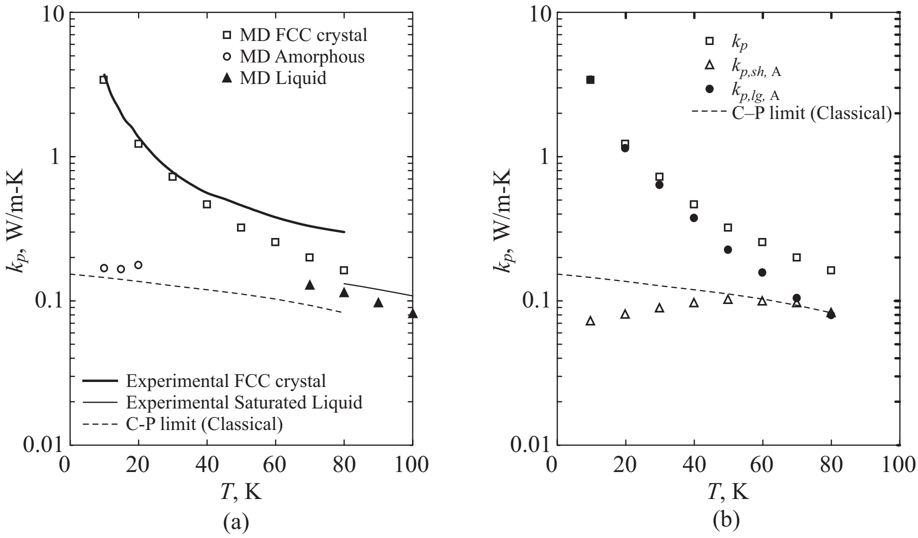

Figure 4.33. Temperature dependence of the experimental and predicted L–J Ar thermal conductivities [317].

temperatures, as the mean relaxation time gets smaller, the overall behavior approaches that of a damped oscillator (i.e., a monotonic decay), as opposed to a set of coupled oscillators (as seen at low temperatures), which can gain and lose energy.

4.12.3 Comparison with Experiment

The predicted thermal conductivities, experimental values [465], and the C–P limit for Ar are shown in Figure 4.33(a) as functions of temperature. Also included are the MD results given in [280], obtained under very similar simulation conditions. In Figure 4.33(b), the decomposition of the FCC crystal thermal conductivity into $k_{p,sh,\mathrm{A}}$ and $k_{p,lg,\mathrm{A}}$ is shown along with the C–P limit (4.131). The FCC crystal MD results are in reasonable agreement with the trend and magnitude of the experimental data (a decrease above the experimental peak value, which is near a temperature of 6 K), justifying the neglection of quantum effects. The data are in good agreement with those in [280].

As given in (4.110), the C-P limit is a quantum, harmonic expression. The MD simulations are classical and anharmonic. As such, for use in Figure 4.33, the classical limit of the C-P limit (4.131) is taken [i.e., the mode specific heat $k_\mathrm{B}x^2e^x/(e^x-1)^2$ equal to k_B], to give

$$k_{p,\text{C-P}} = \frac{1}{2}(\frac{\pi}{6})^{1/3}\beta k_\mathrm{B} n^{2/3}\sum_\alpha u_{p,\alpha}. \tag{4.185}$$

The number density, n, is taken from the FCC crystal MD results. Because of anharmonic effects at finite temperatures, the specific heat will deviate from the classical value, which is accounted for by the factor β ($0.5 \le \beta \le 1$). The FCC crystal data are used for the calculations, as the amorphous phase is stable only up to a temperature of 20 K. The temperature dependence of the sound speeds, $u_{p,\alpha}$ (of which there are three, one longitudinal and two transverse), is obtained from quasi-harmonic dispersion curves in the [100] direction based on the FCC crystal simulation cell sizes. There will be a difference between the amorphous sound speeds and those for the FCC crystal. As no sound speed data are available for the amorphous L–J phase, the FCC crystal values are used, scaled by a factor of 0.8 (typical for Si and Ge [69, 199]). Under these approximations, the C-P limit is plotted with the understanding that there will be some errors in the calculated values.

4.13 Phonon Conductivity Decomposition: Optical Phonons

Optical phonons contribute to phonon conductivity, but their contributions are weakly temperature dependent and generally small, except for low thermal conductivity crystals. An example is shown for silica structures in [318], where dense (quartz) and cage (zeolites) crystals have been studied by use of MD. The structures are shown in Figure 1.7. The G-K autocorrelation decay decomposition (4.182) for acoustic phonons is now extended to include optical phonons, i.e.,

$$\begin{aligned}\frac{\langle \boldsymbol{q}(t)\cdot\boldsymbol{q}(0)\rangle}{3} &= A_{sh,\mathrm{A}}\exp(-t/\tau_{p,sh,\mathrm{A}}) + A_{lg,\mathrm{A}}\exp(-t/\tau_{p,lg,\mathrm{A}})\\ &\quad + \sum_i B_{\mathrm{O},i}\exp(-t/\tau_{p,\mathrm{O},i})\cos(\omega_{p,\mathrm{O},i}t). \qquad (4.186)\end{aligned}$$

Then, using the G-K relation listed in Table 3.9, similar to (4.183), we find that the phonon conductivity is

$$\begin{aligned}k_p &= \frac{1}{k_\mathrm{B}VT^2}\Big(A_{sh,\mathrm{A}}\tau_{p,sh,\mathrm{A}} + A_{lg,\mathrm{A}}\tau_{p,lg,\mathrm{A}} + \sum_i \frac{B_{\mathrm{O},i}\tau_{p,\mathrm{O},i}}{1+\tau^2_{p,\mathrm{O},i}\omega^2_{p,\mathrm{O},i}}\Big)\\ &\equiv k_{p,sh,\mathrm{A}} + k_{p,lg,\mathrm{A}} + k_{p,\mathrm{O}}. \qquad (4.187)\end{aligned}$$

The results for quartz at the temperature of 250 K are shown in Table 4.7. The five most distinguished optical-phonon branches are listed (the dispersion results are given in Figure 4.7). For quartz, the optical-phonon contribution is small. Their MD results for the four structures, along with the experimental results for quartz, an amorphous silica, are shown in Figure 4.34.

The contribution of the short- and long-range acoustic phonons, and the optical phonon, are shown separately in Figure 4.35. The optical-phonon contribution is the most significant for zeolite LTA, which has the lowest conductivity. As was mentioned, the optical-phonon contribution is rather temperature independent.

Although not mentioned here, the direct (or nonequilibrium) methods (imposing a temperature gradient) have also been used for the prediction of k_p. Some aspects of these methods are reviewed in [320].

Table 4.7. *Thermal conductivity decomposition for quartz (a direction) at $T = 250$ K. The time constant for the short-range acoustic-phonon component is obtained from the energy correlation analysis [318].*

Component	τ_p, ps	$\omega/2\pi$, THz	$k_{p,i}$, W/m-K
Short-range acoustic $k_{p,sh,\mathrm{A}}$	0.016	–	1.143
Long-range acoustic $k_{p,lg,\mathrm{A}}$	2.37	–	9.494
Optical $k_{p,\mathrm{O}}$			
1	3.19	14.2	0.087
2	1.65	18.3	0.436
3	2.50	21.6	0.052
4	1.24	22.8	0.242
5	2.82	32.8	0.070
			0.887
Total, k_p			11.524

4.14 Quantum Corrections to MD/G-K Predictions

Because of their classical nature, MD simulations cannot explicitly take quantum effects into account. From the standpoint of lattice dynamics, there are two significant points to consider. First, the energy of the phonon modes is quantized in units of $\hbar\omega_k$. This is not true of the classical system, in which the mode energies are continuous. The second point, and the focus of this section, is the temperature dependence of the mode excitations. As predicted by the Bose–Einstein distribution, there are significant temperature effects in the quantum system that are not present in a classical description. The MD approach is thus not suitable near and below the maximum in the crystal-phase thermal conductivity (observed experimentally around one-tenth of the Debye temperature [302], and for Ar at a temperature of 6 K [91]), where quantum effects on the phonon mode populations are important. The thermal conductivity in this region is also strongly affected by impurities and boundary

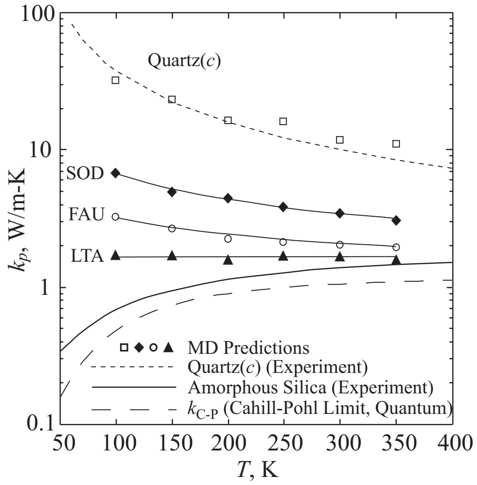

Figure 4.34. MD predicted and experimental thermal conductivities plotted as functions of temperature for silica crystals. All the structures are shown in Figure 1.7. The zeolite MD data are joined by best-fit power-law curves to guide the eye [318].

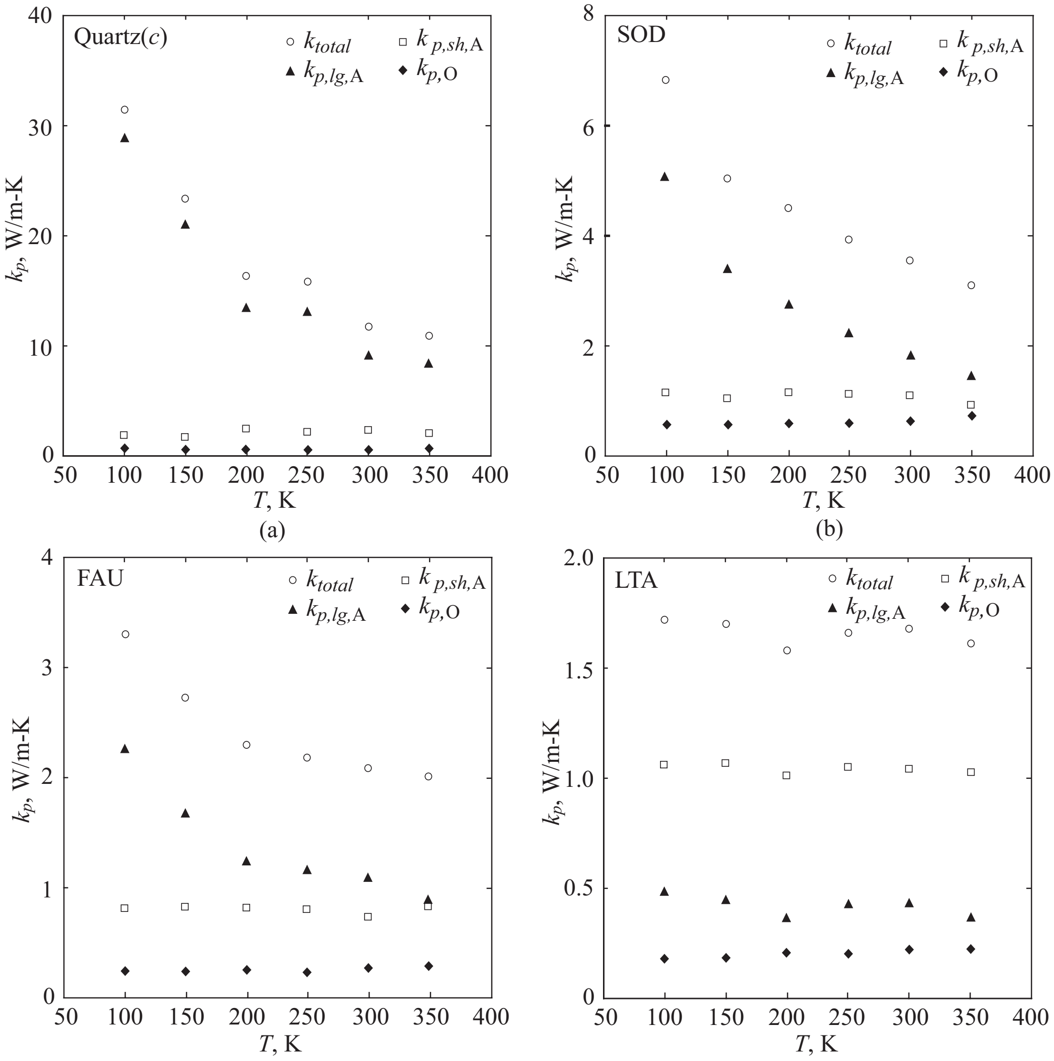

(a) (b) (c) (d)

Figure 4.35. Thermal conductivity decomposition for (a) quartz (c direction), (b) SOD, (c) FAU, and (d) LTA [318].

effects, which are not considered here. As such, an MD simulation of a perfect crystal with periodic boundary conditions will lead to an infinite thermal conductivity at zero temperature, as opposed to the experimental value, which goes to zero.

The classical nature of the MD simulations is perhaps most evident when we are considering the predicted specific heat, and how they differ from the quantum-mechanical calculations. The reason for the discrepancy is that in a classical-anharmonic system at a given temperature, all modes are excited approximately equally. The expectation value of the mode energy is about $k_B T$. In a harmonic system, the excitation is exactly the same for all modes, and the expectation value of the energy is exactly $k_B T$. In the quantum system, there is a freezing out of high-frequency modes at low temperatures. Only above the Debye temperature are all modes excited approximately equally. The quantum system also has a zero-point energy not found in the MD system.

There is no simple way to explicitly include quantum effects in the MD simulations. In fact, the whole idea behind the simulations is to save significant computational resources by ignoring quantum effects. That being said, some effort has been made to address the classical-quantum issue by mapping the results of MD simulations onto an equivalent quantum system. Using the results for the L–J FCC crystal, one of these approaches [273, 281, 301, 483], is presented and assessed here. The main idea is to scale the temperature and thermal conductivity (after the simulations have been completed) using simple quantum-mechanical calculations and/or arguments. For the remainder of this section, T_{MD} and k_{MD} are used to represent the temperature and thermal conductivity of the MD system, and T and k are used to represent the values for the real, quantum system. A critical assessment of these corrections is given in [470].

The temperature in the MD system is calculated from the relation (Table 2.4)

$$\langle \sum_i \frac{1}{2} m_i |\boldsymbol{u}_i|^2 \rangle = \frac{3}{2}(N-1) k_B T_{\mathrm{MD}}, \tag{4.188}$$

which equates the average kinetic energy of the particles (summed over the index i) to the expectation value of the kinetic energy of a classical system. For a harmonic system, where equipartition of energy exists between the kinetic and potential energies, and between the modes, the total system energy will be given by $3(N-1)k_B T_{\mathrm{MD}}$. The temperature of the real system is found by equating this energy to that of a quantum phonon system (4.50), as suggested in [273, 281] from (4.50), we have

$$3(N-1) k_B T_{\mathrm{MD}} = \sum_\alpha \hbar\omega_\alpha [\frac{1}{2} + \frac{1}{\exp(\hbar\omega_\alpha / k_B T) - 1}], \tag{4.189}$$

where the summation is over the α normal modes of the system. A similar relation has been proposed without the zero-point energy included [i.e., the factor of $\hbar\omega_\alpha/2$ on the right-hand side of (4.189) is not considered] [301, 483].

For the thermal conductivity, it has been proposed [273, 483, 281] that the conduction heat flux $\boldsymbol{q}$, in the classical and quantum systems, should be the same. Written in one dimension,

$$q_{k,x} = -k_{p,\mathrm{MD}} \frac{\mathrm{d}T_{\mathrm{MD}}}{\mathrm{d}x} = -k_p \frac{\mathrm{d}T}{\mathrm{d}x}, \tag{4.190}$$

such that

$$k_p = k_{p,\mathrm{MD}} \frac{\mathrm{d}T_{\mathrm{MD}}}{\mathrm{d}T}. \tag{4.191}$$

The predicted T_{MD} and $\mathrm{d}T_{\mathrm{MD}}/\mathrm{d}T$ curves for the cases of both including and neglecting the zero-point energy are shown in Figure 4.36(a). The data are plotted up to a temperature of 87 K, the melting point of the MD system.

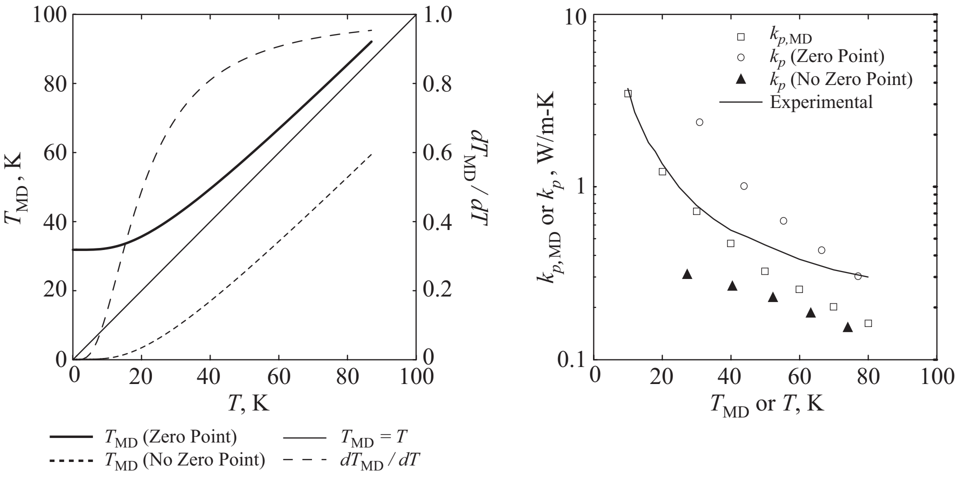

(a) (b)

Figure 4.36. (a) Temperature and thermal conductivity scaling relations. (b) Scaled thermal conductivities with raw Ar FCC MD predictions and experimental data [317].

When the zero-point energy is included, the MD simulations are of interest only at temperatures of 31.8 K and higher. This is an indication of the magnitude of the zero-point energy. The T_{MD} curve approaches T as the temperature is increased, and more modes are excited in the quantum system. The value of T_{MD} will always be higher than T because of the zero-point energy. The thermal conductivity scaling factor starts at zero. This ensures that the thermal conductivity will be zero at zero temperature. As the temperature increases, the scaling factor approaches unity.

When the zero-point energy is not included, the temperature scaling has the same shape as before, but has been shifted downward. In this case, T_{MD} will always be lower than T because of the manner in which the energy is distributed in the modes of the quantum system. The T_{MD} value of zero is relevant in this case, because the associated quantum system can have zero energy. The thermal conductivity scaling factor is identical to when the zero-point energy is included, as the energies differ only by a scalar.

The scaled thermal conductivities and unscaled Ar FCC MD predictions are given in Table 4.8 and shown in Figure 4.36(b) along with the experimental data. To obtain these results, the T values corresponding to the available T_{MD} values are obtained. Because of the nature of the scaling relation, not all the T_{MD} values have a corresponding T. The appropriate thermal conductivity scaling factor is then determined. Overall, the agreement with the experimental data worsens for either of the scaling possibilities compared with the raw MD data. Others have found an improved agreement (for β-SiC including the zero-point energy [281], and for Si, not including the zero-point energy [483]). This lack of consistency raises a high level of doubt about the validity of this approach and its possible widespread acceptance.

The main idea behind this somewhat *ad hoc* temperature scaling procedure is to map the classical MD results onto an equivalent quantum system. By not including

Table 4.8. *Scaled temperatures and thermal conductivities. The first two columns correspond to the raw Ar FCC MD data. The third through fifth columns correspond to the inclusion of the zero-point energy. The last three columns correspond to ignoring the zero-point energy [317].*

		Zero-point			No Zero-point		
$T_{\rm MD}$, K	$k_{p,\rm MD}$, W/m-K	T, K	$\mathrm{d}T_{\rm MD}/\mathrm{d}T$	k_p, W/m-K	T, K	$\mathrm{d}T_{\rm MD}/\mathrm{d}T$	k_p, W/m-K
10	3.44	–	–	–	31.0	0.684	2.36
20	1.22	–	–	–	43.9	0.831	1.01
30	0.718	–	–	–	55.4	0.889	0.639
40	0.467	27.3	0.656	0.306	66.4	0.921	0.430
50	0.323	40.6	0.815	0.263	77.2	0.940	0.304
60	0.255	52.3	0.881	0.225	–	–	–
70	0.201	63.3	0.916	0.184	–	–	–
80	0.162	74.2	0.938	0.151	–	–	–

the zero-point energy, a true quantum system is not being considered. For this reason, if such corrections are to be used, the zero-point energy should be included.

As it stands, there are a number ways that this method could be improved. These are related to the harmonic nature of the energy calculations on both sides of (4.189). The classical energy is based on an assumption of equipartition of energy. The average, total energy of the MD system is in fact less than $3(N-1)k_{\rm B}T_{\rm MD}$ because of anharmonic effects. As shown in Figure 2.15, at a temperature of 20 K, the deviation is 2.6%, and increases to 12.6% at a temperature of 80 K. This correction is straightforward to implement. The phonon-space energy is most easily calculated with the zero temperature, harmonic dispersion relation. However, temperature has a significant effect on the phonon dispersion, and temperature-dependent normal modes would make the the temperature scaling more rigorous.

That being said, it is unlikely that these modifications would lead to a much improved model. The main drawback of this temperature/thermal conductivity scaling approach, as discussed in [280], is that it is a postprocessing step that maps the entire MD system onto a quantum description. The effects are manifested on a mode-by-mode basis, and on the basis of how the energy is distributed, therefore making corrections on an integrated level simply not suitable. In [280], it is suggested to link the classical MD system to a quantum description through the BTE.

In [81] a more general approach is used to investigate the classical-quantum issue by comparing the general forms of the classical and the quantum HCACFs. They do not find evidence to support the use of quantum corrections with MD thermal conductivity predictions. They argue that this is because long-wavelength phonons are the dominant contributors to the thermal transport, which are active even at low temperatures. This is in contrast to the specific heat, for which it is the high-frequency (short-wavelength) modes that get excited as the temperature of the quantum system is increased and lead to the significant temperature dependence up to the Debye temperature.

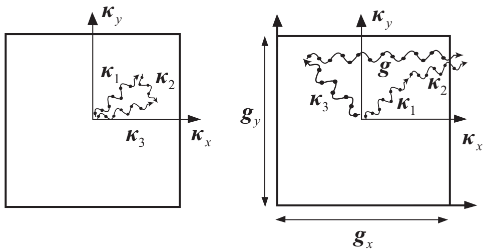

(a) N–Processes (b) U–Processes

Figure 4.37. The N– and U–interphonon-scattering processes and momenta shown in reciprocal lattice space.

As discussed, the MD simulations are classical because it is within this framework that computational costs become reasonable enough to perform simulations of big systems or for long times. When comparing the results of MD simulations with experiments, there are additional factors beyond their classical nature that need to be considered. These include the interatomic potential used, size effects, and the simulation procedures. It is difficult to isolate these effects. Efforts are needed on all fronts to increase the confidence in the results of MD simulations.

4.15 Phonon Conductivity from BTE: Variational Method

Interphonon scattering, which dominates the phonon conductivity at high temperature, has in turn been assumed to be dominated by the three-phonon scattering processes. These are shown in Figure 4.37. There are two types of such interactions: type I ($1 \rightarrow 2+3$) and type II ($1+2 \rightarrow 3$). Because these scatterings change the energy of each phonon involved, it is not expected that they can be accurately presented by a relaxation-time approximation. These three-phonon interactions are divided into the N–Processes, in which the crystal momentum (and energy) is conserved, and the U–Processes, where the crystal momentum is not conserved (however, energy is). These are shown in Figures 4.15(c) and 4.37, and we write

$$\boldsymbol{\kappa}_1 + \boldsymbol{\kappa}_2 = \boldsymbol{\kappa}_3 \text{ (momentum)}, \quad \omega_1 + \omega_2 = \omega_3 \text{ (energy)}, \qquad (4.192)$$

three-phonon N–Processes

$$\boldsymbol{\kappa}_1 + \boldsymbol{\kappa}_2 = \boldsymbol{\kappa}_3 + \boldsymbol{g}, \quad \omega_1 + \omega_2 = \omega_3, \quad \text{three-phonon U–Processes}, \qquad (4.193)$$

where $\boldsymbol{g}$ is the reciprocal lattice vector. The reciprocal lattice vector is not limited to a process that flips the wave-vector summation to the neighboring reciprocal space unit cell only but can involve other cells.

In addition to (4.193) and (4.193), there are other restrictions on 3-phonon interactions, for example, inspection of both energy and momentum conservations (N–Processes) indicates that such interactions cannot involve phonons of the same polarization ($\alpha_1, \alpha_2, \alpha_3$) [33], whereas the U–Processes allow for the probability of this occurrence.

The Peierls interphonon interactions (scattering) are given by the in-and-out scattering (3.1.3) and the FGR (3.27), as [175]

$$\begin{aligned}\frac{\partial \langle f_{p,1}\rangle}{\partial t}|_s = \sum_{\kappa_2}\sum_{\alpha_2}[\sum_{\alpha_3}&\dot{\gamma}_{p,\alpha_1,\alpha_2,\alpha_3}(\boldsymbol{\kappa}_1,\boldsymbol{\kappa}_2,-\boldsymbol{\kappa}_3)\langle f_{p,3}(f_{p,2}+1)(f_{p,1}+1)\\ &-(f_{p,3}+1)f_{p,2}f_{p,1}\rangle\delta_{\mathrm{D}}(\omega_1+\omega_2-\omega_3)\\ &+\frac{1}{2}\sum_{\alpha_3}\dot{\gamma}_{p,\alpha_1,\alpha_2,\alpha_3}(-\boldsymbol{\kappa}_1,\boldsymbol{\kappa}_2,\boldsymbol{\kappa}_3)\langle(f_{p,1}+1)f_{p,2}f_{p,3}\\ &-f_{p,1}(f_{p,2}+1)(f_{p,3}+1)\rangle\delta_{\mathrm{D}}(\omega_1-\omega_2-\omega_3)],\\ &\text{three-phonon scattering rate,}\end{aligned}\tag{4.194}$$

or in terms of the scattering rate the results are[†]

$$\begin{aligned}\dot{\gamma}_{p,\alpha_1,\alpha_2,\alpha_3}(\boldsymbol{\kappa}_1,\boldsymbol{\kappa}_2,\boldsymbol{\kappa}_3) = \frac{1}{\tau_{p\text{-}p,\alpha 1,\alpha 2,\alpha 3}(\boldsymbol{\kappa}_1,\boldsymbol{\kappa}_2,\boldsymbol{\kappa}_3)} &= \frac{\pi\hbar}{4\rho^3V^2\omega_1\omega_2\omega_3}\\ &\times[\sum_{i,j,k}\sum_{\alpha,\beta,\gamma}\frac{\partial^3\langle\varphi\rangle}{\partial d_{i,\alpha}\partial d_{j,\beta}\partial d_{k,\gamma}}|_{\mathrm{o}}e_\alpha^{\boldsymbol{\kappa}_1,\alpha_1}e_\beta^{\boldsymbol{\kappa}_2,\alpha_2}e_\gamma^{\boldsymbol{\kappa}_3,\alpha_3}\\ &\times\ \exp\{i(\boldsymbol{\kappa}_1\cdot\boldsymbol{x}_{o,i}+\boldsymbol{\kappa}_2\cdot\boldsymbol{x}_{o,j}+\boldsymbol{\kappa}_3\cdot\boldsymbol{x}_{o,k})\}]^2\\ &\text{three-phonon scattering relaxation time.}\end{aligned}\tag{4.195}$$

The first triple summation is over the atoms in the system and the second is over the Cartesian coordinates. An example of an MD calculation of this scattering rate, for Ar FCC, is given in [319], where they also discuss the phonon–phonon interaction rules within classical MD simulations.

Note that the scattering matrix element is third-order in the interatomic potentials. The variational method is applied to the BTE [16, 62, 126, 177, 445], in which the phonon distribution function is explicitly involved. The deviation from equilibrium is

$$f_p'(\boldsymbol{\kappa}) = f_p^\circ(\boldsymbol{\kappa}) - \phi_\kappa\frac{\partial f_p^\circ(\boldsymbol{\kappa})}{\partial E_\kappa} = f_p^\circ(\boldsymbol{\kappa}) + \phi_\kappa\frac{f_p^\circ(1+f_p^\circ)}{k_{\mathrm{B}}T},\tag{4.196}$$

where we have used (Table 1.2)

$$f_p^\circ(E_p) = \frac{1}{\exp(\dfrac{E_p}{k_{\mathrm{B}}T})-1}.\tag{4.197}$$

[†] As an example, for acoustic-optical phonon upconversion (+) and downconversion (−) we have

$$\dot{\gamma}_{p,\mathrm{A+A\to O}} = \frac{\hbar}{8\pi\rho^3}\frac{M^2_{\mathrm{A+A\to O}}R}{u^7_{p,\mathrm{A}}u^2_{p,\mathrm{O}}}\omega_{p,\mathrm{A},1}\omega^3_{p,\mathrm{O}}\omega_{p,\mathrm{A},2}f_p^\circ(\omega_{p,\mathrm{A},1})f_p^\circ(\omega_{p,\mathrm{A},2})[f_p^\circ(\omega_{p,\mathrm{O}})\pm 1],$$

where the interaction matrix is

$$M^2_{\mathrm{A+A\to O}} = 4\rho^2\gamma_{\mathrm{G}}^2u^2_{p,\mathrm{A}}u^2_{p,\mathrm{O}},$$

and R is related to the force constants of the constituent atomic pairs [445].

The left-hand side of the BTE (Table 3.1) can be written as (4.95)

$$-\boldsymbol{u}_p \cdot \nabla T \frac{\partial f_p}{\partial T} = \frac{\partial f_p}{\partial t}|_s. \tag{4.198}$$

For three-phonon scattering processes, shown by (4.193) and (4.193), we have

$$(\boldsymbol{\kappa}_1, \alpha_1) + (\boldsymbol{\kappa}_2, \alpha_2) \rightarrow (\boldsymbol{\kappa}_3, \alpha_3), \tag{4.199}$$

where the scattering rate $\partial f_p / \partial T|_s$ is written in terms of the transition rate $\dot{\gamma}^{\boldsymbol{\kappa}_3}_{\boldsymbol{\kappa}_1,\boldsymbol{\kappa}_2}$ [from FGR (3.27)]. Then the BTE becomes

$$\begin{aligned} -\boldsymbol{u}_p(\boldsymbol{\kappa})\nabla T \frac{\partial f_p(\boldsymbol{\kappa})}{\partial T} = & \int\int (\{f_p(\boldsymbol{\kappa}_1) f_p(\boldsymbol{\kappa}_2)[1 + f_p(\boldsymbol{\kappa}_3)] \\ & - [1 + f_p(\boldsymbol{\kappa}_1)][1 + f_p(\boldsymbol{\kappa}_2)] f_p(\boldsymbol{\kappa}_3)\} \dot{\gamma}^{\boldsymbol{\kappa}_3}_{\boldsymbol{\kappa}_1,\boldsymbol{\kappa}_2} \\ & + \frac{1}{2}\{f_p(\boldsymbol{\kappa}_1)[1 + f_p(\boldsymbol{\kappa}_2)][1 + f_p(\boldsymbol{\kappa}_3)] \\ & - [1 + f_p(\boldsymbol{\kappa}) f_p(\boldsymbol{\kappa}_2) f_p(\boldsymbol{\kappa}_3)]\} \dot{\gamma}^{\boldsymbol{\kappa}_2,\boldsymbol{\kappa}_3}_{\boldsymbol{\kappa}_1}) \mathrm{d}\boldsymbol{\kappa}_2 \mathrm{d}\boldsymbol{\kappa}_3. \end{aligned} \tag{4.200}$$

With the deviation from the equilibrium given by (4.196), the isotropic phonon thermal conductivity is given by [33]

$$k_p^{-1} = \frac{1}{2k_\mathrm{B}T^2} \frac{\int\int\int (\phi_{\boldsymbol{\kappa}_1} + \phi_{\boldsymbol{\kappa}_2} - \phi \boldsymbol{\kappa}_3)^2 \dot{\gamma}^{\boldsymbol{\kappa}_3}_{\boldsymbol{\kappa}_1,\boldsymbol{\kappa}_2} \mathrm{d}\boldsymbol{\kappa}_1 \mathrm{d}\boldsymbol{\kappa}_2 \mathrm{d}\boldsymbol{\kappa}_3}{|\boldsymbol{u}_p \phi_{\boldsymbol{\kappa}} \frac{\partial f^\circ_{\boldsymbol{\kappa}}}{\partial T} d\boldsymbol{\kappa}|^2}, \tag{4.201}$$

which is based on the variational principles and should have the minimum when the trial function $\phi_{\boldsymbol{\kappa}}$ satisfies the BTE. The introduction of trial functions is discussed in [177].

The numerical results of [177] for the predicted phonon resistivity $1/k_p$ of Ge are shown in Figure 4.38, along with experimental results (experimental results were also given in Figure 4.20). To predict the low-temperature regime, where impurity and crystal boundary effects dominate, these numerical results are included in the model (similar to treatment of Section 4.9.7). The U–Processes dominate at high temperature and are influenced by the N–Processes with this influence increasing with decreasing temperature. The resistance is minimum when the interphonon interaction diminishes and the impurity effect begins to dominate. The very low-temperature regime is dominated by crystal boundary scattering (Figure 4.17).

Note that in Section 4.9.7 the many constants in Tables 4.2 and 4.3 were adjusted for best fit with the experiment, including $\tau_{p\text{-}p,\mathrm{U}}$. Whereas here no fitting constant is used for $\tau_{p\text{-}p,\mathrm{N}}$ and $\tau_{p\text{-}p,\mathrm{U}}$.

4.16 Experimental Data on Phonon Conductivity

Figure 4.39 shows typical measured phonon conductivity results as functions of temperature [465]. The theoretical treatments of Sections 4.9 and 4.11 predicts these trends. The results for amorphous phases of Se and Si are also shown. The theoretical treatments of Section 4.10 predict these trends.

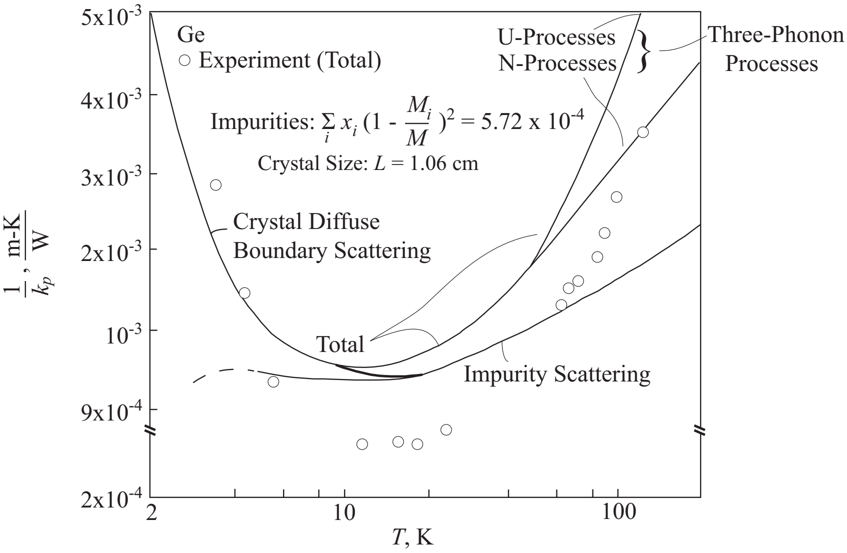

Figure 4.38. Prediction of the variational method, including the three-phonon interactions, for the variation of the phonon resistivity($1/k_p$) of Ge, as a function of temperature. The experimental results are also shown [177].

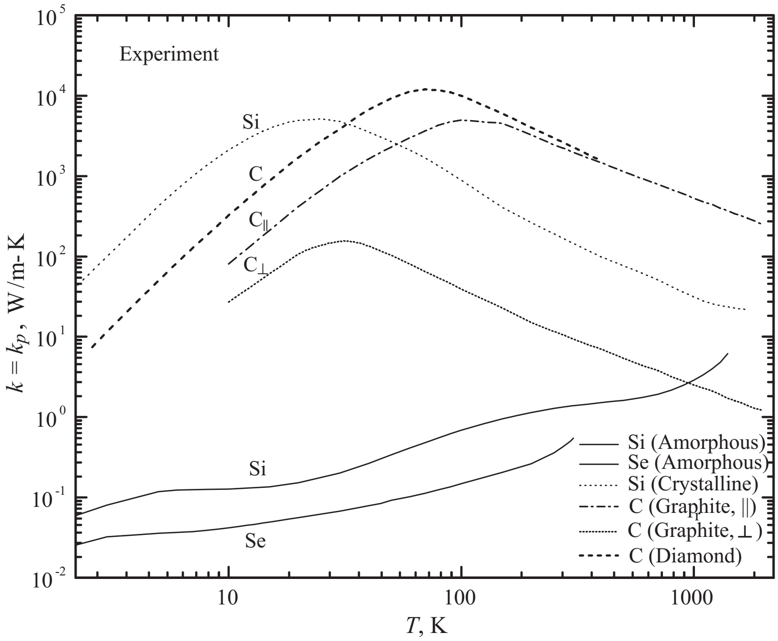

Figure 4.39. Measured variations of measured phonon conductivity, for a few elements in crystalline and amorphous phases, as functions of temperature [465]. For C, the diamond and graphite (anisotropic) crystalline phases are shown. For Si both single crystal and amorphous phases are shown (electronic contribution to k is very small), and for Se only the amorphous phase (low phonon conductivity) is shown.

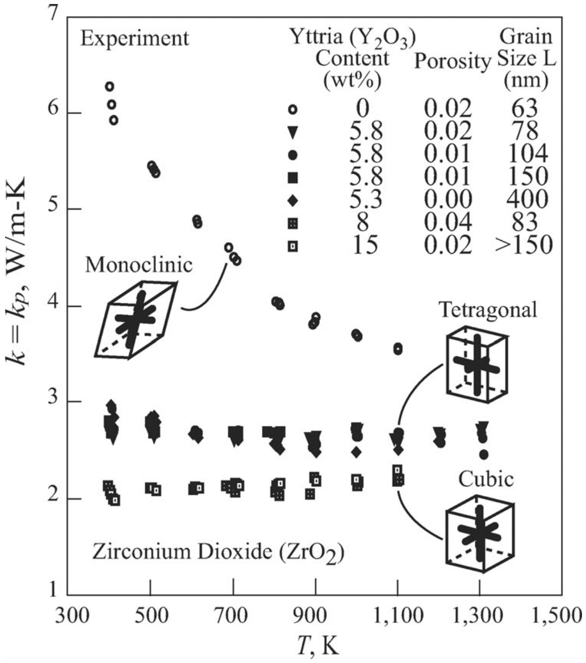

Figure 4.40. Measured variations of high-temperature phonon thermal conductivity of crystallized zirconia (ZrO_2) with respect to temperature. The effects of impurity [yttria, used to make the material a better ion conductor (electrolyte)], grain boundary, and pore scatterings, are shown [413]. These scatterings lower k_p and nearly eliminate the temperature dependence at high temperatures (i.e., the long-range acoustic phonons are suppressed).

For crystalline dielectrics, a maximum in k_p occurs at a fraction of the Debye temperature T_D, whereas for the amorphous phases, the conductivity increases monotonically with temperature and will eventually reaches a plateau (as shown in Figure 4.17). Some intermediate plateaus are also observed.

Figure 4.40 shows how the impurity, pores, and grain size can reduce the phonon conductivity of crystallized ZrO_2. The lattice structure change resulting from impurities are also shown. It is expected that would result in diminishing long-range acoustic-phonon contribution to thermal conductivity (Sections 4.12 and 4.13), i.e., $k_{p,lg,A} \rightarrow 0$.

4.17 Phonon Boundary Resistance

At interfaces between two materials (discontinuity), the mismatch between phonon populations (including maximum frequency) and speeds across the interface results in a resistance to the heat current. This is most pronounced at low temperatures where mismatch in phonon populations is significant. This interfacial resistance is generally referred to as the Kapitza resistance, because of phonon scattering.

Currently two theories have been applied to the prediction of the phonon boundary resistance [453]. The first is the acoustic mismatch model (AMM), which assumes scattering because of the difference in acoustic impedance (product of density and speed of sound) and does not distinguish between various phonon wavelengths (for example, if the surface roughness is of the same order of magnitude as the phonon wavelength). The second theory is the diffuse mismatch model (DMM), which assumes that all phonons incident upon the interface will scatter diffusely (i.e., a rough interface with diffuse reflections). For this, the interface roughness $\langle \delta^2 \rangle^{1/2}$ is larger than the dominant phonon wavelengths, estimated as $(T_{\rm D}/T)a$, where a is the lattice spacing. Then for grain boundaries (same materials on both sides) the AMM prediction that no scattering occurs at the interface is reasonable at very low temperatures, where the phonon wavelength is larger ($\kappa \rightarrow 0$) than the interface length scales. As the temperature increases the phonon wavelength decreases, compromising the AMM theory. Both theories have their shortcomings, but at high temperatures, DMM results are in better agreement with the measurements and MD results.

The analysis of [366] shows that, by using the measured phonon DOS (compared with the Debye DOS), the DMM predicts the phonon boundary resistance relating accurately. The details of the DMM derivation are given in Appendix D and here we use the results.

The net conduction heat flux q_k from material 1 at temperature T_1 to material 2 at temperature T_2 is

$$\frac{1}{AR_{p,b}} = \frac{G_{p,b}}{A} = \frac{q_k}{T_1 - T_2} \quad \text{phonon boundary thermal resistance and conductance,} \tag{4.202}$$

where $R_{p,b}$(K/W) is the phonon boundary thermal resistance, $G_{p,b}$ (W/K) is the phonon boundary conductance, A is the area, and q_k is the conduction heat flux across boundary.

Starting with the general expression for the energy transported per unit time from material 1 to material 2, and assuming that the transmission coefficient $\tau_{b,1\text{-}2}$ is independent of the temperature on either side of the interface (only one side of the interface is considered), from (D.14), we have for the dimensional and dimensionless DMM phonon boundary resistance and for $T_1 \rightarrow T_2 \rightarrow T$,

$$\frac{1}{AR_{p,b}} = \frac{G_{p,b}}{A} = \frac{h_{\rm P}\tau_{b,1\text{-}2}}{8\pi(T_1 - T_2)} \sum_\alpha u_{p,1,\alpha} \int_0^{\omega_{\rm D}} D_p(\omega_p)\omega_p [\frac{1}{\exp(\dfrac{h_{\rm P}\omega_p}{2\pi k_{\rm B} T_1}) - 1} - \frac{1}{\exp(\dfrac{h_{\rm P}\omega_p}{2\pi k_{\rm B} T_2}) - 1}] {\rm d}\omega_p,$$

or

$$\frac{1}{(AR_{p,b})^*} \equiv \frac{1}{AR_{p,b}} \frac{8\pi^2\hbar^3}{k_{\rm B}^4 T_{\rm D}^3 \tau_{b,1\text{-}2} \sum_\alpha u_{p,1,\alpha}^{-2}} = \frac{1}{T_{\rm D}^3(T_1 - T_2)} \times \left[T_1^4 \int_0^{T_{\rm D}/T_1} \frac{x^3}{\exp(x) - 1} {\rm d}x - T_2^4 \int_0^{T_{\rm D}/T_2} \frac{x^3}{\exp(x) - 1} {\rm d}x \right], \tag{4.203}$$

where $\omega_{\rm D}$ and $T_{\rm D}$ are the lower (softer) of those for the two media, and α is the phonon polarization.

The DMM phonon boundary transmission coefficient is approximated as[†]

$$\tau_{b,1\text{-}2} = \frac{\sum\limits_{\alpha} u_{p,2,\alpha}^{-2}}{\sum\limits_{\alpha} u_{p,1,\alpha}^{-2} + \sum\limits_{\alpha} u_{p,2,\alpha}^{-2}} \quad \text{phonon boundary transmission coefficient.} \tag{4.204}$$

Since u_p is related to modulus through (4.72), then when 2 is much harder than 1, a small fraction of phonons are transmitted from 1 to 2. This is due to higher population of the low energy phonons in the softer material. The high energy phonons of harder material do not transmit.

For $T > T_{\rm D}$, (4.203) gives $1/(AR_{p,b})^* = 1/3$ (Figure D.1), for $T_1 \rightarrow T_2 \rightarrow T$ (independent of T_1, T_2, and T).

For three-phonon wave speeds (two transverse and one longitudinal), we have from (4.57)

$$\sum_{\alpha} u_{p,1,\alpha}^{-2} = \frac{1}{u_{p,1,{\rm L}}^{2}} + \frac{2}{u_{p,1,{\rm T}}^{2}}. \tag{4.205}$$

The phonon model speed $u_{p,i,\alpha}$ is related to the Debye temperature $T_{{\rm D},i,\alpha}$ through (4.63) and to the Debye angular frequency $\omega_{{\rm D},i,\alpha}$ through (4.60).

For $\hbar\omega_{\rm D}/k_{\rm B}T \gg 1$, we find an exact solution. Using these, the dimensionless phonon boundary conductance becomes

$$\frac{1}{(AR_{p,b})^*} \equiv \frac{8\pi^2\hbar^3}{(AR_{p,b})k_{\rm B}^4 T_{\rm D}^3 \tau_{b,1\text{-}2} \sum\limits_{\alpha} u_{p,1,\alpha}^{-2}} = 24[1 - C(\frac{T_{\rm D}}{T})](\frac{T}{T_D})^3, \quad \frac{\hbar\omega_{\rm D}}{k_{\rm B}T} \gg 1, \tag{4.206}$$

where $C(T_{\rm D}/T)$ is defined as

$$C(\frac{T_{\rm D}}{T}) = \exp(-\frac{T_{\rm D}}{T})[1 + (\frac{T_{\rm D}}{T}) + \frac{1}{2}(\frac{T_{\rm D}}{T})^2 + \frac{1}{6}(\frac{T_{\rm D}}{T})^3], \quad T_{\rm D} \text{ of softer material.} \tag{4.207}$$

Figure 4.41(a) shows the measured and the Debye model of D_p for $\rm Bi_2Te_3$ and $\rm Sb_2Te_3$ (thermoelectric material discussed in Sections 5.16 and 5.17). The variation of the phonon boundary conductance $AR_{p,b}$ (4.206) as a function of temperature for $\rm Bi_2Te_3$ with a Cu interface is shown in Figure 4.41(b). The Cu $T_{\rm D}$ = 315 K (Table A.2), and $T_{\rm D}$ for $\rm Bi_2Te_3$ is 165 K (softer material). As $T_{\rm D}$ of $\rm Bi_2Te_3$ (softer material) is reached, all its high energy phonons are occupied. The minimum is associated with the interplay between D_p and $f_p^{\rm o}$ in (4.203). For $\rm Bi_2Te_3$, $V_c^{-1} = 5.95 \times 10^{27}$ m^{-3}, and this and other properties are given in [106].

[†] The general expression for normal incidences is (D.24),

$$\tau_{b,1\text{-}2} = \frac{4\rho_1 u_{p,{\rm A},1}\rho_2 u_{p,{\rm A},2}}{(\rho_1 u_{p,{\rm A},1} + \rho_2 u_{p,{\rm A},2})^2}.$$

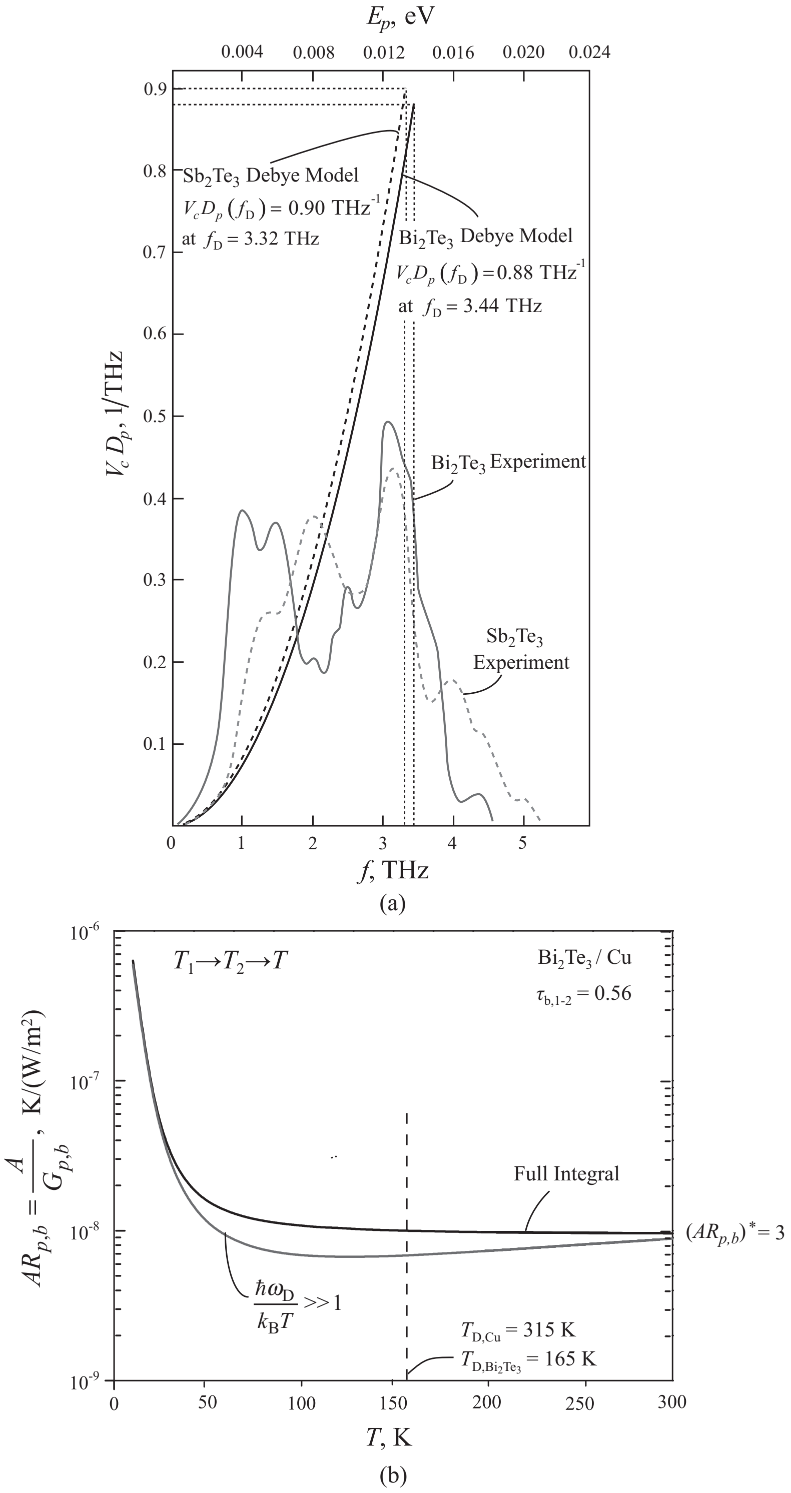

Figure 4.41. (a) Variation of predicted phonon density of states $V_c D_p(f)$ with respect to frequency f, for Bi_2Te_3 and Sb_2Te_3. The experimental results are also shown. The Debye density of states $D_{p,\mathrm{D}}$ and the numerical integration results are also shown [106]. (b) The phonon boundary resistance of Bi_2Te_3/Cu as a function of temperature. The low temperature approximation is for $T_1 \rightarrow T_2 \rightarrow T$, and the full integral results are for $T_1 - T_2 = 1$ K.

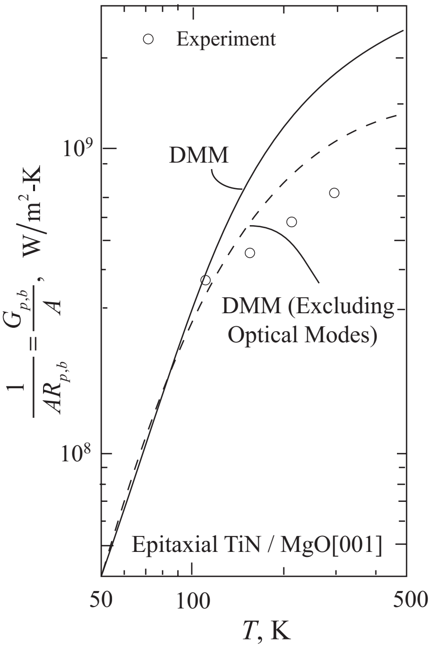

Figure 4.42. Variation of the measured and predicted phonon boundary conductances of the epitaxial TiN/MgO[001] interface as a function of temperature. The solid curve is the DMM prediction for TiN/MgO, and the dashed curve is the DMM with acoustic phonons only. The Debye temperature of TiN is 740 K [100].

The full solution has an asymptotic high-temperature ($T > T_{\mathrm{D},1}$) limit. As the temperature increases and more and more modes are excited, the phonon boundary resistance reaches its minimum value. The solution for $\hbar\omega/k_{\mathrm{B}}T \gg 1$ also has the same asymptotic high-temperature limit.

Note that in many cases the Debye model is not an accurate representation. The numerical evaluation of the (4.203) should be performed [425]. Figure 4.42 compares the experimental results of [100] with the prediction of (4.203) for TiN deposited (epitaxy) on a MgO substrate. By excluding the optical phonon heat capacity (when the optical phonons are removed from the DOS), a better agreement is found. This is because they are not expected to contribute to transport due to their low velocities.

4.18 Absorption of Ultrasound Waves in Solids

In previous sections we have discussed phonon heat capacity and thermal conductivity (storage and transport). We now consider an energy conversion (heating) involving phonons. The external sound wave (long wavelength, elastic waves) attenuation in a crystalline dielectric can be treated using BTE, allowing for deviation from the equilibrium distribution function f_p' of thermal phonons caused by absorption of sound waves. This is referred to as the thermoelectric internal friction [243] and the attenuation is by phonon scattering. The theoretical treatment allows the absorbed energy to transfer to an ideal bath, thus making for a steady-state, isothermal treatment [500].

For these dielectric, crystalline solids, in the low-temperature limit, the spectral acoustic absorption coefficient for a sound wave of angular frequency ω is [500]

$$\sigma_{p,\omega} = \gamma_{\mathrm{G}}^2 \frac{c_{v,p} T}{2u_{p,\mathrm{A}}^3} \frac{\omega^2 \tau_p}{1 + 2\omega^2 \tau_p^2}, \ \gamma_{\mathrm{G}} = \frac{3\beta E_p}{\rho c_v}, \tag{4.208}$$

where γ_{G} is the Grüneisen parameter (4.162), β is the solid linear thermal expansion coefficient, E_p is the isothermal bulk modulus, and τ_p is the single-phonon relaxation time (4.109), i.e.,

$$\tau_p = \frac{3k_p}{\rho c_{v,p} u_{p,\mathrm{A}}^2}, \tag{4.209}$$

where we have used $u_{p,\mathrm{A}}$ as defined in (4.57).

The Grüneisen parameter is near unity and is generally assumed independent of temperature. The two frequency limits for (4.198) are

$$\sigma_{p,\omega} = \gamma_G^2 \frac{\omega^2 k_p T}{\rho u_{p,\mathrm{A}}^5} \quad \omega\tau_p \ll 1, \tag{4.210}$$

and

$$\sigma_{p,\omega} = \frac{\pi}{4} \gamma_G^2 \frac{\omega c_{v,p} T}{\rho u_{p,\mathrm{A}}^5} \quad \omega\tau_p \gg 1. \tag{4.211}$$

These show ω^2 dependence at low frequency and a linear dependence at high frequencies.

The acoustic-wave (mechanical) absorption heating rate is given in terms of the external acoustic intensity I_{ac} as [500]

$$\dot{s}_{p\text{-}p,\omega} = \dot{s}_{m,ac} = 2\sigma_{p,\omega} I_{ac} \ \ \text{ultrasound heating.} \tag{4.212}$$

Examples of acoustic intensities and spectral acoustic absorption coefficients are given in [232].

Using the relaxation time (4.209) and the fluid particle viscosity (6.91), a phonon viscosity μ_p has been suggested [310] with application to motion of dislocations.

4.19 Size Effects

4.19.1 Finite-Size Effect on Phonon Conductivity

When the length (average linear dimension) of the solid L is not significantly larger than the average phonon mean free path λ_p (4.109), then the interface scattering occurs [Casimir effect discussed in Section 4.9.4(A)]. A simpler model for this effect is to define the phonon mean free path using $L \to \infty$, and then including the finite-size effect by using [412]

$$\frac{1}{k_p} = \frac{2}{n k_{\mathrm{B}} u_{p,\mathrm{A}}} \left(\frac{1}{\lambda_p} + \frac{4}{L}\right), \tag{4.213}$$

where $n = 4/a^3$ (FCC), and $n = 2/a^3$ (BCC), where a is the lattice constant. Here $L/4$ is the average distance a phonon travels after the last anharmonic scattering

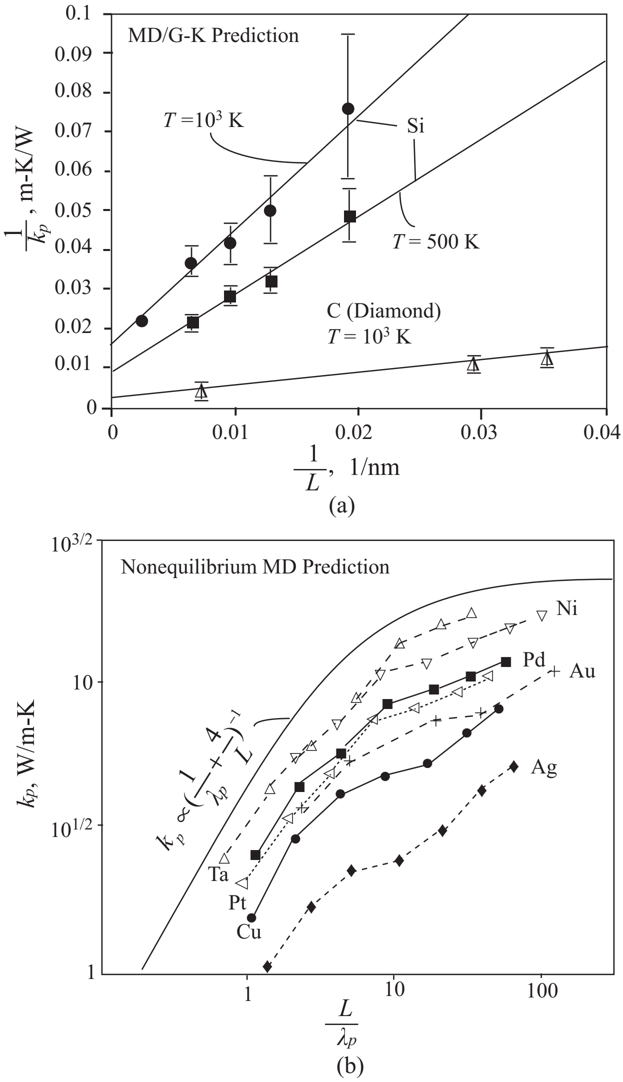

Figure 4.43. (a) Variations of the inverse of predicted lattice conductivity (for nonmetals), with respect to the inverses of computational (solid) linear dimensions [412]. (b) Variations of the inverse of predicted lattice conductivity (for metals), with respect to inverse ratios of computational (solid) linear dimensions to the phonon mean free path [186].

event. We note that for $L/\lambda_p \rightarrow \infty$, (4.213) becomes $k_p = k_B n u_{p,A} \lambda_p/2$, which is 1/2 of k_p in (4.109). This is because the specific heat per atom in (4.213) is taken $3k_B/2$, i.e., half of total phonon $c_{v,p}$, to correct for the optical phonons which do not have significant travel speed.

The MD and direct method [315] predictions of [412] for Si and C(diamond) are shown in Figure 4.43(a) and follow the relation just given.

Similar MD predictions (using the direct method, where a temperature gradient is imposed across the sample, also called nonequilibrium method [320]) results are found for the lattice thermal conductivity of metals [186], where k_p is a small

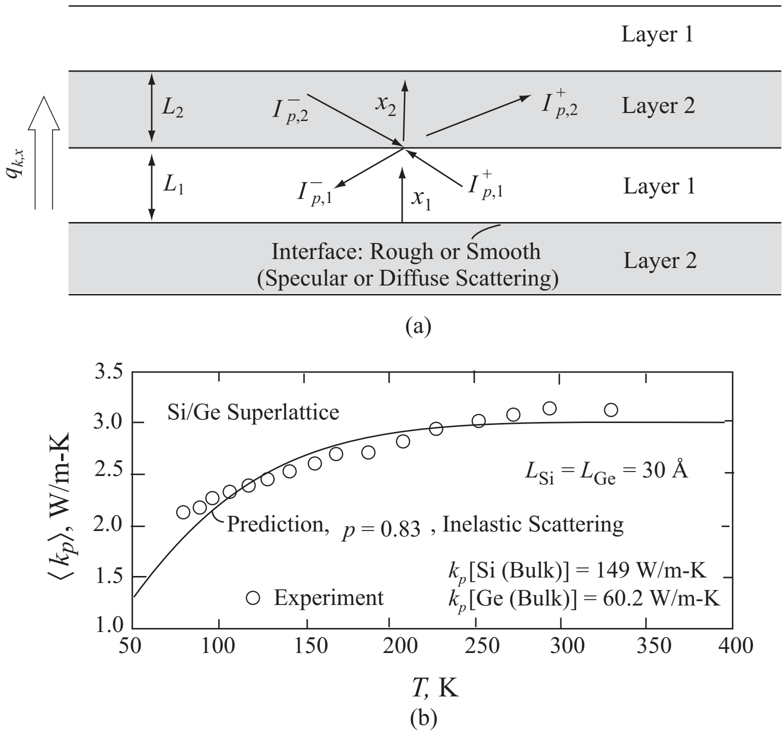

Figure 4.44. (a) Two alternating layers making a superlattice. The heat flow is in the cross-plane direction. The phonon intensity I_p is divided into forward and backward components (so-called two-flux model). (b) Variation of predicted [84] effective lattice conductivity, with respect to temperature, for a Si/Ge superlattice and comparison with experiment [272].

fraction of k for these metals. These results are shown in Figure 4.43(b), along with the proportionality of (4.213).

A more general analytical model is derived in [321] for thin films (in- and cross-plane) and wires, using $\tau_{p\text{-}p}$ and $\tau_{p\text{-}b}$. It is based on a dimensionless length $3k_{\mathrm{B}}u_{p,\mathrm{A}}L/2u_{p,\infty}V_c$, where $k_{p,\infty}$ is the bulk phonon conductivity and V_c is the primitive cell volume. For wire $4D/\pi$ replaces $3L/2$.

4.19.2 Superlattice Phonon Conductivity

A superlattice is a crystalline solid with periodic, alternating (Section 5.22.2 gives a general definition of molecularly constructed layers), very thin layers of two or more substances. Their properties (including lattice conductivity) are vastly different in the in-plane (along layers) and in the cross-plane directions. Because of scattering at the layer interfaces, both the in-plane and cross-plane lattice conductivities decrease compared with the thick-layer composites. Phonon boundary scattering is discussed in Section 4.17 and in Appendix D, where the scattering is because of the abrupt charge in the material acoustic impedance $\rho_i u_{p,\mathrm{A},i}$. Figure 4.44(a) shows a superlattice made of two alternating layers (made of substances 1 and 2) having thickness L_1 and L_2. In a superlattice these layer thicknesses are much smaller than the phonon mean free path of the respective materials, i.e., $L_1 \ll \lambda_{p,1}$ and $L_2 \ll \lambda_{p,2}$ (using a single, average mean free path for each substance). This regime is called the ballistic phonon transport regime, because the boundary scattering dominates the bulk scattering mechanisms.

The one-dimensional BTE has been solved for this two-layer superlattice for the general case of inelastic, diffuse–specular scattering interface [84].

The intensity form of the BTE for a phonon is similar to that derived for a photon in Section 7.6. The resulting effective cross-plane phonon thermal conductivity $\langle k_p \rangle$ of the superlattice is

$$\langle k_p \rangle = \frac{q_{\kappa,x}(L_1+L_2)}{\Delta T|_{L_1+L_2}} = \frac{0.5(L_1+L_2)\rho_2 c_{v,2} u_{p,\mathrm{A},2} \displaystyle\int_0^1 \frac{2p\tau_{s,2\text{-}1}+A}{B}\mu_2 \mathrm{d}\mu_2}{1-2(1-p)\displaystyle\int_0^1 \frac{C}{B}\mu_2 \mathrm{d}\mu_2}$$

cross-plane effective lattice conductivity of superlattice, $\mu = \cos\theta$,

$$p = \begin{cases} 1 \text{ totally specular} \\ 0 \text{ totally diffuse} \end{cases}$$

$$A = (1-p)\tau_{d,2\text{-}1}(1+p\rho_{s,1\text{-}2}+pD\tau_{s,1\text{-}2})$$

$$B = (1+p\rho_{s,2\text{-}1})(1+p\rho_{s,1\text{-}2}) - p^2\tau_{s,1\text{-}2}\tau_{s,2\text{-}1}$$

$$C = (1+p\rho_{s,1\text{-}2})(-\rho_{d,2\text{-}1}+\tau_{d,1\text{-}2}) + pD\tau_{s,1\text{-}2}(-\rho_{d,1\text{-}2}+\tau_{d,2\text{-}1})$$

$$D = \frac{\mu_2 \mathrm{d}\mu_2}{\mu_1 \mathrm{d}\mu_1}$$

$$\rho_{d,i\text{-}j} = \tau_{d,j\text{-}i} = 1-\tau_{d,i\text{-}j}$$

$$\tau_{d,i\text{-}j} = \frac{\rho_j c_{v,j} u_{p,\mathrm{A},j}}{\rho_i c_{v,i} u_{p,\mathrm{A},i} + \rho_j c_{v,j} u_{p,\mathrm{A},j}}$$

$$\rho_{s,i\text{-}j} = |\frac{\rho_i u_{p,\mathrm{A},i}\mu_i - \rho_j u_{p,\mathrm{A},j}\mu_j}{\rho_i u_{p,\mathrm{A},i}\mu_i + \rho_j u_{p,\mathrm{A},j}\mu_j}|^2, \quad \mu_i = \cos\theta_i$$

$$\tau_{s,i\text{-}j} = \frac{4\rho_i u_{p,\mathrm{A},i}\rho_j u_{p,\mathrm{A},j}\mu_i\mu_j}{(\rho_i u_{p,\mathrm{A},i}\mu_i + \rho_j u_{p,\mathrm{A},j}\mu_j)^2}$$

$$\frac{\sin\theta_1}{u_{p,\mathrm{A},1}} = \frac{\sin\theta_2}{u_{p,\mathrm{A},2}} \quad \text{elastic scattering}$$

$$\frac{\sin\theta_1}{\sin\theta_2} = [\frac{(\rho c_v u_{p,\mathrm{A}})_2}{(\rho c_v u_{p,\mathrm{A}})_1}]^{1/2} \quad \text{inelastic scattering.} \tag{4.214}$$

The specular parameter p is found to have an intermediate value when the proceeding prediction is matched with the experiment [84].

Figure 4.44(b) shows the predicted and measured [272] results for $\langle k_p \rangle$ as a function of temperature for a Si/Ge superlattice [84]. The specular reflection parameter is set to $p = 0.83$. The bulk k_p for Si and Ge at $T = 300$ K are given in Table A.1 and are 149 and 60.2 W/m-K. The mean free paths for these (based on acoustic-phonon heat capacity only) are 260 and 199 nm [84].

The experimental results [272] show that $\langle k_p \rangle$ does not monotonically decrease with $L_1 = L_2$, suggesting that the phonon tunneling is not completely described by the proceeding treatment.

The cross-plane phonon thermal conductivity has also been calculated for superlattices, by use of the MD-G–K [267], verifying the boundary phonon scattering and reduced effective thermal conductivity.

The wave treatment and interference for the larger thickness smaller than mean free path shows a minimum $\langle k_p \rangle$ [431].

4.19.3 Phonon Density of States of Nanoparticles

The deviation of lattice vibration from bulk behavior occurs when the solid size decreases. Here we examine MD results for nanoparticles. The Debye DOS has a parabolic distribution resulting from an assumption of an isotropic medium with no dispersion, or any effect of the optical phonons. The measured phonon DOS of nanostructures, however, deviates from that for bulk crystals, because of quantum size effects [502].

The phonon DOS may be calculated with lattice-dynamics calculations or MD simulations [288]. In lattice-dynamics calculations, the dynamical matrix is diagonalized and the vibrational eigenvalues and eigenvectors determined. This approach actually calculates the harmonic modes, e.g., at $T = 0$ K. In MD, the velocity autocorrelation function is calculated for each species and the partial phonon DOS is then obtained by taking the Fourier transforms of this autocorrelation function. The results of these two approaches have been found to agree well with one another at low temperatures [288], as expected. However, at high temperatures the first method is not suitable, because it is harmonic. Also, for systems containing more than a few thousand atoms, it becomes unfeasible to calculate the frequencies of the vibrational modes by diagonalization of the dynamical matrix. For this reason, here $D_p(\omega)$ is calculated with MD simulations [3, 327]. The solid material used is Y_2O_3, which has applications in lasers, including laser cooling [397]. More details are reported in [398].

(A) *Nanoparticle Atomic Structure and MD*

The X-ray diffraction [361] and neutron diffraction [352] experiments have shown that Y_2O_3 has a FCC structure, which is retained in nanocrystals [252]. Eight metal ions are in the positions $(1/4, 1/4, 1/4)$; the remaining 24 occupy the sites $(u, 0, 1/4)$. The 48 oxygen ions are in general positions (x, y, z), arranged in distorted octahedra around the metal ions, the metal–oxygen bonding distances being unequal. The values of u, x, y, z are listed in [361, 352]. The crystal structure is shown in Figure 4.45.

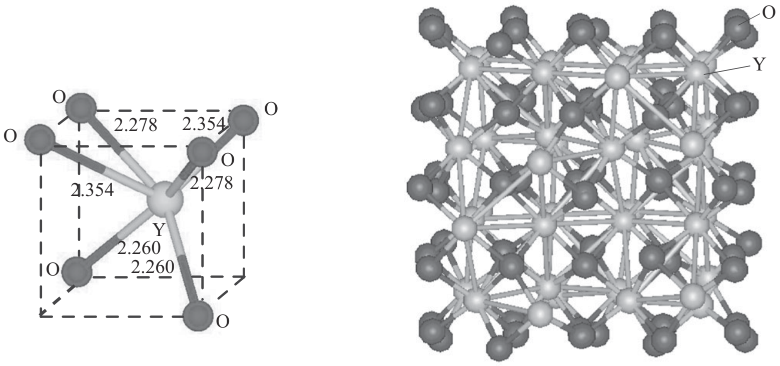

(a) (b)

Figure 4.45. Crystal structure of Y_2O_3. (a) The oxygen ions are arranged in distorted octahedra around the yttrium ions. The listed measured equilibrium bond lengths are in Å. (b) The structure of a cubic unit cell.

The nanopowder is generated by cutting a sphere out of a much larger bulk crystal, as shown in Figure 4.46. Note that the center of the sphere can be randomly selected; we have many possible configurations given the diameter.

In a MD simulation, we predict the phase-space trajectory of a system of particles by solving the Newton equations. The required inputs are an atomic structure and a suitable interatomic potential, which can be obtained from experiments and/or *ab initio* calculations [90].

The interatomic potential is the modified B-K-S potential (2.10), i.e.,

$$\varphi(r_{ij}) = \frac{q_i q_j}{r_{ij}} + A_{ij}\exp(-\frac{r_{ij}}{r_{\mathrm{o},ij}}) + \frac{C_{ij}}{r_{ij}^6}, \tag{4.215}$$

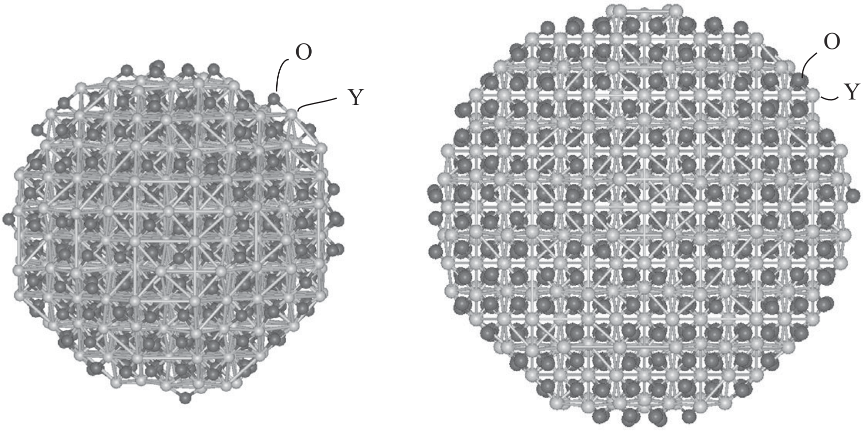

(a) $d_s = 3$ nm (b) $d_s = 4$ nm

Figure 4.46. The structure of the spherical Y_2O_3 nanoparticle (cluster) used in the MD simulations. The boundary is free and the particle structure is relaxed. (a) $d_s = 3$ nm, and (b) $d_s = 4$ nm [397].

Table 4.9. *Parameters used in the Buckingham potential, atomic charges:* $q_Y = 3e_c$, $q_O = -2e_c$.

Atom-Atom	A_{ij}, eV	$r_{o,ij}$, Å	C_{ij}, eV-Å^6	Reference
Y–Y	0	1	0	[60]
Y–O	1345.6	0.3491	0	[60, 279]
O–O	22799	0.149	27.93	[60, 279]

where $\varphi(r_{ij})$ is the interaction energy of atoms i and j, which consists of a Coulomb term and a covalent (short-range) contribution, cast into the usual Buckingham potential [65]. Here q_i is an effective charge of the ith atom, r_{ij} is the interatomic distance between atoms i and j, A_{ij} ($r_{o,ij}$ and C_{ij} are parameters for covalent interactions). For ionic materials, this Buckingham interatomic potential model has been shown to perform well. The parameters in (4.215), obtained from [60, 279], are listed in Table 4.9. This potential set has been verified to reproduce the bulk properties (lattice constant, lattice position, bulk modulus, elastic constant, etc.) well [237].

To determine the DOS of the bulk crystal, MD simulations are carried out in a cubic computation domain that contains $2 \times 2 \times 2 = 8$ unit cells containing $N = 640$ atoms (256 Y and 384 O). The computational method developed in [317] is used. Periodic boundary conditions are applied in all directions. For the nanopowder, the computation domain is a sphere of diameter d_s, which is cut from a much larger bulk crystal, as shown in Figure 4.46. It should be noted that a nanopowder generated in this way may not be neutral in charge; thus some atoms at the surface may need to be removed accordingly to eliminate any net charge of the nanopowder. Also, because the center of the sphere can be randomly selected, we have many possible configurations given the diameter. As such, a number of spherical particles with different configurations are considered in this study, and their behaviors are compared. The free boundary condition is used.

For both bulk crystal and nanocrystals, an initialization period of 5×10^4 time steps is used, with the time step $\Delta t = 1.6$ fs. The system is run in the NVT [Section 2.5.1(A)] ensemble. To set the temperature for the NVT ensemble, the potential energy of the system is monitored every time step. When it reaches a value within 10^{-4}% of the desired value, the ensemble is switched to NVE [Section 2.5.1(A)], and the system is run until the total number of time steps is 1.5×10^5.

(B) *Simulation Results and Analysis*

Typically, the normalized velocity–velocity autocorrelation function is determined for each species in the system. Here we have yttrium and oxygen atoms, and the autocorrelation function for the species α (α = Y, O) is

$$u_\alpha^{2*}(t) = \langle \sum_{i_\alpha=1}^{N_\alpha} \boldsymbol{u}_{i_\alpha}(t) \cdot \boldsymbol{u}_{i_\alpha}(0) \rangle / \langle \sum_{i_\alpha=1}^{N_\alpha} \boldsymbol{u}_{i_\alpha}(0) \cdot \boldsymbol{u}_{i_\alpha}(0) \rangle, \ \alpha = \mathrm{Y, O}, \tag{4.216}$$

Table 4.10. *Number and fraction of atoms for the nanocrystals, for several diameters d_s.*

Particle	Surface Y		Internal Y		Surface O		Internal O	
diameter d_s, nm	$N_{\alpha\beta}$	%	$N_{\alpha\beta}$	%	$N_{\alpha\beta}$	%	$N_{\alpha\beta}$	%
3	182	19.4	198	21.1	265	28.3	293	31.2
4	349	15.7	512	23.0	543	24.4	825	37.0
5	564	12.9	1203	27.4	839	19.1	1782	40.6
6	825	10.9	2212	30.0	1225	16.1	3340	43.9

where N_α is the number of atoms of species α, $\boldsymbol{u}_{i_\alpha}$ is the velocity of atom i_α, and $\langle\ \rangle$ is an ensemble average.

For nanocrystals, the internal and surface atoms vibrate differently. The crystal structure of the internal region is similar to that of bulk crystals, which implies that the internal atoms behave as if they were in a bulk crystal. On the other hand, the surface structure deviates much from the bulk structure because surface atoms lose their outer neighboring atoms, leading to different bond lengths, bond angles, etc. It is straightforward to consider the internal and surface regions separately, although the exact boundary between these regions cannot be well defined. In our practice, the spherical shell with a thickness of 3 Å is taken as the surface region, and the more inside region is considered as the internal region. All atoms are hence decomposed into four categories: surface yttrium atoms, internal yttrium atoms, surface oxygen atoms, and internal oxygen atoms. The number and population fraction for these four categories are shown in Table 4.10 for nanoparticles with increasing size. As expected, the surface region takes a smaller portion as the particle becomes larger, and the limit is that the surface effects can be neglected as the system is extremely large to recover the bulk phase.

The autocorrelation function for species α (α = Y, O), region β (β = surface, internal) is given by

$$u^{2*}_{\alpha\beta}(t) = \langle \sum_{i_{\alpha\beta}=1}^{N_{\alpha\beta}} \boldsymbol{u}_{i_{\alpha\beta}}(t)\cdot\boldsymbol{u}_{i_{\alpha\beta}}(0)\rangle / \langle \sum_{i_{\alpha\beta}=1}^{N_{\alpha\beta}} \boldsymbol{u}_{i_{\alpha\beta}}(0)\cdot\boldsymbol{u}_{i_{\alpha\beta}}(0)\rangle,$$

$$\alpha = \text{yttrium, oxygen}, \quad \beta = \text{surface, internal}, \tag{4.217}$$

where the double subscript $\alpha\beta$ denotes atoms of species α and in region β; then $N_{\alpha\beta}$ is the number of atoms of species α and in region β, $\boldsymbol{u}_{i_{\alpha\beta}}$ is the velocity of atom $i_{\alpha\beta}$.

The velocity–velocity autocorrelation functions are calculated for these four categories of atoms, and are shown in Figure 4.47. The vibrational frequencies of yttrium atoms are considerably lower than those for oxygen atoms, because the atomic mass for the yttrium atom is much larger. However, no evident difference is observed between the surface and internal regions for the same species, and it will be resolved in the phonon DOS in the next section.

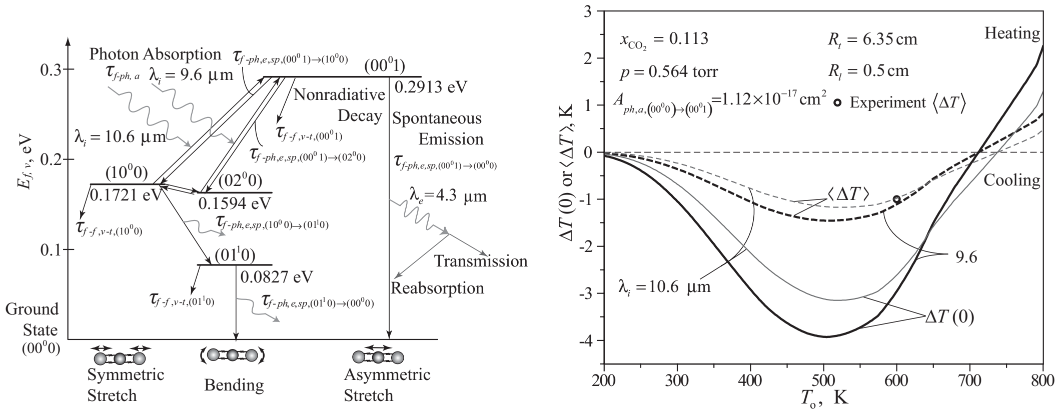

(a) (b)

Figure 4.47. Velocity–velocity autocorrelation functions for (a) surface yttrium atoms, (b) internal yttrium atoms, (c) surface oxygen atoms, and (d) internal oxygen atoms [397, 398].

(C) D_p for Nanoparticles

The frequency spectrum of the normalized velocity autocorrelation function gives the partial $D_{p,\alpha\beta}(\omega)$ as

$$D_{p,\alpha\beta}(\omega) = \int_0^\tau u^{2*}_{\alpha\beta}(t)\cos(\omega t)\mathrm{d}t. \tag{4.218}$$

Generally, the partial phonon DOS calculated in this way can give only the shape of the spectrum, and the absolute values are meaningless. Recognizing that a system with $N_{\alpha\beta}$ atoms has $3N_{\alpha\beta}$ modes, where 3 is the number of degrees of freedom, we can scale $D_{p,\alpha\beta}(\omega)$,

$$D_{p,\alpha\beta,N_{\alpha\beta}} = c_1 D_{p,\alpha\beta}, \tag{4.219}$$

where c_1 is a constant such that from (4.56)

$$\int_0^\infty D_{p,\alpha\beta,N_{\alpha\beta}}(\omega)\mathrm{d}\omega = 3N_{\alpha\beta}. \tag{4.220}$$

Then these partial phonon DOSs are addable, and the total phonon DOS of a system is just the summation of the partial phonon DOS,

$$D_p(\omega) = \sum_\alpha \sum_\beta D_{p,\alpha\beta,N_{\alpha\beta}}. \tag{4.221}$$

It is evident that $D_{p,\alpha\beta,N_{\alpha\beta}}$ is dependent on $N_{\alpha\beta}$, the size of the system. To compare the spectra shapes for systems with different numbers of atoms, it is necessary to define a normalized partial phonon DOS, as

$$D^*_{p,\alpha\beta} = \frac{D_{p,\alpha\beta,N_{\alpha\beta}}}{3N_{\alpha\beta}}. \tag{4.222}$$

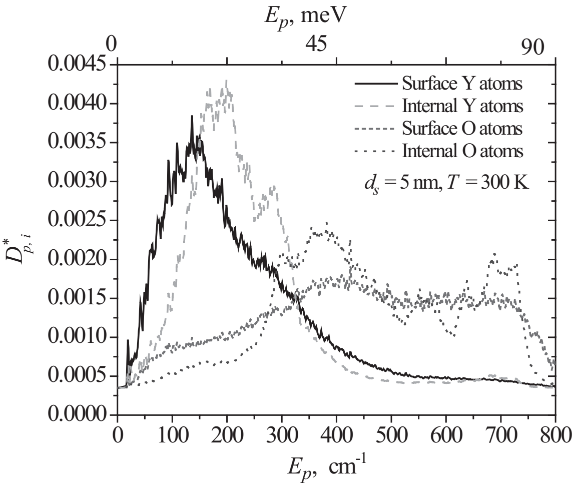

Figure 4.48. Normalized partial phonon DOS of the surface Y atoms, internal Y atoms, surface O atoms, and internal O atoms [398].

Therefore $D^*_{p,\alpha\beta}(\omega)$ satisfies the condition

$$\int_0^\infty D^*_{p,\alpha\beta}(\omega)\mathrm{d}\omega = 1, \tag{4.223}$$

and therefore it is called a normalized partial phonon DOS. The normalized partial $D^*_{p,\alpha\beta}(\omega)$ are calculated for a Y_2O_3 nanoparticle with $d_s = 5$ nm, and the results are shown in Figure 4.48. As indicated by the velocity–velocity autocorrelation function, oxygen atoms have more high-frequency modes than yttrium atoms, because of their lighter mass. For yttrium species, the surface region has more modes in high- and low-frequency tails, whereas the internal region has more modes in the intermediate frequency range. Similar behavior is observed for oxygen species.

These normalized partial phonon DOSs can be used as building blocks for higher-level partial DOSs. For example, the normalized partial DOS for the species α is given by

$$D^*_{p,\alpha} = \sum_\beta \frac{c_{\alpha\beta}}{c_\alpha} D^*_{p,\alpha\beta}, \tag{4.224}$$

where c_α is the population weight for species α, given by

$$c_\alpha = \sum_\beta c_{\alpha\beta}. \tag{4.225}$$

Similarly, the normalized partial DOS for the region β is given by

$$D^*_{p,\beta} = \sum_\alpha \frac{c_{\alpha\beta}}{c_\beta} D^*_{p,\alpha\beta}, \tag{4.226}$$

where c_β is the population weight for region β, given by

$$c_\beta = \sum_\alpha c_{\alpha\beta}. \tag{4.227}$$

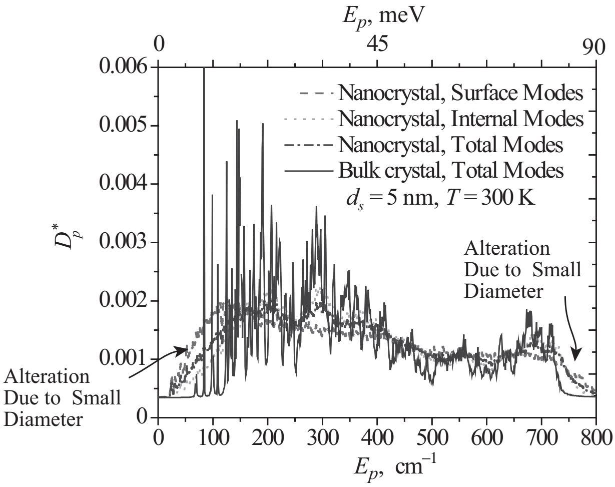

Figure 4.49. Comparison of the phonon DOS of the bulk crystal and nanocrystal for Y_2O_3. The nanocrystal DOS possesses extended low- and high-frequency tails [398].

The total phonon DOS is obtained by summing over the partial DOS weighted with the population, i.e.,

$$D_p^* = \sum_\alpha \sum_\beta c_{\alpha\beta} D_{p,\alpha\beta}^*. \tag{4.228}$$

The normalized partial $D_{p,\beta}^*(\omega)$ for the surface and internal regions are calculated for the same nanocrystal, and the results are shown in Figure 4.49. Also shown are the total phonon DOS for the nanocrystal and for the bulk material [the bulk D_p is also shown in Figure 4.8(c)]. It can be seen that the phonon DOS of nanocrystals is distinct from that of the bulk crystal, in its broadened peaks, and extended tails at low and high frequencies. The bulk crystal has sharp, well-defined peaks (or modes) related to the rigorous periodic structure, while these peaks are broadened in the nanocrystal, because of the loss to some extent of this periodicity. The high frequency tail in the nanocrystal phonon DOS is believed to result from the surface atoms. Because of the loss of the attraction from their outer neighbors, these atoms have contracted bonds with their inner neighbors, compared with the bulk crystal. This leads to a harder surface and the increased vibrational frequencies.

4.19.4 Phonon Conductivity Rectification in Anisotropic, One-Dimensional Systems

Nanotubes have one-dimensional thermal conductivity, and adding heavy atoms to the outside of the nanotube and in a manner to create a gradient in the added-atom layer thickness can result in greater conductivity along the decreasing thickness [79]. Figure 4.50 shows the added heavy molecules $C_9H_{16}Pt$ used in experiment reported in [79], on carbon nitride, and boron nitride multiwell nanotubes (MWNT), with outer diameters of $d_\circ = 30$ to 40 nm.

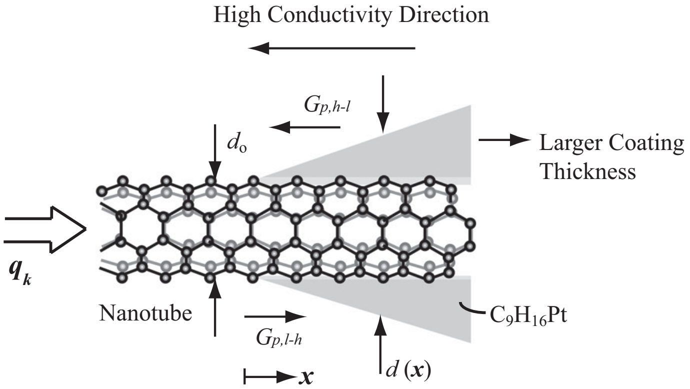

Figure 4.50. Asymmetric phonon conductance for heat flow along decreasing thickness $G_{p,h\text{-}l}$, is larger than the opposite direction $G_{p,l\text{-}h}$ when nanotube of diameter d_0 is nonuniformally coated with amorphous heavy molecules [79].

The rectification R is defined in term of asymmetric conductance along decreasng coating thickness $G_{p,h-l}$ and increasing coating thickness $G_{p,l-h}$, i.e.,

$$R = \frac{G_{p,h-l} - G_{p,l-h}}{G_{p,l-h}}, \tag{4.229}$$

and they report up to $R = 0.07$ (7% rectification).

They suggest the transport is by a stable, single phonon soliton (nonperturbative solutions of nonlinear systems) in nanotubes. These localized particle entities collide with each other without changing shape.

The thermal rectifiers have also been suggested in a linear-chain lattice with a nonlinear (anharmonic) interatomic potential [365]. This nonlinear lattice represents soft molecules attached (locally), with temperature dependent vibration, on an atomic chain (such as a nanotube). It is suggested that the variable wall thickness of a nanotube (multilayer nanotubes) will result in similar thermal rectification.

Thermal rectification in nanodevices has been discussed in [417] based on anharmonicity and structural asymmetry (spin-boson nanojunction).

4.19.5 Heat Flow in Molecular Wire

Pumping of heat by vibration of a nano-molecular element bridging two solids is addressed in [501, 416]. Heat flows between distinct solids when the bridge suffers stochastic thermal fluctuations, with significant representation of these fluctuations in the phonon density of states of one of the solids. The interface of soft and hard solids is discussed in [74].

In a molecular chain or wire (subsystem) connecting two thermal reservoirs, shown in Figure 4.51, under steady state, the conduction heat flow vector from the master-equation quantum mechanics (Glossary) is [417, 501, 416, 418]

$$\mathbf{q}_k = \frac{1}{2A}\sum_{n,m}(E_m - E_n)|S_{n,m}|^2 f_n\left(\frac{1}{\tau_{n\rightarrow m,L}} - \frac{1}{\tau_{n\rightarrow m,R}}\right)\mathbf{s}_{LR}, \tag{4.230}$$

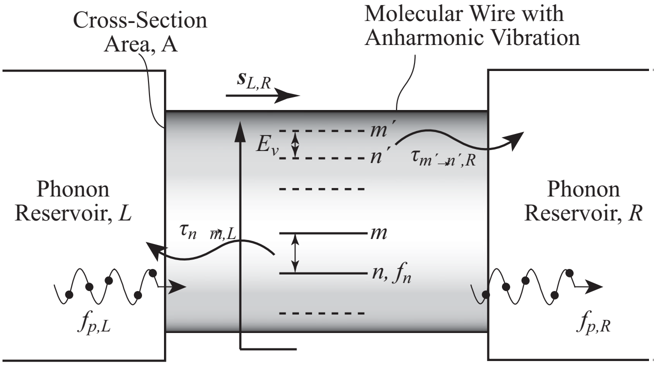

Figure 4.51. Heat flow through a molecular wire connecting two phonon baths [501, 416].

where the subsystem is excited from state E_n (with normalized population f_n and no transfer of population between subsystem and reservoirs) to energy state E_m. Here $S_{n,m}$ is a subsystem operator and for an harmonic model is given as

$$|S_{n,m}|^2 = |\langle n|x|m\rangle|^2 = (1+n)\delta_{m,n+1} + n\delta_{m,n-1}. \tag{4.231}$$

The interactions with reservoirs are at rates $\tau^{-1}_{n\to m,L}$ and $\tau^{-1}_{n\to m,R}$.

Equation 4.231 expresses excitation induced by L minus that excitation relaxation by R, and similarly for excitation by R in relation to L. Under steady state these two are added and then divided by 2.

The results of [418] show that, using an alkane chain, temperature dependence of the wire conductance depends on the cut-off frequency of the reservoirs, the degree of localization of molecular normal modes, and the interaction rates. They also find that the classical (Fourier) conduction overestimates the heat conduction.

4.19.6 Quantum Vibrational Energy Flow in Nanostructures

The Landauer formulation for electron transport across a nanostructure is extended to phonons [45], which gives the phonon junction conductance $G_{p,j}$ as

$$G_{p,j} = \frac{\langle Q_k\rangle}{T_1 - T_2} = \frac{\pi k_B^2 T}{6\hbar} \sum_{n,n'} \int_{E_{n,o}/k_BT}^{\infty} g\tau_{12}\mathrm{d}E_p^*, \tag{4.232}$$

$$g = \frac{3E_{pl}^* E_p^*}{\pi^2(e^{E_p^*}-1)^2}, \qquad E_p^* = \frac{E_p}{k_BT}, \tag{4.233}$$

where T_1 and T_2 are the temperature on the two sides of the junction (and T is the average), and τ_{12} is the joint transmission of energy E_p in sub-band n of side 1 transmitted into sub-band n' of side 2. Also, g satisfies

$$\int_0^{\infty} g\mathrm{d}E_p^* = 1. \tag{4.234}$$

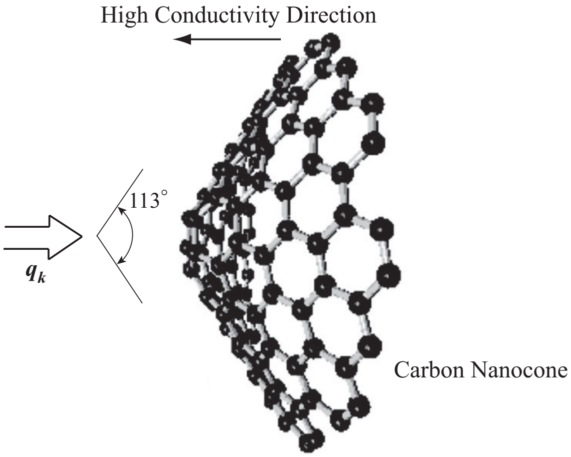

Figure 4.52. Carbon nanocone of 113° diverging angle.

Then in the absence of scattering ($\tau_{12} = 1$) a sub-band n contributes to the conductance (in the limit of $E_{n,o}/k_B T \rightarrow 0$)

$$\begin{aligned}\frac{G_{p,j,\mathrm{o}}}{T} &= \frac{\pi k_\mathrm{B}^2}{6\hbar} \text{ per mode,} \\ &= 9.465 \times 10^{-13} \ \mathrm{W/K^2},\end{aligned} \qquad (4.235)$$

which is called the universal phonon quantum transport (per mode).

4.19.7 Nanocone Conductivity

Nonequilibrium MD results for carbon nanocone (Figure 4.52) show larger phonon conductivity along the decreasing area [503]. The rectification in a 14 nm long nanocone is predicted to be more than 100% at 200 K and decreases with an increase in temperature. The directional thermal conductivity is found to be insensitive to the nanocone length (unlike nanotubes).

4.20 Problems

Problem 4.1

Describe the Born potential model given by the equation. What is the potential energy of a single bond in the Born potential model? The Born model is similar to the harmonic potential given in Table 2.1, where only the leading terms are taken, and assumes a slight displacement and considers bond stretching Γ_s and bond bending Γ_ϕ, i.e.,

$$\varphi_{i,j} = \frac{1}{2}\Gamma_s[\boldsymbol{s}_{i,j} \cdot (\boldsymbol{d}_j - \boldsymbol{d}_i)]^2 + \frac{1}{2}\Gamma_\phi\{|\boldsymbol{d}_j - \boldsymbol{d}_i|^2 - [\boldsymbol{s}_{i,j} \cdot (\boldsymbol{d}_j - \boldsymbol{d}_i)]^2\},$$

where $s_{i,j}$ is the unit vector in the equilibrium direction from atom i to atom j and $\boldsymbol{d}_i$ and $\boldsymbol{d}_j$ are the displacement vectors for atoms from atom i to atom j, respectively.

Problem 4.2

(a) Using the Born potential model (Table 2.1), also given below, which considers only the nearest-neighbor interactions, write the expression for the potential energy of a one-dimensional (along x) monatomic chain in terms of the atomic displacements from the equilibrium positions. Use an interatomic distance a.

$$\varphi = \frac{1}{2}\Gamma[d(x) - d(x-a)]^2 + \frac{1}{2}\Gamma[d(x) - d(x+a)]^2 \quad \text{Born potential.}$$

(b) Using the expression for the potential energy, determine the force ($F = -\partial\varphi/\partial d$) on a given atom in the crystal in terms of its displacement and the displacements of its neighboring atoms. Write the atomic location using $\exp(\kappa x)$.

(c) Derive the expression for the dynamical matrix, in $\boldsymbol{M}^{-1}\boldsymbol{D}(\boldsymbol{\kappa}) = \omega^2\boldsymbol{I}$, where $\boldsymbol{I}$ is the identity tensor. Note that the single component of the dynamical matrix gives $D = \partial^2\varphi/\partial d^2$.

(d) Derive the dispersion relation using this dynamical matrix and compare the result with (4.6), in the case of $m_1 = m_2 = m$.

Problem 4.3

Consider the case of one-dimensional displacement of a chain of atoms with two different atoms in the primitive basis.

(a) Using the Born potential model (Table 2.1, also Problem 4.2) that considers only the nearest-neighbor interactions, write the expression for the potential energy of atom m_1 in the one-dimensional (along x), two-mass atoms per primitive basis (m_1 and m_2). Use a single spring constant Γ, and the atomic displacements from the equilibrium positions. Start with φ_1 written in terms of relative displacement of atom 1 with respect to its right and left neighbors.

(b) Use the expression for the potential energy to determine the force on a given atom in the crystal in terms of its displacement and the displacements of its neighboring atoms. Use $F_1 = -\partial\varphi_1/\partial d_1$, etc. Note that for harmonic potential used in the dynamical matrix, the second derivative of the potential is used to obtain the components of the matrix. The components of the dynamical matrix have the form given by (4.40).

(c) Derive the expression for the dynamical matrix $\boldsymbol{D}$. Note that $\boldsymbol{M}^{-1}\boldsymbol{D}(\boldsymbol{\kappa}) = \omega^2\boldsymbol{I}$, where $\boldsymbol{I}$ is the identity tensor. Use $D_{ij} = \partial^2\varphi/\partial d_i \partial d_j$.

(d) Derive the dispersion relation using the dynamical matrix (by setting the determinant equal to zero) and compare the result with (4.6). Note that a symbolic solver can be used to determine the determinant of the matrix.

Problem 4.4

For the longitudinal phonon in a linear, monatomic lattice, the exponential displacement of the jth atom in the chain given by (4.3) is written as the real part of the exponential function, i.e.,

$$d_j = d_\text{o} \cos(-j\kappa a + \omega t).$$

Using this and for a monatomic chain with the nearest-neighbor interaction (force) constant Γ, show the following about the phonon energy.

(a) Show that the total phonon energy E_p (the sum of kinetic and potential energy) of the wave is

$$E_p = E_{p,k} + E_{p,p} = \frac{1}{2} m \sum_j (\frac{\mathrm{d}d_j}{\mathrm{d}t})^2 + \frac{1}{2}\Gamma \sum_j (d_j - d_{j+1})^2,$$

where j is over all atoms.

(b) Use the proceeding expression for d_j and show that the time-averaged, total modal energy per atom is

$$\begin{aligned} E_p &= \frac{1}{4} d_\text{o}^2 m\omega^2 + \frac{1}{2} d_\text{o}^2 \Gamma[1 - \cos(\kappa a)] \\ &= \frac{1}{2} d_\text{o}^2 m\omega^2, \end{aligned}$$

using the dispersion relation for monatomic chain $\omega^2 = (4\Gamma/m)\sin^2(\kappa a/2)$. This shows that the modal (and average) kinetic and potential energies of this harmonic lattice motion are equal. When placing a thermostat on this system, for a single degree of freedom, the kinetic energy is equal to $k_\text{B}T/2$. Note that $1 - \cos(\kappa a) = 2\sin^2(\kappa a/2)$.

Note that

$$\int_0^{\pi/\omega} \sin^2(b + \omega t)\mathrm{d}t = \pi/2\omega,$$

where b is a constant. Also $\cos(x) - \cos(y) = 2\sin[(x + y)/2]\sin[(x - y)/2]$.

Problem 4.5

Consider a monatomic lattice chain (acoustic phonon only) and show that the equation of motion (3.11) becomes the one-dimensional elastic wave equation,

$$\frac{\partial^2 d}{\partial t^2} = u_{p,\text{L}}^2 \frac{\partial^2 d}{\partial x^2},$$

for $\kappa \rightarrow 0$ (i.e., $u_{p,g} = u_{p,p}$ or linear dispersion).

Note that

$$\frac{\mathrm{d}^2 d}{\mathrm{d}x^2} = \frac{d^{j+1} + d^{j-1} - 2d^j}{a^2},$$

where a is the interatomic spacing.

Note that the elastic, longitudinal, wave phase speed (Section 4.7.2) is found from ω/κ because of (4.9), i.e.,

$$u_{p,\mathrm{L}} = \frac{\omega}{\kappa} = (\frac{\Gamma a^2}{m})^{1/2} = a(\frac{\Gamma}{m})^{1/2}\ \kappa \rightarrow 0.$$

In Table 3.11 and Section 4.7.2, the elastic wave equation becomes evident. Note that for a constant volume, compression wave speed is $u_{p,\mathrm{L}} = (E_\mathrm{Y}/\rho)^{1/2}$, where E_Y is the Young modulus.

Problem 4.6

(a) Derive (4.5) by substituting (4.3) and (4.4), into (4.1) and (4.2), and setting the determinant of the coefficients to zero.

(b) Plot the dispersion curve (in dimensional form) for a linear chain of Ar atoms, using Table 2.7 for the spring (force) constant. The scales used to convert to dimensional forces are given by (4.8).

(c) Increase the mass of the alternating (every other one) atoms (so the optical phonons are also present) by a factor of 2, and repeat (b). Note that this gives $m_1^* = 1/3$, whereas Figure 4.5 is for $m_1^* = 0.5$ and 0.75.

Problem 4.7

Use the Debye–Gaussian DOS model (4.51) to curve fit the FCC Ar phonon MD results given in Figure 4.7. The results should appear similar to those of Figure 4.8(c). Comment on the suitability of this model for representing (a) the peaks, (b) the low-frequency regime, and (c) the area under the curve. (d) What is the magnitude of the dimensionless frequency at which the dimensionless form of the model D_p^* peaks?

Problem 4.8

The FCC Ar phonon dispersion graph shown in Figure 4.7 can be produced by use of the dynamical matrix.

(a) Using the Matlab code, plot the dispersion curve, showing the three acoustic branches for FCC Ar along Γ–K, from Γ to $\kappa^* = 1$. The $\boldsymbol{\kappa}$ direction results are along Γ to K, and only a portion of the results of Figure 4.7.

(b) Comment about the behavior of the branches in the Γ–K line.

(c) Examine the code and comment about the dimension of the dynamical matrix.

Problem 4.9

Write the primitive lattice vector for the FCC zinc-blende structures, such as SiC, GaAs, and ZnS.

Problem 4.10

The cubic zinc-blende structure may be viewed as two FCC structures displaced from each other by 1/4 of a body diagonal. Write these reciprocal lattices of FCC.

Problem 4.11

Consider SiC crystal and assume that Si is at the origin (see the figure). Around this atom, there are four carbon atoms, all at an equal distance from this central Si. The basis consists of Si at the center and C at $a(0.5, 0.5, 0.5)$. Show that the primitive and reciprocal lattice vectors are those given in the figure.

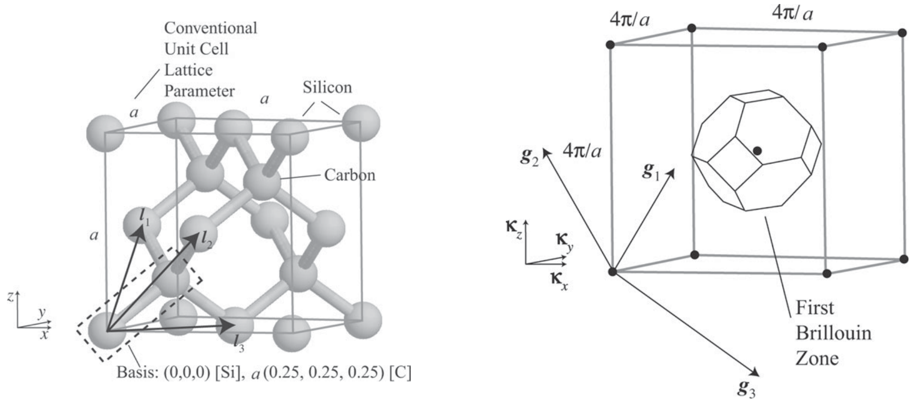

(a) Primitive lattice vectors for SiC: $l_1 = a(0, 0.5, 0.5)$, $l_2 = a(0.5, 0, 0.5)$, $l_3 = a(0.5, 0.5, 0)$

(b) Reciprocal space lattice vectors for SiC: $g_1 = (2\pi/a)(-1, 1, 1)$, $g_2 = (2\pi/a)(1, -1, 1)$, $g_3 = (2\pi/a)(1, 1, -1)$

Problem 4.11. Primitive and reciprocal space lattices for FCC SiC.

Problem 4.12

Show that the following are the unit vectors from C to Si atoms (place Si at the origin) as given as Problem 4.6 for SiC $3^{-1/2}a(\boldsymbol{s}_x + \boldsymbol{s}_y + \boldsymbol{s}_z)$

$3^{-1/2}a(-\boldsymbol{s}_x - \boldsymbol{s}_y + \boldsymbol{s}_z)$
$3^{-1/2}a(\boldsymbol{s}_x - \boldsymbol{s}_y - \boldsymbol{s}_z)$
$3^{-1/2}a(-\boldsymbol{s}_x + \boldsymbol{s}_y - \boldsymbol{s}_z)$.

Use the figure in Problem 4.11.

Problem 4.13

Using the Born potential model that considers only the nearest-neighbor interactions, derive the expression for the potential energy of SiC in terms of their displacements from equilibrium.

Use vectors $\boldsymbol{A}$ to $\boldsymbol{H}$ to represent the vectors in the Ath and Hth unit-cell, components of linear superpositions of the FCC unit lattice. Note that

$$\varphi = \sum_{i,j} \varphi_{i,j} = \sum_{i=1}^{4}\sum_{j=1}^{4}\{\frac{1}{2}\Gamma_S[\boldsymbol{s}_{i,j}\cdot(\boldsymbol{d}_j-\boldsymbol{d}_i)]^2 + \frac{1}{2}\Gamma_\phi\{|\boldsymbol{d}_j-\boldsymbol{d}_i|^2 - [\boldsymbol{s}_{i,j}\cdot(\boldsymbol{d}_j-\boldsymbol{d}_i)]^2\}\}$$

$$\begin{aligned}
\varphi = {} & \frac{1}{2}\Gamma_s|\boldsymbol{l}_A\cdot(\boldsymbol{d}_1(\boldsymbol{x})-\boldsymbol{d}_2(\boldsymbol{x})|^2 \\
& + \frac{1}{2}\Gamma_s|\boldsymbol{l}_B\cdot(\boldsymbol{d}_1(\boldsymbol{x})-\boldsymbol{d}_2(\boldsymbol{x}+\boldsymbol{B}))|^2 \\
& + \frac{1}{2}\Gamma_s|\boldsymbol{l}_C\cdot(\boldsymbol{d}_1(\boldsymbol{x})-\boldsymbol{d}_2(\boldsymbol{x}+\boldsymbol{C}))|^2 \\
& + \frac{1}{2}\Gamma_s|\boldsymbol{l}_D\cdot(\boldsymbol{d}_1(\boldsymbol{x})-\boldsymbol{d}_2(\boldsymbol{x}+\boldsymbol{D}))|^2 \\
& + \frac{1}{2}\Gamma_\phi\{|\boldsymbol{d}_1(\boldsymbol{x})-\boldsymbol{d}_2(\boldsymbol{x})|^2 - |\boldsymbol{l}_A\cdot(\boldsymbol{d}_1(\boldsymbol{x})-\boldsymbol{d}_2(\boldsymbol{x}))|^2\} \\
& + \frac{1}{2}\Gamma_\phi\{|\boldsymbol{d}_1(\boldsymbol{x})-\boldsymbol{d}_2(\boldsymbol{x}+\boldsymbol{B})|^2 - |\boldsymbol{l}_B\cdot(\boldsymbol{d}_1(\boldsymbol{x})-\boldsymbol{d}_2(\boldsymbol{x}+\boldsymbol{B}))|^2\} \\
& + \frac{1}{2}\Gamma_\phi\{|\boldsymbol{d}_1(\boldsymbol{x})-\boldsymbol{d}_2(\boldsymbol{x}+\boldsymbol{C})|^2 - |\boldsymbol{l}_C\cdot(\boldsymbol{d}_1(\boldsymbol{x})-\boldsymbol{d}_2(\boldsymbol{x}+\boldsymbol{C}))|^2\} \\
& + \frac{1}{2}\Gamma_\phi\{|\boldsymbol{d}_1(\boldsymbol{x})-\boldsymbol{d}_2(\boldsymbol{x}+\boldsymbol{D})|^2 - |\boldsymbol{l}_D\cdot(\boldsymbol{d}_1(\boldsymbol{x})-\boldsymbol{d}_2(\boldsymbol{x}+\boldsymbol{D}))|^2\} \\
& + \frac{1}{2}\Gamma_s|-\boldsymbol{l}_F\cdot(\boldsymbol{d}_2(\boldsymbol{x})-\boldsymbol{d}_1(\boldsymbol{x}+\boldsymbol{F}))|^2 \\
& + \frac{1}{2}\Gamma_s|-\boldsymbol{l}_G\cdot(\boldsymbol{d}_2(\boldsymbol{x})-\boldsymbol{d}_1(\boldsymbol{x}+\boldsymbol{G}))|^2 \\
& + \frac{1}{2}\Gamma_s|-\boldsymbol{l}_H\cdot(\boldsymbol{d}_2(\boldsymbol{x})-\boldsymbol{d}_1(\boldsymbol{x}+\boldsymbol{H}))|^2 \\
& + \frac{1}{2}\Gamma_\phi\{|\boldsymbol{d}_2(\boldsymbol{x})-\boldsymbol{d}_1(\boldsymbol{x}+\boldsymbol{F})|^2 - |-\boldsymbol{l}_F\cdot(\boldsymbol{d}_2(\boldsymbol{x})-\boldsymbol{d}_1(\boldsymbol{x}+\boldsymbol{F}))|^2\} \\
& + \frac{1}{2}\Gamma_\phi\{|\boldsymbol{d}_2(\boldsymbol{x})-\boldsymbol{d}_1(\boldsymbol{x}+\boldsymbol{G})|^2 - |-\boldsymbol{l}_G\cdot(\boldsymbol{d}_2(\boldsymbol{x})-\boldsymbol{d}_1(\boldsymbol{x}+\boldsymbol{G}))|^2\} \\
& + \frac{1}{2}\Gamma_\phi\{|\boldsymbol{d}_2(\boldsymbol{x})-\boldsymbol{d}_1(\boldsymbol{x}+\boldsymbol{H})|^2 - |-\boldsymbol{l}_H\cdot(\boldsymbol{d}_2(\boldsymbol{x})-\boldsymbol{d}_1(\boldsymbol{x}+\boldsymbol{H}))|^2\},
\end{aligned}$$

where $\boldsymbol{l}_A$ to $\boldsymbol{l}_H$ are defined as $\boldsymbol{l}_A = 3^{-1/2}(\boldsymbol{s}_x+\boldsymbol{s}_y+\boldsymbol{s}_z)$, $\boldsymbol{l}_B = 3^{-1/2}(-\boldsymbol{s}_x-\boldsymbol{s}_y+\boldsymbol{s}_z)$, $\boldsymbol{l}_C = 3^{-1/2}(\boldsymbol{s}_x-\boldsymbol{s}_y-\boldsymbol{s}_z)$, $\boldsymbol{l}_D = 3^{-1/2}(-\boldsymbol{s}_x+\boldsymbol{s}_y-\boldsymbol{s}_z)$, $\boldsymbol{l}_F = -\boldsymbol{l}_B$, $\boldsymbol{l}_G = -\boldsymbol{l}_C$, and $\boldsymbol{l}_H = -\boldsymbol{l}_D$.

Considering $\boldsymbol{d}_1(\boldsymbol{x}) = d_{1x}(\boldsymbol{x})\boldsymbol{s}_x + d_{1y}(\boldsymbol{x})\boldsymbol{s}_y + d_{1z}(\boldsymbol{x})\boldsymbol{s}_z$,

$\boldsymbol{d}_2(\boldsymbol{x}) = d_{2x}(\boldsymbol{x})\boldsymbol{s}_x + d_{2y}(\boldsymbol{x})\boldsymbol{s}_y + d_{2z}(\boldsymbol{x})\boldsymbol{s}_z$

$\boldsymbol{d}_1(\boldsymbol{x}+\boldsymbol{B}) = d_{1x}(\boldsymbol{x}+\boldsymbol{B})\boldsymbol{s}_x + d_{1y}(\boldsymbol{x}+\boldsymbol{B})\boldsymbol{s}_y + d_{1z}(\boldsymbol{x}+\boldsymbol{B})\boldsymbol{s}_z$, then,

$$
\begin{aligned}
\varphi = {} & \frac{1}{2}\Gamma_s|3^{-1/2}\{d_{1x}(\boldsymbol{x}) - d_{2x}(\boldsymbol{x}) + d_{1y}(\boldsymbol{x}) - d_{2y}(\boldsymbol{x}) + d_{1z}(\boldsymbol{x}) - d_{2z}(\boldsymbol{x})\}|^2 \\
& + \frac{1}{2}\Gamma_s|3^{-1/2}\{-d_{1x}(\boldsymbol{x}) + d_{2x}(\boldsymbol{x}+\boldsymbol{B}) - d_{1y}(\boldsymbol{x}) + d_{2y}(\boldsymbol{x}+\boldsymbol{B}) + d_{1z}(\boldsymbol{x}) - d_{2z}(\boldsymbol{x}+\boldsymbol{B})\}|^2 \\
& + \frac{1}{2}\Gamma_s|3^{-1/2}\{d_{1x}(\boldsymbol{x}) - d_{2x}(\boldsymbol{x}+\boldsymbol{C}) - d_{1y}(\boldsymbol{x}) + d_{2y}(\boldsymbol{x}+\boldsymbol{C}) - d_{1z}(\boldsymbol{x}) + d_{2z}(\boldsymbol{x}+\boldsymbol{C})\}|^2 \\
& + \frac{1}{2}\Gamma_s|3^{-1/2}\{-d_{1x}(\boldsymbol{x}) + d_{2x}(\boldsymbol{x}+\boldsymbol{D}) + d_{1y}(\boldsymbol{x}) - d_{2y}(\boldsymbol{x}+\boldsymbol{D}) - d_{1z}(\boldsymbol{x}) + d_{2z}(\boldsymbol{x}+\boldsymbol{D})\}|^2 \\
& + \frac{1}{2}\Gamma_\phi\{(d_{1x}(\boldsymbol{x}) - d_{2x}(\boldsymbol{x}))^2 + (d_{1y}(\boldsymbol{x}) - d_{2y}(\boldsymbol{x}))^2 + (d_{1z}(\boldsymbol{x}) - d_{2z}(\boldsymbol{x}))^2\} \\
& - \frac{1}{2}\Gamma_\phi|3^{-1/2}\{d_{1x}(\boldsymbol{x}) - d_{2x}(\boldsymbol{x}) + d_{1y}(\boldsymbol{x}) - d_{2y}(\boldsymbol{x}) + d_{1z}(\boldsymbol{x}) - d_{2z}(\boldsymbol{x})\}|^2 \\
& + \frac{1}{2}\Gamma_\phi\{(d_{1x}(\boldsymbol{x}) - d_{2x}(\boldsymbol{x}+\boldsymbol{B}))^2 + (d_{1y}(\boldsymbol{x}) - d_{2y}(\boldsymbol{x}+\boldsymbol{B}))^2 + (d_{1z}(\boldsymbol{x}) - d_{2z}(\boldsymbol{x}+\boldsymbol{B}))^2\} \\
& - \frac{1}{2}\Gamma_\phi|3^{-1/2}\{-d_{1x}(\boldsymbol{x}) + d_{2x}(\boldsymbol{x}+\boldsymbol{B}) - d_{1y}(\boldsymbol{x}) + d_{2y}(\boldsymbol{x}+\boldsymbol{B}) + d_{1z}(\boldsymbol{x}) - d_{2z}(\boldsymbol{x}+\boldsymbol{B})\}|^2 \\
& + \frac{1}{2}\Gamma_\phi\{(d_{1x}(\boldsymbol{x}) - d_{2x}(\boldsymbol{x}+\boldsymbol{C}))^2 + (d_{1y}(\boldsymbol{x}) - d_{2y}(\boldsymbol{x}+\boldsymbol{C}))^2 + (d_{1z}(\boldsymbol{x}) - d_{2z}(\boldsymbol{x}+\boldsymbol{C}))^2\} \\
& - \frac{1}{2}\Gamma_\phi|3^{-1/2}\{d_{1x}(\boldsymbol{x}) - d_{2x}(\boldsymbol{x}+\boldsymbol{C}) - d_{1y}(\boldsymbol{x}) + d_{2y}(\boldsymbol{x}+\boldsymbol{C}) - d_{1z}(\boldsymbol{x}) + d_{2z}(\boldsymbol{x}+\boldsymbol{C})\}|^2 \\
& + \frac{1}{2}\Gamma_\phi\{(d_{1x}(\boldsymbol{x}) - d_{2x}(\boldsymbol{x}+\boldsymbol{D}))^2 + (d_{1y}(\boldsymbol{x}) - d_{2y}(\boldsymbol{x}+\boldsymbol{D}))^2 + (d_{1z}(\boldsymbol{x}) - d_{2z}(\boldsymbol{x}+\boldsymbol{D}))^2\} \\
& - \frac{1}{2}\Gamma_\phi|3^{-1/2}\{-d_{1x}(\boldsymbol{x}) + d_{2x}(\boldsymbol{x}+\boldsymbol{D}) + d_{1y}(\boldsymbol{x}) - d_{2y}(\boldsymbol{x}+\boldsymbol{D}) - d_{1z}(\boldsymbol{x}) + d_{2z}(\boldsymbol{x}+\boldsymbol{D})\}|^2 \\
& + \frac{1}{2}\Gamma_s|-3^{-1/2}\{-d_{2x}(\boldsymbol{x}) + d_{1x}(\boldsymbol{x}+\boldsymbol{F}) - d_{2y}(\boldsymbol{x}) + d_{1y}(\boldsymbol{x}+\boldsymbol{F}) + d_{2z}(\boldsymbol{x}) - d_{1z}(\boldsymbol{x}+\boldsymbol{F})\}|^2 \\
& + \frac{1}{2}\Gamma_s|-3^{-1/2}\{d_{2x}(\boldsymbol{x}) - d_{1x}(\boldsymbol{x}+\boldsymbol{G}) - d_{2y}(\boldsymbol{x}) + d_{1y}(\boldsymbol{x}+\boldsymbol{G}) - d_{2z}(\boldsymbol{x}) + d_{1z}(\boldsymbol{x}+\boldsymbol{G})\}|^2 \\
& + \frac{1}{2}\Gamma_s|-3^{-1/2}\{-d_{2x}(\boldsymbol{x}) + d_{1x}(\boldsymbol{x}+\boldsymbol{H}) + d_{2y}(\boldsymbol{x}) - d_{1y}(\boldsymbol{x}+\boldsymbol{H}) - d_{2z}(\boldsymbol{x}) + d_{1z}(\boldsymbol{x}+\boldsymbol{H})\}|^2 \\
& + \frac{1}{2}\Gamma_\phi\{(d_{2x}(\boldsymbol{x}) - d_{1x}(\boldsymbol{x}+\boldsymbol{F}))^2 + (d_{2y}(\boldsymbol{x}) - d_{1y}(\boldsymbol{x}+\boldsymbol{F}))^2 + (d_{2z}(\boldsymbol{x}) - d_{1z}(\boldsymbol{x}+\boldsymbol{F}))^2\} \\
& - \frac{1}{2}\Gamma_\phi|-3^{-1/2}\{-d_{2x}(\boldsymbol{x}) + d_{1x}(\boldsymbol{x}+\boldsymbol{F}) - d_{2y}(\boldsymbol{x}) + d_{1y}(\boldsymbol{x}+\boldsymbol{F}) + d_{2z}(\boldsymbol{x}) - d_{1z}(\boldsymbol{x}+\boldsymbol{F})\}|^2 \\
& + \frac{1}{2}\Gamma_\phi\{(d_{2x}(\boldsymbol{x}) - d_{1x}(\boldsymbol{x}+\boldsymbol{G}))^2 + (d_{2y}(\boldsymbol{x}) - d_{1y}(\boldsymbol{x}+\boldsymbol{G}))^2 + (d_{2z}(\boldsymbol{x}) - d_{1z}(\boldsymbol{x}+\boldsymbol{G}))^2\} \\
& - \frac{1}{2}\Gamma_\phi|-3^{-1/2}\{d_{2x}(\boldsymbol{x}) - d_{1x}(\boldsymbol{x}+\boldsymbol{G}) - d_{2y}(\boldsymbol{x}) + d_{1y}(\boldsymbol{x}+\boldsymbol{G}) - d_{2z}(\boldsymbol{x}) + d_{1z}(\boldsymbol{x}+\boldsymbol{G})\}|^2 \\
& + \frac{1}{2}\Gamma_\phi\{(d_{2x}(\boldsymbol{x}) - d_{1x}(\boldsymbol{x}+\boldsymbol{H}))^2 + (d_{2y}(\boldsymbol{x}) - d_{1y}(\boldsymbol{x}+\boldsymbol{H}))^2 + (d_{2z}(\boldsymbol{x}) - d_{1z}(\boldsymbol{x}+\boldsymbol{H}))^2\} \\
& - \frac{1}{2}\Gamma_\phi|-3^{-1/2}\{-d_{2x}(\boldsymbol{x}) + d_{1x}(\boldsymbol{x}+\boldsymbol{H}) + d_{2y}(\boldsymbol{x}) - d_{1y}(\boldsymbol{x}+\boldsymbol{H}) - d_{2z}(\boldsymbol{x}) + d_{1z}(\boldsymbol{x}+\boldsymbol{H})\}|^2
\end{aligned}
$$

Problem 4.14

Use the expression for the potential energy to determine the force on a given atom in the crystal in terms of its displacement and the displacements of its neighboring atoms. Note that force is

$$F_{ij,x} = -\frac{\partial \varphi_{ij}}{\partial x_{ij}},$$

$$\begin{aligned}
F_x = &- \frac{\partial}{\partial d_{1,x}} \sum_{i=1}^{4} \sum_{j=1}^{4} \frac{1}{2}\Gamma s[\boldsymbol{b}_{i,j} \cdot (\boldsymbol{d}_j - \boldsymbol{d}_i)]^2 + \frac{1}{2}\Gamma_\phi \{|\boldsymbol{d}_j - \boldsymbol{d}_i|^2 - [\boldsymbol{b}_{i,j} \cdot (\boldsymbol{d}_j - \boldsymbol{d}_i)]^2\} \\
\frac{\partial \varphi}{\partial d_{1x}} = &\ \frac{\Gamma_s}{3}\{d_{1x}(\boldsymbol{x}) - d_{2x}(\boldsymbol{x}) + d_{1y}(\boldsymbol{x}) - d_{2y}(\boldsymbol{x}) + d_{1z}(\boldsymbol{x}) - d_{2z}(\boldsymbol{x})\} \\
&- \frac{\Gamma_s}{3}\{-d_{1x}(\boldsymbol{x}) + d_{2x}(\boldsymbol{x}+\boldsymbol{B}) - d_{1y}(\boldsymbol{x}) + d_{2y}(\boldsymbol{x}+\boldsymbol{B}) + d_{1z}(\boldsymbol{x}) - d_{2z}(\boldsymbol{x}+\boldsymbol{B})\} \\
&+ \frac{\Gamma_s}{3}\{d_{1x}(\boldsymbol{x}) - d_{2x}(\boldsymbol{x}+\boldsymbol{C}) - d_{1y}(\boldsymbol{x}) + d_{2y}(\boldsymbol{x}+\boldsymbol{C}) - d_{1z}(\boldsymbol{x}) + d_{2z}(\boldsymbol{x}+\boldsymbol{C})\} \\
&- \frac{\Gamma_s}{3}\{-d_{1x}(\boldsymbol{x}) + d_{2x}(\boldsymbol{x}+\boldsymbol{D}) + d_{1y}(\boldsymbol{x}) - d_{2y}(\boldsymbol{x}+\boldsymbol{D}) - d_{1z}(\boldsymbol{x}) + d_{2z}(\boldsymbol{x}+\boldsymbol{D})\} \\
&+ \Gamma_\phi(d_{1x}(\boldsymbol{x}) - d_{2x}(\boldsymbol{x})) \\
&- \frac{\Gamma_\phi}{3}\{d_{1x}(\boldsymbol{x}) - d_{2x}(\boldsymbol{x}) + d_{1y}(\boldsymbol{x}) - d_{2y}(\boldsymbol{x}) + d_{1z}(\boldsymbol{x}) - d_{2z}(\boldsymbol{x})\} \\
&+ \Gamma_\phi(d_{1x}(\boldsymbol{x}) - d_{2x}(\boldsymbol{x}+\boldsymbol{B})) \\
&+ \frac{\Gamma_\phi}{3}\{-d_{1x}(\boldsymbol{x}) + d_{2x}(\boldsymbol{x}+\boldsymbol{B}) - d_{1y}(\boldsymbol{x}) + d_{2y}(\boldsymbol{x}+\boldsymbol{B}) + d_{1z}(\boldsymbol{x}) - d_{2z}(\boldsymbol{x}+\boldsymbol{B})\} \\
&+ \Gamma_\phi(d_{1x}(\boldsymbol{x}) - d_{2x}(\boldsymbol{x}+\boldsymbol{C})) \\
&- \frac{\Gamma_\phi}{3}\{d_{1x}(\boldsymbol{x}) - d_{2x}(\boldsymbol{x}+\boldsymbol{C}) - d_{1y}(\boldsymbol{x}) + d_{2y}(\boldsymbol{x}+\boldsymbol{C}) - d_{1z}(\boldsymbol{x}) + d_{2z}(\boldsymbol{x}+\boldsymbol{C})\} \\
&+ \Gamma_\phi(d_{1x}(\boldsymbol{x}) - d_{2x}(\boldsymbol{x}+\boldsymbol{D})) \\
&+ \frac{\Gamma_\phi}{3}\{-d_{1x}(\boldsymbol{x}) + d_{2x}(\boldsymbol{x}+\boldsymbol{D}) + d_{1y}(\boldsymbol{x}) - d_{2y}(\boldsymbol{x}+\boldsymbol{D}) - d_{1z}(\boldsymbol{x}) + d_{2z}(\boldsymbol{x}+\boldsymbol{D})\} \\
&+ 0 \\
&+ 0 \\
&+ 0 \\
&+ 0 \\
&+ 0 \\
&+ 0 \\
&+ 0 \\
&+ 0 \\
&+ 0.
\end{aligned}$$

The zero force is because the various contributions exactly cancel each other.

$$\begin{aligned}
\frac{\partial\varphi}{\partial d_{1x}} = {} & \Gamma_s[\tfrac{4}{3}d_{1x}(\boldsymbol{x}) & -\frac{1}{3}d_{2x}(\boldsymbol{x}) - \frac{1}{3}d_{2y}(\boldsymbol{x}) - \frac{1}{3}d_{2z}(\boldsymbol{x}) \\
& & -\frac{1}{3}d_{2x}(\boldsymbol{x}+\boldsymbol{B}) - \frac{1}{3}d_{2y}(\boldsymbol{x}+\boldsymbol{B}) + \frac{1}{3}d_{2z}(\boldsymbol{x}+\boldsymbol{B}) \\
& & -\frac{1}{3}d_{2x}(\boldsymbol{x}+\boldsymbol{C}) + \frac{1}{3}\Gamma_s d_{2y}(\boldsymbol{x}+\boldsymbol{C}) + \frac{1}{3}d_{2z}(\boldsymbol{x}+\boldsymbol{C}) \\
& & -\frac{1}{3}d_{2x}(\boldsymbol{x}+\boldsymbol{D}) + \frac{1}{3}d_{2y}(\boldsymbol{x}+\boldsymbol{D}) - \frac{1}{3}d_{2z}(\boldsymbol{x}+\boldsymbol{D})] \\
& +\Gamma_\phi[4d_{1x}(\boldsymbol{x}) & -d_{2x}(\boldsymbol{x}) - d_{2x}(\boldsymbol{x}+\boldsymbol{B}) - d_{2x}(\boldsymbol{x}+\boldsymbol{C}) - d_{2x}(\boldsymbol{x}+\boldsymbol{D})] \\
& -\Gamma_\phi[\tfrac{4}{3}d_{1x}(\boldsymbol{x}) & -\frac{1}{3}d_{2x}(\boldsymbol{x}) - \frac{1}{3}d_{2y}(\boldsymbol{x}) - \frac{1}{3}d_{2z}(\boldsymbol{x}) \\
& & -\frac{1}{3}d_{2x}(\boldsymbol{x}+\boldsymbol{B}) - \frac{1}{3}d_{2y}(\boldsymbol{x}+\boldsymbol{B}) + \frac{1}{3}d_{2z}(\boldsymbol{x}+\boldsymbol{B}) \\
& & -\frac{1}{3}d_{2x}(\boldsymbol{x}+\boldsymbol{C}) + \frac{1}{3}\Gamma_s d_{2y}(\boldsymbol{x}+\boldsymbol{C}) + \frac{1}{3}d_{2z}(\boldsymbol{x}+\boldsymbol{C}) \\
& & -\frac{1}{3}d_{2x}(\boldsymbol{x}+\boldsymbol{D}) + \frac{1}{3}d_{2y}(\boldsymbol{x}+\boldsymbol{D}) - \frac{1}{3}d_{2z}(\boldsymbol{x}+\boldsymbol{D})]
\end{aligned}$$

$$\begin{aligned}
& = \frac{4}{3}(\Gamma_s + 2\Gamma_\phi)(d_{1x}(\boldsymbol{x})) \\
& \quad -\frac{1}{3}(\Gamma_s + 2\Gamma_\phi)(d_{2x}(\boldsymbol{x}) + d_{2x}(\boldsymbol{x}+\boldsymbol{B}) + d_{2x}(\boldsymbol{x}+\boldsymbol{C}) + d_{2x}(\boldsymbol{x}+\boldsymbol{D})) \\
& \quad -\frac{1}{3}(\Gamma_s - \Gamma_\phi)(d_{2y}(\boldsymbol{x}) + d_{2y}(\boldsymbol{x}+\boldsymbol{B}) - d_{2y}(\boldsymbol{x}+\boldsymbol{C}) - d_{2y}(\boldsymbol{x}+\boldsymbol{D})) \\
& \quad -\frac{1}{3}(\Gamma_s - \Gamma_\phi)(d_{2z}(\boldsymbol{x}) - d_{2z}(\boldsymbol{x}+\boldsymbol{B}) - d_{2z}(\boldsymbol{x}+\boldsymbol{C}) + d_{2z}(\boldsymbol{x}+\boldsymbol{D})) \\
& = \frac{4}{3}(\Gamma_s + 2\Gamma_\phi)d_{1x}(\boldsymbol{x}) \\
& \quad -\frac{1}{3}(\Gamma_s + 2\Gamma_\phi)(1 + e^{i\boldsymbol{\kappa}\cdot\boldsymbol{B}} + e^{i\boldsymbol{\kappa}\cdot\boldsymbol{C}} + e^{i\boldsymbol{\kappa}\cdot\boldsymbol{D}})d_{2x}(\boldsymbol{x}) \\
& \quad -\frac{1}{3}(\Gamma_s - \Gamma_\phi)(1 + e^{i\boldsymbol{\kappa}\cdot\boldsymbol{B}} - e^{i\boldsymbol{\kappa}\cdot\boldsymbol{C}} - e^{i\boldsymbol{\kappa}\cdot\boldsymbol{D}})d_{2y}(\boldsymbol{x}) \\
& \quad -\frac{1}{3}(\Gamma_s - \Gamma_\phi)(1 - e^{i\boldsymbol{\kappa}\cdot\boldsymbol{B}} - e^{i\boldsymbol{\kappa}\cdot\boldsymbol{C}} + e^{i\boldsymbol{\kappa}\cdot\boldsymbol{D}})d_{2z}(\boldsymbol{x}).
\end{aligned}$$

Other terms $\left[\frac{\partial\varphi}{\partial d_{1y}(\boldsymbol{x})}, \frac{\partial\varphi}{\partial d_{1z}(\boldsymbol{x})}, \frac{\partial\varphi}{\partial d_{2x}(\boldsymbol{x})}, \frac{\partial\varphi}{\partial d_{2y}(\boldsymbol{x})}, \frac{\partial\varphi}{\partial d_{2z}(\boldsymbol{x})}\right]$ can be also obtained by similar mathematical processes.

Problem 4.15

Derive the expression for the dynamical matrix using

$$D_{ij}(\boldsymbol{\kappa}) = \sum_{i=1}^{4}\sum_{j=1}^{4}\sum_{\boldsymbol{x}_p}(\partial^2 \frac{\varphi}{\partial d_i[x_s + x_p]\partial d_j[x_s]})e^{-i(\boldsymbol{\kappa}\cdot\boldsymbol{x}_p)},$$

$$\boldsymbol{D}(\boldsymbol{\kappa}) = \begin{array}{cc} \begin{array}{cccccc} d_{1x} & d_{1y} & d_{1z} & d_{2x} & d_{2y} & d_{2z} \end{array} & \\ \left[\begin{array}{cccccc} A & 0 & 0 & B & C & D \\ 0 & A & 0 & C & B & E \\ 0 & 0 & A & D & E & B \\ B^\dagger & C^\dagger & D^\dagger & A & 0 & 0 \\ C^\dagger & B^\dagger & E^\dagger & 0 & A & 0 \\ D^\dagger & E^\dagger & B^\dagger & 0 & 0 & A \end{array}\right] & \begin{array}{c} d_{1x} \\ d_{1y} \\ d_{1z} \\ d_{2x} \\ d_{2y} \\ d_{2z} \end{array} \end{array},$$

where

$$A = 4(\frac{\Gamma_s + 2\Gamma_\phi}{3}),$$

$$B = (\frac{\Gamma_s + 2\Gamma_\phi}{3})(1 + e^{i(\kappa_x+\kappa_y)a/2} + e^{i(\kappa_y+\kappa_z)a/2} + e^{i(\kappa_z+\kappa_x)a/2}),$$

$$C = (\frac{\Gamma_\phi - \Gamma_s}{3})(1 + e^{i(\kappa_x+\kappa_y)a/2} - e^{i(\kappa_y+\kappa_z)a/2} - e^{i(\kappa_z+\kappa_x)a/2}),$$

$$D = (\frac{\Gamma_\phi - \Gamma_s}{3})(1 - e^{i(\kappa_x+\kappa_y)a/2} - e^{i(\kappa_y+\kappa_z)a/2} + e^{i(\kappa_z+\kappa_x)a/2}),$$

$$E = (\frac{\Gamma_\phi - \Gamma_s}{3})(1 - e^{i(\kappa_x+\kappa_y)a/2} + e^{i(\kappa_y+\kappa_z)a/2} - e^{i(\kappa_z+\kappa_x)a/2}).$$

Problem 4.16

Use the Matlab code for the dynamic matrix of SiC. Examine and comment on the structure of the matrix.

Problem 4.17

Use the Matlab code for the SiC dispersion curve (ω-κ relation). It uses the function developed in Problems 4.14 and 4.15. Draw the dispersion curve along $\Gamma-\mathrm{X}-\mathrm{L}-\Gamma$, $\Gamma-\mathrm{L}$, $\mathrm{X}-\mathrm{L}$, and X. Use the relation $\boldsymbol{M}^{-1}\boldsymbol{D}(\boldsymbol{\kappa})\boldsymbol{s}_\alpha = \omega^2\boldsymbol{s}_\alpha$ and properties for SiC (force constants $\Gamma_s = 414.14$ kg/s^2, $\Gamma_\phi = 53.405$ kg/s^2, lattice constant $a = 4.35 \times 10^{-10}$ m, and mass of Si and C: $m_1 = 4.66 \times 10^{-26}$ kg, $m_2 = 1.99 \times 10^{-26}$ kg).

Problem 4.18

Use the Matlab code for the DOS of SiC and draw the D_p versus ω curve.

Problem 4.19

Plot the dimensional phonon DOS (4.24) for Problem 4.18, parts (b) and (c). Comment on the differences. Note that both $D_p(\kappa)$ and $\omega(\boldsymbol{\kappa})$ relations should be used.

Problem 4.20

Use the Matlab code for the specific heat capacity of SiC (use the DOS developed in Problem 4.18), and plot the $c_{v,p}$ versus T curve.

Problem 4.21

(a) Plot the specific heat capacity per atom for a Cu crystal as a function of temperature (up to $2T_\mathrm{D}$), using the Debye model of lattice specific heat capacity.

(b) Compare with the experimental results, at selected temperatures, given in the following table (in J/kg-K). Note that the high-temperature experimental data do not match the Debye model. The low-temperature data agree better [232]. At higher temperatures, the contribution from conduction electrons (Section 5.8) becomes noticeable.

T, K	$c_{v,p}$, J/kg-K
200	356.1
250	374.1
300	385.0
350	392.6
400	398.6
500	407.7
600	416.7

Problem 4.22

Use the Matlab code for the specific heat of SiC, apply the Debye model and the Einstein model. Draw $c_{v,p}$ as a function of temperature and compare the results with the experimental results. Use the cut-off frequency in the Debye model as $f_\mathrm{D} = 1.58 \times 10^{14}$ Hz. Use the frequency in the Einstein model as that of the highest frequency in the DOS found in Problem 4.18.

Problem 4.23

(a) Show that the specific internal energy per unit mass and per unit volume (4.53) can be written as

$$\begin{aligned} e_p &= \frac{1}{m}\int_0^{\omega_\mathrm{D}} \hbar\omega f_p^\mathrm{o} D_{p,\mathrm{D}} \mathrm{d}\omega \\ &= \frac{3k_\mathrm{B}^4 T^4}{2m\pi^2 u_{p,\mathrm{A}}^3 \hbar^3}\int_0^{T_\mathrm{D}/T} \frac{x^3}{e^x - 1}\mathrm{d}x \\ &= 9\frac{k_\mathrm{B}T}{m}(\frac{T}{T_\mathrm{D}})^3 n \int_0^{T_\mathrm{D}/T} \frac{x^3}{e^x - 1}\mathrm{d}x. \end{aligned}$$

(b) For $T \ll T_\mathrm{D}$, $T_\mathrm{D}/T \to \infty$, and

$$\int_0^\infty \frac{x^3}{e^x - 1}\mathrm{d}x = \frac{\pi^4}{15},$$

show that for $T \ll T_\mathrm{D}$, (4.64) becomes

$$c_{v,p} = \frac{12\pi^4 k_\mathrm{B}}{5m} n (\frac{T}{T_\mathrm{D}})^3,$$

which is the so-called Debye T^3-law.

Problem 4.24

(a) By expanding the exponential terms in (4.64), for small x ($T \gg T_\mathrm{D}$), show that (per atom)

$$c_{v,p} = 3\frac{k_\mathrm{B}}{m},$$

which is the Dulong–Petit limit for harmonic lattice vibration.

(b) Similar to Figure 4.13(a), using (4.64), plot $c_{v,p}m/k_\mathrm{B}$ (per atom) versus temperature (T_D is given in Table A.2) for Cu, and for $T = 300$ K, use the value in Table A.1 to compare. Note that the tabulated $c_{v,p}$ value is in J/kg-K.

Problem 4.25

(a) Use (4.98) and plot $f_p^\circ + f_p'$ as a function of $E_p/k_\mathrm{B}T$, for Si using $u_p = 6.4\times10^3$, $T = 300$ K, $\tau_p = 10^{-11}$ s, $\nabla T = a_1 s_x$, with (i) $a = 0$, (ii) 5×10^8 K/m and (iii) 10^9 K/m.

(b) Considering a cut-off energy of 0.07 eV, repeat (a) using E_p (eV) and plot the population up to the cut-off energy. Use $a_1 = 10^9$ K/m, and $T = 300$ and 1000 K.

Problem 4.26

Derive the Callaway phonon conductivity model (4.108), starting from (4.106). State all the assumptions. Use (4.55) to write $c_{v,p} = k_\mathrm{B}x^2e^x/(e^x - 1)^2$. Note that all three acoustic-phonon modes are treated the same in the Callaway model. Use (4.63) for the relation between T_D and $u_{p,\mathrm{A}}$ (in the Debye model only this average phonon speed is used).

Problem 4.27

The porous crystal, MOF-5 shown in the figure is made of BDC ($C_8H_6O_4$) links with Zn_4O corners and has a lattice spacing $a = 12.92$ Å.

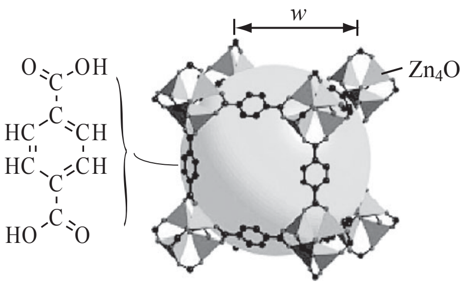

Problem 4.27. Metal–organic porous crystal is made of BDC links and Zn_4O corners.

(a) For a single crystal, determine the number density n. Also, find the molecular weight.

(b) For amorphous solids, we have three acoustic modes, one longitudinal and two transverse. Assuming the longitudinal and transverse velocities are 2500 and 1250 m/s, respectively, use the following relation to predict the Debye temperatures

$$T_{\mathrm{D},i} = \frac{\hbar}{k_\mathrm{B}} u_{p,i} (6\pi^2 n)^{1/3}, \qquad i = \mathrm{L}, \mathrm{T},$$

and compare to the simplified average value 102 K.

(c) The C–P model (4.131) for the minimum thermal conductivity of amorphous solids is

$$k_{p,\text{C-P}} = (\frac{\pi}{6})^{1/3} k_\mathrm{B} n^{2/3} \sum_i [u_i (\frac{T}{T_{\mathrm{D},i}})^2 \int_0^{T_{\mathrm{D},i}/T} \frac{x^3 e^x}{(e^x - 1)} \mathrm{d}x],$$

where the summation is over the three acoustic modes. Determine k_{min} at room temperature (T = 300 K). What major assumption did we make in using the equation?

(d) The Slack [437] relation for the phonon thermal conductivity of crystals at high temperatures is (4.132), i.e.,

$$k_p = k_{p,\mathrm{S}} = \frac{3.1 \times 10^4 \langle M \rangle T_D^3}{T n^{1/3} \gamma_\mathrm{G}^2 N_\circ^{2/3}},$$

where $\langle M \rangle$ is the average molecular weight of the constituents (4.65), γ_G is the Grüneisen parameter (Section 4.11), and $N_\circ$ is the number of atoms per primitive cell. Note that 3.1×10^4 has a unit such that k_p is in W/m-K. Assuming γ_G = 1.5 (the structure includes ionic and covalent bonds) and using the higher Debye temperature, predict the thermal conductivity at room temperature. Is this higher than $k_{p,\text{C-P}}$? If not, explain possible reasons.

(e) Compare this with k_p from (4.177), i.e., the mean-free-path model, using $c_v = 3k_\mathrm{B}$ and n from the atomic structure. Use $\lambda_p = w = 7.6$ Å, and the average acoustic phonon velocity $u_{p,\mathrm{A}}$. The MD simulations (Table 4.6) give $k_{p,\mathrm{MD}} = 0.32$ W/m-K.

Problem 4.28

The high-temperature thermal conductivity of crystals is given by the Slack relation (4.132)

$$k_p = k_{p,\mathrm{S}} = \frac{3.1 \times 10^4 \langle M \rangle T_\mathrm{D}^3}{T n^{1/3} \gamma_\mathrm{G}^2 N_\circ^{2/3}},$$

where $\langle M \rangle$ is the average molecular weight of constituents, T_D is the Debye temperature, n is the number density (atom/volume), γ_G is the Grüneisen parameter, and $N_\circ$ is the number of atoms per primitive cell. Note that 3.1×10^4 has a unit such that k_p is in W/m-K.

(a) For diamond-structure crystals, diamond C, Si, and Ge, determine n.

(b) Predict the room temperature (T = 300 K) thermal conductivity of C, Si, and Ge. Obtain theoretical values of γ_G and T_D from Table 4.5 for these diamond-structure crystals, and use $N_\circ = 2$ (Section 4.3.3).

(c) Determine the percentage error between the predicted and tabulated (Table A.1) values. Note that the measured k_p for diamond may be for crystals containing isotopes, thus this value may be lower than that for pure samples. The Slack model prediction is within about 30% of the experimental results in Table A.1. However, he used his own experimental results for comparison in Table 4.5.

Problem 4.29

Starting from (4.64) divided by n (so $c_{v,p}$ is per atom), derive the first term of the extended Callaway phonon conductivity model in the extended Callaway lattice conductivity model [70]

$$k_p = (48\pi^2)^{1/3}\frac{1}{a}\frac{k_B^3}{h_P^2}\frac{T^3}{T_D}[g_1(f,T,\tau_p) + \frac{g_2^2(f,T,\tau_p,\tau_{p\text{-}p,n})}{g_3(f,T,\tau_p,\tau_{p\text{-}p,N},\tau_{p,r})}],$$

using (4.119) to divide the phonon scattering into normal and resistive groups.

The integrals g_n, $g_{r,1}$, and $g_{r,2}$ and the relaxation times $\tau_{p,n}$, $\tau_{p,r}$, and τ_p are defined as

$$g_1 = \int_0^{T_D/T} \tau_p \frac{x^4 e^x}{(e^x-1)^2}\mathrm{d}x$$

$$g_2 = \int_0^{T_D/T} \frac{\tau_p}{\tau_{p\text{-}p,N}} \frac{x^4 e^x}{(e^x-1)^2}\mathrm{d}x$$

$$g_3 = \int_0^{T_D/T} \frac{\tau_p}{\tau_{p\text{-}p,N}\tau_{p,r}} \frac{x^4 e^x}{(e^x-1)^2}\mathrm{d}x$$

$$\frac{1}{\tau_p} = \frac{1}{\tau_{p\text{-}p,N}} + \frac{1}{\tau_{p,r}}, \quad \frac{1}{\tau_{p,r}} = \sum_i \frac{1}{\tau_{p,r,i}}, \quad x = \frac{\hbar\omega}{k_B T}.$$

State all the assumptions. The second term involves treatment of the normal and resistive processes, whereas the normal processes conserve momentum.

Start from the thermal conductivity relation based on the mean free path (4.109), i.e., $k_p = \rho c_{v,p} u_{p,A} \lambda_p/3$, $\lambda_p = u_{p,A}\tau_p$.

Problem 4.30

(a) Plot the variation of the phonon conductivity with respect to temperature, using the Callaway model (4.108) and (4.109) and the following relaxation resistive and the normal relaxation time, and the data for crystalline alumina (sapphire)

Al_2O_3 given below, for $0 \le T \le 400$ K.

$$\frac{1}{\tau_{p,r}} = \frac{1}{\tau_{p\text{-}d}} + \frac{1}{\tau_{p\text{-}im}} + \frac{1}{\tau_{p\text{-}p,\mathrm{U}}} + \frac{1}{\tau_{p\text{-}b}}$$

$$= A(\frac{2\pi k_{\mathrm{B}}}{h_{\mathrm{P}}})^4 T^4 x^4 + A(\frac{2\pi k_{\mathrm{B}}}{h_{\mathrm{P}}})^4 T^4 x^4 + a_{\mathrm{U}}(\frac{2\pi k_{\mathrm{B}}}{h_{\mathrm{P}}})^2 T^3 e^{-T_{\mathrm{D}}/(\alpha T)} x^2 + \frac{u_{p,\mathrm{A}}}{L}$$

$$\frac{1}{\tau_{p\text{-}p,\mathrm{N}}} = a_{\mathrm{N}} \frac{k_{\mathrm{B}}}{\hbar} T^5 x.$$

Note that Umklapp scattering has a extra, exponential temperature dependence.

(b) Plot the various relaxation times, with respect to temperature at $\omega = \omega_{\mathrm{D}}$ (note that $\hbar\omega_{\mathrm{D}}/k_{\mathrm{B}}T = T_{\mathrm{D}}/T$).

(c) Examine the role of scattering mechanisms on the conductivity, by repeating (a), while suppressing individual scattering contributions (setting relaxation time constant to a very large value).

(d) Show that the Umklapp scattering $\tau^{-1}_{p\text{-}p,\mathrm{U}}$ dominates at high temperatures.

For crystalline Al_2O_3, we have $a_{\mathrm{N}} = 2.7\times10^{-13}$ 1/K^4, $A = 4.08\times10^{-46}$ s^3, $a_{\mathrm{U}} = 1.7\times10^{-18}$ s/K, $T_{\mathrm{D}} = 596$ K, $a = 0.35$ nm, $L = 4.12$ mm, $\alpha = 2$, and $u_{p,\mathrm{A}} = 7009$ m/s.

Verify that the peak value is 7097 W/m-K, and occurs at $T = 29$ K. The peak value is sensitive to the accuracy of the integration scheme.

As a check against the experiment, at $T = 300$ K, the measured conductivity is 29.2 W/m-K.

Problem 4.31

Using the structural metrics for the phonon conductivity at high temperatures, i.e., the Slack relation (4.132) and the relations for the associated properties, predict the phonon conductivity of GaAs taking the following steps. Find the force constant Γ for the diatomic compound GaAs using to the combination rule (4.148) with $s = 1$, and the pair force constants from Table 4.4.

(a) Find the Gruneisen parameters γ_{G} using (4.170) and the electronegativity from Table A.2.

(b) Using Γ as the equivalent force constant for the conventional cubic unit cell, calculate the Debye temperature from (4.160).

(c) Using the Slack relation, calculate the phonon conductivity of GaAs (experimental value at 300 K is 55 W/m-K).

The lattice constant for GaAs is 5.56 Å. Note that $\langle M \rangle$ is the average atomic weight and M is the mass of a unit cell which here contains 8 atoms.

Problem 4.32

Derive the expression for phonon boundary transmission (D.13) for the Debye phonon DOS model, starting from (D.12).

Problem 4.33

(a) Plot the variation of the dimensional phonon boundary conductance $AR_{p,b}$, using (4.203), as a function of temperature ($0 \le T \le T_{\mathrm{D}}$), for Bi_2Te_3 (material 1) bounded by Cu (material 2). The properties to be used are a single Debye temperature $T_D = T_{D,1} = 165$ K, and $n = 5.95\times10^{27}$ 1/m^3, and use the Debye phonon speed $u_{p,A}$ from (4.27) to determine $u_{p,1,\alpha}$ (for all modes). For $u_{p,2,\alpha}$ (for Cu), use $u_{p,2,L} = 4760$, and $u_{p,2,T} = 2325$ m/s.

(b) Plot $AR_{p,b}$ using the high-temperature approximation (4.206), for $0 \le T \le 300$ K, for $T_1 - T_2 = 1$ K, $T_1 = T$, and compare with results of (a). Note that Figure 4.41(b) shows these results.

(c) Comment on the difference between the results of part (a) and part (b).

Problem 4.34

Use the expression for the effective lattice conductivity of a superlattice, (4.214), and calculate the effective lattice conductivity $\langle k_p \rangle$ of a Si/Ge superlattice, for the following conditions, and for inelastic scattering:

$(\rho c_v)_{\rm Si} = 0.93 \times 10^6$ J/m^3-K, $(\rho c_v)_{\rm Ge} = 0.87\times10^6$ J/m^3-K, $u_{p,A,\rm Si} = 1804$ m/s, $u_{p,A,\rm Ge} = 1042$ m/s, $L_{\rm Si} = L_{\rm Ge}$, and $p = 0.8$.

(a) Plot $\langle k_p \rangle$ versus L, $L = L_{\rm Si} + L_{\rm Ge}$, for $10 < L < 1000$ Å.

(b) Plot $\langle k_p \rangle$ versus p $(0 \le p \le 0.8)$, for $L_{\rm Si} = L_{\rm Ge} = 50, 200$, and 1000 Å.

Note that $(\rho c_v)_i$ is for the acoustic phonons only [84]. Use Table A.1 for densities. Also note that the definite integrals can be evaluated numerically.

Problem 4.35

(a) Consider high-temperature phonon scattering ($T \gg T_D$) dominatd phonon conductivity k_p and a constant $\tau_{p\text{-}p}$ (for a given temperature T). Then using (4.108), show that this $\tau_{p\text{-}p}$ can be found from known k_p through

$$\tau_{p\text{-}p} = \frac{3h_{\rm p}^2 k_p}{(48\pi^2)^{1/3} n^{1/3} k_{\rm B}^3 T_{\rm D}^2}.$$

(b) Using the given properties of CoSb$_3$ at T = 300 K, calculate $\tau_{p\text{-}p}$. Note that this is a poor estimate, since $\tau_{p\text{-}p}$ is frequency and temperature dependent (Table 4.3). k_p = 10 W/m-K, $n^{-1/3}$ = 2.886 Å, and T_D = 307 K [Journal of Applied Physics 80: 4442 (1996)].

Problem 4.36

Consider the high-temperature phonon conductivity with interphonon and defect scatterings (Table 4.2), i.e., $\tau_p^{-1} = BT\omega^2 + A\omega^4$, then use (4.108) to shows that

(a) For $A \to 0$,

$$k_p = (\frac{3}{4\pi^4})^{1/3} \frac{k_{\rm B}}{aBT}.$$

i.e., similar to the Slack the $1/T$ relation. Here a is the lattice constant

(b) For high defect content [use $\tan^{-1}(DT_D/T) = \pi/2$, $D^2 = Ak_BT/B\hbar$]

$$k_p = (\frac{3}{32\pi})^{1/3} \frac{\hbar}{aT_{\rm D}(ABT)^{3/2}}.$$

i.e., the $1/T^{1/2}$ relation.

Problem 4.37

Starting from the Landauer relation (4.232)

$$G_{p,j} = \int_0^\infty \frac{1}{2\pi}\hbar\omega\tau_{12}\frac{\partial f_p^\circ}{\partial T}\mathrm{d}\omega,$$

and using $\tau_{12} = 1$, show that

$$G_{p,j} = G_{p,j,\circ} = \frac{\pi k_\mathrm{B}^2 T}{6\hbar}.$$

Problem 4.38

The cross-plane phonon boundary resistance can become very significant in thin films of thickness L (which can be smaller than the phonon mean free path λ_p). This resistance can also be included as part of the bulk resistance (or conductivity) and one such attempt is given in Liu and Asheghi, *ASME J. Heat Transfer*, 128:75-83, 2006 by modifying (4.109) as

$$k_{p,\perp} = \frac{1}{3}\sum_\alpha u_{p,\alpha}^2 \int_0^{T_\alpha/T} c_{v,p,\alpha}\tau_{p\text{-}p,\alpha} z(L^*)\mathrm{d}x, \quad \alpha = \mathrm{L, T, TU},$$

where

$$z(L^*) = 1 - \frac{3}{8L^*} + \frac{3}{2L^*}\int_1^\infty (\frac{1}{y^3} - \frac{1}{y^5})\exp(-L^* y)\mathrm{d}y$$

$$L^* = \frac{L}{\lambda_{p,\alpha}}, \ \lambda_{p,\alpha} = u_{p,\alpha}\tau_{p\text{-}p,\alpha}.$$

In this model the length along which $k_{p,\perp}$ is predicted and scaled with respect to the phonon mean free path $\lambda_{p,\alpha}$ and $\tau_{p\text{-}p,\alpha}$ is the bulk (no interfacial boundary effect) relaxation time (4.119), based on the following relaxation time only.

Using only the three interphonon scattering relaxation times $\tau_{p\text{-}p,\mathrm{L,N}}$, $\tau_{p\text{-}p,\mathrm{T,N}}$, and $\tau_{p\text{-}p,\mathrm{TU}}$ in the low-T regime in Table 4.2 (constants given in Table 4.3, also use ω ¿ ω_1) for Si, plot k_p as a function of L (log-log scale), for $1 \le L < 1000$ nm, and $T = 300$ K. Assume $c_{v,p,\alpha} = c_{v,p}$ and use (4.55) without the integration. Note that with this $k_p(L)$ model, $k_p(L \to \infty)$ is about 80 W/m-K.

5

Electron Energy Storage, Transport and Transformation Kinetics

The solid electric thermal conductivity tensor $\boldsymbol{K}_e$, in addition to the phonon thermal conductivity tensor (i.e., total conductivity $\boldsymbol{K} = \boldsymbol{K}_e + \boldsymbol{K}_p$), determines heat conduction in solids through the Fourier law $\boldsymbol{q}_k = -\boldsymbol{K} \cdot \nabla T$. The heat capacity of an electron $c_{v,e}$ when in local thermal equilibrium with the lattice (i.e., phonon) is small, except at very high temperatures. Electrons can also have a net motion under an applied electric field $\boldsymbol{e}_e$, thus creating opportunities for exchange of their gained kinetic energy, e.g., with the lattice through inelastic scattering in Joule heating. The coupling of electronic and thermal transport, known as thermoelectricity, leads to Peltier heating/cooling.

In Section 2.6.5, we examined the electronic energy states of an idealized electron gas by solving the Schrödinger equation for the case of a collection of free electrons while for metals the conduction electron density $n_{e,c}$ does not change with temperature, for semiconductors $n_{e,c}(T = 0 \text{ K}) = 0$ for intrinsic (non-doped) semiconductors and increases with temperature. In Section 2.6.6 we also derived the electronic energy states of hydrogenlike atoms, along with the designation of the quantum numbers and atomic orbitals. As atoms gather in a cluster or a bulk phase, their orbiting electrons and their energy states are altered because of various nuclear and electronic interactions (Section 2.2), including representation as interatomic potentials. These interactions may increase or decrease the energy gaps between the electron orbital states of individual atoms. The electrons can gain sufficient energy to be free (conduction) electrons or lack this and be bounded (valence) electrons. If a significant electronic energy gap exists between these two electron states, then this cluster or bulk matter may become an electrical insulator. Once an electron is in the conduction state (or band), its kinetic energy can be increased by imposition of an electrical field or by other excitations (such as absorption of photons).

Figure 5.1(a) gives an idealized presentation of the electronic orbital overlaps and the formation of finer energy states (sublevels). The band formed from the ground-state valence level is called the valence band. The band immediately preceding is called the conduction band. The interval between the top of the valence and the bottom of the conduction bands is called the forbidden energy gap $\Delta E_{e,g}$. For ideal electrical insulators, $\Delta E_{e,g} \rightarrow \infty$.

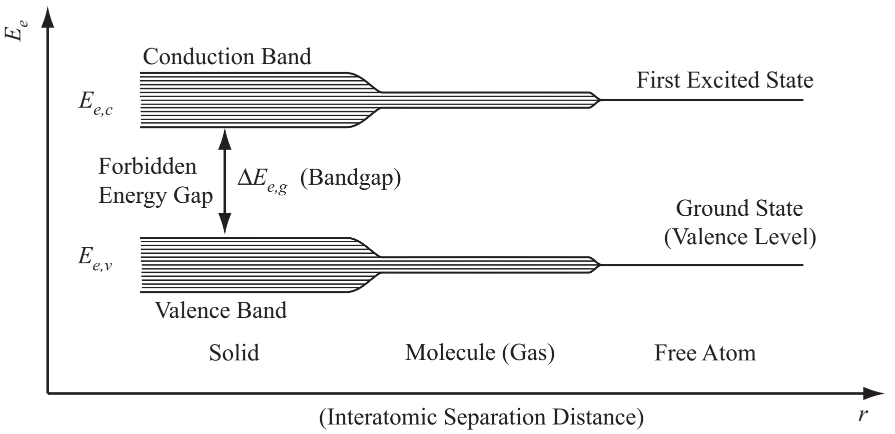

(a) Idealized Band Gap

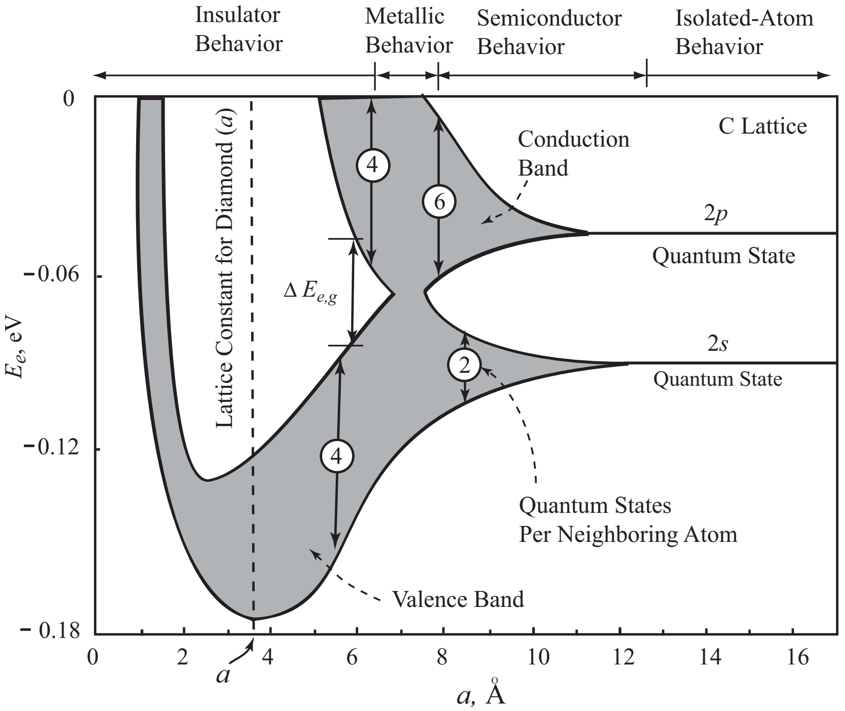

(b) Band Formation in Solid C

Figure 5.1. (a) Idealization of formation of electronic bands (sublevels) and bandgaps as atoms C lattice approach each other and electronic orbitals (energy levels) overlap. (b) Quantitative energy bands for C lattice as a functions of interatomic spacing a [475].

Figure 5.1(b) gives these energy bands quantitatively for C (Table A.2, $1s^22s^22p^2$, group 14) atoms as they form covalent bonds (four valence electrons) equilibrium in a lattice, as a function of lattice constant. This diamond lattice constant (diamond lattice constant in Table A.2) is marked. The isolated carbon atoms contain six electrons occupying $1s$, $2s$, and $2p$ orbitals in pairs (Section 2.2.1)[†]. The $2s$ and $2p$ orbitals are shown in Figure 5.1(b), and as the wave functions overlap by reduced spacing (and because of the Pauli exclusion), energy-level splitting occurs, giving $2N$ states (spin splitting) in $2s$ and $6N$ (due to spin splitting of $2p$ orbitals) states in $2p$, where N is the number of neighboring atoms in the crystal. The $2s$ bands will grow to $4N$ (due further splitting and overlap) as the distance is further decreased, but the $2p$ bands decrease to $4N$ (due to overlap). Figure 5.1(b) shows quantum states per atom and suggests that, with a lattice constant of about 7 Å, a metallic behavior (no bandgap and constant conduction electron density) can be found in this carbon (C) structure, such as in graphene and carbon nanotubes (one delocalized, electron per atom in graphene).

Figure 5.2(a) shows the electronic energy states in bulk solid metals, semiconductors (conduction electron density depends on temperature), and insulators (very low conduction electron density, even at high temperatures). Also, for intrinsic semiconductors the number density of conduction electrons and holes are the same. When electrons are allowed to equilibrate with a reservoir (or a source), their chemical potential equilibrates with this reservoir (and this is represented by the Fermi energy). Metallic solids have very closely spaced electronic energy states, and there are also possibilities of energy overlap (this will be discussed in Section 5.16). These energy states are readily accessible by the thermal energy $k_{\rm B}T$. Also shown in Figure 5.2(a) are the p- and n-type semiconductors (Glossary), which have moderate gaps (for example $\Delta E_{e,g} = 1.13$ eV for Si). The valence band is fully occupied, and some electrons can be thermally promoted to the conduction band. For insulators these gaps are rather large [$\Delta E_{e,g} = 5.45$ eV for C in the diamond phase, Figure 5.1(b)], compared with the thermal energy, so no promotion of an electron to the conduction band occurs.

Figure 5.2(b) contrasts the electronic band structure of a semiconducting crystal with that of a molecule. In molecules, the bandgap is the difference between the lowest unoccupied molecular orbital (LUMO) and highest occupied molecular orbital (HOMO). Quantum dots are nanoscale, three-dimensional (isolated or embedded) structures and have larger bandgap energy and discrete energy levels.

[†] The C ground state is

$$\underset{1s}{\underline{\uparrow\downarrow}}\ \underset{2s}{\underline{\uparrow\downarrow}}\ \underset{2p_x}{\underline{\ \uparrow\ }}\ \underset{2p_y}{\underline{\ \uparrow\ }}\ \underset{2p_z}{\underline{\quad}}.$$

The first step in hybridization is

$$\underset{1s}{\underline{\uparrow\downarrow}}\ \underset{sp^3}{\underline{\ \uparrow\ }}\ \underset{sp^3}{\underline{\ \uparrow\ }}\ \underset{sp^3}{\underline{\ \uparrow\ }}\ \underset{sp^3}{\underline{\ \uparrow\ }},\ sp^3,$$

which forms four sp^3 valence electrons. There are also sp^2 and sp hybridization giving double and triple bonds, i.e.,

$$\underset{1s}{\underline{\uparrow\downarrow}}\ \underset{sp^2}{\underline{\ \uparrow\ }}\ \underset{sp^2}{\underline{\ \uparrow\ }}\ \underset{sp^2}{\underline{\ \uparrow\ }}\ \underset{2p}{\underline{\ \uparrow\ }},\ sp^2,\ \text{delocalized}$$

$$\underset{1s}{\underline{\uparrow\downarrow}}\ \underset{sp}{\underline{\ \uparrow\ }}\ \underset{sp}{\underline{\ \uparrow\ }}\ \underset{2p}{\underline{\ \uparrow\ }}\ \underset{2p}{\underline{\ \uparrow\ }},\ sp,\ \text{delocalized.}$$

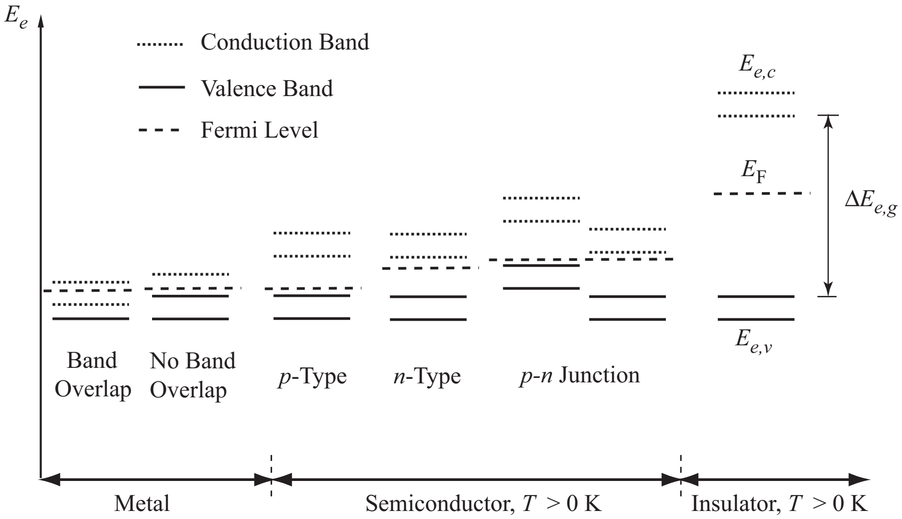

(a) Bulk Crystals

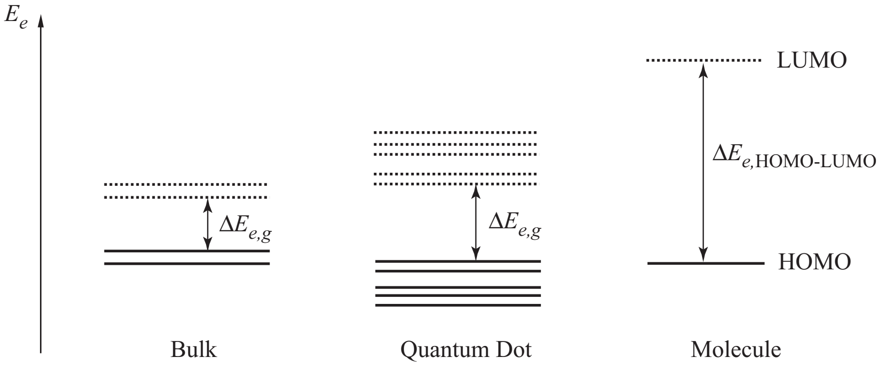

(b) Size Effect in Semiconductors

Figure 5.2. (a) The electron energy states in bulk metals, semiconductors ($T > 0$ K), and insulators. Progressively higher Fermi energy (chemical potential) is needed to conduct electrons (b) Size effects in semiconductor band structure and bandgap in molecules.

In this chapter, we begin with a discussion of electron energy bands structure $E_e(\boldsymbol{\kappa})$ in solids. Then we discuss its electronic transport properties which use these $E_e(\boldsymbol{\kappa})$ in BTE. We do not consider electron (or charged particles, in general) beams, but we consider electron currents in solids. When electrons are part of a particle mixture, such as in thermal plasmas (high temperature, charged gases), we will use some of the fluid particle features discussed in Chapter 6. Finally, we discuss size effects.

5.1 Schrödinger Equation for Periodic-Potential Electronic Band Structure

In Section 2.6.5 we found the solution to the Schrödinger equation for free electrons in periodic structure, as it applies to free (conduction) electrons in metals. However, for bound electrons their interaction with the nuclei should be included, as was done in Section 2.6.6 for hydrogenlike, single atoms. Here we extend this to periodic structures (crystal) and potentials.

As two atoms approach, the electronic energy levels of the atom pair split because of the Pauli exclusion principle. The potential energy of the shared electrons is the average of the energy levels of the valence electrons. For an N-atom system, the energy levels split into N levels, with the inner shell overlapping to a lesser extent. For large N, the spacing can be large, resulting in energy bands. Bands are energy levels for the crystal. Between bands, forbidden energy ranges exist, and each band may be from several atomic energy levels. Electron conductivity requires mobile electrons (i.e., electrons in the conduction bands).

The time-independent Schrödinger equation (Table 2.8) for electrons is

$$[-\frac{\hbar}{2m_e}\nabla^2 + \varphi_c(\boldsymbol{x})]\psi_{e,\boldsymbol{\kappa}}(\boldsymbol{x}) = E_e\psi_{e,\boldsymbol{\kappa}}(\boldsymbol{x}). \tag{5.1}$$

The crystal periodic lattice potential $\varphi_c(\boldsymbol{x})$ is presented (assumed to be the stationary form of the lattice used for the lattice vibration in Chapter 4) as a Fourier series used as the basis of the solution for ψ_e. The symmetry of the reciprocal lattice space (and Brillouin zone, Section 4.3) is most useful, and therefore the crystal potential is given as a series [satisfying $\varphi_c(\boldsymbol{x}+\boldsymbol{l}) = \varphi_c(\boldsymbol{x})$ where $\boldsymbol{l}$ is the lattice real-space vector] expansion in $\boldsymbol{g}$ as

$$\varphi_c(\boldsymbol{x}) = \sum_{\boldsymbol{g}} \varphi_{\boldsymbol{g}} \exp[i(\boldsymbol{g}\cdot\boldsymbol{x})] \quad \text{periodic crystal potential}, \tag{5.2}$$

where $\boldsymbol{g}$ is the reciprocal lattice vector, where $\varphi_{\boldsymbol{g}}$ are constants. For the Coulomb potential, $\varphi_{\boldsymbol{g}}$ decreases rapidly with increasing $\boldsymbol{g}$. The square-well potential is a simplified model, representing infinitely fast decay outside a cut-off region. The periodic (crystal) potential is a Fourier series in reciprocal lattice space.

The Bloch wave function, using an orbital centered around a (translational) lattice vector $\boldsymbol{l}$, is the solution for $\psi_{e,\kappa}$ along (2.68), i.e.,

$$\psi_{e,\boldsymbol{\kappa}}(\boldsymbol{x}) = \sum_{\boldsymbol{\kappa}} a_{\boldsymbol{\kappa}} \exp[i(\boldsymbol{\kappa}\cdot\boldsymbol{x})] \quad \text{Bloch plane-wave series}. \tag{5.3}$$

Substituting these $\psi_{e,\boldsymbol{\kappa}}$ and φ_c in (5.1), we have

$$\sum_{\boldsymbol{\kappa}} -\frac{\hbar^2}{2m_e}\kappa^2 a_{\boldsymbol{\kappa}} \exp[i(\boldsymbol{\kappa}\cdot\boldsymbol{x})] + \sum_{\boldsymbol{g}}\sum_{\boldsymbol{\kappa}} \varphi_{\boldsymbol{g}} a_{\boldsymbol{\kappa}} \exp\{i[(\boldsymbol{g}+\boldsymbol{\kappa})\cdot\boldsymbol{x}]\} = E_e \sum_{\boldsymbol{\kappa}} a_{\boldsymbol{\kappa}} \exp[i(\boldsymbol{\kappa}\cdot\boldsymbol{x})]. \tag{5.4}$$

Using the orthogonality of $e^{-i(\boldsymbol{\kappa}'\cdot\boldsymbol{x})}$, we have the delta function

$$\frac{1}{V}\int \exp[-i(\boldsymbol{\kappa}'\cdot\boldsymbol{x})]\exp[i(\boldsymbol{\kappa}\cdot\boldsymbol{x})]\mathrm{d}V = \delta\boldsymbol{\kappa}'\boldsymbol{\kappa}, \tag{5.5}$$

where $\delta_{\boldsymbol{\kappa}',\boldsymbol{\kappa}}$ is the Kronecker delta. Then (5.4) becomes

$$\frac{\hbar^2}{2m_e}\kappa'^2 a_{\boldsymbol{\kappa}'} + \sum_{\boldsymbol{g}} \varphi_{\boldsymbol{g}} a_{\boldsymbol{\kappa}'-\boldsymbol{g}} = E_e a_{\boldsymbol{\kappa}'}. \tag{5.6}$$

The preceding set of algebraic equations is called the central (or secular) equation for quantized energy E_e.

By rearranging, this equation becomes

$$[\frac{\hbar^2(\kappa^2-g^2)}{2m_e}-E_e]a_{\kappa-g}+\sum_{g'}\varphi_{g'-g}a_{\kappa-g'}=0 \quad \text{central eigenvalue equation.} \tag{5.7}$$

Note that for the time-independent Schrödinger equation (5.1), we have

$$\mathrm{H}\psi_{e,\boldsymbol{\kappa}}(\boldsymbol{x})=E_e(\boldsymbol{\kappa})\psi_{e,\boldsymbol{\kappa}}(\boldsymbol{x}), \tag{5.8}$$

or

$$\int \psi^{\dagger}_{e,\boldsymbol{\kappa}}\mathrm{H}\psi_{e,\boldsymbol{\kappa}}\mathrm{d}V=\int \psi^{\dagger}_{e,\boldsymbol{\kappa}}E_e\psi_{e,\boldsymbol{\kappa}}\mathrm{d}V=E_e$$

$$\text{relation between energy and wave function.} \tag{5.9}$$

The central role of the periodic potential $\varphi_c(\boldsymbol{x})$ is to create the eigenvalues of electron energy E_e, with energy gaps, and this distinguishes it from the nonperiodic potential of hydrogenlike atom electrons treated in Section 2.6.5.

In (5.7), for a given $\boldsymbol{\kappa}$, only coefficients $a_{\boldsymbol{\kappa}-\boldsymbol{g}}$ are needed, and for $\boldsymbol{\kappa}$ in the first Brillouin zone, $\boldsymbol{g}$ is evaluated in the neighboring zones (multiples of the reciprocal lattice vector). Then (5.7) gives the solution to $E_{e,n}(\boldsymbol{\kappa})$, i.e., the eigenvalues of the central equations, where n is the electron band number.

We now proceed with an example of a linear lattice with a single, periodic crystal potential.

5.2 Electronic Band Structure in One-Dimensional Ionic Lattice

To demonstrate the electronic energy gaps occurring for conduction electrons in periodic lattice (ionic) potentials, consider the one- dimensional (linear) atomic chain shown in Figure 5.3 [245].

The one-dimensional form of (5.1) along x, is

$$[-\frac{\hbar}{2m_e}\frac{\mathrm{d}^2}{\mathrm{d}x^2}+\varphi_c(x)]\psi_{e,\kappa}(x)=E_e\psi_{e,\kappa}(x) \quad \text{periodic potential,} \tag{5.10}$$

where $\varphi_c(x)$ is the periodic crystal (lattice) potential[†]. In Section 2.6.5, we found the solution for $\varphi_c = 0$, i.e., the free electron in a box which is the idealized metallic behavior of conduction electrons. Here by using a nonzero φ_c, the dispersion relation $E_e(\boldsymbol{\kappa})$ is no longer the explicit relation (2.94), and this also leads to the energy bandgap. When the potential is idealized as having the square-well potential distribution also shown in Figure 5.3. This is called the periodic Kronig–Penny potential model of electron in an ionic lattice.

[†] This potential, for a lattice parameter a, is of the form [287]

$$\varphi_c=\varphi_o+2\varphi_1\cos(2\pi x/a)+2\varphi_2\cos(4\pi x/a)+\cdots, \tag{5.11}$$

and has a nonlinear, periodic variation as shown depicted in Figure 5.3

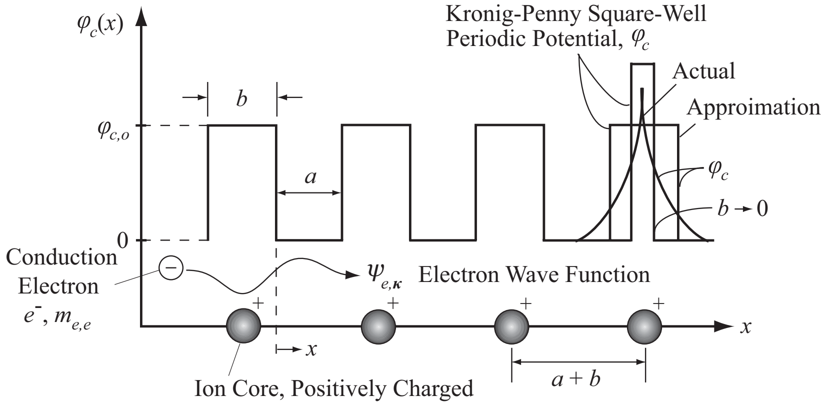

Figure 5.3. A linear, ionic chain lattice and the periodic potential experienced by an electron, causing electronic energy gaps. The electron wave function $\psi_{e,\kappa}(x)$ is expressed as plane waves. Various approximation of the periodic potential are also shown.

In region $0 \leq x \leq a$, $\varphi_c = 0$, and in $-b \leq x \leq 0$, we have $\varphi_c = \varphi_{c,\text{o}}$ (well potential). Then, the periodic behavior is

$$\varphi_c(x) = \varphi_c(x + a + b). \tag{5.12}$$

In region $0 \leq x \leq a$, the wave function (5.3) is the solution to (5.10) with $\varphi_c = 0$, and we have

$$\psi_{e,\kappa}(x) = Ae^{i\kappa_1 x} + Be^{-i\kappa_1 x}, \ 0 \leq x \leq a, \tag{5.13}$$

with $E_e = \hbar^2\kappa_1^2/2m_e$ as in (2.97).

For $-b \leq x \leq 0$, we have $\varphi_c = \varphi_{c,o}$ and the solution becomes

$$\psi_{e,\kappa}(x) = Ce^{\kappa_o x} + De^{-\kappa_o x}, \quad \kappa_\text{o}^2 = \frac{2m_e}{\hbar^2}(\varphi_{c,o} - E_e), \ -b \leq x \leq 0, \tag{5.14}$$

where κ_o is wave number corresponding to energy $\varphi_{c,o} - E_e$. The periodic condition (Brillouin zone boundary) would require that

$$\psi_{e,\kappa}(a \leq x \leq a + b) = \psi_{e,\kappa}(-b \leq x \leq 0)e^{i\kappa(a+b)}. \tag{5.15}$$

We determine the four constants are determined by evaluating the two solutions $\psi_{e,\kappa}$ and their first derivatives $\partial\psi_{e,\kappa}/\partial x$ at $x = 0$ and $x = a$ and setting them equal. These give for $x = 0$ (two equations) and for $x = a$ (two equations)

$$A + B = C + D \tag{5.16}$$

$$i\kappa_1(A - B) = \kappa_\text{o}(C - D) \tag{5.17}$$

$$Ae^{i\kappa_1 a} + Be^{-i\kappa_1 a} = (Ce^{-\kappa_o b} + De^{\kappa_o b})e^{i\kappa(a+b)} \tag{5.18}$$

$$i\kappa_1(Ae^{i\kappa_1 a} - Be^{-i\kappa_1 a}) = \kappa_\text{o}(Ce^{-\kappa_o b} - De^{\kappa_o b})e^{i\kappa(a+b)}, \tag{5.19}$$

where we have referred to the wave number in $0 \leq x \leq a$ as κ_1. Note that, from (5.15), $\psi_{e,\kappa}(a) = \psi_{e,\kappa}(-b)e^{i\kappa(a+b)}$.

The nontrivial solution requires that the determinant of the coefficient matrix of the constants to vanish. This gives the characteristic equation (end-of-chapter problem)

$$\frac{\kappa_o^2-\kappa_1^2}{2\kappa_o\kappa_1}\sinh(\kappa_o b)\sin(\kappa_1 a)+\cosh(\kappa_o b)\cos(\kappa_1 a)=\cos[\kappa(a+b)]. \tag{5.20}$$

This is the eigenfunction (or characteristic equation) for the discrete values of $E_e(\kappa)$. From (5.14) we also have

$$E_e=\frac{\hbar^2\kappa_o^2}{2m_e}+\varphi_{c,o}, \tag{5.21}$$

which is an extension of (2.94).

Now consider a simplified case. For $\kappa_o \gg \kappa_1$ and $\kappa_o b \ll 1$, and for the special limiting case of $b \rightarrow 0$ and $\varphi_{c,o} \rightarrow \infty$, we define

$$\frac{\kappa_o^2 ab}{2}=\frac{m_e ab}{\hbar^2}(\varphi_{c,o}-E_e)\equiv s \quad \text{potential strength } s \text{ is finite.} \tag{5.22}$$

Here s (dimensionless) is the strength of the potential well. For $s=0$, there is no potential, and we have the free electron (Section 2.6.6).

Then using s and these limits, the characteristic equation (5.20) becomes

$$\frac{s}{\kappa_1 a}\sin(\kappa_1 a)+\cos(\kappa_1 a)=\cos(\kappa a),\ b\rightarrow 0,\ \varphi_{c,o}\rightarrow\infty. \tag{5.23}$$

Using the electron energy, the dimensionless wave number is defined as

$$\kappa_1^*=\frac{\kappa_1 a}{\pi}=(\frac{2m_e E_e a^2}{\pi^2\hbar^2})^{1/2}, \quad \text{or } E_e=\frac{\hbar^2\kappa_1^2}{2m_e}. \tag{5.24}$$

This makes (5.23) along with the periodicity at the Brillouin zone boundaries give the constrained characteristic equation

$$\frac{s}{\pi\kappa_1^*}\sin(\pi\kappa_1^*)+\cos(\pi\kappa_1^*)=\cos(\pi\kappa^*),\ \ -1\le\cos(\pi\kappa^*)\le 1,\ \kappa^*=\frac{\kappa a}{\pi}. \tag{5.25}$$

Then only discrete values of κ_1^* are allowed for a given s.

For $s=2$, 6, and 18, the preceding characteristic equation is plotted in Figure 5.4, and the first three areas where the solution exists are highlighted. For example, for $\kappa_1^*=0$, no solution exists. Note that $\kappa_1^{*2}=E_e^*$, i.e.,

$$E_e^*=\frac{2m_e E_e a^2}{\pi^2\hbar^2}=\kappa_1^{*2}. \tag{5.26}$$

Figure 5.5 shows the allowed energies in the $E_e^*(\kappa^*)$ space, where $\kappa^*=0$ is designated as the center and $\kappa^*=1$ is the edge of the first Brillouin zone. The energy gap at the edge of the Brillouin zone is evident.

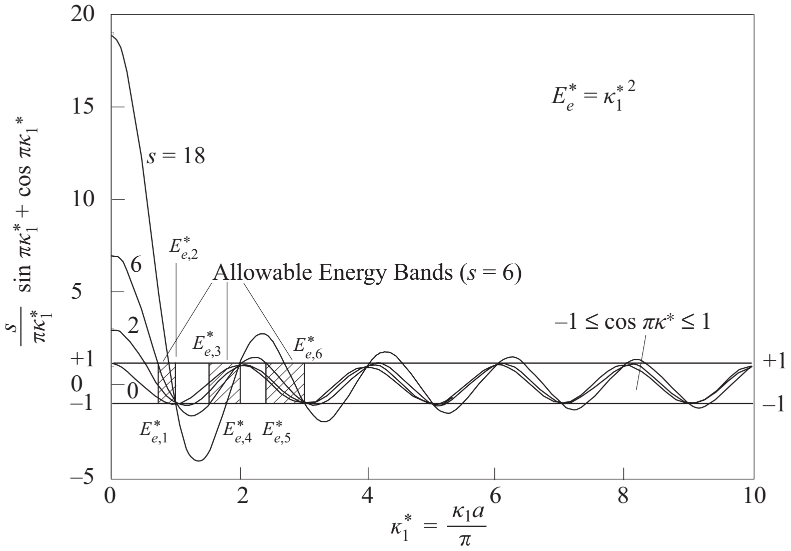

Figure 5.4. The left- and right-hand sides of the characteristic equation, for $s = 2$, 6, and 18. The right-hand side is represented by the bounds (+/−1).

Numerically, the electron energy equation (band structure) is found by solving

$$\frac{s}{\pi E_e^{*1/2}} \sin (\pi E_e^{*1/2}) + \cos (\pi E_e^{*1/2}) = \cos (\pi \kappa^*), \tag{5.27}$$

and allowing for progressively larger eigenvalues E_e^*. So, this replaces (2.94) for $E_e(\boldsymbol{\kappa})$ of the bound electrons. This is the electron dispersion relation.

Note that in this simple model the only parameters are s, m_e, and a. Also, note that to obtain the solution for the free electron, we need to use $s = 0$, and also apply the boundary condition $\psi_{e,\boldsymbol{\kappa}}(0) = \psi_{e,\boldsymbol{\kappa}}(L) = 0$. These would lead to the results given in Section 2.6.5.

The solution for $s = 0$ is also shown in Figures 5.4 and 5.5. The parabolic relation between E_e^* and κ^*, (2.94), is evident in Figure 5.5. Also note some similarity between the electron energy of Figure 5.5 and the phonon energy of Figure 4.3, including energy gaps.

5.3 Three-Dimensional Bands Using Tight-Binding Approximation

In semiconductors the valence atomic electrons in s and p orbitals, when brought together in a crystal, become perturbed. The core electrons are not perturbed much and perturbed outer orbitals are presented with the atomic orbitals as their basis in the tight-binding approximation reviewed here.

In the tight-binding method, the energy eigenstates of (5.7) are determined near the band edges, using the outermost (highest principal quantum number) orbitals, thus excluding those electrons tightly bound to their nuclei. In particular,

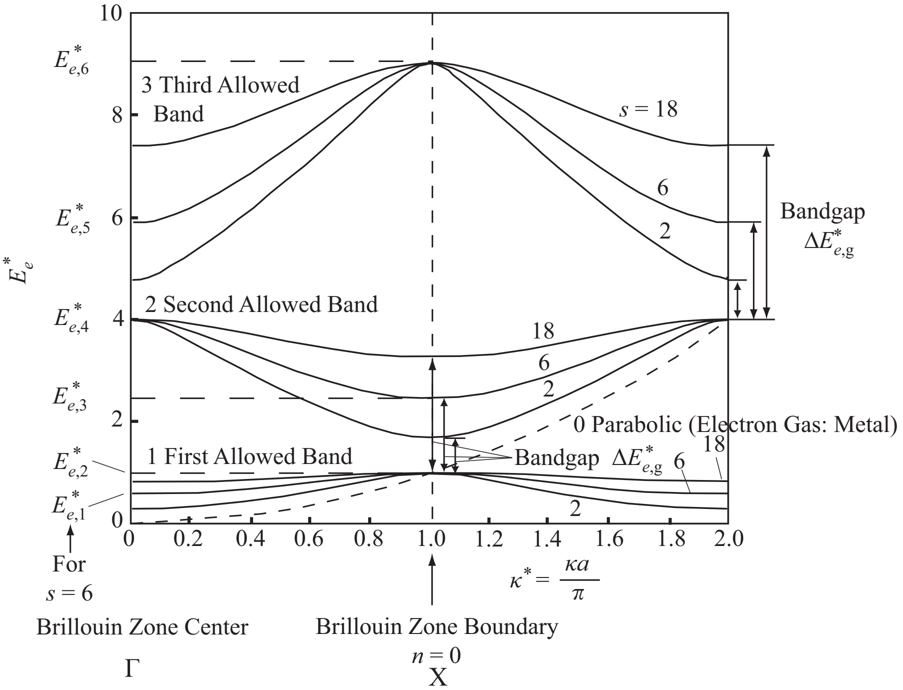

Figure 5.5. The Kronig-Penny electron dispersion relation. The first three electronic bands and the first two bandgaps for the limit ($b \to 0$) square potential with linear, atomic chain. The results are for $s = 2$, 6, and 18. The electron gas model is also shown.

when this assumption is used along with the linear combination of the atomic orbitals (LCAO) to the energy eigenstates, it makes for a simplified treatment for the semiconductors [433].

5.3.1 General LCAO

As we did for the hydrogenlike isolated atoms in Section 2.6.7 for an isolated atom with an electronic structure, we use the Hamiltonian $\mathrm{H_o}$ ($\mathrm{H_o} = -\hbar^2\nabla^2/2m_e + \varphi_e$, where φ_e is the Coulombic potential) and represent the eigenstates of the time-independent Schrödinger equation by

$$\mathrm{H_o}\psi_{e,n} = E_{e,n}\psi_{e,n} \quad n = 1, 2, \ldots, N \text{ for orbitals of isolated atom,} \tag{5.28}$$

where N is the number of atoms. The crystal is now made of these atoms with a known atomic electronic structure represented by $\psi_{e,n}$ [i.e., (2.113)].

The LCAO methods allow for the construction of crystal wave function from the preceding relations by use of the Bloch wave form [433]

$$\psi_{e,\boldsymbol{\kappa}}(\boldsymbol{x}) = \sum_{n,\boldsymbol{x}_\mathrm{o}} \psi_{e,n}(\boldsymbol{x} - \boldsymbol{x}_\mathrm{o})e^{i(\boldsymbol{\kappa}\cdot\boldsymbol{x})} = \sum_{n,x_\mathrm{o}} \phi(\boldsymbol{x} - \boldsymbol{x}_\mathrm{o})e^{i(\boldsymbol{\kappa}\cdot\boldsymbol{x})}, \tag{5.29}$$

where $\boldsymbol{x}_\mathrm{o}$ is the center of orbital n, and the basis function ϕ is constructed with the atomic eigenfunctions, i.e.,

$$\phi(\boldsymbol{x}) = \sum_{n=1}^{N} a_n \psi_{e,n}(\boldsymbol{x}). \tag{5.30}$$

The following steps are for the determination of constant a_n.

The perturbation Hamiltonian is due to the neighboring atoms $\mathrm{H}' = \varphi_c$, where φ_c is the crystal potential, thus we have

$$\mathrm{H} = \mathrm{H}_\mathrm{o} + \mathrm{H}'(\boldsymbol{x}), \tag{5.31}$$

or using (5.1), we have

$$(\mathrm{H}_\mathrm{o} + \mathrm{H}')\psi_{e,\boldsymbol{\kappa}} = E_e(\boldsymbol{\kappa})\psi_{e,\boldsymbol{\kappa}}. \tag{5.32}$$

Because $\psi_{e,n}$ functions are orthogonal, by multiplying by $\psi^{\dagger}_{e,m}$ and integrating, we have

$$\int \psi^{\dagger}_{e,m}\{[\mathrm{H}_\mathrm{o} + \mathrm{H}'] \sum_{n,\boldsymbol{x}_\mathrm{o}} a_n \psi_{e,n}(\boldsymbol{x} - \boldsymbol{x}_\mathrm{o}) e^{i(\boldsymbol{\kappa}\cdot\boldsymbol{x})}$$
$$- E_e(\boldsymbol{\kappa}) \sum_{n,\boldsymbol{x}_\mathrm{o}} a_n \psi_{e,n}(\boldsymbol{x} - \boldsymbol{x}_\mathrm{o}) e^{i(\boldsymbol{\kappa}\cdot\boldsymbol{x})}\}\mathrm{d}\boldsymbol{x} = 0. \tag{5.33}$$

The result is (seperating $\boldsymbol{x}_\mathrm{o} = 0$, and $\boldsymbol{x}_\mathrm{o} \neq 0$ terms)

$$[E_e(\boldsymbol{\kappa}) - E_{e,m}]a_m = -[E_e(\boldsymbol{\kappa}) - E_{e,m}] \sum_{n=1}^{N} a_m$$
$$\times [\sum_{\boldsymbol{x}_\mathrm{o}\neq 0} \int \psi^{\dagger}_{e,m}(\boldsymbol{x}) \psi_{e,n}(\boldsymbol{x} - \boldsymbol{x}_\mathrm{o}) e^{i(\boldsymbol{\kappa}\cdot\boldsymbol{x}_\mathrm{o})}\mathrm{d}\boldsymbol{x}]$$
$$+ \sum_{n=1}^{N} a_n \int \psi^{\dagger}_{e,m}(\boldsymbol{x}) \mathrm{H}'(\boldsymbol{x}) \psi_{e,n}(\boldsymbol{x})\mathrm{d}\boldsymbol{x}$$
$$+ \sum_{n=1}^{N} a_m \sum_{\boldsymbol{x}_\mathrm{o}\neq 0} \int \psi^{\dagger}_{e,m}(\boldsymbol{x}) \mathrm{H}'(\boldsymbol{x}) \psi_{e,n}(\boldsymbol{x} - \boldsymbol{x}_\mathrm{o}) e^{i(\boldsymbol{\kappa}\cdot\boldsymbol{x}_\mathrm{o})}\mathrm{d}\boldsymbol{x}, \tag{5.34}$$

where

$$E_{e,m}\delta_{mn} = \int \psi^{\dagger}_{e,m}(\boldsymbol{x}) \mathrm{H}_\mathrm{o} \psi_{e,n}\mathrm{d}\boldsymbol{x}, \quad \delta_{nm} = \int \psi^{\dagger}_{m}(\boldsymbol{x}) \psi_{n}(\boldsymbol{x})\mathrm{d}\boldsymbol{x}, \tag{5.35}$$

which is of the form given in (5.9). Here δ_{mn} is the Kronecker delta. Note that $\int \psi^{\dagger}_{e,m}(\boldsymbol{x}) \psi_{e,n}(\boldsymbol{x} - \boldsymbol{x}_\mathrm{o}) \neq \delta_{mn}$, for $\boldsymbol{x}_\mathrm{o} \neq 0$.

In the tight-binding approximation, the first integral term on the right-hand side of (5.34) is set to zero by assuming negligible overlap between neighboring atomic wave functions, i.e., atomic functions are tightly bound to atoms [433].

For most potentials, the second integral term also vanishes [433].

The preceding equation is solved for the eigenvalues $E_e(\boldsymbol{\kappa})$, and is a set of $N \times N$ coupled equations. Also, for each $\boldsymbol{\kappa}$, there are N solutions, which provide the N-band E_e-$\boldsymbol{\kappa}$ structure.

5.3.2 Example of Tight-Binding Approximation: FCC, Single s-Band

As an example, consider a monoatomic crystal with a single orbital s. Cu for example, has a 4s electron in its outmost orbital. Because there is only one energy level, $\{a_m\} = 0$, except for the coefficient, $a_s = 1$. Then (5.34) is only one equation, i.e.,

$$E_e(\boldsymbol{\kappa}) - E_s = \int \psi^\dagger_{e,s}(\boldsymbol{x})\mathrm{H}'(\boldsymbol{x})\psi_{e,s}(\boldsymbol{x})\mathrm{d}\boldsymbol{x}$$

$$+ \sum_{\boldsymbol{x}_\mathrm{o} \neq 0} \int \psi^\dagger_{e,s}(\boldsymbol{x})\mathrm{H}'(\boldsymbol{x})\psi_{e,s}(\boldsymbol{x} - \boldsymbol{x}_\mathrm{o})e^{i(\boldsymbol{\kappa}\cdot\boldsymbol{x}_\mathrm{o})}\mathrm{d}\boldsymbol{x}. \quad (5.36)$$

This is written as

$$E_e(\boldsymbol{\kappa}) = E_s - \beta_s - \sum_{\boldsymbol{x}_\mathrm{o}} \gamma(\boldsymbol{x})e^{i(\boldsymbol{\kappa}\cdot\boldsymbol{x}_\mathrm{o})}, \quad (5.37)$$

where using the periodic crystal potential $\mathrm{H}' = \varphi_c$, we have

$$\beta_s \equiv - \int \psi^\dagger_{e,s}(\boldsymbol{x})\mathrm{H}'(\boldsymbol{x})\psi_{e,s}(\boldsymbol{x})\mathrm{d}\boldsymbol{x} \quad (5.38)$$

$$\gamma(\boldsymbol{x}_\mathrm{o}) \equiv - \int \psi^\dagger_{e,s}(\boldsymbol{x})\varphi_c(\boldsymbol{x})\psi_{e,s}(\boldsymbol{x} - \boldsymbol{x}_\mathrm{o})\mathrm{d}\boldsymbol{x} \ \ \text{overlap energy integral.} \quad (5.39)$$

The wave function for $\psi_{e,1s}$ and $\psi_{e,2s}$ are listed in Table 2.10. Here β_s and γ can be treated as given constants, and then it becomes clear that, because of $\exp[i(\boldsymbol{\kappa} \cdot \boldsymbol{x}_\mathrm{o})]$, thecontribution from other than the nearest neighbors may be neglected. Also note that $\gamma(\boldsymbol{x}_\mathrm{o}) = \gamma(-\boldsymbol{x}_\mathrm{o})$.

For example, for the FCC crystals, the 12 nearest neighbors around the atom at $\boldsymbol{x} = 0$ are given by (4.33), i.e.,

$$\boldsymbol{x}_\mathrm{o} = a(\pm 0.5, \pm 0.5, 0);\ a(\pm 0.5, 0, \pm 0.5);\ a(0, \pm 0.5, \pm 0.5), \quad (5.40)$$

and the first Brillouin zone designations for FCC are shown in Figure 4.6(d).

Then the electron energy equation (or scalar equation) (5.36) becomes

$$\begin{aligned} E_e(\boldsymbol{\kappa}) &= E_s - \beta_s - \gamma \sum e^{i(\boldsymbol{\kappa}\cdot\boldsymbol{x}_\mathrm{o})} \\ &= E_s - \beta_s - \gamma[e^{ia(\kappa_x+\kappa_y)/2} + e^{ia(\kappa_x-\kappa_y)/2} + e^{ia(-\kappa_x+\kappa_y)/2} + e^{ia(-\kappa_x-\kappa_y)/2} + \ldots] \\ &= E_s - \beta_s - 4\gamma[\cos(\frac{a\kappa_x}{2})\cos(\frac{a\kappa_y}{2}) + \cos(\frac{a\kappa_y}{2})\cos(\frac{a\kappa_z}{2}) \\ &\quad + \cos(\frac{a\kappa_z}{2})\cos(\frac{a\kappa_x}{2})],\ -\frac{2\pi}{a} \le \kappa_i \le \frac{2\pi}{a}\ \text{(first Brillouin zone).} \end{aligned} \quad (5.41)$$

Figure 5.6(a) shows the variation of $E_e(\boldsymbol{\kappa})$ along the $\boldsymbol{\kappa}$ space L–Γ–X–K–Γ–W. This is a typical presentation of the band structure (having only one band s). The results are for $\gamma = 1.0$ eV and $E_s - \beta_s = 0$, and the width of the band is 16γ.

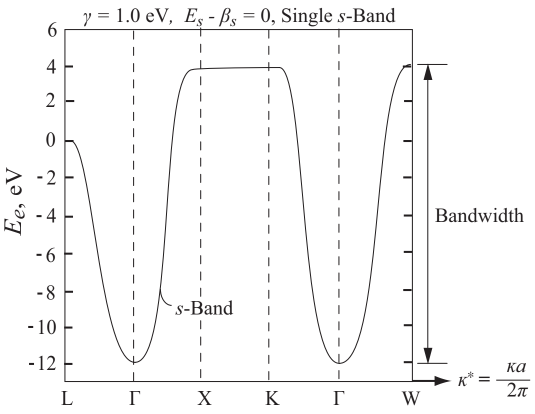

(a) Predicted for a single s-Band Using Tight-Binding Approximation

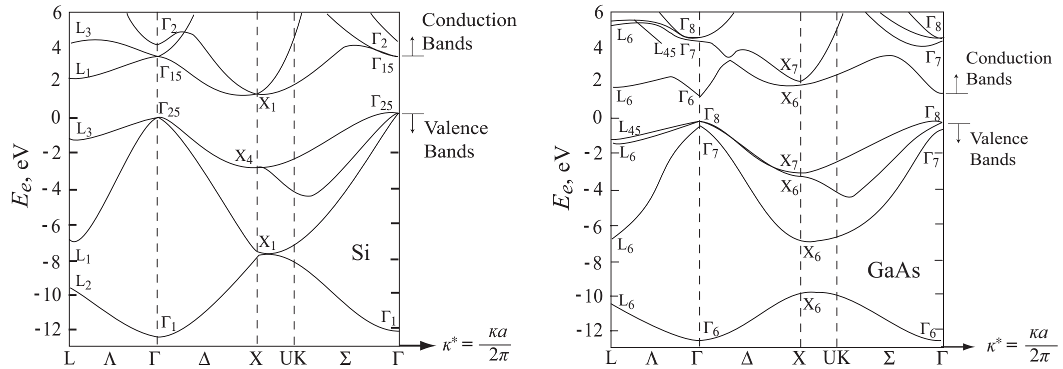

(b) Full-Band Structure of Si(Indirect Bandgap)

(c) Full-Band Structure of GaAs(Direct Bandgap)

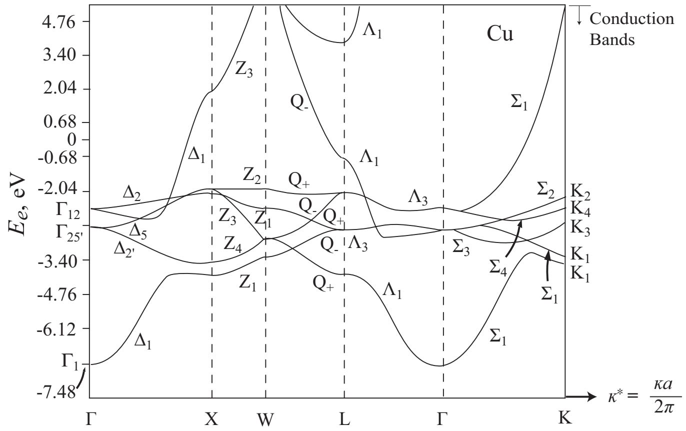

(d) Full-Band Structure of Cu

Figure 5.6. Predicted electron-band structure for (a) an idealized s-band model (tight-binding approximation) and full bands of (b) Si (indirect bandgap) [433], (c) GaAs (direct bandgap) [433], and (d) Cu (overlapped bands resulting in conduction (delocalized) electrons) [67] at $T = 300$ K.

This constant-energy surface in $\{\kappa_x, \kappa_y, \kappa_z\}$ space or the reciprocal lattice is the Fermi surface. The constant-energy surface for (5.41) can be shown in the $\boldsymbol{\kappa}$-space and is an end-of-chapter problem.

Near the zone center Γ, where $\kappa_x = \kappa_y = \kappa_z$ and $\kappa a \ll 1$ (small κ), (5.41) becomes (end-of-chapter problem)

$$E_e(\boldsymbol{\kappa}) = E_s - \beta_s - 12\gamma + \gamma a^2 \kappa^2,$$

$$\text{parabolic energy relation for } \kappa a \ll 1, \text{ for electron in a crystal,} \tag{5.42}$$

compared with the free-electron energy (Section 2.6.4), i.e.,

$$E_e(\boldsymbol{\kappa}) = E_e(\boldsymbol{p}) = E_{e,0} + \frac{\hbar^2\kappa^2}{2m_e} \quad \text{parabolic energy relation for electron gas,} \tag{5.43}$$

which provides the parabolic model for small κ.

Based on this, the effective electron mass $m_{e,e}$ [will be defined in (5.45] is defined as $\hbar^2/2\gamma a^2$.

Note that the overlap energy integral γ (has units of energy through φ_c) depends on a. Also note that Cu has a FCC structure and atomic orbital of (Table A.2) [Ar] $3d^{10}4s^1$, and the s-band in Figure 5.6(a) has similar Γ-point behavior as Figure 5.6(d).

The preceding example can now be generalized. By combining (5.29) and (5.30), the wave function is written as

$$\psi_{e,\boldsymbol{\kappa}}(\boldsymbol{x}) = \sum_{\boldsymbol{x}_i}\sum_{m=1}^{N_o}\sum_{j=1}^{N_a} a_{m,j}(\boldsymbol{\kappa})\phi_{m,j}(\boldsymbol{x} - \boldsymbol{x}_j - \boldsymbol{x}_{o,i})e^{i(\boldsymbol{\kappa}\cdot\boldsymbol{x}_{o,i})}, \tag{5.44}$$

where the sum is over the unit cells, m is for the different atomic functions $\phi_{m,j}$ (up to N_o orbitals) used as the basis, and j is the atoms in each unit cell (up to N_a atoms).

The Hubbard model [205] improves on the tight-binding model, and describes the transition between conductor and insulator. In this model the Hamiltonian has a kinetic term (allowering for hopping or tunneling) and a potential term for the on-site interactions (not included in tight binding).

5.4 *Ab Initio* Computation of Electron Band Structure

Amongst methods for calculation of the electronic band structures are the nearly free-electron model [298], tight-binding method [12, 433], Green function [12, 254], orthogonalized plane wave method [101, 189], and pseudopotentials [12, 101, 258]. When the unit cell contains a large number of atoms, only the density functional theory (DFT) offers sufficient accuracy and computational efficiency. DFT is based on one-to-one correspondence between the ground-state density of a many-electron system and the external potential. The accuracy of this method depends on the relation between the energy of the electrons and their density. The most accurate approximation is the generalized gradient approximation (GGA). The combination of GGA, full-potential, linearized augmented plane-wave (LAPW), and local orbits

(LO) methods, leads to the most accurate scheme for the band structure calculation, which is an all-electron scheme (including relativistic effects) [101]. This method is used in an available computer program WIEN2k [101, 43] and is widely tested. Figure 5.7(a) shows the band structure of CoSb$_3$, a high-temperature thermoelectric material, and its structure is also shown in Figure 5.7(b), calculated using WIEN2k. The input data is given in the footnotes.[†]

[†] I. Input crystal structure

- (1) Click "Execution StructGen$^{\text{TM}}$" to start the struct-file generator
- (2) Input the configuration of atoms as given in table below

Title	CoSb3
Lattice	204_Im-3
a	9.0385 Å(select the Ang button)
b	9.0385 Å
c	9.0385 Å
α, β, γ	90^o, 90^o, 90^o
Atom	Co, enter position (0.25, 0.25, 0.25)
Atom	Sb, enter position (0.0, 0.3351, 0.1602)

- (3) Save structure.
- (4) Click "save file and clean up"

II. Initialize the calculation

- (1) Click "Execution initialize calc"
- (2) Click "x nn" (use "2" for nn-band length factor)
- (3) Click "view outputnn" (don't change any parameter)
- (4) Click "x sgroup"
- (5) Click "View outputsgroup". Do not use the struct-file generated by "sgroup"
- (6) Click "x symmetry"
- (7) Click "copy struct_st"
- (8) Click "x lstart" [use "GGA (Perdew-Burke-Ernzerhof96)" for exchange correlation potential and "- 6.0 Ry" for energy to separate core and valence states]
- (9) Click "view outputst"
- (10) Click "check CoSb3.in1_st"
- (11) Click "check CoSb3.in2_st"
- (12) Click "check CoSb3.inm_st"
- (13) Click "Prepare input files"
- (14) Click "x kgen". Use 3000 for the k-mesh, and choose "Yes" to shift mesh
- (15) Click "view CoSb3.klist"
- (16) Click "x dstart"
- (17) Click "view CoSb3.outputd"
- (18) Do not perform spin-polarized calculation
- (19) Click "Continue with SCF"

III. Submit the calculation and start SCF cycle (for convergence criteria, choose 0.001 Ry for energy, 1 mRy/au for force, and 0.0001 e_c for charge)

IV. Calculate band structure.

- (1) Click "Band Structure" in "Tasks" menu
- (2) Click "Create CoSb3.klist_band"
- (3) Click "x lapw1 -band" to Calculate eigenvalues
- (4) Edit CoSb3.insp. Select an energy range from -2.0 to 2.0 eV, and set Fermi energy to be 0.56372 Ry (this is slightly different from the value calculated by the program)
- (5) Click "x spaghetti" to calculate band structure
- (6) Plot band structure (needs "ghostscript" installed).

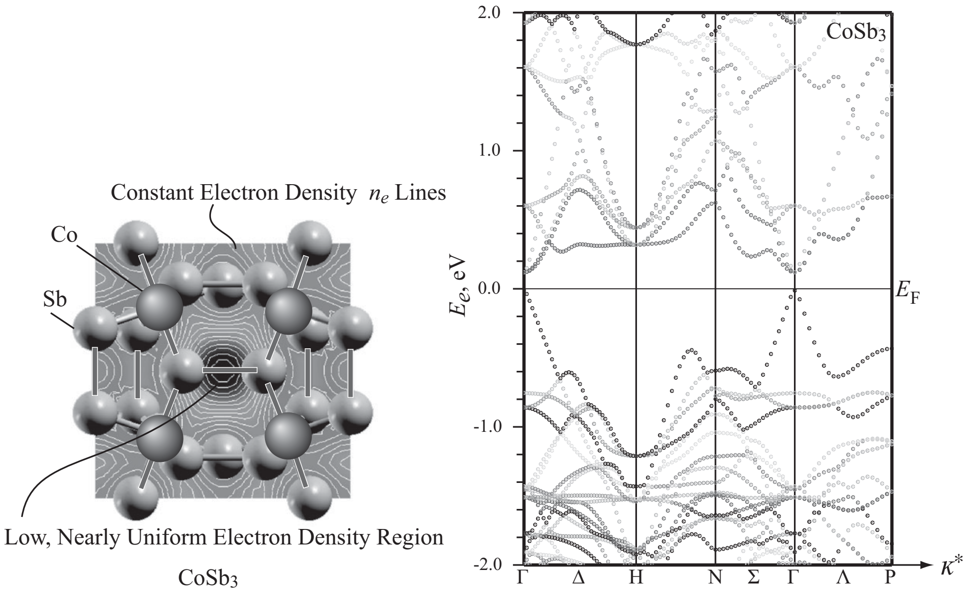

(a) (b)

Figure 5.7. (a) Atomic structure of $CoSb_3$. The constant electron density lines in a unit cell are also shown. (b) Calculated band structure of $CoSb_3$, using WIEN2k.

WIEN2k can also take into account the spin–orbit coupling, which is important for calculations of valence band structure and bandgap, especially for heavy atoms [44, 101].

Another program using GGA is VASP, which uses the pseudopotentials to deal with the core electrons. Since VASP only needs to deal explicitly with the valence electrons (rather than full electrons as in WIEN2k), VASP is much more efficient and can handle much larger system. Though VASP makes a pseudopotential approximation, its accuracy is acceptable and similar to that of the LAPW method in many cases [44, 257, 197]. In general, WIEN2k is suitable for the accurate investigation of small systems, while for large systems VASP is suggested because of its high efficiency.

5.5 Electron Band Structure for Semiconductors and Effective Mass

The electrons in the periodic potential of a crystal are represented by the eigenvalue wave functions in $\boldsymbol{\kappa}$-space. These energy-states that are periodic in $\boldsymbol{\kappa}$-space are separated by certain energy gaps or forbidden energy regions (energies not reached by any real $\boldsymbol{\kappa}$).

This electron band structure $E_{e,n}(\boldsymbol{\kappa})$ found from (5.7) depends on the constituent atoms (their electrical orbits). The semiconductors have the most complex band structures. Table A.2 (perodic table) gives the electron orbits, and for example Si has a $1s^2 2s^2 2p^6 3s^2 3p^2$ electron structure and the last $s-$ and $p-$orbit do tend to influence the bandgaps separating the valence and conduction bands [Figure 5.1(b)].

Each band has $2N$ (because of spin degeneracy) allowed $\boldsymbol{\kappa}$ states and each unit cell (basis) in the crystal contributes electrons to these states.

Figures 5.6(a) and (b) show the predicted electron band structures for Si and GaAs, respectively. There are four valance bands ($E_{e,v} \leq 0$) for Si and three conduction bands. There are many band overlaps. Figure 5.6(c) shows the band structure for Cu. Note the lack of bandgap in Cu.

The three-dimensional eigenfunction $E_e(\boldsymbol{\kappa})$ for semiconductors is rather complex, and therefore simplification is made in their presentation. Figure 5.8(a) shows the model band structure for diamond and zinc-blende crystals (e.g., Si, GaAs). For them, the conduction band has three minima, namely at $\Gamma(\boldsymbol{\kappa} = 0)$, at L (along the $\langle 111 \rangle$ direction at boundary of the first Brillouin zone), and at Δ (along the Δ line). The modal semiconductor also has three valence bands, each having a maximum at $\boldsymbol{\kappa} = 0$, and one is split-off by the spin–orbit interaction [294].

The $\boldsymbol{\kappa}$-space designation for the first Brillouin zone is given in Figure 5.8(b), for FCC lattice. More complete designations are given in Section 4.3.

Figure 5.8(c) shows the six valleys (constant-energy surfaces) in the E_e-$\boldsymbol{\kappa}$-space of Figure 5.6(b), for Si. Note that none of these valleys is located on the Brillouin zone edges. With phonon-induced transitions (scatterings), conduction electrons can transit between these valleys (intervalley scattering). This will be discussed in Section 5.15.3.

In the periodic electron gas treatment of Section 2.6.5, the electron energy dispersion was presented by the wave-number parabolic relation (2.94). Using the parabolic band model, an effective electron mass is defined as the electron kinetic energy (as a function of wave number) expressed through the Taylor series expansion as

$$E_{e,k}(\boldsymbol{p}) = E_{e,k}(\boldsymbol{\kappa}) = E_e(0) + \left.\frac{\partial E_e(\kappa)}{\partial \kappa}\right|_{\kappa=0} \kappa + \left.\frac{\partial^2 E_e(\kappa)}{\partial \kappa^2}\right|_{\kappa=0} \frac{\kappa^2}{2} + \cdots +$$

$$\equiv E_e(0) + \frac{\hbar^2 \kappa^2}{2m_{e,e}}, \quad m_{e,e} \equiv \frac{\hbar^2}{\left.\dfrac{\partial^2 E_e(\kappa)}{\partial \kappa^2}\right|_{\kappa=0}}$$

$$\text{effective mass in parabolic energy band,} \tag{5.45}$$

where the first derivative $\partial E_e(\kappa)/\partial\kappa|_{\kappa=0} = 0$ because of assumed symmetry and $m_{e,e}$ is the effective electron mass (which can be smaller or larger than the electron mass m_e).

Then for a direct gap (when the minimum of conduction electron and maximum of valence electron occur at $\boldsymbol{\kappa} = 0$), we can use the parabolic dispersion (2.97) approximation, i.e.,

$$E_e(\boldsymbol{\kappa}) = \pm\frac{\hbar^2|\boldsymbol{\kappa}|^2}{2m_{e,e}}, \quad + \text{conduction}, \ - \text{valence}, \ \text{band at } \Gamma, \ \text{direct band}, \tag{5.46}$$

which represents a band as a spherical energy surface (but is called parabolic) in $\boldsymbol{\kappa}$-space. This single effective mass indicates an isotropic E_e-$\boldsymbol{\kappa}$.

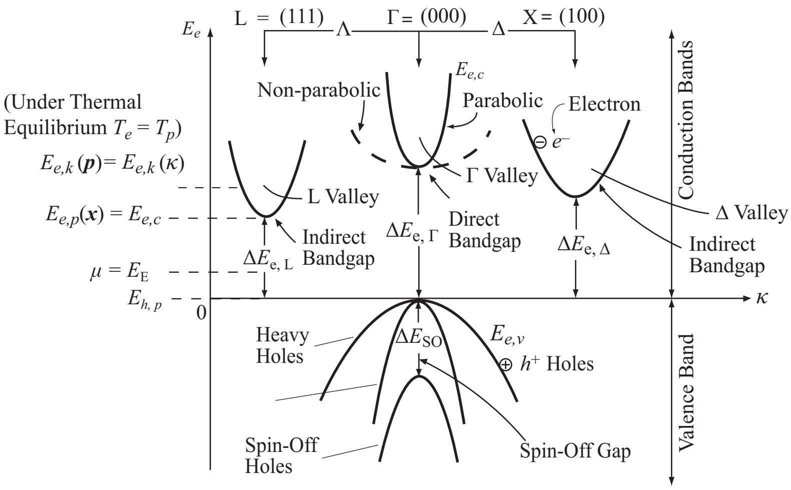

(a) Zinc-Blende Semiconductor Electron Band Structure Model (Parabolic Bands)

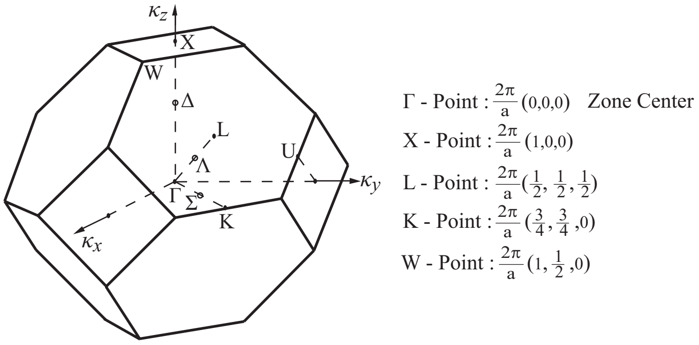
κ_z
X
W
Δ
L
Λ
U
Γ
Σ
K
κ_x
κ_y
Γ - Point : $\frac{2\pi}{a}(0,0,0)$ Zone Center
X - Point : $\frac{2\pi}{a}(1,0,0)$
L - Point : $\frac{2\pi}{a}(\frac{1}{2},\frac{1}{2},\frac{1}{2})$
K - Point : $\frac{2\pi}{a}(\frac{3}{4},\frac{3}{4},0)$
W - Point : $\frac{2\pi}{a}(1,\frac{1}{2},0)$

(b) First Brillouin Zone for Face-Centered Cubic (Zinc-Blende) Lattice

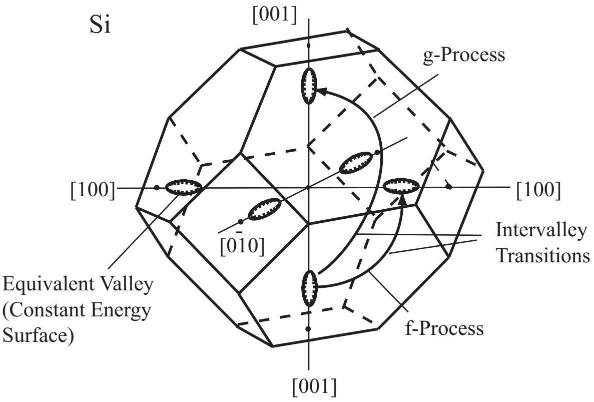

(c) Equivalent Valley in Conduction Bands of Si and Intervalley Transitions

Figure 5.8. (a) Model electronic band structure for diamond and zinc-blende crystal semiconductor. The kinetic energy $E_{e,k}(\boldsymbol{p}) = E_{e,k}(\boldsymbol{\kappa})$ and potential energy $E_{e,p}(\boldsymbol{x})$ and valleys are also shown. (b) Standard notation for labeling high-symmetry lines and points in FCC lattice Brillouin zone [294]. (c) Six equivalent valleys (constant-energy surfaces) in the conduction bands of Si (the f and g intervalley scatterings are also shown) [294].

Table 5.1. *Model band parameters of common cubic semiconductors [433] at $T = 300$ K. $m_{e,e}$ is for parabolic and $m_{e,e,\mathrm{L}}$ and $m_{e,e,\mathrm{T}}$ are for ellipsoidal band (dispersion) models. The crystal structure is also listed. DIM (diamond), ZB (zinc blende), SP (sphalerite), and (–) indicates unusual structure.*

Compound	Crystal structure	$\Delta E_{e,\Gamma}$, eV	$\Delta E_{e,L}$, eV	$\Delta E_{e,\Delta}$, eV	ΔE_{SO}, eV	$\frac{m_{e,e}}{m_e}$	$\frac{m_{e,e,\mathrm{L}}}{m_e}$	$\frac{m_{e,e,\mathrm{T}}}{m_e}$
C	DIM	11.67	12.67	5.45	0.006	–	1.4	0.36
Si	DIM	4.08	1.87	1.13	0.044	–	0.98	0.19
Ge	DIM	0.89	0.76	0.96	0.29	–	1.64	0.082
AlSb	ZB	2.5	2.39	1.6	0.75	–	1.64	0.23
GaP	ZB	2.7	2.7	2.2	0.08	–	1.12	0.22
GaAs	ZB	1.42	1.71	1.90	0.34	0.067	–	–
GaSb	SP	0.67	1.07	1.30	0.77	0.045	–	–
InP	ZB	1.26	2.0	2.3	0.13	0.080	–	–
InAs	ZB	0.35	1.45	2.14	0.38	0.023	–	–
InSb	ZB	0.23	0.98	0.73	0.81	0.014	–	–
ZnS	ZB	3.8	5.3	5.2	0.07	0.28	–	–
ZnSe	ZB	2.9	4.5	4.5	0.43	0.14	–	–
ZnTe	ZB	2.56	3.64	4.26	0.92	0.18	–	–
CdTe	ZB	1.80	3.40	4.32	0.91	0.098	–	–

Then the electron group velocity (4.15) is

$$\boldsymbol{u}_{e,g} = \frac{1}{\hbar}\nabla_{\kappa}(\boldsymbol{\kappa})E_e(\boldsymbol{\kappa}) = \frac{\hbar\boldsymbol{\kappa}}{m_{e,e}}, \tag{5.47}$$

and the momentum is (de Broglie relation)

$$\boldsymbol{p} = \hbar\boldsymbol{\kappa} = m_{e,e}\boldsymbol{u}_{e,g} \quad \text{de Broglie relation.} \tag{5.48}$$

For indirect bandgap, for bands at L and along Δ, the ellipsoidal dispersion of(5.45) is given by

$$E_{e,k}(\boldsymbol{p}) = E_e(\boldsymbol{\kappa}) = \frac{\hbar^2}{2}\left(\frac{\kappa_{\mathrm{L}}^2}{m_{e,e,\mathrm{L}}} + \frac{\kappa_{\mathrm{T}}^2}{m_{e,e,\mathrm{T}}}\right)$$

$$\text{ellipsoidal energy dispersion model at L and along } \Delta, \text{ in direct band.} \tag{5.49}$$

Table 5.1 gives the model band parameters of common cubic semiconductors. For the ellipsoidal bands, the conduction band is flatter (larger effective mass) and thus have a larger DOS (to be shown in Section 5.7). For Si, a single effective mass of 1.08 m_e is used for electrons.

As an approximation a single wave vector is also used with a correction for high energies, called the Kane model [294],

$$E_e(\boldsymbol{\kappa})[1 + \frac{E_e(\boldsymbol{\kappa})}{\Delta E_{e,g}}] = \pm\frac{\hbar^2\kappa^2}{2m_{e,e,\mathrm{o}}} \quad \text{nonparabolic dispersion model,} \tag{5.50}$$

where $m_{e,e,\mathrm{o}}$ is the DOS average effective mass equal to $(m_{e,e,\mathrm{L}}m_{e,e,\mathrm{T}}^2)^{1/3}$.

We will further discuss the Kane model (including relaxation times) in Section 5.17.3, in connection with thermoelectric property predictions.

As will be shown, when using the BTE, it is more convenient to use $E_e(\boldsymbol{p})$ in place of $E_e(\boldsymbol{\kappa})$ by using (5.48) for the convection term.

The bandgap energy $\Delta E_{e,g}$ is temperature dependent (for most semiconductors, decreases with increase in temperature; exceptions include PbTe). Empirical relations such as $\Delta E_{e,g}(T) = \Delta E_{e,g} - aT^2/(T+b)$ are used. For Si and the Δ bandgap, $a = 0.473 \times 10^{-3}$ eV/K, and $b = 636$ K. As will be discussed, Table 5.6 includes some data on $\Delta E_{e,g}$ at 0 and 300 K.

5.6 Periodic Electron Gas Model for Metals

The Fermi surface separates the occupied from unoccupied levels. Then the Fermi momentum $\hbar\kappa_{\rm F} = p_{\rm F}$ and its energy $E_{\rm F}$, is the highest occupied energy level. As we discussed in Section 2.6.5, the Fermi wave vector is given by (2.101) as $\kappa_{\rm F} = (3n_{e,c}\pi^2)^{1/3}$, where $n_{e,c}$ is the number density of conduction electrons. The Fermi velocity is $u_{\rm F} = p_{\rm F}/m_e$.

The Fermi energy is defined through (2.94) and number density from (1.19), i.e.,

$$E_{\rm F} \equiv \frac{\hbar^2\kappa_{\rm F}^2}{2m_e} \quad \text{parabolic energy dispersion relation for metals} \tag{5.51}$$

$$n_{e,c} = \int_0^\infty D_e(E_e) f_e {\rm d}E_e. \tag{5.52}$$

For metals, $n_{e,c}$ is found directly from the number of conduction (delocalized) electrons and is independent of temperature, i.e., (2.103). For semiconductors, $n_{e,c}$ depends on temperature and on $E_{\rm F}$, as we will show in Section 5.7, or if $n_{e,c}$ and T are known, $E_{\rm F}$ is determined. Using $D_e(E_e) = {\rm d}n_{e,c}/{\rm d}E_e = 3n_{e,c}/2E_e = 2^{1/2}m_e^{3/2}E_e^{1/2}/(\pi^2\hbar^3)$ (end-of-chapter problem).

For metals using (1/17), we have [Figure 2.17(c)]

$$\begin{aligned} n_{e,c} &= \int_0^\infty D_e(E_e) f_e^{\rm o} {\rm d}E_e = nz_e, \quad D_e(E_e) = \frac{m_e\kappa_{\rm F}}{\pi^2\hbar^2} = \frac{2^{1/2}m_e^{3/2}E_e^{1/2}}{\pi^2\hbar^3} \\ &= \int_0^{E_{\rm F}} D_e {\rm d}E_e = \frac{1}{3\pi^2}(\frac{2m_e}{\hbar^2}E_{\rm F})^{3/2} \quad \text{metals,} \end{aligned} \tag{5.53}$$

which is the same as (2.101), where z_e is the number of electrons per atom. We have used $f_e^{\rm o} = 1$ for $E_e \le E_{\rm F}$, for $E_{\rm F}/k_{\rm B}T \gg 1$ (Chapter 1 problem). Note that metals have large nz_e, and therefore, large $E_{\rm F}$.

Also note that, by combining (5.53) and (5.53), we have

$$n_{e,c} = \frac{\kappa_{\rm F}^3}{3\pi^2} = nz_e. \tag{5.54}$$

Also from (5.53), we have the Fermi energy for an electron gas

$$E_{\rm F} = \frac{\hbar^2}{2m_e}(3\pi^2 n_{e,c})^{2/3} \quad \text{metals.} \tag{5.55}$$

Table 5.2. *The number of free electrons per atom, free-electron number densities, Fermi energies, Fermi temperatures, Fermi wave numbers, and Fermi velocities, for metals [12]. The crystal structure is also listed, BCC (body-centered cubic), FCC (face-centered cubic), HCP (hexagonal close packed), and (–) indicates unusual structure.*

Element (structure)	z_e	$n_{e,c}$, 10^{28} m^{-3}	E_F, eV	T_F, 10^4 K	κ_F, 10^{10} m^{-1}	u_F, 10^6 m/s
Li (BCC)	1	4.70	4.74	5.51	1.12	1.29
Na (BCC)	1	2.65	3.24	3.77	0.92	1.07
K (BCC)	1	1.40	2.12	2.46	0.75	0.86
Rb (BCC)	1	1.15	1.85	2.15	0.70	0.81
Cs (BCC)	1	0.91	1.59	1.84	0.65	0.75
Cu (FCC)	1	8.47	7.00	8.12	1.36	1.57
Ag (FCC)	1	5.86	5.49	6.38	1.20	1.39
Au (FCC)	1	5.90	5.53	6.42	1.21	1.40
Be (HCP)	2	24.7	14.3	16.6	1.94	2.25
Mg (HCP)	2	8.61	7.08	8.23	1.36	1.58
Ca (FCC)	2	4.61	4.69	5.44	1.11	1.28
Sr (FCC)	2	3.55	3.93	4.57	1.02	1.18
Ba (FCC)	2	3.15	3.64	4.23	0.98	1.13
Nb (BCC)	1	5.56	5.32	6.18	1.18	1.37
Fe (BCC)	2	17.0	11.1	13.0	1.71	1.98
Mn (–)	2	16.5	10.9	12.7	1.70	1.96
Zn (–)	2	13.2	9.47	11.0	1.58	1.83
Cd (–)	2	9.27	7.47	8.68	1.40	1.62
Hg (–)	2	8.65	7.13	8.29	1.37	1.58
Al (FCC)	3	18.1	11.7	13.6	1.75	2.03
Ga (–)	3	15.4	10.4	12.1	1.66	1.92
In (–)	3	11.5	8.63	10.0	1.51	1.74
Tl(HCP)	3	10.5	8.15	9.46	1.46	1.69
Sn (–)	4	14.8	10.2	11.8	1.64	1.90
Pb (FCC)	4	13.2	9.47	11.0	1.58	1.83
Bi (–)	5	14.1	9.90	11.5	1.61	1.87
Sb (–)	5	16.5	10.9	12.7	1.70	1.96

For completeness, we also repeat (2.103), i.e.,

$$n_{e,c} = nz_e = \frac{N_A}{M}\rho z_e \quad \text{metals,} \tag{5.56}$$

where N_A is the Avogadro number, M is the molecular weight, ρ is the density, and z_e is the number of free electrons per atom. This is the number of valence electrons for each atom in the metallic bond (Section 2.1.2). This is related to the *npms* electron becoming delocalized. Table A.2 shows the outmost electron orbitals, and for example, for Cu we have one $4s$ ($4s^1$) electron, while we have two $2s$ ($2s^2$) electrons for Be. Bi and Sb used in thermoelectic compounds, have $z_e = 5$, which is 2 from the s orbital and 3 from the p orbital. This also corresponds to one of the oxidation states listed in Table A.2. Table 5.2 lists z_e, $n_{e,c}$, E_F, T_F, κ_F, and u_F for metals. As we discussed in Section 2.6.4, for $n_{e,c}$ conductive electrons per unit volume, the ground state is formed by occupying all single-particle levels with $\kappa < \kappa_F$ and leaving all levels with $\kappa > \kappa_F$ unoccupied.

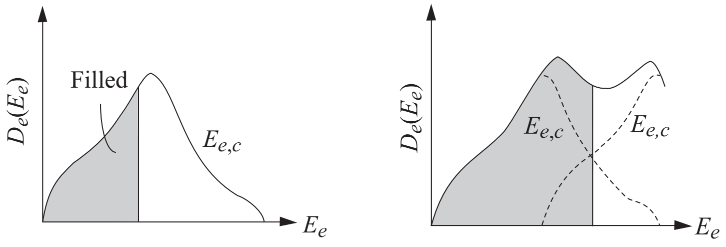

(a) Metal (Single Partially Filled Band) (b) Metal (Overlapping Bands)

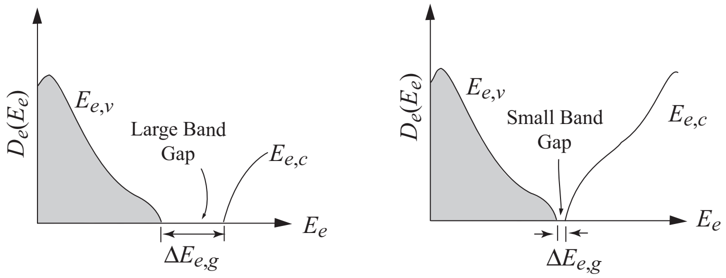

(c) Insulator (d) Semiconductor (Direct Band)

Figure 5.9. Electron DOS $D_e(E_e)$ for metals, insulators, and direct-band semiconductors, at $T = 0$ K [63]. The shaded region shows the filled (occupied) states. Thermal excitation (of the order of $k_B T$) moves the electron across the gap for semiconductors.

Then the Fermi velocity based on E_F and m_e is

$$u_F = \left(\frac{2E_F}{m_e}\right)^{1/2}. \tag{5.57}$$

The Fermi temperature is

$$T_F = \frac{E_F}{k_B}, \tag{5.58}$$

and the Fermi momentum is

$$p_F = 2(m_e E_F)^{1/2}. \tag{5.59}$$

The electron group velocity $\boldsymbol{u}_{e,g}$ is defined similarly to that for phonons (4.15) as

$$\boldsymbol{u}_{e,g} = \frac{1}{\hbar}\nabla_{\boldsymbol{\kappa}} E_e(\boldsymbol{\kappa}) \quad \text{electron group velocity.} \tag{5.60}$$

5.7 Electron/Hole Density of Carrier and States for Semiconductors

The electron DOS $D_e(E_e)$ will allow for determination of the transport properties as well as the electron number density. For metals, insulators, and semiconductors, the general distribution of $D_e(E_e)$ is shown in Figure 5.9 for $T = 0$ K. For metals there is no energy bandgap and for insulators this gap is very large (so all electrons are in the ground state at all temperatures), and for semiconductors at $T = 0$ K all electrons are in the valence band and as the temperature increases more move to the conduction band. The conductive electron density is (5.52)

$$n_{e,c} = \int_0^\infty D_e(E_e) f_e(E_e) \mathrm{d}E_e \equiv \sum_{\boldsymbol{\kappa}} f_e[E_e(\boldsymbol{\kappa})]. \tag{5.61}$$

The electron equilibrium distribution function f_e^{o} is given in Table 1.2.

For a general treatment of electrons, the electron energies $E_e(\boldsymbol{x}, \boldsymbol{p})$ is the sum of the potential and kinetic energy, $E_{e,p}(\boldsymbol{x})$ and $E_{e,k}(\boldsymbol{p})$, and using the Fermi energy in place of the chemical potential μ, we have [294]

$$\begin{aligned} f_e^{\mathrm{o}} &= \frac{1}{\exp[\dfrac{E_e(\boldsymbol{x}, \boldsymbol{p}) - \mu}{k_{\mathrm{B}}T}] + 1}, \quad \mu = E_{\mathrm{F}} \\ &= \frac{1}{\exp[\dfrac{E_{e,p}(\boldsymbol{x}) + E_{e,k}(\boldsymbol{p}) - E_{\mathrm{F}}}{k_{\mathrm{B}}T}] + 1}, \quad E_e = E_{e,p}(\boldsymbol{x}) + E_{e,k}(\boldsymbol{p}), \end{aligned} \tag{5.62}$$

where $\mu = E_{\mathrm{F}}$.[†]

The potential energy $E_{e,p}(\boldsymbol{x})$ is the same as the lowest energy of the conduction band, as shown in Figure 5.8(a). For the nondegenerative approximation ($E_e - E_{\mathrm{F}} \gg k_{\mathrm{B}}T$, or for small $n_{e,c}$), and $E_{e,k} = p^2/2m_{e,e}$, we have

$$f_e^{\mathrm{o}} = \exp(-\frac{E_e - E_{\mathrm{F}}}{k_{\mathrm{B}}T}) = \exp(\frac{E_{\mathrm{F}} - E_{e,p}}{k_{\mathrm{B}}T}) \exp(-\frac{p^2}{2m_{e,e}k_{\mathrm{B}}T}). \tag{5.63}$$

Then the nondegeneracy equilibrium conduction-band electron density is given as based on momentum integration of (3.11); (5.61) becomes

$$\begin{aligned} n_{e,c} &= \frac{1}{\hbar^3} \sum_{\boldsymbol{p}} f_e^{\mathrm{o}}(\boldsymbol{p}) = \frac{1}{4\pi^3\hbar^3} \int_{\boldsymbol{p}} \exp[(-E_{e,p} - \frac{p^2}{2m_{e,e}} + E_{\mathrm{F}}) \frac{1}{k_{\mathrm{B}}T}] \mathrm{d}\boldsymbol{p} \\ &= \frac{1}{4\pi^3\hbar^3} \int_0^\infty \exp(-\frac{p^2}{2m_{e,e}k_{\mathrm{B}}T}) \exp(\frac{-E_{e,p} + E_{\mathrm{F}}}{k_{\mathrm{B}}T}) 4\pi p^2 \mathrm{d}p \\ &= \frac{1}{4} (\frac{2m_{e,e}k_{\mathrm{B}}T}{\pi\hbar^2})^{3/2} \exp(\frac{E_{\mathrm{F}} - E_{e,p}}{k_{\mathrm{B}}T}) \quad \text{for } \frac{E_e - E_{\mathrm{F}}}{k_{\mathrm{B}}T} \gg 1 \\ &\equiv n_{e,\mathrm{F}} \exp(\frac{E_{\mathrm{F}} - E_{e,p}}{k_{\mathrm{B}}T}), \quad n_{e,\mathrm{F}} = 2(\frac{m_{e,e}k_{\mathrm{B}}T}{2\pi\hbar^2})^{3/2} \end{aligned} \tag{5.64}$$

equilibrium $n_{e,c}$ and effective $n_{e,\mathrm{F}}$ conduction (nondegenerate) electron densities,

where we have allowed for two possible spin states. The effective electron density assumes all states are at the bottom (edge) of the conduction band ($E_{\mathrm{F}} - E_{e,p}$) = 0.

[†] For the free-electron gas, the chemical potential μ is replaced with the Fermi energy E_{F}, but there is a temperature dependence given by [12]

$$\mu = E_{\mathrm{F}}[1 - \frac{1}{3}(\frac{\pi k_{\mathrm{B}}T}{2E_{\mathrm{F}}})^2 + \cdots].$$

which is negligible for $T \ll \frac{E_{\mathrm{F}}}{k_{\mathrm{B}}}$.

This presentation of the states makes for a $T^{3/2}$ dependency. The effective density of conduction band $n_{e,\mathrm{F}}$ has a counter-part for the valence band (e.g., the hole density). The intrinsic carrier density n_i is related to $n_{e,\mathrm{F}}$, $n_{h,\mathrm{F}}$ and $\Delta E_{e,g}$.[†]

Figures 5.10(a)(i) and (ii) show the variations of the intrinsic (electron e^- or hole h^+) density $n_i = n_{h,i} = n_{e,i}$ for Ge and Si (end-of-chapter problem), as a function of temperature. For the extrinsic semiconductors, the charge carrier which has the larger number density is called the majority carrier (so p-type semiconductors have excess holes which are the majority and n-type has excess electron, so holes are the minority). Also, for the extrinsic carriers, we still have $n_{e,c}n_{h,c} = n_i^2$, i.e., the product of the minority and majority carrier densities is constrained by n_i.

The general (degenerate) form of f_e^{o}, (5.62) leads to integrals called the Fermi–Dirac integral of order j, where the integrand is $E_{e,k}^j/\{\exp[(E_{e,k}+E_{e,p}-E_{\mathrm{F}})/k_{\mathrm{B}}T]+1\}$ (Chapter 3 problem). The exponential term is called the Fermi function.

Equation (5.64) relates the equilibrium conduction electron density $n_{e,c}$ to the Fermi energy E_{F}, and $n_{e,\mathrm{F}}$. Here $n_{e,\mathrm{F}}$ is the effective electron DOS (conduction band) for the case of $E_{e,p} = E_{e,c} = E_{\mathrm{F}}$ [Figure 5.8(a)]. We have also used $E_{e,c}$ for the conduction-band-edge energy. So, unlike metals where $n_{e,c}$ and E_{F} are stated through (2.102), for semiconductors $n_{e,c}$ and E_{F} are related through the temperature-dependent relation (5.64).

From (5.64), the larger the Fermi energy (chemical potential), the larger are the number of conduction electrons (carriers). Compared with metals that have large E_{F}, semiconductors have a small E_{F} (or $n_{e,c}$). Doped semiconductors have larger carrier concentrations than those of shown in Figure 5.10(a)(i) and (ii), however they are yet much smaller than $n_{e,c}$ listed for metals in Table 5.2. Then, E_{F} in semiconductors is generally smaller than $k_{\mathrm{B}}T$. We will use this in treatment of the semiconductors in Section 5.9.

The semiconductor Fermi energy can be determined from (5.64), where $n_{e,c}$ is known. The density of electronic states in energy space $D_e(E_e)$ is the number of

---

[†] The Fermi energy of semiconductors can be found from [Figure 5.7(a)]

$$E_{\mathrm{F}} = E_{e,p} + k_{\mathrm{B}}T \ln \frac{n_{e,c}}{n_{e,\mathrm{F}}}.$$

The hole (h^+) counterpart of this is

$$E_{\mathrm{F}} = E_{h,p} - k_{\mathrm{B}}T \ln \frac{n_{h,c}}{n_{h,\mathrm{F}}},$$

or

$$E_{\mathrm{F}} = \frac{E_{e,p}+E_{h,p}}{2} + \frac{k_{\mathrm{B}}T}{2} \ln \frac{n_{h,\mathrm{F}}}{n_{e,\mathrm{F}}},$$

where $n_{h,c}$ is the valence-band density (conduction hole density) and $n_{h,\mathrm{F}}$ is the effective-valence-band density. By eliminating E_{F} between the above two relations, the intrinsic carrier density is defined as (the mass action law)

$$n_i = (n_{e,\mathrm{F}}n_{h,\mathrm{F}})^{1/2} \exp(-\frac{\Delta E_{e,g}}{2k_{\mathrm{B}}T}), \quad \Delta E_{e,g} = E_{e,p} - E_{h,p}.$$

For evaluation of $n_{h,\mathrm{F}}$, the effective hole mass $m_{h,e}/m_e$ is used.

Also, similar to (5.64) the equilibrium conduction hole density is

$$n_{h,c} = n_{h,\mathrm{F}} \exp(\frac{E_{h,p}-E_{\mathrm{F}}}{k_{\mathrm{B}}T}), \quad n_{h,\mathrm{F}} = 2(\frac{m_{h,e}k_{\mathrm{B}}T}{2\pi\hbar^2})^{3/2}.$$

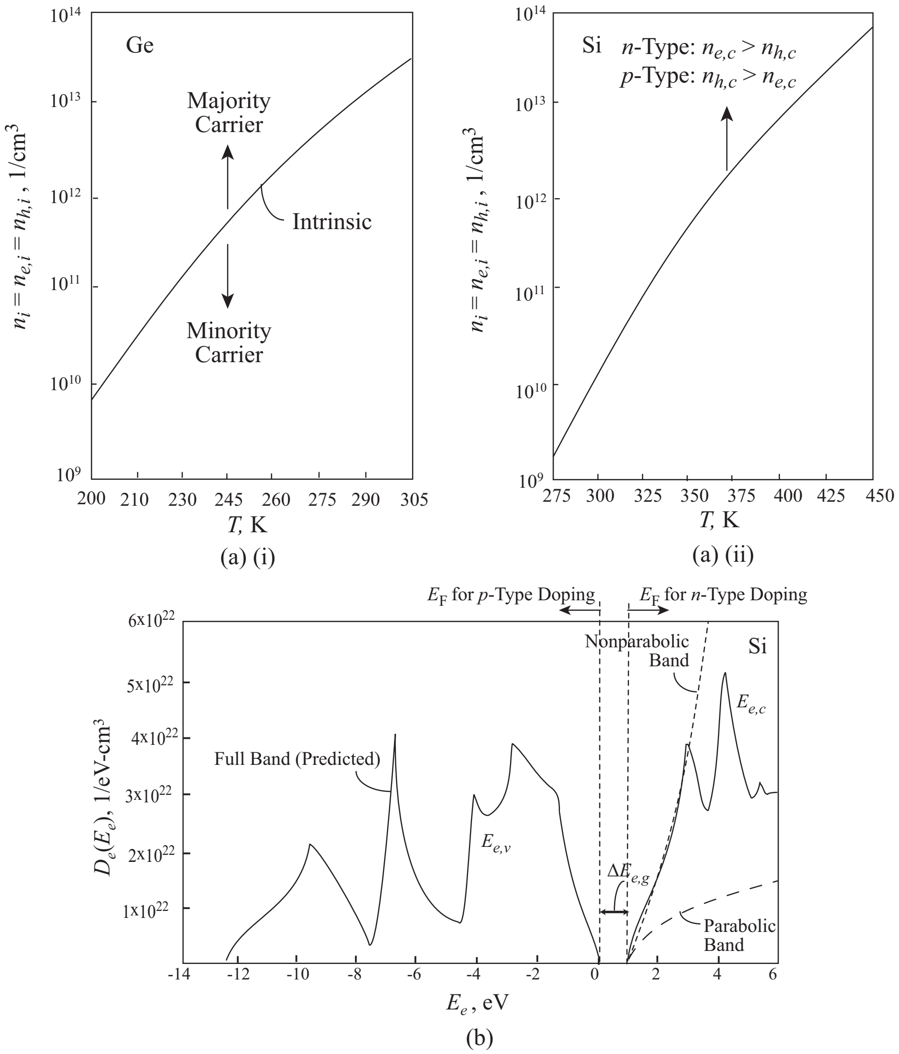

Figure 5.10. (a) Intrinsic electron (equal to hole) density for (i) Ge, and (ii) Si. Because $\Delta E_{e,g}$ is smaller for Ge, its n_i is larger than Si (at a given T) [245]. (b) Predicted DOS for the electron bands of Si [82, 260]. The nonparabolic density of states is given in footnote of Section 5.4. Also shown are the parabolic and nonparabolic models.

electric states having energy $E_e(\kappa)$ and is also represented as (2.99) or (per volume V) by (2.99) or (4.21), i.e.,

$$
\begin{aligned}
D_e[E_e(\boldsymbol{\kappa})] &= \sum_{\alpha} \int_{\boldsymbol{\kappa}'} \frac{\mathrm{d}\boldsymbol{\kappa}'}{(2\pi)^3} \delta_{\mathrm{D}}[E_e(\boldsymbol{\kappa}) - E_e(\boldsymbol{\kappa}')] \\
&\equiv \sum_{\boldsymbol{\kappa}',\alpha} \delta_{\mathrm{D}}[E_e(\boldsymbol{\kappa}) - E_e(\boldsymbol{\kappa}')]. \qquad (5.65)
\end{aligned}
$$

Then, for parabolic energy bands [near the band maximum and minimum given by (5.45)], and for two spins, we have

$$
\begin{aligned}
D_e[E_e(\boldsymbol{\kappa})] &= \frac{1}{4\pi^3}\int_{\kappa'} \delta_{\rm D}(\frac{\hbar^2\kappa^2}{2m_{e,e}} - \frac{\hbar^2\kappa'^2}{2m_{e,e}})4\pi\kappa'^2 {\rm d}\kappa' \\
&= \frac{1}{4\pi^3}\int_{\kappa'} \frac{2m_{e,e}}{2\kappa'\hbar^2}\delta_{\rm D}(\frac{\hbar^2\kappa'^2}{2m_{e,e}} - \frac{\hbar^2\kappa^2}{2m_{e,e}})4\pi\kappa'^2 {\rm d}(\frac{\hbar^2\kappa'^2}{2m_{e,e}} - \frac{\hbar^2\kappa^2}{2m_{e,e}}) \\
&= \frac{2^{1/2}m_{e,e}^{3/2}E_e^{1/2}}{\pi^2\hbar^3}
\end{aligned}
$$

Semiconductor DOS parabolic energy band (same as electron gas), (5.66)

i.e., $D_e(E_e)$ is proportional to $E_e^{1/2}$. This is the same as (5.53) shown graphically in Figure 2.17(c) for metals, except here we use the effective mass and bond energy $E_e(\boldsymbol{\kappa})$[†].

The same is obtained using the definition given in the Glossary, $D_e(\kappa) = 4\pi\kappa^2{\rm d}\kappa\ \ /(2\pi)^3$, i.e., (4.19), and noting that for metallic dispersion ${\rm d}\kappa/{\rm d}E_e = m_{e,e}/\hbar^2\kappa(m_{e,e}/2\hbar^2E_e)^{1/2}$ and $4\pi\kappa^2{\rm d}\kappa\ \ /{\rm d}E_e = 4\pi m_{e,e}\kappa/\hbar^2 = 4\pi 2^{1/2}m_{e,e}^{3/2}E_e^{1/2}/\hbar^3$, allowing for the particle spin of 2, and divided by $(2\pi)^3$, we have (5.66). This shows that the electron dispersion relation is quadratic for the parabolic model. Also note that the electron group velocity is related to ${\rm d}E_e/{\rm d}\kappa$, through (5.60).

For the ellipsoidal band model (5.49), the effective mass in (5.66) becomes $(m_{\rm L}m_{\rm T})^{1/2} = m_{e,e,\circ}$ and is called the density-of-states effective mass. Figure 5.10(b) shows the DOS $D_e(E_e)$ for model (parabolic and nonparabolic) and full-electron-band structure for Si. The parabolic model bands do not predict the full-band results, leaving out the high energy electrons. The nonparabolic band approximation, (5.49), overpredicts the density of high-energy electrons. However, for the conduction electrons only, the parabolic model is satisfactory. Note that for electron gas (or free electrons) the DOS is that given by (5.66), except m_e is used instead of $m_{e,e}$.

5.8 Specific Heat Capacity of Conduction Electrons

When the conduction electron is in thermal equilibrium with the lattice, (phonon), i.e., $T_e = T_p = T$, below we will show that electron specific heat is not large compared with that of the phonon (lattice). In Sections 5.18 and 5.19, we will discuss the case of local thermal nonequilibrium, $T_e \neq T_p$.

For metals, in the electron-gas approximation the electrons have an equilibrium energy pdf (fermion) that gives their energy with respect to the chemical potential

---

[†] The nonparabolic band model (5.50) gives, after integration, the $D_e(E_e)$ given by (5.65) as (Section 5.17.3)

$$D_e(E_e) = \frac{2^{1/2}m_{e,e,\circ}^{3/2}}{\pi^2\hbar^3}E_e^{1/2}(1+\frac{E_e}{\Delta E_{e,g}})^{1/2}(1+2\frac{E_e}{\Delta E_{e,g}}).$$

μ and thermal energy $k_\mathrm{B}T$ as (Table 1.2)

$$f_e^\circ = \frac{1}{\exp(\dfrac{E_e-\mu}{k_\mathrm{B}T})+1} = \frac{1}{\exp(\dfrac{E_e-E_\mathrm{F}}{k_\mathrm{B}T})+1}, \tag{5.67}$$

where μ is assumed to be equal to the electron Fermi energy E_F. In solids, $T = T_p$ is the lattice temperature. As will be shown, because E_F is large, the high energy electrons are not excited until very high temperatures and this tends to vanish the equilibrium electron heat capacity at low and moderate temperatures.

The specific heat of the electron gas is defined similarly to (4.53) and given in terms of the electron DOS D_e as

$$n_{e,c}c_{v,e} = \frac{\partial(\langle E_e\rangle - E_\mathrm{F})}{\partial T}|_V, \tag{5.68}$$

where the energy of a system of electrons is given as

$$\langle E_e\rangle = \int_0^\infty (E_e - E_\mathrm{F}) f_e^\circ D_e(E_e)\mathrm{d}E_e. \tag{5.69}$$

Then,

$$n_{e,c}c_{v,e} = \int_0^\infty (E_e - E_\mathrm{F})\frac{\partial f_e^\circ}{\partial T} D_e(E_e)\mathrm{d}E_e, \tag{5.70}$$

or using (5.85), we have

$$c_{v,e} = \int_0^\infty (E_e - E_\mathrm{F}) D_e(E_e)\frac{\partial}{\partial T}\frac{1}{\exp(\dfrac{E_e-E_\mathrm{F}}{k_\mathrm{B}T})+1}\mathrm{d}E_e. \tag{5.71}$$

We can approximate this by changing the limit of the integral by noting that $D_e(E_e) \simeq D_e(E_\mathrm{F})$ and then moving this outside the integral; then by also making a variable substitution $x = (E_e - E_\mathrm{F})/k_\mathrm{B}T$, we have

$$n_{e,c}c_{v,e} = k_\mathrm{B}^2 T D_e(E_\mathrm{F}) \int_{-E_\mathrm{F}/k_\mathrm{B}T}^\infty \frac{x^2 e^x}{(e^x+1)^2}\mathrm{d}x. \tag{5.72}$$

On using (5.53), we have

$$\begin{aligned} n_{e,c}c_{v,e} &= k_\mathrm{B}^2 T \frac{3n_{e,c}}{2E_\mathrm{F}} \int_{-E_\mathrm{F}/k_\mathrm{B}T}^\infty \frac{x^2 e^x}{(e^x+1)^2}\mathrm{d}x \\ &= k_\mathrm{B}^2 T \frac{2^{1/2} m_e^{3/2} E_\mathrm{F}^{1/2}}{\pi^2\hbar^3} \int_{-E_\mathrm{F}/k_\mathrm{B}T}^\infty \frac{x^2 e^x}{(e^x+1)^2}\mathrm{d}x \\ &\quad \text{electron-gas specific heat capacity.} \end{aligned} \tag{5.73}$$

We can use (5.53) to introduce $n_{e,c}$ as the coefficient of (5.73).

Figure 5.11 shows the specific heat capacity ($n_{e,c}c_{v,e}$ divided by $k_\mathrm{B}n_{e,c}$) of Cu electrons, where E_F (7.00 eV for Cu) is given in Table 5.2. Because $E_\mathrm{F}/k_\mathrm{B}T$ is rather large at moderate temperatures, the integral in (5.73) is small, and therefore the specific heat capacity of electron gas is small. This is because electrons with energy

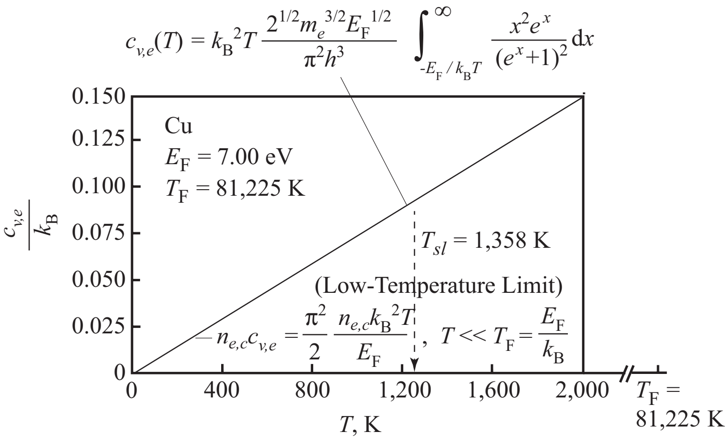

Figure 5.11. Variation of predicted specific heat capacity (per conduction electron) of Cu conduction electrons, with respect to temperature. The low-temperature limit is also shown. Because the Fermi energy is rather very large (compared with $k_B T$), the electron specific heat capacity is small.

less than the Fermi energy are already occupied. So, very small fraction of electrons, those within $k_B T$ of E_F are able to contribute to $c_{v,e}$.

Because at moderate temperatures $k_B T \ll E_F$, and by using (2.101) for $n_{e,c}$ and using that in (5.56), we have (end-of-chapter problem)

$$D_e(E_F) = \frac{3n_{e,c}}{2E_F} \quad \text{low-temperature limit,} \tag{5.74}$$

and now by using this in (5.72) for $E_F \gg k_B T$ we have (end-of-chapter problem)

$$n_{e,c} c_{v,e} = (\frac{\pi^2 k_B T}{2E_F}) n_{e,c} k_B \quad \text{for } k_B T \ll E_F \text{ electron gas,} \tag{5.75}$$

which, if the classical behavior for a particle were used, would be $3n_{e,c}k_B/2$, which is independent of the temperature and extremely large for low and moderate temperatures.

Similarly, using (5.64) for $E_F/k_B T \ll 1$, we also have the same result for a nondegenerate semiconductor with parabolic bands, i.e.,

$$n_{e,c} c_{v,e} = \frac{\pi^2}{2} \frac{k_B^2 T}{E_F} n_{e,c}(T) \quad \text{for } T \ll \frac{E_F}{k_B} = T_F \quad \text{nondegenerate semiconductors.} \tag{5.76}$$

where $n_{e,c} c_{v,e}$ here is per unit volume. This shows a linear temperature dependence of electron specific heat capacity at moderate temperatures in addition to the $n_{e,c}(T)$ dependence given by (5.64).

This is unlike the lattice specific heat $c_{v,p}$, shown in Figure 4.13(a) and given by (4.64). Note that here $T_e = T_p = T$ is the lattice temperature, because the kinetic energy of the electrons (which leads to their temperature) was not defined and used here.

The free-electron specific heat in metals and semiconductors is much less than $3k_{\rm B}/2$, which may be assigned based on its temperature. Therefore, in $nc_v = n_{e,c}c_{v,e} + nc_{v,p}$ (per atom or per kg or per m^3), in general for solids only the lattice specific heat is used.

When thermal nonequilibrium is used between the free electrons and the lattice (Sections 5.18 and 5.19) or when gases with thermal nonequilibrium are used between electrons and heavier species (Section 6.13), the temperature of the electron is defined based on its kinetic energy, and then the classical limit of translational kinetic energy is used for the specific heat capacity.

5.9 Electron BTE for Semiconductors: Thermoelectric Force

Similar to our treatment of k_p in Section 4.9, we now address the transport properties of electrons in solids. The thermoelectric (TE) transport properties are k_e (electric thermal conductivity), σ_e (electrical conductivity), $\alpha_{\rm S}$ (Seebeck coefficient), and $\alpha_{\rm P}$ (Peltier coefficient). The theoretical treatment of electron transport is given in [515] and for semiconductors in [294] and is briefly reviewed here using the treatment of [294].

Using the bond structure model of Figure 5.8)(a), the equilibrium distribution (5.62) can be written as ($\boldsymbol{p} = \hbar\boldsymbol{\kappa}$, $E^*_{e,k} = p^2/2m_{e,e}k_{\rm B}T$)

$$f_e^{\rm o} = \frac{1}{\exp[\dfrac{E_{e,k}(\boldsymbol{p}) + E_{e,p}(\boldsymbol{x}) - E_{\rm F}(\boldsymbol{x})}{k_{\rm B}T}] + 1} \equiv \frac{1}{\exp(E_e^* - E_{\rm F}^*) + 1}, \tag{5.77}$$

where $E_{\rm F}$ is the quasi (nonequilibrium) Fermi energy. Assuming that under an applied force $\boldsymbol{F}_e$, the distribution is altered to $f_e^{\rm o} + f_e'$ ($f_e^{\rm o}$ is symmetric and f_e is asymmetric), with $f_e' \ll f_e^{\rm o}$, the relaxation-time approximation of the BTE (Table 3.1) becomes

$$f_e = f_e^{\rm o} + f_e' \tag{5.78}$$

$$\left.\frac{\partial f_e}{\partial t}\right|_s = \frac{\partial f_e^{\rm o}}{\partial t} - \frac{\partial f_e'}{\partial t} = -\frac{\partial f_e'}{\partial t} \simeq -\frac{f_e'}{\tau_e(\boldsymbol{p})} \tag{5.79}$$

$$\boldsymbol{u}_e \cdot \nabla(f_e^{\rm o} + f_e') + \boldsymbol{F}_e \cdot \nabla_{\boldsymbol{p}}(f_e^{\rm o} + f_e') = -\frac{f_e'}{\tau_e(\boldsymbol{p})}. \tag{5.80}$$

Assuming that the applied force $\boldsymbol{F}_e = -\nabla E_{e,p}$, we have

$$\boldsymbol{u}_e \cdot \nabla f_e^{\rm o} - \nabla E_{e,p} \cdot \nabla_{\boldsymbol{p}} f_e^{\rm o} = -\frac{f_e'}{\tau_e(\boldsymbol{p})} \tag{5.81}$$

or

$$\boldsymbol{u}_e \cdot \frac{\partial f_e^{\rm o}}{\partial E_e^*}\nabla E_e^* - \nabla E_{e,p} \cdot \frac{\partial f_e^{\rm o}}{\partial E_e^*}\nabla_{\boldsymbol{p}} E_e^* = -\frac{f_e'}{\tau_e}. \tag{5.82}$$

Using (5.77), we have for the two derivations of E_e

$$\nabla E_e^* = \frac{1}{k_\mathrm{B}T}(\nabla E_{e,p} - \nabla E_\mathrm{F}) + (E_{e,k} + E_{e,p} - E_\mathrm{F})\nabla\frac{1}{k_\mathrm{B}T} \tag{5.83}$$

$$\nabla_p E_e^* = \frac{\boldsymbol{u}_e}{k_\mathrm{B}T}. \tag{5.84}$$

Then solving for f_e' in (5.82), we have the solution to the asymmetric (deviation) distribution function as

$$\begin{aligned} f_e' &= \frac{\tau_e(\boldsymbol{p})}{k_\mathrm{B}T}(\frac{\partial f_e^\mathrm{o}}{\partial E_e^*})\boldsymbol{u}_e \cdot [\nabla E_\mathrm{F} - T(E_{e,k} + E_{e,p} - E_\mathrm{F})\nabla\frac{1}{T}] \\ &\equiv \frac{\tau_e(\boldsymbol{p})}{k_\mathrm{B}T}(-\frac{\partial f_e^\mathrm{o}}{\partial E_e^*})\boldsymbol{u}_e \cdot \boldsymbol{F}_{te}, \end{aligned} \tag{5.85}$$

where

$$\boldsymbol{F}_{te} = -\nabla E_\mathrm{F} + T(E_{e,k} + E_{e,p} - E_\mathrm{F})\nabla\frac{1}{T}. \tag{5.86}$$

Here $\boldsymbol{F}_{te}$ is called the generalized thermoelectric force. This can be written in indexed form as

$$F_{te,i} = -\frac{\partial E_F}{\partial x_i} + T(E_{e,k} + E_{e,p} - E_\mathrm{F})\frac{\partial}{\partial x_i}\frac{1}{T}, \tag{5.87}$$

which has an electrochemical potential E_F, and a thermal component $1/T$. This shows the effect of gradients in an electrochemical potential, and in the inverse of absolute temperature, on the nonequilibrium distribution function. Similar treatment is given in [71]. So, in the Onsager relation (3.56), these should appear as the thermoelectric transport forces, i.e., (3.61) and (3.62). However, as will be discussed in Section 5.12, the choice of $\boldsymbol{e}_e$ and ∇T are more directly comparable with experimental measurables.

In Appendix G we present a statistical entropy treatment of the Seebeck coefficient.

5.10 Electron Relaxation Time and Fermi Golden Rule

Electrons can be scattered by a scattering potential φ_s, as it appears in the Schrödinger equation given in Table 2.8. Here the transition rate is expressed by FGR (3.27), where the complete derivation is given in Appendix E. The transition rate is derived from the time-dependent Schrödinger equation, using the perturbation of the unperturbed Hamiltonian (no scattering) solution. We briefly discuss the steps below. We use $\boldsymbol{\kappa}$ or $\boldsymbol{p}$, when convenient, and they are related as $\boldsymbol{p} = \hbar\boldsymbol{\kappa}$. We will also use the parabolic model of band structure with a single effective mass, i.e., (5.46).

Assuming that the solution for $\varphi_s = 0$ ($\mathrm{H} = \mathrm{H_o}$) is given by Ψ_κ^o (time dependent), similar to (2.67), we have (for plane electron wave function)

$$\Psi_\kappa^\mathrm{o}(\boldsymbol{x}, t) = \sum_\kappa a_\kappa(t)\psi_{\kappa_\mathrm{o}}(\boldsymbol{x})\exp[-i\frac{E_e(\boldsymbol{\kappa}_\mathrm{o})t}{\hbar}], \quad \mathrm{H_o}\psi_\kappa = E_e(\boldsymbol{\kappa})\psi_\kappa. \tag{5.88}$$

Consider that this scattering results in a change of the electron wave packet (wave vector) from $\boldsymbol{\kappa}$ to $\boldsymbol{\kappa}'$.

As outlined in Section 5.1 and 5.3, the solution for $\varphi_s = 0$ ($\mathrm{H} = \mathrm{H_o}$) is used to construct the function for $\varphi_s \neq 0$ ($\mathrm{H} = \mathrm{H_o} + \mathrm{H}'$, $\mathrm{H}' = \varphi_s$ is the perturbation Hamiltonion), starting from the Schrödinger equation

$$i\hbar \frac{\partial \Psi}{\partial t} = (\mathrm{H_o} + \mathrm{H}')\Psi = (\mathrm{H_o} + \varphi_s)\Psi, \tag{5.89}$$

where $\mathrm{H_o}$ is the Hamiltonian for $\varphi_s = 0$.

Now using (5.88) in (5.89), we have

$$i\hbar \sum_{\boldsymbol{\kappa}} \frac{\partial a_{\boldsymbol{\kappa}}}{\partial t} \psi_{\boldsymbol{\kappa}} \exp[-\frac{iE_e(\boldsymbol{\kappa})t}{\hbar}] = \varphi_s \sum_{\boldsymbol{\kappa}} a_{\boldsymbol{\kappa}}(t)\psi_{\boldsymbol{\kappa}} \exp[-\frac{iE_e(\boldsymbol{\kappa})t}{\hbar}]. \tag{5.90}$$

Using the definition (Table 2.8) of the wave function, the probability of finding the electron with wave vector $\boldsymbol{\kappa}'_{\mathrm{o}}$ (as a result of scattering) is

$$P(\boldsymbol{\kappa}') = \lim_{t\to\infty} |a_{\boldsymbol{\kappa}'}(t)|^2. \tag{5.91}$$

For an electron wave packet centered at $\boldsymbol{\kappa}_{\mathrm{o}}$ entering and interacting with φ_s and emerging at $\boldsymbol{\kappa}'_{\mathrm{o}}$, at $t = 0$ we have $a_{\mathrm{o},\boldsymbol{\kappa}}(t = 0) = 1$ and $a_{\mathrm{o},\boldsymbol{\kappa}}(t = 0) = 0$ for $\boldsymbol{\kappa} \neq \boldsymbol{\kappa}_{\mathrm{o}}$. From the definition of the scattering rate, from $\boldsymbol{\kappa}$ to $\boldsymbol{\kappa}'$, which is time derivative of (5.91), we have [294]

$$\dot{\gamma}_e(\boldsymbol{\kappa}, \boldsymbol{\kappa}') = \lim_{t\to\infty} \frac{|a_{\boldsymbol{\kappa}'}(t)|^2}{|a_{\mathrm{o},\boldsymbol{\kappa}}|^2 t} = \lim_{t\to\infty} \frac{|a_{\boldsymbol{\kappa}'}(t)|^2}{t}. \tag{5.92}$$

Now we determine $a_{\boldsymbol{\kappa}'}$ for $\varphi_s = 0$ by first multiplying both sides of (5.90) by $\psi^\dagger_{\boldsymbol{\kappa}'} \exp[iE_e(\boldsymbol{\kappa}')t/\hbar]$, using the orthogonality of $\psi_{\boldsymbol{\kappa}}$, and then integrating over the unit cell (assuming Bloch wave form; details are given in Appendix E). Then (5.90) becomes

$$i\hbar \frac{\partial a_{\boldsymbol{\kappa}'}}{\partial t} = \sum_{\boldsymbol{\kappa}} M_{\kappa',\kappa} a_{\boldsymbol{\kappa}} \exp[\frac{i[E_e(\boldsymbol{\kappa}') - E_e(\boldsymbol{\kappa})]t}{\hbar}]. \tag{5.93}$$

Here $M_{\mathrm{o},\boldsymbol{\kappa}',\boldsymbol{\kappa}}$ is called the matrix element [appearing in (3.27)] of the scattering potential (or transition) between electron states $\boldsymbol{\kappa}'$ and $\boldsymbol{\kappa}$, and here becomes (Appendix E) [294]

$$\begin{aligned} M_{\mathrm{o},\boldsymbol{\kappa}',\boldsymbol{\kappa}} &= |\langle \psi_{\kappa'} | \varphi_s | \psi_{\kappa} \rangle| = |\langle \kappa' | \varphi_s | \kappa \rangle| \\ &\equiv \frac{1}{V} \int_{cell} \psi^\dagger_{\boldsymbol{\kappa}'}(\boldsymbol{x}) \varphi_s \psi_{\boldsymbol{\kappa}}(\boldsymbol{x}) \mathrm{d}\boldsymbol{x}. \end{aligned} \tag{5.94}$$

For example, using the Bloch planar wave in a one-dimensional form of the matrix element results in [294]

$$M_{\mathrm{o},\boldsymbol{\kappa}',\boldsymbol{\kappa}} = \frac{1}{L} \int_{-L/2}^{L/2} e^{-i\kappa' x} \varphi_s(x) e^{i\kappa x} \mathrm{d}x \quad \text{one-dimensional matrix element.} \tag{5.95}$$

For scattering by a periodic, point defect, this leads to a simple expression.[†]

In general, φ_s is three dimensional and in most cases is given as a series solution involving the Bloch waves.

Using (3.27), the electron-scattering rate $\dot{\gamma}_e$ (5.92) is then represented in terms of the preceding matrix element as [389]

$$\dot{\gamma}_e(\boldsymbol{\kappa}', \boldsymbol{\kappa}) = \sum_{\boldsymbol{\kappa}'}\{\frac{2\pi}{\hbar}|M_{\mathrm{o},\boldsymbol{\kappa}',\boldsymbol{\kappa}}|^2\delta_{\mathrm{D}}[E_e(\boldsymbol{\kappa}') - E_e(\boldsymbol{\kappa}) - \hbar\omega] + \frac{2\pi}{\hbar}|M_{\mathrm{o},\boldsymbol{\kappa}',\boldsymbol{\kappa}}|^2\delta_{\mathrm{D}}[E_e(\boldsymbol{\kappa}') - E_e(\boldsymbol{\kappa}) + \hbar\omega]\}. \tag{5.96}$$

The first term is nonzero when energy $\hbar\omega$ is absorbed and the second when it is emitted. For elastic scattering, $\hbar\omega = 0$. This is similar to the form given in (3.12).

In addition to the energy conservation, there is a requirement of momentum conservation. For example, for electron–phonon interactions, the momentum conservation is

$$\boldsymbol{\kappa} - \boldsymbol{\kappa}' \pm \boldsymbol{\kappa}_p = 0. \tag{5.97}$$

As an example, consider elastic scattering by a delta function perturbing potential, such that (5.96) is written as [294]

$$\dot{\gamma}_e(\boldsymbol{p}', \boldsymbol{p}) = \frac{2\pi}{\hbar}\frac{\varphi_{\mathrm{o}}^2}{L^2}\sum_{\boldsymbol{p}'}\delta_{\mathrm{D}}(E_e' - E_e) \equiv c\sum_{\boldsymbol{p}'}\delta_{\mathrm{D}}(E_e' - E_e), \tag{5.98}$$

where c represents the constants. Then performing the integral similar to (5.64) but using (3.12), we have for the momentum relaxation time

$$\begin{aligned}\frac{1}{\tau_e(\text{momentum})} &= \dot{\gamma}_e(\boldsymbol{p}', \boldsymbol{p}) \\ &= \frac{c}{4\pi^2\hbar^3}\int_0^{\pi}\int_0^{2\pi}\int_0^{\infty}\delta_D(\frac{p'^2}{2m_{e,e}} - \frac{p^2}{2m_{e,e}})p'^2\mathrm{d}p'\sin\theta\mathrm{d}\phi\mathrm{d}\theta \\ &= c\frac{(4m_{e,e})^{2/3}}{4\pi^2\hbar^3}E_e^{1/2}(\boldsymbol{p}) = cD_e(\boldsymbol{p}) \\ &= \frac{2\pi}{\hbar}M_{\mathrm{o},\boldsymbol{\kappa}',\boldsymbol{\kappa}}^2 D_e(\boldsymbol{p}) = \frac{2\pi}{\hbar}\frac{\varphi_{\mathrm{o}}^2}{L^2}D_e(\boldsymbol{p}),\end{aligned} \tag{5.99}$$

where we have used (5.66) for $D_e(\boldsymbol{p})$. This is the FGR expression given in footnote of Section 3.2.3.

Here we have related τ_e and $\dot{\gamma}_e$ by assuming isotropic scattering and the domination of the out-scattering, as discussed in Section 5.11. Equation (5.99) indicates that the higher the electron DOS $D_e(\boldsymbol{p})$ (the higher the final energy), the higher the

---

[†] For $\varphi_s(x) = \varphi_{\mathrm{o}}\delta(x)$, (5.95) becomes

$$M_{\mathrm{o},\boldsymbol{\kappa}',\boldsymbol{\kappa}} = \frac{1}{L}\int_{-L/2}^{L/2}\varphi_{\mathrm{o}}(x)e^{-i(\kappa'-\kappa)x}\mathrm{d}x = \frac{\varphi_{\mathrm{o}}}{L},$$

i.e., the interaction matrix element is constant.

scattering rate. Note that here the energy is conserved (elastic scattering), and this is the momentum relaxation time. In this example, $\hbar\omega = 0$.

Because, in general, scattering is anisotropic, i.e., the deflection of $\boldsymbol{p}$ is rather small, the relaxation time in the momentum equation ($\boldsymbol{p}^1$-moment of BTE) is extended to include this. Also, this results in a distinction between the momentum (which is direction dependent) and the energy relaxation. The momentum relaxation time is (3.23), i.e., given by

$$\frac{1}{\tau_e(\text{momentum})} = \sum_{\boldsymbol{p}'} \dot{\gamma}_e(\boldsymbol{p}, \boldsymbol{p}')(1 - \frac{|\boldsymbol{p}'|}{|\boldsymbol{p}|}\cos\theta) \text{ momentum relaxation time}, \quad (5.100)$$

where θ is the polar angle between $\boldsymbol{p}$ and $\boldsymbol{p}'$. This weights each collision by the fractional change in the direction of momentum. For isotropic scattering, $\tau_e^{-1}(\text{momentum}) = \sum_{\boldsymbol{p}'} \dot{\gamma}_e(\boldsymbol{p}, \boldsymbol{p}')$.

The energy relaxation time appears in the energy equation ($\boldsymbol{p}^2$-moment of BTE) is given by (3.24), i.e.,

$$\frac{1}{\tau_e(\text{energy})} = \sum_{\boldsymbol{p}'} \dot{\gamma}_e(\boldsymbol{p}, \boldsymbol{p}')[1 - \frac{E_e(\boldsymbol{p}')}{E_e(\boldsymbol{p})}] = \sum_{\boldsymbol{p}'} \dot{\gamma}_e(\boldsymbol{p}, \boldsymbol{p}')[\frac{E_e(\boldsymbol{p}) - E_e(\boldsymbol{p}')}{E_e(\boldsymbol{p})}]$$

$$\text{energy relaxation time}. \quad (5.101)$$

This weights each collision by the fractional change in the energy.

For elastic scattering, $\boldsymbol{p} = \boldsymbol{p}'$, $E_e(\boldsymbol{p}') = E_e(\boldsymbol{p})$, then $\tau_e(\text{energy}) \rightarrow \infty$.

5.11 Average Relaxation Time $\langle\langle\tau_e\rangle\rangle$ for Power-Law τ_e (Momentum) (E_e)

The scattering alters the distribution function f_e (increase of f_e is called an in-scattering and decrease is called an out-scattering process). The rate of scattering is given by (3.8), as described in Section 3.1.3, i.e,

$$\frac{\partial f_e}{\partial t}|_s = \sum_{\boldsymbol{p}'} f_e(\boldsymbol{p}')[1 - f_e(\boldsymbol{p})]\dot{\gamma}_e(\boldsymbol{p}', \boldsymbol{p}) - f_e(\boldsymbol{p})[1 - f_e(\boldsymbol{p}')]\dot{\gamma}_e(\boldsymbol{p}, \boldsymbol{p}'), \quad (5.102)$$

where $\dot{\gamma}_e(\boldsymbol{p}', \boldsymbol{p})$ is the transition rate of scattering from state $\boldsymbol{p}'$ to state $\boldsymbol{p}$. Using the relaxation-time approximation of the scattering term (3.11), we have for $f_e(\boldsymbol{p}) \ll 1$

$$\left.\frac{\partial f_e}{\partial t}\right|_s = \sum_{\boldsymbol{p}'} f_e(\boldsymbol{p}')\dot{\gamma}_e(\boldsymbol{p}', \boldsymbol{p}) - f_e(\boldsymbol{p})\dot{\gamma}_e(\boldsymbol{p}, \boldsymbol{p}')$$

$$\equiv -\frac{f_e'}{\tau_e(\boldsymbol{p})}, \quad (5.103)$$

where $\tau_e(\boldsymbol{p})$ is the relaxation time between collisions.

For isotropic scattering and for nondegenerate semiconductors ($f_e \ll 1$), and considering out-scattering only, we have from (3.8)

$$\frac{1}{\tau_e(\boldsymbol{p})} = \sum_{\boldsymbol{p}'} \dot{\gamma}_e(\boldsymbol{p}, \boldsymbol{p}') \text{ isotropic, out-scattering.} \tag{5.104}$$

This will allow us to use the FGR (5.96) for the determination of the relaxation time (Section 5.15).

As an example for evaluation of the average relaxation time, consider electron transport in a uniform, one-dimensional electric field $e_{e,x}\boldsymbol{s}_x$, so BTE (5.80) becomes

$$-e_c e_{e,x}\boldsymbol{s}_x \cdot \nabla_{\boldsymbol{p}} f_e = -\frac{f_e'}{\tau_e(\boldsymbol{p})}, \tag{5.105}$$

where $f_e = f_e^{\rm o} + f_e'$, and $f_e^{\rm o} \gg f_e'$.

Now, using $\nabla_{\boldsymbol{p}} f_e^{\rm o} \gg \nabla_{\boldsymbol{p}} f_e'$, we have

$$-e_c e_{e,x}\boldsymbol{s}_x \cdot \nabla_{\boldsymbol{p}} f_e^{\rm o} = -\frac{f_e'}{\tau_e(\boldsymbol{p})}. \tag{5.106}$$

From the equilibrium distribution (5.77) and using $E_{e,k} = p^2/2m_{e,e}$, we have (5.84) again

$$\nabla_{\boldsymbol{p}} f_e^{\rm o} = -\frac{\boldsymbol{p}}{m_{e,e}}\frac{1}{k_{\rm B}T} f_e^{\rm o} = -\frac{\boldsymbol{u}_e}{k_{\rm B}T} f_e^{\rm o}. \tag{5.107}$$

Then, using this in (5.106), we have

$$f_e' = -\frac{e_c e_{e,x}\tau_e u_{e,x}}{k_{\rm B}T} f_e^{\rm o}. \tag{5.108}$$

This shows that deviation from equilibrium is caused by the imposed field $e_{e,x}$.

The average velocity is called the drift velocity $\overline{u}_{ex} = \langle u_{e,x}\rangle$ and is

$$\overline{u}_{e,x} \equiv \langle u_{e,x}\rangle \equiv \frac{\displaystyle\sum_{\boldsymbol{p}} u_{e,x}(f_e^{\rm o} + f_e')}{\displaystyle\sum_{\boldsymbol{p}} (f_e^{\rm o} + f_e')} = \frac{\displaystyle\sum_{\boldsymbol{p}} u_{e,x} f_e'}{\displaystyle\sum_{\boldsymbol{p}} f_e^{\rm o}}, \tag{5.109}$$

where in the denominator we use $f_e^{\rm o} \gg f_e'$, and because $f_e^{\rm o}$ is symmetric in $u_{e,x}$, the product $u_{e,x} f_e^{\rm o}$ is odd and that summation vanishes in the numerator. Then, using (5.64) and (5.108), we have

$$\langle u_{e,x}\rangle = -e_c e_{e,x} \frac{\displaystyle\sum_{\boldsymbol{p}} u_{e,x}^2 \tau_e f_e^{\rm o}}{n_{e,c} k_{\rm B}T}, \tag{5.110}$$

where T is the lattice temperature. Next, we use the average equilibrium kinetic energy $\langle E_{e,k}\rangle = \sum_{\boldsymbol{p}} E_{e,k} f_e^{\rm o} = (3/2)k_{\rm B}Tn_{e,c}$ (based on equipartition of translational energy), and $u_{e,x}^2 = u_e^2/3$ (based on spherical symmetry, will show this in

Table 5.3. *Power-law constant s for common electron-scattering mechanisms in semiconductors [294].*

Mechanism i	s
Acoustic phonon	$-1/2$
Nonpolar optical phonon	$-1/2$
Ionized impurity(weakly screened)	$+3/2$
Ionized impurity(strongly screened)	$-1/2$
Neutral impurity	0
Piezoelectric (semiconductors)	$+1/2$

Section 5.12), to write for the drift velocity[†] along x

$$\begin{aligned}\langle u_{e,x}\rangle &= \frac{-e_c e_{e,x}}{m_{e,e}}\frac{\dfrac{1}{3}\displaystyle\sum_{p}\frac{1}{2}m_{e,e}u_e^2\tau_e(E_e)f_e^{\text{o}}(E_e)}{\dfrac{1}{3}\langle E_e\rangle}\\ &\equiv \frac{-e_c}{m_{e,e}}\frac{\langle E_e\tau_e(E_e)\rangle}{\langle E_e\rangle}\,e_{e,x}\\ &= \frac{-e_c}{m_{e,e}}\langle\langle\tau_e\rangle\rangle\,e_{e,x}\\ &\equiv -\mu_{e,x}e_{e,x},\quad \langle\langle\tau_e\rangle\rangle(\text{momentum}) \equiv \frac{\langle E_e\tau_e(E_e)\rangle}{\langle E_e\rangle}\\ &\qquad\qquad \text{average relaxation time,}\end{aligned}\tag{5.111}$$

where $\mu_{e,x}$ (along x) is the electron mobility, generally presented in units of cm^2/V-s. Therefore the electron mobility and its relaxation time are equivalent. We have also used (5.64) for definition of $n_{e,c}$. We assume a power-law relation for the relaxation time, i.e.,

$$\tau_e(E_e) = \tau_e[E_e(\boldsymbol{p})] = \tau_{e,\text{o}}[\frac{E_e(\boldsymbol{p})}{k_\text{B}T}]^s \quad \text{energy-dependent relaxation time,}\tag{5.112}$$

where $\tau_{e,\text{o}}$ is a constant and s depends on the type of scattering. Note that this also shows the temperature dependence T^{-s}, in addition to any temperature dependence of $\tau_{e,\text{o}}$.

In Section 5.15 we will examine electron–phonon scattering closely and summarize the relaxation-time relation for the various scattering mechanisms given in Table 5.3.

[†] Typical drift speed in Cu conductors is 10^{-4} m/s, whereas the random thermal speed of a free electron at room temperature is 1.2×10^5 m/s $[(3k_\text{B}T/m_e)^{1/2}]$, and the Fermi velocity is 1.6×10^6 m/s.

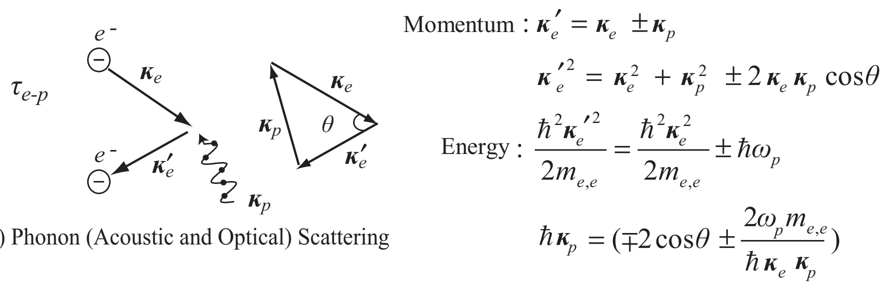
e^-
$\tau_{e\text{-}p}$
κ_e
e^-
κ_e'
κ_p
κ_e
κ_p
θ
κ_e'
Momentum : $\kappa_e' = \kappa_e \pm \kappa_p$
$\kappa_e'^2 = \kappa_e^2 + \kappa_p^2 \pm 2\kappa_e\kappa_p\cos\theta$
Energy : $\frac{\hbar^2\kappa_e'^2}{2m_{e,e}} = \frac{\hbar^2\kappa_e^2}{2m_{e,e}} \pm \hbar\omega_p$
$\hbar\kappa_p = (\mp 2\cos\theta \pm \frac{2\omega_p m_{e,e}}{\hbar\kappa_e\kappa_p})$

(a) Phonon (Acoustic and Optical) Scattering

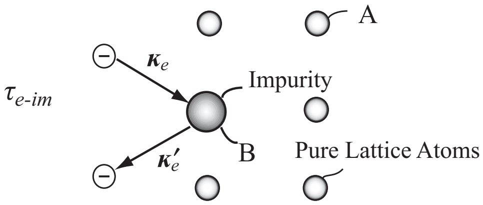

(b) Ionized and Neutral Impurity (B) Scattering

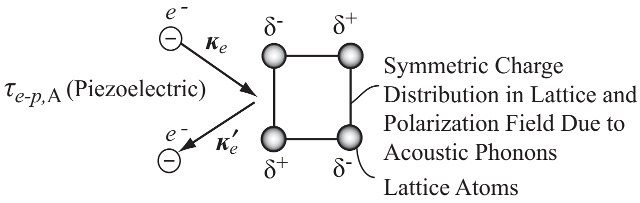
e^-
κ_e
δ^-
δ^+
Symmetric Charge Distribution in Lattice and Polarization Field Due to Acoustic Phonons
$\tau_{e\text{-}p,\mathrm{A}}$ (Piezoelectric)
e^-
κ_e'
δ^+
δ^-
Lattice Atoms

(c) Piezoelectric Scattering (Semiconductors)

Figure 5.12. Electron scattering by (a) phonon (acoustic and optical), (b) impurity (ionized and neutral), and (c) piezoelectric (semiconductors).

Table 5.3 gives the value of the power-law constant s for common elastic scattering mechanisms in semiconductors. These are for phonon, impurity, and piezoelectric scatterings, as also shown in Figure 5.12. Note the momentum and energy conservation in the interactions, as shown for the electron–phonon scattering. If the absorbed/emitted phonon energy is small, it is assumed elastic, but this is not the case for the optical phonons. So, in Figure 3.3, the scattering of electrons from state $\boldsymbol{\kappa}_e'$ to state $\boldsymbol{\kappa}$ may not be elastic. In Section 5.15, the derivation of the electron–phonon relaxation time (and the relation $s = -1/2$ for acoustic phonons) in semiconductors will be derived.

From the power-law relaxation time (3.25), we find that the averaged relaxation time (5.111) becomes[†]

[†] Using $y = p^2/2m_{e,e}k_{\mathrm{B}}T$, (5.113) is written as

$$\langle\langle\tau_e\rangle\rangle = \tau_{e,\mathrm{o}}\frac{\displaystyle\int_0^\infty y^{s+3/2}e^{-y}\mathrm{d}y}{\displaystyle\int_0^\infty y^{3/2}e^{-y}\mathrm{d}y},$$

which leads to the final form of (5.113), using (5.114).

$$
\begin{aligned}
\langle\langle\tau_e\rangle\rangle &= \tau_{e,\mathrm{o}}\frac{\sum_{\boldsymbol{p}} \frac{p^2}{2m_{e,e}}(\frac{p^2}{2m_{e,e}k_\mathrm{B}T})^s \exp(-\frac{p^2}{2m_{e,e}k_\mathrm{B}T})}{\sum_{\boldsymbol{p}} \frac{p^2}{2m_{e,e}} \exp(-\frac{p^2}{2m_{e,e}k_\mathrm{B}T})} \\
&= \tau_{e,\mathrm{o}}\frac{\int_0^\infty (\frac{p^2}{2m_{e,e}k_\mathrm{B}T})^s \exp(-\frac{p^2}{2m_{e,e}k_\mathrm{B}T}) p^4 \mathrm{d}p}{\int_0^\infty \exp(-\frac{p^2}{2m_{e,e}k_\mathrm{B}T}) p^4 \mathrm{d}p} \\
&\equiv \tau_{e,\mathrm{o}}\frac{\Gamma(s+\frac{5}{2})}{\Gamma(\frac{5}{2})}, \quad \text{for } \tau_e[E_e(\boldsymbol{p})] \equiv \tau_{e,\mathrm{o}}[\frac{E_e(\boldsymbol{p})}{k_\mathrm{B}T}]^s \\
&\qquad \text{power-law energy dependent average relaxation time.}
\end{aligned}
\tag{5.113}
$$

Among the properties of the gamma function $\Gamma(z)$ are

$$
\begin{aligned}
\Gamma(z) &\equiv \int_0^\infty y^{z-1}e^{-y}\mathrm{d}y \\
\Gamma(n) &= (n-1)! \\
\Gamma(n+1) &= n\Gamma(n) \\
\Gamma(\frac{1}{2}n) &= \frac{(n-2)!!\pi^{1/2}}{2^{(n-1)/2}} \\
\Gamma(\frac{1}{2}) &= \pi^{1/2}, \quad \Gamma(\frac{3}{2}) = \frac{\pi^{1/2}}{2}, \quad \Gamma(\frac{5}{2}) = \frac{3\pi^{1/2}}{4} \\
\Gamma(\frac{7}{2}) &= \frac{15\pi^{1/2}}{8}, \quad \Gamma(\frac{9}{2}) = \frac{105\pi^{1/2}}{16},
\end{aligned}
\tag{5.114}
$$

where $n!!$ is the double fractional.[†] When there is multiple scattering, $\mu_e^{-1} = \sum_i \mu_{e,i}^{-1}$, and because the electrical resistivity ρ_e is proportional to μ_e^{-1}, this states that $\rho_e = \sum_i \rho_{e,i}$ [Matthiessen rule (4.111)]. Thus using $\sigma_e(1/\rho_e)$ proportional to μ_e (5.112), we have

$$
\dot{\gamma}_e(\boldsymbol{p}) = \frac{1}{\tau_e} = \sum_i \frac{1}{\tau_{e,i}(\boldsymbol{p})},
\tag{5.115}
$$

where some of the mechanisms i are listed in Table 5.3. Because the mobility is defined through the drift velocity and electric field as $\langle \boldsymbol{u}_e\rangle = \boldsymbol{u}_e = -\mu_e\boldsymbol{e}_e$, generally (5.111) is used to determine $\langle\langle\tau_e\rangle\rangle$(momentum). The momentum relaxation time is also determined through (5.114), with $\tau_{e,\mathrm{o}}$ given empirically. For isotropic scattering, the energy relaxation time is related to the momentum relaxation time (examples are given in Table 5.4 and Section 5.19).

[†] $n!! = n(n-2)\ldots 5\times 3\times 1$ for n odd, and $n!! = n(n-2)\ldots 4\times 2$, for n even.

Table 5.4. *Some electron scattering relaxation time relations.*

Source of scattering	Relaxation time
Electron-alloy [433]	$\tau^{-1}_{e\text{-}a} = \frac{3\pi V_\mathrm{o}\varphi_s^2 x(1-x)m^{3/2}_{e,e}E^{1/2}_e}{2^{1/2}8\hbar^4}(\boldsymbol{p})$ V_o is $a^3/4$, φ_s is scattering potential, x is alloy atomic fraction
Electron-ionized impurity (generalized form) (momentum) [433]	$\tau^{-1}_{e\text{-}im} = n_{im}\frac{1}{1+2^{1/2}\pi}(\frac{ze_c^2}{\epsilon_e\epsilon_\mathrm{o}})^2\frac{1}{m^{1/2}_{e,e}E^{3/2}_e(\boldsymbol{p})}\times$ $\{\ln[1+\frac{8m_{e,e}E_e(\boldsymbol{p})\lambda^2}{\hbar^2}] - \frac{1}{1+\frac{\hbar^2}{8m_{e,e}E_e(\boldsymbol{p})\lambda^2}}\}$ z is the charge of impurity, λ is screening length
Electron–phonon [294, 433]	momentum (acoustic phonon, elastic): $\tau^{-1}_{e\text{-}p,\mathrm{A}}(\text{momentum}) = \frac{m_e\mu_e}{e_c}(\text{metals})$ $\tau^{-1}_{e\text{-}p,\mathrm{A}}(\text{momentum}) = \frac{2^{1/2}m^{3/2}_{e,e}k_\mathrm{B}T\varphi^2_{d,\mathrm{A}}E^{1/2}_e(\boldsymbol{p})}{\pi\hbar^4_\mathrm{P}\rho u^2_{p,\mathrm{A}}}$ $\tau_{e\text{-}p,\mathrm{A}}(\text{energy}) = \frac{k_\mathrm{B}T}{2m_{e,e}u_p^2}\tau_{e\text{-}p,\mathrm{A}}(\text{momentum})$ momentum (piezoelectric) $\tau^{-1}_{e\text{-}p,\mathrm{A}} = (\frac{m_{e,e}}{8})^{1/2}(\frac{e_c e_{pz}}{\epsilon_\mathrm{o}\epsilon_e})^2\frac{k_\mathrm{B}T}{\rho u^2_{p,\mathrm{A}}}E^{1/2}_e(\boldsymbol{p})$ momentum (nonpolar, optical phonon): absorption $\tau^{-1}_{e\text{-}p,\mathrm{O}} = \frac{\varphi'^2_{d,\mathrm{O}}f^\circ_p(\omega_{p,\mathrm{O}})m^{3/2}_{e,e}[E_e(\boldsymbol{p})+\hbar\omega_{p,\mathrm{O}}]^{1/2}}{2^{1/2}\pi\hbar^3\rho\omega_{p,\mathrm{O}}}$, emission $\tau^{-1}_{e\text{-}p,\mathrm{O}} = \frac{\varphi'^2_{d,\mathrm{O}}[f^\circ_p(\omega_{p,\mathrm{O}})+1]m^{3/2}_{e,e}[E_e(\boldsymbol{p})-\hbar\omega_{p,\mathrm{O}}]^{1/2}}{2^{1/2}\pi\hbar^3\rho\omega_{p,\mathrm{O}}}$, intervalley scattering (g- and f-scattering): $\tau^{-1}_{e\text{-}p,iv} = \sum_\alpha\frac{\pi\varphi'^2_{iv,i\alpha}Z_i D_e[E_e(\boldsymbol{p})\pm\hbar\omega_{p,iv,\alpha}-\Delta E_{e,iv}](f^\mathrm{o}_p+\frac{1}{2}\mp\frac{1}{2})}{2\rho\omega_{iv,i,\alpha}}$ emission and absorption momentum (polar optical phonon): $\tau^{-1}_{e\text{-}p,\mathrm{PO}} = \frac{e_c^2\omega_{p,\mathrm{O}}m^{1/2}_{e,e}}{2\pi\hbar[2E_e(\boldsymbol{p})]^{1/2}}(\frac{1}{\epsilon_\mathrm{o}\epsilon_{e,\infty}}-\frac{1}{\epsilon_\mathrm{o}\epsilon_{e,s}})[f^o_p(\omega_{p,\mathrm{O}})]$ $\sinh^{-1}(\frac{E_e(\boldsymbol{p})}{\hbar\omega_{p,\mathrm{O}}})^{1/2}Z_i$ absorption $\tau^{-1}_{e\text{-}p,\mathrm{PO}} = \frac{e_c^2\omega_{p,\mathrm{O}}m^{1/2}_{e,e}}{2\pi\hbar[2E_e(\boldsymbol{p})]^{1/2}}(\frac{1}{\epsilon_\mathrm{o}\epsilon_{e,\infty}}-\frac{1}{\epsilon_\mathrm{o}\epsilon_{e,s}})[f^o_p(\omega_{p,\mathrm{O}})+1]$ $\sinh^{-1}(\frac{E_e(\boldsymbol{p})}{\hbar\omega_{p,\mathrm{O}}}-1)^{1/2}$ emission energy (polar and nonpolar optical phonon): $\tau^{-1}_{e\text{-}p,\mathrm{O}}(\text{energy}) = \sum_{\boldsymbol{p}'}\dot{\gamma}_{e\text{-}p}(\boldsymbol{p},\boldsymbol{p}')[1-\frac{E_e(\boldsymbol{p}')}{E_e(\boldsymbol{p})}] =$ $\frac{\hbar\omega_{p,\mathrm{O}}}{E_e(\boldsymbol{p})}\tau^{-1}_{e\text{-}p,\mathrm{O}}$ (momentum) for high E_e
Electron–photon (momentum) [433]	$\tau^{-1}_{e\text{-}ph} = \frac{4\pi^2e_c^2}{m_e^2\omega_{ph}\epsilon_\mathrm{o}\epsilon_e}f^o_{ph}D_{ph}(\omega_{ph})\frac{2p^2_{cv}}{3}$ absorption $\tau^{-1}_{e\text{-}ph} = \frac{4\pi^2e_c^2}{m_e^2\omega_{ph}\epsilon_\mathrm{o}\epsilon_e}(f^o_{ph}+1)D_{ph}(\omega_{ph})\frac{2p^2_{cv}}{3}$ emission p_{cv} is the electric transition dipole
Phonon-assisted electron–photon	$\tau^{-1}_{e\text{-}ph\text{-}p} = \frac{2\pi}{\hbar}(\frac{\omega_{e,g}}{\omega_{ph,i}})^2\frac{(\boldsymbol{s}_{ph,i}\cdot\boldsymbol{\mu}_e)^2}{2\epsilon_\mathrm{o}}\frac{a^2_{i\text{-}p}}{2\rho u^2_{p,\mathrm{A}}}\frac{D_p(E_p)f^\mathrm{o}_p(E_p)}{E_p}e_{ph,i}$ (Section 7.12)

5.12 Thermoelectric Transport Property Tensors for Power-Law $\tau_e(E_e)$

In Section 3.4, from the Onsager transport relations, we discussed presentation of fluxes in terms of gradients. In presence of an electric field $\mathbf{e}_e$ and a temperature gradient ∇T, the electrical and heat flux vectors are given in terms of the macroscopic gradients (and including the coupling tensors $\boldsymbol{L}_{et}$ and $\boldsymbol{L}_{te}$) by

$$\boldsymbol{j}_e = \boldsymbol{L}_{ee}\cdot\boldsymbol{e}_e + \boldsymbol{L}_{et}\cdot\nabla T \tag{5.116}$$

$$\boldsymbol{q} = \boldsymbol{L}_{te}\cdot\boldsymbol{e}_e + \boldsymbol{L}_{tt}\cdot\nabla T. \tag{5.117}$$

However, as was shown by (5.87), in an electron BTE, the gradients in the Fermi energy ∇E_F and the inverse of temperature $\nabla(1/T)$ are the relevant potential gradients. These fluxes are also related to the macroscopic transport, starting with the electrical current density given by

$$\boldsymbol{j}_e \equiv -e_c\boldsymbol{j}_n = -\frac{e_c}{\hbar^3}\sum_{\boldsymbol{p}}\boldsymbol{u}_e f_e'. \tag{5.118}$$

The heat flow rate can be written using the thermodynamic relation of Table 2.4 as (using $\mu = E_\mathrm{F}$, as the quasi-Fermi electrochemical potential)

$$\mathrm{d}Q = \mathrm{d}E_e - E_\mathrm{F}\mathrm{d}N_e, \tag{5.119}$$

where the E_F varies with position. Now using $E_e = E_{e,k} + E_{e,p}$ and (5.83) and (5.119) with time derivative and per unit area (i.e., flux vector form), we have

$$\boldsymbol{q} = \boldsymbol{q}_e - E_\mathrm{F}\boldsymbol{j}_n = \frac{1}{\hbar^3}\sum_{\boldsymbol{p}}(E_{e,k} + E_{e,p} - E_\mathrm{F})\boldsymbol{u}_e f_e'. \tag{5.120}$$

Next, using (5.85) in (5.118) and (5.119), we have

$$\begin{aligned}\boldsymbol{j}_e &= -\frac{e_c}{\hbar^3 k_\mathrm{B}T}\sum_{\boldsymbol{p}}\boldsymbol{u}_e\tau_e\Big(-\frac{\partial f_e^\mathrm{o}}{\partial E_e^*}\Big)(\boldsymbol{u}_e\cdot\boldsymbol{F}_{te})\\ &= -\frac{e_c}{\hbar^3 k_\mathrm{B}T}\sum_{\boldsymbol{p}}\boldsymbol{u}_e\tau_e\Big(-\frac{\partial f_e^\mathrm{o}}{\partial E_e^*}\Big)\{\boldsymbol{u}_e\cdot[-\nabla E_\mathrm{F} + T(E_{e,k} + E_{e,p} - E_\mathrm{F})\nabla\frac{1}{T}]\}\end{aligned} \tag{5.121}$$

$$\begin{aligned}\boldsymbol{q} &= \frac{1}{\hbar^3 k_\mathrm{B}T}\sum_{\boldsymbol{p}}\boldsymbol{u}_e\tau_e\Big(-\frac{\partial f_e^\mathrm{o}}{\partial E_e^*}\Big)(E_{e,k} + E_{e,p} - E_\mathrm{F})(\boldsymbol{u}_e\cdot\boldsymbol{F}_{te})\\ &= \frac{1}{\hbar^3 k_\mathrm{B}T}\sum_{\boldsymbol{p}}\boldsymbol{u}_e\tau_e\Big(-\frac{\partial f_e^\mathrm{o}}{\partial E_e^*}\Big)(E_{e,k} + E_{e,p} - E_\mathrm{F})\\ &\quad\{\boldsymbol{u}_e\cdot[-\nabla E_\mathrm{F} + T(E_{e,k} + E_{e,p} - E_\mathrm{F})\nabla\frac{1}{T}]\}.\end{aligned} \tag{5.122}$$

We write $\boldsymbol{F}_{te}$ in terms of $\nabla(E_\mathrm{F}/e_c)$ and $\nabla(1/T)$, i.e., (5.87), and also begin to use index notation.

We now define the thermoelectric (TE) transport tensors $\boldsymbol{A}_{ee}$, $\boldsymbol{A}_{et}$, $\boldsymbol{A}_{te}$, $\boldsymbol{A}_{tt}$, and we also introduce their components (elements) $\alpha_{ee,ij}$, etc., by writing (5.121) and

(5.122) as

$$\boldsymbol{j}_e = \boldsymbol{A}_{ee} \cdot \nabla \frac{E_{\rm F}}{e_c} + \boldsymbol{A}_{et} \cdot \nabla \frac{1}{T}, \quad j_{e,i} = \alpha_{ee,ij} \frac{\partial}{\partial x_j} \frac{E_{\rm F}}{e_c} + \alpha_{et,ij} \frac{\partial}{\partial x_j} \frac{1}{T} \tag{5.123}$$

$$\boldsymbol{q} = \boldsymbol{A}_{te} \cdot \nabla \frac{E_{\rm F}}{e_c} + \boldsymbol{A}_{tt} \cdot \nabla \frac{1}{T}, \quad q_i = \alpha_{te,ij} \frac{\partial}{\partial x_j} \frac{E_{\rm F}}{e_c} + \alpha_{tt,ij} \frac{\partial}{\partial x_j} \frac{1}{T}. \tag{5.124}$$

Note that the subscript j here is a repeated summation index (from $\boldsymbol{u}_e \cdot \boldsymbol{F}_{te}$). Then, we have the Onsager transport coefficients for the $\nabla(E_{\rm F}/e_c)$ and $\nabla(1/T)$ forces as

$$\alpha_{ee,ij} = \frac{e_c^2}{\hbar^3 k_{\rm B} T} \sum_{\boldsymbol{p}} u_{e,i} u_{e,j} \tau_e (-\frac{\partial f_e^{\rm o}}{\partial E_e^*}) \tag{5.125}$$

$$\alpha_{et,ij} = \frac{-e_c}{\hbar^3 k_{\rm B} T} \sum_{\boldsymbol{p}} u_{e,i} u_{e,j} \tau_e T (E_{e,k} + E_{e,p} - E_{\rm F}) (-\frac{\partial f_e^{\rm o}}{\partial E_e^*}) \tag{5.126}$$

$$\alpha_{te,ij} = \frac{-e_c}{\hbar^3 k_{\rm B} T} \sum_{\boldsymbol{p}} u_{e,i} u_{e,j} \tau_e (E_{e,k} + E_{e,p} - E_{\rm F}) (-\frac{\partial f_e^{\rm o}}{\partial E_e^*}) \tag{5.127}$$

$$\alpha_{tt,ij} = \frac{1}{\hbar^3 k_{\rm B} T} \sum_{\boldsymbol{p}} u_{e,i} u_{e,j} \tau_e T (E_{e,k} + E_{e,p} - E_{\rm F})^2 (-\frac{\partial f_e^{\rm o}}{\partial E_e^*}). \tag{5.128}$$

Note that the Onsager conditions among the transport coefficients, e.g., (3.59), do not apply here since we did not address the entropy and other thermodynamic properties[†]. However, (5.126) and (5.127) are different only be a factor of T.

For nondegenerate conductors (most semiconductors), we have $E_{\rm F}/k_{\rm B}T \ll 1$, and for degenerate conductors, (metals) we have $E_{\rm F}/k_{\rm B}T \gg 1$. To evaluate (5.125) to (5.128), further specifications are needed, and here we consider the simplest of them, i.e., a nondegenerate distribution $[e^{(E_e^*-E_{\rm F})^*} \gg 1]$ in (5.77), and spherical (energy surfaces), parabolic energy (energy variation with momentum or wave vector) semiconductor bands, centered around $\boldsymbol{\kappa}' = \{0,0,0\}$. Then from (5.63) we have

$$f_e^{\rm o} = e^{-(E_e^*-E_{\rm F}^*)}, \quad -\frac{\partial f_e^{\rm o}}{\partial E_e^*} = f_e^{\rm o} \text{ nondegenerate distribution.} \tag{5.129}$$

The integration over $\boldsymbol{p}$ is in both direction and magnitude. The direction integral (for spherical symmetry) gives

$$\frac{1}{\displaystyle\int_0^\pi \sin\theta {\rm d}\theta} \int_0^\pi u_{e,i} u_{e,j} \sin\theta {\rm d}\theta = \frac{1}{3} u_e^2 \delta_{ij}, \tag{5.130}$$

[†] For more complete calculation the Seebeck coefficient is expressed as the sum of $\alpha_{\rm S,presence}$ and $\alpha_{\rm S,transport}$ [132, 10]. Here $\alpha_{\rm S,presence}$ is the sum of contributions to the carrier-induced entropy change, i.e., $\alpha_{\rm S,presence} = \alpha_{\rm S,mix} + \alpha_{\rm S,spin} + \alpha_{\rm S,vibration}$, where the right hand side terms are change of the entropy-of-mixing, spin entropy, and vibrational entropy upon adding a charge carrier, respectively. The other contribution $\alpha_{\rm S,transport}$ is equal to the net energy transferred in moving a carrier divided by qT, where q is the carrier charge. In our treatment in this section, we approximate that $\alpha_{\rm S,mix}$ is the dominant and the only contribution, i.e., $\alpha_{\rm S,spin}$, $\alpha_{\rm S,vibration}$, and $\alpha_{\rm S,transport}$ are negligible. In Appendix G, we will discuss the cases where due to thermal disorder (called phonon softening effect) these contributions are large and should be included.

because $u_{e,i}u_{e,j} = u_{e,i}^2\delta_{ij}$ and $u_e^2 = 3u_{e,i}^2$; here δ_{ij} is the Kronecker delta.

Then for $\alpha_{ee,ij}$, we have (using the average kinetic energy $\langle E_{e,k}\rangle = 3k_\mathrm{B}T/2 = 3m_{e,e}\langle u_{e,i}^2\rangle/2$, where T is the lattice temperature), similar to (5.111),

$$\begin{aligned}
\alpha_{ee,ij} &= \frac{e_c^2}{\frac{3}{2}k_\mathrm{B}T}\frac{1}{\hbar^3}\sum_{\boldsymbol{p}}\frac{u_e^2}{2}\tau_e f_e^\mathrm{o}\delta_{ij}\\
&= \frac{e_c^2\frac{1}{\hbar^3}\sum\limits_{\boldsymbol{p}} f_e^\mathrm{o}}{\frac{1}{\hbar^3}\sum\limits_{\boldsymbol{p}}\frac{3}{2}k_\mathrm{B}Tf_e^\mathrm{o}}\frac{1}{\hbar^3}\sum_{\boldsymbol{p}}\frac{E_{e,k}}{m_{e,e}}\tau_e f_e^\mathrm{o}\delta_{ij}\\
&= \frac{n_{e,c}e_c^2}{m_{e,e}}\langle\langle\tau_e\rangle\rangle\delta_{ij}, \quad \langle\langle\tau_e\rangle\rangle(\text{momentum}) \equiv \frac{\langle E_{e,k}\tau_e(E_{e,k})\rangle}{\langle E_{e,k}\rangle}\\
&= n_{e,c}e_c\mu_e\delta_{ij}, \ \mu_e = \frac{e_c\langle\langle\tau_e\rangle\rangle}{m_{e,e}}.
\end{aligned} \tag{5.131}$$

Since $n_{e,c}$ does not influence the mobility μ_e, this is used to separate the carrier concentration from its kinetics, when presenting σ_e. In (5.131)

$$\langle E_{e,k}\rangle = \frac{1}{4\pi^3\hbar^3}\int_{\boldsymbol{p}} E_{e,k}(p)f_e^\mathrm{o}(p)\mathrm{d}\boldsymbol{p} = \frac{1}{8\pi^3\hbar^3 m_{e,e}}\int_{\boldsymbol{p}} p^2 f_e^\mathrm{o}(p)\mathrm{d}\boldsymbol{p}. \tag{5.132}$$

The integrals over $\boldsymbol{p}$ are given by (5.113).

The electron drift velocity vector is presented by the electron mobility (and conductivity) as

$$\boldsymbol{u}_e = -\mu_e\boldsymbol{e}_e = -\frac{e_c\boldsymbol{e}_e}{m_{e,e}}\langle\langle\tau_e\rangle\rangle \ \text{ electron drift velocity,} \tag{5.133}$$

which is the vectorial form of (5.111). Note that μ_e has units of $|\boldsymbol{u}_e|/|\boldsymbol{e}_e|$ or m^2/V-s or cm^2/V-s. We also used the definition of $n_{e,c}$ from (5.66) in (5.131). The average electron drift velocity $\boldsymbol{u}_e$ and the time constant $\langle\langle\tau_e\rangle\rangle$ have been used, where the last is given by (5.111).

Now, for $\alpha_{et,ij}$, (5.26) we have

$$\begin{aligned}
\alpha_{et,ij} &= \frac{-e_c}{\hbar^3 k_\mathrm{B}}\frac{2}{3m_{e,e}}[(E_{e,p}-E_\mathrm{F})\sum_{\boldsymbol{p}}E_{e,k}\tau_e f_e^\mathrm{o} + \sum_{\boldsymbol{p}}E_{e,k}^2\tau_e f_e^\mathrm{o}]\delta_{ij}\\
&= \frac{-n_{e,c}e_cT}{m_{e,e}}[(E_{e,p}-E_\mathrm{F})\frac{\langle E_e\tau_e\rangle}{\langle E_e\rangle} + \frac{\langle E_e^2\tau_e\rangle}{\langle E_e\rangle}]\delta_{i,j}.
\end{aligned} \tag{5.134}$$

Now, using the properties of the Γ function, given by (5.114), we have, similar to (5.113),

$$\frac{\langle E_{e,k}^2 f_e^\mathrm{o}\tau_e\rangle}{\langle E_{e,k}f_e^\mathrm{o}\rangle} = k_\mathrm{B}T\tau_{e,\mathrm{o}}\frac{\Gamma(s+\frac{7}{2})}{\Gamma(\frac{5}{2})} = (s+\frac{5}{2})k_\mathrm{B}T\langle\langle\tau_e\rangle\rangle. \tag{5.135}$$

using $\mu_e = e_c\langle\langle\tau_e\rangle\rangle/m_{e,e}$, and from (5.64)

$$\frac{E_\mathrm{F} - E_{e,p}}{k_\mathrm{B}T} = \ln\frac{n_{e,F}}{n_{e,c}} \tag{5.136}$$

$$\alpha_{et,ij} = -\frac{k_\mathrm{B}T^2}{e_c}[\ln\frac{n_{e,\mathrm{F}}}{n_{e,c}} + (s + \frac{5}{2})]\alpha_{ee,ij}. \tag{5.137}$$

By inspection of (5.126) and (5.127), we have

$$\alpha_{te,ij} = \frac{1}{T}\alpha_{et,ij}. \tag{5.138}$$

The last coefficient given by (5.125) becomes

$$\begin{aligned}\alpha_{tt,ij} &= \frac{1}{\hbar^3 k_\mathrm{B}}\sum_p u_{e,i}^2 f_e^\mathrm{o}\tau_e(E_{e,p} + E_{e,k} - E_\mathrm{F})^2 \\ &= \frac{2}{3\hbar^3 k_\mathrm{B}m_{e,e}}\sum_p E_{e,k}\tau_e f_e^\mathrm{o}[(E_{e,p} - E_\mathrm{F})^2 + 2E_{e,k}(E_{e,p} - E_\mathrm{F}) + E_{e,k}^2]\delta_{ij} \\ &= \frac{n_{e,c}T}{m_{e,e}}(k_\mathrm{B}T)^2\ln(\frac{n_{e,\mathrm{F}}}{n_{e,c}})^2\frac{\langle E_e\tau_e(E_e)\rangle}{\langle E_e\rangle} + \frac{2n_{e,c}T}{m_{e,e}}(k_\mathrm{B}T)\ln(\frac{n_{e,\mathrm{F}}}{n_{e,c}})^2\frac{\langle E_e^2\tau_e(E_e)\rangle}{\langle E_e\rangle} + \\ &\quad \frac{n_{e,c}T}{m_{e,e}}\frac{\langle E_e^3\tau_e(E_e)\rangle}{\langle E_e\rangle},\end{aligned} \tag{5.139}$$

where the angle brackets indicate integral over $\boldsymbol{p}$ space, as shown in (5.111).

Now, using definition (5.125), the Γ function properties (5.114), and the result for $\alpha_{ee,ij}$ (5.131), we have

$$\alpha_{tt,ij} = \frac{k_\mathrm{B}^2T^3}{e_c^2}\{[\ln\frac{n_{e,\mathrm{F}}}{n_{e,c}} + (s + \frac{5}{2})]^2 + (s + \frac{5}{2})\}\alpha_{ee,i,j}. \tag{5.140}$$

5.13 TE Transport Coefficients for Cubic Semiconductors

5.13.1 Seebeck, Peltier, and Thomson Coefficients, and Electrical and Thermal Conductivities

Alternatively, coupled thermoelectric (TE) transport equations (5.121) and (5.122) can be written as the electric-field intensity vector and the heat flux vector, in terms of $\boldsymbol{e}_e$, $\boldsymbol{j}_e$, and ∇T. These are the conventional forms through which electrical and thermal transports are defined. Then for isotropic (cubic) materials we have (end-of-chapter problem)

$$\boldsymbol{j}_e = \alpha_{ee}\boldsymbol{e}_e - \frac{\alpha_{et}}{T^2}\nabla T \tag{5.141}$$

$$\boldsymbol{e}_e = \alpha_{ee}^{-1}\boldsymbol{j}_e + \frac{\alpha_{ee}^{-1}\alpha_{et}}{T^2}\nabla T \tag{5.142}$$

$$\boldsymbol{q} = \alpha_{te}\alpha_{ee}^{-1}\boldsymbol{j}_e - \frac{1}{T^2}(\alpha_{tt} - \alpha_{te}\alpha_{ee}^{-1}\alpha_{et})\nabla T$$

semiconductors of cubic symmetry, (5.143)

Note that $\nabla\varphi_e = -e_c^{-1}\nabla\mu = -\boldsymbol{e}_e$, here we have assumed $\nabla\mu = \nabla E_{\rm F}$ (valid for $T \ll \frac{E_{\rm F}}{k_{\rm B}}$), so $\nabla E_{\rm F}/e_c$ in (5.13) is equal to $\boldsymbol{e}_e$ [as it appears in (5.144)]. We now define the TE transport properties as

$$\boldsymbol{j}_e = \sigma_e \boldsymbol{e}_e - \sigma_e \alpha_{\rm S} \nabla T \qquad (5.144)$$

$$\boldsymbol{e}_e \equiv \rho_e \boldsymbol{j}_e + \alpha_{\rm S}\nabla T, \quad \rho_e = \frac{1}{\sigma_e}, \quad \alpha_{ee} \equiv \sigma_e, \quad \frac{\alpha_{et}\alpha_{ee}^{-1}}{T^2} \equiv \alpha_{\rm S} \qquad (5.145)$$

$$\boldsymbol{q} \equiv \alpha_{\rm P}\boldsymbol{j}_e - k_e \nabla T, \;\; \alpha_{\rm P} = \alpha_{\rm S} T, \quad \alpha_{te}\alpha_{ee}^{-1} \equiv \alpha_{\rm P},$$

$$\frac{\alpha_{tt} - \alpha_{te}\alpha_{ee}^{-1}\alpha_{et}}{T^2} \equiv k_e, \qquad (5.146)$$

where ρ_e(Ω-m) is the electrical resistivity, $\alpha_{\rm S}$(V/K) is the Seebeck coefficient, $\alpha_{\rm P}$(V) is the Peltier coefficient, and k_e(W/m-K) is the electric thermal conductivity (the total thermal conductivity is $k = k_e + k_p$, where k_p is the phonon thermal conductivity). The Seebeck coefficient (also called the thermopower) is the electrical potential induced by temperature differences, causing the diffusion of electrons or holes toward the cold region.

We note that electrical conductivity is the product of conduction electron density, electron charge, and electron mobility, and that electron mobility and relaxation time are equivalent. For insulators, k_p is the sole contributor and for metals (and to a large extent for semiconductors at and preceding room temperature) k_e dominates. For nondegenerate, isotropic (cubic structure) semiconductors, with spherical and parabolic electrical bands, we have

$$\sigma_e = \frac{1}{\rho_e} = \frac{n_{e,c}e_c^2\langle\langle\tau_e\rangle\rangle}{m_{e,e}} = \frac{n_{e,c}e_c^2}{m_{e,e}}\tau_{e,\rm o}\frac{\Gamma(s+\frac{5}{2})}{\Gamma(\frac{5}{2})} \equiv n_{e,c}e_c\mu_e$$

$$\text{electricalconductivity} \qquad (5.147)$$

$$\alpha_{\rm S} = \mp\frac{k_{\rm B}}{e_c}[\ln\frac{n_{e,\rm F}}{n_{e,c}} + (s+\frac{5}{2})] \qquad \text{Seebeck coefficient}$$

$$= \mp\frac{k_{\rm B}}{e_c}[\frac{E_{\rm F}-E_{e,p}}{k_{\rm B}T} + (s+\frac{5}{2})] \;\; + \text{ for } n\text{-type}, - \text{ for } p\text{-type} \qquad (5.148)$$

$$\alpha_{\rm P} = \alpha_{\rm S} T \qquad \text{Kelvin relation and Peltier coefficient} \qquad (5.149)$$

$$k_e = \sigma_e \frac{k_{\rm B}^2 T}{e_c^2}(s+\frac{5}{2}) \qquad \text{electronic thermal conductivity,} \qquad (5.150)$$

where μ_e and $\langle\langle\tau_e\rangle\rangle$ are given by (5.131). The effective mass defined in (5.45) is listed in Table 5.1. The n- and p-type semiconductors are defined in the Glossary. Note that $\alpha_{\rm S}$ and $\alpha_{\rm P}$ do not contain the kinetics $\tau_{e,\rm o}$, but σ_e and k_e do.

For multiband structures, $\alpha_{\rm S}$ is summed over the number of bands j (Section 5.17). We will show in Section 5.17.1 how $\alpha_{\rm S}$ varies with the chemical potential (i.e., $E_{\rm F}$, which represents the carrier concentration). In extrinsic semiconductors (p- or

n-type are desired), the Fermi energy is optimized along with the transport properties. In a two-band structure (one valence and one conduction with no band degeneracy) the energy difference $E_{e,p} - E_\mathrm{F}$ is replaced with the bandgap energy $\Delta E_{e,g}$.

For match with experiment, a constant is added after $s + 5/2$ in (5.148) and is referred to as the phonon drag [163].

Note that k_B/e_c is 86 μV/K, and this gives the order of magnitude for the Seebeck coefficient.

The relation

$$\frac{k_e}{\sigma_e T} = \frac{k_\mathrm{B}^2}{e_c^2}(s + \frac{5}{2}) \equiv N_\mathrm{L} \quad \text{Wiedemann–Franz–Lorenz law,} \tag{5.151}$$

is called the Wiedemann–Franz–Lorenz law, and N_L is called the Lorenz number and depends on s.

The Thomson coefficient α_T(V/K), is defined as

$$\alpha_\mathrm{T} \equiv \frac{\dfrac{1}{j_e}\dfrac{\mathrm{d}q}{\mathrm{d}x}}{\dfrac{\mathrm{d}T}{\mathrm{d}x}} = T\frac{\mathrm{d}\alpha_\mathrm{S}}{\mathrm{d}T} \quad \text{Thomson coefficient.} \tag{5.152}$$

This gives $\mathrm{d}q_x/\mathrm{d}x = \alpha_\mathrm{T} j_e \mathrm{d}T/\mathrm{d}x$, which shows that in the presence of a temperature gradient, an electric conductor can absorb ($\alpha_\mathrm{T} > 0$) or release heat.

Then from the linear relation for α_S in (5.148), we have

$$\alpha_\mathrm{T} = \mp\frac{k_\mathrm{B}}{e_c}\frac{\Delta E_{e,g}}{k_\mathrm{B}T} \quad - \text{ for } n\text{-type and } + \text{ for } p\text{-type,} \tag{5.153}$$

where we have used the relation between the effective carrier density and the intrinsic carrier density (Section 5.7) to remove E_F and use the bandgap energy.

The Thomson coefficient expresses the extent of heat flux induced by an electrical current in a nonisothermal conductor.

5.13.2 Electron Mean Free Path for Metals

For a free-electron gas, the Fermi speed is (5.57), and gives

$$u_\mathrm{F} = (\frac{2E_\mathrm{F}}{m_e})^{1/2}. \tag{5.154}$$

and $c_{v,e}$ is given by (5.73), for $T_e = T_p$ (electrons in thermal equilibrium with the lattice). For $T_e \neq T_p$, $c_{v,e} = 3k_\mathrm{B}T/2$, per electron (Section 5.18).

Then the mobility is given in terms of the relaxation time by (5.147) and can in turn be written in terms of the electron mean free path $\lambda_e = u_\mathrm{F}\langle\langle\tau_e\rangle\rangle$, and then the electrical conductivity becomes

$$\sigma_e = n_{e,c}e_c^2\frac{\lambda_e}{m_{e,e}u_\mathrm{F}}. \tag{5.155}$$

The electronic thermal conductivity can be defined because of the kinetic form of the thermal conductivity, similar to (4.110) for phonons. Then we have [30]

$$k_e = \frac{1}{3} n_{e,c} c_{v,e} u_{\mathrm{F}} \lambda_e. \tag{5.156}$$

Next, using (5.57), (5.74), (5.155), and (5.156), we have

$$\frac{k_e}{\sigma_e T} = N_{\mathrm{L,o}} = \frac{\pi^2}{3}\frac{k_{\mathrm{B}}^2}{e_c^2} = 2.442 \times 10^{-8}\ \frac{\mathrm{W}\text{-}\Omega}{\mathrm{K}^2} \quad \text{Lorenz number}, \tag{5.157}$$

i.e., the Lorenz number N_{L} is expected to be a constant for metals, however, as will be shown in Section 5.16 when we review experimental results, N_{L} decreases substantially as inelastic phonon scattering becomes important at small T/T_{D}.

5.14 Magnetic Field and Hall Factor and Coefficient

In the presence of a magnetic field, indicated by the magnetic induction vector $\boldsymbol{b}_e$, (5.80) becomes (i.e., added Lorentz force)

$$\boldsymbol{u}_e.\nabla(f_e^{\mathrm{o}} + f_e') - (e_e \boldsymbol{e}_c + e_c \boldsymbol{u}_e \times \boldsymbol{b}_e).\nabla_{\boldsymbol{p}}(f_e^{\mathrm{o}} + f_e') = -\frac{f_e'}{\tau_e(\boldsymbol{p})}. \tag{5.158}$$

When $\boldsymbol{b}_e$ is perpendicular to $\boldsymbol{j}_e$, there is induced a potential $\Delta\varphi_{\mathrm{H}}$ (Hall voltage) perpendicular to both of them (and a corresponding Hall field $\boldsymbol{e}_{\mathrm{H}}$). This deflects the carriers and moves them to the surface (opposite change build up on opposite surfaces). Using a treatment similar to that given for the electric field alone, we write the electrical current with the additional induced current as[†] [294]

$$\boldsymbol{j}_e = \sigma_e \boldsymbol{e}_e - \sigma_e \mu_{\mathrm{H}} \boldsymbol{e}_e \times \boldsymbol{b}_e, \tag{5.159}$$

where μ_{H} is the Hall mobility and is related to the drift mobility μ_e, in (5.131), through

$$\mu_{\mathrm{H}} = \mu_e r_{\mathrm{H}} \quad \text{Hall mobility}$$

$$r_{\mathrm{H}} = \frac{\langle\langle \tau_e^2 \rangle\rangle}{\langle\langle \tau_e \rangle\rangle^2} = \frac{\Gamma(2s + \frac{5}{2})\Gamma(\frac{5}{2})}{[\Gamma(s + \frac{5}{2})]^2} \quad \text{Hall factor}, \tag{5.160}$$

where r_{H} is the Hall factor (a constant).

The Hall coefficient R_{H} is defined as

$$R_{\mathrm{H}} = \frac{r_{\mathrm{H}}}{\mp n_{i,c} e_c} \quad \text{Hall coefficient}, - \text{for } i = e \text{ and} + \text{for } i = h. \tag{5.161}$$

For negative Hall coefficient we have n-type semiconductor, and vice versa for p-type. For metals R_{H} is a constant. The magnitude of r_{H} is near unity. Then using

---

[†] Under force equilibrium, we have

$$e_c \boldsymbol{e}_{\mathrm{H}} = -e_c \mu_e \boldsymbol{e}_e \times \boldsymbol{b}_e \quad \boldsymbol{e}_{\mathrm{H}} = -\mu_e \boldsymbol{e}_e \times \boldsymbol{b}_e \quad R_{\mathrm{H}} = \frac{\boldsymbol{e}_{\mathrm{H}}}{\boldsymbol{b}_e \times \boldsymbol{j}_e}.$$

Table 5.3 and (5.114), r_H is $3\pi/8$ for acoustic phonon and strongly screened ionized impurity scattering, and is 1.93 for weakly screened ionized impurity scattering. In practice, measured R_H is used to determine the electron and hole concentration (density) or Fermi energy in semiconductors, which in general is temperature dependent.[†]

5.15 Electron–Phonon Relaxation Times in Semiconductors

Electron scattering by a phonon is illustrated in Figure 5.12. The electron-scattering rate is given by (5.96), in terms of the interaction matrix element $M_{\boldsymbol{\kappa}',\boldsymbol{\kappa}}$ and the energy and momentum conservation requirements expressed by the Dirac delta function δ_D. The matrix element in turn includes the scattering potential φ_s. It is generally assumed that there is only one phonon involved in the electronic transition.

The electron–phonon interaction is mostly inelastic, and the most important ones are the acoustic phonon, polar optical phonon (e.g., Figure 4.9 for Si), nonpolar optical phonons (e.g., Figure 4.10 for GaAs), equivalent intervalley phonon, and piezoelectric phonon (for very low temperatures).

The scattering of electrons (and holes in semiconductors) that is due to dislocation of atoms in the lattice, is referred to as strain and can be related with deformation scattering theory. This involves specification of the deformation potential $\varphi_d(\boldsymbol{x})$ in the Brillouin zone.

The electron perturbation produced by phonons is by the acoustic phonons (relative displacement of atoms and piezoelectric effect in semiconductors) and by the optical phonons (relative displacement of neighboring atoms and in polar crystal produces polarization fluctuation). For these phonon scatterings the perturbation potential relates to atomic displacement d through [i.e., (2.120), $\mathrm{H} = \mathrm{H}_\circ + \varphi_{s,e-p}\epsilon + \cdots$] [371]

$$\begin{aligned}
&\varphi_{s,e\text{-}p} \sim \varphi_{d,\mathrm{A}}\partial d/\partial x && \text{acoustic phonon (one-dimensional strain)}\\
&\varphi_{s,e\text{-}p} \sim \frac{e_c e_{pz}}{\epsilon_\mathrm{o}\epsilon_e} d && \text{piezoelectric (acoustic phonons)}\\
&\varphi_{s,e\text{-}p} \sim \varphi'_{d,\mathrm{O}} d && \text{nonpolar optical phonon (displacement)}\\
&\varphi_{s,e\text{-}p} \sim q_e d && \text{polar optical phonon,}
\end{aligned} \tag{5.162}$$

where $\boldsymbol{d}$ is the atomic displacement vector, $\varphi_{d,\mathrm{A}}$ and $\varphi'_{d,\mathrm{O}}$ are scattering potential constants, and q_e is the effective charge. Here e_{pz}(C/m^2) is the piezoelectric constant. The acoustic phonon scattering can be presented by treating the nuclei (ions) as a charged elastic continuum with charge density fluctuation of $-n_{e,c}e_c z\nabla \cdot \boldsymbol{d}$.

[†] Using (5.161) and (5.64), we have for electron

$$n_{e,c}(E_\mathrm{F}) = -\frac{r_\mathrm{H}}{R_\mathrm{H} e_c},$$

and this gives an explicit relation for E_F.

The intervalley electron-phonon scattering is treated similar to the nonpolar optical phonon scattering. Both the momentum conservation and energy conservation are imposed by $\delta_{\rm D}(\boldsymbol{\kappa}_e \pm \boldsymbol{\kappa}_p - \boldsymbol{\kappa}'_e)$ and $\delta_{\rm D}(E_{e,\boldsymbol{\kappa}'} - E_{e,\boldsymbol{\kappa}} \mp \hbar\omega_p)$. Here we drop the electron subscript in $\boldsymbol{\kappa}$ for simplicity.

The displacement vector $\boldsymbol{d}$ is determined as outlined in Section 4.8 and in a form given by (4.70).

5.15.1 Electron–Phonon Wave Function

The quantum lattice-vibration displacement is given by (4.47), and the normal displacement coordinate $Q_{\kappa_p,\alpha}$ is defined as [433]

$$Q_{\kappa_p,\alpha} = (\frac{\hbar}{2m\omega_\alpha})^{1/2}(b^\dagger_{-\boldsymbol{\kappa}_p} + b_{\boldsymbol{\kappa}_p}). \tag{5.163}$$

Then (4.47) becomes

$$\boldsymbol{d} = \frac{1}{N^{1/2}} \sum_{\boldsymbol{\kappa}_p,\alpha} \{[Q_{\boldsymbol{\kappa}_p,\alpha}\boldsymbol{s}_{\boldsymbol{\alpha}} e^{i(\boldsymbol{\kappa}_p\cdot\boldsymbol{x}_{\rm o})}] + [Q_{\boldsymbol{\kappa}_p,\alpha}\boldsymbol{s}_{\boldsymbol{\alpha}} e^{i(\boldsymbol{\kappa}_p\cdot\boldsymbol{x}_{\rm o})}]^\dagger\}, \tag{5.164}$$

where † indicates the complex conjugate and $\boldsymbol{x}_{\rm o}$ is the lattice center location.

The electron is presented by an initial state $|\boldsymbol{\kappa}\rangle$ and the phonon by the product state $\prod |f_{p,\boldsymbol{\kappa}_p,\alpha}(Q_{\boldsymbol{\kappa}_p,\alpha})\rangle$, which describes the phonon distribution. In the final state (after scattering), the electron is represented by $|\boldsymbol{\kappa}'\rangle$ and the phonon by a new distribution $\prod |f_{p,\boldsymbol{\kappa}'_p,\alpha}(Q_{\boldsymbol{\kappa}'_p,\alpha})\rangle$. Then the initial and final states of the electron–phonon wave function for the system, appearing in the matrix element (5.94) are

$$\psi_i = \psi_{\boldsymbol{\kappa}}(\boldsymbol{x}) \prod_{\boldsymbol{\kappa}_p,\alpha} |f_{p,\boldsymbol{\kappa}_p}(Q_{\boldsymbol{\kappa}_p,\alpha})\rangle \tag{5.165}$$

$$\psi_f = \psi_{\boldsymbol{\kappa}'}(\boldsymbol{x}) \prod_{\boldsymbol{\kappa}'_p,\alpha} |f_{p,\boldsymbol{\kappa}'_p}(Q_{\boldsymbol{\kappa}_p,\alpha})\rangle \quad \text{electron–phonon wave function.} \tag{5.166}$$

In the matrix element, the phonon portion is

$$\prod_{\boldsymbol{\kappa}''_p,\alpha''} \prod_{\boldsymbol{\kappa}'_p,\alpha'} \langle f_{p,\boldsymbol{\kappa}''_p,\alpha''} | Q_{\boldsymbol{\kappa},\alpha} | f_{p,\boldsymbol{\kappa}',\alpha'}\rangle. \tag{5.167}$$

Now we use the normal coordinate displacement in terms of the phonon creation and destruction (ladder) operators (Section 2.6.2) and note that the only nonvanishing elements are [433]

$$\langle (f_{p,\boldsymbol{\kappa}_p,\alpha} - 1)| b_{\boldsymbol{\kappa}_p} | f_{p,\boldsymbol{\kappa}_p,\alpha}\rangle = f^{1/2}_{p,\boldsymbol{\kappa}_p,\alpha} \tag{5.168}$$

$$\langle (f_{p,\boldsymbol{\kappa}_p,\alpha} + 1)| b^\dagger_{\boldsymbol{\kappa}_p} | f_{p,\boldsymbol{\kappa}_p,\alpha}\rangle = (f_{p,\boldsymbol{\kappa}_p,\alpha} + 1)^{1/2}. \tag{5.169}$$

The interaction matrix element containing $Q_{\boldsymbol{\kappa}_p,\alpha}$ is [433]

$$\frac{\hbar}{2m\omega_{\boldsymbol{\kappa}_p,\alpha}} \delta_{\rm D}(\boldsymbol{\kappa}_p, \boldsymbol{\kappa}'_p, \boldsymbol{\kappa}''_p)\delta_{\rm D}(\alpha, \alpha', \alpha'')[f^{1/2}_{p,\boldsymbol{\kappa}_p}\delta_{\rm D}(f_{p,\boldsymbol{\kappa}'_p} - 1, f_{p,\boldsymbol{\kappa}_p})$$

$$+ (f_{p,\boldsymbol{\kappa}_p} + 1)^{1/2}\delta_{\rm D}(f_{p,\boldsymbol{\kappa}'_p} + 1, f_{p,\boldsymbol{\kappa}_p})], \tag{5.170}$$

which represents the phonon absorption and emission. At equilibrium, we have f_p^{o}.

The electronic portion has an e-p interaction Hamiltonian expressed by (5.164), i.e.,

$$\mathrm{H}_{e\text{-}p} = \varphi_{s,e\text{-}p} = \sum_{\kappa_p}\{[\varphi_{s,\kappa_p,\alpha} Q_{\kappa_p,\alpha} e^{i(\kappa_p\cdot x_{\mathrm{o}})}] + [\varphi_{s,\kappa_p,\alpha} Q_{\kappa_p,\alpha} e^{i(\kappa_p\cdot x_{\mathrm{o}})}]^\dagger\}, \tag{5.171}$$

For Bloch plane waves, the electronic portion of $M_{\kappa',\kappa}$ is

$$\frac{1}{V}\int d^\dagger(f_{p,\kappa_p'},\boldsymbol{\kappa}')e^{-i(\kappa'\cdot x)}\varphi_{s,\kappa_p,\alpha}(\boldsymbol{x})e^{\pm i(\kappa_p\cdot x)}d(f_{p,\kappa_p},\boldsymbol{\kappa})e^{i(\kappa\cdot x)}\mathrm{d}\boldsymbol{x}. \tag{5.172}$$

The spatial integral is over a primitive cell, giving

$$\begin{aligned}&\frac{1}{V}\int_{\mathrm{cell}}\psi^\dagger(f_{p,\kappa_p'},\boldsymbol{\kappa}')\varphi_{s,\kappa_p,\alpha}\psi^\dagger(f_{p,\kappa_p},\boldsymbol{\kappa})\sum_{\boldsymbol{R}}[i(\boldsymbol{\kappa}+\boldsymbol{\kappa_p}-\boldsymbol{\kappa}')\cdot \boldsymbol{x}_{\mathrm{o}}]\\ &=\frac{1}{V}\int_{\mathrm{cell}}\psi^\dagger(f_{p,\kappa_p'},\boldsymbol{\kappa}')\varphi_{s,\kappa_p,\alpha}\psi^\dagger(f_{p,\kappa_p},\boldsymbol{\kappa})\mathrm{d}\boldsymbol{x}\,\delta_{\mathrm{D}}(\boldsymbol{\kappa}\pm\boldsymbol{\kappa_p}-\boldsymbol{\kappa}',\boldsymbol{g}),\end{aligned} \tag{5.173}$$

assuming that, because of the small cell size, $\exp[i(\boldsymbol{\kappa}-\boldsymbol{\kappa}')\cdot\boldsymbol{x}]=1$. For the normal processes $\boldsymbol{g}=0$ and for the Umklapp processes $\boldsymbol{g}\neq 0$ (Section 4.15). Then we define the interaction (coupling) coefficient $C_{\kappa_p,\alpha}$ as

$$\begin{aligned}M_{\kappa,\kappa'}(\text{electronic}) &= \frac{1}{V}C_{\kappa_p,\alpha}G(\boldsymbol{\kappa},\boldsymbol{\kappa}')\delta_{\mathrm{D}}(\boldsymbol{\kappa}\pm\boldsymbol{\kappa_p}-\boldsymbol{\kappa}',\boldsymbol{g}),\\ C_{\kappa_p,\alpha}G(\boldsymbol{\kappa},\boldsymbol{\kappa}') &\equiv \int_{\mathrm{cell}}\psi^\dagger(f_{p,\kappa_p'},\boldsymbol{\kappa}')\varphi_{s,\kappa_p,\alpha}\psi^\dagger(f_{p,\kappa_p},\boldsymbol{\kappa})\mathrm{d}\boldsymbol{x}\\ &=\varphi_{s,\kappa_p,\alpha}G(\boldsymbol{\kappa},\boldsymbol{\kappa}'),\end{aligned} \tag{5.174}$$

where for the last equality it is assumed that $\varphi_{s,\kappa_p,\alpha}$ does not vary significantly over the unit cell. The quantity $G(\boldsymbol{\kappa},\boldsymbol{\kappa}')$ represents the overlap of the cell periodic part of the initial and final electronic states.

The electron–phonon matrix elements for Bloch plane waves, $\exp(i\boldsymbol{\kappa}'\cdot\boldsymbol{x})$ and $\exp(i\boldsymbol{\kappa}\cdot\boldsymbol{x})$, become

$$\begin{aligned}M^2_{\kappa,\kappa'} &= \langle\psi_f|\varphi_{s,e\text{-}p}|\psi_i\rangle^2\\ &=\frac{\hbar}{2Nm}\frac{C^2_{\kappa_p,\alpha}G(\boldsymbol{\kappa},\boldsymbol{\kappa}')}{\omega_{p,\alpha}}[f_p(\omega_{p,\alpha})+\frac{1}{2}\mp\frac{1}{2}]\delta_{\mathrm{D}}(\boldsymbol{\kappa}\pm\boldsymbol{\kappa_p}-\boldsymbol{\kappa}',0)\\ &\quad(+\text{ absorption, }-\text{ emission of phonons) for the normal processes.}\end{aligned} \tag{5.175}$$

The final form of the electron-scattering rate (by phonons) (5.96), for which the equilibrium phonon distribution instead, is [433]

$$\begin{aligned}\dot{\gamma}_{e\text{-}p} = \frac{1}{\tau_{e\text{-}p}} &= \frac{1}{8\pi^2 Nm}\int\frac{C^2_{\kappa_p,\alpha}G(\boldsymbol{\kappa},\boldsymbol{\kappa}')}{\omega_{p,\alpha}(\kappa_p,\alpha)}[f_p^\circ(\omega_{p,\alpha})+\frac{1}{2}\mp\frac{1}{2}]\\ &\quad\times\delta_{\mathrm{D}}(\boldsymbol{\kappa}\pm\boldsymbol{\kappa}_p-\boldsymbol{\kappa}')\,\delta_{\mathrm{D}}(E_{e,\kappa'}-E_{e,\kappa}\mp\hbar\omega_{p,\alpha})\mathrm{d}\boldsymbol{\kappa}'\\ &\quad\text{electron–phonon scattering,}\end{aligned} \tag{5.176}$$

where

$$G(\boldsymbol{\kappa}, \boldsymbol{\kappa}') = 1 \ \text{ for parabolic bands,} \tag{5.177}$$

and $C_{\kappa_p,\alpha}$ is related to the integral of $\varphi_{s,e\text{-}p}$ taken over the cell (5.174), and can be a complex variable. Again, N is the number of unit cells, and m is the mass of the oscillator. For nonparabolic bands, $G(\boldsymbol{\kappa}, \boldsymbol{\kappa}')$ is given in [433] for both electrons and holes.

5.15.2 Rate of Acoustic-Phonon Scattering of Electrons

Acoustic-phonon scattering of electrons (and holes in semiconductors), i.e., fluctuation in electron energy caused by strain (deformation potential scattering), are nearly elastic, and from using (5.162) and (5.164) we have

$$\begin{aligned}
\varphi_{s,e\text{-}p} &= \varphi_{d,\mathrm{A}} \frac{\mathrm{d}d}{\mathrm{d}x} \\
&= \frac{1}{N^{1/2}} \sum_{\boldsymbol{\kappa}_p} \{[i Q_{\boldsymbol{\kappa}_p,\alpha} \varphi_{d,\mathrm{A}} \boldsymbol{s}_{\boldsymbol{\alpha}} \cdot \boldsymbol{\kappa}_{\boldsymbol{p}} e^{i(\boldsymbol{\kappa}_p \cdot \boldsymbol{x}_\mathrm{o})}] \\
&\quad + [i Q_{\boldsymbol{\kappa}_p,\alpha} \varphi_{d,\mathrm{A}} \boldsymbol{s}_\alpha \cdot \boldsymbol{\kappa}_{\boldsymbol{p}} e^{i(\boldsymbol{\kappa}_p \cdot \boldsymbol{x}_\mathrm{o})}]^\dagger\}.
\end{aligned} \tag{5.178}$$

Then, using (5.174), we have

$$C^2_{\kappa_p,\alpha} = \varphi^2_{d,\mathrm{A}} \kappa^2_p. \tag{5.179}$$

Using the $\boldsymbol{\kappa}_p \to 0$ approximation for the acoustic phonons (Section 4.1), we have for the acoustic-phonon dispersion

$$\omega_p = u_{p,\mathrm{A}} \kappa_p. \tag{5.180}$$

Using Table 1.2 for f_p°, we have the classical limit for bosons (including phonons, Figure 1.1)

$$f_p^\circ = \frac{1}{\exp(\dfrac{\hbar\omega_p}{k_\mathrm{B}T}) - 1} \simeq \frac{k_\mathrm{B}T}{\hbar\omega_p} \quad \text{for} \quad \hbar\omega_p \ll k_\mathrm{B}T. \tag{5.181}$$

Then, using (5.179) to (5.181) in (5.176), we have the acoustic-phonon-scattering rate of electrons as

$$\begin{aligned}
\dot{\gamma}_{e\text{-}p,\mathrm{A}} = \frac{1}{\tau_{e\text{-}p,\mathrm{A}}} &= \frac{4\pi^3}{8\pi^2 N m} \int \frac{\varphi^2_{d,\mathrm{A}} \kappa^2_p}{\omega_p} [f_p^\circ + \frac{1}{2} \mp \frac{1}{2}] \delta_\mathrm{D}(\boldsymbol{\kappa} \pm \boldsymbol{\kappa}_p - \boldsymbol{\kappa}') \\
&\quad \times \delta_\mathrm{D}(E_{e,\boldsymbol{\kappa}'} - E_{e,\boldsymbol{\kappa}} \mp \hbar\omega_p) \mathrm{d}\boldsymbol{\kappa}' \\
&= \frac{\varphi^2_{d,\mathrm{A}} k_\mathrm{B} T}{8\pi^2 \hbar \rho u^2_{p,A}} \int \delta_\mathrm{D}(\boldsymbol{\kappa} \pm \boldsymbol{\kappa}_p - \boldsymbol{\kappa}') \delta_\mathrm{D}(E_{e,\boldsymbol{\kappa}'} - E_{e,\boldsymbol{\kappa}} \mp \hbar\omega_p) \mathrm{d}\boldsymbol{\kappa}',
\end{aligned} \tag{5.182}$$

where $\rho = mN/V$. For low-energy phonons $f_p^\circ \gg 1$, so we have neglected the 1/2 terms. Also for low-energy phonons [classical limit, from (5.181), for bosons], $f_p^\circ \simeq k_\mathrm{B}T/\hbar\omega_p$.

We also note that, from (5.65),

$$\frac{1}{8\pi^3}\int \delta_{\rm D}[E_e(\boldsymbol{\kappa}) - E_e(\boldsymbol{\kappa}')]{\rm d}\boldsymbol{\kappa}' = D_e[E_e(\boldsymbol{\kappa})]. \tag{5.183}$$

Now, for elastic scattering (dropping $\hbar\omega_p$), and because $\boldsymbol{p}_e = \hbar\boldsymbol{\kappa}_e$, we have [433]

$$\frac{1}{\tau_{e\text{-}p,A}} = \frac{\pi\varphi_{d,{\rm A}}^2 k_{\rm B}T D_e[E_e(\boldsymbol{p})]}{\hbar\rho u_{p,{\rm A}}^2} . \tag{5.184}$$

Now, using (5.66) for D_e, we have

$$\frac{1}{\tau_{e\text{-}p,{\rm A}}(\text{momentum})} = \frac{2^{1/2}m_{e,e}^{3/2}\varphi_{d,{\rm A}}^2 k_{\rm B}T E_e^{1/2}(\boldsymbol{p})}{\pi\hbar^4\rho u_{p,{\rm A}}^2}$$

$$\text{elastic acoustic-phonon scattering,} \tag{5.185}$$

which is listed in Table 5.4. Note that T here is the lattice temperature. Writing this in terms of power-law relation (5.113), we have $s = -1/2$ (Table 5.3), i.e.,

$$\tau_{e\text{-}p,{\rm A}}(\text{momentum}) = (\tau_{e\text{-}p,{\rm A}})_{\rm o}[\frac{E_e(\boldsymbol{p})}{k_{\rm B}T}]^{-1/2},$$

$$(\tau_{e\text{-}p,{\rm A}})_{\rm o}(\text{momentum}) = \frac{\pi\hbar^4\rho u_{p,{\rm A}}^2}{2^{1/2}m_{e,e}^{3/2}\varphi_{d,{\rm A}}^2(k_{\rm B}T)^{3/2}}. \tag{5.186}$$

To use this, the perturbation deformation potential $\varphi_{d,{\rm A}}$ should be known (of the order of 1 eV, Table 5.5). The average acoustic-phonon speed $u_{p,{\rm A}}$ is found from $u_{p,{\rm A}} = u_{p,g,{\rm A}}$ given by (4.61). Also the larger $E_e(\boldsymbol{p})$ the shorter the relaxation time.

The total scattering is the sum of emission and absorption, and because they are the same here (neglecting $\hbar\omega_p$), $\tau_{e\text{-}p,{\rm A}}$ total is twice (5.184).

The variation of $\tau_{e\text{-}p,{\rm A}}^{-1}$, with respect to E_e, for Si, is shown in Figure 5.13(a).

5.15.3 Rate of Optical-Phonon Scattering of Electrons

(A) *Nonpolar Optical Phonons*

The scattering potential for nonpolar (Section 4.6) optical phonons is given by the perturbation Hamiltonian [433]

$$\varphi_{s,e\text{-}p} = \boldsymbol{\varphi}_{d,{\rm O}}' \cdot \boldsymbol{d} \quad \text{optical-phonon perturbation Hamiltonian,} \tag{5.187}$$

where $\boldsymbol{\varphi}_{d,{\rm O}}'$ is the nonpolar optical deformation potential derivative vector. Then after evaluation of (5.187) in (5.96), we have [433]

$$C_{\kappa_p,\alpha}^2 = \varphi_{d,{\rm O}}'^2. \tag{5.188}$$

Using the $\kappa_p \to 0$ approximation of the optical-phonon dispersion (Section 4.1), we use a constant phonon frequency (dispersionless) $\omega_{p,{\rm O}}$ (zone center), and the

Table 5.5. *Parameters used in the electron scattering relaxation-time relations, for Si and GaAs [433].*

Parameter	Symbol	Magnitude, Si	Magnitude, GaAs
Mass density (g/cm^3)	ρ	2.329	5.36
Lattice constant	a	5.43	5.642
Low frequency dielectric constant	$\epsilon_{e,s}$	11.7	12.90
High frequency dielectric constant	$\epsilon_{e,\infty}$	–	10.92
Piezolelectric constant (C/m^2)	e_{pz}	–	0.160
LA velocity ($\times 10^5$ cm/s)	$u_{p,\mathrm{LA}}$	9.04	5.24
TA velocity ($\times 10^5$ cm/s)	$u_{p,\mathrm{TA}}$	5.34	3.0
LO phonon energy (eV)	$\hbar\omega_{p,\mathrm{O}}$	0.063	0.03536
Electron effective mass	$m^*_{e,e}$	–	0.067
(lowest valley)(m_e)	$m^*_{e,e,\mathrm{L}}, m_{e,e,\mathrm{T}}$	0.916, 0.19(X)	–
Electron effective mass	$m^*_{e,e}$	–	0.222(L)
(upper valley) (m_e)	$m^*_{e,e}$	–	0.58(X)
	$m^*_{e,e,\mathrm{L}}, m_{e,e,\mathrm{T}}$	1.59,0.12(L)	–
Nonparabolicity parameter (eV^{-1})	α	0.5(X)	0.610,0.461(L), 0.204(X)
Energy separation	$\Delta E_{e,\Gamma\mathrm{L}}$	–	0.29
between valleys (eV)	$\Delta E_{e,\Gamma\mathrm{X}}-$	0.48	
Electron acoustic deformation potential (eV)	$\varphi_{d,\mathrm{A}}$	9.5	7.0(Γ) 9.2(L) 9.0(X)
Electron optical deformation potential ($\times 10^8$ eV/cm)	$\varphi'_{d,\mathrm{O}}$	–	3.0(L)
Optical-phonon energy (eV)	$\omega_{p,\mathrm{O}}$	0.0642	0.0343
Hole acoustic deformation potential (eV)	$\varphi_{d,h,\mathrm{A}}$	5.0	3.5
Hole optical deformation potential ($\times 10^8$ eV/cm)	$\varphi'_{d,h,\mathrm{O}}$	6.00	6.48
Intervalley parameters, g-type(X-X) ($\times 10^8$ eV/cm), (eV)	$\varphi'_{iv}, \hbar\omega$	0.5, 0.012(TA) 0.8, 0.019(LA) 11.0,0.062(LO)	
Intervalley parameters, f-type(X-X) ($\times 10^8$ eV/cm), (eV)	$\varphi'_{iv}, \hbar\omega$	0.3, 0.019(TA) 2.0, 9.947(LA) 2.0,0.059(LO)	
Intervalley parameters (X-L) ($\times 10^8$ eV/cm), (eV)	$\varphi'_{iv}, \hbar\omega$	2.0, 0.058 2.0, 0.055 2.0,0.041 2.0,0.017	
Intervalley deformation potential ($\times 10^8$ eV/cm)	$\varphi'_{d,\mathrm{O}}(\Gamma\mathrm{L})$ $\varphi'_{d,\mathrm{O}}(\Gamma\mathrm{X})$ $\varphi'_{d,\mathrm{O}}(\mathrm{LL})$, $\varphi'_{d,\mathrm{O}}(\mathrm{LX})$ $\varphi_{d\mathrm{A}}(\mathrm{XX})$	–	10.0 10.0 10.0 5.0 7.0
Intervalley phonon energy (eV)	$(\hbar\omega)_i$	–	0.0278,0.0299 0.0290, 0.0293 0.0299

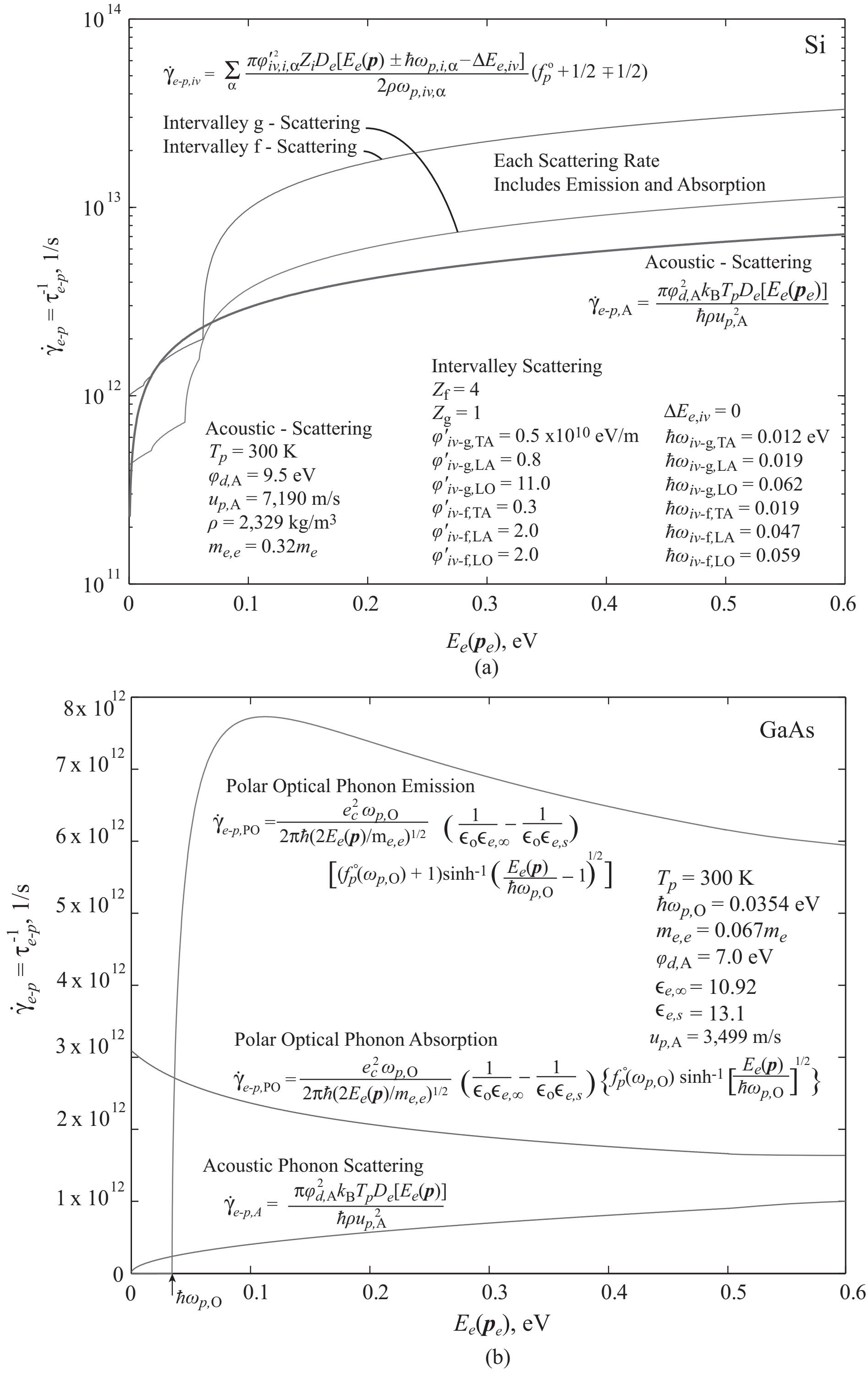

Figure 5.13. (a) Predicted variations of the phonon relaxation times in Si with respect to the electron kinetic energy. For the intervalley scattering the contributions from phonon emission and absorption are added. (b) Variations of the optical-phonon and acoustic-phonon-scattering relaxation times for electrons in GaAs, with respect to the electron kinetic energy. The results are for $T_p = 300$ K.

result for (5.176) is [433] (also an end-of-chapter problem)

$$\frac{1}{\tau_{e\text{-}p,\mathrm{O}}(\text{momentum})} = \frac{\pi\varphi_{d,\mathrm{O}}^{\prime 2}}{2\rho\omega_{p,\mathrm{O}}} f_p^\circ(\omega_{p,\mathrm{O}}) D_e[E_e(\boldsymbol{p}) + \hbar\omega_{p,\mathrm{O}}]$$

$$\text{nonpolar optical-phonon absorption} \qquad (5.189)$$

$$\frac{1}{\tau_{e\text{-}p,\mathrm{O}}(\text{momentum})} = \frac{\pi\varphi_{d,\mathrm{O}}^{\prime 2}}{2\rho\omega_{p,\mathrm{O}}} [f_p^o(\omega_{p,\mathrm{O}}) + 1] D_e[E_e(\boldsymbol{p}) - \hbar\omega_{p,\mathrm{O}}]$$

$$\text{nonpolar optical-phonon emission,} \qquad (5.190)$$

where we have used (5.65), for $D_e(E)$, with spin degeneracy, and $nm = \rho$, as our analysis is per-unit volume. Typical values of $\varphi'_{d,\mathrm{O}}$ are listed in Table 5.5. Since D_e is given by (5.66), the $\tau_{e\text{-}p,\mathrm{O}}$ presents a power-law relation with $s = -1/2$.

For nonpolar semiconductors, the electron scattering (transition) is dominated by phonon-induced transitions between the valleys in the constant-energy surface and requires optical phonons. Figure 5.8(c) shows the six equivalent conduction-band valleys of Si. The scattering between opposite valleys, e.g., [100] to [$\bar{1}$00] is called the g-process, and that between nonopposite valleys is called the f-process. These are shown in Figure 5.8(c). The momentum is conserved, and the intervalley scattering involves an Umklapp process (5.97). The indirect bands of Si are shown in Figure 5.6(a), and the minimum in the conduction band is not at the zone edge (X-point). Then 0.3 times the dimensionless wave vector away from the zone edge, or $0.3(2\pi/a[100])$ phonon energy, is needed for a g-process. The intervalley (or interband) scattering is similar to the nonpolar optical phonon scattering and the relations for both absorption and emission are given in Table 5.4. For Si, the intervalley scattering is also shown in Figure 5.13(a). The properties are listed in Table 5.5. The electron-photon interaction for the case of emission, is similar to the spontaneous emission relation (3.43).

(B) *Polar Optical Phonons*

In the polar optical phonon–electron interaction, the LO phonon modes create a polarization that is due to an effective charge q_e, which is expressed in terms of low-frequency (static) and high-frequency dielectric constants, $\epsilon_{e,s}$ and $\epsilon_{e,\infty}$ (3.50). The polar optical phonons were discussed in Section 4.6, showing that at the Brillouin zone center $E_{p,\mathrm{LO}} > E_{p,\mathrm{TO}}$ (Figure 4.16).

The polarization and the effective charge density q_e/V_c in (5.162), where V_c is the unit-cell volume, are given by

$$\boldsymbol{p}_e(0) = \frac{1}{4\pi}(\frac{\epsilon_{e,s} - 1}{\epsilon_{e,s}})\boldsymbol{d}, \quad \boldsymbol{p}_e(\infty) = \frac{1}{4\pi}(\frac{\epsilon_{e,\infty} - 1}{\epsilon_{e,\infty}})\boldsymbol{d}$$

$$\frac{q_e^2}{V_c} = \frac{\epsilon_\mathrm{O}\rho\omega_{p,\mathrm{O}}^2}{\epsilon_{e,\infty}}(\frac{\epsilon_{e,\infty}}{\epsilon_{e,s}} - 1)$$

$$\text{effective charge in polar optical-phonon scattering,} \qquad (5.191)$$

where $(\epsilon_{e,\infty}/\epsilon_{e,s})-1$ is a measure of strength of the polar dipole (Section 4.6) [294].

For polar optical-phonon scattering (Section 4.6), the Debye model electric permittivity (dielectric function) of the solid (3.50) is used, and the expressions for $\tau_{e\text{-}p,\mathrm{PO}}$ are listed in Table 5.4.

The variation of $\tau^{-1}_{e\text{-}p,\mathrm{A}}$ and $\tau^{-1}_{e\text{-}p,\mathrm{PO}}$ (emission and absorption) with respect to E_e, for GaAs, is shown in Figure 5.13(b). The phonon dispersion for GaAs is shown in Figure 4.9.

Note that the smallest $\tau_{e\text{-}i}$ controls the electric transport, according to (5.115), and from the results shown in Figures 5.13(a) and (b), this depends on the electron kinetic energy (and also on the lattice temperature T_p).

5.15.4 Summary of Electron-Scattering Mechanisms and Relaxation-Time Relations

A summary of various electron scatterings is given in Table 5.4.[†] The parameters used in the expressions for two semiconductors, Si and GaAs, are listed in Table 5.5.

These include the electron–alloy, electron-impurity, electron–phonon (acoustic, polar optical, and nonpolar optical), electron–photon and phonon-assisted electron–photon scatterings.

Distinctions are made between the momentum and energy-scattering relaxation times (Section 3.1.6); and we will further discuss these in Section 5.18.

5.16 TE Transport Coefficients Data for Metals and Semiconductors

5.16.1 Structural Defects in Crystalline Solids

Various formation defects cause deviation, from the ideal phonon and electron transport properties, and these should be considered when one is comparing experimental results with the theoretical predictions. A stable crystalline lattice can accept defects up to a threshold maximum concentration (number density) n_d; beyond this point the lattice breaks down, and either a different crystal structure is formed or the structure becomes amorphous. Crystal defects are thermodynamically controlled phenomena and formation of defects, and the most probable defect is simply that which leads to the lowest free energy for the crystal.

An intrinsic defect is a stoichiometric defect, i.e., a structural defect that preserves the overall ideal chemical stoichiometry, e.g., the 1:1 ratio of cation to anion in NaCl. An extrinsic defect is a nonstoichiometric defect, i.e., a defect that leads to a fractional change in stoichiometry. A point defect is a defect involving

---

[†] In addition, for TE materials, such as telluride compounds, more specific relaxation-time models have been developed, including the Kane model further described in Section 5.17.3.

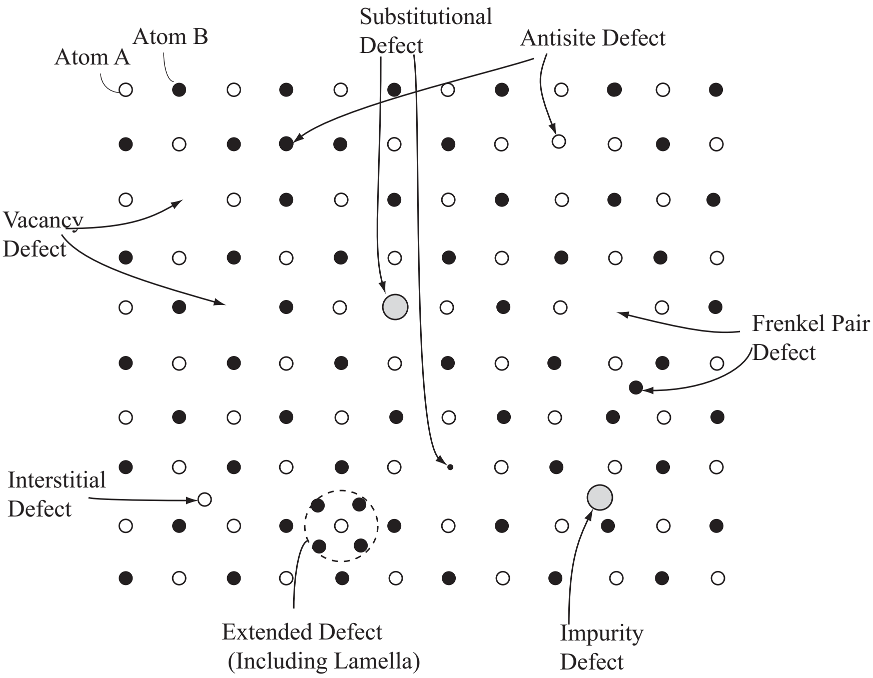

Figure 5.14. Some typical crystalline solid structure defects affecting phonon and electron transport.

isolated atom or ion sites in the lattice. The extended (topology) defects include line defects (also called dislocations, including those from lamella) and plane defects. In Frenkel defects, one atom is displaced off its regular lattice site into an interstitial location.

Figure 5.14 shows examples of crystal structural defects that can influence the phonon and electron transport coefficients. In TE materials, both point and extended defects contribute to nonideal properties. The point defects include antisite, impurity, interstitial, substitutional, and vacancy.

5.16.2 Metals

For metals (degenerate conductors), the number density of conducting electrons $n_{e,c}$ is constant and the Fermi energy (level) lies well preceding the conduction band edge, and

$$f_e^{\rm o}(E_e) = \frac{1}{e^{E_e^* - E_{\rm F}^*} + 1}, \quad E_{\rm F}^* = \frac{E_{\rm F}}{k_{\rm B}T} \gg 1 \quad \text{metals.} \tag{5.192}$$

The Fermi energy [related to $n_{e,c}$ through (5.55)] for metals is listed in Table 5.2. Then the electrical conductivity (5.131), which when using (5.53) for $n_{e,c}$ becomes

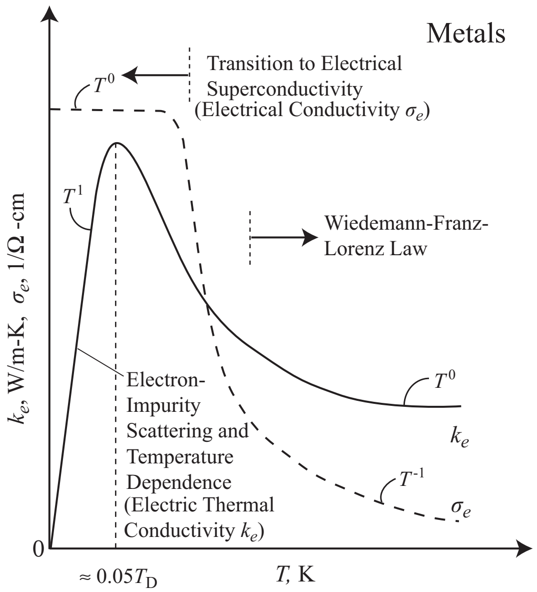

Figure 5.15. Variation of the electrical conductivity and the electronic thermal conductivity of metals, with respect to temperature. At low temperatures, the electron-impurity (defect) scattering affects the electronic thermal conductivity, more pronounced resulting in vanishing thermal conductivity, whereas the electrical conductivity reaches a plateau [30].

[163][†] (for power-law relaxation time)

$$\sigma_e = n_{e,c} e_c \mu_e = \frac{8\pi}{3}\left(\frac{1}{2\pi^2\hbar^2}\right)^{3/2} e_c^2 m_e^{1/2} \tau_{e,\mathrm{o}} \left(\frac{E_\mathrm{F}}{k_\mathrm{B} T}\right)^{s+3/2}$$

$$\text{electrical conductivity for metals.} \qquad (5.193)$$

To obtain (5.193), (5.125) is evaluated under the degenerate conductor treatment of $E_\mathrm{F}/k_\mathrm{B}T \gg 1$. Wiedemann–Franz–Lorenz law (5.151) holds at higher temperatures, where the electron–phonon scattering dominates. Thus we can use (5.186) in $\tau_{e,\mathrm{O}} = (\tau_{e\text{-}p,\mathrm{A}})_\mathrm{o}$. At low temperatures, the electronic thermal conductivity is pronouncedly more affected by impurity scattering (compared to the electrical conductivity). These trends are shown in Figure 5.15. Note that k_e has similar temperature dependence as k_p shown in Figure 4.17. Both k_e and k_p diminish as $T \rightarrow 0$. At high temperatures, in metals σ_e is proportional to $1/T$ [will be shown in Figure 5.16(a)], so k_e becomes nearly independent of T, while, k_p has the $1/T$ behavior presented by the Slack model (4.132). The peak in k_e and k_p is around 0.05 and 0.1 T_D,

---

[†] Note that for a power-law relaxation time we have

$$\int_0^\infty E_e^{j+s+3/2} \frac{\partial f_e^\mathrm{o}}{\partial E_e} \mathrm{d}E_e = -(j+s+3/2)\int_0^\infty E_e^{j+s+1/2} f_e^\mathrm{o}(E_e)\mathrm{d}E_e,$$

and for metals we have

$$\int_0^\infty E_e^n f_e^\mathrm{o}(E_e) \simeq \frac{1}{n+1}\left(\frac{E_\mathrm{F}}{k_\mathrm{B}T}\right)^{n+1}.$$

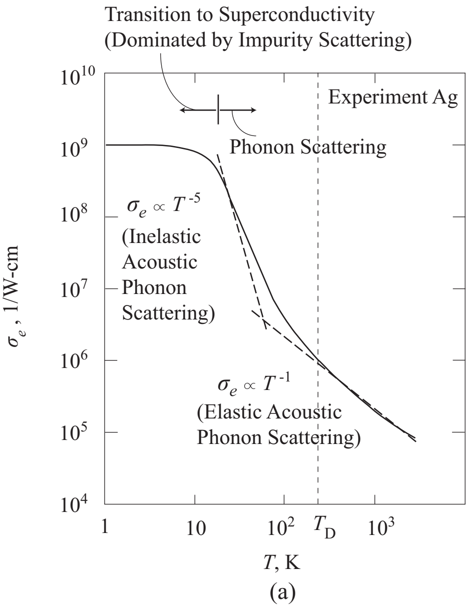

(a)

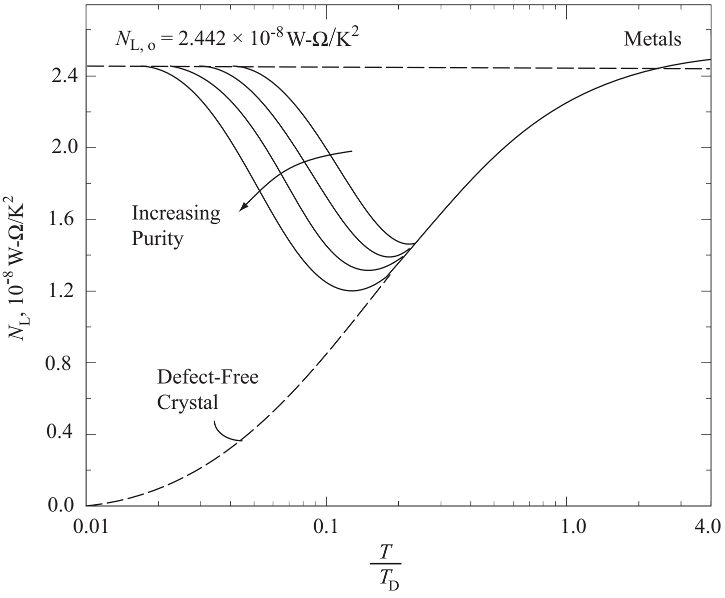

(b)

Figure 5.16. (a) Typical temperature dependence of the electrical conductivity for Ag [63]. (b) Variation of the Lorenz number with respect to T/T_D for metals [30].

respectively. We will discuss this further in the next section, where the experimental results are presented.

Based on acoustic-phonon-dominated scattering ($s = -1/2$ in Table 5.3), (5.193) shows that σ_e is proportional to $1/T$, which is characteristic of metallic electrical conductivity at high temperatures.

Also, for metals the Seebeck coefficient is found from (5.126) and (5.143) as [163]

$$\alpha_S = \mp\frac{\pi^2}{3}\frac{k_B}{e_c}\frac{s+\frac{3}{2}}{\frac{E_F}{k_B T}} = \mp\frac{\pi^2}{3}\frac{k_B^2}{e_c E_F}(s+\frac{3}{2})T \quad \text{Seebeck coefficient for metals.} \quad (5.194)$$

Note that $k_B/e_c = 86\ \mu\text{V/K}$, giving the order of magnitude of the Seebeck coefficient.

The Fermi energies of metals are listed in Table 5.2.

Also, from (5.157), for metals we have

$$k_e = N_{L,o}\sigma_e T = 2.442 \times 10^{-8}\sigma_e T$$

$$\text{Lorenz number for metals at high temperatures.} \quad (5.195)$$

We note that this overpredicts k_e for some metals, especially at moderate temperatures. Then the Lorenz number (or Lorenz ratio) N_L depends on temperature, as shown in Figure 5.16(b) for metals [30]. Note that, for pure metals, the Lorenz number becomes fairly small as $T \rightarrow 0$.

Thomson coefficient (5.152) for metals becomes the same as the Seebeck coefficient (5.194).

Figure 5.16(a) shows the measured variation of the electrical conductivity of Ag with respect to temperature. There are three distinct regimes, starting with the constant high conductivity at low temperatures (limited by impurity scattering). Then there is a high-scattering regime (inelastic acoustic-phonon scattering) with a very strong temperature dependence and large drop in conductivity. This is then followed by the largely elastic acoustic-phonon-scattering regime with a T^{-1} dependency. Then (5.193) can predict the high temperature behavior of σ_e, with $s = -1/2$.

Bloch [18] has suggested an approximate analysis for the scaled electrical resistivity, using the Debye temperature. He found that, for all metals, the following relation holds with relatively good accuracy [18]:

$$\frac{\rho_e}{\rho_e(T_D)} = \frac{\sigma_e(T_D)}{\sigma_e} = 3.7(\frac{T}{T_D})^5 \int_0^{T_D/T} \frac{x^5 e^x}{(e^x-1)^2}\mathrm{d}x$$

$$\text{Bloch model for metal electrical conductivity.} \quad (5.196)$$

This relation is shown in Figure 5.17, along with the data for several metals.

Figure 5.18(a) shows the variation of measured thermal conductivity of some metals (including Cu) with respect to temperature.

To examine the validity of the Wiedemann–Franz–Lorenz law, the results from using it along with the experimental results for Cu [196], to predict the thermal conductivity, are shown in Figure 5.18(b). The Debye temperature of Cu is 315 K (Table A.2). The peak in the experimental value of k_e (we assume that $k_p \simeq 0$) is located around $T = 10$ K. The Wiedemann–Franz–Lorenz law (with constant Lorenz number) along with the experimental result for σ_e [283] follows the experimental k_e, with better agreement at higher temperatures. Note that the temperature-dependent Lorenz number of Figure 5.16(b) allows for a match with experimental results.

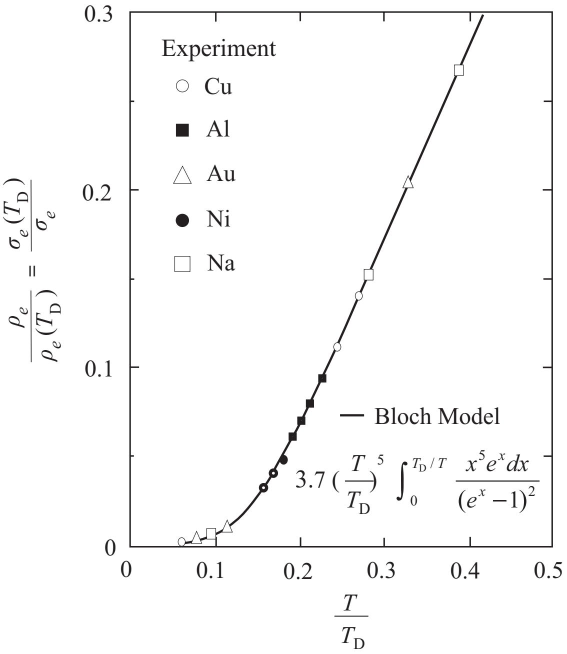

Figure 5.17. Temperature dependence of the electrical resistivity for five different metals as a function of the scaled temperature [18]. The Bloch model is also shown.

Also shown in Figure 5.18(b) is that the Bloch model of the electrical conductivity (5.196) overpredicts σ_e at low temperatures, and there is better agreement in the predicted k_e for higher temperatures.

In this example, (5.195) overpredicts k_e and (5.196) should be used at higher temperatures. Also note that the experimental results are for $k = k_p + k_e$. The relation $\sigma_e T$ vanishes as $T \rightarrow 0$. Both k_p and k_e are strongly reduced by impurity scattering at low temperatures (k_p is also reduced at low temperatures, due to reduction in $c_{v,p}$).

Because of the lack of data for k_p, we can only suggest the difference between the predicted k_e and the measured k at low temperatures is due to k_p.

The measured Seebeck coefficient of some metals, as a function of temperature, is shown in Figure 5.19. There is a general agreement with the temperature to the power-unity relation given in (5.194) for moderate high temperatures. Platinum has a peak in the positive region and then has a negative α_S at larger temperatures. Normal metals refers to those having $D_e(E_e)$ presented by (5.66), i.e., parabolic relation, and include Na, K, and Al. On the other hand, Pt is an abnormal metal. The diffusion of electrons from a hot to a cold region is influenced by the lattice vibration (phonon) and ion scattering and the electron DOS is therefore altered, resulting in a change of sign in α_S (which is expected to be negative for normal metals).

For metals, the TE figure of merit (Section 5.16.4) $Z_e T = \alpha_S^2 \sigma_e T/(k_e + k_p)$, for $s = 0$, and using (5.157) and (5.194) becomes $Z_e T \leq 3\pi^2/4(E_F/k_B T)$, then for $E_F/k_B T > 4$,

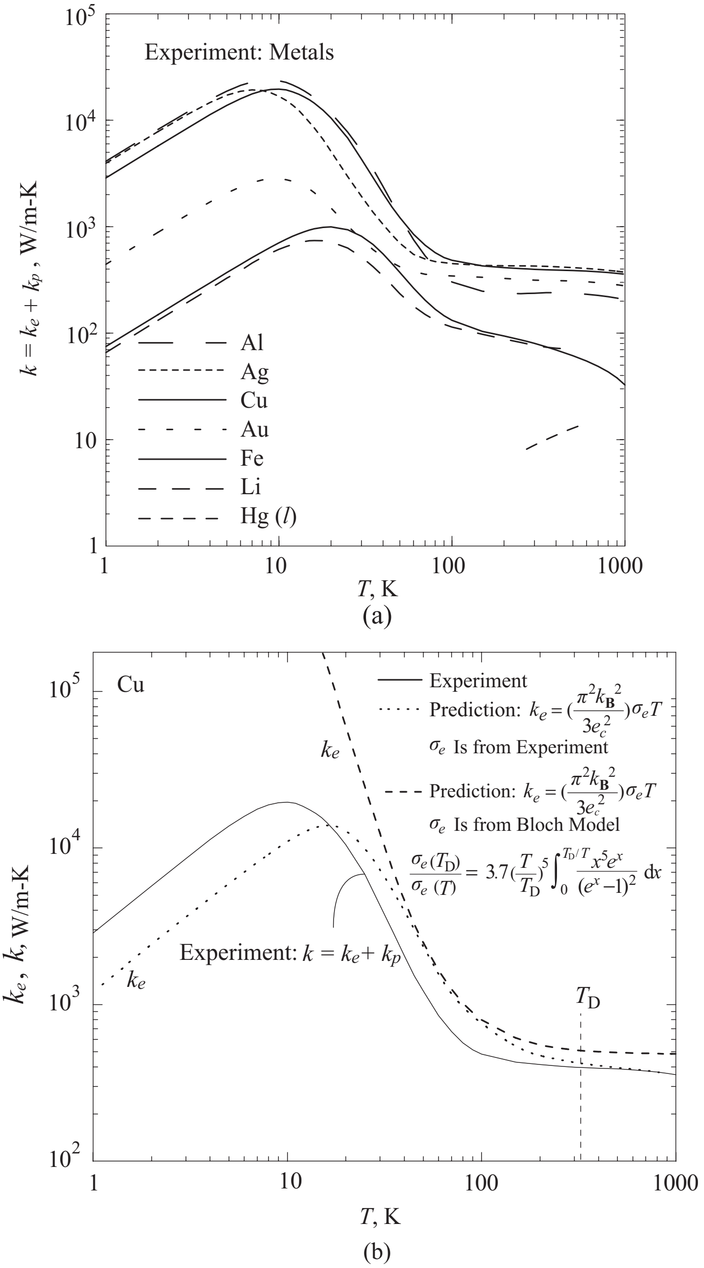

Figure 5.18. (a) Metal (mostly electronic) thermal conductivity for some metals. For Hg, the liquid conductivity is shown [196]. The conductivity for metals is dominated by electronic contribution. (b) Variations of the electronic and total thermal conductivities with respect to temperature, for Cu. In addition to the experimental results, the results obtained with the experimental results for the electrical conductivity along with the use of the Wiedemann–Franz–Lorenz law, are shown. Also shown is the prediction using the Bloch model of the electrical conductivity along with the Wiedemann–Franz–Lorenz law.

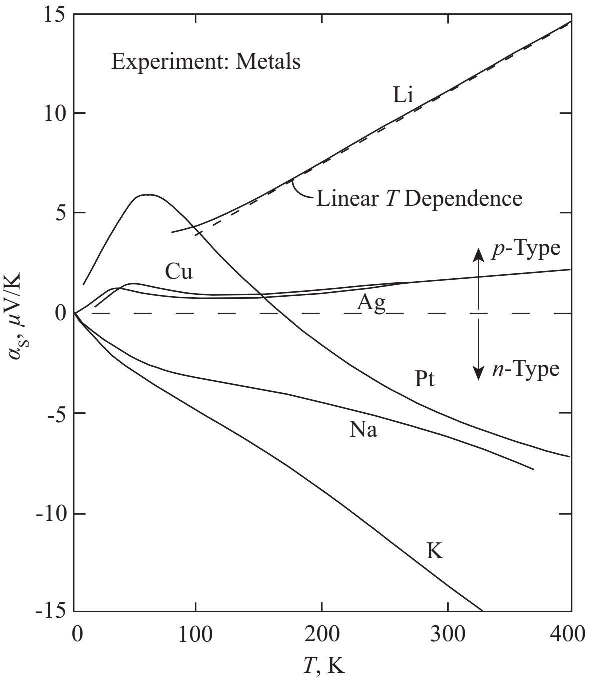

Figure 5.19. Variation of the Seebeck coefficient of some metals with respect to temperature [120].

we have an upper limit of $Z_eT \leq 0.46$. This inequality is because we used the limit of $k_p = 0$. As we will be shown in Section 5.16.4, for semiconductors can have higher Z_eT.

5.16.3 Semiconductors

The room-temperature ranges of the conduction electron density and the electrical conductivity of various materials are shown in Figure 5.20. Metals are marked with having $n_{e,c} > 10^{21}$ 1/cm^3. Doped semiconductors (n- and p-type semiconductors are defined in the Glossary) reach the electron density and conductivity of metals. Metals are also marked with having $\sigma_e > 10^3$ 1/Ω-cm.

The temperature dependences of the electrical conductivity of metals, semiconductors, and insulators are shown in Figure 5.21. Although both metals and insulators have their electrical conductivities decreasing with temperature, those of intrinsic semiconductors increase with temperature. The n-type dopants move the behavior of semiconductors toward metals, as expected. For the n-type doping (excess electron over intrinsic electron density), As, P, and Sb (group 15, five valence electrons) are used, while for the p-type, Al and B (group 13, three valence electrons) are used. For the moderately doped Si shown in Figure 5.21, as the temperature is lowered, there is deactivation of the ionized dopants and this is called dopant freeze out.

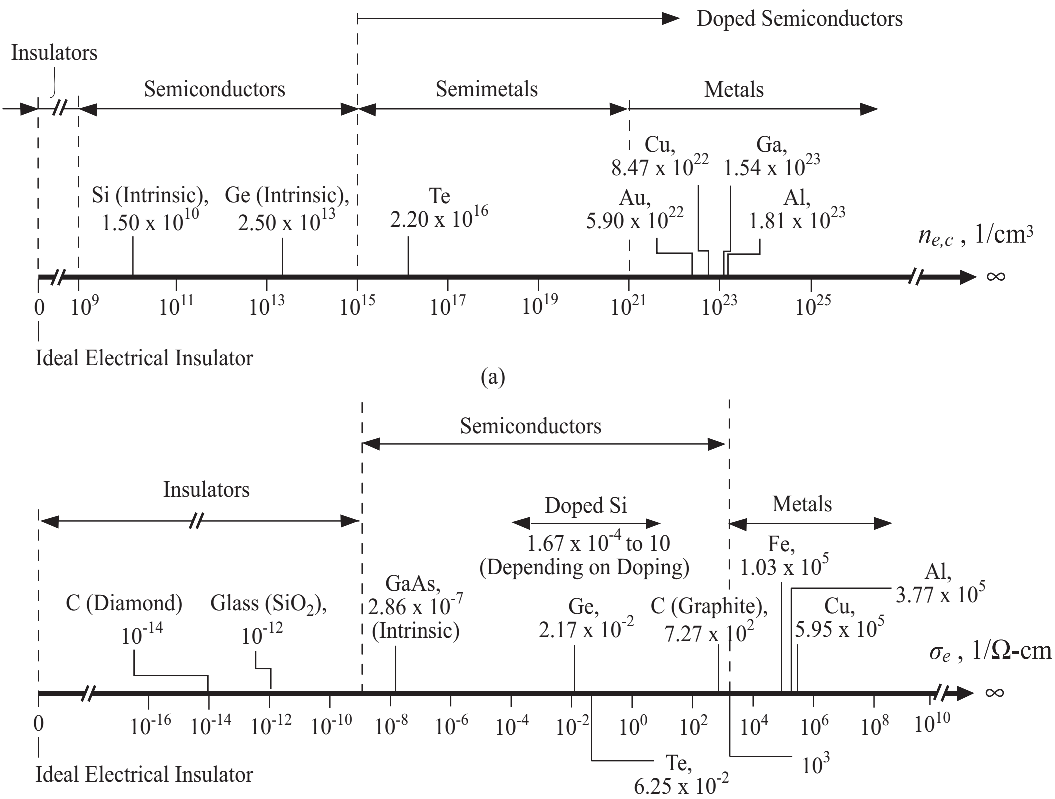

(a)

(b)

Figure 5.20. (a) Range of the measured conduction electron density $n_{e,c}$ of metals (few electrons per atom), semimetals, semiconductors, and insulators. (b) Range of the electrical conductivity of some metals, semiconductors, and insulators. The results are for $T = 300$ K.

As an example of the electrical and thermal properties of intrinsic and doped semiconductors, Figures 5.22 to 5.25 show the hole (holes h^+ have a change of $+e_c$) concentration $n_{h,c}$, hole mobility μ_h, total electrical conductivity σ_e, and thermal conductivity k of doped Si. The total electric conductivity is

$$\sigma_e = e_c(n_{h,c}\mu_h + n_{e,c}\mu_e). \tag{5.197}$$

Table 5.6 lists the effective bandgap at 0 and 300 K, and the electron and hole mobilities at 300 K, for some semiconductors. As mentioned in Section 5.5, for most semiconductors $\Delta E_{e,g}$ decreases with temperature. Exceptions include PbTe, for which there is a transition from direct to indirect bandgap (around 420 K), it is the direct bandgap (at L-point) which is temperature dependent.

For low electric fields, the drift velocity–electric field relation is linear, and also, using the average momentum relaxation time (5.113), the electron mobility is

$$\mu_e = \frac{e_c\langle\langle\tau_e\rangle\rangle}{m_{e,e}}, \tag{5.198}$$

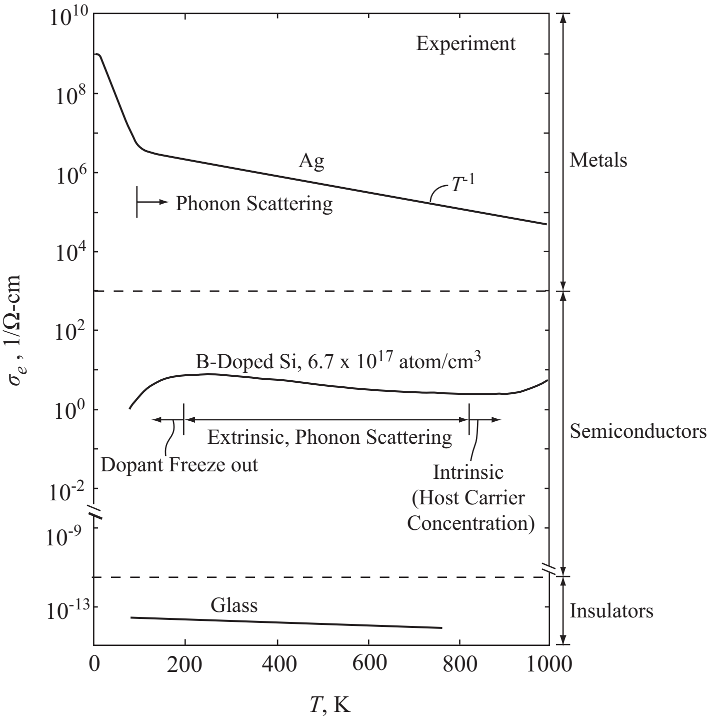

Figure 5.21. Variations of the measured electrical conductivity of a typical metal, semiconductor (intrinsic and doped), and insulator, with respect to temperature. Dopant freeze out relates to a lack of activation energy to ionize dopants.

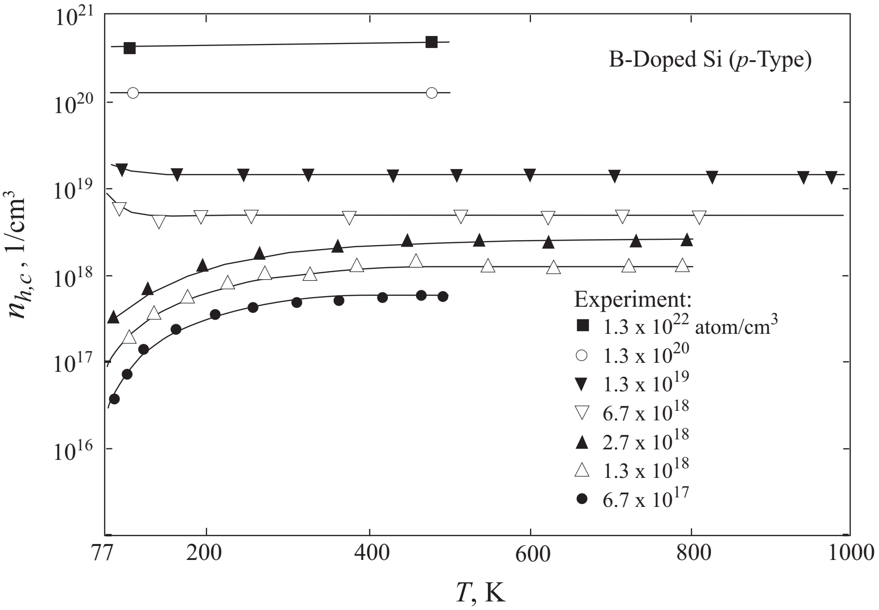

Figure 5.22. Variation of the hole concentration for intrinsic and B-doped Si with respect to temperature [297].

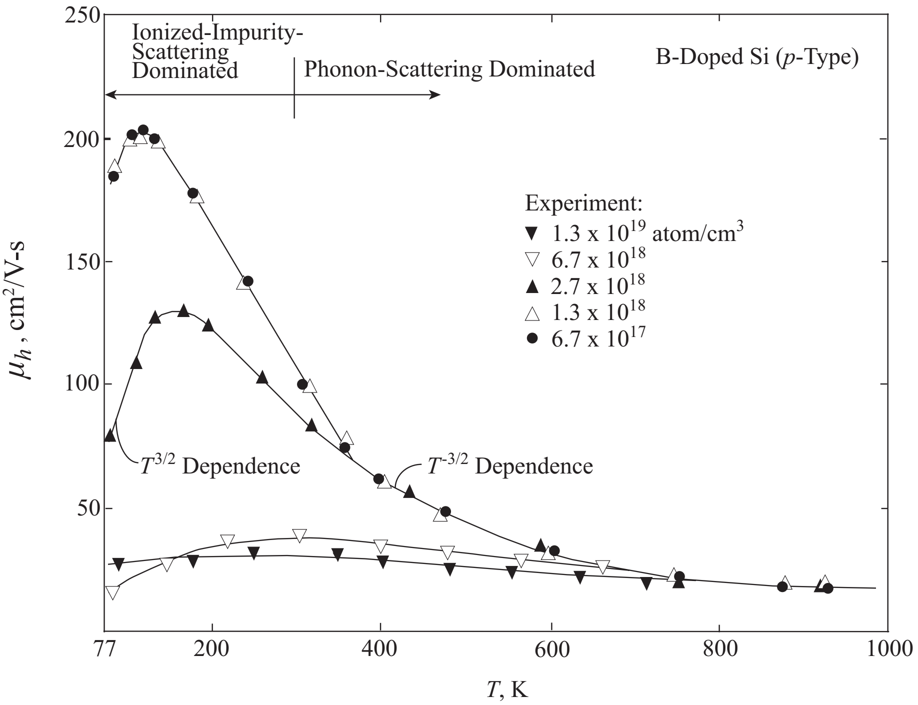

Figure 5.23. Variation of the hole mobility for B-doped Si with respect to temperature [297]. The low-temperature impurity-scattering and high-temperature acoustic-phonon-scattering are evident.

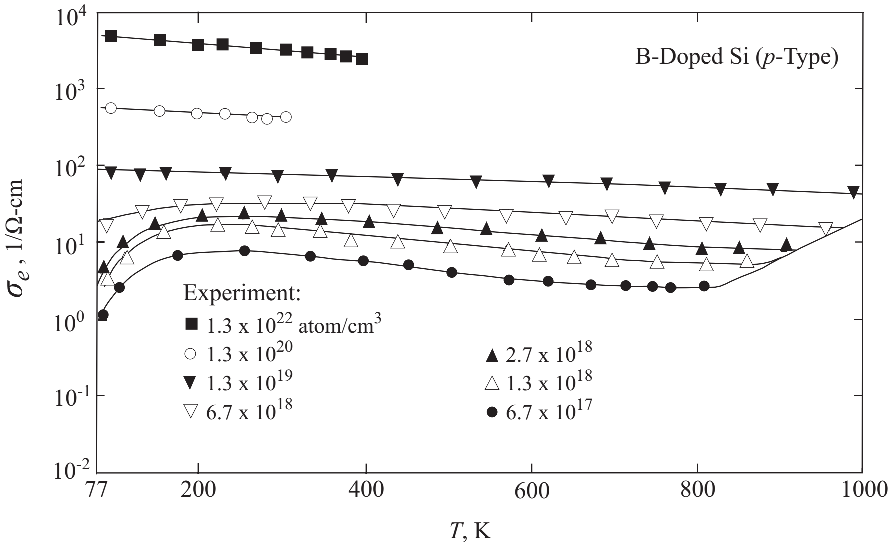

Figure 5.24. Variation of the total electrical conductivity for B-doped Si (p-type) with respect to temperature [297].

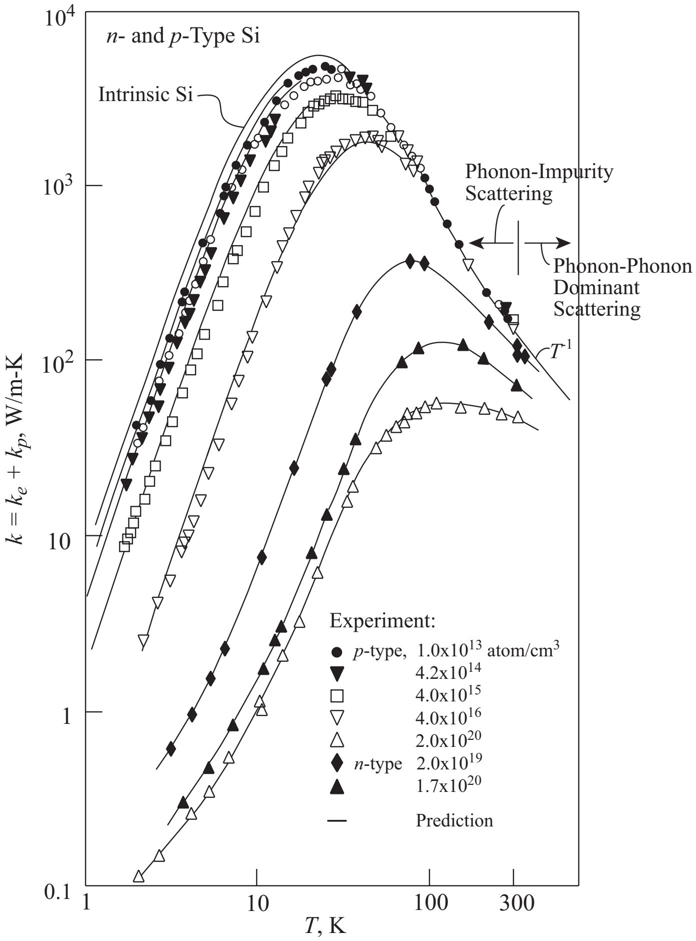

Figure 5.25. Predicted and measured variations of total (mostly phonon) thermal conductivity, for intrinsic and p- and n-type doped Si, with respect to low and intermediate temperatures [33]. The predictions are based on the Callaway SMRT phonon conductivity model. The contribution for the electronic thermal conductivity is very small.

where the contribution from all scatterers are combined using (4.111), i.e., the Matthiessen rule (series),

$$\frac{1}{\tau_e} = \sum_j \frac{1}{\tau_{e,j}} \quad \text{Matthiessen rule (series).} \tag{5.199}$$

The energy-dependent relaxation time for scattering of electrons by impurity, acoustic phonon, optical phonon, etc., are given in Table 5.4. Then the averaged energy $\langle\langle\tau_e\rangle\rangle$ is found from (5.113).

Table 5.6. *The smallest or effective bandgap and the electron and the hole mobilities for some semiconductors. The bandgaps are at $T = 0$ K and $T = 300$ K [433]. For most the bandgap decreases with temperature, for PbTe this is reversed.*

	Bandgap $\Delta E_{e,g}$,eV		Mobility μ_e, μ_h at 300 K, cm^2/V-s	
Material	300 K	0 K	μ_e	μ_h
C	5.47	5.48	1800	1200
Ge	0.66	0.74	3900	1900
Si	1.12	1.17	1500	450
α-SiC	3.00	3.30	400	50
GaSb	0.72	0.81	5000	850
GaAs	1.42	1.52	8500	400
GaP	2.26	2.34	110	75
InSb	0.17	0.23	80000	1250
InAs	0.36	0.42	33000	460
InP	1.35	1.42	4600	150
CdTe	1.48	1.61	1050	100
PbTe	0.31	0.19	6000	4000

For impurity scattering, and using the energy that maximizes τ_{e-im}, the electron mobility becomes (power-law $\tau_{e\text{-}im}$, Table 5.4)

$$\tau_{e\text{-}im} = \tau_{e,\text{o}}(\frac{E_e}{k_\text{B}T})^{3/2}$$

$$\mu_e = \frac{82^{1/2}\epsilon_e(k_\text{B}T)^{3/2}}{\pi^{3/2}e_c^3 m_{e,e}^{1/2} n_{im}[\ln(1+\gamma_m^2) - \gamma_m^2/(1+\gamma_m^2)]}$$

$$\gamma_m \equiv \frac{(24 m_{e,e} k_\text{B}T)^{1/2}}{\hbar\lambda} \quad \text{impurity-scattering-dominated mobility,} \qquad (5.200)$$

where λ is the screening length. This shows that the mobility increases with temperature (which dominates the low-temperature behavior) as nearly $T^{3/2}$ (Figure 5.23).

The acoustic-phonon-dominated mobility is (using power-law $\tau_{e\text{-}p,\text{A}}$, Table 5.4)

$$\mu_e = \frac{2^{3/2}e_c\hbar^4\rho u_{p,\text{A}}^2}{3\varphi_{d,\text{A}}^2 m_{e,e}^{5/2}(k_\text{B}T)^{3/2}} \quad \text{acoustic-phonon-scattering-dominated mobility,}$$

$$\tau_{e\text{-}p,\text{A}} = \tau_{e,\text{o}}(\frac{E_e}{k_\text{B}T})^{-1/2}. \qquad (5.201)$$

This shows a $T^{-3/2}$ dependence that represents the high-temperature behavior (Figure 5.23). Similar results are expected for holes.

The total thermal conductivity is based on parallel transport [232]

$$k = k_e + k_p \quad \text{parallel transport.} \qquad (5.202)$$

The concept of the mean free path used in (4.109) and (5.156) for phonon and electron thermal conductivity by introducting a single velocity and a single mean free path for each carrier gives

$$k = \frac{1}{3}\rho c_{v,p} u_p \lambda_p + \frac{1}{3} n_{e,c} c_{v,e} u_{\mathrm{F}} \lambda_e. \tag{5.203}$$

As we noted in Section 5.3, $c_{v,e}$ (here per free electron) is rather small at low temperatures (temperature dependent). The $c_{v,e}$ relation is given by (5.72), and the electrons are assumed to be at the lattice temperature, i.e., in thermal equilibrium with phonons.

Among the elements, for metals k_e dominates k, for semiconductors k_p dominates k. For compounds, e.g., in Bi_2Te_3, the contributions of k_e and k_p are nearly equal [106]. Generally, when both k_e and k_p are significant, k is not large.

Figure 5.22 shows the increase in hole concentration with an increase in B concentration in Si, and its dependence on temperature. At high dopant concentrations, the strong temperature dependence, characteristic of intrinsic semiconductors, disappears. In general, mobility of high-electrical-conductivity semiconductors (such as PbTe) is over 1000 cm^2/V-s. Table 5.6 lists the mobility (electron and hole) of some semiconductors at $T = 300$ K [433], where phonon scattering dominates.

Figure 5.23 shows the variation of the hole mobility in the B-doped Si. Note that, at high dopant concentrations, the mobility drops to its value for intrinsic Si. Also, for the moderate dopant concentrations, there is a notable increase in hole mobility at low temperatures, which is due to suppression of phonon scattering.

Figure 5.24 shows that the electrical conductivity of B-doped silicon increases substantially and becomes nearly temperature independent. In contrast, the intrinsic Si has a very strong temperature-dependent electrical conductivity, which is due mostly to the variation of the conduction electron density with temperature.

The thermal conductivity of doped Si is shown in Figure 5.25. As is clear, the phonon-dominated thermal conductivity decrease is due to the presence of dopants. It also shows that the phonon-scattering effect of these dopants surpasses any electronic contributions to thermal conductivity.

Variations of the measured Seebeck coefficient of intrinsic and doped Si, with respect to temperature, are shown in Figure 5.26. From (5.148), because of the $\ln(n_{e,\mathrm{F}}/n_{e,c})$ relation, at low and moderate temperatures, $n_{e,c}$ is low and α_{S} is rather large. The intrinsic Si has an n-type behavior at high temperatures; because of the increase in conduction electron density, the effect of doping disappears and α_{S} tends toward zero at high temperatures.

5.16.4 TE Figure of Merit Z_e

TE materials are used in TE power generation and in TE cooling. In addition to the Seebeck coefficient α_{S}, the electrical resistivity and thermal conductivity play significant roles [232]. The TE figure of merit is defined as $Z_e = \alpha_{\mathrm{S}}^2 \sigma_e / k = \alpha_{\mathrm{S}}^2 / \rho_e k$. The product $\alpha_{\mathrm{S}}^2 \sigma_e$ is called the thermoelectric power factor. Because of

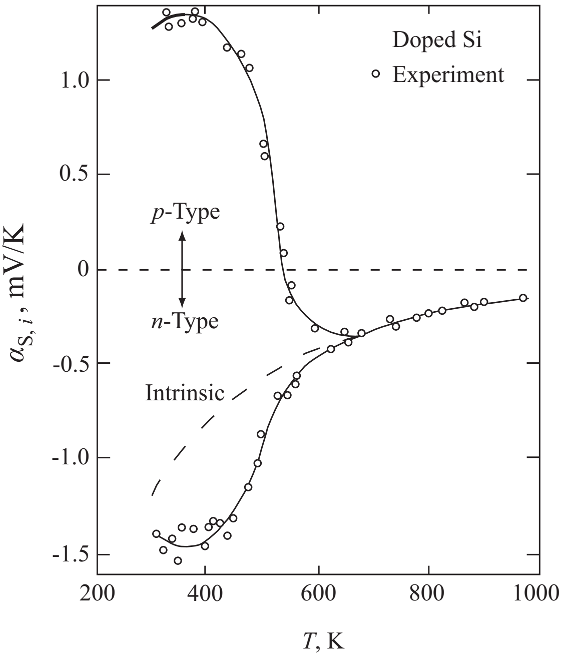

Figure 5.26. Variations of measured Seebeck coefficients, with intrinsic, and p- and n-type behaviors, for doped Si, as functions of temperature [158, 120]. The n-type generally uses As and P, and the p-type doped Si uses B.

the high TE figure of merit Z_e, semiconductors have been the choice materials for thermoelectricity. Figure 5.27 shows the measured Z_e with respect to temperature for various high-Z_e materials.

The TE figure of merit can be expressed with (5.148) for α_S (5.147) for σ_e, (5.147) and (5.64) for $n_{e,c}$, (5.202) for k, and (5.151) to relate k_e and σ_e. Then this expression becomes (end-of-chapter problem)

$$Z_eT = \frac{\alpha_S^2\sigma_e}{k_p + k_e}T = \frac{[\xi - (s + \frac{5}{2})]^2}{[2\frac{k_B^2T}{e_c}AB\exp(\xi)]^{-1} + s + \frac{5}{2}},$$

$$\xi \equiv \frac{\Delta E_{e,g}}{k_BT}, \quad A \equiv \frac{\mu_e}{k_p}(\frac{m_{e,e}}{m_e})^{3/2}, \quad B \equiv (\frac{m_ek_BT}{2\pi\hbar^2})^{3/2}. \tag{5.204}$$

The maximum in Z_eT taken with respect to ξ gives (end-of-chapter problem)

$$\xi_o + 4(s + \frac{5}{2})\frac{k_B^2T}{e_c}AB\exp(\xi_o) \equiv \xi_o + (s + \frac{5}{2})2\beta = s + \frac{1}{2}$$

$$\beta = \frac{k_B^2\sigma_eT}{e_c^2k_p} \quad \text{Chasmar-Stratton coefficient.} \tag{5.205}$$

Here we have used the relation between the intrinsic carrier concentration and the effective band density (Section 5.7) to remove the Fermi energy and replace it with bandgap energy, i.e., $E_{e,c} - E_{e,v} = \Delta E_{e,g}$. The dimensionless

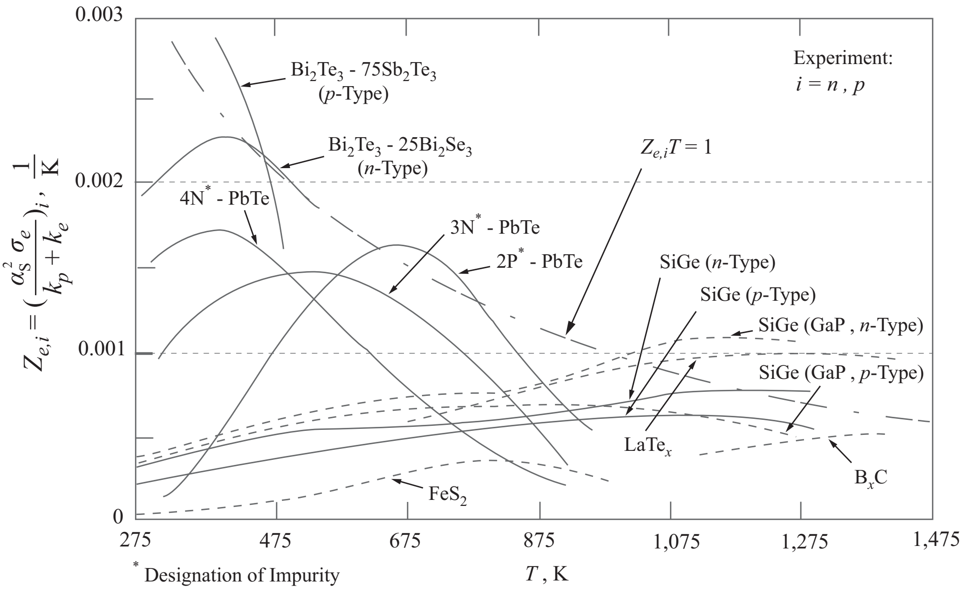

Figure 5.27. Variations of individual (p- or n-type) figures of merit $Z_{e,i}$ for selected bulk TE (semiconductor) material, as functions of temperature [396].

coefficient $\beta \equiv 2k_B^2 TAB/e_c = k_B^2 \sigma_e T/e_c^2 k_p$ [note similarity to Wiedemann–Franz–Lorenz law (5.151), except here we have k_p instead of k_e] is referred to as the Chasmar-Stratton coefficient and is < 0.5 for all known materials. Useful TE materials have $\beta \exp(\xi)$ between 0.05 and 0.2, with α_S about $\pm$ 200 μV/K [163].

Figures 5.28(a) and (b) show the crystal structure of Bi_2Te_3. Figure 5.28(c) shows the band structure for Bi_2Te_3 predicted with the tight-binding approximation [271]. The band edges are not located along the high-symmetry lines, but are in the reflection planes. Figures 5.29(a) and (b) show the variation of the measured electrical conductivity and Seebeck coefficient with respect to temperature for Pb-doped Bi_2Te_3 [368].

Note that even the crystal with zero Pb concentration has an electrical conductivity that behaves like that of metals (nondegenerate) because of the inherent defects. When comparing theoretical predictions with experimental results (Section 5.16.1), account has to be made of the inherent defects, through specification (prescription) of carrier concentrations. We will discuss this in Section 5.17.3. As Pb concentration increases, σ_e increases and α_S decreases[†]. Similar structures include Sb_2Te_3. As the expected, the phonon conductivity is anisotropic. The atomic spacings are also rather large, resulting in a small total phonon and electron conductivity. The optimal figure of merit is discussed in [396] and in Section 5.17.3.

[†] Some high carrier concentration compounds have large α_S. Example as $B_{13}C_2$, that due to phonon softening has large contribution from vibration to entropy and α_S. For these, the effect of vibration should be separately included [10]. This is discussed in Appendix G.

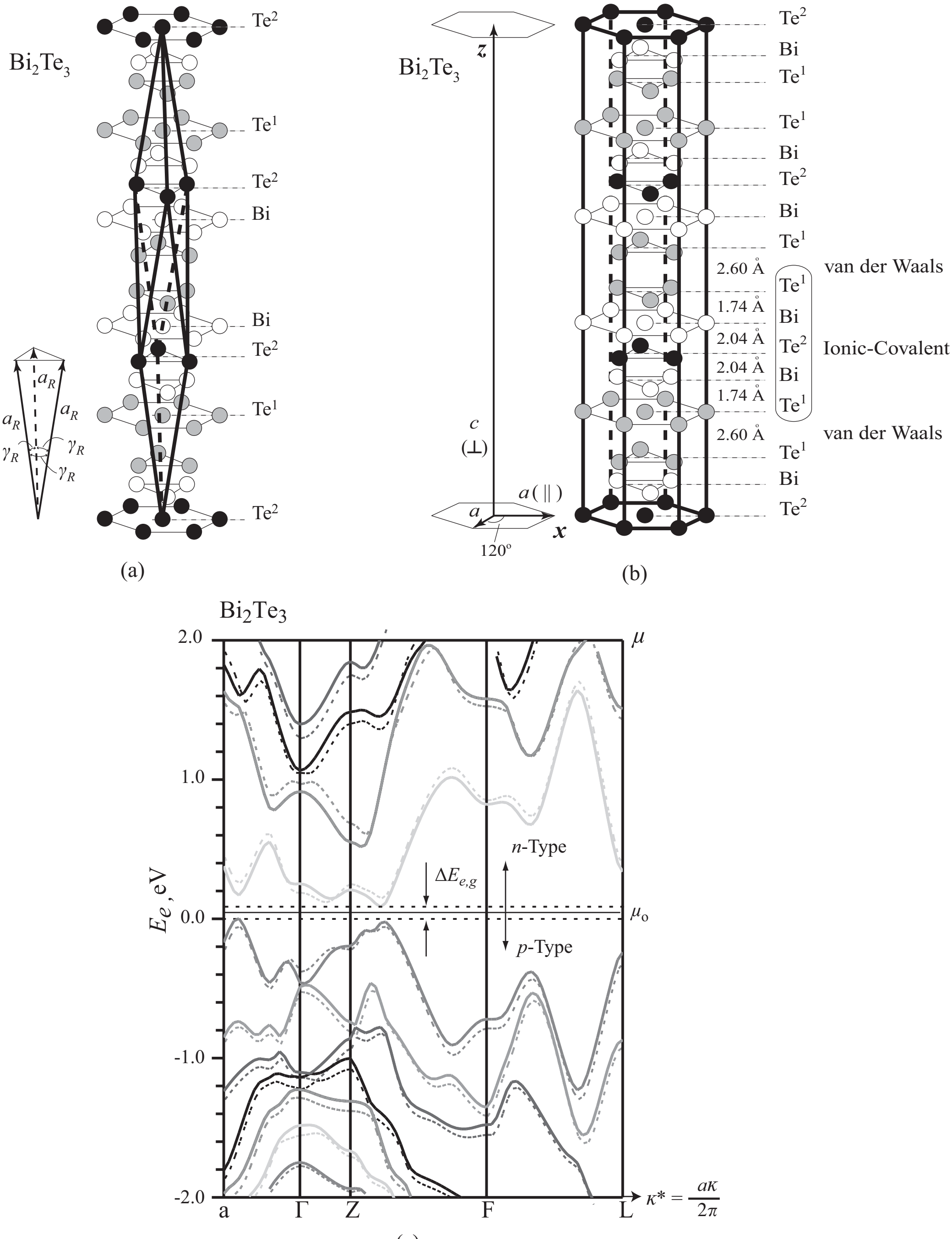

(a)

(b)

(c)

Figure 5.28. The crystal structure of Bi_2Te_3 (a tetradymite-type structure). (a) Rhombohedral primitive unit cell, and (b) hexagonal nonprimitive unit cell, $c = 30.487$ Å, $a = 4.384$ Å [396]. The rhombohedral cell parameters are $a_R = (3a^2 + c^2)^{1/2}/3$, $\sin(\gamma_R/2) = 3/2[3 + (c/a)^2]^{1/2}$. (c) Band structure of Bi_2Te_3 calculated with (solid curve) and without (dashed curve) $p_{1/2}$ corrections [202]. On the right vertical axis, the reference chemical potential (used in Section 5.17.4) is also marked.

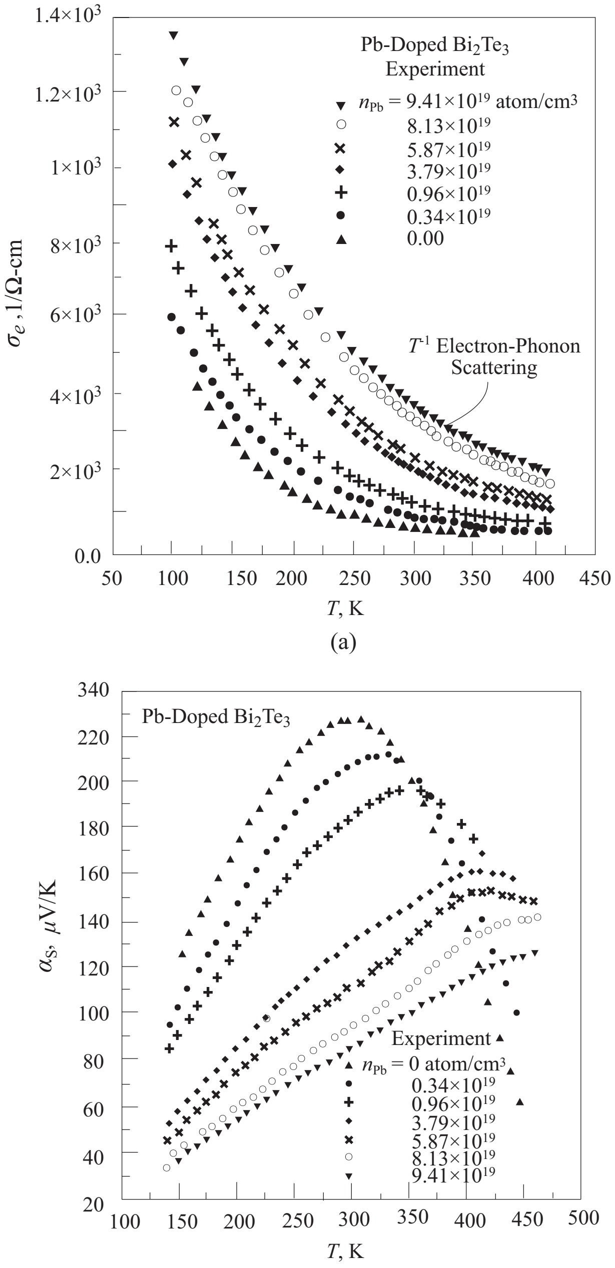

(a)

(b)

Figure 5.29. (a) Temperature dependences of the measured electrical conductivity (along *c*) of the Pb-doped Bi_2Te_3 crystals [368]. Note the metal behavior (monotonic decrease with increase in temperature), even for the pure Bi_2Te_3. This is due to lattice defects. (b) Temperature dependence of the measured Seebeck coefficient (along *c*) of the Pb-doped Bi_2Te_3 (*p*-type) crystals [368].

It is also customary to use the dimensionless TE figure of merit Z_eT. The best TE materials (semiconductors) have Z_eT of unity or higher (Figure 5.27)[†].

The Peltier cooling/heating rate $\dot{S}_{e\text{-}p}$ for a p-type material connected to an n-type material through an electrical conductor (metal) with a current $J_e = j_eA$, is

$$\dot{S}_{e\text{-}p} = \dot{S}_{e,\mathrm{P}} = (\alpha_{\mathrm{S},p} - \alpha_{\mathrm{S},n})J_eT, \tag{5.206}$$

where T is the junction temperature.

5.17 *Ab Initio* Computation of TE Transport Property Tensors

Using band structures from *ab initio* calculation, we can also calculate TE transport properties on the basis of appropriate electron-scattering models. Most such calculations are based on the BTE and relaxation-time approximations.

5.17.1 TE Transport Tensors and Variable Chemical Potential

The TE transport properties are derived from the BTE as introduced in Section 5.12, with the relaxation-time approximation. Here we do not assume nondegeneracy and include all electron bands. The most general form of the relations [(5.125) to (5.128)] for TE properties are [202, 299]

$$\begin{aligned}
\boldsymbol{A}_{\mathrm{S},j} &= 2\int \frac{\mathrm{d}\boldsymbol{\kappa}}{(2\pi)^3}\boldsymbol{u}_{e,j,\boldsymbol{\kappa}} f'_{e,j}(\boldsymbol{\kappa},T)(E_{e,j}-\mu)/(T\boldsymbol{\Sigma}_{e,j})\\
\boldsymbol{\Sigma}_{e,j} &= 2q_j\int \frac{\mathrm{d}\boldsymbol{\kappa}}{(2\pi)^3}\boldsymbol{u}_{e,j,\boldsymbol{\kappa}} f'_{e,j}(\boldsymbol{\kappa},T)\\
\boldsymbol{K}^{\circ}_{e,j} &= \frac{2}{q_jT}\int \frac{\mathrm{d}\boldsymbol{\kappa}}{(2\pi)^3}\boldsymbol{u}_{e,j,\boldsymbol{\kappa}} f'_{e,j}(\boldsymbol{\kappa},T)(E_{e,j}-\mu)^2\\
\boldsymbol{K}_{e,j} &= \boldsymbol{K}^{\circ}_{e,j} - [2\int \frac{\mathrm{d}\boldsymbol{\kappa}}{(2\pi)^3}\boldsymbol{u}_{e,j,\boldsymbol{\kappa}} f'_{e,j}(\boldsymbol{\kappa},T)(E_{e,j}-\mu)]^2/(T\boldsymbol{\Sigma}_{e,j})
\end{aligned}$$

$$f'_{e,j}(\boldsymbol{\kappa},T) \equiv q_j\boldsymbol{u}_{e,j,\boldsymbol{\kappa}}\tau_e[E_{e,j}(\boldsymbol{\kappa})](\frac{\partial f^{\mathrm{o}}_{e,j}}{\partial E_{e,j}})|_{E_{e,j}=\mu}, \tag{5.207}$$

where $\boldsymbol{A}_{\mathrm{S}}$ is the Seebeck coefficient tensor, $\boldsymbol{\Sigma}_e$ is the electrical conductivity tensor, $\boldsymbol{K}_e$ is the electrical thermal conductivity tensor, j is the band index, q_j is the charge of carrier, $\boldsymbol{\kappa}$ is the wave vector, $\boldsymbol{u}_{e,j,\boldsymbol{\kappa}}$ is the group velocity vector (in the jth band and wave vector $\boldsymbol{\kappa}$), $f^{\mathrm{o}}_e(\boldsymbol{\kappa}) = \{e^{[E_e(\boldsymbol{\kappa})-\mu]/k_{\mathrm{B}}T}+1\}^{-1}$ is the equilibrium Fermi–Dirac distribution function (Table 1.2, note the distribution function is band dependent), μ is the chemical potential, and E_e is the total energy of electrons. Accordingly, the band structure $E_{e,j}(\boldsymbol{\kappa})$, chemical potential μ and relaxation times τ_e are required

---

[†] For metals, using $k_e = k$, along with (5.195), and (5.194) with $s = 0$, we have

$$Z_eT = \frac{3\pi^2}{4\xi^2}, \quad \xi = \frac{E_{\mathrm{F}}}{k_{\mathrm{B}}T}.$$

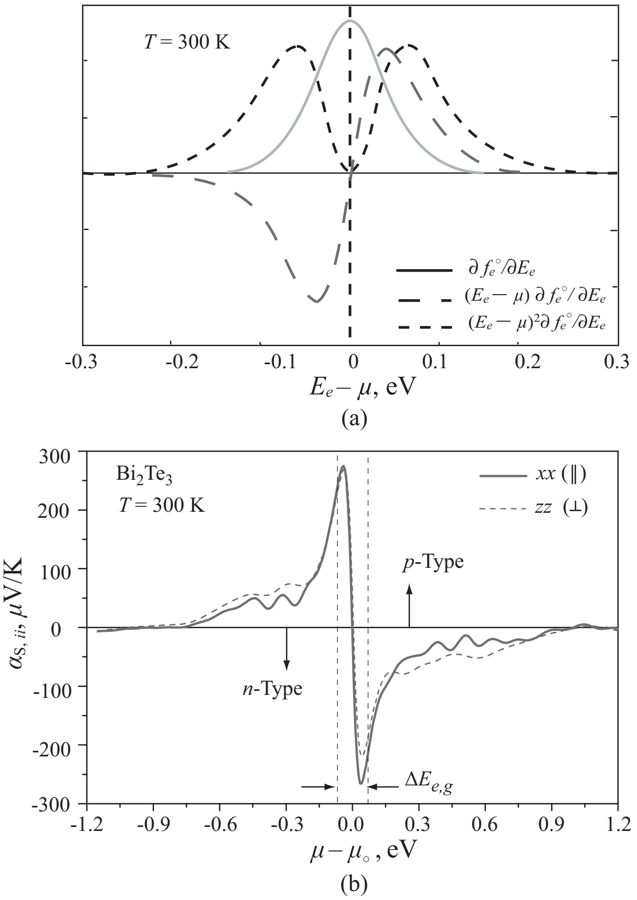

Figure 5.30. (a) Variation of the integrand factor $\partial f_e^\circ/\partial E_e$, $(E_e - \mu)\partial f_e^\circ/\partial E_e$, and $(E_e - \mu)^2\partial f_e^\circ/\partial E_e$, in (5.207), with respect to $E_e - \mu$ [298]. (b) The *ab initio* calculated (BoltzTraP) variation of the directional Seebeck coefficient elements of Bi_2Te_3 with respect to the chemical potential. Only the xx and zz [Figure 5.28(b)] components of the tensor are shown [298].

inputs. (5.207) allows for the investigation of contributions from each band and even each mode of electrons (or holes).

As an example, consider Bi_2Te_3 TE material. Figures 5.28(a) to (c) show the atomic structure and the calculated band structure. Figures 5.29(a) and (b) show the variation of the measured electrical conductivity and Seebeck coefficient (for various Pb doping) as a function of temperature.

The Seebeck coefficient involves $(E_e - \mu)\partial f_e^{\mathrm{o}}/\partial E_e$ and is very sensitive to the magnitude of chemical potential [see Figure 5.30(a)], which in turn is affected by the composition uncertainties (Figure 5.14). The intrinsic chemical potential can be directly obtained based on the intrinsic electron density and DOS of electrons from *ab initio* calculations. However, in real crystals, defects or dopants will also contribute some carriers (hole or electron), resulting in a different chemical potential. The total electron density includes both the extrinsic electron density (can be obtained from the defect density) and the intrinsic electron density. With the assumption that the effects of defects or dopants on the band structure and DOS are negligible, the real chemical potential is generally fitted from experiments instead of the intrinsic electron density.

5.17.2 Introduction to BoltzTraP

BoltzTraP [298] is a program for calculating the semiclassical transport coefficients based on the BTE (5.207). To calculate the TE transport coefficients by use of the BTE, the group velocity of electrons should be known. As the interpolated bands pass exactly through the calculated band-energies, the precision of the direct differential approach is limited by possible band crossings where the band derivatives will be calculated incorrectly. BoltzTraP relies on a Fourier expansion of the band-energies where the space group symmetry is maintained by the use of star functions

$$E_{e,j}(\boldsymbol{\kappa}) = \sum_{\boldsymbol{l}} c_{lj} S_l(\boldsymbol{\kappa}), \quad S_l(\boldsymbol{\kappa}) = \frac{1}{N_p} \sum_{\Lambda} e^{i\boldsymbol{\kappa}\cdot\Lambda l}, \tag{5.208}$$

where $\boldsymbol{l}$ is a lattice vector ($\boldsymbol{x}_\text{o}$) and $\{\Lambda\}$ are the N_p point group rotations. The expansion coefficients are given as

$$\begin{aligned} c_{\boldsymbol{x}j} &= E_{e,i}(\boldsymbol{\kappa}_N) - \sum_{\boldsymbol{l}\neq 0} c_{li} e^{i\boldsymbol{\kappa}\cdot\boldsymbol{l}}, \quad \boldsymbol{l} = 0 \\ &= \rho_l^{-1} \sum_{\boldsymbol{\kappa}\neq\boldsymbol{\kappa}_N} \lambda_l (S_{li}^* - S_{0i}^*), \quad \boldsymbol{l} \neq 0, \end{aligned} \tag{5.209}$$

where ρ_l is the roughness function $\rho_l = [1 - \frac{3}{4}(|\boldsymbol{l}|/|\boldsymbol{l}_{min}|)^2]^2 + \frac{3}{4}(|\boldsymbol{l}|/|\boldsymbol{l}_{min}|)^6$ ($\boldsymbol{l}_{min}$ is the smallest nonzero lattice vector) and λ_l are calculated by solving

$$\begin{aligned} \Delta E_{e,j}(\boldsymbol{\kappa}) &= E_{e,j}(\boldsymbol{\kappa}) - E_{e,i}(\boldsymbol{\kappa}_N) \\ &= \sum_{\boldsymbol{\kappa}'\neq\boldsymbol{\kappa}_N} \sum_{\boldsymbol{l}\neq 0} \frac{[S_l(\boldsymbol{\kappa}) - S_l(\boldsymbol{\kappa}_N)][S_l^*(\boldsymbol{\kappa}') - S_l^*(\boldsymbol{\kappa}_N)]}{\rho_l} \lambda_l^j. \end{aligned} \tag{5.210}$$

In this way, the extrapolated energies can be exactly equal to the calculated band-energies and the necessary derivatives for the BTE can be straightforwardly and accurately calculated. This approach has been tested by comparison with the recent calculations in which the group velocity is from the momentum matrix elements, which are in turn calculated directly from the wave functions, and good agreements are found [298].

BoltzTraP uses the BTE [as shown in (5.207)] to calculate the TE transport properties. The relaxation time τ_e, in principle, is dependent on both the band index and the $\boldsymbol{\kappa}$ direction. However, in BoltzTraP, the relaxation time τ_e is assumed to be a constant, so BoltzTraP outputs only σ_e/τ_e. For use of a different relaxation-time model, for example, the Kane model, one needs to modify the code (subroutine FERMIINTEGRALS).

Table 5.7. *Input parameters for BoltzTraP.*

WIEN	bandstyle (format of band structure to be input)
0 0 0 0.0	iskip (not presently used), idebug (output level), setgap (logic switch for bandgap manipulation), shiftgap
0.34517 0.0005 0.3 78.0	eferm (Fermilevel,in Ry), delatae (energygrid, in Ry), ecut (energy span around Fermilevel), number of valence electrons
CALC	CALC (calculate expansion coeff), NOCALC (read from file)
5	lpfac (number of lattice-points per κ-point)
BOLTZ	run mode (only BOLTZ is supported)
0.15	efcut (energy range of chemical potential around Fermilevel)
600. 50.	Tmax (max temperature for integrations), deltat (temperature step)
0.0	(energy range of bands given individual DOS output)

The code of BoltzTraP is interfaced to the band-structure code WIEN2k [43], but can also be easily interfaced to any other band-structure codes. Table 5.7 shows the input parameters in the input file case.intrans, using Bi_2Te_3 as an example.

To run BoltzTrap, a user must enter the directory containing the band-structure file [for WIEN2k, it is case.energy file or case.energyso file (if the spin–orbit coupling is specified)]. The user can run BoltzTrap by the following command:

```
"path to BoltzTrap"/SRC BoltzTrap1/x trans BoltzTraP
```

The traces of the tensors calculated in (5.207) are written as functions of μ and T in the output file called case.trace. Users must write their own program to extract the information they need. Figure 5.30(b) shows the variation of the Seebeck coefficient with respect to the chemical potential. It can be seen that the Seebeck coefficient is very sensitive to the change of the chemical potential.

The tensors of $\boldsymbol{\Sigma_e}/\tau_e$ and $\boldsymbol{A}_S$ are written in the file called case.condtens; the tensors of the Hall coefficient are written in the file called case.halltens.

5.17.3 Relaxation Times Based on Kane Band Model

The relaxation-time models simplify the calculation of BTE, but condense all the complexities into the relaxation time τ_e. In principle, the scattering relaxation time can be obtained with the FGR and the perturbation theory. The scattering of electrons is related to the perturbation of the Hamiltonian for an electron, which is

$$\mathrm{H} = -\frac{\hbar^2}{2m_e}\nabla^2 + \frac{e_c^2}{4\pi\epsilon_\circ}\int \frac{n_e g_e(\boldsymbol{r}')}{|\boldsymbol{r}-\boldsymbol{r}'|}\mathrm{d}\boldsymbol{r}' + \varphi_{ec} + \varphi_{ext} + \mathrm{H}' \tag{5.211}$$

$$\begin{aligned}\mathrm{H}' &= \mathrm{H}'_{e\text{-}p,\mathrm{A}} + \mathrm{H}'_{e\text{-}p,\mathrm{O}} + \mathrm{H}'_{e\text{-}p,\mathrm{PO}} + \mathrm{H}'_{e\text{-}v,d} + \mathrm{H}'_{e\text{-}v,\mathrm{C}} + \cdots \\ &= \varphi_{e\text{-}p,\mathrm{A}}\frac{\partial \boldsymbol{d}}{\partial \boldsymbol{r}} + \varphi'_{e\text{-}p,\mathrm{O}}\boldsymbol{d} - \frac{e_c q_e}{V_\circ}\sum_{\kappa_p}\frac{\kappa_p}{\kappa_p^2+\lambda^{-2}}(iQ_{\boldsymbol{\kappa}_p}e^{i\boldsymbol{\kappa}_p\cdot\boldsymbol{r}}) + \varphi_{v,c} + \frac{Ze_c^2}{4\pi\epsilon r}e^{-r/\lambda} + \cdots\end{aligned} \tag{5.212}$$

where $g_e(\boldsymbol{r})$ is the electron radial distribution function, φ_{ec} is the exchange-correlation energy, φ_{ext} is the external potential excluding the perturbation, H' is the perturbation Hamiltonian that is due to scatterings, $\mathrm{H}'_{e\text{-}p,\mathrm{A}}$, $\mathrm{H}'_{e\text{-}p,\mathrm{O}}$, $\mathrm{H}'_{e\text{-}p,\mathrm{PO}}$, $\mathrm{H}'_{e\text{-}v,d}$, and $\mathrm{H}'_{e\text{-}v,\mathrm{C}}$ are the perturbation Hamiltonians for the acoustic-phonon scattering, nonpolar optical-phonon scattering, polar optical-phonon scattering, short-range scattering by impurity, and scattering by Coulomb potential, respectively. Here $\varphi_{e\text{-}p,\mathrm{A}}$ and $\varphi'_{e\text{-}p,\mathrm{O}}$ are the deformation potentials for the acoustic and optical phonons, q_e is the effective charge, $\varphi_{v,c}$ is the scattering potential of impurity. $\boldsymbol{d} = N^{-1/2}\sum_{\boldsymbol{\kappa}_p} Q_{\boldsymbol{\kappa}_p}\boldsymbol{s}_{\boldsymbol{\kappa}_p}\exp(i\boldsymbol{\kappa}_p\cdot\boldsymbol{r})$ (N is the number of unit cells and $\boldsymbol{s}_{\boldsymbol{\kappa}_p}$ is the polarization vector) is the normal coordinate form of lattice displacement, $\boldsymbol{\kappa}_p$ is the phonon wave vector, $Q_{\boldsymbol{\kappa}_p}$ is the normal coordinate, λ is the screening length, and Ze_c is the effective charge of impurity.

The electron relaxation time τ_e for a mode $\boldsymbol{\kappa}$ can be represented as [434]

$$\frac{1}{\tau_e(\boldsymbol{\kappa})} = \sum_i \frac{1}{\tau_{e,i}(\boldsymbol{\kappa})} = \int \frac{\mathrm{d}\boldsymbol{\kappa}'}{(2\pi)^3}\dot{\gamma}_{\boldsymbol{\kappa},\boldsymbol{\kappa}',i}\left(1 - \frac{f'_{\boldsymbol{\kappa}'}}{f'_{\boldsymbol{\kappa}}}\frac{f^{\circ}_{\boldsymbol{\kappa}}}{f^{\circ}_{\boldsymbol{\kappa}'}}\right), \tag{5.213}$$

where $f^{\circ}_{\boldsymbol{\kappa}}$ is the carrier equilibrium distribution , $f'_{\boldsymbol{\kappa}} = f_{\boldsymbol{\kappa}} - f^{\circ}_{\boldsymbol{\kappa}}$ is the perturbation of the distribution, $\dot{\gamma}_{\boldsymbol{\kappa},\boldsymbol{\kappa}',i}$ is the transition rate from state $\boldsymbol{\kappa}$ to $\boldsymbol{\kappa}'$ by the ith scattering, which can in turn be given by the FGR as [434]

$$\dot{\gamma}_{\boldsymbol{\kappa},\boldsymbol{\kappa}',i} = \frac{2\pi}{\hbar}\delta[E_e - E_e(\boldsymbol{\kappa}')]|M_{\boldsymbol{\kappa},\boldsymbol{\kappa}',i}|^2$$

$$M_{\boldsymbol{\kappa},\boldsymbol{\kappa}',i} = \langle\boldsymbol{\kappa}'|\mathrm{H}'_i|\boldsymbol{\kappa}\rangle = \int \psi^{\dagger}(\boldsymbol{\kappa}',\boldsymbol{r})\mathrm{H}'_i\psi(\boldsymbol{\kappa},\boldsymbol{r})\mathrm{d}\boldsymbol{r}, \tag{5.214}$$

where H'_i is the perturbation Hamiltonian for the scattering mechanism i, and $\psi(\boldsymbol{\kappa},\boldsymbol{r})$ is the wave function for mode $\boldsymbol{\kappa}$. The Bloch wave function corresponding to the electron wave vector $\boldsymbol{\kappa}$ can be written as

$$\psi(\boldsymbol{\kappa}',\boldsymbol{r}) = \frac{1}{V^{1/2}}\sum_o C'_J \sum_{\boldsymbol{g}} C^{\boldsymbol{\kappa}}_{\boldsymbol{g}} e^{i(\boldsymbol{\kappa}+\boldsymbol{g})\cdot\boldsymbol{r}}, \tag{5.215}$$

where V is the volume, C and C' are coefficients, and the subscripts J and $\boldsymbol{g}$ denote the different orbitals and reciprocal lattice vectors. Therefore,

$$M_{\boldsymbol{\kappa},\boldsymbol{\kappa}'} = \frac{1}{V^{1/2}}\sum_{J'}\sum_{J} C'^{\dagger}_{J'}C'_J \sum_{\boldsymbol{g}'}\sum_{\boldsymbol{g}} e^{i(-\boldsymbol{\kappa}'-\boldsymbol{g}')\cdot\boldsymbol{r}}\mathrm{H}' e^{i(\boldsymbol{\kappa}+\boldsymbol{g})\cdot\boldsymbol{r}}. \tag{5.216}$$

If the wave function and the perturbation potential can be obtained from the first-principle calculation, $\tau_{e,i}$ can be directly determined. This calculation is very challenging, and here we just introduce an analytical relaxation-time model, which is also based on the FGR and incorporates the nonparabolic Kane model for the energy dispersion.

Many semiconductors with narrow bandgaps, e.g., lead chalcogenides, exhibit significant nonparabolicity of their energy bands. The two-band model is one of the models proposed to account for this for theoretical calculations of transport coefficients. The main features of the two-band model are as follows: the conduction- and valence-band extrema are located at the same $\boldsymbol{\kappa}$ point of the $\boldsymbol{\kappa}$-space, for example, Γ point, with the energy separation from other bands at this κ point being essentially larger than the main energy gap; at the same time, the momentum operators have nonzero matrix elements between the states corresponding to the extremal points. The energy dispersion for each valley is of the nonparabolic ellipsoidal form (5.50)

$$E_e(1+\frac{E_e}{\Delta E_{e,g}})=\frac{\hbar^2\kappa_{\rm T}^2}{m_{e,e,{\rm T}}}+\frac{\hbar^2\kappa_{\rm L}^2}{2m_{e,e,{\rm L}}}, \tag{5.217}$$

where $m_{e,e,\rm L}$ and $m_{e,e,\rm T}$ are longitudinal and transverse components of the effective mass tensor near the extremum, as given in (5.49), and $\kappa_{\rm L}$ and $\kappa_{\rm T}$ are longitudinal and transverse components of the wave vector. The DOS average effective mass is defined as

$$m_{e,e,\circ}=(m_{e,e,{\rm L}}m_{e,e,{\rm T}}^2)^{1/3} \quad \text{for conduction, direct band.} \tag{5.218}$$

Then the DOS D_e (5.66) becomes [using (5.50) to represent (5.217)]

$$D_e=\frac{2^{1/2}m_{e,e,\circ}^{3/2}}{\pi^2\hbar^3}E_e^{1/2}(1+\frac{E_e}{\Delta E_{e,g}})^{1/2}(1+2\frac{E_e}{\Delta E_{e,g}}). \tag{5.219}$$

In the framework of the Kane model, five electron-scattering mechanisms are normally considered, namely because of the deformation potential of the acoustic phonons $\tau_{e\text{-}p,\rm A}$, deformation potential of the optical phonons $\tau_{e\text{-}p,\rm O}$, polar scattering by the optical phonons $\tau_{e\text{-}p,\rm PO}$, short-range deformation potential of vacancies $\tau_{e\text{-}v,\rm d}$, and Coulomb potential of vacancies $\tau_{e\text{-}v,\rm C}$. According to (5.115), the total scattering relaxation time is expressed as

$$\frac{1}{\tau_e}=\frac{1}{\tau_{e\text{-}p,\rm A}}+\frac{1}{\tau_{e\text{-}p,\rm O}}+\frac{1}{\tau_{e\text{-}p,\rm PO}}+\frac{1}{\tau_{e\text{-}v,d}}+\frac{1}{\tau_{e\text{-}v,\rm C}}. \tag{5.220}$$

At low temperatures, charge carriers are scattered mainly by the charged vacancy. At low carrier densities, scattering by the Coulomb potential of the vacancies dominates, whereas for high carrier densities, the Coulomb potential is screened by the carriers and scattering by the short-range potential of vacancies dominates. As the temperature increases, scattering by thermal phonons becomes more and more important. When the temperature is above room temperature, scattering by acoustic phonons and optical phonons normally makes the main contribution to the total relaxation time [36].

Within the Kane model, the expressions for different scattering mechanisms are given as follows [36, 202, 381, 509].

(A) *Scattering by Deformation Potential of Acoustic Phonons* $\tau_{e\text{-}p,\mathrm{A}}$

The relaxation time for electrons dispersed on the deformational potential of acoustic phonons, when the Kane model of dispersion is used, can be given as

$$
\begin{aligned}
\tau_{e\text{-}p,\mathrm{A}} &= \frac{(\tau_{e\text{-}p,\mathrm{A}})_\circ (E_e + \frac{E_e^2}{\Delta E_{e,g}})^{-1/2}}{(1+2\frac{E_e}{\Delta E_{e,g}})[(1-A)^2 - B]} \\
A &\equiv \frac{\frac{E_e}{\Delta E_{e,g}}(1-a_\mathrm{A})}{(1+2\frac{E_e}{\Delta E_{e,g}})}, \quad a_\mathrm{A} = \frac{\varphi_{e\text{-}p,\mathrm{A},v}}{\varphi_{e\text{-}p,\mathrm{A},c}} \\
B &\equiv \frac{8\frac{E_e}{\Delta E_{e,g}}(1+\frac{E_e}{\Delta E_{e,g}})a_\mathrm{A}}{3(1+2\frac{E_e}{\Delta E_{e,g}})^2} \\
(\tau_{e\text{-}p,\mathrm{A}})_\circ &\equiv \frac{2\pi\hbar^4 c_l}{\varphi^2_{e\text{-}p,\mathrm{A},c} k_\mathrm{B} T (2m_{e,e,\circ})^{3/2}},
\end{aligned}
\qquad (5.221)
$$

where $\Delta E_{e,g}$ is the band energy gap, $\varphi_{e\text{-}p,\mathrm{A},c}$ and $\varphi_{e\text{-}p,\mathrm{A},v}$ are the acoustic deformation potential coupling constants for the conduction and valence band, c_l is a combination of elastic constants, a_A is the ratio of the acoustic deformation potential coupling constants for the valence and conduction bands, and $m_{e,e,\circ}$ is the DOS effective mass for a single ellipsoid.

(B) *Scattering by Deformation Potential of Optical Phonons* $\tau_{e\text{-}p,\mathrm{O}}$

$$
\begin{aligned}
\tau_{e\text{-}p,\mathrm{O}} &= \frac{(\tau_{e\text{-}p,\mathrm{O}})_\circ (E_e + \frac{E_e^2}{\Delta E_{e,g}})^{-1/2}}{(1+2\frac{E_e}{\Delta E_{e,g}})[(1-A)^2 - B]} \\
A &\equiv \frac{\frac{E_e}{\Delta E_{e,g}}(1-a_\mathrm{O})}{(1+2\frac{E_e}{\Delta E_{e,g}})}, \quad a_\mathrm{O} = \frac{\varphi_{e\text{-}p,\mathrm{O},v}}{\varphi_{e\text{-}p,\mathrm{O},c}} \\
B &\equiv \frac{8\frac{E_e}{\Delta E_{e,g}}(1+E_e/\Delta E_{e,g})a_\mathrm{O}}{3(1+2\frac{E_e}{\Delta E_{e,g}})^2} \\
(\tau_{e\text{-}p,\mathrm{O}})_\circ &\equiv \frac{2\hbar^2 a_R^2 \rho (\hbar\omega_{p,\mathrm{O}})^2}{\pi\varphi^2_{e\text{-}p,\mathrm{O},c} k_\mathrm{B} T (2m_{e,e,\circ})^{3/2}},
\end{aligned}
\qquad (5.222)
$$

where a_R is lattice constant, ρ is the density, $\omega_{p,\mathrm{O}}$ is the frequency of the optical phonons, and $\varphi_{e\text{-}p,\mathrm{O},c}$ and $\varphi_{e\text{-}p,\mathrm{O},v}$ are the optical deformation potential coupling constants for conduction and valence bands. Equation (5.222) is similar to (5.186).

(C) *Scattering by Polar-Optical Phonons* $\tau_{e\text{-}p,\mathrm{PO}}$

In a simple isotropic parabolic model, the relaxation time for polar LO phonons has the form [381]

$$\tau^{-1}_{e\text{-}p,\mathrm{PO}} \sim \frac{1}{u_e \kappa^2} \int_0^{2\kappa} \kappa_p \mathrm{d}\kappa_p, \tag{5.223}$$

where u_e is the velocity of electrons. When the integral takes into account all phonons, we have

$$\tau_{e\text{-}p,\mathrm{PO}} = \frac{\hbar^2 u_e}{2k_\mathrm{B} T e_c^2[(\epsilon_\mathrm{o}\epsilon_{e,s})^{-1} - (\epsilon_\mathrm{o}\epsilon_{e,\infty})^{-1}]}. \tag{5.224}$$

Inclusion of nonparabolicity and screening effects will lead to

$$\begin{aligned}
\tau_{e\text{-}p,\mathrm{PO}} &= \frac{\hbar^2 (E_e + \frac{E_e^2}{\Delta E_{e,g}})^{1/2} F^{-1}}{e_c^2 (2m_{e,e,\circ})^{1/2} k_\mathrm{B} T[(\epsilon_\mathrm{o}\epsilon_{e,s})^{-1} - (\epsilon_\mathrm{o}\epsilon_{e,\infty})^{-1}](1 + 2\frac{E_e \epsilon}{\Delta E_{e,g}})} \\
F &\equiv 1 - \delta \ln(1 + \delta^{-1}) - \frac{2\frac{E_e}{\Delta E_{e,g}}(1 + \frac{E_e}{\Delta E_{e,g}})}{(1 + 2\frac{E_e}{\Delta E_{e,g}})^2}[1 - 2\delta + 2\delta^2 \ln(1 + \delta^{-1})] \\
\delta &\equiv (2\kappa \lambda_\mathrm{o})^{-2},
\end{aligned} \tag{5.225}$$

where $\epsilon_{e,s}$ and $\epsilon_{e,\infty}$ are the static and high-frequency relative permitivities, κ is the carrier wave vector, and λ_o is the screening length of the optical phonons.

(D) *Scattering by Short-Range Deformation Potential of Vacancies* $\tau_{e\text{-}v,d}$

$\tau_{e\text{-}v,d}$ also has a form similar to the relaxation time of electron–acoustic-phonon scattering, because of a similar deformation potential $\varphi_{e\text{-}v,d}$, which is

$$\begin{aligned}
\tau_{e\text{-}v,d} &= \frac{(\tau_{e\text{-}v,d})_\circ (E_e + \frac{E_e^2}{\Delta E_{e,g}})^{-1/2}}{(1 + 2\frac{E_e}{\Delta E_{e,g}})[(1 - A)^2 - B]} \\
A &\equiv \frac{\frac{E_e}{\Delta E_{e,g}}(1 - a_v)}{(1 + 2\frac{E_e}{\Delta E_{e,g}})}, \quad a_v = \frac{\varphi'_{e\text{-}v,d,v}}{\varphi'_{e\text{-}v,d,c}} \\
B &\equiv \frac{8\frac{E_e}{\Delta E_{e,g}}(1 + E_e/\Delta E_{e,g})a_v}{3(1 + 2\frac{E_e}{\Delta E_{e,g}})^2} \\
(\tau_{e\text{-}v,d})_\circ &\equiv \frac{\pi \hbar^4}{\varphi^2_{e\text{-}v,d,c} m_{e,e,\circ} (2m_{e,e,\circ})^{1/2} n_v},
\end{aligned} \tag{5.226}$$

where n_v is the vacancy density, and a_v is the ratio of the short-range deformation potential coupling constants of vacancies for valence and conduction bands.

(E) *Scattering by Coulomb Potential of Vacancies* $\tau_{e\text{-}v,\mathrm{C}}$

$$\tau_{e\text{-}v,\mathrm{C}} = \frac{\epsilon_s^2(2m_{e,e,\mathrm{o}})^{1/2}(E_e + \frac{E_e^2}{\Delta E_{e,g}})^{3/2}}{\pi(Ze_c^2)^2 n_v[\ln(1+\xi) - \xi/(1+\xi)](1+2\frac{E_e}{\Delta E_{e,g}})}$$

$$\xi \equiv (2\kappa\lambda_v)^2, \qquad (5.227)$$

where Ze_c is the vacancy charge, and λ_v is the screening radius of the vacancy potential, which is given as

$$\lambda_v^{-2} = \frac{4\pi e_c^2}{\epsilon_s} D_e(\mu), \quad \mu = E_\mathrm{F}$$

$$D_e(\mu) \equiv \frac{2^{1/2}(m_{e,e,\circ})^{3/2}}{\pi^2\hbar^3}(\mu + \frac{\mu^2}{\Delta E_{e,g}})^{1/2}(1+2\frac{\mu}{\Delta E_{e,g}}), \qquad (5.228)$$

where $D_e(\mu)$ is the DOS at the Fermi level.

5.17.4 Predicted Seebeck Coefficient and Electrical Conductivity

With the knowledge of the relaxation-time models and the band structure, we can predict the key TE properties by using (5.207). Here we use the example of Bi_2Te_3 (anisotropic, tetradymite-type structure shown in Figure 5.28) and modify the BoltzTraP code to incorporate the Kane relaxation-time models. Figure 5.31 shows the variation of $\alpha_{\mathrm{S},xx}$ of Bi_2Te_3 with temperature, predicted with (5.207). The calculation was carried out using BoltzTraP, a software package adopting BTE. Both the energy-dependent relaxation-time models and the constant relaxation-time model were used. The BoltzTraP code was modified and the relaxation-time model was incorporated into the integration, as BoltzTrap assumes a constant relaxation time. To incorporate the temperature dependence of the band structure, the band structure was assumed not to change with temperature, and the conduction band was shifted in the calculation to include the temperature dependence of the bandgap $\Delta E_{e,g}$ (Section 5.5). Figure 5.31 shows that the constant $\Delta E_{e,g}$ leads to much higher values for $T > 300$ K (intrinsic regime), whereas results predicted with the temperature-dependent $\Delta E_{e,g} = 0.13 - 1.08 \times 10^{-4} T$ agree quite well with the experimental results. However, in the extrinsic regime ($T \le 300$ K), there is only a minor difference between the results with the two different settings for $\Delta E_{e,g}$. As shown in Figure 5.31, with the same temperature-dependent $\Delta E_{e,g} = 0.13 - 1.08 \times 10^{-4} T$ eV, the two relaxation-time models give very similar results in the extrinsic regime, because one kind of carriers dominates the electrical transport. However, some small deviation appears in the intrinsic regime, where the concentrations of the holes and electrons become comparable, and it increases with the increasing temperature. This phenomenon indicates that the temperature dependences of the mobilities of holes and electrons are different.

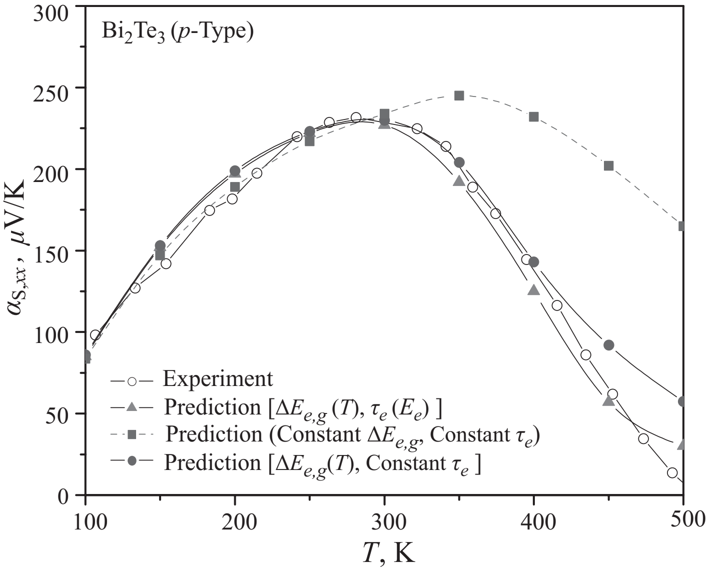

Figure 5.31. Variation of the predicted Seebeck coefficient for p-type Bi$_2$Te$_3$ with respect to temperature, compared with the available experimental results [216]. Both a temperature-dependent bandgap $\Delta E_{e,g} = 0.13 - 1.08 \times 10^{-4}T$ eV and a constant $\Delta E_{e,g} = 0.13$ eV are used. Also shown are the predictions made with the energy-dependent relaxation times and the constant relaxation-time model [202].

The band structure calculated with the experimental lattice parameters at 300 K was used in the calculations for α_S in Figure 5.30(b). Temperature changes not only the carrier concentrations but also the lattice parameters. However, the band-structure calculations adopting the lattice parameters under different temperatures show that the thermal expansion has negligible effects on the band structure. The change of the lattice parameters from 0 to 300 K results in only less than a 2% change in the bandgap. Compared with the actual temperature dependence of the bandgap, it seems that the temperature variation of the bandgap is mainly because of lattice vibration.

Figure 5.30(b) shows the variation of α_S along the xx and zz directions, with respect to the chemical potential μ, at 300 K. Apparently, the two curves are very similar, indicating the isotropy of α_S. Figure 5.30(b) shows that, for p-type Bi$_2$Te$_3$, the α_S peaks along the xx and zz directions almost overlap. However, for n-type Bi$_2$Te$_3$, the absolute peak value α_S along the xx direction is larger than that along the zz direction, though the peak positions are identical. In Figure 5.30(b), $\mu_\circ$ is the chemical potential value at which $\alpha_S = 0$. It is useful to rewrite the relation for α_S as

$$\alpha_S = -\frac{k_B}{e_c}\frac{\langle E_e - \mu\rangle_{\sigma_e(E_e,\mu)}}{k_B T}, \quad \langle E_e - \mu\rangle_{\sigma_e(E_e,\mu)} = \frac{\int \sigma_e(E_e,\mu)(E_e-\mu)\mathrm{d}E_e}{\int \sigma_e(E_e,\mu)\mathrm{d}E_e}. \tag{5.229}$$

Here $\langle E_e - \mu\rangle_{\sigma_e(E_e,\mu)}$ is the $\sigma_e(E_e,\mu)$-averaged energy deviation from the chemical potential. Then we have

$$\mu_\circ = \langle E_e\rangle_{\sigma_e(E_e,\mu_\circ)}, \tag{5.230}$$

which is the $\sigma_e(E_e)$-averaged energy and close to the middle of the bandgap [marked on the right-hand side of Figure 5.28(c)]. Therefore,

$$\alpha_{\rm S} = -\frac{k_{\rm B}}{e_c}\frac{[\langle E_e\rangle_{\sigma_e(E_e,\mu)} - \langle E_e\rangle_{\sigma_e(E_e,\mu_\circ)}] - (\mu - \mu_\circ)}{k_{\rm B}T}. \tag{5.231}$$

Here $\langle E_e\rangle_{\sigma_e(E_e,\mu)}$ has a simple form, where the nondegenerate approximation is used, i.e.,

$$\begin{aligned}\langle E_e\rangle_{\sigma_e(E_e,\mu)} &\simeq \frac{\sigma_{e,e}\Delta E_{e,g}}{\sigma_{e,e}+\sigma_{e,h}}\\ &= \frac{1}{1+be^{-2\epsilon/(k_{\rm B}T)}}\Delta E_{e,g},\end{aligned} \tag{5.232}$$

where $\sigma_{e,e}$ and $\sigma_{e,h}$ are the electrical conductivity contributed by electrons and holes, $b = (\mu_h/\mu_e)(m_{e,h}/m_{e,e})^{3/2}$ (μ_h and μ_e are the mobilities of electrons and holes), and $\epsilon = \mu - \Delta E_{e,g}/2$ is the distance of the chemical potential above the middle of the bandgap. For semiconductors with large bandgap ($\Delta E_{e,g} > 10k_{\rm B}T$), the maximum value of $\alpha_{\rm S}$ can be estimated as [similar in form to (5.153)]

$$|\alpha_{\rm S}|_{max} = \frac{k_{\rm B}}{e_c}\frac{\Delta E_{e,g}}{2k_{\rm B}T}. \tag{5.233}$$

For small $2\epsilon/k_{\rm B}T$, we have

$$\langle E_e\rangle_{\sigma_e(E_e,\mu)} \simeq \frac{\Delta E_{e,g}}{1+b}[1+\frac{2b\epsilon/(k_{\rm B}T)}{1+b}] \tag{5.234}$$

Therefore,

$$\alpha_{\rm S} \simeq -\frac{k_{\rm B}}{e_c}\frac{[\frac{2b\Delta E_{e,g}}{(1+b)^2k_{\rm B}T} - 1](\mu-\mu_\circ)}{k_{\rm B}T}. \tag{5.235}$$

For a narrow bandgap semiconductor, as shown in Figure 5.30(b), (5.235) is a good approximation for $\alpha_{\rm S}$ when $|\mu - \mu_\circ| < \Delta E_{e,g}/2$. When μ is close to the band edge, the effects of the opposite charges become smaller. While μ moves farther into the band edge, $\langle E_e\rangle_{\sigma_e(E_e,\mu)}$ is closer to μ. Therefore, $\alpha_{\rm S}$ will achieve the maximum near the band edge, and the maximum value can be estimated from (5.235). Assuming $b = 1$ and that the maximum is achieved at the band edge, for Bi_2Te_3 at 300 K, then $|\alpha_{\rm S}|_{max} \simeq 320\ \mu$V/K, which is close to the results in Figure 5.30(b).

Figure 5.32 shows the predicted electrical conductivity of Bi_2Te_3 along the xx and zz directions, wherein the Kane-band-model-based relaxation times are used. The temperature-dependent bandgap $\Delta E_{e,g} = 0.13 - 1.08 \times 10^{-4}T$ eV are adopted in the calculation. Some parameters, for example, the deformation coupling potentials, are fitted to the experimental results and listed in Table 5.8. Below 300 K the ratio $\sigma_{e,xx}/\sigma_{e,zz}$, is around 2.2 and almost temperature independent. But above 300 K, $\sigma_{e,xx}/\sigma_{e,zz}$ increases with increasing temperature. From the results shown in Figure 5.32, this is because $\sigma_{e,xx}$ changes much faster than $\sigma_{e,zz}$ at high temperatures. Note that the predicted $\sigma_{e,xx}/\sigma_{e,zz}$ is lower than the experimental values (around 2.95). A reason can be the neglect of the direction dependence of the effective masses.

Table 5.8. *Parameters used in the Kane nonparabolic relaxation-time models for Bi_2Te_3.*

Parameter	Magnitude	Parameter	Magnitude
$m_{h,e,\circ}/m_e$	0.08	$m_{e,e,\circ}/m_e$	0.06
n_v, 1/m^3	1.04×10^{25}	ρ, kg/m^3	7.86×10^3
$\epsilon_{e,\mathrm{o}}$	400	$\epsilon_{e,\infty}$	69.8
c_l, N/m^2	0.71×10^{11}	$\hbar\omega_{\mathrm{o}}$, eV	0.0076
Z	0.1	$\varphi_{e\text{-}p,\mathrm{A},c}$, eV	35
$\varphi_{e\text{-}p,\mathrm{O},c}$, eV	40	$\varphi_{e\text{-}v,d,c}$, J-m^3	1.2×10^{-46}
$a_{\mathrm{A}}, a_{\mathrm{O}}, a_v$	1.0	n_v, 1/m^3	1.04×10^{25}
$\Delta E_{e,g}$, eV	$0.13 - 1.08 \times 10^{-4}T$	a_R, Å	10.45

Figure 5.33 shows the variations of average values of various relaxation times, i.e., $\langle\langle\tau_{e\text{-}i}\rangle\rangle$ calculated from the relaxation-time models based on the Kane model (Section 5.17.3), as functions of temperature. The largest is $\langle\langle\tau_{e-v,\mathrm{C}}\rangle\rangle$, and the shortest are $\langle\langle\tau_{e\text{-}p,\mathrm{A}}\rangle\rangle$ and $\langle\langle\tau_{e\text{-}p,\mathrm{O}}\rangle\rangle$. The three phonon scatterings, $\langle\langle\tau_{e\text{-}p,\mathrm{A}}\rangle\rangle$, $\langle\langle\tau_{e\text{-}p,\mathrm{O}}\rangle\rangle$, and $\langle\langle\tau_{e\text{-}p,\mathrm{PO}}\rangle\rangle$, make up most of the total $\langle\langle\tau_e\rangle\rangle$. Note that (5.221), (5.222), and (5.224) show a T^{-1} relation.

5.17.5 Electric and Phonon Thermal Conductivities

For semiconductors, the total thermal conductivity includes two parts, i.e., electric thermal conductivity k_e and lattice conductivity k_p [(5.202)]. Currently it is not

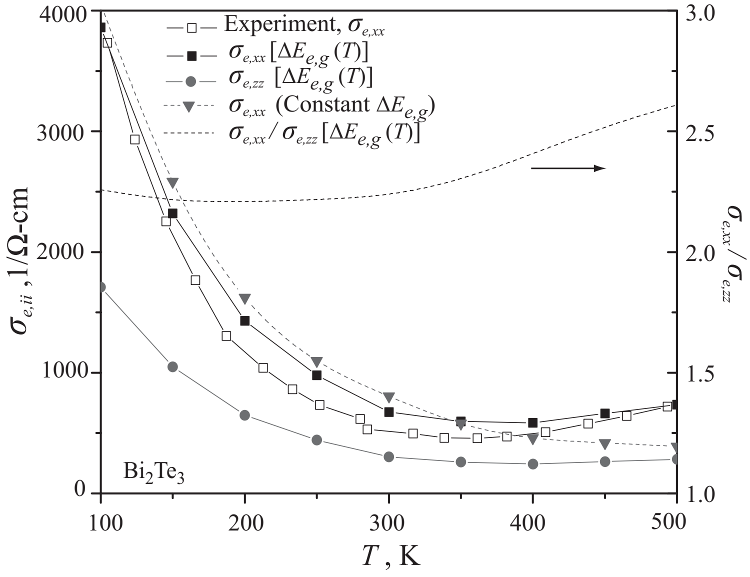

Figure 5.32. Variations of predicted directional electrical conductivities for Bi_2Te_3 with respect to temperature, using the Kane band model and energy-dependent relaxation times, and comparison with the available experimental results [216].

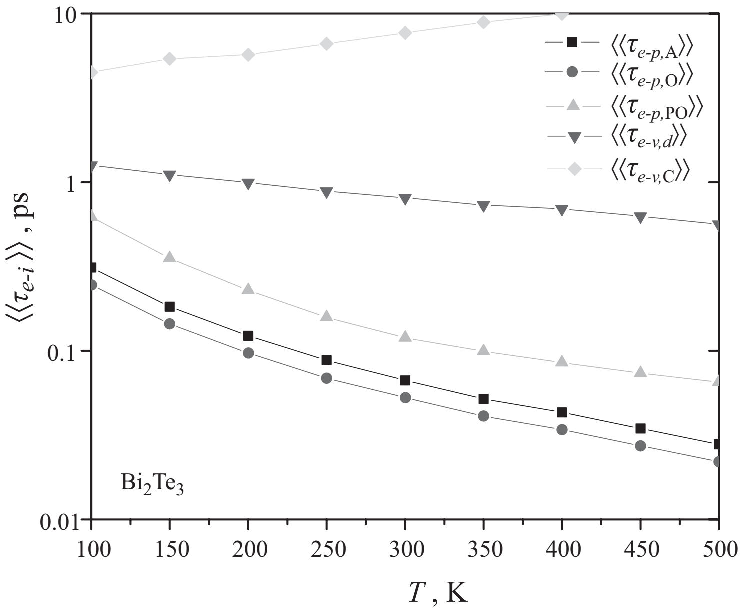

Figure 5.33. Variations of predicted electron relaxation times for Bi_2Te_3 with respect to temperature, using the Kane band model for energy dispersion.

possible to measure k_p and k_e separatively, so it is the total thermal conductivity $k = k_e + k_p$ that is measured, and k_e is generally derived from the Wiedemann–Franz law (5.151). The difference between the measured k and the derived k_e is used for k_p. However, as shown in Figure 5.16, the Lorenz number is not a constant and may be subject to many nonapplicable assumptions. Using (5.207), we can also predict k_e using the BTE (implemented in BoltzTraP) based on the full-band structure and the relaxation-time models.

(A) *Electric Thermal Conductivity*

Traditionally, the Wiedemann–Franz law (5.151), $k_e = N_{\mathrm{L}}\sigma_e T$, is used to calculate the electric thermal conductivity k_e on the basis of σ_e. However, for semiconductors, N_{L} may not be the value used for metals [$N_{\mathrm{L},\circ} = (\pi^2/3)k_{\mathrm{B}}^2/e_c^2$, (5.195)], especially when the chemical potential is near the center of the bandgap. When the sample is heavily doped (the chemical potential is deep inside the valence or conduction band), $N_{\mathrm{L}}/N_{\mathrm{L},\circ}$ is close to 1.0. However, for intermediate doping, $N_{\mathrm{L}}/N_{\mathrm{L},\circ}$ can be smaller than 1.0, and the minimum is around 0.7. For small doping concentrations or intrinsic regime, $N_{\mathrm{L}}/N_{\mathrm{L},\circ}$ may be much larger than 1.0. Figure 5.34(a) shows the temperature dependence of the electric thermal conductivity calculated according to Eq. (5.207). The results show that k_e for both directions increase with increasing temperature. Due to the significant changes of N_{L} in the intrinsic regime, using $N_{\mathrm{L},\circ}\sigma_e T$ underestimates k_e at high temperatures.

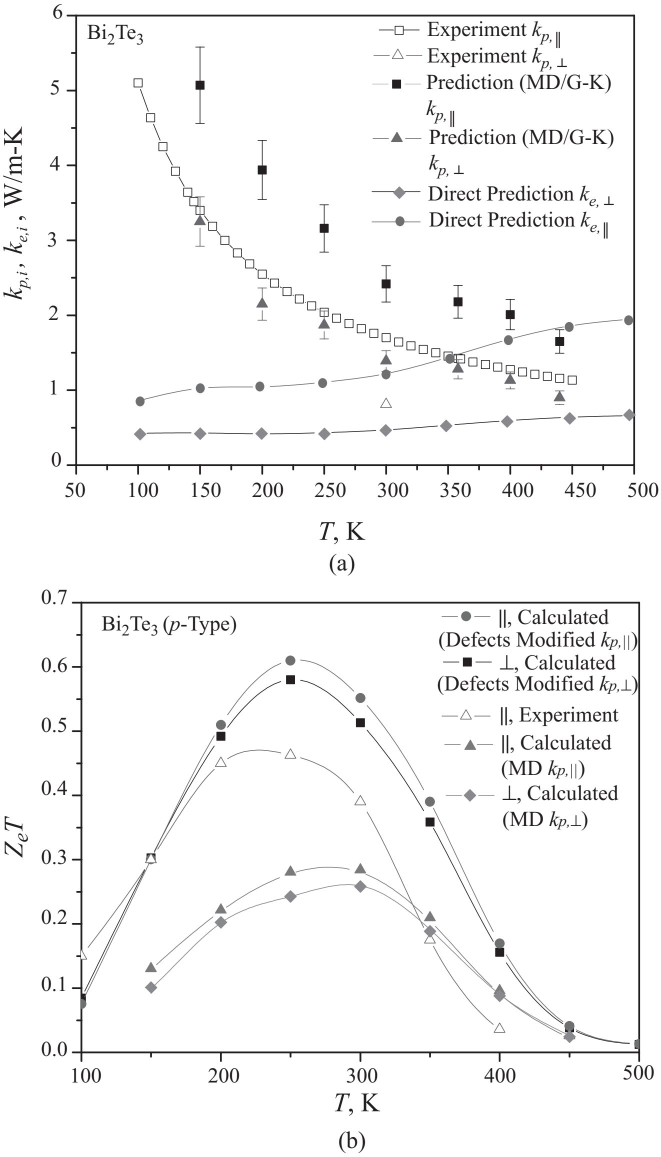

(a)

(b)

Figure 5.34. (a) Predicted electrical and phonon thermal conductivities of Bi$_2$Te$_3$. The electrical thermal conductivity is directly predicted using the BTE and the Kane relaxation-time models. The phonon thermal conductivity is predicted using MD simulation and the G–K method [202]. Available experimental results are also shown [216]. (b) Variation of calculated directional figure of merit for Bi$_2$Te$_3$ (along ∥ and ⊥), with respect to temperature. Both the results with the directly calculated k_p and that modified by defects are presented. The experimental results [216] are also shown.

(B) *Phonon Thermal Conductivity*

In semiconductors, phonons are scattered by the grain boundary, defects, and other phonons and carriers. According to the Matthiessen rule (4.111) and phonon-scattering mechanisms of (4.120), we have

$$\frac{1}{k_p} = \frac{1}{k_{p\text{-}b}} + \frac{1}{k_{p\text{-}im}} + \frac{1}{k_{p\text{-}p}} + \frac{1}{k_{p\text{-}e}}, \tag{5.236}$$

where $k_{p\text{-}b}$, $k_{p\text{-}im}$, $k_{p\text{-}p}$, and $k_{p\text{-}e}$ are the thermal conductivities limited by the scattering by the grain boundary, defects, phonons (U–processes only), and by charged carriers, respectively.

For semiconductors, the thermal resistivity that is due to the phonon–carrier scattering $1/k_{p\text{-}e}$, is normally very small. We can evaluate $1/k_{p\text{-}e}$ by using the electrical resistivity ρ_e. This relation has been derived by ignoring the difference between the N- and U–processes between carriers and phonons [30, 516], and using the Bloch model for ρ_e (5.196):

$$\frac{1}{k_{p\text{-}e}} = \frac{3.7\rho_e(T_{\rm D})}{N_{{\rm L},\circ}T}\left(\frac{T_{\rm D}}{T}\right) I_5 \frac{\pi^2 z_e^2}{27 I_4^2} \tag{5.237}$$

$$\rho_e = 3.7\rho_e(T_{\rm D})\left(\frac{T}{T_{\rm D}}\right)^5 I_5 \quad \text{Bloch model of metal } \rho_e. \tag{5.238}$$

Here

$$I_n = \int_0^{T_{\rm D}/T} \frac{x^n e^x}{(e^x - 1)^2}\,{\rm d}x. \tag{5.239}$$

In the proceeding relations, z_e is the number of free electrons per atom, $N_{\rm L}$ is the Lorenz constant, and $T_{\rm D}$ is the Debye temperature. Then we have

$$\frac{1}{k_{p\text{-}e}} = \frac{\rho_e}{N_{{\rm L},\circ}T}\frac{(T_{\rm D}/T)^6}{27 I_4^2}\pi^2 z_e^2. \tag{5.240}$$

For $T/T_{\rm D}$ increasing from 0.1 to 10, $(T_{\rm D}/T)^6/I_4(T_{\rm D}/T)^2$ decreases from 97 to 9. Also, for normal dopant concentrations ($< 10^{19}$ cm^{-3}), z_e is of the order of 10^{-3}. Then for a wide temperature range ($0.1 \le T/T_{\rm D} \le 10$), $1/k_{p,e}$ is only about 10^{-4} of the electrical thermal resistivity $1/k_e$ found from the Wiedemann–Franz law, and is therefore negligible for this semiconductor.

Then, for bulk semiconductors, the lattice thermal conductivity is mainly limited by the phonon–phonon scattering (U–processes). The lattice conductivity can be predicted using the MD simulation and the G–K method, as introduced in Section 4.12. The most important is the appropriate interatomic potentials used to predict the lattice vibrations, including both the anharmonic and harmonic behaviors. Normally those potentials can be developed by fitting the energy surface computed with *ab initio* methods, for example, DFT. This approach, which is rather involved, is used here, and the resulting potentials need to be verified by use of the bulk properties and crystal structures. The potentials used here for Bi_2Te_3 are reported in [202]. Figure 5.34 shows the temperature-dependent, in-plane and cross-plane (Figure 5.28 shows the crystal structure) lattice conductivities of Bi_2Te_3. Note that the predicted in-plane and cross-plane k_p are higher than the experimental results. This is expected, considering the defects (e.g., isotopes, displacements, lamellas, etc.) in a real semiconductor crystal (Figure 5.14), which will reduce the thermal conductivity according to (5.236).

The lattice conductivities in both directions follow the $1/T$ law [202], similar to insulators, i.e., the Slack relation (4.132). The predicted cross-plane thermal conductivity $k_{p,\perp}$ is lower than the in-plane $k_{p,\|}$. Because the average cross-plane sound velocity (1631 m/s) is very close to the in-plane sound velocity (1775 m/s), the difference between the two thermal conductivities is mainly due to the anharmonicity along the different directions. This can be verified by the directional Grüneisen parameter $\gamma_{\mathrm{G},i}$ along the direction i. For Bi_2Te_3, the in-plane Grüneisen parameter $\gamma_{\mathrm{G},\|}$ is 1.17, and the cross-plane Grüneisen parameter $\gamma_{\mathrm{G},\perp}$ is 1.86 at 300 K [19]. The large difference in the anharmonicity originates from the unique bond characteristics in the layered structure (Figure 5.28), in which the intralayer bonds are covalent but the inter-layer bonds are hybrids of the electrostatic interactions and van der Waals interactions [202]. Furthermore, when the thermal conductivity is decomposed (Sections 4.12 and 4.13), we find that the contribution from the short-range acoustic phonons $k_{p,sh,\mathrm{A}}$, and that from the optical phonons $k_{p,\mathrm{O}}$, in the two different directions, are almost the same. The difference is due only to the contribution from the long-range acoustic phonons $k_{p,sh,\mathrm{A}}$. More details are reported in [202].

(C) *Figure of Merit*

Figure 5.34(b) shows the variation of the figure of merit Z_eT (5.204) for the p-type Bi_2Te_3 specimen of experiment [216] along the $\|$ and $\perp$ directions, with respect to temperature. The lower two curves are based on the directly (MD) calculated k_p. Because k_p as well as σ_e is very sensitive to defects, which are always present in fabricated specimens, for comparison between the calculated and measured Z_eT we used a modified k_p and the results are shown with the top two curves. Due to the difficulty in including the various defects, the modified k_p was obtained by fitting the total thermal conductivity to the experimental results [216] at 300 K and then using the Slack $1/T$ law at other temperatures. The experimental results are also shown in Fig. 5.34(b). The Z_eT with a modified k_p is higher than experimental results above 200 K, mainly due to the overestimation of σ_e. The calculated Z_eT reaches its maximum around 250 K. Z_eT along the $\|$ direction is higher than that along the $\perp$ direction between 200 K and 400 K, due to the larger ratio $\sigma_{e,\|}/\sigma_{e,\perp}$ compared to $k_{p,\|}/k_{p,\perp}$. Note that the experimental $\sigma_{e,\|}/\sigma_{e,\perp}$ is larger than the calculated results (discussed above), so the difference in the figure of merits along the $\|$ and $\perp$ direction is expected to be even larger.

5.18 Electron and Phonon Transport Under Local Thermal Nonequilibrium

Conduction electrons can acquire kinetic energy by an imposed electric field, by absorbing photons, or by other energy transitions. This kinetic energy can be harvested before inelastic scattering (in particular with phonons) results in conversion of this electronic energy to heat. Here we address this electronic carrier transport and interactions, while considering local thermal nonequilibrium between the electrons and phonons (each carrier and subcarrier has a temperature).

In many semiconductor devices, because of spatial variations in carrier (electron and hole) concentrations, the carrier diffusion also becomes important. An average particle (semiclassical) treatment is made starting from the Boltzmann transport equation (with appropriate moments) [47, 294, 302].

5.18.1 Derivations

The BTE (Table 3.1) for carrier $i = e$, is written as

$$\frac{\partial f_i}{\partial t} + \boldsymbol{u}_i \cdot \nabla f_i + \boldsymbol{F}_i \cdot \nabla_{\boldsymbol{p}} f_i = \frac{\partial f_i}{\partial t}|_s + \dot{s}_{f,i\text{-}j}. \tag{5.241}$$

As we discussed in Chapter 3, the BTE describes the statistical particle transport, including electron and phonon. The conservation equations that are encountered in fluid mechanics, heat transfer, and electron transport are found by taking different moments of the BTE.

Taking a function of electron momentum $\phi(\boldsymbol{p}_e)$, its weighed sum (or integral) is (note that here for electrons we have allowed for two spins)

$$\langle \phi(\boldsymbol{p}_e) \rangle \equiv \frac{1}{\hbar^3} \sum_{\boldsymbol{p}_e} \phi(\boldsymbol{p}_e) f_e(\boldsymbol{x}, \boldsymbol{p}_e, t). \tag{5.242}$$

Multiplying BTE by $\phi(\boldsymbol{p}_e)$ and summing over the momentum gives the BTE moment equation

$$\frac{1}{\hbar^3} \sum_{\boldsymbol{p}} \phi(\boldsymbol{p}) \frac{\partial f_e}{\partial t} + \frac{1}{\hbar^3} \sum_{\boldsymbol{p}_e} \phi(\boldsymbol{p}_e) \nabla \cdot \boldsymbol{u}_e f_e + \frac{1}{\hbar^3} \sum_{\boldsymbol{p}_e} \phi(\boldsymbol{p}_e) \boldsymbol{F}_e \cdot \nabla_{\boldsymbol{p}} f_e$$

$$= \frac{1}{\hbar^3} \sum_{\boldsymbol{p}_e} \phi(\boldsymbol{p}_e) \frac{\partial f_e}{\partial t}|_s + \frac{1}{\hbar^3} \sum_{\boldsymbol{p}} \phi(\boldsymbol{p}_e) \dot{s}_{f,e}. \tag{5.243}$$

The summation implies integrations (3.11) and (3.12), depending on symmetry. Also, the average of relaxation-time approximation (3.13) gives

$$\frac{1}{\hbar^3} \sum_{\boldsymbol{p}} \phi(\boldsymbol{p}) \frac{\partial f_e}{\partial t}|_s \equiv -\langle\langle \tau_{e,\phi}^{-1} \rangle\rangle (\langle \phi(\boldsymbol{p}_e) \rangle - \langle \phi(\boldsymbol{p}_e)^\circ \rangle), \tag{5.244}$$

where $\tau_{i,\phi}$ indicates the continuity τ_e(continuity), momentum τ_e(momentum), or energy τ_e(energy) relaxation time, depending on ϕ (Section 5.10).

For $\phi = \boldsymbol{p}_e^\circ$, the BTE gives the continuity equation for a carrier (here written for conduction electrons, but for the holes a similar equation is written)

$$\frac{\partial n_{e,c}}{\partial t} + \nabla \cdot \boldsymbol{u_e} n_{e,c} + \sum_i \dot{n}_{e,c,i} = \frac{\partial n_{e,c}}{\partial t} + \frac{1}{e_c} \nabla \cdot \boldsymbol{j_e} + \sum_i \dot{n}_{e,c,i} = 0, \qquad (5.245)$$

where we have used $\boldsymbol{j}_e = e_c \boldsymbol{u}_e n_{e,c}$ where $\boldsymbol{u}_e$ is the drift velocity $\boldsymbol{u}_e = \langle \boldsymbol{u}_e \rangle$. This is also given in Table 3.6.

For the carrier (electron) momentum, $\phi(\boldsymbol{p}_e) = \boldsymbol{p}^1 = m_{e,e} \boldsymbol{u_e}$, we have

$$\langle \phi(\boldsymbol{p}) \rangle = \frac{1}{4\pi^3 \hbar^3} \sum_{\boldsymbol{p}_e} \boldsymbol{p}_e f_e = n_{e,c} m_{e,e} \boldsymbol{u_e} \qquad (5.246)$$

$$\frac{1}{\hbar^3} \sum_{\boldsymbol{p}_e} \boldsymbol{p}_e \nabla \cdot \boldsymbol{u_e} f_e = \nabla_i (n_{e,c} m_{e,e} \boldsymbol{u}_{e,i} \boldsymbol{u}_{e,j} + n_{e,c} k_{\mathrm{B}} T_e)$$

$$= n_{e,c} m_{e,e} \boldsymbol{u}_e \nabla \boldsymbol{u}_e + \nabla n_{e,c} k_{\mathrm{B}} T_e. \qquad (5.247)$$

where we have used the thermal velocity and expressed it in terms of $k_{\mathrm{B}} T$ using the equipartition of translational kinetic energy.

These equations give the momentum conservation equation

$$n_{e,c} m_{e,e} [\frac{\partial \boldsymbol{u}_e}{\partial t} + (\boldsymbol{u}_e \cdot \nabla) \boldsymbol{u}_e] = -n_{e,c} e_c \boldsymbol{e_e} - \nabla n_{e,c} k_{\mathrm{B}} T_e - \frac{n_e m_{e,e} \boldsymbol{u}_e}{\tau_{e\text{-}p}(\text{momentum})}. \qquad (5.248)$$

The electron momentum (and energy) relaxation times are given in Table 5.4.

Under a steady-state condition, and by neglecting the gradient of electron drift velocity, (5.248) gives the drift–diffusion equation, i.e.,

$$\boldsymbol{j_e} = n_{e,c} e_c \mu_e \boldsymbol{e_e} + e_c D_e \nabla n_{e,c} + n_{e,c} \mu_e k_{\mathrm{B}} \nabla T_e \qquad \text{drift–diffusion equation,} \qquad (5.249)$$

where $D_e = k_{\mathrm{B}} T_e \mu_e / e_c$. This is also given in Table 3.6.

For energy, $\phi = E_{e,\kappa}(\boldsymbol{p}_e) = \boldsymbol{p}_e^2 / 2m_{e,e}$, and we define

$$\langle \phi(\boldsymbol{p}_e) \rangle = \frac{1}{\hbar^3} \sum_{\boldsymbol{p}_e} E_{e,\kappa}(\boldsymbol{p}_e) f_e = \frac{E_e}{V} = \frac{3}{2} n_{e,c} k_{\mathrm{B}} T_e + \frac{1}{2} n_{e,c} m_{e,e} u_e^2. \qquad (5.250)$$

Next, we note that

$$\langle\langle \tau_\phi^{-1} \rangle\rangle (\langle \phi(\boldsymbol{p}_e) \rangle - \langle \phi(\boldsymbol{p}_e)^{\mathrm{o}} \rangle) = \langle\langle \tau_{e\text{-}p}^{-1}(\text{energy}) \rangle\rangle (\frac{E_e}{V} - \frac{E_e^\circ}{V}) \qquad (5.251)$$

$$\frac{1}{\hbar^3} \sum_{\boldsymbol{p}_e} E_{e,\kappa} \nabla \cdot \boldsymbol{u_e} f_e = \frac{1}{\hbar^3} \sum_{\boldsymbol{p}_e} \frac{1}{2} m_{e,e} u_e^2 \nabla \cdot \boldsymbol{u}_e f_e$$

$$= \nabla \frac{1}{2} n_{e,c} m_{e,e} \langle u_e^2 \boldsymbol{u}_e \rangle$$

$$= \nabla (\frac{E_e}{V} \boldsymbol{u}_e + \boldsymbol{u}_e \cdot n_{e,c} k_{\mathrm{B}} T_e + k_e \nabla T_e). \qquad (5.252)$$

Equation (5.252) is called the heat flux term, as the last term represents heat conduction by an electron.

Using the proceeding equations, we find that the energy conservation equation is [47]

$$\begin{aligned}\frac{\partial(E_e/V)}{\partial t} &= -\nabla\cdot(\frac{E_e}{V}\boldsymbol{u}_e + n_{e,c}k_\mathrm{B}T_e\boldsymbol{u}_e + k_e\nabla T_e) + \boldsymbol{j}_e\cdot\boldsymbol{e}_e\\ &\quad -\frac{E_e - E_e^\circ}{\langle\langle\tau_e^{-1}(\text{energy})\rangle\rangle} + \sum_i \dot{s}_{e\text{-}i}(\text{energy})\\ \frac{E_e}{V} &= \frac{3}{2}n_{e,c}k_\mathrm{B}T_e + \frac{1}{2}n_{e,c}m_{e,e}u_e^2.\end{aligned}\tag{5.253}$$

Note that the total kinetic energy of the carrier E_e is the sum of translational (3 translational degrees of freedom) and drift motions. Here the carrier temperature T_e is defined by use of the electron collision velocity $\langle u_e'^2\rangle^{1/2}$, such that $3n_{e,c}k_\mathrm{B}T_e/2 = m_{e,e}n_{e,c}\langle u_e'^2\rangle^{1/2}/2$. The collision velocity is also called the thermal speed (for the random component of the velocity), where $\langle u_e'\rangle = 0$. This defines the carrier temperature based on the classical equipartition of energy ($k_\mathrm{B}T/2$ per degree of freedom). Note that this does not include the quantum effects on the specific heat capacity, as included in (5.73).

By substituting the continuity equation (5.245) and momentum conservation equation (5.248) into the the energy conservation equation (5.253), we have [47]

$$\begin{aligned}\frac{\partial T_e}{\partial t} + \nabla\cdot\boldsymbol{u}_e T_e &= \frac{2}{3n_e k_\mathrm{B}}\nabla\cdot k_e\nabla T_e + \frac{1}{3}T_e\nabla\cdot\boldsymbol{u}_e - \frac{T_e - T_{p,\mathrm{O}}}{\tau_{e\text{-}p,\mathrm{O}}}\\ &\quad -\frac{T_e - T_{p,\mathrm{A}}}{\tau_{e\text{-}p,\mathrm{A}}} + \frac{m_{e,e}u_e^2}{3k_\mathrm{B}}[\frac{2}{\tau_{e\text{-}p}(\text{momentum})} - \frac{1}{\tau_{e\text{-}p,\mathrm{O}}} - \frac{1}{\tau_{e\text{-}p,\mathrm{A}}}]\\ &\quad +\frac{2}{3n_{e,c}k_\mathrm{B}}\sum_i \dot{s}_{e\text{-}i}(\text{energy}).\end{aligned}\tag{5.254}$$

This distinguishes between scattering by the acoustic and the optical phonons. Note that this includes the Joule heating (first term in the square brackets).[†]

The thermal-phonon energy equations are derived from the first law of thermodynamics. The BTE for a phonon is applicable for energy conservation and is written separately for the optical phonon and the acoustic phonon.

5.18.2 Phonon Modal Energy Equations

Starting from (5.241) and using the same momentum power formulation and averages. The optical- and acoustic-phonon systems are treated separatively (having

---

[†] The volumetric Joule heating is found using (5.147) as

$$\rho_e j_e^2 = \frac{m_{e,e}}{e_c^2 n_{e,c}\tau_{e\text{-}p}(\text{momentum})}e_c^2 n_{e,c}^2 u_e^2 = \frac{m_{e,e}n_{e,c}u_e^2}{\tau_{e\text{-}p}(\text{momentum})}.$$

Then, dividing by $3k_\mathrm{B}n_{e,c}$, we have the term in (5.254).

temperatures $T_{p,\mathrm{O}}$ and $T_{p,\mathrm{A}}$ related to their energies and nonequilibrium occupancies) [151]. The optical-phonon energy conservation equation is based on BTE, with no transport terms (assuming $\boldsymbol{u}_{p,\mathrm{O}} = 0$ and $\boldsymbol{F}_{p,\mathrm{O}} = 0$ for the optical phonons) [151]

$$\frac{\partial E_{p,\mathrm{O}}}{V\partial t} = -\frac{\partial E_e}{V\partial t}|_s + \frac{\partial E_{p,\mathrm{O}}}{V\partial t}|_s. \tag{5.255}$$

Substituting for scattering terms for (5.254), we have [151]

$$nc_{p,\mathrm{O}}\frac{\partial T_{p,\mathrm{O}}}{\partial t} = \frac{3n_{e,c}k_\mathrm{B}}{2}\frac{T_e - T_{p,\mathrm{O}}}{\tau_{e\text{-}p,\mathrm{O}}} + \frac{n_{e,c}m_{e,e}u_e^2}{2\tau_{e\text{-}p,\mathrm{O}}} - nc_{p,\mathrm{O}}\frac{T_{p,\mathrm{O}} - T_{p,\mathrm{A}}}{\tau_{p,\mathrm{A}}}, \tag{5.256}$$

where n is the number of atoms per unit volume.

The acoustic-phonon energy conservation equation ($\boldsymbol{F}_{p,\mathrm{A}} = 0$) is

$$\frac{\partial E_{p,\mathrm{A}}}{V\partial t} + \nabla\cdot k_p\nabla T_{p,\mathrm{A}} = -\frac{\partial E_{p,\mathrm{O}}}{V\partial t}|_s \tag{5.257}$$

or

$$nc_{p,\mathrm{A}}\frac{\partial T_{p,\mathrm{A}}}{\partial t} = \nabla\cdot k_p\nabla T_{p,\mathrm{A}} + nc_{p,\mathrm{O}}\frac{T_{p,\mathrm{O}} - T_{p,\mathrm{A}}}{\tau_{p,\mathrm{A}}} + \frac{3n_{e,c}k_\mathrm{B}}{2}\frac{T_e - T_{p,\mathrm{A}}}{\tau_{e\text{-}p,\mathrm{A}}}. \tag{5.258}$$

Note that the specific heat is divided into the acoustic and optical components.

The acoustic phonon heat capacity is given by (4.64) and optical phonon by (C.1).

In addition to the conservation equations there is the Poisson equation (Table 3.5), which satisfies the Gauss law, i.e.,

$$\nabla^2\varphi_e = -\frac{e_c}{\epsilon_\mathrm{o}\epsilon_e}(n_{e,c} + n_{e,b}), \tag{5.259}$$

where $n_{e,b}$ is the bond electron density, which should be included.

The set of equations derived in this section is used for electron–phonon thermal nonequilibrium analysis of semiconductor devices.

5.18.3 Summary of Conservation (Electrohydrodynamic) Equations

Because of their similarity to the Navier–Stokes equations (Table 3.10), including the mechanical energy equation (6.123), the carrier conservation equations are called the hydrodynamic equations. The summary of carrier balance equations are subsequently given. The electronic carrier (electron or hole) continuity equation, i.e., (5.245), is

$$\frac{\partial n_{e,c}}{\partial t} + \frac{1}{e_c}\nabla\cdot\boldsymbol{j_e} + \sum_i \dot{n}_{e,c,i} = 0. \tag{5.260}$$

The electronic carrier drift–diffusion equation, i.e., (5.249), is

$$\boldsymbol{j_e} = e_c n_{e,c}\mu_e\boldsymbol{e_e} + e_c D_e\nabla n_{e,c} + n_{e,c}\mu_e k_\mathrm{B}\nabla T_e, \quad D_e = \frac{k_\mathrm{B}T_e\mu_e}{e_c}. \tag{5.261}$$

The electron energy equation is

$$\frac{\partial T_e}{\partial t} + \nabla \cdot \boldsymbol{u}_e T_e = \frac{2}{3n_{e,c}k_\mathrm{B}} \nabla \cdot k_e \nabla T_e + \frac{1}{3} T_e \nabla \cdot \boldsymbol{u}_e - \frac{T_e - T_{p,\mathrm{O}}}{\tau_{e\text{-}p,\mathrm{O}}(\text{energy})}$$
$$- \frac{T_e - T_{p,\mathrm{A}}}{\tau_{e\text{-}p,\mathrm{A}}(\text{energy})} + \frac{m_{e,e}u_e^2}{3k_\mathrm{B}} [\frac{2}{\tau_{e\text{-}p}(\text{momentum})} - \frac{1}{\tau_{e\text{-}p,\mathrm{O}}(\text{energy})}$$
$$- \frac{1}{\tau_{e\text{-}p,\mathrm{A}}(\text{energy})}] + \frac{2}{3n_{e,c}k_\mathrm{B}} \sum_i \dot{s}_{e\text{-}i}(\text{energy}). \tag{5.262}$$

Note again that $\boldsymbol{u}_e$ is the drift velocity. The optical-phonon energy equation (including electron kinetic energy transfer) is

$$nc_{p,\mathrm{O}} \frac{\partial T_{p,\mathrm{O}}}{\partial t} = \frac{3n_{e,c}k_\mathrm{B}}{2} \frac{T_e - T_{p,\mathrm{O}}}{\tau_{e\text{-}p,\mathrm{O}}(\text{energy})} + \frac{n_{e,c}m_{e,e}u_e^2}{2\tau_{e\text{-}p,\mathrm{O}}(\text{energy})}$$
$$- n_{e,c}c_{p,\mathrm{O}} \frac{T_{p,\mathrm{O}} - T_{p,\mathrm{A}}}{\tau_{p,\mathrm{A}}(\text{energy})}. \tag{5.263}$$

The acoustic-phonon energy equation (includes conduction) is

$$nc_{p,\mathrm{A}} \frac{\partial T_{p,\mathrm{A}}}{\partial t} = \nabla \cdot k_p \nabla T_{p,\mathrm{A}} + n_{e,c}c_{p,\mathrm{O}} \frac{T_{p,\mathrm{O}} - T_{p,\mathrm{A}}}{\tau_{p,\mathrm{A}}(\text{energy})}$$
$$+ \frac{3n_{e,c}k_\mathrm{B}}{2} \frac{T_e - T_{p,\mathrm{A}}}{\tau_{e\text{-}p,\mathrm{A}}(\text{energy})}. \tag{5.264}$$

5.19 Cooling Length in Electron–Phonon Local Thermal Nonequilibrium

From the results of Section 5.18, the electron and phonon transport equations, under thermal nonequilibrium, can be written as spectral (energy resolved) or energy-averaged forms. Here the averaged forms are used, those giving electron and lattice temperatures T_e and T_p along with a single, average relaxation time. For simplicity, only the acoustic phonons are considered. To generalize the results, we assume TE transport over a solid conductor, as shown in Figure 5.35. The problem is further described in [106].

The kinetics of electrons and phonons in an electric field or in a temperature field is described by the coupled BTE for electrons and phonons (Section 5.18). In one dimension and for steady state, with constant properties, these equations are the simplified forms of (5.262) [108, 227]

$$- k_e \frac{d^2 T_e}{dx^2} = \rho_e j_e^2 - \frac{n_{e,c}k_\mathrm{B}}{\tau_{e\text{-}p}(\text{energy})}(T_e - T_p) \tag{5.265}$$

$$- k_p \frac{d^2 T_p}{dx^2} = \frac{n_{e,c}k_\mathrm{B}}{\tau_{e\text{-}p}(\text{energy})}(T_e - T_p), \tag{5.266}$$

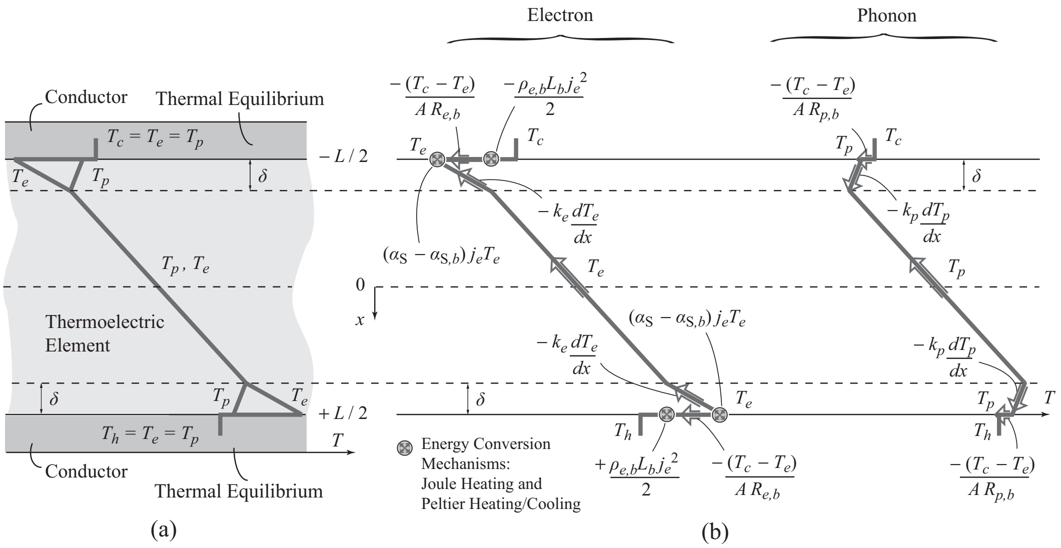
Electron
Phonon
Conductor
Thermal Equilibrium
$T_c = T_e = T_p$
T_e
T_p
δ
T_p, T_e
Thermoelectric Element
$T_h = T_e = T_p$
$-L/2$
$+L/2$
0
x
T
$-\frac{(T_c - T_e)}{A R_{e,b}}$
$-\frac{\rho_{e,b} L_b j_e^2}{2}$
T_c
$-k_e \frac{dT_e}{dx}$
$(\alpha_S - \alpha_{S,b}) j_e T_e$
$-\frac{(T_c - T_e)}{A R_{p,b}}$
$-k_p \frac{dT_p}{dx}$
T_h
$+\frac{\rho_{e,b} L_b j_e^2}{2}$
$-\frac{(T_c - T_e)}{A R_{e,b}}$
$-\frac{(T_c - T_e)}{A R_{p,b}}$
Energy Conversion Mechanisms: Joule Heating and Peltier Heating/Cooling
(a)
(b)

Figure 5.35. (a) Temperature distributions for electron and lattice subsystem, assuming equilibrium in the connectors. (b) Energy conversion mechanisms and heat transfer paths of electron and lattice subsystem [106].

where j_e is the electrical current density and $\tau_{e\text{-}p}$(energy) is the average, electron–phonon energy relaxation time. These are the energy equations for the electron and phonon subsystems.

Note that the volumetric Joule heating (3.54), $\boldsymbol{j}_e \cdot \boldsymbol{e}_e = \rho_e j_e^2 = m_{e,e} n_{e,c} u_e^2 / \tau_{e\text{-}p}$ (momentum) (footnote in Section 5.18.1). In [108, 227], with some justifications, the coefficient 3/2 in (5.263) and (5.264) is replaced with 1, as it appears in (5.265) and (5.266).

Assuming that ρ_e, $n_{e,c}$, $\tau_{e\text{-}p}$(energy), k_e, and k_p are constant, we solve the proceeding equations by defining a center-of-thermal-conductivity temperature $kT_{ctc} = k_e T_e + k_p T_p$ [24]. The solution is

$$T_e = A_1 + A_2 \frac{x}{L} + \frac{\rho_e j_e^2 [(\frac{L}{2})^2 - x^2]}{2k} + \frac{\rho_e j_e^2 \delta^2}{\gamma k} - \frac{1}{\gamma}[A_3 \cosh(\frac{x}{\delta}) + A_4 \sinh(\frac{x}{\delta})] \tag{5.267}$$

$$T_p = A_1 + A_2 \frac{x}{L} + \frac{\rho_e j_e^2 [(\frac{L}{2})^2 - x^2]}{2k} - \frac{\rho_e j_e^2 \delta^2}{k} + [A_3 \cosh(\frac{x}{\delta}) + A_4 \sinh(\frac{x}{\delta})], \tag{5.268}$$

where

$$\delta = \delta_{e\text{-}p} = (\frac{\tau_{e\text{-}p}}{n_{e,c} k_B} \frac{k_e k_p}{k_e + k_p})^{1/2} \text{ cooling length}$$

$$\tau_{e\text{-}p}(\text{energy}) = \frac{k_{\rm B}T_p}{2m_{e,e}u_{p,A}^2}\tau_{e\text{-}p}(\text{momentum}),$$

$$\tau_{e\text{-}p}(\text{momentum}) = \langle\langle\tau_e\rangle\rangle(\text{momentum}) = \frac{m_{e,e}\mu_e}{e_c}$$

$$\text{average electron–phonon relaxation time,} \tag{5.269}$$

where $\gamma = k_e/k_p$ and L is the thermoelectric element thickness.

The relation between $\tau_{e\text{-}p}$(energy) and $\tau_{e\text{-}p}$(momentum) is for the acoustic deformation potential (end-of-chapter problem). The various $\tau_{e\text{-}p}$ are listed in Table 5.4.

In [227], the constant 2 in (5.269) is replaced with similar constants for low and high temperatures (with respect to the Debye temperature).

The four unknown constants A_1, A_2, A_3, and A_4 are determined [105] by the boundary conditions for the flow of heat by electrons and phonons at the boundaries, as presented in Figure 5.35. Also, for simplicity, it is assumed that electrons and phonons are in equilibrium in the connectors, i.e, $T_p = T_e = T_c$ at $x = -L/2$ and $T_p = T_e = T_h$ at $x = L/2$.

The phonon boundary conditions are

$$-\frac{T_c - T_p}{AR_{p,b}} - k_p\frac{dT_p}{dx} = 0, \quad \text{at } x = -\frac{L}{2} \tag{5.270}$$

$$-\frac{T_p - T_h}{AR_{p,b}} - k_p\frac{dT_p}{dx} = 0, \quad \text{at } x = \frac{L}{2}, \tag{5.271}$$

where $AR_{p,b}$ is the phonon boundary resistance. This resistance is because of a change in acoustic properties at the interface, as discussed in Section 4.13. The electron boundary conditions are

$$-\frac{T_c - T_e}{AR_{e,b}} - k_e\frac{dT_e}{dx} + (\alpha_{\rm S} - \alpha_{{\rm S},b})\, j_e T_e - \rho_{e,b}L_b\frac{j_e^2}{2} = 0, \quad \text{at } x = -\frac{L}{2} \tag{5.272}$$

$$-\frac{T_e - T_h}{AR_{e,b}} - k_e\frac{dT_e}{dx} + (\alpha_{\rm S} - \alpha_{{\rm S},b})\, j_e T_e + \rho_{e,b}L_b\frac{j_e^2}{2} = 0, \quad \text{at } x = \frac{L}{2}, \tag{5.273}$$

where $AR_{e,b}$ is the electron thermal boundary resistance [106] and $\alpha_{{\rm S},b}$ and $\rho_{e,b}L_b$ are the boundary Seebeck coefficient and the electrical boundary resistance (multiplied by area).

The first term in the proceeding equations represents the heat flow as defined by the phonon (electron) boundary resistance, and the second term is the heat flow predicted by the Fourier law. The third terms (5.272) and (5.273) represent the Peltier cooling and heating, respectively. The Joule heating at the boundaries is represented by the fourth term.

The bulk Seebeck coefficient $\alpha_{\rm S}$ is given by (5.274), the n- and p-type thermoelectric materials. The boundary Seebeck coefficient $\alpha_{{\rm S},b}$, assuming that tunneling is the dominant electron transport mechanism across the metal/semiconductor interfaces, is given by [24]

$$\alpha_{\mathrm{S},b} = (\frac{k_{\mathrm{B}}}{e_c})\frac{\pi^2}{3}k_{\mathrm{B}}T(\frac{h_{\mathrm{P}}^2 E_{e,o}}{8\pi^2 m_{e,e}^* d^2})^{-1/2}, \tag{5.274}$$

where $E_{e,o}$ is the height of the boundary electron energy barrier. Equations (5.267) and (5.268) were solved analytically with (5.270) to (5.273). The resulting expressions for the coefficients A_j are in general very complicated. For electrical current j_e equal to zero, the coefficients A_j are

$$A_1 = \frac{T_h + T_c}{2}$$

$$A_2 = \frac{\gamma L^* \mathrm{coth} L^* + \frac{R_e^* R_p^* (1+\gamma)^2}{2R_k^*}}{R_e^* + \frac{R_e^* R_p^* (1+\gamma)^2}{2R_k^*} + \frac{\gamma L^* \mathrm{coth} L^*}{(1+2R_k^*)^{-1}} + R_p^* \gamma^2}(T_h - T_c)$$

$$A_3 = 0$$

$$A_4 = \frac{\gamma^2 R_p^* - \gamma R_e^*}{R_e^* + \frac{R_e^* R_p^* (1+\gamma)^2}{2R_k^*} + \frac{\gamma L^* \mathrm{coth} L_{te}^*}{(1+2R_k^*)^{-1}} + R_p^* \gamma^2} \frac{(T_h - T_c)}{2\mathrm{sinh} L^*}, \quad \text{for } j_e = 0, \tag{5.275}$$

where the dimensionless parameters (*) are given by

$$R_e^* = \frac{(\frac{1}{AR_{p,b}} + \frac{1}{AR_{e,b}})^{-1}}{AR_{e,b}}, \quad R_p^* = \frac{(\frac{1}{AR_{p,b}} + \frac{1}{AR_{e,b}})^{-1}}{AR_{p,b}},$$

$$R_k^* = \frac{(\frac{1}{AR_{p,b}} + \frac{1}{AR_{e,b}})^{-1}}{\frac{L}{k_e + k_p}}, \quad L^* = \frac{L}{2\delta}. \tag{5.276}$$

More details, as well as a numerical example, are given in [106].

5.20 Electronic Energy States of Ions in Crystals

The slightly altered electronic states of doped ions in dielectric crystals allow for precise, spectral electron transitions that can be used, for example, in solid-state lasers, and in laser heating and cooling of solids. The electron state in the crystal host is altered, including the occurrence of energy splitting, and these are briefly reviewed in the following discussion.

We first look at ions in f block that have a weakly interacting $4f$ orbital because the $4f$ shell is deeply embedded inside the $5s$ and $5p$ shells, as seen in Figure 5.36. Because of the relatively weak interaction with the lattice, the energy calculation is much simpler. The Hamiltonian can be written for an individual rare-earth ion and decomposed as [112]

$$\mathrm{H} = \mathrm{H}_{free\ ion} + \mathrm{H}_{ion-lattice}, \tag{5.277}$$

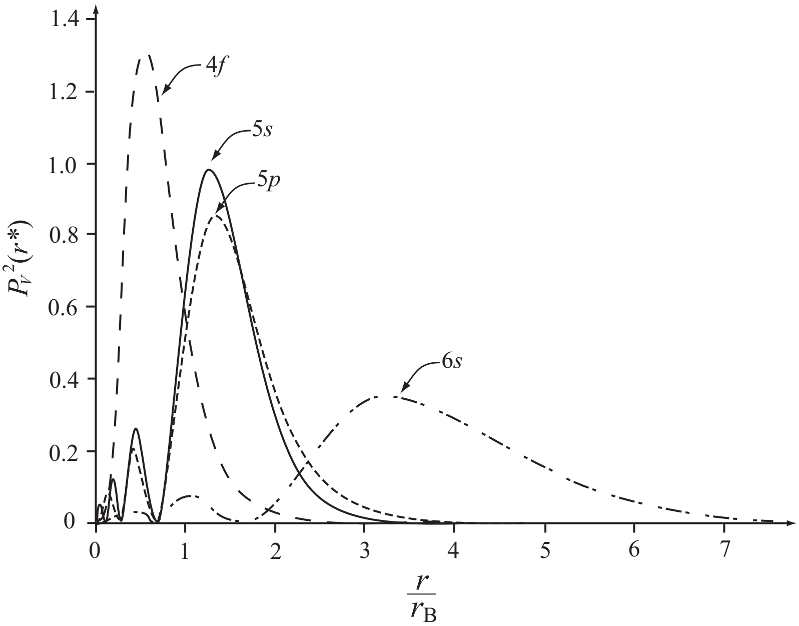

Figure 5.36. Square of the radial electron distribution probability distribution $P_V(r^*) = \psi^\dagger\psi \mathrm{d}r^*$ for $4f$, $5s$, $5p$, and $6s$ electron orbits of Gd^{3+} [147].

where $\mathrm{H}_{free\ ion}$ is the Hamiltonian of the ion in complete isolation, and $\mathrm{H}_{ion-lattice}$ contains the static interactions of the ion with the host, which is also referred to as the crystal field.

The standard approach for treating $\mathrm{H}_{free\ ion}$ is to employ the central-field approximation, in which each electron is assumed to move independently in a spherically symmetric potential formed by the nucleus and the average potential of all other electrons. The solutions are then included as a product of a radial and an angular function. Whereas the radial function depends on the details of the potential, the spherical symmetry ensures that the angular component is identical to that of a hydrogen atom and can be expressed as spherical harmonics.

Using the radial function dependence on a potential, a semiempirical approach has been employed in which the attempt is made to identify these effective interactions operating within the f electrons that produce the observed structure [347]. Based on this method of interpretation, $\mathrm{H}_{free\ ion}$ (the free ion Hamiltonian) of the system is written as

$$\begin{aligned}\mathrm{H}_{free\ ion} = &\sum_{k=0,2,4,6} F_k \mathrm{I}^k + \xi S \cdot L + \alpha L(L+1) + \beta G(G_2) + \gamma G(R_7) \\ &+ \sum_{i=2,3,4,6,7,8} \Upsilon^i t_i + \sum_{k=0,2,4} M^k m_k + \sum_{2,4,6} P^k p_k,\end{aligned} \tag{5.278}$$

Table 5.9. *The semiempirical atomic properties of rare-earth ions [347] in cm*$^{-1}$. *N is the number of electrons in the f shell. (1 cm*$^{-1}$ *= 0.12398 meV, Table 1.4.)*

N	Ground state	Ion, z	F_2, cm^{-1}	ξ, cm^{-1}	Ionic radius Å
0	$^1S_0$	La^{3+}, 57			1.061
1	$^2F_{5/2}$	Ce^{3+}, 58		640	1.034
2	$^3H_4$	Pr^{3+}, 59	320	759	1.013
3	$^4I_{9/2}$	Nd^{3+}, 60	327	885	0.995
4	$^5I_4$	Pm^{3+}, 61			0.979
5	$^6H_{5/2}$	Sm^{3+}, 62	370	1200	0.964
6	$^7F_0$	Eu^{3+}, 63	401	1320	0.950
7	$^8S_{7/2}$	Gd^{3+}, 64	408	1470	0.938
8	$^7F_6$	Tb^{3+}, 65	434	1705	0.923
9	$^6H_{15/2}$	Dy^{3+}, 66	420	1900	0.908
10	$^5I_8$	Ho^{3+}, 67	450	2163	0.894
11	$^4I_{15/2}$	Er^{3+}, 68	433	2393	0.881
12	$^3H_6$	Tm^{3+}, 69	447	2617	0.869
13	$^2F_{7/2}$	Yb^{3+}, 70		2883	0.858
14	$^1S_0$	Lu^{3+}, 71			0.848

where F_k are the Slater integral parameters,[†] which represent the effective Coulomb interaction between $4f$ electrons. Here, I^k are the angular integrals over spherical harmonics, ξ is the spin–orbit parameter, and α, β and γ are coefficients of the Casimir operators for the full rotation group and the nonsymmetry groups G_2 and R_7 [375]. Also, here Υ^i are known as Trees parameters [466], M^k are the spin and orbital magnetic moments of the electrons, and P^k are three-electron electrostatic correlations. The Slater and the spin–orbit parameters for rare-earth ions in $LaCl_3$ are tabulated in Table 5.9.

Then assuming that the $4f$ radial wave functions are for hydrogen, as discussed in Section 2.6.6, the relationship between F_k are obtained as [223]

$$F_4/F_2 = 41/297 = 0.138$$

$$F_3/F_2 = 7.25/81.143 = 0.0151. \tag{5.279}$$

For the $4f$ shells a good estimate of F_2 is made with

$$F_2 = 12.4(z - 34) \ \text{cm}^{-1}, \tag{5.280}$$

where z is the atomic number of the rare-earth ion. Assuming that the lattice forms approximately hexagonal symmetry (D_{3h}), $H_{ion\text{-}lattice}$ (crystal field Hamiltonian) can be expanded as

$$H_{ion\text{-}lattice} = \sum_{k,q} B_q^k C_q^k = B_0^2 c_0^2 + B_0^4 c_0^4 + B_0^6 c_0^6 + B_0^2 (c_6^6 + c_{-6}^6), \tag{5.281}$$

[†] The Slater radial integrals are defined as

$$F_k(i.j) = \int_0^\infty \int_0^\infty \frac{r^{<k}}{r^{>k+1}} [P_i(r_1)P_i(r_2)]^2 \mathrm{d}r_1 \mathrm{d}r_2,$$

which is a parameter representing the radial distribution of the electrons.

Table 5.10. *Crystal field parameters of Nd^{3+} in LaF_3 and $LaCl_3$ crystals [111].*

Nd^{3+}: LaF_3 (D_{3h} approximation)	Nd^{3+}: $LaCl_3$ (C_{3h} approximation)
$\alpha = 21.28$	$\alpha = 22.1$
$\beta = -583$	$\beta = -650$
$\gamma = 1443$	$\gamma = 1586$
$\Upsilon^2 = 306$	$\Upsilon^2 = 377$
$\Upsilon^3 = 41$	$\Upsilon^3 = 40$
$\Upsilon^4 = 59$	$\Upsilon^4 = 63$
$\Upsilon^6 = -283$	$\Upsilon^6 = -292$
$\Upsilon^7 = 326$	$\Upsilon^7 = 358$
$\Upsilon^8 = 298$	$\Upsilon^8 = 354$
$M^0 = 2.24$	$M^0 = 2.1$
$M^2 = 1.25$	
$M^4 = 0.84$	
$P^2 = 213$	$P^2 = 255$
$P^4 = 160$	
$P^6 = 106.5$	
$B_0^2 = 216$	$B_0^2 = 163$
$B_0^4 = 1225$	$B_0^4 = -336$
$B_0^6 = 1506$	$B_0^6 = -713$
$B_6^6 = 770$	$B_6^6 = 462$

where B_q^k are the crystal field parameters and c_q^k is a tensor operator acting on the normal coordinate of the electron. The nonvanishing component of c_q^k is dependent on the symmetry of the ion complex and their values should be looked up in references that deal with group theory. Some examples of crystal field parameters are listed in Table 5.10. These parameters are used to map the complete energy spectrum of the rare-earth ions [111]. Detailed examples are shown in [96]. Note that, for transition metals, comprehensive examples can be found in [170] using Dq parameters.

Because the solutions are constructed from hydrogenlike states, the total orbital angular momentum L and the total spin S are the quantum numbers. Here L and S are the vector sums of the orbital and spin quantum numbers for all the $4f$ electrons on the ion. Each f electron contributes an orbital quantum number of 3 and a spin of 1/2. Total orbital angular momenta are specified by the letters S, P, D, F, G, H, I, K, ..., to represent L = 0, 1, 2, 3, 4, 5, 6, 7, ..., respectively. Russell–Saunders coupling (LS coupling) is most often used. In this scheme, L and S are vectorially added to form the total angular momentum J, and the states are labeled using atomic term symbol $^{2S+1}L_J$ [171]. The quantum numbers (L, S, J, and another arbitrary one) define the terms of the configuration, all of which are the degeneration of the central-field approximation, as shown in Figure 5.37. The electrostatic interaction lifts the angular degeneracy and produces a spectrum of states with energies depending on L and S, but not on J.

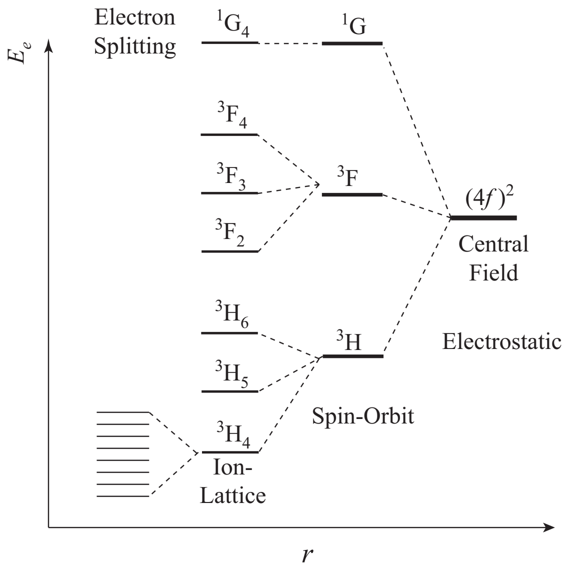

Figure 5.37. Energy diagram (electronic energy as a function of distance between ion and its nearest neighbor) illustrating hierarchy of energy splittings, resulting from electron–electron and electron–host (ion) interactions for the f-block atoms (Table A.2) [112].

Next in the hierarchy is the spin–orbital, the strongest of the magnetic interactions. Spin–orbit lifts the degeneracy in the total angular momentum and splits the LS terms into J levels. This uses the Hund rules for J for a particular atom [157]. The Hund first rule states that, all other being equal, the state with the highest total spin will have the lowest energy. The Hund second rule states that if a subshell is no more than half filled, then the lowest energy level has $J = |L - S|$; if it is more than half filled, then $J = L + S$ has the lowest energy.

The host has the least influence on the electronic structure and changes the positions of these levels only slightly. The static effects of the host on the rare-earth dopant customarily are treated by replacing the host with an effective crystal field potential at the ion site.

Two examples of energy levels of rare-earth ion-doped crystals are shown in Figure 5.38.

In Section 7.12, we will discuss application of electron transition of ions embedded in host crystals in the laser cooling of solids.

5.21 Electronic Energy States of Gases

The electronic configurations of gas molecules provide precise, spectral electron transitions similar to the rare-earth ion-doped crystals. This is because gas atoms and molecules and ions dopant in crystals are relatively isolated, so they do not form energy bands like atoms in a lattice structure.

The electronic energy states of a gas molecule are defined by the associated wave function of the molecule. The central field approximation and LCAO method

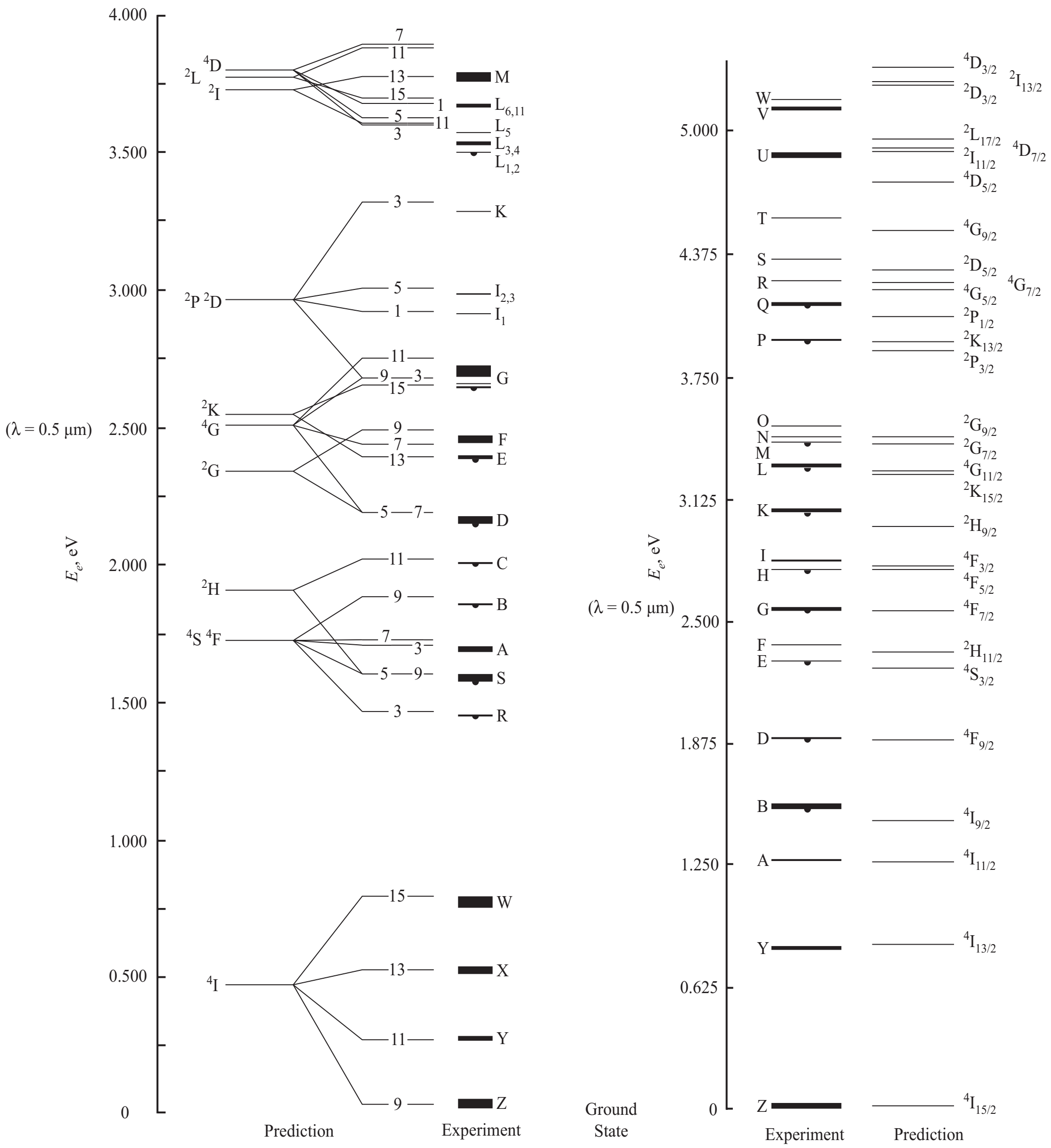

(a) Nd^{3+}: $LaCl_3$

(b) Er^{3+}: $LaCl_3$

Figure 5.38. Empirical and computed energy levels of (a) $Nd^{3+}(4f^3)$ and (b) $Er^{3+}(4f^{11})$ in ion-doped $LaCl_3$. The semicircles indicate fluorescence (resonance R) in the $LaCl_3$ structure [112, 369].

(Section 5.3) can be applied to calculate the energy states of a molecule from the Schrödinger equation, as discussed in Section 2.6.7.

The notation used to represent the electronic energy states of gas molecules typically includes the LS coupling introduced in Section 5.21. In addition to the coupling, a prefix is included to indicate the excitation level of the atom. For instance, the ground state configuration of Ne is 1S0, and the second excited state with the same quantum spin (opposing spin of the excited electrons) would also be $^1S_0$, which

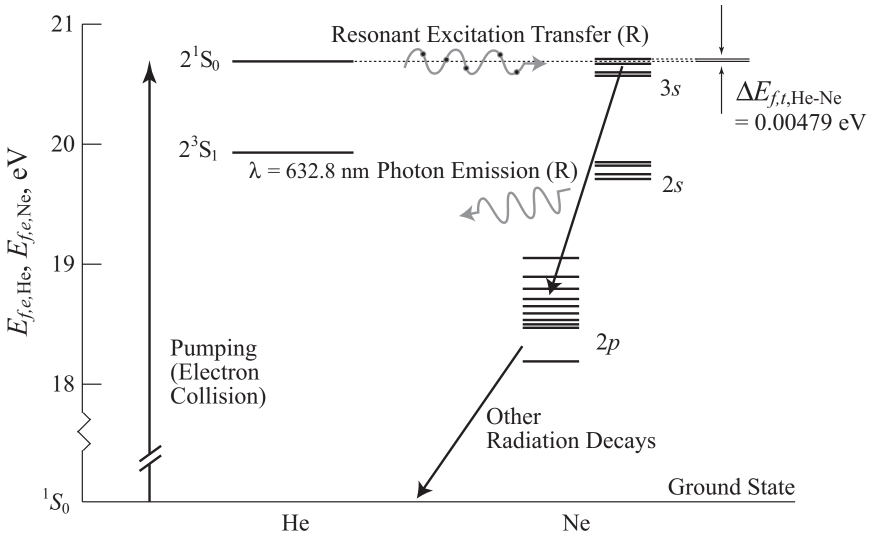
21
20
19
18
$^1S_0$
$E_{f,e,\text{He}}, E_{f,e,\text{Ne}}$, eV
2^1S_0
2^3S_1
Resonant Excitation Transfer (R)
3s
$\Delta E_{f,t,\text{He-Ne}}$
= 0.00479 eV
λ = 632.8 nm Photon Emission (R)
2s
2p
Pumping
(Electron
Collision)
Other
Radiation Decays
Ground State
He
Ne

Figure 5.39. A partial energy diagram showing electronic energy states, a translational energy transfer, and a common laser transition found in the atomic He–Ne laser system [494].

we refer to as 2^1S_0 for clarity. The energy states of He are represented in this notation in Figure 5.39, which shows experimentally determined energy states of He and Ne atoms in a partial energy diagram.

For the excited states of Ne in Figure 5.39, the Paschen notation [494] is used to refer to groups of electron configurations more easily. This represents a group of configurations based on the outermost electron shell, where the ground state electron configuration is assumed to be the 1*s* orbital. For example, the ground-state electron configuration of Ne is normally $2s^2 2p^5 3s^1$, but becomes 1*s* in the Paschen notation system. The Ne $2s_{2-5}$ electron configurations are equivalent to LS notation $^1P_1$, $^3P_0$, $^3P_1$, and $^3P_2$. Here P indicates that the principal quantum number of the 2*s* subshell is 2, and the other quantum numbers arise from the possible spin configurations of S = 0 or S = 1.

There are at least three basic electronic energy transfers involved in the 632.8 nm He–Ne laser cycle: electrical excitation of He, resonant excitation transfer from He to Ne, and the subsequent laser transition in Ne to a lower energy level.

Electrical discharge is used to electronically excite (pump) gas. For discharge to occur, atoms are forced to ionize to conduct electricity. Not only does the ionization energy necessarily excite and free electrons, but traveling electrons also collide with atoms and can stimulate upper electronic energy levels in those atoms. In an electrical discharge through He, the atoms become overexcited and quickly relax to their uppermost stable energy state, He 2^1S_0. A high population of these molecules accumulates (population inversion).

Resonant excitation transfer is a collisional process that transfers electronic energy between fluid particles. This occurs only when energy states are sufficiently close, so that an electron–electron impact between fluid particles can transfer electronic energy from one fluid particle to the other. The energy coincidence between the He 2^1S_0 and Ne 3*s* energy levels allows for resonant energy transfer between the two molecules, electronically exciting the Ne 3*s* energy level. The reversible excitation can be represented as a spin-conserving energy transfer:

$$E_{f,e,\mathrm{He}}(2^1\mathrm{S}_0) + E_{f,e,\mathrm{Ne}}(^1\mathrm{S}_0) = E_{f,e,\mathrm{He}}(^1\mathrm{S}_0) + E_{f,e,Ne}(^3\mathrm{S}_2) - \Delta E_{f,t,\mathrm{He\text{-}Ne}}. \tag{5.282}$$

Photon emission of electronic energy states of gases occurs only under special circumstances. Nonradiative decay processes compete with photon emission. If the relaxation times of electronic energy states of a fluid particle are too high, collisional deactivation will take place before radiation occurs. The rate of collisions, particle velocity, and the magnitude of energy transfer all affect the quickness of nonradiative decay processes.

For lasing to occur, more atoms must be in an excited state than in the ground state; this is called population inversion. Ideally, for lasing, atoms should be excited very selectively into a single, upper energy level. It is important to give atoms the same energy states, so they can emit the same photon. If atoms are excited in different energy states they cannot give the same energy photon, and stimulated emission will not occur. When the rate of excitation is high enough to produce a population inversion, stimulated emission occurs.

There are a number of factors in the He–Ne system that collectively produce the population inversion. A high number of He atoms are selectively excited into their stable, upper electronic energy level. The He atoms very selectively excite the Ne $3s^2$ energy level by excitation transfer. Also, because of the large energy gaps between electronic energy states of gases, it is difficult to deactivate the energy levels through collisional processes. The population of excited Ne atoms accumulates, and stimulated emission becomes favorable, producing laser light.

Although the laser produces relatively high-energy, short-wavelength laser light, this transition is not a high power source of laser energy because it produces a relatively low rate of photon emission. The efficiency of a typical He–Ne laser is around 0.1%. Inefficiencies arise because of the difficulty in forcing an increase in the electronic states of gases, and a significant portion of the energy in the cycle does not produce lasing. The remaining energy is dissipated as heat and must be removed from the laser system. Usually this is accomplished by cycling gases. The major benefits provided by the atomic He–Ne laser system are the high stability that it has compared with that of other lasers, a long operating lifetime, and low manufacturing costs. The energies of some other electronic transitions in gases are shown in Figure 5.40, although there are a number of electronic transition energies for any gaseous atom or molecule. We will discuss atomic and molecular lasers in Sections 7.2 and 7.13.

5.22 Size Effects

Thin (comparable with the de Broglie wavelength) layers of semiconductors (intrinsic and doped) can trap (confine) conduction electrons within them, and these

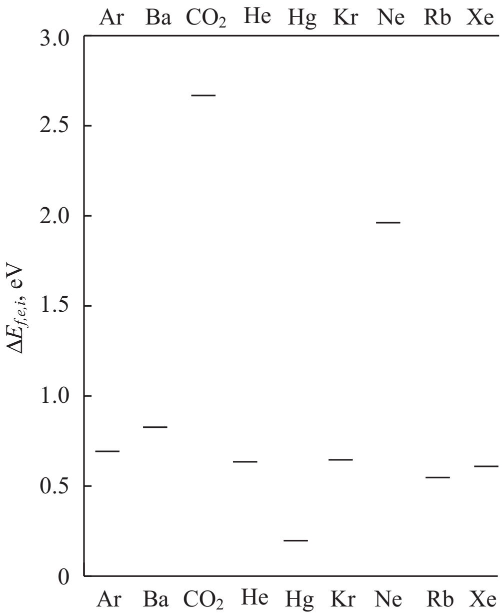

Figure 5.40. Some electronic transition energies for Ar, Ba, CO$_2$, He, Hg, Kr, Ne, Rb, and Xe gaseous atoms or molecules [337, 494].

electrons behave as quantum wave packets (as compared with particles). This confining structure is called a quantum well (QW). The electron energy bands become discrete and are called the subbands. Confining the electron along a second dimension produces quantum wire (QWIRE) (including rectangular crosssection) and along all three directions gives quantum box or dot (QD).

The unique characteristic of a QD is that the trapped electron behaves as it belongs to an atom (but subject to the symmetry of the lattice). Because of the discrete energy states, the quantum well, wire, and dot have discrete distributions of the DOS. Using (4.19), we note that $(\mathrm{d}n_{e,c}/\mathrm{d}\kappa)_{2\text{-D}} = 2(L/2\pi)^2 2\pi\kappa$, and $(\mathrm{d}n_{e,c}/\mathrm{d}\kappa)_{1\text{-D}} = 2(L/2\pi)^2$, when 2 is for the two spins. Then using $D_e(E_e) = \mathrm{d}n_{e,c}/\mathrm{d}E_e$, we have $D_e(E_e)_{2\text{-D}} = 4\pi m_{e,e}/h_p^2$, and $D_e(E_e)_{1\text{-D}} = (4m_{e,e}/h_p^2)^{1/2}(E_e - E_{e,i})^{-1/2}$, where E_e is from the band reference $E_e(0) = E_{e,c}$, as in (5.45), and E_i is the discrete state. The 2-D confinement makes for constant energy, and 1-D confinement makes for a singularities at $E_{e,n}(0)$. Figure 5.41 shows the general distribution of the electron DOS $D_e(E_e)$ for these as compared with the bulk semiconductors (idealized), given by (5.66), which show an $E_e^{1/2}$ dependence. Quantum dots have the most discrete $D_e(E_e)$ DOS representing only singularities.

5.22.1 Quantum Well for Improved TE Z_eT

As indicated above, the quantum wells have $D_e(E_e)$ with discrete distribution, i.e., zero variance around $E_{e,i}$ where $E_{e,i}$ is a sub-band. Here, following [300] it is shown that such discontinuity maximizes the TE figure of merit Z_eT defined by (5.204). We

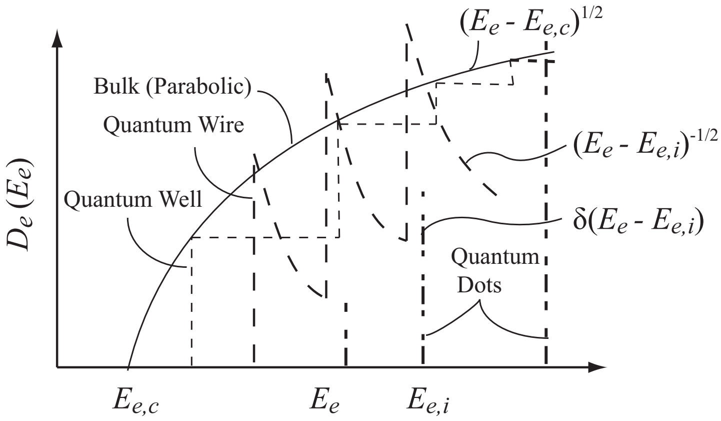

Figure 5.41. Distribution of electron DOS for idealized bulk (parabolic), QW, quantum wire, and QD semiconductors [86]. The first three have continuous distributions, whereas the quantum dots have singularities (subbands) only.

begin by rewriting (5.125) to (5.128), or (5.207), as [300]

$$\sigma_e = e_c^2 \int_{-\infty}^{\infty} (-\frac{\partial f_e^{\rm o}}{\partial E_e}) G(E_e) {\rm d}E_e \tag{5.283}$$

$$T\sigma_e \alpha_{\rm S} = e_c \int_{-\infty}^{\infty} (-\frac{\partial f_e^{\rm o}}{\partial E_e}) G(E_e)(E_e - \mu) {\rm d}E_e \tag{5.284}$$

$$Tk_{e,{\rm o}} = e_c \int_{-\infty}^{\infty} (-\frac{\partial f_e^{\rm o}}{\partial E_e}) G(E_e)(E_e - \mu)^2 {\rm d}E_e \tag{5.285}$$

$$k_e = k_{e,{\rm o}} - T\sigma_e \alpha_{\rm S}^2 \tag{5.286}$$

$$G(E_e) = \sum_{\boldsymbol{\kappa}} u_{e,g,\kappa}^2 \tau_e(\boldsymbol{\kappa}) \delta_{\rm D}[E_e - E_e(\boldsymbol{\kappa})] \tag{5.287}$$

$$-\frac{\partial f_e^{\rm o}}{\partial E_e} = \frac{1}{k_{\rm B}T} \frac{\exp(\dfrac{E_e - \mu}{k_{\rm B}T})}{[\exp(\dfrac{E_e - \mu}{k_{\rm B}T}) + 1]^2}, \tag{5.288}$$

where $G(E_e)$ is the transport distribution function and $k_{e,{\rm o}}$ is the electrical thermal conductivity with zero electrochemical potential gradient.

Using $\partial f_e^{\rm o}/\partial E_e$, the transport coefficients are written in terms of integrals I_n as

$$\sigma_e = \sigma_{e,{\rm o}} I_0, \;\; \sigma_{e,{\rm o}} = \frac{e_c^2}{\hbar r_{\rm B}} \tag{5.289}$$

$$\sigma_e \alpha_{\rm S} = \frac{k_{\rm B}}{e_c} \sigma_{e,{\rm o}} I_1 \tag{5.290}$$

$$k_{e,\mathrm{o}} = (\frac{k_\mathrm{B}}{e_c})^2 T\sigma_{e,\mathrm{o}} I_2 \tag{5.291}$$

$$I_n = \int_{-\infty}^{\infty} \frac{e^x}{(e^x+1)^2} G^*(x) x^n \mathrm{d}x \tag{5.292}$$

$$G^* = \hbar r_\mathrm{B} G(\mu + x k_\mathrm{B} T), \tag{5.293}$$

where r_B is the Bohr radius (Table 1.4).

Then we have for (5.204)

$$Z_e T = \frac{\dfrac{T\sigma_e \alpha_\mathrm{S}^2}{k_p}}{\dfrac{k_{e,\mathrm{o}}}{k_p} - \dfrac{T\sigma_e \alpha_\mathrm{S}^2}{k_p} + 1} = \frac{B\dfrac{I_1^2}{I_0}}{BI_2 - B\dfrac{I_1^2}{I_0} + 1}$$

$$\equiv \frac{\xi}{1-\xi+C}, \ \xi = \frac{I_1^2}{I_0 I_2}, \ C = \frac{1}{AI_2}, \ B = (\frac{k_\mathrm{B}}{e_c})^2 \frac{T\sigma_{e,\mathrm{o}}}{k_p}, \tag{5.294}$$

where B is related to the Chasmar–Stratton coefficient defined in relation to (5.204).

Because $\xi \ll 1$, the maximum $Z_e T$ is at $\xi = 1$, i.e.,

$$Z_e T \le \frac{1}{C} = \frac{k_{e,\mathrm{o}}}{k_p}. \tag{5.295}$$

For parabolic bands, we have

$$G(E_e) = D_e(E_e) u_{e,g,x}^2 (E_e) \tau_e(E_e), \tag{5.296}$$

and it is shown in [300] that, when $D_e(E_e)$ has a Dirac function behavior, then $\xi \to 1$. Also, when the dimensionless $G^*(x)$ is expressed as

$$G^*(x) = H(x)\delta_\mathrm{D}(x - E^*), \tag{5.297}$$

we have for the transport coefficients

$$\sigma_e = \sigma_{e,\mathrm{o}} H(E^*) \frac{e^{E^*}}{(e^{E^*}+1)^2}, \ E^* = \frac{E_{e,m}}{k_\mathrm{B} T} \tag{5.298}$$

$$\alpha_\mathrm{S} = \frac{k_\mathrm{B}}{e_c} E^* \tag{5.299}$$

$$k_{e,\mathrm{o}} = (\frac{k_\mathrm{B}}{e_c})^2 T\sigma_{e,\mathrm{o}} H(E^*) E^{*2} \frac{e^{E^*}}{(e^{E^*}+1)^2}, \tag{5.300}$$

where $E_{e,m}$ is the peak energy with respect to Fermi level.

To maximize $k_{e,\mathrm{o}}$ (and $Z_e T$), if $H(E^*) = H$ is assumed constant (from Figure 5.30, we note that α_S has a maximum where $\mu_\circ$ is about a few $k_\mathrm{B} T$ from the Fermi level), then the maximum in $E^{*2} e^{E^*}/(e^{E^*}+1)^2$ is at $E^* = 2.4$, i.e., having resonance $E_e = 2.4 k_\mathrm{B} T$ above the Fermi level. Using this gives $\alpha_\mathrm{S} = 207\ \mu$V/K, as we also found from (5.204). Then the optimal $Z_e T$ is

$$(Z_e T)_{max} = 0.439(\frac{k_\mathrm{B}}{e_c})^2 \frac{\sigma_{e,\mathrm{o}} T}{k_p} H. \tag{5.301}$$

Then the QWs having a Dirac delta function $D_e(E_e)$ can maximize the TE figure of merit. Quantum dots offer the possibility of having a single delta function and are the preferred material. These carrier pockets are discussed in [61, 180, 250].

5.22.2 Reduced Electron–Phonon Scattering Rate in Quantum Wells

In molecularly constructed (e.g., epitaxy), multilayer (including superlattice) semiconductors, with a layer thickness of the order of 10 Å, the electron confinement also modifies its scattering by phonons [390]. Multiple QW structures consist of a series of QWs made of alternating layers of wells and barriers. When the barrier thickness is large ($\geq$ 40 Å), no significant electronic coupling occurs between neighboring wells and it is called a QW, and for this barrier ($\leq$ 40 Å), electronic coupling occurs and it is called a superlattice.

Confinement of electrons (and holes) influences their phonon-scattering rate, and in the case of harvesting hot electrons (and holes), excess kinetic energy, generated in photon absorption by semiconductors (as in solar cells, Section 7.14), reduction of $\tau_{e\text{-}p}$ is desirable [351]. The electron energy for the case of a QW is the solution to the Schrödinger equation for the extended case of a particle in a box (Section 2.6.6) for a finite barrier height φ_{o}, and gives [351]

$$E_{e,n} = \frac{\hbar^2\kappa^2}{2m_{e,e}} - \varphi_{\mathrm{o}}, \ \kappa = \frac{n\pi}{L}, \ n = 1, 2, 3, \ldots, \qquad (5.302)$$

where L is the well width.

As shown in Figure 5.41, the ideal QW D_e is a steplike function with each plateau given by

$$D_e = \frac{nm_{e,e}}{\pi\hbar^2}, \quad n = 1, 2, 3, \ldots. \qquad (5.303)$$

The hot-electron cooling time $\tau_{e\text{-}p}$, Figure 5.42(a), is measured with the energy-loss technique, after photon absorption [351], and the average relaxation time [which is because of electron scattering by LO phonons, i.e., the polar optical phonon emission branch of Figure 5.13(b)] is found from

$$-\frac{\mathrm{d}E_e}{\mathrm{d}t} = \frac{\hbar\omega_{p,\mathrm{LO}}}{\tau_{e\text{-}p,a}} \exp(-\frac{\hbar\omega_{p,\mathrm{LO}}}{k_{\mathrm{B}}T_e}), \qquad (5.304)$$

where T_e is the electron temperature. The experimental results for multiple 250-Å GaAs/250-Å $\mathrm{Al_{0.38}Ga_{0.62}As}$ QWs are shown in Figure 5.42(b) [351].

The electron temperature (kinetic energy) was deduced from the time-resolved luminesce spectra [351]. The carrier densities calculated from photon absorption are 10^{19}, 5×10^{18}, and 2×10^{18} 1/cm^3 for the 25-, 12.5-, and 5-mW laser (pumping) powers.

The e-p relaxation time for GaAs was shown in Figure 5.13(b), and the phonon emission branch shows an initial strong energy dependence. The measured average relaxation time at high electron temperatures [note that using $E_e = 3k_{\mathrm{B}}T/2$ as in (5.253) is not valid at high energies since the distribution becomes degenerate],

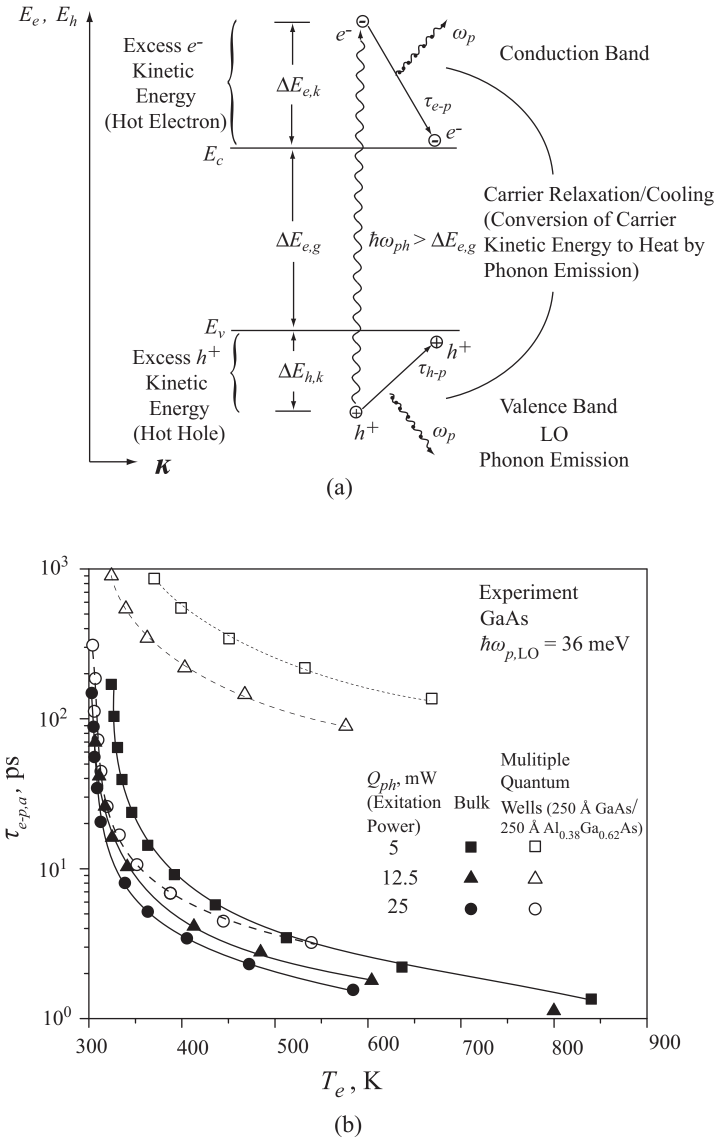

Figure 5.42. (a) Hot electrons (excess kinetic energy that is due to photon absorption) and holes in semiconductors, and phonon emission during their decay. (b) Variation of the average electron–phonon relaxation times for a GaAs bulk and multiple QWs, with respect to electron temperature (or kinetic energy). The hot electrons are generated by photon (laser) absorption [351].

is larger than the predicted value, but the energy dependencies are similar. This is in part due to the photoexcitation charge carrier averaging. The results for Figure 5.42(b) show that the cooling rate $1/\tau_{e\text{-}p}$ is slower in the metallic QWs (by up to two orders of magnitude). They also show that the higher photogenerated carrier density, the slower the cooling rate, especially in the QWs. This is referred to as the hot-phonon bottleneck, because of the significant nonequilibrium distribution of phonons (in particular, LO) caused by the hot carriers. The relaxation time

$\tau_{p\text{-}p}$(LO), Table 4.2, is not small enough to return phonons to equilibrium quickly (with the crystal bath) to keep up with the phonon emission rate, especially in the QWs where phonon modes are also modified.

The reduced $\tau_{e\text{-}p}$ shown in Figure 5.42(b) can help in harvesting the hot electrons (through impact ionization or multiple exciton generation) before they cooled [394].

5.22.3 Electronic and Phonon Thermal Conductance of Graphene–Flake Junctions

The bottleneck in the electronic and phonon transport of graphene-based composites [447], promising for their superior electrical and thermal transport properties, is in the interflake resistance. It is due to the very weak interflake interactions compared to the strong covalent bonds in the graphene flakes. Here, we examine the interflake thermal energy transport using the quantum thermal energy transport treatments, while considering that applications of graphene may include its inevitable passivated form. The graphene flakes are commonly edge (and side) passivated with various atomic groups, and these edge passivations influence the graphene properties [270]. We consider those O- or H-passivations of graphene flake edges that do not corrugate the graphene plane, so there are three interflake junction arrangements: O-H, O-O, and H-H. Then the carrier scattering is concentrated in the interflake junction when considering the long intragraphene mean free path for the energy carriers compared with the flake dimension. The nanoscale thermal transport addresses the quantum features and the carrier wave effects, and within that the nonequilibrium Green's function (NEGF) formalism is used in [424]. Also, for phonon transport in heterostructures the semi-classical acoustic mismatch model (AMM) or diffuse mismatch model (DMM) and molecular dynamics (MD) can provide limited, but more intuitive insights into the phonon transport. However, MD based on the classical Newtonian mechanics has limitations when considering the quantum effects, even though it can easily include the anharmonic effects, and the conventional semi-classical AMM and DMM do not include the atomic details of the interfaces and the quantum and wave natures of the phonon transport. In [424], they use both the NEGF formalism and the AMM treatment for the interflake phonon transport across the edge-passivated graphene, and although the electronic thermal transport is expected to be small in this system, they include it for insight into the force fields and to complete treatment of the thermal transport.

The relaxed structures of the joined, passivated graphene flakes (zigzag edges) show restructuring within the first four C atoms from the edge (and negligible difference from the bulk, within less than 0.01 Å, beyond that). In the Green's function formalism, we consider a central region connected to two semi-infinite regions representing the bulk graphene, as shown in Figure 5.43. The central region is divided into two "contact cells or electrodes" on each side with four carbon atoms each and a "scattering region or junction" with four carbon atoms on each side of the passivated atoms, also shown in Figure 5.43.

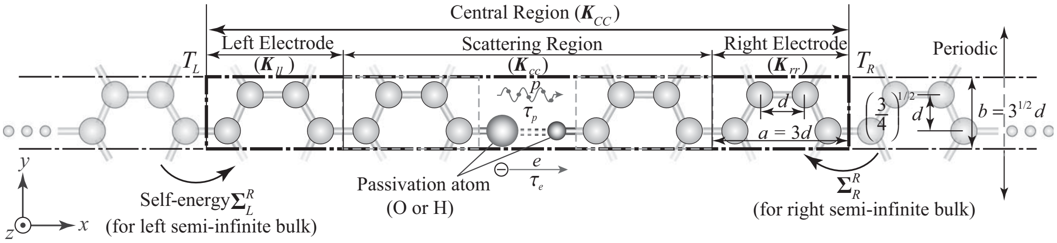

Figure 5.43. The edge-passivated graphene-flake junction used for the thermal transport calculations. The entire domain is divided into a central and two semi-infinite regions, and the central region is divided into a scattering and two electrode regions. The temperatures T_L and T_R are prescribed. d is the interatomic distance, and a and b is the width and height of the periodic bulk cell.

For calculations of the self-energy and the bulk graphene properties, the scattering region is replaced with the same structure as the left and right electrodes. The graphene phonon dispersion is obtained using the dynamical matrix from the DFT calculations with the lattice dynamics relation with the Born-von Karman boundary condition [486],

$$[\omega_p^2(\kappa_x^*, \kappa_y^*, \alpha)\boldsymbol{I} - \boldsymbol{K}_{cc}(\kappa_y^*) - \boldsymbol{K}_{cl}(\kappa_y^*)e^{i\kappa_x^*} - \boldsymbol{K}_{cr}(\kappa_y^*)e^{-i\kappa_x^*}]\boldsymbol{s}(\kappa_x^*, \kappa_y^*, \alpha) = 0, \tag{5.305}$$

where κ_x^* is the dimensionless wave number in the transport direction ($\kappa_x^* = \kappa_x a$ and κ_x is the wave number in the x direction), α is the polarization [4 atoms in each unit cell and three degrees of freedom per each atom, so that the number of total branches (α) is 12], $\boldsymbol{s}$ is the eigenvector, and $\boldsymbol{K}_{cl}$ ($\boldsymbol{K}_{cr}$) is the dynamical matrix for the interaction between the left (right) electrode and the scattering region. The phonon dispersion found from Eq. (5.305) is unfolded to show it for the primitive cell of graphene composed of two C atoms. The dispersion curve from Γ to M ($\kappa_y^* = 0$) is in good agreement with the experiments, as demonstrated in Figure 5.44(a). Because the passivated atoms are linearly aligned and the transport with the $\boldsymbol{\kappa}$ vector (wavevector) propagating in the transport direction is expected to dominate (when expanding to the longer functional groups, it would be more dominant), we first focus on the dominant transport direction ($\kappa_y^* = 0$). In the ideal ballistic transport, when all modes are transmitted without scattering, the phonon transmission is the number of modes at frequency ω_p, and the NEGF transmission for graphene is similar to this ballistic limit with a small η, as shown in Figure 5.44(b). Phonons incident from the graphene are transported through the passivated edges in the three junctions with significantly suppressed transmissions. The τ_p for the O-H junction is the largest of the three, and in all three the phonons with low energy (less than 30 meV) and some high energies have relatively high transmissions.

In 1–D transport with a given κ_y^*, the phonon conductance is evaluated using the Landauer formula [266, 388],

$$G_{p,1\mathrm{D}}(\kappa_y^*)\ [\mathrm{W/K}] = \int_0^\infty \frac{\mathrm{d}\omega_p}{2\pi}\hbar\omega_p\tau_p(\kappa_y^*, \omega_p)[\frac{\partial f_p^\circ(\omega_p, T)}{\partial T}], \tag{5.306}$$

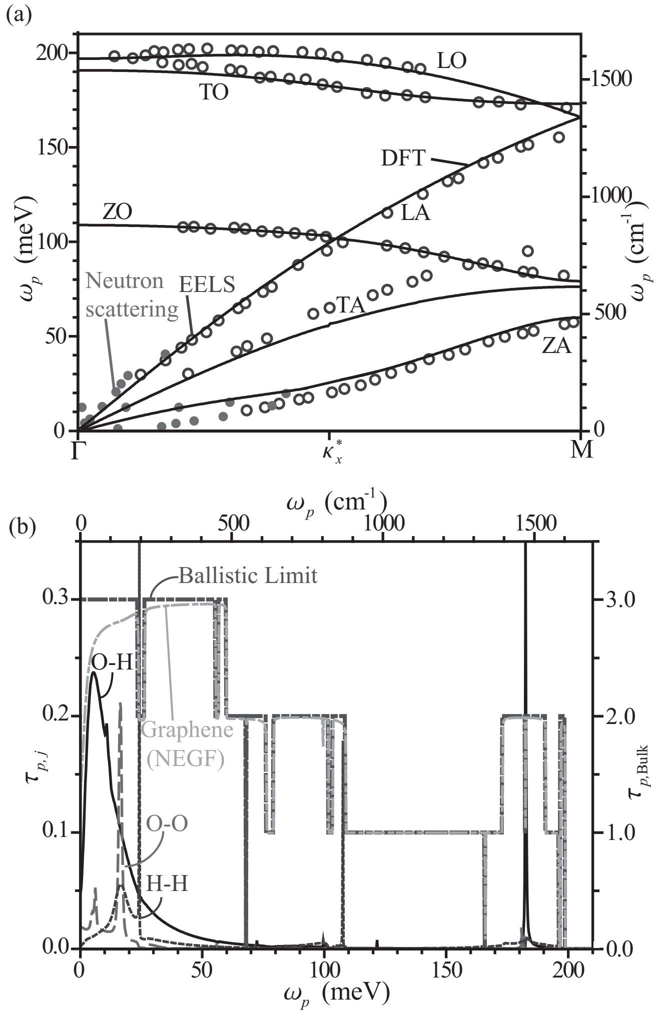

Figure 5.44. (a) The phonon dispersion from Γ to M for the bulk graphene. The solid line is from the DFT dynamical matrix calculations. The red solid circles are from the neutron scattering data and the blue open circles are from the electron energy loss spectroscopy (EELS) data [355]. (b) The variations of the phonon transmission with the transport direction ($\kappa_y^* = 0$) with respect to the phonon energy, for the bulk graphene and the passivated junctions. The transmissions for the passivated junctions are largely suppressed, while the O-H junction has the largest transmission.

where T is the temperature, $\hbar$ is the the reduced Planck constant, the equilibrium Bose-Einstein distribution function is $f_p^\circ(\omega_p, T) = [\exp(\hbar\omega_p/k_\mathrm{B}T) - 1]^{-1}$, and k_B is the Boltzmann constant. To include contributions from all wavevectors (as well as $\kappa_y^* = 0$), we sample κ_y^* values (200 points in the first Brillouin zone, $-\pi \leq \kappa_y^* < \pi$) and integrate 1–D conductance for each direction for the 2–D conductance as [511],

$$G_{p,\mathrm{2D}}\ [\mathrm{W/m\text{-}K}] = \frac{1}{b}\int_{-\pi}^{\pi} \mathrm{d}\kappa_y^* G_{p,\mathrm{1D}}(\kappa_y^*). \tag{5.307}$$

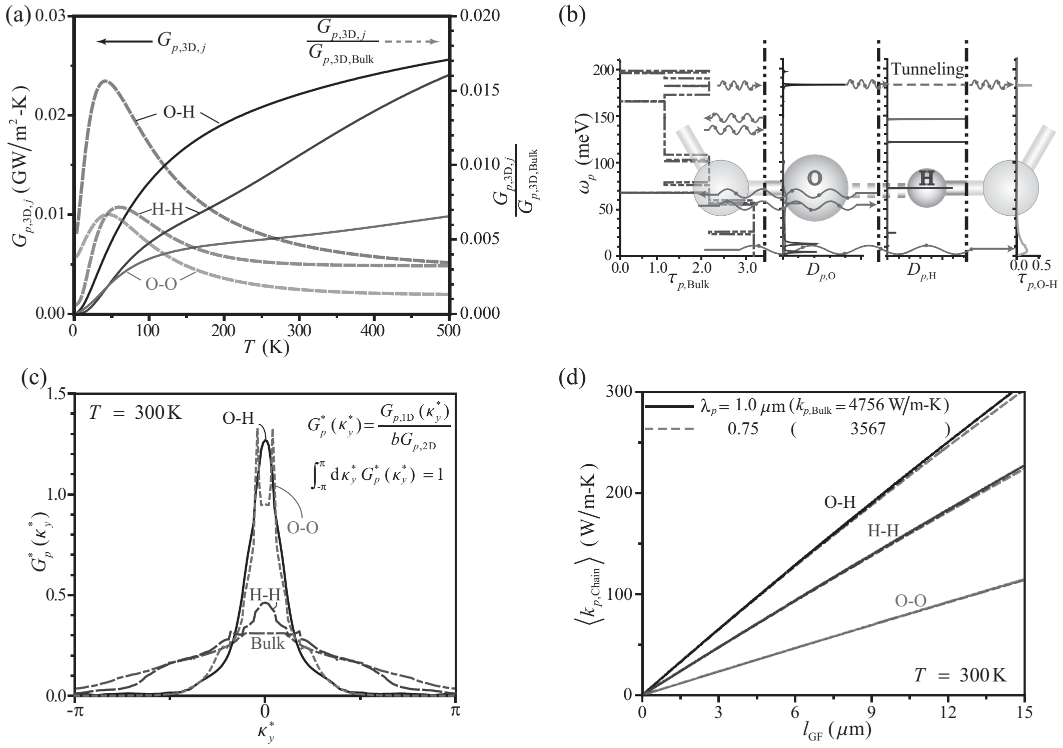

Figure 5.45. (a) Variations of the phonon conductance ($G_{p,3\text{D},j}$, solid lines) of the three passivated flake junctions with respect to temperature, from the NEGF calculations, and comparison with the bulk behavior (dash lines). (b) Phonon transport channels and the mechanism of phonon transport suppression in the O-H passivated junction. (c) The contribution of wavevectors to thermal conductance $[G^*_p(\kappa^*_y)]$ at T = 300 K. (d) The effective thermal conductivity of linear chains composed of graphene flakes with three cases of edge passivated junctions at T = 300 K, as a function of the flake length. Two mean free paths, $\lambda_p = 1.0$ μm ($k_{p,\text{Bulk}}$ = 4756 W/m-K) and $\lambda_p = 0.75$ μm ($k_{p,\text{Bulk}}$ = 3567 W/m-K), are used [160, 350].

The phonon conductance per unit width ($G_{p,2\text{D}}$, W/m-K) is calculated by Eqs. (5.306) and (5.307). Using the layer separation distance (0.335 nm) in the graphite as the thickness, we find the phonon conductance per unit area ($G_{p,3\text{D}}$, W/m^2-K), which is shown in Figure 5.45(a). $G_{p,3\text{D}}$'s for the edge-passivated graphene junctions are largely suppressed to less than 1% of bulk graphene $G_{p,3\text{D,Bulk}}$ at 300 K (4.76 GW/m^2-K from this work) because only phonons with low energy or tunneled resonant energy can be transmitted through the interflakes, as shown in Figure 5.45(b). Figure 5.45(c) shows the contribution of wavevectors to thermal conductance $[G^*_p(\kappa^*_y) = G_{p,1\text{D}}(\kappa^*_y)/(bG_{p,2\text{D}})$ satisfying $\int_{-\pi}^{\pi} d\kappa^*_y G^*_p(\kappa^*_y) = 1$], and it confirms that phonons with the transport direction are dominant. This is also the case for the phonon transport in the passivated graphene junctions at lower temperature.

Because hetero-structure systems experience a large decrease in the transport caused by the Kapitza resistance at the interfaces, the reduction in thermal conductance of the graphene junctions with edge passivation drastically reduces the effective thermal conductivity of the graphene composite. The total thermal resistance of the linear chain of graphene flakes ($1/G_{p,\mathrm{3D,Chain}}$) is the sum over the resistances for the graphene flakes and the interflakes junctions, i.e.,

$$\frac{1}{G_{p,\mathrm{3D,Chain}}} = n_j\left(\frac{1}{G_{p,\mathrm{3D,GF}}} + \frac{1}{G_{p,\mathrm{3D},j}}\right) + \frac{1}{G_{p,\mathrm{3D,GF}}}, \tag{5.308}$$

where n_j is the number of the interflake junctions in the chain, and $G_{p,\mathrm{3D,GF}}$ and $G_{p,\mathrm{3D},j}$ are the thermal conductance of the graphene flake and the interflake junction, respectively. With uniform length for the graphene flakes (l_{GF}), the effective thermal conductivity of the chain with sufficiently long length $L_c = (n_j + 1)l_{\mathrm{GF}}$ is

$$\langle k_{p,\mathrm{Chain}}\rangle = G_{p,\mathrm{3D,Chain}}L_c = \frac{G_{p,\mathrm{3D,GF}}G_{p,\mathrm{3D},j}}{G_{p,\mathrm{3D,GF}} + G_{p,\mathrm{3D},j}}l_{\mathrm{GF}}. \tag{5.309}$$

Since the conductance calculated in this work is based on the ballistic transport, the thermal conductivity of graphene flakes depends on l_{GF} and the phonon mean free path λ_p [350], i.e.,

$$k_{p,\mathrm{GF}} = G_{p,\mathrm{3D,GF}}l_{\mathrm{GF}} = G_{p,\mathrm{3D,Bulk}}\frac{l_{\mathrm{GF}}\lambda_p}{l_{\mathrm{GF}} + \lambda_p}. \tag{5.310}$$

The phonon thermal conductivity of undisrupted graphene $k_{p,\mathrm{Bulk}}$ (i.e., $l_{\mathrm{GF}} \rightarrow \infty$) is $G_{p,\mathrm{3D,Bulk}}\lambda_p$ (4756 W/m-K with $\lambda_p = 1.0$ μm and 3567 W/m-K with $\lambda_p = 0.75$ μm). Using the phonon conductance of interflake junction and the graphene flake, we find the effective thermal conductivity of the linear chain composed of graphene flakes with uniform length. Figure 5.45(d) shows variation of the effective thermal conductivity as a function of the flake length. ($\langle k_{p,\mathrm{Chain}}\rangle$ increases with l_{GF}.) Here we confirm the large reduction in the effective thermal conductivity compared to the undisrupted graphene.

The electronic thermal conductance is calculated using the NEGF and the TranSIESTA module within the SIESTA code (with the GGA-PBE exchange correlation, the CG relaxation, and a single ζ-plus-polarization basis set) [57] and the same configuration shown in Figure 5.43. For infinitesimal voltage and temperature differences, the electronic thermal conductance is [135]

$$G_{e,\mathrm{2D}}\ [\mathrm{W/m\text{-}K}] = \frac{1}{bT}\left(K_2 - \frac{K_1^2}{K_0}\right), \tag{5.311}$$

where K_n is defined as $K_n = (1/\pi\hbar)\int \mathrm{d}E_e(E_e - E_{\mathrm{F}})^n\tilde{\tau}_e(E_e)[-\partial f_e^\circ(E_e,T)/\partial E_e]$, E_{F} is the Fermi level defined by the external electrode, $\tilde{\tau}_e$ is the average electron transmission over the sampled $\boldsymbol{\kappa}$ vectors (200 points in the y direction) with regard to the electron energy, and f_e° is the equilibrium fermion distribution, $f_e^o(E_e,T) = \{\exp[(E_e - E_{\mathrm{F}})/k_{\mathrm{B}}T) + 1\}^{-1}$. $G_{e,\mathrm{3D}}$ for bulk and three junctions are calculated with the layer separation distance as in $G_{p,\mathrm{3D}}$ and compared with $G_{p,\mathrm{3D}}$ in Figure 5.46(a). The reduction of G_e from the bulk value is more pronounced than G_p, when no external bias potential is applied. Figure 5.46(b) presents the charge-density isosurface ($\rho_e^* = 0.02$) and the wavefunction of the first eigenstate below the E_{F} (at the Γ point). The low charge density present between the flakes and the localized orbital

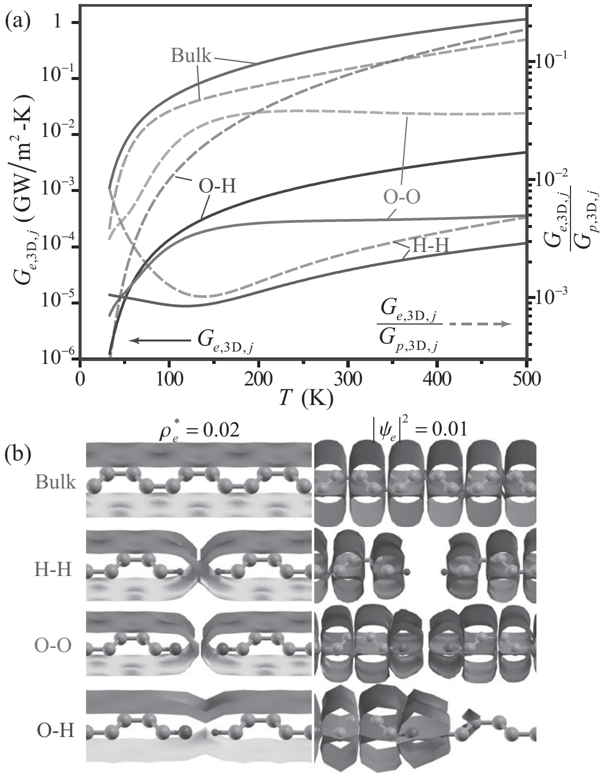

Figure 5.46. (a) Variations of the electronic thermal conductance ($G_{e,3D,j}$, solid lines) on the left and that scaled with $G_{p,3D,j}$ ($G_{e,3D,j}/G_{p,3D,j}$, dash lines) on the right, without an external bias potential, with respect to temperature. (b) The charge-density iso-surface ($\rho_e^* = 0.02$) on the left and the wavefunction ($|\psi_e|^2 = 0.01$) of the first eigenstate below the E_F (at the Γ point) on the right, for the bulk and the three junctions. Different colors (blue and red) in the wavefunctions correspond to the opposite signs.

near the passivated edge for the symmetric junctions differs from the chemical σ- or π-bond between the passivation atom and the nearest C [270] and the delocalized π-bond in the bulk graphene. These differences lead to the large drop in the magnitude of G_e. For the asymmetric junction O-H, the G_e is less suppressed because of the delocalization in the molecular orbital due to the asymmetric charge distribution. As shown in the right side of Figure 5.46(a), the G_e for all the three junctions is smaller than the G_p, especially at low temperatures, with the O-H junction suffering the least reduction.

5.22.4 Heterobarrier for Converting Hot–Phonon Energy to Electric Potential

Various decays, recombinations, and drags in energy conversions and many resistive processes (e.g., in electronic circuits) emit phonons, hindering energy relaxation and transport in devices [137, 391, 469]. Among the phonon modes, energy relaxation through optical-phonon emission is dominant in semiconductors. An emission rate larger than decay can overpopulate the optical modes compared to their equilibrium population, and "hot phonons" represent this excess occupancy [249]. Examples include high-power electronic devices [313], frustrated-vibration relaxation of chemisorbed molecules [406], lattice electron stoppage of charged fission fragments [162], and nonradiative decay of hot electrons in optoelectric devices [97]. These hot phonons are finally thermalized, converting their energy to waste heat and generating entropy. To improve the efficiency and mitigate heat generation, the thermalized phonons can be recycled by the anti-Stokes cooling process (photon-assisted absorption of phonon), resulting in lower device operating temperatures [401, 239]. Photonics including light-emitting diodes show enhanced efficiency through thermoelectrically pumped heat [410]. However, using the hot phonons before thermalization is expected to further improve the efficiency. Also, removal of the excess phonons through this harvesting will lead to improved thermal management and device performance (reducing the phonon friction in electron transport) [312].

In [426], an unassisted absorption of hot phonons for direct electric potential gain using semiconductor heterobarriers is analyzed. Barrier structures have been used in thermionics, thermoelectrics, and photovoltaics [420, 421, 241, 376] and for the selective transmission of hot electrons (for TE performance enhancement) and heat absorption to restore the equilibrium electron distribution. Here, the heterobarrier structure is designed as an embedded structure rather than a standalone device, so that we can place the structure near the hot-phonon source for effective pre-thermalization harvesting. This requires kinetics optimization between phonon absorption and emission (lifetime $\tau_{p\text{-}e}$) and between up- and downconversion ($\tau_{p\text{-}p}$). The Monte Carlo method is employed to simulate this electron transport and phonon energy conversion in the diffusive regime, showing electric potential gain and phonon energy absorption.

A heterobarrier structure composed of GaAs and $\mathrm{Al}_x\mathrm{Ga}_{1-x}\mathrm{As}$ (x or x_{Al} is the Al content) is chosen for this study. Since $\mathrm{Al}_x\mathrm{Ga}_{1-x}\mathrm{As}$ has a larger bandgap than GaAs and the interface has a band edge discontinuity in the conduction ($\Delta E_c = 0.79x_{\mathrm{Al}}, x_{\mathrm{Al}} < 0.41$) and valence bands ($\Delta E_v = -0.46x_{\mathrm{Al}}$) depending on x_{Al} (type I), the barrier height φ_b can be controlled with x_{Al} [514, 278]. We consider electrons as the main charge carriers and barriers in the conduction band. Potential barriers can cause an adverse (or reverse) current by reflection or potential change, so a large, forward local electric field formed by x_{Al} grading is introduced in the barrier to compensate for this adverse effect [421]. Figure 5.47 shows the spatial distributions of (i) x_{Al}, (ii) electric field, e_e, (iii) product of electric potential and electron charge, $e_c\varphi_e$ (in the conduction band edge), and (iv) optical and acoustic phonon temperatures, $T_{p,\mathrm{O}}$ and $T_{p,\mathrm{A}}$, in the hot-phonon absorbing barrier (HPAB) structure. The electric current density j_e, drift velocity $u_{e,d}$, and electron transition processes involving phonon absorption are also shown.

The lowest conduction band in GaAs has three valleys, at Γ, L, and X, where Γ is heavily populated at room temperature. Electrons in the band are scattered through various mechanisms, and the overall interaction rates are shown in Figure 5.48(a). The Γ-valley polar optical phonon interaction, which absorbs or emits

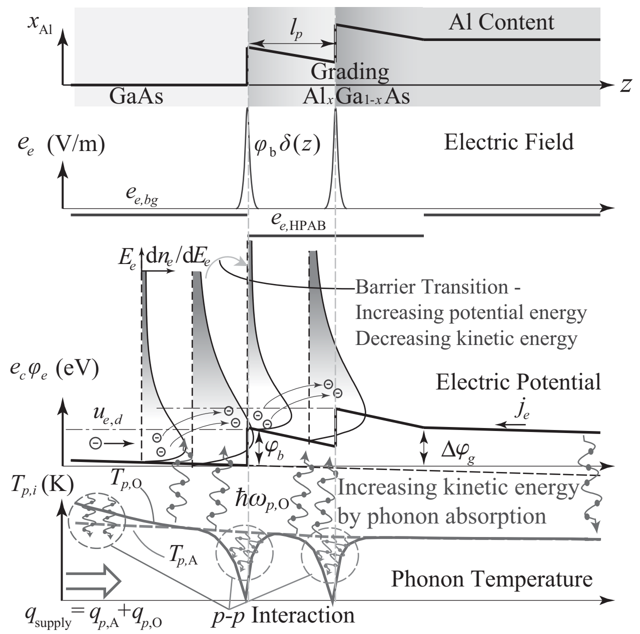

Figure 5.47. Spatial distributions of Al content, electric field and potential, and phonon temperatures in the hot-phonon absorbing barrier structure. $x_{\rm Al}$ abruptly increases, creating the potential barrier (with height φ_b) in the conduction band edge, while the grading maintains the current. Phonon absorption populates electrons with higher energy than barrier height ($E_e > \varphi_b$) before or after the barrier transition, and this energy is converted to electric potential. The population of optical phonons quickly decreases at the barriers and recovers by upconversion.

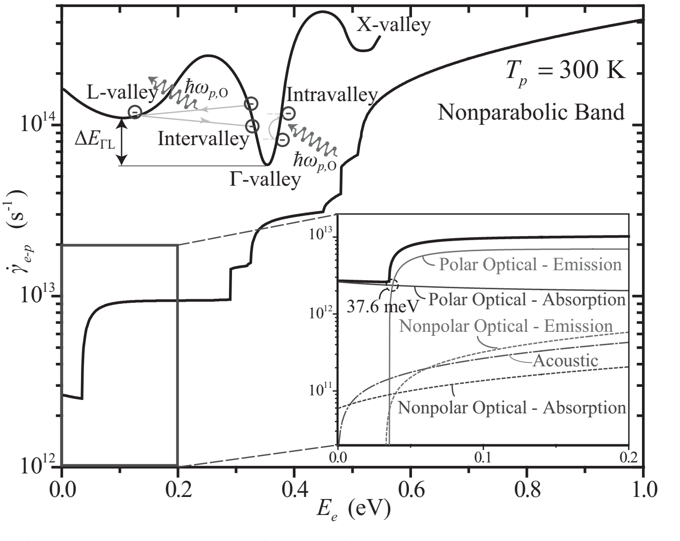

Figure 5.48. Variations of the electron interaction rates in the lowest conduction band, as a function of electron energy (E_e) for $T_p = 300$ K. Insets show the band structure and various interaction mechanisms (left) and the interaction rates for low-E_e Γ-valley electrons (right). Polar optical phonon scattering is dominant at low E_e, and intervalley scattering rates increase with E_e.

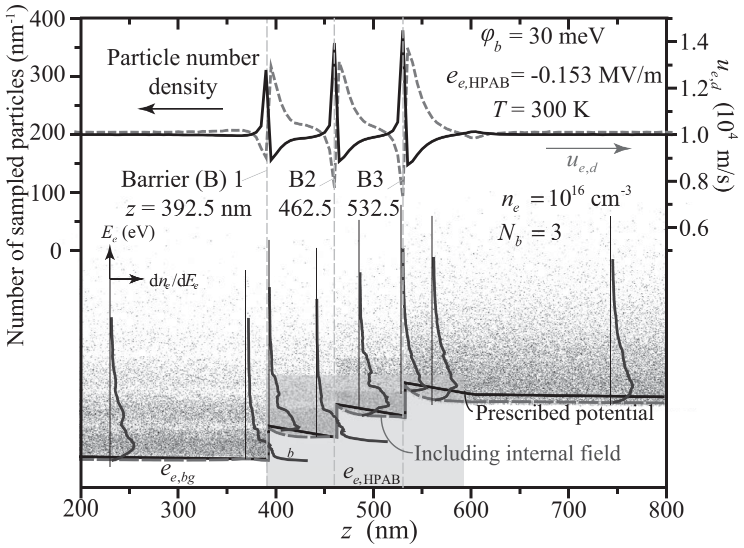

Figure 5.49. Sampled particle number density, drift velocity ($u_{e,d}$), and particle-energy distributions over the simulation cell. Electrons are accumulated behind barriers and low-energy electrons are highly populated near barriers.

longitudinal optical (LO) phonon, dominates for low E_e, and intervalley scattering is dominant when $E_e > \Delta E_{\Gamma\mathrm{L}}$ (energy difference between Γ- and L-valleys). Average absorption $\langle \dot{\gamma}_{p\to e}\rangle$ and emission $\langle \dot{\gamma}_{e\to p}\rangle$ rates for Γ-valley are obtained considering LO phonon temperature $T_{p,\mathrm{LO}}$ ($= E_{p,\mathrm{LO}}/\{k_\mathrm{B}[\ln(f_{p,\mathrm{LO}}+1) - \ln(f_{p,\mathrm{LO}})]\}$) and electron distribution $\mathrm{d}n_e/\mathrm{d}E_e$ ($D_e f_e^\circ$, where D_e is the density of states and f_e° is the equilibrium electron distribution).

The particle density and velocity distributions in Figure 5.49 show the electron accumulation and the low electron velocity behind the barriers. As Figure 5.49 also shows, the potential profile near the barriers is bent by this nonuniform charge distribution, and this effect is not significant for small n_e ($< 10^{17}$ cm^{-3}). Whereas the electron energy distribution $\mathrm{d}n_e/\mathrm{d}E_e$ without a barrier is consistent and close to equilibrium, the low-energy electron density is large in the proximity of the barriers. This is because of the low transmission and energy loss caused by the barrier. The phonon energy absorption rate ($\dot{s}_{p\text{-}e} = \dot{S}_{p\text{-}e}/V$, $\mathrm{W/m^3}$) is determined from the electron energy distribution ($\mathrm{d}n_e/\mathrm{d}E_e$), i.e.,

$$\dot{s}_{p\text{-}e} = \sum_j \int_{E_e} [\dot{\gamma}_{p\to e,j}(E_e) - \dot{\gamma}_{e\to p,j}(E_e)] E_{p,j} \frac{\mathrm{d}n_e(E_e)}{\mathrm{d}E_e} \mathrm{d}E_e, \tag{5.312}$$

where j is an interaction mechanism. The simulation results show an efficiency of 18.8% (of phonons converted to electric potential), when $u_{e,d} = 6.2 \times 10^4$ m/s and $\phi_b = 30$ meV.

5.23 Problems

Problem 5.1

(a) In the Kronig–Penney model, for $s = 5$, determine the first five allowed electronic energy bands using (5.25) and plot the results similar to Figure 5.4.

(b) Then plot E_e(eV) versus κ(1/nm) similar to Figure 5.5, using (5.27) to find the roots κ^* of constant E_e^*. Use the Si lattice constant a from Table A.2. Scan κ^* and obtain roots E_e^*, and then convert to dimensional values.

Problem 5.2

Show that the small κa limit of the s-orbital energy equation for the s-orbital, FCC tight-binding model becomes $E_e(\boldsymbol{\kappa}) = E_s - \beta_s - 12\gamma + \gamma a^2\kappa^2$.

Problem 5.3

Make a three-dimensional $\{\kappa_x, \kappa_y, \kappa_z\}$ contour plot of a constant electron-energy surface, which is based on the s-orbital energy equation for the s-orbital, FCC tight-binding model (5.41). Note that there is no need to specify the constants when using $(E_e - E_s + \beta_s)/|\gamma| = 2$ as the constant energy surface. Also use $-1 \le a\kappa_i/2\pi \le 1$. The contour, is similar to that shown in the figure.

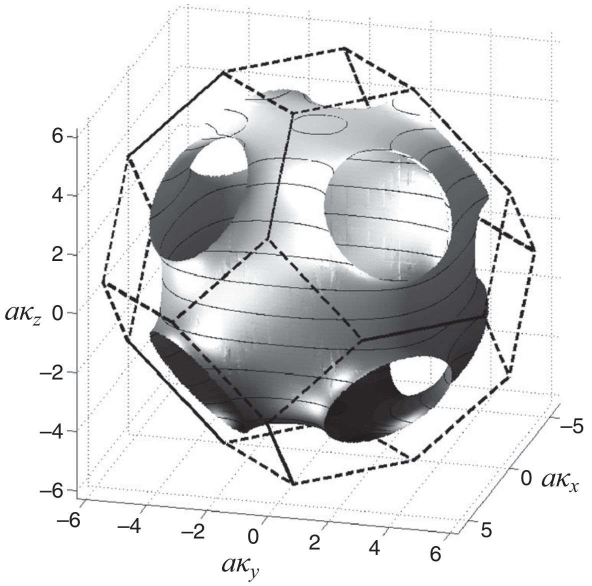

Problem 5.3. Constant energy surface (Fermi Surface), $(E_e - E_s + \beta_s)/|\gamma|$, in reciprocal lattice space, for s-orbital, FCC lattice, with the nearest-neighbor only, tight-binding approximation.

Problem 5.4

(a) Comment on the approximations (tight binding and others) made in the SiC electronic band structure Matlab codes.

(b) Run the SiC Matlab codes and comment on the discrepancies in the predicted absolute values of the band energies.

Problem 5.5

Show that (5.20) is the determinant of the coefficient matrix of the vector of constants $\{A, B, C, D\}$ when set equal to zero.

Problem 5.6

Plot the tight-binding approximated, single s-band structure $E_e(\kappa a/2\pi)$, (5.41), for $\gamma = 1.0$ eV and $E_{e\text{-}\beta} = 0$, and for $\boldsymbol{\kappa}$ along L–Γ–X–K–Γ–W [Figure 5.6(a)].

The coordinates of the Brillouin zone symmetry points for a FCC lattice are given in Figure 5.7(b), and these lead to lines such as

$$\begin{aligned}
&\Gamma - \mathrm{X} : 0 \leq \kappa_x \leq \frac{2\pi}{a}, \quad \kappa_y = \kappa_z = 0 \\
&\Gamma - \mathrm{L} : 0 \leq \kappa_x = \kappa_y = \kappa_z \leq \frac{\pi}{a} \\
&\Gamma - \mathrm{K} : 0 \leq \kappa_x = \kappa_y \leq \frac{3\pi}{2a}, \quad \kappa_z = 0, \text{ etc.}
\end{aligned}$$

Problem 5.7

(a) Use the software Materials Studio (use DFT method, Section 5.4) for the *ab initio* computation of the electronic band structure in Si. Use the default setting and plot $E_e(\kappa)$, which is along W–L–Γ–X–W–K. This graph is similar to (but not the same as) Figure 5.6(b).

(b) Comment on the direct versus indirect bandgaps, and the lowest energy bandgap in Si.

Problem 5.8

(a) Table 5.2 shows that $-E_{\mathrm{F}}/k_{\mathrm{B}}T = -T_{\mathrm{F}}/T$ can be represented by $-\infty$ for moderate temperatures. Using this, show that the integral in (5.72) becomes

$$\int_{-\infty}^{\infty} \frac{x^2 e^x}{(e^x+1)^2} \mathrm{d}x = \frac{\pi^2}{3},$$

by dividing the integral into two equal parts $\int_{-\infty}^{0}$ and $\int_{0}^{\infty}$, and using $\exp(ax)$ to keep x positive for both integrals. Then use integration by parts [$u = x^2$, $\mathrm{d}v = e^x(e^x + 1)^{-2}\mathrm{d}x$] to change $(e^x + 1)^{-2}$ to $(e^x + 1)^{-1}$. Then the integral containing $(e^x + 1)^{-1}$ is available in handbooks. Symbolic integral solvers can also be used.

(b) Starting with (2.101), show that

$$\ln n_{e,c} = \frac{3}{2} \ln E_{\mathrm{F}} + c$$

$$\frac{\mathrm{d}n_{e,c}}{n_{e,c}} = \frac{3}{2}\frac{\mathrm{d}E_{\mathrm{F}}}{E_{\mathrm{F}}},$$

and that the free-electron energy DOS is (5.74), i.e.,

$$D_e(E_e) \equiv \frac{\mathrm{d}n_{e,c}}{\mathrm{d}E_\mathrm{F}} = \frac{3n_{e,c}}{2E_\mathrm{F}}.$$

(c) Use the result of part (b) in (5.72) and the result of part (a), to arrive at (5.76)

$$c_{v,e} = \frac{\pi^2}{2}\frac{n_{e,c}}{E_\mathrm{F}}k_\mathrm{B}^2 T.$$

Problem 5.9 Complete the integration to arrive at the energy-averaged relaxation time (5.113), and evaluate the gamma function for the scattering mechanisms given in Table 5.3.

Problem 5.10

Complete the steps and derive (5.131) from (5.125).

Problem 5.11

Complete the steps and derive (5.137) from (5.126).

Problem 5.12

(a) Complete the steps and derive (5.140) from (5.128).

(b) Show how the transport coefficient in (5.141) to (5.143) are related to those appearing in (5.123) and (5.124).

(c) Derive the relations among σ_e, k_e, α_S, and α_P, and α_{ee}, α_{et}, α_{te}, and α_{tt} as given in (5.145) to (5.146).

Problem 5.13

(a) Use $m_{e,e}/m_e = 1.08$ for Si and $T = 300$ K to show that $n_{e,F} = 2.80\times10^{19}$ 1/cm^3.

(b) Use $m_{h,e}/m_e = 0.81$ for Si and $T = 300$ K to show that $n_{h,F} = 1.83\times10^{19}$ 1/cm^3.

(c) Use the relation for intrinsic carrier density (footnote of Section 5.7),

$$n_i = (n_{e,\mathrm{F}}n_{h,\mathrm{F}})^{1/2}\exp(-\frac{\triangle E_{e,g}}{2k_\mathrm{B}T}),\ i = e \text{ or } h,$$

with gap energy $\triangle E_{e,g} = 1.12$ eV, for Si and $T = 300$ K to show that $n_i = 9.056\times10^9$ 1/cm^3. Check this against Figure 5.10(a)(ii).

(d) Using the expression for the intrinsic Fermi energy

$$E_\mathrm{F} - E_\mathrm{F,i} = k_\mathrm{B}T\ln\frac{n_{e,c}}{n_i} \quad \text{for } n\text{-type}$$

$$E_\mathrm{F} - E_\mathrm{F,i} = -k_\mathrm{B}T\ln\frac{n_{h,c}}{n_i} \quad \text{for } p\text{-type},$$

plot $E_\mathrm{F} - E_{\mathrm{F},i}$ (x axis) (in eV) versus $n_{e,c}$ (y axis, logarithmic scale), for $n_i < n_{e,c}(n_{h,c}) < 10^{21}$ 1/cm^3 and for $T = 300$ K. This gives the relation between the chemical potential $\mu = E_\mathrm{F}$ and the extrinsic carrier density $n_{e,c}$ (or $n_{h,c}$), which is separately determined from the measured Hall coefficient, (5.161).

Problem 5.14

In (5.176) and (5.174), explain the physical significance of the FGR and the interaction matrix element.

Problem 5.15

(a) For electron–acoustic-phonon (deformation-potential) scattering, starting from (5.176), use (5.179) and replace $E_e(\boldsymbol{p}) - E_e(\boldsymbol{p}')$ with $\hbar\omega_p$ (for emission of one phonon). Then use this approximate form (no phonon population dependence)

$$\dot{\gamma}_{e\text{-}p,\mathrm{A}} = \int \frac{\varphi_{d,\mathrm{A}}^2 \kappa_p^2}{8\pi^2 \rho \omega_p} \delta_\mathrm{D}(\boldsymbol{p}' - \boldsymbol{p} + \hbar\boldsymbol{\kappa}_p)\delta_\mathrm{D}(E_{e,\boldsymbol{\kappa}'} - E_{e,\boldsymbol{\kappa}} - \hbar\omega_p)\mathrm{d}\kappa_p,$$

and find the energy relaxation time $\tau_{e\text{-}p,\mathrm{A}}$(energy).

Note that, by using the momentum and energy conservations, we have

$$E_e(\kappa') = E_e(\kappa) \pm \hbar\omega_p, \quad \frac{\hbar^2\kappa'^2}{2m_{e,e}} = \frac{\hbar^2\kappa^2}{2m_{e,e}} \pm \hbar\omega_p$$

$$\boldsymbol{\kappa}' = \boldsymbol{\kappa} \pm \boldsymbol{\kappa}_p, \ \text{ or } \kappa'^2 = \kappa^2 + \kappa_p^2 \pm 2\kappa\kappa_p \cos\theta,$$

and also use the properties of the Dirac delta function, i.e.,

$$\delta_\mathrm{D}(\kappa' - \kappa \pm \kappa_p)\delta_\mathrm{D}(E_{e,\kappa'} - E_{e,\kappa} \mp \hbar\omega_p) = \frac{m_{e,e}}{\hbar^2\kappa\kappa_p}\delta_\mathrm{D}(\pm\cos\theta + \frac{\kappa_p}{2\kappa} \mp \frac{\omega_p m_{e,e}}{\hbar\kappa\kappa_p}).$$

Note that due to lack of spherical symmetry, using (3.12), we have [294]

$$\begin{aligned}
\frac{1}{\tau_{e\text{-}p,\mathrm{A}}(\text{energy})} &= \frac{\varphi_{d,\mathrm{A}}^2}{4\pi E_e \rho u_e}\int_0^\infty \int_{-1}^{1} \delta_\mathrm{D}(-\cos\theta + \frac{\kappa_p}{2\kappa} + \frac{u_{p,\mathrm{A}}}{u_e})\mathrm{d}(\cos\theta)\kappa_p^3 \mathrm{d}\kappa_p \\
&= \frac{\varphi_{d,\mathrm{A}}^2}{4\pi E_e \rho u_e}\int_{\kappa_{p,min}}^{\kappa_{p,max}} \kappa_p^3 \mathrm{d}\kappa_p \\
&= \frac{\varphi_{d,\mathrm{A}}^2 \kappa_{p,max}^4}{16\pi E_e \rho u_e} = \frac{2^{3/2} m_{e,e}^{5/2} \varphi_{d,\mathrm{A}}^2 E_e^{1/2}}{\pi\hbar^4 \rho}, \quad \kappa_{p,max} = \frac{2p_e}{\hbar}, \quad E_e = \frac{p_e^2}{2m_{e,e}}.
\end{aligned}$$

Note that the ϕ part of the integral yields 2π, since the integral of δ_D over the entire domain (-1 to 1) is equal to 1 (Glossary).

(b) Using $\tau_{e\text{-}p,\mathrm{A}}$(energy) just given, and $\tau_{e\text{-}p,\mathrm{A}}$(momentum) given by (5.185), show that

$$\tau_{e\text{-}p,\mathrm{A}}(\text{energy}) = \frac{k_\mathrm{B}T}{2m_{e,e}u_{p,\mathrm{A}}^2}\tau_{e\text{-}p,\mathrm{A}}(\text{momentum}).$$

Problem 5.16

Using (5.65), show that for $\hbar\omega = 0$ and a constant interaction matrix, the FGR (5.96) becomes

$$\dot{\gamma}_e(\boldsymbol{\kappa}', \boldsymbol{\kappa}) = \frac{2\pi}{\hbar}|M_{\kappa',\kappa}|^2 D_e[E_e(\kappa)],$$

where D_e is the electron DOS. Allow for electron spin.

Problem 5.17

Assume the piezoelectric-scattering potential and the displacement distribution

$$\varphi_{s,e\text{-}p} = \frac{e_c e_{pz}}{\epsilon_o \epsilon_e} d, \; d = d_o e^{\pm i(\boldsymbol{\kappa}_p \cdot \boldsymbol{x})},$$

for the LO phonon scattering of electrons. Here d_o is the magnitude of lattice-vibration displacement.

Then write (5.95) for the matrix element as

$$\begin{aligned} M_{\boldsymbol{p}',\boldsymbol{p}} &= \frac{1}{V_c}\int \frac{e_c e_{pz}}{\epsilon_o \epsilon_e} d_o \exp[\frac{-i(\boldsymbol{p}' - \boldsymbol{p} \mp \hbar\boldsymbol{\kappa}_p)\cdot \boldsymbol{x}}{\hbar}]d\boldsymbol{x} \\ &= \frac{e_c e_{pz} d_o}{\epsilon_o \epsilon_e}\frac{1}{V_c}\int \exp[\frac{-i(\boldsymbol{p}' - \boldsymbol{p} \mp \hbar\boldsymbol{\kappa}_p)\cdot \boldsymbol{x}}{\hbar}]d\boldsymbol{x}. \end{aligned}$$

The displacement is given as [294]

$$d_o^2 = \frac{\hbar}{2\rho V_c \omega_{p,\text{O}}}(\frac{k_\text{B}T}{f_p^\circ + \frac{1}{2} \mp \frac{1}{2}}), \quad f_p^\circ = \frac{k_\text{B}T}{\hbar\omega_{p,\text{O}}}.$$

Using $\omega_p/\kappa_p = u_{p,A}$, show that

$$|M_{\boldsymbol{p}',\boldsymbol{p}}|^2 = \frac{e_c^2 e_{pz}^2 k_\text{B}T}{2\epsilon_o^2 \epsilon_e^2 E_p \kappa_p^2 V_c}\{\frac{1}{V_c}\int \exp[\frac{-i(\boldsymbol{p}' - \boldsymbol{p} - \hbar\boldsymbol{\kappa}_p)\cdot \boldsymbol{x}}{\hbar}]d\boldsymbol{x}\}^2, \text{ for the } -\frac{1}{2} \text{ case,}$$

where, from (4.72), $u_{p,A} = u_{p,b}$ and is

$$u_{p,\text{A}} = (E_p/\rho)^{1/2},$$

where E_p is the bulk modulus of elasticity.

Problem 5.18

The atomic displacement (d) in optical phonons produces a change in lattice spacing directly, so the perturbation potential for optical phonons is generally assumed to be proportional to d ($\varphi_{s,e\text{-}p} = \varphi'_{e\text{-}p}d$), as in (5.162) ($\varphi'_{e\text{-}p} = \varphi'_{d,\text{O}}$ for nonpolar optical phonons and $\varphi'_{e\text{-}p} = q_e$ for polar optical phonons). Using (5.163), (5.165), and (5.166), the displacement and the initial and final states of the electron-phonon wave functions are simplified as

$$d = [\hbar/(2m\omega_{p,\text{O}})]^{1/2}(b^\dagger + b), \; |\psi_i\rangle = |\psi_{e,i}\rangle|f_p\rangle, \text{ and } |\psi_f\rangle = |\psi_{e,f}\rangle|f_{p'}\rangle,$$

where $|\psi_e\rangle$ and $|f_p\rangle$ are the wave functions for electron and phonon. The final state of phonon is $|f_{p'}\rangle = |f_p + 1\rangle$ for the phonon emission and $|f_{p'}\rangle = |f_p - 1\rangle$ for the phonon absorption.

(a) Using the simplified (5.96) [the first term is absorption and the second term is emission]

$$\dot{\gamma}_{e\text{-}p} = \sum_{\kappa'} \frac{2\pi}{\hbar} |\langle \psi_f | \varphi_{s,e\text{-}p} | \psi_i \rangle|^2 \delta_{\rm D}(E_{e,f} - E_{e,i} \pm E_{p,{\rm O}}),$$

show the interaction rate for phonon emission and absorption is

$$\dot{\gamma}_{e\text{-}p} = \sum_{\kappa'} \frac{\pi}{m\omega_{p,{\rm O}}} |\langle \psi_{e,f} | \varphi'_{e\text{-}p} | \psi_{e,i} \rangle|^2 |\langle f_p \pm 1 | b^\dagger + b | f_p \rangle|^2 \delta_{\rm D}(E_{e,f} - E_{e,i} \pm E_{p,{\rm O}}).$$

(b) Using the properties of ladder operators [see the footnote in Section 2.6.4]

$$b^\dagger |f_p\rangle = (f_p + 1)^{1/2} |f_p + 1\rangle \text{ and } b|f_p\rangle = f_p^{1/2} |f_p - 1\rangle,$$

show $|\langle f_p \pm 1 | b^\dagger + b | f_p \rangle|^2 = f_p + 1/2 \pm 1/2$.

(c) Using the parabolic band approximation for D_e $[= (2^{1/2} m_{e,e}^{3/2} E_e^{1/2})/(\pi^2 \hbar^3)$, as in (5.66)], calculate the scattering rate between electron and nonpolar optical phonon, and compare the result with that in Table 5.4.
Hint: For nonpolar optical phonon scattering,

$$\sum_{\kappa'} |\langle \psi_{e,f} | \varphi'_{e\text{-}p} | \psi_{e,i} \rangle|^2 \delta_{\rm D}(E_{e,f} - E_{e,i} \mp E_{p,{\rm O}}) = \varphi'^2_{d,{\rm O}} D_e(E_{e,f}) \frac{V}{N}.$$

V/N is added because the unit of D_e is J^{-1}m^{-3} (per unit energy range per volume), and N is the number of atoms in a primitive cell ($N = 2$).

Problem 5.19

(a) Derive expression (5.204) for the thermoelectric figure of merit.

(b) Show that optimum value ($\partial Z_e T/\partial \xi = 0$, use $\eta = \exp \xi$ and take derivative $\partial Z_e T/\partial \eta$) of $\xi_{\rm o}$ is found from

$$\xi_{\rm o} + 4(s + \frac{5}{2}) \frac{k_{\rm B}^2 T}{e_c} AB \exp(\xi_{\rm o}) = s + \frac{1}{2}$$

Then

$$\xi_{\rm o} \simeq s + \frac{1}{2} \text{ for negligible } k_e.$$

(c) Using Table 5.3 and the $k_e = 0$ results, show that for acoustic-phonon scattering $\xi_{\rm o} = 0$, and for weak ionized impurity scattering $\xi_{\rm o} = 2$.

Problem 5.20

(a) Plot $Z_e(T)$ for n-type Bi_2Te_3, using the following parameters [163] and the optimum Fermi energy, $E_{\rm F} \simeq \xi_{\rm o} k_{\rm B} T = (s + 1/2) k_{\rm B} T$ (for negligible k_e).

$k_p = 0.7$ W/m-K (parallel to c axis), $s = -1/2$, $m_{e,e} = 0.58 m_e$, and $\mu_e = 0.120$ m^2/V-s, at 300 K.

(b) Comment on the occurance of a maximum and compare with Figure 5.27.

Problem 5.21

(a) Using (5.147) to (5.150), calculate σ_e, α_S, α_P, and k_e, for the p-type Bi_2Te_3, at $T = 300$ K, assuming that the acoustic-phonon scattering dominates (Table 5.3), and using a single, effective bandgap ($\Delta E_{e,g} = E_{e,p} - E_{h,p}$, at minimum bandgap location) of $\Delta E_{e,g} = 0.13$ eV, $n_{e,c} = 6\times10^{24}$ 1/m^3, and $\mu_e = 0.1$ m^2/V-s.

Note that, for the p-type semiconductors, we have from (5.148) using the bandgap energy

$$\alpha_{S,p} = -\frac{k_B}{e_c}[\frac{E_{v,p} - E_{e,p}}{k_B T} + (s + \frac{5}{2})] = \frac{k_B}{e_c}[\frac{\Delta E_{e,g}}{k_B T} - (s + \frac{5}{2})],$$

where $E_{v,p}$ is the valance-band potential energy.

(b) For $k = k_e + k_p = 1.7$ W/m-K, calculate k_p at $T = 300$ K and then calculate $Z_e T$.

(c) Compare the calculated (predicted) values with those reported in the literature (e.g., *CRC Handbook of Thermoelectrics* [396]). The values vary depending on the doping used, and amongst the reported values are $\alpha_{S,p} = 230$ μV/K and $\rho_e = 10^{-5}$ Ω-m.

Problem 5.22

(a) Show that the solution to (5.265) and (5.266) for the case of $T_e = T_p$ at $x \rightarrow 0$ (assuming thermal equilibrium at the surface), and finite $T_e - T_p$ for $x \rightarrow \infty$ (away from the surface), is

$$T_e - T_p = \frac{\rho_e j_e^2 \delta^2}{k_e}(1 - e^{-x/\delta}),$$

where δ is the cooling length.

(b) Evaluate the $T_e - T_p$ expression for $x \rightarrow \infty$ for Si at $T = 300$ K, $k_p = 148$ W/m-K, $k_e = 1$ W/m-K, $\rho_e = 2.33 \times 10^3$ Ω-m, $\delta = 5 \times 10^{-7}$ m, and $j_e = 10^{12}$ A/m^2.

Problem 5.23

Show that solutions (5.267) and (5.268) satisfy (5.265) and (5.266).

Problem 5.24

(a) Determine the cooling length δ for Al, Si (intrinsic), and Te, at $T = 300$ K. Use Table A.1 for the total thermal conductivity, and Figure 5.20(b) for electrical conductivity. Then use the Wiedemann–Franz relation (assume phonon scattering is dominant) to find the electronic thermal conductivity. Next use these to determine the phonon conductivity. Also determine the relaxation time from the electrical conductivity (5.147). Figure 5.20(a) gives $n_{e,c}$ for the three elements. The average acoustic phonon speed for Si is given in Figure 5.13(a), for Al it is 6240 m/s, and for Te = 2610 m/s.

(b) Comment on the accuracy of the Wiedemann–Franz relations for semiconductors and metals.

(c) Comment on the ability (spatial constraints) of harvesting hot electrons in these materials. Use data in handbooks, etc., as well as those given in the text.

Problem 5.25

(a) Consider a Sb_2Te_3 thermoelectric element with length L and its two ends at T_h and T_c [106]. Using the one-dimensional solution for the temperature distributions of electrons and phonons in thermal nonequilibrium, plot the electron and phonon temperatures $T_e(x)$, $T_p(x)$, $-2 \le x \le +2$ μm, assuming the coefficients for zero electric current ($j_e = 0$) (A_1 through A_4) given in (5.275) are valid. Use the following conditions and for (i) $J_e = 0$, 15, and (ii) 30 mA.

$T_h = 300$ K, $T_c = 285$ K, $\alpha_S = 171$ μV/K, $\rho_e = 1.04\times10^{-5}$ Ω-m, $k_e = 0.6$ W/m-K, $k_p = 1.5$ W/m-K, $k = k_e + k_p$, $L = 4$ μm, $AR_{k,e,b} = 9.3\times10^{-7}$ K/(W/m^2), $A = 80$ μm^2, $AR_{k,p,b} = 8.0\times10^{-8}$ K/(W/m^2), and $\delta = 156$ nm.

Note that all conductances are per unit area. Also note that the temperatures for $j_e = 0$ and $j_e > 0$ do not match near the two ends. The numerical solution to this problem [i.e., not using (5.275) coefficients] is given in [106].

(b) Comment on the extent of thermal nonequilibrium within the element.

Problem 5.26

Consider conduction boundary resistance at the interface of a metal and a dielectric [303]. The interface is at $x = 0$, and the metal occupies $x \ge 0$.

In the electron–phonon (lattice) thermal nonequilibrium (Section 5.19), the carrier energy equations are given as

$$k_e \frac{\mathrm{d}^2 T_e}{\mathrm{d}x^2} = \frac{n_e k_\mathrm{B}}{\tau_{e\text{-}p}}(T_e - T_p) \quad 0 \le x < \infty$$

$$k_p \frac{\mathrm{d}^2 T_p}{\mathrm{d}x^2} = -\frac{n_e k_\mathrm{B}}{\tau_{e\text{-}p}}(T_e - T_p) \quad 0 \le x < \infty.$$

(a) Using $\Delta T = T_e - T_p$, and

$$\frac{1}{\delta^2} = \frac{1}{\delta_e^2} + \frac{1}{\delta_p^2}, \quad \delta_i^2 = \frac{k_i \tau_{e\text{-}p}}{n_e k_\mathrm{B}},$$

and using $\Delta T = 0$ for $x \to \infty$, show that $\Delta T = a_1 \exp(-x/\delta)$, where a_1 is a integration constant.

(b) Using this in the electron energy equation, show that

$$T_e = a_1 (\frac{\delta}{\delta_e})^2 \exp(-\frac{x}{\delta}) + a_2 x + a_3.$$

Using $\mathrm{d}T_e/\mathrm{d}x|_{x=0} = 0$, show that

$$T_e = a_1 (\frac{\delta}{\delta_e})^2 \exp(-\frac{x}{\delta}) + a_1 \frac{\delta}{\delta_e^2} x + a_3$$

$$T_p = a_1 [(\frac{\delta}{\delta_e})^2 - 1] \exp(-\frac{x}{\delta}) + a_1 \frac{\delta}{\delta_e^2} x + a_3.$$

(c) Now, the boundary thermal conditions for T_p and T_e are given in Section 5.19, as

$$k_p \frac{\mathrm{d}T_p}{\mathrm{d}x} = \frac{T_p - T}{AR_{p,b}} \quad \text{at } x = 0$$

$$k_e \frac{\mathrm{d}T_e}{\mathrm{d}x} = 0, \; k_p \frac{\mathrm{d}T_p}{\mathrm{d}x} = k \frac{\mathrm{d}T}{\mathrm{d}x} \quad \text{at } x = 0,$$

where k and T are for the dielectric, $x \le 0$ (dielectric material), and $1/AR_{p,b}$ is the phonon–phonon boundary conductance. Use this to show that the linear temperature distribution in the dielectric is [starting with $T = a_4(x) + a_5$]

$$T(|x|) = -\frac{k_p}{k}\frac{a_1}{\delta}|x| - a_1[1 + \frac{AR_{p,b}\delta}{k_p} - (\frac{\delta}{\delta_e})^2] + a_3,$$

so the unknown constants are a_1 and a_3.

(d) Now using

$$\frac{1}{AR_b} = \frac{q}{T_e'(0) - T(0)}, \; q = -k\frac{\mathrm{d}T}{\mathrm{d}x}|_{x=0},$$

where $T_e'(0) = a_3$ is the slip electron temperature, show that the interface (boundary) resistance R_b is

$$AR_b = \frac{\delta}{k_p}[1 + \frac{k_p AR_{p,b}}{\delta} - (\frac{\delta}{\delta_e})^2], \; \frac{1}{\delta^2} = \frac{n_e k_\mathrm{B}}{\tau_{e\text{-}p}}(\frac{1}{k_e} + \frac{1}{k_p}) = \frac{n_e k_\mathrm{B}}{\tau_{e\text{-}p}}\frac{k_p + k_e}{k_e k_p},$$

where the cooling length $\delta = \delta_{e\text{-}p}$ is the same as that given by (5.269).

Problem 5.27

The hyperbolic heat conduction equation based on finite wave speed has been suggested for from the electron heat transfer in metals for short-pulse-laser heating [305] in thin-metal films. Start with the conduction energy equation (Table 1.1), i.e.,

$$n_{e,c}c_{p,e}\frac{\partial T_e}{\partial t} + \nabla \cdot \boldsymbol{q}_e = \dot{s},$$

and use the constitutive relation for the thermal wave and its Taylor series expansion, i.e.,

$$\boldsymbol{q}_e(\boldsymbol{x}, t + \tau_e) = -k_e \nabla T_e$$

$$\boldsymbol{q}_e(\boldsymbol{x}, t) + \frac{\partial \boldsymbol{q}_e}{\partial t}\tau_e + \cdots = -k_e \nabla T_e,$$

where τ_e is the free electron relaxation time and it is assumed to be small.

Then starting from the above energy equation and $\boldsymbol{q}_e$, show that hyperbolic electron heat conduction equation becomes

$$\frac{\partial T_e}{\partial t} - \alpha_e \nabla^2 T_e = \frac{1}{n_{e,c}c_{p,e}}(\dot{s} + \frac{\alpha_e}{u_{e,\omega}^2}\frac{\partial \dot{s}}{\partial t}) - \frac{\alpha_e}{u_{e,\omega}^2}\frac{\partial^2 T_e}{\partial t^2}$$

hyperbolic electron heat conduction equation,

where

$$\alpha_e = \frac{k_e}{n_{e,c}c_{p,e}} \quad \text{thermal diffusivity}, \quad \tau_e = \frac{\alpha_e}{u_{e,\omega}^2}$$

and $u_{e,\omega}$ is the electron wave speed (second sound speed), given as [305]

$$u_{e,\omega} = [\frac{p_{\rm F}^2}{3m_e m_{e,e}}(1+{\rm F_o})]^{1/2}$$

$$\simeq (\frac{1}{3})^{1/2} u_{\rm F}.$$

Here $\rm F_o$ is a dimensionless interaction parameter.

For $\dot{s} = 0$, this becomes

$$\frac{\partial T_e}{\partial t} = \alpha_e \nabla^2 T_e + \frac{\alpha_e}{u_{e,\omega}^2}\frac{\partial^2 T_e}{\partial t^2}.$$

For $\tau_e \rightarrow 0$ $(\alpha_e/u_{\rm F} \rightarrow 0)$, the Fourier law is recovered.

The quantum limit of the proceeding equation is discussed in [255].

Problem 5.28

(a) Using the Taylor series expansion (around solution at $t = t_{\rm o}$) for the time-dependent wave function

$$\Psi(\boldsymbol{x}, t+t_{\rm o}) = \sum_{n=0}^{\infty} \frac{t_{\rm o}^n}{n!}(\frac{\partial}{\partial t})^n \Psi(\boldsymbol{x}, t),$$

satisfying the time-dependent Schrödinger equation (Table 2.8), show that

$$\Psi(\boldsymbol{x}, t+t_{\rm o}) = \exp(-\frac{i{\rm H}t_{\rm o}}{\hbar})\Psi(\boldsymbol{x}, t).$$

Note that H does not explicitly depend on t. Also, note that the proceeding series represents an exponential function, and that it is related to $\partial/\partial t$.

(b) Show that the expectation value of the dynamical variable $\phi(\boldsymbol{x}, \boldsymbol{p}, t)$ at time $t + t_{\rm o}$

$$\langle\phi\rangle_{t+t_{\rm o}} = \langle\Psi(\boldsymbol{x}, t+t_{\rm o})|\phi(\boldsymbol{x}, \boldsymbol{p}, t+t_{\rm o})|\Psi(\boldsymbol{x}, t+t_{\rm o})\rangle$$

is

$$\langle\phi\rangle_{t+t_{\rm o}} = \langle\Psi^\dagger(\boldsymbol{x}, t)|e^{\frac{i{\rm H}t_{\rm o}}{\hbar}}\phi(\boldsymbol{x}, \boldsymbol{p}, t+t_{\rm o})e^{-\frac{i{\rm H}t_{\rm o}}{\hbar}}|\Psi(\boldsymbol{x}, t)\rangle.$$

Note that the Hermiticity of H gives

$$(e^{-\frac{i{\rm H}t_{\rm o}}{\hbar}})^\dagger = e^{\frac{i{\rm H}t_{\rm o}}{\hbar}}.$$

(c) Using the kinetics definition of temperature (kinetic energy)

$$E_k = \frac{p^2}{2m},$$

show that in quantum mechanics

$$\langle \boldsymbol{p} \rangle = -i\hbar \int \Psi^\dagger \nabla \Psi \mathrm{d}\boldsymbol{x} = \int \Psi^\dagger (\frac{\hbar}{i}) \nabla \Psi \mathrm{d}\boldsymbol{x}$$

and

$$\langle E_k \rangle = -\frac{\hbar^2}{2m} \int \Psi^\dagger \nabla^2 \Psi \mathrm{d}\boldsymbol{x}.$$

Problem 5.29

Show that for an electron in an electromagnetic field [φ_e is the electric field scalar potential, and $\varphi_\circ(\boldsymbol{\kappa})$ is the other potential] with

$$\mathrm{H} = \frac{(\boldsymbol{p}_e - e_c \boldsymbol{a}_e)^2}{2m_e} + e_c \varphi_e + \varphi_\circ(\boldsymbol{x}),$$

the first-order perturbation $\mathrm{H} = \mathrm{H}_\circ + \mathrm{H}'(t)$ gives

$$\mathrm{H}'(t) = \frac{e_c}{m_e} \boldsymbol{a}_e \cdot \boldsymbol{p}_e,$$

which is a linearly polarized, monochromatic plane wave with $\varphi_e = 0$.

This is used in the derivation of the electron transition rate (transition dipole moment) and the relation between spontaneous and stimulated emissions (Section 7.4.2).

Problem 5.30

Use (5.65) (not allowing for spin) and the plane wave approximation with the periodic boundary condition, $(\kappa_1, \kappa_2, \kappa_3) = (2\pi/L)(n_1, n_2, n_3)$, $n_i = 0, 1, 2, \ldots$, and derive (E.35).

Problem 5.31

In thermionic emission [332], the electron current (5.118) written in terms of energy integral is

$$j_{e,x} = -e_c \int D_e f_e^\circ u_{e,x} \mathrm{d}E_e,$$

where D_e is given by (5.53), and $E_e = m_e u_e^2/2 = m(u_{e,x}^2 + u_{e,y}^2 + u_{e,z}^2)/2$, $u_{e,x\min} \le u_{e,x} < \infty$, $-\infty \le u_{e,y} < \infty$, $-\infty \le u_{e,z} < \infty$, so electron can escape.

The minimum velocity corresponds to the energy barrier height

$$\Delta E_\circ = -e_c \varphi_\omega - E_\mathrm{F} = \frac{m_e u_{e,x}^2}{2},$$

where $\varphi_\omega < 0$ is the work function energy needed for removal of the electron from surface.

Show that

$$j_{e,x} = -\frac{e_c m_e k_\mathrm{B}^2}{2\pi^2 \hbar^3} T^2 e^{-e_c \varphi_\omega / k_\mathrm{B} T},$$

This is called the Richardson thermionic emission relation and is an upper limit since there are interfacial reflection and other effects.

Problem 5.32

Acoustic lattice vibration also produces electric field $\boldsymbol{e}_e$, and this scatters electrons, most notably at high temperatures. For a one-dimensional motion, the interaction (scattering) potential $\varphi_{s,e\text{-}p}$ is generally

$$\varphi_{s,e\text{-}p}(x,t) = -e_c \int e_{e,x} \mathrm{d}x.$$

Requiring periodic deformation potential gives, using displacement along $\boldsymbol{x}$, for piezoelectric scattering,

$$\epsilon_{\mathrm{o}}\epsilon_e e_{e,x} = -e_{pz}\frac{\partial d_x}{\partial x},$$

or

$$e_{e,x} = -\frac{e_{pz}}{\epsilon_{\mathrm{o}}\epsilon_e}\frac{\partial d_x}{\partial x},$$

where e_{pz} is the piezoelectric constant.

Using these, show that

$$\varphi_{s,e\text{-}p}(x,t) = \frac{e_c e_{pz}}{\epsilon_{\mathrm{o}}\epsilon_e} d_x(x,t).$$

6

Fluid Particle Energy Storage, Transport, and Transformation Kinetics

Fluid particle refers to matter in a gas or liquid phase, with the particle being the smallest unit (made of atoms or molecules) in it, for which further breakdown would change the chemical identity of the particle. For a fluid in motion, the convection heat flux vector $\boldsymbol{q}_u = \rho_f c_{p,f} \boldsymbol{u}_f T$ and the surface-convection heat flux vector $\boldsymbol{q}_{ku}$ (which describes the interfacial heat transfer between two phases in relative motion, in which at least one phase is a fluid) are influenced by the specific heat capacity $c_{p,f}$ of the fluid particle (whereas $\boldsymbol{q}_{ku}$ also depends on the isotropic fluid thermal conductivity k_f, viscosity μ_f, and velocity). The fluid (gas or liquid) velocity $\boldsymbol{u}_f$ can be subsonic or supersonic, and for contained gases at low pressures or in small spaces, it is possible for fluid particle–surface collisions to dominate over the interparticle collisions. In this chapter, we examine energy storage and transport in fluids, as well as fluid interactions with surfaces (and the associated fluid flow regimes). We will discuss how the effective conductivity of the fluid $\langle k_f \rangle$ can be influenced by suspended particle, turbulence, and free electrons.

Fluid particles can be monatomic, diatomic, or polyatomic, mononuclear or polynuclear, with various molecular symmetries and asymmetries, and can have five types (forms) of energy: potential (among the constituent atoms and molecules), electronic, translational, vibrational, and rotational (Figure 1.1). The electronic energy is part of potential energy, however, here we use the potential energy for inter fluid particle interactions only. With the partition function, each form of energy can be considered separately, and the total energy is the summation of these five energies. The maximum vibrational and rotational energies a molecule can attain are limited by the dissociation energy φ_e. Above this energy, the atoms of a molecule have an excess of internuclear energy that overcomes the bonding force between them, causing the atoms to dissociate. Similarly, the maximum electronic energy a fluid particle can obtain is the first ionization energy, which is the energy at which an electron has enough energy to escape the pull of the atom. Figure 6.1(a) gives examples of the magnitudes of these energies for gaseous CO, CO_2, He, Ne, and N_2 used in gas lasers. Unlike phonons, the energy states of the fluid particles are in general discrete. As a reference, the average translational energy of a monatomic gas is also shown for $T = 300$ K. For CO_2 and Ne, the energy of photon emission is also

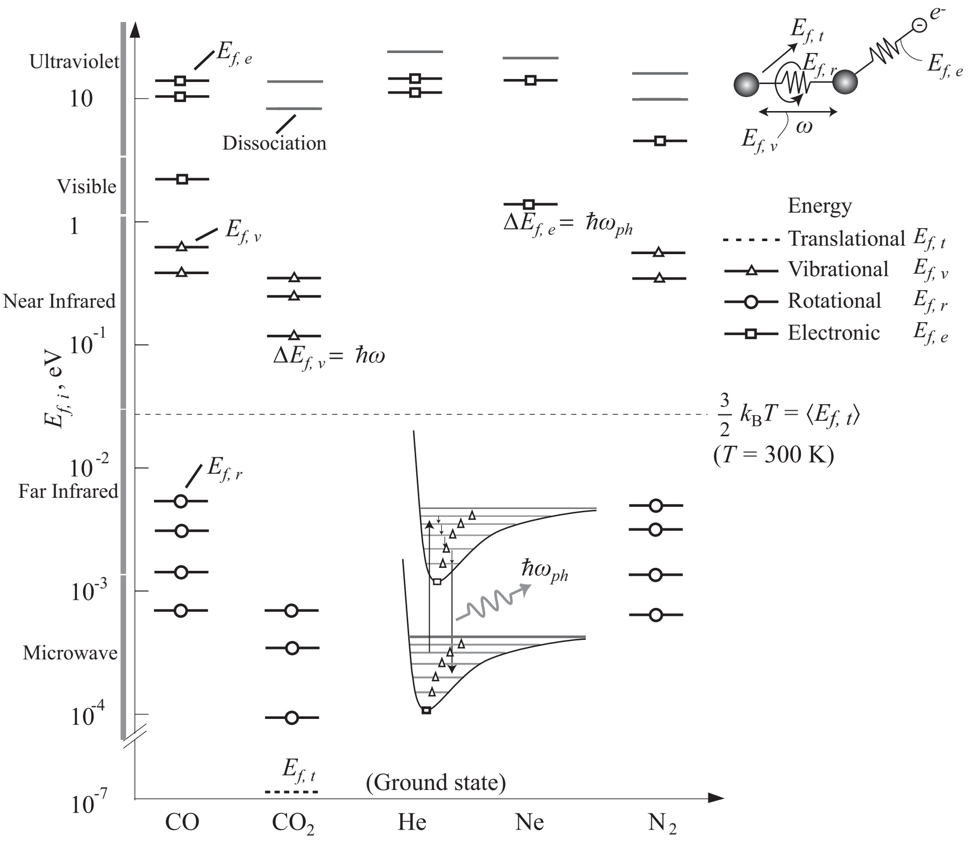

(a) Examples of Various Fluid Particle Internal Energies

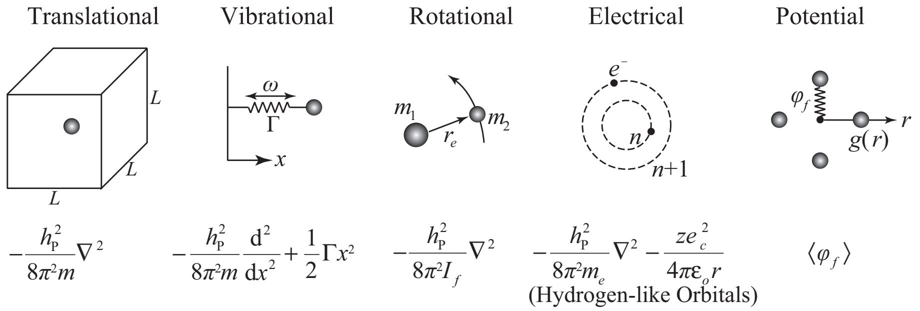
Translational
Vibrational
Rotational
Electrical
Potential
L
L
L
ω
Γ
x
m_1
m_2
r_e
e^-
n
$n+1$
φ_f
r
$g(r)$
$-\frac{h_P^2}{8\pi^2 m}\nabla^2$
$-\frac{h_P^2}{8\pi^2 m}\frac{d^2}{dx^2}+\frac{1}{2}\Gamma x^2$
$-\frac{h_P^2}{8\pi^2 I_f}\nabla^2$
$-\frac{h_P^2}{8\pi^2 m_e}\nabla^2-\frac{ze_c^2}{4\pi\epsilon_o r}$
(Hydrogen-like Orbitals)
$\langle \varphi_f \rangle$

(b) Fluid Particle Hamiltonians

Figure 6.1. Examples of the magnitude of various (translational, vibrational, rotational, and electronic) fluid particle energies [125, 409, 494], for some monatomic (He, Ne), diatomic (CO, N_2), and polyatomic (CO_2) gases. The average monotonic-gas translational kinetic energy $3k_BT/2$, for $T = 300$ K, is also shown. For CO_2 and Ne, their lasing frequencies (and energy) are also shown (related to vibrational energy). (b) The Hamiltonian for the translational, vibrational, rotational, electronic, and potential energy.

shown (vibrational energy). The rotational and translational energies are low, while the vibrational and electronic energies are high. Also shown is the potential energy for nonideal (dense) gases. The calculations of these energies (including numerical solutions) are described in Section 6.1, and their transformation and transport mechanisms are discussed throughout this chapter.

6.1 Fluid Particle Quantum Energy States and Partition Functions

The fluid particle (monatomic, diatomic, or polyatomic) may undergo translational, vibrational and rotational motions (a fluid particle made of N_o atoms has $3N_o$ modes of motion), and dense fluids also have interparticle potential energy. The electronic energy of the fluid particle is where energy is stored by displacing its electrons with respect to its nucleus. Then the fluid particle energy (and Hamiltonian) is divided into potential, electronic, translational, vibrational, and rotational energies [Figure 6.1(b)], i.e.,

$$E_f = \sum_i E_{f,i} = E_{f,p} + E_{f,e} + E_{f,t} + E_{f,v} + E_{f,r}$$

$$\mathrm{H}_f = \sum_i \mathrm{H}_{f,i} = \langle \varphi_f \rangle + \mathrm{H}_{f,e} + \mathrm{H}_{f,t} + \mathrm{H}_{f,v} + \mathrm{H}_{f,r}. \tag{6.1}$$

The Hamiltonians for various energies are listed in Figure 6.1. In Section 6.1.5, we will discuss the numerical solution to the Schrödinger equation and here we proceed with the thermodynamic treatment, including the fluid temperature.

The partition function Z defined through (2.21), using the fluid particle Hamiltonian, is partitioned into various energies. First it is divided into potential, electronic, and kinetic energy partitions. Then, for each type of motion, i.e., translation, vibration, or rotation, the kinetic energy is further partitioned. Based on the definition of Z, the total partition function is the product of each of these and from Table 2.4, i.e.,

$$Z_f = \prod_i Z_{f,i} = Z_{f,p} Z_{f,e} Z_{f,t} Z_{f,v} Z_{f,r},$$

$$E_f = k_\mathrm{B} T^2 N \frac{\partial \ln Z_f}{\partial T}|_{N,V}, \tag{6.2}$$

The particle in a box model of fluid particles is used to derive the translational quantum energy states. Similarly, other quantum kinetic and electronic energy states are treated (derivations are outlined below). For the case of no potential energy (field free), we have $E_{f,p} = \langle \varphi_f \rangle = 0$ $(Z_{f,p} = 1)$.

6.1.1 Translational Energy and Partition Function

Considering translational motion, the energy is the translational kinetic energy and the Hamiltonian is $\mathrm{H}_{f,t} = -(h_\mathrm{P}^2/8\pi^2 m)\nabla^2$, shown in Figure 6.1, i.e.,

$$E_{f,t} = \frac{1}{2} m u_f^2 = \frac{1}{2m} p_f^2, \quad u_f = |\boldsymbol{u}_f|, \quad p_f = |\boldsymbol{p}_f|, \tag{6.3}$$

where $\boldsymbol{p}_f$ is the fluid particle momentum vector. Then similar to Section 2.6.5 for periodic free electron, the time-independent Schrödinger equation (2.62) becomes

$$\mathrm{H}_{f,t}\psi_{f,t} = \mathrm{E}_{f,t}\psi_{f,t}, \ \frac{h_\mathrm{P}}{8\pi^2 m}\nabla^2\psi_{f,t} + \frac{1}{2m}p_{f,t}^2\psi_{f,t} = 0. \tag{6.4}$$

Assuming that the box (containing one gas particle) is impermeable, it would require that $\psi_{f,t} = 0$ on the wall (and also outside the box). The solution to $\psi_{f,t}$ can be separated into three independent Cartesian-coordinate components, i.e.,

$$\psi_{f,t}(\boldsymbol{x}) = \psi_{f,x}(x)\psi_{f,y}(y)\psi_{f,z}(z). \tag{6.5}$$

For a box of volume L^3, the boundary conditions are (similar to electron gas of Section 2.6.5)

$$\psi_{f,i}(0) = \psi_{f,i}(L) = 0, \ \ i = x, y, z. \tag{6.6}$$

The solution for each component, e.g., x, is

$$\psi_{f,x}(0) = A_x \sin{(2\pi\frac{p_{f,x}}{h_\mathrm{P}}x)} + B_x \cos{(2\pi\frac{p_{f,x}}{h_\mathrm{P}}x)}. \tag{6.7}$$

While (6.6) the constants are determined and the the eigenvalues are

$$p_{f,x} = \frac{h_\mathrm{P}}{2}\frac{n_x}{L}, \quad n_x = 1, 2, 3, \cdots \tag{6.8}$$

The resulting energy states are

$$E_{f,t,n} = \frac{h_\mathrm{P}^2}{8m}(\frac{n_x^2}{L^2} + \frac{n_y^2}{L^2} + \frac{n_z^2}{L^2}) \ \text{translational energy states}, \tag{6.9}$$

where n_x, n_y, n_z are the translational quantum numbers.

Note that quantum translational energies can be very small. For example, for $\mathrm{CO_2}$, with $L = 3.4$ nm (p of nearly 1 atm at 300 K), $h_\mathrm{P}^2/8mL^2$ (i.e., $n = 1$) is 4×10^{-7} eV. The nonground states have much larger energies but still small compared to vibrational energy. Because of this very small quantum translational energies, they are excited and occupied at very low temperature (approaching 0 K). Noting that the fluid particle translational energy follows the M–B distribution (Table 1.2), partition function (2.27) for translational energy (6.9) is [73]

$$\begin{aligned} Z_{f,t} &= \sum_{i=0}^{\infty} g_{f,t,i}\exp(-\frac{E_{f,t,i}}{k_\mathrm{B}T}) \\ &= \prod_{j=1}^{3}\sum_{n_x=1}^{\infty} g_{f,t,i}\exp(-\frac{n_x^2}{L^2}\frac{h_\mathrm{P}^2}{8mk_\mathrm{B}T}) = \int_0^\infty \frac{\pi}{4}(\frac{8mV^{2/3}}{h_\mathrm{P}^2})^{3/2}E_{f,t}^{1/2}e^{-E_{f,t}/k_\mathrm{B}T}\mathrm{d}E_{f,t} \\ &= V(\frac{2\pi m k_\mathrm{B}T}{h_\mathrm{P}^2})^{3/2} = \frac{V}{\lambda_\mathrm{dB}^3}, \ V = L^3, \end{aligned} \tag{6.10}$$

where $\lambda_{\rm dB}$ is the de Broglie wavelength. The degeneracy is

$$g_{f,t,i} = \frac{4\pi(8mV^{2/3}h_{\rm P}^2)^{3/2}E_{f,t,i}^{1/2}}{4}. \tag{6.11}$$

This can be used to define the criterion for having an ideal gas[†].

Using the relation for translational internal energy (6.1), then from (6.10) the translational energy is (Chapter 2 problem)

$$E_{f,t} = k_{\rm B}T^2\frac{\partial \ln Z_{f,t}}{\partial T} = \frac{3}{2}k_{\rm B}T \quad \text{average translational energy.} \tag{6.12}$$

So, here only the translational energy of the particle gives the temperature. If the ensemble energy also includes rotational and vibrational energy, then the temperature relates to the total partition function and the total degrees of motion freedom. The energies can be expressed in terms of thermal energy with $E_{f,i} = k_{\rm B}T_i$. While the ground translational energy states are occupied near 0 K, the ground rotational energy state becomes occupied at $0 < T < 100$ K, and vibration energy states at $T > 100$ K, (Table 6.2).

6.1.2 Vibrational Energy and Partition Function

For polyatomic gases, the vibrational energy is also determined from the Schrödinger equation. For example, for diatomic gases, the quantum vibrational energy is (the treatment of a simple harmonic oscillator applicable to diatomic molecules, where $\mathrm{H}_{f,v} = -(h_{\rm P}^2/8\pi^2 m)\mathrm{d}^2/\mathrm{d}x^2 + \frac{1}{2}\Gamma x^2$, is given in Section 2.6.4)

$$E_{f,v,l} = \hbar\omega_f(l+\frac{1}{2}), \quad l = 0, 1, 2, \cdots \quad \text{diatomic gas vibrational energy states,} \tag{6.13}$$

where l is the vibrational (or vibronic) quantum number. For polyatomic molecules with multiple vibrational modes, an expanded form of (6.13) is used (Section 7.13.1).[‡] The scale for the vibrational frequency is similar to that used for phonons, (2.51), i.e., for harmonic pair vibration, $\omega_f = (\Gamma/m)^{1/2}$, where Γ is the spring

---

[†] Using (6.10), $Z_{f,t} \equiv V/\lambda_{\rm dB}^3$, where $\lambda_{\rm dB} = (h_{\rm P}^2/2\pi m k_{\rm B}T)^{1/2}$ is the thermal de Broglie wavelength (see Glossary), and the dilute- (ideal-) gas criterion is defined as

$$n_f^* = \frac{\lambda_{\rm dB}^3}{V/N} = \lambda_{\rm dB}^3 n_f = \frac{(h_{\rm P}^2/2\pi m k_{\rm B}T)^{3/2}}{k_{\rm B}T/p} \gg 1 \ \text{ideal-gas condition (Maxwell-Boltzmann statistics).},$$

where n_f^* is the dimensionless number of fluid particles per unit volume (also called quantum concentration). Also, see Glossary on Bose-Einstein condensate and Section 7.13.

[‡] For polyatomic gases with for k indicating the vibrational modes given in Table 6.1, we have

$$E_{f,v} = \sum_k (l_k + \frac{1}{2})\hbar\omega_{f,v,k}.$$

constant and is the second derivative of the interatomic potential evaluated at equilibrium position. Then the partition function becomes

$$
\begin{aligned}
Z_{f,v} &= \sum_{l=0}^{\infty} \exp[-(l+\frac{1}{2})\frac{\hbar\omega_f}{k_\mathrm{B}T}] = \exp(-\frac{\hbar\omega_f}{2k_\mathrm{B}T})\sum_{l=0}^{\infty}\exp(-l\frac{\hbar\omega_f}{k_\mathrm{B}T}) \\
&\simeq \exp(-\frac{\hbar\omega_f}{2k_\mathrm{B}T})\frac{1}{1-\exp(-\dfrac{\hbar\omega_f}{k_\mathrm{B}T})} \\
&= \frac{\exp(-\dfrac{T_{f,v}}{2T})}{1-\exp(-\dfrac{T_{f,v}}{T})}, \quad T_{f,v} \equiv \frac{\hbar\omega_f}{k_\mathrm{B}},
\end{aligned}
\tag{6.14}
$$

where $T_{f,v}$ is defined as the single characteristic temperature for vibration for diatomic particle (this will be given for some diatomic gases in Table 6.2). We will discuss triatomic and larger molecules in Section 6.2. This is the same as the partition function for the simple harmonic oscillator given by (2.88). In Section 7.13.1, we will discuss vibrational transitions of polyatomic, molecular gases in gas lasers. These vibrational transistions have energies in the near-infrared regime.

6.1.3 Rotational Energy and Partition Function

Similarly, the rotational energy for diatomic gas particles, where the rigid-rotor Hamiltonian is $\mathrm{H}_{f,r} = -(h_\mathrm{P}^2/8\pi^2 I_f)\nabla^2$, is [†]

$$
\begin{aligned}
E_{f,r,j} &= \frac{h_\mathrm{P}^2}{8\pi^2 I_f} j(j+1) \equiv B_{f,r} j(j+1), \\
I_f &= \frac{m_1 m_2}{m_1+m_2} r_e^2, \; j = 0, 1, 2, \cdots \quad \text{rotational energy states,}
\end{aligned}
\tag{6.15}
$$

where I_f is moment of inertia for the molecule, j is the rotational quantum number, and r_e is the equilibrium separation distance discussed in Section 2.2. Here $B_{f,r}$ is the rotational constant $h_\mathrm{P}^2/8\pi^2 I_f$.

The partition function for the fluid particle rotational energy is [73]

$$
\begin{aligned}
Z_{f,r} &= \sum_{j=0}^{\infty} g_{f,r,j}\exp(-\frac{E_{f,r,j}}{k_\mathrm{B}T}) \;=\; \sum_{j=0}^{\infty}(2j+1)\exp[\frac{-j(j+1)h_\mathrm{P}^2}{8\pi^2 I_f k_\mathrm{B} T}] \\
&\simeq 1 + 3\exp(\frac{-2T_{f,r}}{T}) + 5\exp(\frac{-6T_{f,r}}{T}) + \cdots + \\
&\simeq \frac{T}{T_{f,r}}(1+\frac{1}{3}\frac{T_{f,r}}{T}+\frac{1}{15}\frac{T_{f,r}^2}{T^2}+\cdots),
\end{aligned}
\tag{6.16}
$$

[†] The rigid-rotor approximation leads to constant energy gaps between adjacent levels, and this is not consistent with experiments (Section 6.1.5) [323].

where $T_{f,r}$ is the rotational temperature defined as (will be given for some diatomic and polyatomic gases in Table 6.2)

$$T_{f,r} \equiv \frac{h_{\rm P}^2}{8\pi^2 I_f k_{\rm B}} = \frac{B_{f,r}}{k_{\rm B}}. \tag{6.17}$$

The ground-state quantum rotational energies of polyatomic gases are of the order of 10^{-4} eV. H_2 having a small atomic mass, has a small I_f and large $E_{f,v}$. Therefore they are excited at low temperatures.

The practical form of (6.16) uses a symmetry number N_s and is [479],

$$Z_{f,r} = \frac{T}{N_s T_{f,r}} \begin{cases} N_s = 1 & \text{for heteronuclear polyatomic gas} \\ N_s = 2 & \text{for homonuclear polyatomic gas.} \end{cases} \tag{6.18}$$

6.1.4 Electronic Energy and Partition Function

The electronic Hamiltonian $\mathrm{H}_{f,e}$ is given in the footnote of Section 2.2.2 as $\mathrm{H}_{f,e} - \mathrm{H}_{e\text{-}n} + \mathrm{H}_{e\text{-}e} + \mathrm{H}_{n\text{-}n}$, for the electron-nuclear, electron-electron, and nuclear-nuclear interactions. The solution for the hydrogen-like atoms based on $\mathrm{H}_{e\text{-}n} = -ze_c^2/4\pi\epsilon_{\rm o}r$ was given in Section 2.6.6 (with four quantum numbers). So these quantum electronic transition will be given by $\Delta E_{e,n} = -(e_c^2/8\pi\epsilon_{\rm o}r_{\rm B})[n^{-2} - (n \pm 1)^{-2}]$. The dissociation energies are listed for some atomic pair in Table 2.3, for H_2 it is 4.52 eV (or $T_{f,e,\mathrm{H}_2} = 5.24 \times 10^4$ K), and we will discuss dissociation and ionization in Section 6.13 on thermal plasmas. The first ionization energy of elements is given in Table A.2 (e.g., 15.72 eV for Ar). The electronic energy of some gases were discussed in Section 5.21 and some values were listed in Figures 5.39 and 5.40. The electronic energies are much larger than the kinetic energies.

Here we use a simple thermodynamic treatment, since the electronic energy does not make a significant contribution to the fluid particle specific heat capacity and its thermal conductivity.

The partition function for electronic energy states $E_{f,e,k}$ is represented through the electronic excitation temperature $T_{f,e,k}$, where k is the electronic quantum number. Then

$$\begin{aligned} Z_{f,e} &= \sum_{k=0}^{\infty} g_{f,e,k} \exp(-\frac{E_{f,e,k}}{k_{\rm B}T}) = \sum_{k=0}^{\infty} g_{f,e,k} \exp(-\frac{T_{f,e,k}}{T}) \\ &= g_{f,e,0} + g_{f,e,1} \exp(-\frac{T_{f,e,1}}{T}) \ldots, \quad T_{f,e,k} = \frac{E_{f,e,k}}{k_{\rm B}} \\ & E_{f,e,k} \ \text{electronic energy states.} \end{aligned} \tag{6.19}$$

We discuss the potential energy $E_{f,p} = \langle \varphi_f \rangle$ and its partition function $Z_{f,p}$ in Section 6.3 when examining dense fluids. It is also customary to combine the potential and vibrational energies for diatomic and polyatomic gases (Section 6.2). Figure 6.2 shows the discrete electronic, vibrational, and rotational energies of H_2. Their ground states, as well as their excited states, are shown. The variation of interatomic

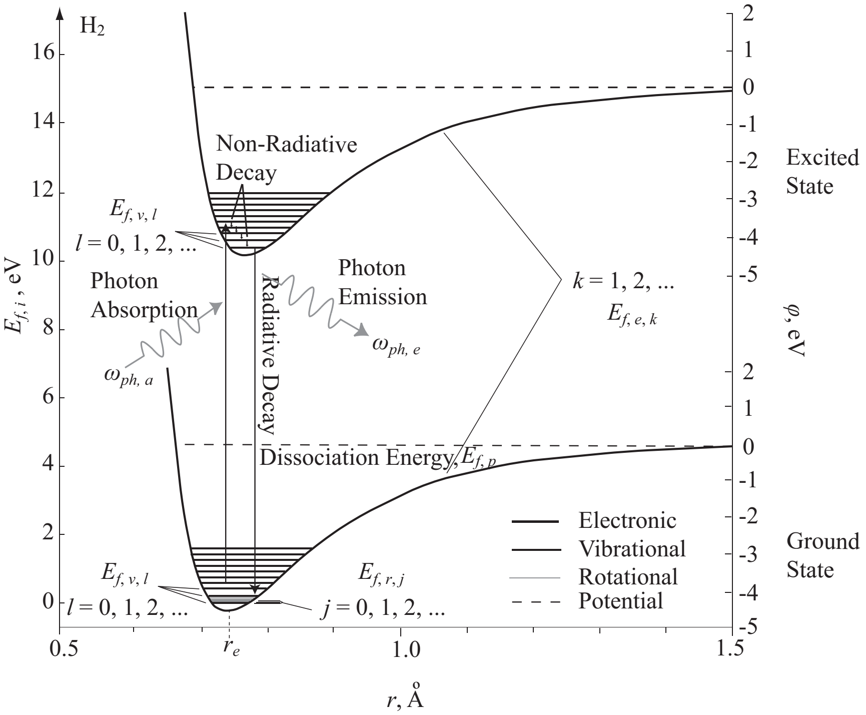

Figure 6.2. Discrete electronic, vibrational, and rotational energies (left) of H_2 for the ground (lowest) and excited state. The variation of the interatomic potential (right) with respect to the separation distance is also shown.

potential, with respect to the interatomic spacing, is also shown (L–J potential model). The potential is only slightly different from the excited electronic state (for H_2, but not in general). The large energy transitions are by photon (radiation) absorption/emission, whereas the smaller ones are nonradiative (mechanical). Note the large electronic energy transitions (around 10 eV). The translational energies are generally small (of the order of millielectronvolts).

Since the electronic energy excitation temperature $T_{f,e,k}$ is very large, generally only the ground state is used (and does not contribute to internal energy e_f and $c_{v,f}$). In Section 7.13.2, we discuss electronic transition of atomic gases in laser cooling. As an example, rotational and vibrational modes of H_2O molecules are shown. The force constant is calculated using the procedure described in Section 4.11.2 (also in Section 7.13.1). Also, note that for all kinetic energies we have had the equilibrium distribution and the same temperature. Nonequilibrium distribution, including steady-state population inversion, occurs in gas lasers (Section 7.13), chemical reactions, and so on.

6.1.5 *Ab Initio* Computation of Vibrational and Rotational Energy States

Using the Gaussian computer code series discussed in Section 2.2.2, the vibrational and rotational energy states of molecules can be calculated. For example, for

CO_2, the first excited, bending vibration mode $\hbar\omega(0,1,0)$ has the calculated energy of 0.08014 eV (the vibrational quantum numbers are discussed in Section 7.8.2). The symmetric and asymmetric stretching vibration modes are $\hbar\omega(1,0,0) = 0.1751$ eV and $\hbar\omega(0,0,1) = 0.2957$ eV. The experimental value is close at 0.0828 eV.[†] The rigid-rotor energy states given by (6.15) written as $E_{f,r,j} = B_{f,r}j(j+1)$, and the rotational constant $B_{f,r}$ found from Gaussian are also given in the footnote. The calculated value is (since this is a linear molecule, the two rotation directions are degenerate) $B_{f,r} = 0.0486$ meV. Then the first excited, rotational state has energy of $E_{f,r,1} = 9.72 \times 10^{-5}$ eV (also marked in Figure 1.4). However, the rigid-rotor approximation is not generally valid because it results in a constant energy gap between energy levels [323]. For the nonrigid rotor, the rotational energy is expanded as $E_{f,r,j} = B_{f,r}j(j+1) - D_{f,r}j^2(j+1)^2 + H_{f,r}j^3(j+1)^3 + \ldots$, and generally $D_{f,r}$ and $H_{f,r}$ are found empirically.

For H_2O and the structure shown in Table 6.1, the calculated [Gaussian, HF 6-31G(d) keyword = Anharmonic VibRot mode] rotational constants $B_{f,r,i}(i = x,y,z)$ are 3.388 meV (819.13 GHz, 39.31 K), 1.807 meV (436.91 GHz, 20.97 K), and 1.178 meV (284.93 GHz, 13.67 K). Note the low rotational temperatures $T_{f,r}$. Also, the symmetric, asymmetric, and bending vibrational frequencies are 117.6, 120.8, and 55.8 THz, respectively (or 0.4862, 0.4995, and 0.2309 eV) (or 5641, 5796, and 2680 K). Note that the Hatree-Fock levels contain known systematic errors,

---

[†] Gaussian 03 (Gaussian 4 using Windows)
1. Create CO_2 molecule. Select a carbon divalent and oxygen atoms.
2. Give the interatomic distances and angles (1.16 as bond length and 180° as interatomic angle).
3. Set the calculation mode

```
Calculation mode
Job Type : Frequency
Method: Ground State, Theoretical: Hartree-Fock, wave function Type: restricted
Basis Set: 6-31G
Charge 0 Spin: Singlet
Additional Keyword: Freq=anharm
```

4. Submit this input

```
%chk=C:\G03W\CO2_Input.chk
# freq=anharm rhf/6-31g
Title Card Required
0 1
 C        0.00000000      0.00000000       0.00000000
 O        0.00000000      0.00000000       1.16000000
 O        0.00000000      0.00000000      -1.16000000
Output:
ROTATIONAL CONSTANT (GHz)          11.740573
ROTATIONAL CONSTANT (cm-1)          0.391623
1         2         3         4
PIU       PIU       SGG       SGU
Frequencies – 653.6297 653.6297 1412.4694 2384.7165
Red. masses – 12.8774 12.8774 15.9949 12.8774
Frc consts – 3.2415 3.2415 18.8014 43.1470
IR Inten – 67.2745 67.2745 0.0000 921.4059
(1,0,0)       1412.4694 cm-1       0.1751239 eV
(0,0,1)       2384.7165 cm-1       0.2956672 eV
(0,1,0)        653.6297 cm-1       0.0810397 eV
(0,2,0)       1307.2594 cm-1       0.1620795 eV
```

Table 6.1. *Degrees of freedom in translational, rotational, and vibrational motions of linear and nonlinear polyatomic molecules made of* N_o *atoms. The 9 degrees of freedom of* H_2O *molecule are also shown, as an example.*

Motion	Linear polyatomic molecules	Nonlinear polyatomic molecules
Translation, N_t	3	3
Rotation, N_r	2	3
Vibration, N_v	$3N_o - 5$	$3N_o - 6$
Total	$3N_o$	$3N_o$

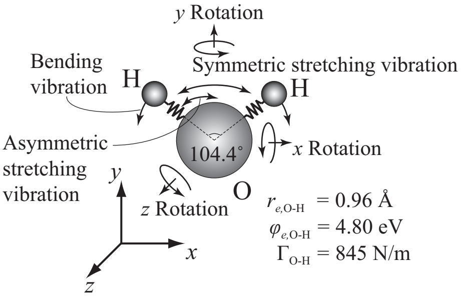
y Rotation
Bending vibration
Symmetric stretching vibration
H
H
Asymmetric stretching vibration
104.4°
x Rotation
y
z Rotation
O
$r_{e,\text{O-H}}$ = 0.96 Å
$\varphi_{e,\text{O-H}}$ = 4.80 eV
$\Gamma_{\text{O-H}}$ = 845 N/m
x
z

due to neglecting the electron correlation, and this results in overestimating the frequency by about 10%–12% (the values here are corrected). We list the H_2O photon absorption bands in Table 7.3.

6.2 Ideal-Gas Specific Heat Capacity

The average specific internal energy e is related to the partition function through (6.12), i.e.,

$$e_f = \frac{R_g}{M} T^2 \frac{\partial \ln Z_f}{\partial T}|_{N,V}, \tag{6.20}$$

where $R_g = k_B N_A$, and product rule (6.2) is used for $Z_{f,i}$, i.e., the contribution from each mechanism of energy storage in the fluid particle.

The ideal gas equation of states (obtained from Z_f, as will be shown in Section 5.3) is

$$p = \frac{R_g}{M} \rho_f T = n_f k_B T,\ n_f = \frac{p}{k_B T} \quad \text{ideal-gas equation of states,} \tag{6.21}$$

where M is the molecular weight, $M = mN_A$.

For ideal, diatomic gases, the electronic energy is assumed negligible, and using (6.20) and the partition functions of Section 6.1 ($E_{f,p} = 0$, no potential energy for

Table 6.2. *Rotation and vibration temperatures for some diatomic gases and vibrational temperatures for some linear and nonlinear polyatomic molecules [73].*

Molecule	$T_{f,r}$, K	$T_{f,v}$, K	Molecule	$T_{f,v,k}$, K
Cl_2	0.351	808	CCl_4	310(2), 450(3), 660, 1120(3)
H_2	85.3	6215	CH_4	1870(3), 2180(2), 4170, 4320(3)
I_2	0.054	308	CO_2	954(2), 1890, 3360
N_2	2.88	3374	H_2O	2290, 5160, 5360
O_2	2.07	2256	NH_3	1360, 4800, 4880(2), 2330(2)
CO	2.77	3103	NO_2	850(2), 1840, 3200
HCl	15.2	4227	SO_2	750, 1660, 1960
HI	9.06	3266		

ideal gas), we have the specific heat capacity at constant volume as (Table 2.4)(end-of-chapter problem)

$$c_{v,f} = \frac{\partial e_f}{\partial T}|_V = \frac{R_g}{M}\{\frac{3}{2} + (\frac{T_{f,v}}{T})^2 \frac{\exp(T_{f,v}/T)}{[\exp(T_{f,v}/T) - 1]^2} + 1 + \frac{2}{15}(\frac{T_{f,r}}{T})^2\}$$

$$\text{diatomic ideal gas,} \qquad (6.22)$$

where we have used (6.16) for the rotational energy. Here the first term is due to translation, the second is due to vibration, and the last two are due to rotation. Since $T_{f,r}$ is low, then the rotational contribution to (6.22) is $k_B T$ due to the two degrees of freedom (for all linear polyatomic gases).

For linear molecules (e.g., CO_2, Figure 2.10)., there are two axes for rotation, and a three for nonlinear molecules (e.g., H_2O, Figure 2.10). Also, there are $3N_o - 5$ (N_o is the number of atoms in molecule) vibration modes for linear and $3N_o - 6$ modes for nonlinear polyatomic ideal gases. There are $3N_o$ total degrees of freedom per molecule. These are summarized in Table 6.1. The selection rule for the allowed rotational and vibrational modes follows the group theory of quantum mechanics [462]. This selection will include the degenerate modes.

For a linear, diatomic gas there is one vibrational mode. However, it is customary to think of the vibrational mode as having a kinetic and a potential component, so this contribution is R_g/M. At large temperatures, the limit of $7R_g/2M$ is reached. At yet higher temperatures, the contribution from the electronic energy storage should be included. Table 6.2 lists the empirical values for $T_{f,v}$ and $T_{f,r}$, for some common diatomic gases. Note that the low-energy rotational modes are excited (occupied) at much lower temperatures, compared with the vibrational modes (Figure 6.1), i.e., $T_{f,r} < T_{f,v}$. Also note that the lighter molecules have higher transition temperatures.

For monatomic gases, the only contribution is from the translational motion. Then

$$c_{v,f} = \frac{3R_g}{2M} \quad \text{or} \quad c_{v,f} = \frac{3}{2}k_B \quad \text{monatomic ideal gas.} \qquad (6.23)$$

Here $c_{v,f}$ is first given in J/kg-K and then per fluid particle (here atom).

For three or more atoms the relative position of the atoms should be included, and for a nonlinear arrangement of atoms, the specific heat capacity for an N_o-atom molecule is assumed to be dominated by translation, rotation, and vibration, and given by [73]

$$c_{v,f} = \frac{R_g}{M}\{3 + \sum_k^{3N_o-6} (\frac{T_{f,v,k}}{T})^2 \frac{\exp(T_{f,v,k}/T)}{[\exp(T_{f,v,k}/T) - 1]^2}\}, \quad T_{f,v,k} = \frac{\hbar\omega_{f,v,k}}{k_B}.$$

$$\text{nonlinear, polyatomic ideal gas.} \qquad (6.24)$$

Here the translational and rotational energies are assumed fully occupied compared with the vibrational energy (i.e., the vibrational energy has the highest transition temperature.) Also, note that each vibrational degree of freedom adds one R_g/M to $c_{p,f}$ (combines it with potential energy). The relation for a linear polyatomic molecule is similar, except 3 is replaced with 5/2, and $3N_o - 6$ is replaced with $3N_o - 5$ (Table 6.1). The empirical values for $T_{f,v,k}$ are also listed in Table 6.2 for some common polyatomic gases. Repeated temperatures, in Table 6.2, are indicated in parentheses.

Figure 6.3(a) shows the variations of the specific heat capacity of homonuclear H_2 and N_2 with respect to temperature. These predicted results are close to experimental values. From Table 6.2, we note that $T_{f,r}$ for H_2 is only 85.3 K, whereas $T_{f,v}$ is 6215 K. Both of these are lower for N_2 (due to larger mass of N). For H_2, the value of 7/2 is reached at about 6000 K. Note that at $T = 300$ K, $c_{p,f} = c_v + k_B$ per molecules is $3.5k_B$ or 1.038×10^3 J/kg-K, as also listed in Table A.1. As we will discuss in Section 7.13, for CO_2, the first four vibrational excited states are the bending mode (which is degenerate, so there are two of the same mode) with energy $E_{f,v}(0,1,0) = 82.8$ meV (or $T_{f,v} = E_{f,v}/k_B = 960.7$ K, close to that in Table 6.2), $E_f(1,0,0) = 172.3$ meV (or 1999 K) for symmetric stretch, and $E_{f,v}(0,0,1) = 291.5$ meV (or 3383 K) for asymmetric stretch. So, the listed $T_{f,r}$ in Table 6.2 are the first excited vibrational states of these polyatomic gases.

Figure 6.3(b) shows the same for CH_4 and H_2O. Note that this H_2O vibrational energies (or temperature) are close to that found from the *ab initio* calculations in Section 6.1.5. Also note that for heteronuclear CH_4, the specific heat capacity increases significantly with temperature (the first $T_{f,v,j}$ is 1870 K, Table 6.2). For water vapor $c_{v,f}$ per molecule can reach as high as 6, but it dissociates before all its vibrational states are excited. Note that the softer (weaker) bonds in CCl_4 make for small $E_{f,v}$ (and $T_{f,v}$), so some of its vibrational states are well occupied at room temperature (i.e., large room-temperature $c_{v,f}$). We discussed the van der Waals, ionic/metallic, and covalent bonds in Section 4.11.2.

In general, as the temperature increases, the vibrational energy states become occupied. At very high temperatures, the classical limit of $k_B/2$ for each degree of motion freedom is reached. The two (constant-pressure and constant-volume) specific heat capacities are related through

$$c_{p,f} = c_{v,f} + T(\frac{\partial p}{\partial T}|_v \frac{\partial v}{\partial T}|_p) \equiv c_{v,f} + T\frac{\beta^2}{\rho_f \kappa}, \ \kappa_p = \frac{1}{\rho_f}\frac{\partial \rho_f}{\partial p}|_T, \qquad (6.25)$$

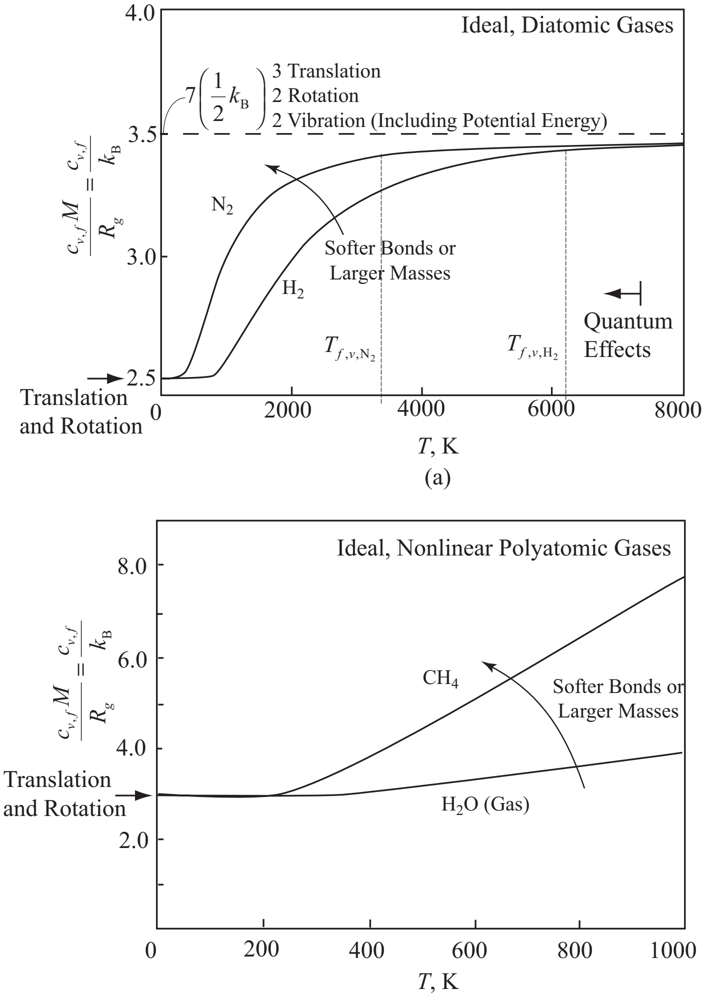

(a)

(b)

Figure 6.3. Predicted (with empirical transition temperatures, Table 6.2) scaled variation of the specific heat capacity of (a) diatomic, and (b) nonlinear polyatomic gases, with respect to temperature. Here $c_{v,f}$ is in per kg (when using M/R_g) or per fluid particle.

where β is the volumetric thermal expansion coefficient and κ_p is the isothermal compressibility ($\kappa_p = 1/E_p$. E_p is the bulk modulus). For ideal gas, $T^2\beta/\rho_f\kappa_p = R_g/M$.

The specific heat capacity per molecule (of mass m) can be written as $\alpha(T)k_B/m$, where $\alpha(T)$ is dimensionless and expresses the degrees of freedom of temperature dependence ($\alpha = 3/2$ for monatomic gases). Then, noting that the product of $\rho_f c_{p,f} T$ appears in the macroscopic energy equation of Table 1.1, for an ideal gas ($p = k_B\rho_f T/m$) (6.21), we have

$$\rho_f c_{p,f} T = p\alpha(T)T \quad \text{ideal-gas specific heat capacity,} \tag{6.26}$$

i.e., the sensible heat content per unit volume is proportional to the pressure.

6.3 Dense-Fluid Specific Heat Capacity: van der Waals Model

The phonon theory of liquid thermodynamics is presented in [48], based on the Frenkel model of liquid particle jump at frequency $\omega_{\rm F}$ is able to support shear waves for frequencies larger than $\omega_{\rm F}$. The internal energy of the liquid is given a function of a Debye $\omega_{\rm D}$ in addition to this frequency.[†] Here we use a classical treatment which leads to the equation of states for dense fluids.

The partition function for a single-component, dense fluid accounts for the interparticle force-field interactions and is given as (Table 2.4)

$$Z_f = \frac{1}{N_f!} Z_{f,p} Z_{f,t} Z_{f,r}, \qquad (6.27)$$

where $Z_{f,p}$ is the classical configuration integral accounting for the particle interactions (includes vibration), $Z_{f,t}$ is the translation component of the molecular partition function, and $Z_{f,r}$ is the rotational component. The factor $1/N_f!$ accounts for the indistinguishability of the molecules.

The Hamiltonian in the partition function relation (6.1) is written as

$$\mathrm{H}_f = \langle \varphi_f \rangle_{N_f}(\boldsymbol{x}) + \mathrm{H}_{f,t}(\boldsymbol{p}) + \mathrm{H}_{f,r}(\boldsymbol{p}). \qquad (6.28)$$

The translation component

$$Z_{f,t} = \frac{1}{h_{\rm P}^{3N_f}} [\int \exp{(-\frac{1}{k_{\rm B}T}\frac{p^2}{2m})}\mathrm{d}\boldsymbol{p}]^{N_f}. \qquad (6.29)$$

Then similar to (6.10), (6.27) is written as [73]

$$Z_f = \frac{(2\pi m k_{\rm B} T)^{3N_f/2}}{h_{\rm P}^{3N_f}} Z_{f,r} Z_{f,p}, \qquad (6.30)$$

where $Z_{f,p}$ includes the modified volume term, not shown as part of $Z_{f,t}$. The rotational component is given for both linear and nonlinear polyatomic molecules, as [73]

$$Z_{f,r} = \frac{\pi^{(N_{t\text{-}r}-5)N_f/2}}{N_s^{N_f}} (\frac{T}{T_{f,r}})^{(N_{t\text{-}r}-3)N_f/2}, \qquad (6.31)$$

where $N_{t\text{-}r}$ $(= N_t + N_r)$ is the total number of translational and rotational energy storage modes (Table 6.1), N_s is the symmetry number for a polyatomic molecule

---

[†] Based on the Frenkel theory, the liquid internal energy is

$$e_f = k_{\rm B}T(1 + \frac{\beta_f T}{2})[3g(\frac{\hbar\omega_{\rm D}}{T}) - (\frac{\omega_{\rm F}}{\omega_{\rm D}})^3 g(\frac{\hbar\omega_{\rm F}}{T})],$$

where function g is

$$g(x) = \frac{3}{x^3}\int_0^x \frac{z^3}{e^z - 1}\mathrm{d}z.$$

$$\omega_{\rm F} = \frac{2\pi G_\infty}{\mu_f},$$

and G_∞ is the high-frequency shear modulus, and μ_f is the viscosity. For monatomic liquids $\omega_{\rm D}$ is taken as that of the solid phase.

(the number of ways the molecule can be rotated into itself), and $T_{f,r}$ is the characteristic temperature for rotation. For polyatomic molecules, $N_s = 2$ for H_2O and $N_s = 3$ for NH_3, etc.

The potential component of the molecular partition function (2.21) is based on the effective potential $\langle \varphi_f \rangle$

$$Z_{f,p} = \int \exp\,[-\frac{1}{k_B T}\langle \varphi_f \rangle_{N_f}(\boldsymbol{x}_1, \boldsymbol{x}_2 \cdots \boldsymbol{x}_N)]\mathrm{d}\boldsymbol{x}_1\boldsymbol{x}_2 \cdots \boldsymbol{x}_N. \tag{6.32}$$

Using the radial distribution function $g(r)$, Section 2.2.5, and for L–J potential (2.47) the total effective potential energy of the fluid is [similar to (2.49)]

$$\begin{aligned} E_{f,p} = \langle \varphi_f \rangle_{N_f} &= \frac{N_f}{2}\int_d^\infty \frac{N_f}{V} 4\pi r^2 \varphi_{\mathrm{LJ}}(r) g(r)\mathrm{d}r = \frac{2\pi N_f^2}{V}\int_d^\infty r^2 \varphi_{\mathrm{LJ}}(r)\mathrm{d}r \\ &\equiv -\frac{aN_f^2}{V}, \;\; g(r) = 0 \text{ for } r < d, \;\; g(r) = 1 \text{ for } r \geq d \end{aligned} \tag{6.33}$$

$$a = -2\pi \int_d^\infty r^2 \varphi_{\mathrm{LJ}}(r)\mathrm{d}r = \frac{8\pi \epsilon_{\mathrm{LJ}} \sigma_{\mathrm{LJ}}^6}{3d^3}(1 - \frac{\sigma_{\mathrm{LJ}}^6}{3d^6}), \tag{6.34}$$

where a is the van der Waals coefficient, and d is the diameter of the molecule (this is sometimes taken as the molecular collision diameter, which will be discussed in Section 6.5). Note that the $g(r)$ approximation in (6.33) matches well the distribution in Figure 2.11(b) for liquids.

The integral in (6.32) is over the volume V and is repeated for N_f molecules leading to V^{N_f}. However, for dense fluids, the fluid particles occupy a relatively large percentage of the physical space. These occupied volumes are not accessible and should not be included in the integral over all the coordinates. Therefore, $(V - N_f b)^{N_f}$ is used instead of V^{N_f}, where b is a van der Waals constant representing the mean volume occupied by a fluid particle in the system. Then the potential energy component is [73]

$$Z_{f,p} = \exp(\frac{aN_f{}^2}{Vk_B T})(V - N_f b)^{N_f}. \tag{6.35}$$

When all three contributions (6.30), (6.31), and (6.35), are substituted into (6.27), the dense-fluid molecular partition function is (end-of-chapter problem)

$$Z_f = \frac{1}{N_f!}\frac{(2\pi m k_B T)^{3N_f/2}}{h_{\mathrm{P}}^{3N_f}}\frac{\pi^{(N_{t\text{-}r}-5)N_f/2}}{N_s^{N_f}}(\frac{T}{T_{f,r}})^{(N_{t\text{-}r}-3)N_f/2}\exp(\frac{aN_f{}^2}{Vk_B T})(V - N_f b)^{N_f}. \tag{6.36}$$

The pressure is given in terms of the partition function from Table 2.4 as

$$p = k_B T\frac{\partial \ln Z_f}{\partial V}|_{T,N_f}. \tag{6.37}$$

Table 6.3. *L–J parameters and van der Waals coefficients for some common compounds [73].*

Compound	$\epsilon_{\rm LJ}/k_{\rm B}$, K	$\sigma_{\rm LJ}$, Å	a, 10^{-49} Pa-m^6/molecule^2	b, 10^{-29}m^3/molecule	$N_{t\text{-}r} = N_t + N_r$
H_2O	78	3.17	15.20	5.05	6
N_2	95	3.70	3.76	6.40	5
O_2	118	3.58	3.78	5.23	5
CO_2	198	4.33	10.10	7.09	5
CH_4	149	3.78	6.31	7.09	6

Substituting partition function (6.36) into the preceding equation and using the Stirling approximation, i.e., $\ln N_f! = N_f \ln N_f - N_f$, we have (end-of-chapter problem)

$$p = \frac{N_f k_{\rm B} T}{V - N_f b} - \frac{a {N_f}^2}{V^2} = k_{\rm B} T (\frac{n_f}{1 - b n_f}) - a n_f^2, \ n_f = \frac{N_f}{V},$$

dense-fluid van der Waals equation of states, (6.38)

where as in (6.21) n_f is the fluid particle number density, and (6.38) is quadratic in n_f and the second term reduces the pressure due to the interactions, similar to that in Table 2.4.

Note that since V is only in the potential energy partition function, the pressure is only dependent on $Z_{f,p}$. For $b n_f \ll 1$ and $a n_f^2 \ll 1$, ideal-gas equation of states (6.21) is obtained. The coefficients of a and b can be related to the L–J coefficients. The definition of a in (6.34) can be simplified as $a = 16\pi\epsilon_{\rm LJ}\sigma_{\rm LJ}^3/9$, if we assume that $d = \sigma_{\rm LJ}$. The parameter b is interpreted as the volume of space occupied by each molecule, which is $b \simeq \pi d^3/6$. Thus assuming that $d = \sigma_{\rm LJ}$, we have $b = \pi\sigma_{\rm LJ}^3/6$. However, these assumptions underestimate a and b.

Table 6.3 lists the L–J potential parameters and the van der Waals coefficients for a few common compounds. Note that these potentials treat each molecules as a particle, so they represent the force field of the molecules (as compared to the individual atoms). For example, this H_2O–H_2O potential represents mostly the O–O force field. Potentials other than the L–J more accurately model the partially-charged oxygens [373], among the potential models is the simple rigid pointcharge (SPC). The empirical values for a and b (based on actual d) are also listed, as well as the value of $N_{t\text{-}r}$.

From the definition of enthalpy and by re-writing (6.20) not per unit mass but per particle, we have [†]

$$h_f = e_f + pV, \quad e_f = k_{\rm B} T^2 \frac{\partial \ln Z_f}{\partial T}|_{N_f,V}. \tag{6.39}$$

[†] Using (6.39), we have

$$h_f = \frac{N_{t-r} N_f}{2} k_{\rm B} T + \frac{V/N_f}{V/N_f - b} N_f k_{\rm B} T - \frac{2 a N_f^2}{V}.$$

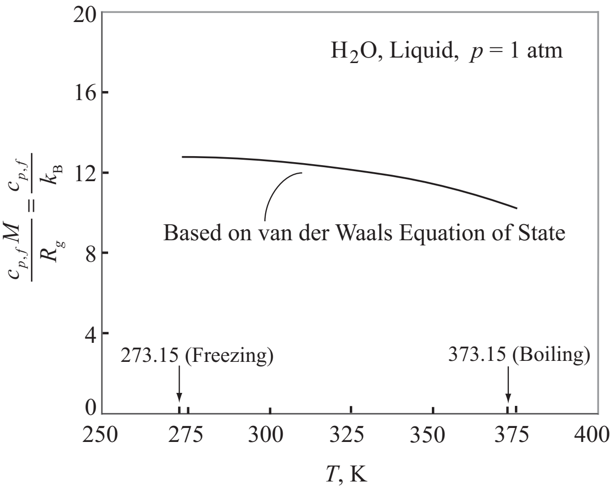

Figure 6.4. Predicted variations of specific heat capacities (at constant pressure) of saturated liquid water (p = 1 atm) with respect to temperature. $c_{p,f}$ is given in per kg and per fluid particle.

For N_f particles, this is multiplied by N_f. Now using the van der Waals equation of states (6.38), we find that the specific heat capacity at constant pressure (per unit mass, i.e., using R_g/M) for a van der Waals fluid is (end-of-chapter problem)

$$c_{p,f} = \frac{\partial h_f}{\partial T}|_p = \frac{R_g}{M}\{(\frac{N_{t\text{-}r}}{2} + \frac{V/N_A}{V/N_A - b}) - \frac{[\frac{2a}{(V/N_A)^2} - \frac{bk_BT}{(V/N_A - b)^2}](\frac{1}{V/N_A - b})}{\frac{2a}{(V/N_A)^3} - \frac{k_BT}{(V/N_A - b)^2}}\}$$

$$\text{van der Waals heat capacity.} \tag{6.40}$$

Note that we first use $N_f = N_A$ to find $c_{v,f}$ per mole and then use M to find $c_{v,f}$ per mass. Note that all three components $Z_{f,i}$ contribute to $c_{p,f}$.

Here we have used the Maxwell relation [73]

$$\frac{\partial h_f}{\partial T}|_{p,N_f} = \frac{\partial h}{\partial T}|_{V,N_f} - \frac{\partial h_f}{\partial V}|_{T,N_f}\frac{\partial p/\partial T|_{N_f,V}}{\partial p/\partial V|_{T,N_f}}. \tag{6.41}$$

Figure 6.4 shows the predicted specific heat capacities of saturated ($p = 1$ atm) liquid water obtained with (6.40). The results are about 30% over the experimental results. For triatomic liquid H_2O, the results of Figure 6.4 show that per atom $c_{p,f}m/k_B$ is larger than 3 at lower (relative) temperatures. The energy is the intermolecular potential energy and is also a reason for the large heat of evaporation of water. Unlike gases, the liquid specific heat capacity decreases with temperature.

Noting that the liquid potential energy is large, this energy is released when liquid is transformed to gas, and this energy is nearly the heat of evaporation. Also note the lower specific heat of gaseous water (per molecule) shown in Figure 6.3(b). We will further discuss this in Section 6.11.5.

The two specific heats ($c_{v,f}$ and $c_{p,f}$) are related through (6.25) and are nearly equal for most liquids. In general, an accurate prediction of the liquid specific heat is more challenging (compared with that of gases) [73].

6.4 Gas BTE, $f_f^{\rm o}$ and Thermal Velocities

The BTE (Table 3.1) requires specification of the collision term on the right-hand side, which here is considered to be the dynamics of the collision of two particles. In the kinetic theory of gases, Boltzmann considered dilute gases and analyzed the elementary collision processes between pairs of molecules. The evolution of the equilibrium distribution function is described by the BTE.

6.4.1 Interparticle Collisions

If there were no collisions, the particles would have positions and momentum distributions such that the probability distribution function at time t and t+dt is that given by (3.5), i.e.,

$$f_f(\boldsymbol{x} + \boldsymbol{u}\mathrm{d}t, \boldsymbol{p} + \boldsymbol{F}_f\mathrm{d}t, t + \mathrm{d}t) = f_f(\boldsymbol{x}, \boldsymbol{p}, t), \tag{6.42}$$

where $\boldsymbol{F}_f$ denotes an external force acting on fluid particles at point $(\boldsymbol{x}, \boldsymbol{p})$.

The collisions (scattering) change this, and they are represented as $\partial f_f/\partial t|_s$ and the BTE (Table 3.1) becomes

$$(\frac{\partial}{\partial t} + \boldsymbol{u}_f \cdot \nabla_{\boldsymbol{x}} + \boldsymbol{F}_f \cdot \nabla_{\boldsymbol{p}}) f_f(\boldsymbol{x}, \boldsymbol{p}, t) = \frac{\partial f_f}{\partial t}|_s. \tag{6.43}$$

Here we consider elastic scattering and $\dot{s}_f = 0$. Boltzmann assumed binary collisions with $\boldsymbol{F}_f = 0$. He also assumed that the velocity and position of a molecule are uncorrelated (assumption of molecular chaos). He constructed a moving-coordinate, and the relation is subsequently briefly described [460] and is shown in Figure 6.5, where the superscript $'$ indicates before collision.

Each particle is designated by a mass, a diameter (hard sphere), and phase-space coordinates $(\boldsymbol{x}, \boldsymbol{p})$. The effect of the binary collisions is expressed in terms of a differential scattering cross section describing the probability for a change of velocities

$$\{\boldsymbol{u}'_{f,1}, \boldsymbol{u}'_{f,2}\}_{before} \rightarrow \{\boldsymbol{u}_{f,1}, \boldsymbol{u}_{f,2}\}_{after}, \tag{6.44}$$

where ϕ thus denotes the relative orientation of the vectors $(\boldsymbol{u}'_{f,2} - \boldsymbol{u}'_{f,1})$ and $\boldsymbol{u}_{f,21} = (\boldsymbol{u}_{f,2} - \boldsymbol{u}_{f,1})$, as shown in Figure 6.5. In Section 6.5, we will discuss the equilibrium collision (scattering) rate.

In Section 6.5 we will write the energy and momentum conservations for a binary, elastic collision and will show that $|\mathbf{u}_{f,21}| = |\mathbf{u}_{f,2} - \mathbf{u}_{f,1}|$ is conserved. We will also use the same scattering rate for in- and out-scattering (due to symmetry). This scattering rate is $\dot{\gamma}_{f\text{-}f} = n_{f,2}|\mathbf{u}_{f,12}|\mathrm{d}A_{ff}$, where $\mathrm{d}A_{ff}$ is the differential scattering cross-section area in the center of mass frame of Figure 6.5. We use the equivalent collision (Section 6.5) and write $\mathrm{d}A_{ff}$ in terms of $\eta\mathrm{d}\eta$ defined in Figure 6.5. We assume the hard spheres potential of Figure 2.3, but also show the actual particle

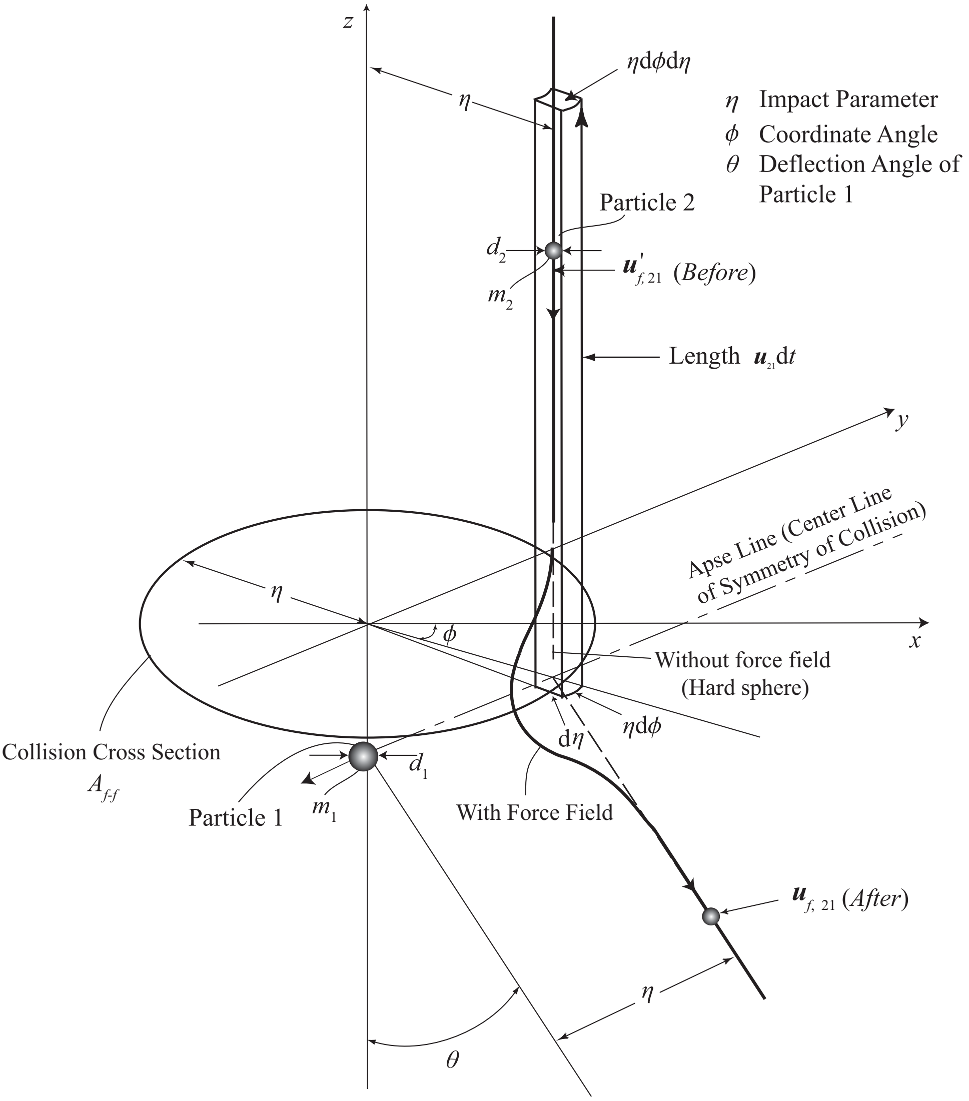
z
η
ηdφdη
η Impact Parameter
φ Coordinate Angle
θ Deflection Angle of Particle 1
Particle 2
d_2
m_2
$\boldsymbol{u}'_{f,21}$ (Before)
Length $\boldsymbol{u}_{21}$dt
y
Apse Line (Center Line of Symmetry of Collision)
η
φ
x
Without force field (Hard sphere)
ηdφ
dη
Collision Cross Section $A_{f\text{-}f}$
d_1
Particle 1
m_1
With Force Field
$\boldsymbol{u}_{f,21}$ (After)
η
θ

Figure 6.5. A general three-dimensional (moving-coordinate) rendering of the binary encounter of gas particle (hard sphere) 2 with gas particle (hard sphere) 1 with a relative velocity $\boldsymbol{u}_{21}$. The geometrical variables used in the collision integral are shown. The apse line passes through both particle centers [460].

path with realistic interparticle force field in Figure 6.5. Including this nonequilibrium binary scattering term, (6.43) becomes [460]

$$
\begin{aligned}
&\left(\frac{\partial}{\partial t} + \boldsymbol{u}_f \cdot \nabla_{\boldsymbol{x}} + \boldsymbol{F}_f \cdot \nabla_{\boldsymbol{p}}\right) f_{f,1} \\
&= \frac{\partial f_f}{\partial t}\Big|_s = \int_\eta \int_\phi \int_{\boldsymbol{u}_2} (f'_{f,1} f'_{f,2} - f_{f,1} f_{f,2}) n_{f,2} |\boldsymbol{u}_{f,21}| \eta \, \mathrm{d}\boldsymbol{u}_2 \, \mathrm{d}\psi \, \mathrm{d}\phi \\
&\text{BTE with binary collisions,} \qquad (6.45)
\end{aligned}
$$

where $\boldsymbol{p}_2 = m_2\boldsymbol{u}_2$, and $f_{f,1} \equiv f(\boldsymbol{x}, \boldsymbol{p}, t)$, $f'_{f,1} \equiv f(\boldsymbol{x}, \boldsymbol{p}', t)$, and so on. Note that here f_f is not dimensionless, but $f_f \mathrm{d}\mathbf{u}_f$ is (this will be given in the next section).

Then using

$$\boldsymbol{u}_f \cdot \nabla_{\boldsymbol{x}} f_f \equiv u_x \frac{\partial f_f}{\partial x} + u_y \frac{\partial f_f}{\partial y} + u_z \frac{\partial f_f}{\partial z} \tag{6.46}$$

$$\boldsymbol{F}_f \cdot \nabla_{\boldsymbol{p}} f_f \equiv F_x \frac{\partial f_f}{\partial p_x} + F_y \frac{\partial f_f}{\partial p_y} + F_z \frac{\partial f_f}{\partial p_z}. \tag{6.47}$$

Integrodifferential equation (6.45) describes the spatial–temporal behavior of a dilute gas. Given an initial distribution $f_f(\boldsymbol{x}, \boldsymbol{p}, t = 0)$, the solution $f_f(\boldsymbol{x}, \boldsymbol{p}, t)$ describes the distribution changes over time. Because f_f is difficult to visualize, there are certain moments of f_f that represent averages such as the local particle density, which can be determined as measured. Chapman and Enskog [235] developed a general procedure for the approximate solution of the BTE. For certain simple model systems such as hard spheres, their method produces predictions for $f_f(\boldsymbol{x}, \boldsymbol{p}, t)$ (and its moments). The BTE is generally used to describe nonequilibrium processes. The equilibrium distribution $f_f^{\rm o}(\boldsymbol{x}, \boldsymbol{p})$ is that solution of BTE that is stationary, i.e., given by (3.6),

$$\frac{\mathrm{D} f_f^{\rm o}(\boldsymbol{x}, \boldsymbol{p}, t)}{\mathrm{D}t} = 0 \;\; \text{equlilibrium distribution.} \tag{6.48}$$

For the case of $\boldsymbol{F}_f = 0$ this gives the M–B equilibrium distribution function $f_f^{\rm o}$ for a spatially and temporally uniform stationary ideal gas (Section 6.5). We will evaluate the binary collision rate appearing on the right-hand side of ideal gases (6.45) in Section 6.5. Then we use $f_f^{\rm o}$ and a driving force, along with the collision rate, to evaluate k_f.

6.4.2 Equilibrium Distribution Function for Translational Energy

Consider translational energy only (e.g., monatomic, ideal gas). Gases have a nondegenerate behavior (M–B), except at very low temperatures (Section 7.13.2). Assuming that the molecular velocities are isotropic (in the absence of external fields) and that the distribution of molecular speeds in any one component of velocity is independent of that in any other component, the probability of finding a molecule in a given element of velocity space, $\mathrm{d}\boldsymbol{u}_f$, is then

$$P[(u_x, u_y, u_z), (u_x + \mathrm{d}u_x, u_y + \mathrm{d}u_y, u_z + \mathrm{d}u_z)] = f_f^{\rm o}(\boldsymbol{u}_f)\mathrm{d}\boldsymbol{u}_f \;\; \text{probability,} \tag{6.49}$$

and, using the directional independence, we have variable separation given by

$$P(u_x, u_x + \mathrm{d}u_x) = X(u_x)\mathrm{d}u_x \tag{6.50}$$

$$P(u_y, u_y + \mathrm{d}u_y) = Y(u_y)\mathrm{d}u_y \tag{6.51}$$

$$P(u_z, u_z + \mathrm{d}u_z) = Z(u_z)\mathrm{d}u_z. \tag{6.52}$$

From the second assumption, we have

$$f_f^{\rm o}(\boldsymbol{u}_f)\mathrm{d}\boldsymbol{u} = X(u_x)\mathrm{d}u_x Y(u_y)\mathrm{d}u_y Z(u_z)\mathrm{d}u_z \tag{6.53}$$

or

$$f_f^{\rm o}(\boldsymbol{u}_f) = X(u_x)Y(u_y)Z(u_z). \tag{6.54}$$

From the preceding assumption, we know that functions X, Y, and Z should have the same form; therefore

$$f_f^{\rm o}(\boldsymbol{u}_f) = X(u_x)X(u_y)X(u_z). \tag{6.55}$$

Noting that $u_f^2 = u_x^2 + u_y^2 + u_z^2$, we can choose an appropriate functional form for X (including symmetry around $u_x = 0$, etc.), such as $X(u_x) = A\ \exp(Bu_x^2)$, then

$$f_f^{\rm o}(\boldsymbol{u}_f) = A^3\exp[B(u_x^2 + u_y^2 + u_z^2)]. \tag{6.56}$$

The coefficients of A and B are determined based on two constraints, namely the conservation of number density of the fluid particles and the kinetic-theory (translational thermal motion) and equipartition of energy definition of the temperature (Table 2.4), i.e.,

$$\int_{\boldsymbol{u}_f} f_f^{\rm o}(\boldsymbol{u}_f)\mathrm{d}\boldsymbol{u}_f = [\int_{-\infty}^{\infty} f_f^{\rm o}(u_x)\mathrm{d}u_x]^3 = [2\int_0^{\infty} f_f^{\rm o}(u_x)\mathrm{d}u_x]^3 = 1$$

$$\text{particle number conservation,} \tag{6.57}$$

$$\frac{m}{3k_{\rm B}}\int_{\boldsymbol{u}_f} u_f^2 f_f^{\rm o}(\boldsymbol{u}_f)\mathrm{d}\boldsymbol{u}_f = \frac{m}{3k_{\rm B}}\langle u_f^2\rangle \quad = T \quad \text{definition of temperature,} \tag{6.58}$$

where

$$\langle u_f^2\rangle^{1/2} \equiv (\frac{3k_{\rm B}T}{m})^{1/2} \quad \text{RMS thermal speed.} \tag{6.59}$$

Note that alternatively $f_f^{\rm o}$ could be defined such that the integral (6.57) yields the total number of fluid particles N_f or the number of fluid particles per unit volume (number density) n_f[†].

Using the preceding gives

$$A = (\frac{m}{2\pi k_{\rm B}T})^{1/2}, \qquad B = -\frac{m}{2k_{\rm B}T}. \tag{6.60}$$

[†] To include the number density of fluid particles n_f in f_f^o, we start with (6.49), written as

$$P = \frac{f_f^o(\boldsymbol{u}_f)\ \mathrm{d}\boldsymbol{u}_f}{n_f}.$$

Then (6.61), (6.59), and (6.57) become (end-of-chapter problem)

$$f_f^{\rm o}(\boldsymbol{u}_f) = n_f(\frac{m}{2\pi k_{\rm B}T})^{3/2}\exp(\frac{-mu_f^2}{2k_{\rm B}T}), \quad \int_0^{\infty} 4\pi u_f^2 f_f^{\rm o}(\boldsymbol{u}_f)\ \mathrm{d}u_f = n_f.$$

This is the same as the momentum integral ($p_f = mu_f$) given as a Chapter 1 problem.

Then the M–B (or Maxwellian) velocity (or momentum) distribution function becomes

$$f_f^{\circ}(\boldsymbol{u}_f) = (\frac{m}{2\pi k_{\rm B}T})^{3/2}\exp(\frac{-m\boldsymbol{u}_f\cdot\boldsymbol{u}_f}{2k_BT}) = (\frac{m}{2\pi k_{\rm B}T})^{3/2}\exp(-\frac{mu_f^2}{2k_{\rm B}T})$$

M–B velocity vector (momentum) probability distribution function. (6.61)

Figure 6.6(a) gives this distribution for N_2 at two temperatures.

To find the speed in a given direction, for example, for the x component of the velocity, we use $\boldsymbol{u}_f = u_{f,x}\boldsymbol{s}_x$.

The distribution of the fluid speed can be obtained by considering the probability of finding the particle in the shell of $u_f < |\boldsymbol{u}_f| < u_f + \mathrm{d}u_f$, which has the volume of $4\pi u_f^2\mathrm{d}u_f$, so $f_f^{\circ}(u_f)\mathrm{d}u_f = f_f^{\circ}(\boldsymbol{u}_f)4\pi u_f^2\mathrm{d}u_f$. Then

$$f_f^{\circ}(u_f) = 4\pi u_f^2 f_f^{\circ}(\boldsymbol{u}_f) = 4\pi(\frac{m}{2\pi k_{\rm B}T})^{3/2}u_f^2\exp(\frac{-mu_f^2}{2k_{\rm B}T})$$

M–B speed probability distribution (occupancy) function. (6.62)

This is referred to as the Maxwell distribution function.

Using (6.62), the average (or mean) speed is defined as [†]

$$\langle u_f\rangle = \int_0^{\infty} f_f^{\circ}(u_f)u_f\mathrm{d}u_f$$

$$= (\frac{8}{\pi}\frac{k_{\rm B}T}{m})^{1/2} \quad \text{average thermal speed.} \tag{6.63}$$

The most probable speed is found from $\partial f_f^{\circ}(u_f) = \partial u_f = 0$ and is $(2k_{\rm B}T/m)^{1/2}$. For N_2 at $T = 300$ K, $m = 4.652\times10^{-26}$ kg, and we have $\langle u_f^2\rangle^{1/2} = 516.8$ m/s and $\langle u_f\rangle = 476.2$ m/s, i.e., $\langle u_f\rangle$ is slightly smaller [by $(8/3\pi)^{1/2}] = 0.92$]. The two thermal speeds are also shown in Figure 6.6(a). The relation with the speed of sound a_s will be give in Section 6.8.

Noting that $E_f = mu_f^2/2$, we have $\mathrm{d}E_f = mu_f\mathrm{d}u_f$; then we have for the energy distribution function

$$f_f^{\circ}(E_f)\mathrm{d}(E_f) = f_f^{\circ}(u_f)\mathrm{d}(u_f) = f_f^{\circ}[(\frac{2E_f}{m})^{1/2}]\frac{\mathrm{d}E_f}{mu_f}$$

$$= 2\pi(\pi k_{\rm B}T)^{-3/2}E_f^{1/2}\exp(-\frac{E_f}{k_{\rm B}T})\mathrm{d}E_f, \tag{6.64}$$

or

$$f_f^{\circ}(E_f^*) = \frac{2}{\pi^{1/2}}E_f^{*1/2}\exp(-E_f^*), \quad E_f^* = \frac{E_f}{k_{\rm B}T},$$

$$\langle E_f\rangle = \int_0^{\infty} E_f^* f_f^{\circ}(E_f)\mathrm{d}E_f = \frac{3}{2}k_{\rm B}T$$

M–B energy probability occupancy distribution function. (6.65)

[†] Note that $\langle u_f\rangle$ is not the net flow, and we use $\overline{u}_f$ for the net flow (Sections 6.11 and 6.12).

This is the dimensionless energy M–B energy distribution function listed in Figure 1.1. The mean (average) energy per fluid particle in translational motion is $3k_{\rm B}T/2$ (Chapter 1 problem).

6.4.3 Inclusion of Gravitational Potential Energy

When a gravitational potential energy is added to the particle energy, i.e., from (6.1), $E_f = E_{f,t} + E_{f,p} = mu_f^2/2 + mgz$, with $\boldsymbol{g}$ pointing against z, the equilibrium distribution function for $\boldsymbol{F} = m\boldsymbol{g}$, (6.61) becomes

$$f_f^{\rm o}(\boldsymbol{u}_f, \boldsymbol{x}) = (\frac{m}{2\pi k_{\rm B}T})^{3/2} \exp{(-\frac{mgz}{k_{\rm B}T})}\exp(\frac{-mu_f^2}{2k_{\rm B}T})$$

$$E_f = \frac{1}{2}mu_f^2 + mgz, \tag{6.66}$$

satisfying the equilibrium distribution (and under steady state) (6.48), i.e., no collision ideal-gas BTE. Then (6.48) becomes

$$\frac{{\rm D}f_f^{\rm o}}{{\rm D}t} = \boldsymbol{u} \cdot \nabla f_e^{\rm o} + m\boldsymbol{g} \cdot \nabla_{\boldsymbol{p}} f_e^{\rm o} = 0. \tag{6.67}$$

6.5 Ideal-Gas Binary Collision Rate and Relaxation Time

Consider the binary collision of ideal-gas particles (hard spheres) 1 and 2, as shown in Figure 6.5. The mass and diameters are m_1 and m_2, d_1 and d_2, and velocities are $\boldsymbol{u}_1$ and $\boldsymbol{u}_2$, or the relative velocity $\boldsymbol{u}_{f,21} = \boldsymbol{u}_{f,2} - \boldsymbol{u}_{f,1}$. The particle collisions are elastic (the energy remains in the translational energy of the colliding particles). The total momentum and kinetic energy of the two colliding particle are conserved, and if in the kinetic energy conservation it is assumed that the particles have the same mass, it simplifies the analysis (the momentum conservation will be applied for the general cases of m_1 and m_2). Then conservations of momentum and kinetic (translational) energy (elastic collision) are applied and they result in (end-of-chapter problem)

$$(m_1\boldsymbol{u}'_{f,1} + m_2\boldsymbol{u}'_{f,2})_{before} = (m_1\boldsymbol{u}_{f,1} + m_2\boldsymbol{u}_{f,2})_{after}$$

$$\text{momentum conservation (elastic collision)} \tag{6.68}$$

$$|\boldsymbol{u}'_{f,21}|_{before} = |\boldsymbol{u}'_{f,2} - \boldsymbol{u}'_{f,1}|_{before} = |\boldsymbol{u}_{f,21}|_{after} = |\boldsymbol{u}_{f,2} - \boldsymbol{u}_{f,1}|_{after}$$

$$\text{kinetic (translational) energy conservation,} \tag{6.69}$$

where subscripts $before$ and $after$ indicate before and after the collision.

We now derive the scattering rate for the case of equilibrium distribution functions. We refer to Figures 6.5 and 6.6, to arrive at the scattering rate per unit volume, along the formulation used in deriving (6.45). The number of particles 2 approaching particles 1 during time interval dt and per unit of volume $u_{f,21}\ \eta\ {\rm d}\phi{\rm d}\eta{\rm d}t$ is

$$n_{f,2}f_{f,2}^{\rm o}u_{f,21}\eta{\rm d}\phi{\rm d}\eta{\rm d}t{\rm d}\boldsymbol{u}_2, \quad u_{f,21} = |\boldsymbol{u}_{f,2} - \boldsymbol{u}_{f,1}|. \tag{6.70}$$

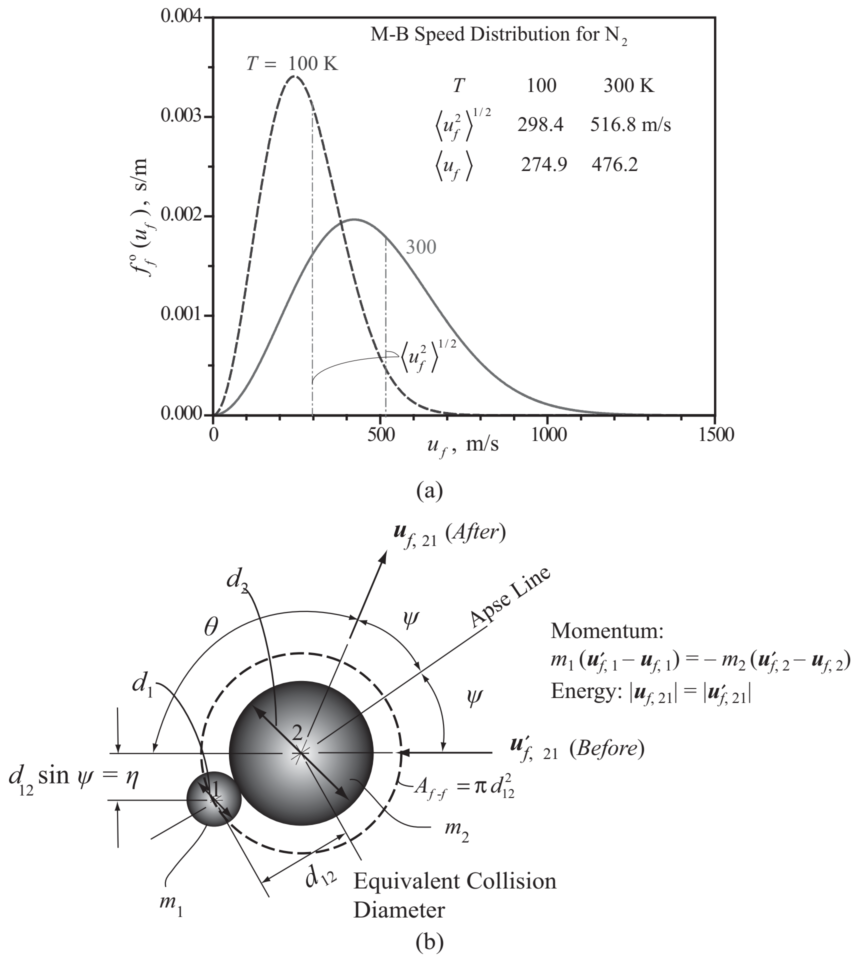
M-B Speed Distribution for N$_2$
T = 100 K
300
T 100 300 K
$\langle u_f^2 \rangle^{1/2}$ 298.4 516.8 m/s
$\langle u_f \rangle$ 274.9 476.2
$\langle u_f^2 \rangle^{1/2}$
$f_f^o(u_f)$, s/m
u_f, m/s
0.000
0.001
0.002
0.003
0.004
0
500
1000
1500
(a)
$\mathbf{u}_{f,21}$ (After)
Apse Line
d_2
θ
ψ
ψ
d_1
2
1
$d_{12} \sin\psi = \eta$
$\mathbf{u}'_{f,21}$ (Before)
$A_{f\text{-}f} = \pi d_{12}^2$
m_2
m_1
d_{12} Equivalent Collision Diameter
Momentum:
$m_1(\mathbf{u}'_{f,1} - \mathbf{u}_{f,1}) = -m_2(\mathbf{u}'_{f,2} - \mathbf{u}_{f,2})$
Energy: $|\mathbf{u}_{f,21}| = |\mathbf{u}'_{f,21}|$
(b)

Figure 6.6. (a) M–B speed distribution function for N$_2$ at $T = 100$ and 300 K. (b) Two-dimensional (in moving coordinates) rendering of binary collision and the collision equivalent diameter ideal-gas particles (hard spheres), showing the geometrical variables appearing in collision integral [460]. The equivalent collision diameter d_{12} is also shown.

The number of particles 1 colliding with particles 2 is similarly

$$n_{f,1} f_{f,1}^{\mathrm{o}} u_{f,21} \eta \mathrm{d}\phi \mathrm{d}\eta \mathrm{d}t \mathrm{d}\boldsymbol{u}_1. \tag{6.71}$$

Then the total number of collisions is [also related to $\partial f_f/\partial t|_s$ in (6.45), dominated by occupancies before collision]

$$\dot{n}_{f,12}\,\mathrm{d}V\,\mathrm{d}t = \int_\eta \int_\phi \int_{\boldsymbol{u}_2} n_{f,1} n_{f,2} f_{f,1}^{\mathrm{o}}\,\mathrm{d}V \mathrm{d}\boldsymbol{u}_1 f_{f,2}^{\mathrm{o}} u_{f,21} \eta \mathrm{d}\phi \mathrm{d}\eta \mathrm{d}t \mathrm{d}\boldsymbol{u}_2 \tag{6.72}$$

or

$$\dot{n}_{f,12} = \int_{\boldsymbol{u}_2} \int_{\boldsymbol{u}_1} \int_\eta \int_\phi n_{f,1} n_{f,2} f_{f,1}^{\mathrm{o}} f_{f,2}^{\mathrm{o}} u_{f,21} \eta \mathrm{d}\phi \mathrm{d}\eta \mathrm{d}\boldsymbol{u}_1 \mathrm{d}\boldsymbol{u}_2. \tag{6.73}$$

We have used equilibrium distribution. Now, we define a collision equivalent diameter (the diameter of the sphere of collision) by using the geometrical variables of Figure 6.6, and we have

$$\eta \equiv d_{12}\sin\psi, \quad \eta\,\mathrm{d}\eta = d_{12}^2\cos\psi\sin\psi\mathrm{d}\psi, \quad d_{12} = (d_1+d_2)/2,$$

$$\text{equivalent collision diameter,} \qquad (6.74)$$

where ψ is related to θ as shown in Figure 6.6. The collision cross-section area $A_{ff} = \pi d_{12}^2$ is determined with the individual collision diameters. Then we have

$$\dot{n}_{f,12} = \int_{\boldsymbol{u}_1}\int_{\boldsymbol{u}_2} n_{f,1}n_{f,2}f_{f,1}^{\mathrm{o}}f_{f,2}^{\mathrm{o}}u_{f,21}d_{12}^2\mathrm{d}\boldsymbol{u}_1\mathrm{d}\boldsymbol{u}_2\int_0^{\pi/2}\cos\psi\sin\psi\mathrm{d}\psi\int_0^{2\pi}\mathrm{d}\phi, \qquad (6.75)$$

where

$$u_{f,21} = |\boldsymbol{u}_{f,1}-\boldsymbol{u}_{f,2}| = (u_{f,1}^2+u_{f,2}^2-2\boldsymbol{u}_{f,1}\cdot\boldsymbol{u}_{f,2})^{1/2}. \qquad (6.76)$$

Note that for a general treatment $\boldsymbol{u}_{f,1}\cdot\boldsymbol{u}_{f,2}$ can be set to zero. The integrations over ψ and θ gives π. The equilibrium M–B distribution function for velocity is given by (6.61) and for particle 1 is

$$f_{f,1}^{\mathrm{o}}(\boldsymbol{u}_f) = (\frac{m_1}{2\pi k_{\mathrm{B}}T})^{3/2}\exp(-\frac{m_1u_f^2}{2k_{\mathrm{B}}T}) \text{ M–B distribution (occupancy) function,} \qquad (6.77)$$

where m_1 is M_1/N_{A}. Then, in the integration of (6.75), for the approximation we have

$$\int_{\boldsymbol{u}_1}\int_{\boldsymbol{u}_2} f_{f,1}^{\mathrm{o}}f_{f,2}^{\mathrm{o}}(u_{f,1}^2+u_{f,2}^2-2\boldsymbol{u}_{f,1}\cdot\boldsymbol{u}_{f,2})^{1/2}\mathrm{d}\boldsymbol{u}_1\mathrm{d}\boldsymbol{u}_2$$

$$\simeq \int_{\boldsymbol{u}_1}\int_{\boldsymbol{u}_2}[(f_{f,1}^{\mathrm{o}}u_{f,1}\mathrm{d}\boldsymbol{u}_1)^2+(f_{f,2}^{\mathrm{o}}u_{f,2}\mathrm{d}\boldsymbol{u}_2)^2-2f_{f,1}^{\mathrm{o}}f_{f,2}^{\mathrm{o}}(\boldsymbol{u}_{f,1}\cdot\boldsymbol{u}_{f,2})\mathrm{d}\boldsymbol{u}_1\mathrm{d}\boldsymbol{u}_2]^{1/2},$$

$$\langle u_{f,i}\rangle = \int_0^\infty f_{f,i}^{\mathrm{o}}u_{f,i}\mathrm{d}u_i = \int_0^\infty f_{f,i}^{\mathrm{o}}(u_{f,i})u_{f,i}\mathrm{d}u_{f,i} \text{ average thermal speed,} \qquad (6.78)$$

where we have used (6.63).

As was mentioned, the contribution from $\boldsymbol{u}_{f,1}\cdot\boldsymbol{u}_{f,2}$ term is zero. Using M–B distribution (6.77), the other two terms each give the square of the average thermal speed (6.63) for each mass group. Then (6.75) becomes (end-of-chapter problem)

$$\dot{n}_{f,12} = 2n_{f,1}n_{f,2}d_{12}^2[\frac{2\pi k_{\mathrm{B}}T(m_1+m_2)}{m_1m_2}]^{1/2}, \qquad (6.79)$$

where $n_{f,1}$ and $n_{f,2}$ are the number density of each particle, and the universal gas constant is defined as $R_g = k_{\mathrm{B}}N_{\mathrm{A}}$, and $M = mN_{\mathrm{A}}$. The preceding is the volumetric rate of collision of particles 1 with particles 2. For a monatomic ideal gas, this volumetric collision rate $\dot{n}_{f\text{-}f}$ becomes

$$\dot{n}_{f\text{-}f} = 4n_f^2d_f^2(\frac{\pi k_{\mathrm{B}}T}{m})^{1/2} = \frac{4\pi^{1/2}d_f^2p^2}{(k_{\mathrm{B}}T)^{3/2}m^{1/2}}$$

$$\text{single component gas, binary collision rate,} \qquad (6.80)$$

Table 6.4. *Estimates of collision diameter and mean free path (at 298 K and 1 atm) for some gaseous molecules (or atoms) modeled as hard spheres [235].*

Gas	λ_f, nm	d_f, Å	Species	λ_f, nm	d_f, Å
Air	64.0	3.72	He	186.2	2.18
Ar	66.6	3.64	Hg	83.2	4.26
CH_4	51.6	4.14	Kr	51.2	4.16
CO_2	41.9	4.59	Ne	132.8	2.59
C_2H_4	36.1	4.95	NH_3	45.1	4.43
C_2H_6	31.5	5.30	N_2	62.8	3.75
HCl	44.4	4.46	O_2	67.9	3.61
H_2	117.7	2.74	Xe	37.6	4.85
H_2O	41.8	4.60			

where we have used n_f from (6.21). The estimated (from measurements of properties such as gas viscosity) collision (hard-sphere) diameter, and the mean free path (at 298 K and 10 atm) for some gaseous molecules are listed in Table 6.4 [235]. Note that He has the smallest collision diameter among the atoms and molecules listed (the collision cross-section area is $A_{ff} = \pi d_f^2$). The mean free path is also the largest for He (we will discuss the mean free path of ideal gas in the following section). For example, for N_2 at $p = 1.013 \times 10^5$ Pa, and $T = 300$ K, we have $n_f = 2.662 \times 10^{25}$ 1/m^3 and $\dot{n}_{f\text{-}f} = 2.031 \times 10^{35}$ 1/m^3-s. We can also define the collision relaxation time as

$$\tau_{f\text{-}f} = \frac{1}{\dot{\gamma}_{f\text{-}f}} = \frac{n_f}{\dot{n}_{f\text{-}f}} = \frac{m^{1/2}}{4\pi^{1/2} d_f^2 (k_{\rm B} T)^{1/2} n_f} = \frac{1}{2^{1/2}\pi d_f^2 n_f \langle u_f \rangle}$$

single component gas binary collision relaxation time, (6.81)

where $\langle u_f \rangle$ is given by (6.63). From (6.81), $\tau_{f\text{-}f}$ increases as m increases, and as d_f, T, and n_f decrease.

Thus for the preceding N_2 example, we have $\tau_{f\text{-}f} = 1.311 \times 10^{-10}$ s.

6.6 Ideal-Gas Mean Free Path and Viscosity

The interparticle collision relaxation time $\tau_{f\text{-}f,i}$ is defined as

$$\tau_{f\text{-}f,i} \equiv \frac{n_{f,i}}{\sum\limits_j \dot{n}_{f,ij}}. \qquad (6.82)$$

Then, using (6.79), we have

$$\tau_{f\text{-}f,i} = \frac{1}{\sum\limits_j 2 n_{f,j} d_{ij}^2 \, [\dfrac{2\pi k_B T (m_i + m_j)}{m_i m_j}]^{1/2}}. \qquad (6.83)$$

The mean free path λ_f is defined as

$$\lambda_{f,i} \equiv \tau_{f\text{-}f,i}\langle u_{f,i}\rangle \text{ mean free path definition,} \tag{6.84}$$

where the average molecular (thermal) speed $\langle u_{f,i}\rangle$ (6.63) is

$$\langle u_{f,i}\rangle = (\frac{8}{\pi}\frac{k_{\rm B}T}{m_i})^{1/2}. \tag{6.85}$$

Then

$$\lambda_{f,i} = \frac{1}{\sum\limits_j \pi n_{f,j} d_{ij}^2 (\frac{m_j}{m_i}+1)^{1/2}}$$

$$\text{mean free path for multicomponent, ideal-gas.} \tag{6.86}$$

For a single component ideal-gas, we have

$$\lambda_f = \frac{1}{2^{1/2}\pi n_f d_f^2} = \frac{1}{2^{1/2} n_f A_{ff}},\ n_f = \frac{p}{k_{\rm B}T}$$

$$\text{single component, ideal-gas mean free path,} \tag{6.87}$$

where A_{ff} is the particle-particle collision cross-section area. Table 6.4 gives the mean free paths for some common gases at $T = 298$ K and $p = 1.013 \times 10^5$ Pa. These values are of the order of 10 nm. For the smaller-diameter-lighter atoms, H_2 and He, they are of the order of 100 nm for N_2 we have $\lambda_f = 62.8$ nm (close to air value). Note that the ratio $\lambda_f/n_f^{1/3} = [2^{1/2}\pi n_f^{2/3} d_f^2]^{-1}$ gives multiples of the average particle distance $n_f^{1/3}$ in distance λ_f, and this for the N_2 examples is 18.8.

Some other useful relationships can be developed. Although the net flow of fluid particles across a planar surface is zero, the flux of particles moving along a direction is not. This flux of particles (through a surface with normal vector $\boldsymbol{s}_n$, where i is along a positive Cartesian coordinate axis) is [73]

$$\begin{aligned} j_{f,i} &= \int_0^\infty n_f u_{f,i} f_f^{\rm o}(u_{f,i}) {\rm d}u_{f,i} \\ &= \int_0^\infty n_f u_{f,i} (\frac{m}{2\pi k_{\rm B}T})^{1/2} \exp(-\frac{m u_{f,i}^2}{2k_{\rm B}T})\ {\rm d}u_{f,i} \quad \text{ideal-gas flux,} \end{aligned} \tag{6.88}$$

where we have used (6.61) for only one direction.

Then the gas mass flux moving in a direction is found by multiplying (6.88) by the mass of each particle and can be related to the average thermal velocity according to [using $\int_0^\infty x \exp(-ax^2){\rm d}x = 1/2a$]

$$\dot{m}_f = m j_{f,i} = \frac{1}{4} m n_f (\frac{8k_{\rm B}T}{\pi m})^{1/2} = \frac{1}{4} m n_f \langle u_f\rangle \text{ ideal-gas directional mass flux.} \tag{6.89}$$

The momentum flux (or stress) is related to the dynamic viscosity according to

$$\tau_{ij} = m n_f \int u_{f,i} u_{f,j} f_f^{\rm o}(\boldsymbol{u}_f) {\rm d}\boldsymbol{u}_f \equiv -\mu_f \frac{\partial \overline{u}_{f,i}}{\partial x_j} \text{ dynamic viscosity.} \tag{6.90}$$

From this the gas viscosity [†] is (end-of-chapter problem)

$$\mu_f = \frac{1}{3} m n_f \langle u_f \rangle \lambda_f = \frac{1}{3} \rho_f \langle u_f \rangle \lambda_f = \frac{1}{3} \rho_f \langle u_f \rangle^2 \tau_{f\text{-}f} = \frac{1}{2^{1/2} 3\pi} \frac{m \langle u_f \rangle}{d_f^2}$$

$$\text{monatomic ideal-gas viscosity.} \qquad (6.91)$$

Note that here we have used the average mean thermal speed $\langle u_f \rangle$ given by (6.63), which is slightly different from the mean thermal speed $\langle u_f^2 \rangle^{1/2}$ given by (6.59).

The pressure is related to the average thermal speed through (6.89)

$$p = n_f k_B T = \frac{1}{3} m n_f \langle u_f \rangle^2 = \frac{1}{3} \rho_f \langle u_f \rangle^2. \qquad (6.92)$$

Then, using $\tau_{f\text{-}f} = \lambda_f / \langle u_f \rangle$, we have $\mu_f = p \tau_{f\text{-}f}$, i.e., dynamic viscosity is the product of pressure and relaxation time for ideal gases.

6.7 Kinetic-Limit Evaporation/Condensation Heat Transfer Rate

The mass flux given by (6.89) is used to determine the theoretical maximum heat flux through a liquid–vapor interface A_{lg}, undergoing condensation–evaporation. For a single-component fluid, having a heat of vaporization–condensation Δh_{lg} (or Δh_{gl}) under ideal conditions of no limit to the supply–removal of heat to the liquid–vapor interface, no limit to the supply of make-up liquid–vapor to the interface, and complete ideal (no resistance) removal of the produced vapor–liquid, the theoretical maximum heat transport rate to the interface is the product of mass flux (6.89) and the heat of phase change, i.e., [155]

$$\frac{\dot{S}_{f\text{-}f,lg,max}}{A_{lg}} = \dot{m}_{lg,max} \Delta h_{lg} = \left(\frac{R_g T_{lg}}{2\pi M}\right)^{1/2} \rho_g \Delta h_{lg}, \qquad (6.93)$$

and similarly for $q_{gl,max}$.

Since the saturation temperature $T_{lg}(p_g)$ increases, ρ_g increases, whereas Δh_{lg} decreases (and vanishes at the critical temperature T_c), and $\dot{S}_{f\text{-}f,lg,max}/A_{lg}$ will reach a maximum as the temperature (or pressure) increases. This is plotted in Figure 6.7(a) for water, ethanol, and refrigerant R-12 as $\dot{S}_{f\text{-}f,lg,max}/A_{lg}$ as a function of the reduced pressure p/p_c. Water has the highest heat of evaporation of any natural and synthesized fluid and, as shown in Figure 6.7(a) it also has the highest peak in $q_{lg,max}$ (over 10^{10} W/m^2).

The ideal assumptions regarding liquid–vapor supply are not realized in practice because of hydrodynamic resistances, and similarly the heat supply–removal that is due to heat transfer resistances, resulting in achievable values much less than

---

[†] Note that the kinematic viscosity is

$$\nu_f = \frac{\mu_f}{\rho_f} = \frac{1}{3} \langle u_f \rangle \lambda_f = \frac{1}{3} \langle u_f \rangle^2 \tau_{f\text{-}f},$$

i.e., product of thermal speed and mean free path.

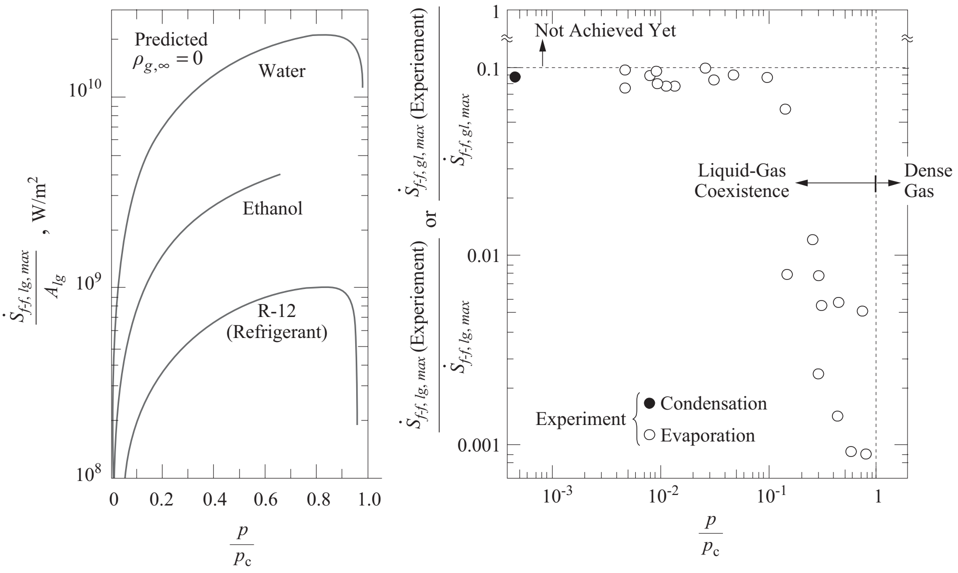

(a) (b)

Figure 6.7. (a) Variations of the theoretical maximum heat flux for evaporation for water, ethanol, and Freon-12 with respect to reduced pressure. (b) Variations of the ratio of the measured maximum heat flux for evaporation and condensation to the theoretical limit, with respect to the reduced pressure [155].

$\dot{S}_{f\text{-}f,lg,max}/A_{lg}$ or $\dot{S}_{f\text{-}f,gl,max}/A_{lg}$. So far, only one-tenth of this limit has been reached in the most exhaustive efforts to reduce these resistances. Figure 6.7(b) shows the experimental results in evaporation and condensation experiments to reach these theoretical maxima.

When the far-field vapor concentration is not zero, i.e, there is no vacuum away from the liquid–vapor interface, the preceding theoretical limit is modified as

$$\frac{\dot{S}_{f\text{-}f,lg,max}}{A_{lg}} = (\frac{R_g}{2\pi M})^{1/2}\Delta h_{lg}(\rho_g T_{lg}^{1/2} - \rho_{g,\infty}T_{lg,\infty}^{1/2}), \qquad (6.94)$$

where $\rho_{g,\infty}$ and $T_{lg,\infty}(p_{g,\infty})$ are the far-field vapor density and temperature (assumed to be the saturation condition).

6.8 Ideal-Gas Thermal Conductivity from BTE

6.8.1 Nonequilibrium BTE and Relaxation-Time Approximation

The fluid particle BTE (6.43), under no external force and written for a fluid particle group $f_{f,i}$ is

$$\frac{\partial f_{f,i}}{\partial t} + \boldsymbol{u}_{f,i} \cdot \nabla f_{f,i} = \frac{\partial f_{f,i}}{\partial t}|_s, \qquad (6.95)$$

This represents the net rate of change in this fluid particle (molecules) population that is due to collision with particles of different positions and momenta.

Continuing with the collision rate, from Figure 6.6 and also from (6.70), the number of particles of group j approaching particle i, during time interval dt with $f^{\text{o}}_{f,j}$ is

$$f_{f,j}|\boldsymbol{u}_{f,ji}|\mathrm{d}t\ \eta\mathrm{d}\eta\mathrm{d}\phi\mathrm{d}\boldsymbol{u}_j, \tag{6.96}$$

where $\boldsymbol{u}_{f,ji}$ is the relative velocity, and η and ϕ are defined as in Figure 6.6. Then we rewrite the right-hand side of (6.45) as

$$\frac{\partial f_{f,i}}{\partial t}|_s = \int_\eta\int_\phi\int_{\boldsymbol{u}_j}(f'_{f,i}f'_{f,j} - f_{f,i}f_{f,j})|\boldsymbol{u}_{f,ji}|\mathrm{d}t\ \eta\mathrm{d}\eta\mathrm{d}\phi\mathrm{d}\boldsymbol{u}_j, \tag{6.97}$$

where the prime indicates distribution functions that restore equilibrium. Under equilibrium, we have $f'_{f,i}f'_{f,j} = f_{f,i}f_{f,j}$.

The collision rate signifies the ability of the system to return to the equilibrium distribution function $f^{\text{o}}_{f,i}$; the larger it is, the faster this return.

As discussed in Section 3.1.4, one of the approximations made in simplifying the collision rate is the perturbation approximation; using a perturbation parameter ϵ and the Taylor series expansion, we have

$$f^{\text{o}}_{f,i} = f_{f,i}|_\epsilon + (\frac{\partial f_{f,i}}{\partial\epsilon}|_\epsilon)\epsilon + (\frac{\partial f^2_{f,i}}{\partial\epsilon^2}|_\epsilon)\frac{\epsilon^2}{2} + \cdots + \tag{6.98}$$

or

$$\frac{\partial f_{f,i}}{\partial\epsilon}|_\epsilon = -\frac{f_{f,i}|_\epsilon - f^{\text{o}}_{f,i}}{\epsilon} \quad \text{for } \epsilon \to 0. \tag{6.99}$$

Using the interparticle collision relaxation time $\tau_{f\text{-}f,i}$ from (6.82), and noting that the collision restores $f^{\text{o}}_{f,i}$, we write

$$\frac{\partial f_{f,i}}{\partial t}|_s = -\frac{f_{f,i} - f^{\text{o}}_{f,i}}{\tau_{f\text{-}f,i}}. \tag{6.100}$$

Next we use this to derive the relation for the ideal-gas thermal conductivity.

6.8.2 Thermal Conductivity

Independent of the BTE, the kinetic theory of gas allows for derivation of a relation between the ideal-gas thermal conductivity k_f and the mean free path [460]. Here we derive the relation from the ideal-gas BTE (6.95); by using a treatment similar to those used in Chapters 4 and 5 for phonons and electrons [440]. The relaxation-time approximation of (6.100) gives

$$\frac{\partial f_f}{\partial t}|_s = -\frac{f_f - f^{\text{o}}_f}{\tau_{f\text{-}f}}, \tag{6.101}$$

where f^{o}_f is the equilibrium M–B particle distribution function, Table 1.2, and $\tau_{f\text{-}f}$ is the momentum-independent fluid particle (gas) thermal collision relaxation time given by (6.82). Then BTE (6.95) becomes

$$\frac{\partial f_f}{\partial t} + \boldsymbol{u}_f \cdot \nabla f_f + \boldsymbol{F}_f \cdot \nabla_{\boldsymbol{p}} f_f = -\frac{f_f - f_f^{\rm o}}{\tau_{f\text{-}f}}, \tag{6.102}$$

where $\tau_{f\text{-}f}$ is assumed to be independent of $\boldsymbol{p}$.

In the presence of a temperature gradient ∇T, from Onsager relation (3.56), there will be a conduction heat flux (given by the Fourier law) (Table 1.1) and for isotropic behavior we have

$$\boldsymbol{q}_k = -k_f \nabla T, \;\; \boldsymbol{q}_{k,j} = -k_f \frac{\partial T}{\partial x_j}, \tag{6.103}$$

where k_f is the gas thermal conductivity. With no net motion, heat flow is due to the thermal motion and deviation of the energy distribution from the thermal equilibrium distribution. Similar to (4.93) and (5.120), the conduction heat flux is also given in terms of the molecular energy flux that is due to a deviation in population $f_f^{'} = f_f - f_f^{\rm o}$ as

$$\boldsymbol{q}_k = \frac{1}{(2\pi\hbar)^3}\int E_f \boldsymbol{u}_f f_f^{'} {\rm d}\boldsymbol{p}_f = \frac{1}{(2\pi\hbar)^3}\int E_f \boldsymbol{u}_f (f_f - f_f^{\rm o}) {\rm d}\boldsymbol{p}_f, \tag{6.104}$$

where we are using the fluid particle momentum (instead of the wave vector). Under the steady-state condition ($\partial f_f/\partial t = 0$); they (6.102) becomes

$$\boldsymbol{u}_f \cdot \nabla f_f = -\frac{f_f - f_f^{\rm o}}{\tau_{f\text{-}f}}. \tag{6.105}$$

Now we linearize the $\boldsymbol{u}_f \cdot \nabla f_f$ term by approximating f_f with $f_f^{\rm o}$, i.e., using the local equilibrium distribution condition, $\nabla f_f \simeq \nabla f_f^{\rm o}$. Then, we expand $\nabla f_f^{\rm o}$ in terms of ∇T. We use the classical M–B $f_f^{\rm o}$, i.e., the equilibrium distribution function for energy given in Table 1.2 as

$$f_f^{\rm o} = \exp(-\frac{E_f - \mu}{k_{\rm B} T}), \quad E_f = \frac{1}{2} m u_f^2, \tag{6.106}$$

where μ is the chemical potential.

Next, expanding $f_f^{\rm o}$, using E_f, T, and μ, we have

$$\begin{aligned}
\boldsymbol{u}_f \cdot \nabla f_f^{\rm o} &= \boldsymbol{u}_f (\frac{\partial f_f^{\rm o}}{\partial E_f}\nabla E_f + \frac{\partial f_f^{\rm o}}{\partial T}\nabla T + \frac{\partial f_f^{\rm o}}{\partial \mu}\nabla \mu) \\
\frac{\partial f_f^{\rm o}}{\partial T} &= -\frac{E_f - \mu}{T}\frac{\partial f_f^{\rm o}}{\partial E_f} \\
\frac{\partial f_f^{\rm o}}{\partial \mu} &= -\frac{\partial f_f^{\rm o}}{\partial E_f} \\
\nabla E_f &= 0.
\end{aligned} \tag{6.107}$$

Then

$$\begin{aligned}\boldsymbol{u}_f \cdot \nabla f_f^{\mathrm{o}} &= -\frac{\partial f_f^{\mathrm{o}}}{\partial E_f}\, \boldsymbol{u}_f \cdot (\frac{E_f}{T}\nabla T - \frac{\mu}{T}\nabla T + \nabla \mu) \\ &= -\frac{\partial f_f^{\mathrm{o}}}{\partial E_f}\, \boldsymbol{u}_f \cdot \nabla T \frac{1}{T}[E_f - (\mu - T\frac{\mu}{T}|_p)],\end{aligned} \tag{6.108}$$

where p is the pressure.

We now use the thermodynamics relation

$$\mu - T\frac{\partial \mu}{\partial T}|_p = h, \tag{6.109}$$

where h is the specific enthalpy. Then (6.108) becomes

$$\boldsymbol{u}_f \cdot \nabla f_f^{\mathrm{o}} = -\frac{\partial f_f^{\mathrm{o}}}{\partial E_f}\frac{E_f - h}{T}(\boldsymbol{u}_f \cdot \nabla T). \tag{6.110}$$

Also, using (6.105), we have

$$\frac{\partial f_f^{\mathrm{o}}}{\partial E_f} = -\frac{f_h^{\mathrm{o}}}{k_{\mathrm{B}} T}. \tag{6.111}$$

Using these, the Boltzmann transport equation (6.102) becomes

$$f_f^{\mathrm{o}}\frac{E_f - h}{k_{\mathrm{B}} T^2}(\boldsymbol{u}_f \cdot \nabla T) = -\frac{f_f - f_f^{\mathrm{o}}}{\tau_{f\text{-}f}}\ , \tag{6.112}$$

or

$$\frac{f_f - f_f^{\mathrm{o}}}{f_f^{\mathrm{o}}} = \frac{f_f'}{f_f^{\mathrm{o}}} = -\frac{1}{k_{\mathrm{B}} T^2}\tau_{f\text{-}f}(E_f - h)(\boldsymbol{u}_f \cdot \nabla T). \tag{6.113}$$

The thermal conductivity is found by use of the deviation $f_f^{'}$. We write conduction flux (6.104) for direction j and arrive at

$$\begin{aligned} q_{k,j} &= \frac{1}{(2\pi\hbar)^3}\int u_{f,j} E_f f_f' \mathrm{d}\boldsymbol{p}_f \\ &= -\frac{\tau_{f\text{-}f}}{(2\pi\hbar)^3 k_{\mathrm{B}} T^2}\int u_{f,j} E_f (E_f - h) u_{f,j} f_f^{\mathrm{o}} \frac{\partial T}{\partial x_j}\mathrm{d}\boldsymbol{p}_f,\end{aligned} \tag{6.114}$$

where we have used the energy-independent τ_{f-f} (6.81), i.e., unlike the treatment of the phonon (4.108) and electron (5.131). We replace the velocity with E_f and define the integral as [similar to (5.63)]

$$\begin{aligned} q_{k,j} &= -\frac{2 n_f \tau_{f\text{-}f}}{3 m k_{\mathrm{B}} T^2}\langle (E_f - h) E_f^2 \rangle \frac{\partial T}{\partial x_j},\quad n_f = \frac{1}{\hbar^3}\int f_f^{\mathrm{o}} \mathrm{d}\boldsymbol{p}_f \\ &\equiv -k_f \frac{\partial T}{\partial x_j},\end{aligned} \tag{6.115}$$

where from the isotropic assumption (6.57) we have equal translational energy in all three directions, leading to

$$u_{f,j}^2 = \frac{u_f^2}{3} = \frac{2E_f}{3m}. \tag{6.116}$$

We have used the $f_f^{\rm o}$ form that includes n_f. We will subsequently evaluate the integral shown by $\langle\ \rangle$. Note that we have introduced the particle number conservation also through n_f by using (5.64) (footnote of Section 6.4.2). We have used (6.103) in (6.115). We now

$$k_f = \frac{2}{3}\frac{n_f \tau_{f\text{-}f}}{m k_{\rm B} T^2}\langle (E_f - h)E_f^2\rangle. \tag{6.117}$$

Next the specific enthalpy $h = E_f + pv_f = 5k_{\rm B}T/2$ is used for monatomic gases. Then

$$E_f - h = -k_{\rm B}T. \tag{6.118}$$

Now, evaluating the integral, we start with

$$\langle (E_f - h)E_f^2\rangle$$

$$= \frac{1}{(2\pi\hbar)^3 n_f}\int (E_f - \frac{5}{2}k_{\rm B}T)E_f^2 \exp[-\frac{(E_f-\mu)}{k_{\rm B}T}]\mathrm{d}\boldsymbol{p}_f \quad \text{monatomic gas.} \tag{6.119}$$

Then, we convert the momentum differential to energy differential using $E_f = p_f^2/2m$, i.e.,

$$\mathrm{d}\boldsymbol{p}_f = 4\pi p_f^2 \mathrm{d}p_f = 2\pi m^2 E_f \frac{m}{(2E_f)^{1/2}}\mathrm{d}p_f = \frac{8\pi}{2^{1/2}} m^{3/2} E_f^{1/2} \mathrm{d}E_f. \tag{6.120}$$

Note that in (6.114) similar results would have been found if we had used (6.64) directly and performed the integration over the fluid energy. This shows the consistency of the classical limit for energy distribution function (6.106).

In a constant pressure process, we take $\mu = \mu_{\rm o} = 0$, and we have

$$\langle (E_f - h)E_f^2\rangle = \langle E_f^3\rangle - h\langle E_f^2\rangle. \tag{6.121}$$

Now, returning to the averages similar to (5.113), we have the general form

$$\langle E_f^n\rangle \equiv \frac{\displaystyle\int_{E_f} f_f^{\rm o} E_f^n \mathrm{d}\boldsymbol{p}_f}{\displaystyle\int_{E_f} f_f^{\rm o}\mathrm{d}\boldsymbol{p}_f} = \frac{\displaystyle\int_{E_f} f_f^{\rm o} E_f^n \frac{8\pi}{2^{1/2}} m^{3/2} E_f^{1/2}\mathrm{d}E_f}{\displaystyle\int_{E_f} f_f^{\rm o} \frac{8\pi}{2^{1/2}} m^{3/2} E_f^{1/2}\mathrm{d}E_f}$$

$$= \frac{\displaystyle\int_{E_f} E_f^{n+1/2}\exp(-E_f/k_{\rm B}T)\mathrm{d}E_f}{\displaystyle\int_{E_f} E_f^{1/2}\exp(-E_f/k_{\rm B}T)\mathrm{d}E_f} = \frac{\Gamma(n+1/2+1)/(k_{\rm B}T)^{-(n+1/2+1)}}{\Gamma(1/2+1)/(k_{\rm B}T)^{-3/2}}$$

$$= (k_{\rm B}T)^n \frac{\Gamma(n+3/2)}{\Gamma(3/2)}, \tag{6.122}$$

where the Γ function is defined in (5.114).

Again, note that we have used classical limit (6.106). Then,

$$
\begin{aligned}
\langle E_f^3\rangle - h\langle E_f^2\rangle &= (k_\mathrm{B}T)^3\frac{\Gamma(9/2)}{\Gamma(3/2)} - \frac{5}{2}k_\mathrm{B}T(k_\mathrm{B}T)^2\frac{\Gamma(7/2)}{\Gamma(3/2)}\\
&= (k_\mathrm{B}T)^3(\frac{105}{8} - \frac{5}{2}\times\frac{15}{4})\\
&= \frac{15}{4}(k_\mathrm{B}T)^3, \qquad (6.123)
\end{aligned}
$$

where the values of $\Gamma(9/2)$, $\Gamma(7/2)$ and $\Gamma(3/2)$ are also given in (5.114).

Next, we use this in (6.117) to arrive at

$$
\begin{aligned}
k_f &= \frac{2}{3}\frac{n_f\tau_{f\text{-}f}}{mk_\mathrm{B}T^2}\frac{15}{4}(k_\mathrm{B}T)^3 = \frac{5}{2}\frac{n_f\tau_{f\text{-}f}}{mk_\mathrm{B}T^2}(k_\mathrm{B}T)^3\\
&= \frac{5}{2}k_\mathrm{B}\,\frac{n_f\tau_{f\text{-}f}}{m}k_\mathrm{B}T = \frac{1}{3}\rho_f c_{p,f}\langle u_f^2\rangle\tau_{f\text{-}f}, \qquad (6.124)
\end{aligned}
$$

where $\rho_f = n_f m$ is the density of the gas (kg/m^3), $c_{p,f}$ is the specific heat capacity (J/kg-K), and $\langle u_f^2\rangle^{1/2}$ is the RMS thermal velocity $(3k_\mathrm{B}T/m)^{1/2}$ given by (6.84), which is also simply found from the equipartition of translational energy, from $m\langle u_f^2\rangle/2 = 3k_\mathrm{B}T/2$.

Similar to (6.84), the product of $\tau_{f\text{-}f}\langle u_f^2\rangle^{1/2} = \lambda_f$ is the mean free path of the colliding gas molecules (but here we use the RMS thermal velocity). Then by using this relation, we find that the the preceding expression for the gas thermal conductivity becomes

$$
k_f = \frac{1}{3}\rho_f c_{p,f}\langle u_f^2\rangle^{1/2}\lambda_f \quad \text{monatomic ideal gas}, \qquad (6.125)
$$

which is the common form of the result from the so-called elementary kinetic theory[†] (end-of-chapter problem), except for the appearance of $c_{p,f}$ instead of $c_{v,f}$, i.e.,

$$
k_f = \frac{1}{3}\rho_f c_{v,f}\langle u_f^2\rangle^{1/2}\lambda_f = \frac{1}{3}n_f c_{v,f}\langle u_f^2\rangle^{1/2}\lambda_f, \qquad (6.126)
$$

where in the second expression we have used $c_{v,f}$ per fluid particle (Section 6.2). Note that n_f, $\langle u_f^2\rangle^{1/2}$, and λ_f are given by (6.59) and (6.87), and $c_{v,f}$ is given by (6.25) and (6.22), or (6.23) or (6.24). The kinetic-theory-based treatment of the thermal conductivity (end-of-chapter problem) uses $\langle u_f\rangle$ in place of $\langle u_f^2\rangle^{1/2}$, as was used in the derivation of μ_f relation (6.91).

[†] Note that thermal diffusivity of gas is [using (6.125)]

$$
\alpha_f = \frac{k_f}{\rho_f c_{p,f}} = \frac{1}{3}\langle u_f^2\rangle^{1/2}\lambda_f = \frac{1}{3}\langle u_f^2\rangle\tau_{f\text{-}f},
$$

i.e., similar to the kinematic viscosity, it is the product of thermal speed and mean free path. Also, thermal effusivity of gas is

$$
(\rho_f c_{p,f}k_f)^{1/2} = (\frac{1}{3}\rho_f^2 c_{p,f}^2\langle u_f^2\rangle\tau_{f\text{-}f})^{1/2}.
$$

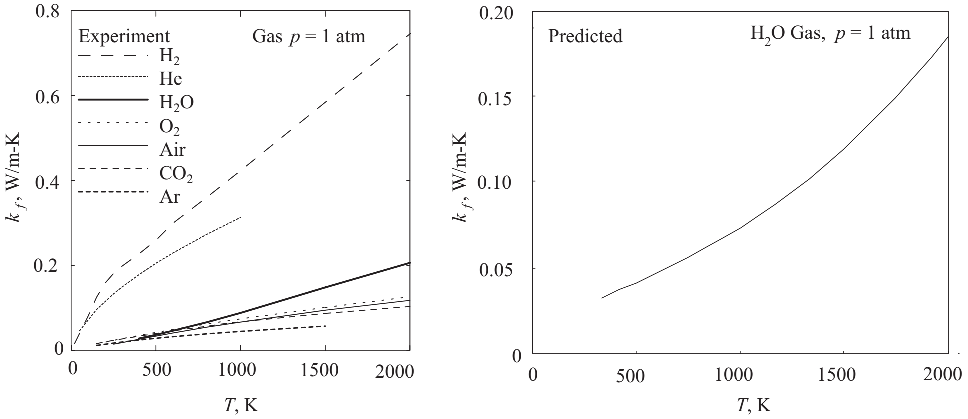

(a) (b)

Figure 6.8. (a) Variations of measured thermal conductivity of some typical gases with respect to temperature [465]. (b) Variations of predicted thermal conductivity of gaseous H_2O, using the mean free path model (6.128), with respect to temperature.

Note the similarity also with the relation for the gas viscosity, (6.91). Also, note that $\mu_f c_{p,f}/k_f = \mathrm{Pr}$, i.e., the gas Prandtl number, which is equal to unity when (6.126) is used. The Prandtl number of gases is nearly unity [231]. The speed of sound for an ideal gas is

$$a_s \equiv (\frac{\partial p}{\partial \rho_f})_s^{1/2} = (\frac{c_{p,f}}{c_{v,f}}\frac{\partial p}{\partial \rho_f}|_T)^{1/2} = (\frac{c_{p,f}}{c_{v,f}}\frac{E_p}{\rho_f})^{1/2} = (\frac{c_{p,f}}{c_{v,f}}\frac{R_g}{M}T)^{1/2}$$

$$= (\frac{c_{p,f}}{3c_{v,f}})^{1/2}\langle u_f^2\rangle^{1/2} = (\frac{\gamma}{3})^{1/2}\langle u_f^2\rangle^{1/2}, \quad \gamma = \frac{c_{p,f}}{c_{v,f}}. \qquad (6.127)$$

Note that $\rho_f^{-1}\partial\rho_f/\partial p|_T$ is the isothermal compressibility $(1/E_p)$ (Table 3.11), and we have used the Maxwell relations among thermodynamic properties [73].

Note that the average thermal speed is defined in (6.63) and is related to $\langle u_f^2\rangle^{1/2}$ through $\langle u_f\rangle = (8/3\pi)^{1/2}\langle u_f^2\rangle^{1/2}$. Also, note that for N_2 at $T = 300$ K, $a_s = 353.1$ m/s. For polyatomic gases a more rigorous derivation gives [277], along with using a_s, i.e.,

$$k_f = \frac{1}{3}\rho_f\frac{15\pi}{32}(c_{v,f} + \frac{9}{4}\frac{R_g}{M})(\frac{8}{\pi\gamma})^{1/2}a_s\lambda_f \quad \text{polyatomic, ideal gas,} \qquad (6.128)$$

where $c_{v,f} = 3R_f/2M$, and for monatomic gases the coefficient $15\pi/32$ and the term $9R_g/4M$ are dropped. The mean free path is given by (6.87). Figure 6.8(a) shows the variations of measured thermal conductivity of some typical gases with respect to temperature. The gas conductivity increases with temperature, as the speed of sound increases with temperature. Figure 6.8(b) shows the predicted thermal conductivity of gaseous H_2O as a function of temperature using (6.128).

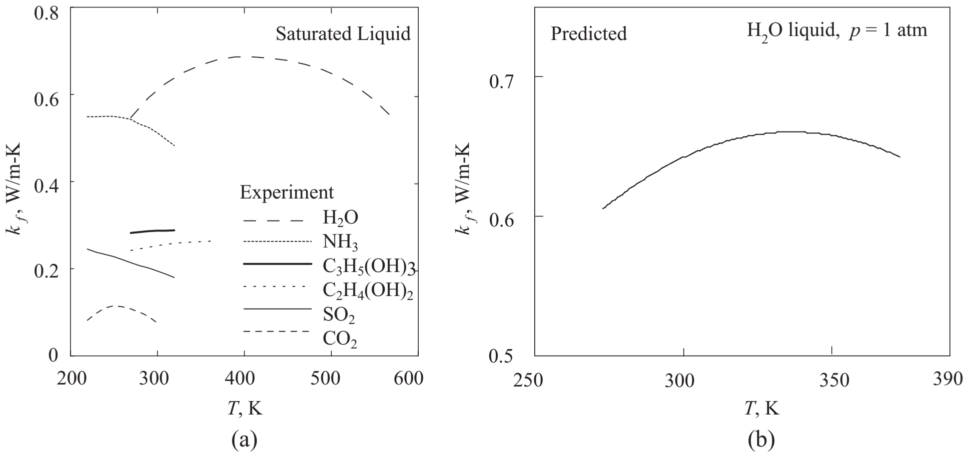

Figure 6.9. (a) Variations of the measured thermal conductivity of some typical (nonmetallic) liquids with respect to saturation temperature [465]. (b) Variations of the predicted thermal conductivity of liquid H_2O with respect to temperature at $p = 1$ atm.

6.9 Liquid Thermal Conductivity from Mean Free Path and Molecular Dynamics

Figure 6.9(a) shows variations of measured thermal conductivity of some typical (single component nonmetallic) liquids with respect to saturation temperature. Note that generally for a given pressure, there is a small temperature range over which there is liquid phase. The liquid metals have a thermal conductivity close to their solid-state values (e.g., Hg), as shown in Figure 5.18(a).

Over the range of equilibrium liquid-phase existence (saturation), the variations in k_f are not very large. The liquid thermal conductivity can be predicted with the result from the Bridgman kinetic theory [59].

As was mentioned in Section 1.1.4, liquid particles collide at a much higher rate than the gases. Therefore, we expect a smaller mean free path for liquids compared with gases. In this theory, Bridgman [41, 59] theory assumes a simple cubic arrangement of atoms, with a spacing of $a = (1/n_f)^{1/3} = (M/\rho_f N_\mathrm{A})^{1/3}$, using (1.11). Bridgman then approximates the fluid thermal conductivity relation (6.126) as

$$k_f = \frac{1}{3}\rho_f c_{v,f}\langle u_f^2\rangle^{1/2}\lambda_f = \rho_f c_{v,f} a_s n_f^{-1/3} \quad \text{nonmetallic liquid conductivity}, \tag{6.129}$$

by using the mean free path as nearly equal to the fluid particle spacing, i.e., $\lambda_f = 3n_f^{-1/3}$, and the RMS thermal speed equal to the speed of sound a_s [defined in (6.127)]. Assuming rigid spheres, the heat capacity is taken as $Mc_{v,f} = 3R_g$, although for liquid $c_{v,f}$ can be larger. Using this in (6.129), we have

$$\begin{aligned} k_f &= \rho_f \frac{3R_g}{M} a_s (\frac{M}{\rho_f N_\mathrm{A}})^{1/3} \\ &= \rho_f \frac{3R_g}{M} (\frac{c_{p,f}}{c_{v,f}} \frac{\partial \rho_f}{\partial p}|_T)^{1/2} (\frac{M}{\rho_f N_\mathrm{A}})^{1/3}. \end{aligned} \tag{6.130}$$

Rearranging this, we have

$$\begin{aligned} k_f &= \frac{3R_g}{N_{\rm A}^{1/3}}\frac{\rho_f^{2/3}}{M^{2/3}}(\frac{c_{p,f}}{c_{v,f}}\frac{1}{\rho_f\kappa_f})^{1/2} \\ &= \frac{3R_g}{N_{\rm A}^{1/3}}\frac{\rho_f^{1/6}}{M^{2/3}}(\frac{c_{p,f}}{c_{v,f}}\frac{1}{\kappa_f})^{1/2},\ \kappa_f = \frac{1}{\rho_f}\frac{\partial \rho_f}{\partial p}|_T = \frac{1}{E_p} \\ &\qquad \text{nonmetallic liquid conductivity.} \end{aligned} \qquad (6.131)$$

For example, for water at $T = 300$ K, this gives $k_f = 0.6437$ W/m-K by using $\kappa_f = 4.46 \times 10^{-10}$ Pa^{-1}, which is close to the experimental result of 0.613 W/m-K [232]. Note that for liquids, $c_{p,f} \simeq c_{v,f}$. Figure 6.9(b) shows the variations of the predicted thermal conductivity of liquid water with respect to temperature for $p =$ 1 atm (this limits the temperature range to freezing and boiling temperatures at this pressure). The temperature dependence is through ρ_f, $c_{p,f}/c_{v,f}$, and κ_f, where $\rho_f(T)$ decreases monotonically, $(c_{p,f}/c_{v,f})(T)$ increases monotonically, and $\kappa_f(T)$ has a minimum in the middle of the temperature range.

Equilibrium classical MD simulations and the Green-Kubo integration of the heat current correlation function $\langle \boldsymbol{q}(t) \cdot \boldsymbol{q}(0)\rangle$ (Sections 3.6 and 4.12 and 4.13) have been made in the microcanonical ensemble for water at $T = 300$ and 255 K [31]. They find good agreement with the experimental results. They use the extended simple point charge (SPC/E) intermolecular potential model of H_2O. They find that large high-frequency oscillation of $\langle \boldsymbol{q}(t) \cdot \boldsymbol{q}(0)\rangle$ is a distinctive feature of water around 30 THz. Similar to the results for crystals, they find two low-frequency exponential-like decay modes with first being faster (short range), with a decay rate of the order of the collision time 0.03 ps and temperature independent. The second decay is slower and temperature dependent. The nonequilibrium classical MD simulations of water in [393] predict the anomalous initial increase of the thermal conductivity with temperature and the thermal conductivity maximum shown in Figure 6.9(b). They also use the TIP(transferable intermolecular potential)4P/2005 intermolecular potential model which yields similar results. This and SPC/E are rigid non-polarizable empirical models.

The theory of electrical conductivity of liquid metals and their alloys is given in [136]. The electron mean free path is only a few atomic separation distance long and the σ_e relation includes the atomic structure through the structure factor. For liquid metals the heat transfer is dominated by charge (electron) transport, and from the electric thermal conductivity, the Wiedemann-Franz law (5.193) with the Lorenz number can be used to predict the thermal conductivity of liquid metals [161]. The electrical conductivity of liquid metals has been calculated using *ab initio* MD and the Kubo–Greenwood relation in [343].

6.10 Effective Conductivity with Dispersed Particles in Thermal Motion

The derivation of the Brownian diffusion by Einstein and that by Langevin are summarized in [93]. These are given here along with a simple effective thermal conductivity model.

6.10.1 Langevin Derivation of Brownian Diffusion

A spherical particle of diameter d_s and mass m_s dispersed in a viscous liquid (viscosity μ_f) under isothermal (T_f) conditions and under the thermal motion (no other driving force) experiences displacement as governed by the Langevin stochastic particle dynamics equation [93] given in Table 3.7 for $\boldsymbol{F}_{k,s} = 0$, i.e.,

$$m_s \frac{d^2x}{dt^2} = -3\pi\mu_f d_s \frac{dx}{dt} + F(t) \quad \text{one-dimensional Langevin equation}, \tag{6.132}$$

where the hindering force is the viscous force on the solid, spherical particle (called the Stokes force). This force is $3\pi\mu_f d_s u_s$, where u_s is the particle speed $\mathrm{d}x/\mathrm{d}t$[†]. In (6.132) $F(t)$ is the stochastic (thermal) driving force which gives the average particle velocity through this kinetic energy as $m_s\langle u_s^2\rangle/2 = 3k_\mathrm{B}T/2$ and also through the force correlation given in Table 3.7. Multiplying (6.132) by x and using the chain rule, we have

$$\frac{m_s}{2}\frac{\mathrm{d}^2x^2}{\mathrm{d}t^2} - m_s(\frac{\mathrm{d}x}{\mathrm{d}t})^2 = -\frac{3}{2}\pi\mu_f d_s \frac{\mathrm{d}x^2}{\mathrm{d}t} + F(t)x(t). \tag{6.133}$$

Now taking the ensemble average over a $\langle\rangle$ (Section .3)and assuming that $\langle F(t)x(t)\rangle = 0$, i.e., the instantaneous thermal force and the instantaneous particle positions are not correlated, then

$$\frac{m_s\langle u_s^2\rangle}{2} = \frac{m_s}{2}\frac{\mathrm{d}}{\mathrm{d}t}\langle\frac{\mathrm{d}x^2}{\mathrm{d}t}\rangle + \frac{3}{2}\pi\mu_f d_s\langle\frac{\mathrm{d}x^2}{\mathrm{d}t}\rangle = m_s\langle(\frac{\mathrm{d}x}{\mathrm{d}t})^2\rangle. \tag{6.134}$$

Noting that, from the equipartition of energy, we have

$$\frac{1}{2}m_s\langle(\frac{\mathrm{d}x}{\mathrm{d}t})^2\rangle \equiv \frac{1}{2}m_s\langle u_s^2\rangle \equiv \frac{3}{2}k_\mathrm{B}T_f, \tag{6.135}$$

then we have

$$\frac{m_s}{3\pi\mu_f d_s}\frac{\mathrm{d}}{\mathrm{d}t}\langle\frac{\mathrm{d}x^2}{\mathrm{d}t}\rangle + \langle\frac{\mathrm{d}x^2}{\mathrm{d}t}\rangle = \frac{2\times 3k_\mathrm{B}T_f}{3\pi\mu_f d_s}. \tag{6.136}$$

The solution to (6.136) is

$$\langle\frac{\mathrm{d}x^2}{\mathrm{d}t}\rangle = \frac{2\times 3k_\mathrm{B}T_f}{3\pi\mu_f d_s} + Ae^{-\frac{3\pi\mu_f d_s}{m_s}t}. \tag{6.137}$$

The viscous relaxation time τ_μ is defined as

$$\tau_\mu = \frac{m_s}{3\pi\mu_f d_s}, \tag{6.138}$$

which is independent of temperature (except through μ_f), and it is of the order of 10^{-9} s for small particles in liquids.

Then for $t/\tau_\mu \gg 1$, we have

$$\langle\frac{\mathrm{d}x^2}{\mathrm{d}t}\rangle = \frac{2\times 3k_\mathrm{B}T_f}{3\pi\mu_f d_s}, \quad \frac{t}{\tau_\mu} \gg 1. \tag{6.139}$$

[†] This gives the Stokes drag coefficient equal to 24/Re_d, where the Reynolds number is $\mathrm{Re}_d = \rho_f u_s d_s/\mu_f$ [232].

Using x_o at $t = 0$, the integration gives

$$\langle x^2 \rangle - \langle x_\mathrm{o}^2 \rangle = \frac{2 \times 3 k_\mathrm{B} T_f}{3\pi \mu_f d_s} t = \frac{2 \times 3 k_\mathrm{B} T_f}{m_s} t \equiv \langle \delta^2 \rangle, \tag{6.140}$$

where $\langle \delta^2 \rangle^{1/2}$ is the RMS of the displacements of a particle in Brownian motion. The more general solution is (3.65)[†]

The Einstein (Brownian) diffusion coefficient is defined through

$$\langle \delta^2 \rangle \equiv 6 D_\mathrm{E} t, \tag{6.141}$$

or

$$D_\mathrm{E} = \frac{k_\mathrm{B} T_f}{3\pi \mu_f d_s} \quad \text{Einstein (Brownian) diffusion coefficient.} \tag{6.142}$$

As an example, for $d_s = 2$ μm particle in water at 300 K ($\mu_f = 9.2 \times 10^{-4}$ Pa-s), $D_\mathrm{E} = 0.24$ $\mu\mathrm{m}^2/s$, and for $d_s = 2$ nm gives $D_\mathrm{E} = 240$ $\mu\mathrm{m}^2/s$ (i.e., $\langle \delta^2 \rangle^{1/2} = 38$ nm in one second). This shows the solid particle diffuses through liquid more effectively when temperature is raised, or liquid viscosity or particle diameter is decreased.

From (6.141), the root-mean-square displacement in any direction is $(2 D_\mathrm{E} t)^{1/2}$. The Brownian diffusion time (time it takes for a displacement of $d_s/2^{1/2}$) is defined as

$$\tau_\mathrm{E} = \frac{d_s^2}{4 D_\mathrm{E}} = \frac{3\pi \mu_f d_s^3}{4 k_\mathrm{B} T} \quad \text{Brownian diffusion time,} \tag{6.143}$$

which becomes very long as the solid particle diameter increases.

6.10.2 Thermal Relaxation Time and Effective Fluid Thermal Conductivity

In enhanced thermal conductivity liquids, due to the suspension of nanoparticles, the lack of thermal equilibrium between the particle and the liquid (in a temperature gradient ∇T_f field) also plays a role [213].

Here we take an alternative and simple approach. The effective conductivity of liquids with particle suspensions $\langle k_f \rangle$ may be expressed as a parallel (or additive) contribution of conductivities, i.e.,

$$\langle k_f \rangle = k_f + k_{f,\mathrm{E}} \quad \text{dilute suspension,} \tag{6.144}$$

where k_E is the contribution that is due to the Brownian motion (nanoparticle concentration is low enough that interparticle collisions are rate) of constituents and increases the ability of the particles to diffuse, store heat, and transfer heat through its surface (a continuum or semicontinuum concept). The

---

[†] Note that the velocity distribution follows the M–B relation (6.61) for $t \to \infty$ [323], i.e.,

$$\langle u_f^2 \rangle = \frac{3 k_\mathrm{B} T}{m} + (u_\mathrm{o}^2 - \frac{3 k_\mathrm{B} T}{m}) e^{-2t/\tau_\mu},$$

where u_o is the velocity at $t = 0$. This shows $\langle u_f^2 \rangle$ reaches equipartition as $t \to \infty$.

storage/boundary–resistance/surface–convection is represented by thermal relaxation time (6.82) $\tau_\alpha = \lambda_s/\langle u_s^2\rangle^{1/2}$, where λ_s is the thermal mean free path of the solid particle. Then, using (6.126), $k_{f,\mathrm{E}}$ can be written as

$$\begin{aligned} k_{f,\mathrm{E}} &= \frac{1}{3} n_s c_{v,s} \langle u_s^2\rangle^{1/2}\lambda_s = \frac{1}{3} n_s c_{v,s}\langle u_s^2\rangle \tau_\alpha, \ \ \tau_\alpha = R_t c_{v,s} \\ &= \frac{1}{3} n_s c_{v,s}\langle u_s^2\rangle R_t c_{v,s} = \frac{\pi d_s^3}{18}\rho_s c_{v,s}^2 \frac{3k_\mathrm{B}T}{m_s} R_t, \end{aligned} \tag{6.145}$$

where n_s is the number of particles per unit volume, $c_{v,s}$ is its heat capacity per particle [(4.66), the classical limit for a monatomic solid $3Nk_\mathrm{B}$ for a crystal with $T > T_\mathrm{D}$], $N = N_\mathrm{A}\rho_s \pi d_s^3/6M_s$, where ρ_s and M_s are the density and molecular weight of solid particles. N is the number of atoms in the particle, and R_t is the sum of the internal and external resistances to heat flow (heat loss from the particle) [232]. As n_s increases, the mean free path of the solid particle λ_s will be limited by solid interparticle collisions.

Because of the coalescing of the solid particles (as in colloids in general), solid particle clusters are formed (i.e., not monodispersed). The cluster form favors the dominance of the internal resistance due to relatively small cluster effective conductivity $\langle k\rangle_c$. This low value of $\langle k\rangle_c$ is in part due to the size effect in the thermal conductivity of the solid particles [Section 4.9.4(A)]. Also, note that, where clusters are formed, $\langle d\rangle_c$, $\langle n\rangle_c$, and $\langle c_v\rangle_c$ should be used in (6.145), which increases the diameter and reduces the number of particles per unit volume. For a sphere (here the cluster) to lose a substantial amount of its heat content, the Fourier number should be nearly 0.1 [232], i.e.,

$$\mathrm{Fo}_d = \frac{4\langle\alpha\rangle_c \tau_\alpha}{\langle d\rangle_c^2} = \frac{4\langle k\rangle_c\tau_\alpha}{\langle\rho c_p\rangle_c \langle d_s\rangle_c^2} = 0.1, \tag{6.146}$$

or the thermal relaxation (diffusion) time (Table 3.12) given by

$$\tau_\alpha = 0.1\frac{\langle\rho c_p\rangle_c\langle d\rangle_c^2}{4\langle k\rangle_c} = 0.1\frac{\langle n\rangle_s\langle c_v\rangle_c\langle d\rangle_c^2}{4\langle k\rangle_c}. \tag{6.147}$$

Then for clusters, $\langle d\rangle_c$ is larger and $\langle k\rangle_c$ is smaller (compared with nonclustered d_s and k_s), resulting in large thermal relaxation time τ_α and larger $k_{f,\mathrm{E}}$. Note that this thermal relaxation time can be longer than the viscous relaxation time (6.138) suggested in some analyses [234].

For dominant external resistance, under very small Reynolds number $\rho\langle u_s^2\rangle^{1/2} d_s/\mu_f$, the resistance is $1/2\pi d_s k_f$. Then the relaxation time is $c_{v,s}/2\pi d_s k_f$. If there is no cluster, then this relaxation time is larger than that based on internal resistance.

Note that even with a small volume fraction, the particles can form a colloidal network [percolation threshold, similar to Figure 2.9(b)(v) for soots]. Then the heat conduction through the connected matrix should be considered (instead of the Brownian motion)(, which assumes well-dispersed particles).

6.11 Interaction of Moving Fluid Particle and Surface

The fluid mean free path presents the probability distance a fluid particle travels before undergoing collision with another fluid particle. In the presence of a condensed phase, i.e., a surface (or interface), there is also the probability that the fluid particle collides with this surface. Representing the geometry for the surface containing the fluid particles by a clearance distance l, then the ratio of the probability of the fluid–fluid collision to the fluid–surface collision is given by the Knudsen number Kn_l as

$$\mathrm{Kn}_l = \frac{\lambda_f}{l} \quad \text{Knudsen number.} \tag{6.148}$$

For liquids, λ_f is three times the molecular spacing $3(M/\rho_f N_\mathrm{A})^{1/3}$, and therefore $\mathrm{Kn}_l \ll 1$.

6.11.1 Fluid Flow Regimes

For large Kn_l, the probability of the fluid particle–surface interaction (collision) is larger than that among fluid particles and this is the free-molecular-flow regime ($\mathrm{Kn}_l > 1$). For small Kn_l, the interfluid particle collisions dominate, and it is called the viscous-flow regime ($\mathrm{Kn}_l \ll 1$). Between these two is the transitional-flow regime ($0.01 < \mathrm{Kn}_l < 1$). Figure 6.10(a) shows results of the Knudsen experiment with $\mathrm{CO_2}$ flow in capillary tube, ($l = d = 3.33 \times 10^{-2}$ mm, and length $L = 2$ cm), at 25°C with varying pressure [230]. The measured mass flow rate divided by pressure drop is plotted versus the pressure (in cm-Hg). For isothermal flow, $\dot{m}_f/(\Delta p/L) = \mathrm{d}^2 Mp/32 M_f R_g T$, is proportional to p, in the viscous regime. In this experiment the transition to viscous regime is around $\mathrm{Kn}_l = 0.14$, but for general geometry consideration, this may be lower. Figure 6.10(b) gives approximate boundaries for these regimes. The viscous-flow regime is described by the Navier–Stokes equations of fluid motion listed in Table 3.10 (momentum and mass conservation equations). These equations can be derived from the BTE, by taking the appropriate moments of this equation [73, 459]. The viscous-flow regime in turn is classified based on the flow Reynolds number Re_L, where L is the characteristic (hydrodynamic) length for the surface (or object). The Reynolds number is the ratio of the inertial to viscous forces, i.e.,

$$\mathrm{Re}_L = \frac{\rho_f \overline{u}_f L}{\mu_f} \quad \text{Reynolds number,} \tag{6.149}$$

where $\overline{u}_f$ is the macroscopic (net) fluid velocity. The low-Reynolds-number flow is characterized by zero-velocity fluctuations, i.e., laminar-flow regime. At a high Reynolds number, the flow becomes unstable and turbulent (chaotic fluctuations), i.e., turbulent-flow regime. One type of turbulent-flow structure is the boundary-layer turbulence, as depicted in Figure 6.10. The regime between the laminar and the turbulent-flow is the transitional, viscous-flow regime. The transition for boundary-layer turbulence is around $\mathrm{Re}_L = 5 \times 10^5$.

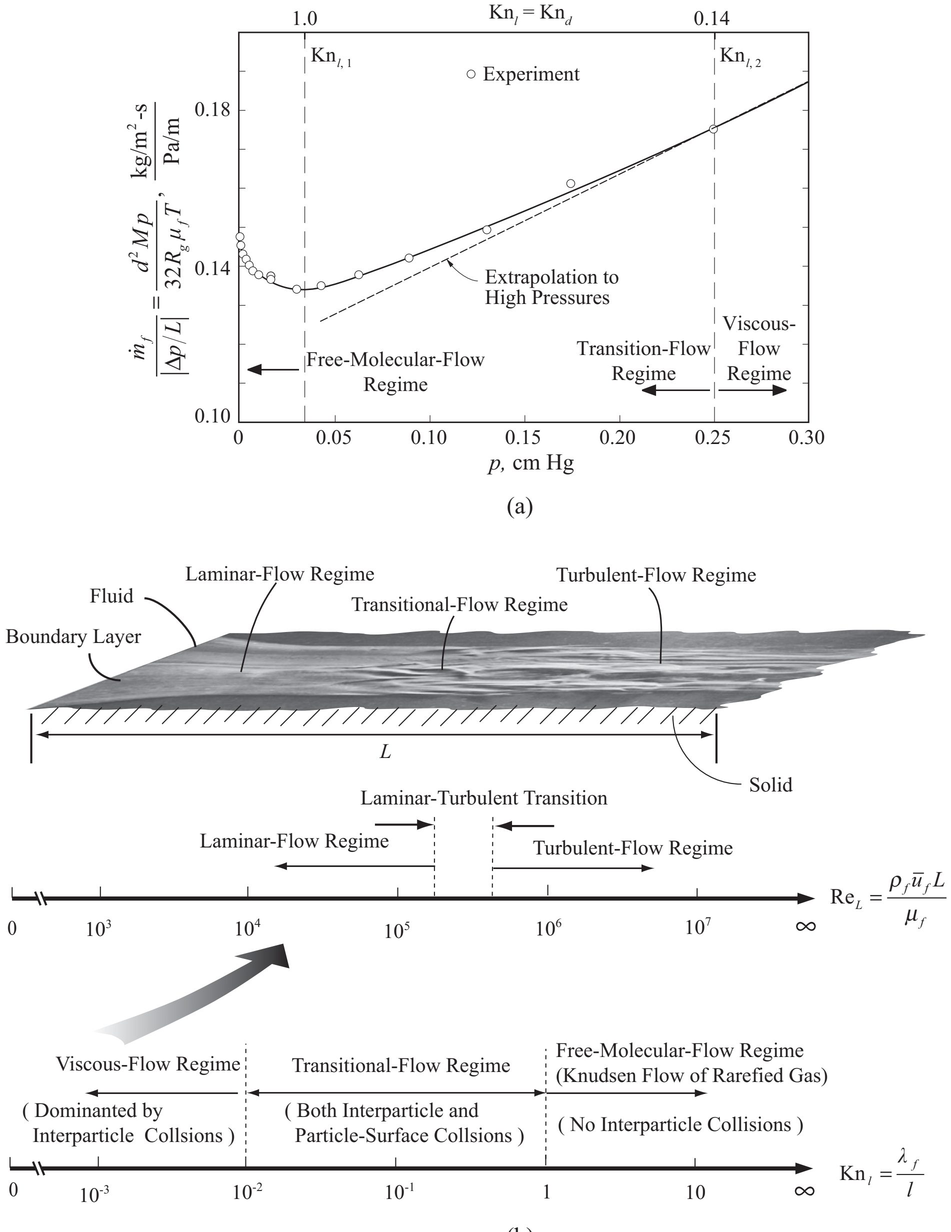

Figure 6.10. (a) The results of the Knudsen experiment showing the mass flow rate through a bundle of capillary tubes of diameter d at various absolute pressures [230]. (b) The free-molecular, transitional-flow, and viscous-flow regimes, as marked by the magnitude of the Knudson number Kn_l (l is clearance distance) and the expanded viscous-flow regime, as marked by the magnitude of the Reynolds number Re_L (showing laminar, laminar–turbulent transitional, and turbulent-flow regimes).

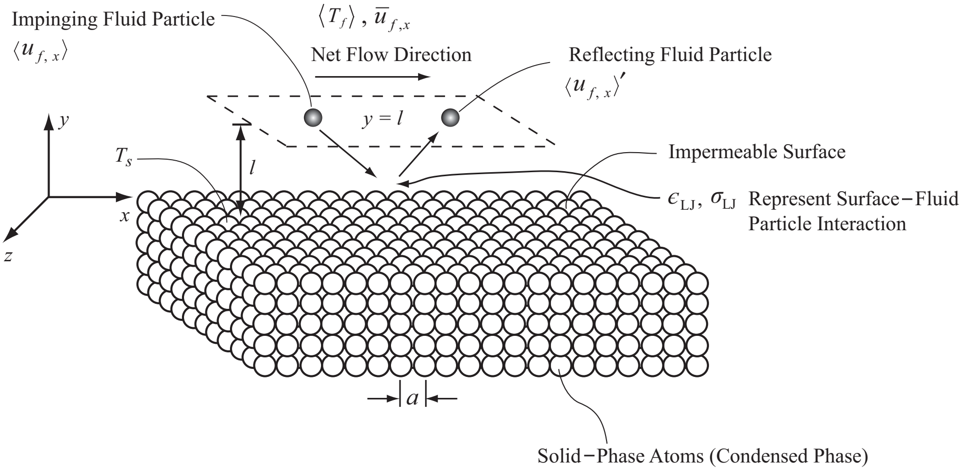
Impinging Fluid Particle
$\langle u_{f,x} \rangle$
$\langle T_f \rangle$, $\overline{u}_{f,x}$
Net Flow Direction
Reflecting Fluid Particle
$\langle u_{f,x} \rangle'$
$y = l$
y
x
z
T_s
l
Impermeable Surface
$\epsilon_{\rm LJ}$, $\sigma_{\rm LJ}$ Represent Surface−Fluid Particle Interaction
a
Solid−Phase Atoms (Condensed Phase)

Figure 6.11. Fluid particle–surface interaction showing an impinging fluid particle with a y-component velocity colliding and reflecting from a solid surface.

Both gas and liquid flows can be sonic or supersonic. The Mach number Ma $= u_f/a_s$, where a_s is the speed of sound in the fluid, is used to show the effect of reaching and surpassing the speed of sound in fluid flow and its compressibility and shock formation features (in gases, in particular, this results in the formation of various shocks that are discontinuities in pressure, etc.).

6.11.2 Knudson-Flow-Regime Surface Accommodation and Slip Coefficients

Consider free-molecular flow ($\mathrm{Kn}_l > 1$), as depicted in Figure 6.11. The fluid particles interact only with the surface. The particles approach the surface with velocity (averaged over many realizations) $\langle u_{f,x} \rangle$ and leave with an altered tangential velocity, $\langle u_{f,x} \rangle'$. The energy transfer to the solid is mostly through the f-p channels (as compared to f-e) [307]

Then the Maxwell tangential momentum (translational) accommodation coefficient a_u, defined as

$$a_u = \frac{\langle u_{f,x} \rangle - \langle u_{f,x} \rangle'}{\langle u_{f,x} \rangle} \quad \text{momentum accomodation coefficient,} \tag{6.150}$$

represents the tangential velocity slip. Noting that the average fluid velocity at the surface is the average of these two, we have for the surface slip velocity u_i, by using the net flow quantities, i.e., $\overline{u}_{f,x}$,

$$u_i = \frac{\overline{u}_{f,x} + (1 - a_u)\overline{u}_{f,x}}{2} = (\frac{2 - a_u}{2})\overline{u}_{f,x} \text{velocity slip for free-molecular-flow regime.}$$

Here we first consider a thermal fluid–solid surface, i.e., $\langle T_f \rangle = T_s = T$. The MD results for a monatomic gas with L–J potential and FCC solid of lattice parameter a, are obtained in [6]. The L–J potential parameters are $\epsilon_{\rm LJ}$ and $\sigma_{\rm LJ}$ for fluid particle-solid interatomic interaction. In the MD simulations, the M–B distribution is used for $\langle u_{f,x} \rangle$. Figure 6.12(a) shows the variation of a_u with respect to $\sigma_{\rm LJ}/a$, for

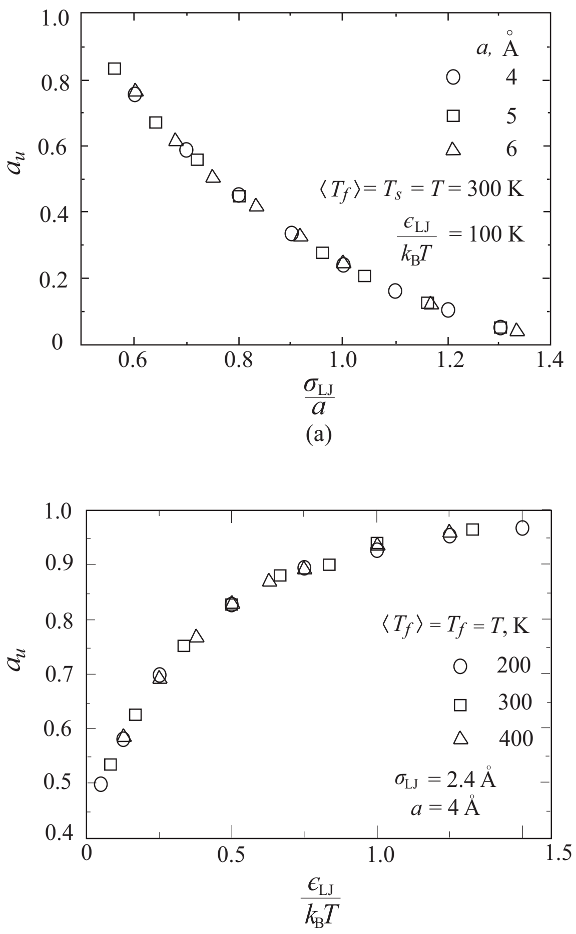

(a)

(b)

Figure 6.12. (a) Variation of MD predicted momentum (translational) accommodation coefficient with respect to the normalized L–J potential separation constant. (b) Same, but with respect to the normalized interaction energy constant [6].

$T = 300$ K, $\sigma_{\rm LJ}/k_{\rm B} = 100$ K, and three values of a. As the equilibrium interatomic distance represented by $\sigma_{\rm LJ}/a$ increases, $a_u \rightarrow 0$, i.e., the reflected molecules have the same tangential momentum as those impinging. For a very small interatomic equilibrium distance, all the tangential momentum is lost by the interaction with the surface ($a_u \rightarrow 1$). Figure 6.12(b) shows the variations of a_u with respect to $\epsilon_{\rm LJ}/k_{\rm B}T$, for $\sigma_{\rm LJ} = 2.4$ Å, $a = 4$ Å, and $T = 200,\ 300,$ and 400 K. Again, as the interaction energy increases (or the temperature decreases), the reflected tangential momentum decreases ($a_u \rightarrow 1$).

Under thermal nonequilibrium between the gas and the solid surface ($\langle T_f \rangle \neq T_s$), the thermal accommodation coefficient is defined as [46]

$$a_T = \frac{\langle q_{f,y} \rangle - \langle q_{f,y} \rangle'}{\langle q_{f,y} \rangle - \langle q_{f,y}(T_s) \rangle}, \tag{6.151}$$

Table 6.5. *Experimental values for momentum accommodation coefficient a_u for some gas–surface pairs for near $T = 300$ K [444].*

Gas	Surface	a_u
Air	machined brass	1.00
Air	old shellac	1.00
Air	fresh shellac	0.79
Air	oil	0.9
Air	glass	0.9
N_2	glass	0.95
CO_2	machined brass	1.00
CO_2	old shellac	1.00
CO_2	oil	0.92
H_2	oil	0.93
He	oil	0.87

where $\langle q_{f,y} \rangle$ is the energy flux incident upon the surface, $\langle q_{f,y} \rangle'$ is the energy flux reflected from the surface, and $\langle q_{f,y}(T_s) \rangle$ is the stream of fluid particles leaving the surface and carrying the same mean energy per particle as a stream issuing from a gas in equilibrium at the surface temperature T_s. For $a_T = 1$, there is a complete thermal accommodation (called diffuse re-emission).

Tabulated values for a_T are given in [444] and for a very clean surface and weakly interacting fluid particle–surface molecules, a_T can be very small ($a_T \rightarrow 0$). However, for polar gas molecules, we have $a_T \rightarrow 1$.

For monatomic gases (translational kinetic energy only), $\langle q_{f,y} \rangle$ is proportional to T (translation kinetic energy) and the proportionality constant is the same for all quantities in (6.151); then $a_T = (\langle T_f \rangle - \langle T_f \rangle')/(\langle T_f \rangle - T_s)$. However, for polyatomic gases the impact changes the proportions of the rotational and vibrational (and at high temperatures the electronic) energies, and therefore this simplification does not hold [107]. For fluid particles with rotational motion, a rotational (and vibrational) accommodation coefficient is similarly defined [107] using the moment of inertia (6.15).

The MD results for thermal (energy) accommodation of a diatomic gas with both translation and rotational energy are reported in [46]. They simulate the fluid–solid pair N_2–Pt, using the L–J potential, and examine both the directly scattered as well as the adsorbed–desorbed fluid (Section 6.11.5) particles. For $\mathrm{Kn}_l \rightarrow 0$ (viscous-flow regime), we have $a_u = a_T = 1$, and the fluid velocity and temperature at the surface become the solid surface values. These are called the viscous-flow-regime, no-slip surface conditions.

Tables 6.5 and 6.6 list experimental values for a_u and a_T for typical gas–surface pairs, stating the surface condition and temperature [444]. For some noble gases and He with very smooth, low-surface-energy solids, a_T is very small (approximately zero). Note that for Ne on clean W, there is a small temperature dependence of a_T, while a_u changes significantly with temperature, as in Figure 6.12(b). The momentum accommodation coefficient is generally close to unity. We will use a_u and a_T in

Table 6.6. *Experimental values for thermal accommodation coefficient a_T for some gas–solid-surface pairs (at specified temperature) [444].*

Gas	Surface	Surface condition (adsorbed gas)	T, K	a_T
Air	bronze	indeterminate		0.88-0.95
	cast iron	indeterminate		0.87-0.96
	aluminum	indeterminate		0.87-0.97
N_2	W	indeterminate	305	0.624
	Pt	indeterminate		0.5
	glass	indeterminate	103	0.38
O_2	Pt, bright	indeterminate		0.81
	Pt, black	indeterminate		0.93
	Pt	saturated	303	0.38
CO_2	W, bright	CO_2	305	0.990
	Pt	saturated	303	0.76
H_2	Pt, bright	indeterminate		0.32
	Pt, black	indeterminate		0.74
	Pt	saturated	303	0.220
	glass	indeterminate	308	0.29
	glass	indeterminate	103	1.0
He	W, flashed	indeterminate	298	0.17
	W, not flashed	indeterminate	298	0.53
	W	clean	303	0.0169
	W	clean	248	0.0153
	W	clean	83	0.0151
	W	K on H_2	298	0.106
	W	H_2 on K	298	0.096
	W	O on K	298	0.22
	W	K on O	298	0.12
	Pt	saturated	303	0.238
	K	clean	298	0.0826
	Na	clean	298	0.0895
	glass	clean	302	0.31
	glass	indeterminate	298	0.35
Ne	W	clean	303	0.0412
	W	clean	243	0.0395
	W	clean	77	0.0495
	W	H_2	295	0.17
	W	N_2	79	0.32
	Pt	saturated	303	0.57
	K	clean	298	0.1987
	Na	clean	298	0.19
	glass	indeterminate	298	0.7
Ar	W	clean	303	0.272
	W	clean	243	0.294
	W	clean	77	0.549
	Pt	saturated	303	0.89
	K	clean	298	0.444
	Na	clean	298	0.459
Kr	W	clean	303	0.462
	W	clean	243	0.498
	W	clean	77	0.926
Xe	W	clean	303	0.773
	W	clean	243	0.804
	W	clean	90	0.942

the slip model in the following Sections 6.11.3 and 6.11.4, and also for size effect on effective conductivity of confined gas in Section 6.14.1.

6.11.3 Slip Coefficients in Transitional-Flow Regime

In the translational-flow regime ($10^{-2} \leq \mathrm{Kn}_l \leq 1$) and in the presence of a gradient in the mean gas velocity $\overline{\boldsymbol{u}}_f$, the tangential surface velocity slip is defined through

$$u_i = \alpha_u \frac{\partial \overline{u}_{f,x}}{\partial y} \quad \text{on a solid surface, velocity slip for translational-flow regime,} \tag{6.152}$$

where α_u is the velocity slip coefficient, i.e., $u_i = 0$ corresponds to no velocity slip.

Also, the flux of molecules impinging on the surface is given by (6.89), and the tangential momentum flux is the product of this molecular flux and the change in the tangential velocity. Then, using (6.90) for this change, we have

$$\tau_{xy} = \frac{1}{4} m n_f \langle u_f \rangle a_u \overline{u}_{f,x}. \tag{6.153}$$

This tangential momentum flux is also the fluid viscous shear stress, and for a Newtonian fluid (6.90) it is

$$\tau_{xy} = \mu_f \frac{\partial \overline{u}_{f,x}}{\partial y}, \tag{6.154}$$

where μ_f is the fluid viscosity. Then substituting (6.151) and (6.152) into the equations (6.153) and (6.154), we have

$$\frac{1}{4} m n_f \langle u_f \rangle a_u \overline{u}_{f,x} = \mu_f \frac{\partial \overline{u}_{f,x}}{\partial y} = \mu_f \frac{u_i}{\alpha_u} = \mu_f \frac{2 - a_u}{2} \frac{1}{\alpha_u} \overline{u}_{f,x}, \tag{6.155}$$

or

$$\alpha_u = \frac{2\mu_f}{m n_f \langle u_f \rangle} \frac{2 - a_u}{a_u} \quad \text{Maxwell velocity slip coefficient.} \tag{6.156}$$

This is the Maxwell velocity slip coefficient relation.

Now noting that $\mu_f = m n_f \langle u_f^2 \rangle^{1/2} \lambda_f / 3$, (6.92) (end-of-chapter problem), it is customary to approximate (6.156) with

$$\alpha_u = \frac{2 - a_u}{a_u} \lambda_f \equiv a_u^* \lambda_f. \tag{6.157}$$

The temperature slip coefficient α_T is similarly defined through (i.e., $\alpha_T = 0$ corresponds to no temperature slip)

$$T_i - T_s = \alpha_T \frac{\partial \langle T_f \rangle}{\partial y}, \quad \text{temperature slip coefficient on interface.} \tag{6.158}$$

As an approximation, α_T is related to α_u through the Kennard relation [444]

$$\alpha_T = \alpha_u \frac{2\gamma}{\gamma+1}\frac{1}{\mathrm{Pr}} \equiv \alpha_T^* \lambda_f \quad \text{Kennard temperature slip coefficient}$$

$$\gamma = \frac{c_{p,f}}{c_{v,f}}, \quad \mathrm{Pr} = \frac{\mu_f c_{p,f}}{k_f}, \tag{6.159}$$

where γ is the specific heat ratio and Pr is the Prandtl number. Note that α_u^* and α_T^* are dimensionless and are of the order of unity. These show that the velocity and temperature slip coefficients are proportional to the gas mean free path (6.87), and, as λ_f decreases, these slip coefficients tend to vanish (viscous-flow regime).

6.11.4 Solid Particle Thermophoresis in Gases

In the presence of a temperature gradient in a gas with solid particle suspensions, the gas kinetic energy difference on different parts of the particle surface can move the particle in the direction of a lower temperature. This is referred to as particle thermophoresis. For the motion to be significant (compared with, for example, the buoyancy force), the particles should be small, compared with the mean free path of gas, i.e., $\mathrm{Kn}_d = 2\lambda_f/d_s$ (d_s is the solid particle diameter) can become large. This problem has been analyzed [454] where for the velocity slip, in addition to α_u^* discussed in Section 6.11.3, is also affected by the temperature variation around the particle. This is presented using the temperature slip using a thermodiffusive slip coefficient $\alpha_{u,T}^*$, such that the tangential (polar) slip velocity is given as

$$u_{\theta,i} = \alpha_u^* \lambda_f r \frac{\partial}{\partial r}\frac{u_\theta}{r} + \alpha_{u,T}^* \frac{2\mu_f}{\rho_f T_f d_s}\frac{\partial T_f}{\partial \theta}, \quad \text{at } r = \frac{d_s}{2}. \tag{6.160}$$

Also, the temperature slip is given similar to (6.158), using α_T^*, as

$$T_f - T_s = \alpha_T^* \lambda_f \frac{\partial T_f}{\partial r}, \quad \text{at } r = \frac{d_s}{2}. \tag{6.161}$$

These allow for fluid temperature variation $T_f(r,\theta)$ around the solid particle.

The result for the thermophoretic force $\boldsymbol{F}_T$ on the solid particle as [454]

$$\boldsymbol{F}_T = -\frac{6\pi\mu_f^2 \alpha_{u,T}^* d_s \left(\frac{k_f}{k_s} + \alpha_T^* \mathrm{Kn}_d\right)\frac{\nabla T_f}{T_f}}{\rho_f (1 + 3\alpha_u^* \mathrm{Kn}_d)\left(1 + 2\frac{k_f}{k_s} + 2\alpha_T^* \mathrm{Kn}_d\right)}, \tag{6.162}$$

where k_f and k_s are the fluid and solid conductivity, and $\mathrm{Kn}_d = 2\lambda_f/d_s$. In [454], $\alpha_u^* = \alpha_{u,T}^* = 1.14$ and $\alpha_T^* = 2.18$ are suggested.

The thermophoretic velocity is [454]

$$\boldsymbol{u}_T = \boldsymbol{F}_T \frac{1}{3\pi\mu_f d_s}\{1 + \mathrm{Kn}_d[a_1 + a_2 \exp(-\frac{a_3}{\mathrm{Kn}_d})]\}$$

$$\text{particle thermophoretic velocity.} \tag{6.163}$$

In [454] it is also suggested that $a_1 = 1.20$, $a_2 = 0.41$, and $a_3 = 0.88$. When $\mathrm{Kn}_d \rightarrow 0$, the Stokes velocity $3\pi\mu_f d_s \boldsymbol{F}_T$ is recovered. This is the same as the velocity used in Brownian motion as presented in Section 6.10.

6.11.5 Physical Adsorption and Desorption

When an involatile solid is in contact with a gas, the gas molecules adsorb (stick) to the solid (the solid is called the adsorbent or substrate, and the adsorbed gas is called the adsorbate). Surface adsorption differs from absorption (which requires penetration into the bulk solid phase). In physical adsorption (or physisorption) the gas molecules are held to the surface by the relatively weak van der Waals forces as shown in Figure 6.13(a). In the chemical adsorption (chemisorption), the chemical reaction occurs at the surface and the gas molecules are held to the surface with strong chemical bonds.

The amount of gas adsorbed to a surface at a given temperature depends on the gas pressure and equilibrium condition. This is called the adsorption isotherm and is generally given as the mole of gas per gram of adsorbent as a function of pressure (or normalized by the saturation pressure for a given temperature). Figure 6.13(b) gives the adsorption isotherm for H_2O adsorbed on Pt, for $T = 298$ and 313 K. The adsorption isotherm is also presented as the amount of fluid particles adsorbed per unit area of solid surface. As the temperature increases, less fluid particles are adsorbed. Also, as the saturation pressure of the fluid is reached the fluid liquifies on the surface and the adsorbed amount increases substantially (capillary condensation) [54].

Figure 6.13(c) shows MD adsorption results, the variation of the number of adsorbed Ar atoms per unit surface area of Pt with respect to the surface temperature, $85 < T < 1320$ K, i.e., $0.06 < \epsilon_{sf}/k_{\mathrm{B}}T < 0.931$ [206]. A full surface coverage by a monolayer is also marked. Note that the surface temperature ranges from the triple-point to above the critical-point temperature of Ar, where $\epsilon_{sf}/k_{\mathrm{B}}T_c = 0.525$ at the critical-point temperature of Ar, and $\epsilon_{sf}/k_{\mathrm{B}}T_{tp} = 0.931$ at the triple-point temperature [Figure 2.13(a)]. Minor adsorption is found at high temperatures, due to large kinetic energy compared with surface force, with an exponential increase with decreasing temperature due to a decrease in kinetic energy compared with surface force. This is associated with relatively weak fluid-solid interatomic interaction. This weak interaction results in a small decrease in adsorption at high temperatures, however, once fluid particles adsorb onto the surface, interatomic interactions (potential) promote further adsorption. This is more pronounced at high pressure, $N_f = 900$. A transition occurs at $\epsilon_{sf}/k_{\mathrm{B}}T \simeq 0.7$ for $N_f = 600$, whereas at $\epsilon_{sf}/k_{\mathrm{B}}T \simeq 0.6$ for $N_f = 900$. This transition in turn affects the accommodation coefficients and the effective thermal conductivity. Near the triple-point temperature, a fully-covered adsorbed layer is found. For $N_f = 900$, the number of adsorbed atoms continue to decrease as the temperature increases, whereas for $N_f = 600$, those are nearly constant above the critical temperature. This residual adsorption at high pressures

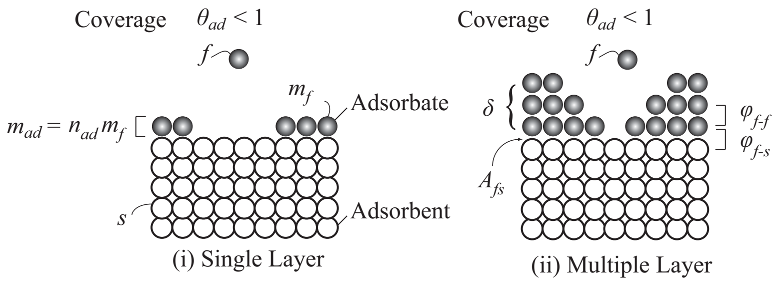

(a) Physical Adsorption

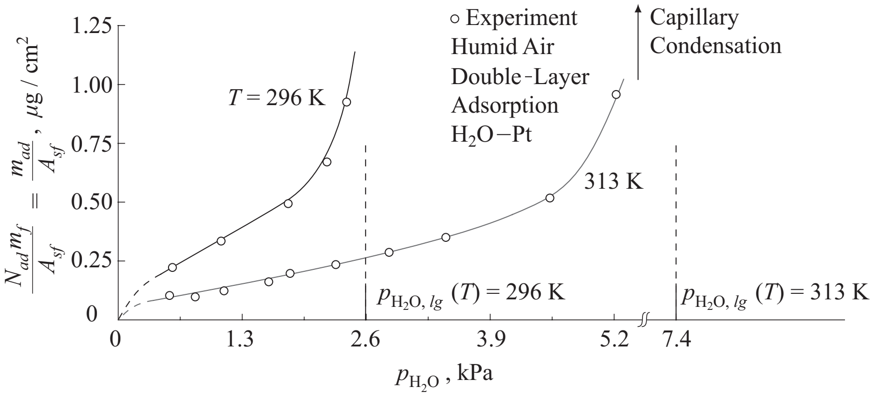

(b) Adsorption Isotherm for Water Adsorbed on Gold Surface

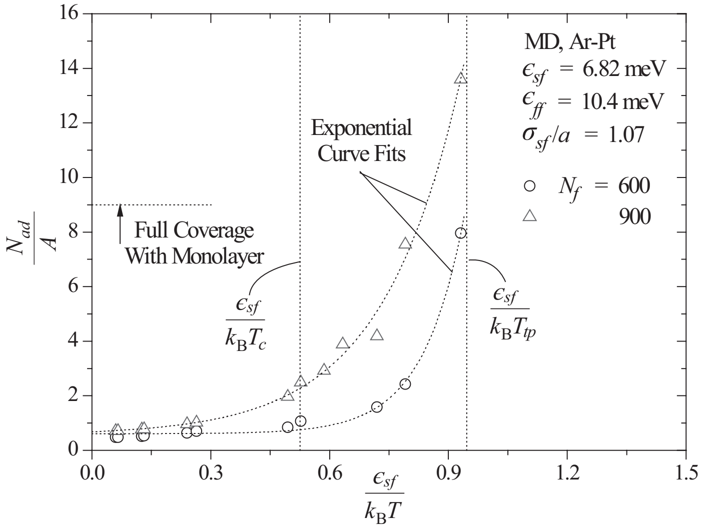

(c)

Figure 6.13. (a) Simple and multilayer physical adsorption, and (b) experimental adsorption isotherm for H_2O–Pt at $T = 296$ and 313 K [54]. (c) MD results showing variation of the number of adsorbed Ar atoms per unit surface area in the nanogap for $N_f = 600$ and 900, as a function of dimensionless inverse temperature $\epsilon_{sf}/k_B T$. Exponential curve fits to the MD results are also shown. The full surface coverage by a monolayer is also marked.

leads to pressure-dependent a_u and a_T, but is expected to disappear at very high temperature (large gas superheat).

(A) *Single-Layer Pure Gas Adsorption*

Desorption is the process of removing the adsorbent gas molecules and is achieved by raising the temperature or lowering the pressure.

The fraction of surface area covered by gas molecules is θ_{ad}, and it is generally allowed that first this fraction reaches unity as the adsorption proceeds and then after completion of a single molecular layer (monolayer), additional layers are formed until the van der Waals forces emanating from the surface are not able to affect the gas molecules sufficiently far from the surface. These are shown in Figure 6.13(a).

The simplest analysis is for single-layer, single component gas adsorbed fluid particle is called the Langmuir adsorption model. It is for a planar, homogeneous surface, with no reaction among adsorbed species, and a monolayer adsorption only. The rate of adsorption is the integrated flux of gas molecules moving toward the surface with energy sufficiently large to overcome the adsorption barrier E_{ad}. Note that this is proportional to the fraction of surface not covered by adsorbed particle. This is expressed as [37]

$$\frac{\mathrm{d}n_{ad}}{\mathrm{d}t} = n_f(1-\theta_{ad})\int_{u_{f,\mathrm{o}}}^{\infty} f_f^{\mathrm{o}}(\boldsymbol{u}_f)\alpha_{ad}\mathrm{d}u_{f,y} \text{ Langmuir adsorption model,} \quad (6.164)$$

where $u_{f,\mathrm{o}}$ is defined from the threshold energy,

$$E_{ad} \equiv \frac{1}{2}mu_{f,\mathrm{o}}^2, \quad (6.165)$$

which defines the threshold gas velocity $u_{f,\mathrm{o}}$ for adsorption and α_{ad} is called the sticking probability (assumed to be independent of $u_{f,y}$ and is generally between 0.8 and 1.0). The equilibrium distribution function $f_f^{\mathrm{o}}(\boldsymbol{u}_f)$ is given by (6.61), and the integration gives

$$\frac{\mathrm{d}n_{ad}}{\mathrm{d}t} = n_f(\frac{k_{\mathrm{B}}T}{2\pi m})^{1/2}\exp(-\frac{E_{ad}}{k_{\mathrm{B}}T})(1-\theta_{ad})\alpha_{ad} \equiv \dot{\gamma}_{ad}n_f(1-\theta_{ad}), \quad (6.166)$$

where $\dot{\gamma}_{ad}$ is the adsorption rate coefficient per fluid particle. The desorption rate is assumed to be proportional to the surface coverage θ_{ad}, i.e.,

$$\frac{\mathrm{d}n_{ad}}{\mathrm{d}t} = \dot{\gamma}_{de}\theta_{ad}\exp(-\frac{E_{de}}{k_{\mathrm{B}}T}), \quad (6.167)$$

where $\dot{\gamma}_{de}$ is desorption rate coefficient and E_{de} is the desorption activation barrier. There are other adsorption and desorption kinetic models, in which the dependence on the surface vacancy $1-\theta_{ad}$ and coverage θ_{ad} is not linear. The first-order-models given preceding are among the simpler ones.

At equilibrium, we have $\mathrm{d}n_{ad}/\mathrm{d}t = \mathrm{d}n_{de}/\mathrm{d}t$, and from this we have

$$\frac{(\frac{k_\mathrm{B}T}{2\pi m})^{1/2}\alpha_{ad}\exp(\frac{\Delta E_{ad}}{k_\mathrm{B}T})}{\dot{\gamma}_{de}}n_f \equiv \frac{\dot{\gamma}_{ad}}{\dot{\gamma}_{de}}n_f = \frac{\theta_{ad}}{1-\theta_{ad}}, \quad \Delta h_{ad} = E_{de} - E_{ad}. \tag{6.168}$$

Rearranging this gives

$$\theta_{ad} = \frac{\frac{\dot{\gamma}_{ad}}{\dot{\gamma}_{de}}n_f}{1+\frac{\dot{\gamma}_{ad}}{\dot{\gamma}_{de}}n_f} = \frac{\frac{\dot{\gamma}_{ad}}{\dot{\gamma}_{de}}p}{1+\frac{\dot{\gamma}_{ad}}{\dot{\gamma}_{de}}p}, \quad p = n_f k_\mathrm{B}T. \tag{6.169}$$

At low pressures, $\theta_{ad} = (\dot{\gamma}_{ad}/\dot{\gamma}_{de})p$, and at high pressures, $\theta_{ad} = 1$. Assuming a monolayer adsorption, where V_{max} is the volume of completely covered ($\theta_{ad} = 1$) gas particles, then the volume of adsorbent is ($\theta_{ad} = V_{ad}/V_{max}$)

$$V_{ad} = \frac{V_{max}\frac{\dot{\gamma}_{ad}}{\dot{\gamma}_{de}}p}{1+\frac{\dot{\gamma}_{ad}}{\dot{\gamma}_{de}}p}, \quad p = n_f k_\mathrm{B}T \quad \text{Langmuir adsorption isotherm.} \tag{6.170}$$

There are other adsorption isotherm models, including the Brunauer–Emmett–Teller (BET) isotherm for multilayer adsorption. Examples of isotherms are given in [230].[†]

(B) *Heat of Adsorption*

The net energy Δh_{ad} is the differential (per molecule) isosteric (constant θ_{ad}) enthalpy (or heat) of adsorption and is related to p and T (similarly to the Clausius–Clapeyron relation for liquid–vapor equilibrium) as [277]

$$\frac{\partial \ln p}{\partial T}|_\theta = \frac{\Delta h_{ad}}{k_\mathrm{B}T^2} \quad \text{ideal gas.} \tag{6.171}$$

In general $\Delta h_{ad} = \Delta h_{ad}(T, \theta_{ad})$. This heat (enthalpy) of adsorption is similar to the heat (enthalpy) of evaporation. The specific enthalpy is defined in terms of the specific internal energy (and pressure and specific volume v) as

$$h = e + pv. \tag{6.172}$$

Then we can write for the enthalpy of evaporation, at conditions T and p,

$$\Delta h_{lg} = (c_{g,v} - c_{l,v})T + p(v_g - v_l). \tag{6.173}$$

The enthalpy of evaporation per molecule (or atom) is the energy required for changing a molecule of a liquid into the gaseous state. This energy breaks down the intermolecular attractive force, and also provides the energy necessary to expand the gas $p(v_g - v_l)$. There is no potential energy (internal energy is the molecular

---

[†] The BET equation is [504]

$$\frac{p}{V_{ad}(p_{eq}-p)} = \frac{1}{V_\mathrm{max}c} + \frac{c-1}{V_\mathrm{max}}\frac{p}{p_{lg}}, \quad c = \exp(\frac{\Delta E_{ad}}{k_\mathrm{B}T}),$$

where p_{lg} is the saturation pressure $p_{lg}(T)$, and ΔE_{ad} is generally found empirically.

kinetic energy) for an ideal gas. For example, for H_2O the enthalpy of evaporation at $p = 1$ atm and $T = 373.15$ K is 0.39 eV; from Figures 6.3 and 6.4, we note that this is mostly associated with $p(v_g - v_l)$, compared with $(c_{g,v} - c_{l,v})T$.

An example of the prediction of $\theta_{ad}(T)$ and $\Delta h_{ad}(T, \theta_{ad})$ for H_2O adsorption on SiO_2 is given in [373]. They find that Δh_{ad} is larger than the bulk heat of evaporation Δh_{lg} and show that SiO_2 distorts (elongates and changes the bond angle) the hydrogen bond in H_2O compared with the bulk (or free) H_2O.

In high solid–fluid surface area per unit volume A_{sf}/V adsorbers (such as dessicants), up to 25% of the mass of the adsorber occurs. For spherical particles of diameter d packed with porosity ϵ, we have $A_{sf}/V = 6(1-\epsilon)/d$, and as d approaches a few micrometers, A_{sf}/V becomes very large.

6.11.6 Disjoining Pressure in Ultrathin-Liquid Films

The pressure in thin-liquid films is affected by the interatomic forces of the liquid and the solid substrate. The integral force can be presented as the pressure difference between the vapor and the liquid (assuming a single component fluid) across this interface, $p_g - p_l$. For a L–J fluid with a similar L–J (2.9) interaction with the solid atoms, this relation has been derived in [75], i.e.,

$$\varphi_{f\text{-}f} = 4\epsilon_{\text{LJ},f\text{-}f}[(\frac{\sigma_{\text{LJ},f\text{-}f}}{r})^{12} - (\frac{\sigma_{\text{LJ},f\text{-}f}}{r})^{6}] \tag{6.174}$$

$$\varphi_{f\text{-}s} = 4\epsilon_{\text{LJ},f\text{-}s}[(\frac{\sigma_{\text{LJ},f\text{-}s}}{r})^{12} - (\frac{\sigma_{\text{LJ},f\text{-}s}}{r})^{6}]. \tag{6.175}$$

The mean-field potential that a fluid atom experiences at the vapor–liquid interface is $(r^2 = x^2 + z^2)$

$$\langle\varphi_f\rangle = \int_\delta^\infty \int_0^\infty n_s \varphi_{f\text{-}s} 2\pi x \mathrm{d}x \mathrm{d}z, \tag{6.176}$$

where x is measured for the vapor–liquid (δ is the liquid-film thickness) interface, and n_s is the solid atomic number density. This gives

$$\begin{aligned}\langle\varphi_f\rangle &= -\frac{4\pi n_s \epsilon_{\text{LJ},f\text{-}s}\sigma^6_{\text{LJ},f\text{-}s}}{6\delta^3} + \frac{4\pi n_s \epsilon_{\text{LJ},f\text{-}s}\sigma^{12}_{\text{LJ},f\text{-}s}}{45\delta^9}\\ &\equiv \frac{A_\text{H}}{6\pi n_f \sigma^3_{\text{LJ},f\text{-}s}}[\frac{2}{15}(\frac{\sigma_{\text{LJ},f\text{-}s}}{\delta})^9 - (\frac{\sigma_{\text{LJ},f\text{-}s}}{\delta})^3],\end{aligned} \tag{6.177}$$

where $A_\text{H} = 4\pi^2 n_s n_f \epsilon_{\text{LJ},f\text{-}s}\sigma^6_{\text{LJ},f\text{-}s}$ is called the Hamaker constant. Note that this gives a mean surface potential with exponent is 9–3 as compared with 12–6 used for the pairs in (6.174) and (6.175).

The first term is generally very small and negligible; then we have the pressure difference [73]

$$p_l - p_g = p_d = -\frac{A_\text{H}}{6\pi\delta^3}. \tag{6.178}$$

This pressure difference is called the disjoining pressure p_d.

6.12 Turbulent-Flow Structure and Boundary-Layer Transport

Turbulent flow is marked by random fluctuations in the fluid velocity $\boldsymbol{u}_f$. For a boundary-layer flow, with the Cartesian coordinate system and with u_f being the velocity in the x direction, Figure 6.14(a) renders this turbulent velocity function. Figures 6.14(c) and (d) show the structures of the viscous and thermal boundary layers for laminar and turbulent flows. The distributions of the velocity and temperature are shown in terms of the dimensionless velocity u_f^* and temperature T_f^*. As with the laminar flow, the near-field nonuniformities are confined to regions adjacent to the surface and are marked by the viscous and thermal boundary-layer thicknesses $\overline{\delta}_\nu$ and $\overline{\delta}_\alpha$. For turbulent boundary layers, the fluctuations vanish far away and very close to the surface. The region adjacent to the surface is called the laminar sublayer. The laminar viscous sublayer has a thickness $\delta_{l,\nu}$, and the laminar thermal sublayer has a thickness $\delta_{l,\alpha}$. These are marked in Figures 6.14(c) and (d). In turbulent boundary layers, although the disturbed region is larger than its laminar counterpart, most of the changes in the velocity and the temperature occur very close to the surface. As such, adjacent to the surface the gradients of the velocity and the temperature are much larger than those in the laminar boundary layers.

It is customary to decompose the fluid velocity into a time-averaged (or mean) $\overline{\boldsymbol{u}}_f$ and a fluctuating component $\boldsymbol{u}'_f$ [195], i.e.,

$$\boldsymbol{u}_f = \overline{\boldsymbol{u}}_f + \boldsymbol{u}'_{f,t}, \quad \overline{\boldsymbol{u}}_f \equiv \frac{1}{\tau}\int_0^\tau \boldsymbol{u}_f \mathrm{d}t \quad \text{mean and fluctuating components of } \boldsymbol{u}_f, \tag{6.179}$$

where τ(s) is the time period for averaging and is taken to be long enough such that $\overline{\boldsymbol{u}}_f$ no longer changes by any further increase in τ.

The temperature is also decomposed as

$$T_f = \overline{T}_f + T'_f, \quad \overline{T}_f \equiv \frac{1}{\tau}\int_0^\tau T_f \mathrm{d}t \quad \text{mean and fluctuating components of } T_f. \tag{6.180}$$

Turbulence can be produced within the boundary layer when the flow becomes unstable. This is called the boundary-layer turbulence. The boundary-layer turbulence, in an otherwise parallel laminar flow (far field), occurs at a transition Reynolds number $\mathrm{Re}_{L,t}$. This boundary-layer transition Reynolds number is $\mathrm{Re}_{L,t} = 5 \times 10^5$ [413].

Turbulence can also be present in the far-field flow and this is called the free-stream turbulence. This can be caused by propellers, the presence of grid nets, other interactions with solid surfaces, or by instabilities in the far-field flow. Our discussion here is limited to boundary-layer turbulence.

Although on the solid surface $\boldsymbol{u}_f = 0$, the surface-convection heat transfer is influenced by the velocity and temperature fluctuations near the surface, similar to the laminar-flow case. The turbulent velocity fluctuations are three dimensional, and the component perpendicular to the surface makes the largest contribution to the surface-convection heat transfer.

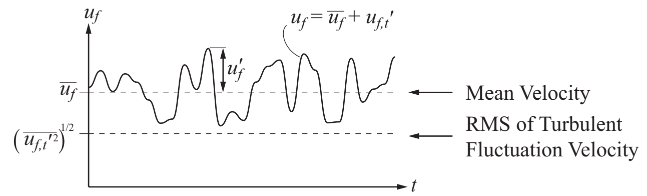

(a) Fluid Particle Turbulent Velocity Fluctuations in the x direction, $u_{f,t}$

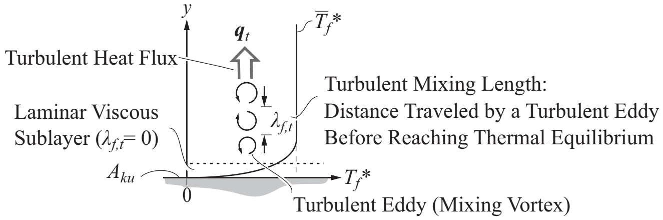
y
$\boldsymbol{q}_t$
$\overline{T}_f^*$
Turbulent Heat Flux
Turbulent Mixing Length: Distance Traveled by a Turbulent Eddy Before Reaching Thermal Equilibrium
Laminar Viscous Sublayer ($\lambda_{f,t}$= 0)
$\lambda_{f,t}$
A_{ku}
T_f^*
0
Turbulent Eddy (Mixing Vortex)

(b) Turbulent Mixing Length, $\lambda_{f,t}$

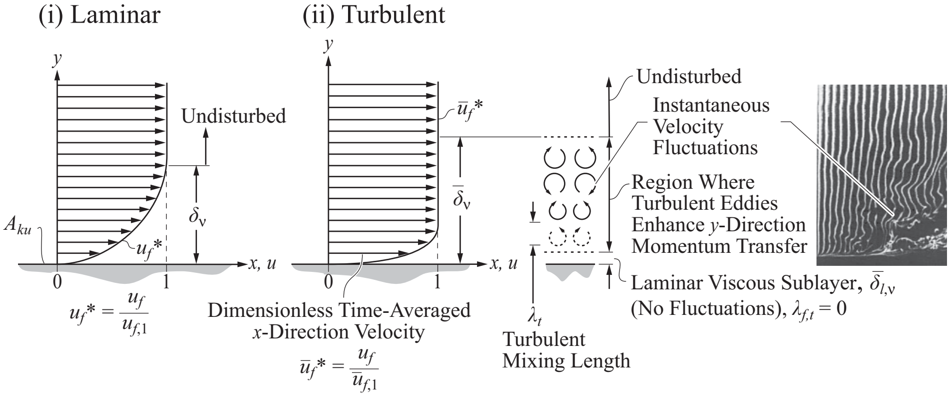
(i) Laminar
(ii) Turbulent
y
Undisturbed
δ_ν
A_{ku}
u_f^*
x, u
0
1
$u_f^* = \frac{u_f}{u_{f,1}}$
$\overline{u}_f^*$
$\overline{\delta}_\nu$
Dimensionless Time-Averaged x-Direction Velocity
$\overline{u}_f^* = \frac{u_f}{\overline{u}_{f,1}}$
Undisturbed
Instantaneous Velocity Fluctuations
Region Where Turbulent Eddies Enhance y-Direction Momentum Transfer
Laminar Viscous Sublayer, $\overline{\delta}_{l,\nu}$ (No Fluctuations), $\lambda_{f,t} = 0$
λ_t
Turbulent Mixing Length

(c) Viscous Laminar and Turbulent Boundary Layers, δ_ν and $\overline{\delta}_\nu$

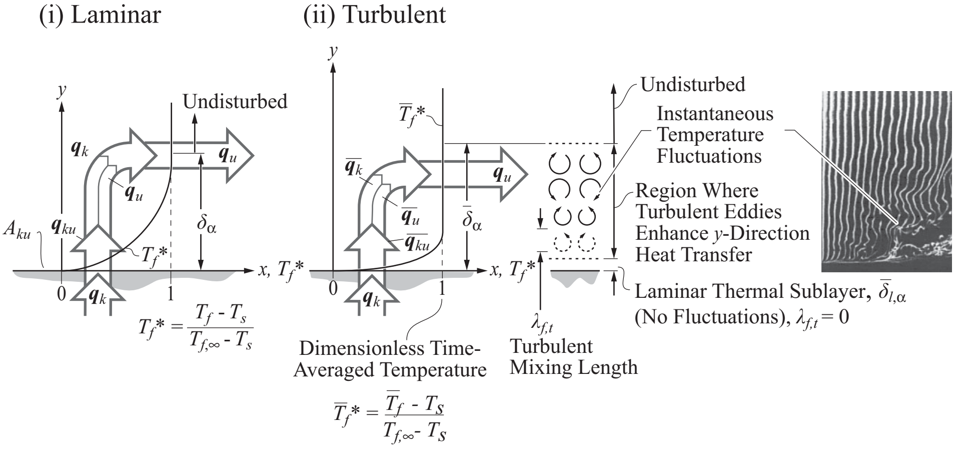
(i) Laminar
(ii) Turbulent
y
Undisturbed
$\boldsymbol{q}_k$
$\boldsymbol{q}_u$
$\boldsymbol{q}_{ku}$
A_{ku}
δ_α
T_f^*
x, T_f^*
0
1
$T_f^* = \frac{T_f - T_s}{T_{f,\infty} - T_s}$
$\overline{T}_f^*$
$\overline{\boldsymbol{q}}_k$
$\overline{\boldsymbol{q}}_u$
$\overline{\boldsymbol{q}}_{ku}$
$\overline{\delta}_\alpha$
Dimensionless Time-Averaged Temperature
$\overline{T}_f^* = \frac{\overline{T}_f - T_S}{T_{f,\infty} - T_S}$
Undisturbed
Instantaneous Temperature Fluctuations
Region Where Turbulent Eddies Enhance y-Direction Heat Transfer
Laminar Thermal Sublayer, $\overline{\delta}_{l,\alpha}$ (No Fluctuations), $\lambda_{f,t} = 0$
$\lambda_{f,t}$
Turbulent Mixing Length

(d) Thermal Laminar and Turbulent Boundary Layers, δ_α and $\overline{\delta}_\alpha$

Figure 6.14. (a) Turbulent velocity fluctuations showing the mean and fluctuating components of the x-direction velocity $u'_{f,t}$. (b) A rendering of turbulent mixing length. (c) Structure of the viscous laminar and turbulent boundary layers. (d) Structure of the thermal laminar and turbulent boundary layers, (c) and (d) include renderings of the turbulent eddies (and turbulent mixing lengths) that contribute to the lateral (y-direction) heat transfer.

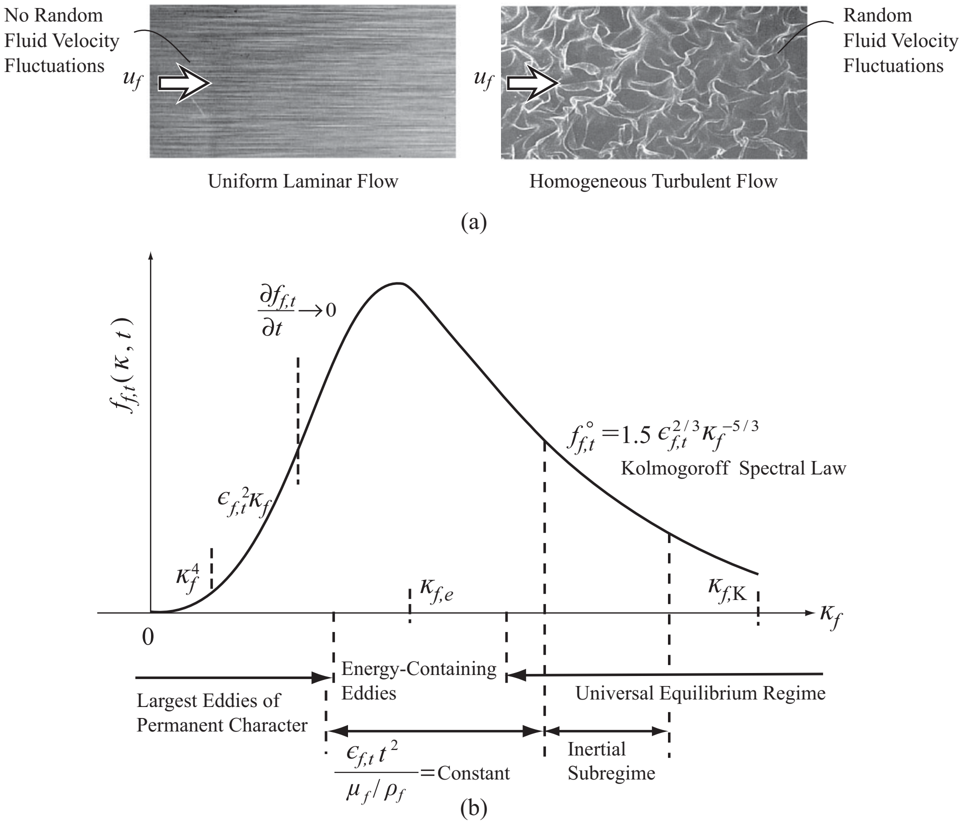

Figure 6.15. (a) Homogeneous turbulence in a unidirectional flow. (b)Turbulent energy spectrum, i.e, turbulent energy distribution function verses turbulent wave number, showing the various regimes [195]. The Kolmogoroff spectrum law applies to the large wave number (inertial) subregime. The results are homogeneous, equilibrium (balance between production and dissipation) turbulence.

6.12.1 Turbulent Kinetic Energy Spectrum for Homogeneous Turbulence

The idealized turbulent flow is the homogeneous, isotropic turbulence (spatial homogeneity in mean properties). This is rendered in Figure 6.15(a). In comparison with the boundary-layer turbulence, the homogeneous turbulence is in the free stream (away from any surface). The turbulent kinetic energy equation is obtained from the Navier–Stokes equations given in Table 3.10 and is [195]

$$E_{f,t} = \frac{1}{2}u'_{f,i}u'_{f,i}, \quad \overline{u^2_{f,i}} = \overline{u^2_{f,j}} \quad \text{isotropic, turbulent kinetic energy } E_{f,t}. \tag{6.181}$$

$$\frac{\mathrm{D}}{\mathrm{D}t}\overline{E}_{f,t} = -\frac{\partial}{\partial x_i}\overline{u'_{f,i}(\frac{p'}{\rho_f} + E_{f,t})} - \overline{u'_{f,i}u'_{f,j}}\frac{\partial \bar{u}_f}{\partial x_i}$$
$$+ \frac{\mu_f}{\rho_f}\frac{\partial}{\partial x_i}\overline{u'_{f,j}(\frac{\partial u'_{f,i}}{\partial x_j} + \frac{\partial u'_{f,j}}{\partial x_i})} - \frac{\mu_f}{\rho_f}\overline{(\frac{\partial u'_{f,i}}{\partial x_j} + \frac{\partial u'_{f,j}}{\partial x_i})\frac{\partial u'_{f,j}}{\partial x_i}}. \tag{6.182}$$

The first term on the right is the convective diffusion of the turbulent mechanical energy, the second is the work of deformation of the mean motion by the turbulent stresses, the third is the viscous shear stress of the turbulent motion, and the last one is the viscous dissipation.

Under homogeneous turbulence only the time-dependent part of the left-hang side and the viscous dissipation on the right are nonzero. For this case, any existing turbulent fluctuation decays in time by viscous dissipation. Then

$$\frac{\partial \overline{E}_{f,t}}{\partial t} = \frac{\partial}{\partial t}\frac{3}{2}\overline{u'^2_{f,i}} = \frac{\mu_f}{\rho_f}\overline{\left(\frac{\partial u'_{f,i}}{\partial x_j} + \frac{\partial u'_{f,j}}{\partial x_i}\right)\frac{\partial u'_{f,j}}{\partial x_i}} \equiv \epsilon_{f,t} \quad \text{homogeneous turbulence,} \tag{6.183}$$

where $\epsilon_{f,t}$ is the viscous dissipation rate of the turbulent kinetic energy.

The turbulent velocity fluctuation for an incompressible fluid ($\nabla \cdot \boldsymbol{u}_f = 0$) can be Fourier decomposed by the wave vector $\boldsymbol{\kappa}$ and the angular frequency ω as

$$\boldsymbol{u}'_f(\boldsymbol{x}, t) = \iint \boldsymbol{U}'_f(\kappa_f, \omega)\exp(i\boldsymbol{\kappa}_f \cdot \boldsymbol{x} - \omega t)\, \mathrm{d}\boldsymbol{\kappa}_f\, \mathrm{d}\omega, \tag{6.184}$$

and the incompressibility requires that

$$\boldsymbol{\kappa}_f \cdot \boldsymbol{U}'_f = 0. \tag{6.185}$$

This states that the only disturbances allowed are transverse (not longitudinal). Such turbulent elements are called turbulent eddies. Then it is said the turbulent velocity field is made of eddies of different sizes (wave numbers). The eddies of large sizes are created by the mean flow, and they in turn exchange their energy with the smaller eddies (this is called turbulent energy cascading).

To describe the turbulent fluctuations (kinetic energy) in terms of distribution over wave number (or frequency), we define the turbulent energy distribution function $f_{t,t}$ through

$$\overline{E}_{f,t} = \frac{3}{2}\overline{u'^2_{f,1}} = \int_0^\infty f_t(\kappa_f, t)\, \mathrm{d}\boldsymbol{\kappa}_f \quad \text{turbulent energy distribution function,} \tag{6.186}$$

where the wave number and the angular frequency are assumed to be related through $\kappa_f = \omega/\overline{u}_{f,1}$, where $\overline{u}_{f,1}$ is the mean velocity. Here $f_{f,t}$ has units of m^3/s^2. Figure 6.15(b) gives the variation of the turbulent energy distribution function f_t with respect to the wave number as compiled from measurements and theoretical predictions. This is also called the turbulent energy spectrum. Figure 6.15(b) shows that for the smallest wave number (largest-size) eddies, we have a κ_f^4 relation for the turbulent distribution function and very slow decay (viscosity is not important). The intermediate wave-number eddies contain most of the turbulent kinetic energy and are referred to as the energy-containing eddies. The peak is designated by $\kappa_{f,e}$. The smallest eddy size is the Kolmogoroff length $\kappa_{f,\mathrm{K}} = 2\pi/\lambda_{f,\mathrm{K}}$.

The eddies of length $\lambda_{f,t}$ that have velocity $u_{f,t}$ have Reynolds number $\mathrm{Re}_t = \rho_f u_{f,t}\lambda_{f,t}/\mu_f$, and for large eddies (larger Re_t) their energy is not dissipated by viscosity, but cascaded to smaller eddies. The eddies with $\mathrm{Re}_t \simeq 1$ are dissipated because of viscosity, and this gives the smallest eddy, which has a length $\lambda_{f,\mathrm{K}}$ (Kolmogoroff length) and velocity $u_{f,\mathrm{K}}$

$$\lambda_{f,\mathrm{K}} = \frac{\mu_f/\rho_f}{u_{f,\mathrm{K}}} \quad \text{Kolmogoroff length, smallest eddies.} \tag{6.187}$$

Using (6.183), Kolmogoroff (Kolmogorov) suggested that the velocity of the smallest eddies must follow (replacing the time derivative with $u_{f,\mathrm{K}}/\lambda_{f,\mathrm{K}}$)

$$\frac{u^3_{f,\mathrm{K}}}{\lambda_{f,\mathrm{K}}} \simeq \epsilon_{f,t} \quad \text{viscous dissipation rate,} \tag{6.188}$$

and using this in (6.187), we have

$$\lambda_{f,\mathrm{K}} = [(\frac{\mu_f}{\rho_f})^3 \frac{1}{\epsilon_{f,t}}]^{1/4}, \quad u_{f,\mathrm{K}} = (\frac{\mu_f}{\rho_f}\epsilon_{f,t})^{1/4} \quad \text{Kolmogoroff length and velocity scales.} \tag{6.189}$$

Then, using $\kappa_{f,\mathrm{K}} = 2\pi/\lambda_{f,\mathrm{K}}$, we can show that [334]

$$f^{\mathrm{o}}_{f,t}(\kappa) = 1.5\,\epsilon^{2/3}_{f,t}\kappa_f^{-5/3} \quad \text{turbulent energy distribution function for inertial subregime.} \tag{6.190}$$

This is the Kolmogoroff −5/3 spectral law for equilibrium, homogeneous turbulence.

6.12.2 Boundary-Layer Turbulent Heat Flux

As with (6.179) and (6.180), the convection heat flux vector is similarly averaged, and we have

$$\begin{aligned} \overline{\boldsymbol{q}_u} &= \overline{\boldsymbol{q}_{u,m}} + \overline{\boldsymbol{q}_{u,t}} \\ &= \underbrace{(\rho c_p)_f \overline{\boldsymbol{u}}_f \overline{T}_f}_{\substack{\text{mean convection} \\ \text{heat flux vector } \overline{\boldsymbol{q}_{u,m}}}} + \underbrace{(\rho c_p)_f \overline{\boldsymbol{u}'_{f,t} T'_{f,t}}}_{\substack{\text{turbulent convection} \\ \text{heat flux vector } \overline{\boldsymbol{q}_{u,t}}.}} \end{aligned} \tag{6.191}$$

The turbulent fluctuations contribute to the heat transfer in a way similar to the molecular fluctuations discussed in Section 6.4. There we used the molecular (thermal) velocity fluctuations and the RMS thermal speed $\langle \overline{u_f^2} \rangle^{1/2}$ and through (3.14) showed how the heat was transfered by these fluctuations. Here, the combined effects of the turbulent velocity fluctuation $(\overline{\boldsymbol{u}'_{f,t} \cdot \boldsymbol{u}'_{f,t}})^{1/2}$, the ability of the fluid to store/release heat $(\rho c_p)_f$, and the ability of the fluctuations to carry the fluid content a short distance before reaching thermal equilibrium also result in heat transfer in the presence of a temperature nonuniformity. This is shown in Figure 6.14(b).

From (6.57), we write the y component (i.e., perpendicular to the surface) of the turbulent convection heat flux as

$$(\overline{q_{u,t}})_y = (\rho c_p)_f \overline{v'_{f,t} T'_{f,t}}. \tag{6.192}$$

We now proceed to relate $\overline{v'_{f,t}T'_{f,t}}$ to mean quantities that are more readily measured or predicted.

6.12.3 Turbulent Mixing Length and Turbulent Thermal Conductivity

Using an analogy with the conduction in gases (which is due to molecular fluctuations), as given by (6.125), the heat transfer that is due to turbulent fluctuations is expressed as [195, 413]

$$(\overline{q_{u,t}})_y = (\rho c_p)_f \overline{v'_{f,t}T'_{f,t}} \equiv -\mathrm{Pr}_t^{-1}(\rho c_p)_f(\overline{v'^2_{f,t}})^{1/2}\lambda_{f,t}\frac{\mathrm{d}\overline{T}_f}{\mathrm{d}y}, \tag{6.193}$$

where $\lambda_{f,t}$ is the turbulent mean free path and is also called the turbulent mixing length [shown in Figure 6.14(b)]. This is a representation of the distance traveled by a fluid particle before reaching equilibrium (either thermal or mechanical). It varies with the distance from the bounding surface. The constant Pr_t (called the turbulent Prandtl number) is determined empirically and is near unity. Here $(\overline{v'^2_{f,t}})^{1/2}$ is the RMS of the turbulent velocity fluctuation in the y direction.

We note that the proportionality of $\overline{v'_{f,t}T'_{f,t}}$ to $\mathrm{d}\overline{T}_f/\mathrm{d}y$, similarly exists for velocity and temperature deviation caused by spatial (instead of temporal) nonuniformities. This is discussed and the proportionality shown in [231].

Because in (6.193) the turbulent heat transfer is related to the gradient of the mean temperature, a turbulent thermal conductivity $k_{f,t}$ is defined by

$$(\overline{q_{u,t}})_y \equiv -k_{f,t}\frac{\mathrm{d}\overline{T}_f}{\mathrm{d}y} \quad \text{turbulent thermal conductivity.} \tag{6.194}$$

Then from (6.194) and (6.193), $k_{f,t}$ is found as

$$k_{f,t} \equiv (k_{f,t})_\perp = \mathrm{Pr}_t^{-1}(\rho c_p)_f(\overline{v'^2_{f,t}})^{1/2}\lambda_{f,t}, \tag{6.195}$$

where subscript $\perp$ indicates perpendicular to the surface.

Next $(\overline{v_{f,t}{}'^2})^{1/2}$ is related to the gradient of the component of the fluid mean velocity along the surface, i.e., $|\partial\overline{u}_f/\partial y|$. This is because, from the examination of the momentum equation, we find that the magnitude of the fluctuations increases as the velocity gradient becomes larger. When we use the turbulent mixing length $\lambda_{f,t}$ again, and we have $(\overline{v_{f,t}{}'^2})^{1/2} \equiv \lambda_{f,t}|\partial\overline{u}_f/\partial y|$. Again, this is because as $\mathrm{d}\overline{T}_f/\mathrm{d}y$ was the source for $\overline{v'_{f,t}T'_{f,t}}$, $|\mathrm{d}\overline{u}_f/\mathrm{d}y|$ is the source for $(\overline{v'^2_{f,t}})^{1/2}$. Then (6.61) becomes

$$k_{f,t} = \mathrm{Pr}_t^{-1}(\rho c_p)_f\lambda^2_{f,t}|\frac{\partial\overline{u}_f}{\partial y}|, \ \alpha_{f,t} = \frac{k_{f,t}}{(\rho c_p)_f}, \tag{6.196}$$

where $\alpha_{f,t}$ is the turbulent thermal diffusivity (or eddy diffusivity). Note that $\mathrm{Pr}_t = \nu_{f,t}/\alpha_{f,t}$, where ν_t is the turbulent kinematic viscosity.

We can extend the results to the three-dimensional heat flow. The turbulent convection heat flux vector $(\rho c_p)_f\overline{\boldsymbol{u}'_{f,t}T'_{f,t}}$ is proportional to the gradient of $\overline{T}_f$, i.e., $\nabla\overline{T}_f$. Therefore, as $\nabla\overline{T}_f$ becomes larger, $(\rho c_p)_f\overline{\boldsymbol{u}'_{f,t}T'_{f,t}}$ increases. Then, assuming that k_t is isotropic (i.e., the same in all directions), from (6.194) the vectorial form of $\boldsymbol{q}_t$ is

$$\overline{\boldsymbol{q}_{u,t}} = (\rho c_p)_f \overline{\boldsymbol{u}'_{f,t} T'_{f,t}} \equiv -k_{f,t} \nabla \overline{T}_f, \qquad (6.197)$$

where we note that the turbulent convection heat flux vector is related to the gradient of mean temperature.

We note that in general $k_{f,t}$ is anisotropic (and should be represented by a tensor).

6.12.4 Spatial Variation of Boundary-Layer Turbulent Mixing Length

For fully-turbulent flows at high Reynolds numbers, $k_{f,t}$ can be larger than k_f (the molecular thermal conductivity) at some locations near the solid surface. Also, $k_{f,t}$ vanishes in the laminar sublayer. Therefore $k_{f,t}$ (or $\boldsymbol{u}'_{f,t}$ and $\lambda_{f,t}$) varies with the distance from the surface and enhances the convection heat transfer. For parallel flows, this enhancement is noticeable in the direction perpendicular to the flow (y direction), where the mean velocity $\overline{v}_f$ is small and the heat transfer is otherwise dominated by molecular conduction.

The smallest turbulent mixing length is the Kolmogoroff length $\lambda_{f,\mathrm{K}}$, (6.189), and the largest is the characteristic length of confining solid L (in the direction of turbulent transport).

Empirical results show that for the flow over a semi-infinite flat plate, the variation of the mixing length in the turbulent boundary layer, adjacent to surface, is approximated as [233]

$$\lambda_{f,t} = \begin{cases} 0 & 0 \le y \le \delta_{l,i} & \text{laminar sublayer (molecular } \lambda_f) \\ \kappa_{\mathrm{vK}}(y - \delta_{l,\nu}) & \delta_{l,\nu} \le y \le 0.21\overline{\delta}_{t,\nu} & \text{inner turbulent core} \\ 0.085\overline{\delta}_{t,\nu} & 0.21\overline{\delta}_{\nu} \le y \le \overline{\delta}_{t,\nu} & \text{outer turbulent core} \\ 0 & & \text{outside turbulent boundary layer} \end{cases}$$

$$\text{distribution of turbulent mixing length}, \qquad (6.198)$$

where $i = \alpha$ or ν (thermal or viscous), κ_{vK} (von Kármán universal constant) is typically equal to 0.41 and $\overline{\delta}_{t,\nu}$ is the the turbulent viscous boundary-layer thickness that will be subsequently given below [233]. The laminar sublayer thickness is given in terms of the wall shear stress $\overline{\tau}_s$ as $\delta_{l,\nu} = 10.8\mu_f/(\overline{\tau}_s/\rho_f)^{1/2}$, and $\delta_{l,\alpha} = 13.2\,\mathrm{Pr}\delta_{l,\nu}/10.8$. The mixing length is zero in the laminar sublayer where there are no turbulent fluctuations. Above the sublayer, the mixing length increases linearly with the distance from the bounding surface until $y = 0.21\overline{\delta}_{t,\nu}$, above which $\lambda_{f,t}$ is proportional to the boundary-layer thickness. Outside the boundary-layer (in the free stream) there are no turbulent fluctuations and $\lambda_{f,t} = 0$. In practice it is assumed that $\overline{\delta}_{t,\alpha} \simeq \overline{\delta}_{t,\nu}$, i.e, turbulent thermal and fluctuation boundary layer thickness are equal.

The turbulent wall shear stress related to the wall friction factor and boundary-layer thickness, are

$$\frac{\overline{\tau}_s}{\rho} = \frac{c_f \overline{u}^2_{f,\infty}}{2} \tag{6.199}$$

$$\frac{c_f}{2} = 0.0296 \, \mathrm{Re}_L^{-0.2} \tag{6.200}$$

$$\delta_{l,\nu} = 10.8 \frac{\mu_f}{(\overline{\tau}_s/\rho_f)^{1/2}}, \quad \frac{\delta_{t,\nu}}{L} = 0.037 \, \mathrm{Re}_L^{-0.2}. \tag{6.201}$$

Figure 6.16(a) shows the distribution of turbulent mixing length (dimensionless) as a function of the distance (dimensionless) from the edge of the laminar sublayer [4]. The results are deduced from the measured velocity distribution. Figure 6.16(b) shows the variation of the dimensional, directional fluid conductivity $\langle k_f \rangle_\perp = k_f + k_{f,t,\perp}$ with respect to the distance from the solid surface, calculated with the experimental results of [4]. The results are for air at T = 300 K, and $\mathrm{Re}_L = 3.55 \times 10^5$, which is close to the transition Reynolds number. The laminar sublayer and the turbulent boundary-layer thicknesses are also shown. For this experiment, the total conductivity reaches about 3.0 W/m-K (k_f = 0.026 W/m-K).

The distribution of the mean, x-direction velocity $\overline{u}_f$ is generally determined from empirical relations that include the dependence on y and Re_L [233].

Figures 6.14(c) and (d) give a rendering of this enhanced heat transfer. The fluctuations in the velocity and in the temperature are characterized by the turbulent eddies (i.e., small vortices with a large range of sizes and frequencies). The turbulent mixing length $\lambda_{f,t}$ is also shown.

6.12.5 Turbulent Mixing Using Lagrangian Langevin Equation

In [330], a modified Langevin equation is used to describe the turbulent mixing of thermal markers. They show results for a point source (or a sink) located on the wall of a channel with turbulent flow. This requires adding to the Brownian motion treatment, the direct influence of molecular thermal diffusion and the mechanism by which the dispersing markers are removed from the wall. This is done by considering that the markers are displaced both by convection and by a random walk associated with molecular diffusion. Because of molecular diffusion, the marker need not follow a fluid particle. This effect is taken into account by allowing the time-scales in the Langevin equation to depend on the Prandtl number (or the Péclet number). They use a modified Langevin equation to describe dispersion in an inhomogeneous field.

6.13 Thermal Plasmas: Plasma Thermal Conductivity

Electrically charged gases (i.e., plasmas) are heated by Joule heating through imposing an electric current. Gases become charged (i.e., ionized) at high temperatures (T_f > 2000 K). When very high temperature gases (i.e., T_f > 4000 K) are needed,

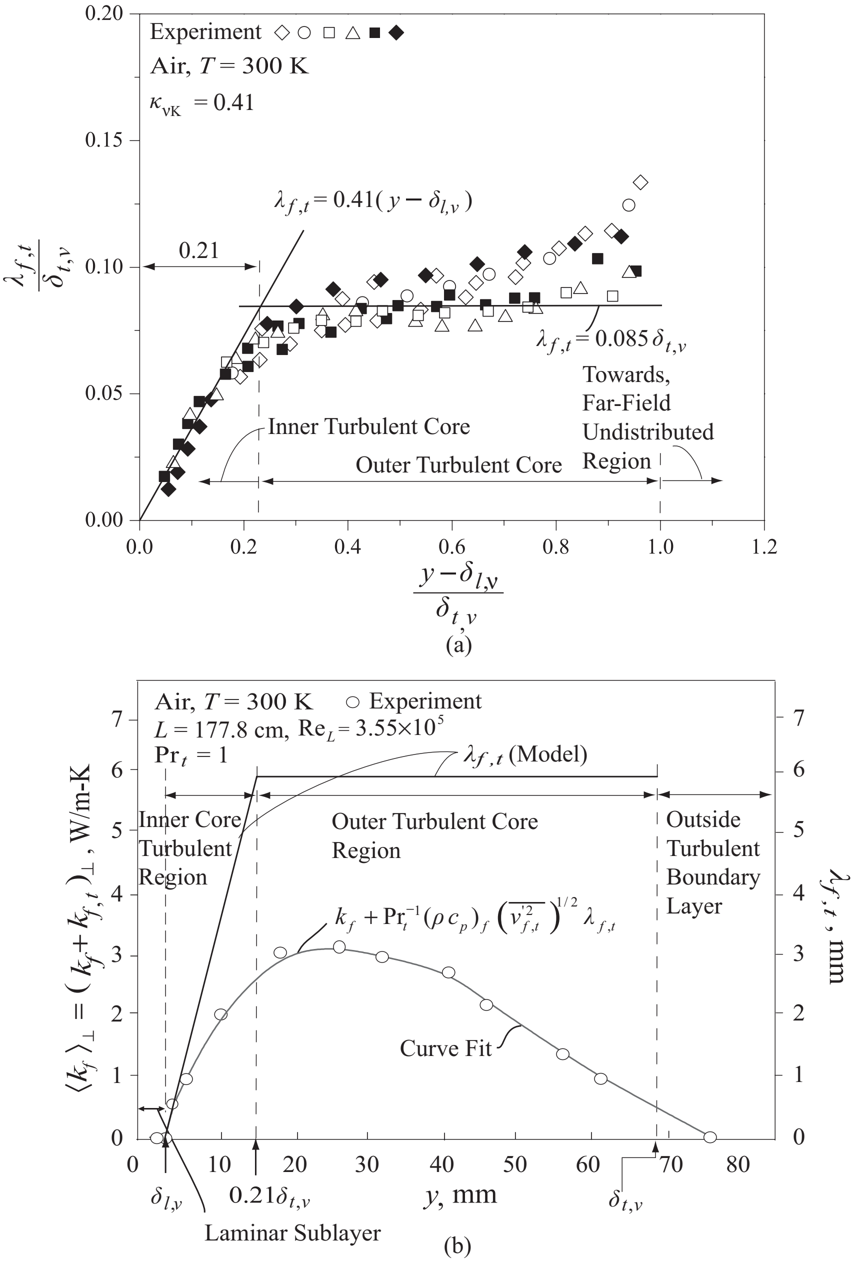

Figure 6.16. (a) Variations of the mixing length deduced from the measured velocity distribution, as fractions of the distance from the edge of the laminar sublayer [4]. (b) Variations of effective fluid directional thermal conductivity (left) and the model mixing length (right) with respect to distance from the surface [4].

Joule heating is used and the process is called thermal plasma generation. Figure 6.17 shows the typical temperatures in natural and engineered thermal plasmas and the associated force electron density $n_{e,c}$ (1/cm^3). A thermal plasma is made of electrons, ions, and neutral molecules and atoms. Compared with the conduction

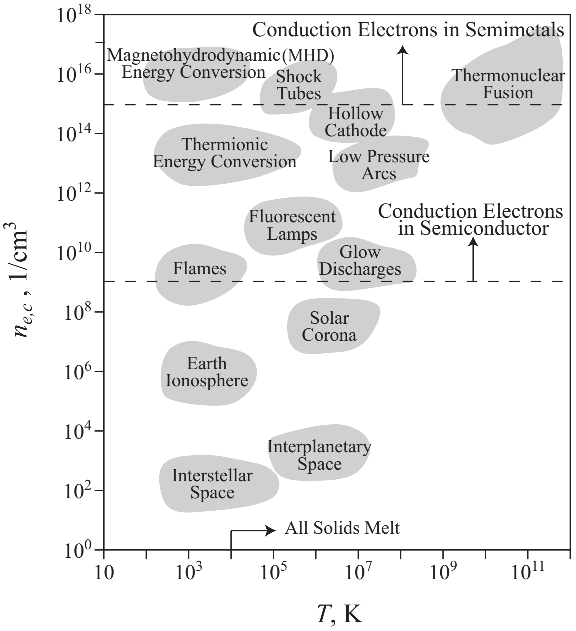

Figure 6.17. Typical temperatures for thermal plasmas and their associated force electron densities [253].

electrons in solids, Figure 5.20 for example, fluorescent lamps have higher conduction electron densities than some semiconductors. Also, the plasma in magnetohydrodynamics (MHD) has higher electron density than semimetals. Because electrons are much lighter than the rest of the species in the plasma, they heat up much faster. Therefore, unless there are many collisions among all the species, there can be a thermal nonequilibrium among them. Once the heat source (e.g., Joule heating) is removed, thermal equilibrium is quickly achieved, except for very short elapsed times and at very low pressures.

Among the common gases used in thermal plasmas are Ar, H_2, O_2, N_2, air, Ar–H_2, Ar–He, and CO_2. Laboratory units with the capability of $\dot{S}_{e,\mathrm{J}} = 30$ to 50 kW and industrial units of up to 1-MW power are used. Because of the high temperatures, there are some desired heat losses to prevent the solids in contact with the plasma from melting. There are also some undesired heat losses. Therefore the temperature in the gas drops over a short distance, but the center of the plasma has temperatures of about 10,000 K.

6.13.1 Free Electron Density and Plasma Thermal Conductivity

Thermal plasmas are used in manufacturing and materials processing, for example in the heating of sprays of paint particles in dry painting, in chemical vapor deposition, in welding, and in surface-material removal. Because of the free electrons, plasmas have a high electrical conductivity σ_e, and, depending on the gas, they can

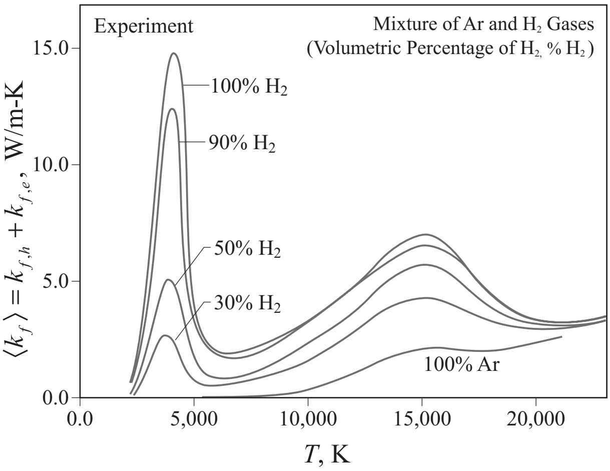

Figure 6.18. Thermal conductivity of Ar–H_2 gas mixture at elevated temperatures [53].

also have a high thermal conductivity. The plasma thermal conductivity $\langle k_f \rangle$ can be decomposed as

$$\langle k_f \rangle = k_{f,h} + k_{f,e} = \sum_h \frac{1}{3} n_h c_{v,h} u_h \lambda_h + \sum_e \frac{1}{3} n_e c_{v,e} u_e \lambda_e, \tag{6.202}$$

where $k_{f,h}$ represents the conductivity of heavier species and $k_{f,e}$ is for free electrons. Note that u_e used here is based on T_e, which may not be equal to T_h Section (6.13.2), and from (6.63) using the electron mass (Table A.3, $m_e = 5.45 \times 10^{-4}\ m_p$, where m_p is the proton mass), the electron thermal speed is rather large. This results in a large contribution from $k_{f,e}$. The collision diameter for e–h collision is also small, making λ_e large [according to (6.87)]. Figure 6.18 gives the thermal conductivity of Ar–H_2 mixture as a function of temperature and for various hydrogen volume fractions [53]. Note that, around $T = 3500$ K, the conductivity of hydrogen reaches a value of 15 W/m-K (because $k_{f,e} > k_{f,h}$ in ionized gases, this magnitude is typical of some metallic solids). Because of this high thermal conductivity, such thermal plasmas can very effectively heat the entrained particles (sensible heating rates $\mathrm{d}T/\mathrm{d}t$, of the order of 10^5 to 10^7 K/s are achieved).

The gas is charged by injection of charged particles, by pilot electrodes, by high frequency starting circuits, or by an initial increase in the gas temperature, for example, by an C_2H_2–O_2 torch. For the Joule heating of charged gases, the steady-state energy equation is given in Table 1.1. In thermal plasma generation, the volumetric radiation heat transfer becomes significant and needs to be included. Under local thermal equilibrium for all species in the plasma, the energy equation from Table 1.1 is written as

$$\nabla \cdot (\boldsymbol{q}_k + \boldsymbol{q}_u + \boldsymbol{q}_r) = \dot{s}_{ij} + \dot{s}_{e,\mathrm{J}} = \dot{s}_{ij} + \sigma_e \overline{\boldsymbol{e}_e \cdot \boldsymbol{e}_e} = \dot{s}_{ij} + \sigma_e \overline{e_e^2}$$

$$\text{thermal equilibrium energy equation,} \tag{6.203}$$

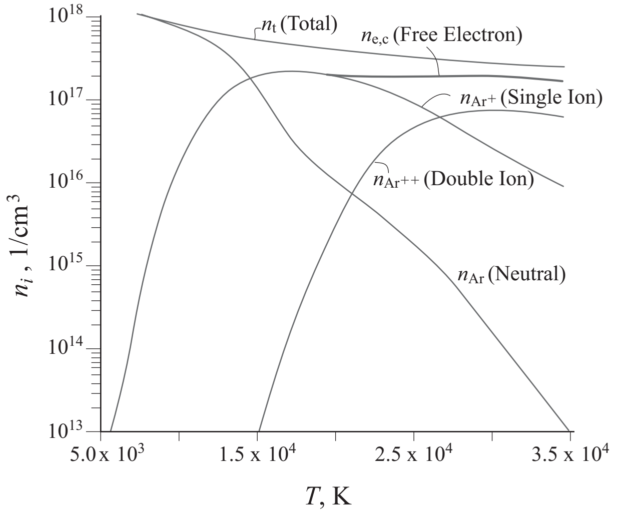

(a) Equilibrium Composition of Argon Plasma (p = 1 atm)

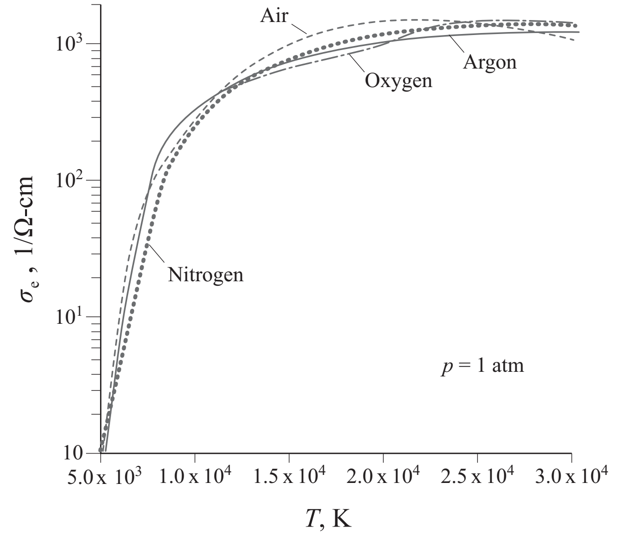

(b) Electrical Conductivity of Air, Argon, Nitrogen, and Oxygen Plasmas

Figure 6.19. (a) Equilibrium composition of argon plasma as a function of temperature at 1–atm pressure. (b) Electrical conductivities of air, argon, nitrogen, and oxygen plasmas as functions of temperature, at 1–atm pressure [263].

where $\dot{s}_{ij}$ is the dissociation-ionization energy conversion rate $\dot{s}_{ij} < 0$, and $\boldsymbol{e}_e$(V/m) is the electric-field intensity vector and can be steady or oscillating (i.e., time periodic). For time periodic fields use (3.52). Then a portion of $\dot{s}_{e,\mathrm{J}}$ is used for the dissociation–ionization. Figure 6.19(a) shows the equilibrium composition of the argon plasma as a function of temperature and at 1-atm pressure. Note that the concentration of free electrons n_e, c rises rapidly as $T = 1.5 \times 10^4$ K is reached and

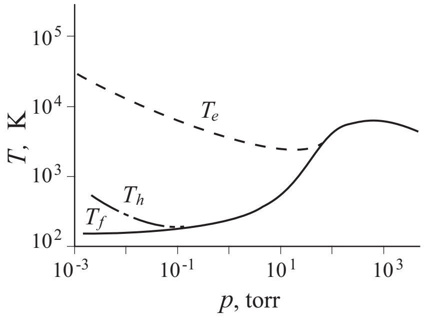

Figure 6.20. The thermal equilibrium, or lack of it, between electrons T_e, ions (heavier charged species) T_h, and the gas temperatures T_f including neutral atoms, as a function of pressure [253]. As the pressure (and collision rate) increases, thermal equilibrium is reached.

increases at a much lower rate shortly after that. The number of neutral species n_A decreases rapidly for $T > 10^4$ K and becomes relatively rare at $T = 3.5 \times 10^4$ K. In Figure 5.20 it was mentioned that solid semimetals have electron concentrations of 10^{15} to 10^{21} electrons/cm^3, and this places these thermal plasmas in the electronic conduction range of semimetals. The electrical conductivities of several gases are given in Figure 6.19(b), as functions of temperature. Again note that for $T > 10^4$ K a plateau is reached. These electrical conductivities are very large for the gas phase, but smaller than those of the metals.

Determination of $\dot{s}_{ij}$ involves determining the most significant dissociation and ionization reactions, which in turn requires knowledge of the associated equilibrium compositions and the energy needed for breaking each of these bonds. This is not addressed here, and details can be found in [263].

Plasmas are multicomponent high-temperature gases containing neutral particles and atoms and molecules, and electrons and ions with continuous and extensive interactions among them. The plasma state of matter and plasma physics are described in [83, 427]. The plasmas are further divided into cold and thermal plasmas. In cold plasmas, the lighter electron temperature is much higher than the other heavier gas constituents (i.e., ions and neutral atoms or molecules), and therefore thermal nonequilibrium exists between the electrons and the remainder gas species referred to as the heavier particles (T_h). In thermal plasmas, there exists a near-thermal equilibrium. In [253], it is shown that the increase in the pressure (or the molecular density) leads to thermal equilibrium. Figure 6.20 shows this trend toward thermal equilibrium with the increase in pressure (1 torr is equal to 1/760 of 1–atm pressure and one atmosphere is 1.013×10^5 Pa), where T_f stands for the gas temperature (electrons, ions, and neutral atoms) and T_e is the electron temperature. These ions are included in the heavier species. For $p > 100$ torr, thermal equilibrium is attained. The neutral atoms have the lowest temperature, thus reducing the average gas temperature. Then the atmospheric pressure plasmas are in equilibrium. The binary collision rate is given by (6.79) and p^2 dependence is shown in (6.80)

Plasmas can be under external applied electric or magnetic fields, and they generate (i.e., induce) a magnetic field as they flow. From the heat transfer characteristics, plasmas are a subset of the MHD, but they are generally treated separately for the following reasons.

Because of the very high temperatures, the radiative heat transfer is generally significant, and the multiple constituents have various constituent size, mass, and initial conditions, and therefore can be in local thermal nonequilibria [122]. The electrical conductivity of the dissociated and ionized gases also becomes significantly large with the increase in temperature, and, in general, the thermoelectrophysical property variations must also be considered. In low-pressure plasmas, the mean free path of the molecules may be of the order of the momentum and thermal boundary-layer thickness, and therefore in a transition-flow regime (Knudsen regime, discussed in Section 6.11), or a molecular-flow regime treatment may be necessary.

The equilibrium population density of the excited states of the various species are determined from the kinetic theory [253] and is in general treated similar to the chemical reactions. Treatments of the species equations and other transport and thermodynamic properties of plasmas are reviewed [122].

An example of plasma flow under an applied field is given in [468], where allowance for a velocity slip is made for electrons flowing at much higher velocities than the rest of the constituents. An example that includes chemical reactions among the constituents is given in [338].

6.13.2 Thermal Nonequilibrium Plasma Energy Equation

The thermal energy conservation equations for the electrons and for the heavier species are written assuming monatomic species. The specific heat capacity at constant pressure for ideally behaving monatomic gases is given by (6.23) using (6.21), i.e, per atom (particle) we have

$$c_p = c_v + k_\mathrm{B} = \frac{5}{2}k_\mathrm{B}. \tag{6.204}$$

The free-electron energy equation, similar to (5.265), but for a free-electron subsystem, becomes

$$\begin{aligned}\frac{1}{r^2}\frac{\partial}{\partial r}r^2\frac{5}{2}k_\mathrm{B}n_{e,c}T_e u + \frac{1}{r\sin\theta}\frac{\partial}{\partial\theta}\frac{5}{2}k_\mathrm{B}n_{e,c}T_e v\sin\theta &= \frac{1}{r}\frac{\partial}{\partial r}k_{f,e}r^2\frac{\partial}{\partial r}T_e \\ + \frac{1}{r^2\sin\theta}\frac{\partial}{\partial\theta}k_{f,e}\sin\theta\frac{\partial}{\partial\theta}T_e - \Delta E_\mathrm{I}\dot{n}_{e,c} + \nabla\cdot\boldsymbol{q}_r + \dot{s}_{e,J} - \dot{s}_{e\text{-}h},\end{aligned} \tag{6.205}$$

where ΔE_I is the ionization energy, $\dot{s}_{e,J}$ is volumetric Joule heating, and $\dot{s}_{e\text{-}h}$ is the rate of energy transfer from the electron to the heavier species. Also, u and v designate r and θ components of the gas velocity. The heavier species energy equation becomes

$$\begin{aligned}&\frac{1}{r^2}\frac{\partial}{\partial r}r^2\frac{5}{2}k_\mathrm{B}n_h T_h u + \frac{1}{r\sin\theta}\frac{\partial}{\partial\theta}\frac{5}{2}k_\mathrm{B}n_h T_h v\sin\theta \\ &\quad = \frac{1}{r^2}\frac{\partial}{\partial r}k_{f,h}r^2\frac{\partial}{\partial r}T_h + \frac{1}{r^2\sin\theta}k_{f,h}\sin\theta\frac{\partial}{\partial\theta}T_h + \dot{s}_{e\text{-}h}.\end{aligned} \tag{6.206}$$

The $\dot{n}_{e,c}$ in (6.205) is determined from a kinetic model and is a function of the electron temperature and the concentration of the electrons and atoms (as described in Section 6.13.3). The interaction kinetics rate between the electron and heavier species $\dot{s}_{e\text{-}h}$ is divided into the interaction between the electrons and ions and the interaction between the electrons and atoms. These interactions are determined by the proper kinetic models and depend on T_h and T_e as well as on $n_a, n_i (n_h = n_i + n_a)$, and $n_{e,c}$. These kinetic models are discussed in [78] and are reviewed in Section 6.13.4.

The two-medium (two-temperature) descriptions of the energy transport and the fluid dynamics just given for the electrons and the heavier species, with the viscosity (including the second viscosity), density, and the thermal conductivities being strong functions of the temperature, constitute a continuum description that now requires specification of the boundary conditions. The presumed low pressure of the plasma would require the modeling of these boundary conditions through the slip coefficients. These are discussed next.

6.13.3 Species Concentrations for Two-Temperature Plasmas

Consider the single ionization–recombination reaction for a monatomic gas

$$\mathrm{A} \rightleftharpoons \mathrm{A}^+ + e^-. \tag{6.207}$$

The law of mass action having the equilibrium constant in terms of the number densities of atoms, ions, and electrons, n_a, n_i, and n_e (for A, A^+, and e^-), which is derived in [87] for the case of local thermal nonequilibrium between the electrons and the heavier species (T_e and T_h). This is

$$\begin{aligned}
&\frac{p_e p_i}{p_a} = 2\frac{Z_{f,i}(T_e)}{Z_{f,a}(T_e)}\left(\frac{2\pi m_e k_\mathrm{B} T_e}{h_\mathrm{P}^2}\right)^{3/2} k_\mathrm{B} T_e \exp\left(-\frac{\Delta E_I}{k_\mathrm{B} T_e}\right) \quad \text{law of mass action} \\
&p_e = n_{e,c} k_\mathrm{B} T_e, \quad p_a = n_a k_\mathrm{B} T_h, \quad p_i = n_i k_\mathrm{B} T_h, \\
&Z_{f,a}(T_e) = \sum_k g_{a,k} \exp\left(-\frac{\Delta E_{a,k}}{k_\mathrm{B} T_e}\right), \quad Z_{f,i}(T_e) = \sum_k g_{i,k} \exp\left(-\frac{\Delta E_{i,k}}{k_\mathrm{B} T_e}\right),
\end{aligned} \tag{6.208}$$

or

$$\frac{n_{e,c} n_i}{n_a} = 2\frac{Z_{f,i}(T_e)}{Z_{f,a}(T_e)}\left(\frac{2\pi m_e k_\mathrm{B} T_e}{h_\mathrm{P}^2}\right)^{3/2} \exp\left(-\frac{\Delta E_I}{k_\mathrm{B} T_e}\right), \tag{6.209}$$

where ΔE_I is the effective ionization energy of the atom and $\Delta E_{a,k}$ and $\Delta E_{i,k}$ are the differences between the kth and ground-state energies. It is assumed that $m_a = m_i = m_h$.

The preceding equation is referred to as the Saha equation.

6.13.4 Kinetics of Energy Exchange Between Electrons and Heavier Species

The energy exchange between electrons and heavier species is based on collision frequency (similar to Section 6.5) extended to multicomponent gas, and is written

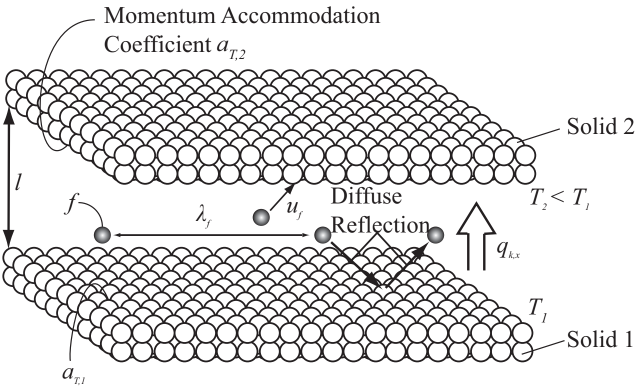

Figure 6.21. Conduction heat transfer across a confined (by two parallel solid surfaces) gas layer where $\mathrm{Kn}_l = \lambda_f / l$ is larger than unity.

as [78, 364]

$$\dot{s}_{e\text{-}h} = \dot{s}_{e\text{-}i} + \dot{s}_{e\text{-}a} \tag{6.210}$$

$$\dot{s}_{e\text{-}i} = \frac{2n_i e_c^4}{3m_n(4\pi\epsilon_o)^2}\left(\frac{8\pi m_e}{k_\mathrm{B}T_e}\right)^{1/2}\frac{1}{T_c}\ln\left[\frac{9(4\pi\epsilon_o k_\mathrm{B}T_e)^3}{4\pi n_{e,c}e_c^6}\right](T_e - T_h) \tag{6.211}$$

$$\dot{s}_{e\text{-}a} = 3k_\mathrm{B}n_{e,c}\frac{m_e}{m_h}\frac{(1-\alpha)\rho_g}{m_h}\left(\frac{8\pi m_e}{k_\mathrm{B}T_e}\right)^{1/2}A_{ea}(T_h - T_e), \tag{6.212}$$

where α is the degree of ionization, $A_{ea} = \pi d_{ea}^2/4$ is the electron-neutral collision cross-section area [212], and d_{ea} is the effective equivalent diameter for this collision (6.74). The collision frequency for electrons (and similarly for ions and neutrals) is expressed using (6.81) and is written as [212]

$$\frac{1}{\tau_e} = \sum_{k=i,a} n'_k A_{ek}(\langle u_e\rangle^2 + \langle u_k\rangle^2)^{1/2}\frac{2m_{ek}}{m_e}, \tag{6.213}$$

from (6.83), $m_{ek} = m_e m_k/(m_e + m_k)$. Empirical relations are used for the cross-section areas, including [212], i.e.,

$$A_{ea}(\mathrm{cm}^2) \simeq (-0.35 + 0.775 \times 10^{-4}T_e) \times 10^{-18}. \tag{6.214}$$

Numerical examples are given in [78].

6.14 Size Effects

6.14.1 Effective Thermal Conductivity in Gas-Filled Narrow Gaps

(A) *Regimes and Closed-Form Solutions*

At low gas densities or in small gaps, the probability of collision of fluid particles with the confining solid becomes larger than that of the interparticle collision. This is depicted in Figure 6.21 for two parallel plates, separated by a distance l, confining

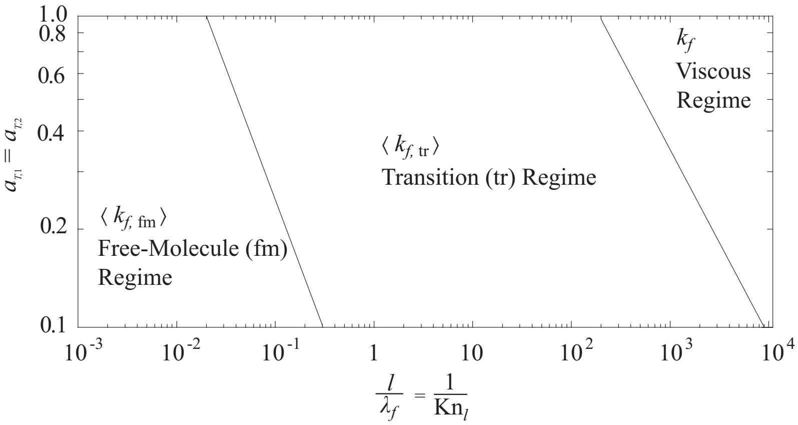

Figure 6.22. Classification of free-molecular, transition, and continuum (viscous) regimes for heat conduction across a gas confined between parallel plates for $a_{T,1} = a_{T,2}$ [444].

a gas in thermal motion (no net flow). Using the thermal accommodation coefficient (6.151), the monatomic, free-molecular (fm) regime effective gas thermal conductivity is [235, 441]

$$\frac{\langle k_{f,fm} \rangle}{l} = \frac{p(c_{v,f} + \frac{R_g}{2})}{\frac{1}{a_{T,1}} + \frac{1}{a_{T,2}} - 1} \frac{1}{(2\pi M R_g T)^{1/2}} \tag{6.215}$$

monatomic gas effective thermal conductivity in free-molecular regime,

where $c_{v,f}$ is the molar heat capacity and $R_g = k_{\rm B} N_{\rm A}$. This Knudsen number regime is $\text{Kn}_l = \lambda_f / l \rightarrow \infty$ (i.e., ballistic transport), so no Knudsen number appears. For the transition regime (intermediate Knudsen number), the preceding relation is modified as [444]

$$\langle k_{f,tr} \rangle = \langle k_{f,fm} \rangle (1 + \frac{4}{15} \frac{1}{\text{Kn}_l} \frac{a_{T,1} a_{T,2}}{a_{T,1} + a_{T,2} - a_{T,1} a_{T,2}})^{-1} \tag{6.216}$$

monatomic gas effective thermal conductivity in transition regime.

This includes the Knudsen number effect and the range of λ_f / l (and momentum accommodation coefficients $a_{T,1}$ and $a_{T,2}$), where (6.215) (free-molecular regime), (6.216) (transition regime), and (6.126) (continuum or viscous regime) are valid, and are shown in Figure 6.22. Note that $\text{Kn}_l = 1$ is in the transition regime.

For fluid particle–solid surface pairs with small a_T (Table 6.6), the transition to the continuum regime occurs at higher $1/\text{Kn}_l$, i.e., higher pressure [from (6.87)]. The small thermal accommodation coefficients would generally lead to smaller effective gas thermal conductivity. For example, for Ne–W pair, the transition to continuum regime occurs around 10^7 Pa (at 300 K), due to long mean free path and smaller a_T.

Figure 6.23 shows the variation of the effective thermal conductivity of Ar gas between two W plates separated by 1 μm, at 300 K, as a function of the gas pressure. The thermal accommodation coefficient is from Table 6.6. Note that $\langle k_{f,\text{fm}} \rangle$ increases

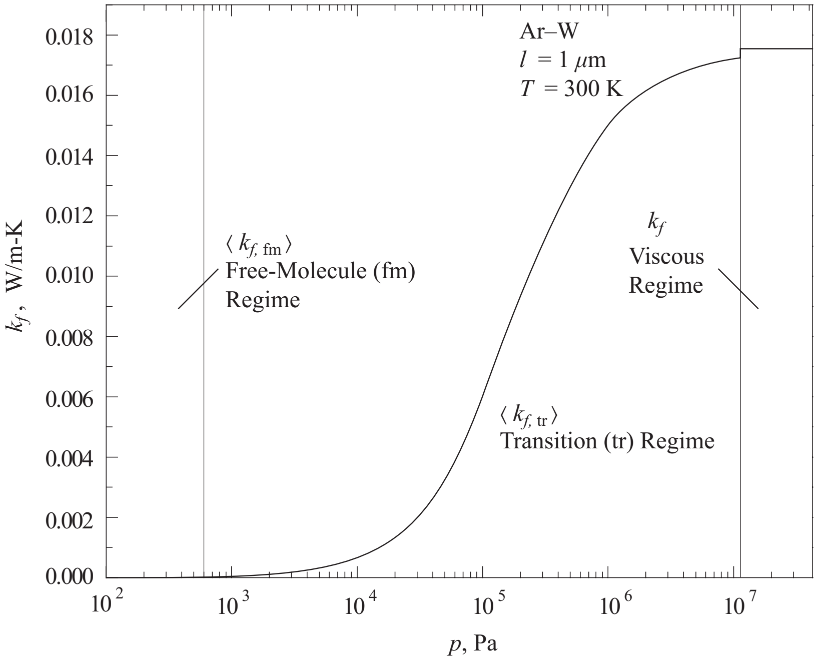

Figure 6.23. Variation of the effective thermal conductivity of Ar gas occupying spacing between two W plates separated by 1 μm, at $T = 300$ K, as a function of pressure.

linearly with p, whereas $\langle k_{f,\mathrm{tr}} \rangle$ has a middle exponential behavior bounded by a linear and a plateau behavior. There is a slight jump at the continuum (viscous) regime boundary. For the continuum regime, we have used $k_f = \beta n_f c_{v,f} \langle u_f \rangle \lambda_f / 2$, where $\beta = 5/2$ for monatomic gases [460]. Note that for this example, p for the beginning of the continuum regime is more than 100 atm. Also, note that the ballistic heat transfer by particles to the solid surface is not addressed here. So, $\langle k_f \rangle$ accounts for heat transfer through the particle-particle collision and the particle-wall collision.

(B) *MD Simulations Including Adsorption*

The effect of adsorption on momentum a_u and thermal a_T accommodation coefficients and effective thermal conductivity $\langle k_f \rangle$ of Ar vapor-filled Pt nanogap and nanocavity is examined using nonequilibrium MD simulations and L–J potentials [206]. Near the saturation temperature, condensable gas adsorbs onto the the confining surface by interatomic/molecular potential, and this adsorbed layer enhances thermal a_T and momentum a_u accommodation coefficients due to an increase in the fluid particles-confining surface interactions. This increased thermal accommodation in turn enhances the effective thermal conductivity, and the larger momentum accommodation increases viscous shear stress at the confining surface. This adsorption-affected heat transfer is significant in gas-filled nanopores, such as thermal insulation aerogels [200, 290], and in polymer electrolyte of fuel cells [99, 207], where the effective thermal conductivity and accommodation coefficients must be addressed. However, the effect of adsorption had not been addressed in the derivation of the closed-form solutions of the effective thermal conductivities in the molecular- and transition-flow regimes (6.215) and (6.216), and in the treatment of the momentum and thermal [46] accommodation coefficients.

For the confining surfaces, a three-layered, face-centered-cubic (FCC) (111) plane solid Pt is modeled using the harmonic potential with $N_s = 3,136$ atoms. The solid temperatures are controlled using the Langevin thermostat with phantom molecules as described in [309, 308, 484]. The parameters are as follows: The force constant $\Gamma = 46.8$ N/m, the mass of Pt is $m_s = 3.24 \times 10^{-1}$ yg, the equilibrium distance (distance to the neighboring atoms) $r_{\rm o} = 0.28$ nm, the friction (damping) coefficient $\gamma = 5.184 \times 10^{-12}$ kg/s, and the random excitation force of the Gaussian distribution with the standard deviation $\sigma_F = (2\Gamma k_{\rm B} T_s/\Delta t)^{1/2}$. The temperature difference between the two surfaces is from 10 to 120 K for the accommodation coefficients, (so it is larger than the temperature fluctuation of the solid), whereas 10 K is used for the effective thermal conductivity calculations.

For the Ar-Pt interactions, L–J potential is used in the nanogap, whereas a one-dimensional potential between Ar and the adiabatic side walls is used in the nanocavity. This is [308, 484]

$$\varphi_{sf}(l) = \frac{4\pi 3^{1/2}\epsilon_{sf}}{15}(\frac{\sigma_{sf}}{r_o})^2[2(\frac{\sigma_{sf}}{l})^{10} - 5(\frac{\sigma_{sf}}{l})^4], \tag{6.217}$$

where $\epsilon_{sf} = 6.82$ meV [442], $\sigma_{sf} = 0.309$ nm [484], l is the distance between the fluid particles and side walls, and the cut-off distance is $3.5\sigma_{sf}$. To reach steady state, 5×10^6 time steps are simulated; then we calculate ensemble-averaged thermodynamic properties, a_u, a_T, and $\langle k_f \rangle$ over another 5×10^6 time steps. The gas pressure is calculated using the ideal gas law. The accommodation coefficients are evaluated form of (6.151) and (6.150), following the recipes described in [442, 443]. An imaginary line is used to separate incident and reflecting particles and is placed at the cut-off distance of the solid-fluid interaction (1 nm from the surface). The selection of distance is based on two requirements [442, 443]. One is that the reflected particles must not be interfered with by surface forces, and the other is that the reflected particles should not collide with the adjacent fluid particles before passing through this imaginary line. For $N_f > 1,000$, the second requirement is violated due to the small mean free path ($\lambda_f \sim 2$ nm). Thus, we use $N_f = 1536$ only near the triple-point temperature, where adsorption significantly reduces the number of gaseous particles (to about 100).

The ensemble averaged heat flux is calculated similar to () as [353, 484],

$$\langle q_{k,g} \rangle = \frac{1}{V}[\sum_i \frac{1}{2} m_i (\boldsymbol{u}_i \cdot \boldsymbol{u}_i) u_{i,z} + \sum_i \varphi_i u_{i,z} + \frac{1}{2}\sum_i \sum_j z_{ij}(\boldsymbol{u_i} \cdot \boldsymbol{F_{ij}})], \tag{6.218}$$

where V is the volume, m_i is the mass of particle i, $\boldsymbol{u}_i$ is the velocity, $u_{i,z}$ is the z-component of the velocity, φ_i is the potential energy, z_{ij} is the z-component of the displacement separation, and F_{ij} is the interaction force between i and j particles. Note that $\langle\ \rangle$ represents the ensemble average. Then, the effective thermal conductivity is evaluated from the Fourier law, $\langle k_f \rangle = -\langle q_{k,g} \rangle/(\partial T/\partial z)$. Note that $\langle q_{k,g} \rangle$ is

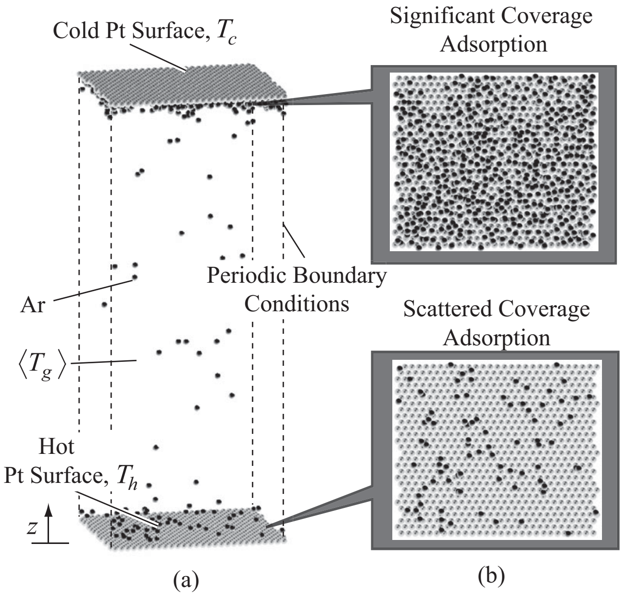
Cold Pt Surface, T_c
Significant Coverage Adsorption
Periodic Boundary Conditions
Ar
$\langle T_g \rangle$
Hot Pt Surface, T_h
z
Scattered Coverage Adsorption
(a)
(b)

Figure 6.24. (a) 3-D snapshot of simulated Ar atoms ($N_f = 600$, $\mathrm{Kn}_l = 2.1$) in the nanogap at $\langle T_g \rangle = 85$ K, showing larger adsorption on the top cold surface, and (b) stereo view of the top and bottom surface showing larger adsorption at the cold surface.

the same as the heat flowing into the hot and leaving the cold surface $\langle q_{k,s} \rangle$, which are calculated integrating the net damping and random forces with respect to time in the Langevin equation. Radiation heat transfer is neglected among the walls.

A snapshot of MD simulation in the nanogap, including adsorption, at $\langle T_g \rangle =$ 85 K with $N_f = 600$, is shown in Figures 6.24(a) and (b). The cold surface is below the triple-point temperature ($T_{tp} = 85$ K [219]), $T_c = 80$ K, whereas the hot surface is above it, $T_h = 90$ K. Noting that the triple-point temperature of Ar confined in Vycor glass nanopore is only 2 K larger than that for the bulk Ar [219], thus we expect the equilibrium phase diagram of the confined Ar to be different. Here we only use the bulk triple-point temperature as a reference when addressing phase change in the Ar-Pt nanogap. Near surfaces, thermodynamic equilibrium (chemical potential) between gas and adsorbed phase determines the surface coverage.

Adsorption influences the surface momentum and energy exchange as manifested through a_u and thermal a_T accommodation coefficients. In Figures 6.25 and 6.26, variations of MD-simulated a_u and a_T are shown with respect to surface temperatures, $75 < T < 1,320$ K (i.e., $0.06 < \epsilon_{sf}/k_\mathrm{B}T < 1.13$). The a_u has a low value ($a_u \simeq 0.33$) at high temperature $\epsilon_{sf}/k_\mathrm{B}T \rightarrow 0$ and increases toward unity (diffuse and no temperature slip) with decreasing temperature $\epsilon_{sf}/k_\mathrm{B}T \rightarrow \infty$. At low temperature, the kinetic energies of incident particles are small enough for significant solid-fluid interactions (adsorption) (i.e., the adsorbed particles fluctuate several times due to the attractive surface force before escaping out of the potential well). In addition, the adsorbed particles exchange kinetic energies with the neighboring adsorbed particles. These cause the increased a_u, and result in the

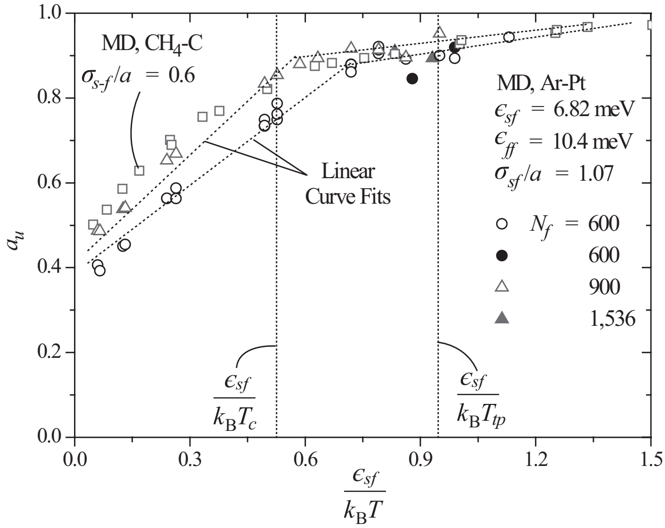

Figure 6.25. Predicted momentum accommodation coefficient a_u using $N_f = 600$, 900, or 1536 as a function of dimensionless inverse temperature $\epsilon_{sf}/k_B T$, showing transitions at $\epsilon_{sf}/k_B T = 0.7$ for $N_f = 600$ and $\epsilon_{sf}/k_B T = 0.6$ for $N_f = 900$. For $N_f = 600$, solid circles are the MD results for the hot surface above the triple-point temperature and the cold surface below it. Other simulation results are shown [6]. The linear curve fits, critical-, and triple-point temperature of Ar are also shown.

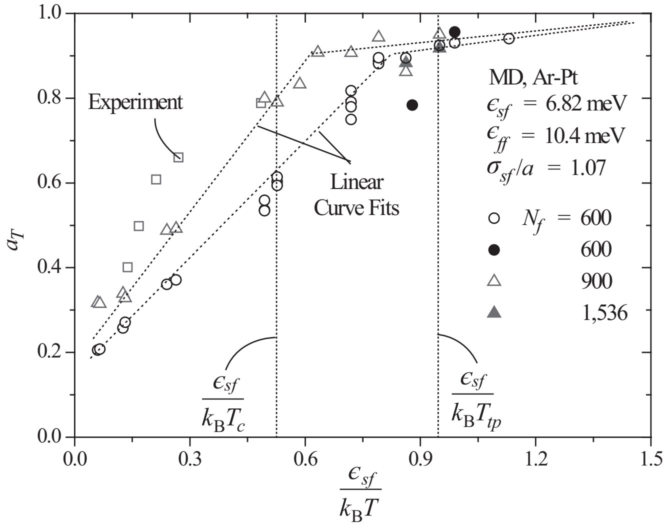

Figure 6.26. Predicted thermal accommodation coefficient a_T using $N_f = 600$, 900, or 1,536 as a function of dimensionless inverse temperature $\epsilon_{sf}/k_B T$, showing transitions at $\epsilon_{sf}/k_B T = 0.7$ for $N_f = 600$ and $\epsilon_{sf}/k_B T = 0.6$ for $N_f = 900$. For $N_f = 600$, solid circles represent the simulation results for the hot surface above the triple-point temperature and the cold surface below it. Experimental results are shown [50]. The linear curve fits, critical-, and triple-point temperature of Ar are also shown.

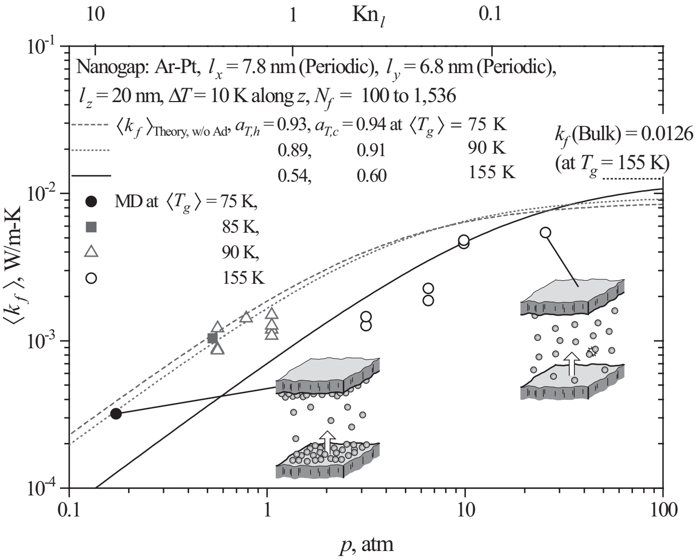

Figure 6.27. MD results for the effective thermal conductivity $\langle k_f \rangle$ in the nanogap with respect to vapor pressure $\langle p_g \rangle$ and Kn_l, at a few vapor temperatures $\langle T_g \rangle$.

transition at $\epsilon_{sf}/k_\mathrm{B}T \simeq 0.7$ which is related to the temperature where no significant adsorption occurs.

In the nanogap, the effective thermal conductivity in the transition regime is calculated between the triple-point and critical-point temperature and is compared with (6.216) using the predicted a_T as shown in Figure 6.27. Overall, the MD results are in good agreement with the closed-form solution within 20% uncertainty, even at low temperatures (significant adsorption). The closed-form solution is derived using the Maxwell integral equations of transfer, the Maxwell velocity distribution function of fluid particles, and the gas temperatures near the confining surfaces predicted by the accommodation coefficients and confining surface temperatures, neglecting adsorption as the boundary conditions. This approach is still valid even with adsorption because the thermal accommodation coefficients account for the effective fluid-wall molecular interactions. The MD results show that high temperatures allow for a large number density of gaseous particles, n_f small Kn_l without significant adsorption and large mean thermal velocity, which increase $\langle k_f \rangle$. However, the absence of adsorption results in low a_T, limiting $\langle k_f \rangle$. At low temperatures, small kinetic energy leads to significant adsorption, which, in turn, increases $\langle k_f \rangle$ by increasing a_T, whereas it causes large Kn_l and small mean thermal velocity that reduces $\langle k_f \rangle$.

6.14.2 Thermal Creep (Slip) Flow in Narrow Gaps

Thermal creep (slip) flow of a gas along a surface (nonadsorbing gas, i.e., no gas-surface interactions) with a temperature gradient results in flow from the colder region toward the higher-temperature region. In a tube with a relatively small temperature gradient along its surface, the density does not change appreciably over points a few mean free paths apart. Then the molecules striking it from one direction (i.e., the warmer side) supply it with an impulse proportional to the average thermal speed corresponding to the higher temperature, and those from the other direction give it an impulse proportional to the average thermal speed corresponding to the lower temperature. This difference in impulse (force) acting on the wall results in the differential force on the layer of the gas closer to the wall, thus resulting in the streaming of molecules from the cold to the hot end of the tube. Because the streaming is from the colder side toward the warmer side, the momentum that is due to the streaming gas would also reach the wall, and this would be opposite to the direction of increasing temperature, because it is in this direction that the wall acts on the nearest gas layers with their tangential forces.

Consider a temperature gradient along the x direction on the surface, given by $\mathrm{d}T/\mathrm{d}x$. Using the velocity equilibrium distribution function (6.61), which includes n_f, the probability distribution functions at a reference temperature T_o and at the varying temperature $T(x)$, we have

$$f_f^\mathrm{o}(T) = n_f(\frac{m}{2\pi k_\mathrm{B}T})^{3/2}\exp(-\frac{mu_f^2}{2k_\mathrm{B}T}) \tag{6.219}$$

$$f_f^\mathrm{o}(T_\mathrm{o}) = n_{f,\mathrm{o}}(\frac{m}{2\pi k_\mathrm{B}T_\mathrm{o}})^{3/2}\exp(-\frac{mu_f^2}{2k_\mathrm{B}T_\mathrm{o}}) \tag{6.220}$$

or

$$\frac{f_f^\mathrm{o}(T)}{f_f^\mathrm{o}(T_\mathrm{o})} = \frac{n_f}{n_{f,\mathrm{o}}}(\frac{T_\mathrm{o}}{T})^{3/2}\exp[\frac{mu_f^2}{2k_\mathrm{B}}(\frac{1}{T_\mathrm{o}}-\frac{1}{T})]. \tag{6.221}$$

Now using a linear variation in the temperature, we have

$$T = T_\mathrm{o}(1+\frac{1}{T}\frac{\mathrm{d}T}{\mathrm{d}x}x) \tag{6.222}$$

$$n_f = n_{f,\mathrm{o}}(1+\frac{1}{T}\frac{\mathrm{d}T}{\mathrm{d}x}x)^{-1} \text{ from } p = n_f k_\mathrm{B}T. \tag{6.223}$$

Using these, we have

$$\begin{aligned}\frac{f_f^\mathrm{o}(T)}{f_f^\mathrm{o}(T_\mathrm{o})} &= \frac{1}{1+\frac{1}{T}\frac{\mathrm{d}T}{\mathrm{d}x}x}\frac{1}{(1+\frac{1}{T}\frac{\mathrm{d}T}{\mathrm{d}x}x)^{3/2}}\exp[\frac{mu_f^2}{2k_\mathrm{B}T_\mathrm{o}}(1-\frac{1}{1+\frac{1}{T}\frac{\mathrm{d}T}{\mathrm{d}x}x})]\\ &\simeq (1-\frac{5}{2}\frac{1}{T}\frac{\mathrm{d}T}{\mathrm{d}x}x)\exp(\frac{1}{T}\frac{\mathrm{d}T}{\mathrm{d}x}x\frac{mu_f^2}{2k_\mathrm{B}T})\\ &\simeq 1-\frac{5}{2}\frac{1}{T}\frac{\mathrm{d}T}{\mathrm{d}x}x+\frac{1}{T}\frac{\mathrm{d}T}{\mathrm{d}x}x\frac{mu_f^2}{2k_\mathrm{B}T}\\ &= 1+\frac{1}{T}\frac{\mathrm{d}T}{\mathrm{d}x}x(\frac{mu_f^2}{2k_\mathrm{B}T}-\frac{5}{2}),\end{aligned}$$

where the Taylor series expansion is used twice.

Now the disturbed distribution function is given in terms of the equilibrium distribution function and a perturbation parameter ϕ

$$\begin{aligned} f_f &= f_f^{\rm o}(T)(1+\phi) \\ &= f_f^{\rm o}(T_{\rm o})[1+\frac{1}{T}\frac{{\rm d}T}{{\rm d}x}x(\frac{mu_f^2}{2k_{\rm B}T}-\frac{5}{2})](1+\phi) \\ &\simeq f_f^{\rm o}(T_{\rm o})[1+\frac{1}{T}\frac{{\rm d}T}{{\rm d}x}x(\frac{mu_f^2}{2k_{\rm B}T}-\frac{5}{2})+\phi]. \end{aligned} \quad (6.224)$$

Next the gas BTE (6.102) becomes

$$\begin{aligned} \boldsymbol{u}_f \cdot \nabla f_f &= \frac{\partial f}{\partial t}|_s \\ u_{f,r}\frac{\partial f_f}{\partial r} + u_{f,x}\frac{\partial f_f}{\partial x} &= \frac{\partial f}{\partial t}|_s \\ u_{f,r}\frac{\partial \phi}{\partial r} + u_{f,x}\frac{1}{T}\frac{{\rm d}T}{{\rm d}x}(\frac{mu_f^2}{2k_{\rm B}T}-\frac{5}{2}) &= \frac{\partial \phi}{\partial t}|_s = -\frac{\phi}{\tau_{f\text{-}f}}. \end{aligned} \quad (6.225)$$

Next, the solution to (6.225) is found and after lengthy steps, the thermal slip (creep) speed at the surface is given by [235, 292]

$$u_{i,T} = \sigma_T \frac{\mu_f}{p}\frac{R_g}{M}\frac{{\rm d}T}{{\rm d}x} \quad \text{thermal slip (creep) speed } u_{i,T} \text{ and constant } \sigma_T, \quad (6.226)$$

where σ_T is the thermal slip constant. Then using (6.92) for μ_f, we have

$$u_{i,T} = \frac{\sigma_T}{3}\langle u_f^2\rangle^{1/2}\lambda_f\frac{1}{T}\frac{{\rm d}T}{{\rm d}x}, \quad \sigma_T = \frac{3}{4} \quad \text{Kennard thermal slip constant} \quad (6.227)$$

Kennard [235] derives a relation that gives $\sigma_T = 3/4$.

As an example for the thermal slip speed of air, at $T = 298$ K and $p = 1.013 \times 10^5$ Pa, we have $\langle u_f^2\rangle^{1/2} = 413.7$ m/s, and $\lambda_f = 64.0 \times 10^{-9}$ m, and then $u_{i,T} = 2.221 \times 10^{-8}{\rm d}T/{\rm d}x$. On reducing the pressure, for example to 1.013×10^2 Pa, this speed increases by a factor of 10^3. Further refinement of (6.226) is reported in [292] and [422]. In the latter, a value of 1.175 is computed for σ_T, with a relatively small dependence on the mixture composition.

For flow through the tube of radius R, for the case of high ${\rm Kn}_R = \lambda_f/R$ (R is the tube radius), we have only the thermal creep flow, and for small ${\rm Kn}_R$, we also have the viscous-flow contribution. Figures 6.28(a) and (b) show these two flow regimes. Now the combined the thermal slip (6.227) and the Knudsen slip (6.152) for radial geometry give the total velocity slip at the tube wall as

$$u_i = -\alpha_u \frac{\partial \overline{u}_{f,x}}{\partial r} + \sigma_T \frac{\mu_f}{p}\frac{R_g}{M}\frac{{\rm d}T}{{\rm d}x} \quad \text{at } r = R. \quad (6.228)$$

The momentum equation is given in Table 3.10, and for $\overline{u}_{f,x}$ and ${\rm d}p/{\rm d}x$ (using the symmetry at the center line, $r = 0$), we have

$$\overline{u}_{f,x} = -\frac{1}{4\mu_f}(R^2 - r^2 + 2\alpha_u R)\frac{{\rm d}p}{{\rm d}x} + \sigma_T\frac{\mu_f}{p}\frac{R_g}{M}\frac{{\rm d}T}{{\rm d}x}. \quad (6.229)$$

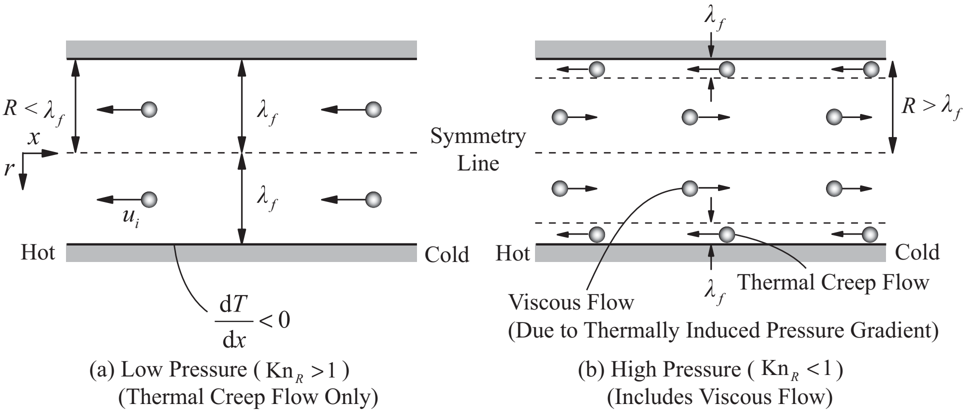

(a) Low Pressure ($\mathrm{Kn}_R > 1$)
(Thermal Creep Flow Only)

(b) High Pressure ($\mathrm{Kn}_R < 1$)
(Includes Viscous Flow)

Figure 6.28. (a) Knudsen-, and (b) viscous-flow regimes of the thermal creep flow (temperature gradient along the tube surface)

The fluid flow rate is

$$\dot{M}_f = -\frac{\pi}{8}\frac{R^4 pM}{\mu_f R_g T}(1+4\frac{\alpha_u}{R})\frac{\mathrm{d}p}{\mathrm{d}x} + \sigma_T \pi \frac{\mu_f R^2}{T}\frac{\mathrm{d}T}{\mathrm{d}x}. \tag{6.230}$$

Note that for $\dot{M}_f = 0$ we have (for nonadsorbing gas), (6.230) giving the induced pressure gradient as

$$\frac{\mathrm{d}p}{\mathrm{d}x} = \frac{8\sigma_T \mu_f^2 R_g}{MR^2 p(1+4\frac{\alpha_u}{R})}\frac{\mathrm{d}T}{\mathrm{d}x} \quad \text{thermally induced pressure gradient for } \dot{M}_f = 0. \tag{6.231}$$

This thermally induced pressure gradient (in the viscous-flow regime) returns the thermal creep flow, resulting in the zero net flow rate. Note that $\mathrm{d}p/\mathrm{d}x$ follows $\mathrm{d}T/\mathrm{d}x$, i.e., pressure is lower where the temperature is lower.

6.15 Problems

Problem 6.1

Use the software Gaussian to obtain the rotational constant, and the first four vibrational states of CO_2. The values are listed in Section 6.1.5 and its footnote.

Problem 6.2

Derive the specific heat capacity relation (6.22) using the definitions for the ideal gas and the diatomic molecule, translational (6.10), vibrational (6.14), and rotational (6.16) partition functions.

For rotational partition function, an approximation $\ln[1 + T_{f,r}/3T + \cdots] \cong T_{f,r}/3T + \cdots$. can be used, but is not necessary.

Problem 6.3

Show that the dense fluid total partition function is (6.36), using the partition function for the individual energies.

Problem 6.4

Derive van der Waals equation of state (6.38), using the dense-fluid total partition function.

Problem 6.5

Derive the relation for the specific heat capacity (at constant pressure) for the van der Waals dense fluid, i.e., (6.40), using (6.36), (6.38), and (6.39).

Problem 6.6

Using M–B speed distribution function $f_f^{\rm o}(u_f)$, show that the ideal-gas average thermal speed is $\langle u_f \rangle = (8k_{\rm B}T/\pi m)^{1/2}$, i.e., (6.63).

Problem 6.7

Using (6.24) and Table 6.2, plot $Mc_{v,f}/R_g$ for CH_4 (methane) as a function of temperature, up to 2500 K, as in Figure (b), and comment on its molecular degrees of freedom of motion changing with temperature.

Problem 6.8

Complete the integration (6.88) to show the relation (6.89) for the ideal-gas mass flux.

Problem 6.9

Show that the integral (6.119) will give the same result (6.123) when we use (6.64) for the particle equilibrium distribution function and take the integral directly over the energy (instead of the momentum space).

Problem 6.10

(a) Use the three-dimensional liquid MD code and plot the trajectory of a fluid particle (start near the center of the computational cube).

(b) Plot the velocity distribution function (use x-direction velocity and divide the negative and positive velocities into small bins and enter the number of particles with velocity in a particular bin and then plot this number versus velocity).

(c) Comment on the distribution found in part (b) and compare with the M–B distribution function (6.77).

Problem 6.11

(a) Show that (6.34) is the result of integration (6.33).

(b) Assuming $d = \sigma_{\rm LJ}$ and using Table 6.3, evaluate a and b for H_2O and compare with the tabulated values (Table 6.4). Comment on the validity of the assumption $d = \sigma_{\rm LJ}$.

Problem. 6.12

Consider a one-dimensional ideal gas flow along x, with a velocity $U_{f,x}(y) = u_{f,x} + \overline{u}_{f,x}(y)$, where $\overline{u}_{f,x}(y)$ is the average velocity. Assume that

(i) $(\partial f_f/\partial t)_s = -(f_f - f_f^{\rm o})/\tau_{f\text{-}f}$, where $\tau_{f\text{-}f}$ is the relaxation time to restore equilibrium, which is the time between molecular collisions.

(ii) $\partial f_f/\partial y = \partial f_f^{\rm o}/\partial y$,

(iii) no external forces, and

(iv) steady-state condition.

(a) Show that the gas BTE leads to

$$f_f - f_f^{\rm o} = \tau_{f\text{-}f} U_{f,y} \frac{f_f^{\rm o}}{u_{f,x}} \frac{\partial \overline{u}_{f,x}}{\partial y}.$$

(b) Then using (6.91) for the definition of the viscous shear stress, show that the gas viscosity is (6.91), i.e., $\mu_f = \rho_f \tau_{f\text{-}f} \langle u_f^2 \rangle/3$, where $\rho_f = mn_f$ is the density of the gas, and $\langle u_f^2 \rangle^{1/2}$ is the RMS thermal (fluctuation) speed, which is given by $\langle u_f^2 \rangle = \int u_f^2 f_f^{\rm o}(\boldsymbol{u}_f)\mathrm{d}\boldsymbol{u}_f$.

The definitions of viscous shear stress and viscosity are given by (6.90), i.e.,

$$\tau_{xy} \equiv \int_{\boldsymbol{u}} m u_{f,x} u_{f,y} f_f^{\rm o} \mathrm{d}\boldsymbol{u}_f. \quad \tau_{xy} \equiv -\mu_f \frac{\partial \overline{u}_{f,x}(y)}{\partial y}.$$

Note that $\langle u_f^2 \rangle = 3\langle u_{f,y}^2 \rangle$ with the isotropic assumption. Also, note that the integral $\int u_{f,x} u_{f,y} f_f^{\rm o} \mathrm{d}\boldsymbol{u}_f$ is zero, i.e.,

$$\int u_{f,x} u_{f,y} f_f^{\rm o} \mathrm{d}\boldsymbol{u}_f = \int f_{f,z}^{\rm o} \mathrm{d}u_z \int u_x f_{f,x}^{\rm o} \mathrm{d}u_x \int u_y f_{f,y}^{\rm o} \mathrm{d}u_y,$$

where $u_{f,x} f_{f,x}^{\rm o}$ is an odd function of $u_{f,x}$, then $\int u_{f,x} f_{f,x}^{\rm o} \mathrm{d}u_{f,x} = 0$. Similarly, $\int u_{f,y} f_{f,y}^{\rm o} = 0$, etc.

Problem 6.13

(a) Using one-dimensional motion, show that the relative speed of colliding particles remains the same before and after elastic collision, i.e., show (6.69) using the momentum and energy conservation during the collision.

(b) Derive (6.79) for the particle collision rate, by completing the integration in (6.75). Take $\boldsymbol{u}_{f,1} \cdot \boldsymbol{u}_{f,2} = 0$ for a general treatment.

(c) Determine the collision rate and the mean free path for ideal gas air at $p = 1$ atm and $T = 300$ K, using the molecular collision diameter from Table 6.4.

Note that the integration over ψ and ϕ are separated and, show that this integral is equal to π.

Problem 6.14

(a) Use the relation for the thermal conductivity of a polyatomic, ideal gas (6.128) to predict the thermal conductivity of air at $T = 300$ K and $p = 1$ atm. In (6.128) $c_{v,f} = 3R_g/2M$, then (6.25) for ideal gas and $c_{p,f} = 5R_g/2M$. Compare this with the available the measured value. The prediction can be improved using experimental values for $c_{v,f}$, $c_{p,f}$, ρ_f, $a_{\rm s}$, and λ_f.

(b) Use the Bridgman liquid thermal conductivity relation (6.131) to calculate the thermal conductivity of liquid water at $T = 300$ K, and $p = 1$ atm.

Problem 6.15

Using the fluid particle velocity probability distribution function that satisfies the fluid particle number density n_f for the ideal gas,

$$f_f^{\rm o}(\boldsymbol{u}_f) = n_f(\frac{m}{2\pi k_{\rm B}T})^{2/3}\exp(\frac{-mu_f^2}{2k_{\rm B}T}),$$

which is also listed in footnote of Section 6.4.2, show that $\int f_f^{\rm o}{\rm d}\boldsymbol{u}_f = n_f$.

Problem 6.16

Consider the effect of nanoparticles (in Brownian motion) on the effective conductivity of host liquid.

(a) Use effective conductivity $\langle k_f\rangle$ relation (6.144), for water at $T = 300$ K, with alumina (Al_2O_3, five atoms per molecule) nanoparticles, and assume the particles are not in a cluster form (i.e., are well-dispersed). Then calculate $\langle k_f\rangle$ for the following conditions. $d_s = 10$ nm, $n_s = 10^{20}$ 1/cm^3, $c_{v,s} = 3\times 5Nk_{\rm B}$, number of molecules per particle $N = N_A\rho_s\pi d_s^3/(6M_s)$, where 5 in the $c_{v,s}$ expression is the number of atoms in Al_2O_3, $\rho_s = 4000$ kg/m^3, and M_s are the density and molecular weight of the particles, $k_s = 36$ W/m-K (no size effect assumed, but it can reduce k_s significantly), and the water properties at 300 K. Use (6.145) for the diffusion thermal relaxation time, and $\tau_\alpha = 0.1\times 3c_{v,s}/2\pi d_sk_s$, with $\langle u_s^2\rangle = 3k_{\rm B}\,T_f/m_s$.

(b) Repeat for $d_s = 50$ nm, while keeping the mole fraction of nanoparticle the same. Note that $n_s = 6/\pi d_s^3$.

(c) Use $d_s = 10$ nm, and repeat with external resistance and time constant $\tau_\alpha = c_{v,s}/2\pi d_sk_f$.

(d) Comment on the conductivity enhancement that is due to nanoparticles in Brownian motion, is it significant? Note that the larger particles do not remain suspended and tend to precipitate.

Problem 6.17

The mean free path concept, the classical specific heat capacity, and fluid particle flux can be directly used for fluid particle thermal conductivity (6.126) for ideal gas. The figure shows the direction of conduction heat flow along direction x, where the temperature distribution is given by $T = T(x)$. The smallest distance we can use as our differential (vanishing length) is the average of the mean free path.

(a) Show that the number of particles that cross $x = 0$ moving in the $+x$ direction with a given speed u, making an angle between θ and $\theta + {\rm d}\theta$ with the x axis, is proportional to $\sin\theta\cos\theta{\rm d}\theta$.
Hint: use

$$f_f^{\rm o}(u_f) = (\frac{m}{2\pi k_B T})^{3/2}\exp(\frac{-mu_f^2}{2k_{\rm B}T})u_f^2{\rm d}\Omega,$$

similar to (6.62). Also the differential solid angle ${\rm d}\Omega = 2\pi\sin\theta{\rm d}\theta$.

(b) Show that the average distance traveled along the x direction is $2\lambda_f/3$.

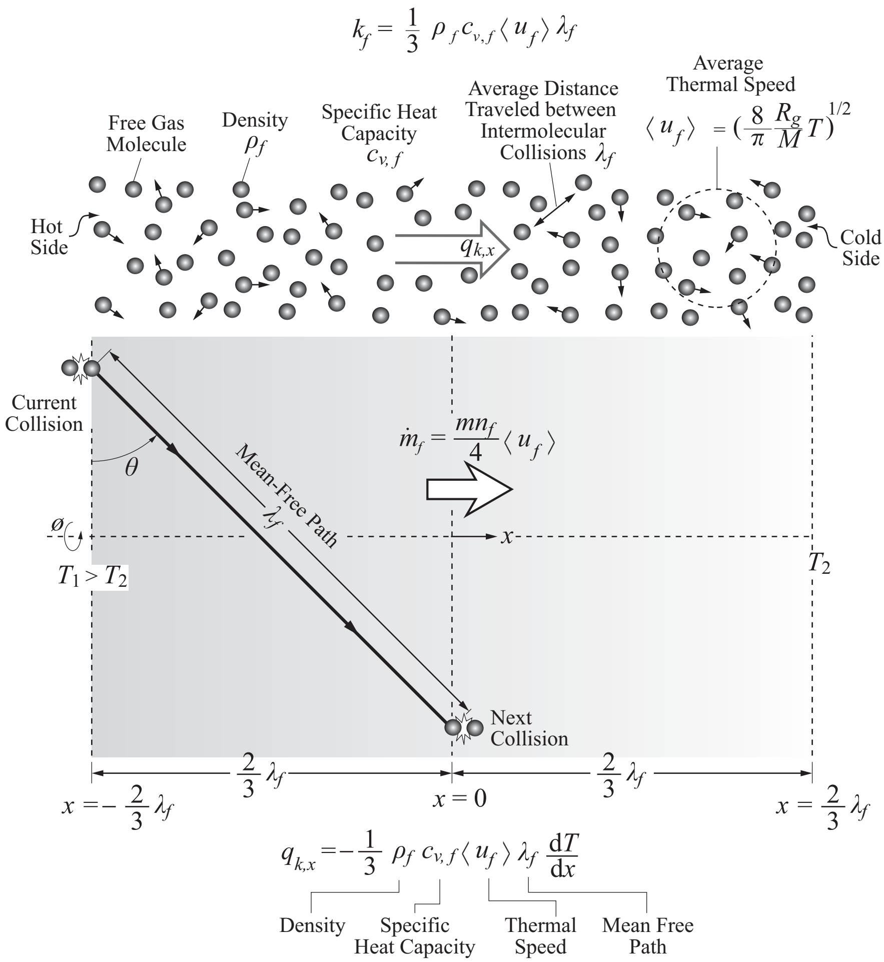
$k_f = \frac{1}{3}\,\rho_f c_{v,f} \langle u_f \rangle \lambda_f$
Free Gas Molecule
Density ρ_f
Specific Heat Capacity $c_{v,f}$
Average Distance Traveled between Intermolecular Collisions λ_f
Average Thermal Speed
$\langle u_f \rangle = (\frac{8}{\pi}\frac{R_g}{M}T)^{1/2}$
Hot Side
Cold Side
$q_{k,x}$
Current Collision
θ
Mean-Free Path λ_f
$\dot{m}_f = \frac{mn_f}{4}\langle u_f \rangle$
ø
x
$T_1 > T_2$
T_2
Next Collision
$\frac{2}{3}\lambda_f$
$\frac{2}{3}\lambda_f$
$x = -\frac{2}{3}\lambda_f$
$x = 0$
$x = \frac{2}{3}\lambda_f$
$q_{k,x} = -\frac{1}{3}\,\rho_f\, c_{v,f} \langle u_f \rangle \lambda_f \frac{\mathrm{d}T}{\mathrm{d}x}$
Density
Specific Heat Capacity
Thermal Speed
Mean Free Path

Problem 6.17. Derivation of k_f from kinetic theory of gases.

(c) Using the fluid particle (molecular) mass flux (6.89) and the Fourier law of conduction (6.103), show that the conduction heat flux is [this is an alternative (6.114) which uses BTE]

$$
\begin{aligned}
q_{k,x} &= \frac{1}{4} m n_f \langle u_f \rangle (e_{f,1} - e_{f,2}) \\
&= \frac{1}{4} m n_f \langle u_f \rangle \frac{\mathrm{d}e}{\mathrm{d}T}\frac{\mathrm{d}T}{\mathrm{d}x}(-\Delta x) \\
&= \frac{1}{4} m n_f \langle u_f \rangle \frac{\mathrm{d}e}{\mathrm{d}T}\frac{\mathrm{d}T}{\mathrm{d}x}(-\frac{4}{3}\lambda_f).
\end{aligned}
$$

(d) Using the definition of $c_{v,f}$ (Table 2.4) show that

$$
q_{k,x} = -\frac{1}{3}\rho_f c_{v,f} \langle u_f \rangle \lambda_f \frac{\mathrm{d}T}{\mathrm{d}x}, \quad \rho_f = m n_f.
$$

Note that here the average internal energy is used, while in (6.114) the phase-space internal energy is used. However, the final results are the same.

Problem 6.18

(a) Show that integral (6.176) gives the relation (6.177) for the mean-field potential $\langle \varphi_f \rangle$.

(b) Using $n_s = n_f = 2{\times}10^{28}$ 1/m^3, $\sigma_{\mathrm{LJ},f\text{-}s} = 3.0$ Å, and $\epsilon_{\mathrm{LJ},t\text{-}s} = 1.7{\times}10^{-21}$ J, calculate the Hamaker constant in J and in eV.

(c) Plot the disjoining pressure p_d versus the liquid film thickness, using (6.178), for the fluid-solid pair in (b), and for $5 < \delta < 1000$ Å.

Problem 6.19

Determine the thermophoretic force on an alumina ($\mathrm{Al_2O_3}$) particle with diameter of 100 nm in air at $T = 800$ K and a temperature gradient of 500 K/mm.

Problem 6.20

(a) Using the available thermodynamics data for saturated water, and (6.93), plot $\dot{S}_{f\text{-}f,lg,max}/A$ as a function reduced pressure p/p_c [as shown in Figure 6.7(a)].

(b) At one atom pressure, the critical heat flux (dryout limit) of a pool of boiling water under normal gravity is about 1.2 MW/m^2. What fraction of (a) is this? Comment on the limitation of pool boiling (buoyancy driven flow) and how this boiling critical heat flux can be increased.

Problem 6.21

The high thermal conductivity of thermal plasmas (Figure 6.18) is due to the collisions of large number density charged and neutral particles ($n_{e,c}$ and n_a) moving at high thermal speeds.

(a) Consider the electrons with the largest thermal speed (smallest mass) to dominate the thermal conductivity, i.e., use (6.202) as electronic thermal conductivity only $\langle k_f \rangle = k_{f,e} = n_{e,c} c_{v,e} u_e \lambda_e / 3$. For pure $\mathrm{H_2}$ thermal plasma at $T_e = 4000$ K, use k_f from Figure 6.18, and $n_{e,c} = 10^{16}$ 1/cm^3. Then using $c_{v,e} = 3k_{\mathrm{B}}/2$ per free electron, and u_e from (6.59), calculate the electron mean free path λ_e.

(b) Using this λ_e, estimate the electron-atom collision diameter d_{ea} from (6.87), assuming $n_e \gg n_a$.

(c) Comment on the magnitude of d_{ea} and the applicability of this analysis.

Problem 6.22

(a) Using (6.128), (6.215), and (6.216), for air–Al (even though this is a diatomic gas mixture) at $T = 300$ K, with a gap size $l = 1$ μm, plot $\langle k_f \rangle$ as a function of pressure for 10^2 to 2×10^8 Pa. Use Table 6.6 for the thermal accommodation coefficient, then using this value in Figure 6.22 find the marking for the viscous, transition, and free-molecular regimes

(b) Repeat part (a) for Ne–W using $k_f = \frac{1}{2}\beta n_f c_{v,f} \langle u_f \rangle \lambda_f$ [460], $\beta = 5/2$ for monatomic gases.

(c) Comment on the trends and any jumps (discontinuities) in the curves. Note that the accommodation coefficient is temperature dependent, increasing as the temperature decreases [Section 6.14.1(B)].

Problem 6.23

Consider application of the Fermi golden rule (FGR) to the kinetics of vibrational energy transfer from an adsorbed CO molecule to its metallic substrate crystalline Ni. In the adsorbed state, the CO vibration is affected by the surface force field and is called the frustrated vibration. This CO vibration is transmitted through the CO-Ni stretching vibration which is in turn damped via a multi-phonon process (phonon emission). These are shown in the figure below.

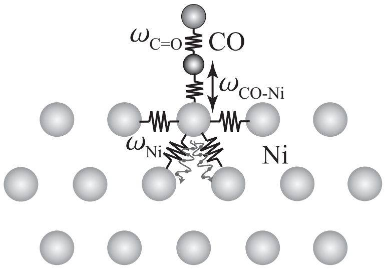

Problem 6.23. Adsorbed CO molecule on solid, ideally smooth Ni substrate. The vibrational energy transfer to the substrate is shown.

The maximum frequency of Ni, $\omega_{D,\mathrm{Ni}}$ is 36.6 meV (295 cm^{-1}) and the vibrational frequency of CO-Ni, $\omega_{\mathrm{CO-Ni}}$ is 49.0 meV (395 cm^{-1}). Assume that the energy between CO and Ni can be described by a Morse potential model (Table 2.1), $\varphi(d_{\mathrm{CO}} - d_{\mathrm{Ni}}) = \varphi_{\mathrm{o}}(\{1 - \exp[-a_{\mathrm{o}}(d_{\mathrm{CO}} - d_{\mathrm{Ni}})]\}^2 - 1)$, where d_{CO} (d_{Ni}) is the displacement of CO (Ni) from the equilibrium position, φ_{o} is the adsorption energy (1.8 eV), a_{o} is $(m_{r,\mathrm{CO-Ni}}\omega^2_{\mathrm{CO-Ni}}/2\varphi_{\mathrm{o}})^{1/2}$ (from the second derivative of the Morse potential), and the reduced mass is $m_{r,\mathrm{CO-Ni}} = (m^{-1}_{\mathrm{CO}} + m^{-1}_{\mathrm{Ni}})^{-1}$.

(a) Using the Taylor series expansion and expand the Morse potential in power of $(d_{\mathrm{CO}} - d_{\mathrm{Ni}})$ to find the total Hamiltonian of the vibrational properties of the CO (adsorbate) and Ni (metal) system. The total Hamiltonian H is the sum of the Hamiltonians of the localized adsorbate vibration H_f and the phonons H_p, each expressed with the creation and nnihilation operators ($b^{\dagger}_{\mathrm{CO-Ni}}$ and $b_{\mathrm{CO-Ni}}$ for the localized CO-Ni vibration, $b^{\dagger}_{\mathrm{Ni},\kappa\alpha}$ and $b_{\mathrm{Ni},\kappa\alpha}$ for the Ni phonons), and the interaction Hamiltonian $\mathrm{H}_{f\text{-}p}$. In $\mathrm{H}_{f\text{-}p}$, the relaxation of the CO-Ni stretching vibration is through the two-phonon emission process, for the lowest order in the perturbation theory. Hint: d^2_{Ni} for two phonon emissions and d_{CO} for the relaxation of the CO-Ni vibration are required.

(b) From the Fermi golden rule (3.27), the transition probability rate, from state κ to κ', is $\dot{\gamma}_{\kappa,\kappa'} = (1/\tau_{\kappa,\kappa'}) = (2\pi/\hbar)|M_{\kappa,\kappa'}|^2\delta_D(E_{\kappa'} - E_\kappa \mp \hbar\omega)$. Using the interaction Hamiltonian in part (a), derive the expression for the relaxation rate of the CO-Ni stretching vibration via two-phonon emissions, $\dot{\gamma}_{f\text{-}p,N_p=2}$. Using the creation and annihilation operators, the displacement $d_{\mathrm{CO}} = [\hbar/(2m_{r,\mathrm{CO-Ni}}\omega_{\mathrm{CO-Ni}})]^{1/2}(b^{\dagger}_{\mathrm{CO-Ni}} + b_{\mathrm{CO-Ni}})$ and $d_{\mathrm{Ni}} = \sum_{\kappa,\alpha}[\hbar/(2m_{\mathrm{Ni}}\omega_{\mathrm{Ni},\kappa\alpha}N_{\mathrm{Ni}})]^{1/2}(b_{\mathrm{Ni},\kappa\alpha} + b^{\dagger}_{\mathrm{Ni},\kappa\alpha})\hat{\boldsymbol{z}} \cdot \boldsymbol{s}_\alpha$, where N_{Ni} is the number of Ni atom. In this transition, the initial state is represented as $|n_{\text{CO-Ni}} = 0, f_{\text{Ni},\kappa\alpha}+1, f_{\text{Ni},\kappa'\alpha'}+1\rangle$ and the final state is $|n_{\text{CO-Ni}} = 1, f_{\text{Ni},\kappa\alpha}, f_{\text{Ni},\kappa'\alpha'}\rangle$. To simplify this problem, assume that $\omega_{\text{Ni},\kappa\alpha}$ is only dependent on κ (i.e. $\omega_{\text{Ni},\kappa\alpha} = \omega_{\text{Ni},\kappa}$), and use the fact that $\sum_{\alpha}(\hat{\boldsymbol{z}} \cdot \boldsymbol{s}_\alpha)^2 = 1$ and $(1/N_{\text{Ni}}^2)\sum_{\kappa,\kappa'}\delta_D(\omega_{\text{CO-Ni}} - \omega_{\text{Ni},\kappa} - \omega_{\text{Ni},\kappa'}) = \int \mathrm{d}\omega_{\text{Ni}} D_p(\omega_{\text{Ni}}) D_p(\omega_{\text{CO-Ni}} - \omega_{\text{Ni}})$, where $D_p(\omega_{\text{Ni}}) = (1/N_{\text{Ni}})\sum_{\kappa}\delta_D(\omega_{\text{Ni}} - \omega_{\text{Ni},\kappa'})$.

(c) Using the relation in part (b), find the relaxation time of the vibrational energy between adsorbate CO and adsorbent Ni by the two-phonon emissions at 300 K and then estimate the energy transfer rate. For the phonon density of states $D_p(\omega_p)$ use the Debye model, $D_p(\omega_p) = [3(\omega_p/\omega_D)^2\delta(1-\omega_p/\omega_D)]$, where $\delta(x)$ is the Heaviside step function [$\delta(x) = 1$, if $x > 0$ and $\delta(x) = 0$, if $x < 0$] and ω_D is the cut-off phonon frequency.

7

Photon Energy Storage, Transport, and Transformation Kinetics

The radiative heat flux vector $\boldsymbol{q}_r$ is given in terms of the photon intensity I_{ph} in Table 1.1. The photon intensity, in turn, is determined by the source of radiation (including emission) and its interactions with matter (including absorption, reemission, and elastic scattering) as it travels at the speed of light in that matter. In addition to thermal emission, which is related to temperature of matter and is generally random in direction over a wide range of wavelengths, there are other stimulated and ordered emissions. Photons are also central in a wide range of energy conversions $\dot{s}_{i\text{-}j}$ (e.g., solar, flames, lasers). In this chapter, we examine various photon emission, absorptions, scatterings, and other interactions. These interactions are strongly dependent on the photon energy $\hbar\omega$, where ω is the angular frequency.

We refer to a propagating, coherent, EM wave and its energy (as described by the Maxwell equations), as well as a quantized wave packet (or quantum-particle), both as photons. Historically, radiative heat transfer had been constructed assuming broadband radiation, but with the emergence of lasers, very narrow or discrete photon energy has become common. Here we use discrete, nonequilibrium photon energy distributions, as well as blackbody (Planck law) thermal radiation (as in a photon gas), to treat photon transport and interactions with electronic entities (e.g., electrons in isolated atoms or ions, conduction electrons, valence electrons, molecular dipoles) in matter. We begin by reviewing photon energy and electric energy transitions in matter (atoms or molecules) without first discussing electromagnetic field interactions. These include some interaction (transition) selection rules. However, for a complete quantitative treatment of the interaction, the classical wave nature of a photon is used. This is due to a relative ease of use and the success the classical method had in explaining experimental results.

Blackbody radiation is an important experimental discovery that played a central role in the development of quantum mechanics. Using classical wave theory, the spectral, hemispherical, emissive power is given by the Rayleigh–Jeans law (Sections 1.4 and 7.2). However, it was found that the Rayleigh–Jeans law was applicable only for long wavelengths. The entire spectrum was understood only when Planck suggested that an EM wave with frequency ω exchanges energy with matter in a quantum given by $E_{ph} = \hbar\omega$ (discussed in the quantum–mechanical description of the simple harmonic oscillator in Section 2.6.4). This assumption suggests that light waves have a well-defined energy just as particles do. The derivation of blackbody radiation will be given in the next section.

In the photoelectric experiment light impinges upon a material and electrons are emitted because of the interaction of the light with electrons. Experiments show that, if the frequency of light is below a threshold value, there is no emission of electrons, regardless of intensity. The Planck blackbody radiation was used by Einstein to explain the photoelectric effect (the photoelectric transition rate is reviewed in Section G.2, Appendix E, as an application of the FGR) as light being made of particles with energy $E_{ph} = \hbar\omega$. Electrons are emitted by a single (it can also involve multiple photons, but with much lower probability) photon knocking the electron out; thus the energy per photon must exceed the electron work function.

The quantum treatment of a photon as a harmonic oscillator, along the lines of the treatments given in Section 2.6.4 (2.90), and Section 4.5 (for phonon), gives the energy of the photon occupation number (probability) $f_{ph}(\boldsymbol{\kappa}, \alpha)$, as

$$E_{ph,\boldsymbol{\kappa},\alpha} = \hbar\omega_\alpha(\boldsymbol{\kappa})[f_{ph}(\boldsymbol{\kappa}, \alpha) + \frac{1}{2}], \tag{7.1}$$

for wave vector $\boldsymbol{\kappa}$ and polarization α. We will further discuss the quantum-particle treatment of photon and the radiation field Hamiltonian in Section 7.3.1.

In general, the low-frequency EM waves (for example, microwave) are well treated using the classical wave theory (Maxwell equations), whereas the high-frequency (high-energy) waves are treated using quantum mechanics, when electronic transitions are involved. In this chapter, we start with the quasi-particle treatment, then coherent wave treatment, and make some comparisons.

The photon energy can reach very high values, as shown in Figure 7.1(a), where the various regimes of the EM waves are shown. These are starting from the lowest photon energy, long, medium, and short wave and very-high frequency radio, covering down to wavelength of 1 m, then microwave, infrared, visible, ultraviolet, X-rays, γ-rays, and cosmic rays. This large range for phonons allows for interactions with very low energy entities (such as the rotational energy state in fluid particles) to very high energy entities (e.g., causing ejection of electrons from atoms).

Comparing the energies of different wavelengths (frequencies), we find that $\lambda = 5\ \mu$m (microwave) has $\omega = 3.770 \times 10^{11}$ rad/s, and $\hbar\omega = 248.2\ \mu$eV (close to rotational transitions); $\lambda = 50\ \mu$m (far infrared) has $\omega = 3.770 \times 10^{13}$ rad/s, and $\hbar\omega = 24.82$ meV (close to $k_B T = 25.85$ meV for $T = 300$ K, Figure 1.4); $\lambda = 5\ \mu$m (near infrared) has $\omega = 3.770 \times 10^{14}$ rad/s, and $\hbar\omega = 0.2480$ eV (in the range of photodissociation of ozone and oxygen molecule, and close to the first vibrational transition of N_2, 0.2890 eV, Figure 1.4); $\lambda = 0.5\ \mu$m (visible, green) has $\omega = 3.770 \times 10^{15}$ rad/s, and $\hbar\omega = 2.482$ eV (close to the electronic gap energy of AlSb, 2.50 eV, Table 5.1); $\lambda = 0.05\ \mu$m (ultraviolet) has $\omega = 3.770 \times 10^{16}$ rad/s, and $\hbar\omega = 24.82$ eV (close to first ionization energy of He, 24.58 eV, Table A.2); $\lambda = 0.005\ \mu$m $= 5$ nm (X-rays) has $\omega = 3.770 \times 10^{17}$ rad/s, and $\hbar\omega = 248.2$ eV [close to first photoionization energy

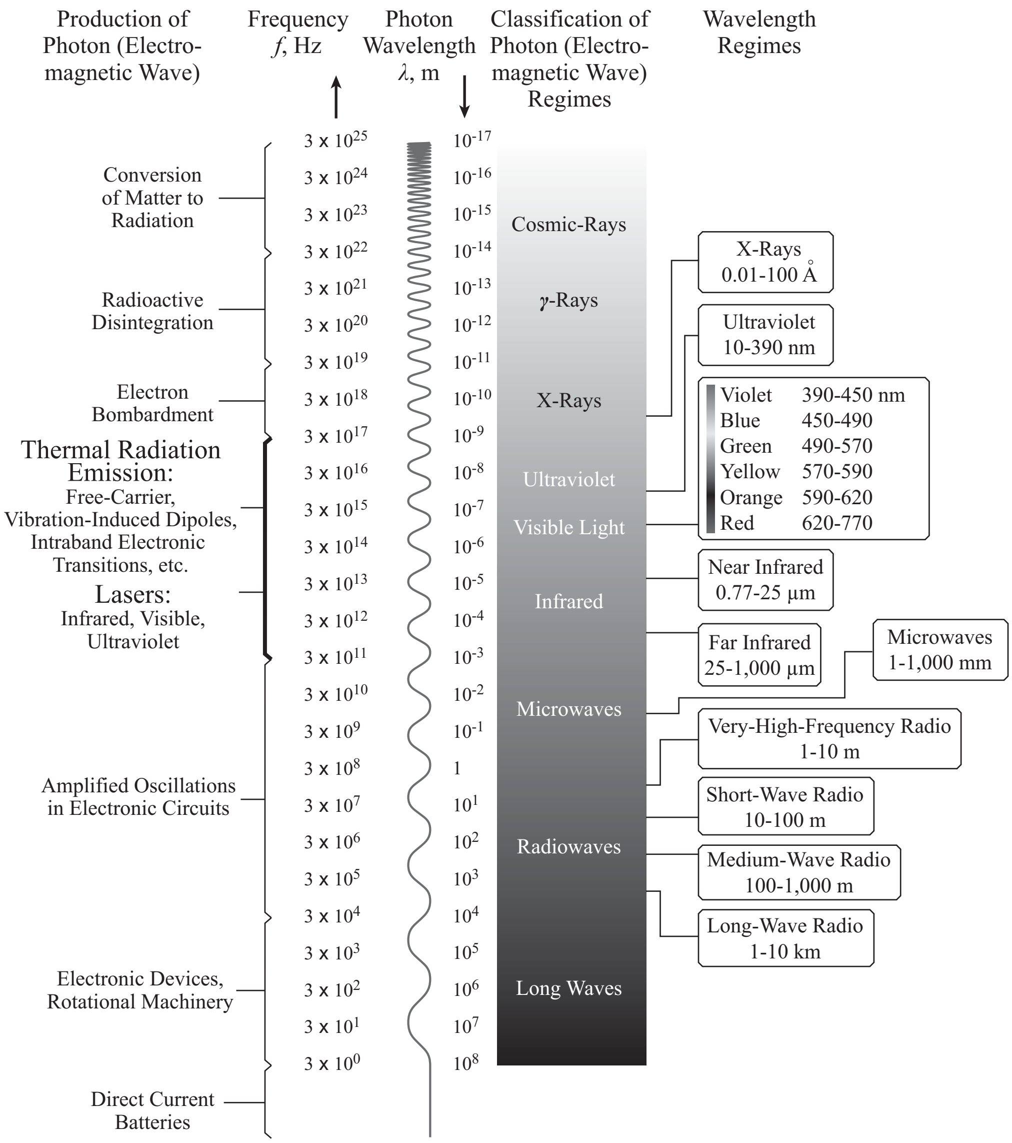

(a) Radiation Spectrum

Figure 7.1. (a) Spectra (wavelength and frequency) of the EM wave (radiation) regimes and their production.

of Al, Figure 7.1(b)], and $\lambda = 5 \times 10^{-5}$ μm $= 0.5$ Å (X-rays) has $\omega = 3.770 \times 10^{19}$ rad/s, and $\hbar\omega = 24.82$ keV.

Figure 7.1(b) shows examples of spectral (frequency dependent) absorption coefficient $\sigma_{ph,\omega}$ of matter (gas, liquid, and solid, and polymer, oxide, semiconductor, and metal), over a large range of photon energies from the microwave regime to the γ-rays regime. The inverse of $\sigma_{ph,\omega}$ is the spectral photon mean free path $\lambda_{ph,\omega}$. High absorptions are associated with electronic dipole transitions driven by atomic

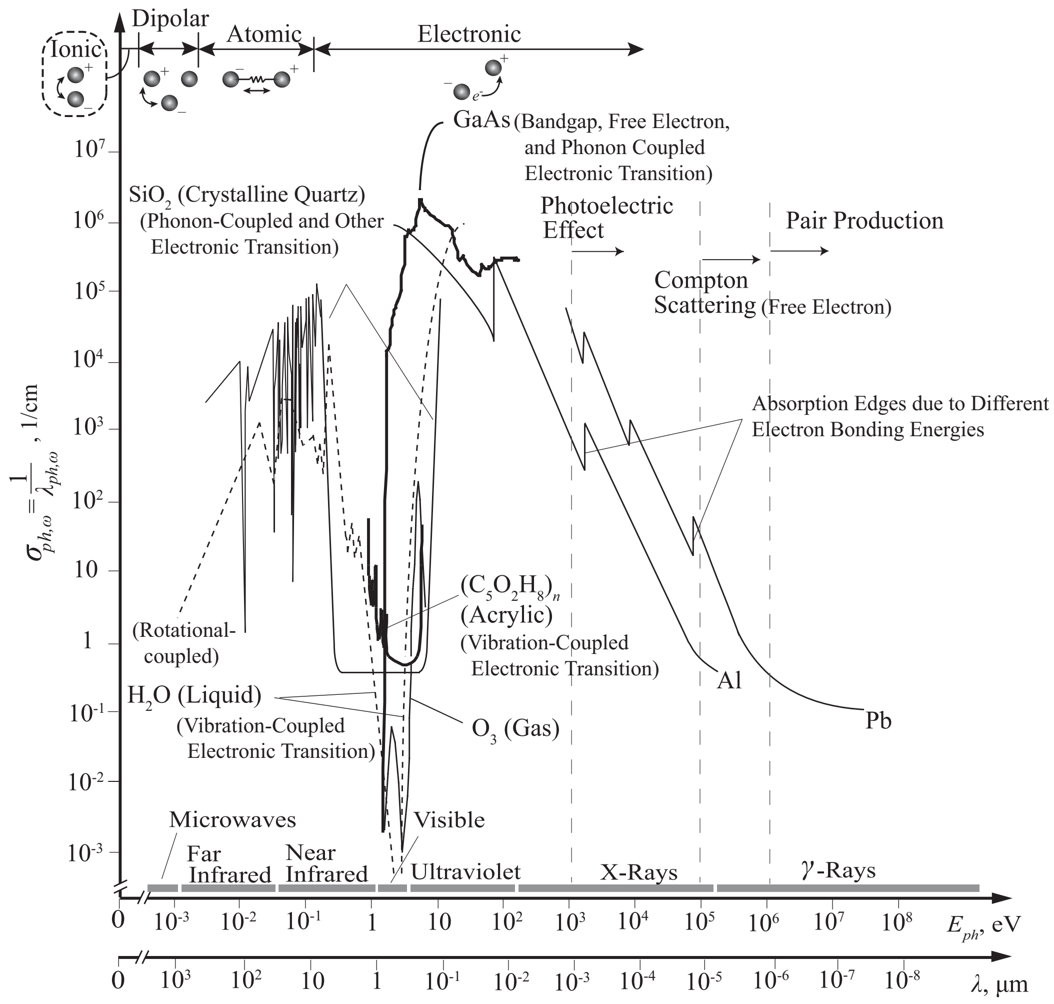

(b) Absorption Spectrum

Figure 7.1 (*cont.*) (b). Spectral photon absorption coefficient for typical gas, liquid, and solid phases. For the solid phase, examples of polymer, oxide, semiconductor, and metals are given. The spectral photon mean free path $\lambda_{ph,\omega}$ is the inverse of $\sigma_{ph,\omega}$. As the photon energy progressively increases, it interacts with larger energy entities, starting with low-energy, rotational–vibrational–electronic energy of polyatomic gases, to electron ejection from metals.

vibration (in gases, liquids, and solids), electronic transitions including bandgaps, and free charge carriers (e.g., electrons) transitions. For example, the vibration (phonon) energy range for crystalline SiO_2 (quartz) was shown in Figure 4.8(a) and the electronic band structure of GaAs was shown in Figure 5.6(c).

In this chapter we start with the ideal quantum-particle (photon gas) treatment and the blackbody spectral intensity. Next we examine nonblackbody photon emissions, such as lasers. Then we discuss the quantum and semi-classical treatments of photon–matter interactions. Next we consider two-level electronic transition systems and introduce the Einstein spontaneous and stimulated emission coefficients.

Then we use these in the photon BTE to formulate the photon particle transport equation (equation of radiative transport). We will show that, in the optically thick limit, $\lambda_{ph,\omega} \ll L$, where L is the distance traveled by a photon, we can use the Fourier law and define a radiant conductivity. We also examine EM wave treatment of radiation and discuss field localization resulting from coherent interference of the waves as they travel through an ideal, one-dimensional, absorbing multilayer medium. We also contrast this with the particle treatment of this phenomena. Then we examine various photon–matter interactions, including continuous and band absorptions and emissions. Next, examples are given of photon–matter interactions in energy conversion, using laser cooling of solids and gases, and photovoltaics, as examples. Finally, we consider size effects in photon emission and transport.

7.1 Quantum-Particle Treatment: Photon Gas and Blackbody Emission

Photon particle (or gas) treatment allows us to examine its thermalized (or thermal equilibrium) energy distribution (and also assign pressure and entropy to it as with fluid particle gas). In photon gas the interphoton collisions are absent (however, the wave treatment of the photon allows for interference, etc.), but the photon interacts with electric entities (such as a free electron or oscillating dipole).

We start with the quantum energy of the simple harmonic oscillator, neglecting the zero point ($T = 0$ K, from Figure 1.1, $f_{ph}^{\mathrm{o}} = 0$) energy and expressing the quantum energy as $\hbar\omega$.

For simplicity, we assume only the frequency dependence of the photon energy and write the photon energy (7.1), dropping the 1/2 term, density $e_{ph,\omega}$, similar to (3.38), using the photon distribution function $f_{ph,\omega}$, in frequency range ω to $\omega + \mathrm{d}\omega$ as

$$e_{ph,\omega} = \frac{\mathrm{d}E_{ph,\omega}}{V} = \hbar\omega f_{ph} D_{ph,\omega}\mathrm{d}\omega. \qquad (7.2)$$

Similarly, the photon number density is defined.[†] The blackbody density of state $D_{b,\omega}$ [which is defined similar to (4.19) for phonon and (5.65) for electron] is for dispersionless (linear dispersion relation) phase speed (4.16), which is equal to the group speed (4.15), $u_{ph} = \mathrm{d}\omega/\mathrm{d}\kappa = \omega/\kappa$

$$\begin{aligned} D_b(\kappa) &= \sum_{\alpha} \int_{\kappa'} \frac{4\pi\kappa^2 \mathrm{d}\kappa'}{(2\pi)^3}\, \delta_{\mathrm{D}}(\kappa' - \kappa) \\ D_{b,\omega} &= \frac{1}{\pi^2} \int_{\omega'} \frac{1}{u_{ph}^3} \omega'^2 \mathrm{d}(\omega' - u_{ph}\kappa)\delta_{\mathrm{D}}(\omega' - u_{ph}\kappa) \\ &= \frac{\omega^2}{\pi^2 u_{ph}^3}, \qquad [\omega = u_{ph}(\omega)\kappa, \quad \text{dispersion relation}] \\ &\qquad \text{blackbody photon DOS and phase speed,} \end{aligned} \qquad (7.3)$$

[†] Photon number density is found from (1.19) as $n_{ph} = \int_0^\infty f_{ph}(\omega) D_{ph}(\omega)\mathrm{d}\omega$. For blackbody emission, $n_{ph,b}$ is proportional to T^3 (end-of-chapter problem).

where the number of polarizations α is 2. Debye phonon DOS (4.26) is based on this, except that Debye introduced the cut-off frequency to constrain the number of oscillators (to $3n$ for monatomic, cubic crystals). Both assume a linear dispersion relation (group and phase velocities are equal and constant). The general dispersion relation for the photon, in terms of the complex index of refraction m_λ ($\kappa = \kappa_{\rm o} m_\lambda = m_\lambda \omega / u_{ph,{\rm o}}$) is given in Table 3.5. Then

$$\frac{\mathrm{d}E_{ph,\omega}}{V} = \frac{\hbar\omega^3 f_{ph}\mathrm{d}\omega}{\pi^2 u_{ph}^3}\frac{D_{ph,\omega}}{D_{b,\omega}}. \tag{7.4}$$

The spectral photon intensity $I_{ph,\omega}$[†] is related to the photon energy density through (dividing by the total solid angle $\Omega = 4\pi$[‡] and multiplying by the velocity u_{ph})

$$\begin{aligned}\mathrm{d}I_{ph,\omega}(\omega, T) &= \frac{u_{ph}}{4\pi}\frac{\mathrm{d}E_{ph,\omega}}{V} = \frac{1}{4\pi}u_{ph}\hbar\omega f_{ph}D_{ph}\mathrm{d}\omega \\ &= \frac{u_{ph}}{4\pi}\frac{\hbar\omega^3 f_{ph}\mathrm{d}\omega}{\pi^2 u_{ph}^3}\frac{D_{ph,\omega}}{D_{b,\omega}} \\ &= \frac{\hbar\omega^3 f_{ph}\mathrm{d}\omega}{4\pi^3 u_{ph}^2}\frac{D_{ph,\omega}}{D_{b,\omega}}. \end{aligned}\tag{7.5}$$

The total intensity is found by integrating over angular frequency $I_{ph} = \int \mathrm{d}I_{ph,\omega}$. Similarly, the radiation heat flux is $\mathrm{d}q_{ph} = \mathrm{d}I_{ph}/4$.[§] Note that we have not included the angular variations of I_{ph}, although it can be significant and can be included starting from (7.2).

[†] The phonon intensity is defined similarly to (7.5) as

$$\mathrm{d}I_{p,\omega}(\omega) = \frac{u_{p,\mathrm{A}}}{4\pi}\hbar\omega f_p D_p(\omega)\mathrm{d}\omega.$$

[‡] The differential solid angle is $\mathrm{d}\Omega = \sin\theta\mathrm{d}\phi\mathrm{d}\theta$, where θ is the polar and ϕ is the azimuthal angle and for azimuthal symmetry $\mathrm{d}\Omega = 2\pi\sin\theta\mathrm{d}\theta = 2\pi\mathrm{d}\cos\theta \equiv -2\pi\mathrm{d}\mu$, where $\mu = \cos\theta$. This is used in Table 1.1. Integration over $-1 \le \mu \le 1$ gives $\Omega = 4\pi$.

[§] The radiation heat flux q_{ph} for photon gas is

$$\mathrm{d}q_{ph,\omega} = \frac{e_{ph}u_{ph}}{4},$$

which is similar to the mass flux for fluid particles (6.89). Then using (7.2), we have

$$\mathrm{d}q_{ph,\omega} = \frac{1}{4}u_{ph}\hbar\omega f_{ph}D_{ph}\mathrm{d}\omega.$$

In general (for directional I_{ph}) the relation between $\mathrm{d}q_{ph,\omega}$ and $\mathrm{d}I_{ph,\omega}$ is

$$\begin{aligned}\mathrm{d}q_{ph,\omega} &= \int_{\Omega=4\pi}\mathrm{d}I_{ph,\omega}\mathrm{d}\Omega \\ &= \int_0^{2\pi}\int_0^{\pi/2}\mathrm{d}I_{ph,\omega}\cos\theta\sin\theta\mathrm{d}\theta\mathrm{d}\phi,\end{aligned}$$

when the integral is over the solid angle of a unit hemisphere.

Under equilibrium distribution, $f_{ph} = f_{ph}^{\rm o}$ (Table 1.2) and for vacuum $u_{ph,\rm o} = c_{\rm o}$, the blackbody radiation intensity is given by

$$\begin{aligned} {\rm d}I_{b,\omega}(\omega, T) &= \frac{\hbar\omega^3 f_{ph}^{\rm o}{\rm d}\omega}{4\pi^3 u_{ph,\rm o}^2} \\ &= \frac{\hbar\omega^3}{4\pi^3 u_{ph,\rm o}^2}\frac{{\rm d}\omega}{\exp(\hbar\omega/k_{\rm B}T) - 1}, \end{aligned} \tag{7.6}$$

or by using the relation $\lambda = 2\pi/\kappa = 2\pi u_{ph,\rm o}/\omega$, we have[†]

$$\begin{aligned} {\rm d}I_{b,\lambda}(\lambda, T) &= \frac{\hbar(8\pi^3)u_{ph,\rm o}}{4\pi^3\lambda^3}\frac{2\pi u_{ph,\rm o}{\rm d}\lambda/\lambda^2}{\exp(2\pi\hbar u_{ph,\rm o}/\lambda k_{\rm B}T) - 1} \\ &= \frac{4\pi\hbar u_{ph,\rm o}^2}{\lambda^5\,[\exp(2\pi\hbar u_{ph,\rm o}/\lambda k_{\rm B}T) - 1]}{\rm d}\lambda \quad \text{Planck law.} \end{aligned} \tag{7.7}$$

The Planck law describes the ideal, quantized (harmonic oscillator) spectral distribution of the EM energy (photon) in thermal equilibrium (called thermal radiation).

The maximum in $I_{b,\lambda}$ ($\partial I_{b,\lambda}/\partial\lambda = 0$) occurs at $\hbar\omega/k_{\rm B}T = \hbar\omega/\lambda k_{\rm B}T = 4.965$ or $\lambda_{max}T = 2898$ μm-K (called the Wien displacement law), whereas the maximum in $I_{b,\omega}$ ($\partial I_{b,\omega}/\partial\omega = 0$), which gives the most likely frequency, is at $\hbar\omega/k_{\rm B}T = 2.821$ (both are end-of-chapter problems).

The solar radiation is produced through nuclear fusion reactions, originally as very high energy gamma rays and after billions of collisions with matter it reaches the surface and then escapes. The core of the sun is solid-like dense (10^7 K, H fusion) while its surface is a very low-density (10^{-3} kg/m^3) plasma (with turbulent convection currents). So, 5780 K is an effective temperature, dominated by emission and transmission of radiation through its thin (500 km) photosphere

The blackbody, spectral emissive power $E_{b,\lambda}$ is $I_{b,\lambda}\cos\theta$ and when integrated over θ gives

$$\begin{aligned} {\rm d}E_{b,\lambda} \equiv \pi{\rm d}I_{b,\lambda} &= \frac{4\pi^2\hbar u_{ph,\rm o}^2}{\lambda^5\,[\exp(2\pi\hbar u_{ph,\rm o}/\lambda k_{\rm B}T) - 1]}{\rm d}\lambda \\ &\qquad \text{blackbody spectral emissive power.} \end{aligned} \tag{7.8}$$

This is generally referred to as the the Planck law of blackbody radiation. Almost all (98 %) blackbody thermal emission is between λT =1444 and 22,890 μm-K [232].

This variation of ${\rm d}E_{b,\lambda}/{\rm d}\lambda$ as a funciton of λ is shown in Figure 7.2(a), for four different temperatures. The Draper point marked there identifies the threshhold of radiation detection by the human eye.

[†] The frequency-dependent (7.7) and (7.8) are

$$ {\rm d}I_{b,\omega} = \frac{\hbar\omega^3{\rm d}\omega}{2\pi^2 u_{ph,\rm o}^2[\exp(\hbar\omega/k_{\rm B}T) - 1]}, $$

$$ {\rm d}E_{b,\omega} = \frac{\hbar\omega^3{\rm d}\omega}{2\pi u_{ph,\rm o}^2[\exp(\hbar\omega/k_{\rm B}T) - 1]}. $$

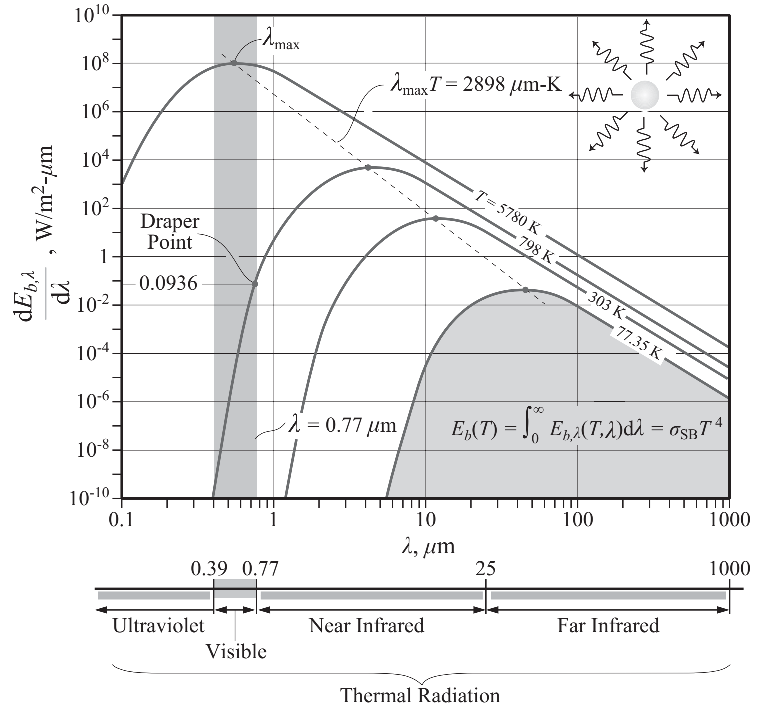

(a) Blackbody Spectral Emissive Power

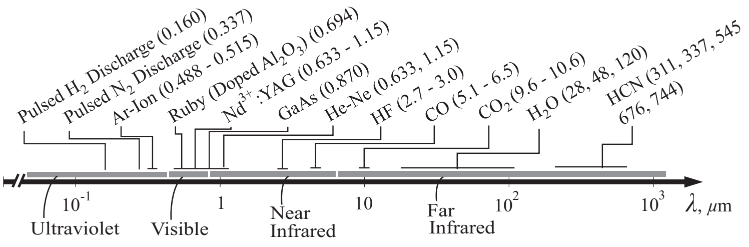

(b) Laser Wavelengths

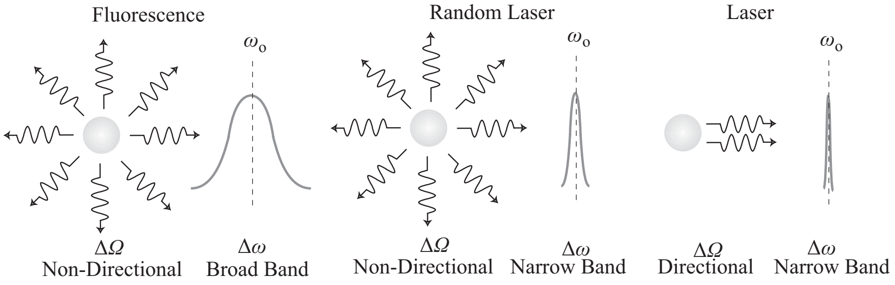

(c) Order in Radiation Emission

Figure 7.2. (a) Blackbody spectral emission power as a function of wavelength (b) Examples of wavelengths of typical lasers. The numbers in parentheses indicate the wavelength in micrometers (some have multiple wavelengths). (c) Illustration of the solid angle span and bandwidth (around ω_o) of some light sources. The solid angle $\Delta\Omega$ describes the direction of radiation.

The total, blackbody emissive power E_b is found by integrating the spectral, blackbody emissive power $E_{b,\lambda}$ over the wavelength range $(0 \leq \lambda \leq \infty)$, and this gives

$$E_b(T) = \int_0^\infty E_{b,\lambda} \mathrm{d}\lambda = \sigma_{\mathrm{SB}} T^4, \ \sigma_{\mathrm{SB}} = \frac{\pi^2 k_{\mathrm{B}}{}^4}{60\hbar^3 u_{ph,\mathrm{o}}^2} \ \text{Stefan–Boltzmann law.} \tag{7.9}$$

This is the Stefan–Boltzmann law, and σ_{SB} is the Stefan–Boltzmann constant[†], which is $\sigma_{\mathrm{SB}} = 5.6705 \times 10^{-8}$ W/m^2-K^4.

For very large wavelengths, the exponential term in (7.8) is approximated by a two-term Taylor series solution (end-of-chapter problem), leading to

$$\mathrm{d}E_{b,\lambda} = \frac{2\pi u_{ph,\mathrm{o}} k_{\mathrm{B}} T}{\lambda^4} \mathrm{d}\lambda \ \text{Rayleigh–Jeans law for large } \lambda. \tag{7.10}$$

The same result is obtained using $\hbar \rightarrow 0$ in (7.8), i.e., allowing photons of arbitrary small energy content, as postulated by the classical mechanics. Thus (7.10) is identical to the one derived by Rayleigh and Jeans using the classical mechanics and is called the Rayleigh–Jeans distribution. Because in (7.10), as $\lambda \rightarrow 0$, $\mathrm{d}E_{b,\lambda} \rightarrow \infty$, it is called the ultraviolet catastrophe.

7.2 Lasers and Near-Field (EM Wave) Thermal Emission

7.2.1 Lasers and Narrow-Band Emissions

Laser (light amplification of stimulated emitted radiation) is a device generating or amplifying light (wavelengths ranging from the far-infrared regime to X-rays and γ-rays regimes). The laser beams have high directionality (indicated by their solid angle $\Delta\Omega$, spectral purity (very narrow bands $\Delta\omega$), and intensity. Figure 7.2(b) gives examples of the primary wavelengths emitted by some lasers [429] and covers four orders of magnitude (from ultraviolet to far infrared). Different atoms and atomic combinations (and in different phases and states), creating various quantum energy states and state transition possibilities, are used as the emitting medium. Various excitation mechanisms (energies) are used to create transitions in this medium. Generally mirrors (optical cavity) are used for the amplification (feedback).

There are gas lasers (e.g., He, Ne, Ar, Kr, Xe ion, N_2, CO_2), chemical lasers (e.g., HF), dye lasers, metal-vapor lasers (e.g., HeCd, NeCu), rare-earth doped solid-state lasers (e.g., ruby, Nd^{3+}:YAG, Ti^{3+}:Al_2O_3), semiconductor lasers (e.g., GaN, AlGaAs, InGaAsP), etc. Some lasers reach the ideal monochromatic ($\Delta\omega \rightarrow 0$), unidirectional output ($\Delta\Omega \rightarrow 0$), but some, including random lasers, may have significant directional distributions, or might have broadbands. For example, He-Ne laser has a band width $\Delta\omega = 1.5 \times 10^6$ Hz (0.002 nm around the central wavelength

---

[†] Similarly, the phonon Stefan–Boltzmann coefficient (not constant) is arrived at using the Debye model and a single phonon speed, as (using $c_{v,p}$ per kg)

$$\sigma_{\mathrm{SB}}(\text{phonon}) = \frac{\rho c_{v,p} u_{p,\mathrm{A}}}{16 T^3}.$$

of 633 nm), while Ti^{3+}:Al_2O_3 laser has $\Delta\omega = 1.28 \times 10^{14}$ Hz (300 nm centered around 800 nm). These are illustrated in Figure 7.2(c). As mentioned, various mirrors and cavities are used for creating the directional preference, and various methods are used to create a narrow-band resonance [429].

7.2.2 Classical EM Wave Near-Field Thermal Emission

The fluorescent emission is expected to be random in direction and also has a bandwidth. The radiation entropy aspect of laser cooling has been analyzed in [403]. The radiation that is due to thermally vibrating dipoles and other electric transitions occurring at a distance below the surface and also for an object of linear dimension d or for objects separated by a distance d, when the wavelength of the EM wave λ is nearly the same as the clearance distance $2\pi d/\lambda \leq 1$, the EM field is referred to as being in the near-field region.[†] The blackbody radiation discussed in Section 7.1 is the ideal emission in the far-field region, where the distance from the source of emission (local dipoles, etc.) is several times larger than the wavelength. The thermal radiation emission can be presented as the thermal fluctuation of charges in matter. This fluctuating electric field $\boldsymbol{e}_e(\boldsymbol{x}, \omega)$ is given as [344, 383, 481]

$$\boldsymbol{e}_e(\boldsymbol{x}, \omega) = i\omega\mu_{\rm o} \int_V \boldsymbol{G}_e(\boldsymbol{x}, \boldsymbol{x}', \omega) \cdot \boldsymbol{j}_e(\boldsymbol{x}, \omega) {\rm d}\boldsymbol{x}', \tag{7.11}$$

where $\boldsymbol{G}_e$ (V/m) is the dyadic Greens function from the source located at $\boldsymbol{x}'$ and $\boldsymbol{j}_e$ is the Fourier transform of the current density vector that is due to thermal fluctuations. The electric field is due to the thermal fluctuations in the dipole moment $\boldsymbol{p}_e(\omega)$. The fluctuation in $\boldsymbol{p}_e$ is represented by a correlation [221], which in turn is related to temperature, frequency, and the imaginary component of the polarizability $\alpha_{e,c}$ (3.41).[‡]

The radiative heat transfer between two spheres is found from the Poynting vector (Table 3.5) normal to the surface and has been numerically calculated in [344]. We subsequently consider the analytical solution in the limit of small clearing distance.

When two dielectric solid surfaces at different temperatures T_1 and T_2 (for example a tip and a surface) are brought very close (submicrometer distance) and in a vacuum, one of the near-field interactions is through fluctuating dipoles in each solid. This is the near-field radiation (Coulomb interaction) dipole–dipole energy

---

[†] $2\pi d/\lambda$ is called the size parameter and is key in the particle scattering theory [230].

[‡] Writing (3.41) using a polarizability tensor, we have $\boldsymbol{p}_{e,l} = \epsilon_{\rm o}\alpha_{e,lk}\boldsymbol{e}_{e,k}$, $\boldsymbol{j}_e = -i\omega\boldsymbol{p}_{e,k}$. The correlation function for the dipole moment becomes [221]

$$\langle p_{e,k}(\omega)p^\dagger_{e,l}(\omega')\rangle = \hbar\coth(\frac{\hbar\omega}{2k_{\rm B}T}){\rm Im}[\epsilon_{\rm o}\alpha_{e,kl}(\omega)]2\pi\delta(\omega-\omega').$$

Also, the mean energy of the harmonic oscillator is [same as (7.1)]

$$\frac{\hbar\omega}{2}\coth\frac{\hbar\omega}{2k_{\rm B}T} = \hbar\omega[\frac{1}{2} + \frac{1}{\exp(\frac{\hbar\omega}{k_{\rm B}T}) - 1}] = E_{ph}.$$

transfer (known as the Foster energy transfer [115]). The rate of net radiation energy transfer between a solid 1 and a solid 2 is

$$q_{ph,1\text{-}2}(\omega) = \frac{\omega\epsilon_o}{2}\alpha_{e,c,2}|\boldsymbol{e}_e(\boldsymbol{x})|^2, \quad \alpha_{e,c,j} = \alpha_{e,c,j}(\epsilon_{e,j}), \tag{7.12}$$

where the strongly frequency dependent [at transitions, Figure 7.1(b)] $\alpha_{e,c,2}$ is the imaginary part of the polarizability (3.41) (ability of an ion to distort the electron of the other ion) of solid 2, and $\boldsymbol{e}_e$ is the incident electric field vector produced by the dipoles excited by lattice thermal energy. The polarization in turn is related to the electric permittivity ϵ_e, which in turn is a signature of the electric entity of material (Section 3.3.5).[†] It has been shown that (7.12) can be written in terms of temperatures T_1 and T_2 as [115]

$$q_{ph,1\text{-}2} = \frac{3}{4\pi^2}\frac{\alpha_{e,c,1}\alpha_{e,c,2}}{d^6}[E_{ph}(\omega,T_1) - E_{ph}(\omega,T_2)], \tag{7.13}$$

where d is the separation distance and photon energy $E_{ph}(\omega, T)$ is

$$E_{ph} = \hbar\omega f_{ph}^{o} = \frac{\hbar\omega}{\exp(\frac{\hbar\omega}{k_B T}) - 1}. \tag{7.14}$$

For d of the order of one nanometer, this energy transfer rate is many orders of magnitude larger than that corresponding to the far-field radiation heat flux for the emission and absorption of photons, which is [115]

$$q_{ph,1\text{-}2} = \frac{\omega^4\alpha_{e,c,1}\alpha_{e,c,2}}{32\pi^3 u_{ph}^2 d^2}[E_{ph}(\omega,T_1) - E_{ph}(\omega,T_2)]. \tag{7.15}$$

Note the vastly different dependence (or lack of) on ω and d for (7.14) and (7.15).

The near-field radiation heat transfer is further discussed in Section 7.15.1, under sized effects. The experimental results of [242] for a tip-sample (scanning thermal microscopy) distance below 10 nm show deviation from the preceding theory. These are due to local variations in material-dependent properties, for which the macroscopic semiclassical (Maxwell) description of dielectric properties may fail.

7.3 Quantum and Semiclassical Treatments of Photon–Matter Interaction

The formalism of quantized radiation field, based on quantum operators, is introduced in the next sections. Then we will discuss the photon–matter interaction by using these operators. These are needed for the photon–electron interactions (i.e., Section 7.12).

[†] For spheres of diameter d_s, the relation is

$$\alpha_{e,c}(\omega) = \mathrm{Im}[\alpha_e(\omega)] = 4\pi d_s^3 \frac{3\,\mathrm{Im}[\epsilon_e(\omega)]}{[\epsilon_e(\omega)+2]^2},$$

where $\epsilon_e(\omega)$ is the frequency dependent electric permittivity (3.44).

7.3.1 Hamiltonians of Radiation Field

Quantization of electrodynamics begins by presenting the EM field by the vector potential [407]. Using the EM field described by the vacuum Maxwell equations summarized in Table 3.5, we use the vector potential $\boldsymbol{a}_e$ with the radiation or Coulomb gauge ($\nabla \cdot \boldsymbol{a}_e = 0$, also called transversality condition, as the transverse component of $\boldsymbol{a}_e$ accounts for EM radiation of a moving charged particle) to arrive at the current for Ampere law written as (Chapter 3 problem) [95]

$$\nabla^2 \boldsymbol{a}_e(\boldsymbol{x}, t) - \frac{1}{u_{ph,\mathrm{o}}^2}\frac{\partial^2}{\partial t^2}\boldsymbol{a}_e(\boldsymbol{x}, t) = 0, \tag{7.16}$$

$$\boldsymbol{e}_e = -\frac{\partial \boldsymbol{a}_e}{\partial t}, \qquad \boldsymbol{b}_e = \nabla \times \boldsymbol{a}_e, \tag{7.17}$$

where $\boldsymbol{a}_e$, $\boldsymbol{e}_e$, and $\boldsymbol{b}_e$ are the vector potential and electric field and magnetic field vectors of the EM radiation defined in Section 3.3.1 (Table 3.5).

We assume time–space separations, $\boldsymbol{a}_{e,\alpha}(\boldsymbol{x}, t) = q_\alpha(t)\boldsymbol{a}_\alpha(\boldsymbol{x})$, and use the separation of variables method to find

$$\nabla^2 \boldsymbol{a}_\alpha + \frac{\omega_\alpha^2}{u_{ph,\mathrm{o}}^2}\boldsymbol{a}_\alpha = 0, \qquad \frac{\partial^2 q_\alpha}{\partial t^2} + \omega_\alpha^2 q_\alpha = 0, \tag{7.18}$$

where ω_α is the separation constant (eigenvalues). The solutions are (plane-wave expansion) [407]

$$q_\alpha = q_\alpha e^{-i\omega_\alpha t}, \qquad \boldsymbol{a}_{e,\alpha}(\boldsymbol{x}) = \boldsymbol{s}_{ph,\alpha}(\frac{1}{\epsilon_\mathrm{o} V})^{1/2} e^{i\boldsymbol{\kappa}_\alpha \cdot \boldsymbol{x}},$$

$$\boldsymbol{a}_{e,\alpha}(\boldsymbol{x}, t) = |q_\alpha|(\frac{1}{\epsilon_\mathrm{o} V})^{1/2}\boldsymbol{s}_{ph,\alpha} e^{i(\boldsymbol{\kappa}_\alpha \cdot \boldsymbol{x} - \omega_\alpha t)}, \tag{7.19}$$

where V is the interaction volume, $\boldsymbol{s}_{ph,\alpha}$ is the unit polarization vector for the α mode and $\kappa_\alpha = \omega_\alpha u_{ph}$ is the wave vector. Note that, unlike EM waves generated by a point charge (i.e., electron having mass and charge), EM wave in vacuum (free space) does not have mass or charge. Therefore the vector potential is written in a quantity per an imaginary particle having the mass and charge of an electron.

Using the preceding, the Coulomb gauge condition gives

$$\nabla \cdot \boldsymbol{a}_{e,\alpha} = 0 = \boldsymbol{s}_{ph,\alpha} \cdot \boldsymbol{\kappa}_\alpha i(\frac{1}{\epsilon_\mathrm{o} V})^{1/2} e^{i\boldsymbol{\kappa}_\alpha \cdot \boldsymbol{x}} q_\alpha e^{i\omega_\alpha t}. \tag{7.20}$$

From the preceding, we note that $\boldsymbol{s}_{ph,\alpha} \cdot \boldsymbol{\kappa}_\alpha = 0$; therefore the polarization and propagation vectors are perpendicular (i.e., the field is composed of transverse waves only).

Summing over all modes $\boldsymbol{a}_{e,\alpha}$ (by including negative κ_α and ω_α), (7.19) becomes

$$\boldsymbol{a}_e(\boldsymbol{x}, t) = \sum_\alpha [q_\alpha(t)\boldsymbol{a}_{e,\alpha}(\boldsymbol{x}) + q_\alpha^\dagger(t)\boldsymbol{a}_{e,\alpha}^\dagger(\boldsymbol{x})]. \tag{7.21}$$

Using the preceding, $\boldsymbol{e}_e$ and $\boldsymbol{b}_e$,for a plane wave with polarization along the y direction and motion along the x direction (for example) become [from (7.17)]

$$\begin{aligned}\boldsymbol{e}_{e,\alpha} &= \frac{i\omega}{u_{ph,\mathrm{o}}}(q_\alpha \boldsymbol{a}_{e,\alpha} - q_\alpha^\dagger \boldsymbol{a}_{e,\alpha}^\dagger)\\ &= \frac{i\omega}{u_{ph,\mathrm{o}}}|q_\alpha|(\frac{1}{\epsilon_\mathrm{o} V})^{1/2}\boldsymbol{s}_y[e^{i(\kappa_{\alpha x}x-\omega_\alpha t)} - e^{-i(\kappa_{\alpha x}x-\omega_\alpha t)}]\\ &= -\kappa_{\alpha x}|q_\alpha|\boldsymbol{s}_y(\frac{1}{\epsilon_\mathrm{o} V})^{1/2}2\sin(k_{\alpha x}x-\omega_\alpha t)\end{aligned} \tag{7.22}$$

$$\begin{aligned}\boldsymbol{b}_{e,\alpha} &= \boldsymbol{s}_z\frac{\partial a_{e,y}}{\partial y}\\ &= \boldsymbol{s}_z i\kappa_{\alpha x}|q_\alpha|(\frac{1}{\epsilon_\mathrm{o} V})^{1/2}\boldsymbol{s}_z[e^{i(\kappa_{\alpha x}x-\omega_\alpha t)} - e^{-i(\kappa_{\alpha x}x-\omega_\alpha t)}]\\ &= -\kappa_{\alpha x}|q_\alpha|\boldsymbol{s}_z(\frac{1}{\epsilon_\mathrm{o} V})^{1/2}2\sin(\kappa_{\alpha x}x-\omega_\alpha t),\end{aligned} \tag{7.23}$$

where $\boldsymbol{s}_x$, $\boldsymbol{s}_y$, and $\boldsymbol{s}_z$ are the unit vectors. The Hamiltonian (energy) of the radiation field is given by (assuming a vacuum)

$$\begin{aligned}\mathrm{H} &= \frac{1}{2}\int(\epsilon_\mathrm{o}\boldsymbol{e}_e^2 + \mu_\mathrm{o}^{-1}\boldsymbol{b}_e^2)\mathrm{d}V = \int \epsilon_\mathrm{o}\boldsymbol{e}_e^2 dV\\ &= \frac{1}{4\pi}\int[\sum_\alpha \frac{i\omega_\alpha}{u_{ph,\mathrm{o}}}(q_\alpha \boldsymbol{a}_{e,\alpha} - q_\alpha^\dagger \boldsymbol{a}_{e,\alpha}^\dagger)][\sum_{\alpha'} \frac{i\omega_\alpha'}{u_{ph,\mathrm{o}}}(q_{\alpha'} \boldsymbol{a}_{e,\alpha'} - q_{\alpha'}^\dagger \boldsymbol{a}_{e,\alpha'}^\dagger)]\mathrm{d}V.\end{aligned} \tag{7.24}$$

Note that magnitude of the magnetic field is the same as the magnitude of the electric field, as evident in (7.22) and (7.23). Then we have for the integrals

$$\begin{aligned}&\int \boldsymbol{a}_{e,\alpha}\cdot\boldsymbol{a}_{e,\alpha'}dV = \frac{1}{\epsilon_\mathrm{o}}\delta_{\alpha,\alpha'}\\ &\int \boldsymbol{a}_{e,\alpha}\cdot\boldsymbol{a}_{e,\alpha}\mathrm{d}V = 0 = \int \boldsymbol{a}_{e,\alpha}^\dagger\cdot\boldsymbol{a}_{e,\alpha}^\dagger\mathrm{d}V\\ &\int \boldsymbol{a}_{e,\alpha}^\dagger\cdot\boldsymbol{a}_{e,\alpha}dV = \frac{1}{\epsilon_\mathrm{o}}.\end{aligned} \tag{7.25}$$

Therefore, the classical Hamiltonian of EM field becomes

$$\begin{aligned}\mathrm{H} &= -\frac{1}{4\pi u_{ph,\mathrm{o}}^2}\sum_{\alpha,\alpha'}\int[(q_\alpha q_\alpha' \boldsymbol{a}_{e,\alpha}\cdot\boldsymbol{a}_{e,\alpha'} + q_\alpha^\dagger q_{\alpha'}^\dagger \boldsymbol{a}_{e,\alpha}^\dagger\cdot\boldsymbol{a}_{e,\alpha'}^\dagger)\\ &\quad - (q_\alpha q_\alpha'^\dagger \boldsymbol{a}_{e,\alpha}\cdot\boldsymbol{a}_{e,\alpha'}^\dagger + q_\alpha^\dagger q_{\alpha'} \boldsymbol{a}_{e,\alpha}^\dagger\cdot\boldsymbol{a}_{e,\alpha'})]\mathrm{d}V\\ &= \epsilon_\mathrm{o}\sum_\alpha \omega_\alpha^2 2q_\alpha q_\alpha^\dagger\frac{1}{\epsilon_\mathrm{o}}\\ &= 2\sum_\alpha \omega_\alpha^2 q_\alpha q_\alpha^\dagger.\end{aligned} \tag{7.26}$$

Now we replace q_α and $q_\alpha^\dagger$ with the following coordinates and momenta

$$Q_\alpha = q_\alpha + q_\alpha^\dagger \tag{7.27}$$

$$p_\alpha = \frac{\partial Q_\alpha}{\partial t} = -i\omega_\alpha(q_\alpha - q_\alpha^\dagger). \tag{7.28}$$

Then

$$q_\alpha = \frac{1}{2}(Q_\alpha - \frac{1}{i\omega_\alpha}p_\alpha), \qquad q_\alpha^\dagger = \frac{1}{2}(Q_\alpha + \frac{1}{i\omega_\alpha}p_\alpha), \tag{7.29}$$

and (7.26) becomes

$$\mathrm{H} = 2\sum_\alpha \omega_\alpha^2 q_\alpha q_\alpha^\dagger = \frac{1}{2}\sum_\alpha (p_\alpha^2 + \omega_\alpha^2 Q_\alpha^2). \tag{7.30}$$

This is the Hamiltonian for the harmonic oscillator.

We have just formulated the dynamics of EM radiation as its mechanical analog, a simple harmonic oscillator. Thus, the EM field can be treated as an ensemble of harmonic oscillators with their frequency and polarization.

In the quantum treatment of the EM field, we treat $Q,\ p,\ q$, and $q^\dagger$ as operators, with the following commutation relations (2.72) (Chapter 2 problem)

$$[Q_\alpha, p_{\alpha'}] = i\hbar\delta_{\alpha\alpha'}$$

$$[Q_\alpha, Q_{\alpha'}] = [p_\alpha, p_{\alpha'}] = 0. \tag{7.31}$$

Then (7.31) gives

$$[q_\alpha, q_{\alpha'}^\dagger] = \frac{\hbar}{2\omega_\alpha}\delta_{\alpha\alpha'}$$

$$[c_\alpha, c_{\alpha'}^\dagger] = \delta_{\alpha\alpha'}, \tag{7.32}$$

where $c^\dagger$ and c are creation and annihilation operators, respectively (Section 2.6.4) and $\delta_{\alpha,\alpha'}$ is the Kronecker delta. The creation and annihilation operators are here defined as

$$c_\alpha = (\frac{2\omega_\alpha}{\hbar})^{1/2} q_\alpha, \qquad c_\alpha^\dagger = (\frac{2\omega_\alpha}{\hbar})^{1/2} q_\alpha^\dagger. \tag{7.33}$$

Then the Hamiltonian of the EM field (7.30) becomes [similar to those given by (2.85) and (4.50)]

$$\mathrm{H}_{ph} = \sum_\alpha \hbar\omega_\alpha(c_\alpha^\dagger c_\alpha + \frac{1}{2}), \tag{7.34}$$

similar to (4.49) for phonons. Using these operators, vector potential (7.21) becomes

$$\boldsymbol{a}_e(\boldsymbol{x}, t) = \sum_\alpha (\frac{\hbar}{2\epsilon_{\mathrm{o}}\omega_\alpha V})^{1/2} \boldsymbol{s}_{ph,\alpha}(c_\alpha e^{i\boldsymbol{\kappa}_\alpha\cdot\boldsymbol{x}} + c_\alpha^\dagger e^{-i\boldsymbol{\kappa}_\alpha\cdot\boldsymbol{x}}). \tag{7.35}$$

We have used $\epsilon_{\mathrm{o}} = 1/\mu_{\mathrm{o}} u_{ph,\mathrm{o}}^2$, where ϵ_{o} is the free-space permittivity and μ_{o} is the free-space permeability.

The preceding photon Hamiltonian will be used in photon–matter interaction, including in Section 7.12.1, where we develop the theory of laser cooling.

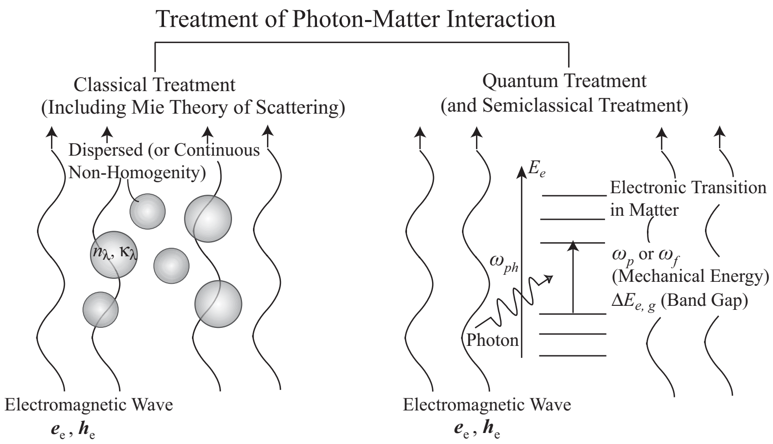

(a) Photon–Matter Interation Treatments

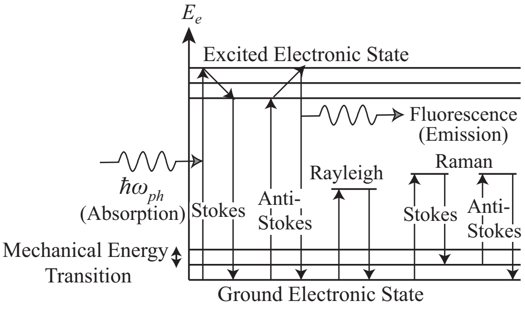

(b) Photon Scattering Mechanisms

Figure 7.3. (a) Classical (optical constant) treatment and semiclassical (classical EM wave $\boldsymbol{e}_e$ and $\boldsymbol{h}_e$ and discrete electronic energy) treatment of photon–matter interactions. (b) Elastic and inelastic photon–atom interactions showing Rayleigh (elastic scattering), fluorescence (mechanical and electronic transitions) and Raman (mechanical transitions) scatterings. In anti-stokes scattering, the emitted photon has higher energy than the absorbed photon.

7.3.2 Photon-Matter Interactions

In the semiclassical treatment of EM wave (represented by $\boldsymbol{e}_e$ and $\boldsymbol{h}_e$) interaction with matter, the bulk optical properties of the matter are represented by the complex spectral index of refraction $m_\lambda = n_\lambda - i\kappa_\lambda$ (Table 3.5). Here n_λ is the spectral index of refraction and κ_λ is the spectral index of extinction (loss). The Mie scattering theory is an example of this treatment [236] and results in prediction of scattering and absorption characteristics of the particles. Rayleigh elastic scattering is the limit of this for small particles (size parameter $\pi d/\lambda$ is $\ll 1$, where d is the particle diameter) [230].

In the semiclassical treatment of EM wave–matter interactions, the wave is treated as classical, whereas the atom is treated as a quantum system with discrete EM states undergoing transitions because of absorption of photons. These two treatments are shown in Figure 7.3(a). Figure 7.3(b) shows the classical elastic Rayleigh scattering, with no absorption (the radiation intensity only undergoes scattering), as well as some quantum energy absorption and transitions (inelastic). The examples are fluorescence, in which the photon energy matches the electronic transitions, and Raman scattering, in which the atomic kinetic energy is also excited (in addition to electronic transitions). In the next few sections, the focus will be on the semi-classical treatment of the absorption (and emission), when the detailed electronic transition and the associated atomic kinetic energy changes can be analyzed and used for heating, cooling, or other energy conversions.

In the quantum treatment of EM wave–matter, the photon–electron interaction Hamiltonian becomes [23]

$$\begin{aligned} \mathrm{H}_{ph\text{-}e} &= -\frac{e_c}{m_e}(a+a^\dagger)\boldsymbol{a}_e \cdot \boldsymbol{p_e} \\ &= -\frac{e_c}{m_e}(\frac{\hbar}{2\epsilon_{\mathrm{o}}\omega_\alpha V})^{1/2}(\boldsymbol{s}_{ph,\alpha}\cdot\boldsymbol{p_e})(a+a^\dagger)(ce^{i\boldsymbol{\kappa}\cdot\boldsymbol{x}}+c^\dagger e^{-i\boldsymbol{\kappa}\cdot\boldsymbol{x}}) \\ &= -(\frac{\hbar}{2\epsilon_{\mathrm{o}}\omega_\alpha V})^{1/2}(\boldsymbol{s}_{ph,\alpha}\cdot e_c\frac{\partial \boldsymbol{x}}{\partial t})(a+a^\dagger)(ce^{i\boldsymbol{\kappa}\cdot\boldsymbol{x}}+c^\dagger e^{-i\boldsymbol{\kappa}\cdot\boldsymbol{x}}) \\ &= -(\frac{\hbar\omega_\alpha}{2\epsilon_{\mathrm{o}} V})^{1/2}(\boldsymbol{s}_{ph,\alpha}\cdot e_c\boldsymbol{x})(a+a^\dagger)(ce^{i\boldsymbol{\kappa}\cdot\boldsymbol{x}}+c^\dagger e^{-i\boldsymbol{\kappa}\cdot\boldsymbol{x}}), \end{aligned} \tag{7.36}$$

where $\boldsymbol{s}_{ph,\alpha}$ is the polarization vector of the EM wave, $\boldsymbol{p_e}$ is the dipole moment vector (electric entity here), ω_α is the EM wave frequency, and $a(a^\dagger)$ is the operator describing the internal motion (excitation) of the electron. We have used the commutation relationship[†] for the transition dipole moment $\boldsymbol{\mu}_e = \langle\psi_f|\boldsymbol{p}_e|\psi_i\rangle = im_e\omega_\alpha\langle\psi_f|\boldsymbol{x}|\psi_i\rangle$.

In a typical atomic transition in the optical regime, the photon wavelength (of the order of several thousand angstrom) is much larger than the linear dimension of the atom (of the order of 1 Å). Then we can use the expansion $e^{-i\boldsymbol{\kappa}\cdot\boldsymbol{x}} = 1 - i\boldsymbol{\kappa}\cdot\boldsymbol{x} - (\boldsymbol{\kappa}\cdot\boldsymbol{x})^2/2 - \ldots$ and take the leading term, which is 1.

This Hamiltonian from the quantum treatment of EM wave–matter interaction will be used in Section 7.12.1, when we develop the interaction rate using the FGR (3.27).

7.4 Photon Absorption and Emission in Two-Level Electronic Systems

As mentioned, the classical description of absorption and emission of photons, based on the complex dielectric constant (and its relationship with the complex index of refraction, is given in [127]). Here we start with a quantum treatment.

We begin the photon absorption by introducing the quantum two-level electronic transitions and the Einstein model for interaction of photon and matter (its

---

[†] Note that

$$[\mathrm{H},\boldsymbol{x}] = \frac{\hbar}{i}\frac{\partial x}{\partial t} = \frac{\hbar}{i}\frac{\boldsymbol{p}}{m_e}$$

$$\begin{aligned} \frac{\hbar}{im_e}\langle\psi_f|\boldsymbol{p}|\psi_i\rangle &= \langle\psi_f|[\mathrm{H},\boldsymbol{x}]|\psi_i\rangle = \langle\psi_f|\mathrm{H}x - x\mathrm{H}|\psi_i\rangle \\ &= (E_f - E_i)\langle\psi_f|\boldsymbol{x}|\psi_i\rangle = \hbar\omega_\alpha\langle\psi_f|\boldsymbol{x}|\psi_i\rangle. \end{aligned}$$

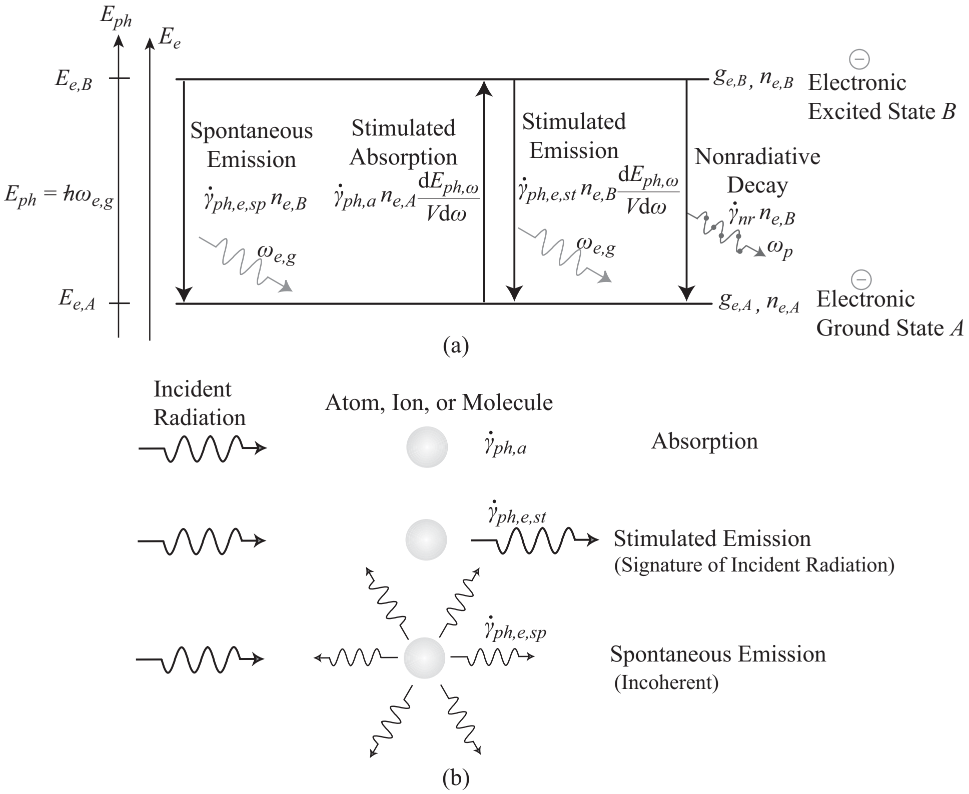
E_{ph}
E_e
$E_{e,B}$
$E_{ph} = \hbar\omega_{e,g}$
$E_{e,A}$
Spontaneous Emission
$\dot{\gamma}_{ph,e,sp}\, n_{e,B}$
$\omega_{e,g}$
Stimulated Absorption
$\dot{\gamma}_{ph,a}\, n_{e,A} \frac{dE_{ph,\omega}}{V d\omega}$
Stimulated Emission
$\dot{\gamma}_{ph,e,st}\, n_{e,B} \frac{dE_{ph,\omega}}{V d\omega}$
$\omega_{e,g}$
Nonradiative Decay
$\dot{\gamma}_{nr}\, n_{e,B}$
ω_p
$g_{e,B},\ n_{e,B}$ Electronic Excited State B
$g_{e,A},\ n_{e,A}$ Electronic Ground State A
(a)
Incident Radiation
Atom, Ion, or Molecule
$\dot{\gamma}_{ph,a}$
Absorption
$\dot{\gamma}_{ph,e,st}$
Stimulated Emission
(Signature of Incident Radiation)
$\dot{\gamma}_{ph,e,sp}$
Spontaneous Emission
(Incoherent)
(b)

Figure 7.4. (a) Electron transitions and photon emission in an irradiated, two-level electron system. Both spontaneous and stimulated emission are shown, as well as the stimulated absorption. (b) Stimulated emission follows the direction of incident radiation, but spontaneous emission does not.

electronic structure). Figure 7.4(a) shows the model for absorption and emission in this electron system. When the photon emission is influenced by the absorption of the photon, distinction should be made between the spontaneous photon emission (which is due to fluctuations, including thermal motion) and the stimulated emission (which depends on the absorbed photon). In principle, the excitation and emission can also be due to phonons and molecular vibration (e.g., CO_2 laser in Figure 7.39). We have already discussed spontaneous emission by transition dipole, e.g., (3.43), and at finite temperatures there will always be a spontaneous emission present. We now seek the relations between the spontaneous and stimulated emissions in excited systems. Figure 7.4(b) shows that the stimulated emission follows the direction of incident radiation, whereas the spontaneous emission is random in its angular distribution.

7.4.1 Einstein Excited-State Population Rate Equation

Consider photon irradiation with frequency ω on an electron system with populations $n_{e,A}$ in the ground state and $n_{e,B}$ in the excited state (because of absorption of photons), as shown in Figure 7.4. The spectral energy density of photon is given by (7.4), and, using this, we find that the electron system population rate equation is [†]

$$\frac{\mathrm{d}n_{e,B}}{\mathrm{d}t} = \underbrace{-\dot{\gamma}_{ph,e,sp} n_{e,B}}_{\text{spontaneous emission}} + \underbrace{\dot{\gamma}_{ph,a} n_{e,A} \frac{\mathrm{d}E_{ph,\omega}}{V\mathrm{d}\omega}}_{\text{stimulated absorption}} - \underbrace{\dot{\gamma}_{ph,e,st} n_{e,B} \frac{\mathrm{d}E_{ph,\omega}}{V\mathrm{d}\omega}}_{\text{stimulated emission}} - \underbrace{\dot{\gamma}_{nr} n_{e,B}}_{\text{nonradiative decay}}$$

population rate equation. (7.37)

The last term is due to nonradiative decay (Section 7.11), and can be for example by phonon emission. This is referred to as the Einstein population rate equation [291].[‡] Note that $\dot{\gamma}_{ph,e,sp}$ is in units of (1/s) and $\dot{\gamma}_{ph,e,st}$ and $\dot{\gamma}_{ph,a}$ are in (m^3-rad/s)/(J-s). This is needed to make the stimulated absorption and emission proportional to the incident radiation.

Population inversion and amplification occurs when $n_{i,B} > n_{i,A}$, i.e., the population of the excited state is larger than the ground state (for any energy carrier i). Then the population is not in thermal equilibrium (and does not follow the distribution functions of Table 1.2). To maintain steady-state population inversion, a three or larger level system is needed (Section 7.13.1 for CO_2 laser). As in Figure 5.39 for He-Ne laser, a pumping level, and a lasing upper level (metastable) and a lower level are needed. If the lower level is the ground state, this is a three-level laser, if not, it is a four-level laser (e.g., He-Ne).

The spontaneous (without means to influence the process) emission (no prior field) or relaxation transition is a spontaneous drop from B to A while emitting a photon (EM wave) or phonon at the transition frequency. This is also called fluorescence, and signifies that each electric or magnetic entity behaves as a random oscillation antenna (e.g., electric dipole antenna). Spontaneous emission is incoherent emission. The stimulated (in presence of prior field) responses or stimulated transitions (absorption and emission) result in each electric or magnetic entity acting as a miniature, passive resonant antenna and oscillates in response to the applied signal only. This is a phase-coherent internal transition and emission.

Note that in this two-level system $\mathrm{d}n_{e,A}/\mathrm{d}t = -\mathrm{d}n_{e,B}/\mathrm{d}t$. Under steady-state, we have $\mathrm{d}n_{e,B}/\mathrm{d}t = 0$.

[†] The Einstein coefficients A, B_{AB}, B_{BA} in (7.37) are

$$\frac{\mathrm{d}n_{e,B}}{\mathrm{d}t} = -An_{e,B} + B_{AB} n_{e,A} \frac{\mathrm{d}E_{ph,\omega}}{V\mathrm{d}\omega} - B_{BA} n_{e,B} \frac{\mathrm{d}E_{ph,\omega}}{V\mathrm{d}\omega} - \dot{\gamma}_{nr} n_{e,B}.$$

[‡] Under spontaneous decay only, the solution to (7.37), with initial condition of $n_{e,B}(0)$, is

$$n_{e,B}(t) = n_{e,B}(0) e^{-t/\tau_{ph,e,sp}},$$

where the life time is $\tau_{ph,e,sp} = \dot{\gamma}_{ph,e,sp}^{-1}$.
In general, the radiation (decay) lifetime is

$$\frac{1}{\tau_r} = \frac{1}{\tau_{ph,e,sp}} + \frac{1}{\tau_{ph,e,st}} + \frac{1}{\tau_{nr}}.$$

Under general condition, spontaneous emission dominates, but in lasers, the stimulated emission dominates.

Under $\dot{\gamma}_{nr} = 0$, the steady-state result gives the relation between the coefficients (Kirchhoff law)

$$\dot{\gamma}_{ph,a} n_{e,A} \frac{\mathrm{d}E_{ph,\omega}}{V\mathrm{d}\omega} = \dot{\gamma}_{ph,e,sp} n_{e,B} + \dot{\gamma}_{ph,e,st} n_{e,B} \frac{\mathrm{d}E_{ph,\omega}}{V\mathrm{d}\omega}. \tag{7.38}$$

We note that for $\mathrm{d}E_{ph,\omega}/V\mathrm{d}\omega$ in (7.2), f_{ph} is not required to be the equilibrium distribution and, as in lasers, can have a very narrow band of energy with a population far from equilibrium. One can write $E_{ph,\omega}/V\mathrm{d}\omega$ as a sum of the thermal contribution and external (nonthermal) contribution [291].

In Section 7.11, we will list examples of $\tau_{ph,e,sp}$ for some materials, as well as the expression for the classical oscillating electron emission. Also, in Section 7.4.4, we discuss the relation between $\dot{\gamma}_{ph,a}$ and the absorption coefficient and cross-section area. In Section 7.8, we will discuss calculation of absorption coefficient, using FGR. Once $\dot{\gamma}_{ph,a}$ is known, for equilibrium population, $\dot{\gamma}_{ph,e,st}$ and $\dot{\gamma}_{ph,e,sp}$ are found from (7.40) and (7.42). Similarly, when $\dot{\gamma}_{ph,e,sp}$ is known, the other two are found.

7.4.2 Einstein Coefficients for Equilibrium Electronic Population

Under classical equilibrium energy occupancy, and for $\dot{\gamma}_{nr} = 0$, the electronic energy distribution functions can be presented by use of the degree of degeneracies $g_{e,A}$ and $g_{e,B}$ (for $g_{e,i} = 1$, there is no degeneracy) defined in the partition function (2.27) as[†]

$$\frac{n_{e,B}}{n_{e,A}} = \frac{g_{e,B}}{g_{e,A}} \exp(-\frac{\hbar\omega_{e,g}}{k_\mathrm{B}T}), \ \hbar\omega_{e,g} = E_{e,B} - E_{e,A}. \tag{7.39}$$

Then (7.39) requires that for equilibrium thermal source $\mathrm{d}E_{ph,\omega}/V\mathrm{d}\omega$ is given by (7.4) as $\hbar\omega f_{ph}^{\mathrm{o}} D_{b,\omega}$, we have

$$g_{e,A}\dot{\gamma}_{ph,a} = g_{e,B}\dot{\gamma}_{ph,e,st} \quad \text{equilibrium condition 1.} \tag{7.40}$$

This states that, for nondegenerate systems ($g_{e,A} = g_{e,B} = 1$), the stimulated emission and absorption rates are equal.

Also, rearranging (7.40) and using (7.38) and (7.39), we have

$$\begin{aligned} \frac{dE_{ph,\omega}}{Vd\omega} &= \frac{\dot{\gamma}_{ph,e,sp}}{\frac{g_{e,A}}{g_{e,B}}\exp(\frac{\hbar\omega}{k_\mathrm{B}T})\dot{\gamma}_{ph,a} - \dot{\gamma}_{ph,e,st}} \\ &= \frac{\hbar\omega^3}{\pi^2 u_{ph}^3}\exp(-\frac{\hbar\omega}{k_\mathrm{B}T}) \end{aligned} \tag{7.41}$$

[†] There are some special nonequilibrium conditions, namely,

$$\frac{g_{e,A}n_{e,B}}{g_{e,B}n_{e,A}} \ll 1 \quad \text{low excitation condition}$$

$$\frac{g_{e,A}n_{e,B}}{g_{e,B}n_{e,A}} = 1 \quad \text{saturation}$$

$$\frac{g_{e,A}n_{e,B}}{g_{e,B}n_{e,A}} > 1 \quad \text{amplification (inversion).}$$

The last one exists in lasers.

$$\frac{\dot{\gamma}_{ph,e,sp}}{\dot{\gamma}_{ph,e,st}} = \frac{\hbar\omega_{e,g}^3}{\pi^2 u_{ph}^3} \text{ equilibrium condition 2.} \tag{7.42}$$

Therefore, all three terms are present, i.e., using (7.40) along with (7.42), there is need for the stimulated emission.

Equations (7.38), (7.40), and (7.41) describe the so-called inverse processes under equilibrium and are called the detailed balance relations.

The three Einstein coefficients $\dot{\gamma}_{ph,i}$ (or A, B_{AB}, and B_{BA} coefficients) are similarly related through (7.40) and (7.42), under equilibrium (this also makes for homogeneous and isotropic radiation).

The absorbed power (including stimulated emission), per unit volume, is

$$\dot{s}_{ph\text{-}e} = \hbar\omega_{e,g}\left.\frac{\mathrm{d}n_{e,B}}{\mathrm{d}t}\right|_{AB} = \hbar\omega_{e,g}\left(\dot{\gamma}_{ph,a}n_{e,A}\frac{\mathrm{d}E_{ph,\omega}}{V\mathrm{d}\omega} - \dot{\gamma}_{ph,e,st}n_{e,B}\frac{\mathrm{d}E_{ph,\omega}}{V\mathrm{d}\omega}\right). \tag{7.43}$$

The spontaneous radiative lifetime $\tau_{ph,e,sp} = 1/\dot{\gamma}_{ph,e,sp}$ is part of the radiative lifetime and in the absence of stimulated emission becomes the radiative lifetime τ_r (Section 7.12.2).

7.4.3 Spontaneous Versus Stimulated Emissions in Equilibrium Thermal Cavity f_{ph}^{o}

Consider the source of photons to be thermal, so f_{ph} appearing in E_{ph} in (7.2) is that continuous equilibrium bosons, i.e.,

$$f_{ph}^{\mathrm{o}} = \frac{1}{\exp(\frac{\hbar\omega}{k_{\mathrm{B}}T}) - 1} \quad \text{photon equilibrium distribution.} \tag{7.44}$$

Under steady-state and equilibrium photon distribution, from (7.38) we have

$$\frac{\mathrm{d}E_{ph,\omega}}{V\mathrm{d}\omega} = \frac{\dot{\gamma}_{ph,e,sp}}{\frac{n_{e,A}}{n_{e,B}}\dot{\gamma}_{ph,a} - \dot{\gamma}_{ph,e,st}}. \tag{7.45}$$

Now for equilibrium electronic distribution, using (7.39), (7.40), and (7.44), we have

$$\frac{\mathrm{d}E_{ph,\omega}}{V\mathrm{d}\omega} = \frac{\dot{\gamma}_{ph,e,sp}}{\dot{\gamma}_{ph,e,st}} f_{ph}^{\mathrm{o}}. \tag{7.46}$$

Note that the sum of the stimulated and spontaneous emission rates is

$$\dot{\gamma}_{ph,e,st}\frac{\mathrm{d}E_{ph,\omega}}{V\mathrm{d}\omega} + \dot{\gamma}_{ph,e,sp} = \dot{\gamma}_{ph,e,sp}(f_{ph}^{\mathrm{o}} + 1). \tag{7.47}$$

Writing (7.46) for stimulated emission, we have

$$\dot{\gamma}_{ph,e,st}\frac{\mathrm{d}E_{ph,\omega}}{V\mathrm{d}\omega} = \dot{\gamma}_{ph,e,sp} f_{ph}^{\mathrm{o}}. \tag{7.48}$$

We now examine two limits. From (7.44), for $\hbar\omega/k_{\mathrm{B}}T \ll 1$ and $T = 300$ K (radio-frequencies and microwave regimes), we have $f_{ph}^{\mathrm{o}} \to \infty$, and (7.48) gives

$$\dot{\gamma}_{ph,e,sp} \ll \dot{\gamma}_{ph,e,st}\frac{\mathrm{d}E_{ph,\omega}}{V\mathrm{d}\omega} \quad \text{for } \omega \ll \frac{k_{\mathrm{B}}T}{\hbar} = 3.928 \times 10^{13} \text{ rad/s}$$

$$\text{stimulated emission dominates,} \tag{7.49}$$

i.e., in thermal cavity, the stimulated emission rate is much larger than the spontaneous emission rate.

Similarly, for $\hbar\omega/k_\mathrm{B}T \gg 1$ and $T = 300$ K (near-infrared, visible, etc.), we have $f^\mathrm{o}_{ph} \rightarrow 0$, and from (7.48)

$$\dot{\gamma}_{ph,e,sp} \gg \dot{\gamma}_{ph,e,st}\frac{\mathrm{d}E_{ph,\omega}}{V\mathrm{d}\omega} \quad \text{for } \omega \gg \frac{k_\mathrm{B}T}{\hbar} = 3.928 \times 10^{13}\ \mathrm{rad/s}$$
$$\text{spontaneous emission dominates,} \qquad (7.50)$$

i.e., the spontaneous emission rate is much larger than the thermally stimulated emission (and absorption) of thermal radiation.

As the temperature increases, so does this frequency. Therefore, at high temperatures the thermally excited energy density increases, whereas at low temperatures (including room temperature) it is not that significant when considering transition energy ($\hbar\omega$) in the near-infrared, visible, and ultraviolet regimes.

When the stimulated and spontaneous emission rates are equal, it is called the saturation condition (saturation photon energy density), and using (7.42) we have

$$\frac{\mathrm{d}E_{ph,\omega}}{V\mathrm{d}\omega} = \frac{\dot{\gamma}_{ph,e,sp}}{\dot{\gamma}_{ph,e,st}} = \frac{\hbar\omega^3}{\pi^2 u^3_{ph}} \quad \text{saturation energy density.} \qquad (7.51)$$

This corresponds to $f^\mathrm{o}_{ph} = 1$ in (7.2). From (7.5), using the intensity $I_{ph,\omega}\Delta\omega = u_{ph}\mathrm{d}E_{ph,\omega}/V$ (assuming unidirectional radiation, i.e., not divided by 4π), for $\omega = 3\times 10^{15}$ rad/s (red light), and $\Delta\omega = 6\times 10^{10}$ rad/s (conventional, narrow-band light sources [291]), for the thermal emission light source under saturation (maximum) energy density we have

$$\int I_{ph,\omega}\mathrm{d}\omega = \frac{\hbar\omega^3\Delta\omega}{\pi^2 u^3_{ph}} = 1.924 \times 10^5\ \mathrm{W/m^2}$$
$$\text{maximum narrow-band,} \quad \text{directed thermal emission of red light } (f^\mathrm{o}_{ph} = 1). \qquad (7.52)$$

This would require a very high temperature. Laser light sources (nonequilibrium populations) can have intensities larger than this maximum thermal emission value (even with narrow $\Delta\omega$), especially the pulsed lasers.

7.4.4 Spectral Absorption Coefficient and Cross–Section Area

We define the spectral absorption coefficient $\sigma_{ph,\omega}$ through volumetric photon absorption rate, i.e.,

$$\dot{s}_{ph\text{-}e} \equiv \sigma_{ph,\omega} u_{ph} \int_\omega \frac{\mathrm{d}E_{ph,\omega}}{V} \quad \text{spectral absorption coefficient.} \qquad (7.53)$$

We include the stimulated emission in the net absorption, so $\sigma_{ph,\omega}$ is related to the Einstein coefficients through (7.43) as

$$\begin{aligned}\sigma_{ph,\omega} &= \frac{\hbar\omega(\dot{\gamma}_{ph,a}n_{e,A} - \dot{\gamma}_{ph,e,st}n_{e,B})}{u_{ph}\int_\omega \mathrm{d}\omega}\\ &= \frac{\hbar\omega\dot{\gamma}_{ph,a}n_{e,A}(1 - \frac{g_{e,A}}{g_{e,B}}\frac{n_{e,B}}{n_{e,A}})}{u_{ph}\int_\omega \mathrm{d}\omega},\end{aligned} \tag{7.54}$$

where $\int_\omega \mathrm{d}\omega$ is over a small bandwidth, centered around ω. The bandwidth (shape) function $g(\omega)$ was introduced in Table 3.5, subject to a normalization condition.

Under equilibrium (7.39), we have

$$1 - \frac{g_{e,A}}{g_{e,B}}\frac{n_{e,B}}{n_{e,A}} = 1 - \exp(\frac{-\hbar\omega}{k_\mathrm{B}T}). \tag{7.55}$$

Then

$$\sigma_{ph,\omega} = \frac{\hbar\omega\dot{\gamma}_{ph,a}n_{e,A}[1 - \exp(\frac{-\hbar\omega}{k_\mathrm{B}T})]}{u_{ph}\int_\omega \mathrm{d}\omega}. \tag{7.56}$$

Hence we can define the photon absorption cross-section area as

$$\begin{aligned}A_{ph,a}(\omega) &\equiv \sigma_{ph,\omega}n_{e,A}[1 - \exp(\frac{-\hbar\omega}{k_\mathrm{B}T})]\\ &= \frac{\hbar\omega\dot{\gamma}_{ph,a}}{u_{ph}\int_\omega \mathrm{d}\omega} \quad \text{absorption cross-section area.}\end{aligned} \tag{7.57}$$

The spontaneous emission power (per unit volume) is

$$\dot{s}_{e\text{-}ph} = \hbar\omega\dot{\gamma}_{ph,e,sp}n_{e,B} \quad \text{spontaneous emission.} \tag{7.58}$$

Then under thermal equilibrium, making the preceding substitutions, we have

$$\begin{aligned}\dot{s}_{e\text{-}ph} &= \hbar\omega[\frac{\hbar\omega^3}{\pi^2 u_{ph}^3}\dot{\gamma}_{ph,a}\frac{g_{e,A}}{g_{e,B}}][n_{e,A}\frac{g_{e,B}}{g_{e,A}}\exp(\frac{-\hbar\omega}{k_\mathrm{B}T})]\\ &= \hbar\omega\dot{\gamma}_{ph,a}n_{e,A}\frac{\hbar\omega^3}{\pi^2 u_{ph}^3}\exp(\frac{-\hbar\omega}{k_\mathrm{B}T})\\ &= \frac{\sigma_{ph,\omega}u_{ph}\int_\omega \mathrm{d}\omega}{1 - \exp(\frac{-\hbar\omega}{k_\mathrm{B}T})}\frac{\hbar\omega^3}{\pi^2 u_{ph}^3}\exp(\frac{-\hbar\omega}{k_\mathrm{B}T})\\ &= \sigma_{ph,\omega}\frac{\hbar\omega^3}{\pi^2 u_{ph}^3}\frac{1}{\exp(\frac{\hbar\omega}{k_\mathrm{B}T}) - 1}\int_\omega \mathrm{d}\omega\\ &= \sigma_{ph,\omega}u_{ph}\int_\omega \frac{\mathrm{d}E_{ph,\omega}}{V}\end{aligned}$$

$$\text{spontaneous emission rate} \quad \text{in terms of absorption coefficient.} \tag{7.59}$$

Writing (7.56) in terms of $\dot{\gamma}_{ph,e,sp}$ from (7.40) and (7.42), we have

$$\begin{aligned}\sigma_{ph,\omega} &= \frac{\hbar\omega\dot{\gamma}_{ph,a}n_{e,A}[1-\exp(\frac{-\hbar\omega}{k_{\rm B}T})]}{u_{ph}\int_{\omega}{\rm d}\omega}\\ &= \frac{\hbar\omega[\frac{\dot{\gamma}_{ph,e,sp}}{\hbar\omega^3}\pi^2u_{ph}^3\frac{g_{e,A}}{g_{e,B}}][n_{e,B}\frac{g_{e,A}}{g_{e,B}}\exp(\frac{\hbar\omega}{k_{\rm B}T})][1-\exp(\frac{-\hbar\omega}{k_{\rm B}T})]}{u_{ph}\int_{\omega}{\rm d}\omega}\\ &= \frac{\pi^2u_{ph}^2n_{e,B}\dot{\gamma}_{ph,e,sp}}{\omega^2\int_{\omega}{\rm d}\omega}\frac{1}{f_{ph}^{\rm o}}. \qquad (7.60)\end{aligned}$$

Comparing with (7.56), i.e., $\sigma_{ph,\omega} = n_{e,B}A_{ph,e}/f_{ph}^{\rm o}$, we have for the photon emission cross-section area in terms of $\dot{\gamma}_{ph,e,sp}$

$$A_{ph,e}(\omega) \equiv \frac{\pi^2u_{ph}^2\dot{\gamma}_{ph,e,sp}}{\omega^2\int_{\omega}{\rm d}\omega} \quad \text{emission cross-section area.} \qquad (7.61)$$

Note that (7.57) and (7.61) relate the absorption and emission cross-section areas to the Einstein rate coefficients.

In most applications, the spontaneous emission dominates over the stimulated emission.

7.5 Particle Treatment: Photon BTE with Absorption, Emission, and Scattering

The BTE (Table 3.1) written for photon as a particle having momentum $\boldsymbol{p}_{ph} = \hbar\omega\boldsymbol{s}/u_{ph}$, along direction $\boldsymbol{s}$, and for ph-e scattering, absorption/emission $\dot{s}_{f,ph\text{-}e}$, and any other generation/removal presented by $\dot{s}_{f,ph,i}$, is

$$\frac{\partial f_{ph}}{\partial t} + u_{ph}\boldsymbol{s}\cdot\nabla f_{ph} = \left.\frac{\partial f_{ph}}{\partial t}\right|_{s} + \dot{s}_{f,ph\text{-}e} + \dot{s}_{f,ph,i}. \qquad (7.62)$$

Here we have assumed that the external force $\boldsymbol{F}_{ph}$ is zero.

In Sections 7.8 and 7.9, we will discuss various photon–electron interactions, including those assisted by phonons, in solids (ranging from electrical insulators, to semiconductors, metals and gases). Also in Section 7.12 we will discuss photon–electron interactions in gases, including those assisted by fluid particle kinetic energy.

Here we continue with the two-level electronic transition, as shown in Figure 7.5, to derive the relations for various terms in (7.62). The source term $\dot{s}_{f,ph\text{-}e}$ representing the absorption and emission of photons of angular frequency ω can be written as [408]

$$\begin{aligned}\dot{s}_{f,ph\text{-}e}(\omega) = u_{ph}\sum_{A,B}\{&-n_{e,A}(\omega_A)A_{ph,a}(\omega)f_{ph}(\omega)\\ &+n_{e,B}(\omega_B)A_{ph,e}(\omega)[1+f_{ph}(\omega)]\} \quad \text{absorption and emission,} \qquad (7.63)\end{aligned}$$

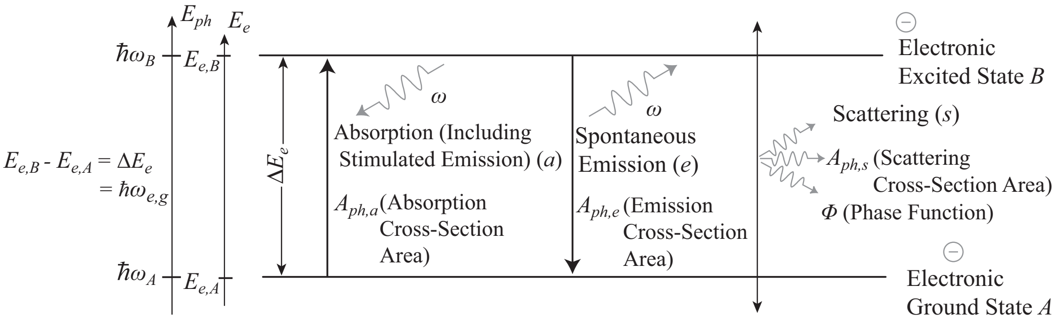
E_{ph}
E_e
$\hbar\omega_B$
$E_{e,B}$
$E_{e,B} - E_{e,A} = \Delta E_e$
$= \hbar\omega_{e,g}$
$\hbar\omega_A$
$E_{e,A}$
ΔE_e
ω
Absorption (Including Stimulated Emission) (a)
$A_{ph,a}$ (Absorption Cross-Section Area)
ω
Spontaneous Emission (e)
$A_{ph,e}$ (Emission Cross-Section Area)
Electronic Excited State B
Scattering (s)
$A_{ph,s}$ (Scattering Cross-Section Area)
Φ (Phase Function)
Electronic Ground State A

Figure 7.5. A two-level, electron transition photon–electron interaction presentation of the source term in the photon BTE (the absorption and emission are represented by effective cross-sectional areas $A_{ph,a}$ and $A_{ph,e}$). The ground state is designated as A and the excited state as B.

where ω_A is the frequency of the lower-energy state A and ω_B is the frequency of the higher-energy state B, and $n_{e,A}$ and $n_{e,B}$ are the number of absorption and emission (spontaneous and stimulated) systems per unit volume. As in Section 7.4, the interaction cross-section areas $A_{ph,a}$ and $A_{ph,e}$ represent the photon absorption (stimulated absorption minus stimulated emission) and emission effectiveness for these electronic transitions. These are generally determined from the FGR (3.27), as will be discussed in Sections 7.8 and 7.9, or empirically.

During the transition from ω_B to ω_A, a photon is emitted, and in the reverse a photon is absorbed.

Now in the scattering term of (7.62), consider a photon of angular frequency ω traveling in the direction $\boldsymbol{s}$ as shown in Figure 7.6. This photon is scattered by a boson or a fermion particle i. The initial photon state is given by ω and $\boldsymbol{s}$, and its final state is given by ω_2 and $\boldsymbol{s}_2$. The particle i has an initial state given by $\boldsymbol{p}_{i,j}$ and final state given by $\boldsymbol{p}_{i,k}$. The photon-scattering cross-section area is $A_{ph,s}$. The general scattering integral (3.8) is written as [408]

$$\left.\frac{\partial f_{ph,\omega}(\boldsymbol{s})}{\partial t}\right|_s = -\sum_{i,j,k}\frac{u_{ph}}{(2\pi\hbar)^3}\int\!\!\int \mathrm{d}\boldsymbol{p}\mathrm{d}A_{ph,s}(\boldsymbol{p}_{i,j},\omega,\boldsymbol{s}\rightarrow\boldsymbol{p}_{i,k},\omega_2,\boldsymbol{s}_2)$$
$$\times f_{i,j}(\boldsymbol{p}_{i,j})[1\pm f_{i,k}(\boldsymbol{p}_{i,k})]\{\underbrace{f_{ph,\omega}(\boldsymbol{s})[1+f_{ph,\omega_2}(\boldsymbol{s}_2)]}_{\text{out-scattering}}$$
$$\underbrace{-\,f_{ph,\omega_2}(\boldsymbol{s}_2)[1+f_{ph,\omega}(\boldsymbol{s})]\times\frac{[1\pm f_{i,j}(\boldsymbol{p}_{i,j})]f_{i,k}(\boldsymbol{p}_{i,k})}{[1\pm f_{i,k}(\boldsymbol{p}_{i,k})]f_{i,j}(\boldsymbol{p}_{i,j})}}_{\text{in-scattering}}$$
$$+\ \text{boson},\ -\ \text{fermion}. \qquad (7.64)$$

The preceding photon absorption/emission and scattering expressions are subsequently further developed and discussed.

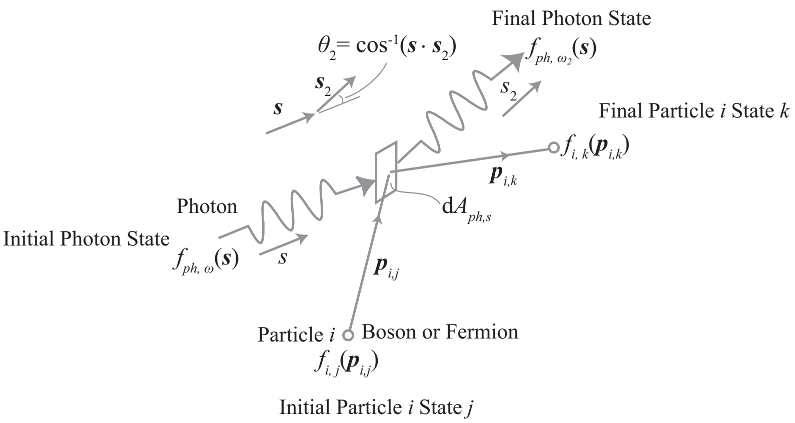
Final Photon State
$\theta_2 = \cos^{-1}(\boldsymbol{s}\cdot\boldsymbol{s}_2)$
$f_{ph,\omega_2}(\boldsymbol{s})$
$\boldsymbol{s}_2$
$\boldsymbol{s}$
s_2
Final Particle i State k
$f_{i,k}(\boldsymbol{p}_{i,k})$
$\boldsymbol{p}_{i,k}$
Photon
$\mathrm{d}A_{ph,s}$
Initial Photon State
$f_{ph,\omega}(\boldsymbol{s})$
s
$\boldsymbol{p}_{i,j}$
Particle i
Boson or Fermion
$f_{i,j}(\boldsymbol{p}_{i,j})$
Initial Particle i State j

Figure 7.6. General rendering of binary interaction and photon scattering by a material particle i (boson or fermion). The scattering is designated by scattering cross-section area $A_{ph,s}$ and scattering direction change $\boldsymbol{s}\cdot\boldsymbol{s}_2$.

7.5.1 Combining Absorption and Emission

The absorption and emission cross-section areas in (7.63) are related for the two-level system through (7.60), (7.61) as (7.55) [408]

$$A_{ph,a}(\omega) = \frac{g_{e,B}(\omega_B)}{g_{e,A}(\omega_A)} A_{ph,e}(\omega)$$

$$\text{relation between emission and absorption cross-section areas,} \qquad (7.65)$$

where $g_{e,i}$ is the degeneracy for the electronic states A and B with their two corresponding frequencies shown in Figure 7.5.

Using this, (7.63) becomes

$$\begin{aligned}\dot{s}_{f,ph\text{-}e} &= u_{ph}\sum_{A,B} n_{e,A}(\omega_A)A_{ph,a}(\omega)[1-\frac{g_{e,A}(\omega_A)n_{e,B}(\omega_B)}{g_{e,B}(\omega_B)n_{e,A}(\omega_A)}]\\ &\times[\frac{1}{\dfrac{g_{e,B}(\omega_B)n_{e,A}(\omega_A)}{g_{e,A}(\omega_A)n_{e,B}(\omega_B)}-1} - f_{ph,\omega}(s)]\\ &\equiv u_{ph}\sigma_{ph,\omega}[f^n_{ph}(T) - f_{ph}(\boldsymbol{s})], \end{aligned} \qquad (7.66)$$

where, similar to (7.60), the radiation (photon) spectral absorption coefficient $\sigma_{ph,\omega}$ is defined as

$$\sigma_{ph,\omega} = \sum_{A,B} n_{e,A}(\omega_A)A_{ph,a}[1-\frac{g_{e,A}(\omega_A)n_{e,B}(\omega_B)}{g_{e,B}(\omega_B)n_{e,A}(\omega_A)}],$$

$$\text{spectral absorption coefficient.} \qquad (7.67)$$

The inverse of $\sigma_{ph,\omega}$ is referred to as the photon mean free path λ_{ph}.

The distribution function (including thermal nonequilibrium) $f_{ph}(\omega, T)$ is

$$f_{ph}(\omega, T) = \frac{1}{\dfrac{g_{e,B}(\omega_B)n_{e,A}(\omega_A)}{g_{e,A}(\omega_A)n_{e,B}(\omega_B)} - 1}. \tag{7.68}$$

Under the special case of local thermal equilibrium (all particles in the differentialchap7:fig:GasLaserLevel collision area are at temperature T) for the distribution of absorbing and emitting systems, the population ratio is given by

$$\frac{g_{e,A}(\omega_A)n_{e,B}(\omega_B)}{g_{e,B}(\omega_B)n_{e,A}(\omega_A)} = \exp(-\frac{E_B - E_A}{k_\mathrm{B}T}) = \exp(\frac{-\hbar\omega_{e,g}}{k_\mathrm{B}T}) \tag{7.69}$$

$$E_{e,B} - E_{e,A} = \hbar(\omega_B - \omega_A) = \hbar\omega_{e,g}. \tag{7.70}$$

Using this in (7.66), we have

$$\dot{s}_{f,ph\text{-}e}(\omega) = u_{ph}\sigma_{ph,\omega}[f_{ph}^{\mathrm{o}}(T) - f_{ph}(s)] \text{ local thermal equilibrium.} \tag{7.71}$$

Finally, the absorption coefficient (7.67), using (7.69), becomes

$$\begin{aligned}\sigma_{ph,\omega} &\equiv \sum_{\omega_A} n_{e,A}(\omega_A)A_{ph,a}(\omega_{e,g})[1 - \exp(-\frac{\hbar\omega}{k_\mathrm{B}T})]\\ &= \sum_{\omega_B} \frac{n_{e,B}(\omega_B)A_{ph,e}(\omega)}{f_{ph}^{\mathrm{o}}(T)} \text{ local thermal equilibrium,}\end{aligned} \tag{7.72}$$

where as in (7.44) we have

$$f_{ph}^{\mathrm{o}}(\omega, T) = \frac{1}{\exp(\dfrac{\hbar\omega}{k_\mathrm{B}T}) - 1}. \tag{7.73}$$

In (7.72) the summation is over all two-level systems with energy gap $\hbar\omega$. Then the spectral absorption coefficient given by (7.72) depends on the number density of the available electronic transitions and the absorption/emission cross-section areas.

Then $f_{ph}(s)$ needs to be different than the equilibrium distribution at T, i.e., $f_{ph}^{\mathrm{o}}(T)$, in order to have a net emission–absorption.

7.5.2 Photon–Free Electron Elastic Scattering Rate and Cross–Section Area

Photon elastic scattering by free-conduction electrons is called Compton (or Thomson) scattering. This allows for a rather simple treatment of scattering rate and this angular distribution (scattering angle θ_2). We sum over the initial and final electron spin states (by doubling the scattering cross section). Then (7.64) written for a fermion becomes

$$\frac{\partial f_{ph,\omega}(\omega,\boldsymbol{s})}{\partial t}\bigg|_s = -\sum_{i,j,k}\frac{2u_{ph}}{(2\pi\hbar)^3}\int_{\boldsymbol{p}_e}\mathrm{d}\boldsymbol{p}_e\int \mathrm{d}A_{ph,s}(\boldsymbol{p}_e,\omega,\boldsymbol{s}\rightarrow \boldsymbol{p}_{e,2},\omega_B,\boldsymbol{s}_2)$$
$$\times f_e(\boldsymbol{p}_e)[1-f_e(\boldsymbol{p}_{e,2})]\{f_{ph,\omega}(\boldsymbol{s})[1+f_{ph,\omega_B}(\boldsymbol{s}_2)]$$
$$-f_{ph,\omega_B}(\boldsymbol{s}_2)[1+f_{ph,\omega}(\boldsymbol{s})]\times\frac{[1-f_e(\boldsymbol{p}_e)]f_e(\boldsymbol{p}_{e,2})}{[1-f_e(\boldsymbol{p}_{e,2})]f_e(\boldsymbol{p}_e)}\}, \qquad (7.74)$$

where $\boldsymbol{p}_{e,2}$ represents the final momentum of the electron participating in the collision. Assuming equilibrium distribution and using f_e^{o} from Table 1.2, we have

$$\frac{[1-f_e\boldsymbol{p}_e)]f_e(\boldsymbol{p}_{e,2})}{[1-f_e(\boldsymbol{p}_{e,2})]f_e(\boldsymbol{p}_e)} = \exp[-\frac{\hbar(\omega-\omega_B)}{k_{\mathrm{B}}T}], \qquad (7.75)$$

where we have used the conservation of energy between the colliding photon and electron, i.e.,

$$E_e(\boldsymbol{p}_{e,2})-E_e(\boldsymbol{p}_e) = E_{ph}(\omega_B)-E_{ph}(\omega)$$
$$=\hbar(\omega_B-\omega). \qquad (7.76)$$

For the elastic scattering we have $\hbar(\omega-\omega_B)=0$ and the right-hand side of (7.75) is nearly unity.

The differential scattering cross-section area for nonpolarized radiation is approximated as the Thomson cross-section area,[†] i.e.,

$$\mathrm{d}A_{ph,s} = (\frac{e_c^2}{4\pi m_e\epsilon_{\mathrm{o}}u_{ph}^2})^2\frac{1+\cos^2\theta_2}{2}\mathrm{d}(\cos\theta_2)\mathrm{d}\phi_2$$
$$\mathrm{d}\Omega = \sin\theta_2\mathrm{d}\theta_2\mathrm{d}\phi_2 = \mathrm{d}\cos\theta_2\mathrm{d}\phi_2, \qquad (7.77)$$

where $\mathrm{d}\Omega$ is the differential solid angle of the scattering angle θ_2 and

$$\theta_2 = \cos^{-1}(\boldsymbol{s}\cdot\boldsymbol{s}_2), \qquad (7.78)$$

and ϕ_2 is the azimuthal angle.

[†] Derivation is given as an end-of-chapter problem.
The classical free-electron motion (displacement) (Table 2.5) under an oscillating EM field gives [a simplified form of (3.45)]

$$m_e\frac{d^2x}{dt^2} = -e_ce_{e,o}\sin\omega t,$$

or

$$x = \frac{e_ce_{e,o}}{m_e\omega^2}\sin\omega t.$$

The oscillating electric dipole (3.40) is

$$\boldsymbol{p}_e = -e_cx\boldsymbol{s}_x = p_{e,o}\sin(\omega t)\boldsymbol{s}_x,$$

where $p_{e,o} = e_c^2e_{e,o}/m_e\omega^2$.

Now substituting this in (7.74), we have for the scattering rate (and its angular distribution)

$$\left.\frac{\partial f_{ph,\omega}(\omega,\boldsymbol{s})}{\partial t}\right|_s = -\pi u_{ph} n_{e,c} \Big(\frac{e_c^2}{4\pi m_e \epsilon_{\rm o} u_{ph}^2}\Big)^2 \int_{-1}^{1} (1+\cos^2\theta_2)$$

$$\times [f_{ph,\omega}(\boldsymbol{s}) - f_{ph,\omega_B}(\boldsymbol{s}_2)]\mathrm{d}(\cos\theta_2),\quad \frac{\hbar\omega}{m_e u_{ph}^2} \ll 1,\quad \frac{p_e}{m_e u_{ph}} \ll 1$$

$$\Phi(\theta_2,\phi) = 1 + \cos^2\theta_2 \ \ \text{phase function for free-electron scattering.} \tag{7.79}$$

The angular distribution (inside the integral) of the scattering is represented by the scattering phase function $\Phi(\theta_2, \phi)$.

As given in (5.64), we have

$$n_{e,c} = \frac{2}{(2\pi\hbar)^3} \int_{\boldsymbol{p}_e} f_e(\boldsymbol{p}_e)\mathrm{d}\boldsymbol{p}_e. \tag{7.80}$$

Here $n_{e,c}$ is the number of free (conduction) electrons per unit volume and the factor 2 is for the two possible spin states.

In the Compton effect, the photon wavelength (X-rays and γ-rays regimes) increases because of absorption by the free electrons (kinetic energy of electron increases). Note that both energy and momentum are conserved in this collision. By performing the integration over θ_2, the average scattering cross-section area (7.77) is

$$\langle A_{ph,s}\rangle = \frac{8\pi}{3} r_{\rm C}^2,\quad r_{\rm C} = \frac{e_c^2}{4\pi m_e \epsilon_{\rm o} u_{ph,o}^2},\quad \sigma_{ph,s} = n_{e,c}\langle A_{ph,s}\rangle$$

$$\text{Compton (or Thomson) scattering by free electron,} \tag{7.81}$$

where $r_{\rm C}$ is the classical (Compton) electron radius (Table 1.4), $n_{e,c}$ is the number density of scatterers, and $\sigma_{ph,s}$ is the scattering coefficient $\langle A_{ph,s}\rangle = 6.649\times10^{-29}$ m^2 = 6.649×10^{-25} cm^2. A unit for scattering of photons is barn (b), which is 10^{-24} cm^2 = 10^{-8} Å^2 = 10^2 fm^2. This is nearly the cross-section area of uranium nucleus. So Compton cross-section area is close to nuclear cross-section area. This shows that, for this free electron, the scattering cross-section area is independent of the frequency of the incident EM wave.

The general treatment of photon (classical EM wave) scattering is described in [236], and this includes the Mie scattering that covers the entire range of the size parameter (defined by $\alpha_\lambda = \pi d/\lambda$, where d is the particle diameter). These are also discussed in [230]. The treatment includes the definition of the phase function, which gives the angular distribution of the scattered wave, similar to that in (7.77). For a very small size parameter, $\alpha_\lambda \ll 1$, we have the Rayleigh scattering (which is for atoms, molecules, and bound electrons) that shows $A_{ph,s}$ is proportional to

λ^{-4} (or ω^4) of incident EM wave.[†] This gives the red sunset, since the longer light wavelengths are scattered less, and the blue sky, since the short wavelengths are scattered most.

7.6 Photon Intensity: Equation of Radiative Transfer

The equation of radiative transfer (ERT) refers to the BTE for photons written in terms of the radiation intensity I_{ph}. This intensity is the general, nonequilibrium intensity (including laser radiation) given by (7.5). The absorption, emission, and scattering can now be made more general. Here we derive this equation and also show the results for the case of absorption–emission dominated (no scattering and source/sink) transport under strong absorption (called the optically thick limit).

7.6.1 General Form of ERT

Using the spectral absorption coefficient in (7.66), the BTE (7.62) can be written as

$$\frac{\partial f_{ph}}{\partial t} + u_{ph}\boldsymbol{s} \cdot \nabla f_{ph} = \left.\frac{\partial f_{ph}}{\partial t}\right|_s + u_{ph}\sigma_{ph,\omega}[f_{ph}(\omega, T) - f_{ph}(\boldsymbol{s})] + \dot{s}_{f,ph,i}. \tag{7.82}$$

Multiplying (7.82) by $\hbar\omega^3/4\pi^3 u_{ph}^2$ for photon density of states, i.e., $I_{ph,\omega} = u_{ph} f_{ph}\hbar\omega\, D_{ph,\omega}/4\pi$ using the definition of intensity (7.5), and applying (7.71) we

---

[†] Starting from the classical treatment of bound [in an atomic potential (2.54)] electron motion (Table 2.5) in a time-periodic EM field, we have [extension of (3.45)]

$$m_e \frac{\mathrm{d}^2 x}{\mathrm{d}t^2} - m_e\omega_{n,e}^2 x = -e_c e_{e,o} \sin\omega t,$$

where $\omega_{n,e}$ is natural frequency of the bound electron (similar to harmonic interatomic bonding), we have for the solution

$$x = \frac{e_c e_{e,o}}{m_e(\omega^2 - \omega_{n,e}^2)} \sin\omega t.$$

The dipole moment vector (3.40) of this electron is

$$\boldsymbol{p}_e = -e_c x \boldsymbol{s}_x = -p_{e,o} \sin\omega t \boldsymbol{s}_x, \;\; p_{e,o} = \frac{e_c^2 e_{e,o}}{4\pi\epsilon_{\mathrm{o}} m_e(\omega^2 - \omega_{n,e}^2)}.$$

Then the Rayleigh scattering cross-section area, found similarly to (7.77) is

$$\frac{\mathrm{d}A_{ph,s}}{\mathrm{d}\Omega} = \frac{\omega^4}{(\omega^2 - \omega_{n,e}^2)^2} r_{\mathrm{C}}^2 \sin\omega,$$

or

$$\langle A_{ph,s}\rangle = \frac{8\pi}{3} r_{\mathrm{C}} \frac{\omega^4}{(\omega^2 - \omega_{n,e}^2)^2}, \;\; \sigma_{ph,s} = n_s A_{ph,s} \text{ Rayleigh scattering by bound electron.}$$

For $\omega \ll \omega_{n,e}$ (e.g., visible incident radiation versus the ultraviolet vibration), we have from (7.81)

$$\sigma_{ph,s} = n_s \frac{8\pi}{3} r_{\mathrm{C}}^2 \frac{\omega^4}{\omega_{n,e}^4} = n_s \frac{8\pi}{3} \frac{r_{\mathrm{C}}^2}{\omega_{n,e}^4} \frac{(2\pi u_{ph})^4}{\lambda^4}.$$

have

$$\frac{\partial I_{ph,\omega}(\omega,\boldsymbol{s})}{u_{ph}\partial t}+\boldsymbol{s}\cdot\nabla I_{ph,\omega}(\omega,\boldsymbol{s})=\left.\frac{\partial I_{ph,\omega}(\omega,\boldsymbol{s})}{u_{ph}\partial t}\right|_{s}$$

$$+\,\sigma_{ph,\omega}[I_{ph,\omega}(\omega,T)-I_{ph,\omega}(\omega,\boldsymbol{s})]+\dot{s}_{ph,i}. \qquad (7.83)$$

Note that here we have used f_{ph} instead of $f_p'h$ [as used in transport relations such as (3.22)]. This is the spectral (and directional) ERT.

Under local thermal equilibrium, (7.83) becomes

$$\frac{\partial I_{ph,\omega}(\omega,\boldsymbol{s})}{u_{ph}\mathrm{d}t}+\boldsymbol{s}\cdot\nabla I_{ph,\omega}(\omega,\boldsymbol{s})=\left.\frac{\partial I_{ph,\omega}(\omega,\boldsymbol{s})}{u_{ph}\partial t}\right|_{s}$$

$$+\,\sigma_{ph,\omega}[I_{b,\omega}(\omega,T)-I_{ph,\omega}(\omega,\boldsymbol{s})]+\dot{s}_{ph,i}\quad \text{local thermal equilibrium}, \qquad (7.84)$$

where we have used the blackbody intensity (7.6) for the photon emission.

The elastic scattering term $\partial I_{ph}/\partial t|_s$ is in turn represented as in- and out-scattering, as in Section 3.1.3, or in the case of Compton scattering it is given by (7.79). This presentation involves a scattering cross-section area, the number density of scatterers, and the phase function [230].

It is customary [230] to use a scattering coefficient $\sigma_{ph,s,\omega}$ to represent $\partial I_{ph}/\partial t|_s$, and then an extinction coefficient as the sum of the absorption and scattering coefficients, $\sigma_{ph,ex,\omega}=\sigma_{ph,\omega}+\sigma_{ph,s,\omega}$. This form of the ERT is presented in Section 7.7.3. The radiative net heat flux vector $\boldsymbol{q}_{ph}$ is given by

$$\boldsymbol{q}_r=\boldsymbol{q}_{ph}=\int_0^\infty\int_{4\pi}\boldsymbol{s}I_{ph,\omega}\mathrm{d}\Omega\mathrm{d}\omega=\int_0^\infty\int_{-1}^{1}\boldsymbol{s}I_{ph,\omega}\mathrm{d}\mu\mathrm{d}\omega, \qquad (7.85)$$

where $\mu=\cos\theta$. Note that symmetric $I_{ph,\omega}$ leads to $\boldsymbol{q}_{ph}=0$, i.e., we need asymmetric $I_{ph,\omega}$ (attenuation or increase) for radiative heat flow.

The divergence of the total radiative heat flux, which is used in the energy equation (Table 1.1), is found from[†]

$$\nabla\cdot\boldsymbol{q}_r=\nabla\cdot\boldsymbol{q}_{ph}=\int_0^\infty\int_{4\pi}\nabla\cdot\mathbf{s}I_{ph,\omega}\mathrm{d}\Omega\mathrm{d}\omega=4\pi\int_0^\infty\sigma_{ph,\omega}I_{ph,n,\omega}(\omega,T)\mathrm{d}\omega$$

$$-\,2\pi\int_0^\infty\sigma_{ph,\omega}\int_{-1}^{1}I_{ph,\omega}(\omega,\boldsymbol{s})\mathrm{d}\mu\mathrm{d}\omega+2\pi\int_0^\infty\int_{-1}^{1}\dot{s}_{ph,i}\mathrm{d}\mu\mathrm{d}\omega. \qquad (7.87)$$

When $\nabla\cdot\boldsymbol{q}_{ph}>0$, then the net radiation heat transfer leaving a differential control volume (Table 1.1) is larger than that arriving, i.e., thermal emission and other sources dominate over absorption. Then $\nabla\cdot\boldsymbol{q}_{ph}$ is balanced with the rest of the heat

---

[†] Absorption of EM radiation is a common heating method, and the volumetric rate of heating is expressed as

$$\dot{s}_{ph,a}=\dot{s}_{e,\sigma}=-\nabla\cdot\boldsymbol{q}_r=\sigma_{ph}q_{r,\mathrm{o}}e^{-\sigma_{ph}x}, \qquad (7.86)$$

for a columnar radiation with $q_r=q_{r,\mathrm{o}}(x=0)$.

transfer mechanism, heat storage, and energy conversion, according to the energy equation given in Table 1.1. The solution to the ERT is discussed in [428], among others. These include close-form, exact, and approximate solutions, and numerical solutions. In the P-N methods, moments of ERT and the expansion of I_{ph} in terms of spherical harmonics are used. In the discrete ordinate method, angular integration over a fraction of the total solid angle (4π) is made, thus dividing this into finite angular regimes. For example, one forward region and one backward regions are used (we will employ this in Section 7.7.3). The numerical techniques applied to BTE (Section 3.1.8) are also used for the ERT.

7.6.2 Optically Thick Limit, Mean Free Path, and Radiant Conductivity

When the optical thickness defined by $\sigma^*_{ph} = \sigma_{ph} L$ for a medium of thickness L and absorption coefficient σ_{ph} is larger than 1, the ERT, for an emitting medium with a strong absorption is approximated as follows. Since for optically thick media, the local emission and absorption dominate (absorption dominates over scattering), then in (7.84), under $\dot{s}_{ph,i} = 0$, for steady-state and local thermal equilibrium conditions, and for a plane-parallel geometry radiation with $I_{ph,\omega}$ changing only along the x direction (with $\mathbf{s}$ making an angle θ with the x direction), we have

$$\frac{\mathrm{d}I_{ph,\omega}}{\mathrm{d}(x/\cos\theta)} = \sigma_{ph,\omega}(I_{b,\omega} - I_{ph,\omega}) \quad \text{plane-parallel radiation.} \tag{7.88}$$

Note that we have used $\mathbf{s}I_{ph,\omega} \cdot \mathbf{s}_x = I_{ph,\omega}\cos\theta$. Taking the integral over all possible frequencies and also assuming that the spatial variations of $I_{ph,\omega}$ and $I_{ph,b,\omega}$ are identical, we have, using (7.9)

$$\frac{\mathrm{d}I_{ph}}{\mathrm{d}(x/\cos\theta)} = \sigma_{ph}(I_b - I_{ph}),$$
$$\pi I_b = \pi\int_0^\infty I_{b,\omega}\mathrm{d}\omega = E_b = \sigma_{\mathrm{SB}}T^4, \tag{7.89}$$

where $x/\cos\theta$ is the photon path as it travels between surfaces located at x and $x + \Delta x$.

The radiation heat flux $q_{ph,x}$ (Table 7.1) is found by the integration of I_{ph} over a unit sphere, i.e.,

$$q_{ph,x} = \int_0^{2\pi}\int_0^{\pi} I_{ph}\cos\theta\sin\theta\mathrm{d}\theta\mathrm{d}\phi, \tag{7.90}$$

where we have used $\mathbf{s} = \mathbf{s}_x\cos\theta$. Note that this integral is over a complete sphere (since we are interested in the net radiation flux). Also note that $I_{ph,b}$ is independent of θ and ϕ (diffuse radiation).

The equation of radiative transfer (7.90) can be rearranged as

$$I_{ph} = -\frac{\mathrm{d}I_b\cos\theta}{\sigma_{ph}\mathrm{d}x} + I_b. \tag{7.91}$$

Table 7.1. *Spectral ERT (photon transport equation for absorbing/emitting/scattering media), under local thermal nonequilibrium.*

$$I_{ph} = \frac{u_{ph}\hbar\omega D_{ph} f_{ph}}{4\pi}$$

$$\frac{\partial I_{ph,\omega}(\omega, \boldsymbol{s})}{u_{ph}\partial t} + \boldsymbol{s}\cdot\nabla I_{ph,\omega}(\omega, \boldsymbol{s})$$

$$= \frac{\partial I_{ph,\omega}(\omega, \boldsymbol{s})}{u_{ph}\partial t}|_s + \sigma_{ph,\omega}[I_{ph,n,\omega}(\omega, T) - I_{ph,\omega}(\omega, \boldsymbol{s})] + \dot{s}_{ph\text{-}i}$$

$$\boldsymbol{q}_r = \boldsymbol{q}_{ph} = 2\pi\int_0^\infty\int_{4\pi}\boldsymbol{s}I_{ph,\omega}\mathrm{d}\Omega\mathrm{d}\omega = \int_0^\infty\int_{-1}^1\boldsymbol{s}I_{ph,\omega}\mathrm{d}\mu\mathrm{d}\omega$$

$$\nabla\cdot\boldsymbol{q}_r = \nabla\cdot\boldsymbol{q}_{ph} = \int_0^\infty\int_{4\pi}\nabla\cdot\boldsymbol{s}I_{ph,\omega}\mathrm{d}\Omega\mathrm{d}\omega = 4\pi\int_0^\infty\sigma_{ph,\omega}I_{ph,n,\omega}(\omega, T)\mathrm{d}\omega -$$

$$2\pi\int_0^\infty\sigma_{ph,\omega}\int_{-1}^1 I_{ph,\omega}(\omega, \boldsymbol{s})\mathrm{d}\mu\mathrm{d}\omega + 2\pi\int_0^\infty\int_{-1}^1\dot{s}_{ph,i}\mathrm{d}\mu\mathrm{d}\omega$$

$I_{ph,\omega}$	spectral, directional photon intensity (7.5), W/(m^2-sr-rad/s)
$I_{b,\omega}$	blackbody (equilibrium) spectral photon intensity for, W/(m^2-sr-rad/s), used instead of $I_{ph,n,\omega}$
$I_{ph,n,\omega}$	nonequilibrium, but only temperature-dependent spectral emission intensity, W/(m^2-sr-rad/s)
$\boldsymbol{q}_r$	net radiative heat flux vector, W/(m^2)
$\boldsymbol{s}$	unit vector
u_{ph}	speed of light, m/s
$\dot{s}_{ph,i}$	photon generation rate other than the absorption/emission in *ph-e* interactions, W/(m^3-sr-rad/s)
$\sigma_{ph,\omega}$	spectral absorption coefficient, 1/m
$\mathrm{d}\Omega$	$\sin\theta\mathrm{d}\theta\mathrm{d}\phi$, solid angle, sr
μ	$\cos\theta$, θ is polar angle

Upon integration, we have for $q_{ph,x}$

$$q_{ph,x} = \int_0^{2\pi}\int_0^{\pi}(-\frac{\mathrm{d}I_{ph}\cos\theta}{\sigma_{r,a}\mathrm{d}x} + I_b)\cos\theta\sin\theta\mathrm{d}\theta\mathrm{d}\phi. \qquad (7.92)$$

Now, noting that $I_{ph,b}$ is independent of θ and ϕ, we have

$$\begin{aligned} q_{ph,x} &= -\frac{\mathrm{d}I_b}{\sigma_{ph}\mathrm{d}x}\int_0^{2\pi}\int_0^{\pi}\cos^2\theta\sin\theta\mathrm{d}\theta\mathrm{d}\phi + I_b\int_0^{2\pi}\int_0^{\pi}\cos\theta\sin\theta\mathrm{d}\theta\mathrm{d}\phi \\ &= -\frac{\mathrm{d}I_b}{\sigma_{ph}\mathrm{d}x}\times\frac{4}{3}\pi + I_b\times 0 \\ &= -\frac{4\pi}{3\sigma_{ph}}\frac{\mathrm{d}I_b}{\mathrm{d}x}. \end{aligned} \qquad (7.93)$$

Now, using $\pi I_b = E_b = \sigma_{\rm SB} T^4$, we have

$$q_{ph,x} = -\frac{4}{3\sigma_{ph}}\frac{\mathrm{d}E_b}{\mathrm{d}x} = -\frac{4\sigma_{\rm SB}}{3\sigma_{ph}}\frac{\mathrm{d}T^4}{\mathrm{d}x} = -\frac{16}{3}\frac{\sigma_{\rm SB}T^3}{\sigma_{ph}}\frac{\mathrm{d}T}{\mathrm{d}x}. \tag{7.94}$$

It can be rewritten as

$$\boldsymbol{q}_{ph} = -k_{ph}\nabla T, \quad k_{ph} = \frac{16}{3}\frac{\sigma_{\rm SB}T^3}{\sigma_{ph}}, \quad \text{for } \sigma^*_{ph} \gg 1$$

photon thermal conductivity. (7.95)

Here k_{ph} is called the radiant (photon) conductivity and this optically thick limit $\sigma^*_{ph} = \sigma_{ph}L \gg 1$ is also called the radiation diffusion limit.

Note that in replacing $\mathrm{d}I_{ph}/\mathrm{d}x$ with $\mathrm{d}I_b/\mathrm{d}x$ in the ERT, we are eliminating all the distant radiation heat transfer effects by approximating the local intensity, i.e., rewriting (7.6.2)

$$I_{ph} = I_b - \frac{\cos\theta}{\sigma_{ph}}\frac{\mathrm{d}I_b}{\mathrm{d}x}. \tag{7.96}$$

Also note that E_{ph} is the integral of I_{ph} over a unit hemisphere.

Similar to phonon mean free path (4.109), defining the photon mean free path $\lambda_{ph} = 1/\sigma_{ph}$, (7.95) becomes

$$k_{ph} = \frac{16}{3}\sigma_{\rm SB}T^3\lambda_{ph} = \frac{4\pi^2}{45}\frac{k_{\rm B}^4T^3}{\hbar^3u_{ph,\rm o}^2}\lambda_{ph} = \frac{4\pi^2}{45}\frac{k_{\rm B}^3T^3}{\hbar^3u_{ph,\rm o}^3}k_{\rm B}u_{ph,\rm o}\lambda_{ph}$$

$$= \frac{4\pi^2}{45}\frac{k_{\rm B}^3T^3}{\hbar^3u_{ph,\rm o}^3}k_{\rm B}u_{ph,\rm o}\lambda_{ph} = \frac{1}{3}n_{ph}k_{\rm B}u_{ph,\rm o}\lambda_{ph}, \quad \lambda_{ph} = 1/\sigma_{ph}$$

photon mean free path, (7.97)

where n_{ph} is given by (1.12) (end of chapter problem), and a is a constant.[†] Note that, similar to (4.109), this presents photon conductivity for optically thick media as a product of the principal carrier heat capacity, speed, and mean free path of the carrier. Also note that, with $k_i = n_i c_{v,i} u_i \lambda_i/3$, here the photon heat capacity is $n_{ph}c_{v,ph} = 16\sigma_{\rm SB}T^3/u_{ph,\rm o}$.[‡]

[†] Note that, similar to (4.87), this presents photon conductivity k_{ph} for optically thick media as a product of specific heat capacity, speed, and the mean free path of the carrier.

[‡] Comparing (7.95) with (4.109) for phonons, we arrive at the photon counterpart, i.e.,

$$k_p = \frac{16}{3}\sigma_{\rm SB}(\text{phonon})T^3\lambda_p = \frac{1}{3}n_p c_{v,p} u_{p,\rm A}\lambda_p,$$

where, as mentioned in Section 7.2, we have (using $c_{v,p}$ per phonon)

$$\sigma_{\rm SB}(\text{phonon}) = \frac{n_p c_{v,p} u_{p,\rm A}}{16T^3}.$$

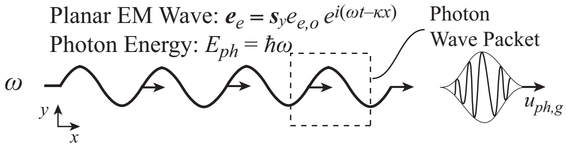
Planar EM Wave: $\boldsymbol{e}_e = \boldsymbol{s}_y e_{e,o}\, e^{i(\omega t - \kappa x)}$
Photon Energy: $E_{ph} = \hbar\omega$
Photon Wave Packet
ω
y
x
$u_{ph,g}$

Figure 7.7. Wave–particle duality of photons, illustrated as a planar wave train propagating along the x direction.

7.7 Wave Treatment: Field Enhancement and Photon Localization

Radiative energy is carried by photons, which are in principle both quasi-particles and waves, according to the theory of wave–particle duality. This is depicted as a planar wave train, where a wave is segmented into parts (photons) and presented as a wave packet, in Figure 7.7. Each photon has an energy $\hbar\omega$ and a well-defined phase relation to other photons. The ERT, developed in the last section, can describe the particle behavior, and the EM wave theory (Section 3.3.2) can capture the wave features. For some absorption, emission, and scattering phenomena, the propagation of radiative energy in a homogeneous/heterogeneous media, the particle or wave distinction is not critical, and both ERT and EM treatments can be used. However, some important phenomena are attributed only to the coherent wave nature, and can only be interpreted by the propagating wave theory. These include interference, diffraction, and tunneling. In this section the photon localization and field enhancement, which are due to wave interference effects, will be discussed as examples.

Photon localization is a size effect in photon transport in nanostructures (heterogeneous media). Figures 7.8(a) to (d) show the different regimes of photon (monochromatic irradiation, e.g., laser) scattering in nanopowders [379]. When the photon mean free path λ_{ph} is much larger than the incident wavelength λ_i, photons may experience a single-scattering event and the transport is diffusive [493]. As λ_{ph} decreases, photons begin to undergo multiple-scattering events. When λ_{ph} is comparable with, or smaller than, the incident wavelength, recurrent scattering occurs, i.e., photons may return to the original location after being scattered many times. In this case, photons do not propagate through the medium and are confined in a small spatial region, forming a cavity. This phenomenon, termed photon localization, is the counterpart of the electron localization suggested in [5]. The EM field of the localized photon, as shown in Figure 7.8(d), can be orders of magnitude larger than the incident field [399]. This is demonstrated is subsequent sections.

7.7.1 Photon Localization in One-Dimensional Multilayer

The simplest model of random heterogeneous medium is the one-dimensional multilayer geometry made of parallel solid layers with random thickness, as shown in Figure 7.9. Regions $l = 1$ and $N + 1$ are semi-infinite vacuum (air) layers. This multilayer medium has $N/2$ (N is an even number here) solid layers and $N/2 - 1$ vacuum layers. The coordinates $x_1, x_2, \ldots, x_N$ are chosen such that the thickness of each

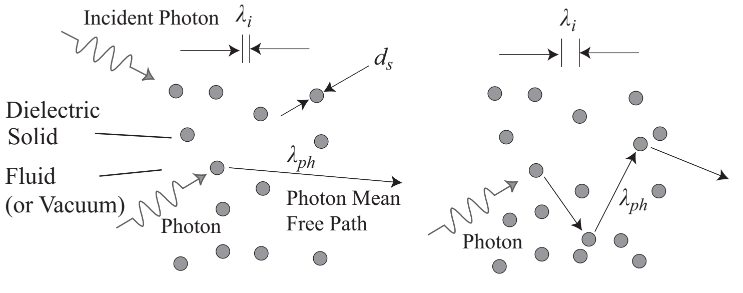

(a) Single Scattering (b) Multiple Scattering

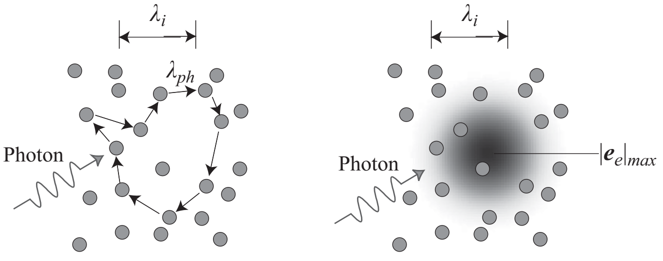

(c) Recurrent Scattering (d) Field Localization

Figure 7.8. (a) Single, (b) multiple, and (c) recurrent scattered photon trajectories in a medium of random scatterers, and (d) a rendering of the electric field intensity distribution for case (c) showing photon localization [379].

layer is random, but obeys a trapezoidal (uniform) distribution (i.e., all thicknesses in a range have equal probability). This multilayer medium has a finite dimension in the direction of the EM wave propagation x, and an infinite length in the plane normal to x. We assume a dielectric solid and use the optical properties Figure 3.4, i.e., the complex refractive index $m_{s,\omega}[= n_{s,\omega} - i\kappa_{s,\omega},$ (3.30) and Table 3.5], which depends on the frequency (or wavelength). All the quantities and parameters are scaled with respect to the incident angular frequency ω_i. Vacuum has a refractive index $m_f (m_f = n_f = 1, \kappa_f = 0)$.

For no current flowing and with uniform charge distribution, the EM wave equation is simplified and we have the one-dimensional, time-periodic Helmholtz equation (3.35) and (3.36), as

$$\frac{\partial^2 e_e(x)}{\partial x^2} + \kappa_o^2 m_i^2 e_e(x) = 0, \quad \boldsymbol{e}_e = \boldsymbol{s}_y e_e(x) e^{i\omega t} = \boldsymbol{s}_y e_e(x) e^{i\kappa_o c m_i t}, \qquad (7.98)$$

where κ_o is the vacuum wave number and m_i is the local complex index of refraction at the incident frequency. The wave form is (3.36). Here we have used an arbitrary y-direction polarization. For the medium shown in Figure 7.9(a), the field is divided into two components, the forward (transmitted) component $e_{e,l}^{+}$ and the backward (reflected) component $e_{e,l}^{-}$. the solution to (7.98) at a particular location x in the lth

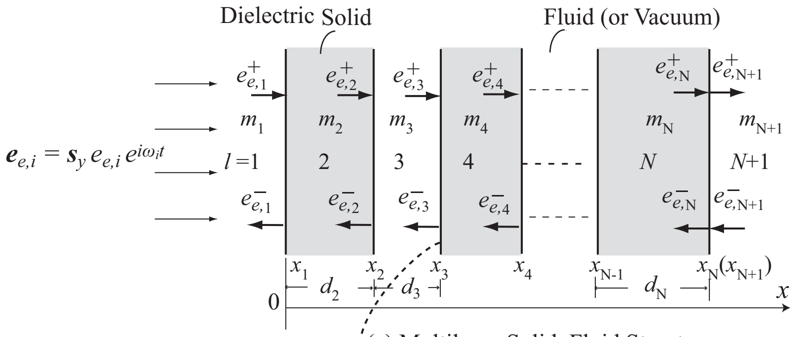
Dielectric Solid
Fluid (or Vacuum)
$e_{e,i} = s_y\, e_{e,i}\, e^{i\omega_i t}$
$e^+_{e,1}$ $e^+_{e,2}$ $e^+_{e,3}$ $e^+_{e,4}$ $e^+_{e,N}$ $e^+_{e,N+1}$
m_1 m_2 m_3 m_4 m_N m_{N+1}
$l=1$ 2 3 4 N $N+1$
$e^-_{e,1}$ $e^-_{e,2}$ $e^-_{e,3}$ $e^-_{e,4}$ $e^-_{e,N}$ $e^-_{e,N+1}$
x_1 x_2 x_3 x_4 x_{N-1} $x_N(x_{N+1})$
d_2 d_3 d_N
0
x

(a) Multilayer Solid–Fluid Structure

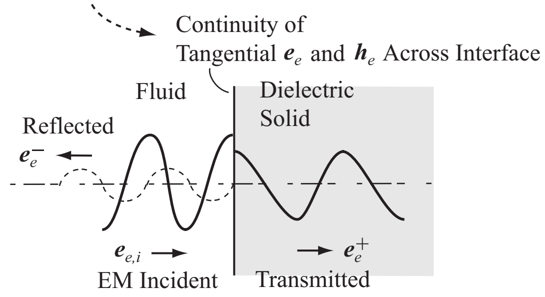

(b) EM Across Fluid–Solid Interface

Figure 7.9. (a) Model random heterogenous medium, consisting of parallel solid (dielectric) and air (vacuum) layers with random thicknesses. The porosity (void fraction, ϵ) is prescribed. (b) Incident transmitted and reflected $\boldsymbol{e}_e$ (tangential components of $\boldsymbol{e}_e$ and $\boldsymbol{h}_e$ are conserved among incident, transmitted, and reflected $\boldsymbol{e}_e$ and $\boldsymbol{h}_e$).

layer is given by

$$e_e(x) = e^+_{e,l} e^{i\kappa_l (x - x_l)} + e^-_{e,l} e^{-i\kappa_l (x - x_l)}, \quad l = 1, 2, \ldots, N+1, \tag{7.99}$$

where x_{N+1} takes the value of x_N, as there are only N interfaces, and $\kappa_l = m_l \omega_i / c_{\rm o}$ is the wave vector, where $c_{\rm o}$ is the speed of light in vacuum. The boundary conditions require that the tangential electric and magnetic field intensities be continuous across each interface as shown in Figure 7.9(b)[†] [289]. The relationship between the amplitudes of the lth and (l+1)th interfaces are given in the matrix form [513][‡]

$$\begin{bmatrix} e^+_{e,l} \\ e^-_{e,l} \end{bmatrix} = \boldsymbol{T}_l^{-1} \boldsymbol{T}_{l+1} \boldsymbol{P}_{l+1} \begin{bmatrix} e^+_{e,l+1} \\ e^-_{e,l+1} \end{bmatrix}, \; l = 1, 2, \ldots, N, \tag{7.100}$$

[†] The tangential components $\boldsymbol{e}_e$ (and $\boldsymbol{h}_e$) is continuous (f stands for fluid and s for solid),

$$\boldsymbol{s}_t \cdot \boldsymbol{e}_{e,f} = \boldsymbol{s}_t \cdot \boldsymbol{e}_{e,s},$$

reflection and incident angles are equal,

$$\theta_i = \theta_r$$

and transmitted wave follows

$$\frac{\sin\theta_t}{\sin\theta_i} = \frac{n_f}{n_s}.$$

[‡] The $\boldsymbol{T}$-matrix method uses the linearity of the Maxwell equations and is applied to planar and axisymmetric (revolution) geometries. The incident and scattered electric fields are expanded in Taylor series, and the coefficient designated as T_{ij} signifies the transition between them.

where

$$\boldsymbol{T}_l = \begin{bmatrix} 1 & 1 \\ m_l & -m_l \end{bmatrix}, \; l = 1, 2, \ldots, N+1, \tag{7.101}$$

and $\boldsymbol{T}_l^{-1}$ is the inverse of $\boldsymbol{T}_l$, and

$$\boldsymbol{P}_l = \begin{bmatrix} e^{-i\kappa_l(x_l - x_{l-1})} & 0 \\ 0 & e^{i\kappa_l(x_l - x_{l-1})} \end{bmatrix}, \; l = 2, 3, \ldots, N+1. \tag{7.102}$$

Hence

$$\begin{bmatrix} e^{+}_{e,j} \\ e^{-}_{e,j} \end{bmatrix} = \begin{bmatrix} M^{(j)}_{11} & M^{(j)}_{12} \\ M^{(j)}_{21} & M^{(j)}_{22} \end{bmatrix} \begin{bmatrix} e^{+}_{e,N+1} \\ e^{-}_{e,N+1} \end{bmatrix}, \; j = 1, 2, \ldots, N, \tag{7.103}$$

where

$$\begin{bmatrix} M^{(j)}_{11} & M^{(j)}_{12} \\ M^{(j)}_{21} & M^{(j)}_{22} \end{bmatrix} = \prod_{l=j}^{N} \boldsymbol{T}_l^{-1} \boldsymbol{T}_{l+1} \boldsymbol{P}_{l+1}, \; j = 1, 2, \ldots, N. \tag{7.104}$$

For a wave incident from medium 1, we have $e^{-}_{e,N+1} = 0$. Therefore,

$$\frac{e^{+}_{e,j}}{e^{+}_{e,1}} = \frac{M^{(j)}_{11}}{M^{(1)}_{11}} \tag{7.105}$$

and

$$\frac{e^{-}_{e,j}}{e^{+}_{e,1}} = \frac{M^{(j)}_{21}}{M^{(1)}_{11}}. \tag{7.106}$$

The use of (7.105) and (7.106) in (7.99) yields the field everywhere. For this time-periodic EM field, the magnetic field is given by the Faraday law for a time-periodic field (Table 3.5) and becomes

$$\boldsymbol{h}_e(x) = \frac{1}{i\omega_i \mu_\mathrm{o} \mu_e} \nabla \times \boldsymbol{e}_e(x), \tag{7.107}$$

where μ_e is the relative magnetic permeability.

The EM energy (3.39) transmissivity is defined as

$$\tau_r = \frac{I_{ph}(N+1)}{I_{ph,i}} = \frac{|\boldsymbol{e}^{-}_{e,N+1}|^2}{|\boldsymbol{e}_{e,i}|^2} = |\boldsymbol{e}_e^{-*}(N+1)|^2 \;\; \text{transmissivity}. \tag{7.108}$$

This transmissivity is computed for a model multilayer with 50 layers in which the layer thicknesses d_s follows a uniform distribution between $\langle d_s \rangle \pm d_s =$ 1000 ± 800 nm, and with the porosity $\epsilon = 0.35$, $n_s = 1.8$ and $\kappa_s = 0$ (n_s and κ_s are for doped yttria compacts off resonance [385], λ_i = 1000 nm). To generate such a multilayer, we have an infinite number of possibilities, each of which is a realization. The nonabsorbing material is used to remove the possibility of causing exponential decay by absorption. To investigate the transmissivity as a function of the sample thickness, we add one layer to the sample at one time and obtain a series of transmissivities. The dots shown in Figure 7.10 represent these transmissivities

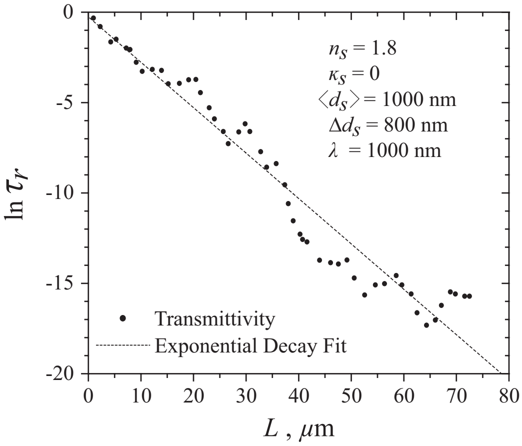

Figure 7.10. Variation of the transmissivity as a function of the medium thickness. The dots are the transmissivities obtained by adding layers to the medium, one at a time, and the dashed line is an exponential decay fit [399].

for one typical realization, where there are 1, 2, . . . , 50 layers. These dots are fitted well by an exponential decay line, indicating that localization exists. From (7.88) for collimated beam (1-D) and using $\lambda_{ph} = 1/\sigma_{ph}$, and with no emission, we have the transmission (7.108) and the ratio of intensities. Then, the localization length of this realization can be obtained from the slope of the fitted line

$$\lambda_{ph} = -\frac{\mathrm{d}L}{\mathrm{d}(\ln \tau_r)}. \tag{7.109}$$

There are infinite possible realizations for this model multilayer, and localization behavior is observed in all realizations that were tried. This supports the statement that random systems in one dimension always exhibit localization [322]. The localization length of this model multilayer is obtained by averaging the localization lengths of numerous realizations. For Figure 7.10 results, λ_{ph} is 3.2 μm, which is 3.2 times $\langle d_s \rangle$.

7.7.2 Coherence and Electric Field Enhancement

The localization is due to the constructive interference among the multiply scattered waves, even though the transmissivity profile in Figure 7.10 does not show any explicit signature of interference. The local field amplitude, rather than the transmissivity, has been examined and strong field enhancement was observed [385], which provides an exact signature of strong, constructive wave interference.

(A) *One-Dimensional Multilayer Geometry*

The local electric field is determined in a model multilayer geometry with 50 layers and subject to the same irradiation as in the previous section. There are also infinite possible realizations for this model multilayer, and the field results for one of them is shown in Figure 7.11(a), where the dimensionless electric field is defined as $|\boldsymbol{e}_e^*| = |\boldsymbol{e}_e|/|\boldsymbol{e}_{e,i}|$.

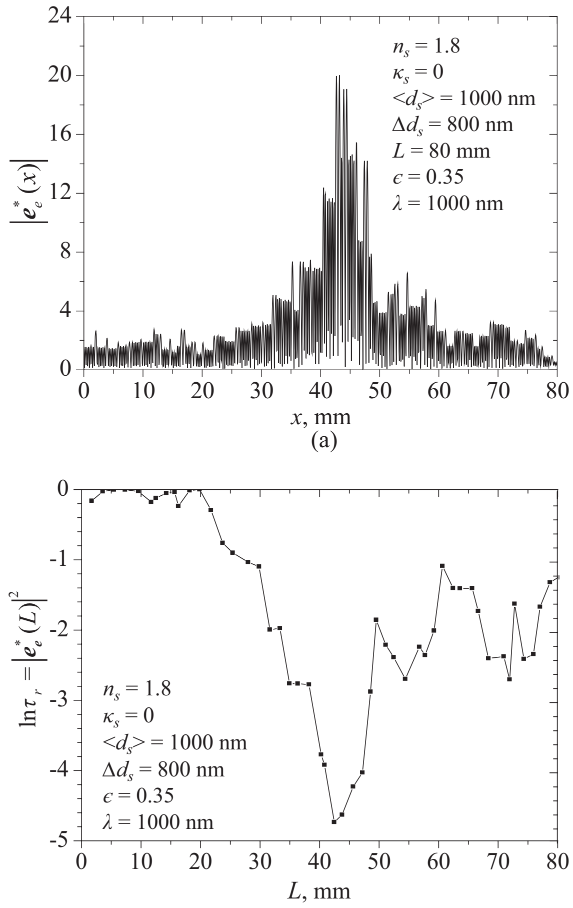

(a)

(b)

Figure 7.11. (a) Local field distribution in a random multilayer, with field enhancement shown. (b) Variations of the transmissivity as functions of the medium thickness in the same multi-layer [399].

From Figure 7.11(a), it is evident that there is field enhancement, i.e., there are peaks in the field inside the medium that can be a few orders of magnitude larger than the incident field. Thus the energy density of the electric field can be two or even more orders of magnitude larger than the incident value. In periodic multilayer geometry, the electric field is also spatially periodic, resulting in no isolated peaks inside the medium (even if the field in this case can also be higher than the incident field). The physical basis of the field enhancement is EM wave interference. In the random multilayer system, the waves will multiply transmit and reflect at all interfaces, and interfere with each other. At some sites for some realizations, the interference is so ideally constructive that it results in an extremely large field. Thus the large field enhancement is directly attributed to randomness and cannot be observed in homogeneous or spatially periodic media. Note the coherence requirement that the medium size be smaller than the coherence length must be satisfied in order to observe the field enhancement. The coherence length is $\lambda^2/\Delta\lambda$ for a central wavelength λ and a spectrum width $\Delta\lambda$ [182]. Here we assume a monochromatic wave, thus satisfying the coherence condition ($\Delta\lambda$ is 0 and the coherence length is infinite). The coherence length of many lasers is several kilometers, satisfying the coherence condition. Note how the transmissivity evolves layer by layer in such a realization, leading to field enhancement, as shown in Figure 7.11(b). Different from Figure 7.10, in which the transmissivity reveals an exponential decay behavior, the variation of transmissivity with respect to the sample thickness, as shown in Figure 7.11(b), has a large fluctuation. The localization occurs and diffusion breaks down, because after local field enhancement, the transmissivity increases, instead of decreases, with an increase in the sample thickness. Note that the transmissivity for large L is much larger than that shown in Figure 7.10, as more photons have to travel through and interfere with each other to establish a large local field. Although realizations allowing field enhancement generally lead to a larger transmissivity, the field is trapped in a wavelength size region, forming a random resonator.

(B) *Two-Dimensional Geometry*

A two-dimensional random porous medium is shown in Figure 7.12(a). The solids are an array of infinitely long (in the y direction) dielectric cylinders with random radii and locations. We again examine the EM wave propagation subject to incidence of a planar EM wave upon this structure, traveling in the x direction. A code that is based on the finite-element method, high-frequency structure simulator (HFSS), is used to numerically solve the field distributions. A finite computation domain is chosen, resulting in six surfaces or boundaries. The two x–z boundaries are taken as periodic to simulate the infinite length in the y direction. The two x–y boundaries are also taken as periodic. The y–z planes are set to be the incident boundary at $x = 0$ and the radiation boundary at $x = L$.

A computation domain of $5\times1\times5$ μm^3 is chosen. Again, the local electric field in this region is determined for a normal incident EM wave of wavelength $\lambda = 1000$ nm for a random medium composed of 20 long cylinders with a random diameter $\langle d_s \rangle \pm \Delta d_s = 1000 \pm 400$ nm, and with $n_s = 1.8$ and $\kappa_s = 0$ in air (vacuum). The results are shown in Figure 7.12(b), in which contours of the constant dimensionless electric field are used. Similar to the one-dimensional case, there are sites of field enhancement within the random porous medium that can be a few orders higher in magnitude compared with the incident field.

7.7.3 Comparison with Particle Treatment (ERT)

(A) *Formulation and Two-Flux Approximation*

The radiation transport within the same composite described in previous sections can also be treated by using the ERT. In this treatment, the scattering properties of a single particle are derived first, using small and large particle-size approximations.

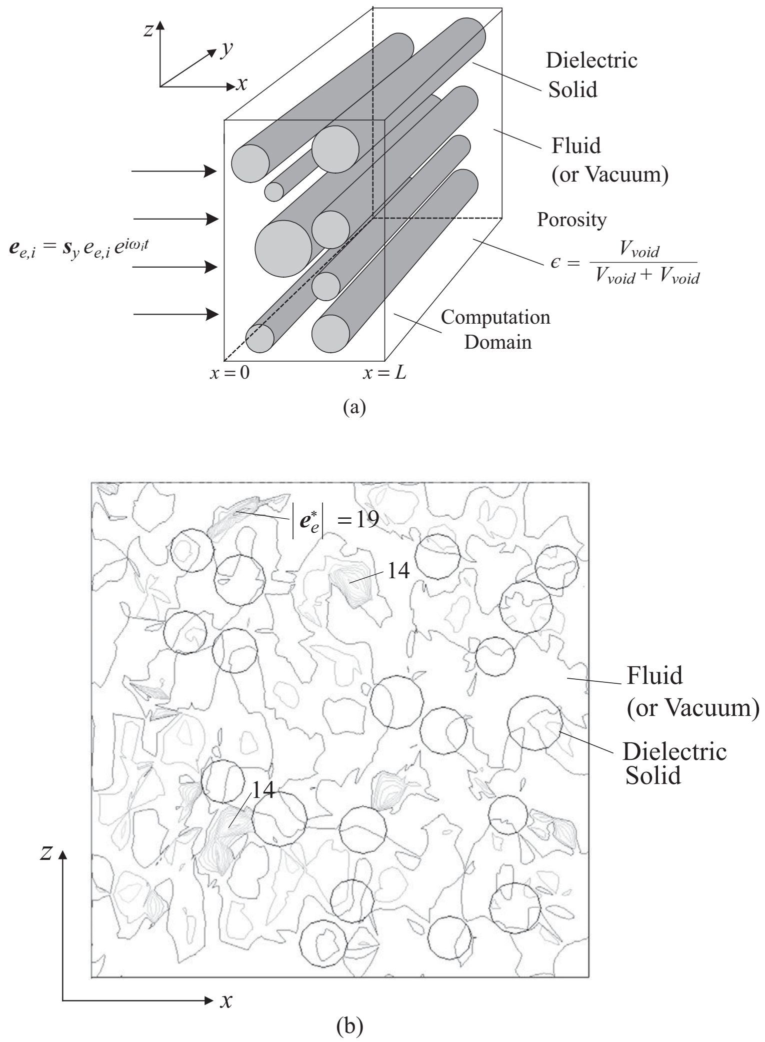
z
y
x
Dielectric
Solid
Fluid
(or Vacuum)
Porosity
$\epsilon = \frac{V_{void}}{V_{void} + V_{void}}$
$\boldsymbol{e}_{e,i} = \boldsymbol{s}_y \, e_{e,i} \, e^{i\omega_i t}$
Computation
Domain
$x = 0$
$x = L$
$|\boldsymbol{e}_e^*| = 19$
14
14
Fluid
(or Vacuum)
Dielectric
Solid
z
x

(a)

(b)

Figure 7.12. (a) The two-dimensional geometry composed of infinitely long cylinders. (b) The two-dimensional distribution of the dimensionless field magnitude $|e_e|^*$ for a realization. The circles are the sections of the cylinders. The porosity is 0.85 [399].

The effective scattering properties are then determined for a cluster of particles, based on the porosity and particle size distribution. The ERT is solved by use of some approximations, such as the two-flux approximation [230].

For a one-dimensional multilayer system, a layer serves as a single scatterer. For the normal incidence of a planar radiation upon a planar particle, as shown in Figure 7.13, the scattering is by reflection. Using the transfer matrix method we find that, the incident, transmitted, and reflected fields are related through

$$\begin{bmatrix} e_{e,i} \\ e_{e,r} \end{bmatrix} = \boldsymbol{T}_1^{-1} \boldsymbol{T}_2 \boldsymbol{T}_2 \boldsymbol{P}_2^{-1} \boldsymbol{T}_3 \begin{bmatrix} e_{e,t} \\ 0 \end{bmatrix}. \tag{7.110}$$

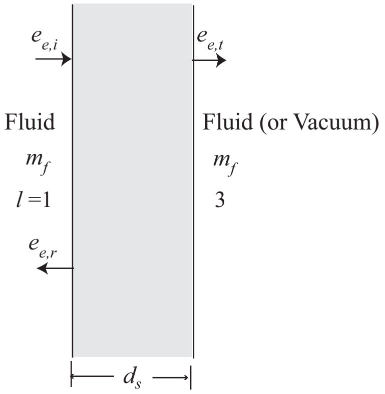

Figure 7.13. One-dimensional transmission and reflection in a single, effective (heterogeneous) layer.

Thus $e_{e,r}$ and $e_{e,t}$ are derived in terms of $e_{e,i}$, and the transmissivity (7.108) is a function of the layer thickness d_s for a given m_f and m_s, i.e.,

$$\tau_r(d_s) = \frac{|e_{e,t}|^2}{|e_{e,i}|^2} = \frac{I_{ph,t}}{I_{ph,i}}. \tag{7.111}$$

The extinction (sum of absorption and scattering, Section 7.6.1) coefficient of the single particle is defined using (7.109) with $\sigma_{ph} = 1/\lambda_{ph}$, as

$$\sigma_{ph,ex}(d_s) = \frac{-\ln \tau_r(d_s)}{d_s}. \tag{7.112}$$

We now turn to the particle (ERT) treatment. For a random multilayer geometry with porosity ϵ, where the layer thickness d_s follows a uniform distribution in the range of $\langle d_s \rangle \pm \Delta d_s$, the effective extinction spectral coefficient becomes

$$\langle \sigma_{ph,ex} \rangle = \frac{\int_{\langle d_s \rangle - \Delta d_s}^{\langle d_s \rangle + \Delta d_s} -\ln \tau_r(d_s) \mathrm{d} d_s}{\int_{\langle d_s \rangle - \Delta d_s}^{\langle d_s \rangle + \Delta d_s} d_s \mathrm{d} d_s}(1-\epsilon). \tag{7.113}$$

Then the effective spectral absorption coefficient is given in term of κ_s as (Table 3.5)

$$\langle \sigma_{ph,a,w} \rangle = \frac{4\pi \kappa_s}{\lambda_i}(1-\epsilon). \tag{7.114}$$

The effective scattering coefficient is found from

$$\langle \sigma_{ph,s} \rangle = \langle \sigma_{ph,ex} \rangle - \langle \sigma_{ph,a} \rangle. \tag{7.115}$$

Because the scattering occurs only in the backward direction, the scattering phase function, $\Phi(\theta)$ defined in (7.79) and represented by the general scattering term in Table 7.1. It is given with various models in [230], and it is a delta function, i.e.,

$$\Phi(\theta) = \delta(\theta - \pi), \quad \int_{-1}^{1} \Phi(\theta) \mathrm{d} \cos\theta = 2. \tag{7.116}$$

Then ERT (7.83), replacing the scattering term with the expression containing the phase function Φ, and under no emission, becomes

$$\begin{aligned}\cos\theta\frac{\mathrm{d}I_{ph}(x,\theta)}{\mathrm{d}x} &= -(\langle\sigma_{ph,s}\rangle+\langle\sigma_{ph,a}\rangle)I_{ph}(x,\theta)\\ &\quad +\frac{\langle\sigma_{ph,s}\rangle}{2}[\int_0^1 I_{ph}(x,\theta_i)\Phi(\theta_i-\theta)\mathrm{d}\cos\theta_i\\ &\quad +\int_{-1}^0 I_{ph}(x,\theta_i)\Phi(\theta_i-\theta)\mathrm{d}\cos\theta_i]. \qquad (7.117)\end{aligned}$$

For normal irradiation on a one-dimensional geometry, the radiative intensity has only two components, namely, forward and backward. Thus the two-flux approximation [230] can be used to solve (7.117). By taking $\theta=0$ and defining $I_{ph}(x,0)=I^+_{ph}$, and $I_{ph}(x,\pi)=I^-_{ph}$, (7.117) gives for the forward intensity

$$\frac{\mathrm{d}I^+_{ph}}{\mathrm{d}x} = -(\langle\sigma_{ph,s}\rangle+\langle\sigma_{ph,a}\rangle)I^+_{ph}+\langle\sigma_{ph,s}\rangle[(1-B)I^+_{ph}+BI^-_{ph}], \qquad (7.118)$$

where using (7.116), we have

$$B=\frac{1}{2}\int_{-1}^1\Phi(\theta_i)\mathrm{d}\cos\theta_i=1. \qquad (7.119)$$

Equation (7.118) can then be simplified to

$$\frac{\mathrm{d}I^+_{ph}}{\mathrm{d}x} = -(\langle\sigma_{ph,s}\rangle+\langle\sigma_{ph,a}\rangle)I^+_{ph}+\langle\sigma_{ph,s}\rangle I^-_{ph}. \qquad (7.120)$$

Similarly, by taking $\theta=\pi$, (7.117) gives for the backward intensity

$$-\frac{\mathrm{d}I^-_{ph}}{\mathrm{d}x} = -(\langle\sigma_{ph,s}\rangle+\langle\sigma_{ph,a}\rangle)I^-_{ph}+\langle\sigma_{ph,s}\rangle I^+_{ph}. \qquad (7.121)$$

The boundary conditions for (7.120) and (7.121) are

$$I^+_{ph}(0)=1,\ I^-_{ph}(L)=0. \qquad (7.122)$$

(B) *Photon Diffusion in Nonabsorbing, Random Media*

Here we show that the particle-based ERT is not capable of predicting photon localization. Again, a nonabsorbing medium ($\sigma_{ph,a}=0$) is used to remove the possibility of causing exponential decay by absorption. Equations (7.120) and (7.121) are simplified to

$$\begin{aligned}\frac{\mathrm{d}I^+_{ph}}{\mathrm{d}x} &= -\langle\sigma_{ph,s}\rangle I^+_{ph}+\langle\sigma_{ph,s}\rangle I^-_{ph}\\ -\frac{\mathrm{d}I^+_{ph}}{\mathrm{d}x} &= -\langle\sigma_{ph,s}\rangle I^-_{ph}+\langle\sigma_{ph,s}\rangle I^+_{ph}. \qquad (7.123)\end{aligned}$$

The solutions subject to the boundary conditions given by (7.122) are

$$I^+_{ph}(x) = \frac{1 + \langle\sigma_{ph,s}\rangle(L - x)}{1 + \langle\sigma_{ph,s}\rangle L}$$

$$I^-_{ph}(x) = \frac{\langle\sigma_{ph,s}\rangle(L - x)}{1 + \langle\sigma_{ph,s}\rangle L}. \tag{7.124}$$

Then the transmissivity is found from

$$\tau_r(L) = I^+_{ph}(L) = \frac{1}{1 + \langle\sigma_{ph,s}\rangle L}. \tag{7.125}$$

In random porous media, $\langle\sigma_{ph,s}\rangle L$ is generally much larger than 1 (optically thick), and $\tau_r(L)$ has an inverse dependence, i.e., $\tau_r(L) = 1/[\langle\sigma_{ph,s}\rangle L]$, which is characteristic of the classical diffusion [480] with a mean free path $\lambda_{ph} = 1/\langle\sigma_{ph,s}\rangle$. Thus photon localization cannot be predicted by the ERT, because the random medium is represented as an effective medium in order to define the effective scattering and absorption properties, where EM wave interference (coherence) effects are not now filtered (i.e, removed).

7.8 Continuous and Band Photon Absorption

7.8.1 Photon Absorption Coefficient for Solids

Photon absorption by matter is described by interaction of EM waves with electric or magnetic entities (e.g., free electron or electric dipoles) as discussed in Section 7.3. The spectral photon absorption coefficient $\sigma_{ph,\omega}$ of a solid is experimentally found through the simplified form of the ERT (Table 7.1) under unidirectional (along x) radiation, steady state, no $\dot{s}_{ph,i}$, and the dominance of absorption, i.e.,

$$\frac{\mathrm{d}I_{ph,\omega}}{\mathrm{d}x} = -\sigma_{ph,\omega} I_{ph,\omega}, \quad \frac{I_{ph,\omega}}{I_{ph,\omega}(x = 0)} = \exp(-\sigma_{ph,\omega} x)$$

$$\text{ERT (Beer–Lambert law) for columnar, absorption dominated radiation,} \tag{7.126}$$

where $\sigma_{ph,\omega}$ is assumed constant. Note that (7.126) is also obtained for a columnar radiation ($\cos\theta = 1$), under no emission, from (7.88). The theoretical prediction of $\sigma_{ph,\omega}$ is through (7.54), where the interaction (transition) probability rate (FGR) (5.96) gives $\tau_{ph,a}$, and using the absorption time constat $\tau_{ph,a}$

$$\sigma_{ph,\omega} = \frac{\hbar\omega\dot{\gamma}_{ph,a} n_e}{u_{ph}\int \mathrm{d}\omega} = \frac{\hbar\omega n_e}{\tau_{ph,a} u_{ph} e_{ph}} \quad \text{absorption time constant,} \tag{7.127}$$

where e_{ph} is given by (7.2).

Using the spectral optical property κ_λ (spectral index of extinction, Table 3.5), $\sigma_{ph,\omega}$ is also given as

$$\sigma_{ph,\omega} \equiv \frac{2\omega\kappa_\lambda}{u_{ph}} = \frac{4\pi\kappa_\lambda}{\lambda} \quad \text{relation with index of extinction.} \tag{7.128}$$

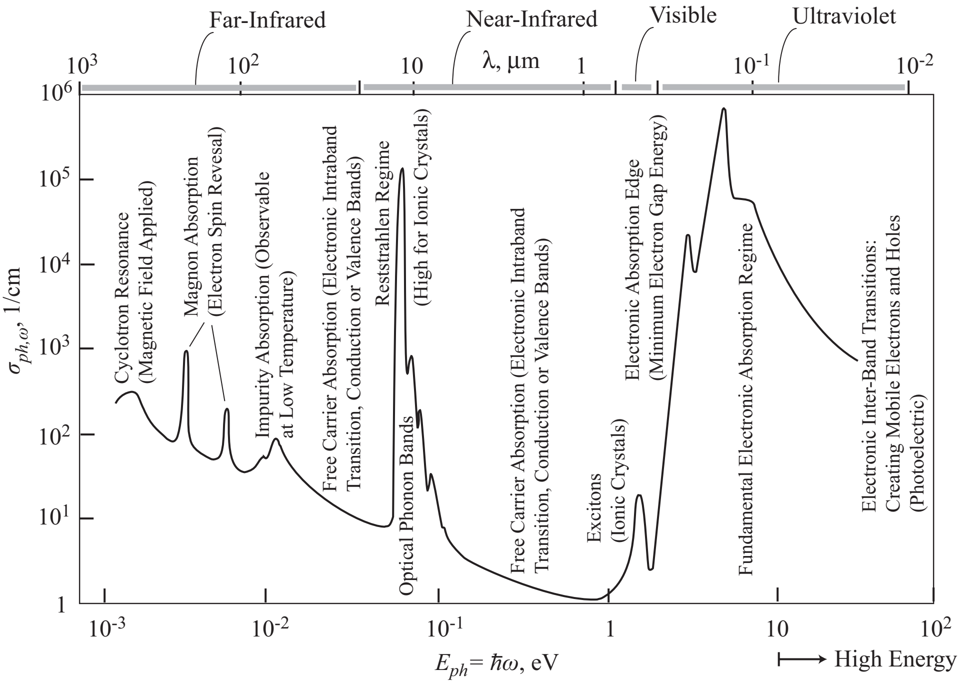

Figure 7.14. Generalized photon absorption spectrum of crystalline semiconductor (typical groups 13–15 elements in Table A.2) [127]. The far-infrared to ultraviolet photon energy regimes are also shown.

In turn, κ_λ is related to σ_e, μ_e, and ϵ_e through the relation given in Table 3.5, using the classical treatment. In doped ions of otherwise transparent solids, and in dilute gases and solutions, the absorption coefficient is given in terms of the absorption cross-section area $A_{ph,a}$ per absorber, and the absorber concentration n_a, as

$$\sigma_{ph,\omega} = A_{ph,a} n_a \quad \text{absorption cross-section area relation,} \tag{7.129}$$

and (7.126) is used to measure $A_{ph,a}$. In general, $A_{ph,a}$ depends on the temperature and pressure (e.g., residual stress in solids). The photon absorption cross-section area is much smaller than the molecular collision cross-section area (Table 6.4).

In addition, the photon spectral absorptance $\alpha_{ph,\omega}$ is defined as

$$\alpha_{ph,\omega} = 1 - \exp(-\sigma_{ph,\omega} L) \quad \text{spectral absorptance,} \tag{7.130}$$

where L is the path length of photons. For small $\sigma_{ph,\omega} L$ (optically thin limit), we have $\alpha_{ph,\omega} = \sigma_{ph,\omega} L$, i.e., absorptance is equal to the optical thickness.[†]

Figure 7.14 shows the hypothetical absorption coefficient of a semiconductor-like crystal, caused by various absorption mechanisms. A rendering of these various photon absorption mechanisms is shown in Figure 7.15. These electronic (including semiconductors), phonon-mediated (exiton), phonon (optical), and other photon absorptions are subsequently described.

[†] $\alpha_{ph,\omega} = 1 - e^{-\sigma_{ph,\omega} L} \simeq 1 - 1 + \sigma_{ph,\omega} L + \cdots = \sigma_{ph,\omega} L$ optically thin limit.

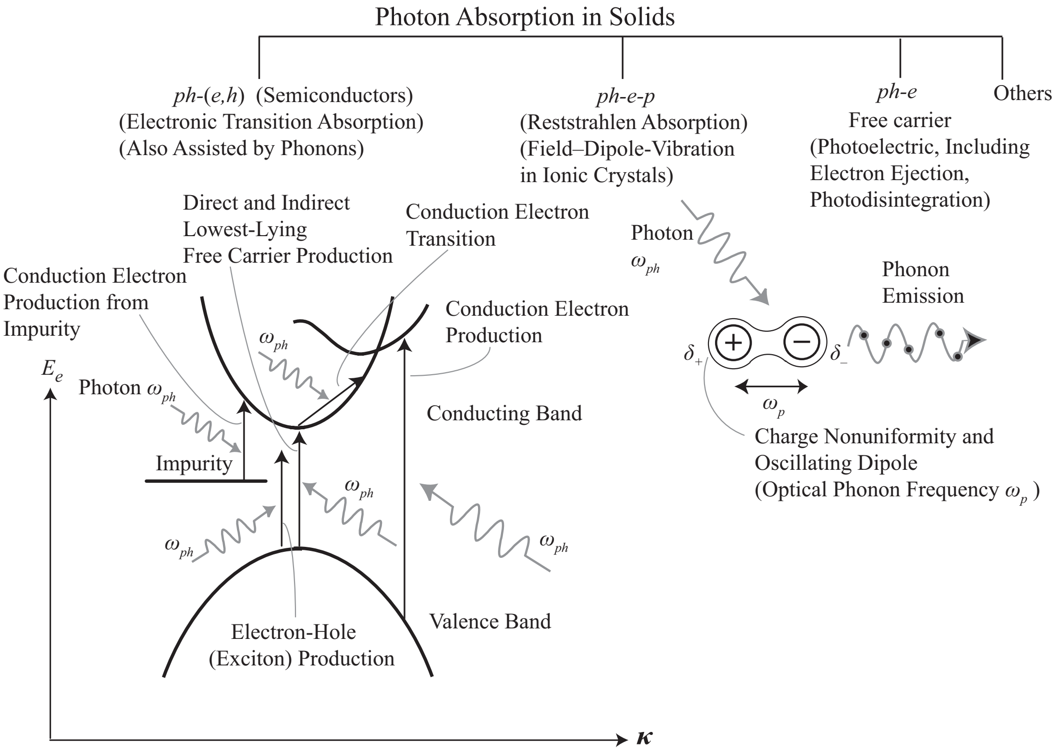

Figure 7.15. Various mechanisms of photon absorption in solids. Examples of photon absorption in metal, semiconductor, and dielectric (electric insulator) are given in Figure 7.1(b).

In Figure 7.14, starting at high frequencies (ultraviolet regime), the absorption of a photon is due to electronic transitions (intraband transition for electrons and holes), resulting in photoconductivity. For high photon energy (greater than 10 eV, as also marked in Figure 1.4) the fall in the absorption coefficient is rather small, but in the visible–near-infrared regime the fall is rather rapid and is called the semiconductor low-energy broadening of the fundamental absorption edge (energy gap $\Delta E_{e,g}$). In this regime, for ionic crystals, exciton absorption becomes significant.

As the far infrared is approached, the intraband conduction or valence electronic transition occurs (free-carrier absorption, especially significant for doped semiconductors). This extends to far-infrared and microwave regimes, and the magnitude of $\sigma_{ph,\omega}$ depends on the mobile electron orbital density (increasing intrinsic carrier density). In metals this is the dominant absorption.

At the end of the near-infrared regime and beginning of the far-infrared regime (photon energy of 0.02 to 0.05 eV, of the order of $k_B T$, for moderate T), the photon–phonon interactions dominate and very high absorption coefficients are found (highest for ionic crystals) along with high reflection.

Impurities also result in the absorption of low-energy photons, and this is detectable only at low temperatures (otherwise the impurities ionize); at yet lower photon energies, absorption that is due to electron spin reversal occurs because of paramagnetic imparities. Some of the low energy absorptions may require imparities of a magnetic field.

The classical optical relation or the FGR is used to arrive at the absorption coefficient, as previously outlined.

The free-electron spectral absorption coefficient for metals is given as (Chapter 3 problem; note that $I_{ph,\omega}$ is proportional to $|\boldsymbol{e}_e|^2$, so $\sigma_{ph,\omega} = 2/\delta_{ph\text{-}e}$, where δ is the skin depth) [118, 145]

$$\sigma_{ph,\omega} = \frac{2\omega\kappa_\omega}{u_{ph}} = (\frac{2n_{e,c}e_c^2\langle\langle\tau_e\rangle\rangle\omega}{\epsilon_{\mathrm{o}}\epsilon_e m_e u_{ph}^2})^{1/2} \quad \text{metals (electron free carrier)}, \tag{7.131}$$

where $\langle\langle\tau_e\rangle\rangle$ is the average momentum electron relaxation time of (5.133) and (5.147) determined from the electrical conductivity.

For absorption, by dielectrics, the complex component of the dielectric function is used for $\kappa_\omega = \epsilon_{e,c}/2n_\omega$. We discussed the dielectric function in Section 3.3.5 and will do again in Section 7.15.1. For semiconductors, the absorption coefficient is defined for the interband (between valence and conduction electrons) transitions [118], similar to (7.127), as

$$\sigma_{ph,\omega} = \frac{\hbar\omega\dot{\gamma}_{ph\text{-}e}}{I_{ph,\omega}} \quad \text{direct interband transition}, \tag{7.132}$$

where $\dot{\gamma}_{ph\text{-}e}$ is the rate of interband transitions per unit volume and per unit time, and $I_{ph,\omega}$ is the incident electromagnetic flux. Then we use the FGR (3.27) along with the interaction matrix element (5.94). The perturbation Hamiltonian is related to the local dipole (end of chapter problem), and leads to the matrix element (transition between valence and conduction electrons)

$$|M_{v,c}|^2 = (\frac{e_c}{m_{e,e}u_{ph}})^2|\boldsymbol{a}_e|^2|\langle\psi_v|e_c\boldsymbol{x}|\psi_c\rangle|^2 = (\frac{e_c}{m_{e,e}u_{ph}})^2|\boldsymbol{a}_e|^2|\boldsymbol{\mu}_e|^2, \tag{7.133}$$

where $\boldsymbol{a}_e$ is the vector potential (Table 3.5) and $e_e\boldsymbol{x} = \boldsymbol{p}_e$ is the local dipole of electronic transition, the expression for $\sigma_{ph,\omega}$ is [118]

$$\sigma_{ph,\omega} = \frac{e_c^2}{\epsilon_{\mathrm{o}}^2 m_{e,e}^2 u_{ph} n_\omega \omega}|\langle\psi_v|e_c\boldsymbol{x}|\psi_c\rangle|^2 D_{ph\text{-}e}[f_e^{\mathrm{o}}(E_{e,v}) - f_e^{\mathrm{o}}(E_{e,c})]$$

$$\text{direct interband transition}, \tag{7.134}$$

where n_ω is the spectral index of refraction, $D_{ph\text{-}e}$ is the joint DOS, and $|\langle v|\boldsymbol{p}_e|c\rangle|$ couples the states with the same $\boldsymbol{\kappa}$ in the valence and conduction bands.

An analytical relation for the resonant photon absorption–emission for the transition rate of the conduction band to the heavy-hole band and the conduction band to the light-hole band (Figure 5.8) is given in [26]. A similar relation is derived for the indirect band, in which phonon energy is absorbed or emitted to match the different $\boldsymbol{\kappa}$ of the valence and conduction bands. There are two coupling coefficients, namely, *ph-e-p* coupling involving phonon absorption ($a_{ph\text{-}e\text{-}p,a}$), and *ph-e-p* coupling involving phonon emission ($a_{ph\text{-}e\text{-}p,e}$).

Table 7.2 lists absorption of photons by atoms, ions, or molecules capable of electronic transition through the transition dipole moment $\boldsymbol{\mu}_e$. The relations to the absorption cross-section area and the Einstein coefficients are also used. Table 7.2 also summarizes the spectral absorption coefficient $\sigma_{ph,\omega}$ for photon absorption that

Table 7.2. *Some relations for spectral photon absorption and scattering coefficients in isolated atoms, ions, or molecules, and in solids (semiconductors and metals).*

Mechanism	Absorption or Scattering Coefficient
Electronic transition (absorption) in atom, ion, or molecule	$\sigma_{ph,\omega} = n_{e,A} A_{ph,a}(\omega) = n_{e,A} \frac{\pi^2 u_{ph}^2}{\omega_{e,g}^2 \int_\omega \mathrm{d}\omega} \dot{\gamma}_{ph,e,sp}$ $n_{e,A}$ is the number density of ground-state atoms (or ions or molecules), $\omega_{e,g}$ is the transition angular frequency, $\dot{\gamma}_{ph,e,sp} = 1/\tau_{ph,e,sp} = 1/\tau_r = \omega_{e,g}^3 \|\boldsymbol{\mu}_e\|^2 / 3\pi \epsilon_{\mathrm{o}} \hbar u_{ph}^3$, $\boldsymbol{\mu}_e$ is the transition dipole moment, $\int_\omega \mathrm{d}\omega$ is the bandwidth
Photoelectric (hydrogen) (Appendix E)	$\sigma_{ph\text{-}e} = n_{\mathrm{H}} A_{ph\text{-}e},\ A_{ph\text{-}e} = \frac{512\pi^2}{3} \frac{r_{\mathrm{B}}^2 e_c^2}{4\pi \epsilon_{\mathrm{o}} \hbar c} (\frac{E_{e,1}}{\hbar\omega})^4 \frac{e^{-4\gamma \cot^{-1}\gamma}}{1 - e^{2\pi\gamma}},$ $\gamma = (\frac{\hbar\omega}{E_{e,1}} - 1)^{-1/2}$ n_{H} is number density of H atoms, $E_{e,1}$ is ground-state energy
Molecular vibrational absorption	$\sigma_{ph,\omega} = \frac{4\pi^2 n_{f,v} \omega}{3\hbar u_{ph} Z_f} (e^{-E_{f,i}/k_{\mathrm{B}}T} - e^{-E_{f,f}/k_{\mathrm{B}}T}) \|\langle \psi_f \| \boldsymbol{p}_e \| \psi_i \rangle\|^2 f(\omega, \omega_{i\text{-}f})$ quantities defined under (7.138)
Compton (free-electron) scattering	$\sigma_{ph,s} = n_{e,c} \frac{8\pi}{3} r_{\mathrm{C}}^2 = n_{e,c} \times (6.649 \times 10^{-29}\ \mathrm{m}^2),\quad r_{\mathrm{C}}^2 = \frac{e_c^2}{4\pi m_e \epsilon_{\mathrm{o}} u_{ph,o}^2}$ $n_{e,c}$ is the number density of free electrons
Rayleigh (bound-electron) scattering	$\sigma_{ph,s,\omega} = n_{e,b} \frac{8\pi}{3} r_{\mathrm{C}}^2 \frac{\omega^4}{(\omega^2 - \omega_{n,e}^2)^2}$ $n_{e,b}$ is the number density of bound electrons
Semiconductor interband electronic transitions [118]	indirect-band absorption: with phonon absorption $\sigma_{ph,\omega} = a_{ph\text{-}e\text{-}p,a} \frac{(\hbar\omega - \Delta E_{e,g} + \hbar\omega_p)^2}{\exp(\hbar\omega_p / k_{\mathrm{B}}T) - 1},$ where $a_{ph\text{-}e\text{-}p,a}$ is the phonon absorption coupling constant indirect-band absorption: with phonon emission $\sigma_{ph,\omega} = a_{ph\text{-}e\text{-}p,e} \frac{(\hbar\omega - \Delta E_{e,g} - \hbar\omega_p)^2}{1 - \exp(-\hbar\omega_p / k_{\mathrm{B}}T)},$ where $a_{ph\text{-}e\text{-}p,e}$ is the phonon emission coupling constant direct-band abosorption: $\sigma_{ph,\omega} = \frac{e_c^2}{\epsilon_{\mathrm{o}}^2 m_{e,e}^2 u_{ph} n_\omega \omega} \|\langle \psi_v \| e_c \boldsymbol{x} \| \psi_c \rangle\|^2 D_{ph\text{-}e} [f_e^{\mathrm{o}}(E_{e,v}) - f_e^{\mathrm{o}}(E_{e,c})],$ where n_ω is the index of refraction, $D_{ph\text{-}e}$ is the joint density of states, and $\|\langle \psi_v \| e_c \boldsymbol{x} \| \psi_c \rangle\| = \|\langle v \| \boldsymbol{p}_e \| c \rangle\|$ couples the states with the same $\boldsymbol{\kappa}$ in the valence and conduction bands for $\hbar\omega > 3$ eV, GaAs, $\sigma_{ph,\omega} = 1.9 \times 10^{-3} \frac{(\hbar\omega - \Delta E_{e,g})^{1/2}}{\hbar\omega}$, (SI units)
Free carrier absorption, low photon energy [118, 52]	absorption in metals: $\sigma_{ph,\omega} = (2\sigma_e \mu_{\mathrm{o}} \mu_e \omega)^{1/2} = (\frac{2 n_{e,c} e_c^2 \langle\langle \tau_e \rangle\rangle \omega}{\epsilon_{\mathrm{o}} \epsilon_e m_e u_{ph}^2})^{1/2}$ absorption in semiconductors: $\sigma_{ph,\omega} = \frac{\omega_{pl}^2}{(4\pi)^{1/2} u_{ph} \omega^2 \langle\langle \tau_e \rangle\rangle},$ ω_{pl}(unscreened plasma frequency) $= (\frac{n_{e,c} e_c^2}{\epsilon_{\mathrm{o}} m_{e,e}})^{1/2}$
Dielectric absorption	$\sigma_{ph,\omega} = \frac{4\pi \kappa_\lambda}{\lambda},\ \kappa_\lambda = \frac{\epsilon_{e,c}}{2 n_\lambda}$

is due to electrons and for conduction (free) electrons (free-carrier absorption) in metals and semiconductors; also listed are $\sigma_{ph,\omega}$ for semiconductor interband (direct- and indirect- band) absorption transitions.

From Table 7.2, the frequency dependence for free carrier absorption in metals is $\omega^{1/2}$, whereas for semiconductors it is ω^{-2}, i.e., much stronger frequency dependence. The frequency dependence of the direct band spectral absorption is $(\hbar\omega - \Delta E_{e,g})^{1/2}/\omega$, after proper substitutions. The phonon absorption–emission assisting in indirect-band absorption gives a $(\hbar\omega - \Delta E_{e,g} \pm \hbar\omega_p)^2$ dependence, which again is much stronger frequency dependent than that for the direct bands.

The inverse of $\sigma_{ph,\omega}$ is referred to as the photon mean free path $\lambda_{ph,\omega} = 1/\sigma_{ph,\omega}$, (7.97). The photon mean free path in metals is very short and is called the skin depth (the metals are also highly reflective). The derivation of $\sigma_{ph,\omega}$ is a Chapter 3 problem.

Absorption (attenuation) of EM waves by dielectrics was discussed in Section 3.3.5. Figure 7.1(b) gives example of $\sigma_{ph,\omega}$ for a metal (Al), a semiconductor (GaAs), a dielectric (SiO_2), and an organic solid (acrylic). These are predictable with the relations previously discussed.

7.8.2 Photon Absorption Coefficient for Gases

The interaction of a photon (EM field) and fluid particle (or atom and molecule in general) is considered as the interaction of an electric field $\boldsymbol{e}_e$ (magnetic field interaction is considered for magnetic materials) with an electric transition dipole moment $\boldsymbol{\mu}_e$, i.e.,

$$\boldsymbol{\mu}_e = \langle \psi_f | e_c \boldsymbol{x} | \psi_i \rangle, \tag{7.135}$$

where ψ_i and ψ_f are the initial- and final- state wave functions of the electron.

The perturbation Hamiltonian is

$$\mathrm{H}' = -|\boldsymbol{\mu}_e| e_{e,o} \cos(\omega t), \;\; \boldsymbol{e}_e = e_{e,o} \cos(\omega t) \boldsymbol{s}_\alpha, \tag{7.136}$$

where $\boldsymbol{s}_\alpha$ is the polarization vector.

The discrete, internal, translational, vibrational, rotational, and electronic energy states of the fluid particle (including the gas phase) were shown in Figure 6.1. Therefore we expect resonant absorption at the discrete energies, and because these internal energies coexist, there are band broadenings when, for example, a vibrational transition is accompanied by one or more rotational transitions.

The spectral absorptance $\alpha_{ph,\omega}$ is defined for a gas having a length L along a collimated beam of frequency ω and is given by (7.130), where $\sigma_{ph,\omega}$ is the absorption coefficient. Figure 7.16(a) shows the near-infrared spectra of absorptance of CO_2, H_2O, and CH_4, for the given temperature, total pressure p, and partial pressure p_i (for CH_4). Using the ideal gas relation (6.21), $p_i = n_{f,i} k_B T$, and as will be shown $\sigma_{ph,\omega}$ is proportional to $n_{f,i}$ which are excited. There are a few absorption bands for each molecule, and strength (absorption) of these bands (and their widths) depend on the temperature, total pressure, and partial pressure of these species. For a given

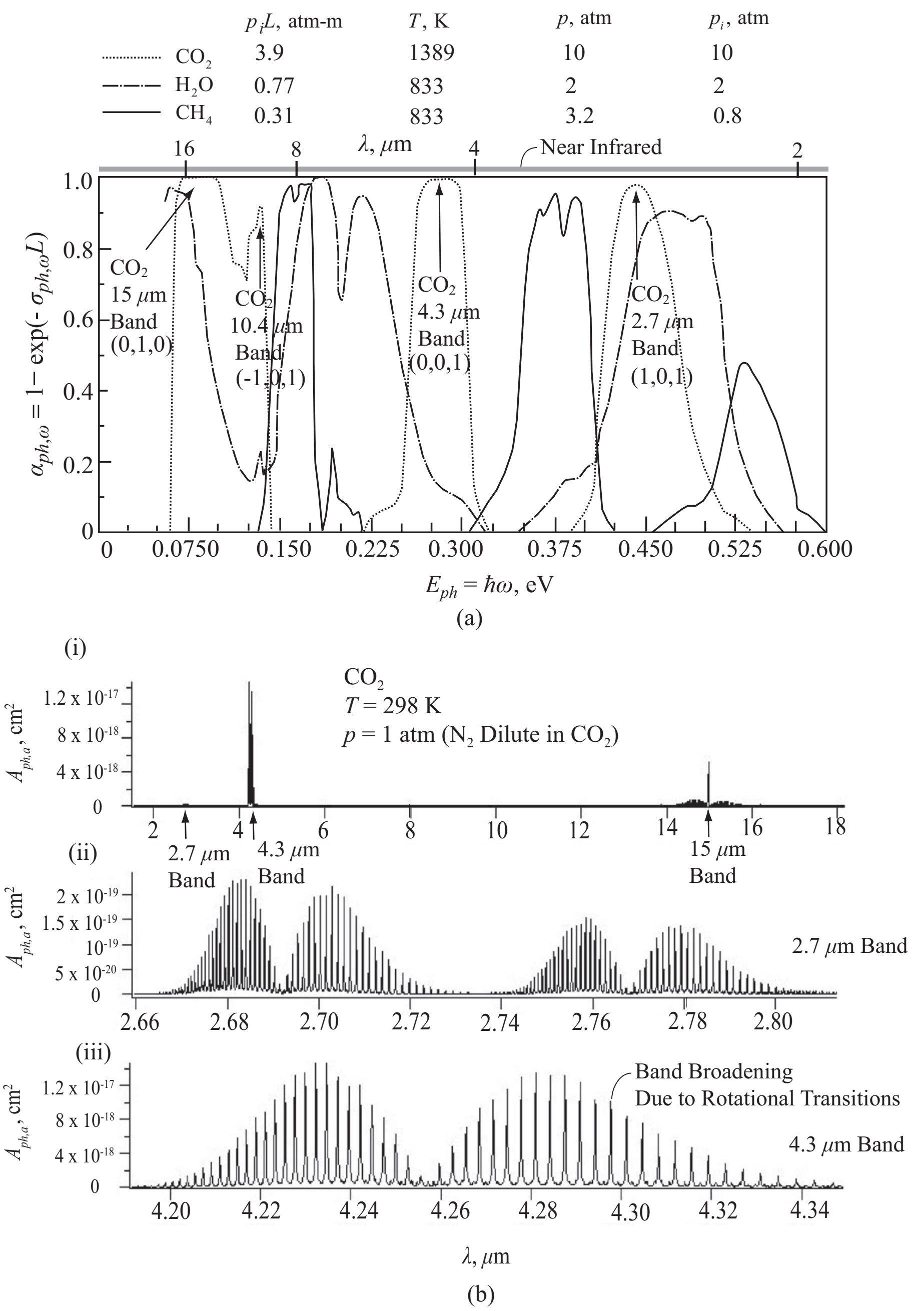

Figure 7.16. (a) Near-infrared variations of the spectral absorptance for CO_2, H_2O, and CH_4 gases, with respect to photon energy, for the listed temperature and total and partial pressures [428]. Each absorption band has a bandwidth that depends on the pressure and temperature. (b) Variations of the measured photon absorption cross-section area of CO_2 (at T = 298 K and p = 1 atm total pressure) as functions of wavelength. The partial pressure of CO_2 is low (N_2 is the background gas). Note the strong absorption around 4.2–4.3 μm which is shown in more detail in (b)(iii) [113, 456]. The combined vibrational–rotational transitions are shown.

temperature, the product of the partial pressure and the beam path length is used to specify the gas conditions. Details on the band models and their calculation are given in [331].

The vibrational energy transitions are larger than the rotational energy transitions (examples will be given in Section 7.13), and also these transitions occur simultaneously. This is the reason for the band-type behavior of the gas photon absorption and emission. The combined rigid-rotor and harmonic-oscillator models gives an energy transition (higher-order Hamiltonians are also used when accuracy requires), which combines (6.14) and (6.16, Section 6.1.5), i.e.,

$$E_{f,v\text{-}r} = \sum_k (l_k + \frac{1}{2})\hbar\omega_{f,v,k} + j(j+1)B_{f,r},\ l_k, j = 1, 2, \ldots \qquad (7.137)$$

Note that allowed transition $\Delta l_k = \pm 1$ combined with $\Delta j = 0, \pm 1, \ldots$, creates distinct branches in each band. For polyatomic gases, the sum is made over the vibrational modes (the number of modes are listed in Table 6.1) Some of the significant bands in common combustion/environmental gases are listed in Table 7.3 (H_2O, CO_2, CO, NO, SO_2, and CH_4) [124]. Note that the H_2O absorption transitions can include more than one modal excitations. For example, H_2O (0,1,1) combines the bending and symmetric-stretching vibrational modes (Table 6.1).

The vibrational degrees of freedom expresses the modes of vibration, and for example, for CO_2, which is a linear molecule, there is a symmetric mode, a bending mode, and an asymmetric (two oxygen atoms oscillate against the carbon atom). The vibrational quantum numbers, l_1, l_2, and l_3 in parentheses in Table 7.3 are for the symmetric, bending, and asymmetric modes. The *ab initio* calculated values of the vibrational and rotational constants for CO_2 are given in Section 6.1.5, and as the temperature increases higher j-levels are occupied.

Figure 7.16(b) shows variations of the measured spectral photon absorption cross-section area (per molecule) of CO_2 as functions of the photon wavelength for $T = 298$ K and a total pressure of 1 atm (dilute CO_2 concentration in N_2). CO_2 has absorption peaks at 2.0, 2.7, 4.3, 4.8, 9.4, 10.4, and 15 μm, and Figure 7.16(b)(i) shows the strongest bands at 4.3 and 15 μm (with another but less significant band at 2.7μm). Note that this vibrational cross-section area is larger than the nuclear cross-section area mentioned in Section 7.5.2, and yet much smaller than the binary fluid-particle collision cross-section area (Section 6.5). Note the band broadening that is due to rotational energy transitions. There is also band broadening that is due to gas particle collisions and due to the Doppler effect (relative velocity of the absorbed photon and the fluid particle thermal translational motion). The Doppler broadening is a signature of the gas temperature. The greenhouse (thermal) emission and absorption with peak around 10 μm effect) is most pronounced with the broad-band, long wavelength (15 μm) broad band of CO_2. The significant H_2O bands are outside the greenhouse range.

The natural (fundamental) frequency $\omega_n = \omega_f$ can be estimated with the inter-atomic spring (force) constant using (2.55). However, in polyatomic gases various vibrational motions occur (Section 6.1.5).

Table 7.3. *Measured major (infrared regime) gas absorption bands for some combustion/environmental gases [124]. The CO_2 bending vibrational modes are degenerate (two modes). l_1 is for symmetric-stretching, l_2 for bending, and l_3 for asymmetric-stretching vibration mode, and each excitation (transition) is represented as (Δl_1, Δl_2, Δl_3), where $\Delta l_i = \pm 1, \pm 2$, etc. The selection rules allowing only certain optical transitions are given in [121].*

	Band center, μm (meV)	Vibrational degrees of freedom	Δl_1, Δl_2, Δl_3
H_2O	71 (17.5)	3	(0,0,0), Δj only
	6.3 (197)		(0,1,0)
	2.7 (459)		(0,2,0)
	1.87 (692)		(0,1,1)
	1.38 (898)		(1,0,1)
CO_2	15 (82.3)	4	(0,1,0)
	10.4 (119)		(−1,0,1)
	9.4 (131)		(0,−2,1)
	4.3 (288)		(0,0,1)
	2.7 (459)		(1,0,1)
	2.0 (646)		(2,0,1)
CO	4.7 (264)	1	(1)
	2.35 (528)		(2)
NO	5.34 (232)	1	(1)
SO_2	19.27 (64.3)	3	(0,1,0)
	8.68 (143)		(1,0,0)
	7.35 (167)		(0,0,1)
	4.34 (286)		(2,0,0)
	4.0 (310)		(1,0,1)
CH_4	7.66 (162)	9	(1,0,0,1)
	3.31 (375)		(0,0,1,0)
	2.37 (523)		(1,0,0,1)
	1.71 (725)		(1,1,0,1)

For quantum calculation, for atmospheric gases, the spectral absorption coefficient of the transition electric dipole resonance is used [358]. This is based on the FGR (3.27) and (7.54), and is given by

$$\sigma_{ph,\omega} = \frac{4\pi^2 n_{f,v}\omega}{3\hbar u_{ph} Z_f}(e^{-E_{f,i}/k_{\mathrm{B}}T} - e^{-E_{f,f}/k_{\mathrm{B}}T})|\langle\psi_f|\boldsymbol{p}_e|\psi_i\rangle|^2 g(\omega,\omega_{i\text{-}f}), \tag{7.138}$$

where $n_{f,v}$ is the number density of the particular vibrational state of the gas molecule, $E_{f,i}$ and $E_{f,f}$ are the lower and upper energies for the transition, Z_f is the partition function, $\boldsymbol{\mu}_e = \langle\psi_f|\boldsymbol{p}_e|\psi_i\rangle$ is the transition dipole moment, and includes $|\psi_i\rangle$ and $|\psi_f\rangle$, which are the states and wave functions of the upper and lower states (7.135, and $g(\omega,\omega_{i\text{-}f})$ is the line-shape function (Table 3.5) to allow for line broadening that is due to molecular collision, etc. Note that the matrix element $|\boldsymbol{\mu}_e|$ is that defined by (3.29) and similarly in (5.94). Equation (7.138) is also listed in Table 7.2. In Section 7.12.6 we discuss the *ab initio* computation of $|\boldsymbol{\mu}_e|$ for a molecular complex.

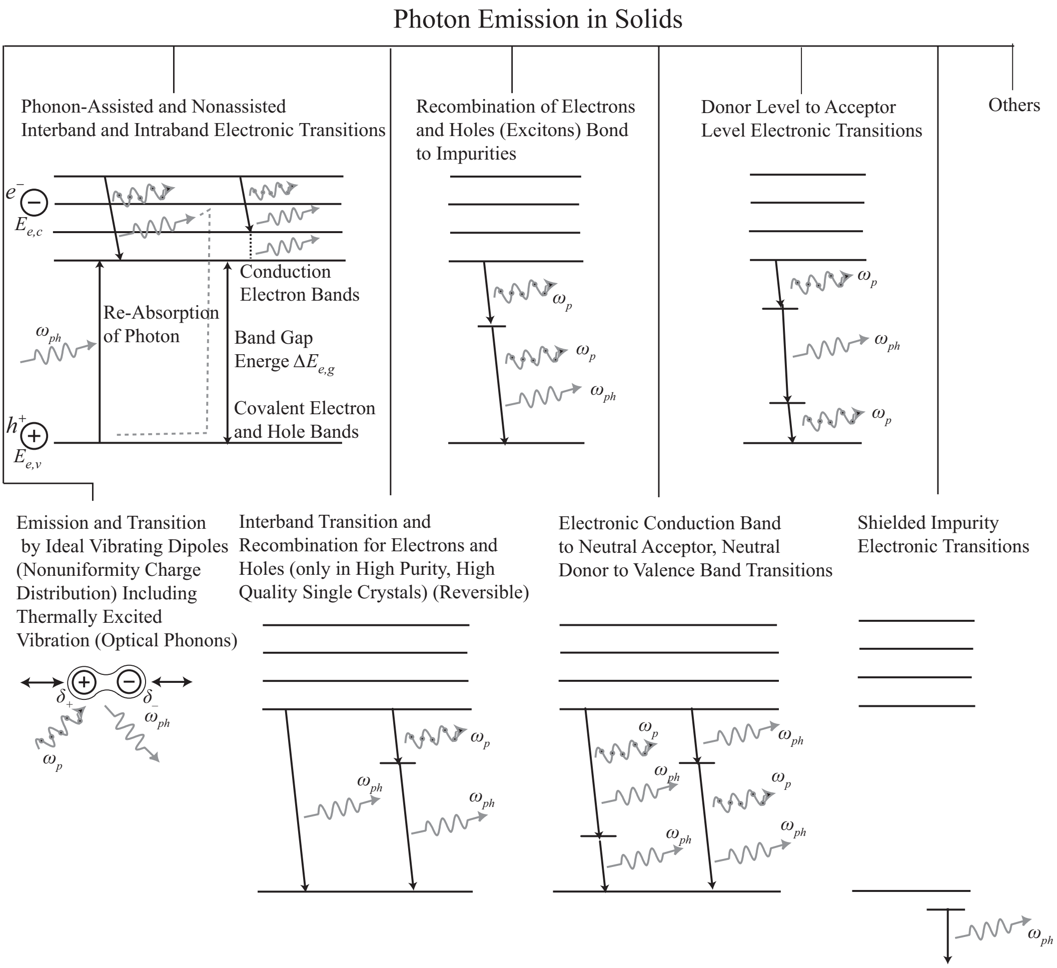
Photon Emission in Solids
Phonon-Assisted and Nonassisted Interband and Intraband Electronic Transitions
Recombination of Electrons and Holes (Excitons) Bond to Impurities
Donor Level to Acceptor Level Electronic Transitions
Others
e^-
$E_{e,c}$
Re-Absorption of Photon
ω_{ph}
Conduction Electron Bands
Band Gap Energe $\Delta E_{e,g}$
Covalent Electron and Hole Bands
h^+
$E_{e,v}$
ω_p
ω_{ph}
Emission and Transition by Ideal Vibrating Dipoles (Nonuniformity Charge Distribution) Including Thermally Excited Vibration (Optical Phonons)
δ_+
δ_-
ω_p
ω_{ph}
Interband Transition and Recombination for Electrons and Holes (only in High Purity, High Quality Single Crystals) (Reversible)
Electronic Conduction Band to Neutral Acceptor, Neutral Donor to Valence Band Transitions
Shielded Impurity Electronic Transitions

Figure 7.17. Various mechanisms of photon emission in solids [127]. These in turn determine the electric permittivity (dielectric function) of the material.

Figure 7.1(b) gives example of $\sigma_{ph,\omega}$ for O_3 (ozone) at 300 K at 1 atm. It also gives $\sigma_{ph,\omega}$ for H_2O at the same thermodynamic conditions.

7.9 Continuous and Band Photon Emission

7.9.1 Emission Mechanisms

Although in some processes the photon emission is the reverse of a photon absorption process, in many cases it is not. The most commonly encountered photon emission mechanisms, which are electronic, but may be phonon assisted, are shown in Figure 7.17.

Photons can be emitted by vibrating dipoles of a multiatom crystal. This is limited in frequency to the highest optical phonons, although multiple phonon contributions are possible (but the probability decreases with the number involved in the interaction).

In the phonon-assisted interband and intraband electron transitions, the electrons in the upper conduction band come to thermal equilibrium with a lattice (i.e., thermalize) rather quickly (Sections 5.19 and 5.22.2). The emitted photon for this mechanism has a range of energy (broad spectral range). In this process, if the photon energy exceeds the gap energy $\Delta E_{e,g}$, it maybe reabsorbed, causing further electronic transitions. The intraband emissions would require special excitation contributions (electron avalanches).

The interband recombination of electrons and holes with photon emission is the reverse of strong photon absorption, but relative to other processes is less likely (except for high-purity crystals). The interband transitions can occur in direct and indirect gap transitions. The emission band width should be of the order of $k_{\rm B}T$, because of thermalization of electrons and holes.

The impurity-related emissions, including acceptors and donors, can be due to annihilation by the exciton band to impurities. Again these are phonon emission or absorption assisted. Transitions between band edges and acceptor or donor impurities are common, and can be phonon assisted. The electrons captured at donor impurity levels can recombine with holes captured at acceptor levels and emit photons.

The optical transition from excited states to ground states of impurities can be influenced by the lattice (strong coupling) or slightly perturbed (well-shielded). The well-shielded impurities result in transitions and photon emission spectra with sharp lines (related to equivalent undisturbed atomic lines). The energy levels of triply ionized rare-earth ion impurities are deduced from fluorescence experimental results. Solid-state lasers use such ion-embedded crystals (such as neodymium ion Nd^{3+} in yttria–aluminum–garnet, YAG).

In Section 7.10, the surface emission of Si will be examined, with particular attention to the lattice-vibration regime. In Section 7.15.1 we consider the near-field emission of Si. The lattice vibration in turn influences the frequency dependence of the dielectric function ϵ_e (Section 3.3.5) and the signature of phonon-resonance-induced peaks in ϵ_e are evident in the near-field emission.

7.9.2 Absorption and Emission Reciprocity (Kirchhoff Law)

We now consider the cross-section area for the photon absorption and emission processes arising for the generalized two electronic energy levels. We continue to assume no phonon emission or absorption. The upper and lower states are shown in Figure 7.18(a). The resonant electronic transition has phonon or electronic sublevels (sidebands). The two levels are characterized by the energies $E_{e,i}$ and $E_{e,j}$ and the degeneracies $g_{e,i}$ and $g_{e,j}$. The emission and absorption cross-section areas can be determined as a summation of the individual cross-section areas $(A_{ph,e})_{ij}$ and $(A_{ph,a})_{ji}$, between the levels. Assume the multiplets A and B are each under their

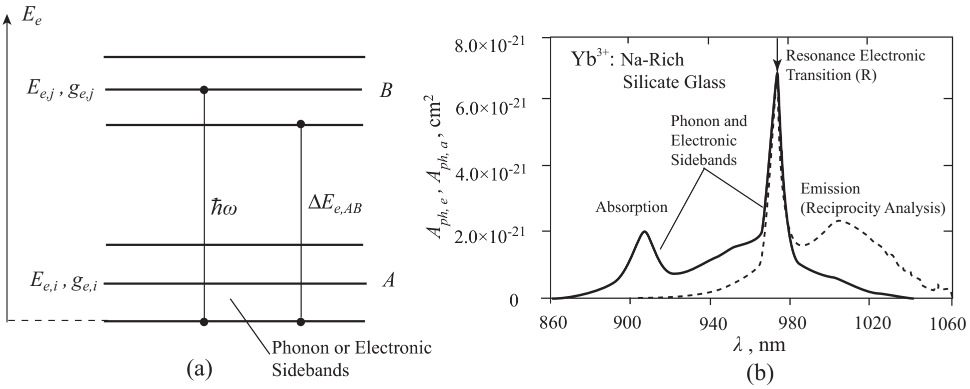

Figure 7.18. (a) Electronic transitions in a two multiplets (A and B) with phonon or electronic sublevels (i and j). The absorbed photon energy is $\hbar\omega$, and the electronic transition is $\Delta E_{e,AB}$. (b) Same showing the absorption and emission cross-section areas for Yb^{3+} in a silicate-blend glass [143], showing red shifting of the emission.

own thermal equilibrium; we have from (7.55), (7.57), and (7.61)

$$A_{ph,e}(\omega) = \sum_{i,j} g_{e,j}\{\frac{\exp[-(E_{e,j} - \Delta E_{e,AB})/k_{\rm B}T]}{Z_B}\}(A_{ph,e})_{ji} g_{e,i} \qquad (7.139)$$

$$A_{ph,a}(\omega) = \sum_{i,j} g_{e,i}[\frac{\exp(-E_{e,i}/k_{\rm B}T)}{Z_A}](A_{ph,a})_{ij} g_{e,j}, \qquad (7.140)$$

where $\Delta E_{e,AB}$ is the energy gap between the two lowest levels of the upper and lower multiplets. Here Z_A and Z_B are the partition functions of the lower and upper multiplets, which are given by

$$Z_B = \sum_j g_{e,j} \exp[-(E_{e,j} - \Delta E_{e,AB})/k_{\rm B}T] \qquad (7.141)$$

$$Z_A = \sum_i g_{e,i} \exp(-E_{e,i}/k_{\rm B}T), \qquad (7.142)$$

and the energy difference is

$$E_{e,j} - E_{e,i} = \hbar\omega. \qquad (7.143)$$

We now divide (7.139) by (7.140), and using $(A_{ph,e})_{ji} = (A_{e,a})_{ij}$, we have

$$\begin{aligned}\frac{A_{ph,e}(\omega)}{A_{ph,a}(\omega)} &= \frac{Z_A}{Z_B}\exp[-(E_{e,j} - \Delta E_{e,AB} - E_{e,i})/k_{\rm B}T]\\ &= \frac{Z_A}{Z_B}\exp[-(\hbar\omega - \Delta E_{e,AB})/k_{\rm B}T] \text{ Kirchhoff law.} \qquad (7.144)\end{aligned}$$

So, the emission is red-shifted compared to absorption. For a simple two-level system (without multiplets), we have $Z_A = Z_B$, and $\hbar\omega = \Delta E_{e,AB}$. Then (7.144) reduces to the simple relation $A_{ph,e}(\omega) = A_{ph,a}(\omega)$. Figure 7.18(b) shows the measured absorption cross-section area $A_{ph,a}(\lambda)$ and the emission cross-section area determined from the reciprocity relation [143]. Note that in general emission can be red or blue shifted depending on the population of the excited state (for inverse population, it is blue shifted).

Once $A_{ph,e}$ is known, for example from absorption, for the general case of emission we have

$$\dot{s}_{e\text{-}ph,\omega} = \sigma_{ph,\omega} u_{ph} \int_\omega \frac{\mathrm{d}E_{ph,\omega}}{V} = n_{e,B} A_{ph,e} u_{ph} \int_\omega \frac{\mathrm{d}E_{ph,\omega}}{V}. \tag{7.145}$$

7.10 Spectral Surface Emissivity

A general treatment (near and far field) of thermally excited surface EM emission is rendered in Figure 7.19(a), and given in [221]. Here we loosely build on the conventional far-field definition of the surface emissivity (this is rather a volumetric description and falls short; the surface treatment outlined in Section 7.15.1 leads to the proper definition of emissivity). The spectral (and directional) emissivity $\epsilon_{ph,\omega}(\theta, \phi, T)$ is defined using the blackbody spectral emissive power (quantum-particle treatment) $E_{b,\omega}$ (7.8), i.e.,

$$\epsilon_{ph,\omega}(\theta, \phi, T) = \frac{\mathrm{d}E_{ph,\omega}(\theta, \phi, T)}{\mathrm{d}E_{b,\omega}(T)}, \tag{7.146}$$

where $E_{ph,\omega}$ is the spectral emissive power. Assuming that $f_{ph} = f_{ph}^{\mathrm{o}}$, from (7.1) we have

$$\epsilon_{ph,\omega,T}(\theta, \phi) = \frac{D_{ph,\omega}(T)}{D_{b,\omega}(T)} \quad \text{for } f_{ph}^{\mathrm{o}} \text{ from photon gas}, \tag{7.147}$$

where the blackbody photon DOS is defined by (7.3).

We briefly discuss semiconductors, insulators, and metals.

Figures 7.19(b) and (c) show the variations of measured normal ($\theta = 0$), spectral emissivity of crystalline Si. Figure 7.19(b) is for $T = 323$ K and the low-energy results are from [465]. The blackbody DOS is also shown, as well as the DOS $D_{ph}(\omega) = \epsilon_{ph,\omega} D_b(\omega)$. The visible regime is dominated by direct and indirect interband transitions.

Figure 7.19(c) shows the variations of normal ($\theta = 0$) spectral emissivity $\epsilon_{ph,\omega}(\omega, T)$ for Si as functions of energy for four different temperatures [411]. This is the low-energy regime, where the lattice vibration dominates (dipole emission). The emissivity first increases with an increase in temperature and then decreases. The peak around $\lambda = 9$ μm is associated with the Si–O bond from oxygen impurity.

Comparing Figure 7.19(b) with the spectral absorption characteristic of semiconductors (Figures 7.14 and 7.15), we see that the high absorption and emission regimes are very similar, as the dominant mechanisms for absorption and emission in the respective regimes are the same.

The near-field and far-field emissions of Si have been predicted in [150] and will be discussed in relation to size effects in Section 7.15.1. The near-infrared regime behavior is dominated by nonpolar, optical-phonon-induced transition dipoles, and by intraband transitions for electrons and holes. Also shown in Figure 7.19(b) is the

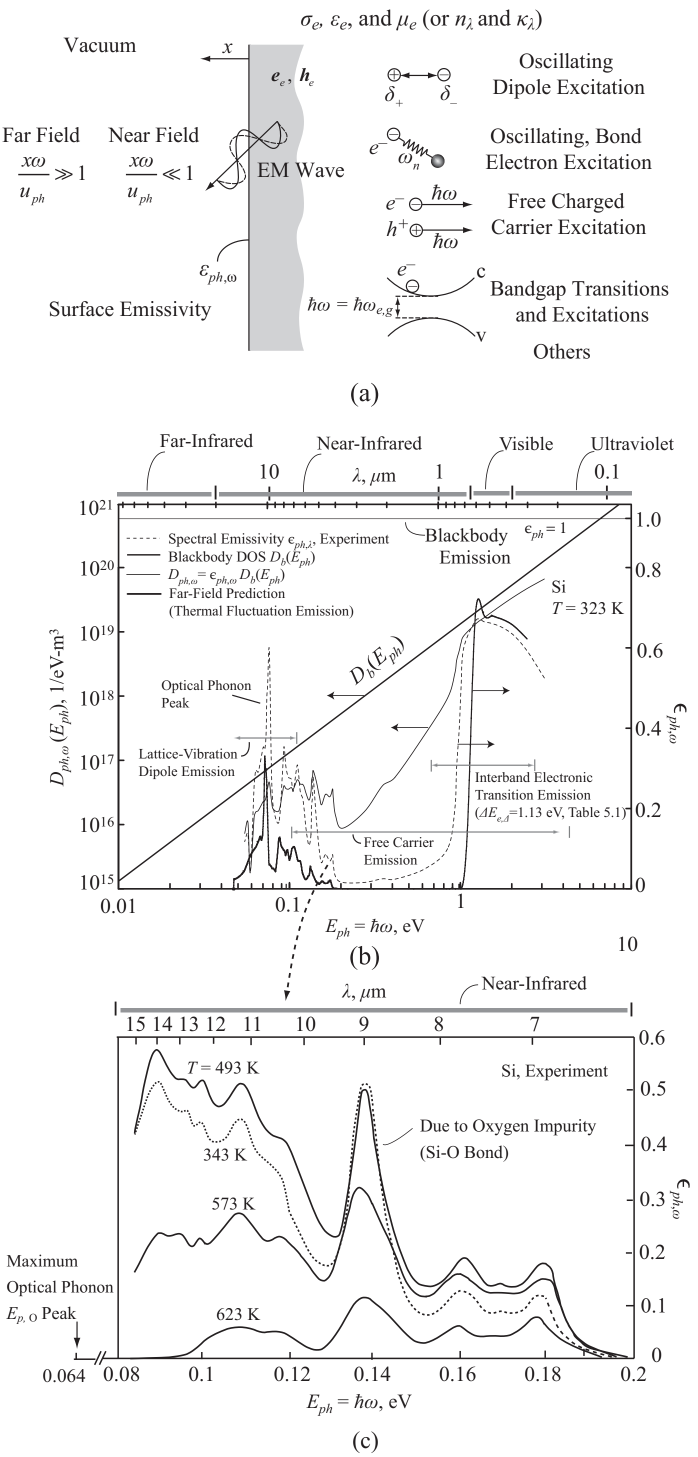

Figure 7.19. (a) EM treatment of surface emissivity. (b) Spectral, normal emissivity $\epsilon_{ph,\omega}(\omega, T)$ of Si. DOS $D_{ph}(E_{ph})$ and $D_b(E_{ph})$, and $\epsilon_{ph,\omega}(\omega, T)$ for low- and high-energy regimes [465]. Also shown are the predicted normal spectral emissivity [150]. (c) The lattice-vibration (near-infrared) dipole radiation (emission) regime and its temperature dependence [411]. The phonon DOS for Si is shown in Figure 4.11, and the peak in the optical-phonon modes is also shown there.

normal spectral emissivity of Si predicted in [150]. The general agreement around the bandgap and the high-energy phonon regimes is rather good, validating the dielectric function model used (Section 7.15.1). As the temperature increases, the higher-energy phonons are excited; however, the Si phonon DOS shown in Figure 4.11 nearly cuts off at $E_{ph} = 0.064$ eV (optical phonon). Then the increase in temperature results in smaller occupancy of the low energy states, and therefore their reduced efficiencies.

The interband electronic transition regime of Figure 7.19(b) begins near the $\Delta E_{e,\Delta}$ bandgap of 1.13 eV for Si (Table 5.1). The spectral reflectivity and emissivity of SiC in the near-infrared regime has been predicted in [153].

The role of optical phonons is through dependence of the electric permittivity on frequency (polar, optical phonons, Section 4.6), and in turn the dependence of the surface (tangent to surface) EM waves (or its wave vector $\kappa_{||}$) on the electric permittivity. For SiC, the following photon dispersion and dielectric function relations are used [153]

$$\kappa_{||} = \frac{\omega^2}{u_{ph}^2}\frac{\epsilon_e}{\epsilon_e + 1} \quad \text{photon dispersion relation,} \tag{7.148}$$

$$\epsilon_e(\omega) = \epsilon_{e,\infty}\left(1 + \frac{\omega_{p,\mathrm{LO}}^2 - \omega_{p,\mathrm{TO}}^2}{\omega_{p,\mathrm{TO}}^2 - \omega^2 - i\tau_e^{-1}\omega}\right)$$

$$\text{oscillator model for dielectric function.} \tag{7.149}$$

For SiC, they use $\hbar\omega_{p,\mathrm{LO}} = 0.127$ eV (10.32 μm), $\hbar\omega_{p,\mathrm{TO}} = 0.0983$ eV (12.61 μm), $\hbar\tau_e^{-1}$ (damping constant) $= 0.000590$ eV, and $\epsilon_{e,\infty} = 6.7$. Then, between 10.32 and 12.61 μm, this dispersion relation has a complex entity and behavior [153], and in turn determines the high near-field emission (coherent and near-resonant emission), and far-field emissivity (high emissivity).

Using the classical EM treatment for the normal, spectral emissivity [428], we have

$$\epsilon_{ph,\omega,n} = \frac{4n_\lambda}{(n_\lambda + 1)^2 + \kappa_\lambda^2}. \tag{7.150}$$

Also, for metals at long wavelengths (infrared), the two components of the complex index of refraction n_λ and κ_λ (Table 3.5) are equal (Chapter 3 problem) and given by

$$n_\lambda = \kappa_\lambda = \left[\frac{\lambda\mu_\mathrm{o}c_\mathrm{o}}{4\pi\rho_e(T)}\right]^{1/2} \quad \text{metals at long wavelengths.} \tag{7.151}$$

Using this, we note that $\epsilon_{ph,\omega,n}$ decreases with an increase in λ, and also increases with T (as ρ_e increases with T for metals, Figure 5.16). The $\epsilon_{ph,\omega,n}(\lambda, \rho_e)$ is called the Hagen–Rubens relation.

For a surface, the sum of the spectral reflectivity, absorptivity, and transmissivity is equal to unity [232]. Here our treatments of photon transport are volumetric and this reference to surface property is for the sake of completeness and is used in the treatment of energy-conversion devices. Also, as a surface property, the spectral

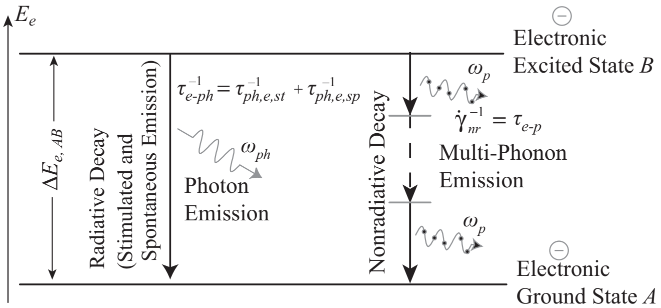

Figure 7.20. Radiative and nonradiative decay processes in a two-level system. The radiative decay is generally dominated by spontaneous photon emission, $\tau_{ph,e,sp}$.

emissivity strongly depends on the surface topology (e.g., roughness), and surface composition (e.g., oxidation adsorption).

7.11 Radiative and Nonradiative Decays and Quantum Efficiency

Using the classical description of a bound, oscillating electron, a damping rate $\dot{\gamma}_e$ can be added for any energy loss.[†] In general, this energy decay in electronic transitions includes both radiative (electromagnetic radiation) and nonradiative contributions (7.37). The radiative decay is the total (spontaneous and stimulated emission) and is in general dominated by the spontaneous emission [429]. The nonradiative decay includes inelastic collision of atoms with each other, or with the molecular and lattice vibration (phonon emission or absorption in solids).

The multiphonon relaxation process (purely nonradiative) is more clearly observed in rare-earth-element doped crystals (Section 5.20). When an electron of the ion is excited from the ground state to the excited state, it will not remain in the excited state long and returns to the ground state, with energy released equal to the energy gap $\Delta E_{e,AB}$ between the two states. As shown in Figure 7.20, this energy can be released through a radiative decay process by emitting a photon with an energy of $\Delta E_{e,AB}$, or through a purely nonradiative decay process by emitting several phonons (vibrational quanta of the host crystal), and the number of phonons emitted is given by $N_p = \Delta E_{e,AB}/\hbar\omega_p$, for energy per phonon $\hbar\omega_p$.

To calculate the total decay rate, the interaction of the isolated rare-earth ion with its crystalline host is interpreted as being due to the modulation of the crystalline electric field by the lattice vibrations. Based on the FGR (3.27) and weak coupling, the total decay rate, which is defined as the fraction of excited electrons

---

[†] The one-dimensional classical equation of motion for conduction electron (Table 2.5) becomes [i.e., (3.45)]

$$\frac{d^2x}{dt^2} + \dot{\gamma}_e \frac{dx}{dt} + \omega^2_{n,e} x = -\frac{e_c}{m_e} e_{e,x},$$

where $\omega_{n,e} = (\Gamma_e/m_e)^{1/2}$ is the natural or resonance angular frequency, $\dot{\gamma}_e = 1/\tau_e$, and Γ_e is the force constant, similar to interatomic force constant (2.54).

decaying per second, is modeled as [42, 369]

$$\dot{\gamma}_{e\text{-}ph\text{-}p}(T) = \frac{1}{\tau_{e\text{-}ph\text{-}p}} = \dot{\gamma}_{e\text{-}ph}(T=0)(1+f_p^{\mathrm{o}})^{N_p}$$

N_p-phonon, purely nonradiative decay model (effective phonon-mode model), (7.152)

where $\tau_{e\text{-}ph\text{-}p}$ is the lifetime of excited electrons, N_p is the number of phonons emitted to fill the energy gap between the two states, and f_p^{o} is the phonon equilibrium distribution (occupation) function (Table 1.2), i.e.,

$$f_p^{\mathrm{o}} = \frac{1}{\exp(\hbar\omega_p/k_{\mathrm{B}}T)-1}. \tag{7.153}$$

Relation (7.152) shows strong dependence of $\gamma_{e\text{-}ph\text{-}p}(T)$ on the number of phonons involved. Finally the temperature-dependent decay rate is given by

$$\dot{\gamma}_{e\text{-}ph\text{-}p}(T) = \dot{\gamma}_{e\text{-}ph}(T=0)[1-\exp(-\hbar\omega_p/k_{\mathrm{B}}T)]^{-N_p}$$

N_p-phonon, purely nonradiative decay model. (7.154)

Here $\dot{\gamma}_{e\text{-}ph}(T=0)$ is the radiative decay rate, because $\dot{\gamma}_{e\text{-}ph\text{-}p}(T) = \dot{\gamma}_{e\text{-}ph\text{-}p}(T=0)$ at $T=0$ when $f_p^{\mathrm{o}}=0$ and the phonon modes are all initially in their ground state. As the temperature is raised, the phonon modes become thermally populated and the multiphonon relaxation rate increases. Thus the radiative decay rate is constant, whereas the nonradiative decay rate increases with temperature. The radiative lifetime is

$$\dot{\gamma}_{e\text{-}ph} = \frac{1}{\tau_{e\text{-}ph}} = \dot{\gamma}_{e\text{-}ph}(T=0). \tag{7.155}$$

Now, using Matthiessen rule (4.111), we have

$$\dot{\gamma}_{e\text{-}ph\text{-}p} = \dot{\gamma}_{e\text{-}ph} + \dot{\gamma}_{e\text{-}p}, \quad \dot{\gamma}_{e\text{-}p}(T) = \dot{\gamma}_{nr} = \frac{1}{\tau_{e\text{-}p}} = \dot{\gamma}_{e\text{-}ph\text{-}p}(T) - \dot{\gamma}_{e\text{-}ph}$$

Matthiessen rule (series), (7.156)

or

$$\frac{1}{\tau_{e\text{-}p}} = \frac{1}{\tau_{e\text{-}ph\text{-}p}} - \frac{1}{\tau_{e\text{-}ph}}, \tag{7.157}$$

where $\tau_{e\text{-}ph}$ is called the radiative lifetime ($\tau_{e\text{-}ph}^{-1} = \tau_{ph,e,st}^{-1} + \tau_{ph,e,sp}^{-1}$, stimulated emission is neglected other than in optical cavities) and $\tau_{e\text{-}p}$ ($= \dot{\gamma}_{nr}^{-1}$) is the nonradiative lifetime (Section 7.4). In general $\tau_{nr} = \tau_{e\text{-}p} < \tau_{e\text{-}ph}$, i.e., nonradiative decays are faster processes, compared to photon producing decays, but for photonics this is reversed and phonon emission is avoided. In Section 7.12.6, we discuss *ab initio* calculations of the nonradiative decay time, using the Huang–Rhys theory of coupling.

Table 7.4. *Examples of radiative decay (emission) times* $\tau_{ph,e,sp} = \dot{\gamma}_{e\text{-}ph}^{-1}$ *of some laser and phosphorous materials [429, 506].*

Material and Transition	**λ**, nm	$\boldsymbol{\tau_{e\text{-}ph}}$, s
Na		
$3s \rightarrow 3p$	589	15.9×10^{-9}
$3s \rightarrow 4p$	330	3.5×10^{-7}
He–Ne		
$3s_2 \rightarrow 4p_4$	633	7.0×10^{-7}
$2s_2 \rightarrow 2p_4$	1153	2.3×10^{-7}
$2s_2 \rightarrow 3p_4$	3392	1.04×10^{-6}
Nd^{3+}: YAG		
${}^4F_{3/2} \rightarrow {}^4I_{3/2}$	1064	1.22×10^{-3}
Ruby		
${}^2E \rightarrow {}^4A_2$	694	4.3×10^{-3}
Mn^{2+}: γ-$Zn_3(PO_4)_2$	635	100×10^{-3}
Ce^{3+}: $Ca_2MgSi_2O_7$	600	100×10^{-3} to 1
Mn^{2+}: MgF_2	585	> 1
Ce^{3+}: CaS	507	7.2×10^{2}
Eu^{2+},Al^{3+}: CaS	650	3.6×10^{3}
Ti^{4+}: Y_2O_2S	565	1.8×10^{4}

An oscillating atom, like an oscillating classical dipole, emits EM energy at its discrete oscillation frequency, and this energy decays in time (emission). The classical electron oscillator (Section 3.3.5) has the radiative decay time of (3.42)

$$\tau_{e\text{-}ph,\mathrm{o}} = \tau_{ph,e,sp,\mathrm{o}} = \dot{\gamma}_{ph,e,sp,\mathrm{o}}^{-1} = \frac{6\pi\epsilon_{\mathrm{o}} m_e u_{ph}^3}{e_c^2\omega^2} = \frac{3\epsilon_{\mathrm{o}} m_e u_{ph}}{2\pi e_c^2}\lambda^2 = 4.504\times10^4\lambda^2$$

$$\text{classical oscillating electron radiative decay time,} \quad (7.158)$$

for spontaneous emission in vacuum.[†] This gives $\tau_{ph,e,sp,\mathrm{o}} = 1.1\times10^{-8}$ s for $\lambda = 0.5$ μm (visible regime), and the larger wavelengths have noticeably larger decay times. The radiation broadening refers to the emission spectra line that has this decay signature and the linewidth is defined as $\Delta\lambda = \lambda^2\dot{\gamma}_{ph,e,sp}/2\pi u_{ph}$. For this example, $\Delta\lambda = 1.2\times10^{-4}$ Å.

Some ions have radiative decay times close to those of preceding classical electron oscillator. Table 7.4 gives examples of the radiative decay times for some laser phosphorous (Glossary) materials . These are dominated by spontaneous emission

---

[†] The average radiation power is [289] (Chapter 3 problem)

$$P_e = \frac{\omega^4 p_{e,o}^2}{12\pi\epsilon_{\mathrm{o}} u_{ph,\mathrm{o}}^3},$$

for an oscillating dipole moment.

(unless the excited-state population reaches saturation, i.e., becomes the same as the ground state). For some of these solids, the decay time is orders of magnitude larger than $\tau_{ph,e,sp,\text{o}}$. For the alkali metal Na, the radiation lifetime is close to that predicted by (7.158), but for rare-earth metals doped glasses it is not as small as that predicted by (3.43) The decay time $\tau_{e\text{-}ph}$ for Nd^{3+}: LaCl_3 of Figure 5.38, for various fluorescent transitions, are reported in [7], and are between 20 to 170 μs.

Phosphorous materials have decay times significantly longer than that of the laser materials. The excited electrons in these materials form a singlet that is surrounded by levels that are not allowed by quantum mechanic exclusions. Although the electrons eventually decay to the ground levels, the time it takes for them to reach the ground state is long, thus the luminescence is prolonged (used in displays).

The temperature dependence of (7.152) has been confirmed by experiments. For example, in a Y_2O_3 crystal doped with Yb^{3+}, the lifetime of the excited electrons ($^2\text{F}_{5/2}$ to $^2\text{F}_{7/2}$) is measured as a function of temperature [384]. The results are shown in Figure 7.21(a). The results are predicted for the multiphonon decay rate using (7.154) with $\hbar\omega_p = 0.1952$ eV and $N_p = 6$ (predicted by the metrics introduced in [238]). This suggests that the decay is a six phonon relaxation process, with the energy of 0.1952 eV per phonon, which corresponds to the highest available phonon mode of the O–O pair. Note that for very large temperatures (reaching the melting temperature of the host crystal), $\tau_{e\text{-}ph\text{-}p}$ tends to zero [from (7.154)]. The prediction of (7.154) is also shown in Figure 7.21(b) for Ti^{3+}: Al_2O_3, and is is good agreement is found with experiments.

Other multiphonon relaxation-time models have been suggested [386], and are more accurate representations of experimental results at low temperatures. Because the population of the excited state deviates from that given for the thermal equilibrium, it needs to be determined using the rate equation. Using (7.37), at steady state, the excitation events from the ground state must be balanced by the decay events from the excited state, i.e.,

$$n_{e,A}(\omega_1)A_{ph,a}(\omega)f_{ph}(\omega) - n_{e,B}(\omega_2)A_{ph,d}(\omega)[1 + f_{ph}(\omega)] = 0, \tag{7.159}$$

where $A_{ph,d}$ is the decay cross section and is related to $A_{ph,e}$ through

$$\eta_{e\text{-}ph} = \frac{A_{ph,e}}{A_{ph,d}} = \frac{\dot{\gamma}_{e\text{-}ph}}{\dot{\gamma}_{e\text{-}ph\text{-}p}(T)} = \frac{\dot{\gamma}_{e\text{-}ph}}{\dot{\gamma}_{e\text{-}ph} + \dot{\gamma}_{e\text{-}p}} = \frac{\tau_{e\text{-}ph\text{-}p}}{\tau_{e\text{-}ph}} \quad \text{quantum efficiency}, \tag{7.160}$$

where $\eta_{e\text{-}ph}$ is the quantum efficiency [374]. The quantum efficiency is the equivalent of the Carnot efficiency (which uses temperatures). Then we have

$$\frac{n_{e,B}}{n_{e,A}} = \frac{A_{ph,a}(\omega)f_{ph}(\omega)}{A_{ph,d}(\omega)[1 + f_{ph}(\omega)]} = \frac{A_{ph,a}(\omega)f_{ph}(\omega)}{\frac{A_{ph,e}(\omega)}{\eta_{e\text{-}ph}}[1 + f_{ph}(\omega)]}. \tag{7.161}$$

Using $\dot{s}_{f,ph}$ given by (7.66), we have the heating rate as

$$\dot{s}_{f,ph} = u_{ph}\sigma_{ph,\omega}[f^n_{ph}(T) - f_{ph}(s)], \quad \sigma_{ph,\omega} = A_{ph,a}n_a. \tag{7.162}$$

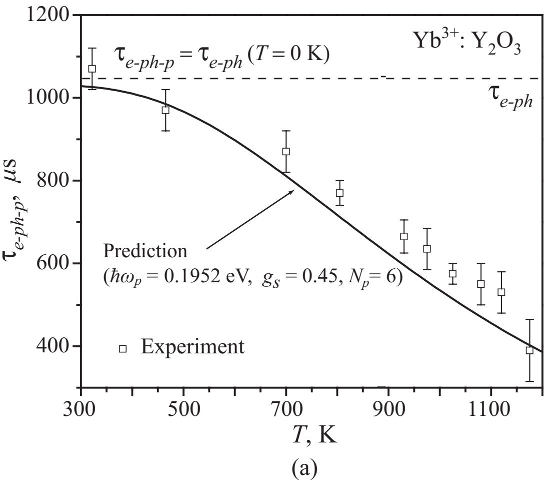

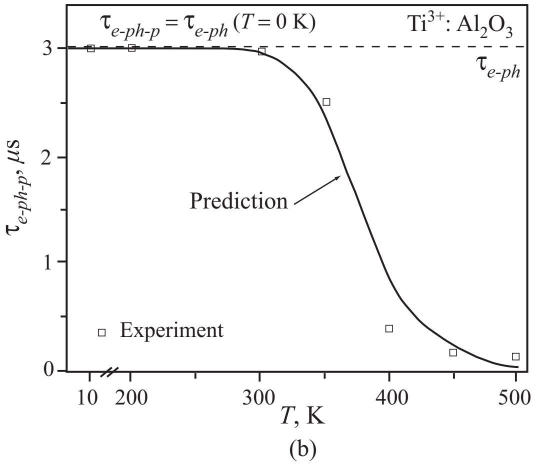

Figure 7.21. Lifetime (decay rate) measured for excited electron in (a) Yb^{3+} doped yttria [384], and (b) Ti^{3+}-doped alumina (sapphire) [369]. For (a) the prediction based on O–O cut-off frequency is also shown [238]. Here g_s is a coefficient that depends on the structure of the crystals.

Here n_a is the number density of absorption sites, and the nonequilibrium distribution function is

$$f^n_{ph}(T) = \frac{1}{\dfrac{g_{e,B}(\omega_2)n_{e,A}(\omega_1)}{g_{e,A}(\omega_1)n_{e,B}(\omega_2)} - 1} = \frac{1}{\dfrac{g_{e,B}(\omega_2)}{g_{e,A}(\omega_1)}\dfrac{A_{ph,a}(\omega)f_{ph}(\omega)}{\frac{A_{ph,e}(\omega)}{\eta_{e\text{-}ph}}[1+f_{ph}(\omega)]}}$$

$$= \frac{\eta_{e\text{-}ph}f_{ph}(\omega)}{1+f_{ph}(\omega)-\eta_{e\text{-}ph}f_{ph}(\omega)}, \qquad (7.163)$$

where we have used (7.65).

When the spontaneous emission dominates over the stimulated emission [i.e., occupation is $f_{ph}(\omega) \ll 1$], then f^n_{ph} is simplified to

$$f^n_{ph}(T) = \eta_{e\text{-}ph} f_{ph}(\boldsymbol{s}). \tag{7.164}$$

Note that $f^n_{ph}(T)$ is nonequilibrium distribution, and here it is proportional to the local distribution function $f_{ph}(\boldsymbol{s})$.

In Section 7.12.6 we will discuss *ab initio* calculations of $\dot{\gamma}_{e\text{-}ph}$ and $\dot{\gamma}_{e\text{-}p}$, for a simple ionic complex.

7.12 Anti-Stokes Fluorescence: Photon–Electron–Phonon Couplings

7.12.1 Anti-Stokes Laser Cooling (Phonon Absorption) of Ion-Doped Solids

Phonon assisted electronic transition by photon absorption, i.e., phonon-assisted, dipole-moment transition, is the cooperative process (Glossary) governing laser cooling of solids. The concept of laser cooling (optical refrigeration) by the anti-Stokes luminescence in solids was introduced in [372], where the thermal vibrational energy can be removed by the anti-Stokes fluorescence in which a material is excited with photons having an energy below the mean fluorescence energy. Initially, it was believed that optical cooling by the anti-Stokes fluorescence contradicted the second law of thermodynamics [476, 477], suggesting that the cycle of excitation and fluorescence is reversible, and hence an energy yield greater than one would be equivalent to the complete transformation of heat to work. This was cleared up when entropy was assigned to radiation [264]. The entropy of a radiation field is proportional to its frequency bandwidth and also to the solid angle through which it propagates. Because the incident laser light has a small bandwidth and propagates in a well-defined direction, it has almost zero entropy. On the other hand, the fluorescence is broadband and is emitted in all directions, so if the power of the emission is equal to or greater than the incident beam, the emission has a comparatively large entropy.

Figures 7.22(a) to (e) show the energy diagram, as well as the steps identifying the mechanisms, in laser cooling of an ion-doped dielectric (otherwise transparent to the laser irradiation) solid. There the host crystal lattice is idealized as transparent to the pumping laser. Typical host crystals include $Y_3Al_5O_{12}$(YAG), $LiYF_4$, $LiSrAlF_6$, $Ca_5(PO_4)_3F$, $LaMgAl_{11}O_{19}$, $Gd_3Sc_2Ga_3O_{12}$, $La_2Be_2O_5$, Al_2O_3, $BeAl_2O_3$, and MgF_2 [369]. Some of its atoms are replaced with optically active, doped ions (e.g., Yb^{3+}), and thus become slightly absorbing. In quantum-mechanics the ion is represented by an effective transition dipole moment(or dipole operator), defined as a quantum mechanical spatial integral of the classical dipole moment $e_c\boldsymbol{x}$ (7.135), i.e.,

$$\boldsymbol{\mu}_e = \int \psi^*_f q \boldsymbol{x} \psi_i \mathrm{d}\boldsymbol{x}, \tag{7.165}$$

where q (here equal to e_c) is the electric charge, $\boldsymbol{x}$ is the position vector, and ψ_i and ψ_f are the initial- and final-state wave functions of the two level system. The electromagnetic field, which has a polarization vector $\boldsymbol{s}_{ph,\alpha}$, may interact with the

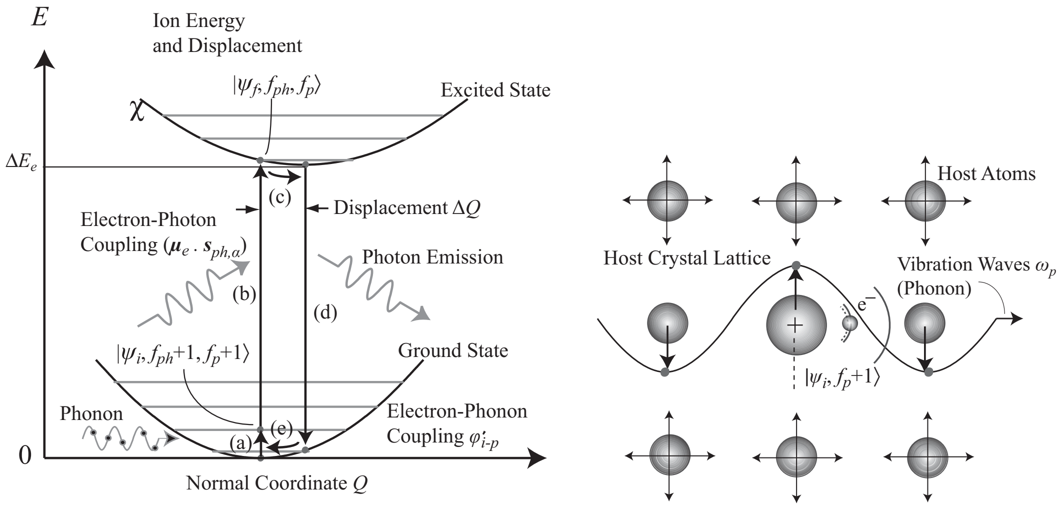

Configuration Coordinate Diagram

(a) Electron-phonon Coupling

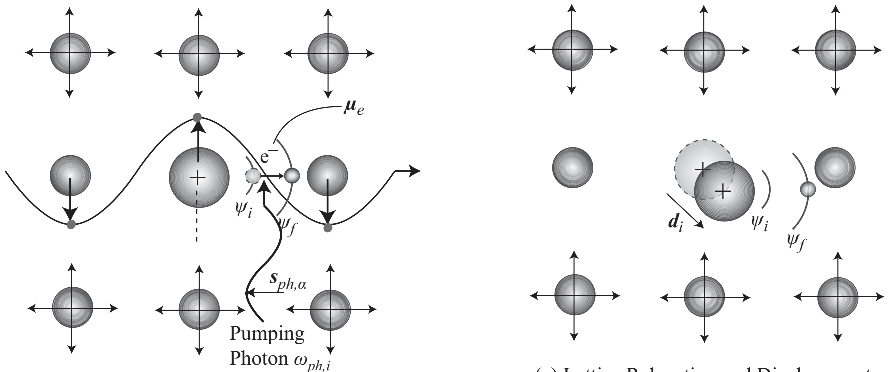

(b) Phonon Assisted Absorption
(under Born-Oppenheimer Approximation)

(c) Lattice Relaxation and Displacement
(under Energy Minimization)

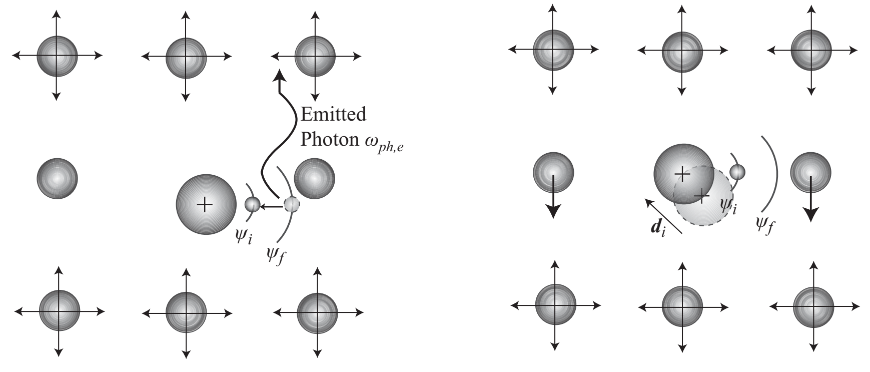

(d) Emission (under Born-Oppenheimer Approximation),
Ending in Ground State (Boltzmann Statistics)

(e) Lattice Relaxation and Restoring
(under Energy Minimization)

Figure 7.22. (a) The energy diagram, (b)–(e) five steps in the photon–electron–phonon couplings in the energy transfer cycle for the laser cooling of ion-doped dielectric solids. Photon absorption is assisted by phonon absorption, thus emitted photon (radiative decay) has a higher energy than the absorbed photon. Both excited and ground state ions couple with phonon through the displacement (shown with normal coordinate).

ion if the coupling factor $\boldsymbol{s}_{ph,\alpha} \cdot \boldsymbol{\mu}_e$ is nonzero (i.e., they are not orthogonal). The principal mechanisms of the photon–electron–phonon interactions resulting in the cooling effect in the solid, are shown in Figures 7.22(a)–(e). In step (a), the electron in the ground state is coupled to a phonon and forms a combined state.

In (b), when the medium is irradiated by laser light with a frequency $\omega_{ph,i}$ that is below the resonance frequency $\omega_{e,g}$ for the energy gap ($F_{5/2}$ to $F_{7/2}$ transition of the $4f$–$4f$ orbital transition, 10,250 cm^{-1} for Yb^{3+} ion in Y_2O_3, similar to results given in Figure 5.38), the electron has some probability of being excited by absorbing a photon from the pumping field and the coupled phonon, such that $\hbar\omega_{ph,i} + \hbar\omega_p = \hbar\bar{\omega}_{ph,e}$, where $\bar{\omega}_{ph,e} =$ mean emission angular frequency. According to the Born–Oppenheimer approximation, this electronic transition is instantaneous and the ion core does not move. In (c), after the electron is in the excited state, the charge distribution around the ion has been alternated, and the lattice will relax to new equilibrium positions. In (d), the electron then undergoes a radiative decay and returns to the ground state, emitting a photon with frequency $\omega_{ph,e}$. It is followed in (d) by another lattice-relaxation process that restores the lattice to its original positions.

If the average emitted photon frequency $\bar{\omega}_{ph,e}$ is larger than $\omega_{ph,i}$, the medium loses thermal energy and is cooled. A local temperature decrease was detected by a photothermal deflection technique, and the cooling efficiencies achieved in ytterbium-doped glass (up to 2%) were more than 10^4 times those observed in Doppler cooling of gases (Section 7.13.2). Since then, various ytterbium-doped glasses and crystals have been cooled [123, 133, 140, 164, 183, 295, 342, 382]. For the f-orbital transitions (rare-earth ions), an approximate relation for $\boldsymbol{\mu}_e$ is developed based on the transition charge distribution overlap [238].

7.12.2 Laser Cooling Efficiency

Figure 7.23(a) shows the energy transfer among photon–electron–phonon for Yb^{3+} ion a dielectric crystal (Y_2O_3). As shown in Figure 7.23(b), because of the ion–lattice coupling, the resonant, zero-phonon line in the absorption spectrum is broadened by the phonon sidebands, in which the electronic excitation may be assisted by absorbing one or more lattice phonons. The average emission wavelength $\bar{\lambda}_{ph,e}$ is independent of the excitation wavelength $\lambda_{ph,i}$ [110, 476]. This is in accordance with the Vavilov empirical rule [476], which states that the shape of the emission spectrum of a transition is essentially independent of the wavelength at which it is excited. Although this is not true for all materials, in the case of ytterbium in crystals, the time scale of thermal interactions ($\sim 10^{-12}$ s to 10^{-9} s) is orders of magnitude shorter compared with the time scale for optical transitions (of the order of 10^{-3} s) [134]. This implies that no matter what photon wavelength $\lambda_{ph,i}$ is used to excite the ytterbium transition, the population distribution in the upper manifold reaches thermal equilibrium before relaxing to the ground-state manifold, so, the emission spectra is independent of the pumping wavelength. The absorption spectrum (dimensionless $E^*_{ph,e}$) of Yb^{3+}: ZBLANP is shown in Figure 7.23(b) [275]. Apart from the strongest

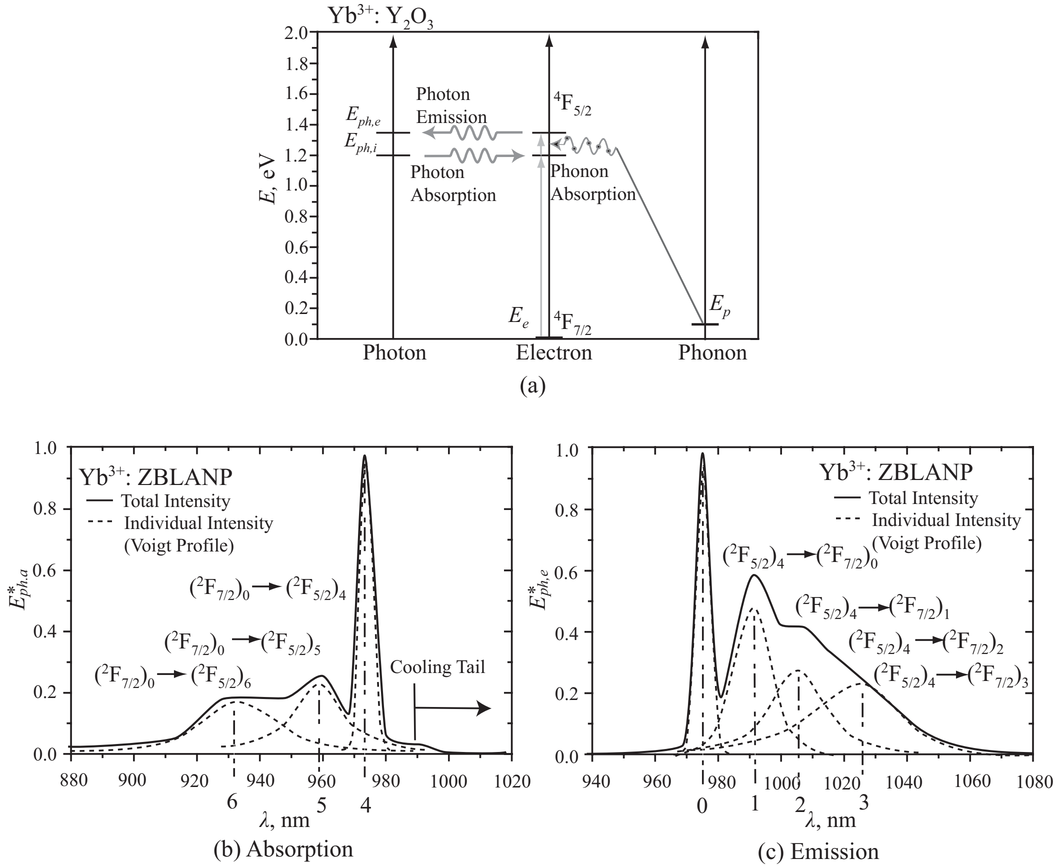

(b) Absorption

(c) Emission

Figure 7.23. (a) Energy spectra of all three energy carriers in irradiated Yb^{3+}:Y_2O_3. Yb^{3+} has only two main electronic levels: $^4F_{7/2}$ and $^4F_{5/2}$. The Russel-Saunders term symbols are used for electronic states. (b) Dimensionless absorption spectrum of Yb^{3+}: ZBLANP at $T = 10$ K. The transitions $(^2F_{5/2})_4 \rightarrow (^2F_{7/2})_{0,1,2,3}$, from the first excited manifold to four ground level manifolds are extrapolated (Voigt profile) and are also shown. (c) Dimensionless emission spectrum for the same [275].

resonance transition $(^2F_{5/2})_4 \rightarrow {}^2(F_{7/2})_0$, there exist 3 phonon sideband transitions designated as (1,2,3). When the mean absorbed phonon energy is larger than the average emitted phonon (the 3 vibronic transitions), cooling occurs. The conditions for cooling and heating are

$$\hbar\omega_{ph,i} - \hbar\bar{\omega}_{ph,e} = \hbar\omega_p < 0 \ \text{ cooling (anti-Stokes process)}$$

$$\hbar\omega_{ph,i} - \hbar\bar{\omega}_{ph,e} = \hbar\omega_p > 0 \ \text{ heating (Stokes process),} \qquad (7.166)$$

where $\omega_{ph,i}$ is the incoming photon frequency, $\bar{\omega}_{ph,e}$ is the average emission photon frequency, and ω_p is the single phonon frequency.

The emission spectrum (dimensionless $E^*_{ph,a}$) of Yb^{3+}: ZBLANP in Figure 7.23(c) shows that there are also three sub-levels in the excited state manifold. Note that the shift of emission to the long wavelengths in Figure 7.23(c) is that also predicted by the reciprocity discussed in Section 7.9.2, and also shown in Figure 7.21(b). In Figure 7.18(b), the mean emission wavelength $\bar{\lambda}_{ph,e}$, shown as the vertical line, is defined as

$$\bar{\lambda}_{ph,e} = \frac{\int_0^\infty E_{ph,\lambda}\lambda \mathrm{d}\lambda}{\int_0^\infty E_{ph,\lambda}\mathrm{d}\lambda}. \quad (7.167)$$

The absorption at wavelengths longer than $\bar{\lambda}_{ph,e}$ is defined as the cooling tail. This is a phonon-assisted absorption process, as was shown in Figure 7.22. Note that $\sigma_{ph,\omega}$ and $E_{ph,\omega}$ are related through the absorption and emission cross-section area, given by reciprocity relation (7.144). Then the laser cooling efficiency is defined as the ratio between the net cooling power and the absorbed laser power, i.e.,

$$\eta_{p\text{-}ph} = \frac{\bar{\omega}_{ph,e} - \omega_{ph,i}}{\omega_{ph,i}} = \frac{\bar{\omega}_{ph,e} - (\omega_{e,g} - N_p\omega_p)}{\omega_{e,g} - N_p\omega_p} = \frac{\lambda_{ph,i} - \bar{\lambda}_{ph,e}}{\bar{\lambda}_{ph,e}} \quad \text{laser cooling efficiency,} \quad (7.168)$$

where N_p is the number of phonons involved in one transition. It is evident that $\eta_{p\text{-}ph}$ increases as $N_p\omega_p$ increases, indicating that higher-energy phonons are desirable, to couple to the anti-Stokes electron excitation.

The cooling efficiency $\eta_{p\text{-}ph}$ increases as the pumping wavelength $\lambda_{ph,i}$ increases. However, the excitation probability $\dot{\gamma}_{ph\text{-}e}$ (which determines the absorption coefficient $\sigma_{ph,\lambda,i}$, and also the extinction index $\kappa_{\lambda,i}$) becomes too small if the pumping wavelength is too long. Thus the cooling efficiency $\eta_{p\text{-}ph}$ of different materials (or structures) are compared at the same excitation probability. We consider the excitation probability in the cooling tail, where the energy $\hbar(\omega_{e,g} - \omega_{ph,i})$ is provided by annihilation of the lattice phonons. This multiphonon-assisted anti-Stokes excitation process is one of the multiphonon phenomena, which also include multiphonon Stokes excitation, multiphonon relaxation, and multiphonon energy transfer. For the multiphonon anti-Stokes excitation, the process involving the smallest number of phonons is the most probable. Thus, as a first approximation, only the cut-off phonons have been assumed to couple effectively to the anti-Stokes excitation of the electron, although phonons of various energies are available in the lattice [14]. However, this approach generally does not give a detailed fit to experimental spectra. To resolve the experimental spectra, different phonon modes should be used according to different pumping wavelengths, so that the energy requirement $\hbar\omega_{ph,i} + \hbar\omega_p = \hbar\omega_{e,g}$ is satisfied without assuming any arbitrary broadening. To do this, the phonon DOS obtained by lattice dynamics calculations should be included. A thorough model (for weak couplings) has been developed for this purpose [140, 141] by considering one phonon absorption, and is confirmed in modeling the laser cooling in bulk materials. Here, the solution procedure is briefly introduced in the next section. Later, we discuss strong couplings and the derivations leading to *ab initio* computations.

7.12.3 Photon–Electron–Phonon Transition Rate Using Weak Coupling Approximation

Because a much longer pumping wavelength than the resonance is used in laser cooling, the probability of a purely electronic transition (the first order process) between electronic sublevels becomes very small. While the phonon-assisted transition, a second-order process, begins to contribute significantly to absorption. As a result, the absorption turns out to be a combination of the first-order and second-order transitions. Because the first-order process does not involve phonons, only the second-order process is analyzed here for the purpose of understanding the role of phonons in laser cooling.

In the second-order process, the ion in its ground state absorbs an incident photon and a phonon, and moves up to the excited state. The probability per unit time of such a process can be evaluated using the perturbation theory. The Hamiltonian for the physical system considered is given by [140]

$$\mathrm{H} = \mathrm{H}_e + \mathrm{H}_p + \mathrm{H}_{ph} + \mathrm{H}_{ph\text{-}e} + \mathrm{H}_{e\text{-}p}. \tag{7.169}$$

The first term is[†] (neglecting the 1/2 energy term)

$$\mathrm{H}_e = \hbar\omega_{e,g} a^\dagger a, \tag{7.170}$$

i.e., the Hamiltonian of the ion electronic levels, where $\hbar\omega_{e,g}$ is the energy difference between the optically active energy levels of the dopant ion (considered as a two-level ion) and $a^\dagger$. (a) is the creation (annihilation) operator of an electronic excitation. Again, we have neglected the 1/2 term appearing in the Hamiltonian by using the ladder operator (Section 2.6.5 footnote)

The second term is (Section 4.5)

$$\mathrm{H}_p = \sum_p \hbar\omega_p b^\dagger b, \tag{7.171}$$

i.e., the phonon field Hamiltonian, where ω_p is the phonon frequency and $b^\dagger(b)$ is the creation (annihilation) operator of a phonon in mode p. Again, we have neglected the 1/2 term.

The third term is (Section 7.3.1)

$$\mathrm{H}_{ph} = \hbar\omega_{ph,i} c^\dagger c, \tag{7.172}$$

i.e., the electromagnetic laser field Hamiltonian, where $\omega_{ph,i}$ is the pumping frequency and $c^\dagger(c)$ is the creation (annihilation) operator of a photon.

The fourth term is that developed in Section 7.3.2, i.e., (7.36), which we write as

$$\begin{aligned}\mathrm{H}_{ph\text{-}e} &= -\boldsymbol{s}_{ph,i}\cdot\boldsymbol{\mu}_e\left(\frac{\hbar\omega_{ph,i}}{2\epsilon_\mathrm{o}V_s}\right)^{1/2}(c^\dagger + c)(a^\dagger + a)\\ &= C_{ph\text{-}e}(c^\dagger + c)(a^\dagger + a),\quad C_{ph\text{-}e} \equiv -\boldsymbol{s}_{ph,i}\cdot\boldsymbol{\mu}_e\left(\frac{\hbar\omega_{ph,i}}{2\epsilon_\mathrm{o}V_s}\right)^{1/2},\end{aligned} \tag{7.173}$$

[†] Following the footnote of Section 2.6.4, we use $(a, a^\dagger)$ for electron, $(b, b^\dagger)$ for phonon , and $(c, c^\dagger)$ for photon.

i.e., the photon–electron interaction Hamiltonian, where $\boldsymbol{s}_{ph,i}$ is the polarization vector of the photon, $\boldsymbol{\mu}_e$ is the transition dipole moment of the electronic transition, $\epsilon_{\rm o}$ is the vacuum permittivity, and V_s is the interacting volume. Note that from (3.36) the term $[\hbar\omega_{ph,i}/(2\epsilon_{\rm o}V_s)]^{1/2}$ is the vacuum electric field per photon.

(A) *Acoustic Phonons*

The fifth term is the electron–phonon interaction Hamiltonian that can be described as distortion of the ligand ions affecting the crystal field. Such a distortion is a function of the local strain; therefore we can expand the crystal field potential in powers of such a strain. The Local strain is defined by the strain term $\epsilon_{i,j}$ as

$$\epsilon_{i,j} = \frac{1}{2}(\frac{\partial \boldsymbol{d}_i}{\partial x_j} + \frac{\partial \boldsymbol{d}_j}{\partial x_i}) \quad (i, j = 1, 2, 3), \tag{7.174}$$

which is also given in Table 3.11. For simplicity we shall assume that

$$\epsilon \approx \frac{\partial \boldsymbol{d}}{\partial x}\ |_{x=0}, \tag{7.175}$$

thus not taking into any account the anisotropy of the elastic waves. We take as origin for the coordinate axes to point of the lattice in which the nucleus of the ion is located.

The displacement $\boldsymbol{d}$ is given by (4.47), and its derivative is expressed as [369]

$$\frac{\partial \boldsymbol{d}}{\partial x}\ |_{x=0} = (\frac{\hbar\omega_p}{2\rho u_p^2})^{1/2}(b - b^\dagger). \tag{7.176}$$

Then the crystal field Hamiltonian, H_c in terms of strain is

$$\mathrm{H}_c = \mathrm{H}_{\rm o} + \varphi_{e\text{-}p,\mathrm{A}}\epsilon, \tag{7.177}$$

where $\mathrm{H}_{\rm o}$ is the static crystal field Hamiltonian term and higher-order terms are neglected. The the interaction Hamiltonian becomes

$$\begin{aligned}\mathrm{H}_{e\text{-}p} &= \varphi_{e\text{-}p,\mathrm{A}}\epsilon\\ &= \varphi_{e\text{-}p,\mathrm{A}}(\frac{\hbar\omega_p}{2\rho u_p^2})^{1/2}(b - b^\dagger)\\ &= C_{e\text{-}p,\mathrm{A}}(b - b^\dagger),\ \ C_{e\text{-}p} \equiv \varphi_{e\text{-}p,\mathrm{A}}(\frac{\hbar\omega_p}{2\rho u_p^2})^{1/2},\end{aligned} \tag{7.178}$$

i.e., the electron–phonon interaction Hamiltonian, where $\varphi_{e\text{-}p,\mathrm{A}}$ is the acoustic interaction potential that is analogous to (5.177), ω_p is the phonon frequency, u_p is the average speed of sound, and ρ is the mass density.

This process appears in the second-order term of the perturbation expansion, and the transition (photon-induced, phonon-assisted absorption) rate $\dot{\gamma}_{ph\text{-}e\text{-}p}$, which (is the dominant rate controlling mechanism; thus we have a weak phonon coupling) is given by the FGR (3.27) [140], i.e,

$$\dot{\gamma}_{ph\text{-}e\text{-}p} = \sum_f \dot{\gamma}_{e,i\text{-}f} = \frac{2\pi}{\hbar}\sum_f |M_{f,i}|^2\delta_{\rm D}(E_f - E_i), \tag{7.179}$$

where E_i and E_f are, respectively, the initial and final energies of the electron system. The interaction matrix element $M_{f,i}$ admits a perturbative expansion given by [140]

$$M_{fi} = \langle f|\mathrm{H}_{int}|i\rangle + \sum_m \frac{\langle f|\mathrm{H}_{int}|m\rangle\langle m|\mathrm{H}_{int}|i\rangle}{E_{e,i} - E_{e,m}} + \sum_{m,n} \frac{\langle f|\mathrm{H}_{int}|m\rangle\langle m|\mathrm{H}_{int}|n\rangle\langle n|\mathrm{H}_{int}|i\rangle}{(E_{e,i} - E_{e,m})(E_{e,i} - E_{e,n})} + \cdots, \tag{7.180}$$

with $\mathrm{H}_{int} = \mathrm{H}_{e\text{-}ph} + \mathrm{H}_{e\text{-}p}$. The summations on m and n include all the intermediate phonon and photon states.

We calculate the transition probability $\dot{\gamma}_{ph,a}$ between initial $|i\rangle = |\psi_i, f_{ph} + 1, f_p + 1\rangle$ and final $|f\rangle = |\psi_f, f_{ph}, f_p\rangle$ states of the system, where the first ket element ψ_i refers to the ion (electronic) state, the second one, f_{ph}, to the photon number in the interacting volume V_s, and the third one, f_p, to the phonon distribution function. These types of processes appear only in the second-order perturbation expansion of the $M_{f,i}$ interaction matrix, which gives [23, 369]

$$\begin{aligned}
M_{fi,2nd} &= \sum_m \frac{\langle f|\mathrm{H}_{int}|m\rangle\langle m|\mathrm{H}_{int}|i\rangle}{E_{e,i} - E_{e,m}} \\
&= \sum_m \Bigg[\frac{\langle \psi_f, f_{ph}, f_p|\mathrm{H}_{e\text{-}ph}|\psi_m, f_{ph}+1, f_p\rangle}{E_i - (E_m - \hbar\omega_p)} \\
&\quad \times \langle \psi_m, f_{ph}+1, f_p|\mathrm{H}_{e\text{-}p}|\psi_i, f_{ph}+1, f_p+1\rangle \\
&\quad + \frac{\langle \psi_f, f_{ph}, f_p|\mathrm{H}_{e\text{-}p}|\psi_m, f_{ph}, f_p+1\rangle}{E_i - (E_m - \hbar\omega_{ph})} \\
&\quad \times \langle \psi_m, f_{ph}, f_p+1|\mathrm{H}_{e\text{-}ph}|\psi_i, f_{ph}+1, f_p+1\rangle \Bigg] \\
&\simeq \sum_m \frac{\langle \psi_f, f_{ph}, f_p|C_{ph\text{-}e}(a^\dagger + a)(c^\dagger + c)|\psi_m, f_{ph}+1, f_p\rangle}{E_i - (E_m - \hbar\omega_p)} \\
&\quad \times \langle \psi_m, f_{ph}+1, f_p|a_{e\text{-}p}C_{e\text{-}p}a^\dagger a(b - b^\dagger)|\psi_i, f_{ph}+1, f_p+1\rangle \\
&= \sum_m \frac{\langle \psi_f, f_{ph}, f_p|C_{ph\text{-}e}(a^\dagger + a)(c^\dagger + c)|\psi_m, f_{ph}+1, f_p\rangle}{E_i - (E_m - \hbar\omega_p)} \\
&\quad \times \langle \psi_m, f_{ph}+1, f_p|C_{e\text{-}p}a^\dagger a(b - b^\dagger)|\psi_i, f_{ph}+1, f_p+1\rangle \\
&= \sum_m \frac{\langle \psi_f, f_{ph}, f_p|C_{ph\text{-}e}(a^\dagger + a)f_{ph}^{1/2}|\psi_m, f_{ph}, f_p\rangle}{E_i - (E_m - \hbar\omega_p)} \\
&\quad \times \langle \psi_m, f_{ph}+1, f_p|C_{e\text{-}p}a^\dagger a f_p^{1/2}|\psi_i, f_{ph}+1, f_p\rangle \\
&= \sum_m C_{ph\text{-}e} f_{ph}^{1/2} C_{e\text{-}p} f_p^{1/2} \frac{\langle \psi_f|(a^\dagger + a)|\psi_m\rangle\langle \psi_m|a^\dagger a|\psi_i\rangle}{E_i - (E_m - \hbar\omega_p)}.
\end{aligned} \tag{7.181}$$

The energy symbol with no subscript indicates the total energy (whereas subscripts e indicate electron system only). The approximation is based on not allowing transition to states lower than the lowest excited manifold, so we have phonon absorption followed by photon absorption [Figure 7.22(a)]. Because the phonon energy $\hbar\omega_p$ is much smaller than the energy gap, it cannot by itself induce an electronic transition. In the perturbation theory the intermediate wave function ψ_m is then approximated as unperturbed, i.e., $\psi_m = \psi_i$, and $E_m = E_i$. Hence, using the definition of matrix element (5.94), (7.181) becomes

$$\begin{aligned} M_{f,i,2nd} &= \sum_p C_{ph\text{-}e} f_{ph}^{1/2} C_{e\text{-}p} f_p^{1/2} \frac{\langle\psi_f|(a^\dagger + a)|\psi_i\rangle\langle\psi_i|a^\dagger a|\psi_i\rangle}{E_i - (E_i - \hbar\omega_p)} \\ &= \sum_m C_{ph\text{-}e} f_{ph}^{1/2} C_{e\text{-}p} f_p^{1/2} \frac{\langle\psi_f|(a^\dagger + a)|\psi_i\rangle\langle\psi_i|a^\dagger a|\psi_i\rangle}{E_i - (E_i - \hbar\omega_p)} \\ &= \sum_m C_{ph\text{-}e} f_{ph}^{1/2} C_{e\text{-}p} f_p^{1/2} \frac{1}{\hbar\omega_p}, \end{aligned} \tag{7.182}$$

where we have used $\langle\psi_i|a^\dagger a|\psi_i\rangle = 1$, $\langle\psi_f|a|\psi_i\rangle = 0$, and $\langle\psi_f|a^\dagger|\psi_i\rangle = 1$. These are due to the use of the number operator, applying the lowering operator to the ground state, and the definition of the raising ladder operator (Section 2.6.4), respectively.

Substituting (7.182) into (7.179), we have [140]

$$\dot{\gamma}_{ph\text{-}e\text{-}p} = \sum_f \dot{\gamma}_{e,i\text{-}f} = \frac{2\pi}{\hbar} \sum_p (\frac{C_{ph\text{-}e} C_{e\text{-}p}}{\hbar\omega_p})^2 f_{ph} f_p \delta_{\rm D}(\hbar\omega_{ph,i} + \hbar\omega_p - \hbar\omega_{e,g}). \tag{7.183}$$

To perform the summation on the phonon modes in (7.183), we must introduce the phonon DOS $D_p(E_p)$. In terms of this distribution function, transition rate (7.183), becomes an integral given as

$$\begin{aligned} \dot{\gamma}_{ph\text{-}e\text{-}p} &= \frac{2\pi}{\hbar} C_{ph\text{-}e}^2 f_{ph} \frac{\varphi_{e\text{-}p,\rm A}^2}{2\rho u_p^2} \int_{E_{min}}^{E_{max}} {\rm d}E_p D_p(E_p) \frac{f_p^{\rm o}(E_p)}{E_p} \\ &\quad \times \delta_{\rm D}(\hbar\omega_{ph,i} + E_p - \hbar\omega_{e,g}) \\ &= \frac{2\pi}{\hbar} C_{ph\text{-}e}^2 f_{ph} \frac{\varphi_{e\text{-}p,\rm A}^2}{2\rho u_p^2} \frac{D_p(E_p) f_p^{\rm o}(E_p)}{E_p}, \end{aligned} \tag{7.184}$$

where E_p is the phonon energy given by $E_p = \hbar\omega_{e,g} - \hbar\omega_{ph,i}$ and $\varphi_{e\text{-}p,\rm A}$ was defined in (7.178). It implies that the excitation spectra can be well associated with the phonon spectra, as observed in [335]. Here we have used the equilibrium distribution functions for phonons. Then (7.184) is rewritten as

$$\begin{aligned} \dot{\gamma}_{ph\text{-}e\text{-}p} &= \frac{2\pi}{\hbar} \frac{(\boldsymbol{s}_{ph,i} \cdot \boldsymbol{\mu}_e)^2}{2\epsilon_{\rm o}} \frac{\varphi_{e\text{-}p,\rm A}^2}{2\rho u_p^2} \frac{D_p(E_p) f_p^{\rm o}(E_p)}{E_p} \hbar\omega_{ph,i} \frac{f_{ph}}{V_s} \\ &= \frac{2\pi}{\hbar} \frac{(\boldsymbol{s}_{ph,i} \cdot \boldsymbol{\mu}_e)^2}{2\epsilon_{\rm o}} \frac{\varphi_{e\text{-}p,\rm A}^2}{2\rho u_p^2} \frac{D_p(E_p) f_p^{\rm o}(E_p)}{E_p} e_{ph,i}, \end{aligned} \tag{7.185}$$

where $e_{ph,i}$ is the incident photon energy density (per unit solid volume) also used in (7.2).

(B) *Optical Phonons*

When specific normal modes of vibration dominate the electron–phonon interaction, it is useful to express the electron–phonon interaction Hamiltonian in terms of normal coordinates, which is presented as (5.163) and (5.164). Because the optical deformation potential that is analogous to (5.187), the crystal field Hamiltonian term (7.177) can be replaced with [238]

$$\mathrm{H}_c = \mathrm{H}_\mathrm{o} + \varphi'_{e\text{-}p,\mathrm{O}} Q_q . \tag{7.186}$$

Again, the higher-order terms have been neglected. Then the interaction Hamiltonian term (7.178) becomes

$$\begin{aligned} \mathrm{H}_{e\text{-}p} &= \varphi'_{e\text{-}p,\mathrm{O}} Q_q \\ &= \varphi'_{e\text{-}p,\mathrm{O}} \left(\frac{\hbar}{2m_{\mathrm{AC}}\omega_p}\right)^{1/2} (b_q + b_q^\dagger) \\ &= C_{e\text{-}p,\mathrm{O}}(b_q + b_q^\dagger), \quad C_{e\text{-}p} \equiv \varphi'_{e\text{-}p,\mathrm{O}} \left(\frac{\hbar}{2m_{\mathrm{AC}}\omega_p}\right)^{1/2}, \end{aligned} \tag{7.187}$$

where $\varphi'_{e\text{-}p,\mathrm{O}}$ is the electron–phonon coupling similar to deformation potential (5.187), ω_p is the phonon frequency, m_{AC} is the mass of the reduced oscillating atom, and $b_q(b_q^\dagger)$ is the creation (annihilation) operator in normal coordinates. Note that $(\hbar/2m_{\mathrm{AC}}\omega_p)^{1/2}$ represents the atomic displacement (2.59). Then going through FGR 3.27) similar to acoustic phonons by using the new interaction matrix, we rewrite (7.185) as

$$\dot{\gamma}_{ph\text{-}e\text{-}p} = \frac{1}{\tau_{ph\text{-}e\text{-}p}} = \frac{\pi\hbar}{2m_{\mathrm{AC}}\epsilon_\mathrm{o}} (\mathbf{s}_{ph,i} \cdot \boldsymbol{\mu}_e)^2 \varphi'^2_{e\text{-}p,\mathrm{O}} \frac{D_p(E_p) f_p^\mathrm{o}(E_p)}{E_p^3} \hbar\omega_{ph,i} \frac{f_{ph}}{V_s}. \tag{7.188}$$

Note that now $D_p(E_p)$ is the phonon DOS for normal (local) modes that may be different from $D_p(E_p)$ for the bulk host material. Also, note that D_p maybe represented by the Debye–Gaussian model (4.29) [e.g., Figure 4.8(c)]. The theoretical treatment of $\varphi'_{e\text{-}p,\mathrm{O}}$ is given in [238], and Figures 7.24(a) to (c) show aspects of the material metrics of laser cooling of solids [238]. Figure 7.24(a) shows the phonon assisted electronic excitation for Yb^{3+}. Figures 7.24(b) and (c) show that although strong phonon coupling is desirable in excitation, it is not desired in the decay (since it reduces the quantum efficiency).

An analytical, harmonic approximation relation for $\varphi'_{e\text{-}p,\mathrm{O}}$ is given in [240]. This gives $\varphi'_{e\text{-}p,\mathrm{O}} = \Gamma_{\mathrm{IAC}} \Delta x^2_{\mathrm{min}}/2r_{nn}$, where Γ_{IAC} is the ion-ligand force constant, Δx_{min} is given by (2.59) and r_{nn} is the distance between the ion and its nearest cation.

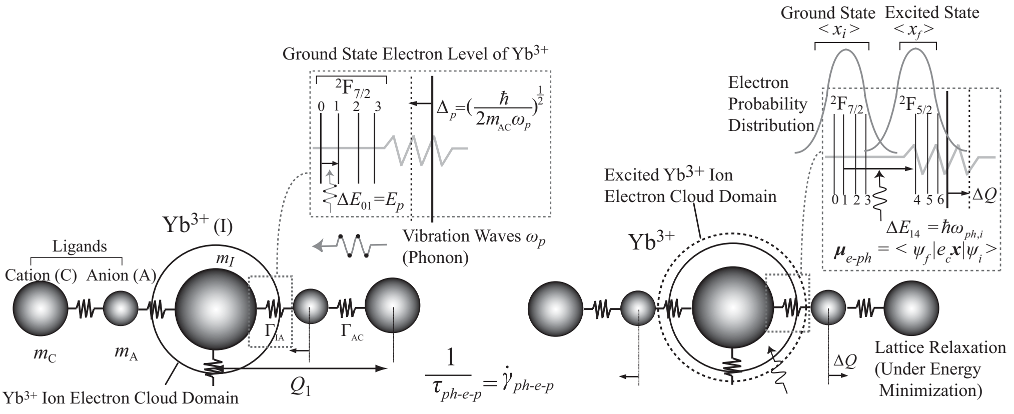
Ground State Electron Level of Yb^{3+}
$^2F_{7/2}$
0 1 2 3
$\Delta_p = (\frac{\hbar}{2m_{AC}\omega_p})^{\frac{1}{2}}$
$\Delta E_{01} = E_p$
Vibration Waves ω_p (Phonon)
Yb^{3+} (I)
Ligands
Cation (C) Anion (A)
m_I
m_C
m_A
Γ_{IA}
Γ_{AC}
Q_1
Yb^{3+} Ion Electron Cloud Domain
$\frac{1}{\tau_{ph\text{-}e\text{-}p}} = \dot{\gamma}_{ph\text{-}e\text{-}p}$
Ground State Excited State
$<x_i>$ $<x_f>$
Electron Probability Distribution
$^2F_{7/2}$ $^2F_{5/2}$
0 1 2 3 4 5 6
ΔQ
$\Delta E_{14} = \hbar\omega_{ph,i}$
$\mu_{e\text{-}ph} = <\psi_f|e_c\mathbf{x}|\psi_i>$
Excited Yb^{3+} Ion Electron Cloud Domain
Yb^{3+}
Lattice Relaxation (Under Energy Minimization)

(a) Photon-Induced, Phonon-Assisted, Electronic Transition in Weak Electron–Phonon Coupling Regime

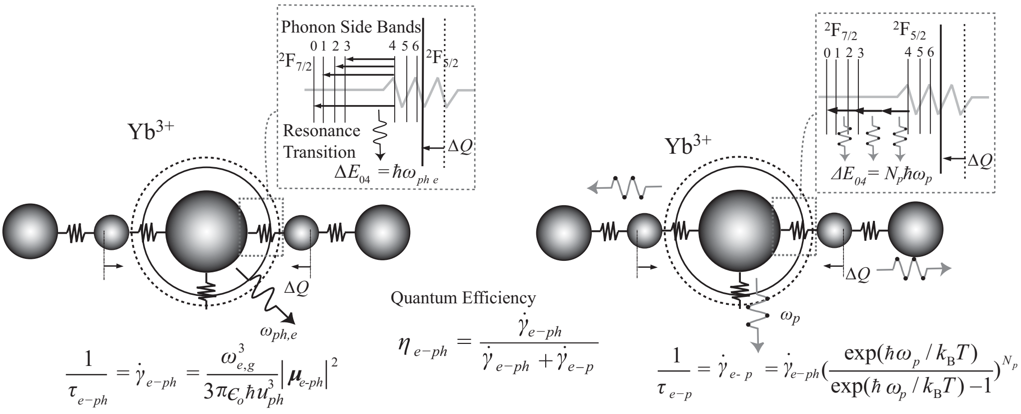
Phonon Side Bands
0 1 2 3 4 5 6
$^2F_{7/2}$ $^2F_{5/2}$
Resonance Transition
$\Delta E_{04} = \hbar\omega_{ph\,e}$
ΔQ
Yb^{3+}
$\omega_{ph,e}$
$\frac{1}{\tau_{e-ph}} = \dot{\gamma}_{e-ph} = \frac{\omega_{e,g}^3}{3\pi\epsilon_o\hbar u_{ph}^3}|\mu_{e\text{-}ph}|^2$
Quantum Efficiency
$\eta_{e-ph} = \frac{\dot{\gamma}_{e-ph}}{\dot{\gamma}_{e-ph} + \dot{\gamma}_{e-p}}$
$^2F_{7/2}$ $^2F_{5/2}$
0 1 2 3 4 5 6
$\Delta E_{04} = N_p\hbar\omega_p$
ΔQ
Yb^{3+}
ω_p
$\frac{1}{\tau_{e-p}} = \dot{\gamma}_{e-p} = \dot{\gamma}_{e-ph}(\frac{\exp(\hbar\omega_p/k_BT)}{\exp(\hbar\omega_p/k_BT)-1})^{N_p}$

(b) Radiative Transition (Resonance)

(c) Multiphonon Nonradiative Transition in Strong Electron–Phonon Coupling Regime

Figure 7.24. Material metrics of the photon–electron–phonon interactions in laser cooling of Yb^{+3}-doped solids. (a) Model for the optical-phonon coupling with a bound electron followed by photon absorption. (b) Purely radiative emission process. The phonon side band transitions are also shown. (c) Purely nonradiative emission process. The quantum efficiency η_{e-ph} is also defined by the ratio of radiative transition rate to total transition rate. The various variables will be discussed in the texts of the related sections [238].

7.12.4 Time Scales for Laser Cooling of Solids (Weak Couplings)

In the weak coupling analysis the kinetics of laser cooling cycle has been presented with various characteristic times, namely, $\tau_{ph\text{-}e}$, $\tau_{e\text{-}p}$ and $\tau_{ph\text{-}e\text{-}p}$.

A variety of parameters can be used to describe the photon–electron interaction, e.g., the Einstein $\dot{\gamma}_{ph,e,sp}$ given in (7.37), $\dot{\gamma}_{ph,a}$ given by (7.184), the radiative lifetime ($\tau_r = \tau_{ph\text{-}e}$), the oscillator strength, or the absorption cross-section area. These parameters are all governed by the transition dipole moment, which is a more fundamental quantity. For example, the Einstein A coefficient $\dot{\gamma}_{ph,e,sp}$ in (7.37) (equivalent to the radiative decay rate $\dot{\gamma}_r$) and the radiative lifetime $\tau_r = \tau_{ph,e,sp} = \tau_{ph\text{-}e}$

(applied to anti-Stokes emission dominated by spontaneous emission, as demonstrated in Section 7.4.3) are related to the transition dipole moment by (3.43) [194]

$$\dot{\gamma}_{ph,e,sp} = \dot{\gamma}_{ph\text{-}e} = \frac{\omega_{e,g}^3}{3\pi\epsilon_{\mathrm{o}}\hbar u_{ph}^3}\langle\mu_{ph\text{-}e}\rangle^2 \tag{7.189}$$

$$\tau_{ph,e,sp} = \tau_{ph\text{-}e} = \frac{1}{\dot{\gamma}_{ph,e,sp}} = \frac{3\pi\epsilon_{\mathrm{o}}\hbar u_{ph}^3}{\omega_{e,g}^3}\frac{1}{\langle\mu_{ph\text{-}e}\rangle^2}, \tag{7.190}$$

where ϵ_{o} is the free-space electric permittivity and $\langle\mu_{ph\text{-}e}\rangle$ is the spatial average of the photon polarization and transition dipole moment vectors and is defined as $\langle\mu_{ph\text{-}e}\rangle^2 = \langle(\mathbf{s}_{ph,i}\cdot\boldsymbol{\mu}_{ph\text{-}e})^2\rangle = (\mu_{ph\text{-}e}/3^{\frac{1}{2}})^2$.

The multiphonon decay process is given by [392] [also given by (7.154)

$$\dot{\gamma}_{e\text{-}p} = \dot{\gamma}_{ph\text{-}e}[1 - \frac{\exp(\hbar\omega_{p,c}/k_{\mathrm{B}}T)}{\exp(\hbar\omega_{p,c}/k_BT) - 1}]^{N_p}, \quad N_p = \frac{E_{e,g}}{\hbar\omega_{p,c}}. \tag{7.191}$$

The photon-induced phonon-assisted transition time $\tau_{ph\text{-}e\text{-}p}$ is given by the inverse of (7.188) assuming that the photon density of state f_{ph} integrates to one for an incoming laser (monochromatic and single-photon interaction). The predicted $\tau_{ph\text{-}e\text{-}p}$ can be directly compared with other transition times by defining the photon-induced, photon-assisted transition dipole moment $\mu_{ph\text{-}e\text{-}p}$ i.e.,

$$\dot{\gamma}_{ph\text{-}e\text{-}p} = \frac{1}{\tau_{ph\text{-}e\text{-}p}} = \frac{\omega_{e,g}^3}{3\pi\epsilon_{\mathrm{o}}\hbar u_{ph}^3}\frac{3\pi^2\hbar^2u_{ph}^3\hbar\omega_{ph,i}}{2m_{\mathrm{AC}}\omega_{e,g}^3V_s}\frac{\varphi'^2_{e\text{-}p,\mathrm{O}}D_p(E_p)f_p^{\mathrm{o}}(E_p)}{E_p^3}\langle\mu_{ph\text{-}e}\rangle^2$$

$$\equiv \frac{\omega_{e,g}^3}{3\pi\epsilon_{\mathrm{o}}\hbar u_{ph}^3}\langle\mu_{ph\text{-}e\text{-}p}\rangle^2. \tag{7.192}$$

In Figure 7.25, variations of the predicted photon-induced, phonon-assisted transition lifetime with respect to temperature, is compared with the experimental results of [164], for Yb^{3+}: ZrF, and good agreement is found. Also shown is the temperature dependence of $\tau_{e\text{-}p} = \dot{\gamma}_{e\text{-}p}^{-1}$.

The sample temperature depends on the balance between the thermal load (radiative heat transfer from surroundings) and the laser cooling rate. The simplified analysis of the laser cooling of a sample used in [164] is given here. The sample is a 7 mm long, 170 μm diameter optical fibre, subject to laser irradiation from one end, as shown in Figure 7.26. The only external load is the thermal radiation from the surroundings. Because the external radiative resistance is much larger than the internal conductive resistance, the sample can be assumed to be at uniform temperature T, and the macroscopic, steady-state, integral-volume energy equation (Table 1.1) is

$$Q_{ph,s} = \dot{S}_{ph\text{-}e\text{-}p}, \tag{7.193}$$

where the thermal radiation load $Q_{ph,s}$ is given by

$$Q_{ph,s} = (\frac{1}{2}\pi D^2 + \pi DL)\epsilon_{ph}\sigma_{\mathrm{SB}}(T_s^4 - T_\infty^4), \tag{7.194}$$

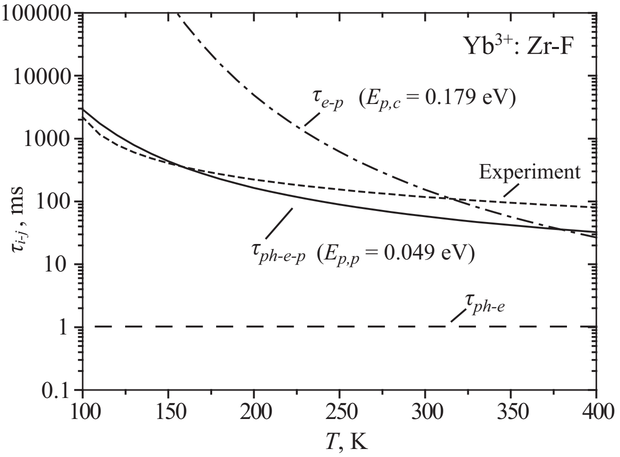

Figure 7.25. Variations of time constants as functions of temperature. The radiative relaxation time is the shortest followed by the phonon-assisted photon absorption at low temperatures. Multiphonon relaxation exhibits strong temperature dependence and is dominant at high temperatures [238]. Comparison with experimental results [164] is also shown.

where ϵ_{ph} is the total surface emissivity. The energy conversion $\dot{S}_{ph\text{-}e\text{-}p}$ is given by

$$\begin{aligned}
\dot{S}_{ph\text{-}e\text{-}p} &= Q_{ph,a} - Q_{ph,e}\\
&= \hbar\omega_{ph,i}\dot{\gamma}_{ph\text{-}e\text{-}p}\int_{V_s} n_d \mathrm{d}V_s - \hbar\omega_{ph,e}\dot{\gamma}_{ph-e}\int_{V_s} n_d \mathrm{d}V_S\\
&= (1-\frac{\bar{\omega}_{ph,e}}{\omega_{ph,i}}\frac{\dot{\gamma}_{e\text{-}ph}}{\dot{\gamma}_{ph\text{-}e\text{-}p}})\hbar\omega_{ph,i}\dot{\gamma}_{ph\text{-}e\text{-}p}\int_{V_s} n_d \mathrm{d}V_s\\
&= (1-\frac{\bar{\omega}_{ph,e}}{\omega_{ph,i}}\eta_{e\text{-}ph})A_{ph,a}n_d u_{ph}\int_{V_s} e_{ph,i}\mathrm{d}V_s \quad A_{ph,a} = \frac{\hbar\omega_{ph,i}\dot{\gamma}_{ph\text{-}e\text{-}p}}{u_{ph}\hbar\omega_{ph,i}n_{ph,i}}\\
&= (1-\frac{\bar{\omega}_{ph,e}}{\omega_{ph,i}}\eta_{e\text{-}ph})\sigma_{ph,i}u_{ph}\hbar\omega_{ph,i}n_{ph,i}V_s\\
&= (1-\frac{\bar{\omega}_{ph,e}}{\omega_{ph,i}}\eta_{e\text{-}ph})\alpha_{ph,i}Q_{ph,i},
\end{aligned} \tag{7.195}$$

where n_d is the dopant concentration, $\sigma_{ph,i}$ is the absorption coefficient (which is the product of $A_{ph,a}$ and n_d), and $n_{ph,i}$ is the number of photons per unit volume.

The spectral absorptance $\alpha_{ph,i}$ of intensity flux $I_{ph,i}$ is related to the absorptance (for optically thin solids, see footnote of Section 7.8) as,

$$\alpha_{ph,i} = 1 - \exp(-\sigma_{ph,i}L), \quad \text{for } \sigma_{ph,i}L \ll 1, \quad \alpha_{ph,i} = \sigma_{ph,i}L, \tag{7.196}$$

and $Q_{ph,a} = AI_{ph,i}\alpha_{ph,i}Q_{ph,i}$, where $Q_{ph,i}$ is the incident laser power.

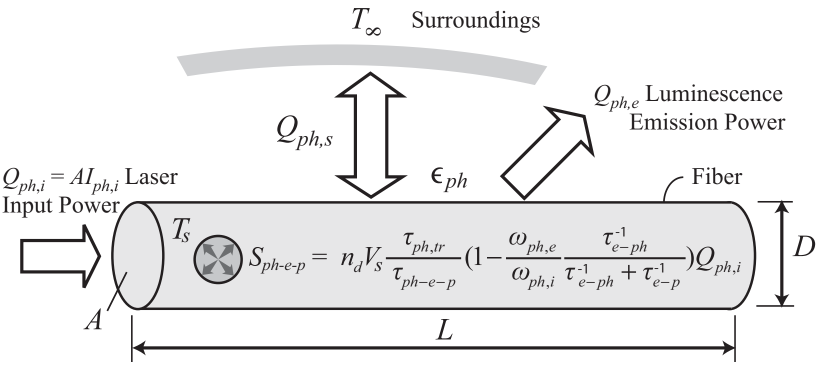

T_∞ Surroundings
$Q_{ph,s}$
$Q_{ph,e}$ Luminescence Emission Power
$Q_{ph,i} = AI_{ph,i}$ Laser Input Power
ϵ_{ph}
Fiber
T_s
$S_{ph\text{-}e\text{-}p} = n_d V_s \frac{\tau_{ph,tr}}{\tau_{ph-e-p}}(1-\frac{\omega_{ph,e}}{\omega_{ph,i}}\frac{\tau^{-1}_{e-ph}}{\tau^{-1}_{e-ph}+\tau^{-1}_{e-p}})Q_{ph,i}$
D
A
L

Figure 7.26. Heat transfer mechanism of laser cooling of a solid rod (fiber). The solid sample exchanges radiation heat with the surroundings through vacuum. The sample temperature is determined by the balance between the net external radiation (thermal load) and the cooling rate.

Thus (7.193) becomes

$$
\begin{aligned}
(\frac{1}{2}\pi D^2 + \pi DL)\epsilon_{ph}\sigma_{\rm SB}(T_s^4 - T_\infty^4) &= (1 - \frac{\bar{\omega}_{ph,e}}{\omega_{ph,i}}\eta_{e\text{-}ph})\alpha_{ph,i}Q_{ph,i} \\
&= (\frac{\lambda_{ph,i}}{\bar{\lambda}_{ph,e}}\eta_{e\text{-}p} - \eta_{p\text{-}ph})\alpha_{ph,i}Q_{ph,i}. \qquad (7.197)
\end{aligned}
$$

from which the sample temperature T_s is determined.

Using the quantum quantities developed in Section 7.12.1, (7.195) becomes

$$
\begin{aligned}
\dot{S}_{ph\text{-}e\text{-}p} &= \frac{\pi\hbar}{2\epsilon_{\rm o} m_{\rm AC}}\langle\mu_{ph\text{-}e}\rangle^2 \varphi'^2_{e\text{-}p,{\rm O}}\frac{D_p(E_p)f_p^{\rm o}(E_p)}{E_p^3}\frac{\hbar\omega_{ph,i}n_d L}{u_{ph}}(1 - \frac{\bar{\omega}_{ph,e}}{\omega_{ph,i}}\eta_{e\text{-}ph})Q_{ph,i} \\
&= n_d V_s \frac{\tau_{ph,tr}}{\tau_{ph\text{-}e\text{-}p}}(1 - \frac{\bar{\omega}_{ph,e}}{\omega_{ph,i}}\frac{\tau^{-1}_{ph\text{-}e}}{\tau^{-1}_{ph\text{-}e} + \tau^{-1}_{e\text{-}p}})Q_{ph,i}, \qquad (7.198)
\end{aligned}
$$

for the optical-phonon absorption, where $\tau_{ph\text{-}e}$, $\tau_{e\text{-}p}$, and $\tau_{ph\text{-}e\text{-}p}$ are the radiative, nonradiative, and phonon-assisted transition time constants respectively, and $\tau_{ph,tr}$ is the photon transit time that is defined by $\tau_{ph,tr} = L/u_{ph}$, where L is the sample length (along the beam). This indicates that, unlike energy transport, the energy conversion process is a product of the time constants of the processes. The cooling rate is directly limited by the the phonon-assisted absorption process, which has a transition rate two orders of magnitude smaller than that of the purely radiative transition. The reabsorption of emitted photons is neglected because it is estimated to be only 0.005% of the total emission rate [400]. Further details are reported in [400] and [238]. The *ab initio* computation of the three carrier interaction rates in the strong coupling regime is introduced in the next section.

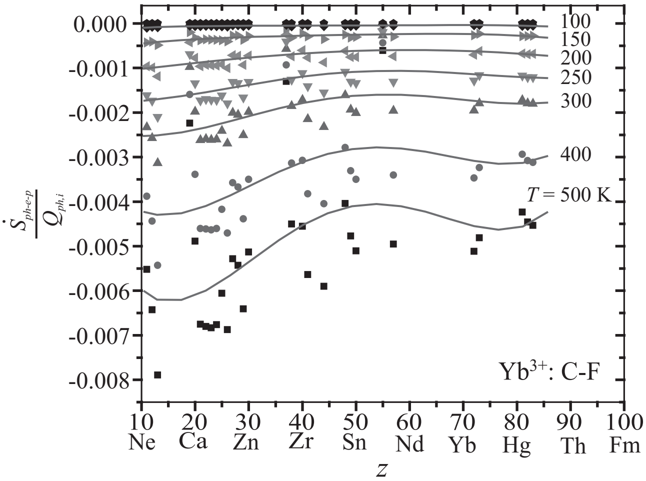

Figure 7.27. Dimensionless cooling rate as a function of atomic number, for discrete values of temperature for Yb^{3+} : C-F where C stands for cation. Some elements are added for reference. Also, a fourth-order polynomial fit is shown to guide the eye. Note that semiconductors and rare-earth materials have been omitted [238].

7.12.5 Optimal Host Material

Figure 7.27 shows distribution of the maximum cooling rate as a function of the atomic number. The trend is fitted to a 4th-order polynomial to guide the eye. The results show that there are two peaks, between atomic numbers 20 and 30 and 75 and 85. This trend supports the recent successes of blending of light and heavy cations as host materials for laser cooling of solids. However, as the temperature decreases and the available high energy phonons diminish rapidly (Bose–Einstein distribution f_p^{o}), the cooling rate is quickly suppressed.

The above analysis provides a guide to the selection of ion-host materials for optimal performance. Here we compare various host materials, based on performance by atomic pairs, and we choose F as one of the atoms. Figure 7.28(a) shows variation of dimensionless cooling rate with respect to temperature, for some C-F pairs with Yb^{3+} ion. The crystal structure assumed is FCC, which has C-F pairs as the ion immediate ligands. Here C is Tl, Zr, Hf, Nb Fe, Mg and Al. These structures may not be realized, for example, AlF$_3$ is an stable, existing compound. However, if a blend of different C-F pairs are made, the contributions of these pair ligands exist at the ion site. Figure 13(a) shows that Al, which has a relatively low phonon peak energy, exhibits high cooling rate over a wide range of temperatures, however, one can expect that the energy removed per transition is low (low capacity). On the contrary, one can expect the energy removed per transition is high (high capacity) for Zr (due to relatively high phonon peak energy), yet the performance decreases rapidly as the temperature decreases. The inset in Figure 7.28(a) shows that at temperatures near 150 K, it is possible to reach even lower temperature with Tl compared to Zr.

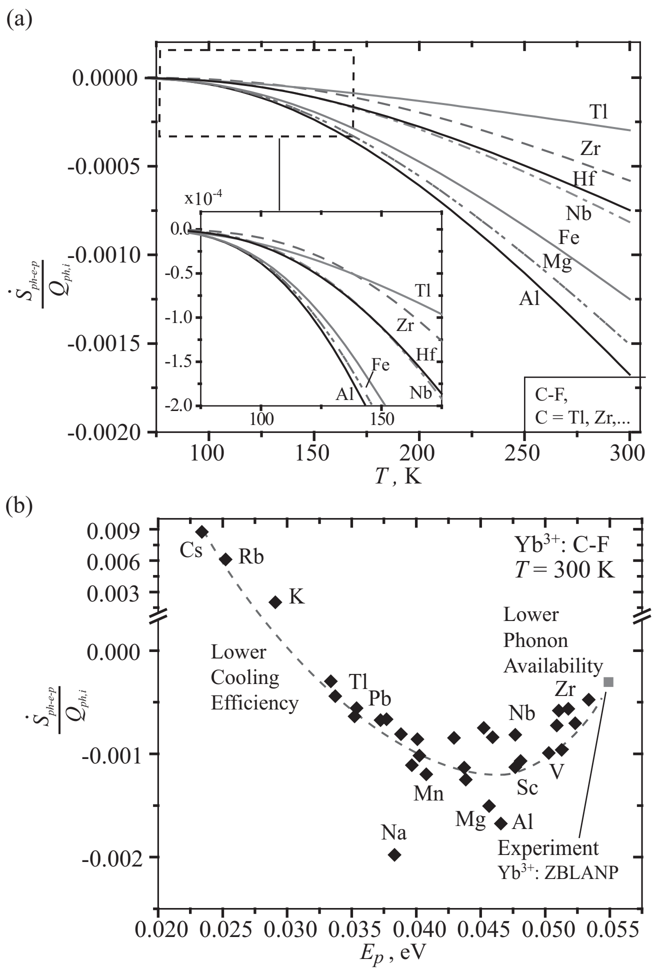

Figure 7.28. (a) Dimensionless cooling rate as a function of temperature, for Yb^{3+}: Tl-F, Zr-F, Hf-F, Nb-F Fe-F, Mg-F, and Al-F. The results are for ideal conditions, i.e., quantum efficiency of one and identical FCC structures. (b) The maximum, normalized cooling rate for various cation-fluoride pairs, as function of phonon energy for Yb^{3+}: C-F. Note that semiconductors and rare-earth materials have been omitted. The dashed line is only intended to guide the eye [238].

The maximum cooling rate for some cation-fluoride pairs are given in Figure 7.28(b). The results show that the first column alkali-metals from the periodic table are not good candidates for laser cooling at T = 300 K. However, due to the relatively lower phonon energy, these elements are expected to be more suitable at lower temperatures with the exception of Cs and Rb. The results are expected from (7.198), which shows that there are several competing processes in laser cooling of solids. These are, (a) higher phonon peak energy results in more energy removed per transition, (b) lower phonon peak energy results in higher phonon distribution values (c) low cut-off frequency results in higher phonon density of states, and (d) higher cut-off frequency results in higher a nonradiative decay.

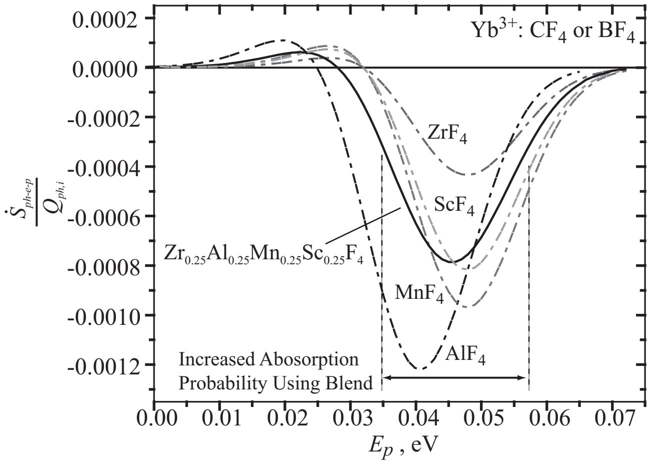

Figure 7.29. Dimensionless cooling rate as a function of phonon energy for diatomic host Yb^{3+}: CF_4 or blend host, BF_4. The cooling rates have been calculated using ideal conditions, i.e., quantum efficiency of one and FCC structure, and are linearly superimposed. Although the magnitude of the cooling rate is moderated, the absorption probability increases as the phonon spectrum broadens. The cooling rates for diatomic hosts are shown in dashed lines and exhibit less broadening [238].

Using the above discussions, it is possible to quantitatively predict the cooling performance of a blended material. Figure 7.29 shows the cooling performance of an example blend of host materials. In practice, the composition discussed here may not be realized, however, the blend here provides an example providing a valuable general guide. The figure shows that blending materials that have different phonon peak energies increases the half width of the transition. This, in turn increases the transition probability. One can expect that as the half width broadens, it increases the probability of various phonon modes available in the lattice coupling with the electron in oscillation. This blending strategy is expected to increase the absorption rate as much as factor of 2.

Results of Figures 7.28(a) and 7.29 suggest using elements Al, Mn, Na and Mg in the host blend. Nevertheless, for optimized cooling performance, a wide range of elements should be present in the blend for increased absorption probability (with the exception of Rb and Cs).

7.12.6 Photon–Electron and Electron–Phonon Transition Rates Using Strong Couplings (Ab Initio Computation)

It was found in the previous section that the absorption rate $\dot{\gamma}_{ph,a}$ is limited by the photon–electron coupling and electron–phonon coupling. It becomes feasible to calculate these coupling parameters by using *ab initio* methods, which may allow for an understanding to link these coupling parameters to the atomic structure, especially in the quantitative level.

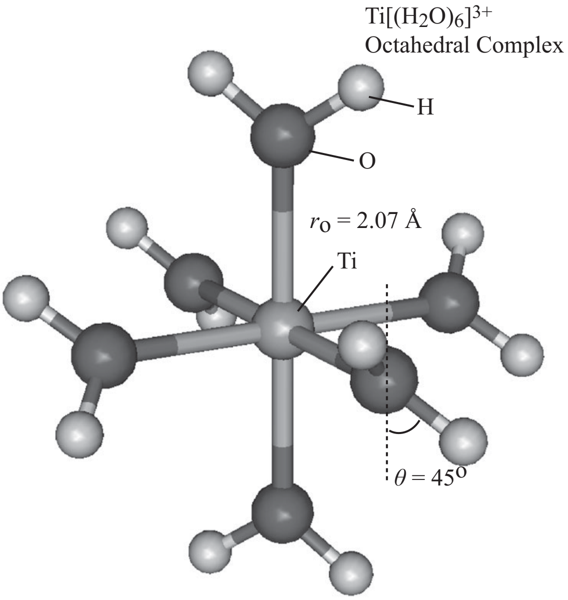

Figure 7.30. The optimized geometry of the ground state of Ti$[(H_2O)_6]^{3+}$ (hydrated titanium) complex.

(A) *Photon–Electron Coupling (Transition Dipole Moment)*

Here we use the Ti$[(H_2O)_6]^{3+}$ complex as the model system. The calculation is performed using Gaussian 03 Package [149] introduced in Chapter 2, with the B3LYP method and the 6-311+G* basis set. The Ti^{3+} ion has a single unpaired electron, which gives a spin multiplicity of 2 for the complex. To avoid convergence problems of the self-consistent function (SCF), a quadratic convergent (QC) procedure has been applied. No symmetry restriction was prescribed at the start of the calculation, and the optimized geometry converges to the D_{3d} all-vertical symmetry, as shown in Figure 7.30. This symmetry is lower than the O_h point group and higher than C_i. The calculated Ti–O bond length is 2.07 Å, which agrees well with the experimental value 2.03 Å [467] and previously reported ground-state calculations on this complex [228, 455].

The energy levels for the complex at the ground state equilibrium geometry can be calculated using the time-dependent DFT (TDDFT), which is believed to be the most accurate method for excited states. For a free-standing Ti^{3+} ion, it has five degenerate *d* levels, with the orbitals shown in Figure 7.31. As the ion is put into an octahedral crystal field (Section 5.20) of the six surrounding oxygen atoms, the levels are split into two groups, three levels for the ground state and two levels for the excited state. The Jahn–Teller effect further splits the ground state into two multiplets, with an energy gap of 6046 cm^{-1}. The Jahn–Teller theorem states that any complex occupying an energy level with an electronic degeneracy is unstable against a distortion that removes that degeneracy in first order. The vibronic coupling of ions in solids can cause a local distortion of the lattice in which the atoms

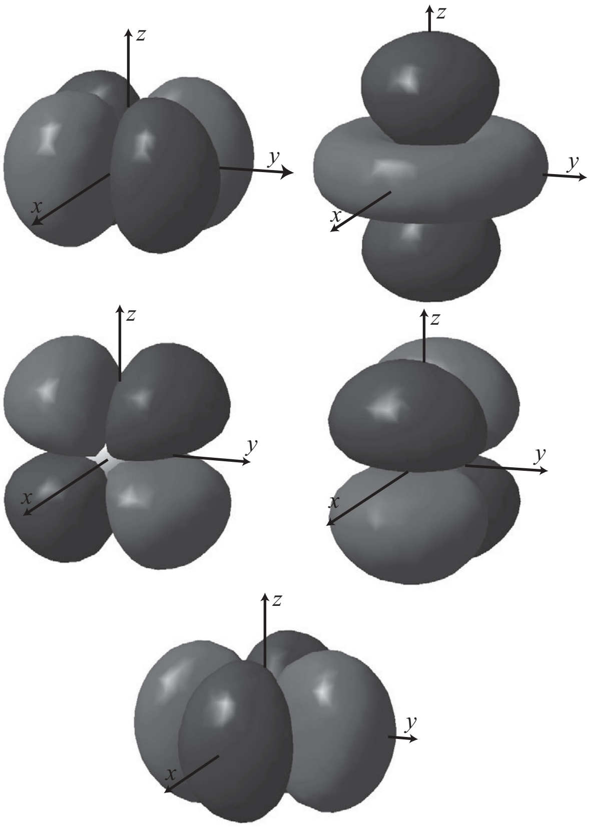

Figure 7.31. The fine degenerate 3*d* orbitals of a single Ti^{3+} ion.

move in the direction of normal-mode displacement to lift the electronic degeneracy. A new equilibrium position is achieved in which the local symmetry is lower than the point-group symmetry of the crystal. Here for the $Ti[(H_2O)_6]^{3+}$ complex the symmetry is lowered from O_h to D_{3d}. The evolution of the energy levels is shown in Figure 7.32.

The ground- and excited-state wave functions are calculated with Gaussian (Section 2.2.2, as shown in Figures 7.33 (a) and (b). The *ab initio* calculations showed that the energies of the orbitals below the HOMO (highest occupied molecular orbital) are approximately the same for the ground and the excited electronic states, so that the differences of the state energies can be discussed with these singly occupied molecular orbital (SOMO) energies. Based on the theory of LCAO [166], the ground state is mainly composed of the $3d_{z^2}$ orbital, and the excited state is dominated by the $3d_{x^2-y^2}$ orbital.

A photon can be absorbed by an ion if the coupling factor $\mathbf{s}_{ph,i} \cdot \boldsymbol{\mu}_e$ is nonzero (i.e., they are not orthogonal), where $\mathbf{s}_{ph,i}$ is the polarization vector of the EM field, and $\boldsymbol{\mu}_e$ is the effective transition dipole moment of the ion. The transition dipole moment is defined as a quantum mechanical spatial integral of the classical dipole

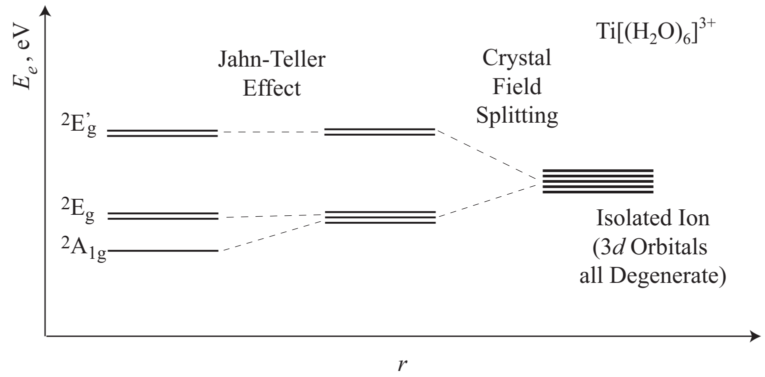

Figure 7.32. Calculated energy levels of the $Ti[(H_2O)_6]^{3+}$ complex at the ground-state equilibrium geometry. The Ti-O bond length is $r_e = 2.07$ Å. The energy multiplets that are due to the crystal field and the Jahn–Teller effect are shown.

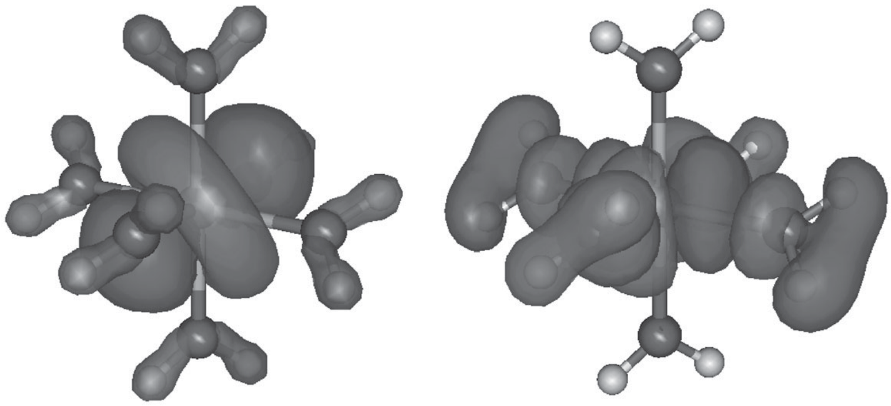

(a) ψ_{ground} (b) ψ_{excited}

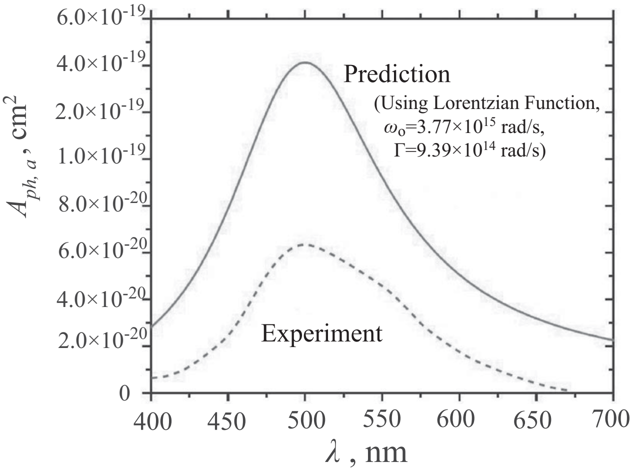

(c)

Figure 7.33. Calculated wave functions for (a) ground- and (b) excited-state $T_i[(H_2O)_6]^{3+}$ [402], and (c) predicted and measured absorption bands. The Lorentzian band-broadening function is defined in Table 3.5.

moment $e_c \boldsymbol{x}$, i.e.,

$$\boldsymbol{\mu}_{e,21} = \sum_{1} |\langle \psi_{f,m_1} | e_c \boldsymbol{x} | \psi_{i,m_2} \rangle|, \tag{7.199}$$

where e_c is the electron charge, $\boldsymbol{x}$ is the position vector, m_1 is the sublevels of the ground state ψ_{f,m_1}, and m_2 is the sublevels of excited state ψ_{i,m_2}. Note that $\boldsymbol{\mu}_{e,21}$ must be independent of m_2; otherwise, the different m_2 levels would have different transition dipole moments and radiative lifetimes (which are not possible in an isotropic environment). The transition dipole moment between a sublevel m_1 of the ground state and a sublevel m_2 of the excited state is then calculated by

$$\boldsymbol{\mu}_{e,sub} = |\langle \psi_{i,m_1} | e_c \boldsymbol{x} | \psi_{i,m_2} \rangle|, \tag{7.200}$$

which gives 0.005259 D (Table A.3) (1.859×10^{-32} C-m). This value is rather small, indicating that the ground state and excited state have very similar symmetry properties.

Because of a strong electron–phonon coupling in Ti^{3+} systems, the ground state has many vibrational sublevels. If we assume there are N sublevels and each has a similar transition dipole moment, then the total transition dipole moment becomes

$$\boldsymbol{\mu}_{e,21} = N \boldsymbol{\mu}_{e,sub}, \tag{7.201}$$

where N will be determined by fitting to experimental value. The lifetime of Ti^{3+}: Al_2O_3 was measured by spectroscopy experiments to be 3 μs [370]. By substituting (7.201) into (7.190), we have $N = 4000$, indicating that the vibronic effect of Ti doped systems is significant.

(B) *Strong Electron–Vibration Coupling (Electron–Phonon Wave Function)*

When the coupling between the electrons of the optically active ion and the lattice vibration is strong (involving many phonons), transitions become broadband with strong temperature dependence. The atoms in a solid are never completely at rest. The thermal vibrations of the atoms modulate the local crystal field at the site of an optically active ion. This modulation can have several effects on the optical properties of the doped ion. For example, it can modulate the position of the electronic energy levels, leading to a broadening and shifting in peak position of the spectral transition. Also it can cause transitions to occur between electronic energy levels accompanied by the absorption or emission of vibrational energy, but with or without the emission or absorption of photons.

The coupling of an electron to a specific vibrational mode is essentially the change of the electronic property in response to the lattice displacement along that vibrational mode. The normal vibrational modes of the $Ti[(H_2O)6]^{3+}$ complex can be conveniently calculated with Gaussian, after the geometry is optimized. The total degrees of freedom for the complex, (neglecting the H atoms we have seven atoms), is found from Table 6.2 to be 21, 3 translational, 3 rotational, and 15 vibrational. Among all calculated vibrational modes, we consider only those that are also

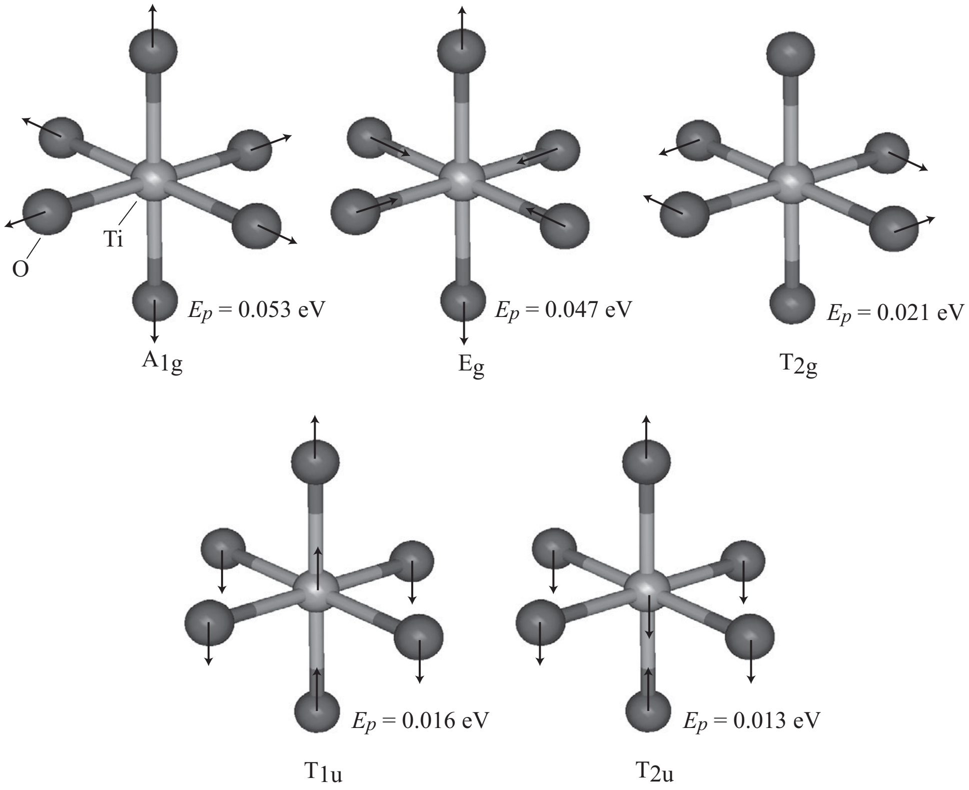

Figure 7.34. The five highest-energy vibrational normal modes along with the frequencies, for $Ti[(H_2O)_6]^{3+}$ complex.

observed for the octahedral TiO_6 core. The modes that are due to the hydrogen atoms only do not contribute significantly to the electron–phonon coupling, because these modes are screened by the more inner oxygen atoms. The five highest vibrational energy normal modes and frequencies are shown in Figure 7.34.

A configuration coordinate diagram is often used to describe transitions between electronic transitions coupled to vibrations. It depicts the variation in the electronic energy levels with respect to the displacement of the normal vibrational coordinate away from its equilibrium position. Here, because the vibration modes that are due to hydrogen atoms have very little effect on the energy level of the Ti^{3+} ion, we are concerned only with the vibration of the octahedral TiO_6 core. For these modes the hydrogen atoms move rigidly with the oxygen atoms.

The configuration coordinate diagram is obtained by calculating the energy levels with respect to the normal coordinate of a specific vibrational mode. Shown in Figure 7.35 is the configuration coordinate diagram corresponding to the A_{1g} normal mode. Five levels resulting from the 3*d* orbitals are shown. As discussed in Figure 7.32, we have the ground state ${}^2A_{1g}$, the first excited state ${}^2E_g$, which is composed of two nearly degenerate levels, and the second excited state ${}^2E'_g$, which is also composed of two nearly degenerate levels. The transition between the ${}^2A_{1g}$ and ${}^2E'_g$

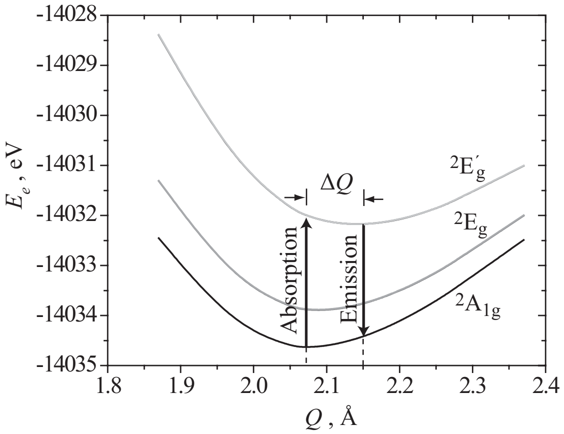

Figure 7.35. Configuration coordinate diagram (energy verses normal coordinate) corresponding to the A_{1g} normal mode, for $Ti[(H_2O)_6]^{3+}$ complex [402].

levels is very important in lasers and luminescent applications and is therefore of concern here. As shown in the figure, the potential energy minimum for the excited state is shifted to the right to that of the ground state, as expected. This shift leads to the well-known Stokes shift in the emission wavelength. For the excited state, the electron is normally farther away from its nuclei than the ground state, repelling the surrounding oxygen atoms. As the result, the equilibrium Ti–O bond length for the excited state becomes longer than that of the ground state, which in turn leads to a smaller force constant and vibrational frequency – the curvature for the excited state is flatter than that for ground state. To take into account the modifications of both normal coordinates (5.164) and frequencies between the electronic states, we can express them in general as follows

$$Q' = Q + \Delta Q \quad \text{shift in normal coordinate} \tag{7.202}$$

$$\omega'_s = \omega_s(1 - F) \quad \text{shift in energy,} \tag{7.203}$$

where ΔQ is the normal coordinate shift of the energy minimum and F is the fraction of the frequency shift. Only those normal modes that have modifications in either normal coordinates or frequencies between the electronic states concerned can contribute to the radiationless transition probability. The Huang–Rhys coupling factor S_s for mode ω_s is

$$S_s = \frac{m\omega_s \Delta Q^2}{2\hbar} \quad \text{Huang–Rhys coupling factor,} \tag{7.204}$$

where M is the mass of the vibrating atom, the O atom here.

In the Born–Oppenheimer approximation, the system wave function ψ is presented as [369]

$$\psi_{i,\nu}(\boldsymbol{x}, Q) = \phi_i(\boldsymbol{x}, Q)\theta_{i,\nu}(Q) \quad \text{electron–phonon wave function.} \tag{7.205}$$

where $\theta_{i,\nu}(Q)$ is the vibrational wave function at a nuclei normal coordinate Q, and $\phi_i(\boldsymbol{x}, Q)$ is the electronic wave function for a fixed position of the nuclei. This implies that the motion of the electron is very rapid compared with the nuclei motion. The Hamiltonian H for the entire system can be chosen as

$$\mathrm{H} = \mathrm{H}_k(Q) + \mathrm{H}_e(\boldsymbol{x}) + \mathrm{H}_{e\text{-}p}(Q), \tag{7.206}$$

where $\mathrm{H}_k(Q)$ is the kinetic energy operator of all nuclear motions, $\mathrm{H}_e(\boldsymbol{x})$ is the electronicenergy operator for electronic states, and $\mathrm{H}_{e\text{-}p}(Q)$ is the electron–lattice interaction potential. In the adiabatic approximation, $\phi_e(\boldsymbol{x}, Q)$ and $\theta_{i,\nu}(Q)$ are solutions of the following Schrödinger equations, i.e., similar to (2.75)

$$[\mathrm{H}_e(r) + \mathrm{H}_{e\text{-}p}(Q)]\phi_i(\boldsymbol{x}, Q) = \varphi_i(Q)\phi_i(\boldsymbol{x}, Q) \quad \text{electronic energy} \tag{7.207}$$

$$[\mathrm{H}_k(Q) + \varphi_i(Q)]\theta_{i,\nu}(Q) = \mathrm{H}_{i,\nu}(Q)\theta_{i,\nu}(Q) \quad \text{phonon energy,} \tag{7.208}$$

where $\varphi_i(Q)$ is the adiabatic potential of the electronic state at the instantaneous position Q and ν signifies the overall vibrational state of the nuclei. Although $\psi_{i,\nu}$ is a good approximation for stationary states, the system oscillates to and from various quantum states of nearly the same energy. This should be interpreted as the transition from one electronic state to another, accompanied by a transition in the quantum states of the nuclear motion. The perturbation Hamiltonian H′ for the nonradiative transition process is given by [284, 369]

$$\mathrm{H}'\psi_{i,\nu}(\boldsymbol{x}, Q) = -\frac{\hbar^2}{2m}\sum_s \frac{\partial\phi_i(\boldsymbol{x}, Q)}{\partial Q_s}\frac{\partial\theta_{i,\nu}}{\partial Q_s} - \frac{\hbar^2}{2m}\sum_s \frac{\partial^2\phi_i(\boldsymbol{x}, Q)}{\partial Q_s^2}\theta_{i,\nu}. \tag{7.209}$$

The nonradiative transition rate $\dot{\gamma}_{e\text{-}p}$ is given by the FGR (3.27):

$$\dot{\gamma}_{e\text{-}p} = \frac{2\pi}{\hbar}\sum_{\nu,\nu'} p_{i\nu}|\langle f\nu'|\mathrm{H}'|i\nu\rangle|^2\delta_{\mathrm{D}}(E_{f,\nu'} - E_{i\nu}), \tag{7.210}$$

where $p_{i\nu}$ is the distribution function for the Boltzmann population of the initial vibrational levels and a δ_{D} function is used for the density of final states to ensure conservation of energy. Using the electronic and vibrational wave functions in (7.210), we have

$$\dot{\gamma}_{e\text{-}p} = \frac{2\pi}{\hbar}\sum_{\nu,\nu'} p_{i\nu}|(-\frac{\hbar^2}{m})\sum_s \langle\phi_f|\frac{\partial\phi_i}{\partial Q_s}\rangle\langle\theta_{f\nu'}|\frac{\partial\theta_{i\nu}}{\partial Q_s}\rangle|^2\delta_{\mathrm{D}}(E_{f\nu'} - E_{i\nu}), \tag{7.211}$$

where Q_s is for mode ω_s.

Here the electronic part of the matrix element can be defined as

$$R_s(fi) = -\frac{\hbar^2}{m}\langle\phi_f|\frac{\partial\phi_i}{\partial Q_s}\rangle. \tag{7.212}$$

The derivative represents how sensitive the electronic wave function is with respect to the displacement along a particular vibrational mode. This is shown in Figure 7.36.

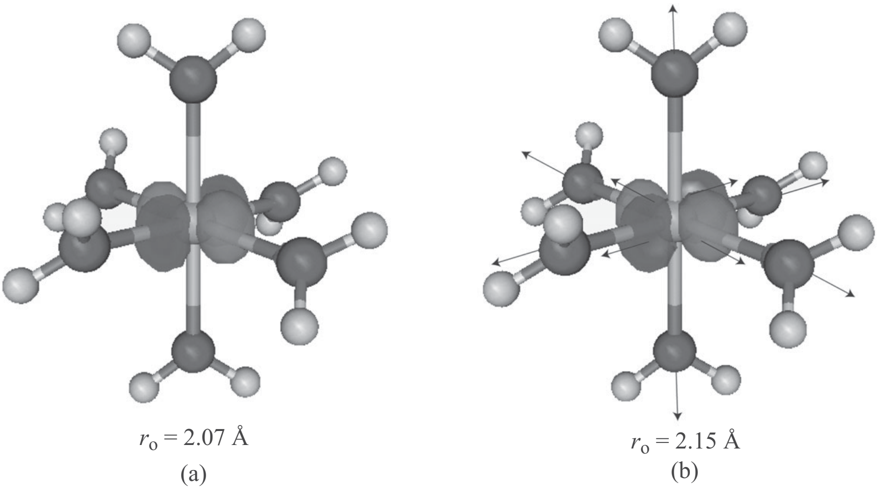

Figure 7.36. The modulations (a) and (b) of the excited state wavefunction with respect to the A_{1g} vibrational mode, for $Ti[(H_2O)_6]^{3+}$.

Equation (7.211) has been evaluated in [284] by replacing the δ_D function with an integral, and the final result of the transition probability of the nonradiative decay is

$$\dot{\gamma}_{e\text{-}p} = \frac{\pi\omega_s}{2\omega_s\hbar^3}|R_s(fi)|^2 \exp[-S_s \coth\frac{\hbar\omega_s}{2k_\mathrm{B}T}][(\coth\frac{\hbar\omega}{2k_\mathrm{B}T}+1)\exp(-i\phi' P_i^+)J_{P_i^+}$$
$$\times(S \operatorname{csch}\frac{\hbar\omega}{2kT}) + (\coth\frac{\hbar\omega}{2k_\mathrm{B}T}-1)\exp(-i\phi' P_i^-)J_{P_i^-}(S \operatorname{csch}\frac{\hbar\omega}{2k_\mathrm{B}T})], \qquad (7.213)$$

where S is the effective Huang–Rhys coupling factor and includes all modes, $J_{P_i^+}$ is the P_i^+th order Bessel function, and P_i^+ and P_i^- are defined as

$$P_i^+ = \frac{1}{\omega}[-\omega_{AB} - \omega_s + \frac{\rho\omega}{2}\coth\frac{\hbar\omega}{2k_\mathrm{B}T}] \qquad (7.214)$$

$$P_i^- = \frac{1}{\omega}[-\omega_{AB} + \omega_s + \frac{\rho\omega}{2}\coth\frac{\hbar\omega}{2k_\mathrm{B}T}], \qquad (7.215)$$

where ω_{AB} is the gap energy between the ground and the excited state.

Using (7.213), the nonradiative decay rate is calculated as a function of temperature, and is shown in Figure 7.37(a). The total decay rate, $\dot{\gamma}_{ph\text{-}e\text{-}p}$ is the summation of the radiative and nonradiative rates as (7.156), i.e.,

$$\dot{\gamma}_{ph\text{-}e\text{-}p}(T) = \dot{\gamma}_{ph,e,sp} + \dot{\gamma}_{e\text{-}p}(T), \qquad (7.216)$$

and the lifetime is given by

$$\tau_{ph\text{-}e\text{-}p} = \frac{1}{\dot{\gamma}_{ph\text{-}e\text{-}p}}. \qquad (7.217)$$

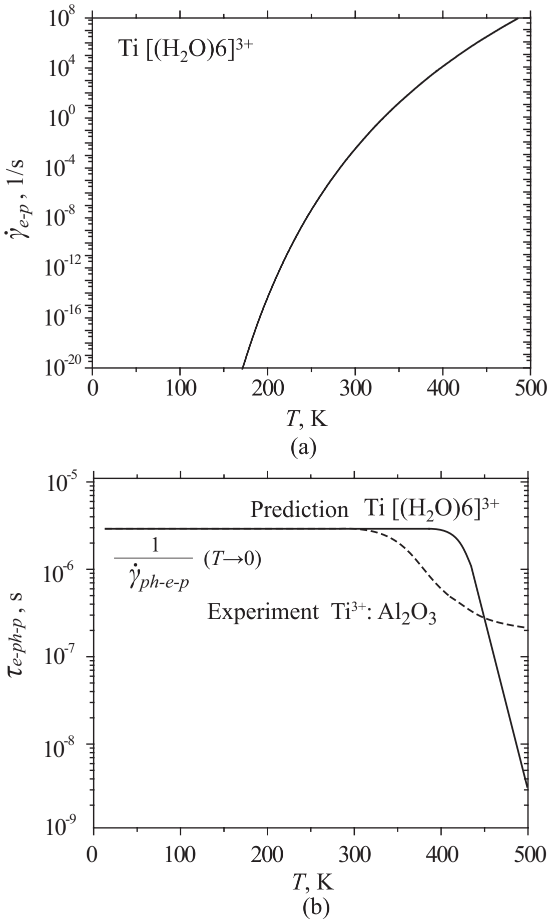

Figure 7.37. (a) Variations of total transition rate with respect to temperature. (b) Variations of lifetime ($1/\tau_d = 1/\tau_r + 1/\tau_{nr}$) with respect to temperature. The experimental results are from Figure 7.37(b) [402].

The calculated lifetime in this way is shown in Figure 7.37(b). Similar to the results given in Figures 7.21(a) and (b), Figure 7.37(b), at low temperatures, the nonradiative decay rate is negligibly small compared with the radiative decay rate, so that the lifetime remains almost a constant. As the temperature increases, more phonons are activated and involved in the decay process, and the nonradiative decay rate is increasing rapidly. At around 250 K, the nonradiative decay rate becomes comparable or even larger than the radiative decay rate, and the lifetime drops significantly with temperature. At high temperatures, the decay process is dominated by the nonradiative decay. The predicted lifetime is compared with that of the Ti:sapphire laser material, which also has an octahedral crystal field around the Ti^{3+} ion. The measured Ti^{+3}: Al_2O_3 lifetime [Figure 7.21(b)] at low temperatures is much shorter than that predicted for $Ti[(H_2O)_6]^{3+}$, because it was not measured at the zero-phonon line, and in real materials defects and impurities may modify the symmetry properties around the Ti ion significantly. At high temperatures, the nonradiative decay rates follow a similar trend. Exact agreement is not expected because the phonon modes for our cluster are different from those in the Ti^{3+}: Al_2O_3 solids.

7.13 Gas Lasers and Laser Cooling of Gases

7.13.1 Molecular-Gas Lasers

In molecular-gas laser systems [494], photons can be emitted from transitions in the vibrational–rotational spectrum of a molecule. The energy of the photon emission is directly related to the fluid particle energies associated with such a laser system.

Unlike solids and liquids, the energy of gaseous fluid particles is completely contained within an individual molecule and not stored in phonons or intermolecular forces. As discussed in Chapter 6, the fluid particle energy is composed of five energies: potential, electrical, translational, vibrational, and rotational energy; however, here we assume that the potential energy is negligible.

Energy states are quantized and have populations as functions of temperature, as given by the M–B distribution. Near room temperature, vibrational and electrical energy states are not significantly populated. However, transitions to excited vibrational and electronic states can occur through special excitation processes.

(A) *Rotational and Vibrational Quantum States*

Transitions between these energy states are governed by selection rules [22, 103]. The most basic selection rule states that the rotational and vibrational quantum numbers (Section 6.1), j and l, can increase or decrease only by a value of one for any transition

$$\Delta j = \pm 1,\ \ \Delta l = \pm 1. \tag{7.218}$$

The low-lowvel rotational energy transition ($\Delta j = -1$) is called the P branch, while $\Delta j = +1$ is called the R branch.

Polyatomic molecules have multiple modes of vibration, and have multiple corresponding vibrational quantum numbers. CO_2 [121] is a triatomic molecule with three modes of vibration, (l_1, l_2, l_3), Table 7.3. These vibrational quantum numbers correspond to modes of vibration referred to as the symmetric stretch, bending, and antisymmetric stretch modes, respectively. Selection rules for this molecule are

$$|\Delta l_2| = \text{even},\ \ |\Delta l_3| = \text{odd} \tag{7.219}$$

or

$$|\Delta l_2| = \text{odd},\ \ |\Delta l_3| = \text{even}. \tag{7.220}$$

Based on the distribution of rotational energy states present in a molecule, there are a number of transitions that can occur in a single vibrational transition. This gives many closely spaced absorption lines (in $\sigma_{ph,\omega}$) that make up a rotational–vibrational spectrum, as shown in Figure 7.38. Each absorption line (in $\sigma_{ph,\omega}$) is

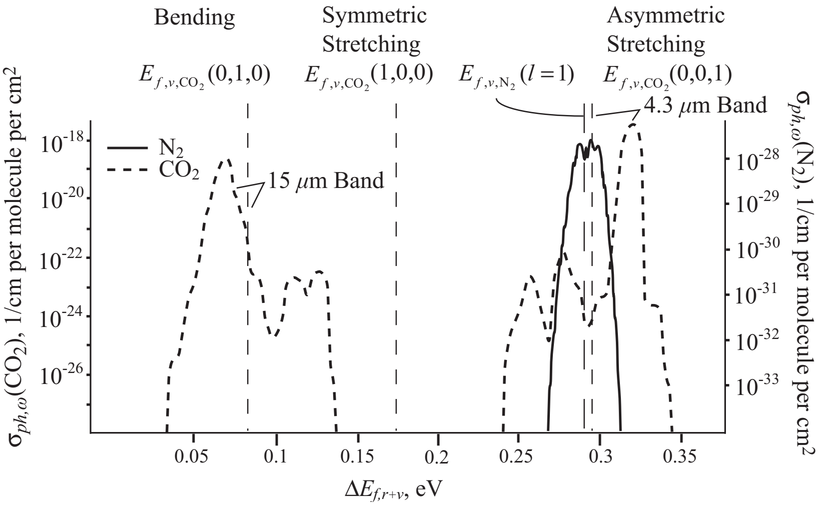

Figure 7.38. Variations of the measured spectral absorption coefficient with respect to energy (infrared regime) for N_2 and CO_2. The rotational–vibrational spectra of N_2 and CO_2 show the first vibrational transition of N_2 and its relation to CO_2 absorption lines [66]. The CO_2 band designations are from Table 7.3.

attributed to a specific rotational–vibrational energy transition from the ground state. The change in vibrational energy between $l = 0$ to $l = 1$ for N_2 occurs at 0.2890 eV. This energy state is, like all energy states in the rotational–vibrational spectrum, quantized and fixed. The spectrum arises because rotational-energy states are not linearly spaced, and as such a change of $j = \pm 1$ is generally not constant.

Not all energy states of a molecule appear in the absorption spectra. According to the selection rules for a triatomic atom, a transition from $l_1 = 0$ to $l_1 = 1$ cannot occur without an accompanying transition in another vibration mode. From the ground state, the (1,0,0) energy level of the CO_2 molecule cannot be accessed and does not show up in the absorption spectra of Figure 7.38. This arises physically because a single collision cannot exert a force that will excite a symmetric stretch mode of vibration from the ground state. A complete set of energy states can be described quantum mechanically.

The energy states of fluid particles can be predicted classically when combined with quantum restrictions from the Schrödinger equation. Quantum restrictions give acceptable rotational energy levels of a fluid particle as $\hbar^2$ times multiples of the rotational quantum number j. The combination of these results gives the rotational energy states defined by (6.15), i.e.,

$$E_{f,r} = \frac{\hbar^2}{2I_f} j(j+1) = B_{f,r} j(j+1), \quad j = 0, 1, 2, 3 \ldots \text{ rotational energy}, \tag{7.221}$$

where I_f is the moment of inertia. Values for the rotational energy states of a gas molecule can be predicted from the interatomic spacing of atoms and their masses. From masses and interatomic separations, the moment of inertia is determined by assuming the molecule rotates as a rigid body about its center of mass. This is called the rigid-rotor assumption (Section 6.1.5), which is not generally valid. The moment of inertia, I_f, is related to reduced mass m_{12} and the separation distance, i.e.,

$$I_f = m_{12}r_e^2 = \frac{m_1 m_2}{m_1 + m_2} r_e^2 \text{ moment of inertia.} \tag{7.222}$$

Vibrational energy states of gas molecules are also determined quantum mechanically from the Schrödinger equation. The quantum restrictions yield the acceptable energy levels in terms of a vibrational quantum number l, i.e., from (6.13), we have for a simple harmonic oscillator

$$E_{f,v} = (l + \frac{1}{2})\hbar\omega_f \text{ diatomic vibrational energy, } l = 0, 1, 2, 3 \ldots \tag{7.223}$$

For a polyatomic molecule such as CO_2, we have

$$E_{f,v}(l_1, l_2, l_3) = \hbar\omega_{f,1}(l_1 + \frac{1}{2}) + \hbar\omega_{f,2}(l_2 + \frac{1}{2}) + \hbar\omega_{f,3}(l_3 + \frac{1}{2}), \tag{7.224}$$

where $\omega_{f,i}$ is smaller or larger than the natural frequency ω_n. The energy of the degenerate modes are added, and the selection rules, which allow only certain optical transitions, are discussed in [121].

Values of the vibrational natural frequency of a gas molecule can be predicted from the potential energy function. To simplify the problem, we assume harmonic oscillation about the equilibrium separation, so that the potential is of the form $\varphi_{ij} = \Gamma_{ij}r_{ij}^2/2$. We create this harmonic approximation of the potential from the Morse potential (Table 2.1). By taking the second derivative of the potential evaluated at the equilibrium separation, we determine the value of the bond force constant Γ. The Morse potential is

$$\begin{aligned} \varphi &= \varphi_o\{[1 - e^{-a_o(r-r_e)}]^2 - 1\} \text{ Morse potential} \\ &= \varphi_o[e^{-2a_o(r-r_e)} - 2e^{-a_o(r-r_e)}], \end{aligned} \tag{7.225}$$

where φ_o is the potential-well depth r_e is the equilibrium separation, and a is the harmonicity parameter. The harmonicity term varies significantly, depending strongly on the type of bonding present between atoms. The second derivative of this function evaluated at $r = r_e$ is the force constant (2.54)

$$\Gamma_{12} = 2a^2\varphi_o \text{ force constant for Morse potential.} \tag{7.226}$$

Note that for L-J pair potential, we have $\Gamma_{\text{LJ}} = (7.560)^2\epsilon_{\text{LJ}}/\sigma_{\text{LJ}}^2$.

The natural frequency of a diatomic bond can then be easily determined from the harmonic oscillation between two molecules about their center of mass. The natural frequency (2.54) becomes

$$\omega_f = (\frac{\Gamma_{12}}{m_{12}})^{1/2} = (\Gamma_{12}\frac{m_1 + m_2}{m_1 m_2})^{1/2},$$

$$\text{natural (fundamental vibrational) frequency for diatomic molecule.} \tag{7.227}$$

Note that for homonuclear, diatomic bond, the reduced mass is replaced with m (e.g., 23.25 yg for N_2), i.e., (2.54).

Table 7.5. *The rotational and force constants for several diatomic molecules calculated using Gaussian [149] with the basis set: 6-31 G(d) and scaling factor 0.8929.*

Atomic pair	$B_{f,r}$, eV	m_{12}, yg	Γ_{12}, N/m	ω_f, Trad/s
B–H	18.3	1.81	575	563
Ca–Ca	0.0571	66.36	14.1	14.6
C=O	2.27	22.32	2732	350
Cu–Cu	0.135	104.50	194	43.1
N≡N	2.47	23.25	4317	431
Ne–Ne	0.683	33.20	679	143
N–H	22.7	1.78	794	667
O–H	24.4	1.77	849	692
Si–H	10.2	1.73	310	423

Table 7.5 lists the parameters φ_o, r_e and a in the Morse potential (7.225) and the rotational constant for several molecules. Note that Morse potential is not the most suitable for all these molecules. The general method for calculation of the force constant is described in Section 4.11.2 for arbitrary pair bonds, using the combinative rules and Table 4.4 which lists values for for mononuclear paris. For polyatomic gases the frequencies of vibration in (7.228) are found from the solution to the Schrödinger equation (e.g., using Gaussian [149], Section 6.1.5)

Translational energies have an impact on the distribution of vibrational and rotational energy levels, as well as the probability of energy transfer between vibrational and rotational energy levels. When a molecule attains an excited vibrational or rotational state, with energy above the ground-state distribution, the primary nonradiative transfer mechanism is through collisional deactivation.

(B) *CO_2 Gas Laser*

In a laser system, the process of radiative emission competes with nonradiative transfer mechanisms (Section 7.11). To decrease the probability of deactivation, it is important to try to reduce the effect of collisional deactivation. Maintaining a high number of molecules in an excited state allows stimulated emission to occur. In the molecular laser system, the stimulated emission $\dot{\gamma}_{f\text{-}ph,e,st}$ that occurs is a transition between the vibrational energy states of the fluid particle (molecule).

An example of a typical molecular laser is the molecular N_2–CO_2 system. Figure 7.39 shows the partial energy diagram representing this molecular laser system. A common CO_2 laser cycle consists of electrically exciting N_2, transferring resonant energy to a CO_2 molecule, and laser emission. There is also He for population control.

CO_2 is a linear, polyatomic gas [Figure 2.10(b)], and its 9 degrees of freedom (Table 6.2) are 3 translational, 2 rotational, and 4 vibrational. The vibrational modes of CO_2 are symmetric stretching, bending (degenerate, 2 modes), and asymmetric stretching.

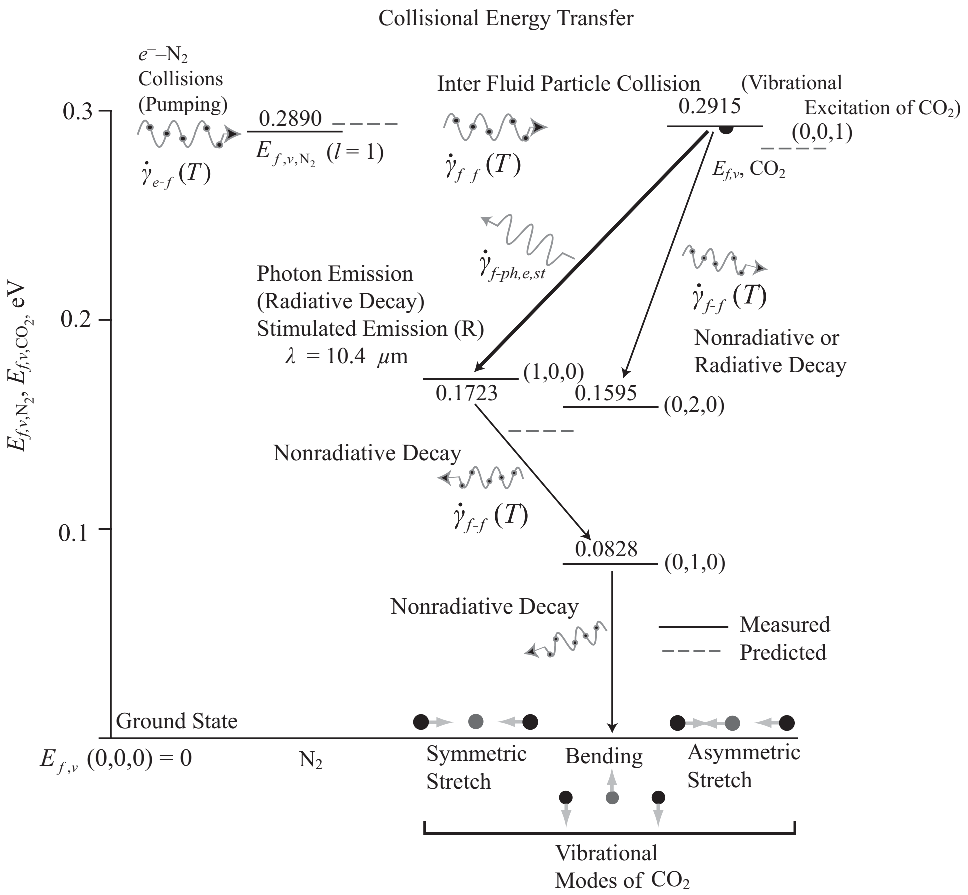

Figure 7.39. The energy-level (5 levels for CO_2) diagram of a CO_2 laser showing λ = 10.4 μm (includes rotational side bands) laser transition and coincident energy levels between the N_2 ($l = 1$) and CO_2 (0,0,1) energy states [494]. Semicircle indicates fluorescence. The *ab initio* calculated values are given in Section 6.1.5.

Nitrogen molecules are excited into their first vibrational state by collision with the accelerated electrons e^-. Figure 7.38 shows the N_2 vibration spectrum. Note that unless excited externally, at $T = 300$ K the thermal equilibrium population of $N_2(l = 1)$ is very low ($T_{f,v} = 3371$ K, Table 6.2). Applying an electrical current ionizes the gas and creates a flow of electron motion, which produces electron–fluid particle collisions. Electrical excitation increases the vibrational–rotational energy states of a fluid particle through electron impact and collisional energy transfer mechanisms. Electron impacts vibrationally excite nitrogen. Also, because transitions between vibrational energy levels in the same electronic state for a homonuclear diatomic molecule are forbidden according to the parity selection rule, the population of nitrogen molecules in the first vibrational energy state is allowed to accumulate.

Energy is then transferred through a resonant collision between nitrogen and carbon dioxide. An inelastic collision can transfer vibrational, rotational, and translational energy between fluid particles, if the energy states are sufficiently close. The near coincidence of the $l = 1$ energy state of nitrogen molecule and the (0,0,1) state of carbon dioxide allows this transition to occur easily near room temperature (The difference in energy is less than $k_B T$). The major absorption bands of CO_2 are listed in Table 7.3, and the quantum numbers in parentheses are explained in Section 7.8.2. The binary collision (Section 6.5) reaction is

$$E_{N_2(l=1)} + E_{CO_2(0,0,0)} \rightarrow E_{N_2(l=0)} + E_{CO_2(0,0,1)} - 2.232 \times 10^{-3} (\text{eV}). \qquad (7.228)$$

A transition of vibrational energy can occur radiatively. Radiative decay occurs most naturally into the next lowest energy state. Nonradiative decay may occur first, and is more likely to occur if the particle velocity is high, the collision rate is great, and the change in energy states is small. For carbon dioxide, a radiative decay from the (0,0,1) energy state to the (1,0,0) state will occur if conditions limit the effectiveness of nonradiative decay.

From the harmonic-oscillator approximation of vibrational energy states, the energy of the $l = 1$ state of nitrogen is estimated [from (7.223)] as 0.2920 eV. For the (0,0,1) and (1,0,0) energy states indicated in Figure 7.39, using the C=O bond vibrational frequency as the natural frequencies of carbon dioxide, gives for the first vibrational energy levels 0.1478 eV and 0.2831 eV. Note that the actual frequencies of (0,0,1) and (1,0,0) are different than these. Therefore, in general, the vibrational frequencies are measured.

The observed energy of the photon emitted in the carbon dioxide molecule (Figure 7.39) is $0.2915 - 0.1723 = 0.1192$ eV. This corresponds to a photon wavelength of 10.41 μm (Table 1.4) in the infrared regime. For the P-branch ($\Delta j = -1$) rotational energy transition, we have $E_{f,r} = B_{f,r}[(j-1)j - j(j+1)] = -2B_{f,r} j$, and for $j = 20$ as the most probable, we have (Section 6.1.5) $0.1192 - 40 \times 4.850 \times 10^{-5} = 0.1173$ eV (or $\lambda = 10.6$ μm). So, if the rotational energy sideband is used, in this case, the vibration-rotation transition energy is lower than the vibration-only transition. There are many other transitions that have been observed in the range between 10.4 and 10.6 μm in the CO_2 molecule, which are due to the rotational sublevel and isotope variations in the same vibrational transition. Note that the fraction of the excited (0,0,1) energy that is used for lasing is $0.1192/0.2915 = 0.4089$. However, the laser efficiency is lower than this due to the pumping, collision, and the nonradiative decay inefficiencies.

A number of factors can be controlled in a molecular laser system. Of primary importance in applications are controlling the wavelength, power and efficiency, and stability of a laser system. The energy transition present in the rotational–vibrational spectrum of the lasing fluid particle is what gives the molecular laser its wavelength, and in this way the wavelength of a laser can be chosen.

The output power and stability of a system are also dependent on the fluid particle energies. Output powers and stability are limited by inefficiencies of energy transfer and inconsistent transition energies. Creating stable operating conditions generates a stable laser system, which is done by reducing the variation in the initial distribution of energy states present by cooling. The addition of low pressures can reduce the collision rate, which in turn reduces the effect of collisional deactivation. Both low temperature and pressure can be obtained through gas cycling and control. Inherent energy losses and ineffective energy transfers can be limited by closely matching energy states between fluid particles and using transition energies that are closer to the ground state, so less energy is dissipated as heat.

(C) *Three-Level Analysis of CO_2 Laser Kinetics*

The three-level CO_2 laser model [336] enables a convenient analysis of the molecular gas-laser kinetics. Here, the $CO_2 - N_2$ gas mixture is initially in the ground states under standard gas conditions ($T = 300$ K, $p = 1$ atm). Figure 7.40 shows this simplified energy diagram, and here the vibrational energy levels are divided into three groups. The level 0 is for both ground states; the level 1, which is represented by (1,0,0) state of CO_2, includes the bending and symmetric stretch modes; and the level 2 includes the first vibration state of N_2 and the asymmetric mode state of CO_2. Since a chemical reaction or dissociation is not considered in this analysis, the total numbers of CO_2 and N_2 molecules are conserved, and it is assumed that radiative decay exists only in transition between (0,0,1) and (1,0,0) states. These energy levels do not include rotational levels (j). For analysis of the radiative decay process, the rotational energy conversions are regarded as transition into $j = 20$, which is assumed to be the most dominant state.

(i) *Rate Equations*

The vibrational energies of CO_2 and N_2 are transferred through several processes, including collisional and radiative transfer processes. As marked in Figure 7.40, the three-level analysis includes the following eight energy transfer processes [336].

$$
\begin{aligned}
&\boxed{1}\ \mathrm{CO_2}(0,0,1) + \mathrm{N_2}(l=0) \underset{\tau_{f\text{-}f,\mathrm{CO_2}\text{-}\mathrm{N_2},\leftarrow}}{\overset{\tau_{f\text{-}f,\mathrm{CO_2}\text{-}\mathrm{N_2},\rightarrow}}{\rightleftharpoons}} \mathrm{CO_2}(0,0,0) + \mathrm{N_2}(l=1) + 2.232\times 10^{-3}\ \mathrm{eV}\\
&\boxed{2}\ \mathrm{N_2}(l=0) + e^- \overset{\tau_{e\text{-}f(\mathrm{N_2})}}{\rightleftharpoons} \mathrm{N_2}(l=1) + e^-\\
&\boxed{3}\ \mathrm{CO_2}(0,0,0) + e^- \overset{\tau_{e\text{-}f,v(\mathrm{CO_2})}}{\rightleftharpoons} \mathrm{CO_2}(0,0,1) + e^-\\
&\boxed{4}\ \mathrm{CO_2}(0,0,1) \xrightarrow{\tau_{f\text{-}ph,e[\mathrm{CO_2}:(0,0,1)\rightarrow(1,0,0)]}} \mathrm{CO_2}(1,0,0) + \hbar\omega_{ph}\\
&\boxed{5}\ \mathrm{CO_2}(0,0,1) + \mathrm{M} \xrightarrow{\tau_{f\text{-}f,v[\mathrm{CO_2}:(0,0,1)\rightarrow(1,0,0)]}} \mathrm{CO_2}(1,0,0) + \mathrm{M} + 0.1192\ \mathrm{eV}\\
&\boxed{6}\ \mathrm{CO_2}(1,0,0) + \mathrm{M} \xrightarrow{\tau_{f\text{-}f,v[\mathrm{CO_2}:(1,0,0)\rightarrow(0,0,0)]}} \mathrm{CO_2}(0,0,0) + \mathrm{M} + 0.1723\ \mathrm{eV}\\
&\boxed{7}\ \mathrm{CO_2}(0,0,1) + \mathrm{N_2}(l=0) \xrightarrow{\tau_{f\text{-}f[\mathrm{CO_2}\text{-}\mathrm{N_2}:(0,0,1),l=0\rightarrow(1,0,0),l=0]}} \mathrm{CO_2}(1,0,0) + \mathrm{N_2}(l=0)\\
&\boxed{8}\ \mathrm{CO_2}(0,0,0) + \mathrm{N_2}(l=1) \xrightarrow{\tau_{f\text{-}f[\mathrm{N_2}\text{-}\mathrm{CO_2}:(0,0,0),l=1\rightarrow(1,0,0),l=0]}} \mathrm{CO_2}(1,0,0) + \mathrm{N_2}(l=0).
\end{aligned}
\tag{7.229}
$$

From the eight energy-exchange processes listed in (7.229), process $\boxed{1}$ (collisional energy transfer between CO_2 and N_2) is the closest to energy resonance. Since the

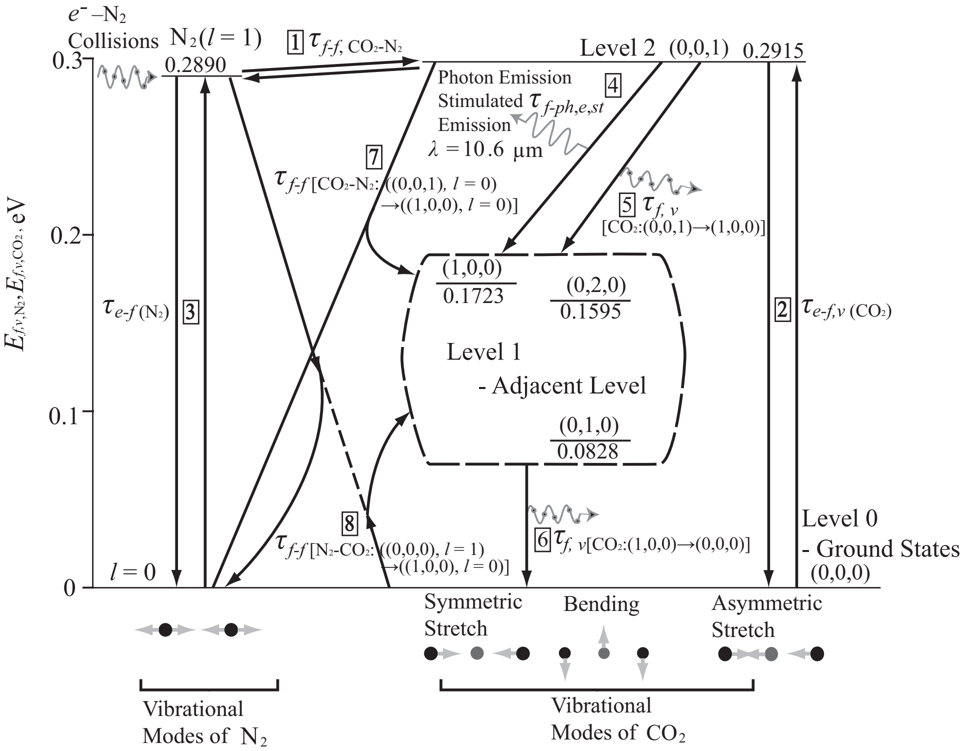

Figure 7.40. The energy-level diagram for a CO_2 laser, showing $\lambda = 10.6$ μm (including the rotational sideband of $j = 20$) laser emission and the eight processes. The time constants and the processes associated with each reaction are also shown [336].

difference in energy is only 2.232×10^{-3} eV, process $\boxed{1}$ is expected to be much faster than other processes. Thus, process $\boxed{1}$ can be independently considered, and the rate equation is

$$-\frac{\mathrm{d}}{\mathrm{d}t}n_{CO_2(0,0,1)} = \frac{n_{N_2(l=0)}n_{CO_2(0,0,1)}}{\tau_{f\text{-}f,CO_2\text{-}N_2,\rightarrow}} - \frac{n_{N_2(l=1)}n_{CO_2(0,0,0)}}{\tau_{f\text{-}f,CO_2\text{-}N_2,\leftarrow}}, \tag{7.230}$$

Note that the first subscript of the time constant includes energy carriers and the second one represents the modes or atomic species. Using the M–B equilibrium distribution function (F.17) at $T = 300$ K and the energies listed in Figure 7.40, the relation between the two time constants in (7.230) is

$$\tau_{f\text{-}f,CO_2\text{-}N_2,\leftarrow} = \frac{\tau_{f\text{-}f,CO_2\text{-}N_2,\rightarrow}}{\exp[(\hbar\omega_{N_2(l=1)} - \hbar\omega_{CO_2(0,0,1)})/k_BT]}\left(= \frac{\tau_{f\text{-}f,CO_2\text{-}N_2,\rightarrow}}{0.914}\right). \tag{7.231}$$

Using (7.231), the solution to (7.230) becomes

$$n_{CO_2(0,0,1)}(t) = n_{CO_2(0,0,1)}|_{t=0}$$
$$\times \frac{0.914n_{CO_2(0,0,0)} + n_{N_2(l=0)}\exp[-(n_{N_2(l=0)} + 0.914n_{CO_2(0,0,0)})\tau^{-1}_{f\text{-}f,CO_2\text{-}N_2,\rightarrow}t]}{0.914n_{CO_2(0,0,0)} + n_{N_2(l=0)}}, \tag{7.232}$$

and assuming that most molecules are in ground states ($n_{\mathrm{CO}_2} \simeq n_{\mathrm{CO}_2(0,0,0)}$, $n_{\mathrm{N}_2} \simeq n_{\mathrm{N}_2(l=0)}$, and $x_{\mathrm{CO}_2} + x_{\mathrm{N}_2} = 1$), the overall time constant between CO$_2$ and N$_2$ is

$$\tau_{f\text{-}f,\mathrm{CO}_2\text{-}\mathrm{N}_2} = \frac{\tau_{f\text{-}f,\mathrm{CO}_2\text{-}\mathrm{N}_2,\rightarrow}}{0.914 x_{\mathrm{CO}_2(0,0,0)} + x_{\mathrm{N}_2(l=0)}} = \frac{\tau_{f\text{-}f,\mathrm{CO}_2\text{-}\mathrm{N}_2,\rightarrow}}{1 - 0.086 x_{\mathrm{CO}_2(0,0,0)}}, \tag{7.233}$$

Now, consider the relaxation processes of excited CO$_2$ and N$_2$ after collision between CO$_2$ and N$_2$. The energy of excited CO$_2(0,0,1)$ and N$_2(l=1)$ molecules are transferred through processes $\boxed{2} - \boxed{8}$, and these processes are presented by four relaxation processes: CO$_2$ − CO$_2$, N$_2$ − CO$_2$,CO$_2$ − N$_2$, and N$_2$ − N$_2$. The overall time constant $\tau_{f\text{-}ph\text{-}f}$ of excited energy can be calculated by the following processes.

First, for $\tau_{\mathrm{CO}_2\text{-}\mathrm{CO}_2}$, in pure CO$_2$ gas, the number densities of CO$_2$ are $n_{\mathrm{CO}_2,(0,0,1)}$ for CO$_2(0,0,1)$ level, and $n_{\mathrm{CO}_2(0,0,0)}$ for CO$_2(0,0,0)$ level. Then for reaction constant $k_{r,\mathrm{CO}_2\text{-}\mathrm{CO}_2}$, the relaxation rate is

$$\tau^{-1}_{\mathrm{CO}_2\text{-}\mathrm{CO}_2} = k_{r,\mathrm{CO}_2\text{-}\mathrm{CO}_2} n_{\mathrm{CO}_2(0,0,1)} n_{\mathrm{CO}_2(0,0,0)}. \tag{7.234}$$

Since process $\boxed{1}$ is very rapid, the exponential term in (7.232) is negligible, and the number density of CO$_2(0,0,1)$ in CO$_2$–N$_2$ mixture (using the molecular fraction) is

$$n_{\mathrm{CO}_2(0,0,1),\mathrm{mix}} = \frac{\tau^{-1}_{f\text{-}f,\mathrm{CO}_2\text{-}\mathrm{N}_2,\leftarrow} x_{\mathrm{CO}_2}}{\tau^{-1}_{f\text{-}f,\mathrm{CO}_2\text{-}\mathrm{N}_2,\rightarrow} x_{\mathrm{N}_2} + \tau^{-1}_{f\text{-}f,\mathrm{CO}_2\text{-}\mathrm{N}_2,\leftarrow} x_{\mathrm{CO}_2}} n_{\mathrm{CO}_2(0,0,1)}. \tag{7.235}$$

Then, from (7.234) and (7.235) we have

$$\tau^{-1}_{\mathrm{CO}_2-\mathrm{CO}_2,\mathrm{mix}} = \tau^{-1}_{\mathrm{CO}_2\text{-}\mathrm{CO}_2} \frac{\tau^{-1}_{f\text{-}f,\mathrm{CO}_2\text{-}\mathrm{N}_2,\leftarrow} x^2_{\mathrm{CO}_2}}{\tau^{-1}_{f\text{-}f,\mathrm{CO}_2\text{-}\mathrm{N}_2,\rightarrow} x_{\mathrm{N}_2} + \tau^{-1}_{f\text{-}f,\mathrm{CO}_2\text{-}\mathrm{N}_2,\leftarrow} x_{\mathrm{CO}_2}}. \tag{7.236}$$

Similarly, we have

$$\tau^{-1}_{\mathrm{CO}_2\text{-}\mathrm{N}_2,\mathrm{mix}} = \tau^{-1}_{\mathrm{CO}_2\text{-}\mathrm{N}_2} \frac{\tau^{-1}_{f\text{-}f,\mathrm{CO}_2\text{-}\mathrm{N}_2,\leftarrow} x_{\mathrm{CO}_2} x_{\mathrm{N}_2}}{\tau^{-1}_{f\text{-}f,\mathrm{CO}_2\text{-}\mathrm{N}_2,\rightarrow} x_{\mathrm{N}_2} + \tau^{-1}_{f\text{-}f,\mathrm{CO}_2\text{-}\mathrm{N}_2,\leftarrow} x_{\mathrm{CO}_2}}, \tag{7.237}$$

$$\tau^{-1}_{\mathrm{N}_2\text{-}\mathrm{CO}_2,\mathrm{mix}} = \tau^{-1}_{\mathrm{N}_2\text{-}\mathrm{CO}_2} \frac{\tau^{-1}_{f\text{-}f,\mathrm{CO}_2\text{-}\mathrm{N}_2,\rightarrow} x_{\mathrm{CO}_2} x_{\mathrm{N}_2}}{\tau^{-1}_{f\text{-}f,\mathrm{CO}_2\text{-}\mathrm{N}_2,\rightarrow} x_{\mathrm{N}_2} + \tau^{-1}_{f\text{-}f,\mathrm{CO}_2\text{-}\mathrm{N}_2,\leftarrow} x_{\mathrm{CO}_2}}, \tag{7.238}$$

$$\tau^{-1}_{\mathrm{N}_2\text{-}\mathrm{N}_2,\mathrm{mix}} = \tau^{-1}_{\mathrm{N}_2\text{-}\mathrm{N}_2} \frac{\tau^{-1}_{f\text{-}f,\mathrm{CO}_2\text{-}\mathrm{N}_2,\rightarrow} x^2_{\mathrm{N}_2}}{\tau^{-1}_{f\text{-}f,\mathrm{CO}_2\text{-}\mathrm{N}_2,\rightarrow} x_{\mathrm{N}_2} + \tau^{-1}_{f\text{-}f,\mathrm{CO}_2\text{-}\mathrm{N}_2,\leftarrow} x_{\mathrm{CO}_2}}. \tag{7.239}$$

Using (7.236), (7.237), (7.238), and (7.239), and the Matthiesen rule (4.111), the overall relaxation time $\tau_{f\text{-}ph\text{-}f}$ is found.

(*ii*) *Time Constants: Theoretical Treatment*

To evaluate the overall relaxation time $\tau_{f\text{-}ph\text{-}f}$, the time constant of each processe should be found theoretically or experimentally. These are classified into collisional (nonradiative) and radiative relaxation processes.

Several models are available for the collisional relaxation processes. Landau and Teller [265] suggested a classical collinear model of the collisional energy transfer with exponential repulsive interaction. Recently, the full quantum-mechanical treatments of the three-dimensional collision dynamics using *ab initio* potential energy fields are reformed [348]. The Schwartz, Slawsky, and Herzfeld (SSH) one-dimensional model [415] gives the relation for $P_{f\text{-}f,v\text{-}t}$ as

$$\tau_{f\text{-}f,v\text{-}t} = \frac{1}{\dot{\gamma}_{f\text{-}f}\, P_{f\text{-}f,v\text{-}t}} = \frac{\tau_{f\text{-}f}}{P_{f\text{-}f,v\text{-}t}}, \tag{7.240}$$

where $\tau_{f\text{-}f,v\text{-}t}$ is the time constant of vibrational-translational energy transfer, $\tau_{f\text{-}f}$ is the time constant of collision, and $P_{f\text{-}f,v\text{-}t}$ is the probability that upon a collision the energy transfer occurs. Using (6.79), (6.80), and (6.81), the collision rate and time constant are found, and (7.240) gives the probability of energy transfer during collision.

$P_{f\text{-}f,v\text{-}t,i\rightarrow f}(u_i)$ is the probability that a system made up of a pair of colliding molecules with relative velocity u_i and vibrational states $l_{i,1}, l_{i,2}, \cdots, l_{i,n}$ will change into vibrational states $l_{f,1}, l_{f,2}, \cdots, l_{f,n}$ through collision. The probability of energy transfer during collision $P_{f\text{-}f,\, v\text{-}t}$ is found by integration with respect to u_i.

Using r as the distance between the centers of gravity of the colliding pair, and normal vibrational coordinates $s_1, s_2, \cdots, s_n$, the interaction potential between the molecules is approximated by a product of the functions of these coordinates [415]:

$$\varphi = \varphi_{\text{o}} f_{\varphi,r}(r) f_{\varphi,s_1}(s_1) \cdots f_{\varphi,s_n}(s_n). \tag{7.241}$$

Following the assumptions and method suggested in [510], $P_{f\text{-}f,v\text{-}t,i\rightarrow f}(u_i)$ is

$$P_{f\text{-}f,v\text{-}t,i\rightarrow f}(u_i) = \frac{4\varphi_{\text{o}}^2}{u_i u_f \hbar^2}[M_{l_{i,1},l_{f,1}} \cdots M_{l_{i,n},l_{f,n}} M_{u_i,u_f}], \tag{7.242}$$

where

$$M_{u_i,u_f} \equiv \int_{-\infty}^{\infty} \psi_{i,r} f_{\varphi,r}(r) \psi_{f,r} \mathrm{d}r = \langle \psi_{i,r} | f_{\varphi,r} | \psi_{f,r} \rangle, \tag{7.243}$$

and

$$M_{l_{i,n},l_{f,n}} \equiv \int_{-\infty}^{\infty} \psi_{i,n} f_{\varphi,s_n}(s_n) \psi_{f,n} \mathrm{d}s_n = \langle \psi_{i,n} | f_{\varphi,s_n} | \psi_{f,n} \rangle, \tag{7.244}$$

where $\psi_{i,r}$ and $\psi_{f,r}$ are the wave functions of the time-independent Schrödinger equation for the motion of a free particle in the potential field $\varphi_{\text{o}} f_{\varphi,r}(r)$, $\psi_{i,n}$ is the initial eigenstate of vibrational state n, and $\psi_{f,n}$ is the eigenstate of vibrational state n after collision.

In [210], a potential $f_{\varphi,r}(r) = e^{-a_{\text{o}} r}$ is used for M_{u_i,u_f}, and we obtain

$$P_{f\text{-}f,v\text{-}t,i\rightarrow f}(u_i) = M^2_{l_{i,1},l_{f,1}} \cdots M^2_{l_{i,n},l_{f,n}} \frac{(p_i^{*2} - p_f^{*2})^2 (e^{p_i^*} - e^{-p_i^*})(e^{p_f^*} - e^{-p_f^*})}{16\pi^2 (e^{p_i^*} + e^{-p_i^*} - e^{p_f^*} - e^{-p_f^*})^2}, \tag{7.245}$$

where $p_i^* \equiv 2\pi m_{12,m} u_i / a_{\text{o}} \hbar$ and $m_{12,m}$ is the reduced mass of the molecules.

When $f_{\varphi,s_n}(s_n) = e^{-a_o A_n s_n}$ is expanded in an infinite series as $f_{\varphi,s_n}(s_n) = 1 + (-a_o A_n s_n) + (-a_o A_n s_n/2!)^2 + \cdots$, we integrate $M_{l_{i,n},l_{f,n}}$ using the properties of the eigenvalues and eigenfunctions in a one-dimensional harmonic oscillator, as

$$M_{l_{i,n},l_{i,n}} = 1 \text{ and } M_{l_{i,n},l_{i,n}\pm 1} = -a_o A_n [\frac{\hbar(l_{i,n} + \frac{1}{2} \pm \frac{1}{2})}{2m_{12,v_n}\omega_n}]^{1/2}, \qquad (7.246)$$

where m_{12,v_n} is the reduced mass of the oscillator vibrating at the frequency ω_n.

Using the M–B velocity distribution at a temperature T, we have

$$P_{f\text{-}f,v\text{-}t} = \langle P_{f\text{-}f,v\text{-}t,i\to f}\rangle = 2(\frac{\mu}{2k_BT})^2 \int_0^\infty u_i^3 P_{f\text{-}f,v\text{-}t,i\to f}(u_i)\exp(\frac{-m_{12,m}u_i^2}{2k_BT})\mathrm{d}u_i \qquad (7.247)$$

For a nonresonant energy exchange, (7.247) gives [415]

$$P_{f\text{-}f,v\text{-}t} = 0.39 M^2_{l_{i,1},l_{f,1}} \cdots M^2_{l_{i,n},l_{f,n}} [\frac{2\pi m_{12,m}\Delta E}{(a_{o,cr})^2\hbar^2}]^2 \frac{\beta^{3/2}e^{-\beta}}{1-e^{2\beta/3}}, \qquad (7.248)$$

where

$$\beta \equiv 3[\frac{\pi^2(\Delta E)^2 m_{12,m}}{(a_{o,cr})^2\hbar^2(2k_BT)}]^{\frac{1}{2}} \pm \frac{\Delta E}{2k_BT}, \quad \Delta E = \frac{1}{2}m_{12,m}(u_i^2 - u_f^2).$$

Here a_o is slightly dependent on the initial relative molecular velocity and consequently on temperature, and $a_{o,cr}$ in (7.248) is the value of a_o at $u_i = u_{i,cr}$, where $u_{i,cr}$ is the value that maximizes the integrand of (7.247). Then, from (7.240) we can theoretically find the time constants of the collisional relaxation processes of energy transfer during collisions.

Relaxation in the CO_2 laser system involves collisional processes, as well as a radiative process between (0,0,1) level and (1,0,0) level. The radiative process depends on vibrational transition dipole moment $\boldsymbol{\mu_e}$ in (3.43), and the spontaneous emission rate is

$$\dot{\gamma}_{f\text{-}ph,e,sp} = \frac{2\omega^3_{e,g}}{3\epsilon_o h_P u^3_{ph}}|\boldsymbol{\mu_e}|^2\frac{S_j}{g_{v',j'}} = \frac{64\pi^4 f^3_{e,g}}{3h_P u_{ph}{}^3 g_{v'j'}}|\boldsymbol{\mu_e}|^2 S_j. \qquad (7.249)$$

Then, using (7.40) and (7.42) in Section 7.4, the stimulated transition rate is

$$\dot{\gamma}_{f\text{-}ph,e,st} = \frac{8\pi^3 S_j}{3h_P^2 g_{vj}}|\boldsymbol{\mu_e}|^2, \qquad (7.250)$$

where j is the rotational quantum number, g_j is the degeneracy ($g_j = 2j+1$), and S_j is the rotational line strength factor with $S_j = j+1$ (R branch, i.e., $j' = j+1$), and $S_j = j$ (P branch, i.e., $j' = j-1$). Using the Füchtbauer–Laudenburg relation [276], the absorption coefficient is

$$\sigma_{ph} = \frac{8\pi^3}{3h_P}(\frac{m}{2\pi k_BT})^{1/2}|\boldsymbol{\mu_e}|^2 S_j(\frac{N_{v,j}}{g_{v,j}} - \frac{N_{v',j'}}{g_{v',j'}}). \qquad (7.251)$$

The vibrational transition dipole moment is found by the measurement of the absorption coefficient. From the measurement [336], $\sigma_{ph} = 0.251\ \text{cm}^{-1}$, and from (7.251), $|\boldsymbol{\mu_e}|^2 = 3.48 \times 10^{-2}$ D for $(0,0,1) \to (1,0,0)$; the spontaneous emission time constant is $\tau_{f\text{-}ph,e,sp} = \dot{\gamma}^{-1}_{f\text{-}ph,e,sp} = 3.13$ s. This value is much greater than the time constants of other processes, and therefore, spontaneous radiative relaxation has a negligible effect on the lasing rate. Stimulated radiative decay rate is proportional to irradiation flux $I_{ph,i}$.

Using the simplified (absorption only) form of (7.126) of the ERT (7.83), and for unidirectional (along x) radiation, under steady state, and $\dot{s}_{ph,i} = 0$,

$$\frac{\mathrm{d}I_{ph,\omega}}{\mathrm{d}x} = -\sigma_{ph,\omega} I_{ph,\omega}, \quad I_{ph}(x=0) = I_{ph,i} \tag{7.252}$$

The net rate at which molecules are stimulated to emit photons, which is the same as the decay rate per unit volume of stimulated radiative decay, is found by dividing (7.252) by photon energy $\hbar\omega_{e,g}$, i.e.,

$$\frac{\dot{\gamma}_{f\text{-}ph,e,st}}{V} = \frac{1}{\tau_{f\text{-}ph,e,sp} V} = -\frac{\mathrm{d}I_{ph,\omega}}{\hbar\omega_{e,g}\mathrm{d}x} = \frac{\sigma_{ph} I_{ph,\omega}}{\hbar\omega_{e,g}}. \tag{7.253}$$

(*iii*) *Time Constants: Experimental Data*

The time constants in a CO_2 laser system are also found experimentally [336]. From measurements [336], the time constant for $\boxed{1}$ is

$$p^{-1}\tau^{-1}_{f\text{-}f,\mathrm{CO_2\text{-}N_2},\rightarrow} = 1.444 \times 10^{7}\ \mathrm{s^{-1}\text{-}atm^{-1}}. \tag{7.254}$$

Using (7.233) at STP, $\tau_{f\text{-}f,\mathrm{CO_2\text{-}N_2}} = 0.072\ \mu$s with $x_{\mathrm{CO_2}} = 0.47$. To find the overall relaxation time constants, the four relaxation processes ($\tau_{\mathrm{CO_2\text{-}CO_2}}$, $\tau_{\mathrm{N_2\text{-}N_2}}$, $\tau_{\mathrm{CO_2\text{-}N_2}}$, and $\tau_{\mathrm{N_2\text{-}CO_2}}$) are needed. Starting with the CO_2-CO_2 relaxation process [(0, 0, 1) → (0, 0, 0) or (1, 0, 0)], which includes processes $\boxed{3}$, $\boxed{4}$, $\boxed{5}$, and $\boxed{6}$, the rate equations are

$$\boxed{3}+\boxed{2}: \quad \frac{\mathrm{d}n_{\mathrm{CO_2}(0,0,0)}}{\mathrm{d}t} = \frac{n_{\mathrm{CO_2}(1,0,0)}}{\tau_{f,v[\mathrm{CO_2}:(1,0,0)\rightarrow(0,0,0)]}} + \frac{n_{\mathrm{CO_2}(0,0,1)}}{\tau_{e\text{-}f(\mathrm{CO_2})}} \tag{7.255}$$

$$\begin{aligned}\boxed{4}+\boxed{5}+\boxed{6}: \quad \frac{\mathrm{d}n_{\mathrm{CO_2}(1,0,0)}}{\mathrm{d}t} &= \frac{n_{\mathrm{CO_2}(0,0,1)}}{\tau_{f\text{-}ph,e[\mathrm{CO_2}:(0,0,1)\rightarrow(1,0,0)]}} + \frac{n_{\mathrm{CO_2}(0,0,1)}}{\tau_{f,v[\mathrm{CO_2}:(0,0,1)\rightarrow(1,0,0)]}} \\ &\quad - \frac{n_{\mathrm{CO_2}(1,0,0)}}{\tau_{f,v[\mathrm{CO_2}:(1,0,0)\rightarrow(0,0,0)]}}\end{aligned} \tag{7.256}$$

$$\begin{aligned}\boxed{4}+\boxed{5}+\boxed{3}: \quad \frac{\mathrm{d}n_{\mathrm{CO_2}(0,0,1)}}{\mathrm{d}t} &= -\frac{n_{\mathrm{CO_2}(0,0,1)}}{\tau_{f\text{-}ph,e[\mathrm{CO_2}:(0,0,1)\rightarrow(1,0,0)]}} \\ &\quad - \frac{n_{\mathrm{CO_2}(0,0,1)}}{\tau_{f,v[\mathrm{CO_2}:(0,0,1)\rightarrow(1,0,0)]}} - \frac{n_{\mathrm{CO_2}(0,0,1)}}{\tau_{e\text{-}f(\mathrm{CO_2})}}.\end{aligned} \tag{7.257}$$

For $I_{ph,\omega} = 0$ (absence of stimulated emission), we have

$$\tau^{-1}_{\mathrm{CO_2\text{-}CO_2}} = \tau^{-1}_{f\text{-}ph,v(\mathrm{CO_2\text{-}CO_2})} = \tau^{-1}_{e\text{-}f(\mathrm{CO_2})} + \tau^{-1}_{f,v[\mathrm{CO_2}:(0,0,1)\rightarrow(1,0,0)]}, \tag{7.258}$$

and for $I_{ph,\omega} \neq 0$,

$$\tau^{-1}_{f\text{-}ph,v(\mathrm{CO_2\text{-}CO_2})} = \tau^{-1}_{e\text{-}f(\mathrm{CO_2})} + \tau^{-1}_{f,v[\mathrm{CO_2}:(0,0,1)\rightarrow(1,0,0)]} + \tau^{-1}_{f\text{-}ph,e,st}. \tag{7.259}$$

Table 7.6. *Time constants in* $CO_2 - N_2$ *gas laser at* $T = 300$ *K and* $p = 1$ *atm [336].*

Time constant	Magnitude, μs	Experiment/Prediction
$\tau_{f\text{-}f,CO_2\text{-}N_2}$	0.072	Prediction
$\tau_{e\text{-}f(N_2)}$	$\approx 10^6$	Prediction
$\tau_{f\text{-}f(N_2\text{-}CO_2,CO_2\text{-}N_2)}$	14.6 ($x_{CO_2} = 0.47$)	Experiment
$\tau_{f\text{-}ph,v(CO_2)}$	29.9	Prediction
$\tau_{f,v(CO_2)}$	132.8	Experiment
$\tau_{f\text{-}ph,st}$	38.5 ($I_{ph,i} = 52$ W/cm^2)	Experiment
$\tau_{f\text{-}ph\text{-}f}$	13.9 ($x_{CO_2} = 0.47$)	Prediction

The N_2-N_2 relaxation involves process $\boxed{2}$ only. Thus, the rate equation for n_{N_2} is

$$\frac{\mathrm{d}n_{N_2(l=0)}}{\mathrm{d}t} = -\frac{\mathrm{d}n_{N_2(l=1)}}{\mathrm{d}t} = \frac{n_{N_2(l=1)}}{\tau_{e\text{-}f(N_2)}}, \quad \text{and} \quad \tau_{N_2\text{-}N_2} = \tau_{e\text{-}f(N_2)}. \tag{7.260}$$

This reaction represents the excitation $[\dot{\gamma}_{e\text{-}f,e(N_2)}]$ and deexcitation process $[\dot{\gamma}_{e\text{-}f,de(N_2)}]$ by electron e^-, and these depend on the electronic temperature by the following relation [471]:

$$\frac{\dot{\gamma}_{e\text{-}f,e(N_2)}}{\dot{\gamma}_{e\text{-}f,de(N_2)}} = \exp(\frac{E_{f,v,N_2}}{k_B T_e}). \tag{7.261}$$

In this model, the electronic temperature almost matches the energy transfer necessary to excite N_2, and thus, the relaxation process of N_2 ($\tau^{-1}_{e\text{-}f(N_2)}$) is rather very slow [328] (i.e., $p\tau_{e\text{-}f(N_2)} > 1$ atm-s). At STP, $\tau_{e\text{-}f(N_2)} \simeq 1$ s (much larger than others), so it is ignored in calculating the overall time constant.

The CO_2-N_2 and N_2-CO_2 processes are related to processes $\boxed{7}$ and $\boxed{8}$ as

$$\tau_{CO_2\text{-}N_2} = \tau_{f\text{-}f[CO_2\text{-}N_2:(0,0,1),l=0\rightarrow(1,0,0),l=0]} \tag{7.262}$$

$$\tau_{N_2\text{-}CO_2} = \tau_{f\text{-}f[N_2\text{-}CO_2:(0,0,0),l=1\rightarrow(1,0,0),l=0)]}. \tag{7.263}$$

The experimental results give $p\tau_{f\text{-}f(N_2\text{-}CO_2,CO_2\text{-}N_2)} = 14.6$ μs-atm for $x_{CO_2} = 0.47$ [336]. Using the above values and relations, the overall time constant is $\tau_{f\text{-}ph\text{-}f} = 13.9 \pm 0.7$ μs. The time constants in this three-level energy analysis are summarized in Table 7.6.

(D) *Laser Cooling of CO_2*

Gas-laser cooling using the Doppler effect discussed in Section 7.13.2 is limited to atomic gases. In contrast, gas-laser cooling by spontaneous anti-Stokes fluorescence (Section 7.12) can be applied to polyatomic gas molecules, which have a multi-energy level system, and have a larger efficiency. The concept of laser cooling by the anti-Stokes fluorescence has long been recognized [372], but the net cooling had not been observed until laser cooling of a low-pressure CO_2–Xe system in

1981 [114]. Here, we use the three-level analysis of the previous section to analyze the anti-Stokes laser cooling of a $CO_2{-}Xe$ system.

(*i*) CO_2 *Laser Cooling Cycle*

The principal mechanism of the anti-Stokes cooling in CO_2 gas-laser systems are shown in Figures 7.41(a)–(c). The energy distribution of CO_2 and Xe molecules in the cooling tube follows the M−B distribution. In Figure 7.42(a), the $CO_2{-}Xe$ gas mixture is irradiated by a CO_2 laser with 10.6 μm wavelength, and CO_2 molecules in level 1 are excited to level 2, the (0,0,1) asymmetric vibration mode, by absorbing photons. In Figure 7.42(b), CO_2 molecules in level 2 undergo radiative decay by spontaneous emission of 4.3 μm wavelength, while the $CO_2{-}Xe$ gas system loses its internal energy through this emission. In Figure 7.41(c), energy exchanges by collisions between CO_2 and CO_2 or Xe replenish the population of fluid particles in level 1, which was reduced during excitation by photon absorption, as in (a). The molecules eventually reach thermal equilibrium by the collisional energy transport, and therefore, the ratio of the number of CO_2 molecules in each level is given by the M−B distribution. This cycle reduces the internal energy of the CO_2 and Xe gas mixture system by the difference between the absorbed energy in step (a) and the emitted energy in spontaneous emission (c), so the cooling energy is

$$\Delta E_{\mathrm{c}} = \hbar\omega_{2\to 0} - \hbar\omega_{2\to 1} = \hbar\omega_{1\to 0}. \tag{7.264}$$

(*ii*) *Calculation of Anti-Stokes Cooling Rate*

The gas mixture is in a tube as shown in Figure 7.41, with the tube wall maintained at temperature T_{o}. The laser beam is centrally located with radius R_L. We begin with some simplifying assumptions. The temperature distribution within the tube is one-dimensional (radial) and in steady state. CO_2 molecules in level 2 undergo nonradiative decays by collisions and radiative decays by spontaneous emission. However, in the cooling effect we do not include 10.6 μm radiative decay to level 1, because this emitted energy in 10.6 μm spontaneous emission is equivalent to the absorbed energy in photon absorption, and thus it does not contribute to cooling or heating.

CO_2 molecules in level 2 decay by spontaneous emission with a time constant $\tau_{f\text{-}ph,e,sp}$, and from (7.264) the decreased internal energy per unit time in the $CO_2{-}Xe$ system is $\tau^{-1}_{f\text{-}ph,e,sp}\hbar\omega_{1\to 0}$. During nonradiative relaxation by vibration-translation energy transfer (inelastic collisions), the internal energy of the gas mixture does not change, whereas the mode of internal energy changes from vibrational to translational. CO_2 molecules in level 2 decay by nonradiative relaxation processes, and the internal energy of the $CO_2{-}Xe$ gas mixture increases by $\tau^{-1}_{f\text{-}f,v\text{-}t}\hbar\omega_{2\to 1}$, where $\tau_{f\text{-}f,v\text{-}t}$ is the time constant of the collisional relaxation process given by (7.240).

The cooling rate (net rate of change in energy) by CO_2 molecules in level 2 is

$$\frac{\mathrm{d}E_{c,h}}{\mathrm{d}t} = -\frac{\hbar\omega_{1\to 0}}{\tau_{f\text{-}ph,e,sp}} + \frac{\hbar\omega_{2\to 1}}{\tau_{f\text{-}f,v\text{-}t}} = -\frac{\hbar\omega_{2\to 0}}{\tau_{f\text{-}ph,e,sp}} + \frac{\hbar\omega_{2\to 1}}{\tau_{f\text{-}ph\text{-}f}}, \tag{7.265}$$

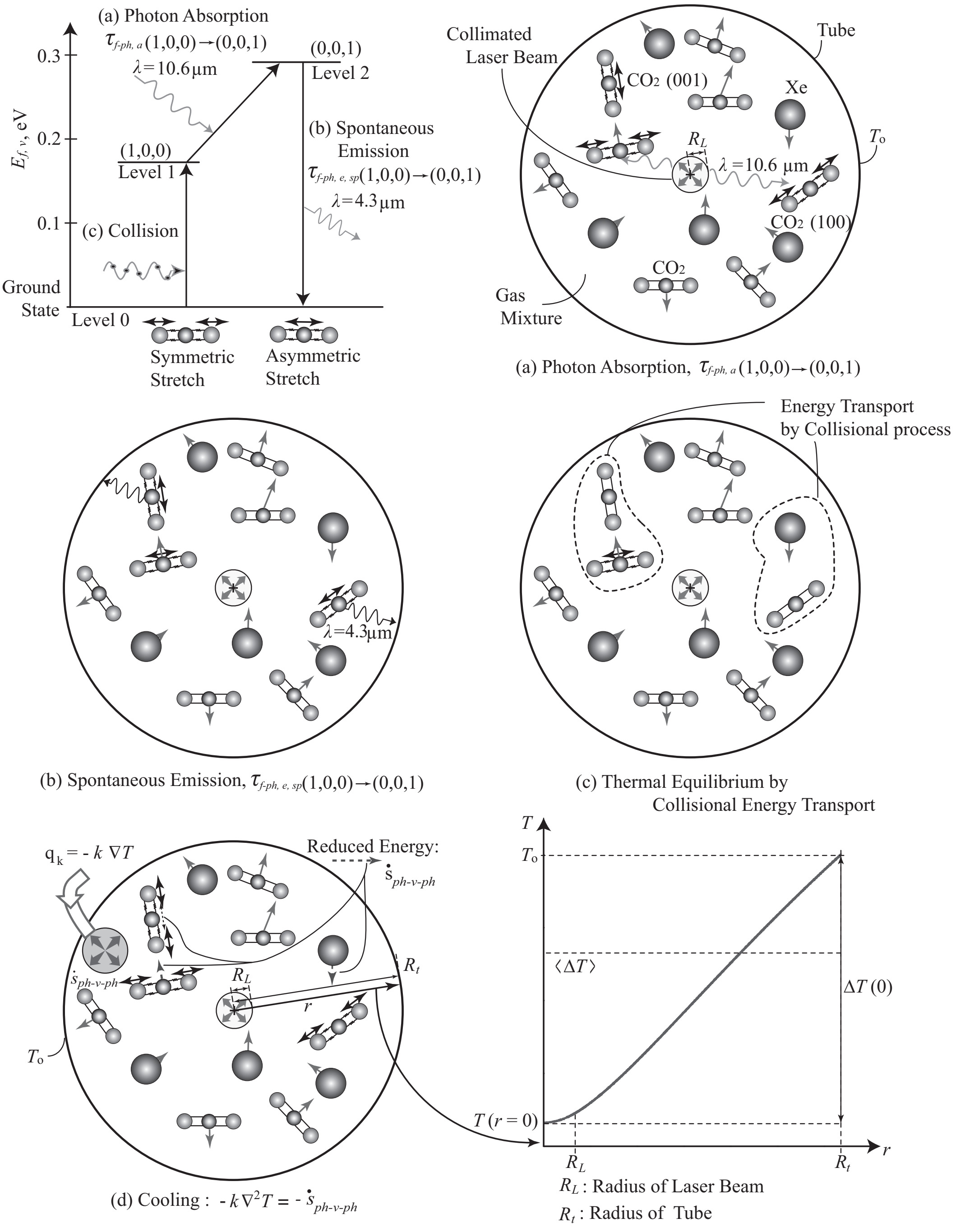
(a) Photon Absorption
$\tau_{f\text{-}ph,\,a}(1,0,0) \rightarrow (0,0,1)$
$\lambda = 10.6\,\mu\mathrm{m}$
(0,0,1)
Level 2
(1,0,0)
Level 1
(b) Spontaneous Emission
$\tau_{f\text{-}ph,\,e,\,sp}(1,0,0) \rightarrow (0,0,1)$
$\lambda = 4.3\,\mu\mathrm{m}$
(c) Collision
$E_{f,\,v}$, eV
0.3
0.2
0.1
Ground State
Level 0
Symmetric Stretch
Asymmetric Stretch
Collimated Laser Beam
Tube
CO_2 (001)
Xe
T_o
R_L
$\lambda = 10.6\ \mu\mathrm{m}$
CO_2 (100)
CO_2
Gas Mixture
Energy Transport by Collisional process
$\lambda = 4.3\,\mu\mathrm{m}$
$q_k = -k\,\nabla T$
Reduced Energy:
$\dot{s}_{ph\text{-}v\text{-}ph}$
$\dot{s}_{ph\text{-}v\text{-}ph}$
R_L
R_t
r
T_o
T
T_o
$\langle \Delta T \rangle$
$\Delta T\,(0)$
$T\,(r=0)$
R_L
R_t
r

(a) Photon Absorption, $\tau_{f\text{-}ph,\,a}(1,0,0) \rightarrow (0,0,1)$

(b) Spontaneous Emission, $\tau_{f\text{-}ph,\,e,\,sp}(1,0,0) \rightarrow (0,0,1)$

(c) Thermal Equilibrium by Collisional Energy Transport

(d) Cooling : $-k\nabla^2 T = -\dot{s}_{ph\text{-}v\text{-}ph}$

R_L : Radius of Laser Beam
R_t : Radius of Tube
T_o : Prescribed Tube Wall Temperature

Figure 7.41. The energy-level diagram for CO_2 laser cooling [114] (a)–(c): Cooling processes. (d) Cooling effect, and (e) gas temperature distribution.

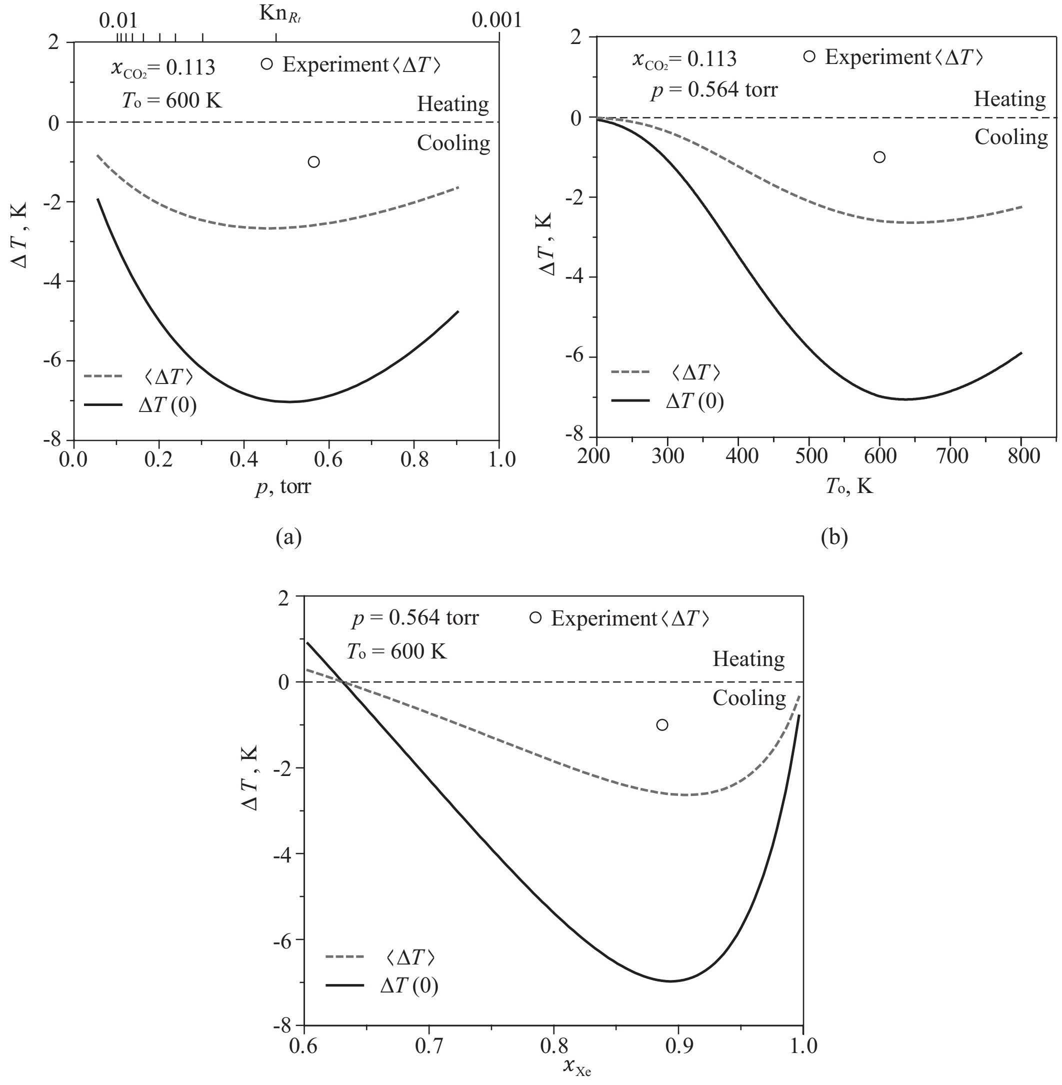

(a)

(b)

(c)

Figure 7.42. Variation of centerline cooling with respect to (a) pressure p, (b) tube temperature T_o, and (c) mole fraction of Xe x_{Xe}. In this analysis, $\tau_{f\text{-}ph,e,sp} = 2.44$ ms, $R_L = 0.50$ cm, and $R_t = 6.35$ cm [114]. Also, as a reference $n_o = 3.88 \times 10^{19}$ 1/m^3, $\tau_{f\text{-}f,v\text{-}t} = 26.8$ ms at $T = 600$ K, and $p = 0.564$ torr [505]. For $\mathrm{Kn}_{R_t} \ll 1$, the gas is in the viscous regime.

where $\tau_{f\text{-}ph\text{-}f}$ is the overall relaxation time constant of CO_2 molecules in level 2, including the radiative $\tau_{f\text{-}ph,e,sp}$ and nonradiative $\tau_{f\text{-}f,v\text{-}t}$. The volumetric cooling rate, $\dot{s}_{ph\text{-}v\text{-}ph}$, varies with the radial direction r and is

$$\dot{s}_{ph\text{-}v\text{-}ph}(r) = n_{\mathrm{CO_2},(0,0,1)}(r)\frac{\mathrm{d}E_{c,h}}{\mathrm{d}t} = n_{\mathrm{CO_2},(0,0,1)}(r)\,(-\frac{\hbar\omega_{2\rightarrow 0}}{\tau_{f\text{-}ph,e,sp}} + \frac{\hbar\omega_{2\rightarrow 1}}{\tau_{f\text{-}ph\text{-}f}}), \qquad (7.266)$$

where $n_{\mathrm{CO_2},(0,0,1)}(r)$ is the number density of CO_2 molecules in level 2 at r. Here we use the saturated values (n_o) in the laser-irradiated region ($0 \le r \le R_L$)

(i.e., $n_{CO_2,(0,0,1)}(r) = n_o$) where n_o is found from the thermal equilibrium density of CO_2 in level 1.

The population rate equation for $n_{CO_2,(0,0,1)}(r)$ is

$$\frac{dn_{CO_2(0,0,1)}(r)}{dt} = -\frac{n_{CO_2(0,0,1)}}{\tau_{f\text{-}ph\text{-}f}}, \tag{7.267}$$

and the species diffusion mass conservation equation (the Fick law) is

$$\begin{aligned} \dot{\boldsymbol{m}}_{CO_2(0,0,1)} &= -D_f \nabla \rho_{CO_2(0,0,1)} = -D_f \nabla n_{CO_2(0,0,1)} m_{CO_2} \\ \nabla \cdot \dot{\boldsymbol{m}}_{CO_2(0,0,1)} &= -\nabla \cdot (D_f \nabla n_{CO_2(0,0,1)} m_{CO_2}) = m_{CO_2} \dot{n}_{CO_2(0,0,1)}, \end{aligned} \tag{7.268}$$

where D_f is the gaseous species (mass) diffusivity for $CO_2(0,0,1)$ in three-level CO_2 and m_{CO_2} is the mass of the CO_2 molecule. Using (7.267), (7.268) for cylindrical coordinate becomes

$$\frac{D_f}{r}\frac{d}{dr}(r\frac{dn_{CO_2(0,0,1)}(r)}{dr}) - \frac{n_{CO_2(0,0,1)}}{\tau_{f\text{-}ph\text{-}f}} = 0. \tag{7.269}$$

Considering the boundary conditions, we find the solution

$$n_{CO_2(0,0,1)}(r) = n_o \frac{K_o[r/(D_f \tau_{f\text{-}ph\text{-}f})^{1/2}]}{K_o[R_L/(D_f \tau_{f\text{-}ph\text{-}f})^{1/2}]} \text{ for } R_L \le r \le R_t, \tag{7.270}$$

where K_o is a modified Bessel function. Using the energy equation [$\nabla \cdot \boldsymbol{q}_k(r) = \dot{s}_{ph\text{-}v\text{-}ph}(r)$, where $\boldsymbol{q}_k$ is the conductive heat flux vector] in Table 1.1, we have

$$-k_f(\frac{1}{r}\frac{d}{dr}r\frac{d\Delta T}{dr}) = \dot{s}_{ph\text{-}v\text{-}ph}(r), \tag{7.271}$$

where k_f is a gas mixture thermal conductivity. Solving (7.271) using the Bessel function J_o, the local cooling [$\Delta T(r) = T(r) - T_o$] is

$$\Delta T(r) = \frac{2}{{R_t}^2} \sum_{n=1}^{\infty} \frac{\langle \dot{s}_{ph\text{-}v\text{-}ph}(\alpha_n) \rangle J_o(\alpha_n r)}{k_f {\alpha_n}^2 [J_1(\alpha_n R_t)]^2}, \tag{7.272}$$

where $\langle \dot{s}_{ph\text{-}v\text{-}ph}(\alpha_n) \rangle = \int_0^{R_T} r \dot{s}_{ph\text{-}v\text{-}ph}(r) J_o(\alpha_n r) dr$ and $\alpha_n R_t$ is the n-th root of $J_o(r) = 0$. Figure 7.41(e) shows variation of $\Delta T(r)$. Dimensionless $\Delta T^*(0)$ is

$$\Delta T^*(0) = \frac{k_f \Delta T(0)}{\dot{s}_{ph\text{-}v\text{-}ph,o} R_t^2} = \sum_{n=1}^{\infty} \frac{2\int_0^1 r^* n^*(r^*) J_1(\alpha_n^* r^*) dr^*}{(\alpha_n^*)^2 [J_1(\alpha_n^*)]^2}, \tag{7.273}$$

where $\dot{s}_{ph\text{-}v\text{-}ph,o} = n_o(dE_{c,h}/dt)$, $\alpha_n^* = \alpha_n R_t$, and $r^* = r/R_t$. The area averaged cooling is given by

$$\langle \Delta T \rangle = \frac{1}{A}\int_{r=0}^{R_t} \Delta T(r)\, 2\pi r dr = \frac{2}{{R_t}^2}\int_0^{R_t} r \Delta T(r) dr. \tag{7.274}$$

(*iii*) *Optimization for Cooling*

In (7.266), cooling occurs when $\dot{s}_{ph\text{-}v\text{-}ph} < 0$ or $\mathrm{d}E_{c,h}/\mathrm{d}t < 0$, i.e.,

$$\tau^{-1}_{f\text{-}ph\text{-}f} < \frac{\omega_{2\rightarrow 0}}{\omega_{2\rightarrow 1}}\tau^{-1}_{f\text{-}ph,e,sp} \quad (= 2.45\tau^{-1}_{f\text{-}ph,e,sp}). \tag{7.275}$$

From (7.265), (7.270), and (7.272), large collisional relaxation time constant $\tau_{f\text{-}f,v\text{-}t}$, large diffusivity D_f, and small thermal conductivity k_f are desirable for larger cooling. From Section 6.6, the collisional time constant (and diffusivity and thermal conductivity) depends on pressure p, temperature T, and the mole fraction of Xe, x_{Xe}. Thus, $\Delta T(0)$ and $\langle \Delta T \rangle$ are maximized through these gas mixture conditions.

Species diffusivity is similar to kinematic viscosity such that $\mu_f/\rho_f D_f$ (Schmidt number) is near unity; then from (6.85), (6.87), and (6.91), we have

$$\frac{\mu_f}{\rho_f} = D_f = \frac{1}{3}\langle u_f \rangle \lambda_f = \frac{2k_{\mathrm{B}}{}^{3/2}}{3\pi^{3/2}m^{1/2}d_{\mathrm{CO}_2}{}^2}\frac{T^{3/2}}{p}. \tag{7.276}$$

In (6.128), the density of the gas ρ_f is proportional to pressure, while the mean free path of the gas λ_f is in inverse proportion to p. Thus, p does not influence the thermal conductivity. Also, from (7.240), the collisional time constant is the inverse of the product of transition probability and the collision rate, and from (6.79), the collision rate is proportional to the number density of CO_2. Therefore, low gas pressure is needed to increase the collisional time constant. However, the small number density of CO_2 in low gas pressure also leads to decrease in the anti-Stokes cooling effect (due to the smaller spontaneous emission from the smaller number density for CO_2 in level 2). Considering these pressure effects, the variation of cooling with respect to pressure is shown in Figure 7.42(a).

As the tube temperature T_{o} increases, from (7.276) D_f increases. From (6.128), k_f is a product of the density ρ_f, thermal speed $\langle u_f \rangle$, and mean free path λ_f. ρ_f is proportional to T_{o}, and λ_f is in inverse proportion to T_{o} from (6.87). Thus, k_f is in proportion to $\langle u_f \rangle$, which is proportional to $T_{\mathrm{o}}^{1/2}$ from (6.127) and (6.128). Then,

$$\tau^{-1}_{f\text{-}f} = \frac{4\pi^{1/2}d^2(k_{\mathrm{B}}T_{\mathrm{o}})^{1/2}n_f}{m^{1/2}} = \frac{4\pi^{1/2}d^2 p}{(k_{\mathrm{B}}m)^{1/2}}T_{\mathrm{o}}^{-1/2}. \tag{7.277}$$

However, from the M–B distribution, the CO_2 population in the higher level increases with T_{o}, inducing the anti-Stokes cooling effect. The combined effects of T_{o} are shown in Figure 7.42(b).

Since k_f of pure Xe gas is fairly low due to its heavy atomic mass, the larger mole fraction of Xe (x_{Xe}), the lower k_f of gas mixture, and the larger $\tau_{f\text{-}f}$. The larger x_{Xe} also makes for smaller p_{CO_2} and larger D_f. The small k_f, large $\tau_{f\text{-}f,v\text{-}t}$, and large D_f (for large x_{Xe}) contribute to increase the cooling. However, the increase in x_{Xe} also decreases the number density of CO_2 in level 2. Considering these effects, we find an optimal x_{Xe} as Figure 7.42(c) shows.

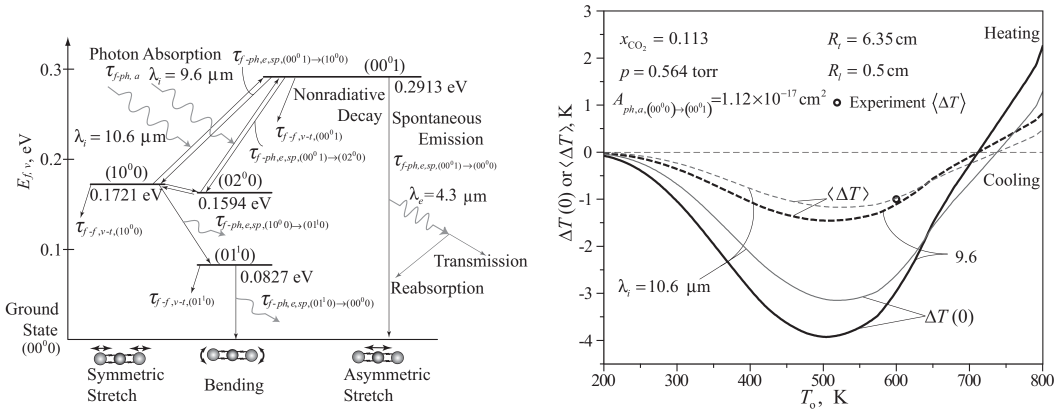

(a) (b)

Figure 7.43. (a) Five-level vibrational energy transitions and their time constants in laser cooling of CO_2 gas. The photon wavelength is selected for the transitions with more effective cooling. (b) Comparison of 9.6 and 10.6 μm wavelength laser cooling, showing variations of cooling with respect to cylinder temperature for both wavelengths. The macroscopic conditions are the same as [114], and the experimental result of [114] for $\lambda_i = 10.6$ μm is also shown.

(*iv*) *Enhanced Cooling using* (02^00) *excitation*

In [423], the enhanced anti-Stokes cooling of CO_2 gas is predicted by the laser irradiation with a 9.6 μm wavelength resonant with the (02^00) level improves. Here, the Herzberg notation [191], $(v_1v_2^lv_3)$, is used for vibrational states, where v_1, v_2, and v_3 are the symmetric, bending, and asymmetric vibrational quantum numbers and l is the angular quantum number of the bending mode. Because the population of overtone vibration levels is low at low vibration temperatures, only levels under (00^01) are considered. Among these, (00^00), (10^00), and (02^00) are possible levels for radiative excitation to (00^01), according to the vibration mode transition selection rule [121]. Covering these three levels, in this analysis, we assume a five-level vibration energy system, as shown in Figure 7.43(a).

Using the time constants in Table 7.7, the anti-Stokes cooling effect in the $CO_2{-}Xe$ gas system is calculated. In spite of the slightly larger photon energy absorption and lower absorption rate due to the smaller transition dipole, when compared to 10.6 μm [251], we found that 9.6 μm resonance with excitation of (02^00) enhances cooling because of the increase in pumped population. The 10.6 and 9.6 μm dual-beam irradiation appears to raise the excited population, but the (00^01) level population cannot exceed the saturated population with a 9.6 μm irradiation. Also, dual irradiation with the 15 μm laser changes the population of other energy levels that have smaller radiative relaxation rates (compared to nonradiative), and this deteriorates cooling. The cooling enhancement of the 9.6 μm wavelength in Figure 7.43(b) shows 3.93 K cooling at a cylinder temperature of 504 K, and 1.05 K with the cylinder at room temperature. All macroscopic conditions are the same as

Table 7.7. *Time constants in laser cooling of CO_2-Xe gas.*

Mechanism	Time Constant	Magnitude
Radiative † Decay	$\tau_{f\text{-}ph,e,sp,\ (00^01)\rightarrow(00^00)}$	2.383 ms
	$\tau_{f\text{-}ph,e,sp,\ (00^01)\rightarrow(02^00)}$	2172
	$\tau_{f\text{-}ph,e,sp,\ (00^01)\rightarrow(10^00)}$	2378
	$\tau_{f\text{-}ph,e,sp,\ (01^10)\rightarrow(00^00)}$	326.3
Nonradiative ‡ Decay	$p\tau_{f\text{-}f,v\text{-}t,\mathrm{CO_2\text{-}CO_2},(00^01)}$ §	3.06 ms-torr
	$p\tau_{f\text{-}f,v\text{-}t,\mathrm{CO_2\text{-}CO_2},(10^00)}$ ‖	0.454
	$p\tau_{f\text{-}f,v\text{-}t,\mathrm{CO_2\text{-}CO_2},(01^10)}$ ‖	5.18
	$p\tau_{f\text{-}f,v\text{-}t,\mathrm{CO_2\text{-}Xe},(00^01)}$ ‖	33.3

† Calculated using transition dipole values from [251].
‡ Data for 300 K, and data for other temperatures estimated using combination of experimental results [88, 449, 346] and theoretical models (Landau-Teller [265] and SSH [415]).
§ [346] and ‖[88].

in [114], and the experimental result of [114] is also shown in Figure 7.43(b). Comparison of laser wavelengths shows that the shorter wavelength results in improved cooling.

Even though k_f and $P_{f\text{-}f,v\text{-}t}$ increase at higher temperatures, the pumped energy level (02^00) population also rises with an increase in (00^01). Higher temperatures increase D_f and maintain a large deviation in (00^01), even in the nonirradiated region. Higher temperatures decrease $\sigma_{ph,a,(00^00)\rightarrow(00^01)}$ due to a decrease in CO_2 number density. The maximum cooling temperature is found when the deteriorating factors–increased k_f and $P_{f\text{-}f,v\text{-}t}$ – are properly compensated by the enhancing factors–large $n_{\mathrm{CO_2},(00^01)}$, D_f and small $\sigma_{ph,a,(00^00)\rightarrow(00^01)}$.

7.13.2 Laser Doppler Cooling of Atomic Gases and Doppler Temperature

Doppler laser cooling provides optical control of atomic motion, and in regard to gases, the speed of atoms can be substantially reduced, thus potentially reaching the absolute zero temperature. As shown in Figure 7.44, the ordinary cryogenic method extends to 0.1 K, whereas the laser cooling of gases can extend to the sub-μK (10^{-6} K) range [326]. The Bose–Einstein condensate is defined in the Glossary.

The kinetic energy of atomic motion is also shown on the right-hand axis of Figure 7.44, along with the regime of energy structure. The molecular regime (MD scale, Table 2.7) designates atomic/molecular translational, rotational, and vibrational energy. The fine structure relates to atomic scales of Table 1.6. The hyperfine structure defined in Section 1.5.2 is a small perturbation in the fine-structure energy.

Doppler laser cooling of atomic gases involves absorption of photons and the consequential emission of photons, with the net effect of reducing the translational kinetic energy of the constituent atoms [178, 326, 367]. This is also called light pressure cooling. It is shown in Figures 7.45(a) to (c). The frequency of irradiation should be in the lower half of the Doppler-broadened absorption (slightly below the atomic resonance frequency) of the atom. This will ensure that only the atoms

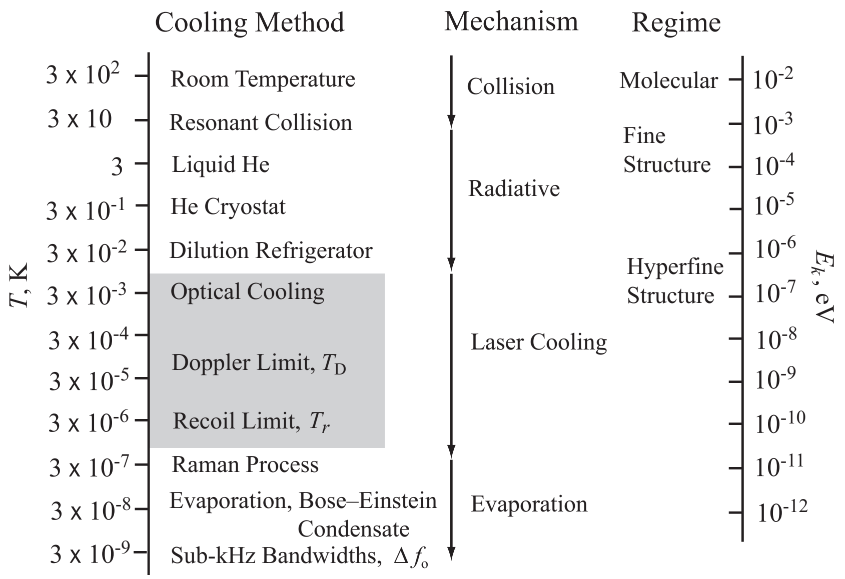

Figure 7.44. Various techniques used for cooling gases to near 0 K. Laser (optical) cooling (shaded areas) provides major subcryogenic cooling, whereas evaporation allows for reaching the nanokelvin regime [334]. The detunning (Doppler) frequency $\Delta f_o = \Delta\omega_o/2\pi$, determines the Doppler temperature.

moving toward the laser source will absorb, thus losing net energy and momentum by scattering the photons. If the photons come from all directions, the atoms lose energy and the Doppler shift detunes any photon traveling in the same direction as the atoms. The laser cooling process results in gas temperatures with a lower limit of the order of $\hbar\dot{\gamma}_{e\text{-}ph}/k_B$, where $\dot{\gamma}_{e\text{-}ph}$ is the spontaneous emission rate of the excited state. The random addition to the average momentum transfer produces a random

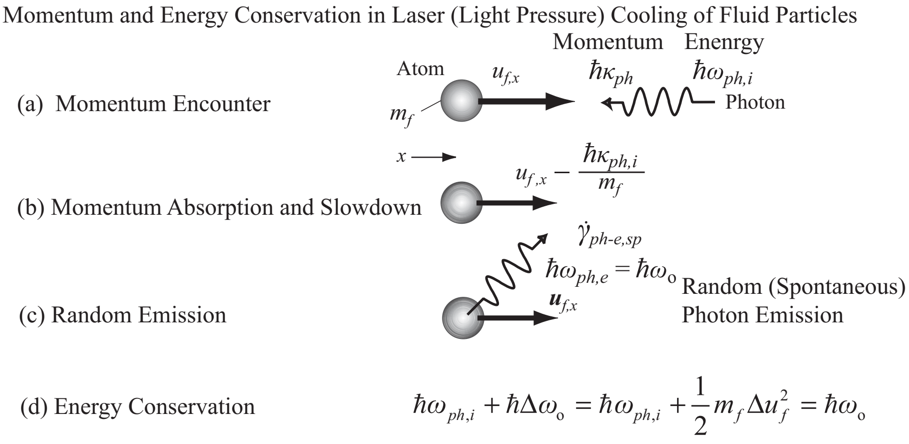
Momentum and Energy Conservation in Laser (Light Pressure) Cooling of Fluid Particles
Momentum
Enenrgy
Atom
$u_{f,x}$
$\hbar\kappa_{ph}$
$\hbar\omega_{ph,i}$
(a) Momentum Encounter
m_f
Photon
x
$u_{f,x} - \frac{\hbar\kappa_{ph,i}}{m_f}$
(b) Momentum Absorption and Slowdown
$\dot{\gamma}_{ph\text{-}e,sp}$
$\hbar\omega_{ph,e} = \hbar\omega_o$
$u_{f,x}$
Random (Spontaneous) Photon Emission
(c) Random Emission
(d) Energy Conservation
$\hbar\omega_{ph,i} + \hbar\Delta\omega_o = \hbar\omega_{ph,i} + \frac{1}{2}m_f\Delta u_f^2 = \hbar\omega_o$

Figure 7.45. (a) A fluid particle with velocity $\boldsymbol{u}_f$ encounters a photon with momentum $\hbar\boldsymbol{\kappa}_{ph}$. (b) After absorbing the photon, the atom is slowed. (c) After emission in a random direction, on average the atom is slower than (a) [367]. (d) Energy conservation for the process.

walk of the atomic momentum and an increase in the mean-square atomic momentum. This heating is balanced by cooling coming from opposing the atomic motion.

The atoms also emit (dominated by spontaneous) photons (in random directions) and their reabsorption results in heating. The translation-assisted electron excitation (absorption) and emission give $\hbar\omega_{ph,i} + \hbar\Delta\omega_{\rm o} = \hbar\omega_{ph,i} + \frac{1}{2}m_f\Delta u_f^2 = \hbar\omega_{\rm o}$, where $\omega_{ph,i}$ is the incident and $\omega_{\rm o} = \omega_{ph,e}$ is the emitted photon frequency. Here $\Delta\omega_{\rm o}$ is the contribution from the motion, i.e., the change in the kinetic energy of fluid particle. The Doppler temperature $T_{\rm D}$ is found from the balance between cooling and heating. The mechanical energy, using the statistical Fokker–Planck equation (3.8) [214] and for a one-dimensional transition along the x direction, is given as [367]

$$\frac{1}{2}m_f\langle u_{f,x}\rangle^2 \equiv \frac{1}{2}k_{\rm B}T_{\rm D} = \frac{\hbar\dot{\gamma}_{ph,e,sp}}{4}\left(\frac{\dot{\gamma}_{ph,e,sp}}{2\Delta\omega_{\rm o}} + \frac{2\Delta\omega_{\rm o}}{\dot{\gamma}_{ph,e,sp}}\right), \qquad (7.278)$$

where $\dot{\gamma}_{ph,e,sp} = 1/\tau_{ph,e,sp}$ (listed for Na in Table 7.4) is the rate of spontaneous emission of the excited state given by (7.189), and $\Delta\omega_{\rm o}$ is the angular frequency of the detuning (Doppler frequency) of the laser from the atomic resonance $\omega_{\rm o}$. The minimum temperature with respect to $2\Delta\omega_{\rm o}/\dot{\gamma}_{ph,e,sp}$ in (7.278) occurs for $\Delta\omega_{\rm o} = \dot{\gamma}_{ph,e,sp}/2$ which gives

$$T_{\rm D} = \hbar\dot{\gamma}_{ph,e,sp}/k_{\rm B} \quad \text{Doppler temperature}, \qquad (7.279)$$

i.e., the Doppler temperature is dependent on the emission rate. It is necessary that the atoms have relatively large electronic transition and because thousands of photons are trapped per atom, the spontaneous emission should be entirely to the ground state. Among atoms used are metastable noble alkali-metal and alkaline-earth atoms. Table 7.8 gives some of strong transitions for some laser materials, including Na. Note that $\omega_{\rm o} = 2\pi u_{ph}/\lambda_{\rm o}$. Figure 7.46 shows the electronic transition (yellow sodium lines) from $3^2{\rm S}_{1/2}$ to $3^2{\rm P}_{3/2}$ using atomic term symbol (Section 5.20) in the Na atom, ($1{\rm s}^2 2{\rm s}^2 2{\rm p}^6 3{\rm s}^1$). It is necessary to use a repumper in order to avoid off-resonance excitation [367]. Na has hyperfine levels which are generally degenerate. Excitation out of one of the hyperfine levels results in radiating to this hyperfine levels.

Then the fluid particle velocity distribution changes from the one time equilibrium M–B speed distribution $f_f^{\rm o}(u_{f,x})$ (6.62) and Figure 6.6(a) to nonequilibrium distribution $f_f^n(u_{f,x})$, as shown in Figure 7.47. Since the peak in speed is around 1100 m/s, the initial temperature from (6.62) is around 1670 K. As shown in Figure 7.44, the laser cooling is the last in series of cooling steps. This for $\dot{\gamma}_{ph,e,sp} = 6.25\times 10^7$ [367] ($\Delta f_{\rm o} = 10^7$ Hz) gives $T_{\rm D} = 238.7$ μK and corresponds to $\langle u_{f,x}\rangle^2$ [given by (7.278), for one-dimensional transition] of 29.38 cm/s (also marked in Figure 7.47). The results given in Figure 7.47 indicate that this low temperature is not reached. The experimental results [367] are for Na vapor with resonance wavelength $\lambda_{\rm o} = 0.5892$ μm (yellow light), or 2.104 eV.

The cooling rate per unit volume is

$$\dot{s}_{ph\text{-}t\text{-}ph} = -n_{ph}\hbar\Delta\omega_{\rm o}\dot{\gamma}_{ph\text{-}t\text{-}ph}, \qquad (7.280)$$

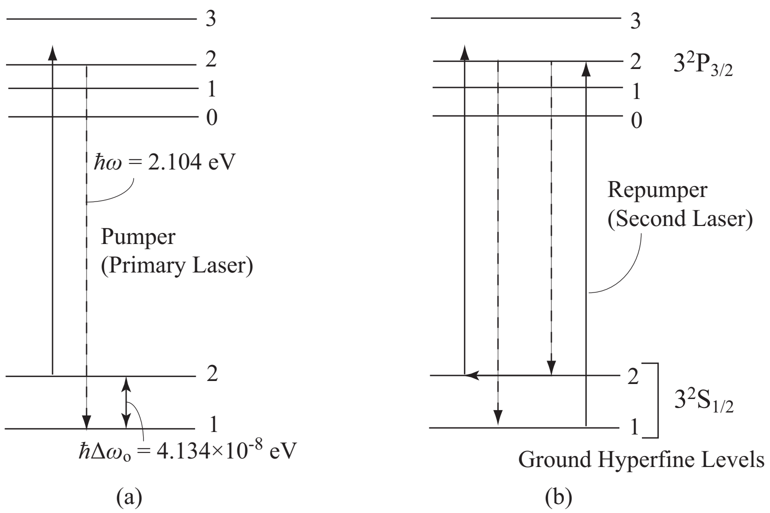

Figure 7.46. Electronic transition in Na atom, using the atomic term symbols (total orbital angular momentum). (a) Recycling is not allowed without repumping. (b) Use of a repumping laser to allow many absorption–emission cycles, for gaseous Na atom laser cooling [367].

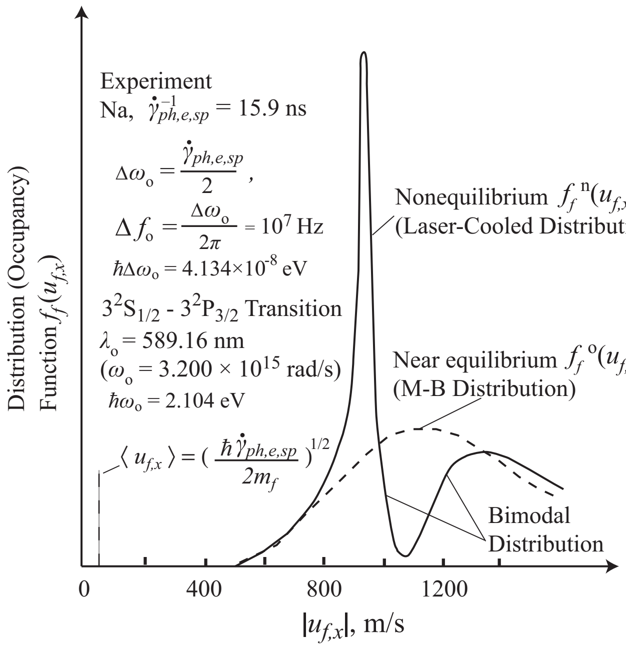

Figure 7.47. Cooling an atomic beam with a fixed frequency laser. The dotted curve is the speed distribution before cooling which at one time was the Maxwell speed distribution [equilibrium distribution f_f^o, from (6.62)], and the solid curve is after cooling (equilibrium distribution f_f^n). Atoms from a narrow speed range are transferred to a slightly narrow range centered on a lower speed [367]. The transition energy of Na, $3^2S_{1/2} - 3^2P_{3/2}$ is 2.104 eV and $\tau_{e\text{-}ph} = \dot{\gamma}_{ph,e,sp}^{-1} = 15.90$ ns [326].

where n_{ph} is the photon density and $\dot{\gamma}_{ph\text{-}t\text{-}ph}$ is the overall rate of absorption of the fluid particle translational energy in this anti-Stokes process. There is a lower-temperature limit, called the recoil temperature T_r, which is defined through

$$\frac{1}{2}m_f\langle u_{f,x}\rangle^2 = \frac{1}{2}\frac{\hbar^2\kappa_{ph}^2}{2m_f} \equiv \frac{1}{2}k_\mathrm{B}T_r, \tag{7.281}$$

or

$$T_r = \frac{\hbar^2\kappa_{ph}^2}{2k_\mathrm{B}m_f} = \frac{\hbar^2\omega_\mathrm{o}^2}{2k_\mathrm{B}u_{ph}^2m_f}. \tag{7.282}$$

This gives for the above Na example, $T_r = 1.20\times10^{-6}$ K $= 1.20$ μK. Both T_D and T_r are marked in Figure 7.44.

The laser cooling of the atomic vapor to very low temperatures ($\simeq 10^{-8}$ K) results in nearly pure condensate (Bose–Einstein condensate, where all gas atoms will be in the ground state, i.e., quantum degenerate gas). From the definition of the Bose–Einstein condensate phase transition given in the Glossary we have

$$\begin{aligned} n_f\lambda_\mathrm{dB}^3 &= 2.612 \\ &= n_f\left(\frac{h_\mathrm{P}^2}{2\pi m_f k_\mathrm{B}T_c}\right)^{1/2}, \end{aligned} \tag{7.283}$$

or

$$T_c = \frac{2\pi\hbar^2}{m_f k_\mathrm{B}}\left(\frac{n_f}{2.612}\right)^{1/2}, \tag{7.284}$$

where T_c is the critical temperature (for uniform, 3-D gas of non-interacting particles with no apparent internal degree of freedom). This shows a dependence on the atomic number density. Below T_c, the ground-state occupation fraction is

$$\frac{n_{f,\mathrm{o}}}{n_f} = 1 - \left(\frac{T}{T_c}\right)^3. \tag{7.285}$$

7.14 Photovoltaic Solar Cell: Reducing Phonon Emission

Photovoltaic cell converts photons to electron-hole pairs and separates them for transport. So special photon absorption and carrier transport properties are sought. From Section 7.1, with the sun at 5760 K, 98% of its radiation energy is between 0.25 and 4.0 μm (125 to 2000 meV). In semiconductors the electronic gap energy $\Delta E_{e,g}$ can be overcome by absorption of a photon of equal energy $\hbar\omega_{e,g}$. When considering a solar irradiation with a multiple photon frequency, there are other interactions and transitions involving holes, electrons, phonons, and photons. Figure 7.48 shows a photon with energy larger than $\Delta E_{e,g}$ absorbed in the semiconductor. The excess energy gives the electron a kinetic energy that is then exchanged in electron–phonon interaction (resulting in phonon emission). There is also the possibility of electron–hole recombination. The electron kinetic energy loss kinetics $\tau_{e\text{-}p}$ (Section 5.19) is

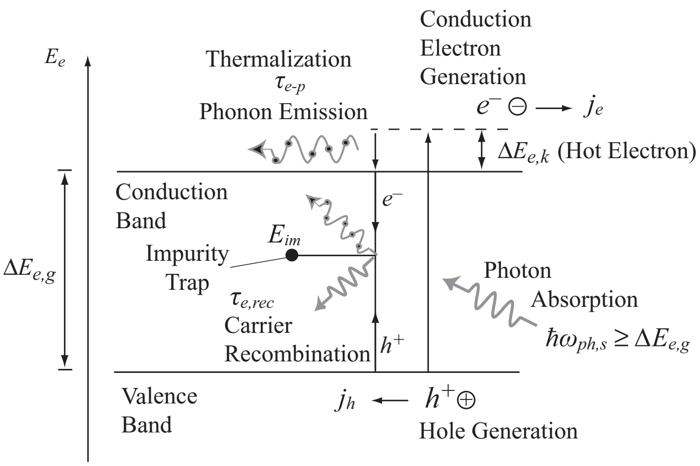

Figure 7.48. A photon of energy larger than the energy gap is absorbed and the excess electron energy (hot electron) results in phonon emission, unless it is slowed down by electron confinement.

quicker than the recombination time $\tau_{e,rec}$ (unless it is slowed down by confinement, Section 5.22.2).

A schematic of the different interactions involved in a p-n single-junction photovoltaic (PV) solar cell are shown in Figure 7.49. The cell is made of layers of n-type (e.g., phosphorous-doped), and p-type (e.g., boron-doped) semiconductors (e.g., Si), with a depletion region, having lengths l_n (about 0.5 μm), l_p (about 300 μm) and l_d.[†] These describe the conversion of the photon flux $E_{b,\omega}(T)/\hbar\omega$ (7.8) to the electron current j_e through an external resistance.

All the processes, which are listed in Table 7.8, are involved in the conversion of solar energy to electric power, the efficiency determined by the effectiveness of each process. The solar irradiation flux is the Planck (blackbody) spectral emissive power $E_{b,\omega}(T_s)$, where T_x is the sun temperature (7.8) and the photon flux is $E_{b,\omega}(T_s)/\hbar\omega$. The total irradiation flux from the sun $q_{ph,s}$ is found using (7.6) for solar emission, along with relation (7.90) and expressing the solid angle as a_s, i.e.,

$$q_{r,s} = q_{ph,s} = \frac{a_s\hbar}{4\pi^2 u_{ph}^2} \int_0^\infty \frac{\omega^3}{\exp(\hbar\omega/k_{\rm B}T_s) - 1} \mathrm{d}\omega, \tag{7.286}$$

The earth–sun solid-angle factor $a_s = 2.18\times 10^{-5}$ and for $T_s = 5760$ K gives $q_{ph,s} = 1,350\ \mathrm{W/m^2}$. For the ambient radiation, T_s is replaced with $T_a = 300$ K and the solid-angle factor a_s is replaced with $a_s = 1$. Note that for blackbody emission, $E_b = \pi I_b$ (7.8). A faction of $\boldsymbol{q}_{ph,s}$ results in electric power generation $\dot{S}_{ph\text{-}e}/A$, and a fraction results in phonon emission $\dot{S}_{ph\text{-}e\text{-}p}/A$. Here we assume. but there is reflection, but

---

[†] The depletion layer combines the p- and n-depletion layers, and for each carrier i is given by

$$l_{d,i} = \left(\frac{2\epsilon_{\rm o}\epsilon_{\rm e}\Delta\varphi_e}{e_c n_i}\right)^{1/2},$$

where $\Delta\varphi_e$ is the built-in potential, and n_i is the carrier i density.

Table 7.8. *Hole, electron, phonon, and photon interactions (processes) in PV energy conversion.*

	Notation	Process
1	$\dot{n}_{ph\text{-}e,s}$	electronic excitation by a solar photon
2	$\dot{n}_{ph\text{-}e,a}$	electronic excitation by an ambient photon
3	$\dot{s}_{ph\text{-}e\text{-}p}/A$	electron relaxation to conduction band edge through phonon emission
4	$\dot{n}_{e,h\text{-}ph}$	electron–hole recombination resulting in photon emission
5	$\dot{n}_{e\text{-}t}$	impurity trap and defect trap assisted recombination
6	$\dot{n}_{e,h\text{-}k}$	recombination by electron–electron or hole–hole kinetic energy exchange

there is radiation exchange with the ambient $q_{r,a}$. The phonon emission leads to a rise in temperature and is transported by conduction $\boldsymbol{q}_k$ (thus decreasing the photovoltac conversion $\dot{S}_{ph\text{-}e}$). These are also shown in Figure 7.49.

In the next section, the PV efficiency is analyzed first for a single-bandgap semiconductor (e.g., Si), then for an ideal multiple-bandgap semiconductor. Finally, the semiempirical efficiency for the actual performances of current PV cells is given.

7.14.1 Single-Bandgap Ideal Solar PV Efficiency

To determine the ideal (including no depletion layer) efficiency of a single direct bandgap PV solar cell we first define some aspects of the power-converting device.

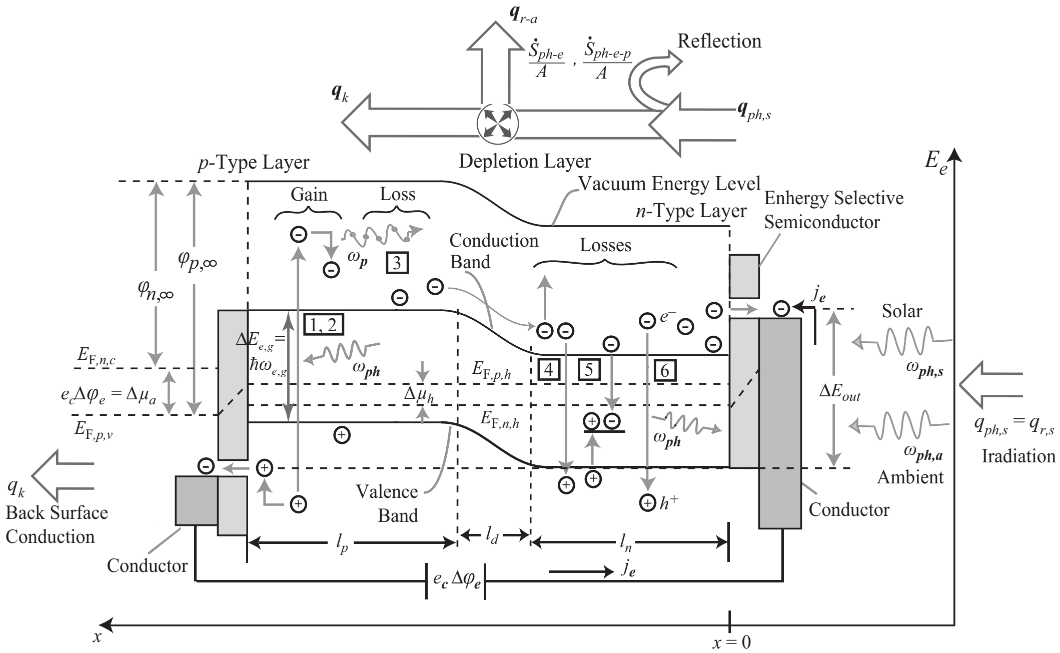

Figure 7.49. Hole, electron, phonon, and photon interactions in the irradiation of a p–n junction PV solar cell. The process numbers are defined in Table 7.8. $E_{F,n,c}$ and $E_{F,p,c}$ are the conductor Fermi levels, $\varphi_{n,\infty}$ and $\varphi_{p,\infty}$ are the vacuum energies, and $E_{F,n,h}$ and $E_{F,p,h}$ are the electron and hole chemical potential in the absorber.

All photons with energy above the bandgap of the semiconductor are absorbed and excite one electron–hole pair. The excited carriers are assumed to immediately come to thermal equilibrium with each other at a temperature T_h, but not with the lattice at T_a. The carriers have infinite mobility, which results in constant quasi-Fermi energies across the cell, as illustrated in Figure 7.49. Also, there is no minority carrier flow across the conductors (i.e., there is no surface recombination).

The efficiency of a PV system is defined as

$$\eta_{ph\text{-}e} = \frac{(\Delta\varphi_e j_e)_{max}}{q_{ph,s}} \quad \text{PV efficiency,} \tag{7.287}$$

where $\Delta\varphi_e$ is the voltage potential, which is equal to $\Delta\mu_a/e_c$, and μ_a is the chemical potential of the carriers at ambient temperature. The distribution of energy for fermions in quasi-equilibrium is given by the Fermi–Dirac distribution (5.62). The difference in quasi-Fermi energies for the hot carrier distribution is $\Delta\mu_h = E_{\mathrm{F},n,h} - E_{\mathrm{F},p,h}$. However, we start with $\Delta\mu_a$; as the conductor is at ambient temperature the carriers need to be extracted at ambient temperature (unless we introduce a device for extraction of hot carriers or take other measures to use the hot-carrier energy), ideally with no loss in energy. A scenario in which this is possible is by isentropic cooling of the carriers at constant energy through an energy selective semiconductor, as illustrated in Figure 7.49. The relationship between $\Delta\mu_h$ and $\Delta\mu_a$ is determined by considering the energy conservation equation, (Table 2.4), i.e.,

$$\mathrm{d}E = T_h \mathrm{d}S + \mu_{h,i}\mathrm{d}N_i. \tag{7.288}$$

By the electron traveling through the external resistance, there is the removal of one particle from both the electron gas and the hole gas, with a change in chemical potential of $\Delta\mu_h$. Per carrier, the conservation equation becomes,

$$\Delta E = T_h \Delta S + \Delta\mu_h. \tag{7.289}$$

Similarly for electrons at ambient temperature, we have

$$\Delta E = T_a \Delta S + \Delta\mu_a. \tag{7.290}$$

With isentropic cooling, the change in entropy by removing a particle from the system is constant and with constant energy, equating the two ΔS gives the relationship between the hot-carrier chemical potential and the ambient chemical potential

$$e_c\Delta\varphi_e = \Delta\mu_a = \Delta\mu_h\frac{T_a}{T_h} + \Delta E_{out}(1 - \frac{T_a}{T_h}). \tag{7.291}$$

In this relationship ΔE_{out} is defined as the utilization pathway for the electrons as illustrated in Figure 7.49. When $T_h = T_a$, $e_c\Delta\varphi_e = \Delta\mu_h$.

With infinite carrier mobility, the current can be determined from the steady-state, one-dimensional carrier continuity equation (5.260), using the carrier generation/removal terms in Figure 7.49 and Table 7.8, neglecting $\dot{n}_{e\text{-}t}$ and $\dot{n}_{e,h\text{-}k}$, i.e.,

$$\frac{1}{e_c}\frac{\mathrm{d}j_e}{\mathrm{d}x} - \dot{n}_{ph\text{-}e,s} - \dot{n}_{ph\text{-}e,a} + \dot{n}_{e,h\text{-}ph} = 0. \tag{7.292}$$

So, the carrier continuity equation includes only three of the generation processes listed and named in Table 7.8. The electron relaxation, $\dot{s}_{e-p}$, does not affect the number of carriers and is therefore not included in the equation. For electron generation, the radiation from both the sun $\dot{n}_{ph-e,s}$ and ambient $\dot{n}_{ph\text{-}e,a}$ are considered. The generation terms, for an optically thick absorber ($\sigma_{ph} l_p > 4$, where the total cell length is $l = l_n + l_d + l_p$ as shown in Figure 7.49), become

$$\dot{n}_{ph\text{-}e,s} = \int_{\omega_{e,g}}^{\infty} \frac{a_s E_{b,s,\omega}}{\hbar \omega l} \mathrm{d}\omega, \qquad \dot{n}_{ph\text{-}e,a} = \int_{\omega_{e,g}}^{\infty} \frac{a_a E_{b,a,\omega}}{\hbar \omega l} \mathrm{d}\omega, \tag{7.293}$$

where a_s and a_a are the solid angles mentioned in relation (7.286). However, note that σ_{ph} is strongly frequency dependent (a general behavior for semiconductors is shown in Figure 7.14).

Here we assume that among the recombination processes, the radiative recombination $\dot{n}_{e,h\text{-}ph}$ is dominant (this is not true in a typical cell, as shown in Figure 7.53). Then the net radiative recombination rate can be determined by considering the rate of photon emission given by (7.8) with the correction that the system is not in chemical equilibrium and assuming all photons emitted with energy above the bandgap energy are the result of carrier recombination, i.e.,

$$\dot{n}_{e,h\text{-}ph} = \dot{n}_{ph\text{-}e,a} \exp(\frac{\Delta \mu_h}{k_{\mathrm{B}} T_h}). \tag{7.294}$$

After the continuity equation (7.292) is integrated along x between $x = 0$ and $x = l$, the current is

$$\frac{j_e}{e_c} = \int_{\omega_{e,g}}^{\infty} \frac{a_s E_{b,s,\omega}}{\hbar \omega} \mathrm{d}\omega + \int_{\omega_{e,g}}^{\infty} \frac{a_s E_{b,a,\omega}}{\hbar \omega} \mathrm{d}\omega - \int_{\omega_{e,g}}^{\infty} \frac{a_s E_{b,a,\omega}}{\hbar \omega} \exp(\frac{\Delta \mu_h}{k_{\mathrm{B}} T_h}) \mathrm{d}\omega. \tag{7.295}$$

The first two terms in (7.295) are constants when using the bandgap energy and the Planck law (7.8), evaluating for $T_s = 5760$ K, and for example $T_a = 300$ K. Also, for (7.291), under the condition of $T_h = T_a$ (ideal) we have $e_c \Delta \varphi_e = \Delta \mu_a = \Delta \mu_h$. Then (7.295) is simplified and gives the short-circuit current dark current, and open circuit potential.[†] To fully characterize the system, we add the energy balance equation, assuming that there is no loss of energy through phonon emission

$$\frac{j_e \Delta E_{out}}{e_c} = \int_{\omega_{e,g}}^{\infty} a_s E_{b,s,\omega} \mathrm{d}\omega + \int_{\omega_{e,g}}^{\infty} a_s E_{b,a,\omega} \mathrm{d}\omega - \int_{\omega_{e,g}}^{\infty} a_s E_{b,a,\omega} \exp(\frac{\Delta \mu_h}{k_{\mathrm{B}} T_h}) \mathrm{d}\omega. \tag{7.296}$$

[†] Under these conditions, (7.295) becomes

$$j_e = j_{sh} - j_{\mathrm{o}}[\exp(\frac{e_c \Delta \varphi_e}{k_{\mathrm{B}} T_h}) - 1],$$

where j_{sh} is the short-circuit and j_{o} is the saturation current, with $j_{sh} = 54.1$ mA/cm^2, and $j_o = 1.72 \times 10^{-12}$ mA/cm^2. For Si with $\Delta E_{e,g} = 1.12$ eV, this gives an open circuit ($j_e = 0$) potential $\Delta \varphi_{\mathrm{o}} = k_{\mathrm{B}} T_h \ln(j_{sh}/j_{\mathrm{o}})/e_c = 0.863$ V, for $T_h = 300$ K. The second term in the above equation is called the dark current, since it turns in the opposite direction.

By defining the bandgap of the semiconductor $\hbar\omega_{e,g}$, the utilization pathway ΔE_{out}, and the voltage $\Delta\varphi_e$ (a fraction of bandgap divided by e_c, Figure 7.49), the maximum power out of the cell is found. In the process the carrier temperature is also determined.

The maximum (hot carrier) efficiency is 66.8% for $\Delta E_{e,g} = \hbar\omega_{e,g} = 0.36$ eV at $T_a = T_h = 3684$ K (found by optimization). It is important to note that the carriers cool through phonon emission very quickly, and it is often assumed the carriers are at the ambient temperature. The maximum efficiency assuming complete electron relaxation through phonon emission ($T_h = T_a = 300$ K) is 30.4% at $\Delta E_{e,g} = 1.26$ eV. The efficiencies are plotted for both scenarios as functions of bandgap energy in Figure 7.50(a). Figure 7.50(b) shows the $j_e - \Delta\varphi_e$ behavior under the ideal condition. For the analysis of carriers in thermal equilibrium with the lattice, the power losses are from several different mechanisms as shown in Figure 7.51.

7.14.2 Multiple-Bandgap Ideal Solar PV Efficiency

The carrier relaxation through phonon emission occurs very quickly (~fs to ps, Figure 5.13) as compared with carrier collection (~ns) and carrier–lattice thermal equilibrium is often assumed. One approach to negate energy loss through phonon emission but allowing the carrier–lattice thermal equilibrium assumption is arranging a system of photovoltaic cells in tandem, each with a reducing bandgap energy, as illustrated in Figure 7.52. The incoming photon is then better matched to a given cell, passing through cells with larger bandgap energy, ideally unabsorbed, until reaching a cell with equal or lower bandgap energy, where it will excite an electron–hole pair. Beyond absorbing a larger portion of the solar spectrum, there will also be recycling of the emitted photons from each cell by neighboring cells. To simplify the efficiency analysis, when there is an infinite number of tandem solar cells, photon recycling has been shown to be equivalent to placing frequency-selective reflectors between cells, which reflect emitted photons with energy above the cell bandgap energy back to the cell [306]. With this assumption the efficiency calculation can be determined similarly to the single-bandgap cell with $T_h = T_a$ and the integral in the current equation taken from the bandgap energy of the given cell to the bandgap energy of the next cell for both absorbtion and emission; (7.295) becomes

$$\begin{aligned}\frac{j_e}{e_c} &= \int_{\omega_{e,g,n}}^{\omega_{e,g,n+1}} \frac{a_s E_{b,s,\omega}}{\hbar\omega} \mathrm{d}\omega + \int_{\omega_{e,g,n}}^{\omega_{e,g,n+1}} \frac{a_s E_{b,a,\omega}}{\hbar\omega} \mathrm{d}\omega \\ &\quad - \int_{\omega_{e,g,n}}^{\omega_{e,g,n+1}} \frac{a_s E_{b,a,\omega}}{\hbar\omega} \exp(\frac{e_c \Delta\varphi_e}{k_\mathrm{B} T_a}) \mathrm{d}\omega. \end{aligned} \tag{7.297}$$

For a finite number of cells, at each cell, the power output is found by determining the maximum product of voltage and current. For the case of infinite tandem cells, $(j_{e,n}\Delta\varphi_{e,n})_{max}$ is determined for each photon frequency. For the total power out, the product of the maximum voltage and maximum current of each cell is integrated

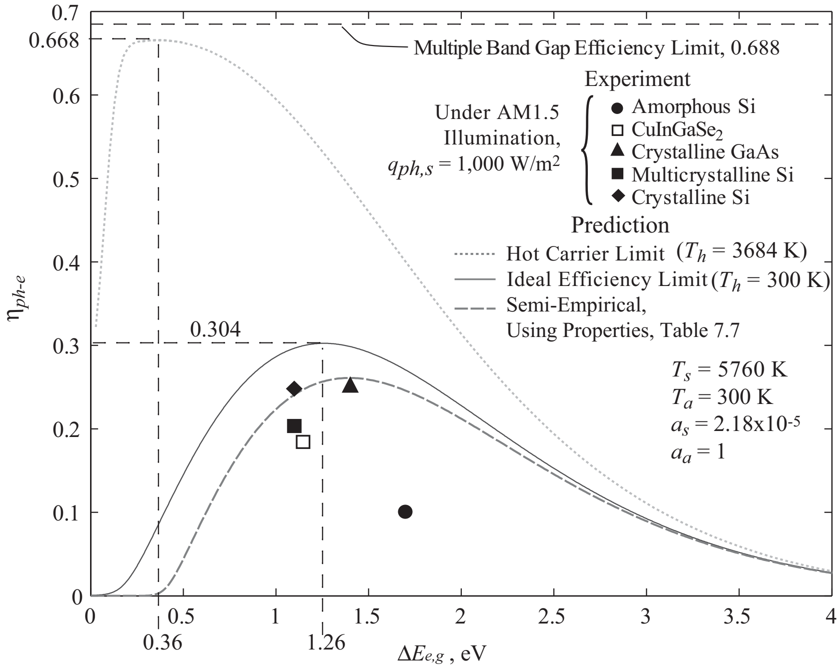

(a)

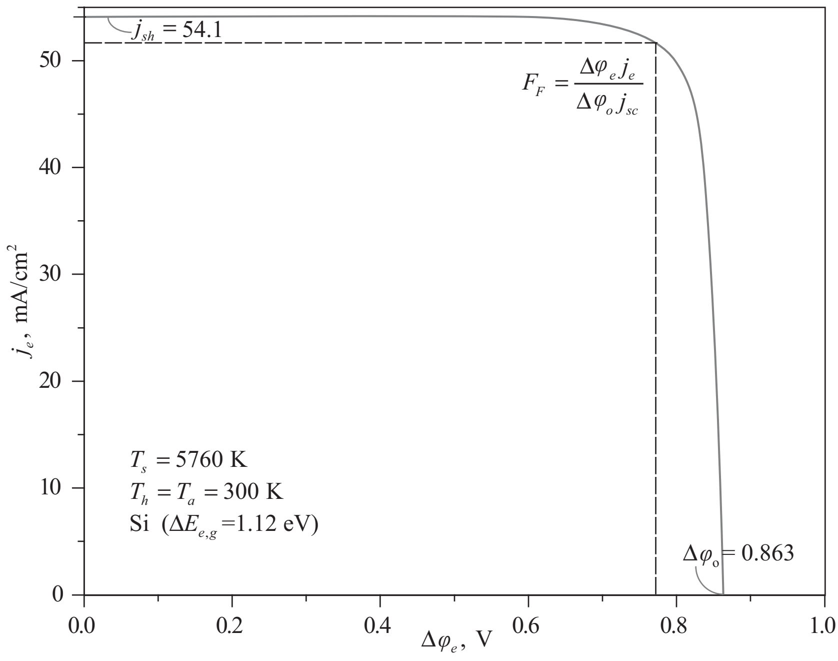

(b)

Figure 7.50. (a) Variations of solar PV efficiency with respect to bandgap energy. Three different analyses are used, namely, ideal analysis with carriers at T_e, ideal with carriers at T_a, and semiempirical, infinite multiple bandgap. Some measured solar cell (Si and GaAs based) performances are also shown [306]. (b) Variations of the current density with respect to electric potential for Si, under the ideal assumption.

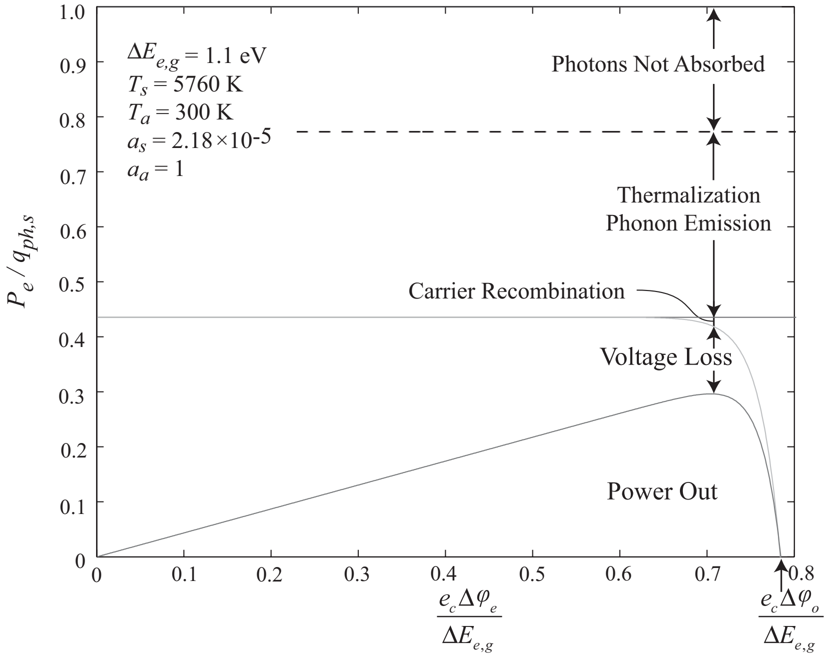

Figure 7.51. Distribution of incoming irradiation energy in PV energy conversion.

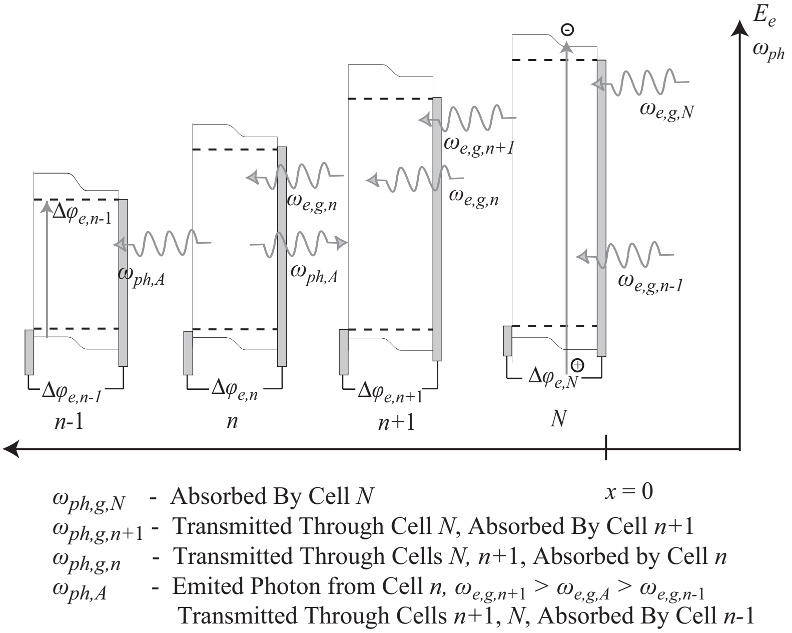
E_e
ω_{ph}
$\omega_{e,g,N}$
$\omega_{e,g,n+1}$
$\omega_{e,g,n}$
$\omega_{e,g,n}$
$\omega_{e,g,n-1}$
$\omega_{ph,A}$
$\omega_{ph,A}$
$\Delta\varphi_{e,n-1}$
$\Delta\varphi_{e,n-1}$
$\Delta\varphi_{e,n}$
$\Delta\varphi_{e,n+1}$
$\Delta\varphi_{e,N}$
⊖
⊕
n-1
n
n+1
N
$x = 0$
$\omega_{ph,g,N}$ - Absorbed By Cell N
$\omega_{ph,g,n+1}$ - Transmitted Through Cell N, Absorbed By Cell n+1
$\omega_{ph,g,n}$ - Transmitted Through Cells N, n+1, Absorbed by Cell n
$\omega_{ph,A}$ - Emited Photon from Cell n, $\omega_{e,g,n+1} > \omega_{e,g,A} > \omega_{e,g,n-1}$ Transmitted Through Cells n+1, N, Absorbed By Cell n-1

Figure 7.52. A rendering of a tandem multiple-bandgap PV solar cell, showing the continuously decreasing bandgap energy with emitted photon recycling.

over all photon frequencies,

$$\frac{\dot{S}_{ph\text{-}e}}{A} = \frac{P_e}{A} = \int_0^\infty (\Delta\varphi_e j_e)_{max} \mathrm{d}\omega. \tag{7.298}$$

The efficiency limit for an infinite tandem cell with $T_s = 5760$ K, $T_a = 300$ K, $a_s = 2.85\times10^{-5}$ and $a_s = 1$ is 68.8%, similar to the limiting efficiency of a hot carrier solar cell.

7.14.3 Semiempirical Solar PV Efficiency

The preceding ideal analyses are very useful investigations because they require minimal information about the PV device. However, for a more realistic analysis, carrier transport must be considered. In the preceding analysis, the mobility of electrons were assumed to be infinite. Without this assumption, a PV solar cell will require an electric field and or a substantial concentration gradient to create a current. Also, recombination rates will include mechanisms other than radiative recombination. Here we analyze a p–n junction PV cell, adding to the analysis the general carrier transport given by the drift–diffusion equation (5.261),

$$\begin{aligned} &j_e = e_c n_{e,c}\mu_e e_e + e_c D_e \frac{\mathrm{d}n_{e,c}}{\mathrm{d}x}, \quad j_h = -e_c n_{h,c}\mu_h e_e - e_c D_h \frac{\mathrm{d}n_h}{\mathrm{d}x} \\ &j_{e,h} = j_e + j_h. \end{aligned} \tag{7.299}$$

The electron diffusion coefficient (Table 3.6) is $D_e = k_B T \mu_e / e_c$, and is similar for that for holes. These equations are used along with the carrier continuity equation (7.292)

$$\frac{1}{e_c}\frac{\mathrm{d}j_e}{\mathrm{d}x} + \dot{n}_e - \dot{n}_{ph\text{-}e,s} = 0, \quad \frac{1}{e_c}\frac{\mathrm{d}j_h}{\mathrm{d}x} - \dot{n}_h + \dot{n}_{ph\text{-}h,s} = 0, \tag{7.300}$$

where the ambient photon contribution is combined with the solar. To determine the current from these equations, several assumptions are made to simplify the analysis. All carriers immediately relax to the conduction band edge. The depletion region of the cell creates a well-defined boundary, where beyond the depletion region there is no electric field present (i.e., the cell is quasi-neutral). The generation rate is constant along the length of the cell. The carrier recombination is linearly dependent on the minority carrier concentration.

The return of e^- and h^+ to their equilibrium distribution is called recombination (Figure 7.49 and Table 7.8) and are by the traps (defects) forming states in the gap, by radiative decay, or by phonons (Auger effect) which is by loss of charge carrier kinetic energy. These are represented by kinetics, $\tau_{e\text{-}h}$, $\tau_{e,h\text{-}ph}$, $\tau_{e\text{-}h\text{-}p}$, etc. [414] The recombination rate for conduction electrons in the p-type region is based on excess minority carrier concentration $n_{e,c}$, $n_{e,i}$, i.e.,

$$\dot{n}_e = \frac{n_{e,c} - n_{e,i}}{\tau_{e,rec}}, \quad n_{e,i} = \frac{n_i^2}{n_{d,p}}, \tag{7.301}$$

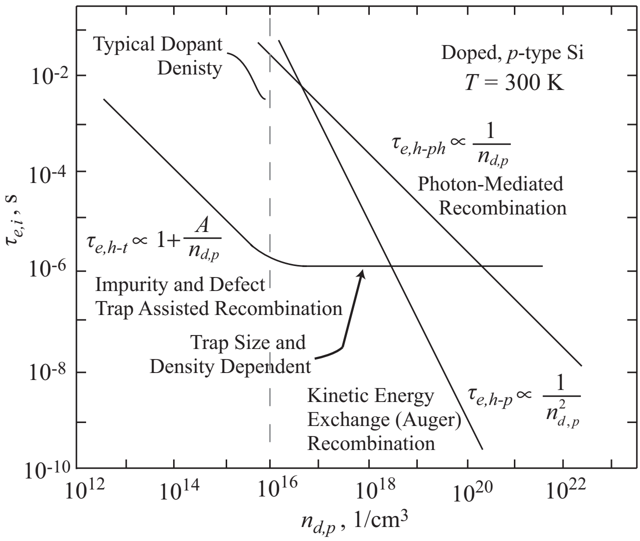

Figure 7.53. Variations of the measured, minority carrier (e^-) lifetimes (kinetics) with respect to dopant concentration for p-type Si [168]. At low $n_{d,p}$, $\tau_{e,h\text{-}t}$ dominates based on (7.302).

$$\frac{1}{\tau_{e,rec}} = \frac{1}{\tau_{e,h\text{-}t}} + \frac{1}{\tau_{e,h\text{-}ph}} + \frac{1}{\tau_{e,h\text{-}p}}, \tag{7.302}$$

where we have used the dominant recombination mechanisms also listed in Table 7.8.

Figure 7.53 shows the minority carrier (e^-) lifetimes (kinetics) $\tau_{e,i}$, as functions of dopant concentrations for p-type Si. Note that the smallest $\tau_{e,i}$ dominates the recombination, for example for $n_{d,p} = 10^{16}$ 1/cm^3, $\tau_{e,h\text{-}t}$ dominates the recombination mechanisms. In addition, the non-recombinative electron-phonon scattering becomes important when attempting to harvest the hot electrons. In Section 5.22.2 we discussed increasing τ_e-p using nanostructures (quantum wells).

To find the current we first consider the minority carrier concentrations as functions of position $n_{e,c}(x)$ in the quasi-neutral regions of the cell. The following derivation is performed for electrons but is similarly applicable to holes. The dimensional parameters are those in Figure 7.49. Combining the drift–diffusion equation and the carrier continuity equation, considering no electric field, we obtain

$$\frac{\mathrm{d}^2 n_{e,c}}{\mathrm{d}x^2} - \frac{\dot{n}_{ph\text{-}e,s}}{D_e} + \frac{n_{e,c} - n_{e,i}}{L_e^2} = 0. \tag{7.303}$$

The diffusion length is introduced as $L_e = (D_e \tau_{e,rec})^{1/2}$. Then the solution is

$$n_{e,c}(x) = A\,\exp(\frac{x + l_n + l_d}{L_e}) + B\,\exp(\frac{-x + l_n + l_d}{L_e}) + \tau_{e,rec}\dot{n}_{ph\text{-}e,s} + n_{e,i}.$$

To solve for the constants, we consider the following boundary conditions. As $x \to \infty$, $n_e(x)$ is finite, therefore $A = 0$. The constant B is found by considering the carriers concentration at the edge of the depletion region $x = l_n + l_d$, defined as [168]

$$n_{e,c} - n_{e,i} = \frac{n_i^2}{n_{d,p}}[\exp(\frac{e_c \Delta\varphi_e}{k_B T_a}) - 1]. \tag{7.304}$$

Therefore, the conduction electron density in the p-type region is

$$n_{e,c}(x) = \tau_{e,rec}\dot{n}_{ph\text{-}e,s} + n_{e,i} + \{\frac{n_i^2}{n_{d,p}}[\exp(\frac{e_c \Delta\varphi_e}{k_B T_a}) - 1] - \tau_{e,rec}\dot{n}_{ph\text{-}e,s}\}\exp(\frac{-x + l_n + l_d}{L_e}). \tag{7.305}$$

The equations governing holes can be set up similarly. The carrier concentrations are then plugged into the drift–diffusion equation to determine the current. For steady state operation the total current across the cell is constant. Therefore, to determine the current, the electron and hole currents are summed at one position in the cell. Now, we define the electron current at the edge of the p-type region and depletion region $l_n + l_d$, as

$$j_e(l_n + l_d) = e_c L_e \dot{n}_{ph\text{-}e,s} - \frac{e_c n_i^2 D_e}{n_{d,p} L_e}[\exp(\frac{e_c \Delta\varphi_e}{k_B T_a}) - 1]. \tag{7.306}$$

The hole current is determined at the edge of the n-type region and depletion region, l_n,

$$j_h(l_n) = e_c L_h \dot{n}_{ph\text{-}e,s} - \frac{e_c n_i^2 D_h}{n_{d,n} L_h}[\exp(\frac{e_c \Delta\varphi_e}{k_B T_a}) - 1]. \tag{7.307}$$

The total current $j_{e,h}$ determined at l_n is $j_h(l_n) + j_e(l_n + l_d)$ plus the electron current generated in the depletion region, $j_{e,dep}$. The current density in the depletion region cannot be solved in the same manner as the other regions because an electric field is present. A simplification for this region can be made by allowing the current to be defined solely by the carrier continuity equation, neglecting recombination, $j_{e,dep} = e_c l_d \dot{n}_{ph\text{-}e,s}$. This simplification is made because the depletion region is relatively small and the electrons and holes are removed quickly by the electric field. From these equations the total current is

$$j_{e,h} = e_c \dot{n}_{ph-e,s}(L_e + L_h + l_d) - e_c n_i^2(\frac{D_e}{n_{d,p} L_e} + \frac{D_h}{n_{d,n} L_h})[\exp(\frac{e_c \Delta\varphi_e}{k_B T_a}) - 1]. \tag{7.308}$$

The efficiency for this approach is plotted in Figure 7.50 as a function of bandgap energy using the material properties of Si listed in Table 7.9. Note that the efficiency is calculated assuming all solar irradiation above the bandgap energy is absorbed over $L_e + L_h + l_d$, equivalent to the width of the cell. Table 7.10 includes observed solar cell operation and other characteristics, for Si, GaAs, and InP based solar PV. The fill factor F_F is the total power out $(\Delta\varphi_e j_e)_{max}$ divided by the product of the open circuit voltage $\Delta\varphi_o$ and short circuit current density j_{sh}. The fill factor F_F [Figure 7.50(b)] is defined such that (7.287) is written as $\eta_{ph\text{-}e} = \Delta\varphi_o j_{sh} F_F / q_{ph,s}$. Note

Table 7.9. *Typical Si PV material properties [345].*

Quantity	Magnitude
D_e	40 cm^2/s
D_h	2 cm^2/s
L_e	14.0 $\mu\mathrm{m}$
L_h	140 $\mu\mathrm{m}$
$n_{d,p}$	10^{16} cm^{-3}
$n_{d,n}$	10^{19} cm^{-3}
$\tau_{e,rec}$	1×10^{-6} s
$\tau_{h,rec}$	5×10^{-6} s

that the crystalline Si has the largest j_{sh}, while the crystalline GaAs has the largest $\Delta\varphi_{\mathrm{o}}$. The largest fill factor is for crystalline InP.

As the temperature increases, the intrinsic carrier concentration increases, thus increasing the recombination rate and reducing performance. Also $\Delta\varphi_{\mathrm{o}}$ decreases with increase in temperature (inverse relation) [296]

7.15 Size Effects

7.15.1 Enhanced Near-Field Radiative Heat Transfer

Thermally excited solid surface waves are due to thermal fluctuations of atoms adjacent to the surface. These surface waves influence the density of states of the emitted EM fields that have intensities that are orders of magnitude larger in the near field than in the far field [76, 221]. Also, the emitted EM waves are quasi-monochromatic (different than blackbody radiation) in the near field.

The EM waves propagating along the interface of two material with distinct EM properties (σ_e, ϵ_e, μ_e), decay exponentially perpendicular to the interface. The surface waves that are due to the coupling between the EM field and a resonant polarization oscillation in the solid are called the surface polaritons. The surface

Table 7.10. *Measured junction PV cells performance of some single $T_a = 298$ K and $q_{r,s} = 10^3$ W/m² [64, 169].*

Material	$\eta_{ph\text{-}e}$	Bandgap	$\Delta E_{e,g}$, eV	l_p, μm	l_n, μm	$\Delta\varphi_o$, V	j_{sh}, mA/cm²	F_F
Crystalline Si	0.247	indirect	1.1	300−500	0.5	0.706	42.2	0.828
Polycrystalline Si	0.203	indirect	1.1	300	0.5	0.664	33.7	0.809
Amorphous Si	0.101	direct	1.7	0.01	0.02	0.539	24.4	0.766
Crystalline GaAs	0.251	direct	1.43	0.5	4	1.022	28.2	0.871
Polycrystalline GaAs	0.182	direct	1.43	–	–	0.994	23.0	0.797
Crystalline InP	0.219	direct	1.35	4.0	0.03	0.878	29.3	0.854
$\mathrm{CuInGaSe_2}$	0.184	direct	1.1–1.2	5.0	0.3	0.669	35.7	0.770

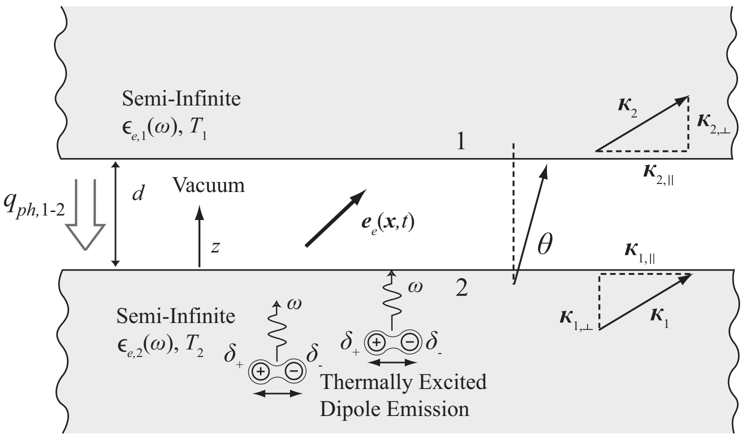

Figure 7.54. Thermally excited surface waves $\boldsymbol{e}_e(\boldsymbol{x}, t)$ and the near-field radiation exchange between two closely placed solid surfaces [150]. Here $\kappa_\parallel$ is the component of wave vector along the surface.

wave of a metal is due to charge density waves or plasmons, and is called the surface-plasmon polarization. For dielectric solids the surface wave is due to the optical phonons and phonon polaritons (which also exist within the solid) and is called the surface-phonon polariton.

In Section 7.2.2 we discussed the near-field surface emission and here we give a quantitative example for two surfaces at different temperatures separated by a vacuum gap of the order of nanometers. Here we examine the formulation of the thermally excited, near-field EM emission and review examples with radiation between two doped Si surfaces separated by a small gap.

Referring to Figure 7.54 for a medium 1 at temperature T, emitting to vacuum (with $T_2 = 0$), the spectral photon energy density (7.24) (for emission) is [221]

$$\begin{aligned}
\frac{\mathrm{d}E_{ph,\omega}}{V\mathrm{d}\omega} &= \frac{\epsilon_o}{2}\langle|\boldsymbol{e}_e|^2\rangle + \frac{\mu_o}{2}\langle|\boldsymbol{h}_e|^2\rangle \\
&= \frac{\hbar\omega^3}{2\pi^2 u_{ph,o}^3[\exp(\frac{\hbar\omega}{k_\mathrm{B}T})-1]}\int_0^{\omega/u_{ph,o}} \frac{\kappa\,\mathrm{d}\kappa}{\frac{\omega}{u_{ph,o}}|\kappa_{\perp,1}|}\,\frac{1-|\rho^s_{r,12}|^2+(1-|\rho^p_{r,12}|^2)}{2} \\
&\qquad\qquad\qquad\qquad\qquad\qquad\qquad \text{propagating waves} \\
&\quad +[\int_{\omega/u_{ph,o}}^{\infty}\frac{4\kappa^3\mathrm{d}\kappa}{\frac{\omega}{u_{ph,o}}\kappa_{\perp,1}}\,\frac{\mathrm{Im}(|\rho^s_{r,12}|)+\mathrm{Im}(|\rho^p_{r,12}|)}{2}e^{-2\mathrm{Im}(\kappa_{\perp,1},z)}], \qquad (7.309) \\
&\qquad\qquad\qquad\qquad\qquad\qquad\qquad \text{evanescent waves}
\end{aligned}$$

where

$$\kappa_{\perp,1} = \epsilon_{e,1}\mu_{e,1}\frac{\omega}{u_{ph,o}} - \kappa^2,\quad \rho^s_{r,12} = \frac{\kappa_{\perp,1}-\kappa_{\perp,2}}{\kappa_{\perp,1}+\kappa_{\perp,2}},\qquad \rho^p_{r,12} = -\frac{\epsilon_{e,1}\mu_{\perp,2}+\epsilon_{e,2}\kappa_{\perp,1}}{\epsilon_{e,1}\kappa_{\perp,2}+\epsilon_{e,2}\kappa_{\perp,1}},$$

where in the s-polarization $\boldsymbol{e}_e$ is perpendicular to y–z plane and the p-polarization $\boldsymbol{e}_e$ lies in y–z plane. $\rho^s_{r,12}$ and $\rho^p_{r,12}$ are the Fresnel reflection factors.

The first integral gives the far-field emission, and when using $2\pi\kappa \mathrm{d}\kappa = \omega^2 \cos\theta \mathrm{d}\Omega / u_{ph,o}^2$, and for $\rho_{r,12}^s = \rho_{r,12}^p = 0$ (for absorbing medium 2), we have

$$\frac{\mathrm{d}E_{ph,\omega}}{\mathrm{d}\omega} = \frac{\mathrm{d}E_{b,\omega}}{\mathrm{d}\omega} = \frac{\hbar\omega^3}{\pi^2 u_{ph,o}^2} \frac{\mathrm{d}\omega}{e^{\hbar\omega/k_\mathrm{B}T} - 1}, \tag{7.310}$$

which is the Planck blackbody spectral energy density (7.4). Note that spectral emissivity $\epsilon_{ph,\omega}$ (7.147) is given in terms of the Fresnel reflection factors as

$$\epsilon_{ph,\omega} = \frac{1 - |\rho_{r,12}^s|^2 + 1 - |\rho_{r,12}^p|^2}{2}, \tag{7.311}$$

which is 1/2 of the sum of the transmission factors for both polarizations.

The spectral energy flux from a dielectric medium 1 to another dielectric medium 2 (Figure 7.54) is given in terms of the exchange function $Z_{1\text{-}2}(\kappa_\parallel)$ as [150]

$$q_{ph,1\rightarrow 2,\omega} = \frac{1}{\pi^2} \frac{\hbar\omega}{\exp(\frac{\hbar\omega}{k_B T_1}) - 1} \int_0^\infty Z_{1\text{-}2}(\kappa_\parallel)\kappa_\parallel \mathrm{d}\omega \mathrm{d}\kappa_\parallel, \tag{7.312}$$

where $\kappa_\parallel$ is the surface-wave-vector component along the surface. This includes the propagating and evanescent waves (exponentially decaying). The net total heat flux is

$$q_{ph,1\text{-}2,\omega} = \frac{1}{\pi^2} \int_0^\infty \int_0^\infty [\frac{\hbar\omega}{\exp(\frac{\hbar\omega}{k_B T_1}) - 1} - \frac{\hbar\omega}{\exp(\frac{\hbar\omega}{k_B T_2}) - 1}] Z_{1\text{-}2}(\kappa_\parallel)\kappa_\parallel \mathrm{d}\omega \mathrm{d}\kappa_\parallel. \tag{7.313}$$

For the near field (7.313) is simplified and becomes (7.15), as shown in [150]. The exchange function is a function of complex dielectric function ϵ_e, and for semiconductors the Drude model (3.49) is extended for each material as [512]

$$\epsilon_e(\omega) = \epsilon_{e,\Delta} - \frac{n_{e,c}e_c^2/\epsilon_\mathrm{o} m_{e,e}}{\omega^2 + i\omega/\tau_e} - \frac{n_{h,c}e_c^2/\epsilon_\mathrm{o} m_{h,e}}{\omega^2 + i\omega/\tau_h}$$

Drude model of dielectric function, (7.314)

where $\epsilon_{e,\Delta}$ is for interband (and lattice vibration) transition; the other terms are for the free-carrier conduction-band electron and valence band hole transitions [150]. The procedure for determining these parameter in the ϵ_e expression is given in [150]. Figure 7.55 shows the variation of the predicted net radiation heat transfer rate between two Si surfaces separated by a gap d.

One surface is at 1000 K (using $\lambda_{max} T$ = 2898 μm-K Section 7.1, gives λ_{max} = 3000 nm) and the other at 300 K (λ_{max} = 10,000 nm) [150]. One Si solid is intrinsic, and the other is doped. The results show that, for $d > 3000$ nm, the far-field behavior is approached, whereas for the doped Si the heat transfer radiation continues to increase with a decrease in the gap spacing. The blackbody radiation (with surface emissivity of unity) is also shown for reference. For doped Si, two different regimes are found, one influenced by doping and one independent of doping.

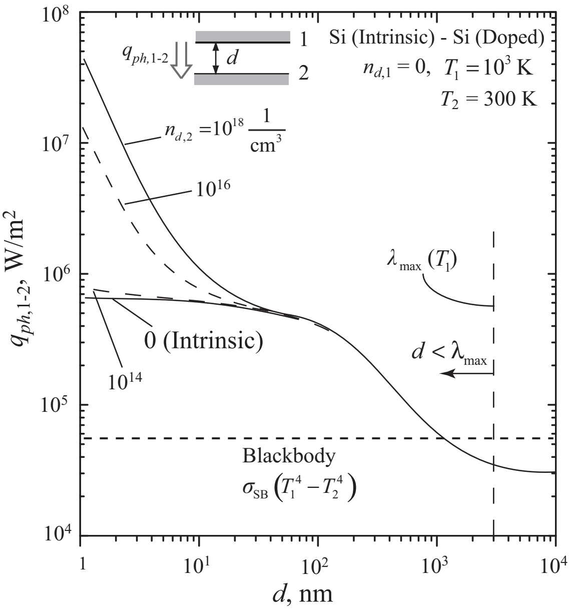

Figure 7.55. Variation of the net radiation heat transfer rate between two Si surfaces as functions of the separation distance. The temperature of each surface and the dopant concentration are also given [150]. $\lambda_{\text{max}} T = 2898$ μm-K.

7.15.2 Photon Energy Confinement by Near-Field Optical Microscopy

Similar to the photon localization of Section 7.7, the electric field intensity in the near field of a probe tip (optical microscope) has been numerically determined using the classical Maxwell equations (Table 3.5) [89]. The probe (cylindrical cone with cone angle of 36°) is made of Si and the substrate is Au. Figures 7.56(a) and (b) show the probe-substrate and the predicted field energy enhancement (confinement) $(|\boldsymbol{e}_e|/|\boldsymbol{e}_{e,i}|)^2$, where $|\boldsymbol{e}_e|$ is the laser irradiation intensity through the probe

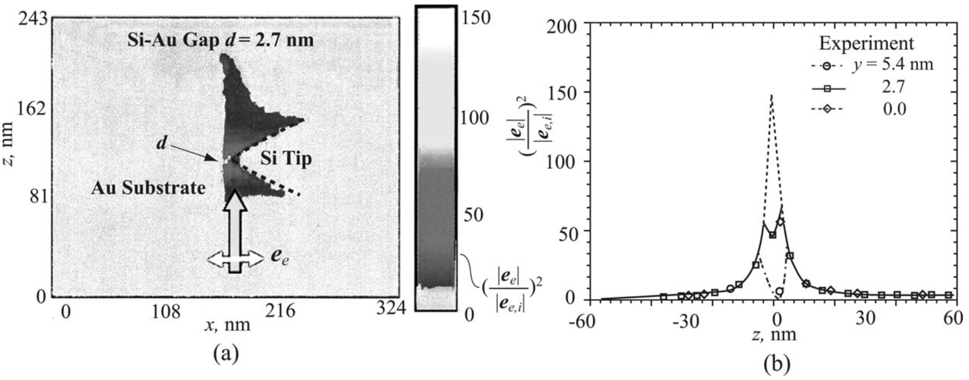

(a) (b)

Figure 7.56. (a) and (b) Normalized electric field energy distribution underneath a Si probe tip irradiated with P-polarization femtosecond laser of $\lambda = 800$ nm in the proximity of the surface of Au film [89]. The tip apex/sample surface separation $d = 2.7$ nm.

(uniform entering the probe). The photon wavelength is 800 nm, with polarization parallel to the incident plane. The top, Au plate separation is $d = 2.7$ nm. Field enhancements as high as 150 appear on the Au surface. The lateral confinement of the high-field-enhancement regime is about 10 nm, allowing for high resolution probing or material alterations.

This photon confinement adjacent to a surface, and where used with sufficiently large, pulsed laser irradiation power, can increase the temperature of the surface. Predicted transient, local temperatures as high as 12,000 K have been reported [89] for metals, under electron, lattice thermal nonequilibrium. (Sections 5.19 and 5.20).

Radiation propagating through subwavelength aperture is concentrated (focused) in the near field of the aperture (near-field optical microscopy) [74, 217, 218]. Amongst the aperture geometries are the O- and H-apertures shown in Figures 7.56(a) and (b) [217], where the former has an analytical solution (to classical Maxwell equations) and the latter is solved numerically.

7.15.3 Hot Phonon Recycling in Photonics

Energy recycling in photonic devices is promising (e.g., high-power lasers, where the laser inefficiency is critical [208]). Laser inefficiency stems from quantum defects (emitted photon energy is lower than that absorbed, $\hbar\omega_{ph,\mathrm{P}} > \hbar\omega_{ph,\mathrm{L}}$), and emitted phonons carry away excess entropy produced during absorption of multimode pumping photons. The second law requires that emitted phonons have higher entropy compared to photons. Thus, in high-power lasers elaborate cooling systems are unavoidable and hinder development of efficient, portable units. Recent efforts on radiation-balanced laser systems have provided alternative to mechanical cooling systems. However, limited photon wavelength contrast of the single-crystal laser medium that is used [55, 56] poses a significant challenge.

In [239], theory is developed and prediction of phonon recycling (phonon excitation and recombination) is made in a multilayer ion-doped laser using the anti-Stokes luminescence.

Anti-Stokes luminescence has cooled ion-doped solids from room temperature to 208 K, and its theory has been advanced recently [458, 134, 139, 400, 238]. It is the reverse of the quantum defect (i.e., $\hbar\omega_{ph,sp} > \hbar\omega_{ph,\mathrm{P}}$), and the excess entropy is removed by multimode incoherent spontaneous photons. The phonon-assisted photon absorption rate strongly depends on the high-energy phonon occupation, making it inefficient at low temperatures [184, 238]. Conversely, at moderate to high temperatures, the high-energy phonons are more accessible. Phonon recycling in ion-doped lasers uses this accessibility by absorbing the high-energy phonons created in the lasing layer to drive the anti-Stokes process in the adjacent cooling layers, as shown by the energy flow diagram in Figure 7.57. Thus, phonon recycling involves dynamics of the three energy carrier [photon (ph), electron (e), and phonon (p)] interactions within and across two heterogeneous layers.

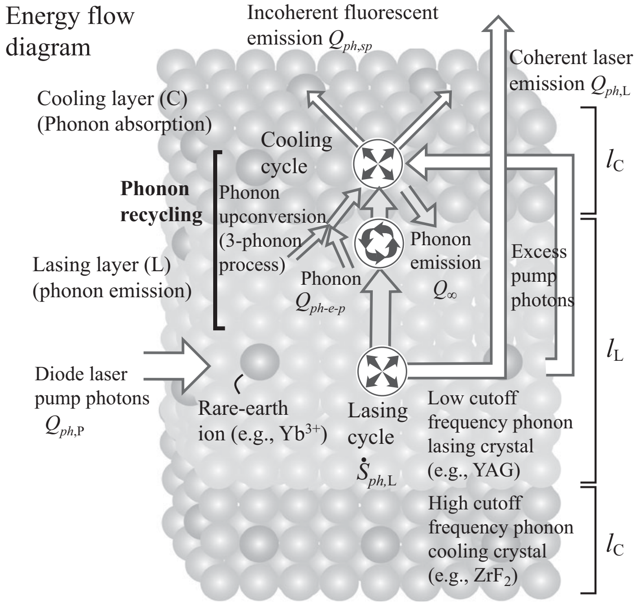
Energy flow diagram
Incoherent fluorescent emission $Q_{ph,sp}$
Coherent laser emission $Q_{ph,\mathrm{L}}$
Cooling layer (C) (Phonon absorption)
Cooling cycle
l_C
Phonon recycling
Phonon upconversion (3-phonon process)
Phonon $Q_{ph\text{-}e\text{-}p}$
Phonon emission Q_∞
Excess pump photons
Lasing layer (L) (phonon emission)
l_L
Diode laser pump photons $Q_{ph,\mathrm{P}}$
Rare-earth ion (e.g., Yb^{3+})
Lasing cycle $\dot{S}_{ph,\mathrm{L}}$
Low cutoff frequency phonon lasing crystal (e.g., YAG)
High cutoff frequency phonon cooling crystal (e.g., ZrF$_2$)
l_C

Figure 7.57. The energy-flow diagram: interactions among ions, photons, and phonons. Photon (clear arrow) and phonon (gray arrow) energy flows and heat flow diagram are also shown.

The second-order transition process is treated using the Fermi golden rule, and the final form of the transition rate (7.188) becomes

$$\dot{\gamma}_{ph\text{-}e\text{-}p} = \frac{\pi\hbar}{2\epsilon_{\mathrm{o}} m_r}(\boldsymbol{s}_{ph,i}\cdot\boldsymbol{\mu}_{ph\text{-}e})^2\varphi'^2_{d,\mathrm{O}}D_p(E_{p,\mathrm{O}})\frac{f_p(E_{p,\mathrm{O}})}{E^3_{p,\mathrm{O}}}\frac{L}{u_{ph}}\frac{Q_{ph,\mathrm{P}}-Q_{ph,a}}{n_{d,\mathrm{C}}V}, \tag{7.315}$$

where m_r is the reduced mass of the host atomic pair, $\boldsymbol{s}_{ph,i}$ is the polarization vector, $\boldsymbol{\mu}_{ph\text{-}e}$ is the electronic transition dipole moment vector, $\varphi'_{e\text{-}p,\mathrm{O}}$ is the optical-phonon deformation potential, $D_p(E_{p,\mathrm{O}})$ is the phonon density of states of phonon having energy $E_{p,\mathrm{O}}$, f_p is the phonon distribution function, L is the photon transit length, u_{ph} is the speed of light, and $(Q_{ph,\mathrm{P}}-Q_{ph,a})/n_{d,\mathrm{C}}V$ represents photon intensity per dopant ion [238]. So, the phonon-assisted photon transition rate is a function of the atomic properties of the dopant ion and host, which are optimized for desired performance [238].

In ion-doped lasers, phonons are emitted in the lasing layer by temperature-independent rapid single-phonon decay and by temperature-dependent multi-phonon decay. These nonequilibrium phonon distributions drive phonon propagation to the adjacent cooling layer. The propagation process involves acoustic-optical phonon up- and downconversion (three-phonon processes) [515, 445] and optical and acoustic-phonon transmission [453], which are influenced by the phonon spectrum of both layers [453].

Figure 7.58(a) shows the Debye-Gaussian model for $D_p(E_p)$ [238] with low cut-off energy $(E_{p,c,\mathrm{L}})$ phonon host in the lasing and high cut-off $(E_{p,c,\mathrm{C}})$ in the cooling

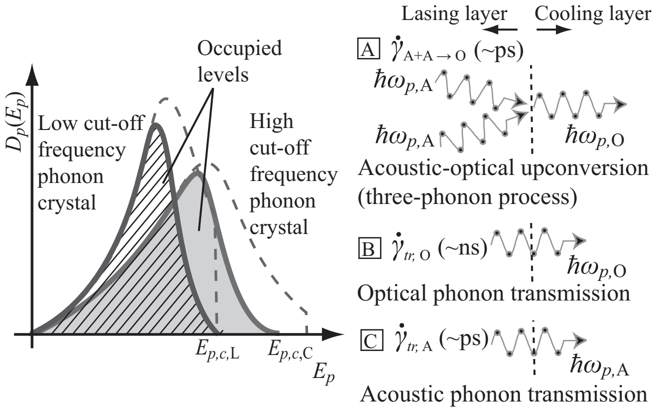
Occupied levels
$D_p(E_p)$
Low cut-off frequency phonon crystal
High cut-off frequency phonon crystal
$E_{p,c,\mathrm{L}}$
$E_{p,c,\mathrm{C}}$
E_p
Lasing layer
Cooling layer
A
$\dot{\gamma}_{\mathrm{A+A}\rightarrow\mathrm{O}}$ (~ps)
$\hbar\omega_{p,\mathrm{A}}$
$\hbar\omega_{p,\mathrm{A}}$
$\hbar\omega_{p,\mathrm{O}}$
Acoustic-optical upconversion (three-phonon process)
B
$\dot{\gamma}_{tr,\mathrm{O}}$ (~ns)
$\hbar\omega_{p,\mathrm{O}}$
Optical phonon transmission
C
$\dot{\gamma}_{tr,\mathrm{A}}$ (~ps)
$\hbar\omega_{p,\mathrm{A}}$
Acoustic phonon transmission

(a) (b)

Figure 7.58. (a) Overlap of phonon DOS (Debye-Gaussian model) for low and high cut-off frequency crystals (not to scale). Filled areas under the curve are the occupied phonon states at a given temperature. Saturation of low-frequency phonons in the cooling layer makes upconversion favorable, and transmission of phonons are needed from the lasing layer. (b) The three-phonon transfer mechanisms.

layer. The three-phonon processes involved in heat transfer across layers are shown in Figure 7.58(b). Note that the figure is not to scale, and the phonon DOS integrates to $3N$, where N is the number of atoms, so depending on the cut-off phonon energies, the curves move up or down. The shaded areas under the curves in Figure 7.58(a) represent occupied phonon levels at a given temperature and are the product of phonon DOS and the boson distribution function. When $E_{p,c,\mathrm{L}} < E_{p,c,\mathrm{C}}$, the average value of $D_p(E_p)$ is higher in the lasing layer, and for a given energy, phonons occupy the lower energy states because of their higher availability. In contrast, for the cooling layer, the value of $D_p(E_p)$ is lower, but extends further into the high-energy regime. Thus, equilibrium phonons occupy higher energy states. During laser operation, generated phonons begin to occupy higher energy states in the lasing laser and create energy nonequilibrium between the lasing and cooling layers. In crossing the interface most low-energy phonon states are already occupied in the cooling layer. Thus, for phonons to propagate into the cooling layer, among the three-phonon processes, the acoustic-optical phonons upconversion process becomes favorable. The added high-energy phonons in the cooling layer are used in the phonon-assisted absorption (anti-Stokes absorption).

Because of phonon transmission and upconversion processes, equilibrium, f_p^{o} used in [400, 238] is no longer valid in calculating the transition rate involving phonon recycling. Calculation of the exact nonequilibrium distribution is very challenging. However, we calculate the time scales for each processes to identify the bottleneck mechanism. It is then reasonable to assume the non-bottleneck processes as equilibria. For example, acoustic phonon thermalization and the upconversion of two acoustic phonons to one optical phonon are of the order of ps [515, 445]. However, due to their low speed, the optical phonon transmission is expected to have a time scale of the order of 10 ns [356], for sub-millimeter travel distance. Thus, the

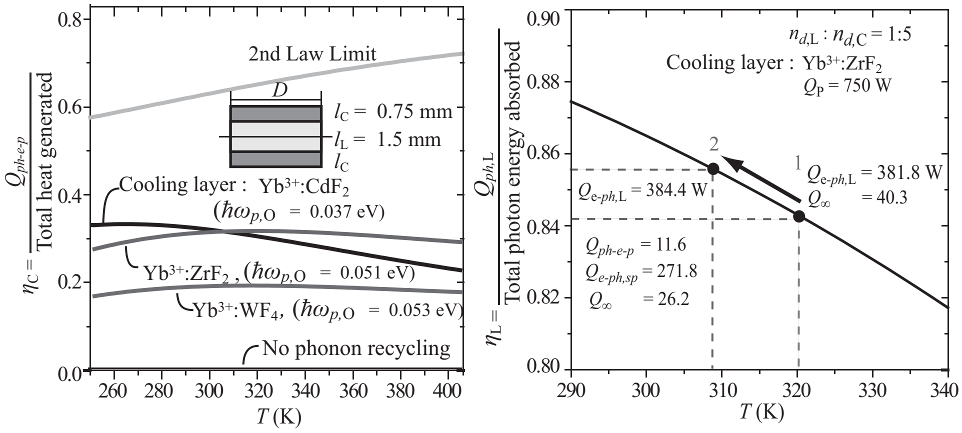

(a) (b)

Figure 7.59. (a) Phonon-cooling performance as a function of temperature for phonon-recycled ion-doped laser using three different cooling crystals. $D = 1$ cm, $l = 1.5$ mm, and $l_C = 0.75$ mm, Yb^{3+} doped disk is used, and emission spectra of Yb^{3+}:ZBLANP are used to calculate the spontaneous emission peak of anti-Stokes cooling [430] and [274]. The second law limit of the anti-Stokes cooling is also shown [341] and [403]. (b) Laser operation conditions as a function of temperature with (2) and without (1) phonon recycling. The reduced cooling load corresponds to a reduced laser crystal temperature and moves the operating condition to 2.

bottleneck process is identified as optical phonon transmission. Therefore, deviation from f_p^o for transmitted optical phonons is accounted for by introducing a transmission coefficient $\tau_{p,tr,O}$, while equilibrium distribution is used for the three-phonon upconversion process. These treatments of the nonequlibrium (hot) phonon populations give

$$f_p = f_p^o(E_{p,O}) + \tau_{p,tr,O} f_p^o(E_{p,O}) + f_p^o(E_{p,A_1}) f_p^o(E_{p,A_2})[f_p^o(E_{p,O}) + 1], \qquad (7.316)$$

where $f_p^o(E_{p,A_1})$ and $f_p^o(E_{p,A_1})$ are distributions of any two acoustic phonon energies that can be annihilated to create one optical phonon of energy $E_{p,O}$, and must be allowed by the phonon dispersion relation and momentum conservation [515]. Note that as the time-scale contrast decreases, the population deviates from equilibrium, resulting in a lower occupation number for the three-phonon process.

The phonon recycling transition rates appear in the macroscopic energy equation, as $Q_{ph\text{-}e\text{-}p} = n_{d,C}\dot{\gamma}_{ph\text{-}e\text{-}p} V$, along with energy conversion $\dot{S}$ and energy transfer Q, for steady-state behavior of ion-doped laser layer and its adjacent anti-Stokes cooling layer. Figure 7.59(a) shows cooling efficiency η_C (heat removed by the anti-Stokes cooling/total heat generated by lasing) as a function of temperature, for three different cooling crystals (ZrF_2, CdF_2, and WF_2) with dopant Yb^{3+}, and Yb^{3+}:YAG (Yttria-Alumina Garnet) as the lasing crystal. The cooling crystal hosts are selected for their high, moderate, and low peak phonon energies; the method for evaluating the necessary atomic quantities in (7.315) is given in [238]; and validity of the electron-phonon interaction potential used there has been confirmed in [240]. The pumping, laser (Yb^{3+}: YAG), and spontaneous emission (Yb^{3+}: ZBLANP) wavelengths are: $\lambda_{ph,\mathrm{P}}$= 998 nm, $\lambda_{ph,\mathrm{L}}$ = 1030 nm, and $\lambda_{ph,sp}$ = 975 nm.

The results shows that for ZrF_2 (optical phonon energy of 0.051 eV), the phonon recycling rate peaks at the conventional laser operation temperatures T_L = 300 to 325 K, with approximately 30% of phonons recycled. At low temperatures, the anti-Stokes cooling rate rapidly diminishes, while the temperature-independent, rapid single-phonon decay remains constant. At high temperatures, the anti-Stokes cooling rate increases, and temperature-dependent multiphonon decay dominates over all other mechanisms and decreases the phonon recycling rate. For crystals with low optical phonon energy (e.g., CdF_2), phonon recycling peaks at lower temperatures, but decreases rapidly at high temperatures (due to a low optical phonon transmission rate). In contrast, high-phonon energy crystals such as WF_4 result in a much lower phonon recycling rate (due to their rather large reduced mass and lower phonon occupancy number). In practice, experiments use combination of materials to achieve maximum cooling, because of statistical distribution of the spontaneous emission spectrum resulting from various defects and impurities [184, 275]. In Figure 7.59(b), variation of laser efficiency η_L (laser emission/total absorption) is shown for a laser system as a function of temperature. The laser with no phonon recycling is pumped by $Q_{ph,\mathrm{P}}$ = 750 W diode laser, while producing $Q_{ph,\mathrm{L}}$ = 381.8 W laser emission and Q_∞ = 40.3 W of heat (the rest of the energy is lost without being absorbed) [430]. With added cooling layers of the same volume and having five times the dopant concentration, we predict $Q_{ph\text{-}e\text{-}p}$ = 12.8 W of heat is removed by the phonon recycling, producing $Q_{ph,sp}$ = 302.2 W of spontaneous emission. When the same external cooling unit is used, for example, Q_∞ = 40.3 W, the reduced cooling load translates to 12 K lower crystal operating temperature, moving the operating conditions to slightly higher laser efficiency. Alternatively, for the same operating temperature, the phonon-recycled laser requires 30% less cooling, resulting in a significant decrease in the cooling unit, which may allow air-cooled units for portability. The thermodynamic limit is found by applying the second law to the phonon-recycled laser [264, 268]. The entropy generation and removal rates are evaluated using the corresponding Q_i/T_i . To find the equilibrium temperatures of the photon source, the thermodynamics of radiation is used, and we find temperatures of 11,000, 44,000, and 4,500 K for diode laser T_P, laser T_L, and spontaneous emission $T_{ph,sp}$, respectively, while the entropy of phonons is evaluated at the laser crystal temperature T [341, 403]. The result is plotted in Figure 7.59(a). This shows that phonon recycling satisfies the second law and is open to future improvement (removing inefficiencies in carrier interactions).

7.16 Problems

Problem 7.1

(a) Derive the expression for the photon Stefan–Boltzmann constant in (7.9).

(b) Starting from the definition of the blackbody intensity, and using the Stefan–Boltzmann law, show that the Stefan–Boltzmann coefficient (but not constant) for a phonon (using the Debye model) is $\rho c_{v,p} u_{p,\mathrm{A}}/(16T^3)$.

Problem 7.2

(a) Derive Rayleigh–Jeans relation (7.10) from blackbody (Planck) distribution function (7.8).

(b) Show that $\mathrm{d}E_{b,\lambda}/\mathrm{d}\lambda$ (7.8) has a maximum at $\lambda_{max}T = 2898\ \mu$m-K (we need to find the root of the transcendental equation resulting from the differentiation). This peak relation is called the Wien displacement law (as T increases, λ_{max} is displaced).

Problem 7.3

(a) Show that $\mathrm{d}I_{b,\omega}$ peaks at $\hbar\omega/k_{\mathrm{B}}T = 2.821$. This is referred to as the most likely frequency for blackbody radiation at temperature T.

(b) Why are the peaks for $I_{b,\lambda}$ and $I_{b,\omega}$ different?

Problem 7.4

(a) Using the blackbody emission, show that the photon number density (1.19)

$$n_{ph,b} = \int_0^\infty f_{ph}^{\mathrm{o}}(\omega)D_{ph}(\omega)\mathrm{d}\omega = \frac{8\pi}{u_{ph}^3}(\frac{k_{\mathrm{B}}T}{h_{\mathrm{P}}})^3\int_0^\infty \frac{x^2}{e^x-1}\mathrm{d}x$$

$$= 2.404 \times 8\pi(\frac{k_{\mathrm{B}}}{h_{\mathrm{P}}u_{ph}})^3T^3.$$

Note that $\int_0^\infty \frac{x^n}{e^x-1}dx = \zeta(n+1)\Gamma(n+1)$, and for $n = 3$, $\zeta(3) = 1.202$ and $\Gamma(3) = 2!$. This shows that the number density of photons in the blackbody emission is proportional to T^3.

(b) Show that the total energy of photons per unit volume is $8\pi^5(k_{\mathrm{B}}T)^4/15(h_{\mathrm{P}}u_{ph})^3$. Note that $\int_0^\infty x^3(e^x-1)^{-1}\mathrm{d}x = \pi^4/15$.

(c) Evaluate this photon number density $n_{ph,b}$ in 1/cm^3, for $T = 10^2$, 10^3, and 10^4 K.

(d) Show that the average energy per photon $\langle E_b\rangle = E_b/Vn_{ph,b}$ is $2.701k_{\mathrm{B}}T$. Evaluate this in eV, for $T = 10^2$, 10^3, and 10^4 K. Compare these with $\hbar\omega$ at the peak of the spectral emissive power of the spectra ($\lambda_{max}T = 2898\ \mu$m-K) (continue to use eV for energy unit).

Problem 7.5

The simple, dipole, spontaneous emission (classical dipole radiation) rate is (3.43) (discussed in Section 3.3.4 and derivation is Problem 7.23)

$$\dot{\gamma}_{ph,e,sp} = \frac{\omega^3|\boldsymbol{\mu}_e|^2}{3\pi\epsilon_{\mathrm{o}}\hbar u_{ph}^3},$$

where $\boldsymbol{\mu}_e$ is the average transition dipole moment.

Then using (7.42), the equilibrium stimulated emission is

$$\dot{\gamma}_{ph,e,st}\frac{\mathrm{d}E_{ph,\omega}}{V\mathrm{d}\omega} = \frac{\pi}{3\epsilon_{\mathrm{o}}\hbar^2}|\boldsymbol{\mu}_e|^2\frac{\mathrm{d}E_{ph,\omega}}{V\mathrm{d}\omega},$$

where $\mathrm{d}E_{ph,\omega}/V\mathrm{d}\omega$ is given by (7.4), and $D_{ph,\omega}/D_{b,\omega} = 1$ for equilibrium.

(a) Show that

$$\frac{\dot{\gamma}_{ph,e,sp}}{\dot{\gamma}_{ph,e,st}\frac{\mathrm{d}E_{ph,\omega}}{V\mathrm{d}\omega}} = \exp(\frac{\hbar\omega}{k_{\mathrm{B}}T}) - 1.$$

(b) For $T = 300$ K, show that for $f = \omega/2\pi \gg 4.35\times10^{12}$ Hz, spontaneous emission dominates.

Problem 7.6

Using (7.29), (7.31), and the commutator relation, $[A, B] = AB - BA$ (Chapter 2 problem), derive the two relations given in (7.32).

Problem 7.7

Consider the derivation of (3.43) expressing the relation for the emission rate (or radiation decay rate) of an electric entity undergoing a transition dipole moment $\boldsymbol{\mu}_e$.

(a) Using the first order perturbation Hamiltonian (E.28), show that, on averaging over all directions, we have ($a_{e,\mathrm{o}} = e_{e,\mathrm{o}}/\omega_i$)

$$\langle f|\mathrm{H}'|i\rangle^2 = \frac{1}{12}\frac{e_c^2 e_{e,\mathrm{o}}^2}{m_e^2\omega_i^2}\langle f|\boldsymbol{p}_e|i\rangle^2,$$

where the average (in all directions) gives $3^{-1/2}$, which is squared here (Problem 7.20). Note, $\exp(i\boldsymbol{\kappa}\cdot\boldsymbol{x}) = 1 + i\boldsymbol{\kappa}\cdot\boldsymbol{x} + \cdots \simeq 1$, because the wavelength of EM radiation emitted is much larger than the typical size of the atom.

(b) Use $[\boldsymbol{x}, \mathrm{H}_\mathrm{o}] = -(i\hbar/m_e)\boldsymbol{p}_e$ (Problem 2.15) and using (7.135) to show that the interaction matrix is

$$|\langle f|\mathrm{H}'|i\rangle|^2 = |M_{fi}|^2 = \frac{1}{12}e_{e,o}^2|\boldsymbol{\mu}_e|^2.$$

Note that $\langle f|i\rangle = 0$.

(c) Use the FGR along with (E.8), (7.2), and (7.3) to show that the stimulated emission rate is

$$\frac{\mathrm{d}E_{ph,\omega}}{V\mathrm{d}\omega}\dot{\gamma}_{ph,e,st} = \frac{\omega_{e,g}^3}{3\pi\epsilon_\mathrm{o}\hbar u_{ph}^3}|\boldsymbol{\mu}_e|^2 f_{ph}^\mathrm{o}.$$

Note that from (3.38), $\epsilon_\mathrm{o}e_{e,\mathrm{o}}^2/2 = \hbar\omega_{e,g}f_{ph}^\mathrm{o}D_{b,\omega}$. Also note that

$$\sum_f \frac{\mathrm{d}E_{ph,\omega}}{V}\delta_D(E_f - E_i - \hbar\omega) = \frac{1}{\hbar}\sum_f \frac{\mathrm{d}E_{ph,\omega}}{V}(\frac{E_f - E_i}{\hbar} - \omega)$$
$$= \frac{\mathrm{d}E_{ph,\omega}}{V}|_\omega = \hbar\omega f_{ph}^\mathrm{o}D_{ph,\omega}.$$

(d) Then using (7.39), (7.5), and (7.6), arrive at (3.43).

Problem 7.8

Show that under thermal equilibrium distribution and under a thermal source the population rate equation (7.37) leads to the two relation (7.40) and (7.42) between the Einstein coefficients.

Problem 7.9

For the case of small absorption (optically thin $\sigma_{ph,L} \ll 1$) and emission domination, consider the following.

(a) Show that the ERT (Table 7.1) under thermal equilibrium, along a path S, and under steady state and $\dot{s}_{ph,i} = 0$, becomes

$$I_{ph,\omega}(S) = \int_0^S \sigma_{ph,\omega} I_{b,\omega} \mathrm{d}S.$$

(b) Using the definition of the mean absorption coefficient,

$$\langle \sigma_{ph} \rangle = \frac{\int_0^\infty \sigma_{ph,\omega} E_{b,\omega} \mathrm{d}\omega}{\int_0^\infty E_{b,\omega} \mathrm{d}\omega} = \frac{\int_0^\infty \sigma_{ph,\omega} E_{b,\omega} \mathrm{d}\omega}{\sigma_{\mathrm{SB}} T^4},$$

which is called the Planck mean absorption coefficient, show that

$$I_{ph} = \int_0^S \langle \sigma_{ph} \rangle \frac{\sigma_{\mathrm{SB}} T^4(S)}{\pi} \mathrm{d}S.$$

(c) Using q_{ph}^+ as the flux (per unit area) emerging from an isothermal slab made of material with $\langle \sigma_{ph} \rangle$, at T having a depth L, i.e.,

$$q_{ph}^+ = 2\pi \int_0^{\pi/2} I_{ph}(\theta) \cos\theta \sin\theta \mathrm{d}\theta,$$

and using $S = L/\cos\theta$, show that this flux is

$$q_{ph}^+ = 2\langle \sigma_{ph} \rangle \sigma_{\mathrm{SB}} L T^4.$$

This can be applied to emitted radiation from a gas or a solid slab that is optically thin.

Problem 7.10

(a) Using (7.126), determine $I_{ph,\omega}/I_{ph,\omega}(x = 0)$, for $x = 1$ mm, $\lambda = 5$ μm (near infrared), and $\lambda = 0.5$ μm (green), at $T = 300$ K, and for (i) Cu (metal), (ii) Si (indirect-band semiconductor), (iii) GaAs (direct-band semiconductor), and (iv) SiO_2 (dielectric). Use available (general literature) $\sigma_{ph,\lambda}$ for Cu, Si, and GaAs. Use available κ_λ for quartz (SiO_2) and $\sigma_{ph,\lambda} = 4\pi\kappa_\lambda/\lambda$.

(b) Explain the mechanism of photon absorption for each of these materials.

Problem 7.11

(a) Show that for an incident radiation intensity of $I_{ph,i}$ (energy per unit area irradiated is $\pi I_{ph,i}$) in a medium with an absorption coefficient σ_{ph}, the divergence (in one dimension, along x) of radiation heat flux q_{ph} is equal to

$-\pi I_{ph,i}\sigma_{ph}\exp(-\sigma_{ph}x)$. In the positive direction, the radiation heat flux at $x=0$ is from (7.32) as

$$q_{ph}(x=0) = 2\pi\int_0^{\pi/2} I_{ph,i}\cos\theta\sin\theta\mathrm{d}\theta = \pi I_{ph,i}.$$

Assume there is no emission and scattering. The divergence of $\boldsymbol{q}_{ph}$ appears in the macroscopic energy equation given in Table 1.1.

(b) Comment on how this term becomes a heat source in the macroscopic energy equation when radiation is absorbed.

Problem 7.12

Derive the expression for Thomson scattering cross-section area, (7.77), starting from a plane-polarized electric field (†):

$$\boldsymbol{e}_e = e_{e,\mathrm{o}}\boldsymbol{s}_\alpha \sin\omega t.$$

Then use

$$\frac{\mathrm{d}A_{ph,s}}{\mathrm{d}\Omega} = \frac{1}{|\bar{\boldsymbol{s}}_e|}\frac{\mathrm{d}\bar{P}_e}{\mathrm{d}\Omega},\quad |\bar{\boldsymbol{s}}_e| = \frac{\epsilon_\mathrm{o}u_{ph}e_{e,o}^2}{2},\quad \mathrm{d}\Omega = \mathrm{d}\cos\theta\mathrm{d}\phi,$$

where $|\bar{\boldsymbol{s}_e}|$ is the time-averaged Poynting vector (Table 3.5), and $\bar{P}_e$ is the time-averaged power per differential solid angle dΩ,

$$\bar{P}_e = \bar{\boldsymbol{s}}_e(r,\theta,\phi)\cdot\boldsymbol{s}_\alpha r^2\mathrm{d}\Omega = \frac{e_c 4e_{e,\mathrm{o}}^2}{32\pi^2\epsilon_\mathrm{o}u_{ph}^3m_e^3}\sin^2\theta.$$

Problem 7.13

Show that the Thomson cross-section area (for photon-free-electron elastic scattering) is $8\pi r_\mathrm{C}^2/3$, where r_C is the classical electron radius and is equal to 6.652×10^{-29} m^2. Note that, as given by (7.81), this is also equal to $e_c^4/6\pi m_e^2\epsilon_\mathrm{o}^2u_{ph,\mathrm{o}}^4$, because $r_\mathrm{C} = e_c^2/4\pi m_e\epsilon_\mathrm{o}u_{ph,\mathrm{o}}^2$.

Hint: Start from the energy of the free electron.

Problem 7.14

(a) Photon scattering from packed particles results in a small photon mean free path $\lambda_{ph} = 1/\sigma_{ph}$. Consider spherical alumina ($\mathrm{Al_2O_3}$) solid particles of diameter $d_s = 1, 10$, and 10^3 μm, surface emissivity of $\epsilon_{ph} = 0.5$, and find the radiant conductivity k_{ph} from the relation [230]

$$k_{ph} = a_1\epsilon_{ph}\tan^{-1}(a_2\frac{k_s^{*a_3}}{\epsilon_{ph}} + a_4)(4d_s\sigma_\mathrm{SB}T^3),$$

$$a_1 = 0.5756,\ a_2 = 1.5353,\ a_3 = 0.8011,$$

$$a_4 = 0.1843,\ k_s^* = \frac{k_s}{4d_s\sigma_\mathrm{SB}T^3},$$

where k_s is the solid particle thermal conductivity, at $T = 500$ K ($k_3 = 20$ W/m-K), for this packed particle bed. Calculate k_{ph}.

(b) Use (7.97) to find λ_{ph} for this medium and express this as multiples of d_s.

(c) The effective thermal conductivity of packed beds $\langle k \rangle$ depends on the solid and the fluid conductivities, k_s and k_f, porosity, particle geometry, and interparticle contact [230]. For a packed bed of spherical particles (porosity 0.38) of amorphous Al_2O_3 ($k_s = 10$ W/m-K), with air ($k_f = 0.0395$ W/m-K) as the fluid, use $\langle k \rangle = 3$ W/m-K [230], and compare with the preceding k_{ph}.

Problem 7.15

Plot the photon spectral absorption coefficient (Table 7.2) at $T = 290$ K, for the followings.

(a) Free-carrier absorption in Al [electrical conductivity of Al is given in Table A.1 and can be used to find $\langle\langle \tau_e \rangle\rangle$ using (5.147), and for metals m_e is used for the electron mass], use $\epsilon_e = 1$. Use up to $E_{ph} = 10$ eV.

(b) Free-carrier absorption in doped Si, with $n_{e,c} = 10^{19}$ 1/cm^3, and $m_{e,e} = 0.32 m_e$, (use σ_e from Figure 5.20 and $\epsilon_e = 1$). Use up to $E_{ph} = \hbar\omega = 1$ eV.

(c) Direct-band absorption for GaAs (Table 5.1, at Γ point). Use E_{ph} from 1.42 to 10 eV. This relation is more accurate for $E_{ph} > 3$ eV.

(d) Indirect-band absorption in Si with optical-phonon cut-off energy of 0.062 eV, determine the coupling constant $a_{ph\text{-}e\text{-}p,a}$ (phonon absorption) from the experimental results given in the figure for energies near the bandgap energy. Photons with energy larger than the bandgap continue to be absorbed (the general behavior is shown in Figure 7.14). The Si lattice constant a is listed in Table A.2. Use units of eV and cm. Use E_{ph} from $\Delta E_{e,g} - \hbar\omega_p$ to 6 eV. Note that this absorption coefficient is for the phonon energies much smaller than the bandgap ($\Delta E_{e,L} = 1.71$ eV). This corresponds to the sharply varying regime to the left of bandgap peak in Figure 7.14.

Use photon frequency over the UV(ultraviolet), V(visible), and NIR(near-infrared) regimes, when appropriate. Compare with any data from the literature. The bandgap data are given in Table 5.1.

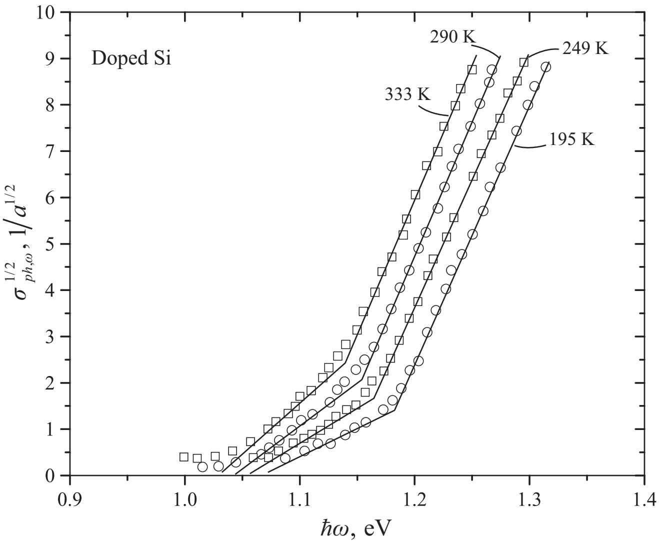

Problem 7.15. Spectral absorption coefficient of doped Si.

Problem 7.16

(a) Use Table 7.5 to calculate the fundamental angular frequency ω_f for CO_2 (C–O bond).

(b) Assume that the collision diameter of CO_2 listed in Table 6.4 can be used for its photon absorption cross-section area $\pi d_f^2/4$.

(c) Compare these with the measured resonant value of $A_{ph,\omega} = 1.4\times10^{-17}$ cm^2 at $\lambda = 4.23$ μm [Figure 7.16 (b)], and comment.

Note that CO_2 has three different vibration frequencies as calculated by Gaussian in Section 6.1.5.

Problem 7.17

In a CO_2 laser, first there is a vibration energy interchange between N_2 (which are excited by electrons) and CO_2 (Figure 7.39). The $l = 1$ vibration of N_2 matches the level (0,0,1) vibration of CO_2, exciting the asymmetric vibration. Then there is a laser (photon emission) to symmetric mode (1,0,0). The presence of He in a CO_2 laser is to maintain the plasma discharge (provide the free electron).

(a) Calculate $\hbar\omega_{f,v}$ of C=O bond, the natural (fundamental) frequency of CO_2, using Table 7.5 and (7.227).

(b) Then using the quantum numbers and energies given in Table 7.5, for triatomic CO_2 along with with (7.225), i.e.,

$$E_{f,v}(l_1, l_2, l_3) = \hbar\omega_{f,1}(l_1 + \frac{1}{2}) + \hbar\omega_{f,2}(l_2 + \frac{1}{2}) + \hbar\omega_{f,3}(l_3 + \frac{1}{2}).$$

Note that when the ground state $E_{f,v}(0,0,0)$ is set to zero then the 1/2 term is removed. Calculate $\omega_{f,1}$, $\omega_{f,2}$, and $\omega_{f,3}$, Then, compare to the calculated values in Section 6.1.5.

(c) Compare the results of (a) and (b), and comment (including the role of rotational energy transitions).

(d) Do (a) for diatomic N_2, using Table 7.4 and compare with Figure 7.39.

Problem 7.18

Determine the fundamental vibrational frequency of N–N (reported value is 2330 1/cm).

Problem 7.19

(a) Using (7.154) to (7.156) and (7.160), plot the variations of (i) $\dot{\gamma}_{e\text{-}ph\text{-}p}$, (ii) $\dot{\gamma}_{e\text{-}ph}$, (iii) $\dot{\gamma}_{e\text{-}p}$, and (iv) $\eta_{e\text{-}ph}$ with respect to temperature for T from 0 to 2500 K, for 1% Yb^{3+}: Y_2O_3 with the following properties (melting temperature of yttria is 2705 K). Use the values $\dot{\gamma}_{e\text{-}ph\text{-}p}(T = 0) = 952.38$ s^{-1}, $\hbar\omega_p = 0.2027$ eV, and $N_p = 6$.

(b) Explain the trend for each of the four (decay rates and efficiency) variables. Note that 0.2027 eV is rather large for a single phonon (even optical phonon).

Problem 7.20

For the radiative (photon) assisted transition from state i to state f shown in the figure, the net electron–hole radiative recombination in volume V is given, similar to (7.132) and (7.133), as in [26] and [27]

$$\dot{\gamma}_{e\text{-}h\text{-}ph}(\mathrm{m}^3/\mathrm{s}) = \frac{tV}{32\pi^6\hbar^2}\int\int\sum_{s_c,s_v}|M_{f,i}|^2 F\frac{1-\cos(x)}{x^2}\mathrm{d}\boldsymbol{\kappa}_{ph}\mathrm{d}\boldsymbol{\kappa}_{e,i}$$

$$x = \frac{t}{\hbar}(E_{e,i} - E_{h,f} - \Delta E_{e,g} - \hbar\omega_{ph})$$

$$F = f_{e,f}(1 - f_{e,i})(f_{ph} + 1) - (1 - f_{e,f})f_{e,i}f_{ph},$$

where s_e and s_v are the spin states, E_{e,κ_e} is the electron kinetic energy in conduction band, and $E_{e,\kappa_e'}$ is for the hole kinetic energy in the valance band.

The matrix element is

$$|M_{f,i}|^2 = \frac{e_c^2\hbar^2}{2Vm_{e,e}^2\epsilon_o\epsilon_e(\omega)\hbar\omega}\sum_{s_c,s_v}\langle f|\boldsymbol{s}_{ph,\alpha}\cdot\boldsymbol{p}_e|i\rangle^2.$$

Show that the direction-averaged matrix element becomes

$$\sum_{s_c,s_v}|M_{f,i}|^2 = \frac{e_c^2}{6V\epsilon_o\epsilon_e(\omega)\hbar\omega}\frac{\hbar^2}{m_{e,e}^2}\sum_{s_c,s_v}\langle f|p_e|i\rangle^2.$$

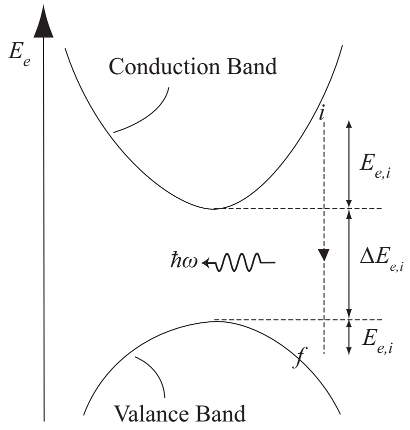

Problem 7.20. Electronic energy designations for radiative recombination.

Problem 7.21

Show that the angular-averaged transition dipole moment is

$$\langle\frac{|\boldsymbol{s}_\alpha\cdot\boldsymbol{\mu}_e|}{|\boldsymbol{\mu}_e|}\rangle = 3^{-1/2},$$

for an electric field with polarity $\boldsymbol{s}_\alpha$ and use $\boldsymbol{\mu}_e = |\boldsymbol{\mu}_e|\boldsymbol{s}_i$.

Note that

$$\boldsymbol{s}_\alpha \cdot \boldsymbol{s}_i = \cos\theta,$$

and that

$$\langle(\boldsymbol{s}_\alpha \cdot \boldsymbol{s}_i)^2\rangle = \frac{\int_0^{2\pi}\int_0^{\pi} \cos^2\theta \sin\theta \mathrm{d}\theta \mathrm{d}\phi}{\int_0^{2\pi}\int_0^{\pi} \sin\theta \mathrm{d}\theta \mathrm{d}\phi}.$$

Problem 7.22

(a) Starting from

$$\frac{\mathrm{d}A_{ph\text{-}e}}{\mathrm{d}\Omega} = 64\pi \frac{e_c^2 r_\mathrm{B}^2}{4\pi\epsilon_\mathrm{o}\hbar u_{ph}} \sin\theta (\frac{E_{e,1}}{\hbar\omega})^4 \frac{e^{-4\gamma\cot^{-1}\gamma}}{1-e^{-2\pi\gamma}},$$

show that

$$A_{ph\text{-}e} = \frac{512\pi^2}{3} \frac{e_c^2 r_\mathrm{B}^2}{4\pi\epsilon_\mathrm{o}\hbar u_{ph}} (\frac{E_{e,1}}{\hbar\omega})^4 \frac{e^{-4\gamma\cot^{-1}\gamma}}{1-e^{-2\pi\gamma}}.$$

Use $\mathrm{d}\Omega = \sin\theta \mathrm{d}\theta \mathrm{d}\phi$ and γ as defined in Table 7.2.

(b) Using the photoelectric absorption relation (also in Table 7.2) (more details are in Section E.3), plot the dimensional ionization cross-section area $A_{ph\text{-}e}$ as a function of incoming photon energy $\hbar\omega$ (in eV), for $\hbar\omega$ between $E_{e,1}$ (2.114) and $10E_{e,1}$.

(c) Using a circular cross-section geometry, comment on the radius of this absorption cross-section area and make comparisons with the Bohr radius.

Problem 7.23

The crystalline calcium resonance transition can be modeled as a two-level system, with $\omega_{e,g} = 4.5\times10^{15}$ rad/s, and its radiative decay lifetimes is $\tau_{ph,e,sp} = 1/\dot{\gamma}_{ph,e,sp} = 4.5\times10^{-9}$ s. This decay is from 4^1P (B level) to 4^1S (A level), where $g_{e,B} = 3$, and $g_{e,A} = 1$.

(a) Find the stimulated emission rate $\dot{\gamma}_{ph,e,st}$ under equilibrium conditions.

(b) Find $\dot{\gamma}_{ph,a}$ (absorption rate) under equilibrium conditions.

(c) Find the absorption cross-section area $A_{ph,a}$, using bandwidth $\int_\omega \mathrm{d}\omega = 10^{12}$ rad/s.

(d) Using (3.43), find the transition electric dipole moment $|\boldsymbol{\mu}_e|$ for this transition. Compare this with Debye electric dipole moment scale $\mathrm{D} = e_c r_\mathrm{B}/2.54$ (Section 1.5.2), where r_B is the Bohr radius. Is this transition dipole moment larger or smaller, and why?

Problem 7.24

Using (7.165) and Table 2.10, calculate the transition dipole moment for the following electronic transition in a hydrogen atom.

(a) $1s \rightarrow 2s$ (answer: $\boldsymbol{\mu}_e = 0$)
(b) $2s \rightarrow 2p_z$ (answer: $\boldsymbol{\mu}_e = -3e_c r_\mathrm{B} \boldsymbol{s}_z$).

Problem 7.25

For the ${}^2\mathrm{F}_{7/2} \rightarrow {}^2\mathrm{F}_{5/2}$ transition of Yb^{3+}, $\Delta E_{e,g} = 1.1998$ eV.

(a) estimate $|\boldsymbol{\mu}_e|$ using $|\boldsymbol{\mu}_e| = g_\mu e_c \Delta R_e$ [238]. Use $g_\mu = 1$, $E_{e,4f} = -19.86$ eV, $\langle R_{4f} \rangle = 0.379$ Å, and

$$\Delta E_{e,g} = A(\frac{1}{R_{e,f}^2} - \frac{1}{R_{e,i}^2}),\ A = E_{e,4f} \langle R_{4f} \rangle^2,$$

$$\frac{1}{R_{e,f}^2} + \frac{1}{R_{e,i}^2} = \frac{2}{\langle R_{4f}^2 \rangle},\ \Delta R_e = R_{e,f} - R_{e,i}.$$

(b) Use this in (7.189) to calculate the spontaneous emission rate.

(c) Using (7.42), find the thermal equilibrium, stimulated emission rate. Note the units are explained in Section 7.4.1.

(d) Using (7.57) and (7.40), calculate the absorption cross-section area for $\int_\omega \mathrm{d}\omega = 10^{12}$ rad/s. Comment on the relation with any other cross-section area (e.g., fluid particle collision).

(e) Using (7.129), find the absorption coeffifient. Use $n_d = 2.8 \times 10^{20}$ cm^{-3}.

Problem 7.26

The laser cooling of solids can be analyzed as described in Section 7.12.4, and here we consider a simplified analysis using empirical absorption cross-section area. The absorption cross-section area is temperature dependent; for example, empirical results show that [164]

$$A_{ph,a}(T) = A_{ph,a,\mathrm{o}} + a_{ph,a}(T_s - T_\mathrm{o}),$$

where for Yb^{+3}: ZBLANP laser cooling material, $A_{ph,o} = 3.70 \times 10^{-26}$ m^2, and $a_{ph,a} = 1.75 \times 10^{-28}$ m^2/K, for $T_\mathrm{o} = 301$ K. In laser cooling involving these materials, use $\lambda_{ph,i} = 1015$ nm, $\lambda_{ph.e} = 999.8$ nm, and a solid in form of a small fiber with $D = 250$ μm, $L = 7$ mm, $\epsilon_{ph} = 0.54$, $n_d = 2.42 \times 10^{20}$ $1/\mathrm{cm}^3$, and $Q_{ph,i} = 2.2$ W in (7.197).

(a) Using the number of dopants per unit volume n_d, and $\alpha_{ph,\lambda,i} = 1 - e^{-\sigma_{ph,\lambda,i} L}$, $\sigma_{ph,\lambda,i} L = A_{ph,a} n_d L$, calculate the absorptance $\alpha_{ph,\lambda,i}$, for target temperature $T_s =$ 300 K.

(b) Using this absorptance, calculate the target temperature T_s, for T_∞= 300 K and $\eta_{e\text{-}ph} = 0.98993$, and $\eta_{p\text{-}ph}$ given by (7.168).

(c) Repeat (a) and (b) with the new target temperature until convergence is reached.

Note that $A_{ph,a}$ is temperature dependent.

Problem 7.27

(a) Show that with $T_a = T_h$ (7.295) written in the ideal, simplified j_e versus $\Delta\varphi_e$ (current versus voltage performance) form, results in the magnitude of constants j_{sh}, $j_{\rm o}$, and $\Delta\varphi_{\rm o}$ listed in the related footnote of Section 7.14.1, for Si with $\Delta E_{e,g} = 1.12$ eV, and $T_a = 300$ K.

(b) Plot j_e (mA/cm^2) versus $\Delta\varphi_e$ (V) for this ideal case [similar to Figure 7.50(b)].

APPENDIX A

Tables of Properties and Universal Constants

A.1 Periodic Table I

Table A.1. *Periodic table of bulk properties of elements.*

	18		← Group Number
	Noble Elements		← Group Name
Element Abreviation →	Ar	18	← z Atomic Number
Element Name →	Argon		
M(kg/kmole) →	39.948	Gas	← State
c_p(J/kg-K) →	521	–	← σ_e(1/Ω-cm)
ρ(kg/m³) →	1.78	4.898×10^{6}	← Δh_{sl}(J/kg)
k(W/m-K) →	0.0177	1.63×10^{5}	← Δh_{lg}(J/kg)
T_{sl}(K) →	84	87	← T_{lg}(K)

Transition Metals

1 Alkali Metals (Except H)	2 Alkaline- Earth Metals	3	4	5	6	7	8	9
H 1 Hydrogen 1.008 Gas 14304 – 0.0899 1.16×10^{5} 0.1815 9.09×10^{5} 14 20								
Li 3 Lithium 6.941 Solid 3582 1.07×10^{5} 534 4.32×10^{5} 84.8 2.134×10^{7} 454 1615	Be 4 Berylium 9.012 Solid 1825 3.08×10^{5} 1850 1.354×10^{6} 201 3.245×10^{7} 1562 2745							
Na 11 Sodium 22.990 Solid 1228 2.11×10^{5} 970 1.13×10^{5} 142 4.263×10^{6} 371 1156	Mg 12 Magnesium 24.305 Solid 1023 2.33×10^{5} 1740 3.68×10^{5} 156 5.242×10^{6} 923 1363							
K 19 Potassium 39.098 Solid 757 1.39×10^{5} 862 6.013×10^{4} 102.5 2.052×10^{6} 337 1032	Ca 20 Calcium 40.078 Solid 647 2.78×10^{5} 1540 2.13×10^{5} 201 3.833×10^{6} 1115 1767	Sc 21 Scandium 44.956 Solid 568 2.1×10^{4} 2990 3.13×10^{5} 15.8 6.989×10^{6} 1814 3109	Ti 22 Titanium 47.880 Solid 523 2.3×10^{4} 4500 3.24×10^{5} 21.9 8.791×10^{6} 1943 3562	V 23 Vanadium 50.942 Solid 489 5.0×10^{4} 6110 4.11×10^{5} 30.7 8.870×10^{6} 2183 3682	Cr 24 Chromium 51.996 Solid 449 7.8×10^{4} 7150 3.256×10^{5} 93.9 6.622×10^{6} 2136 2945	Mn 25 Manganese 54.931 Solid 479 7.2×10^{3} 7300 2.19×10^{5} 7.81 4.112×10^{6} 1519 2335	Fe 26 Iron 55.847 Solid 449 1.02×10^{5} 7870 2.47×10^{5} 80.4 6.259×10^{6} 1811 3135	Co 27 Cobalt 58.993 Solid 421 1.72×10^{5} 8860 2.75×10^{5} 100 6.390×10^{6} 1768 3201
Rb 37 Rubidium 85.468 Solid 363 8.0×10^{4} 1530 2.64×10^{4} 58.2 8.1×10^{5} 313 961	Sr 38 Strontium 87.620 Solid 301 4.7×10^{4} 2640 10.4×10^{4} 35.4 1.585×10^{6} 1042 1655	Y 39 Yttrium 88.906 Solid 298 1.7×10^{4} 4470 1.28×10^{5} 17.2 4.435×10^{6} 1795 3611	Zr 40 Zirconium 91.224 Solid 278 2.4×10^{4} 6520 1.85×10^{5} 22.7 6.376×10^{6} 2128 4682	Nb 41 Niobium 92.906 Solid 265 6.9×10^{4} 8570 2.84×10^{5} 53.7 7.341×10^{6} 2742 5017	Mo 42 Molybdenum 95.940 Solid 251 1.89×10^{5} 10200 4.17×10^{5} 138 6.175×10^{6} 2896 4912	Tc 43 Technetium [98] Solid 243 7×10^{4} 11500 3.32×10^{5} 50.6 5.83×10^{10} 2430 4538	Ru 44 Ruthenium 101.047 Solid 238 1.35×10^{5} 12100 2.56×10^{5} 117 5.838×10^{6} 2607 4423	Rh 45 Rhodium 102.906 Solid 243 2.08×10^{5} 12400 2.65×10^{5} 150 4.798×10^{6} 2236 3970
Cs 55 Cesium 132.905 Solid 242 5.0×10^{4} 1930 1.64×10^{4} 35.9 4.96×10^{5} 302 944	Ba 56 Barium 137.327 Solid 204 2.6×10^{4} 3620 5.7×10^{4} 18.4 1.1×10^{6} 1002 2170		Hf 72 Hafnium 178.490 Solid 144 3.3×10^{4} 13300 1.35×10^{5} 23 3.211×10^{6} 2504 4876	Ta 73 Tantalum 180.948 Solid 140 7.6×10^{4} 16400 1.74×10^{5} 57.5 4.211×10^{6} 3293 5731	W 74 Tungsten 183.850 Solid 132 1.89×10^{5} 19300 1.74×10^{5} 173 4.211×10^{6} 3695 5828	Re 75 Rhenium 186.207 Solid 137 5.4×10^{4} 20800 1.77×10^{5} 48 3.842×10^{6} 3459 5869	Os 76 Osmium 190.200 Solid 130 1.10×10^{4} 22500 2.89×10^{5} 87.6 3.31×10^{6} 3306 5285	Ir 77 Iridium 192.220 Solid 131 1.96×10^{5} 22500 2.13×10^{5} 147 3.185×10^{6} 2720 4701
Fr 87 Francium [223] Solid – – – – 15 – 300 879	Ra 88 Radium [226] Solid 119.5 – 5000 – 18.6 – 973 1900							

Rare-Earth Metals

Lanthanides	La 57 Lanthanum 138.906 Solid 195 1.3×10^{4} 6150 4.46×10^{4} 13.4 2.978×10^{6} 1191 3737	Ce 58 Cerium 140.115 Solid 192 1.2×10^{4} 8160 3.9×10^{4} 11.3 2.955×10^{6} 1071 3716	Pr 59 Praseodymium 140.908 Solid 193 1.5×10^{4} 6770 4.89×10^{4} 12.5 2.105×10^{6} 1204 3793	Nd 60 Neodymium 144.240 Solid 190 1.7×10^{4} 7010 4.95×10^{4} 16.5 1.891×10^{6} 1294 3347	Pm 61 Promethium [145] 7260 – 7220 – 17.9 – 1315 3273	Sm 62 Samarium 150.360 Solid 197 1.0×10^{4} 7520 5.73×10^{4} 13.3 1.107×10^{6} 1347 2067
Actinides	Ac 89 Actinium [227] Solid 120 – 10000 6.3×10^{4} 12 1.75×10^{6} 1324 3473	Th 90 Thorium 232 Solid 113 6.6×10^{6} 11700 6.94×10^{4} 54 2.218×10^{6} 2028 5061	Pa 91 Protactinium 231 Solid 121 – 15370 – 47 6.48×10^{4} 1845 –	U 92 Uranium 238 Solid 116 3.9×10^{4} 19100 3.66×10^{4} 27.5 1.949×10^{6} 1408 4407	Np 93 Neptunium 237 Solid 20450 8.5×10^{3} – – 6.3 – 912 4173	Pu 94 Plutonium [244] Solid 138 7.0×10^{3} 19700 1.17×10^{4} 6.7 1.409×10^{6} 913 3503

10 Transition Metals	**11**	**12**	**13** Boron Group	**14** Carbon Group	**15** Pricogens	**16** Chalcogens	**17** Halogens	**18** Noble Elements
								He 2 Helium 4.002 Gas 5197 – 0.179 2.1×10^{4} 0.152 2.1×10^{5} 3 4
			B 5 Boron 10.811 Solid 1026 – 2340 1.933×10^{6} 27.4 – 2365 4275	C 6 Carbon 12.011 Solid 509 – 3510 – 2300 – 4100 4473	N 7 Nitrogen 14.007 Gas 1039 – 1.24 – 0.026 3.99×10^{5} 63 77	O 8 Oxygen 15.999 Gas 919 – 1.43 – 0.2674 4.26×10^{5} 54 90	F 9 Fluorine 18.998 Gas 828 – 1.7 – 0.0279 3.44×10^{5} 53 95	Ne 10 Neon 20.180 Gas 1030 – 0.9 1.6×10^{5} 0.0493 8.89×10^{4} 24 27
			Al 13 Aluminum 26.982 Solid 897 3.77×10^{5} 2700 3.97×10^{5} 237 1.0875×10^{7} 933 2793	Si 14 Silicon 28.086 Solid 712 - 2330 1.802×10^{6} 149 1.4×10^{7} 1687 3540	P 15 Phosphorus 30.974 Solid 791 - 2690 8.48×10^{4} 12.1 1.799×10^{6} 317 553	S 16 Sulfur 32.066 Solid 732 - 2070 5.34×10^{4} 0.205 2.87×10^{5} 388 718	Cl 17 Chlorine 35.453 Gas 479 - 3.21 1.8×10^{5} 0.0089 5.76×10^{5} 172 239	Ar 18 Argon 39.948 Gas 521 - 1.78 4.898×10^{3} 0.0177 1.63×10^{5} 84 87
Ni 28 Nickel 58.693 Solid 444 1.43×10^{5} 8900 2.91×10^{5} 90.9 6.309×10^{6} 1728 3187	Cu 29 Copper 63.546 Solid 385 5.95×10^{5} 8960 2.07×10^{5} 401 4.726×10^{6} 1358 2836	Zn 30 Zinc 65.390 Solid 388 1.69×10^{5} 7140 1.12×10^{5} 116 1.767×10^{6} 693 1180	Ga 31 Gallium 69.723 Solid 371 6.7×10^{4} 5910 7.97×10^{4} 40.6 3.688×10^{6} 303 2477	Ge 32 Germanium 72.610 Solid 310 – 5323 5.09×10^{5} 60.2 4.557×10^{6} 1211 3107	As 33 Arsenic 74.992 Solid 343 – 5727 – 50.2 1.7×10^{6} 1090 888	Se 34 Selenium 78.960 Solid 339 – 4810 6.62×10^{4} 2.04 1.2×10^{6} 494 958	Br 35 Bromine 79.904 Liquid 226 – 3120 6.6×10^{4} 0.122 1.9×10^{5} 266 332	Kr 36 Krypton 83.800 Gas 248 – 3.73 1.9×10^{5} 0.0095 1.08×10^{5} 116 120
Pd 46 Palladium 106.420 Solid 251 9.5×10^{4} 12020 4.17×10^{5} 71.8 5.567×10^{6} 2896 4912	Ag 47 Silver 107.868 Solid 235 6.21×10^{5} 10500 1.02×10^{5} 429 2.323×10^{6} 1235 2436	Cd 48 Cadmium 112.411 Solid 232 1.38×10^{5} 8690 5.39×10^{4} 96.9 8.86×10^{5} 594 1040	In 49 Indium 114.820 Solid 233 1.14×10^{5} 7310 2.86×10^{4} 81.8 2.019×10^{6} 430 2346	Sn 50 Tin 118.710 Solid 228 9.1×10^{4} 7280 6.07×10^{4} 66.8 2.495×10^{6} 505 2876	Sb 51 Antimony 121.757 Solid 207 2.4×10^{4} 6680 1.66×10^{5} 24.4 – 904 1860	Te 52 Tellurium 127.600 Solid 197 – 6240 1.4×10^{6} 2.35 8.95×10^{6} 723 1261	I 53 Iodine 126.904 Solid 145 – 4953 – 0.449 3.29×10^{5} 387 457	Xe 54 Xenon 131.290 Gas 158 – 5.89 1.7×10^{4} 0.0057 9.63×10^{4} 161 165
Pt 78 Platinum 195.080 Solid 133 9.6×10^{4} 21500 1.15×10^{5} 71.6 2.612×10^{6} 2042 4100	Au 79 Gold 196.967 Solid 129 4.55×10^{5} 19300 6.43×10^{4} 318 1.701×10^{6} 1337 3130	Hg 80 Mercury 200.590 Liquid 140 1.0×10^{4} 13534 1.14×10^{4} 8.3 2.96×10^{5} 234 630	Tl 81 Thallium 204.383 Solid 129 6.1×10^{4} 11800 2.06×10^{4} 46.1 8.06×10^{5} 577 1746	Pb 82 Lead 207.200 Solid 129 4.8×10^{4} 11300 2.32×10^{4} 35.3 8.58×10^{5} 600 2022	Bi 83 Bismuth 208.980 Solid 122 8.6×10^{3} 9790 5.33×10^{4} 7.92 7.3×10^{5} 544 1837	Po 84 Polonium [209] Solid 125 2.2×10^{4} 9320 5.98×10^{4} 20 – 527 1033	At 85 Astatine [210] Solid 140 – – – 1.7 – 575 650	Rn 86 Radon [222] Gas 93.7 – 9.73 1.2×10^{4} 0.0036 7.52×10^{4} 202 211

Rare-Earth Metals

Eu 63 Europium 151.965 Solid 182 1.1×10^{4} 5240 6.06×10^{4} 13.9 9.44×10^{5} 1095 1869	Gd 64 Gadolimium 157.250 Solid 236 7.0×10^{3} 7900 6.36×10^{4} 10.5 2.286×10^{6} 1586 3546	Tb 65 Terbium 158.925 Solid 182 9.0×10^{3} 8230 6.79×10^{4} 11.1 1.42×10^{6} 1629 3503	Dy 66 Dysprosium 162.500 Solid 173 1.1×10^{4} 8550 6.79×10^{4} 10.7 2.083×10^{6} 1685 2840	Ho 67 Holmium 164.930 Solid 165 1.3×10^{4} 8800 1.03×10^{5} 16.2 1.461×10^{6} 1747 2973	Er 68 Erbium 167.260 Solid 168 1.2×10^{4} 9070 1.19×10^{5} 14.5 1.563×10^{6} 1802 3141	Tm 69 Thulium 168.934 Solid 160 1.6×10^{4} 9320 9.9×10^{4} 16.9* 1.130×10^{6} 1818 2223	Yb 70 Ytterbium 173.040 Solid 155 3.8×10^{4} 6900 1.43×10^{4} 34.9* 7.45×10^{5} 1092 1469	Lu 71 Lutetium 174.967 Solid 154 1.9×10^{4} 9840 1.26×10^{5} 16.4* 2.034×10^{6} 1936 3675
Am 95 Americium [243] Solid – – 13670 – 10 – 1449 2284	Cm 96 Curium [247] – – – 13300 – 10 – 1618 –	Bk 97 Berkelium [247] – - – 14790 – 10 – 1323 –	Cf 98 Californium [251] - - - - - 10 - 1173 -	Es 99 Einsteinium [252] – – – – – 10 – 1133 –	Fm 100 Fermium [257] – – – – – 10 – 1800 –	Md 101 Mendelevium [258] – – – – – 10 – 1100 –	No 102 Nobelium [259] – – – – – 10 – 1100 –	Lr 103 Lawrencium [260] – – – – – 10 – 1900 –

A.2 Periodic Table II

Table A.2. *Periodic table of atomic-structure properties of elements.*

Outer Orbit Group Designation	*s* Block
Element Abreviation	Ar
Atomic Radius(Å): Filled Shell Configuration	1.88
Tetrahedral Covalent Bond	–
12-Coordinated Metal	–
Electronic Orbital Structure	$[\mathrm{Ne}]3s^23p^6$
Grüneisen Parameter	2.83
First Ionization Energy(eV)	15.76
Oxidation States	–
Electronegativity	–
Isotopes (Three Most Abundant)	40,36
Crystal Structure	FCC
Lattice Constant(s) (Å)	5.26
Cohesive Energy(eV/atom)	0.080
Mean Debye Temperature (K)	85

LT = Low Temperature Value

FCC - Face Centered Cubic	*a*	ORC - Orthorhombic	*a*/*b*/*c*
BCC - Body Centered Cubic	*a*	HEX - Hexagonal	*a*/*c*
SC - Simple Cubic	*a*	DIA - Diamond	*a*
CUB - Cubic	*a*	RHL - Rhombohedral	*a*/α
TET - Tetragonal	*a*/*c*	MCL - Monoclinic	*a*/*c*

1 *s* Block / 2 *s* Block

Group	Element	Electronic Orbital Structure	Filled Shell Configuration	Tetrahedral Covalent Bond	12-Coordinated Metal	Grüneisen Parameter	First Ionization Energy(eV)	Electronegativity	Crystal Structure	Cohesive Energy(eV/atom)	Oxidation States	Isotopes	Lattice Constant(s) (Å)	Mean Debye Temperature (K)
1	H	$1s^1$	2.08	–	–	–	13.595	2.20	HEX	–	1	1,2	3.75/6.49	110
1	Li	$[\mathrm{He}]2s^1$	0.68	–	1.56	1.06	5.39	0.98	BCC	1.63	1	7,6	3.49	400
1	Na	$[\mathrm{Ne}]3s^1$	0.97	–	1.91	1.49	5.14	0.93	BCC	1.113	1	23	4.23	150
1	K	$[\mathrm{Ar}]4s^1$	1.33	–	2.38	1.65	4.34	0.82	BCC	0.934	1	39,41	5.23	100
1	Rb	$[\mathrm{Kr}]5s^1$	1.48	–	2.55	–	4.18	0.82	BCC	0.852	1	85,87	5.59	56LT
1	Cs	$[\mathrm{Xe}]6s^1$	1.67	–	2.73	–	3.89	0.79	BCC	0.804	1	1.64×10^4	6.05	40LT
1	Fr	$[\mathrm{Rn}]7s^1$	1.75	–	–	–	–	0.70	(BCC)	–	1	–	–	–
2	Be	$[\mathrm{He}]2s^2$	0.35	1.06	1.13	1.28	9.32	1.57	HEX	3.32	2	9	2.29/3.59	1000
2	Mg	$[\mathrm{Ne}]3s^2$	0.65	1.40	1.60	1.71	7.64	1.31	HEX	1.51	2	24,26,25	3.21/5.21	318
2	Ca	$[\mathrm{Ar}]4s^2$	0.99	–	1.98	1.09	6.11	1.00	FCC	1.84	2	40,44,42	5.58	230
2	Sr	$[\mathrm{Kr}]5s^2$	1.13	–	2.15	–	5.69	0.95	FCC	1.72	2	88,86,87	6.08	147LT
2	Ba	$[\mathrm{Xe}]6s^2$	1.35	–	2.24	–	5.21	0.89	BCC	1.90	2	5.7×10^4	5.02	110LT
2	Ra	$[\mathrm{Rn}]7s^2$	1.37	–	–	–	5.28	0.90	BCC	1.66	2	226	–	–

3 4 5 6 7 8 9 *d* Block

Group	Element	Electronic Orbital Structure	Filled Shell Configuration	Tetrahedral Covalent Bond	12-Coordinated Metal	Grüneisen Parameter	First Ionization Energy(eV)	Electronegativity	Crystal Structure	Cohesive Energy(eV/atom)	Oxidation States	Isotopes	Lattice Constant(s) (Å)	Mean Debye Temperature (K)
3	Sc	$[\mathrm{Ar}]3d^14s^2$	0.81	–	1.64	–	6.56	1.36	HEX	3.90	3	45	3.31/5.28	359LT
3	Y	$[\mathrm{Kr}]4d^15s^2$	0.93	–	1.80	–	6.5	1.22	HEX	4.37	3	89	3.65/5.73	256LT
4	Ti	$[\mathrm{Ar}]3d^24s^2$	0.68	–	1.46	–	6.83	1.54	HEX	4.85	4	48,46,47	2.95/4.68	380
4	Zr	$[\mathrm{Kr}]4d^25s^2$	0.80	–	1.60	0.92	6.95	1.33	HEX	6.25	4	90,94,92	3.32/5.15	250
4	Hf	$[\mathrm{Xe}]4f^{14}5d^26s^2$	–	–	1.58	–	6.83	1.30	HEX	6.44	4	180,178,177	3.20/5.06	–
5	V	$[\mathrm{Ar}]3d^34s^2$	–	–	1.35	1.36	6.74	1.63	BCC	5.31	5,3	51,50	3.02	390
5	Nb	$[\mathrm{Kr}]4d^45s^1$	0.67	–	1.47	–	6.77	1.6	BCC	7.57	5,3	93	3.30	275
5	Ta	$[\mathrm{Xe}]4f^{14}5d^36s^2$	–	–	1.47	1.66	7.88	1.50	BCC	8.10	5	181,180	3.31	225
6	Cr	$[\mathrm{Ar}]3d^54s^1$	–	–	1.28	0.90	6.76	1.66	BCC	4.10	6,3,2	52,53,50	2.88	460
6	Mo	$[\mathrm{Kr}]4d^55s^1$	–	–	1.40	1.63	7.18	2.16	BCC	6.82	6,5,4,3,2	98,96,95	3.15	380
6	W	$[\mathrm{Xe}]4f^{14}5d^46s^2$	–	–	1.41	1.71	7.98	2.36	BCC	8.90	6,5,4,3,2	184,186,182	3.16	310
7	Mn	$[\mathrm{Ar}]3d^54s^2$	–	–	1.26	–	7.43	1.55	CUB	2.92	7,6,4,2,3	55	8.89	400
7	Tc	$[\mathrm{Kr}]4d^55s^2$	–	–	1.36	–	7.28	1.90	HEX	6.85	7	93	2.74/4.39	–
7	Re	$[\mathrm{Xe}]4f^{14}5d^56s^2$	–	–	1.38	–	7.87	1.90	HEX	8.03	7,6,4,2,-1	187,185	2.76/4.46	416LT
8	Fe	$[\mathrm{Ar}]3d^64s^2$	–	–	1.27	1.88	7.90	1.83	BCC	4.28	2,3	56,54,57	2.87	400
8	Ru	$[\mathrm{Kr}]4d^75s^1$	–	–	1.34	–	7.36	2.20	HEX	6.74	2,3,4,6,8	102,104,101	2.70/4.28	382LT
8	Os	$[\mathrm{Xe}]4f^{14}5d^66s^2$	–	–	1.35	–	8.7	2.20	HEX	8.17	2,3,4,6,8	192,190,189	2.74/4.33	400LT
9	Co	$[\mathrm{Ar}]3d^74s^2$	–	–	1.25	2.37	7.86	1.88	HEX	4.39	2,3,4	59	2.51/4.07	385
9	Rh	$[\mathrm{Kr}]4d^85s^1$	–	–	1.35	–	7.46	2.28	FCC	5.75	2,3,4	103	3.80	350LT
9	Ir	$[\mathrm{Xe}]4f^{14}5d^76s^2$	–	–	1.36	–	9.1	2.20	FCC	6.94	2,3,4,6	193,191	3.84	430

f Block

Series	Element	Electronic Orbital Structure	Filled Shell Configuration	Tetrahedral Covalent Bond	12-Coordinated Metal	Grüneisen Parameter	First Ionization Energy(eV)	Electronegativity	Crystal Structure	Cohesive Energy(eV/atom)	Oxidation States	Isotopes	Lattice Constant(s) (Å)	Mean Debye Temperature (K)
4*f*	La	$[\mathrm{Xe}]5d^16s^2$	1.15	–	1.88	–	5.77	1.10	HEX	4.47	3	138,139	3.75/6.07	132
4*f*	Ce	$[\mathrm{Xe}]4f^15d^16s^2$	1.10	1.71	1.82	–	5.54	1.12	FCC	4.32	3,4	140,142	5.16	139LT
4*f*	Pr	$[\mathrm{Xe}]4f^36s^2$	–	–	1.84	–	5.46	1.13	HEX	3.70	3,4	141	3.67/5.92	152LT
4*f*	Nd	$[\mathrm{Xe}]4f^46s^2$	–	–	1.82	–	5.53	1.14	HEX	3.40	3	142,143,146	3.66/5.91	157LT
4*f*	Pm	$[\mathrm{Xe}]4f^56s^2$	–	–	1.81	–	5.55	1.13	HEX	–	3	145	–	–
4*f*	Sm	$[\mathrm{Xe}]4f^66s^2$	–	–	1.80	–	5.64	1.17	RHL	2.14	3,2	152,154,147	9.00/23.1	166
5*f*	Ac	$[\mathrm{Rn}]6d^17s^2$	1.11	–	–	–	5.17	1.10	FCC	4.25	3	227	5.31	–
5*f*	Th	$[\mathrm{Rn}]6d^27s^2$	0.99	–	1.80	–	6.08	1.30	FCC	6.20	4	232	5.08	100
5*f*	Pa	$[\mathrm{Rn}]5f^26d^17s^2$	0.90	–	1.63	–	5.89	1.50	TET	–	5,4	231	3.92/3.23	–
5*f*	U	$[\mathrm{Rn}]5f^36d^17s^2$	0.83	–	1.56	–	6.19	1.38	ORC	5.55	6,5,4,3	238,235	2.85/5.86/4.95	210LT
5*f*	Np	$[\mathrm{Rn}]5f^46d^17s^2$	–	–	1.56	–	6.27	1.36	ORC	4.73	6,5,4,3	237	4.72/6.66/4.89	188LT
5*f*	Pu	$[\mathrm{Rn}]5f^67s^2$	–	1.58	1.64	–	6.06	1.28	MCL	3.60	6,5,4,3	244	–	150LT

d Block (10–12)

p Block (13–17)

18
p Block
(Except He: *s* Block)

10	**11**	**12**	**13**	**14**	**15**	**16**	**17**	**18**
								He – – – $1s^{2}$ – 24.58 – – 4 HEX 3.57/5.83 – 26LT
			B 0.23 0.88 0.98 $[He]2s^{2}2p^{1}$ – 8.30 3 2.04 11,10 TET 8.73/5.03 5.81 1250	C 0.15 0.77 0.92 $[He]2s^{2}2p^{2}$ 0.90 11.26 4,2 2.55 12,13 DIA 3.57 7.37 1860	N 1.71 0.70 – $[He]2s^{2}2p^{3}$ – 14.54 3,5,4,2,-3 3.04 14,15 HEX 4.04/6.67 4.92 79LT	O 1.40 0.66 – $[He]2s^{2}2p^{4}$ – 13.61 -2 3.44 16,18 CUB 6.83 2.60 46LT	F 1.36 0.64 – $[He]2s^{2}2p^{5}$ – 17.42 -1 3.98 19 MCL – 0.84 –	Ne 1.36 – – $[He]2s^{2}2p^{6}$ 2.76 21.56 – – 20,22,21 FCC 4.45 0.020 63
			Al 0.50 1.26 1.43 $[Ne]3s^{2}3p^{1}$ 2.41 5.98 3 1.61 27 FCC 4.05 3.39 394	Si 0.41 1.17 1.32 $[Ne]3s^{2}3p^{2}$ 0.44 8.15 4 1.90 28,29,30 DIA 5.43 4.63 645	P 2.12 1.10 – $[Ne]3s^{2}3p^{3}$ – 10.55 3,5,4,-3 2.19 31 CUB 7.17 3.43 –	S 1.84 1.04 – $[Ne]3s^{2}3p^{4}$ – 10.36 2,4,6,-2 2.58 32,34,33 ORC 10.47/24.49/12.87 2.85 –	Cl 1.81 0.99 – $[Ne]3s^{2}3p^{5}$ – 13.01 1,3,5,7,-1 3.16 35,37 ORC 6.24/8.26/4.48 1.40 –	Ar 1.88 – – $[Ne]3s^{2}3p^{6}$ 2.73 15.76 – – 40,36 FCC 5.26 0.080 85
Ni – – 1.25 $[Ar]3d^{8}4s^{2}$ 2.11 7.63 2,3 1.91 58,60,62 FCC 3.52 4.44 375	Cu – 1.35 1.28 $[Ar]3d^{10}4s^{1}$ 2.14 7.72 2,1 1.90 63,65 FCC 3.61 3.49 315	Zn 0.74 1.31 1.39 $[Ar]3d^{10}4s^{2}$ 2.75 9.39 2 1.65 64,66,68 HEX 2.66/4.94 1.35 234	Ga 0.62 1.26 1.41 $[Ar]3d^{10}4s^{2}4p^{1}$ 6.00 3 1.81 69,71 ORC 4.51/7.64/4.51 2.81 240	Ge 0.53 1.22 1.37 $[Ar]3d^{10}4s^{2}4p^{2}$ 0.77 7.88 4 2.01 74,72,70 DIA 5.86 3.85 360	As 2.22 1.18 1.39 $[Ar]3d^{10}4s^{2}4p^{3}$ – 9.81 3,5,-3 2.18 75 RHL 4.16/54.2 2.96 285	Se 1.98 1.14 – $[Ar]3d^{10}4s^{2}4p^{4}$ – 9.75 2,4,6,-2 2.55 80,78,76 HEX 4.36/4.95 2.46 150LT	Br 1.95 1.11 – $[Ar]3d^{10}4s^{2}4p^{5}$ – 11.84 1,5,-1 2.96 79,81 ORC 6.67/8.72/4.48 1.22 –	Kr 2.00 – – $[Ar]3d^{10}4s^{2}4p^{6}$ 2.84 14.00 – 3.00 84,86,82 FCC 5.72 0.116 73LT
Pd – – 1.38 $[Kr]4d^{10}$ 2.47 8.33 2,4 2.20 106,108,105 FCC 3.89 3.89 275	Ag 1.26 1.52 1.45 $[Kr]4d^{10}5s^{1}$ 2.65 7.57 1 1.93 107,109 FCC 4.09 2.95 215	Cd 0.97 1.48 1.57 $[Kr]4d^{10}5s^{2}$ 3.09 8.99 2 1.69 114,112,111 HEX 2.98/5.62 1.16 120	In 0.81 1.44 1.66 $[Kr]4d^{10}5s^{2}5p^{1}$ 2.75 5.78 3 1.78 115,113 TET 4.59/4.94 2.52 129	Sn 0.71 1.40 1.55 $[Kr]4d^{10}5s^{2}5p^{2}$ – 7.34 4,2 1.96 120,118,116 TET 5.82/3.18 3.14 170	Sb 2.45 1.36 1.59 $[Kr]4d^{10}5s^{2}5p^{3}$ – 8.64 3,5,-3 2.05 121,123 RHL 4.51/57.1 2.75 200	Te 2.21 1.32 – $[Kr]4d^{10}5s^{2}5p^{4}$ – 9.01 2,4,6,-2 2.10 130,128,126 HEX 4.45/5.92 2.19 139LT	I 2.16 1.28 – $[Kr]4d^{10}5s^{2}5p^{5}$ – 10.45 1,5,7,-1 2.66 127 ORC 7.27/9.79/4.79 1.11 –	Xe 2.17 – – $[Kr]4d^{10}5s^{2}5p^{6}$ 2.65 12.13 – 2.60 132,129,131 FCC 6.20 0.16 55LT
Pt – – 1.39 $[Xe]4f^{14}5d^{9}6s^{1}$ 2.89 8.96 2,4 2.28 195,194,196 FCC 3.92 5.84 230	Au 1.37 – 1.44 $[Xe]4f^{14}5d^{10}6s^{1}$ 3.17 9.22 3,1 2.54 197 FCC 4.08 3.81 170	Hg 1.10 1.48 1.57 – $[Xe]4f^{14}5d^{10}6s^{2}$ 10.43 2,1 2.00 202,200,199 RHL 2.99/70.8 0.67 100	Tl 0.95 – 1.72 2.36 $[Xe]4f^{14}5d^{10}6s^{2}6p^{1}$ 6.11 3,1 1.62 205,203 HEX 3.46/5.53 1.88 96	Pb 0.84 – 1.75 3.06 $[Xe]4f^{14}5d^{10}6s^{2}6p^{2}$ 7.41 4,2 2.33 208,206,207 FCC 4.95 2.03 88	Bi – – 1.70 – $[Xe]4f^{14}5d^{10}6s^{2}6p^{3}$ 7.29 3,5 2.02 209 RHL 4.75/57.2 2.18 120	Po – – 1.76 – $[Xe]4f^{14}5d^{10}6s^{2}6p^{4}$ 8.43 4,2 2.00 210 SC 3.35 1.50 –	At – – – – $[Xe]4f^{14}5d^{10}6s^{2}6p^{5}$ – 1,3,5,7,-1 2.20 210 – – – –	Rn – – – – $[Xe]4f^{14}5d^{10}6s^{2}6p^{6}$ 10.74 – – 222 (FCC) – 0.202 –

f Block

Eu – 2.04 1.80 $[Xe]4f^{7}6s^{2}$ – 5.67 3,2 1.20 153,151 BCC 4.61 1.86 107LT	Gd – – 1.80 $[Xe]4f^{7}5d^{1}6s^{2}$ – 6.16 3 1.20 158,160,156 HEX 3.64/5.78 4.14 176LT	Tb – – 1.78 – $[Xe]4f^{9}6s^{2}$ 5.86 3,4 1.10 159 HEX 3.60/5.69 4.05 188LT	Dy – – 1.77 $[Xe]4f^{10}6s^{2}$ – 5.94 3 1.22 164,162,163 HEX 3.59/5.65 3.04 186LT	Ho – – 1.77 $[Xe]4f^{11}6s^{2}$ – 6.02 3 1.23 165 HEX 3.58/5.62 3.14 191LT	Er – – 1.76 $[Xe]4f^{12}6s^{2}$ – 6.11 3 1.24 166,168,167 HEX 3.56/5.59 3.29 195LT	Tm – – 1.75 $[Xe]4f^{13}6s^{2}$ – 6.18 3,2 1.25 169 HEX 3.54/5.56 2.42 200LT	Yb – 1.94 1.81 $[Xe]4f^{14}6s^{2}$ – 6.25 3,2 1.10 174,172,173 FCC 5.49 1.60 118LT	Lu – – – – $[Xe]4f^{14}5d^{1}6s^{2}$ 5.43 3 1.27 175,176 HEX 3.51/5.56 4.43 207LT
Am – – 1.81 – $[Rn]5f^{7}7s^{2}$ 5.99 6,5,4,3 1.13 243 HEX – 2.73 –	Cm – – – – $[Rn]5f^{7}6d^{1}7s^{2}$ 6.02 3 1.28 247 HEX – 3.99	Bk – – – – $[Rn]5f^{9}7s^{2}$ 6.23 4,3 1.30 247 HEX – – –	Cf – – – – $[Rn]5f^{10}7s^{2}$ 6.30 3 1.30 251 HEX – – –	Es – – – – $[Rn]5f^{11}7s^{2}$ 6.42 3 1.30 254 HEX – – –	Fm – – – – $[Rn]5f^{12}7s^{2}$ 6.50 3 1.30 257 – – – –	Md – – – – $[Rn]5f^{13}7s^{2}$ 6.58 3,2 1.30 256 – – – –	No – – – – $[Rn]5f^{14}7s^{2}$ 6.65 3,2 1.30 254 – – – –	Lr – – – – $[Rn]5f^{14}6d^{1}7s^{2}$ – 3 – 257 – – – –

A.3 Fundamental Constants

Table A.3. *Fundamental constants, derived quantities, and units conversions [282, 283].*

Symbol	Magnitude and Units
Fundamental constants:	
c_o	speed of light in vacuum, 2.99792458×10^{8} m/s
e_c	electron charge, 1.602×10^{-19} C (1 eV $= 1.602 \times 10^{-19}$ J, where V = J/C)
G_N	Newton (gravitational) constant, 6.673×10^{-11} m^3/kg-s^2
h_P	Planck constant, 6.626×10^{-34} J-s $= 4.136 \times 10^{-15}$ eV-s
$\hbar$	$h_P/2\pi = 1.055 \times 10^{-34}$ J-s $= 6.583 \times 10^{-16}$ eV-s
k_B	Boltzmann constant, 1.381×10^{-23} J/K $= 8.618 \times 10^{-5}$ eV/K
m_e	electron mass, 9.109×10^{-31} kg
m_n	neutron mass, 1.675×10^{-27} kg = 1.675 yg
m_p	proton mass, 1.673×10^{-27} kg = 1.673 yg
N_A	Avogadro number, 6.022×10^{23} molecule/mole $= 6.022 \times 10^{26}$ molecule/kmole
μ_o	free-space magnetic permeability, $4\pi \times 10^{-7} = 1.257 \times 10^{-6}$ N-s^2/C^2

Derived quantities:

$\epsilon_o = \dfrac{1}{c_o^2\mu_o} = 8.854 \times 10^{-12}$ C^2/N-m^2	free-space electric permittivity
D $= e_c r_B/2.54 = 3.3356 \times 10^{-30}$ C-m	Debye (atomic dielectric dipole moment)
$N_{L,o} = \dfrac{\pi^2}{3}\dfrac{k_B T^2}{e_c^2} = 2.442 \times 10^{-8}$ W-Ω/K^2	Lorenz number
$r_C = \dfrac{e_c^2}{4\pi\epsilon_o m_e c_o^2} = 2.8179 \times 10^{-15}$ m	classical (Compton) electron radius
$r_B = \dfrac{4\pi\epsilon_o\hbar^2}{m_e e_c^2} = 5.292 \times 10^{-11}$ m	Bohr radius (atomic length unit)
$\dfrac{e_c^2}{4\pi\epsilon_o r_B} = 27.2114$ eV $= 4.35975 \times 10^{-18}$ J	hartree (atomic energy unit)
$\dfrac{e_c^2}{4\pi\epsilon_o r_B^2} = 8.2378 \times 10^{-8}$ N	atomic force unit
$R_g \equiv k_B N_A = 8.3145 \times 10^{3}$ J/kmole-K	universal gas constant
Ry $= \dfrac{m_e e_c^4}{8\epsilon_o^2 c_o \hbar^3} = 13.606$ eV $= 1.0974 \times 10^{5}$ cm^{-1}	Rydberg ground-state energy of H
$\dfrac{1}{4\pi\epsilon_o} = 8.9876 \times 10^{9}$, Nm^2/C^2	Coulomb constant
$\alpha = \dfrac{e_c^2}{4\pi\epsilon_o\hbar c_o} = 7.29735 \times 10^{-3}$	fine-structure constant
$\sigma_{SB} \equiv \dfrac{\pi^2 k_B^4}{60\hbar^3 c_o^2} = 5.670 \times 10^{-8}$ W/m^2-K^4	Stefan–Boltzmann constant

Units conversions:

1 eV $= 8.0655 \times 10^{3}$ cm^{-1} $= 2.418 \times 10^{14}$ Hz = 11,600 K $= 1.602 \times 10^{-19}$ J = 96.485 kJ/mole

1 cm^{-1} = 0.12398 meV $= 2.998 \times 10^{10}$ Hz

1 Trad/s = 0.6582 meV = 5.309 cm^{-1}

A.4 Unit Prefixes

Table A.4. *Unit prefixes.*

Factor	Prefix	Symbol	Factor	Prefix	Symbol
10^{24}	yotta	Y	10^{-24}	yocto	y
10^{21}	zetta	Z	10^{-21}	zepto	z
10^{18}	exa	E	10^{-18}	atto	a
10^{15}	peta	P	10^{-15}	femto	f
10^{12}	tera	T	10^{-12}	pico	p
10^{9}	giga	G	10^{-9}	nano	n
10^{6}	mega	M	10^{-6}	micro	μ
10^{3}	kilo	k	10^{-3}	milli	m
10^{2}	hecto	h	10^{-2}	centi	c
10^{1}	deka	da	10^{-1}	deci	d

One angstrom is $1\ \text{Å} = 10^{-10}$ m

APPENDIX B

Derivation of Green–Kubo Relation

The Green–Kubo (G–K) development of a time-correlation function expression for the thermal conductivity (the G–K approach) is based in equilibrium classical statistical thermodynamics. Multiple methods can be used to arrive at the final result [517]. Similar approaches can be used to develop expressions for the self-diffusion coefficient, the shear viscosity, and the bulk viscosity. These are all transport coefficients that cannot be obtained by applying a perturbation to the system Hamiltonian, as can be done for some other properties (e.g., the electrical conductivity) for which there is a force that drives the transport. Here, the method of Helfand [187] (applied to mass diffusivity, viscosity, and thermal conductivity) as outlined in [323], is presented step-by-step [315].

B.1 Perturbation Energy Equation and Fourier Transform

The G–K approach is valid in the case of small disturbances from equilibrium and for long times (i.e., the hydrodynamic limit). The key aspect of the derivation is the introduction of a microscopic description of a system to the solution of the macroscopic governing equation.

For the thermal conductivity, a canonical ensemble of particles (i.e., the NVT ensemble) is considered, and the average energy equation (the macroscopic energy equation of Table 1.1, for no net flow $\boldsymbol{u} = 0$, and no radiation heat transfer, with conduction heat flux given by the Fourier law, and using the thermal conductivity tensor $\boldsymbol{K}$) is written for derivation component of energy as

$$nc_v \frac{\partial E'(\boldsymbol{x}, t)}{\partial t} = \nabla \cdot \boldsymbol{K} \cdot \nabla E'(\boldsymbol{x}, t), \tag{B.1}$$

where n is the number of particles per unit volume and c_v is the specific heat per particle.

Here the independent variable $E'(\boldsymbol{x}, t)$ is the deviation (excess) of the energy from its expectation value at position $\boldsymbol{x}$ at time t,

$$E'_i(\boldsymbol{x}, t) = E_i(\boldsymbol{x}, t) - \langle E_i(\boldsymbol{x}, t)\rangle, \qquad E' = \langle E'_i \rangle, \tag{B.2}$$

where $E_i(\boldsymbol{x}, t)$ is the actual energy of particle i at that point and $\langle E(\boldsymbol{x}, t)\rangle$ is its expectation value. The total energy has kinetic and potential energies as $E_i = p_i^2/2m + 1/2\sum_{j\neq i}\varphi_{i\text{-}j}$. The heat flux vector due to conduction is $\boldsymbol{q}_k = \text{-}\nabla \cdot \boldsymbol{K} \cdot \nabla E'/c_v$. There is an initial condition $E'(\boldsymbol{x}, 0)$. The specific heat has units of J/K (i.e., $c_v \propto k_\mathrm{B}$) – particle, and is the number of particles per unit volume. Later (Section B.3) we will show that the heat current is related to the time derivative of the particle j energy E'_j times the particle position $\boldsymbol{x}_j$.

Define the Fourier transform of $E'(\boldsymbol{x}, t)$ as $L(\boldsymbol{\kappa}, t)$, such that

$$L(\boldsymbol{\kappa}, t) = \int \exp(i\boldsymbol{\kappa} \cdot \boldsymbol{x})E'(\boldsymbol{x}, t)\mathrm{d}\boldsymbol{x}. \tag{B.3}$$

Substituting this expression into the energy equation leads to

$$\frac{\mathrm{d}L(\boldsymbol{\kappa}, t)}{\mathrm{d}t} = -\frac{\kappa^2 k}{nc_v}L(\boldsymbol{\kappa}, t), \tag{B.4}$$

with initial condition $L(\boldsymbol{\kappa}, 0)$, which has a solution

$$L(\boldsymbol{\kappa}, t) = L(\boldsymbol{\kappa}, 0)\exp(-\frac{\kappa^2 kt}{nc_v}). \tag{B.5}$$

On a microscopic level, the system energy can be defined on a particle basis as

$$E'(\boldsymbol{x}, t) = \sum_j E'_j(t)\delta[\boldsymbol{x} - \boldsymbol{x}_j(t)], \tag{B.6}$$

where $E'_j(t)$ and $\boldsymbol{x}_j(t)$ are energy and position of particle j, and the sum is over the N particles in the system. The Fourier transform of (B.6) is

$$L(\boldsymbol{\kappa}, t) = \int \sum_j E'_j(t)\delta[\boldsymbol{x} - \boldsymbol{x}_j(t)]\exp(i\boldsymbol{\kappa} \cdot \boldsymbol{x})\mathrm{d}\boldsymbol{x} = \sum_j E'_j(t)\exp[i\boldsymbol{\kappa} \cdot \boldsymbol{x}_j(t)]. \tag{B.7}$$

Multiplying both sides of (B.5) by $L^*(\boldsymbol{\kappa}, 0)$, the complex conjugate of the initial condition, and using (B.7) gives

$$\begin{aligned}&\sum_j E'_j(t)\exp[i\boldsymbol{\kappa} \cdot \boldsymbol{x}_j(t)]\sum_l E'_l(0)\exp[-i\boldsymbol{\kappa} \cdot \boldsymbol{x}_l(0)]\\ &= \{\sum_j E'_j(0)\exp[i\boldsymbol{\kappa} \cdot \boldsymbol{x}_j(0)]\sum_l E'_l(0)\exp[-i\boldsymbol{\kappa} \cdot \boldsymbol{x}_l(0)]\}\exp(-\frac{k\kappa^2 t}{nc_v}).\end{aligned} \tag{B.8}$$

Noting that $\sum_j a_j \sum_l b_l = \sum_j \sum_l a_j b_l$, and taking the ensemble average of both sides, we have

$$\begin{aligned}&\langle\sum_j\sum_l E'_j(t)E'_l(0)\exp\{i\boldsymbol{\kappa} \cdot [\boldsymbol{x}_j(t) - \boldsymbol{x}_l(0)]\}\rangle\\ &= \langle\sum_j\sum_l E'_j(0)E'_l(0)\exp\{i\boldsymbol{\kappa} \cdot [\boldsymbol{x}_j(0) - \boldsymbol{x}_l(0)]\}\rangle\exp(-\frac{k\kappa^2 t}{nc_v}).\end{aligned} \tag{B.9}$$

B.2 Taylor Series Expansion and Ensemble Averaging

An expression for the thermal conductivity is found by expanding both sides of this equation as a Taylor series about $\kappa = 0$ and comparing the coefficients with second order. This procedure is justified by the assumption of small perturbations from equilibrium.

Without losing any generality, the remainder of the derivation is simplified by taking $\boldsymbol{\kappa}$ to be in the x direction [i.e., $\boldsymbol{\kappa} = (\kappa, 0, 0)$]. Consider the left-hand side of (B.9), expanded to second order in κ, with the derivatives evaluated at $\kappa = 0$:

$$\begin{aligned}&\langle\sum_j\sum_l E'_j(t)E'_l(0)\rangle + \kappa\langle\sum_j\sum_l E'_j(t)E'_l(0)i[x_j(t) - x_l(0)]\rangle\\ &+\frac{\kappa^2}{2}\langle\sum_j\sum_l E'_j(t)E'_l(0)i^2[x_j(t) - x_l(0)]^2\rangle.\end{aligned} \tag{B.10}$$

Before proceeding, a number of useful expressions related to the summations and ensemble averages to be evaluated are introduced. First, by conservation of energy,

$$\sum_j E'_j(0) = \sum_l E'_l(t). \tag{B.11}$$

This expression indicates that, although energy is exchanged between the particles, the total value is a constant. Second, the stationary condition for an equilibrium ensemble average states that, for some quantity $\phi(t)$ based on the particle positions and momenta, that

$$\langle\phi(t)\rangle = \langle\phi(0)\rangle. \tag{B.12}$$

Now, consider (B.10) term by term. The first term becomes

$$\begin{aligned}\langle\sum_j\sum_l E'_j(t)E'_l(0)\rangle &= \langle\sum_j E'_j(t)\sum_l E'_l(0)\rangle\\ &= \langle\sum_j E'_j(0)\sum_l E'_l(0)\rangle = \langle\sum_j\sum_l E'_j(0)E'_l(0)\rangle.\end{aligned} \tag{B.13}$$

Using the definition of the energy deviation, and dropping the time label, we have

$$\begin{aligned}\langle\sum_j\sum_l E'_j(t)E'_l(0)\rangle &= \langle\sum_j\sum_l(E_j - \langle E_j\rangle)(E_l - \langle E_l\rangle)\rangle\\ &= \langle\sum_j\sum_l(E_jE_l - E_j\langle E_j\rangle - E_l\langle E_j\rangle + \langle E_j\rangle\langle E_l\rangle)\rangle\\ &= \langle\xi^2 - 2\xi\langle\xi\rangle + \langle\xi\rangle^2\rangle = \langle(\xi - \langle\xi\rangle)^2\rangle = Nk_\mathrm{B}T^2c_v,\end{aligned} \tag{B.14}$$

where ξ represents the total energy in the system [i.e., $\xi = \int E(\boldsymbol{x}, t)\mathrm{d}\boldsymbol{x}$] and $N = nV$ is the number of atoms in the system, where V is the volume of the system. The last step comes from the thermodynamic definition of temperature in the thermal fluctuation and canonical ensemble. (Table 2.4, where c_v contains all the degrees of freedom in atomic motion)

For the first term in (B.10),

$$\begin{aligned}
& i\kappa\langle\sum_j\sum_l E'_j(t)E'_l(0)[x_j(t)-x_l(0)]\rangle \\
&= i\kappa\langle\sum_j\sum_l E'_j(t)E'_l(0)x_j(t)\rangle - i\kappa\langle\sum_j\sum_l E'_j(t)E'_l(0)x_l(0)\rangle \\
&= i\kappa\langle\sum_j E'_j(t)x_j(t)\sum_l E'_l(0)\rangle - i\kappa\langle\sum_j E'_j(t)\sum_l E'_l(0)x_l(0)\rangle \\
&= i\kappa\langle\sum_j E'_j(t)x_j(t)\sum_l E'_l(t)\rangle - i\kappa\langle\sum_j E'_j(0)\sum_l E'_l(0)x_l(0)\rangle \\
&= \kappa\langle\sum_j\sum_l E'_j(t)E'_l(t)x_j(t)\rangle - i\kappa\langle\sum_j\sum_l E'_j(0)E'_l(0)x_l(0)\rangle \\
&= i\kappa\langle\sum_j\sum_l E'_j(0)E'_l(0)x_j(0)\rangle - i\kappa\langle\sum_j\sum_l E'_j(0)E'_l(0)x_l(0)\rangle \\
&= 0.
\end{aligned} \tag{B.15}$$

For the ensemble average in the second-order term,

$$\begin{aligned}
& \langle\sum_j\sum_l E'_j(t)E'_l(0)[x_j(t)-x_l(0)]^2\rangle \\
&= \langle\sum_j\sum_l E'_j(t)E'_l(0)[x_j(t)]^2\rangle - 2\langle\sum_j\sum_l E'_j(t)E'_l(0)x_j(t)x_l(0)\rangle \\
&\quad + \langle\sum_j\sum_l E'_j(t)E'_l(0)[x_l(0)]^2\rangle \\
&= \langle\sum_j E'_j(t)[x_j(t)]^2\sum_l E'_l(0)\rangle - 2\langle\sum_j E'_j(t)x_j(t)\sum_l E'_l(0)x_l(0)\rangle \\
&\quad + \langle\sum_j E'_j(t)\sum_l E'_l(0)[x_l(0)]^2\rangle \\
&= \langle\sum_j E'_j(t)[x_j(t)]^2\sum_l E'_l(t)\rangle - 2\langle\sum_j E'_j(t)x_j(t)\sum_l E'_l(0)x_l(0)\rangle \\
&\quad + \langle\sum_j E'_j(0)\sum_l E'_l(0)[x_l(0)]^2\rangle \\
&= \langle\sum_j\sum_l E'_j(t)E'_l(t)[x_j(t)]^2\rangle - 2\langle\sum_j E'_j(t)x_j(t)\sum_l E'_l(0)x_l(0)\rangle \\
&\quad + \langle\sum_j\sum_l E'_j(0)E'_l(0)[x_l(0)]^2\rangle.
\end{aligned} \tag{B.16}$$

If there is no correlation between the positions and energies of the particles, then

$$\begin{aligned}\langle\sum_j\sum_l E'_j(t)E'_l(t)[x_j(t)]^2\rangle &= \langle\sum_j[x_j(t)]^2[E_j(t)]^2\rangle\\ &= \langle\sum_j E'_j(t)x_j(t)\sum_l E'_l(t)x_l(t)\rangle,\end{aligned} \tag{B.17}$$

so that the second-order term becomes

$$\begin{aligned}&-\frac{\kappa^2}{2}[\langle\sum_j E'_j(t)x_j(t)\sum_l E'_l(t)x_l(t)\rangle - 2\langle\sum_j E'_j(t)x_j(t)\sum_l E'_l(0)x_l(0)\rangle\\ &+\langle\sum_j E'_j(0)x_j(0)\sum_l E'_l(0)x_l(0)\rangle]\\ &= -\frac{\kappa^2}{2}\langle\{\sum_j[x_j(t)E'_j(t) - x_j(0)E'_j(0)]\}^2\rangle.\end{aligned} \tag{B.18}$$

The left-hand side of (B.9) is then

$$Nk_\mathrm{B}T^2c_v - \frac{\kappa^2}{2}\langle\{\sum_j[x_j(t)E'_j(t) - x_j(0)E'_j(0)]\}^2\rangle. \tag{B.19}$$

Now consider the right-hand side of (B.9) expanded term by term about $\kappa = 0$. The zeroth-order term is

$$\langle\sum_j\sum_l E'_j(0)E'_l(0)\rangle, \tag{B.20}$$

which is of the same form as the first term on the left-hand side, and thus equal to $Nk_\mathrm{B}T^2c_v$.

Now, we consider the energy equation (B.1), and will the thermal conductivity. Let the ensemble average on the right-hand side of (B.9) be represented by A and the exponential by B. For the first-order term, the derivative

$$\frac{\partial}{\partial\kappa}(AB) = A\frac{\partial A}{\partial\kappa} + B\frac{\partial B}{\partial\kappa}, \tag{B.21}$$

is required. Letting $C = k_x t/nc_v$ (where k_x is the thermal conductivity in the x-direction), the required derivative is

$$-2AC\kappa\exp(-C\kappa^2) + \exp(-C\kappa^2)\frac{\partial A}{\partial\kappa}. \tag{B.22}$$

For $\kappa = 0$, this expression reduces to $\partial A/\partial\kappa$, so that the first-order term is

$$i\kappa\langle\sum_j\sum_l E'_j(0)E'_l(0)[x_j(0) - x_l(0)]\rangle. \tag{B.23}$$

This term can be evaluated in the same manner as the first-order expansion of the left-hand side, and is equal to zero [see (B.15)].

For the second-order term, the derivative

$$\frac{\partial^2}{\partial \kappa^2}(AB) = A\frac{\partial^2 B}{\partial \kappa^2} + 2\frac{\partial A}{\partial \kappa}\frac{\partial B}{\partial \kappa} + B\frac{\partial^2 A}{\partial \kappa^2}, \tag{B.24}$$

is required. As discussed for the first-order term, the derivative of the exponential goes to zero at $\kappa = 0$, so that the middle term above is zero. For the first term,

$$\begin{aligned} A\frac{\partial^2}{\partial \kappa^2}\exp(-C\kappa^2) &= A\frac{\partial}{\partial \kappa}[-2C\kappa\exp(-C\kappa^2)] \\ &= A[4C^2\kappa^2\exp(-C\kappa^2) - 2C\exp(-C\kappa^2)], \end{aligned} \tag{B.25}$$

which, when evaluated at $\kappa = 0$, gives $2AC$, or

$$2\langle\sum_j\sum_l E'_j(0)E'_l(0)\rangle\frac{k_x t}{nc_v} = \frac{2Nk_{\mathrm{B}}T^2k_x t}{n}. \tag{B.26}$$

Note that $N/n = V$. For the last term in the second order derivative, noting that the exponential goes to unity at $\kappa = 0$,

$$\langle\sum_j\sum_l E'_j(0)E'_l(0)[x_j(0) - x_l(0)]^2\rangle. \tag{B.27}$$

Using the steps shown in (B.16) to (B.18), this term is found to be equal to zero. Multiplying the final result of (B.26) by $-\kappa^2/2$, the second-order term is thus

$$-Vk_{\mathrm{B}}T^2k_x\kappa^2 t, \tag{B.28}$$

and the expansion of the right-hand side of (B.9) is

$$Nk_{\mathrm{B}}T^2c_v - Vk_{\mathrm{B}}T^2k_x\kappa^2 t. \tag{B.29}$$

B.3 Thermal Conductivity Tensor

When the expansions of the two sides of (B.9), (B.19), and (B.29) are brought together, the zeroth-order terms are seen to be equal. Equating the coefficients of the second-order terms and solving for k_x (related to atomic motion in solid or fluid state) gives

$$k_x = \frac{1}{2k_{\mathrm{B}}T^2Vt}\langle\{\sum_j[E'_j(t)x_j(t) - E'_j(0)x_j(0)]\}^2\rangle. \tag{B.30}$$

The final step in the derivation is to transform the ensemble average/summation in (B.30) into the integral of a time correlation function. First, note that

$$\sum_j[E'_j(t)x_j(t) - E'_j(0)x_j(0)] = \int_0^t \frac{\mathrm{d}}{\mathrm{d}t}\sum_j[E'_j(t_1)x_j(t_1)]\mathrm{d}t_1. \tag{B.31}$$

This is done by noting that on the left-hand side the integral of the integrands are evaluated at $t = 0$ and $t = \infty$, so they can be written as time derivatives of an integral. Then because the integration, summation, and differentiation are linear, their order can be changed.

Defining the heat current in the x direction $\dot{w}_x$ as

$$\dot{w}_x(t) \equiv \frac{\mathrm{d}}{\mathrm{d}t}\sum_j [E'_j(t)x_j(t)], \tag{B.32}$$

the ensemble average in (B.30) can be written as

$$\begin{aligned}\langle\{\sum_j [E'_j(t)x_j(t) - E'_j(0)x_j(0)]\}^2\rangle &= \langle\int_0^t \dot{w}_x(t_1)\mathrm{d}t_1 \int_0^t \dot{w}_x(t_2)\mathrm{d}t_2\rangle \\ &= \langle\int_0^t \int_0^t \dot{w}_x(t_1)\dot{w}_x(t_2)\mathrm{d}t_1\mathrm{d}t_2\rangle \\ &= \int_0^t \int_0^t \langle\dot{w}_x(t_1)\dot{w}_x(t_2)\rangle\mathrm{d}t_1\mathrm{d}t_2 \\ &= \int_0^t \int_0^t \langle\dot{w}_x(t_2 - t_1)\dot{w}_x(0)\rangle\mathrm{d}t_1\mathrm{d}t_2,\end{aligned} \tag{B.33}$$

where the last step results from the stationary nature of the equilibrium ensemble $\langle\quad\rangle^\circ$. Using the identity

$$\int_0^t \int_0^t f(t_2 - t_1)\mathrm{d}t_1\mathrm{d}t_2 \equiv 2t\int_0^t (1 - \frac{\tau}{t})f(\tau)\mathrm{d}\tau, \tag{B.34}$$

leads to

$$k_x = \frac{2}{2Vk_\mathrm{B}T^2}\int_0^t (1 - \frac{\tau}{t})\langle\dot{w}_x(\tau)\dot{w}_x(0)\rangle^\circ\mathrm{d}\tau. \tag{B.35}$$

As t can be chosen to be arbitrarily large, τ/t in the integral can be ignored, and the thermal conductivity in the x direction can be written as

$$k_x = \frac{1}{k_\mathrm{B}T^2V}\int_0^\infty \langle\dot{w}_x(t)\dot{w}_x(0)\rangle^\circ\mathrm{d}t. \tag{B.36}$$

To generalize the results, the heat current is expressed as a vectorial flux, i.e.,

$$\dot{\boldsymbol{w}} = \frac{\mathrm{d}}{\mathrm{d}t}\sum_j [E'_j(t)\boldsymbol{x}_j(t)] = \frac{\mathrm{d}}{\mathrm{d}t}\sum_j E_j\boldsymbol{x}_j, \quad \boldsymbol{q} = \frac{\dot{\boldsymbol{w}}}{V}, \tag{B.37}$$

Since $\langle E_j\rangle$ is constant j, giving the thermal conductivity tensor

$$\boldsymbol{K} = \frac{1}{k_\mathrm{B}T^2V}\int_0^\infty \langle\dot{\boldsymbol{w}}(t)\dot{\boldsymbol{w}}(0)\rangle^\circ\mathrm{d}t = \frac{V}{k_\mathrm{B}T^2}\int_0^\infty \boldsymbol{q}(t)\boldsymbol{q}(0)\mathrm{d}t. \tag{B.38}$$

In a system with cubic isotropy, the scalar conductivity is given by

$$k = \frac{V}{k_\mathrm{B}T^2}\int_0^\infty \frac{\langle\boldsymbol{q}(t)\cdot\boldsymbol{q}(0)\rangle^\circ}{3}\mathrm{d}t \quad \text{G–K relation for thermal conductivity.} \tag{B.39}$$

For a two-body potential, the heat current vector can be expressed as

$$\boldsymbol{q} = \frac{1}{V}[\sum_i E_i\boldsymbol{u}_i + \frac{1}{2}\sum_{i,j}(\boldsymbol{F}_{ij}\cdot\boldsymbol{u}_i)\boldsymbol{x}_{ij}] \quad \text{heat current vector,} \tag{B.40}$$

a form readily implemented in MD simulation.

B.4 Physical Interpretation of Heat Current Vector Autocorrelation

Autocorrelation is a measure of how a signature of a dynamic system matches a time-shifted version of itself (i.e., cross correlation of a signature or signal with itself). Developing a physical interpretation of the final result is useful. The argument of the derivative of the heat current can be taken as the energy center of mass of the system. It is a vector that indicates the direction of energy transfer in the system at an instant in time. How long this quantity stays correlated with itself is related to the thermal conductivity. In a material with a high thermal conductivity, the correlation will be long lasting. This can be alternatively stated as a system in which fluctuations from equilibrium dissipate slowly. For a material with a low thermal conductivity, the correlation will be short-lived. One interesting aspect of the G–K approach is that transport properties can be obtained from an equilibrium system. This is an important point for the thermal conductivity, as it is generally thought of in a nonequilibrium system with a temperature gradient. The G–K approach is a real-space formulation, unlike the $\boldsymbol{\kappa}$-space- or $\boldsymbol{p}$-space-based BTE.

APPENDIX C

Derivation of Minimum Phonon Conductivity Relations

C.1 Einstein Thermal Conductivity

The derivation presented in this section and the next is based on that given in [126, 69], with some of the mathematical steps given in more detail. The formulation of the Einstein thermal conductivity, k_E, presented here is that given in [315], which is extended to arrive at the C–P high scatter limit, k_CP, in Section C.2.

In the Einstein approach, the vibrational states do not correspond to phonons, but to the atoms themselves, which are assumed to be on a simple cubic lattice as shown in Figure C.1. As will be discussed, the choice of the crystal structure does not affect the final result. Each atom is treated as a set of three harmonic oscillators in mutually perpendicular directions. Although the atomic motions are taken to be independent, an atom is assumed to exchange energy with its first, second, and third nearest neighbors. The coupling is realized by modeling the atomic interactions as being a result of linear springs (with spring constant Γ) connecting the atoms. A given atom has 6 nearest neighbors at a distance of a, 12 second-nearest neighbors at a distance of $2^{1/2}a$, and 8 third-nearest neighbors at a distance of $3^{1/2}a$.

C.1.1 Conductivity Relation

The derivation starts from the equation written in terms of the mean free path (4.109) ($k_p = nc_{v,p}u_{p,A}\lambda_p/3$). All the vibrational states are assumed to have the same angular frequency of oscillation, ω_E, which leads to a per particle specific heat of from (4.55), as

$$c_{v,p} = 3k_\mathrm{B}\frac{x_\mathrm{E}^2 e^{x_\mathrm{E}}}{(e^{x_\mathrm{E}}-1)^2}, \tag{C.1}$$

where x is defined as $\hbar\omega_\mathrm{E}/k_\mathrm{B}T \equiv T_\mathrm{E}/T$. The mean free path is taken as the distance between first nearest-neighbor atoms ($a = n^{-1/3}$), and the velocity is taken as $a/\tau_{p,\mathrm{E}}$ ($= n^{-1/3}/\tau_{p,\mathrm{E}}$), where τ_E represents the time needed for energy to move from one

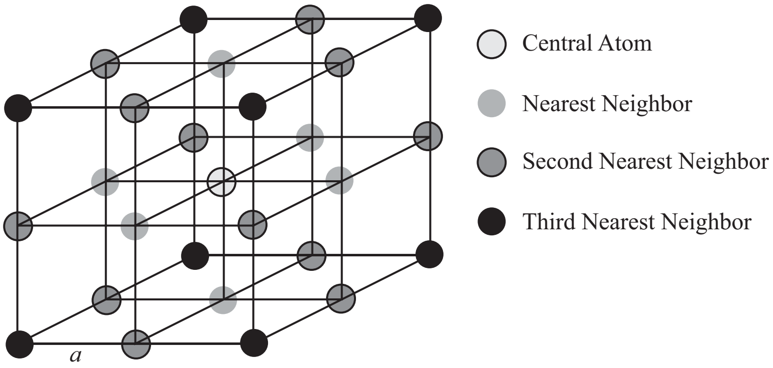

Figure C.1. The simple cubic crystal structure, with the first-, second- and third-nearest neighbors of the central atom shown.

atom to another. Using these specifications in (4.109) leads to

$$k_{p,\mathrm{E}} = \frac{n^{-1/3} k_\mathrm{B}}{\tau_{p,\mathrm{E}}} \frac{x_\mathrm{E}^2 e^{x_\mathrm{E}}}{(e^{x_\mathrm{E}} - 1)^2}. \qquad \text{(C.2)}$$

The value of $\tau_{p,\mathrm{E}}$ must now be specified.

C.1.2 Relaxation Time

Consider a set of two atoms, as shown in Figure C.2. The equation of motion for the central atom in the x direction is desired. As such, consider a displacement of magnitude x ($x \ll a$) of the central atom in the x direction, which will cause the neighbor atom, labeled as atom i, to move along the line of action between it and the central atom by an amount d_i ($d_i \ll a$). The angle formed by these two directions is ϕ_i. The change in the length of the spring is then $(d_i - x\cos\phi_i)$, and the force on the central atom in the x direction is

$$F_{c\text{-}i} = \Gamma(d_i - x\cos\phi_i)\cos\phi_i. \qquad \text{(C.3)}$$

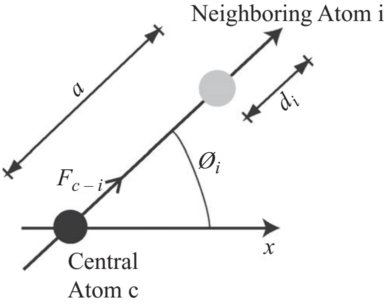

Figure C.2. Two neighboring atoms in the Einstein thermal conductivity formulation.

Summing over the contributions of all the neighbor atoms (26 in total) leads to the equation of motion similar to (4.1)

$$m\frac{\mathrm{d}^2x}{\mathrm{d}t^2} = \sum_i \Gamma(d_i - x\cos\phi_i)\cos\phi_i, \tag{C.4}$$

where m is the mass of an atom. Multiplying through by $(\mathrm{d}x/\mathrm{d}t)\mathrm{d}t$ and integrating over time leads to

$$\begin{aligned}
\int m\frac{\mathrm{d}^2x}{\mathrm{d}t^2}\frac{\mathrm{d}x}{\mathrm{d}t}\mathrm{d}t &= -\int \Gamma x(\sum_i \cos^2\phi_i)\frac{\mathrm{d}x}{\mathrm{d}t}\mathrm{d}t + \int \Gamma(\sum_i d_i\cos\phi_i)\frac{\mathrm{d}x}{\mathrm{d}t}\mathrm{d}t\\
\int \frac{1}{2}m\mathrm{d}[(\frac{\mathrm{d}x}{\mathrm{d}t})^2] &= -\int \frac{1}{2}\Gamma(\sum_i \cos^2\phi_i)\mathrm{d}(x^2) + \int \Gamma(\sum_i d_i\cos\phi_i)\frac{\mathrm{d}x}{\mathrm{d}t}\mathrm{d}t\\
\sum_i \Gamma\cos\phi_i \int d_i\frac{\mathrm{d}x}{\mathrm{d}t}\mathrm{d}t &= \int \mathrm{d}[\frac{m}{2}(\frac{\mathrm{d}x}{\mathrm{d}t})^2 + \frac{\Gamma x^2}{2}\sum_i \cos^2\phi_i].
\end{aligned} \tag{C.5}$$

The variable of integration of the last line of the right-hand side of (C.5) is taken as the energy associated with the central atom (kinetic and potential) so that the integral corresponds to the change of the energy of the atom over a specified time. The left-hand side of the last line of (C.5) represents the work done by the other atoms in the system to bring about this change in energy. Consider a time of one-half of the period of oscillation (π/ω_E), and define the summand of the right-hand side of the last line of (C.5) as η_i and the energy change as ΔE, such that the last line of (C.5) can be written as

$$\Delta E = \sum_i \eta_i. \tag{C.6}$$

Assume that the atomic motions are sinusoidal and uncorrelated such that

$$x = A\ \sin(\omega_\mathrm{E}t) \tag{C.7}$$

$$d_i = A_i\sin(\omega_\mathrm{E}t + \alpha_i), \tag{C.8}$$

where α_i is a random phase angle. This leads to

$$\begin{aligned}
\eta_i &= \Gamma\cos\phi_i \int_0^{\pi/\omega_\mathrm{E}} d_i\frac{\mathrm{d}x}{\mathrm{d}t}\mathrm{d}t\\
&= \Gamma\cos\phi_i \int_0^{\pi/\omega_\mathrm{E}} A_i\sin(\omega_\mathrm{E}t+\alpha_i)A\omega_\mathrm{E}\cos(\omega_\mathrm{E}t)\,\mathrm{d}t\\
&= \Gamma\cos\phi_i AA_i\omega_\mathrm{E}\int_0^{\pi/\omega_\mathrm{E}} [\sin(\omega_\mathrm{E}t)\cos\alpha_i\cos(\omega_\mathrm{E}t)\\
&\quad + \cos(\omega_\mathrm{E}t)\sin\alpha_i\cos(\omega_\mathrm{E}t)]\,\mathrm{d}t.
\end{aligned} \tag{C.9}$$

Consider the first term in the above integral

$$\int_0^{\pi/\omega_\mathrm{E}} \sin(\omega_\mathrm{E}t)\cos(\omega_\mathrm{E}t)\mathrm{d}t = \int_{-\pi/2\omega_\mathrm{E}}^{\pi/2\omega_\mathrm{E}} \frac{1}{2}\sin(2\omega_\mathrm{E}t)\,\mathrm{d}t = 0. \tag{C.10}$$

Then, because of the odd nature of the sine function, the work done becomes

$$\begin{aligned}\eta_i &= \Gamma\cos\phi_i AA_i\omega_{\mathrm{E}}\sin\alpha_i\int_0^{\pi/\omega_{\mathrm{E}}}\cos^2(\omega_{\mathrm{E}}t)\mathrm{d}t \\ &= \Gamma\cos\phi_i AA_i\omega_{\mathrm{E}}\sin\alpha_i\int_0^{\pi/\omega_{\mathrm{E}}}[\frac{1}{2}+\frac{1}{2}\cos(2\omega_{\mathrm{E}}t)]\mathrm{d}t \\ &= \Gamma\cos\phi_i AA_i\omega_{\mathrm{E}}\sin\alpha_i[\frac{t}{2}+\frac{1}{2\omega_{\mathrm{E}}}\sin(2\omega_{\mathrm{E}}t)]|_0^{\pi/\omega_{\mathrm{E}}} \\ &= \frac{\Gamma\cos\phi_i AA_i\sin\alpha_i\pi}{2}. \end{aligned} \tag{C.11}$$

Because the phase angles α_i are random, the average value of the work done by the atoms is zero. As many atoms transfer energy to the central atom as those that obtain energy from it (as would be expected in an equilibrium system). However, the RMS fluctuation of the energy,

$$\langle(\Delta E)^2\rangle = \langle(\sum_i \eta_i)^2\rangle, \tag{C.12}$$

will not be zero. Because the α_i values are uncorrelated, $\langle\eta_i\eta_j\rangle = 0$, such that

$$\langle(\Delta E)^2\rangle = \langle\sum_i \eta_i^2\rangle = \sum_i\langle\eta_i^2\rangle. \tag{C.13}$$

Thus, from (C.11),

$$\eta_i^2 = \frac{\pi^2\Gamma^2\cos^2\phi_i}{4}A^2A_i^2\sin^2\alpha_i, \tag{C.14}$$

and

$$\langle\eta_i^2\rangle = \frac{\pi^2\Gamma^2\cos^2\phi_i}{4}\langle A^2\rangle\ \langle A_i^2\rangle\ \langle\sin^2\alpha_i\rangle. \tag{C.15}$$

If all the atoms are identical, then $A = A_i$. For random α_i, the average is

$$\langle\sin^2\alpha_i\rangle = \int_0^{2\pi}\sin^2\alpha\mathrm{d}\alpha = \frac{1}{2}, \tag{C.16}$$

so that

$$\langle\eta_i^2\rangle = \frac{\pi^2\Gamma^2\cos^2\phi_i}{4}\frac{\langle A^2\rangle^2}{2}, \tag{C.17}$$

and

$$\langle(\Delta E)^2\rangle = \sum_i\frac{\pi^2\Gamma^2\cos^2\phi_i}{4}\frac{\langle A^2\rangle^2}{2} = \frac{\pi^2\Gamma^2\langle A^2\rangle^2}{8}\sum\cos^2\phi_i. \tag{C.18}$$

As can be calculated, the sum in (C.18) is 26/3. Einstein estimated its value at 10, which leads to

$$(\langle(\Delta E)^2\rangle)^{1/2} = (\frac{10}{8})^{1/2}\pi\Gamma\langle A^2\rangle \simeq 3.5\Gamma\langle A^2\rangle \quad \text{Einstein estimation.} \tag{C.19}$$

The size of the energy fluctuations can be compared to the total energy associated with each atom. The potential energy associated with an atom, as seen in the last line of (C.5), is[†]

$$\varphi = \frac{\Gamma x^2}{2} \sum_i \cos^2 \phi_i \simeq 5\Gamma x^2. \tag{C.20}$$

The average potential energy $\overline{\varphi}$ is then

$$\langle \varphi \rangle = 5\Gamma \langle x^2 \rangle, \tag{C.21}$$

where, from (C.7),

$$x^2 = A^2 \sin^2(\omega_{\rm E} t), \tag{C.22}$$

so that

$$\langle x^2 \rangle = \langle A^2 \rangle \, \langle \sin^2(\omega_{\rm E} t) \rangle = \langle A^2 \rangle \frac{1}{2}, \tag{C.23}$$

and

$$\langle \varphi \rangle = \frac{5\Gamma \langle A^2 \rangle}{2} \quad \text{average potential energy.} \tag{C.24}$$

For a harmonic system in which the average kinetic and potential energies are equal (Section 2.5.3), the average total energy is then given by

$$\langle E_p \rangle = 5\Gamma \langle A^2 \rangle. \tag{C.25}$$

This energy is of the same order as the energy fluctuations over a time equal to half of the atomic period of vibration, $\pi/\omega_{\rm E}$, in (C.19), suggesting that this is the appropriate time scale to use as $\tau_{p,{\rm E}}$ in the formulation of the thermal conductivity. This specification leads to

$$\frac{1}{\tau_{p,{\rm E}}} = \frac{\omega_{\rm E}}{\pi} = \frac{T_{\rm E} k_{\rm B}}{\pi \hbar}, \tag{C.26}$$

so that (C.2) becomes

$$k_{p,{\rm E}} = \frac{n^{-1/3} k_{\rm B}^2}{\pi \hbar} T_{\rm E} \frac{x_E^2 e^{x_{\rm E}}}{(e^{x_{\rm E}} - 1)^2} \quad \text{Einstein thermal conductivity,} \tag{C.27}$$

where $T_{\rm E}$ is the Einstein temperature, which can be found by fitting the Einstein specific heat model to experimental data. Unlike (4.116), this phonon relaxation time does not have a temperature dependence. This will lead to a plateau in $k_p(T)$ at high temperatures (Figure 4.17, broken curve).

Because of the approximate nature of the $\tau_{\rm E}$ specification, the geometry initially chosen for the crystal, the assumed form of the atomic displacements (which will not be sinusoidal), the treatment of the potential energy, and the approximation of the summation in (C.18) are of no great consequence.

[†] As mentioned, this is twice the potential energy associated with a single atom.

C.2 Cahill–Pohl Thermal Conductivity

The Cahill–Pohl (C–P) thermal conductivity model is an extension of the Einstein model, but also uses BTE. The derivation is given in [315]. The idea is to include a range of frequencies, instead of the single frequency used by Einstein. The thermal conductivity (4.109) is written as

$$k_p = \sum_{\alpha} \int \frac{1}{3} D_{p,\alpha}(\omega) c_{v,p,\alpha} u_{p,\alpha} \lambda_{p,\alpha} \mathrm{d}\omega, \tag{C.28}$$

where the summation is over the vibrational polarizations (one longitudinal and two transverse), $D_{p,\alpha}(\omega)$ is the volumetric density of vibrational states of polarization α, $c_{v,p}$ is now the specific heat per degree of freedom (and not per particle, as used previously), and $u_{p,\alpha}$ is the low-frequency (long-wavelength) speed of sound for polarization α in the material.

Instead of assuming energy transfer to occur between only nearest-neighbor atoms, one assumes that energy is transferred between vibrating entities with frequency ω and size $\lambda/2$, both of which are variable. Assuming no dispersion of the vibrational waves, we have (4.17)

$$\omega = u_p \kappa = u_p \frac{2\pi}{\lambda}, \tag{C.29}$$

where κ is the wave number and λ is the wavelength (taken as twice the distance over which the energy transfer occurs). Thus, for the mean free path in (C.28),

$$\lambda_{p,\alpha} = \frac{\lambda_\alpha}{2} = \tau_{p\text{-}p,\mathrm{C-P}} u_{p,\alpha} = \frac{\pi u_{p,\alpha}}{\omega} \quad \text{frequency-dependent mean free path.} \tag{C.30}$$

The high-frequency phonons have shorter mean free paths. This does not have a temperature dependence, as compared to (4.116), and correspond to $n = 1$ in (4.116) which is generally valid only for small ω (Figure 4.16). With no dispersion, the Debye density of states for each polarization (4.26) is

$$D_{p,\alpha}(\omega) = \frac{\omega^2}{2\pi^2 u_{p,\alpha}^3}, \tag{C.31}$$

and the specific heat capacity per mode is (C.1), i.e.,

$$c_{v,p} = k_{\mathrm{B}} \frac{x^2 e^x}{(e^x - 1)^2}, \tag{C.32}$$

and the maximum frequency for polarization α is found from (4.28), i.e.,

$$\omega_{\alpha,max} = (6\pi^2 n u_{p,\alpha}^3)^{1/3}, \tag{C.33}$$

which is taken as the upper limit of the integration in (C.28). These specifications lead to

$$\begin{aligned} k_{p,\text{C-P}} &= \sum_{\alpha} \frac{1}{3} \int_0^{\omega_{\alpha,max}} \frac{\omega^2}{2\pi^2 u_{p,\alpha}^3} k_{\text{B}} \frac{x^2 e^x}{(e^x - 1)^2} u_{p,\alpha} \frac{\pi u_{p,\alpha}}{\omega} \mathrm{d}\omega \\ &= \sum_{\alpha} \frac{k_{\text{B}}}{6\pi u_{p,\alpha}} \int_0^{x_{\alpha,max}} x \frac{k_{\text{B}} T}{\hbar} \frac{x^2 e^x}{(e^x - 1)^2} \frac{k_{\text{B}} T}{\hbar} \mathrm{d}x \\ &= \frac{k_{\text{B}}^3 T^2}{6\pi \hbar^2} \sum_{\alpha} \frac{1}{u_{p,\alpha}} \int_0^{x_{\alpha,max}} \frac{x^3 e^x}{(e^x - 1)^2} \mathrm{d}x. \end{aligned} \tag{C.34}$$

A temperature $T_{\text{D},\alpha}$ is found from (4.27)

$$T_{\text{D},\alpha} = u_{p,\alpha} \frac{\hbar}{k_{\text{B}}} (6\pi^2 n)^{1/3}, \tag{C.35}$$

(i.e., $T_{\text{D},\alpha} = x_{i,max} T$, which is not the Debye temperature, as the vibrational polarizations have been differentiated), allowing the thermal conductivity to be written as

$$k_{p,\text{C-P}} = (\frac{\pi}{6})^{1/3} k_{\text{B}} n^{2/3} \sum_{\alpha} u_{p,\alpha} (\frac{T}{T_{\text{D},\alpha}})^2 \int_0^{T_{\text{D},\alpha}/T} \frac{x^3 e^x}{(e^x - 1)^2} \mathrm{d}x \quad \text{C–P thermal conductivity.} \tag{C.36}$$

Unlike the Einstein model, no fitting parameters are required. Both the number density and velocities (the speeds of sound) can be determined experimentally. It is important to note that the value of $k_{p,\text{CP}}$ depends only on the number density of atoms through the upper limit of the integrals. Also, the Einstein assumption of the time for energy transfer between neighboring entities being half the period of oscillation [i.e., $\tau_{p,\text{E}} = \pi/\omega_{\text{E}}$, (C.26)] is not necessary, but follows from the assumption of no dispersion and a mean free path equal to one-half of the wavelength, i.e., (C.30)

$$\tau_{p,\text{E}} = \frac{\lambda_p}{u_{p,A}} = \frac{\lambda/2}{\omega\lambda/2\pi} = \frac{\pi}{\omega_{\text{E}}}. \tag{C.37}$$

The key point that is taken from the Einstein model is the idea of energy transfer occurring between only neighboring vibrational entities. No long-range coherence is assumed to exist [unlike (4.183)]. It is for this reason that the C-P model gives reasonable agreement with the experimental thermal conductivities of amorphous materials, in which short-length-scale interactions are expected to dominate the thermal transport. From a phonon perspective, the C-P thermal conductivity can be interpreted as a model in which all phonons have a mean free path equal to one-half of their wavelength.

The temperature dependence of (C.36) and the Callaway model (4.108) are shown in Figure 4.17. The Single relaxation time (for phonon–phonon interaction) in (C.36) does not allow for a peak in $k_p(T)$, and a monotonic increase in k_p is predicted up to $T_{\text{D},\alpha}$, where a plateau is reached.

APPENDIX D

Derivation of Phonon Boundary Resistance

The following formulation of the interfacial phonon conductance is similar to the quantum junction conductance treatment in [45]. In general, the conductance is controlled by the two distinct phonons in the two contacting solids, with no additional scattering due to interfacial restructuring or any third joint material. At a solid–solid (two semi-infinite media) interface (plane-parallel geometry), the net conduction heat flux q_k that is due to the difference of temperature between T_1 and T_2, assumed uniform in each (semi-infinite medium), for phonons on each side of the interface is [366, 453]

$$q_k = \frac{T_1 - T_2}{AR_{p,b}}, \tag{D.1}$$

where $R_{p,b}$ is the phonon boundary resistance. This resistance is determined by the number of phonons incident upon the interface, the energy carried by each phonon, and the probability of transmission across the interface.

The transmission probability τ_b depends on the side from which phonons arrive at the interface, angle of incidence, phonon frequency, phonon polarization, and T_1 and T_2. Using an analogy with blackbody radiation (7.8), we have

$$q_k = \sigma_{p,2} T_2^4 \tau_{b,2\text{-}1} - \sigma_{p,1} T_1^4 \tau_{b,1\text{-}2}, \tag{D.2}$$

where $\sigma_{\text{SB},i}$(phonon) is the phonon Stefan–Boltzmann constant, given by (Section 7.6.2, footnote)

$$\sigma_{\text{SB},i}(\text{phonon}) = \frac{\rho_i c_{v_{p,i}} u_{p,i}}{16T^3}. \tag{D.3}$$

For $T_1 = T_2$, then $q_k = 0$, and

$$\sigma_{\text{SB},2}(\text{phonon})\tau_{b,2\text{-}1} = \sigma_{\text{SB},1}(\text{phonon})\tau_{b,1\text{-}2}, \tag{D.4}$$

i.e., under thermal equilibrium, the total number of phonons (sum over all phonon states, polarization α and frequency ω_p) leaving one side, is equal to the total number of phonons returning from the other side into that state (called the principle of detailed balance). From this, we define $q_{k,1\text{-}2}(T_1)$ and $q_{k,1\text{-}2}(T_2)$ for the incident phonons at temperatures T_1 and T_2, and write

$$q_k = q_{k,1\text{-}2}(T_1) - q_{k,1\text{-}2}(T_2). \tag{D.5}$$

Using the equilibrium distribution of thermal phonons, we have

$$q_{k,1\text{-}2}(T) = \sum_\alpha \int_0^\infty \int_0^{2\pi} \int_0^{\pi/2} \tau_{b,1\text{-}2}(\theta, \alpha, \omega_p) \times \frac{D_{p,1}(\omega_p) f^o_{p,1}(\omega_p, T_1)}{4\pi} u_{p,1,\alpha} \cos\theta \sin\theta \mathrm{d}\theta \mathrm{d}\phi \hbar\omega_p \mathrm{d}\omega_p. \tag{D.6}$$

The second part inside the integral accounts for the number of phonons with mode α and frequency ω_p, at angles of incidence (θ, φ), speed $u_{p,1,\alpha}$, and energy $\hbar\omega_p$ that are incident from side 1, on the interface, per unit time. When using the Debye DOS, a cut-off frequency is used.

The transmission probability τ_b is given as a function of θ (angle between the phonon propagation direction and the normal to the interface), α, and ω_p, under the assumption that both sides of the interface are isotropic and there is no dependence on temperature. However, when all phonons are diffusely scattered at the interface, τ_b will be a function only of ω_p, and will be determined by the DOS and the principle of detailed balance subsequently given.

D.1 Diffuse Scattering

D.1.1 Transmission Probability for Diffuse Scattering

For diffuse scattering the RMS interface roughness $\langle\delta^2\rangle^{1/2}$ is expected to be larger than the dominant phonon wavelength λ, which is estimated as $\lambda \propto (T_\mathrm{D}/T)^a$, where a is the lattice spacing [366]. We examine (D.6) noting that the number of phonons of frequency ω_p leaving material 1, per unit area and per unit time, is

$$\sum_\alpha \int_0^{2\pi} \int_0^{\pi/2} \tau_{b,1\text{-}2}(\omega_p) \frac{D_{p,1}(\omega_p) f^\mathrm{o}_{p,1}(\omega_p, T_1)}{4\pi} u_{p,1,\alpha} \cos\theta \sin\theta \mathrm{d}\theta \mathrm{d}\phi. \tag{D.7}$$

Because the transmission probability is independent of the incident angles, the angular integral result then is

$$\frac{1}{4} \sum_\alpha \tau_{b,1\text{-}2}(\omega_p) D_{p,1}(\omega_p) f^\mathrm{o}_{p,1}(\omega_p, T_1) u_{p,1,\alpha}. \tag{D.8}$$

From the principle of detailed balance, in which the interface is in thermal equilibrium ($T_1 = T_2 = T$), we can write that

$$\frac{1}{4} \sum_\alpha \tau_{b,1\text{-}2}(\omega_p) D_{p,1}(\omega_p) f^\mathrm{o}_{p,1}(\omega_p, T_1) u_{p,1,\alpha} = \frac{1}{4} \sum_\alpha \tau_{b,2\text{-}1}(\omega_p) D_{p,2}(\omega_p) f^\mathrm{o}_{p,2}(\omega_p, T_2) u_{p,2,\alpha}, \tag{D.9}$$

i.e., the number of phonons leaving side 1 must equal the number of phonons leaving side 2. In addition, because in diffuse scattering a phonon loses the memory of where it comes from, it follows that

$$\tau_{b,1\text{-}2}(\omega_p) = \rho_{b,2\text{-}1}(\omega_p) = 1 - \tau_{b,2\text{-}1}(\omega_p), \tag{D.10}$$

where $\rho_{b,2\text{-}1}$ is the reflectivity. This equation states that the probability of reflection from one side must equal the probability of transmission from the other. Therefore, using (D.9), we have

$$\tau_{b,1\text{-}2}(\omega_p)\sum_\alpha D_{p,1}(\omega_p) f^{\text{o}}_{p,1}(\omega_p, T) u_{p,1,\alpha}$$

$$= [1 - \tau_{b,1\text{-}2}(\omega_p)]\sum_\alpha D_{p,2}(\omega_p) f^{\text{o}}_{p,2}(\omega_p, T) u_{p,2,\alpha}. \tag{D.11}$$

Solving for $\tau_{b,1\text{-}2}(\omega_p)$, we have

$$\tau_{b,1\text{-}2}(\omega_p) =$$

$$\frac{\sum_\alpha D_{p,2}(\omega_p) f^{\text{o}}_{p,2}(\omega_p, T) u_{p,2,\alpha}}{\sum_\alpha D_{p,1}(\omega_p) f^{\text{o}}_{p,1}(\omega_p, T) u_{p,1,\alpha} + \sum_\alpha D_{p,2}(\omega_p) f^{\text{o}}_{p,2}(\omega_p, T) u_{p,2,\alpha}}. \tag{D.12}$$

Using the Debye phonon DOS (4.26) and the phonon equilibrium distribution function (Table 1.2), (D.12) becomes

$$\tau_{b,1\text{-}2} = 1 - \tau_{b,2\text{-}1} = \frac{\sum_\alpha u^{-2}_{p,2,\alpha}}{\sum_\alpha u^{-2}_{p,1,\alpha} + \sum_\alpha u^{-2}_{p,2,\alpha}} \quad \text{Debye transmissivity}, \tag{D.13}$$

i.e, the transmissivity is independent of frequency.

D.1.2 Net Heat Flow for Diffuse Scattering

For diffuse scattering of phonons, (D.1) and (D.5) become

$$\frac{1}{AR_{p,b}} = \frac{G_{p,b}}{A} = \frac{q_{k,1\text{-}2}}{T_1 - T_2} = \frac{\hbar\tau_{b,1\text{-}2}}{4(T_1 - T_2)}\sum_\alpha u_{p,1,\alpha} \times$$

$$\int_0^\infty D_{p,1}(\omega_p)\left[\frac{1}{\exp(\frac{\hbar\omega_p}{k_{\text{B}}T_1}) - 1} - \frac{1}{\exp(\frac{\hbar\omega_p}{k_{\text{B}}T_2}) - 1}\right]\omega_p \mathrm{d}\omega_p, \tag{D.14}$$

where $G_{p,b}$ is the phonon boundary conductance.

Replacing $D_p(\omega_p)$ with the measured phonon DOS, this equation is numerically integrated to yield a value for q, which is substituted into (D.1) to calculate the phonon boundary resistance $R_{p,b}$.

Using the Debye density of states $D_{p,\text{D}}$, i.e.,

$$D_{p,1}(\omega_p) = D_{p,\text{D},1}(\omega_p) = \frac{\omega_p^2}{2\pi^2 u^3_{p,1,\alpha}}, \tag{D.15}$$

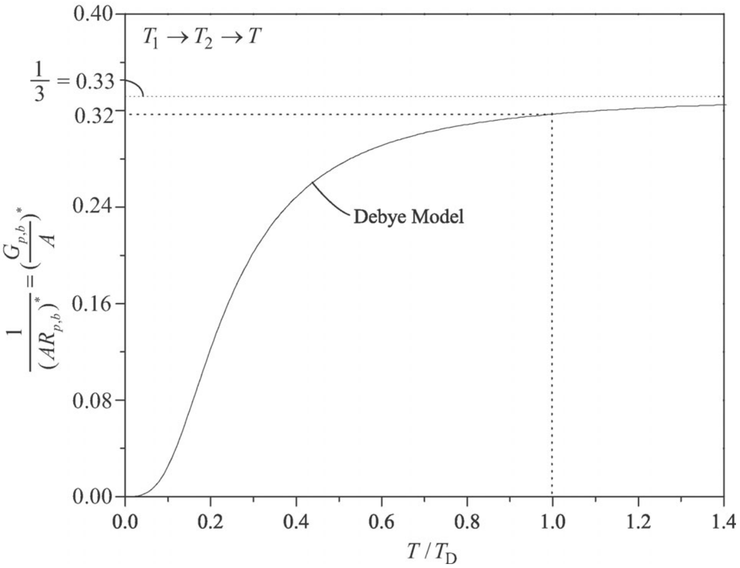

Figure D.1. Variations of dimensionless phonon boundary conductance with respect to dimensionless temperature. The high-temperature limit of 1/3 is also shown.

(D.14) becomes

$$\frac{1}{AR_{p,b}} = \frac{\hbar\tau_{b,1\text{-}2}}{8\pi^2(T_1-T_2)}\sum_\alpha u_{p,1,\alpha}^{-2} \times \int_0^{\omega_D}[\frac{\omega_p^3}{\exp(\frac{\hbar\omega_p}{k_BT_1})-1} - \frac{\omega_p^3}{\exp(\frac{\hbar\omega_p}{k_BT_2})-1}]\mathrm{d}\omega, \tag{D.16}$$

where $\omega_D = \omega_{D,1}$ is the Debye cut-off frequency of side 1.

Using the variable $z = \omega_p/\omega_D$ for normalization, the upper limit of the integral becomes equal to 1, and we have

$$\frac{1}{AR_{p,b}} = \frac{\hbar\tau_{b,1\text{-}2}\omega_D^4}{8\pi^2(T_1-T_2)}\sum_\alpha u_{p,1,\alpha}^{-2} \times \int_0^1[\frac{z^3}{\exp(zT_D/T_1)-1} - \frac{z^3}{\exp(zT_D/T_2)-1}]\mathrm{d}z,$$

$$z = \frac{\omega_p}{\omega_D}, \quad \frac{T_D}{T} = \frac{\hbar\omega_D}{k_BT}. \tag{D.17}$$

Then for $T_1 \to T_2 \to T$, we can use a variable $x = zT_D/T_1 = zT_D/T_2$ and $T_D = T_D$, and (D.17) becomes

$$\frac{1}{AR_{p,b}} = \frac{\tau_{b,1\text{-}2}k_B^4T_D^3}{8\pi^2\hbar^3}\sum_\alpha u_{p,1,\alpha}^{-2}$$

$$\times \frac{1}{T_D^3(T_1-T_2)}[T_1^4\int_0^{T_D/T_1}\frac{x^3}{\exp(x)-1}\mathrm{d}x - T_2^4\int_0^{T_D/T_2}\frac{x^3}{\exp(x)-1}\mathrm{d}x]. \tag{D.18}$$

A dimensionless phonon boundary conductance can be given as

$$\frac{1}{(AR_{p,b})^*} \equiv \frac{1}{AR_{p,b}} \frac{8\pi^2\hbar^3}{k_B^4 T_D^3 \tau_{b,1\text{-}2} \sum_\alpha u_{p,1,\alpha}^2} = \frac{1}{T_D^3(T_1 - T_2)} \times$$

$$\left[T_1^4 \int_0^{T_D/T_1} \frac{x^3}{\exp(x)-1} \mathrm{d}x - T_2^4 \int_0^{T_D/T_2} \frac{x^3}{\exp(x)-1} \mathrm{d}x \right], \qquad \text{(D.19)}$$

and its variation is shown in Figure D.1. The dimensionless phonon boundary conductance initially increases with a temperature, and reaches a plateau at $T/T_D = 1$. The maximum value is $1/(AR_{p,b})^* = 1/3$.

D.2 Specular Scattering

D.2.1 Transmission Probability for Specular Scattering

In specular scattering, phonons are treated as plane waves and the materials that form the interface are treated as continua. This applies to phonons with wavelengths larger than the interfacial roughness.

Because the longitudinal phonons are the quantized LA waves, the transmission probability will be given by the equivalent expression for acoustic waves [286]:

$$\tau_{b,1\text{-}2}(\theta_1) = \tau_{b,2-1}(\theta_2) = 4\frac{\frac{\rho_2 u_{p,2}}{\rho_1 u_{p,1}} \frac{\cos\theta_2}{\cos\theta_1}}{(\frac{\rho_2 u_{p,2}}{\rho_1 u_{p,1}} + \frac{\cos\theta_2}{\cos\theta_1})^2}, \qquad \text{(D.20)}$$

where θ_1 is the incident angle in side 1 and θ_2 is the refraction angle in side 2.

D.2.2 Net Heat Flow for Specular Scattering

For specular scattering of phonons, (D.1), (D.5), and (D.6) become

$$\frac{1}{AR_{p,b}} = \frac{\hbar}{4\pi^2(T_1 - T_2)} \sum_\alpha u_{p,1,\alpha}^{-2} \Gamma_{1,\alpha} \int_0^{\omega_D} [\frac{\omega_p^3}{\exp(\frac{\hbar\omega_p}{k_B T_1}) - 1} - \frac{\omega_p^3}{\exp(\frac{\hbar\omega_p}{k_B T_2}) - 1}] \mathrm{d}\omega_p, \qquad \text{(D.21)}$$

where $\omega_D = \omega_{D,1}$, and

$$\Gamma_{1,\alpha} = \int_0^{\pi/2} \tau_{b,1\text{-}2}(\theta, \alpha) \cos\theta \sin\theta \mathrm{d}\theta, \qquad \text{(D.22)}$$

is calculated numerically. Note that $\tau_{b,1\text{-}2}(\theta, \alpha)$ is assumed to be independent of ω_p for phonons with frequency less than $\omega_{D,1}$, and above that $\tau_{b,1\text{-}2}(\theta, \alpha)$ is zero.

Equation (D.21) can also be normalized with the variable $x = \hbar\omega_p/(k_B T)$, as performed in Section D.1.2. The upper limit of the integral then becomes

$x = \hbar\omega_\mathrm{D}/(k_\mathrm{B}T)$, and for low T, $x \rightarrow \infty$. Therefore, for $[\hbar\omega_p/(k_\mathrm{B}T)] \gg 1$, we have

$$\frac{1}{AR_{p,b}} = \frac{k_\mathrm{B}^4}{4\pi^2\hbar^3(T_1 - T_2)} \sum_\alpha u_{p,1,\alpha}^{-2} \Gamma_{1,\alpha} \int_0^\infty [\frac{T_1^4 x^3}{e^x} - \frac{T_2^4 x^3}{e^x}]\mathrm{d}x,$$

$$x = \frac{\hbar\omega_\mathrm{D}}{k_\mathrm{B}T} \quad \text{for low } T. \tag{D.23}$$

Note that, for normal incidence $\theta_1 = \theta_2 = 0^\circ$, (D.20) becomes

$$\tau_{b,1\text{-}2} = 4\frac{\rho_2 u_{p,2}\ \rho_1 u_{p,1}}{(\rho_2 u_{p,2} + \rho_1 u_{p,1})^2}, \tag{D.24}$$

and we have $\Gamma_{1,\alpha} = \tau_{b,1\text{-}2}/2$, i.e., (D.23) will differ from (D.17) only by the transmission probability.

APPENDIX E

Derivation of Fermi Golden Rule

The Fermi (or Fermi–Dirac) golden rule (FGR) (3.27) allows for calculation of the transition probability rate between two eigenstates of a quantum system using the time-dependent perturbation theory. It is the probability of this scattering-caused transition per unit time. So, the probability is time dependent and is is derived from the time-dependent perturbation theory (the perturbation Hamiltonian, i.e., the scattering potential, is time dependent), under the assumption that the time of the measurement is much larger than the time needed for the transition.

It is the rate of gain of probability per unit time in the manifold of final eigenstate $|\psi_{\kappa'}\rangle$, which is equal to the rate of loss of probability per unit time from the initial eigenstate $|\psi_{\kappa}\rangle$.

A brief derivation of the FGR is given and more details can be found in [94, 294, 325]

E.1 Time-Dependent Perturbation

The general Hamiltonian of interest is of the form (5.89)

$$\mathrm{H} = \mathrm{H_o} + \mathrm{H}', \tag{E.1}$$

where $\mathrm{H_o}$ is a time independent Hamiltonian with a known solution ψ_κ, which is related to Ψ_κ through (2.68), i.e.,

$$\mathrm{H_o}\psi_\kappa = E(\boldsymbol{\kappa})\psi_\kappa \tag{E.2}$$

$$\Psi_\kappa^{\mathrm{o}} = \psi_\kappa \exp[\frac{-iE(\boldsymbol{\kappa})t}{\hbar}], \tag{E.3}$$

and $E(\boldsymbol{\kappa})$ and ψ_κ are time-independent. Here H' causes time-dependent transitions between the states ψ_κ. The time-dependent Schrödinger equation is

$$i\hbar\frac{\partial\Psi}{\partial t} = \mathrm{H}\Psi. \tag{E.4}$$

We now express Ψ as an expansion of the eigenfunctions $\psi_\kappa \exp[-iE_e(\kappa)t/\hbar]$ of the unperturbed system, (2.67), i.e.,

$$\Psi = \sum_\kappa a_\kappa(t)\Psi_\kappa^{\rm o} = \sum_\kappa a_\kappa(t)\psi_\kappa \exp[\frac{-iE(\kappa)t}{\hbar}]. \tag{E.5}$$

The time-dependent problem is solved when the coefficients $a_\kappa(t)$ are known, and from this we will develop time-rate equation, i.e., which is the derivation of the probability of transition.

Substituting (E.5) into (E.4), also using (E.2), we have,

$$\sum_\kappa i\hbar\frac{{\rm d}a_\kappa(t)}{{\rm d}t}\psi_\kappa \exp[\frac{-iE_e(\kappa)t}{\hbar}] + \sum_\kappa a_\kappa(t)E(\kappa)\psi_\kappa \exp[\frac{-iE(\kappa)t}{\hbar}]$$
$$= \sum_\kappa a_\kappa(t)({\rm H_o}+{\rm H}')\psi_\kappa \exp[\frac{-iE(\kappa)t}{\hbar}]. \tag{E.6}$$

Now multiplying by $\psi_{\kappa'}^*$ and integrating over space, we have (using orthogonality of the eigenfunctions)

$$i\hbar\frac{\partial a_{\kappa'}(t)}{\partial t}\exp[\frac{-iE(\kappa')t}{\hbar}] = \sum_\kappa a_\kappa(t)\exp[\frac{-iE(\kappa)t}{\hbar}]\langle\psi_{\kappa'}|{\rm H}'|\psi_\kappa\rangle. \tag{E.7}$$

The interaction matrix element is defined as

$$M_{\kappa',\kappa} = \langle\psi_{\kappa'}|{\rm H}'|\psi_\kappa\rangle = \int \psi_{\kappa'}^*{\rm H}'\psi_\kappa {\rm d}V \quad \text{interaction matrix element.} \tag{E.8}$$

Using this, (E.7) is rewritten as

$$\frac{\partial a_{\kappa'}(t)}{\partial t} = \frac{1}{i\hbar}\sum_\kappa M_{\kappa',\kappa}a_\kappa(t)\exp\{\frac{i[E(\kappa')-E(\kappa)]t}{\hbar}\}, \tag{E.9}$$

which is the equation for $a_{\kappa'}(t)$.

Next we apply the regular perturbation to find an approximation for $a_\kappa(t)$ appearing on the right-hand side of (E.9). Similar to the perturbation approximation used in Section 2.6.7, we have

$$\begin{aligned}{\rm H}' &\rightarrow \epsilon{\rm H}'\\ a_{\kappa'} &= a_{{\rm o},\kappa'} + \epsilon a_{1,\kappa'} + \epsilon^2 a_{2,\kappa'}.\end{aligned} \tag{E.10}$$

Substituting these into (E.9), and collecting the terms with coefficients of the same power ϵ, we have

$$\begin{aligned}\frac{\partial a_{{\rm o},\kappa'}}{\partial t} &= 0\\ \frac{\partial a_{j+1,\kappa'}}{\partial t} &= \frac{1}{i\hbar}\sum_\kappa M_{\kappa',\kappa}a_{j,\kappa}\exp\{\frac{i[E(\kappa')-E(\kappa)]t}{\hbar}\}.\end{aligned} \tag{E.11}$$

To study the time evolution of the problem, we assume that the perturbation H′ is absent at time $t \le 0$ and starts at $t = 0$. With this assumption, the system is in a time-independent state up to $t = 0$. We assume that initially the system is in a single, well-defined state $\psi_{\boldsymbol{\kappa}}$ with

$$a_{\mathrm{o},\boldsymbol{\kappa}}(t = 0) = 1 \tag{E.12}$$

$$a_{\mathrm{o},\boldsymbol{\kappa}'}(t = 0) = \langle \boldsymbol{\kappa}' | \boldsymbol{\kappa} \rangle = 0 \ \text{ if } \boldsymbol{\kappa}' \neq \boldsymbol{\kappa},$$

$$\text{single-state initial conditions.} \tag{E.13}$$

Integration of (E.9) to the first order term gives

$$a_{1,\boldsymbol{\kappa}'}(t) = \frac{1}{i\hbar} \int_0^t M_{\kappa',\kappa} \exp\{\frac{i[E(\boldsymbol{\kappa}') - E(\boldsymbol{\kappa})]t}{\hbar}\} \mathrm{d}t, \tag{E.14}$$

which satisfies initial conditions (E.12) and (E.13).

E.2 Transition Rate

A number of important problems in quantum mechanics involve a perturbation that has time dependence with a time-periodic form. Examples include interactions of electrons with electromagnetic radiation (photons) and electrons in crystals interacting with phonons. In these cases, the time dependence of the perturbation potential is

$$\mathrm{H}' = \mathrm{H}'_x \exp(\mp i\omega t) \quad \text{time-periodic behavior,} \tag{E.15}$$

where H'_x is spatial part (time independent) of the perturbation Hamiltonian. This makes the interaction matrix element (E.8)

$$M_{\kappa',\kappa} = M_{\mathrm{o},\kappa',\kappa} \exp(\mp i\omega t), \quad M_{\mathrm{o},\kappa',\kappa} = \langle \psi_{\boldsymbol{\kappa}'} | \mathrm{H}'_x | \psi_{\boldsymbol{\kappa}} \rangle, \quad \text{time-periodic matrix element.} \tag{E.16}$$

We now integrate (E.14), taking the constant of integration to be zero, as $a_{1,\boldsymbol{\kappa}'} = 0$ for $t \leq 0$ (no perturbation)

$$a_{1,\boldsymbol{\kappa}'}(t) = -\frac{1}{i\hbar} M_{\mathrm{o},\kappa',\kappa} \frac{\exp\{\frac{i[E(\boldsymbol{\kappa}') - E(\boldsymbol{\kappa}) \mp \hbar\omega]t}{\hbar}\} - 1}{\frac{i[E(\boldsymbol{\kappa}') - E(\boldsymbol{\kappa}) \mp \hbar\omega]}{\hbar}}. \tag{E.17}$$

Equation (E.17) states that as $E(\boldsymbol{\kappa}') - E(\boldsymbol{\kappa}) \rightarrow \hbar\omega$ or $E(\boldsymbol{\kappa}') - E(\boldsymbol{\kappa}) \rightarrow -\hbar\omega$ (because of absorption or emission) is reached, the term to the right of $M_{\mathrm{o},\boldsymbol{\kappa}',\boldsymbol{\kappa}}$ will approach its maximum value. Because the probability of finding a state is related to $\psi^2_{\boldsymbol{\kappa}'}$, then this probability is highest for the energies of transition (absorption/emission).

For simplicity, we define

$$\omega' = \frac{[E(\boldsymbol{\kappa}') - E(\boldsymbol{\kappa}) \mp \hbar\omega]}{\hbar}, \tag{E.18}$$

and using the exponential function relation then (E.17) becomes

$$a_{1,\boldsymbol{\kappa}'}(t) = -\frac{1}{i\hbar} M_{\mathrm{o}\kappa',\kappa} \exp(\frac{i\omega' t}{2}) \frac{\sin(\omega' t/2)}{\omega' t/2} t. \tag{E.19}$$

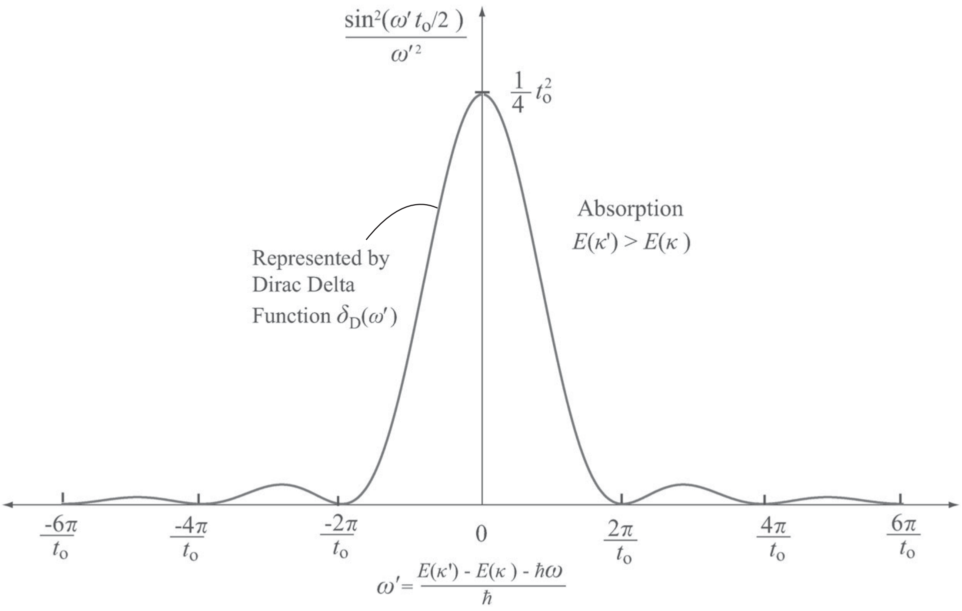

Figure E.1. Variations of the probability of finding the system in a state κ' after the perturbation has been applied at time t_o.

Figure E.1 shows the variation of the probability of transition $\boldsymbol{\kappa} \rightarrow \boldsymbol{\kappa}'$, which is related to $a_{1,\boldsymbol{\kappa}'}^2$ according to (5.91), with absorption of $\hbar\omega$, due to the applied perturbation potential from $t = 0$ to $t = t_o$ (Chapter 3 problem). The probability is $[\sin(\omega' t_o/2)/\omega']^2$. The probability is highest when $E(\boldsymbol{\kappa}') - E(\boldsymbol{\kappa}) \simeq \hbar\omega$ and the peak is proportional to t_o^2.

The transition rate is given by the transition probability (which is related to $a_{\boldsymbol{\kappa}'}^2$) per unit time, (5.91) and (5.92), i.e.,

$$\dot{\gamma}(\boldsymbol{\kappa}', \boldsymbol{\kappa}) = \lim_{t\rightarrow\infty} \frac{|a_{1,\boldsymbol{\kappa}'}(t)|^2}{t} = \lim_{t\rightarrow\infty} \frac{1}{t\hbar^2} |M_{o,\kappa',\kappa}|^2 [\frac{\sin(\omega' t/2)}{\omega' t/2}]^2 t^2. \tag{E.20}$$

Next we note that the integral over the infinite time domain is simplified as

$$\int_{-\infty}^{+\infty} \frac{\sin^2(\omega' t/2)}{(\omega' t/2)^2} \mathrm{d}x = \pi. \tag{E.21}$$

Now using this and the definition of the Dirac delta function δ_D (Glossary), we find the following equality:

$$\lim_{t\rightarrow\infty} [\frac{\sin(\omega' t/2)}{\omega' t/2}]^2 = \pi \delta_D(\frac{\omega' t}{2}) = \frac{2\pi}{t} \delta_D(\omega'). \tag{E.22}$$

Note that here we have used the relation

$$\delta_D(ax) = \frac{1}{a} \delta_D(x) \qquad a \text{ is a constant.} \tag{E.23}$$

Hence, transition rate (E.20) becomes

$$\begin{aligned}\dot{\gamma}(\boldsymbol{\kappa}', \boldsymbol{\kappa}) &= \frac{1}{t\hbar^2}|M_{\mathrm{o},\kappa',\kappa}|^2 \frac{2\pi}{t}\delta_{\mathrm{D}}\{\frac{[E(\boldsymbol{\kappa}') - E(\boldsymbol{\kappa}) \mp \hbar\omega]}{\hbar}\}t^2 \\ &= \frac{2\pi}{\hbar}|M_{\mathrm{o}\kappa',\kappa}|^2 \delta_{\mathrm{D}}[E(\boldsymbol{\kappa}') - E(\boldsymbol{\kappa}) \mp \hbar\omega] \text{ Fermi golden rule.} \end{aligned} \tag{E.24}$$

This is the FGR (3.27).

E.3 Example: Photoelectric Transition Rate for Hydrogen

The hydrogen atom, in ground state when irradiated with photon of energy matching the ionization energy $\hbar\omega$ and amplitude (we will use the electric potential $\boldsymbol{a}_{e,\mathrm{o}}$, Table 3.5), ejects an electron (photoelectric effect) [146]. The transition probability rate is given by (E.24), i.e.,

$$\dot{\gamma}_{ph-e} = \frac{2\pi}{\hbar}|\langle\psi_f|\mathrm{H}'|\psi_i\rangle|^2 \delta_{\mathrm{D}}(E_{e,f} - E_{e,i} - \hbar\omega), \tag{E.25}$$

where f is the final state, i is the initial state, and H' is the time-independent interaction Hamiltonian.

The photon is represented by an EM wave having vector potential $\boldsymbol{a}_e$ (Table 3.5, where $\boldsymbol{b}_e = \nabla \times \boldsymbol{a}_e$, $\nabla \cdot \boldsymbol{a}_e = 0$), i.e.,

$$\boldsymbol{a}_e(\boldsymbol{x}, t) = \boldsymbol{a}_{e,\mathrm{o}}\cos(\boldsymbol{\kappa} \cdot \boldsymbol{x} + \omega t). \tag{E.26}$$

Using this, the electron kinetic energy is (Chapter 5 problem)

$$\mathrm{H}'(t) = -\frac{1}{2m_e}[-e_c(\boldsymbol{p}_e \cdot \boldsymbol{a}_e + \boldsymbol{a}_e \cdot \boldsymbol{p}_e)] = \frac{e_c}{m_e}\boldsymbol{a}_e \cdot \boldsymbol{p}_e. \tag{E.27}$$

Then

$$\begin{aligned}\mathrm{H}'(t) &= \frac{e_e}{m_e}\cos(\boldsymbol{\kappa} \cdot \boldsymbol{x} - \omega t)\boldsymbol{a}_{e,\mathrm{o}} \cdot \boldsymbol{p}_e \\ &= \frac{e_c}{2m_e}[e^{i(\boldsymbol{\kappa}\cdot\boldsymbol{x}-\omega t)} + e^{-i(\boldsymbol{x}\cdot\boldsymbol{\kappa}-\omega t)}]\boldsymbol{a}_{e,\mathrm{o}} \cdot \boldsymbol{p}_e \\ &= \frac{e_c}{2m_e}e^{i\boldsymbol{\kappa}\cdot\boldsymbol{x}}\boldsymbol{a}_{e,\mathrm{o}} \cdot \boldsymbol{p}_e e^{-i\omega t} \\ &= \mathrm{H}'e^{-i\omega t}, \end{aligned} \tag{E.28}$$

as the $\exp(i\omega t)$ corresponding to photon emission is neglected.

The ground-state energy is given by (2.114), i.e., $E_{e,1} = e_c^2/8\pi\epsilon_{\mathrm{o}}r_{\mathrm{B}}$, and its wave function (for hydrogen $z = 1$) is given in Table 2.10, i.e.,

$$|100\rangle = \frac{1}{\pi^{1/2}r_{\mathrm{B}}^{3/2}}e^{-x/r_{\mathrm{B}}}, \tag{E.29}$$

and we assume that the final state is $\psi_f = L^{-3/2}e^{i\boldsymbol{\kappa}_f\cdot\boldsymbol{x}}$. Then the matrix element is (using the Bloch plane wave and time-independent H′)

$$\begin{aligned}\mathrm{M}_{\boldsymbol{\kappa}_f,\boldsymbol{\kappa}} &= \langle\psi_f|\frac{e_c}{2m_eu_{ph}}e^{i\boldsymbol{\kappa}\cdot\boldsymbol{x}}\boldsymbol{a}_{e,\mathrm{o}}\cdot\boldsymbol{p}_e|100\rangle\\ &= \frac{1}{L^{3/2}}\int e^{i\boldsymbol{\kappa}_f\cdot\boldsymbol{x}}\frac{e_c}{2m_eu_{ph}}e^{i\boldsymbol{\kappa}\cdot\boldsymbol{x}}\boldsymbol{a}_{e,\mathrm{o}}\cdot(-i\hbar\nabla)\frac{1}{\pi^{1/2}r_{\mathrm{B}}^3}e^{ix/r_{\mathrm{B}}}\mathrm{d}\boldsymbol{x},\end{aligned}\tag{E.30}$$

where $L^3 = V$ is from the periodic, cubic box treatment of the electron (Section 2.6.6). Because $\lambda \gg r_{\mathrm{B}}$, we set $\exp(i\boldsymbol{\kappa}\cdot\boldsymbol{x}) = 1$.

The integral contains ∇, which is removed by integration by parts, i.e.,

$$\begin{aligned}&\int e^{i\boldsymbol{\kappa}_f\cdot\boldsymbol{x}}\boldsymbol{a}_{e,\mathrm{o}}\cdot(i\hbar\nabla)e^{-x/r_{\mathrm{B}}}\mathrm{d}\boldsymbol{x}\\ &\quad= -\boldsymbol{a}_{e,\mathrm{o}}\cdot\boldsymbol{p}_f\int e^{i\boldsymbol{\kappa}_f\cdot\boldsymbol{r}}e^{-x/r_{\mathrm{B}}}\mathrm{d}\boldsymbol{x}.\end{aligned}\tag{E.31}$$

Taking the z axis along $\boldsymbol{\kappa}_f$, the ϕ integration gives 2π and the θ integration (over $\sin\theta\mathrm{d}\theta$) gives

$$\int_0^{\pi}\int_0^{2\pi}\int_0^{\infty}e^{i\boldsymbol{\kappa}_f\cdot\boldsymbol{s}_z}e^{-z/r_{\mathrm{B}}}\mathrm{d}z\mathrm{d}\phi\sin\theta\mathrm{d}\theta = \frac{8\pi}{r_{\mathrm{B}}}\frac{1}{(r_{\mathrm{B}}^{-2}+\kappa_f^2)^2}.\tag{E.32}$$

Using this, we have

$$\dot{\gamma}_{ph\text{-}e} = \frac{2\pi}{\hbar}|\frac{1}{L^{3/2}}\frac{e_c}{2m_eu_{ph}}\frac{1}{\pi^{1/2}r_{\mathrm{B}}^{3/2}}\boldsymbol{a}_{e,\mathrm{o}}\cdot\boldsymbol{p}_e\frac{8\pi}{r_{\mathrm{B}}}\frac{1}{(r_{\mathrm{B}}^{-2}+\kappa_f^2)^2}|^2\delta_{\mathrm{D}}(E_{e,f}-E_{e,i}-\hbar\omega).\tag{E.33}$$

By taking the average over incidence angle, $\boldsymbol{a}_{e,\mathrm{o}}\cdot\boldsymbol{p}_f = a_{e,\mathrm{o}}p_f\cos\theta$, and noting that $\kappa_f = p_f/\hbar$, this total ionization (photoelectric transition) rate becomes

$$\dot{\gamma}_{ph\text{-}e} = \frac{4m_ep_f}{\pi r_{\mathrm{B}}\hbar^4}(\frac{e_c}{m_eu_{ph}})^2\frac{4\pi a_{e,\mathrm{o}}^2p_f^2}{3}[\frac{1}{r_{\mathrm{B}}^{-2}+(\frac{p_f}{\hbar})^2}]^4$$

$$\text{photoelectric transition rate for hydrogen atom,}\tag{E.34}$$

where we have used from (5.65) and (5.66) (not allowing for spin) that (Chapter 5 problem)

$$L^3\frac{D_e}{2} = \int\delta_{\mathrm{D}}(E_{e,f}-E_{e,i}-\hbar\omega) = (\frac{L}{2\pi})^3 4\pi\kappa_f\frac{m_e}{\hbar^2},\tag{E.35}$$

and $\langle\cos^2\theta\rangle = \int\cos\theta\mathrm{d}\Omega = 1/3$, where $\mathrm{d}\Omega = \sin\theta\mathrm{d}\theta\mathrm{d}\phi$ (Table 7.1).

The cases of $\hbar\omega \gg E_{e,i}$ and $\hbar\omega - E_{e,i} \ll E_{e,i}$ have been examined in [165]. For the case $\hbar\omega - E_{e,i} \simeq E_{e,i}$ (near threshold, where the ejected electron has a very high velocity), we have for the total (integrated over the solid angle) absorption cross-section area

$$A_{ph\text{-}e} = \frac{512\pi^2}{3}\frac{r_{\mathrm{B}}^2e_c^2}{4\pi\epsilon_{\mathrm{o}}\hbar u_{ph}}(\frac{E_{e,1}}{\hbar\omega})^4\frac{e^{-4\gamma\cot^{-1}\gamma}}{1-e^{2\pi\gamma}},\ \gamma = (\frac{\hbar\omega}{E_{e,1}}-1)^{-1/2}.\tag{E.36}$$

Table E.1. *Examples of perturbation Hamiltonian.*

Interaction	Mechanism	Perturbation Hamiltonian
Electron–charge	electron piezoelectric scattering	$\mathrm{H}' = \frac{e_c e_{pz}}{\epsilon_o \epsilon_e}\, \boldsymbol{d} \cdot \boldsymbol{s}$
Electron–phonon	electron scattering by acoustic phonon	$\mathrm{H}' = \varphi_{d,\mathrm{A}} \nabla \cdot \boldsymbol{d}$
	electron scattering by optical phonon	$\mathrm{H}' = \varphi'_{d,\mathrm{O}}\, \boldsymbol{d} \cdot \boldsymbol{s}$
Photon–electron	photon absorption in gases	$\mathrm{H}' = -\lvert \boldsymbol{\mu}_e \rvert e_{e,\mathrm{o}} \cos(\omega t)$
Fluid particle–phonon	adsorbed gas vibration decaying to substrate phonon	$\mathrm{H}' = \mathrm{A} d_f d_s^2,\ A = \frac{9 m_{12} \omega_f^2}{8 \Delta h_{ad}}$

$\boldsymbol{d}$	displacement vector, m
e_{pz}	piezoelectric constant, C/m^2
m_{12}	reduced mass, kg
$\boldsymbol{s}$	unit vector
Δh_{ad}	heat of adsorption, J
$\varphi_{d,\mathrm{A}}$	acoustic scattering potential, J
$\varphi'_{d,\mathrm{O}}$	optical scattering potential, J/m
$\boldsymbol{\mu}_e$	transition dipole moment, C-m

This shows a strong decay in $A_{ph\text{-}e}$ as $\hbar\omega / E_{e,1}$ increases. (Chapter 7 problem)

The transition rate and the absorption (ionization) cross-section area are related through photon energy density (3.38), and is [146]

$$\frac{a_{e,\mathrm{o}}^2 \omega A_{ph\text{-}e}}{8\pi u_{ph}} = \hbar\omega \dot{\gamma}_{ph\text{-}e}. \tag{E.37}$$

E.4 Examples of Perturbation Hamiltonian

Table E.1 gives examples of perturbation Hamiltonian H′ in the interaction matrix element (E.8). These are samples of scatterings/couplings discussed in energy transport and transformation kinetics. The phonon scatterings are discussed in Section 4.9.4. The electron scatterings are discussed in Section 5.15. The photon absorption, and its interaction matrix element, for solids and gases, are discussed in Section 7.8. Other photon couplings are discussed in Section 7.12. Examples of calculations of $\lvert \boldsymbol{\mu}_e \rvert$ and $\varphi'_{d,\mathrm{O}}$ are given in [238].

APPENDIX F

Derivation of Equilibrium, Particle Probability Distribution Functions

The Fermi–Dirac (fermion) and Bose–Einstein (boson) statistics include quantum effects and apply to interacting, indistinguishable particles (Table 1.2). The M–B statistics apply to noninteracting, indistinguishable particles (classical particles), whose wave functions do not overlap and quantum effects vanish (footnote of Section 2.6.5). When the particle concentration is much less than the quantum limit, quantum effects will vanish. The quantum limit is when the particle spacing $n^{-1/3}$ is equal to the de Broglie wavelength $\lambda_{\rm dB}$ (footnote of Section 6.1). All particles can be treated as classical particles, when the ratio of the particle concentration $n = N/V$ and the quantum concentration n_q (the dimensionless concentration) n_q is much less than unity, i.e.,

$$n^* = \frac{n}{n_q} = n\lambda_{\rm dB}^3 = \frac{N}{V}(\frac{2\pi\hbar^2}{mk_{\rm B}T})^{3/2}, \tag{F.1}$$

where N is the number of particles, V is the volume of the system, m is the mass of the particle, and T is the temperature. Therefore both fermions and bosons become the M–B statistics at high temperatures or low concentrations.

Derivation of the particle (including quantum) statistics distribution functions are given in [156, 323].

F.1 Partition Functions

For different ensembles [Section 2.5.1(A)], the partition function may have different forms. For a canonical ensemble, the partition function (2.27) is defined as

$$Z(N, V, T) = \sum_j e^{-E_j/k_{\rm B}T}, \tag{F.2}$$

where j designates the energy state of the system.

For a grand canonical ensemble (μVT), the partition function is defined as

$$Z(\mu, V, T) = \sum_{N=0}^{\infty} Z(N, \mu, V, T,) = \sum_{N=0}^{\infty}\sum_j e^{(E_j-\mu)/k_{\rm B}T}, \tag{F.3}$$

where N is the number of particles, and when it is a constant, then $\mu = 0$, and $Z(\mu, V, T)$ becomes $Z(N, V, T)$, relating (F.2) and (F.3).

The partition function (F.2) and (F.3) can be simplified when the Hamitonian (Table 2.5) is written as the sum of the various energy mechanisms and degrees of freedom, i.e.,

$$E = \mathrm{H} = \varphi + \mathrm{H}_e + \mathrm{H}_t + \mathrm{H}_v + \mathrm{H}_r + \cdots. \tag{F.4}$$

For an N-particle canonical ensemble, the energy of each particle can be expressed as E_j^k, where $k = a, b, c \ldots$ designates the particle (here we assume that they are distinguishable) and j denotes the energy state of the system, the canonical partition function (F.2) becomes

$$\begin{aligned} Z(N, V, T) &= \sum_j e^{-E_j/k_\mathrm{B}T} = \sum_{m,n,l} e^{-(E_m^a + E_n^b + E_l^c + \ldots)/k_\mathrm{B}T} \\ &= \sum_m e^{-E_m^a/k_\mathrm{B}T} \sum_n e^{-E_n^b/k_\mathrm{B}T} \sum_l e^{-E_l^c/k_\mathrm{B}T} \ldots \\ &= Z_a Z_b Z_c \ldots, \quad Z_a = \sum_m e^{-E_m^a/k_\mathrm{B}T}, \end{aligned} \tag{F.5}$$

where m, n, and l, are quantum numbers designating the energy state of each particle. (F.5) means the partition function of the system is the product of the partition functions of the subsystems. Then, for interacting, indistinguishable particles $(Z_a = Z_b = Z_c = \ldots)$, we have

$$Z(N, V, T) = Z(V, T)^N \text{ interacting, indistinguishable particles.} \tag{F.6}$$

This reduces the N-body problem to a one-body problem.

For noninteracting, indistinguishable particles (no wave function overlaps), considering the degeneracy in the energy state of the system, we have [323]

$$Z(N, V, T) = \frac{Z(V, T)^N}{N!} \text{ noninteracting, indistinguishable particles.} \tag{F.7}$$

This also reduces the N-body problem to a one-body problem. For this case the number of available molecular states is much larger than the number of particles N. This is returned to the Boltzmann statistics and becomes increasingly valid at high temperatures.

Using relation (F.5) for the canonical ensemble, the partition function for a grand canonical ensemble is rewritten as

$$\begin{aligned} Z(\mu, V, T) &= \sum_{\{N_j\}} \prod_j e^{-N_j(E_j - \mu)/k_\mathrm{B}T} \\ &= \prod_j [\sum_{N_j} e^{-N_j(E_j - \mu)/k_\mathrm{B}T}] \\ &= \prod_j Z_j, \quad Z_j = \sum_{N_j} e^{-N_j(E_j - \mu)/k_\mathrm{B}T}. \end{aligned} \tag{F.8}$$

Here $\{N_j\}$ designates the configuration of the system, for example, the configuration $\{1, 2, ..\}$ means there is 1 particle in the first energy state, 2 particles in the second energy state, etc. (F.8) states that when an energy state rather than a particle is considered as a subsystem in a grand canonical ensemble, the partition function of the system may have the same relation with the partition functions of the subsystems as in a canonical ensemble [(F.5)].

The probability for a state j in the occupation representation is (2.20), i.e.,

$$P_j = \frac{e^{(E_j-\mu)/k_\mathrm{B}T}}{Z}. \tag{F.9}$$

This is valid for both the grand canonical ensemble and the canonical ensemble (for the canonical ensemble, $\mu = 0$). The mean equilibrium occupancy of particles i ($i = p, e, f, ph$) in the energy state j is therefore

$$f^\circ_{i,j} = \sum N_j P_j = -\frac{\partial \ln Z_j}{\partial \xi_j}, \quad \xi_j = (E_j - \mu)/k_B T. \tag{F.10}$$

The Fermi–Dirac (fermions), Bose–Einsten (bosons) and Maxwell–Boltzmann (M–B) distribution functions are directly derived in the subsequent sections using the statistics for a grand canonical ensemble, as there is no limit for the number of particles.

F.2 Fermi–Dirac Distribution Function f_e^o

In the grand canonical ensemble ($\mu V T$) discussed in Sections 2.5.1 and F.1, the partition function (2.21) for a single-particle state j (of a multiparticle system) with energy E_j, for a quantum gas in a box, is

$$Z_j = \sum_{N_j} e^{-N_j(E_j-\mu)/k_\mathrm{B}T}, \tag{F.11}$$

where N_j is the number of particles in the jth state with energy E_j.

For fermions, a state is occupied by only a single particle or not occupied. This is called a multiplicity of two. Then (F.11) becomes

$$Z_j = \sum_{N_j=0}^{1} e^{-[E_j-\mu]N_j/k_\mathrm{B}T} = e^{-(E_j-\mu)/k_\mathrm{B}T} + 1. \tag{F.12}$$

Then the equilibrium occupation distribution (F.10) is

$$f_e^\mathrm{o} = \frac{e^{-(E_j-\mu)/k_\mathrm{B}T}}{e^{-(E_j-\mu)/k_\mathrm{B}T} + 1} = \frac{1}{e^{(E_j-\mu)/k_\mathrm{B}T} + 1} \quad \text{fermion}. \tag{F.13}$$

F.3 Bose–Einstein Distribution Function f_p°, f_{ph}°

For bosons, there is no limit for the number of particles in a state j. Therefore we have

$$Z_j = \sum_{N_j=0}^{\infty} e^{-(E_j-\mu)N_j/k_{\rm B}T} = \frac{1}{1-e^{-(E_j-\mu)/k_{\rm B}T}}. \tag{F.14}$$

Thus the expected distribution (F.10) becomes

$$\begin{aligned} f_j^{\circ} = f_p^{\circ} = f_{ph}^{\circ} &= \frac{e^{-(E_j-\mu)/k_{\rm B}T}}{1-e^{-(E_j-\mu)/k_{\rm B}T}} \\ &= \frac{1}{e^{(E_j-\mu)/k_{\rm B}T}-1} \quad \text{boson}. \end{aligned} \tag{F.15}$$

F.4 Maxwell–Boltzmann (Classical) Distribution Function f_f°

For noninteracting, indistinguishable (this combination is also called distinguishable) particles (having degeneracy $N_j!$), using $\mu = 0$ and similar to (F.7), we have

$$\begin{aligned} Z_j &= \sum_{N_j=0}^{\infty} \frac{e^{-N_jE_j/k_{\rm B}T}}{N_j!} \\ &= \exp(e^{-E_j/k_{\rm B}T}). \end{aligned} \tag{F.16}$$

Therefore, the expected distribution (F.10) becomes

$$f_f^{\circ} = \frac{1}{e^{E_j/k_{\rm B}T}} \quad \text{M–B}. \tag{F.17}$$

Note that this is the classical model of the more general M–B distribution (6.64), and as shown in Figure 1.1, is valid for large $E_f/k_{\rm B}T$.

F.5 Comparison Among Fermion, Boson, and M–B (Classical) Particles

The mean occupancy $f_i^{\circ}(E_{i,j},\mu,T)$ ($i = p, e, f, ph$) for an orbital with energy $E_{i,j}$ in a system with temperature T and chemical potential μ can be expressed in the generic form

$$f_i^{\circ} = \frac{1}{e^{(E_{i,j}-\mu)/k_BT}+\gamma}, \quad \gamma = 1 \text{ (fermion)},\ 0 \text{ (M-B, Classical)},\ -1 \text{ (boson)}. \tag{F.18}$$

When $(E_{i,j}-\mu)/k_BT \gg 1$, $f_i^{\circ} = 1/e^{(E_{i,j}-\mu)/k_BT}$, where the mean occupancy $f_i^{\circ} \ll 1$. The chemical potential is closely related to the quantum concentration (footnote, Section 6.1)

$$\begin{aligned} n = \frac{N}{V} &= \int \frac{{\rm d}^3p}{h_{\rm P}^3} \exp[-(\frac{p^2}{2m}-\mu)/k_{\rm B}T] = \lambda_{\rm dB}^{-3} e^{\mu/k_{\rm B}T}, \\ \lambda_{\rm dB} &= (\frac{2\pi\hbar^2}{mk_{\rm B}T})^{1/2} \quad \text{de Broglie wavelength}. \end{aligned} \tag{F.19}$$

Then using (F.1) and (F.19), the chemical potential becomes

$$\mu = k_{\rm B} T \ln n_q \lambda_{\rm dB}^3. \tag{F.20}$$

The classical condition $(E_{i,j} - \mu)/k_B T \gg 1$ gives $\mu \ll E_{i,j} - k_B T$, and this leads to $f_i^\circ \ll 1$. Therefore both fermions and bosons can be treated as classical particles at high energies, where $f_i^\circ \ll 1$. This is called the nondegenerate state.

APPENDIX G

Phonon Contributions to the Seebeck Coefficient

The Seebeck effect is the formation of electric potential in the presence of spatial variation of temperature. In 1821, Seebeck observed that a temperature difference between two ends of a metal bar created an electrical current in between, with the voltage (difference in electric potential $\varphi_{e,i}$) being directly proportional to the temperature difference [98]. Physically, when one side of a conductor is hot, electrons have higher thermal energy and diffuse to the cold side. The charge (carrier) concentration increase on the cold side builds an internal electric field that resists the diffusion. The Seebeck voltage is the steady-state potential difference under an open-circuit condition. Here,

$$-(\varphi_{e,2} - \varphi_{e,1}) = \alpha_S (T_2 - T_1), \tag{G.1}$$

where α_S is the Seebeck coefficient and T_i is the temperature of site i.

G.1 Derivation

As shown in Figure G.1, various carriers contribute to the Seebeck coefficient. Their interactions with electrons, magnons, phonons, and other charge carriers (e.g., polarons) also substantially affect the Seebeck coefficient. Figures G.2(a) to (c) show the atomistic schematics for those contributions. The overall Seebeck coefficient can be expressed as the sum of two contributions [130, 131, 132, 339],

$$\alpha_S = \alpha_{S,\mathrm{pres}} + \alpha_{S,\mathrm{trans}}, \tag{G.2}$$

where $\alpha_{S,\mathrm{pres}}$ is the sum of contributions to the carrier-induced entropy change; that is,

$$\alpha_{S,\mathrm{pres}} = \alpha_{S,\mathrm{mix}} + \alpha_{S,\mathrm{spin}} + \alpha_{S,\mathrm{vib}}, \tag{G.3}$$

where the right-hand terms are change of the entropy-of-mixing, spin entropy, and vibrational entropy on adding a charge carrier, respectively. The other contribution $\alpha_{S,\mathrm{trans}}$ is the net energy transferred in moving a carrier divided by qT, where q is the carrier charge [130].

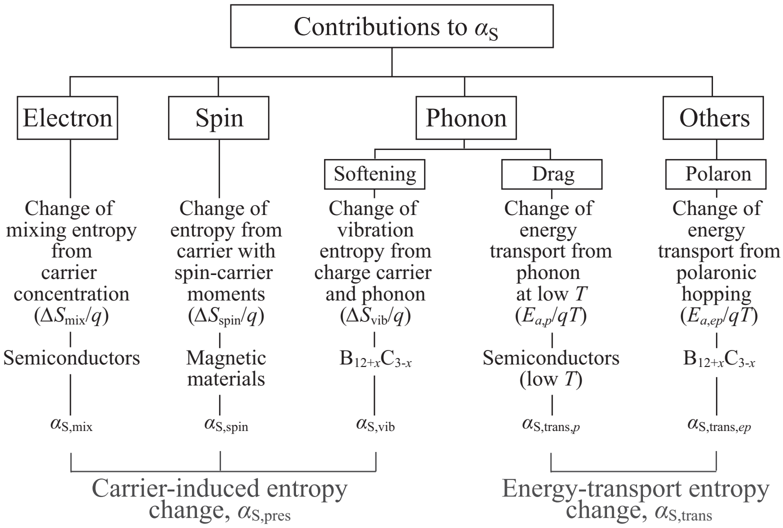
Contributions to α_S
Electron
Spin
Phonon
Others
Softening
Drag
Polaron
Change of mixing entropy from carrier concentration ($\Delta S_{mix}/q$)
Change of entropy from carrier with spin-carrier moments ($\Delta S_{spin}/q$)
Change of vibration entropy from charge carrier and phonon ($\Delta S_{vib}/q$)
Change of energy transport from phonon at low T ($E_{a,p}/qT$)
Change of energy transport from polaronic hopping ($E_{a,ep}/qT$)
Semiconductors
Magnetic materials
$B_{12+x}C_{3-x}$
Semiconductors (low T)
$B_{12+x}C_{3-x}$
$\alpha_{S,mix}$
$\alpha_{S,spin}$
$\alpha_{S,vib}$
$\alpha_{S,trans,p}$
$\alpha_{S,trans,ep}$
Carrier-induced entropy change, $\alpha_{S,pres}$
Energy-transport entropy change, $\alpha_{S,trans}$

Figure G.1. Various contributions to the Seebeck coefficient from different carriers. Their physical interpretation and example of materials for each category are also shown.

Each carrier contributes to the Seebeck coefficient in distinct manner ways and under specific conditions; however, they are highly coupled and interacting. From the phononic point of view, the most prominent contributions to the Seebeck coefficient can be summarized as electron-phonon coupling [132, 154], phonon drag [132, 404], phonon-mediated spin pumping [472], phonon-assisted carrier hopping [131, 132, 499], and carrier-induced phonon softening [131, 132, 339]. Although those effects have been examined in several experimental results [131, 132, 339, 154, 404, 472, 499], no overall coupling consideration or density-functional theory (DFT)–based calculation of phonon contributions to the Seebeck coefficient has been reported yet. The analyses and tuning of its phonon contribution are considered a promising strategy to achieve the high Seebeck coefficient.

G.1.1 Mixing Component

The entropy-of-mixing contribution is usually dominant in lightly doped semiconductors. The change of the entropy-of-mixing on adding a carrier to a system is large because there are very few carriers per thermally available state [131, 185]. Figure G.2(a) shows the electron mixing with a certain temperature gradient. The system is described as spinless fermions (here, electron) on atomic sites. As given in Table 2.4 and Appendix F, the calculated degeneracy for this system is given by $W = N_a!/N!(N_a - N)!$, where N is the number of electrons and N_a is the number of atomic sites per unit cell. The entropy is given by $S = k_B \ln(W) = k_B N \ln(Z) + E/T$. Using the Stirling's approximation, and differentiating with N, we have,

$$\alpha_{S,mix} = \frac{k_B}{q}\ln(\frac{1 - f_e^\circ}{f_e^\circ}), \tag{G.4}$$

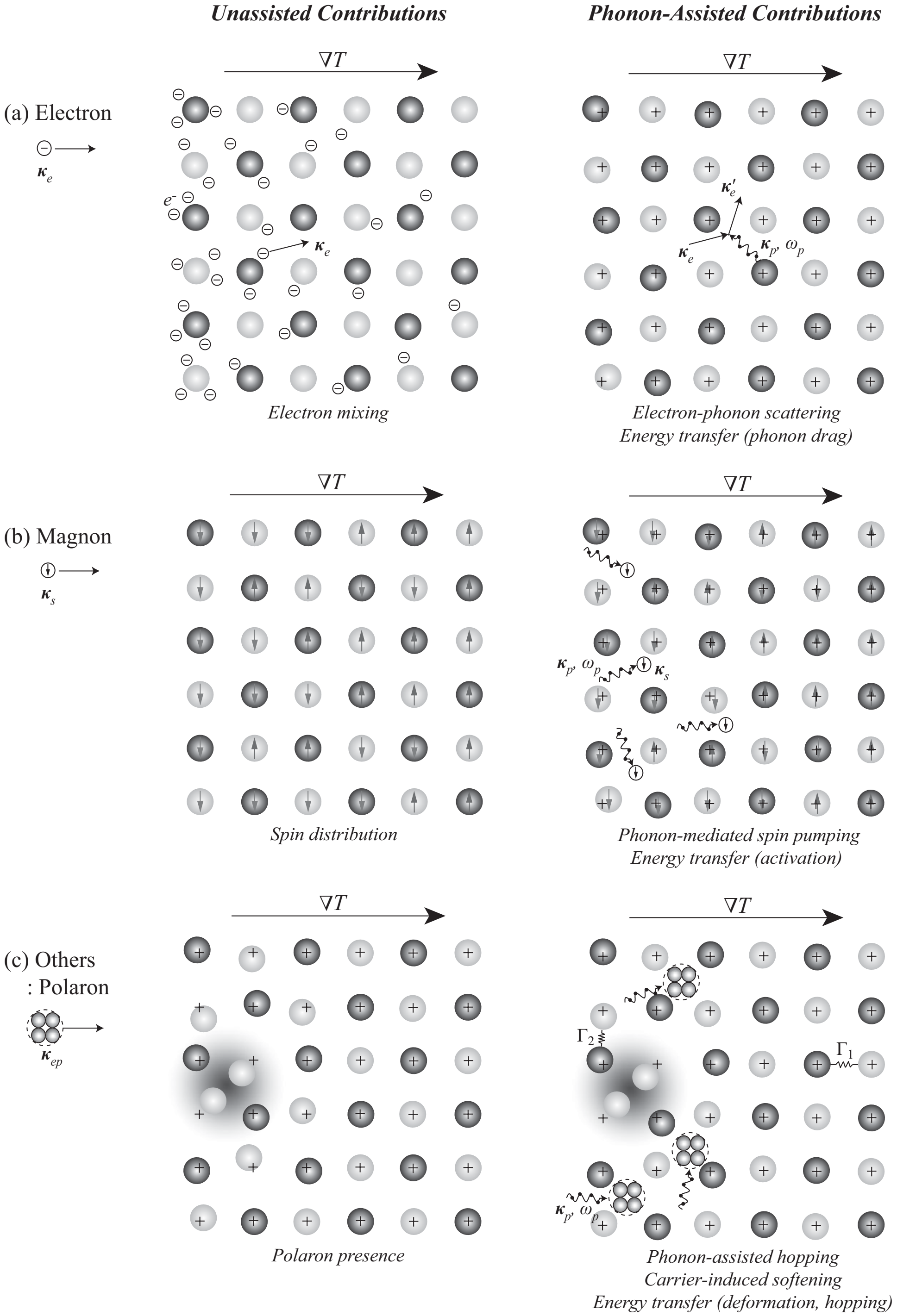

Figure G.2. Atomistic metrics of the Seebeck coefficient contributions in crystals. Model for the temperature-driven entropy change by (a) electron mixing, (b) spin entropy, and (c) polaron-induced phonon softening.

the so-called Heikes formula. Here $f_e^\circ = N/N_a$ is the ratio of electrons to sites (carrier concentration). An alternative form of this simple expression is obtained when the ratio is expressed in terms of the energy of the electronic energy band, the chemical potential (μ) and the thermal energy ($k_\mathrm{B}T$) via the Fermi function, $f_e^\circ = 1/\{\exp[(E_e - \mu)/k_\mathrm{B}T] + 1\}$; that is,

$$\alpha_{\mathrm{S,mix}} = -\frac{k_\mathrm{B}}{q}(\frac{E_e - \mu}{k_\mathrm{B}T}). \tag{G.5}$$

In a high-temperature regime, the electronic energy level shifts with temperature, and the Seebeck coefficient changes. Figure G.2(b) shows the thermal disorder effect caused by a solid's thermal expansion and the electron-phonon interaction.

G.1.2 Spin Component

As given in (G.1), the common Seebeck effect refers to the generation of an electric potential $\Delta\varphi$ by placing a nonmagnetic material in a temperature gradient ΔT. Extending the Seebeck effect to spins, a ferromagnetic alloy [472] can be an example. Two spin channels would introduce different thermoelectric voltages, and consequently a spin voltage would be generated, $\Delta\varphi\uparrow$ - $\Delta\varphi\downarrow$ = $(\alpha_{\mathrm{S,spin}} \uparrow$ - $\alpha_{\mathrm{S,spin}} \downarrow)\Delta T$. The contribution to the Seebeck coefficient that results from the carriers' presence altering the system's spin entropy also becomes simple in the absence of intersite magnetic interactions [Figure G.2(b)]. Then the spin contribution for a carrier confined to a single magnetic site is

$$\alpha_{\mathrm{S,spin}} = \frac{\Delta S_{\mathrm{spin}}}{q} = \frac{k_\mathrm{B}}{q}\ln(\frac{2s+1}{2s_\circ + 1}), \tag{G.6}$$

where $s_\circ$ and s are the net spins of the magnetic site in the absence and presence of the carrier, respectively [131].

G.1.3 Vibration Component

As shown in Figure G.2, there are many vibrational contributions to the Seebeck coefficient. The softening in the vibrational frequencies produces a change in the vibrational entropy, for example. Figure G.2(c) shows the polaron-induced phonon softening and the augmentation of the vibrational component of the Seebeck coefficient. The full crystal Hamiltonian for the vibrational part of the energy is obtained by adding the potential and kinetic energy. As in (4.50), we write the Hamiltonian (for the quantum-harmonic oscillator) as [51, 445]

$$\mathrm{H}_{\mathrm{vib}} = \sum_q \hbar\omega(f_p^\circ + \frac{1}{2}). \tag{G.7}$$

This expression gives the Hamiltonian for the vibrational part of the energy, and it can be used to solve analytically for a number of thermodynamic properties. The free energy is [304]

$$F_{\mathrm{vib}} = -k_{\mathrm{B}}T\ln Z = -k_{\mathrm{B}}T\ln[\sum_{\mathrm{states}} \exp(-\frac{\mathrm{H}_{\mathrm{vib}}}{k_{\mathrm{B}}T})] = k_{\mathrm{B}}T\ln[\sum_{q} \ln[2\sinh\frac{\hbar\omega}{2k_{\mathrm{B}}T}]. \quad \text{(G.8)}$$

This entropy is the negative derivative of the free energy (i.e., [304]):

$$\begin{aligned} S_{\mathrm{vib}} &= -\frac{\partial F_{\mathrm{vib}}}{\partial T} \\ &= 3Nk_{\mathrm{B}}T\int_0^{\omega}\{\frac{\hbar\omega}{2k_{\mathrm{B}}T}\coth(\frac{\hbar\omega}{2k_{\mathrm{B}}T}) - \ln[2\sinh(\frac{\hbar\omega}{2k_{\mathrm{B}}T})]\}D_p(\omega)d\omega, \end{aligned} \quad \text{(G.9)}$$

where $D_p(\omega)$ is the phonon density-of-states for the structure. As in (4.21), the phonon density of states gives the number of modes with a frequency lying in the interval $[\omega, \omega + \mathrm{d}\omega]$. In the high-temperature limit ($k_{\mathrm{B}}T \gg \hbar\omega$) and series expansions of the hyperbolic functions, the above reduces to

$$\begin{aligned} S_{\mathrm{vib}} &= -3Nk_{\mathrm{B}}\int_0^{\infty}[(\frac{\hbar\omega}{2k_{\mathrm{B}}T})(\frac{2k_{\mathrm{B}}T}{\hbar\omega}) - \ln(\frac{\hbar\omega}{2k_{\mathrm{B}}T})]D_p(\omega)d\omega \\ &= -3Nk_{\mathrm{B}}\int_0^{\infty} D_p(\omega)\ln(\omega)d\omega + 3Nk_{\mathrm{B}}[1+\ln(k_{\mathrm{B}}T)]. \end{aligned} \quad \text{(G.10)}$$

(G.10) is given per atom,

$$S_{\mathrm{vib}}/\mathrm{atom} = -k_{\mathrm{B}}\int_0^{\infty} D_p(\omega)\ln(\omega)d\omega + k_{\mathrm{B}}[1+\ln(k_{\mathrm{B}}T)]. \quad \text{(G.11)}$$

The last term is structure independent and cancels out when taking differences. Terms involving $\ln(\hbar)$ are generally left out of (G.11) for convenience (they also cancel when taking differences). Hence, the vibrational contribution to the Seebeck coefficient [130, 131] is simplified in a high-temperature region as

$$\alpha_{\mathrm{S,vib}} = \frac{\Delta S_{\mathrm{vib}}}{q} = \frac{k_{\mathrm{B}}}{q}\sum_i \frac{-\Delta\omega_i}{\omega_i}. \quad \text{(G.12)}$$

G.1.4 Transport Component

As shown in Figure G.1, some charge carriers and their interactions cause a change in net energy transfer. For example, locally induced polarons change the net energy transfer by employing deformation energy and hopping activation/transfer energy [Figure G.2(c)]. To calculate $\alpha_{\mathrm{S,trans}}$ related to the phonon-assisted hopping, we start from $\alpha_{\mathrm{S,trans}} = E_T/qT$, where E_T is the net flow of the vibrational energy that accompanies a phonon-assisted hop from an initial site to a final site [131, 128]; that is,

$$E_T = \frac{k_{\mathrm{B}}T^2}{2}[\frac{\partial\ln(\dot{\gamma}_{1,2}/\dot{\gamma}_{2,1})}{\partial T_1} - \frac{\partial\ln(\dot{\gamma}_{1,2}/\dot{\gamma}_{2,1})}{\partial T_2}]_{T_1=T_2=T}. \quad \text{(G.13)}$$

Here $\dot{\gamma}_{1,2}$ and $\dot{\gamma}_{2,1}$ are the hopping rates from site 1 to site 2 (and from site 2 to site 1), while site 1 is at temperature T_1 and site 2 is at temperature T_2. The ratio of the jump rate is

$$\frac{\dot{\gamma}_{1,2}}{\dot{\gamma}_{2,1}} = \frac{\int_{-\infty}^{\infty} \exp[G(1,2:t)\cos[F_2(1,2:t) + \Delta E_{12}t/\hbar]dt}{\int_{-\infty}^{\infty} \exp[G(2,1:t)\cos[F_2(2,1:t) + \Delta E_{21}t/\hbar]dt}, \tag{G.14}$$

where

$$G(1,2:t) = \sum_q [\varphi^c_{e-p,1}\coth(\frac{\hbar\omega}{2k_\mathrm{B}T_1}) + \varphi_{e-p,2}\coth(\frac{\hbar\omega}{2k_\mathrm{B}T_2})][\cos(\omega t) - 1], \tag{G.15}$$

$$F_2(1,2:t) = \sum_q [\varphi^c_{e-p,1} + \varphi_{e-p,2}]\sin(\omega t), \tag{G.16}$$

and ΔE_{12} is the difference between the final and initial site energies (including lattice-relaxation energies) for a carrier that hops from site 1 to site 2. Here the functions $\varphi_{e-p,1}(\varphi_{e-p,2})$ describe the coupling of the electronic state at site 1 (and site 2) to vibrations of frequency ω_p when unoccupied or occupied by a carrier, respectively. A simple expression for E_T is obtained when one observes that the binding energy varies inversely with the local stiffness, $E_b \sim 1/M\omega^2$, and one considers the limit of a small fractional carrier-induced frequency shift, $(\omega - \omega_c)/\omega = |-\Delta\omega/\omega| \ll 1$. So, (G.13) simplifies to [130, 131]

$$E_T = E_a \sum_i (\frac{-\Delta\omega_i}{\omega_i}) \frac{\hbar\omega_i/2k_\mathrm{B}T}{\sinh(\hbar\omega_i/2k_\mathrm{B}T)}. \tag{G.17}$$

G.2 Example: Phonon Softening and Polaron Hopping for Boron Carbides

Boron carbides ($B_{12+x}C_{3-x}$) have distinctive structures and unconventional bondings. As shown in Figure G.3, a boron carbide unit cell (rhombohedral representation) contains an icosahedron consisting of 12 atoms and of strong covalent bonds linking icosahedra to one another. As a result, boron carbides are very stiff, hard solids with melting temperatures of ∼ 2,600 K [129, 116, 8]. Replacing carbon by boron atoms removes bonding electrons and thereby produces hole-like charge carriers. Such non-stoichiometry results in high densities of p-type charge carriers ($\sim 10^{21}$ cm^{-3}) or about one hole per unit cell [8].

Boron carbides' extraordinary hardness and high carrier densities suggest that these solids would have large thermal conductivities and small Seebeck coefficients. Yet many boron carbides have surprisingly small thermal conductivities and large Seebeck coefficients, suggesting localized charge carriers that move with low mobility by polaronic hopping.

The Seebeck coefficients of a boron carbide sample ($x = 1$) become nearly independent of temperature above about 600 K (Figure G.4). Temperature-independent Seebeck coefficients are commonly observed in solids when high-temperature conduction is dominated by the hopping of constant-density small polarons [10, 9]. Those experimental results are confirmed using the DFT-based direct method, nonequilibrium *ab-initio* molecular dynamics (NEAIMD). From Table 3.5, the

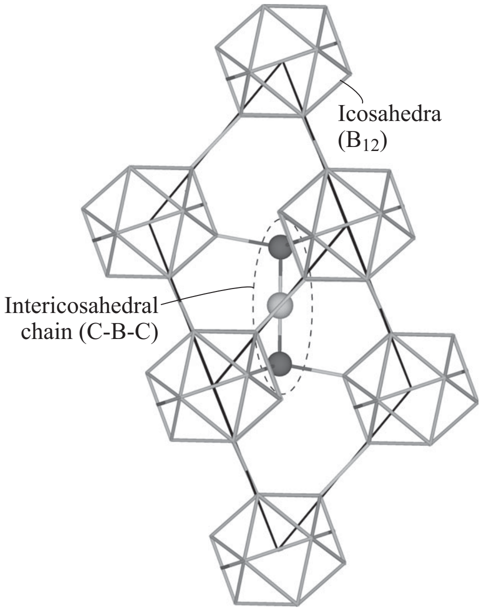

Figure G.3. Atomic structure of boron carbides. Gray and black spheres represent the boron and carbon atom, respectively. To avoid crowding, the boron atoms at the icosahedra are not shown.

potential difference ($\Delta\varphi_e$) is computed as the ratio of the charge difference (Δq) and dielectric value within a certain temperature difference (ΔT),

$$\Delta\varphi_e = \int_0^L \frac{n_e}{\epsilon_e\epsilon_\circ} = \frac{\Delta q L}{\epsilon_e\epsilon_\circ A}, \tag{G.18}$$

where n_e is the charge density, L is the distance from two junctions (hot-cold), ϵ_e is the relative permittivity, $\epsilon_\circ$ is the vacuum permittivity, and A is the cross-sectional area of the simulation cell. For simulations we use the Vienna *ab-initio* simulation package [257] modified to perform NEAIMD-energy exchange [340, 225] as

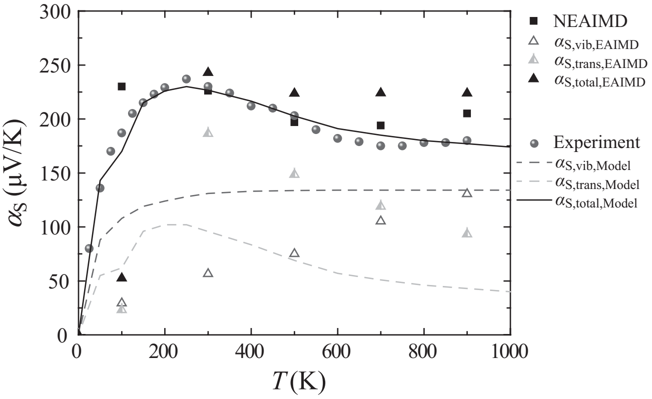

Figure G.4. The Seebeck coefficient of boron carbide (x = 1.0) as a function of temperature. NEAIMD, reported experimental results [10, 9], and analytical model [10, 9] are shown. To clarify its origins, vibration and transport components to the net Seebeck coefficient are also provided.

reported in [446, 485]. The simulations are performed on the supercell of 360 atoms, based on the experimental results for the thermally expanded lattice parameter [457]. We equilibrate each simulation using equilibrium *ab-initio* molecular dynamics (EAIMD) for 1 ps with a 0.5-fs time step. Equilibrium is followed by 22 ps of NEAIMD using a 1-fs time step. To clarify the charge associated with each atom along the simulation cell (hot to cold), Bader's analysis [188] on a charge density grid is used with a DFT charge density.

The Seebeck coefficient is finally obtained from (G.1). As shown in Figure G.4, the NEAIMD predictions of boron carbides agree with experimental results. To clarify the origin of this unusual trend of boron carbides' Seebeck coefficient, Figure G.4 also shows two phonon contributions to the Seebeck coefficient. First, reducing the local vibrational frequencies (phonon softening) increases the vibrational entropy. This entropy is from the negative derivative of the thermodynamic free energy and can be simplified using the high-temperature limit ($k_{\rm B}T \gg \hbar\omega$) and series expansions of the hyperbolic functions (see Section G.1.3). Hence, the vibrational contribution to the Seebeck coefficient is given in (G.12). In addition, some charge carriers and their interactions cause a change in net energy transfer. In boron carbides, locally induced polarons change the net energy transfer by employing deformation energy and hopping activation energy (E_a). To calculate the transport Seebeck component that is related to the phonon-assisted hopping, we start from $\alpha_{\rm S,trans,\mathit{ep}} = E_T/qT$ and (G.13). Using the binding energy relation with the local stiffness, the exact form of E_T simplifies to (G.17). Using (G.17), a simple expression for the net flow of vibrational energy, the transport contribution related to phonon-assisted hopping is calculated. In the temperature-dependent phonon density of states obtained from EAIMD and the Fourier transform of a velocity autocorrelation function over 22 ps (with 1-fs step), we observed the phonon softening of the overall frequency domain. This contribution is to the high-temperature phonon part of the Seebeck coefficient. The vibrational part ($\alpha_{\rm S,vib}$) increases as temperature increases. The other contribution (i.e., $\alpha_{\rm S,trans,\mathit{ep}}$) rises from zero, reaches a peak at about 1/3 of the relevant Debye temperature ($\sim$ 750 K), and then falls to a small value. The sum of these two contributions is in good agreement with the temperature dependence of the boron carbide Seebeck coefficient from NEAIMD and experimental data. Note that our EAIMD decomposition provides different results from those of the Emin approximation [10, 9].

Our theoretical and computational treatment demonstrates that boron carbides have a high-temperature phonon softening and phonon-assisted polaron hopping that contribute to the Seebeck coefficient. This understanding and new predictions show that this material is a good example to demonstrate phonon contributions to the Seebeck coefficient.

APPENDIX H

Monte Carlo Method for Carrier Transport

Monte Carlo (MC) is a broad term and describes an approach to solving problems that involves generating a sequence of random numbers. This approach can be used to solve the Boltzmann transport equation (BTE) for phonon, electron, fluid particle, and photon transport. At first glance, one may ask how randomness can generate a correct solution to the transport equation. However, energy carriers travel according to the scattering probabilities based on the physics, and the uniformly distributed random number decides scattering sequences using the probabilities [498].

The MC simulation is widely used to calculate electron transport and is regarded as one of the most accurate approaches for simulating device performance [294]. The semiclassical MC simulation uses randomly selected scattering mechanisms and relaxation times, which are theoretical based on the quantum mechanical Fermi golden rule (Appendix E), and the classical equations of motion for charge (e.g., electron) carrier transport between scattering events. This is equation of motion represented by

$$\frac{\mathrm{d}\mathbf{r}_e}{\mathrm{d}t} = \frac{1}{\hbar}\nabla_{\kappa_e} E_e(\kappa_e) \text{ and } \frac{\mathrm{d}\kappa_e}{\mathrm{d}t} = \frac{q\mathbf{e}_e}{\hbar}, \tag{H.1}$$

where $\boldsymbol{r}_e$ is the position, E_e is the energy, κ_e is the momentum wavevector of the simulated carrier, $\boldsymbol{e}_e$ is the electric field vector, and q is the electric charge. The energy dispersion relation, or the band structure, $E_e(\kappa_e)$, should be identified for the drift (free flight) of carriers. The random selection procedure for the scattering mechanisms can be simplified through introduction of the self-scattering mechanism [387]. Otherwise, we need the full integral form of the free-flight probability density function for all scattering mechanisms. Scattering rates are generally functions of the energy, so the overall rate [by the Matthiessen rule, 4.111] changes with carrier energy. However, with the self-scattering mechanism, we can use a constant total scattering rate ($\dot{\gamma}_{\mathrm{o}}$), and then by using only one random number, we can cover the various scattering models. This is illustrated in Figure H.1(a). The relaxation time

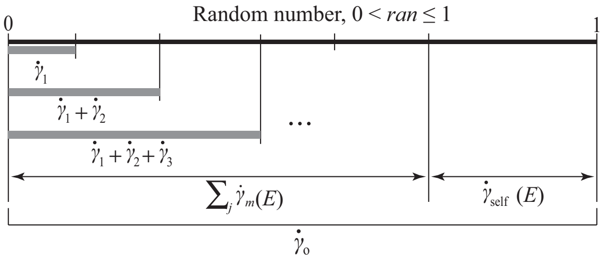
Random number, $0 < ran \le 1$
0
1
$\dot{\gamma}_1$
$\dot{\gamma}_1 + \dot{\gamma}_2$
…
$\dot{\gamma}_1 + \dot{\gamma}_2 + \dot{\gamma}_3$
$\sum_j \dot{\gamma}_m(E)$
$\dot{\gamma}_{\mathrm{self}}(E)$
$\dot{\gamma}_{\mathrm{o}}$

(a) Choice of scattering event with self-scattering

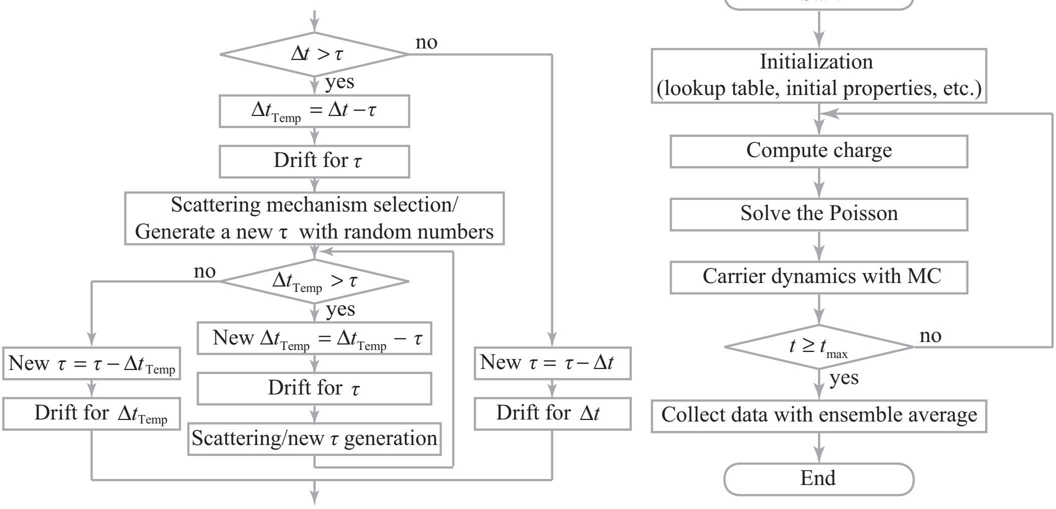
$\Delta t > \tau$
no
yes
$\Delta t_{\mathrm{Temp}} = \Delta t - \tau$
Drift for τ
Scattering mechanism selection/
Generate a new τ with random numbers
no
$\Delta t_{\mathrm{Temp}} > \tau$
yes
New $\Delta t_{\mathrm{Temp}} = \Delta t_{\mathrm{Temp}} - \tau$
Drift for τ
Scattering/new τ generation
New $\tau = \tau - \Delta t_{\mathrm{Temp}}$
Drift for Δt_{Temp}
New $\tau = \tau - \Delta t$
Drift for Δt
Start
Initialization
(lookup table, initial properties, etc.)
Compute charge
Solve the Poisson
Carrier dynamics with MC
$t \ge t_{\max}$
no
yes
Collect data with ensemble average
End

(b) Free-flight and scattering sequence for each carrier within Δt

(c) Algorithm of self-consistent ensemble MC simulation

Figure H.1. (a) Choice of scattering event. The constant scattering rate ($\dot{\gamma}_{\mathrm{o}}$) is composed of overall scattering ($\sum_{m=1}^{j} \dot{\gamma}_m$, j is the total number of possible scattering mechanisms) and the self-scattering rates ($\dot{\gamma}_{\mathrm{self}}$), $\dot{\gamma}_{\mathrm{o}} = \sum_{m=1}^{j} \dot{\gamma}_m + \dot{\gamma}_{\mathrm{self}}$. If the random number, ran, is between $\sum_{m=1}^{i-1} \dot{\gamma}_m/\dot{\gamma}_{\mathrm{o}}$ and $\sum_{m=1}^{i} \dot{\gamma}_m/\dot{\gamma}_{\mathrm{o}}$, the i-th scattering mechanism is selected. If the self-scattering is selected ($ran > \sum_{m=1}^{j} \dot{\gamma}_m$), neither energy nor momentum of the carrier changes. (b) The free-flight and scattering sequence. According to randomly assigned scattering time (τ), a carrier can be scattered or drift within a given time step (Δt). Once it finishes its free flight, a carrier is scattered with randomly selected scattering mechanism and a new scattering time is assigned to the carrier. (c) An algorithm of the self-consistent ensemble MC simulation. Electric potential and field from charge distribution are calculated by solving the Poisson equation, and carrier trajectories are simulated using the MC method with them. Carrier distribution obtained from the simulation is used to update the internal field.

of each carrier (τ) is randomly assigned (with a random number, ran) based on the constant total relaxation time as

$$\tau = -\frac{1}{\dot{\gamma}_{\mathrm{o}}} \ln(ran). \tag{H.2}$$

Each carrier is scattered or drifted during a simulation time step, and Figure H.1(b) outlines an algorithm for this process [198]. Consulting the lookup tables for scattering rates of various mechanisms can save calculation time.

In many electron transport Monte Carlo simulations – the so-called ensemble Monte Carlo simulations – a large ensemble of electrons are simulated at the same time. Then the ensemble average over a long enough time is taken for the calculation of properties such as the electric mobility. The carrier distribution influences the electric field, and the field influences the carrier trajectory, as described with the Poisson equation (Table 3.5) as

$$-\nabla \cdot (\varepsilon_o \varepsilon_e \nabla \varphi_e) = e_c n_e, \tag{H.3}$$

where ε_e is the permittivity, n_e is the charge density, and φ_e is the electric potential. The ensemble MC simulation is coupled with the Poisson equation by the iteration process – the so-called self-consistent process – to make charge distribution consistent with the field, and the field consistent with distribution as shown in Figure H.1(c). This self-consistent ensemble Monte Carlo method is widely used for device simulations [198, 211, 333, 193].

MC simulations are also applied to the BTE for phonon transport, in a similar manner to electron transport, despite the differences between these carriers [314]. The equilibrium phonon occupation number is given by the Bose-Einstein distribution, and the phonon group velocity ($u_{p,g}$) and density of states (D_p) are calculated from the phonon dispersion. Phonons travel with the group velocity and engage in scattering with other phonons, impurity, lattice boundary, electrons, and so on (as discussed in Section 4.9). The ensemble of phonon trajectories is calculated with a stochastic sampling of the scattering events. Phonons can be annihilated and created during the three-phonon interactions, which are representative of phonon scattering as normal and Umklapp processes (Table 4.2). During the Umklapp process, energy is not conserved, posing resistance in energy transport. The MC approach has been applied to phonon transport at nanoscales because of its flexibility in accounting for complicated geometries and the use of proper phonon dispersion relations and different polarization branches [497, 261, 380, 179, 215].

Fluid particles in the transitional-flow regime (Section 6.11) have been simulated with this method. As discussed in Section 6.11, both interparticle and particle-surface collisions are considered in the transition regime ($10^{-2} < \mathrm{Kn}_l < 1$, Kn_l is the Knudsen number defined as λ_f / l, where λ_f is the molecular spacing and l is the clearance distance). The MC for fluid particle transport [also called direct simulation Monte Carlo (DSMC)], treats the fluid particle motion and intermolecular collision separately, based on dilute gas assumption and the kinetic theory [40]. Thus, the DSMC method cannot be applied to dense gases or to highly ionized plasmas dominated by long-range interactions (although it is applied to weakly ionized gases with the Poisson equation to include the electric field effect [452]). This approach was first used for the homogeneous gas relaxation problem and has been used in the flow analysis, such as shock structure [38, 39].

The MC method for photon transport employs the concept of particle beam based on the radiative transfer equation (ERT) discussed in Section 7.6 and summarized in Table 7.1; it has distinct features compared to, for example, electron

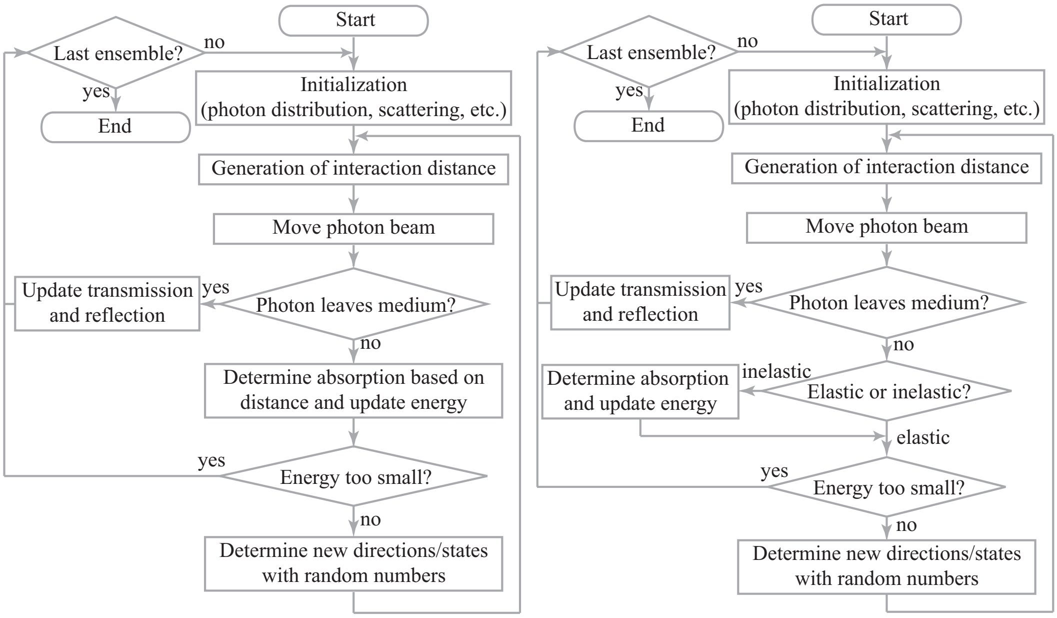
Start
Last ensemble?
no
yes
End
Initialization
(photon distribution, scattering, etc.)
Generation of interaction distance
Move photon beam
Update transmission and reflection
yes
Photon leaves medium?
no
Determine absorption based on distance and update energy
yes
Energy too small?
no
Determine new directions/states with random numbers
Start
Last ensemble?
no
yes
End
Initialization
(photon distribution, scattering, etc.)
Generation of interaction distance
Move photon beam
Update transmission and reflection
yes
Photon leaves medium?
no
Determine absorption and update energy
inelastic
Elastic or inelastic?
elastic
yes
Energy too small?
no
Determine new directions/states with random numbers

(a) Continuous slowing-down approach (CSDA) (b) Discrete inelastic scattering (DIS)

Figure H.2. Flowcharts of the MC simulation of photon transport using (a) CSDA and (b) DIS treatment. Photon beam with randomly initialized spatial distribution travels during a photon interaction time, τ_{ph}. If a photon escapes the computation domain after the free flight and the prescribed number of simulated beams is not sufficient, new photon beams are simulated. Otherwise, the photon beam is scattered and its new energy is updated (when scattering is inelastic), as well as its directions, etc. In energy absorption, if new energy after scattering is smaller than a prescribed criterion, the photon beam is regarded as annihilated and simulation for this beam is stopped.

transport [498, 428]. There are two photon transport treatments: the continuous slowing-down approach (CSDA) and the discrete inelastic scattering (DIS) approach. Both initialize photon beam (photon packet) profiles with random numbers and generally use a spatial uniform or Gaussian beam intensity distribution. The main difference between two treatments is that the CSDA treats inelastic scattering as a continuous event, so energy change corresponds to the distance traveled, but in the DIS approach, the energy change in inelastic scattering events depends on the scattering mechanism [498]. Their algorithms are described in Figure H.2 with flowcharts. They are applied to various biomedical applications for measurements of phonon transport, as well as to similar treatment of electron beam transport as in the scanning electron microscope (SEM) [428, 488, 487].

APPENDIX I

Ladder Operators

This appendix deals with the boson and fermion ladder operators (i.e., annihilation and creation operators). These operators are not only used to find, for example, the eigenspectrum of a the quantum harmonic oscillator (Section 2.6.4); they are also in the second quantization to deal with systems of identical particles, such as, bosons (symmetric particles, e.g., phonons and photons) and fermions (anti-symmetric particles, e.g., electrons). This appendix covers the basics of the second quantization (as compared to the first quantization, of which a brief description is also given here), including the Fock (number) states and the basic forms of the creation and annihilation operators and their commutators (or anti-commutators, in the case of fermion operators). Finally, the use of these operators in creating arbitrary states, the number operators, field operators, and non-interacting and interacting Hamiltonians are discussed.

When dealing with bosons (phonon and photon, symmetric) and fermions (electrons, anti-symmetric), we must represent many identical particles. Consider a simple, non-interacting Hamiltonian

$$\mathrm{H} = \sum_{i}^{N} \mathrm{H}_i, \tag{I.1}$$

where each Hamiltonian H_i generates the identical eigenspectrum ($|\mu_1\rangle$, $|\mu_2\rangle$, $\ldots$, $|\mu_j\rangle, \ldots$) for all N particles. Subscripts on μ denote the state and subscripts on $|\mu_j\rangle$ denote the particle occupying the jth state.

For example, consider a two-particle Hamiltonian with particles in the first two states. The boson and fermion states ($|\psi_\mathrm{B}\rangle$ and $|\psi_\mathrm{F}\rangle$) are

$$\begin{aligned}
|\psi\rangle_\mathrm{B} &= (|\mu_1\rangle_1|\mu_2\rangle_2 + |\mu_2\rangle_1|\mu_1\rangle_2)/2^{1/2} \\
|\psi\rangle_\mathrm{B} &= |\mu_1\rangle_1|\mu_1\rangle_2 \\
|\psi\rangle_\mathrm{B} &= |\mu_2\rangle_1|\mu_2\rangle_2 \\
|\psi\rangle_\mathrm{F} &= (|\mu_1\rangle_1|\mu_2\rangle_2 - |\mu_2\rangle_1|\mu_1\rangle_2)/2^{1/2},
\end{aligned} \tag{I.2}$$

where $|\mu_j\rangle_i$ indicates the jth state (μ) of the ith particle. Note that $|\mu_1\rangle_1|\mu_1\rangle_2$ is naturally symmetrized, such that no similar anti-symmetric system is possible (i.e., there is no equivalent fermion state since the Pauli exclusion principle holds).

This state description becomes cumbersome for many particle systems. Consider the case where N particles are evenly distributed between N states:

$$|\psi\rangle_{\mathrm{B}} = \frac{1}{(N!)^{1/2}} \sum_{ij} \mathrm{P}_{ij} |\mu_1\rangle_1 |\mu_2\rangle_2 \ldots |\mu_N\rangle_N$$

$$|\psi\rangle_{\mathrm{F}} = \frac{1}{(N!)^{1/2}} \begin{vmatrix} |\mu_1\rangle_1 & |\mu_2\rangle_1 & \ldots & |\mu_N\rangle_1 \\ |\mu_1\rangle_2 & |\mu_2\rangle_2 & \ldots & |\mu_N\rangle_2 \\ \vdots & \vdots & \ddots & \vdots \\ |\mu_1\rangle_N & |\mu_2\rangle_N & \ldots & |\mu_N\rangle_N \end{vmatrix}, \tag{I.3}$$

where P_{ij} is a permutation operator switching particle indices i and j and the fermion state is a Slater determinant [439]. (The boson representation is the permanent of a similar matrix.) Note that if two fermions are in the same state, then two columns of the determinant are identical, and the determinant is zero. Thus the fermion system state is zero, and no two particles can share a state (Pauli exclusion principle).

We introduce the second quantization to simplify these forms. Unlike the first quantization, the second quantization does not involve a profound new physical understanding, but is rather a mathematical transformation.

I.1 Fock States

In the second quantization, we represent a system by the number of particles n in each state j to create a Fock state $|n\rangle_j$. For example, consider the states in (I.2):

$$\begin{aligned} |\psi\rangle_{\mathrm{B}} &= (|\mu_1\rangle_1|\mu_2\rangle_2 + |\mu_2\rangle_1|\mu_1\rangle_2)/2^{1/2} && \rightarrow && |1_1, 1_2\rangle \\ |\psi\rangle_{\mathrm{B}} &= |\mu_1\rangle_1|\mu_1\rangle_2 && \rightarrow && |2_1 0_1\rangle \\ |\psi\rangle_{\mathrm{B}} &= |\mu_2\rangle_1|\mu_2\rangle_2 && \rightarrow && |0_1 2_2\rangle \\ |\psi\rangle_{\mathrm{F}} &= (|\mu_1\rangle_1|\mu_2\rangle_2 - |\mu_2\rangle_1|\mu_1\rangle_2)/2^{1/2} && \rightarrow && |1_1 1_2. \end{aligned} \tag{I.4}$$

Note that the fermion Fock states are either full $|1\rangle$ or empty $|0\rangle$. Extended to n particles, it becomes very easy to write, for example, the ground state

$$\begin{aligned} |\psi\rangle_{\mathrm{B}} &= |n\rangle_1 \\ |\psi\rangle_{\mathrm{F}} &= |1\rangle_1|1\rangle_2 \ldots |1\rangle_n. \end{aligned} \tag{I.5}$$

Also, note that μ may describe either a discrete state (e.g., an energy state E_μ in a potential well) or a continuous state (e.g., the wavevector $\boldsymbol{\kappa}$ or momentum $\boldsymbol{p}$ of a free particle). Furthermore, polarizations can be added, with each $\boldsymbol{\kappa}$ being paired with polarization α.

I.2 Annihilation and Creation Operators

To create and alter Fock states and define Hamiltonians (and other operators), we define the creation and annihilation operators. For electrons, phonons, and photons in state μ they are designated a_μ and $a_\mu^\dagger$, b_μ and $b_\mu^\dagger$, and c_μ and $c_\mu^\dagger$ (as in, e.g., Section 7.12.3). The photon and phonon ladder operators behave identically in the following discussion.[†] Therefore, the phonon operator (b) is used to discuss boson ladder operators.

For the bosons, the ladder operators are [15]

$$
\begin{aligned}
&\text{creation:} && b_\mu^\dagger |n\rangle_\mu = (n+1)^{1/2} |n+1\rangle_\mu \\
&\text{that is} && b_\mu^\dagger = \sum_n^\infty (n+1)^{1/2} |n+1\rangle_\mu \langle n| \\
&\text{annihilation:} && b_\mu |n\rangle_\mu = (n)^{1/2} |n-1\rangle_\mu \\
&\text{that is} && b_\mu = \sum_n^\infty n^{1/2} |n-1\rangle_\mu \langle n|. \qquad \text{(I.6)}
\end{aligned}
$$

The commutation relation is

$$
\begin{aligned}
[b_\mu, b_{\mu'}^\dagger] |n\rangle_\mu &= (b_\mu b_{\mu'}^\dagger - b_{\mu'}^\dagger b_\mu) |n\rangle_\mu \\
&= b_\mu \delta_{\mu'\mu} (n+1)^{1/2} |n+1\rangle_\mu - b_{\mu'}^\dagger n^{1/2} |n-1\rangle_\mu \\
&= \delta_{\mu'\mu} (n+1) |n\rangle_\mu - \delta_{\mu'\mu} n |n\rangle_\mu \\
&= \delta_{\mu'\mu}. \qquad \text{(I.7)}
\end{aligned}
$$

Moreover, $[b_\mu, b_{\mu'}] = [b_\mu^\dagger, b_{\mu'}^\dagger] = 0$. This commutator is used in the last step of (4.49). Note that this mirrors the commutation of the ladder operators used to find the eigenspectrum of the quantum harmonic oscillator [172], with the caveat that operators on different states commute.

For fermions the ladder operators are [15]

$$
\begin{aligned}
&\text{creation:} && a_\mu^\dagger |0\rangle_\mu = |1\rangle_\mu \\
&\text{and} && a_\mu^\dagger |1\rangle_\mu = 0 \\
&\text{that is} && a_\mu^\dagger = |1\rangle_\mu \langle 0| \\
&\text{annihilation:} && a_\mu^\dagger |1\rangle_\mu = |0\rangle_\mu \\
&\text{and} && a_\mu^\dagger |0\rangle_\mu = 0 \\
&\text{that is} && a_\mu = |0\rangle_\mu \langle 1|. \qquad \text{(I.8)}
\end{aligned}
$$

[†] When the ladder operators are derived from, for example, the position and momentum operators, there are differences in scaling. However, the ladder operators operate identically on the Fock states and can be used to define the operators, including Hamiltonians, in the same manner [142].

The anti-commutation relation takes the familiar form $\{a_\mu, a^\dagger_{\mu'}\} = a^\dagger_\mu a_\mu + a_\mu a^\dagger_\mu = \delta_{\mu,\mu'}$. Similarly, $\{b_\mu, b_{\mu'}\} = \{b^\dagger_\mu, b^\dagger_{\mu'}\} = 0$. Also, $a_\mu^2 = {a^\dagger_\mu}^2 = 0$, and $|1\rangle_\mu |1\rangle_{\mu'} = a^\dagger_\mu a^\dagger_{\mu'}|\text{vacuum}\rangle = -a^\dagger_{\mu'} a^\dagger_\mu|\text{vacuum}\rangle = |1\rangle_{\mu'}|1\rangle_\mu$ for $\mu' \neq \mu$ in order to satisfy anti-symmetry properties.

I.3 Creating Fock States, Number Operators, and Field Operators

I.3.1 Creating Fock States

To create an arbitrary boson Fock state, creation operators are repeatedly applied to a vacuum state and normalized [142]. For example,

$$|n_1, n_2\rangle_\mu = \frac{{b^\dagger_1}^{n_1} {b^\dagger_2}^{n_2}}{(n_1! n_2!)^{1/2}} |\text{vacuum}\rangle. \tag{I.9}$$

Similarly, to generate an arbitrary fermion Fock state, creation operators are applied to a vacuum state. For example,

$$|1_1, 1_2\rangle = a^\dagger_1 a^\dagger_2 |\text{vacuum}\rangle = -a^\dagger_2 a^\dagger_1 |\text{vacuum}\rangle = -|1_2, 1_1\rangle. \tag{I.10}$$

Note that the order of operators and states is important when creating fermion states.

I.3.2 Number Operators

We can also easily create number operators ($\hat{n}$) for both the bosons and fermions (subscripts B or F), which count the number of particles in each state or the total number of particles in the system (subscripts μ or T). They are

$$\begin{aligned}
\hat{n}_{\mathrm{B},\mu} &= b^\dagger_\mu b_\mu \\
\hat{n}_{\mathrm{B,T}} &= \sum_\mu \hat{n}_{\mathrm{B},\mu} \\
\hat{n}_{\mathrm{F},\mu} &= a^\dagger_\mu b_\mu \\
\hat{n}_{\mathrm{F,T}} &= \sum_\mu \hat{n}_{\mathrm{F},\mu},
\end{aligned} \tag{I.11}$$

with $\hat{n}|n\rangle = n|n\rangle$. That is, the Fock state $|n\rangle$ is an eigenvector of the number operator $\hat{n}$ with eigenvalue n.

I.3.3 Field Operators

The creation and annihilation operators typically exist in momentum space. However, it is often inconvenient to write system Hamiltonians in the momentum space, or conversely, it is more convenient to think about system evolution in position space. For these reasons, among others, we introduce the field operators [$\phi^\dagger(\boldsymbol{x})$ and

$\phi(\boldsymbol{x})$], which describe the quantum field (i.e., quantum field theory [378]). The field operators are the Fourier transform of the creation and annihilation operators for momentum state $\boldsymbol{\kappa}$. That is,

$$\phi^\dagger(\boldsymbol{x}) = \frac{1}{(2\pi)^{3/2}} \int \mathrm{d}\boldsymbol{\kappa}^3 b_{\boldsymbol{\kappa}}^\dagger e^{i\boldsymbol{k}\cdot\boldsymbol{x}}$$

$$\phi(\boldsymbol{x}) = \frac{1}{(2\pi)^{3/2}} \int \mathrm{d}\boldsymbol{\kappa}^3 b_{\boldsymbol{\kappa}} e^{i\boldsymbol{k}\cdot\boldsymbol{x}}, \tag{I.12}$$

for the boson field operators. The field operators mirror the ladder operators. (Substitute ψ for ϕ and a for b for the fermion field operators.)

In the same way that the creation and annihilation operators (of momentum state $\boldsymbol{\kappa}$) add or remove a particle from momentum state $\boldsymbol{\kappa}$, the field operators add or remove a particle from the position $\boldsymbol{x}$. In fact, this is only a naming convention to help clarify whether the formulation is in position or momentum space. Thus, the field operators maintain the same commutation (boson) and anti-commutation (fermion) relations, and the canonical commutation relations arise between both annihilation (or creation) operators (e.g., $[\phi(x), b_p] = i\hbar$).

I.4 Hamiltonians in Second Quantization

Boson and fermion systems may be classified as non-interacting (i.e., a system where the particles do not interact with each other, but may interact with, for example, a potential well) or interacting (i.e., a system where particles attract or repel each other).

Non-interacting Hamiltonians are trivial to describe in the second quantization. Consider a system of non-interacting free bosons. The Hamiltonian is

$$\mathrm{H} = \sum_{\boldsymbol{p}} \frac{\boldsymbol{p}^2}{2m} b_{\boldsymbol{p}}^\dagger b_{\boldsymbol{p}} = \sum_{\boldsymbol{p}} \frac{\boldsymbol{p}^2}{2m} \hat{n}_{\mathrm{B},\boldsymbol{p}}, \tag{I.13}$$

where $\boldsymbol{p}$ is the momentum vector. Similarly, for any non-interacting boson system the Hamiltonian can be written as

$$\mathrm{H} = \sum_{\mu} E_\mu b_\mu^\dagger b_\mu = \sum_{\mu} E_\mu \hat{n}_{\mathrm{B},\mu}, \tag{I.14}$$

where E_μ is the energy of the state μ. For example, in a system of particles trapped in a harmonic potential, $E_\mu = \hbar\omega(\mu + 1/2)$. Thus, the eigenstates of non-interacting systems are those of $\hat{n}_\mu$ (i.e., $|n\rangle_\mu$). For the equivalent fermion system, replace the number operator with its fermion counterpart.

Similar Hamiltonians, for example, are used in (4.49) in Section 4.5 and (7.170–7.172) in Section 7.12.3. These Hamiltonians describe systems of decoupled quantum harmonic oscillators, in which case the annihilation and creation operators may be derived from the polarization and/or position operator and its derivatives (e.g., in the quantum harmonic oscillator [Section 2.6.4] or in phonon wavefunction derivation [Section 4.5 and 5.15.1]). [†]

Now consider the case of an interacting boson system in the first quantization

$$
\begin{aligned}
\mathrm{H} &= \sum_i \frac{\boldsymbol{p}_i^2}{2m} + \frac{1}{2}\sum_{i,j} \varphi(\boldsymbol{x}_i, \boldsymbol{x}_j) \\
&= \int \mathrm{d}\boldsymbol{x} \sum_i |\boldsymbol{x}\rangle_i \left(\frac{-\nabla_i^2}{2m}\right)_i \langle \boldsymbol{x}| + \int\int \sum_{ij} \mathrm{d}\boldsymbol{x}\mathrm{d}\boldsymbol{x}' |\boldsymbol{x}\rangle_i |\boldsymbol{x}'\rangle_j \varphi(\boldsymbol{x}, \boldsymbol{x}')_j \langle \boldsymbol{x}'|_i \langle \boldsymbol{x}|. \qquad \text{(I.15)}
\end{aligned}
$$

By transforming to the second quantization, we eliminate the summation. That is,

$$
\mathrm{H} = \int \mathrm{d}\boldsymbol{x} \phi^\dagger(\boldsymbol{x}')\left(\frac{-\nabla_i^2}{2m}\right)\phi(\boldsymbol{x}) \qquad \text{(I.16)}
$$

$$
+ \int\int \mathrm{d}\boldsymbol{x}\mathrm{d}\boldsymbol{x}' \phi^\dagger(\boldsymbol{x}')\phi^\dagger(\boldsymbol{x}')\varphi(\boldsymbol{x}, \boldsymbol{x}')\phi(\boldsymbol{x})\phi(\boldsymbol{x}). \qquad \text{(I.17)}
$$

Equation (I.16) is the non-interacting Hamiltonian (I.13), whereas (I.17) is the interacting Hamiltonian ($\mathrm{H}_{\mathrm{int}}$). As an example, consider the short-range interaction $\varphi(\boldsymbol{x}, \boldsymbol{x}') = \varphi_o \delta^3(\boldsymbol{x} - \boldsymbol{x}')$, such that

$$
\begin{aligned}
\mathrm{H}_{\mathrm{int}} &= \frac{V_o}{2} \int \mathrm{d}\boldsymbol{x} \phi^{\dagger 2}(\boldsymbol{x})\phi^2(\boldsymbol{x}) \quad (\phi\text{–4 theory}) \\
&= \frac{V_o}{2(2\pi)^3} \sum_{\boldsymbol{k}_2, \boldsymbol{k}_1, \boldsymbol{\kappa}} b^\dagger_{\boldsymbol{\kappa}-\boldsymbol{k}_2} b^\dagger_{\boldsymbol{k}_2} b_{\boldsymbol{\kappa}-\boldsymbol{k}_1} b_{\boldsymbol{k}_1} \quad \text{(momentum space representation).} \qquad \text{(I.18)}
\end{aligned}
$$

Thus, we arrive at the potential examined in ϕ–4 theory [378], where the interaction potential is described by the field to the fourth order. The momentum space representation shows that this interaction results in the exchange of momentum between particles, which, for example, creates quantum depletion in Bose-Einstein condensates (a system of bosons with a finite fraction of particles in the ground state). That is, if we take ($\boldsymbol{\kappa} = \boldsymbol{k}_1 = 0$), the interaction annihilates particles in the ground state and creates them in excited states ($k_2 \neq 0$). [‡]

Finally, consider the Fermi surface. It is rather straightforward to demonstrate the concept in the second quantization for non-interacting fermions ($\mathrm{H} = \sum_\mu E_\mu a_\mu^\dagger a_\mu$). For $T = 0$ K, the ground state is the minimization of $\langle \mathrm{H} - \mu N \rangle$, where N is the number of particles. $\langle \mathrm{H} - \mu N \rangle = \langle \sum_k (E_\kappa - \mu) a_\kappa^\dagger a_\kappa \rangle$, and $a_\kappa^\dagger a_\kappa$ is the number operator n_κ that returns either empty (0) or full (1). Thus, to minimize the energy, μ is selected such that if $E_\kappa - \mu > 0$ then $n_\kappa = 0$, and if $E_\kappa - \mu < 0$ then $n_\kappa = 1$.

[†] The additional $1/2\hbar\omega$ that arises in the harmonic oscillator [e.g., (4.49)] sums to infinity for infinite degrees of freedom (e.g., in a field where the sum is over a continuous variable). By subtracting the same infinity ($1/2\hbar\omega$), the differences resulting from the $\hbar\omega\hat{n}$ term may be investigated. Thus, in boson and fermion formulations, the $1/2\hbar\omega$ term is often dropped [142].

[‡] A more thorough derivation of a mutually interacting system is given in [142].

Nomenclature

A boldface lowercase indicates a vector, and a boldface uppercase letter indicates a tensor; Roman letters are used when proper names are referred to.

a	interatomic spacing (lattice constant), m
a_s	speed of sound in fluids, m/s
$\boldsymbol{a}$	acceleration vector, m/s^2
$\boldsymbol{a}_e$	vector potential, A-kg/m
A	cross-sectional area, m^2
$\boldsymbol{b}_e$	magnetic field vector, V-s/m^2
c_o	speed of light in vacuum, 2.998×10^8 m/s
c_p	specific heat capacity at constant pressure, J/kg-K, or J/K
c_v	specific heat capacity at constant volume, J/kg-K, or J/K
D	Debye, units of electric dipole moment, 3.3356×10^{-30} C-m
D	diameter, m
$D_i(E)$	energy density of states, 1/m^3-eV, for carrier i
$D_i(\omega)$	frequency density of states, 1/m^3-rad/s, for carrier i
$\boldsymbol{d}$	displacement vector, m
E	energy, J
E_p	bulk modulus, Pa
$E_{\rm Y}$	Young modulus, Pa
e	specific energy, J/kg
e_c	electron charge, 1.602×10^{-19} C
$\boldsymbol{e}_e$	electric field intensity vector, V/m
Fo	Fourier number
$\boldsymbol{F}$	force vector, N
f	frequency, 1/s or Hz
f_i	probability distribution function for carrier i
g	degeneracy
$\boldsymbol{g}$	gravity vector, m/s^2
$G_{\rm N}$	Newton (gravitational) constant, 6.673×10^{11} m^3/kg-s^2

G	shear modulus, Pa
G_i	conductance of carrier i, W/K
H	Hamiltonian, J
h	enthalpy, J/kg or J/particle
h_{P}	Planck constant, 6.626×10^{-34} J-s
$\hbar$	$= h_{\mathrm{P}}/2\pi$
$\boldsymbol{h}_e$	magnetic field intensity, A/m
$I_{ph,\omega}$	spectral radiation intensity, W/m^2-(rad/s)
$\boldsymbol{j}_e$	electric current density vector, A/m^2
$\boldsymbol{j}_i$	flux vector for quantity i
$\mathbf{J}$	Jacobian matrix
$\boldsymbol{J}_i$	current vector of quantity i
k	thermal conductivity, W/m-K
k_{B}	Boltzmann constant, 1.381×10^{-23} J/K
Kn_l	Knudson number, λ_f/l
$\boldsymbol{K}$	thermal conductivity tensor, W/m-K
L	length, m
M	molecular weight, kg/kmole
$M_{i,j}$	energy interaction matrix element, J
m	mass, kg
m_e	electron mass, 9.109×10^{-31} kg
m_n	neutron mass, 1.675×10^{-27} kg
m_p	proton mass, 1.673×10^{-27} kg
m_λ	complex index of refraction $n_\lambda - i\kappa_\lambda$
n_i	number density of particle i, 1/m^3
n_λ	spectral index of refraction
$\dot{n}$	particle generation rate, 1/m^3-s
N	number of particle
N_{A}	Avogadro number, 6.022×10^{26} molecule/kmole
$N_{\mathrm{L,o}}$	Lorenz number, 2.44×10^{-8} W-Ω/K^2
p	pressure, Pa, or momentum, N-s
$\boldsymbol{p}$	momentum vector, N-s
$\boldsymbol{p}_e$	dipole moment vector, C-m
P	probability
Pe_{D}	Peclect number, $u_f D/\alpha_f$
Pr	Prandtl number, ν/α_f
Q	heat flow rate, W, or normal coordinate, m
$\boldsymbol{q}$	heat flux vector, W/m^2
q_i	charge of particle i
$\boldsymbol{r}$	radial location, m
$\boldsymbol{r}_{\mathrm{B}}$	Bohr radius, 5.292×10^{-11} m
$\boldsymbol{r}_{\mathrm{C}}$	Compton radius, 2.8179×10^{-15} m
R	resonance
R_g	universal gas constant, 8.3145×10^{3} J/kmol-K

R_t	thermal resistance, K/W
Re_D	Reynolds number, $u_f D/\nu_f$
Ry	Rydberg constant, 1.0974×10^{-5} cm^{-1}, also unit of energy, 13.606 eV
$\dot{S}$	energy conversion rate, W
S	entropy, J/K, or quantum angular momentum spin J-s
$\dot{s}$	volumetric energy conversion rate, $\mathrm{W/m}^3$
$\boldsymbol{s}$	unit vector
$\boldsymbol{s}_e$	Poynting vector, $\mathrm{W/m}^2$
t	time, s
T	temperature, K
$\boldsymbol{u}$	velocity vector, m/s
$\boldsymbol{u}_f$	fluid velocity vector, m/s
V	volume, m^3
$\boldsymbol{\omega}$	heat current vector, W-m
$\boldsymbol{x}$	location, or position vector, m
x, y, z	Cartesian coordinate, m
z	atomic number
Z	partition function
z_e	number of conduction electrons per atom
Z_e	thermoelectric figure of merit, 1/K

Greek

α	diffusivity $= k/\rho c_p$, m^2/s, or fine-structure constant, 7.29735×10^{-3}
α_e	molecular polarization
α_{ph}	photon absorptivity
$\dot{\gamma}_{ad}, \dot{\gamma}_{de}$	adsorption and desorption rate coefficients, $1/\mathrm{m}^3$-s
$\dot{\gamma}_{i,j}$	interaction between carriers i and j, or transition rate between state i and j, 1/s
γ	specific heat capacities ratio, $c_{f,p}/c_{f,v}$
γ_G	Grüneisen constant (or parameter)
Γ	spring constant, N/m
Γ	gamma function
$\delta_\mathrm{D}(E)$	Dirac delta function, 1/J
δ_{ij}	Kronecker delta, $\delta_{ij}(i = j) = 1$, $\delta_{ij}(i \neq j) = 0$.
ϵ_e	electric permittivity (dielectric function)
ϵ_o	free-space electric permittivity, 8.854×10^{-12} A^2-s^2/N-m^2
ϵ_{ph}	emissivity
$\epsilon_{f,t}$	turbulent kinetic energy dissipation rate, $\mathrm{m}^2/\mathrm{s}^3$
η	efficiency
κ	wave number, $\kappa = 2\pi/\lambda$, 1/m
κ_λ	spectral index of extinction
κ_p	isothermal compressibility, Pa^{-1}
$\boldsymbol{\kappa}$	wave vector, 1/m
λ	wavelength, m
λ_i	mean free path of carrier i, m

μ	chemical potential, J/kg, or J/particle, or dynamical viscosity, Pa-s
μ_e	magnetic permeability, N/A^2
$\boldsymbol{\mu}_e$	transition dipole moment, C-m
μ_o	free-space magnetic permeability, 1.257×10^{-6} N/A^2
ν_P	Poisson ratio
ν_f	fluid kinematic viscosity, μ_f/ρ_f, m^2/s
ρ	density, kg/m^3
ρ_e	electrical resistivity, Ω-m
ρ_r	reflectivity
σ_i	absorption coefficient for carrier i, 1/m
σ_e	electrical conductivity, 1/Ω-m
σ_SB	Stefan–Boltzmann constant, 5.670×10^{-8} W/m^2-K^4
τ_a	atomic time scale, 2.4189×10^{-17} s
$\tau_{i\text{-}j}$	relaxation time from interaction between i and j, s
$\tau_{i,j}$	stress tensor component, Pa
τ_r	transmissivity
φ	potential energy, J
Ψ	time-dependent wave function, m$^{-3/2}$
ψ	time-independent wave function, m$^{-3/2}$
Ω	solid angle, sr
ω	angular frequency, $\omega = 2\pi f$, rad/s

Subscripts

A	acoustic
b	blackbody
B	Bohr, or Boltzmann
c	conduction
C	Coulombic, or Compton
C–P	Cahill–Pohl
dB	de Broglie
D	Debye, or Dirac
E	Einstein
e	electron, or electromagnetic, or emission
fm	free molecular
f	fluid particle, fluctuation
F	Fermi
g	group, or gap
G	Grüneisen
h	hole
i	incident, carrier
k	conduction
ku	surface convection
K	Kolmogoroff
l	laminar, or based on length l

L	longitudinal, or Lorenz
LJ	Lennard–Jones
m	molecular
MD	molecular dynamics
n	normal
N	Newton
o	reference value
O	optical
P	Planck, or Peltier, or Poisson
p	phonon, or potential energy, or constant pressure
ph	photon
r	radiation
sp	spontaneous
st	stimulated
s	static
S	Seebeck, or Slack
T	thermal
T	Thomson, or transverse
t	turbulent
tr	transition, or turbulent fluctuation
u	convection
v	valence
Y	Young
α	polarity, or diffusion
ω	frequency
μ	viscous

Superscripts

$'$	turbulent fluctuation
$*$	dimensionless (scaled)
o	equilibrium value
$\dagger$	complex conjugate, or Hermitian conjugate

Others

$\langle\ \rangle$	ensemble average, or spatial average
$-$	time average, or average
$\sim$	nearly
$\propto$	proportional
$O(\ )$	order of magnitude
Δ	difference
$\nabla\cdot$	divergence
∇	gradient
$\partial/\partial t$	time derivative

Abbreviations

AMM	acoustic mismatch model
BCC	body-centered cubic
BDC	1, 4-benzenedicarboxylate
B–K–S	van Beest–Krammer-van Staten
BTE	Boltzmann transport equation
BZBC	Brillouin zone boundary condition
C–P	Cahill–Pohl
DCF	displacement correlation function
DFT	density function theory
DMM	diffuse mismatch model
DOS	density of states
EF	exponential-fit
EM	electromagnetic
ERT	equation of radiative transfer
FAU	faujasite (a zeolite)
FCC	face-centered cubic
FD	first-dip
FGR	Fermi golden rule
fm	free-molecular
GGA	generalized gradient approximation
G–K	Green–Kubo
GTO	Gaussian-type orbital
HCACF	heat current autocorrelation function
HFSS	high-frequency structure simulator
L–J	Lennard–Jones
LA	longitudinal-acoustic
LAPW	linearized augmented plane wave
LCAO	linear combination of atomic orbitals
LDA	local density approximation
LTA	zeolite A (Linde Type A)
LO	longitudinal-optical

M–B	Maxwell–Boltzmann
MD	molecular dynamics
MHD	magnetohydrodynamics
MOF	metal-organic framework
MSD	mean-square displacement
MSRD	mean-square relative displacement
MWNT	multiwall nanotube
NIR	near-infrared regime
NMR	nuclear magnetic resonance
pdf	probability density function
PV	photovoltaic
QC	quadratic convergence
QD	quantum dot
QED	quantum electrodynamics
QW	quantum well
RDF	radial distribution function
RMS	root-mean-square
SC	simple cubic
SCF	self-consistent function
SI	*Systeme International* (system standardizing abbreviations of units)
SMRT	single-mode relaxation time
SOD	sodalite (a zeolite)
SOMO	singly occupied molecular orbital
S–W	Stillenger–Weber
TA	transverse-acoustic
TE	thermoelectric
TDDFT	time-dependent density function theory
TO	transverse-optical
W–K–B	Wentzel–Kramers–Brillouin
YAG	yttria–aluminum–garnet

Glossary

Adiabatic (Born–Oppenheimer) approximation: A technique used to decouple the motion of nuclei and electrons (i.e., separate the variables corresponding to the nuclear and electronic coordinates in the Schrödinger equation associated to the molecular Hamiltonian). It is based on the fact that typical electronic velocities far exceed those of nuclei.

Anti-Stokes emission: When the frequency of emitted photon is equal or larger than the exciting (absorbed) photon. The extra energy can be contributed from phonon absorption (lattice vibration) or from molecular kinetic energy.

Auger effect: One of two principal processes for relaxation of inner-shell electron vacancy in an excited or ionized atom. It is a two-electron process in which an electron makes a discrete transition from a less bound shell to the vacant but tightly bound electron shell. The energy gained in this process is transferred, by means of electron static interaction, to another bound electron, which then escapes from the atom (called the Auger electron).

Ballistic transport: The motion of electrons in ultrasmall (highly confined) regions in semiconductor structures at very high electric field with velocities much higher than their equilibrium thermal velocity. The ballistic electrons are not subjected to scattering, so they can move with ultrahigh velocity. The ballistic transport is determined by the electronic structure of the semiconductor and is different for different semiconductors and this allows ultrafast devices. Ballistic transport is also extended to other microscale energy carriers, indicating transport with no scattering.

Bandgap energy: The energy difference between the bottom of the conduction band and the top of the valence band in a semiconductor or an insulator.

Bloch theorem: This theorem states that the eigenfunction of the Schrödinger equation for a periodic potential is the product of a plane wave times a function that has the same periodicity as the periodic potential.

Bloch wave: A description of an electron in a crystal that takes account of the periodic potential of the positive ions. A free-electron wave, e.g., $\exp[i(\boldsymbol{\kappa} \cdot \boldsymbol{x})]$ is modulated near each atom of the lattice by a periodic potential function $a_{\boldsymbol{\kappa}}(\boldsymbol{x})$. The

Bloch wave is thus represented by

$$\psi_{\kappa}(\boldsymbol{x}) = a_{\kappa}(\boldsymbol{x}) \exp[i(\boldsymbol{\kappa} \cdot \boldsymbol{x})].$$

Bloch showed that the periodic field of the crystal lattice neither scatters nor destroys the free-electron wave, but modulates it.

Boson: A class of particles of the associated with forces, obeying Bose–Einstein statistics.

Bravais lattice: Periodic array in which the repeated units (single or multiatom) of a crystal are arranged. The atoms are presented as points and the infinite array of these discrete points appears exactly the same when viewed from any atom (translational symmetry).

Bose–Einstein condensate: A phase transition at low temperature and high density, corresponding to a phase-space density of

$$n_f \lambda_{\text{dB}}^3 = 2.612,$$

where n_f is the fluid particle number density and λ_{dB} is the de Broglie wavelength (6.10). At this state, a gas of atoms undergoes transition to the Bose–Einstein condensate, which is the lowest accessible quantum state and a new form of matter.

Bremsstrahlung: German word for decelerating radiation. It describes photon emission (or absorption) when a free electron undergoes momentum (energy) change.

Brillouin scattering: Interaction of light in a medium with density variations that change its path. The density variations may be due to acoustic modes (traveling sound waves) or temperature gradient. When the medium is compressed, the index of refraction of light in the medium changes and its path bends. From quantum mechanics, Brillouin scattering is interaction of photons with acoustic phonons. The scattered light wavelength is changed slightly by a variable quantity known as the Brillouin shift.

Brillouin zone: Polyhedral zone in a crystal lattice used to define the frequency or energy of wave motion.

Chirality: The property of an object that cannot be superimposed on its mirror image.

Cohesive energy: The energy of a solid that is required for disassembling it into its constituent parts.

Compton scattering: An increase in the wavelength of a photon (X-ray and γ-ray regimes) due to absorption by free electrons (thus increasing the kinetic energy of the electrons).

Conduction band: A vacant or only partially occupied set of many closely spaced electronic levels resulting from an array of a large number of atoms forming a system in which the electrons can move freely or nearly so.

Cooperative processes: Summing of quanta of energy by the interaction of excited particles resulting in accumulation of excitation energy in one of them. For particles A and B the excitation energy can pass as $\ldots - A^* - A - B - \ldots \rightarrow - A - A - B^* - \ldots$.

Creation and annihilation operators: Creation $a^\dagger$ (annihilation a) operator is the operator in quantum field theory that increases (lowers) the number of particles in a given state by one (i.e., adjacent eigenfunctions of a particle wave function). In the context of the quantum harmonic oscillator, the ladder operators are the creation and annihilation operators, adding or subtracting fixed quanta of energy to the oscillator system. Creation/annihilation operators are different for bosons (integer spin) and fermions (half-integer spin). This is because their wave functions have different symmetry properties.

de Broglie wavelength: A wave associated with an electron (or other quasi-particles) in motion that gives it diffraction and interference characteristics. de Broglie suggested the wave nature of electrons with the momentum given by $\boldsymbol{p} = \hbar\boldsymbol{\kappa}$, where κ is the wave number ($2\pi\lambda$, where $\lambda = h_\mathrm{P}/p = h_\mathrm{P}/mu$ is the wavelength). The thermal de Broglie wavelength use the average thermal momentum $p = (mk_\mathrm{B}T)^{1/2}$, i.e.,

$$\lambda_\mathrm{dB}(\text{thermal}) = (\frac{h_\mathrm{P}^2}{2\pi mk_\mathrm{B}T})^{1/2}.$$

Debye temperature: The temperature corresponding to the crystals highest normal mode of vibration (frequency f_D), i.e., the highest temperature that can be achieved that is due to a single normal vibration f_D and is given by

$$T_\mathrm{D} = h_\mathrm{P} f_\mathrm{D}/k_\mathrm{B}.$$

The Debye temperature is related to atomic force constant and lattice structure as given by (4.161). The value of T_D for elemental solids is given in Table A.2, and for some compounds in Figure 4.26.

Degenerate energy state: Existing in two or more quantum states with the same energy level.

Density of states (DOS): the distribution of a fixed amount of energy among a number of identical particles depends in part on the density of available energy states D_i. The probability that a given energy state will be occupied is given by the distribution function f_i, but if there are more available energy states in a given energy interval, will give greater weight to the probability for that energy interval, i.e.,

$$n_i(E_i) = D_i(E_i) f_i(E_i)\mathrm{d}E_i, \ i = p, e, f, i,$$

where n_i is the number of particles per unit volume with energy E_i to $E_i + \Delta E_i$, $D_i(E)$ is the energy DOS (number of energy states per unit volume in interval ΔE_i), and f_i is the probability distribution function for energy E_i. The density of states depends on the atomic structure of the matter influencing the particular carrier.

The wave number DOS is given by the general expression for spherical energy surfaces as

$$D_i(\kappa)\mathrm{d}\kappa = \frac{4\pi\kappa^2}{(2\pi)^3}\mathrm{d}\kappa.$$

There is also the frequency DOS $Di(\omega)$. The relation between E_i (or ω) and κ is called the dispersion relation $E_i(\kappa)$, [or $\omega_i(\kappa)$], and depends on the particular carrier.

Dirac delta function: This function represents any point action, i.e., action that is highly localized in space and/or time. For interactions involving an energy match requirement, the energy Dirac delta function is defined as

$$\delta_{\rm D}(E-E_i)=0 \text{ for } E\neq E_i,$$

$$\text{and } \delta_{\rm D}(E-E_i)\rightarrow\infty \text{ for } E=E_i,$$

$$\text{and } \int_0^\infty \delta_{\rm D}(E-E_i){\rm d}E=1.$$

Note that $\delta_{\rm D}(E)$ has the unit of inverse energy.[†] Also note that as given by (3.28) and (5.65), the energy integral of the energy Dirac delta function gives the energy DOS.

Dispersion: The frequency or mode dependence of the phase velocity in a medium. The chromatic dispersion of an optical medium is basically the frequency dependence of the phase velocity with which a wave propagates in the medium. More precisely, one defines dispersion of second and higher orders by means of the Taylor expansion of the wave number as a function of the angular frequency ω (around $\omega_{\rm o}$):

$$\kappa(\omega)=\kappa_{\rm o}+\frac{\partial\kappa}{\partial\omega}(\omega-\omega_{\rm o})+\frac{1}{2}\frac{\partial^2\kappa}{\partial\omega^2}(\omega-\omega_{\rm o})^2+\frac{1}{6}\frac{\partial^3\kappa}{\partial\omega^3}(\omega-\omega_{\rm o})^3,$$

where the zeroth-order term describes a common phase shift. The first-order term contains the inverse group velocity and describes an overall time delay without an effect on the pulse shape. The second-order term contains the second-order dispersion (group delay dispersion per unit length). The third-order term contains the third-order dispersion per unit length. The second-order dispersion is often specified in units of $\rm s^2/m$, and is the derivative of the inverse group velocity with respect to the angular frequency. The normal dispersion refers to $\partial^2\kappa/\partial\omega^2>0$ (negative values are called anomalous).

Distinguishable and indistinguishable particles: Particles are considered to be indistinguishable if their wave packets overlap significantly. Two particles can be considered to be distinguishable if their separation is large compared with their de Broglie wavelength.

[†] The Fourier transfer of $F(\kappa)=1$ is

$$f(x)=\int_{-\infty}^{\infty}F(\kappa)e^{i\kappa x}{\rm d}\kappa=\int_{-\infty}^{\infty}e^{i\kappa x}{\rm d}\kappa.$$

Taking the inverse, we have

$$1=\frac{1}{2\pi}\int_{-\infty}^{\infty}f(x)e^{-i\kappa x}{\rm d}x.$$

Then $f(x)$ is zero when $x\neq 0$, and $f(x)$ tends to infinity for $x=0$. Then, using the Dirac delta function, we have

$$\int_{-\infty}^{\infty}f(x)\delta_{\rm D}(x-x_{\rm o}){\rm d}x=f(x_{\rm o}).$$

Note that in the energy Dirac delta function $f(E)$ is equal to 1.

Dopant: In semiconductors a dopant results from introducing impurities into the intrinsic (pure) phase to change its thermoelectric properties. A lightly and moderately doped semiconductor is referred to as extrinsic. A semiconductor that is doped to such high levels that it acts more like a conductor than a semiconductor is called degenerate. For the group 14 semiconductors such as Si or Ge, the most common dopants are group 13 or group 15 elements. Group 13 dopants are electron acceptors (because they are missing the fourth valence electron) and this creates holes; are called the p-type dopants. Group 15 dopants are electron donors, adding extra valence electrons which become unbonded (conduction electrons) from individual atoms and allow the compound to be electrically conductive, and are called the n-type dopants. Heavy (or high) doping refers to the order-of-1 dopant atoms per 10^4 of host atoms. This is often shown as n^+ for n-type doping or p^+ for p-type doping. Dopants are also added to dielectrics (such as oxides).

Drude electron transport model: This model assumes that the conduction electrons (a) do not interact with the cations (free-electron approximation), except for collisions, in which the velocity of the electron abruptly and randomly changes direction as a result of collision (relaxation time approximation), (b) maintain thermal equilibrium through collisions (classical statistics approximation), and (c) do not interact with each other (independent electron approximation).

Effective electron mass: The effective mass of a particle is its apparent mass in the semiclassical model of transport in a crystal. Electrons and holes in a crystal respond to electric and magnetic fields almost as if they were free particles in a vacuum, but with a different mass. This is a fraction of the free-electron mass m_e. Effective mass is defined by analogy with the Newton second law $\boldsymbol{F} = m\boldsymbol{a}$. Using quantum mechanics it can be shown (Chapter 5) that for an electron in an external electric field $\boldsymbol{e}_e$

$$\boldsymbol{a} = \frac{1}{\hbar^2}\frac{\mathrm{d}^2 E_e}{\mathrm{d}\kappa^2} e_c \boldsymbol{e}_e \equiv \frac{\boldsymbol{F}}{m_{e,e}}.$$

Also, in an external electric field, the electron would experience a force of $\boldsymbol{F} = m_{e,e} e_c \boldsymbol{e}_e$, where e_c is the charge. Then the electron effective mass $m_{e,e}$ becomes

$$m_{e,e} = \hbar^2 (\frac{\mathrm{d}^2 E_e}{\mathrm{d}\kappa^2})^{-1}.$$

Elastic collision (scattering): Scattering of an energy carrier by another energy carrier or by other entities (e.g., impurities, in solids) that leaves the energy of the carrier unchanged after the event. For example, impurity scattering and acoustic-phonon scattering of electrons in solids are generally treated as elastic scattering.

Electron bandgap: Under the periodic potential in crystals, electron energy gaps are formed by electrons with localized (nonpropagating) wave functions as opposed to those of electrons in allowed bands that have extended (propagating) wave functions. Bandgap energy is defined by use of this localization as the energy needed to remove an electron from a bond in the solid, enabling the electron to move freely through the solid to conduct electricity.

Electron volt: An amount of energy gained by an unbound electron when accelerated through a static potential of one volt.

Energy relaxation time: The time required for dissipating the carrier energy.

Ergodic hypothesis: This hypothesis states that the time-average behavior of an individual particle in a system is equal to the ensemble-average behavior of the system.

Evanescent wave: Evanescent means tending to vanish, and the intensity of evanescent waves decays exponentially (rather than sinusoidally) with distance from the interface at which they are formed (the wave number is purely imaginary). Evanescent waves are formed when sinusoidal waves are (internally) reflected at an interface at an angle greater than the critical angle so that total internal reflection occurs.

Exciton: The combination of an electron and a hole in an excited semiconductor crystal. An exciton consists of a single electron and a single hole bound by the Coulomb force.

Fermi energy or Fermi level: The energy of the highest occupied energy state of a system of fermions at $T = 0$ K. It is equal to the chemical potential of electrons in a solid (metals, semiconductors, or insulators) or in an electrolyte solution at $T = 0$ K. However, the chemical potential is temperature dependent. For conduction electrons, using a constant chemical potential energy results in negligible error.

Fermi golden rule: This rule states that the electronic transition rate depends on the strength of the coupling between the initial and final states of a system and also depends on the number of ways the transition can occur. This is stated by (3.28). The transition probability is also called the decay probability. A transition will proceed more rapidly if the coupling between the initial and final states is stronger. This coupling term is called the matrix element for the transition and comes from an alternative formulation of quantum mechanics in terms of matrices rather than the differential equations (i.e., Schrödinger approach). The matrix element can be placed in an integral form, in which the interaction that causes the transition is expressed as a Hamiltonian that operates on the initial state wave function. This is stated by (3.29). The transition probability is proportional to the square of the integral of this interaction over the appropriate space.

Fermi surface: The surface of constant electron energy in $\boldsymbol{\kappa}$ (wave-number vector) space. The Fermi surface separates the unfilled orbitals from the filled orbitals at absolute zero. The electrical properties of the metal are determined by the shape of the Fermi surface, because the current is due to changes in the occupancy of states near the Fermi surfaces. The free-electron Fermi surfaces are developed from spheres of radius κ_{F} determined by the valence electron concentration.

Fermion: A class of particles, which unlike bosons, are usually associated with matter and obey the Fermi–Dirac statistics.

Feynman diagram: This diagram visualizes quantum-electrodynamical interactions with lines and vertices (meeting of lines) and is used to derive the probability rate for the interactions (e.g., Fermi golden rule for weak interactions). For example, the single-phonon only (radiationless) electronic transition (absorption and emission) is shown as in the figure.

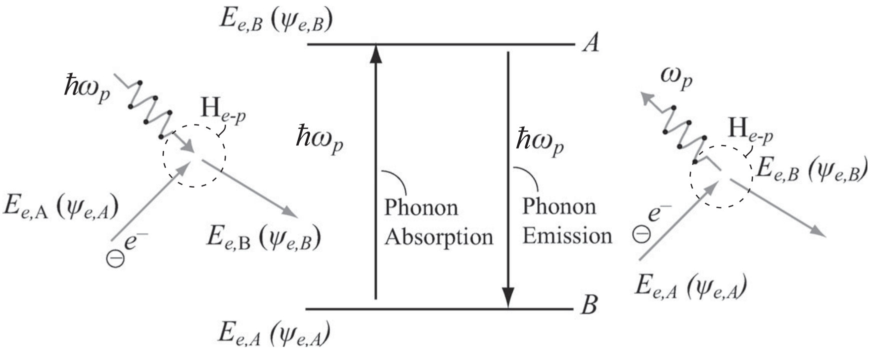

Feynman diagram for nonradiation (phonon absorption/emission) two-level electronic transition. $\mathrm{H}_{e\text{-}p}$ is the electron–phonon interaction Hamiltonian.

Field emission: Emission of electrons and ions by metals (filament) in the presence of an electric field.

Fluid particle: Charged or neutral atoms or molecules in a fluid state undergoing thermal motion (each particle undergoing random, translational, rotational, and vibrational motions representing their kinetic energy and temperature) with or without a net motion (under external force, such as gravitational field, pressure gradient, or electromagnetic field). The simplest treatment of fluid particle transport assumes particles in classical (Newtonian–Hamiltonian), translational thermal motion (Boltzmann theory of gases), subject to the statistical averaging.

Fluorescence: Visible photon emission that is due to X-rays or ultraviolet photon absorption. Fluorescence ends when the source is removed.

Group theory in quantum mechanics: In quantum-mechanical mathematical operations, matrices act on members of a vector space, and only certain members of the space that are symmetrical (with classified symmetry) can be created as described by the group theory theorems.

Grüneisen parameter: Is a dimensionless constant representing the dependence of vibrational frequencies of solid (shift in Debye frequency) on its volume; it is related to the bulk thermodynamic properties through

$$\gamma_{\mathrm{G}} = \frac{3\beta E_p}{\rho c_{v,p}},$$

where β is the linear thermal expansion coefficient and E_p is the isothermal bulk modulus. Section 4.11.2 gives the theoretical prediction and Table A.2 lists the experimental values of γ_{G} for elemental solids and Figure 4.27 for some compounds. The Grüneisen relation can be written as

$$\frac{\partial p}{\partial T}\ |_V\ V = \gamma_{\mathrm{G}} \frac{\partial E}{\partial T}\ |_V,$$

or when integrated as the Grüneisen equation of states for cubic solids it becomes,

$$p(T, V)V = \gamma_G[E(T, V) + G(V)],$$

where E is the phonon energy, and $G(V)$ is called the integration constant. An example of $G(V)$ is

$$G(V) = -A[(\frac{V_o}{V})^{m/3} - (\frac{V_o}{V})^{n/3}],$$

where A, m, and n (4.144) are the L–J potential parameters (Section 4.11.2). The internal energy is $E = E_{\text{elastic}} + \sum_{\kappa,\alpha} \hbar\omega_{\kappa,\alpha}(f_{p,\kappa,\alpha} + 1/2)$.

The modal Grüneisen constant (or parameter) is defined as

$$\gamma_{G,\kappa,\alpha} = -\frac{V}{\omega_{\kappa,\alpha}}\frac{\partial\omega_{\kappa,\alpha}}{\partial V} = -\frac{\partial \ln \omega_{\kappa,\alpha}}{\partial \ln V},$$

where α is the polarization. In the Debye approximation, can have

$$\gamma_{G,\kappa,\alpha} = \gamma_G = -\frac{V}{\omega_D}\frac{\partial\omega_D}{\partial V} = -\frac{\partial \ln \omega_D}{\partial \ln V} \quad \text{Debye approximation.}$$

γ_G is a measure of anharmonicity in a material.

Hamiltonian: Is a function describing the state of a mechanical system in terms of position and momentum (classical mechanics), and in quantum mechanics the Hamiltonian is an operator corresponding to the total energy of a system.

Inelastic collision: A collision between two particles in which part of their kinetic energy is transformed to another form of energy.

Inelastic scattering: The scattering of particle resulting from inelastic collision.

Ionic crystals: Crystals with at least two atoms in their lattice, which are ionized (with zero total charge). The binding is mostly electrostatic, isotropic, and strong. Ionic crystals are insulators (no conduction electron).

Kapitza resistance: In the presence of a heat current there is a discontinuity in temperature at an interface between two different materials, i.e., the interfaces possess a finite thermal resistance known as the Kapitza resistance.

Kinetics: The mechanism by which a physical or chemical change is affected. The microscale energy transformation kinetics describes mechanisms of the energy transition/conversion rate.

Kinetic theory: Particles in thermal motion involving interparticle collisions with the RMS of this thermal velocity being related to the temperature.

Kirchhoff law of radiation: Under local thermal equilibrium (the photon energy distribution function follows the boson distribution), the directional, spectral emissivity of a body is equal to its directional, spectral absorptivity at the same temperature.

Luminescence: Visible photon emission that is not due to thermal radiation emission; this includes phosphorescence and fluorescence.

Magnon: A collective excitation of the electron spin structure in a crystal lattice, i.e., a quantized spin wave.

Master equation: A phenomenological set of first-order differential equations describing time evolution of the probability of a system (similar to the Fokker-Planck equation in Table 3.8) occupying each one of a discrete set of states

$$\frac{\partial P_k}{\partial t} = \sum_l T_{kl} P_l,$$

where P_k is the probability for the system to be in the state k, while the matrix element T_{kl} the k-l transition rate.

Momentum relaxation time: The time required for randomizing the carrier momentum.

n- and p-type semiconductors: Addition of a small atomic percentage of dopant (electron donor and acceptor) atoms in the regular crystal lattice of semiconductor changes the weakly bound outer-shell electrons resulting in significant change in their electrical properties, producing n-type and p-type semiconductors. Group 15 impurity atoms with 5 valence electrons (donors) produce n-type semiconductors by contributing extra electrons. Group 13 impurity (dopant) atoms with 3 valence electrons (acceptors) produce p-type semiconductors by producing a hole (or electron deficiency). Thus the holes are the majority carriers, whereas electrons are the minority carriers in p-type semiconductors, and vice versa. The intrinsic (undoped) semiconductor is called i-type.

Normal displacement coordinates: Normal coordinates comprise a set of coordinates for a coupled system such that the equations of motion each involve one of these coordinates. In lattice displacement, the normal displacement coordinate is a Fourier transform of the lattice displacement and is a complex quantity variable.

Pauli exclusion principle: No two identical fermions may occupy the same quantum state simultaneously. For elements, no two electrons have the same four quantum numbers (n, l, m, and s, Section 2.6.6).

Particle probability distribution function: The probability that a particle is in an energy state E, and is the continuous generalization of discrete probability. There are three distributions, Maxwell–Boltzmann (classical), Bose–Einstein (boson), and Fermi–Dirac (fermion). The distribution functions scale E with $k_{\rm B}T$ and show that the larger $E/k_{\rm B}T$ has a lower probability.

Phonon drag on electron: This refers to the increase in the effective mass of conduction electrons due to its field interactions with the crystal lattice. It also refers to electron–phonon (lattice) inelastic scattering under lack of local thermal equilibrium between the two carriers. At low temperatures (around $0.2T_{\rm D}$, where $T_{\rm D}$ is the Debye temperature), the nonequilibrium distribution of phonons plays a more significant role in electron–phonon scattering and in thermoelectricity this particularly affects the Seebeck coefficient, as phonons force the electrons to move under a temperature gradient.

Phonon gas: A crystal lattice at zero temperature lies in its ground state, and contains no phonons. According to thermodynamics, when the lattice is held at a nonzero temperature its energy is not constant, but fluctuates randomly about some mean value. These energy fluctuations are caused by random lattice vibrations, which can be viewed as a gas of phonons. Because these phonons are generated by the temperature of the lattice, they are sometimes referred to as thermal phonons. Unlike the atoms that make up an ordinary gas, thermal phonons can be created or destroyed by random energy fluctuations. Their behavior is similar to that of the photon gas produced by an electromagnetic cavity, wherein photons may be emitted or absorbed by the cavity walls. This similarity is not coincidental for it turns out that the electromagnetic field (boson) behaves like a set of harmonic oscillators. Both gases obey the Bose–Einstein statistics.

Phonon polariton: The propagating electromagnetic waves coupled to polar optical phonon. For example, the high-frequency dielectric properties are closely related to the optical-phonon modes at THz frequency.

Phosphor: A substance that exhibits the phenomenon of phosphorescence. Transition metal compounds and rare-earth compounds are among phosphors.

Phosphorescence: Visible photon emission that is due to X-ray or ultraviolet photon absorption. Phosphorescence continues for a period of time after the source is removed.

Plasma frequency: The natural frequency of oscillations of electrons in a plasma displaced relative to the ion background; the waves with frequency below the plasma frequency cannot propagate in the plasma.

Plasmon: A quasi-particle resulting from oscillation of plasma (free-electron gas). Plasmons can couple with photon to create plasma polariton.

Polariton: A quasi-particle resulting from coupling of light (photon) with an interacting resonance. Phonon-polariton results from coupling of infrared photon and optical phonon. Exciton-polaiton is coupling of visible light and exciton.

Polaron: A quasi-particle composed of an electron and its accompanying polarization field. In electron–phonon coupling, the electron moving through the crystal carries with it the lattice distortion (polarization) it causes.

Polar and nonpolar semiconductors: In nonpolar semiconductors the longitudinal-optical and the transverse-optical branches of phonon dispersion have the same frequency at the zone center Γ, and in polar semiconductors these two branches split (because of long-range dipolar interactions).

Polar molecules: Molecules in which there exists a permanent spatial separation of the centroid of positive and negative charge or dipole moment.

Potential energy: The energy in matter that is due to its position or the arrangement of its parts. The potential energy appears in gravitational potential, elastic potential, chemical (interatomic) potential, electrical potential, etc.

Primitive cell: A cell that when translated in space will fill the space without overlapping.

Pseudopotential: Effective potential for electrons in a crystal lattice that is calculated in the orthogonalized plane-wave method and in the pseudopotential method. This is a weak potential, because the electrons move rapidly past nuclei in the lattice.

Quantum Hamiltonian: The physical state (total energy) of a system, which may be characterized as a ray in an abstract Hilbert space (or, in the case of ensembles, as a trace class operator with trace 1). It generates the time evolution of quantum states.

Quasi-particle: Is part of the quantum many-body mechanics and presents the combination of a particle and its influence on the local environment, i.e., phonons are treated as quasi-particles with the renormalized self-interactions incorporated into it. Also, in the renormalization of all of the interactions that a single electron (or hole) experiences in a periodic lattice, into self-energy, using an effective mass, the electron is treated as a quasi-particle.

Quantum mechanics: A physical theory that at very small distances produces results that are very different and much more accurate than the results of the classical mechanics. It is derived from a small set of basic principles and applies to at least three general types of phenomena that classical mechanics and classical electrodynamics cannot account for, namely quantization, wave–particle duality (interference of matter particles), and quantum entanglement.

Raman scattering: An inelastic scattering of a photon that creates or annihilates a phonon (and other molecular motion transitions), giving rise to the Stokes and anti-Stokes lines in the scattered spectrum.

Rattler: Loosely bound phonon scatterer (atoms) introduced into a host crystal to result in a short phonon mean free path (reducing lattice conductivity and also resulting in an amorphous phase behavior).

Rayleigh and Mie scatterings: The process by which small particles suspended in a medium of a different index of refraction scatter a portion of the incident radiation in all directions. In elastic scattering, no energy transformation results, only a change in the spatial distribution of the radiation; however, the particles also absorb radiation (inelastic scattering). This scattering varies as a function of the ratio of the particle diameter to the wavelength of the radiation (called the size parameter). When this size parameter is less than about one-tenth, the Rayleigh scattering occurs in which the scattering coefficient varies inversely as the fourth power of the wavelength.

Reciprocal lattice: Every crystal structure has two lattices associated with it, the direct lattice and the reciprocal lattice. A microscope image is a map of the direct lattice whereas the diffraction pattern is a map of the reciprocal lattice. The reciprocal lattice is essential in analytic studies of periodic structures, including the theory of crystal diffraction and the law of momentum conservation, in which the full translational symmetry of free space is reduced to that of a periodic potential.

Relaxation time: Average time between collisions.

Reststrahlen absorption and reflection: Reststrahlen, meaning residue rays in German, is the successive reflection of a broadband photon beam from the surface of a crystal to obtain a narrow-band beam. This is due to the interaction of electromagnetic waves with the vibrating dipoles (molecular vibrations in crystal, i.e., optical phonons).

Rydberg energy, formula, and constant: A unit of electron energy based on the ground-state energy of a hydrogen atom, one Ry energy is

$$\mathrm{Ry} = \frac{m_e e_c^4}{2(4\pi\epsilon_o)^2\hbar^2} = 13.607 \text{ eV}.$$

The Rydberg formula is

$$\frac{1}{\lambda} = \frac{m_e e_c^4}{8c_o\epsilon_o^2\hbar^3}(\frac{1}{n_f^2} - \frac{1}{n_i^2}) = \mathrm{Ry}(\frac{1}{n_f^2} - \frac{1}{n_i^2}),$$

where λ is the wavelength of photon emitted (in vacuum), for $n_f < n_i$, and the Rydberg constant is defined from the above relation as

$$\mathrm{Ry} = \frac{m_e e_c^4}{8c_o\epsilon_o^2\hbar^3} = 1.0974 \times 10^5 \text{ cm}^{-1}.$$

Semiconductors: Solid-state material in which, in contrast to metals and insulators, the electrical conductivity can be controlled by orders of magnitude by adding very small amounts of impurity elements (dopants) thus affecting the negatively charged electrons and positively charged holes. Intrinsic semiconductors have equal free electron and hole concentration, which extrinsics do not (excess hole gives p- and excess electron n-type). Their electrical conductivity is also sensitive to temperature, illumination, and magnetic field. These result from their interatomic bonds (mostly covalent) in which the valence band and the conduction band are separated by the energy gap. Semiconductor properties are displayed by the elements from the group 14 of the periodic table (Tables A.1 and A.2.), i.e., C in the form of diamond, Si, Ge and Sn and their compounds with elements from group 14, e.g., SiGe and SiC, as well as compounds from groups 13 and 15, e.g., GaAs, InP, or GaN, and groups 12 and 16, e.g., CdTe, ZnS.

Skutterudites: Complex minerals, $\mathrm{ReTm_4Pn_{12}}$ (Re: rear earth, Tm: transition metals, Pn: pnicogen), with Re in a simple cubic structure of Tm, each in a tilted pnicogen octahedra.

Spherical, parabolic band: Idealized electron band structure in crystals, in which the energy surfaces are spherical and the energy variation with respect to momentum is parabolic (model band structure).

Spin: A quantum presentation of angular momentum in quantum electrodynamics. It obeys the commutation relation and is a property of all elementary particles (including electrons).

Spontaneous emission: Photon emission that is from perturbations that are due to the vacuum state energy fluctuations (including thermal motion), and the emitted photons are incoherent (no phase relationship).

Stimulated emission: Photon emission that is due to the initial presence of photons in the system and maintains phase coherence with those initial photons.

Stokes law: The frequency of luminescence excited by radiation (photoluminescence) is not higher than the frequency of the exciting radiation.

Surface plasmon: A collective excitation of the electrons at the interface between a conductor and an insulator. On a plane surface, they are nonradiative electromagnetic modes (they cannot be generated by a photon nor decay spontaneously into photons).

Thermophotovoltaic: A device that converts thermal radiation emission from a controlled heat source into electricity. The device is designed for maximum efficiency at the wavelength range of this source.

Thermionic emission: Emission of electrons or ions by metals (filament) heated to high temperatures; the charged particle is called a thermion.

Thomson scattering: In photons (electromagnetic wave) incident upon a charged particle, the electric and magnetic components of the wave exert a Lorentz force on the particle, setting it into motion. Because the wave is periodic in time, so is the motion of the particle. Thus the particle is accelerated and consequently emits radiation.

Tunneling: A quantum mechanical effect allowing transition through a classically forbidden energy state.

Umklapp processes: German word Umklapp for flipping over is the scattering process that conserves the phonon momentum with a wave-vector jump across the Brillouin zone.

Valence band: The highest energy continuum of energy levels in a semiconductor that is fully occupied by electrons at $T = 0$ K.

Wigner–Seitz primitive cell: In crystals (lattices), it is the region of space that is closer to that point than to any other lattice point.

Bibliography

[1] M. Abramowitz and I.A. Stegun. *Handbook of Mathematical Functions*. National Bureau of Standards, Applied Mathematics Series 55, 1972.

[2] S. Adachi. Model dielectric constants of GaP, GaAs, GaSb, InP, InAs, and InSb. *Physical Review B*, 35:7454–7463, 1987.

[3] M.P. Allen and D.J. Tildesley. *Computer Simulation of Liquids*. Clarendon, Oxford, 1989.

[4] P.S. Anderson, W.M. Kays, and R.J. Moffat. Experimental results for the transpired turbulent boundary layer in an adverse pressure gradient. *J. Fluid Mechanics*, 69:353–375, 1975.

[5] P.W. Anderson. Absence of diffusion in certain random lattices. *Physical Review*, 109:1492–1505, 1958.

[6] G. Arya, H.C. Chang, and E.J. McGinn. Molecular simulations of Knudsen wall-slip: Effect of wall morphology. *Molecular Simulations*, 20:697–709, 2003.

[7] C.K. Asawa. Long-delayed fluorescence of Nd^{3+} in pure $LaCl_3$ and in $LaCl_3$ containing Ce^{3+}. *Physical Review*, 155:188–197, 1967.

[8] T.L. Aselage and D. Emin. *Chemistry, Physics and Materials Science of Thermoelectric Materials: Beyond Bismuth Telluride*. Kluwer, Dordrecht, 2003.

[9] T.L. Aselage, D. Emin, and S.S. McCready. Conductivities and Seebeck coefficients of boron carbides: Softening bipolaron hopping. *Physical Review B*, 64:054302–1–8, 2001.

[10] T.L. Aselage, D. Emin, S.S. McCready, and R.V. Duncan. Large enhancement of boron carbides' Seebeck coefficients through vibrational softening. *Physical Review Letters*, 81:2316–2319, 1998.

[11] M. Asen-Palmer, E. Bartkowski, and E. Gmelin. Thermal conductivity of germanium crystals with different isotopic compositions. *Physical Review B*, 56:9431–9447, 1997.

[12] N.W. Ashcroft and N.D. Mermin. *Solid State Physics*. Saunder College Press, Philadelphia, PA, 1976.

[13] R. Astala, S.M. Auerbach, and P.A. Monson. Normal mode approach for predicting the mechanical properties of solids from first principles: Application to compressibility and thermal expansion of zeolites. *Physical Review B*, 71:014112 (1–15), 2005.

[14] F. Auzel. Multiphonon-assisted anti-Stokes and Stokes fluorescence of triply ionized rare-earth ions. *IEEE J. Quantum Electronics*, 35:115–122, 1999.

[15] J.H. Avery. *Creation and Annihilation Operators*. McGraw-Hill, New York, 1977.

[16] R. Bairelein. *Thermal Physics*. Cambridge University Press, Cambridge, 1999.

[17] H. Bao and X. Ruan. *Ab initio* calculations of thermal radiation properties: The semiconductor GaAs. *Int. J. Heat Mass Transfer*, 53:1308–1312, 2010.

[18] J. Bardeen. Electrical conductivity of metals. *J. Applied Physics*, 11:88–111, 1940.

[19] J.O. Barnes and J.A. Rayne. Lattice expansion of Bi_2Te_3 from 4.2 K to 600 K. *Physical Letters A*, 46:317–318, 1974.

[20] S. Baroni, S. de Gironcoli, A. Dal Corso, and P. Giannozzi. Phonons and related crystal properties from density-function perturbation theory. *Review of Modern Physics*, 73:515–562, 2001.

[21] T.H.K. Barron, C.C. Huang, and A. Pasternak. Interatomic forces and lattice dynamics of α-quartz. *J. Physics C*, 9:3925–3940, 1976.

[22] G. Barrow. *The Structure of Molecules*. Benjamin, New York, 1963.

[23] B. Di Bartolo. *Optical Interaction in Solids*. Wiley, New York, 1968.

[24] M. Bartowiak and G.D. Mahan. Heat and electricity transport through interfaces, recent trends in thermoelectric materials. *Semiconductors and Semimetals*, 70:245–271, 2001.

[25] G.K. Batchelor. *The Theory of Homogeneous Turbulence*. Cambridge University Press, Cambridge, 1953.

[26] A.R. Beattie and A.M. White. An analytic approximation with a wide range of applicability for electron initiated Auger transitions in narrow-gap semiconductors. *J. Applied Physics*, 79:802–813, 1996.

[27] A.R. Beattie and A.M. White. An analytic approximation with a wide range of applicability for electron initiated Auger transitions in narrow-gap semiconductors. *Semiconductor Science and Technology*, 12:357–368, 1997.

[28] L.X. Benedict, E.L. Shirley, and R.B. Bohn. Theory of optical absorption in diamond, Si, Ge, and GaAs. *Physics Review B*, 57:R9385–R9387, 1998.

[29] G. Beni and P.M. Platzman. Temperature and polarization dependence of external x-ray absorption fine-structure spectra. *Physical Review B*, 14:1514–1518, 1976.

[30] R. Berman. *Thermal Conduction in Solids*. Clarendon, Oxford, 1974.

[31] D. Bertolini and A. Tani. Thermal conductivity of water: Molecular dynamics and generalized hydrodynamics results. *Physical Review E*, 56:4135–4151, 1997.

[32] R.M. Besancon. *Encyclopedia of Physics*. Second Edition, Van Nostrand Reinhold, New York, 1976.

[33] C.M. Bhandari and D.M. Rowe. *Thermal Conductivity in Semiconductors*. Wiley, New York, 1988.

[34] A.B. Bhatia. *Ultrasonic Absorption*. Dover, New York, 1985.

[35] J.P. Biersack and J.F. Ziegler. Refined universal potentials in atomic collisions. *Nuclear Instruments Methods*, 194:93–100, 1982.

[36] D. Bilc, S.D. Mahanti, and M.G. Kanatzidis. Electronic transport properties of PbTe and $AgPb_mSbTe_{2+m}$ systems. *Physical Review B*, 74:125202–125213, 2006.

[37] G.D. Billing. *Dynamics of Molecule Surface Interactions*. Wiley, New York, 2000.

[38] G.A. Bird. Approach to translational equilibrium in a rigid sphere gas. *Physics of Fluids*, 6:1518–1519, 1963.

[39] G.A. Bird. Shock wave structure in a rigid sphere gas, *In Rarefied Gas Dynamics*, volume 1. Academic Press, New York, 1965.

[40] G.A. Bird. *Molecular Gas Dynamics and the Direct Simulation of Gas Flow*. Second Edition, Oxford University Press, Oxford, 1994.

[41] R.B. Bird, W.E. Stewant, and E.N. Lightfoot. *Transport Phenomena*. Second Edition, Wiley, New York, 2001.

[42] L.A. Bisebergy and H.W. Moos. Multiphonon orbit-lattice relaxation of excited states of rare-earth ions in crystals. *Physical Review*, 174:429–438, 1968.

[43] P. Blaha, K. Schwarz, G. Madsen, D. Kvasnicka, and J. Luitz. *Wien2k User's Guide*. Vienna University of Technology, Getreidemarkt, 2001.

[44] N.P. Blake and H. Metiu. *Chemistry, Physics, and Material Science of Thermoelectric Materials: Beyond Bismuth Telluride*. M.G. Kanatzidis, et al., Editors, Kluwer Academic/Plenum, London, 2003.

[45] M.B. Blencowe. Quantum energy flow in mesoscopic dielectric structures. *Physical Review B*, 59:4992–4998, 1999.

[46] J. Blömer and A. E. Beylich. Molecular dynamic simulation of energy accommodation of internal and translational fluid degrees of freedom at gas-solid interfaces. *Surface Science*, 423:127–133, 1999.

[47] K. Blotekjaer. Transport equations for electrons in two-valley semiconductors. *IEEE Transactions on Electron Devices*, 17:38–47, 1970.

[48] D. Bolmatov, V.V. Brazhkin, and K. Trachenko. The phonon theory of liquid thermodynamics. *Scientific Reports*, 2:421–1–6, 2012.

[49] L. Boltzmann. *Lecture Notes on Gas Theory, Translated from the German Editions (Part 1; 1896, and Part 2; 1898)*. Dover, New York, 1964.

[50] S.F. Borisov, S.A. Litvinenko, Y.G. Semenov, and P.E. Suetin. Experimental investigation of the temperature dependence of the accommodation coefficients for the gases He, Ne, Ar, and Xe on a Pt surface. *J. Engineering Physics and Thermophysics*, 34(5):603–606, 1978.

[51] M. Born and K. Huang. *Dynamical Theory of Crystal Lattice*. Clarendon Press, Oxford, 1954.

[52] M. Born and E. Wolf. *Principles of Optics*. Sixth Edition, Pergamon, Elmsford, 1980.

[53] M.I. Boulos. Thermal plasma processing. *IEEE Transactions on Plasma Science*, 19:1078–1089, 1991.

[54] F.B. Bowden and W.R. Throssell. Adsorption of water vapor on solid surfaces. *Proceedings Royal Society London*, A209:297–308, 1951.

[55] S.R. Bowman. Lasers without internal heat generation. *IEEE J. Quantum Electron*, 35:115–122, 1999.

[56] S.R. Bowman, S.P. O'Connor, and S. Biswal. Ytterbium laser with reduced thermal loading. *IEEE J. Quantum Electron*, 41:1510–1517, 2005.

[57] M. Brandbyge, J.-L. Mozos, P. Ordejon, J. Taylor, and K. Stokbro. Density-functional method for nonequilibrium electron transport. *Physical Review B*, 65:165401–1–17, 2002.

[58] S. Brandt and H.D. Dahmen. *The Picture Book of Quantum Mechanics*. Second Edition, Springer-Verlag, New York, 1995.

[59] P.W. Bridgman. The thermal conductivity of liquids under pressure. *Proceedings of American Academy of Arts and Science*, 99:141–169, 1923.

[60] H.W. Brinkman, W.J. Briels, and H. Verweij. Molecular dynamics simulations of yttria-stabilized zirconia. *Chemical Physics Letters*, 247:386–390, 1995.

[61] D.A. Broido and T.L. Reinecke. Effect of superlattice structure on the thermoelectric figure of merit. *Physical Review B*, 51:13797–13800, 1994.

[62] D.A. Broido, A. Ward, and N. Mingo. Lattice thermal conductivity of silicon from empirical interatomic potentials. *Physical Review B*, 72:014308-1-8, 2005.

[63] R.H. Bube. *Electrons in Solids: An Introductory Survey*. Third Edition, Academic Press, San Diego, 1992.

[64] R.H. Bube. *Photovoltaic Materials, In: Series on Properties of Semiconductor Materials – Vol. 1*. Imperial College Press, New Jersey, 1998.

[65] R.A. Buckingham. The classical equation of state of gaseous helium, neon, and argon. *Proceedings Royal Society London, Series A*, 168:264–283, 1938.

[66] D.E. Burch. *Infrared Absorption by Carbon Dioxide, Water Vapor, and Minor Atmospheric Constituents*. US Department of Commerce Report, Washington, 1962.

[67] G.A. Burdick. Energy band structure of copper. *Physical Review*, 129:138–150, 1963.

[68] D.G. Cahill and S.K. Pohl. Heat flow and lattice vibrations in glasses. *Solid State Communications*, 70:6131–6140, 1992.

[69] D.G. Cahill, S.K. Watson, and R.O. Pohl. Lower limit to thermal conductivity of disordered crystals. *Physical Review B*, 119:1–9, 1992.

[70] J. Callaway. Model for lattice thermal conductivity at low temperatures. *Physical Review*, 113:1046–1051, 1959.

[71] H.B. Callen. The application of Onsager's reciprocal relations to thermoelectric, thermomagnetic, and galvanomagnetic effects. *Physical Review*, 73:1349–1358, 1948.

[72] H.B. Callen. *Thermodynamics and an Introduction to Thermostatistics*. Wiley, New York, 1985.

[73] V.P. Carey. *Statistical Thermodynamics and Microscale Thermophysics*. Cambridge University Press, Cambridge, 1999.

[74] V.P. Carey, G. Chen, C. Grigoropoulos, M. Kaviany, and A. Majumder. A review of heat transfer physics. *Nanoscale and Microscale Thermophysical Engineering*, 12:1–60, 2008.

[75] V.P. Carey and A.P. Wemhoff. Disjoining pressure effects in ultra-thin liquid films in micropassages – comparison of thermodynamic theory with predictions of molecular dynamics simulations. *ASME J. Heat Transfer*, 128:1276–1284, 2006.

[76] R. Carminati, P. Chantrenne, S. Dihaire, S. Gomex, N. Trannoy, and G. Tessier. *Microscale and Nanoscale Heat Transfer*. Springer, Berlin, 2007.

[77] S. Chandrasehkar. *Hydrodynamic and Hydromagnetic Stability*. Dover, New York, 1961.

[78] C.H. Chang and E. Pfender. Heat and momentum transport to particulates injected into low-pressure ($\tilde{8}0$ mbar) nonequilibrium plasmas. *IEEE Transactions on Plasma Science*, 18:958–967, 1990.

[79] C.W. Chang, D. Okawa, A. Majumdar, and A. Zettl. Solid-state thermal rectifier. *Science*, 314:1121–1124, 2006.

[80] P.-O. Chapuis, S. Volz C. Henkel, K. Joulain, and J.-J Greffet. Effects of spatial dispersion in near-field radiative heat transfer between two parallel metallic surfaces. *Physical Review B*, 77:035431(1–9), 2008.

[81] J. Che, T. Cagin, W. Deng, and W.A. Goddard III. Thermal conductivity of diamond and related materials from molecular dynamics simulations. *J. Chemical Physics*, 113:6888–6900, 2000.

[82] J.R. Chelikowsky and M.L. Cohen. Non local pseudopotential calculations for the electronic structure of eleven diamond and zinc-blende semiconductors. *Physical Review B*, 14:556–582, 1976.

[83] F.F. Chen. *Introduction to Plasma Physics and Controlled Fusion*. Plenum, New York, 1984.

[84] G. Chen. Thermal conductivity and ballistic-phonon transport in the cross-plane direction of superlattice. *Physical Review B*, 23:14598–14973, 1998.

[85] G. Chen. *Nanoscale Energy Transport and Conversion*. Oxford University Press, Oxford, 2005.

[86] G. Chen and A. Shakouri. Heat transfer in nanostructures for solid-state energy conversion. *ASME J. Heat Transfer*, 124:242–252, 2002.

[87] X. Chen and P. Han. On the thermodynamic derivation of the Saha equation modified to a two-temperature plasma. *J. Physics D-Applied Physics*, 32:1711–1718, 1999.

[88] P.K. Cheo. Relaxation of CO_2 laser levels by collisions with foreign gases. *IEEE J. Quantum Electronics*, QE-4:587–593, 1968.

[89] A. Chimmalgi, C.P. Grigoropoulos, and K. Komvopoulos. Surface nanostructuring by nano-/femtosecond laser-assisted scanning force microscopy. *J. Applied Physics*, 97:104319–1–12, 2005.

[90] F.C. Chou, J.R Lukes, X.G. Liang, K. Takahashi, and C.L. Tien. Molecular dynamics in microscale thermophysical engineering. *Annual Review of Heat Transfer*, 10:141–176, 1999.

[91] D.K. Christen and G.L. Pollack. Thermal conductivity of solid argon. *Physical Review B*, 12:3380–3391, 1975.

[92] J.D. Chung, A.J.H. McGaughey, and M. Kaviany. Role of phonon dispersion on lattice thermal conductivity modeling. *ASME J. Heat Transfer*, 126:376–380, 2004.

[93] W.T. Coffey, Yu.P. Kalmykov, and J.T. Waldron. *The Langevin Equation*. Second Edition, World Scientific, Hackensack, 2004.

[94] C. Cohen-Tannoudji, B. Diu, and F. Laloe. *Quantum Mechanics*. Wiley, New York, 2007.

[95] C. Cohen-Tannoudji, J. Dupont-Roc, and C. Grynberg. *Atom-Photon Interactions: Basic Processes and Applications*. Wiley-Interscience, Weinheim, 1998.

[96] E.U. Condon and G.H. Shortley. *The Theory of Atomic Spectra*. Cambridge Univeristy Press, London, 1935.

[97] G. Conibeer, R. Patterson, L. Huang, J.-F. Guillemoles, D. König, S. Shrestha, and M.A. Green. Modelling of hot carrier solar cell absorbers. *Solar Energy Materials and Solar Cells*, 94:1516–1521, 2010.

[98] J. Cooper and N. Frankenberger. Thermoelectricity – a ray from the bright tomorrow. *J. American Society for Naval Engineers*, 71:657–664, 1959.

[99] P. Costamagna, S. Grosso, and R. Di Felice. Percolative model of proton conductivity of nafion membranes. *J. Power Sources*, 178(2):537–546, 2008.

[100] R.M. Costescu, M.A. Wall, and D.G. Cahill. Thermal conductance of epitaxial interfaces. *Physical Review B*, 67:054302–1–5, 2003.

[101] S. Cottenier. *Density Functional Theory and the Family of (L)APW-Methods: A Step-by-Step Introduction*. http://www.wien2k.at/reg_user/textbooks/, 2004.

[102] E.G. Cravalho, C.L. Tien, and R.P. Caren. Effect of small spacings on radiative transfer between two dielectrics. *ASME J. Heat Transfer*, 89:351–358, 1967.

[103] P. Cross, J. Decius, and E. Wilson. *Molecular Vibrations*. McGraw-Hill, Totonto, 1955.

[104] S.J. Cyvin. Vibrational mean-square amplitude matrices .1. Secular equations involving mean-square amplitudes of vibration, and approximate computations of mean-square amplitude matrices. *Spectrochemica Acta*, 10:828–834, 1959.

[105] L.W. da Silva. *PhD Thesis: Integrated Micro Thermoelectric Cooler: Theory, Fabrication and Characterization*. University of Michigan, Ann Arbor, 2005.

[106] L.W. da Silva and M. Kaviany. Micro thermoelectric cooler: Interfacial effects on thermal and electrical transport. *Int. J. Heat Mass Transfer*, 47:2417–2435, 2004.

[107] K.J. Daun. Thermal accommodation coefficients between polyatomic gas molecules and soot in laser-induced incandescence experiments. *Int. J. Heat Mass Transfer*, 52:5081–5089, 2009.

[108] G.G. de la Cruz and Yu.G. Gurvich. Electron and phonon thermal waves in semiconductors: An application to photothermal effects. *J. Applied Physics*, 80:1726–1730, 1996.

[109] P.J.U. Debye. *The Collected Papers of Peter J.W. Debye*. Oxbow Press, Woodbridge, 1988.

[110] L.D. Deloach, S.A. Payne, L.L. Chase, L.K. Smith, W.L. Kway, and W.F. Krupke. Evaluation of absorption and emission of Yb^{3+} doped crystals for laser applications. *IEEE J. Quantum Electronics*, 29:1179–1191, 1993.

[111] G.H. Dieke and H.M. Crosswhite. The spectra of the doubly and triply ionized rare earths. *Applied Optics*, 2:675–686, 1963.

[112] M.J.F. Digonnet. *Rare Earth Doped Fiber Lasers and Amplifiers*. Marcel Dekker, New York, 1993.

[113] Y. Ding, A. Campargue, E. Bertseva, S. Tashkun, and V.I. Perevalov. Highly sensitive absorption spectroscopy of carbon dioxide by ICLAS-VeCSEL between 8800 and 9530 cm^{-1}. *J. Molecular Spectroscopy*, 231:117–123, 2005.

[114] N. Djeu and W.T. Whitney. Laser cooling by spontaneous anti-Stokes scattering. *Physical Review Letters*, 46:236–281, 1981.

[115] G. Domingues, S. Volz, K. Joulian, and J.J. Greffet. Heat transfer between two nanoparticles through near field interactions. *Physical Review Letters*, 94:085901–1–4, 2005.

[116] V. Domnich, S. Reynaud, R.A. Haber, and M. Chhowalla. Boron carbide: Structure, properties, and stability under stress. *J. American Ceramic Society*, 94:3605–3628, 2011.

[117] M.T. Dove. *Introduction to Lattice Dynamics*. Cambridge University Press, Cambridge, 1993.

[118] M.S. Dresselhaus. *Solid State Physics, Part II: Optical Properties*. MIT, unpublished, 2005.

[119] S.J. Duclos, K. Brister, R.C. Haddon, A.R. Kortan, and F.A. Thiel. Effects of pressure and stress on C_{60} fullerite to 20 GPa. *Nature*, 351:380–382, 1991.

[120] J.S. Dugdale. *Electical Properties of Metals and Alloys*. Edward Arnold Publishers, London, 1977.

[121] W. Duley. CO_2 *Lasers: Effects and Applications*. Academic Press, London, 1976.

[122] E.R.G. Eckert and E. Pfender. Advances in plasma heat transfer. *Advances in Heat Transfer*, 4:229–310, 1967.

[123] B.C. Edwards, J.E. Anderson, R.I. Epstein, G.L. Mills, and A.J. Mord. Demonstration of a solid-state optical cooler: An approach to cryogenic refrigeration. *J. Applied Physics*, 86:6489–6493, 1999.

[124] E.K. Edwards. *Radiative Heat Transfer Notes*. Hemisphere, Washington, 1981.

[125] K. Eikema, W. Ubachs, W. Vassen, and H. Horgorvorst. Lamb shift measurement in the 1 ^{1}s ground state of helium. *Physical Review A*, 55:1866–1884, 1997.

[126] A. Einstein. Elementare betrachtungen uber die thermische molekularbewegung in festen korpern. *Annalen der Physik*, 35:679–694, 1911.

[127] R.J. Elliott and A.F. Gibson. *An Introduction to Solid State Physics and Its Applications*. Harper & Row, New York, 1974.

[128] D. Emin. Thermoelectric power due to electronic hopping motion. *Physical Review Letters*, 35:882–885, 1975.

[129] D. Emin. Icosahedral boron-rich solids. *Physics Today*, 40:55–62, 1987.

[130] D. Emin. Vibrational contribution to the Seebeck coefficient of bipolaronic carriers in boron carbides. *Physica Status Solidi (b)*, 205:385–390, 1998.

[131] D. Emin. Enhanced Seebeck coefficient from carrier-induced vibrational softening. *Physical Review B*, 59:6205–6210, 1999.

[132] D. Emin. Effects of charge carriers' interactions on Seebeck coefficients, *In Thermoelectrics Handbook: Macro to Nano*. CRC Press, Boca Raton, 2006.

[133] R.I. Epstein, J.J. Brown, B.C. Edwards, and A. Gibbs. Measurements of optical refrigeration in ytterbium-doped crystals. *J. Applied Physics*, 90:4815–4819, 2001.

[134] R.I. Epstein, M.I. Buckwald, B.C. Edwards, T.R. Gosnell, and C.E. Mungan. Observation of laser-induced fluorescent cooling of a solid. *Nature*, 377:500–503, 1995.

[135] K. Esfarjani, M. Zebarjadi, and Y. Kawazoe. Thermoelectric properties of a nanocontact made of two-capped single-wall carbon nanotubes calculated within the tight-binding approximation. *Physical Review B*, 73:085406–1–6, 2006.

[136] T.E. Faber. *Introduction to the Theory of Liquid Metals*. Cambridge University Press, New York, 1972.

[137] J.-N. Fehr, M.-A. Dupertuis, T.P. Hessler, L. Kappei, D. Marti, F. Salleras, M.S. Nomura, B. Deveaud, J.-Y. Emery, and B. Dagens. Hot phonons and Auger related carrier heating in semiconductor optical amplifiers. *IEEE J. Quantum Electronics*, 38:674–681, 2002.

[138] I.D. Feranchuk, A.A. Minkevich, and A.P. Ulyanenkov. Estimate of the Debye temperature for crystal, with polyatomic unit cell. *European Physics: J. Applied Physics*, 19:95–101, 2002.

[139] J. Fernandez, A.J. Garcia-Adeva, and R. Balda. Anti-Stokes laser cooling in bulk erbium-doped materials. *Physical Review Letters*, 97:033001–1–4, 2006.

[140] J. Fernandez, A. Mendioroz, A.J. Garcia, R. Balda, and J.L. Adam. Anti-Stokes laser-induced internal cooling of Yb^{3+}-doped glasses. *Physical Review B*, 62:3213–3217, 2000.

[141] J. Fernandez, A. Mendioroz, A.J. Garcia, R. Balda, J.L. Adam, and M.A. Arriandiaga. On the origin of anti-Stokes laser-induced cooling of Yb^{3+}-doped glass. *Optical Materials*, 16:173–179, 2001.

[142] R.P. Feynman. *Statistical Mechanics: A Set of Lectures*. W.A. Benjamin, Reading, Massachusetts, 1972.

[143] C. Florea and K.A Winick. Ytterbium-doped glass waveguide laser fabricated by ion exchange. *IEEE J. Lightwave Technology*, 17:1593–1601, 1999.

[144] J.B. Foresman and A.E. Frisch. *Exploring Chemistry with Electronic Structure Methods*. Gaussian Inc., Pittsburgh, 1996.

[145] A.R. Forouhi and I. Bloomer. Optical properties of crystalline semiconductors and dielectrics. *Physical Review B*, 38:1865–1874, 1988.

[146] M. Fowler. http://galileo.phys.virginia.edu/classes/752.mf1i.spring03/PhotoelectricEffect.htm, 2004.

[147] A.J. Freeman and R.E. Watson. Theoretical investigation of some magnetic and spectroscopic properties of rare-earth ions. *Physical Review*, 127:2058–2075, 1962.

[148] D. Frenkel and B. Smit. *Understanding Molecular Simulation: From Algorithms to Applications*. Academic, San Diego, 1996.

[149] M.J. Frisch, G.W. Trucks, H.B. Schlegel, G.E. Scuseria, M.A. Robb, J.R. Cheeseman, J.A. Montgomery, T. Vreven, K.N. Kudin, J.C. Burant, J.M. Millam, S.S. Iyengar, J. Tomasi, V. Barone, B. Mennucci, M. Cossi, G. Scalmani, N. Rega, G.A. Petersson, H. Nakatsuji, M. Hada, M. Ehara, K. Toyota, R. Fukuda, J. Hasegawa, M. Ishida, T. Nakajima, Y. Honda, O. Kitao, H. Nakai, M. Klene, X. Li, J.E. Knox, H.P. Hratchian, J.B. Cross, C. Adamo, J. Jaramillo, R. Gomperts, R.E. Stratmann, O. Yazyev, A.J. Austin, R. Cammi, C. Pomelli, J.W. Ochterski, P.Y. Ayala, K. Morokuma, G.A. Voth, P. Salvador, J.J. Dannenberg, V.G. Zakrzewski, S. Dapprich, A.D. Daniels, M.C.

Strain, O. Farkas, D.K. Malick, A.D. Rabuck, K. Raghavachari, J.B. Foresman, J.V. Ortiz, Q. Cui, A.G. Baboul, S. Clifford, J. Cioslowski, B.B. Stefanov, G. Liu, A. Liashenko, P. Piskorz, I. Komaromi, R.L. Martin, D.J. Fox, T. Keith, M.A. Al-Laham, C.Y. Peng, A. Nanayakkara, M. Challacombe, P.M.W. Gill, B. Johnson, W. Chen, M.W. Wong, C. Gonzalez, and J.A. Pople. *Gaussian 03, Revision C.02*. Gaussian, Inc., Wallingford CT, 2004.

[150] C.J. Fu and Z.M. Zhang. Nanoscale radiation heat transfer for silicon at different doping levels. *Int. J. Heat Mass Transfer*, 49:1703–1718, 2006.

[151] K. Fushinobu, A. Majumdar, and K. Hijikata. Heat generation and transport in submicron semiconductor devices. *ASME J. Heat Transfer*, 117:25–31, 1995.

[152] J.D. Gale. Gulp – a computer program for symmetry adapted simulation of solids. *J. Chemical Society, Faraday Transactions*, 93:629–637, 1997.

[153] J. Le Gall, M. Olivier, and J.J. Greffet. Experimental and theoretical study of reflection and coherent thermal emission by a SiC grating supporting a surface-phonon polariton. *Physical Review B*, 55:10105–10114, 1997.

[154] M. Galperin, A. Nitzan, and M. Ratner. Inelastic effects in molecular junction transport: Scattering and self-consistent calculations for the Seebeck coefficient. *Molecular Physics*, 106:397–404, 2008.

[155] W.R. Gambill and J.H. Lienhard. An upper-bound for critical boiling heat fluxes. *ASME J. Heat Transfer*, 111:815–818, 1989.

[156] C. Garrod. *Statistical Mechanics and Thermodynamics*. Oxford University Press, Oxford, 1995.

[157] S. Gasiorowicz. *Quantum Physics*. Third Edition, Wiley, New York, 2003.

[158] T.H. Geballe and G.W. Hall. Seebeck effect in silicon. *Physical Review*, 98:940–947, 1955.

[159] T.H. Geballe and G.W. Hull. Isotopic and other types of thermal resistance in germanium. *Physical Review*, 110:773–775, 1958.

[160] S. Ghosh, I. Calizo, D. Teweldebrhan, E.P. Pokatilov, D.L. Nika, A.A. Balandin, W. Bao, F. Miao, and C.N. Lau. Extremely high thermal conductivity of graphene: Prospects for thermal management applications in nanoelectronic circuits. *Applied Physical Letters*, 92:151911–1–3, 2008.

[161] B. Giordanengo, N. Benazzi, J. Vinckel, J.G. Gasser, and L. Roubi. Thermal conductivity of liquid metals and metallic alloys. *J. Non-crystalline Solids*, 250:377–383, 1999.

[162] A.N. Goland and A. Paskin. Model for fission-fragment damage in thin polycrystalline metal films. *J. Applied Physics*, 35:2188–2194, 1964.

[163] H.J. Goldsmid. *Electronic Refrigeration*. Pion, London, 1986.

[164] T.R. Gosnell. Laser cooling of a solid by 65 K starting from room temperature. *Optics Letters*, 24:1041–1043, 1999.

[165] K. Gottfried and T.M. Yan. *Quantum Mechanics: Fundamentals*. Second Edition, Springer, New York, 2004.

[166] H.B. Gray. *Electrons and Chemical Bonding*. Benjamin, New York, 1964.

[167] R.B. Greegor and F. W. Lytle. Extended x-ray absorption fine structure determination of thermal disorder in Cu: Comparison of theory and experiment. *Physical Review B*, 20:4902–4907, 1979.

[168] M.A. Green. *Solar Cells, Operating Principles, Technology, and Systems Applications*. Prentice-Hall, Englewood Cliffs, 1982.

[169] M.A. Green, K. Emery, D. King, S. Igari, and W. Warta. Solar cell efficiency tables, version 24. *Progress of Photovoltaics: Research and Application*, 12:365, 2004.

[170] J.S. Griffith. *The Theory of Transition Metal Ion*. Cambridge Univeristy Press, London, 1961.

[171] D.J. Griffiths. *Introduction to Quantum Mechanics*. Third Edition, Prentice-Hall, Upper Saddle River, 1995.

[172] D.J. Griffiths. *Introduction to Quantum Mechanics*. Pearson, New York, 2011.

[173] E. Grüneisen and E.S. Goens. Analysis of metal crystals. III. Thermic expansion of zinc and cadmium. *Zeitschrift für Physik (Z. Phys.)*, 29:141–156, 1924.

[174] Y. Guissani and B. Guillot. A numerical investigation of the liquid-vapor coexistence curve of silica. *J. Chemical Physics*, 104:7633–7644, 1996.

[175] V.L. Gurevich. *Transport in Phonon Systems*. North-Holland, Amsterdam, 1986.

[176] F. Halzen and A. Martin. *Quarks & Leptons: An Introductory Course in Modern Particle Physics*. Wiley, New York, 1984.

[177] R.A. Hamilton and J.E. Parrott. Variational calculation of the thermal conductivity of germanium. *Physical Review*, 178:1284–1292, 1969.

[178] T.W. Hansch and A.L. Schawlow. Cooling of gases by laser radiation. *Optics Communications*, 13:68–69, 1975.

[179] Q. Hao, G. Chen, and M.-S. Jeng. Frequency-dependent Monte Carlo simulations of phonon transport in two dimensional porous silicon with aligned pores. *J. Applied Physics*, 106:114321–1–10, 2009.

[180] T.C. Harman, P.J. Taylor, D.L. Spears, and M.P. Walsh. Thermoelectric quantum-dot superlattices with high ZT. *J. Electronic Materials*, 29:L1–L4, 2000.

[181] M. Hayashi, A.M. Mebel, K.K. Liang, and S.H. Lin. *Ab initio* calculations of radiationless transitions between excited and ground singlet electronic states of ethylene. *J. Chemical Physics*, 108:2044–2055, 1998.

[182] E. Hecht. *Optics*. Addison Wesley, San Francisco, 2002.

[183] B. Heeg, M.D. Stone, A. Khizhnyak, G. Rumbles, G. Mills, and P.A. Debarber. Experimental demonstration of intracavity solid-state laser cooling of Yb^{3+}: ZrF_4-BaF_2-LaF_3-AlF_3-NaF glass. *Physical Review A*, 70:021401(1–4), 2004.

[184] M.P. Hehlen, R.I. Epstein, and H. Inoue. Model of laser cooling in the Yb^{3+}-doped fluoroziconate glass ZBLAN. *Physical Review B*, 75:144302–1–13, 2007.

[185] R.R. Heikes and R.W. Ure Jr. *Thermoelectricity: Science and Engineering*. Interscience, New York, 1961.

[186] P. Heino and E. Ristolainen. Thermal conduction at nano scale in some metals by MD. *Microelectronics J.*, 34:773–777, 2003.

[187] E. Helfand. Transport coefficient from dissipation in canonical ensemble. *Physical Review*, 119:1–9, 1960.

[188] G. Henkelman, A. Amaldsson, and H. Jonsson. A fast and robust algorithm for Bader decomposition of charge density. *Computational Materials Science*, 36:354–360, 2006.

[189] C. Herring. A new method for calculating wave functions in crystals. *Physical Review*, 57:1169–1177, 1940.

[190] C. Herring. Role of low-energy phonons in thermal conduction. *Physical Review*, 95:954–965, 1954.

[191] G. Herzberg. *Molecular Spectra and Molecular Structure II. Infrared and Raman Spectra of Polyatomic Molecules*. Van Nostrand, New York, 1945.

[192] G. Herzberg. *Molecuar Spectra and Molecular Structure IV. Constants of Diatomic Molecules*. Van Nostrand, New York, 1979.

[193] K. Hess. *Monte Carlo Device Simulation: Full Band and Beyond*. Springer, New York, 1991.

[194] R.C. Hilborn. Einstein coefficients, cross sections, f values, dipole moments, and all that. *American J. Physics*, 50:982–986, 1982.

[195] J.O. Hinze. *Turbulence*. Second Edition, McGraw-Hill, New York, 1975.

[196] C.Y. Ho and Y.S. Touloukian. *Thermophysical Properties of Matter, the TPRC Data Series*. IFI-Plenum, New York, 1970.

[197] K. Hoang, S.D. Mahanti, J. Androulakis, and M.G. Kanatzidis. Electronic structure of $AgPb_mSbTe_{m+2}$ compounds – implications on thermoelectric properties. *Materials Research Society Symposium Proceedings*, 0886:F05–06.5, 2006.

[198] R.W. Hockney and J.W. Eastwood. *Computer Simulation Using Particle*. Taylor & Francis, New York, 1988.

[199] M.G. Holland. Analysis of lattice thermal conductivity. *Physical Review*, 132:2461–2471, 1963.

[200] L.W. Hrubesh and R.W. Pekala. Thermal properties of organic and inorganic aerogels. *J. Materials Research*, 9(3):731–738, 1994.

[201] B.L. Huang and M. Kaviany. Structural metrics of high-temperature lattice conductivity. *J. Applied Physics*, 100:123507–1–12, 2006.

[202] B.L. Huang and M. Kaviany. *Ab-initio* and MD predictions of electron and phonon transport in bismuth telluride. *Physical Review B*, 77:125209–1–19, 2008.

[203] B.L. Huang, A.J.H. Mcgaughey, and M. Kaviany. Thermal conductivity of metal-organic framework 5 (mof-5): Part 1. Molecular dynamic simulations. *Int. J. Heat Mass Transfer*, 50:393–404, 2006.

[204] B.L. Huang, A.J.H. Mcgaughey, and M. Kaviany. Thermal conductivity of metal-organic framework 5 (mof-5): Part 2. Measurement. *Int. J. Heat Mass Transfer*, 50:405–411, 2006.

[205] J. Hubbard. Electron correlation in narrow energy bands. *Proceedings of the Royal Society A*, 276:238–257, 1963.

[206] G.S. Hwang and M. Kaviany. Molecular dynamics simulation of effective thermal conductivity of vapor-filled nanogap and nanocavity. *J. Applied Physics*, 106:024317–1–6, 2009.

[207] G.S. Hwang, J.H. Nam, M.H. Kim, S.Y. Son, and M. Kaviany. Pore-water morphological transitions in polymer electrolyte and their role on fuel cell performance. *J. Electrochemical Society*, 156:B1192–B1200, 2009.

[208] A. Ikesue and Y.L. Aung. Ceramic laser materials. *Nature Photonics*, 2:721–727, 2008.

[209] J.N. Israelachvili. *Intermolecular and Surface Forces: With Applications to Colloidal and Biological Systems*. Academic, San Diego, 1985.

[210] J.M. Jackson and N.F. Mott. Energy exchange between inert gas atoms and a solid surface. *Proceedings Royal Society London. Series A*, 137:703–717, 1932.

[211] C. Jacoboni and P. Lugli. *The Monte Carlo Method for Semiconductor Device Simulation*. Springer-Verlag, Wien, 1989.

[212] M.Y. Jaffrin. Shock structure in a partially ionized gas. *Physics Fluids*, 8:606–625, 1965.

[213] S.P. Jang and S.U.S. Choi. Role of Brownian motion in the enhanced thermal conductivity of nanofluids. *Applied Physics Letters*, 84:431–4318, 2004.

[214] J. Javanainen. Light-pressure cooling of trapped ions in three dimensions. *Applied Physics A: Materials Science Processing*, 23:175–182, 1980.

[215] M.-S. Jeng, R. Yang, D. Song, and G. Chen. Modeling the thermal conductivity and phonon transport in nanoparticle composites using Monte Carlo simulation. *J. Heat Transfer*, 130:042410–1–11, 2008.

[216] H.W. Jeon, H.P. Ha, D.B. Yun, and J.D. Shim. Electrical and thermoelectrical properties of undoped Bi_2Te_3-Sb_2Te_3 and Bi_2Te_3-Sb_2Te_3-Sb_2Se_3 single crystals. *J. Physics Chemistry of Solids*, 52:579–585, 1991.

[217] E.X. Jin and X. Xu. Radiating transfer through nanoscale apertures. *J. Quantitative Spectroscopy and Radiative Transfer*, 93:163–173, 2005.

[218] E.X. Jin and X. Xu. Obtaining subwavelength optical spots using nanoscale ridge apertures. *ASME J. Heat Transfer*, 129:37–43, 2007.

[219] D.G. Jones and H.M. Fretwell. Phase behaviour of argon and krypton adsorbed in mesoporous Vycor glass. *J. Physics: Condensed Matter*, 15:4709–4715, 2003.

[220] D.D. Joseph. *Stability of Fluid Motion II*. Springer, Berlin, 1976.

[221] K. Joulian, J.P. Mulet, F. Marguier, R. Caminati, and J.J. Greffet. Surface electromagnetic waves thermally excited: Radiative heat transfer, coherence properties and casimir forces revisited in the near field. *Surface Science Reports*, 57:59–112, 2005.

[222] Y.S. Ju and K.E. Goodson. Phonon scattering in silicon films with thickness of order 100 nm. *Applied Physics Letters*, 74:3005–3007, 1999.

[223] B.R. Judd. The theory of spectra of europium salts. *Proceedings Royal Society London. Series A*, 228:120–128, 1955.

[224] C.L. Julian. Theory of conduction in rare-gas crystals. *Physical Review*, 137:A128–137, 1965.

[225] P. Jund and R. Jullien. Molecular-dynamics calculations of the lattice thermal conductivity of vitreous silica. *Physical Review B*, 59:13707–13711, 1999.

[226] H. Kaburaki, J. Li, and S. Yip. Thermal conductivity of solid argon by classical molecular dynamics. *Materials Research Society Symposia Proceedings*, 503:503–508, 1998.

[227] M.I. Kaganov and I.M. Lifshits. *Quasiparticles*. V. Kissin Translator (from Russian), Mir, Moscow, 1979.

[228] B. Kallies and R. Meier. Electronic structure of 3d $[M(H_2O)_6]^{3+}$ ions from Sc^{III}: A quantum mechanical study based on DFT computations and natural bond orbital analyses. *Inorganic Chemistry*, 40:3101–3112, 2001.

[229] M. Kaviany. Onset of thermal convection in a saturated porous medium. *Int. J. Heat Mass Transfer*, 27:2001–2010, 1984.

[230] M. Kaviany. *Principles of Heat Transfer in Porous Media*. Second Edition, Springer, New York, 1995.

[231] M. Kaviany. *Principles of Convective Heat Transfer*. Second Edition, Springer, New York, 2001.

[232] M. Kaviany. *Principles of Heat Transfer*. Wiley, New York, 2001.

[233] W.M. Kays and M.T. Crawford. *Convective Heat Mass Transfer*. Third Edition, McGraw-Hill, New York, 1993.

[234] P. Keblinski and D.G. Cahill. Comment on model for heat conduction in nano fluids. *Physical Review Letters*, 95:209401, 2005.

[235] E.H. Kennard. *Kinetic Theory of Gases*. McGraw-Hill, New York, 1938.

[236] M. Kerker. *The Scattering of Light*. Academic, New York, 1969.

[237] M. Kilo, R.A. Jackson, and G. Borchardt. Computer modelling of ion migration in zirconia. *Philosophical Magazine*, 83:3309–3325, 2003.

[238] J. Kim, A. Kapoor, and M. Kaviany. Material metrics for laser cooling of solids. *Physical Review B*, 77:115127–1–15, 2008.

[239] J. Kim and M. Kaviany. Phonon recycling in ion-doped lasers. *Applied Physics Letters*, 95:074103–1–3, 2009.

[240] J. Kim and M. Kaviany. *Ab-initio* calculations of f-orbital electron-phonon interaction in laser cooling. *Physical Review B*, 79:054103–1–5, 2009.

[241] R. Kim, C. Jeong, and M.S. Lundstrom. On momentum conservation and thermionic emission cooling. *J. Applied Physics*, 107:054502–1–8, 2010.

[242] A. Kittel, W. Müller-Hirsch, J. Parisi, S.A. Biehs, D. Reddig, and M. Holthaus. Near-field heat transfer in a scanning thermal microscope. *Physical Review Letters*, 95:224301–1–4, 2005.

[243] C. Kittel. Ultrasonic resonance and properties of matter. *Reports on Progress in Physics*, 11:205–247, 1946.

[244] C. Kittel. Interpretation of the thermal conductivity of glasses. *Physical Review*, 75:972–974, 1949.

[245] C. Kittel. *Introduction to Solid State Physics*. Seventh Edition, Wiley, New York, 1986.

[246] P.G. Klemens. The thermal conductivity of dielectric solids at low temperatures. *Proceedings Royal Society London, Series A*, 208:108–133, 1951.

[247] P.G. Klemens. The scattering of low-frequency lattice waves by static imperfections. *Proceedings Physical Society London, Series A*, 68:1113–1128, 1955.

[248] P.G. Klemens. Thermal conductivity and Lattice vibration modes. *In: Solid State Physics*. Academic, New York, 1958.

[249] P. Kocevar. Hot phonon dynamics. *Physica B*, 134:155–163, 1985.

[250] T. Koga, X. Sun, S.B. Cronin, and M.S. Dresselhaus. Carrier pocket engineering applied to design useful thermoelectric materials using GaAs/AlAs superlattices. *Applied Physics Letters*, 75:2438–2440, 1998.

[251] T.D. Kolomiĭtsova, A.V. Lyaptsev, and D.N. Shchepkin. Determination of parameters of the dipole moment of the CO_2 molecule. *Optics and Spectroscopy*, 88:648–660, 2000.

[252] A. Konard, U. Herr, R. Tidecks, F. Kummer, and K. Samwer. Luminescence of bulk and nanocrystalline cubic yttria. *J. Applied Physics*, 90:3516–3523, 2001.

[253] M. Konuma. *Film Deposition by Plasma Techniques*. Springer-Verlag, Berlin, 1992.

[254] J. Korringa. On calculation of the energy of a Bloch wave in a metal. *Physica*, 13:392–400, 1947.

[255] M. Kozlowski and J. Marciak-Kozlowska. Beyond the Fourier equation: Quantum hyperbolic heat transport. *arXiv.org:cond-mat/0304052*, April 2003.

[256] G.J. Kramer, N.P. Farragher, B.W.H. van Beest, and R.A. van Saton. Interatomic force fields for silicas, aluminophosphates, and zeolites: Derivation based on *ab initio* calculations. *Physical Review B*, 43:5068–5080, 1991.

[257] G. Kresse and J. Furthmüler. Efficient iterative schemes for *ab initio* total-energy calculations using a plane-wave basis set. *Physical Review B*, 54:11169–11186, 1997.

[258] G. Kresse and J. Furthmüler. *VASP the Guide*. http://cms.mpi.univie.ac.at/vasp/vasp/vasp.html, 2005.

[259] H.W. Kroto, J.R. Heath, S.C. O'Brien, R.F. Curl, and R.E. Smalley. C_{60} Buckminster fullerence *Nature*, 318:162–163, 1985.

[260] T. Kunikiyo, M. Takenaka, and Y. Kamakura. A Monte Carlo simulation of anisotropic electron transport in silicon including full band structure and anisotropic impact-ionization model. *J. Applied Physics*, 75:297–312, 1994.

[261] D. Lacroix, K. Joulain, and D. Lemonnier. Monte Carlo transient phonon transport in silicon and germanium at nanoscales. *Physical Review B*, 72:064305–1–11, 2005.

[262] A.J.C. Ladd, B. Moran, and W.G. Hoover. Lattice thermal conductivity: A comparison of molecular dynamics and anharmonic lattice dynamics. *J. Chemical Physics*, 34:5058–5064, 1986.

[263] J.F. Lancaster. *The Physics of Welding*. Pergamon, Oxford, 1986.

[264] L.D. Landau. On the thermodynamics of photoluminescence. *J. Physics (Moscow)*, 10:503–506, 1962.

[265] L.D. Landau and E. Teller. Theory of sound dispersion (zur theorie der schalldispersion). *in Collected Papers of L. D. Landau*, edited by D. ter Haar (Gordon and Breach, Science Publishers, Inc. and Pergamon Press Ltd., New York, 1965), p.147; *Phys. Z. Sowjetunion*, 10:34–43, 1936.

[266] R. Landauer. Spatial variation of currents and fields due to localized scatterers in metallic conduction. *IBM J. Research and Development*, 1:223–231, 1957.

[267] E.S. Landry, M.I. Hossein, and A.J.H. McGaughey. Complex superlattice unit cell designs for reduced thermal conductivity. *Physical Review B*, 77:184302–1–13, 2008.

[268] P.T. Landsberg and G. Tonge. Thermodynamic energy conversion efficiencies. *J. Applied Physics*, 51:0700R1–20, 1980.

[269] A.R. Leach. *Molecular Modelling Principles and Applications*. Addison-Wesley-Longman, Essex, 1996.

[270] G. Lee and K. Cho. Electronic structures of zigzag graphene nanoribbons with edge hydrogenation and oxidation. *Physical Review B*, 79:165440–1–12, 2009.

[271] S. Lee and P. von Allmen. Tight-binding modeling of thermoelectric properties of bismuth telluride. *Applied Physics Letters*, 88:221071–221073, 2006.

[272] S.M. Lee, D.G. Cahill, and R. Venkatasubramanian. Thermal conductivity of $\mathrm{Si}-\mathrm{Ge}$ superlattices. *Applied Physics Letters*, 70:2957–2959, 1997.

[273] Y.H. Lee, R. Biswas, C.M. Soukoulis, C.Z. Wang, CT. Chan, and K.M. Ho. Molecular-dynamics simulation of thermal conductivity in amorphous silicon. *Physical Review B*, 43:6573–6580, 1991.

[274] G. Lei, J.E. Anderson, M.I. Buchwald, B.C. Edwards, and R.I. Epstein. Determination of spectral linewidth by Voigt profiles Yb^{3+}-doped fluorozirconate glasses. *Physical Review B*, 57:7673–7678, 1998.

[275] G. Lei, J.E. Anderson, M.I. Buchwald, B.C. Edwards, R.I. Epstein, M.T. Murtagh, and G.H. Sigel. Spectroscopic evaluation of Yb^{3+}-doped glasses for optical refrigeration. *IEEE J. Quantum Electronics*, 34:1839–1845, 1998.

[276] B.A. Lengyl. *Introduction to Laser Physics*. John Wiley & Sons, Inc., New York, 1970.

[277] I.N. Levine. *Physical Chemistry*. Third Edition, McGraw-Hill, New York, 1988.

[278] M.E. Levinshtein, S.L. Rumyantsev, and M. Shur. *Handbook Series on Semiconductor Parameters*. World Scientific, London, 1996.

[279] G.V. Lewis and C.R.A. Catlow. Potential models for ionic oxides. *J. Physics C: Solid State Physics*, 18:1149–1161, 1985.

[280] J. Li. *Ph.D. Thesis: Modeling microstrutural effects on deformation resistance and thermal conductivity*. Massachusetts Institute of Technology, Cambridge, 2000.

[281] J. Li, L. Porter, and S. Yip. Atomistic modeling of finite-temperature properties of crystalline $\beta-\mathrm{SiC}$. 2. thermal conductivity and effects of point defects. *J. Nuclear Materials*, 255:139–152, 1998.

[282] M.D. Licker, editor. *Dictionary of Scientific and Technical Terms*. Sixth Edition, McGraw Hill, New York, 2003.

[283] D.R. Lide, editor. *CRC Handbook of Chemistry and Physics*. 82nd Edition, CRC Press, Boca Raton, 2001.

[284] S.H. Lin. Rate of interconversion of electronic and vibrational energy. *J. Chemical Physics*, 44:3759–3767, 1966.

[285] D. Lindley. *Boltzmann's Atoms*. Free Press, New York, 2001.

[286] W.A. Little. The transport of heat between dissimilar solids at low temperatures. *Canadian J. Physics*, 37:334–349, 1959.

[287] P.D. Loly and A.A. Bahurmuz. A comparative study of energy bands in Kronig-Penney and Mathieu potentials. *Physica B*, 100:29–34, 1980.

[288] C.K. Loong, P. Vashishta, R.K. Kalia, W. Jin, M.H. Degani, D.G. Hinks, D.L. Price, J.D. Jorgensen, B. Dabrowski, A.W. Mitchell, D.R. Richards, and Y. Zheng. Phonon density of states and oxgen-isotope effect in $\mathrm{Ba}_{1-x}\mathrm{K}_x\mathrm{BiO}_3$. *Physical Review B*, 45:8052–8064, 1992.

[289] P. Lorrain and D.R. Corson. *Electromagnetic Fields and Waves*. Second Edition, Freeman, San Francisco, 1970.

[290] J. Lou, S. Harrington, and D.-M. Zhu. Effects of physisorption of xenon on the thermal conductivity of resorcinol-formaldehyde aerogels. *Physical Review E*, 60(5):5778–5782, 1999.

[291] R. Loudon. *The Quantum Theory of Light*. Third Edition, Oxford University Press, Oxford, 2000.

[292] S.K. Loyalka. Slip in thermal creep flow. *Physics of Fluids*, 14:21–24, 1971.

[293] V.A. Luchnikov, N.N. Medvedev, Y.I. Naberukhin, and V.N. Novikov. Inhomogeneity of the spatial distribution of vibrational modes in a computer model of amorphous argon. *Physical Review B*, 51:15569–15572, 1995.

[294] M. Lundstrom. *Fundamentals of Carrier Transport*. Second Edition, Cambridge University Press, Cambridge, 2000.

[295] X. Luo, M.D. Eisaman, and T.R. Gosnell. Laser cooling of a solid by 21 k starting from room temperature. *Optics Letters*, 23:639–641, 1998.

[296] A. Luque and S. Hegedus, editors. *Handbook of Photovoltaic Science and Engineering*. Wiley, New York, 1984.

[297] O. Madelung, editor. *Semiconductors – Basic Data*. Springer, Berlin, 1996.

[298] G.K.H. Madsen and D.J. Singh. Boltztrap, a code for calculating band-structure dependent quantities. *Computer Physics Communication*, 175:67–71, 2006.

[299] G.D. Mahan. Good thermoelectrics. *Solid State Physics*, 51:82–152, 1997.

[300] G.D. Mahan and J.O. Sofo. Heat transfer in nanostructures for solid-state energy conversion. *Proceedings of National Academy of Sciences, USA*, 93:7436–7439, 1996.

[301] A. Maiti, G.D. Mahan, and S.T. Pantelides. Dynamical simulations of nonequilibrium processes – heat flow and the Kapitza resistance across grain boundaries. *Solid State Communications*, 102:517–521, 1997.

[302] A. Majumdar. Microscale energy transport in solids. *In Microscale Energy Transport*. Taylor & Francis, Washington, 1998.

[303] A. Majumdar and P. Reddy. Role of electron-phonon coupling in thermal conductance of metal-nonmetal interfaces. *Applied Physics Letter*, 84:4768–4771, 2004.

[304] A.A. Maradudin. *Theory of Lattice Dynamics in the Harmonic Approximation*. Academic Press, New York, 1971.

[305] J. Marciak-Kozlowska. Wave characteristic of femtosecond heat conduction in thin films. *Int. J. Thermophysics*, 14:593–398, 1993.

[306] A. Martí and G. Araújo. Limiting efficiencies for photovoltaic energy conversion in multigap systems. *Solar Energy Materials and Solar Cells*, 43:203–222, 1996.

[307] L. Martin-Gondre, M. Alducin, G.A. Bocan, R. Díez Mui no, and J.I. Juaristi. Competition between electron and phonon excitations in the scattering of nitrogen atoms and molecules off tungsten and silver metal surfaces. *Physical Review Letters*, 108:096101–1–4, 2012.

[308] S. Maruyama. Molecular dynamics method for microscale heat transfer. *Advances in Numerical Heat Transfer*, 2:189–226, 2000.

[309] S. Maruyama and T. Kimura. A study on thermal resistance over a solid-liquid interface by the molecular dynamics method. *Thermal Science and Engineering*, 7(1):63–68, 1999.

[310] W.P. Mason. Phonon viscosity and its effect on acoustic wave attenuation and dislocation motion. *J. Acoustic Society of America*, 32:458–472, 1960.

[311] F.G. Mateo, J. Zuniga, A. Requena, and A. Hidalgo. Energy eigenvalues for Lennard–Jones potential using the hypervirial perturbative method. *J. Physics B: Atomic, Molecular and Optical Physics*, 23:2771–2781, 1990.

[312] A. Matulionis. Hot phonons in GaN channels for HEMTs. *Physica Status Solidi (a)*, 203:2313–2325, 2006.

[313] A. Matulionis, J. Liberis, I. Matulionien, H.-Y. Cha, L.F. Eastman, and M.G. Spencer. Hot-phonon temperature and lifetime in biased 4H-SiC. *J. Applied Physics*, 96:6439–6444, 2004.

[314] S. Mazumder and A. Majumdar. Monte Carlo study of phonon transport in solid thin films including dispersion and polarization. *ASME J. Heat Transfer*, 123:749–759, 2001.

[315] A.J.H. McGaughey. *Ph.D Thesis: Phonon Transport in Molecular Dynamics Simulations: Formulation and Thermal Conductivity Predictions*. University of Michigan, Ann Arbor, 2004.

[316] A.J.H. McGaughey and M. Kaviany. Quantitative validation of the Boltzmann transport equation phonon thermal conductivity model under the single mode relaxation time approximation. *Physical Review B*, 69:94303–1–12, 2004.

[317] A.J.H. McGaughey and M. Kaviany. Thermal conductivity decomposition and analysis using molecular dynamics simulations: Part I. Lennard–Jones argon. *Int. J. Heat Mass Transfer*, 47:1783–1798, 2004.

[318] A.J.H. McGaughey and M. Kaviany. Thermal conductivity decomposition and analysis using molecular dynamics simulations: Part II. Complex silica structures. *Int. J. Heat Mass Transfer*, 47:1799–1816, 2004.

[319] A.J.H. McGaughey and M. Kaviany. Observation and analysis of phonon interactions in molecular dynamics simulations. *Physical Review B*, 71:184305–1–11, 2005.

[320] A.J.H. McGaughey and M. Kaviany. Phonon transport in molecular dynamics simulations: Formulation and thermal conductivity prediction. *Advances in Heat Transfer*, 37:169–225, 2005.

[321] A.J.H. McGaughey, E.S. Landry, D.P. Sellan, and C.H. Amon. Size-dependent model for thin film and nanowire thermal conductivity. *Applied Physics Letters*, 99:131904–1–3, 2011.

[322] A.R. McGurn, K.T. Christensen, F.M. Mueller, and A.A. Maradudin. Anderson localization in one-dimensional randomly disordered optical systems that are periodic on average. *Physical Review B*, 47:13120–13125, 1993.

[323] D.A. McQuarrie. *Statistical Mechanics*. University Science Books, Sausalito, 2000.

[324] D.A. McQuarrie and J.D. Simon. *Physical Chemistry: A molecular Approach*. University Science Books, Sausalito, 1997.

[325] E. Merzbacher. *Quantum Mechanics*. Third Edition, Wiley, New York, 1997.

[326] H.J. Metcalf and P. Van der Straten. *Laser Cooling and Trapping*. Springer, New York, 1999.

[327] R. Meyer, L.J. Lewis, S. Prakash, and P. Entel. Vibrational properties of nanoscale materials: From nanoparticles to nanocrystalline materials. *Physical Review B*, 68:104303(1–9), 2003.

[328] R.C. Millikan and D.R. White. Systematics of vibrational relaxation. *J. Chemical Physics*, 39:3209–3213, 1963.

[329] M.I. Mishchenko, L.D. Travis, and A.A. Lacis. *Scattering, Absorption, and Emission of Light by Small Particles*. Cambridge University Press, Cambridge, 2002.

[330] Y. Mito and T.J. Hanratty. Lagrangian stochastic simulation of turbulent dispersion of heat markers in a channel flow. *Int. J. Heat Mass Transfer*, 46:1063–1073, 2003.

[331] M.F. Modest. *Radiation Heat Transfer*. McGraw-Hill, New York, 1993.

[332] A. Modinos. *Field, Thermionic, and Secondary Electron Emission*. Plenum Press, New York, 1984.

[333] C. Moglestue. *Monte Carlo Simulation for Semiconductor Device*. Chapman and Hall, London, 1993.

[334] A.S. Monin and A.M. Yaglom. *Statistical Fluid Mechanics: Mechanics of Turbulence, Volume 2*. MIT Press, Cambridge, 1979.

[335] E. Montoya, F. Agullo-Rueda, S. Manotas, J. Garciá Solé, and L.E. Bausa. Electron-phonon coupling in Yb^{3+}: $LiNbO_3$ laser crystal. *J. Luminescence*, 94-95:701–705, 2001.

[336] C.B. Moore, R.E. Wood, B.L. Hu, and J.T. Yardley. Vibrational energy transfer in CO_2 lasers. *J. Chemical Physics*, 46:4222–4231, 1967.

[337] M. Morrison, N. Lane, and T. Estle. *Quantum States of Atoms, Molecules, and Solids*. Prentice-Hall, Englewood Cliffs, 1976.

[338] J. Mostaghimi, G.Y. Zhao, and M.I. Boulos. The induction plasma chemical reactor: Part I. Equilibrium model. *Plasma Chemistry and Plasma Processing*, 10:133–150, 1990.

[339] A. Muhlenen, N. Errien, M. Schaer, M.-N. Bussac, and L. Zuppiroli. Thermopower measurements on pentacene transistors. *Physical Review B*, 75: 115338–1–6, 2007.

[340] F. Muller-Plathe. A simple nonequilibrium molecular dynamics method for calculating the thermal conductivity. *J. Chemical Physics*, 106:6082–6085, 1997.

[341] C.E. Mungan. Thermodynamics of radiation-balanced lasing. *J. Optical Society of America B*, 20:1075–1082, 2003.

[342] C.E. Mungan, M.I. Buchwald, B.C. Edwards, R.I. Epstein, and T.R. Gosnell. Internal laser cooling of Yb^{3+}-doped glass measured between 100 and 300 K. *Applied Physics Letters*, 71:1458–1460, 1997.

[343] G. Steinle-Neumann N. de Koker and V. Vlcek. Electrical resistivity and thermal conductivity of liquid FE alloys at high p and t, and heat flux in earth's core. *Proceedings of the National Academy of Sciences*, 109:4070–4073, 2012.

[344] A. Narayanasawmy, D.Z. Chen, and C. Chen. Near-field radiative transfer between two spheres. *IMECE 2006*, 15845, 2006.

[345] J. Nelson. *The Physics of Solar Cells*. Imperial College Press, New Jersey, 2003.

[346] V.V. Nevdakh, L.N. Orlov, and N.S. Leshenyuk. Temperature dependence of the vibrational relaxation rate constants of CO_2 (00^01) in binary mixtures. *J. Applied Spectroscopy*, 70:276–284, 2003.

[347] D.J. Newman. Theory of lanthanide crystal fields. *Advances in Physics*, 20:197–256, 1971.

[348] E.E. Nikitin and J. Troe. 70 years of landau-teller theory for collisional energy transfer – semiclassical three-dimensional generalizations of the classical collinear model. *Physical chemistry chemical physics*, 10:1483–1501, 2008.

[349] G. Nilsson and G. Nelin. Phonon dispersion relations in Ge at 80 K. *Physical Review B*, 3:364–369, 1971.

[350] E. Mu noz, J. Lu, and B.I. Yakobson. Ballistic thermal conductance of graphene ribbons. *Nano Letters*, 10:1652–1656, 2010.

[351] A.J. Nozik. Spectroscopy and hot electron relaxation dynamics in semiconductor quantum wells and quantum dots. *Annual Review of Physical Chemistry*, 52:193–231, 2001.

[352] B.H. O'Connor and T.M. Valentine. A neutron diffraction study of crystal structure of c-form of yttrium sesquioxide. *Acta Crystallographica, Section B*, B25:2140, 1969.

[353] T. Ohara. Contribution of intermolecular energy transfer to heat conduction in a simple liquid. *J. Chemical Physics*, 111(21):9667–9672, 1999.

[354] L. Onsager. Reciprocal relationships in irreversible processes I. *Physical Review*, 37:405–426, 1931.

[355] C. Oshima, T. Aizawa, R. Souda, Y. Ishizawa, and Y. Sumiyoshi. Atomistic structure of band-tail states in amorphous silicon. *Solid State Communications*, 65:1601–1604, 1988.

[356] X.F. Pang and Y.P. Feng. *Quantum Mechanics in Nonlinear Systems*. World Scientific Publishing Company, Singapore, 2005.

[357] J.P. Paolini. The bond order-bond length relationship. *J. Computational Chemistry*, 11:1160–1163, 1990.

[358] J.R. Pardo, J. Cernicharo, and E. Serabyn. Atmospheric transmission at microwaves (atm): An improved model for millimeter/submillimeter applications. *IEEE Transactions Antennas Propagation*, 49:1683–1694, 2001.

[359] S.P. Parker, J.C. Bellows, J.S. Gallagher, and A.H. Hervey. *Encyclopedia of Physics*. Second Edition, McGraw-Hill, New York, 1993.

[360] J.E. Parrott. High temperature thermal conductivity of semiconductor alloys. *Proceedings Physical Society*, 81:726–735, 1963.

[361] M.G. Paton and E.N. Maslen. A refinement of crystal structure of yttria. *Acta Crystallographica*, 19:307–310, 1965.

[362] L. Pauling. *The Nature of Chemical Bonds*. Third Edition, Cornell Universtiy Press, Ithaca, 1960.

[363] R.E. Peierls. On the kinetic theory of thermal conduction in crystals. *Annalen der Physik*, 3:1055–1101, 1929.

[364] H. Petschek and S. Byron. Approach to equilibrium ionization behind story shock waves in argon. *Annals of Physics*, 1:270–315, 1957.

[365] M. Peyrard. The design of thermal rectifier. *Europhysics Letters*, 76:49–55, 2006.

[366] P.E. Phelan. Application of diffuse mismatch theory to the prediction of thermal boundary resistance in thin-film high-t_c superconductors. *ASME J. Heat Transfer*, 120:37–43, 1998.

[367] W.D. Phillips. Laser cooling and trapping of neutral atoms (Nobel lecture). *Review of Modern Physics*, 70:721–741, 1998.

[368] T. Plechacek, J. Navratil, J. Horak, and P. Lostak. Defect structure of Pb-doped Bi_2Te_3 single crystals. *Philosophical Magazine*, 84:2217–2227, 2004.

[369] R.C. Powell. *Physics of Solid-State Laser Materials*. Spinger-Verlag, New York, 1998.

[370] R.C. Powell, G.E. Venikouas, L. Xi, and J.K. Tyminski. Thermal effects on the optical spectra of $Al_2O_3 : Ti^{3+}$. *J. Chemical Physics*, 84:662–665, 1986.

[371] S.S. Prabhu, A.S. Vengurlekar, and S.K. Roy. Nonequilibrium dynamics of hot carriers and hot phonons in CdSe and GaAs. *Physical Review B*, 51:14233–14246, 1995.

[372] P. Pringsheim. Zwei bemerkungen uber den unterschied von lumineszenz und temperaturstrahlung. *Zeitshrift für Physik (Z. Phys.)*, 57:739–746, 1929.

[373] J. Puibasset and R.J.M. Pellanq. A grand canonical Monte Carlo simulation study of water adsoption in Vycor-like hydrophilic mesoporous silica at different temperatures. *J. Physics: Condensed Matter*, 16:S5329–S5243, 2004.

[374] H.T. Quan, Y.-X. Liu, C.P. Sun, and F. Nori. Quantum thermodynamic cycles and quantum heat engines. *Physical Review E*, 76:031105–1–18, 2007.

[375] G. Racah. On the decomposition of tensors by contraction. *Reviews of Modern Physics*, 21:494–496, 1949.

[376] F.W. Ragay, E.W.M. Ruigrok, and J.H. Wolter. GaAs-AlGaAs heterojunction solar cells with increased open-circuit voltage. *IEEE First World Conference on Photovoltaic Energy Conversion*, 2:1934–1937, 1994.

[377] A.D. Rakic and M.L. Majewski. Modeling the optical dielectric function of GaAs and AlAs: Extension of adachi's model. *J. Applied Physics*, 80:5909–5914, 1996.

[378] P. Ramond. *Field Theory: A Modern Primer*. Westview Press, 2001.

[379] S.C. Rand. Bright storage of light. *Optics & Photonics News*, May:32–37, 2003.

[380] J. Randrianalisoa and D. Baillis. Monte Carlo simulation of steady-state microscale phonon heat transport. *J. Heat Transfer*, 130:072404–1–13, 2008.

[381] Y.I. Ravich, B.A. Efimova, and V.I. Tamarchenko. Scattering of current carriers and transport phenomena in lead chalcogenides. I. Theory. *Physica Status Solidi (B)*, 43:11–33, 1971.

[382] A. Rayner, M.E.J. Friese, A.G. Truscott, N.R. Heckenberg, and H. Rubinsztein-Dunlop. Laser cooling of a solid from ambient temperature. *J. Modern Optics*, 48:103–114, 2001.

[383] S.M Raytov, Y.A. Kravtsov, and V.I. Tatarski. *Principles of Statistical Radio Physics*. Third Edition, Springer, New York, 1987.

[384] S.M. Redmond. *Ph.D Dissertation: Luminescence Instabilities and Non-Radiative Processes in Rare-Earth Systems*. University of Michigan, Ann Arbor, 2003.

[385] S.M. Redmond, G.L. Armstrong, H.Y. Chan, E. Mattson, A. Mock, B. Li, R. Potts, M. Cui, S.C. Rand, S.L. Oliveira, J. Marchal, T. Hinklin, and R.M. Laine. Electrical generation of stationary light in random scattering media. *J. Optical Society America B*, 21:214–222, 2004.

[386] E.D. Reed and H.W. Moos. Multiphonon relaxation of excited states of rare-earth ions in YVO_4, $YAsO_4$, and YPO_4. *Physical Review B*, 8:980–987, 1973.

[387] H.D. Rees. Calculation of distribution functions by exploiting the stability of the steady state. *J. Physics and Chemistry of Solids*, 30:643–655, 1969.

[388] L.G.C. Rego and G. Kirczenow. Quantized thermal conductance of dielectric quantum wires. *Physical Review Letters*, 81:232–235, 1998.

[389] O.D. Restrepo, K. Varga, and S.T. Pantelides. First-principles calculations of electron mobilities in silicon: Phonon and coulomb scattering. *Applied Physical Letters*, 94:212103–1–3, 2009.

[390] B.K. Ridley. The electron-phonon interaction in quasi-two-dimensional semiconductor quantum-well structures. *J. Physics C: Solid State Physics*, 15:5899–5977, 1982.

[391] B.K. Ridley, W.J. Schaff, and L.F. Eastman. Hot-phonon-induced velocity saturation in GaN. *J. Applied Physics*, 96:1499–1502, 2004.

[392] L. A. Riseberg and H. W. Moos. Multiphonon orbit-lattice relaxation of excited states of rare-earth ions in crystals. *Physical Review*, 174:429–438, 1968.

[393] F. Römer, A. Lervik, and F. Bresme. Nonequilibrium molecular dynamics simulations of the thermal conductivity of water: A systematic investigation of the SPC/E and TIP4P/2005 models. *J. Chemical Physics*, 137:074503, 2012.

[394] R.T. Ross and A.J. Nozik. Efficiency of hot-carrier solar energy converters. *J. Applied Physics*, 53:3813–3818, 1982.

[395] M. Roufosse and P.G. Klemens. Thermal-conductivity of complex dielectric crystals. *Physical Review B*, 7:5379–5386, 1973.

[396] D.M. Rowe. *CRC Handbook of Thermoelectrics*. CRC Press, Boca Raton, 1995.

[397] X.L. Ruan. *Ph.D Thesis: Fundamentals of Laser Cooling of Rare-Earth-Ion Doped Solids and Its Enhancement Using Nanopowders*. University of Michigan, Ann Arbor, 2006.

[398] X.L. Ruan, H. Bao, and M. Kaviany. Boundary-induced vibrational spectra broadening in nanostructures. *Physical Review Letters*, submitted, 2008.

[399] X.L. Ruan and M. Kaviany. Photon localization and electromagnetic field enhancement in laser irradiated, random porous media. *Nanoscale and Microscale Thermophysical Engineering*, 9:63–84, 2005.

[400] X.L. Ruan and M. Kaviany. Enhanced laser cooling of rare-earth-ion-doped nanocrystalline powders. *Physical Review B*, 73:155422–1–15, 2006.

[401] X.L. Ruan and M. Kaviany. Advances in laser cooling of solids. *ASME J. Heat Transfer*, 129:3–10, 2007.

[402] X.L. Ruan and M. Kaviany. *Ab initio* photon-electron and electron-vibration coupling calculations related to laser cooling of ion-doped solids. *J. Computational Theoretical Nanoscience*, 5:221-229, 2008.

[403] X.L. Ruan, S.C. Rand, and M. Kaviany. Entropy and efficiency in laser cooling of solids. *Physical Review B*, 75:214304–1–9, 2007.

[404] C. Ruf, H. Obloh, B. Junge, E. Gmelin, and K. Ploog. Phonon-drag effect in GaAs-$\mathrm{Al}_x\mathrm{Ga}_{1-x}$. *Physical Review B*, 37:6377–6380, 1998.

[405] A.R. Ruffa. Statistical thermodynamics of insulators. *J. Chemical Physics*, 83:6405–64008, 1985.

[406] S. Sakong, P. Kratzer, X. Han, K. Laß, O. Weingart, and E. Hasselbrink. Density-functional theory study of vibrational relaxation of CO stretching excitation on Si(100). *J. Chemical Physics*, 129:174702–1–11, 2008.

[407] J.J. Sakurai. *Advanced Quantum Mechanics*. Benjamin/Cummings, Menlo Park, 1984.

[408] D.H. Sampson. *Radiative Contributions to Energy and Momentum Transport in Gases*. Wiley, New York, 1965.

[409] R.T. Sanderson. Chemical bonds and bond energy. *Physical Chemistry Series*, 21:174–211, 1971.

[410] P. Santhanam, D.J. Gray, and R.J. Ram. Thermoelectrically pumped light-emitting diodes operating above unity efficiency. *Physical Review Letters*, 108:097403–1–5, 2012.

[411] T. Sato. Spectral emissivity of silicon. *Japanese J. Physics*, 6:339–347, 1967.

[412] P.K. Schelling, S.R. Phillpot, and P. Keblinski. Comparison of atomic-level simulation methods for computing thermal conductivity. *Physical Review B*, 65:144306, 2002.

[413] K.W. Schlichting, N.P. Padture, and P.G. Klemens. Thermal conductivity of dense and porous yttria-stabilized zirconia. *J. Materials Science*, 36:3003–3010, 2001.

[414] E.F. Schubert. *Light Emitting Diodes*. Cambridge University Press, New York, 2006.

[415] R.N. Schwartz, Z.I. Slawsky, and K.F. Herzfeld. Calculation of vibrational relaxation times in gases. *J. Chemical Physics*, 20:1591–1599, 1952.

[416] D. Segal. Stochastic pumping of heat: Approaching the Carnot efficiency. *Physical Review Letters*, 101:260601–1–4, 2008.

[417] D. Segal and A. Nitzan. Spin-boson thermal rectifier. *Physical Review Letters*, 94:034301–1–4, 2005.

[418] D. Segal, A. Nitzan, and P. Hänggi. Thermal conductance through molecular wires. *J. Chemical Physics*, 119:6840–6855, 2003.

[419] H. Septzler, C.G. Sammis, and R.J. O'Connell. Equation of state of sodium chloride ultrasonic measurements to 8 kbar and 800. deg. and static lattice theory. *J. Physics Chemistry of Solids*, 33:1727–1750, 1972.

[420] A. Shakouri and J.E. Bowers. Heterostructure integrated thermionic coolers. *Applied Physics Letters*, 71:1234–1236, 1997.

[421] A. Shakouri, E.Y. Lee, D.L. Smith, V. Narayanamurti, and J.E. Bowers. Thermoelectric effects in submicron heterostructure barriers. *Microscale Thermophysical Engineering*, 2:37–47, 1998.

[422] F. Sharipov and D. Kalempa. Velocity slip and temperature jump coefficients for gaseous mixtures. II. Thermal slip coefficient. *Physics of Fluids*, 16:759–764, 2004.

[423] S. Shin and M. Kaviany. Enhanced laser cooling of $\mathrm{CO_2Xe}$ gas using (02^00) excitation. *J. Applied Physics*, 106:124910–1–6, 2009.

[424] S. Shin and M. Kaviany. Interflake thermal conductance of edge-passivated graphene. *Physical Review B*, 84:235433–1–7, 2011.

[425] S. Shin, M. Kaviany, T. Desai, and R. Bonner. Roles of atomic restructuring in interfacial phonon transport. *Physical Review B*, 82:081302–1–4, 2010.

[426] S. Shin, C. Melnick, and M. Kaviany. Heterobarrier for converting hot-phonon energy to electric potential. *Physical Review B*, 87:075317–1–6, 2013.

[427] J.L. Shohet. *The Plasma State*. Academic, New York, 1971.

[428] R. Siegel and J. Howell. *Thermal Radiation Heat Transfer*. Taylor & Francis, New York, 2002.

[429] A.E. Siegman. *Lasers*. University Science Books, Sausalito, 1986.

[430] W.T. Silfvast. *Laser Fundamentals*. Second Edition, Cambridge University Press, Cambridge, 2004.

[431] M.V. Simkin and G.D. Mahan. Minimum thermal conductivity of superlattices. *Physical Review Letters*, 84:927–930, 2000.

[432] D.J. Singh and L. Nordström. *Planewaves, Pseudopotentials, and the LAPW Method*. Springer, New York, 2006.

[433] J. Singh. *Physics of Semiconductor and Their Heterostructures*. McGraw-Hill, New York, 1993.

[434] J. Singh. *Electronic and Optoelectronic Properties of Semiconductor Structures*. Cambridge University Press, Cambridge, 2003.

[435] D.B. Sirdeshmukh, P.G. Krishna, and K.G. Subhadra. Micro-macro property correlations in alkali halide crystals. *J. Materials Science*, 38:2001–2006, 2003.

[436] G.A. Slack. Effect of isotopes on low-temperature thermal conductivity. *Physical Review*, 105:829–831, 1957.

[437] G.A. Slack. *The Thermal Conductivity of Nonmetallic Crystals, Solid State Physics*. 34, 1–73, Academic Press, New York, 1979.

[438] G.A. Slack and C. Glassbrenner. Thermal conductivity of germanium from 3 k to 1020 k. *Physical Review*, 120:782–789, 1960.

[439] J.C. Slater. The theory of complex spectra. *Physical Review*, 34:1293, 1929.

[440] H. Smith and H.H. Jensen. *Transport Phenomena*. Clarendon, Oxford, 1989.

[441] K.C. Sood and M.K. Roy. Longitudinal and transverse parts of the correction term in the Callaway model for the phonon conductivity. *J. Physics: Condensed Matter*, 5:L245–L246, 1993.

[442] P. Spijker, A.J. Markvoort, P.A.J. Hilbers, and S.V. Nedea. Velocity correlations and accommodation coefficients for gas-wall interactions in nanochannels. *AIP Conference Proceedings*, 1084(1):659–664, 2008.

[443] P. Spijker, A.J. Markvoort, S.V. Nedea, and P.A.J. Hilbers. Velocity correlations between impinging and reflecting particles using MD simulations and several stochastic boundary conditions. *Proceedings of ICNMM, Sixth International Conference on Nanochannels, Microchannels and Minichannels, Darmstadt, Germany*, 1:1–10, 2008.

[444] G.S. Springer. Heat transfer in rarefied gases. *Advances in Heat Transfer*, 7:163–218, 1971.

[445] G.P. Srivastava. *The Physics of Phonons*. Adam Hilger, Bristol, 1995.

[446] S. Stackhouse, L. Stixrude, and B.B. Karki. Thermal conductivity of periclase from first principles. *Physical Review Letters*, 104:208501–1–4, 2010.

[447] S. Stankovich, D.A. Dikin, G.H.B. Dommett, K.M. Kohlhaas, E.J. Zimney, E.A. Stach, R.D. Piner, S.T. Nguyen, and R.S. Ruoff. Graphene-based composite materials. *Nature*, 442:282–286, 2006.

[448] R. Stedman, L. Almqvist, and G. Nillson. Phonon-frequency distribution and heat capacities of aluminum and lead. *Physical Review*, 162:549–557, 1967.

[449] J.C. Stephenson, R.E. Wood, and C.B. Moore. Temperature dependence of intramolecular vibration→vibration energy transfer in CO_2. *J. Chemical Physics*, 54:3097–3102, 1971.

[450] F.H. Stillinger and T.A. Weber. Computer simulation of local order in condensed phases of silicon. *Physical Review B*, 31:5262–5271, 1985.

[451] M.E. Striefler and G.R. Barsch. Lattice dynamics of alpha-quartz. *Physical Review B*, 12:4553–4566, 1975.

[452] A. Sugimurt and W. Vogenitzf. Monte Carlo simulation of ion collection by rocket-borne mass spectrometer. *J. Geophysical Research*, 80:673–684, 1975.

[453] E.T. Swartz and R.O. Pohl. Thermal boundary resistance. *Reviews of Modern Physics*, 61:605–658, 1989.

[454] L. Tablot, R.K. Cheng, R.W. Schefer, and D.R. Willis. Thermophoresis of particle in a heated boundary layer. *J. Fluid Mechanics*, 101:737–758, 1980.

[455] H. Tachikawa, T. Ichikawa, and H. Yoshida. Geometrical structure and electronic states of the hydrated titanium(iii) ion. An *ab initio* CI study. *J. American Chemical Society*, 112:982–987, 1990.

[456] The Pacific Northwest National Laboratory (PNNL) database. *Carbon dioxide images from PNNL, in microns*. http://vpl.astro.washington.edu/spectra/co2pnnlimagesmicrons.htm.

[457] F. Thevenot. Boron carbide – a comprehensive review. *J. European Ceramic Society*, 6:205–225, 1990.

[458] J. Thiede, J. Distel, S.R. Greenfield, and R.I. Epstein. Cooling to 208 K by optical refrigeration. *Applied Physics Letters*, 86:154107, 2005.

[459] C.L. Tien. Thermal radiation properties of gases. *Advances in Heat Transfer*, 5:253–324, 1968.

[460] C.L. Tien and J.H. Lienhard. *Statistical Thermodynamics*. Holt, Rinehart and Winston, New York, 1971.

[461] C.L. Tien, A. Majumdar, and F.M. Gerner. *Microscale Energy Transport*. Taylor & Francis, Washington D.C., 1998.

[462] M. Tinkham. *Group Theory and Quantum Mechanics*. Dover Publications, New York, 2003.

[463] P. Tipler and R. A. Leewelly. *Modern Physics*. Third Edition, Freeman, New York, 2000.

[464] M.D. Tiwari and B.K. Agrawal. Analysis of the lattice thermal conductivity of germanium. *Physical Review B*, 4:3527–3532, 1971.

[465] Y. Touloukian. *Thermophysical Properties of Matter*. Plenum, New York, 1970.

[466] R.E. Trees. Configuration interaction in MN II. *Physical Review*, 83:756–760, 1951.

[467] P.L.W. Tregenna-Piggott, S.P. Best, M.C.M. O'Brien, K.S. Knight, J.B. Forsyth, and J.R. Pilbrow. Cooperative Jahn-Teller effect in titanium alum. *J. American Chemical Society*, 119:3324–3332, 1997.

[468] M.C. Tsai and S. Kou. Heat transfer and fluid flow in welding arcs produced by sharpened and flat electrodes. *Int. J. Heat Mass Transfer*, 33:2089–2098, 1990.

[469] K.T. Tsen, R.P. Joshi, D.K. Ferry, A. Botchkarev, B. Sverdlov, A. Salvador, and H. Morkoç. Nonequilibrium electron distributions and phonon dynamics in wurtzite GaN. *Applied Physics Letters*, 68:2990–2992, 1996.

[470] J.E. Turney, A.J.H. McGaughey, and C.H. Amon. Assessing the applicability of quantumcorrections to classical thermal conductivity predictions. *Physical Review B*, 79:224305–1–7, 2009.

[471] D.C. Tyte. *Advances in Quantum Electronics, Vol 1*. Academic Press, London, 1970.

[472] K. Uchida, H. Adachi, T. An, T. Ota, M. Toda, B. Hillebrands, S. Maekawa, and E. Saitoh. Long-range spin Seebeck effect and acoustic spin pumping. *Nature Materials*, 10:737–741, 2011.

[473] C. Uher. Skutterudites: Prospective novel thermoelectrics. *Semiconductors and Semimetals*, 69:140–253, 2001.

[474] B.W.H. van Beest, G.J. Krammer, and R.A. van Santen. Force field for silica and aluminophosphates based on *ab initio* calculations. *Physical Review Letters*, 64:1955–1958, 1990.

[475] B. van Zeghbroeck. http://ece-www.colorado.edu/~bart/book.

[476] S. Vavilov. Some remarks on the Stokes law. *J. Physics (Moscow)*, 9:68–73, 1945.

[477] S. Vavilov. Photoluminescence and thermodynamics. *J. Physics (Moscow)*, 10:499–501, 1946.

[478] F.J. Vesely. *University of Vienna*. http://homepage.univie.ac.at/franz.vesely/notes/md_neq/mdneq/node1.html, 2007.

[479] W.E. Vincenti and C.H. Kruger. *Introduction to Physical Gas Dynamics*. Wiley, New York, 1965.

[480] Y.A. Vlasov, M.A. Kaliteevski, and V.V. Nikolaev. Different regimes of light localization in a disordered photonic crystal. *Physical Review B*, 60:1555–1562, 1999.

[481] S. Volz. *Microscale and Nanoscale Heat Transfer (Topics in Applied Physics)*. Springer, New York, 2007.

[482] S. Volz, J.B. Saulnier, M. Lallemand, B. Perrin, P. Depondt, and M. Mareschal. Transient Fourier-law deviation by molecular dynamics in solid argon. *Physical Review B*, 54:340–347, 1996.

[483] S.G. Volz and G. Chen. Molecular-dynamics simulation of thermal conductivity of silicon crystals. *Physical Review B*, 61:2651–2656, 2000.

[484] C.S. Wang, J.S. Chen, J. Shiomi, and S. Maruyama. A study on the thermal resistance over solid-liquid-vapor interfaces in a finite-space by a molecular dynamics method. *Int. J. Thermal Sciences*, 46:1203–1210, 2007.

[485] D. Wang, L. Tang, M. Long, and Z. Shuai. Anisotropic thermal transport in organic molecular crystals from nonequilibrium molecular dynamics simulations. *J. Physical Chemistry C*, 115:5940–5946, 2011.

[486] J.-S. Wang, J. Wang, and J.T. Lü. Quantum thermal transport in nanostructures. *European Physical J. B*, 62:381–404, 2008.

[487] L.-H. Wang, S.L. Jacques, and L.-Q. Zheng. Monte Carlo modeling of photon transport in multi-layered tissues. *Computer Methods and Programs in Biomedicine*, 47:131–146, 1995.

[488] L.-H. Wang and H.I. Wu. *Biomedical Optics: Principles and Imaging*. Wiley, Hoboken, 2007.

[489] H.M. Wastergaard. *Theory of Elasticity and Plasticity*. Dover, New York, 1952.

[490] D.P. White. The effect of ionization and displasive radiation on thermal conductivity of alumina. *J. Applied Physics*, 73:2254–2258, 1993.

[491] D.P. White. The effect of ionization and dissipative reaction on the thermal conductivity of alumina at low temperature. *J. Nuclear Materials*, 212–215:1069–1074, 2004.

[492] F. Widulle, T. Ruff, K. Konuma, I. Silier, M. Cordona, W. Kriegseis, and V.I. Ozhogin. Isotope effects in elemental semiconductors: A raman study of silicon. *Solid State Communications*, 118:1–22, 2001.

[493] D.S. Wiersma, P. Bartolini, A. Lagendijk, and R. Righini. Localization of light in a disordered medium. *Nature*, 390:671–673, 1997.

[494] C. Willett. *Introduction to Gas Lasers: Population Inversion Mechanisms*. Pergamon, New York, 1974.

[495] E.B. Wilson, J.C. Decius, and P.C. Cross. *Molecuar Vibrations: The Theory of Infrared and Raman Vibrational Spectra*. McGraw-Hill, New York, 1955.

[496] D. Wolf, P. Keblinski, S.R. Philpot, and J. Eggebrecht. Exact method for the simulation of coulombic systems by direct, pairwise 1/r summation. *J. Chemical Physics*, 110:8254–8282, 1999.

[497] B.T. Wong, M. Francoeur, and M.P. Menguç. A Monte Carlo simulation for phonon transport within silicon structures at nanoscales with heat generation. *Int. J. Heat Mass Transfer*, 54:1825–1838, 2011.

[498] B.T. Wong and M.P. Mengüç. *Thermal Transport for Applications in Micro/Nanomachining*. Springer, New York, 2008.

[499] C. Wood. Transport properties of boron carbides. *AIP Conference Proceedings*, 140:206–215, 1986.

[500] T.O. Woodruff and H. Ehrenrich. Absorption of sound in insulators. *Physical Review*, 123:1553–1559, 1961.

[501] L.A. Wu and D. Segal. Sufficient conditions for thermal rectification in hybrid quantum structure. *Physical Review Letters*, 102:095503–1–4, 2009.

[502] H.S. Yang, K.S. Hong, S.P. Feofilov, B.M. Tissue, R.S. Meltzer, and W.M. Dennis. Electron-phonon interaction in rare earth doped nanocrystals. *J. Luminescence*, 83-84:139–145, 1999.

[503] N. Yang, G. Zhang, and B. Li. Carbon nanocone: A promising thermal rectifier. *Applied Physics Letters*, 93:243111–1–3, 2008.

[504] R.T. Yang. *Gas Separation by Adsorption Processes*. Imperial College Press, London, 1997.

[505] J.T. Yardley and C.B. Moore. Intramolecular vibration-to-vibration energy transfer in carbon dioxide. *J. Chemical Physics*, 46:4491–4495, 1967.

[506] W.M. Yen, S. Shionoya, and H. Yamamoto. *Phosphor Handbook*. CRC Press, Boca Raton, 2002.

[507] R.C. Yu, N. Tea, M.B. Salamon, D. Lorents, and R. Malhotra. Thermal conductivity of single crystal C_{60}. *Physical Review Letters*, 68:2050–2053, 1992.

[508] R. Zallen and M.L. Slade. Influence of pressure and temperature on phonons in molecular chalcogenides: Crystalline As_4S_4 and S_4N_4. *Physical Review B*, 18:5775–5798, 1978.

[509] D.M. Zayachuk. The dominant mechanisms of charge-carrier scattering in lead telluride. *Semiconductors*, 31:173–176, 1997.

[510] C. Zener. Low velocity inelastic collisions. *Physical Review*, 38:277–281, 1931.

[511] W. Zhang, T.S. Fisher, and N. Mingo. Simulation of interfacial phonons transport in Si-Ge heterostructures using an atomistic Green's function method. *J. Heat Transfer*, 129:483–491, 2006.

[512] Z.M. Zhang. *Nano/Microscale Heat Transfer*. McGraw-Hill, New York, 2007.

[513] Z.M. Zhang and M.I. Flik. Predicted absorption of $YBa_2Cu_3O_7$/YSZ/Si multilayer structures for infrared detectors. *IEEE Transactions on Applied Superconductivity*, 3:1604–1607, 1993.

[514] Q.S. Zhu, S.M. Mou, X.C. Zhou, and Z.T. Zhong. Determination of the conduction-band offset of a single AlGaAs barrier layer using deep level transient spectroscopy. *Applied Physics Letters*, 62:2813–2814, 1993.

[515] J.M. Ziman. *Electrons and Phonons: The Theory of Transport Phenomenon in Solids*. Oxford University Press, Oxford, 1960.

[516] J.M. Ziman. *Principles of the Theory of Solids*. Second Edition, Cambridge University Press, Cambridge, 1972.

[517] R. Zwanzig. Time-correlation functions and transport coefficients in statistical mechanics. *Annual Review of Physical Chemistry*, 16:67–102, 1965.

Index

ab initio calculations, 61
ab initio calculation of band structure, 319
absorption of ultrasound waves in solids, 275
acoustic absorption coefficient, 276
acoustic absorption heating, 276
acoustic and optical polarizations, 185
acoustic impedance, 278
acoustic phonon scattering of electron, 354
adiabatic approximation, 727
Ampere law, 140
annihilation and creation operators, 715
annihilation operator, 102, 587
anti-Stokes cooling of CO_2 gas, 626
anti-Stokes emission, 727
anti-Stokes fluorescence, 582
antisite defect, 360
asymmetric phonon conductance, 287
atomic displacement in lattice vibration, 208
atomic electron orbitals, 58
atomic properties, 30
atomic radius, 30
atomic-level resonances, 40
audible sound, 173
auger effect, 727
average Debye DOS model, 185
average sound velocity, 244
average thermal speed, 455
Avogadro number, 22, 666
azimuthal quantum number, 110

ballistic phonon transport regime, 279
ballistic transport, 35, 129, 727
bandgap energy, 727
basis, 190
Beer–Lambert law, 562
Beni–Platzman–Debye MSD model, 210
blackbody photon DOS and phase speed, 523
blackbody radiation, 519
blackbody radiation intensity, 525
blackbody, spectral emissive power, 525
Bloch theorem, 727
Bloch wave, 727
Bohr radius, 22, 666
Boltzmann constant, 20, 22, 666
Boltzmann transport equation (BTE), 120
bond order, 62
Born–Oppenheimer approximation, 96
Bose einstein condensates, 718
Bose–Einstein condensate, 627, 728
Bose–Einstein statistics, 696
boson, 699, 728
boundary Seebeck coefficient, 399
boundary-layer turbulence, 474
boundary-layer turbulent heat flux, 491
bra–ket inner product, 100
Bravais lattice, 728
bravais lattice, 187
bremsstrahlung, 728
Brillouin scattering, 728
Brillouin zone, 186, 728
Brillouin zone planes, 189
Brownian diffusion, 471
Brownian diffusion time, 472
Brownian motion, 154, 472
bulk modulus, 161, 162
bulk properties, 30
bulk properties of elements, 662

Cahill–Pohl model, 232
Cahill–Pohl thermal conductivity, 681
Callaway conductivity model, 211
Callaway phonon thermal conductivity model from BTE, 212
Callaway–Holland thermal conductivity model, 215
canonical ensemble, 83
canonical partition function, 697
carrier density, 40
carrier-induced entropy, 701
Casmir boundary scattering, 218
chirality, 71, 728
classical electron oscillator, 579

classical Hamiltonian, 80
classical molecular dynamics, 81
CO_2 gas laser, 611
cohesive energy, 30, 728
collision (viscous or Langevin) relaxation time, 154
commutation relations, 532
commutator operator, 118
compatibility equation, 162
complex index of refraction, 139
compression wave, 162
Compton scattering, 544, 728
conduction band, 728
configuration coordinate diagram, 603
confluent hypergeometric function, 103
continuity equation, 160
continuous and band photon absorption, 562
continuous and band photon emission in solids, 571
cooling length, 397
cooperative process, 38, 582
cooperative processes, 728
coordination number, 191
correlation function, 159
Coulomb constant, 22, 54, 666
Coulomb law, 54
covalent bonds, 237, 247
coverting hot-phonon energy to electric potential, 418
creating fock states, 716
creation and annihilation operators, 729
creation operator, 102, 587
crystal boundary scattering, 218
crystal structure, 30

de Broglie quantum wave, 98
de Broglie relation, 324
de Broglie wavelength, 728, 729
Debye atomic displacement model, 93
Debye cut-off frequency, 202
Debye model of lattice specific heat capacity, 204
Debye model of the phonon density of states, 201
Debye temperature, 30, 90, 186, 241, 729
Debye–Gaussian model, 186
degenerate conductors, 345
degenerate energy state, 729
dense fluids specific heat capacity: van der Waals model, 447
density, 30
density of electronic energy states, 327
density of states, 40, 106, 729
dielectric function, 139, 148
dielectric heating, 151
diffraction, 552
diffuse scattering, 684
diffusion time, 161
dimensionless dispersion relation, 177
dipole moment, 145
dipole-moment transition, 582
Dirac delta function, 730
disjoining pressure in ultrathin liquid films, 486
dispersion, 730
dispersion relation, 177, 194
distinguishable, 100, 699
distinguishable and indistinguishable particles, 730
dopant, 731
doped semiconductor, 366
Doppler temperature, 629
double bond, 60
Drude electron transport model, 731
Drude–Sommerfeld electron gas model, 105
Dulong–Petit limit, 204
dynamic viscosity, 160, 460
dynamical matrix, 177

effective conductivity with dispersed particles in Brownian motion, 470
effective electron mass, 322, 731
Einstein (Brownian) diffusion coefficiant, 472
Einstein coefficients, 538
Einstein population rate equation, 535, 536
Einstein solid thermal conductivity model, 231
Einstein thermal conductivity, 676
elastic and inelastic scattering, 132
elastic binary collision rate of ideal gas, 456
elastic collision (scattering), 731
elastic constants, 161
electric energy, 440
electric susceptibility, 146
electric susceptivity, 139
electrical conductivity, 30, 128, 139, 367
electromagnetic wave equation, 140
electron, 7
electron and phonon transport equations, 393
electron band structure in crystals, 309
electron band structures for semiconductors, 321
electron bandgap, 731
electron BTE for semiconductors, 334
electron charge, 22, 666
electron density of states, 106
electron energy equation, 397
electron gas specific heat capacity, 332
electron group velocity, 327
electron mass, 22, 666
electron mean free path, 349
electron mobility, 128, 340
electron scattering, 341
electron specific heat capacity, 331
electron volt, 732
electron wave function for hydrogenlike atoms, 109
electron–phonon relaxation time, 351
electron–phonon wave function, 352
electron-scattering relaxation relations, 343
electronegativity, 30, 238
electronic energy states of rare-earth ion-doped crystals, 400

electronic orbital structure, 30
electronic quantum number, 440
emission mechanisms, 571
emissivity, 574
energy gap, 313
energy relaxation time, 338, 732
energy transformation kinetics, 131
ensembles, 82
equation of radiative transfer, 547
equilibrium distribution function for translational energy, 453
ergodic hypothesis, 81, 732
estimation of acoustic velocity, 206
evanescent wave, 644, 732
exciton, 732
exciton-polariton, 736
expectation value, 97
extrinsic, 731
extrinsic defect, 359

f-process, 358
Faraday law, 140
Fermi energy, 108
Fermi energy or Fermi level, 732
Fermi golden rule (FGR), 131, 335, 562, 732
Fermi momentum, 325, 327
Fermi surface, 732
Fermi temperature, 109, 327
Fermi velocity, 109, 327
Fermi–Dirac integral, 165
Fermi–Dirac statistics, 696
fermion, 698, 732
Feynman diagram, 732
field emission, 733
field enhancement, 645
field operators, 716
fine-structure constant, 22, 23, 666
finite size effect, 276
first ionization energy, 30
first quantization, 713
fluid flow regimes, 474
fluid particle, 8, 733
fluid particle BTE and average molecular speed, 451
fluid particle quantum energy states and partition function, 436
fluorescence, 536, 733
Fock states, 714
Fokker–Planck stochastic equation, 156
four quantum numbers, 110
Fourier law of conduction, 1
free-electron energy, 500
free-molecular-flow regime, 474
free-space electric permittivity, 22, 666
free-space magnetic permeability, 22, 666
Frenkel defects, 360
fundamental constants, 22, 666

g-process, 358
gamma function, 342
gas particle translational motion, 436
gas thermal conductivity in narrow gaps, 502
Gauss law, 140
glossary, 727
Grüneisen equation of states, 734
Grüneisen parameter, 233, 244, 733
Grüneisen parameter prediction, 244
grand canonical ensemble, 80, 83
graphene-flake junction, 413
gravitational acceleration vector, 160
Green–Kubo (G–K) relation, 158, 668
Green–Kubo (G–K) transport theory, 156
group theory, 733

Hagen–Rubens relation, 576
Hall coefficient, 350
Hall factor, 350
Hall mobility, 350
Hamaker constant, 486
Hamiltonian, 77, 734
Hamiltonian function, 79
Hamiltonian operator, 79
harmonic approximation, 57, 80
harmonic limit, 57
hartree, 22, 666
heat current, 159
heat current autocorrelation function, 255
heat of evaporation, 30
heat of fusion, 30
heat transfer physics, 32
Heisenberg uncertainty principle, 21
Hermite polynomial, 103
heteronuclear polyatomic gas, 440
Hilbert space, 100
hole, 7
hole concentration, 367
hole density, 329
hole mobility, 367
Hooke law, 159, 162
hot electrons, 419
hot phonons, 419
hot-electron cooling time, 411
hot-phonon bottleneck, 412
hydrogen atom model, 109
hyperbolic heat conduction equation, 430
hyperfine structure, 23
hypersound, 173

ideal-gas mean free path, 459
ideal-gas specific heat capacity, 443
ideal-gas thermal conductivity for BTE, 462
impurity (and isotope and vacancy) scattering, 218
impurity defect, 360
in- and out-scattering, 123
indistinguishable, 100
indistinguishable particles, 697
inelastic collision, 734
inelastic scattering, 734

inner turbulent core, 493
interacting indistinguishable particles, 696
interaction of fluid particle and surface, 474
interaction rate between electrons and heavier species, 501
interatomic forces, 52
interference, 552
intermolecular forces, 52
internal conversion, 137
interparticle collisions, 451
interstitial defect, 360
intrinsic, 731
intrinsic carrier density, 329
intrinsic defect, 359
ionic bonds, 238, 246
ionic crystals, 734
isobaric–isothermal ensemble, 83
isothermal compressibility, 161, 162
isotopes, 30

Joule heating, 151

Kane nonparabolic electron relaxation-time model, 324
Kapitza boundary resistance, 734
Kelvin relation, 348
Kennard thermal slip constant, 510
kinematic viscosity, 461
kinetic energy, 53
kinetic theory, 734
kinetics, 734
Kirchhoff law, 573
Kirchhoff law of radiation, 734
Knudsen number, 474
Knudsen number effect, 503
Knudson-flow-regime surface accommodation coefficients, 476
Kolmogoroff length, 490, 491
Kolmogoroff spectral law, 491
Kronig–Penney potential model, 311

ladder operator, 102
Ladder Operators, 713
laminar sublayer, 493
laminar-flow, 474
Landauer formulation, 288
Langevin equation, 471
Langevin relaxation time, 155
Langevin stochastic dynamic equation, 471
Langevin stochastic equation, 155
Langmuir adsorption isotherm, 485
Langmuir adsorption model, 484
laser cooling of CO_2, 620
laser cooling of atomic gases, 627
laser cooling of solids, 582
lasers and narrow-band emissions, 527
lattice basis, 190
lattice constant, 30
lattice dynamics, 191

Lennard–Jones (L–J) potential, 67
lifetime, 606
linear combination of atomic orbitals (LCAO), 315
liquid–gas interfacial force balance, 160
local thermal equilibrium, 544
localization, 35
longitudinal-acoustic branch, 178
longitudinal-optical branch, 178
Lorenz number, 349
luminescence, 734

Mach number, 476
macroscopic (continuum) energy equation, 1
macroscopic elastic solid-mechanics equations, 159
macroscopic fluid dynamics equations, 159
magnetic quantum number, 110
magnon, 734
majority carrier, 329
master equation, 735
master equation of quantum mechanics, 42
matrix element, 336
Matthiessen rule, 151, 215, 370, 578
Maxwell equations, 140
Maxwell velocity slip coefficient, 480
Maxwell–Boltzmann (M–B), 699
Maxwell–Boltzmann (M–B) energy distribution function, 456
Maxwell–Boltzmann (M–B) statistics, 696
mean free path, 35, 276, 467
mean-field theory, 155
mean-square relative displacement, 209
melting temperature, 30
metallic bonds, 247
microcanonical ensemble, 82
microwave heating, 151
Mie scattering, 546
minimum phonon conductivity relations, 676
mixing length, 492
molecular gas lasers, 608
molecular orbital, 60
molecular weight, 30
molecular wire, 287
momentum accommodation coefficient, 507
momentum relaxation time, 338, 735
Monte Carlo method, 709

n-type doping, 731
n- and *p*-type semiconductors, 735
nanocone conductivity, 289
nanostructurees, 288
nanotube properties, 71
natural angular frequency, 91
Navier equation, 162
Navier–Stokes equations, 159
near-field radiative heat transfer, 642
near-field thermal emission, 528
neutron mass, 22, 666

neutron scattering, 198
Newton (gravitational) constant, 22, 666
Newton and Hamiltonian equations, 80
Newtonian viscous fluid, 160
nonequlibrium (hot) phonon, 649
noninteracting indistinguishable particles, 696
nonparabolic energy band, 324
nonpolar semiconductor, 358
nonradiative decay, 577
normal coordinates, 94, 209, 352, 735
normal modes of vibration, 192
number of phonon branches, 190
number operators, 716

Onsager reciprocity relation, 153
Onsager transport coefficients, 152
Onsager transport relations, 344
optical dispersion relation, 142
optical-phonon contribution to conductivity, 261
optical-phonon energy equation, 397
optically thick limit and radiant conductivity, 549
outer turbulent core, 493
oxidation states, 30

p-type doping, 731
parabolic energy band, 322, 331
particle probability distribution function, 735
particles, 16
partition function, 21, 79
Pauli exclusion principle, 735
Peltier coefficient, 348
Peltier cooling/heating, 377
permutation operator, 714
phase function, 546
phase speed, 179
phase state, 30
phase transformation, 92
phonon, 4
phonon annihilation operator, 196
phonon assisted, 582
phonon boundary conductance, 272
phonon boundary resistance, 271, 683
phonon boundary scattering, 278
phonon boundary thermal resistance, 272
phonon boundary transmission coefficient, 273
phonon contributions to Seebeck coefficient, 701
phonon creation operator, 196
phonon density of states, 181
phonon dispersion, 174
phonon dispersion models, 223
phonon dispersion relation, 177
phonon drag on electron, 735
phonon gas, 735
phonon group velocity, 179
phonon heat capacity, 201
phonon intensity, 524
phonon polariton, 736
phonon recycling, 646
phonon recycling (in photonics), 646
phonon softening, 345, 706
phonon soliton, 287
phonon thermal conductivity, 214
phonon-assisted absorption, 588
phonon-polariton, 736
phonons in photovoltaics, 631
phosphor, 736
phosphorescence, 736
photon, 9
photon absorption and emission, 543
photon absorption and emission in two-level electronic system, 534
photon absorption cross-section area, 540
photon absorption in solids, 562
photon absorption time, 161
photon density of states, 524
photon dispersion relation, 139
photon emission cross-section area, 541
photon energy confinement, 645
photon energy density, 524
photon intensity, 524
photon number density, 523
photon quantum number, 520
photon spectrum, 522
photon–free electron scattering rate, 544
photon-induced, 588
photon-matter interactions, 529
physical adsorption and desorption, 482
pi bond, 60
piezoelectric constant, 351
Planck constant, 21, 22, 666
Planck mean absorption coefficient, 653
plasma frequency, 736
plasma polariton, 736
plasma thermal conductivity, 496
plasmon, 150, 736
Poisson ratio, 159, 162, 208
polar and nonpolar semiconductors, 736
polar molecules, 736
polariton, 736
polarization vector, 143
polaron, 736
polaron hopping, 706
potential energy, 53, 736
potential models, 65
potential well, 53
power-law energy dependent τ_e, 338
Poynting vector, 144
primary wave, 162
primitive cell, 736
primitive lattice vectors, 187
primitive reciprocal lattice vectors, 187
principal energy carriers, 3
principal quantum number, 110
probability density function, 155
probability distribution function, 10
propagating waves, 643
proton mass, 22, 666
pseudopotential, 736

quantum concentration, 696
quantum corrections to MD predictions, 262
quantum dot, 408
quantum efficiency, 580
quantum Hamiltonian, 737
quantum mechanics, 737
quantum theory of lattice vibration, 196
quantum well, 408
quantum well for improved figure of merit, 408
quantum wells, 411
quantum wires, 408
quantumn harmonic oscillator, 197
quasi-particle, 16, 737

radial distribution function, 73
radiation (decay) lifetime, 536
radiation broadening, 579
radiative intensity, 144
radiative lifetime, 592
Raman scattering, 737
random resonator, 558
rattler, 737
Rayleigh and Mie scatterings, 737
Rayleigh scattering, 133, 218, 547
Rayleigh–Jeans law, 519, 527
reciprocal lattice, 186, 737
reciprocity between spectral photon emission and absorption, 572
rectification in anisotropic, one-dimensional systems, 286
reduced mass, 177
relative electric permittivity, 139
relative magnetic permeability, 139
relaxation time, 737
relaxation-time approximation, 124
relaxation-time approximation of gas BTE, 462
relaxation-time models, 215
Reststrahlen absorption and reflection, 737
RMS thermal speed, 454
role of fluid particle motion in gas lasers, 608
rotational constant, 439
rotational energy, 439
rotational quantum number, 439
Rydberg energy, formula, and constant, 738

Saha equation, 501
scales in Lennard Jones (L–J) potential, 92
scattering phase, 546
scattering relaxation times, 217
screened Coulombs potential, 54
second quantization, 713
second viscosity, 160
secondary wave, 162
Seebeck coefficient, 348
semiconductors, 319, 321, 366, 738
semiemprical PV efficiency, 639
shear modulus, 162
shear wave, 162
sigma bond, 60
simple classical harmonic oscillator, 91
simple harmonic oscillator, 101
single-bandgap ideal photovoltaic efficiency, 633
single-mode relaxation time, 211
size effects, 276, 407, 502, 642
size parameter, 219, 546
skutterudites, 738
Slack relation, 233
Slater determinant, 714
slip coefficients in transitional-flow regime, 480
solid angle, 545
species concentrations for two-temperature system, 501
specific heat capacity, 30
spectral absorptance, 563
spectral surface emissivity, 574
specular parameter, 279
specular scattering, 687
speed of light in vacuum, 22, 666
speed of sound for an ideal-gas, 468
speed probability distribution function, 455
spherical, parabolic band, 738
spin, 738
spontaneous and stimulated emissions in thermal cavity, 538
spontaneous emission, 536, 540, 738
spring constant, 91
Stefan–Boltzmann constant, 22, 666
Stefan–Boltzmann law, 527
sticking probability, 484
stimulated absorption, 536
stimulated emission, 536, 738
Stokes law, 738
strain tensor, 162
structural factor, 189
structure defects, 360
substitutional defect, 360
superlattice, 411
surface plasmon, 739
surface polariton, 642
surface tension, 160
surface-phonon polariton, 643
surface-plasmon polarization, 643
symmetry number, 447

T-matrix method, 554
tables of properties, 661
theoretical maximum evaporatoin/condensation heat transfer rate, 461
thermal accommodation coefficient, 477, 507
thermal conductivity, 30, 372
thermal conductivity of ideal gas, 463
thermal conductivity of liquids, 469
thermal conductivity of polymers, 233
thermal creep (slip) flow, 508
thermal diffusivity, 467
thermal effusivity, 467
thermal nonequilibrium, 393

thermal nonequilibrium plasma energy equation, 500
thermal plasma, 494, 496
thermal plasma generation, 495
thermionic emission, 432, 739
thermodynamic relations, 76
thermoelectric (TE) figure of merit, 372, 373
thermoelectric force, 335
thermoelectric power factor, 372
thermophoresis, 481
thermophoretic force, 481
thermophoretic velocity, 481
thermophotovoltaic, 739
Thomson coefficient, 349
Thomson cross-section area, 545
Thomson scattering, 739
three-level analysis of CO_2 laser kinetics, 614
tight-binding approximation, 314, 317
time-dependant Schrödinger equation, 97
Tiwari model, 225
total partition function, 436
transit time, 161
transition dipole moment, 593
transition probability rate, 134, 689
transition Reynolds number, 487
transitional-flow regime, 474
translational quantum numbers, 437
transmission probability for diffuse scattering, 684
transmission probability for specular scattering, 687
triple bond, 60
tunneling, 552, 739
turbulent eddies, 494
turbulent energy distribution function for inertial subregime, 491
turbulent flow, 474
turbulent mean free path, 492
turbulent mixing length, 493
turbulent thermal conductivity, 492
turbulent viscous boundary-layer thickness, 493
turbulent-flow structure and transport, 487

ultrasound, 173
Umklapp processes, 337, 739
universal gas constant, 22, 666
universal phonon quantum transport, 289

vacancy defect, 360
valence band, 739
van der Waals coefficient, 448
van der Waals constant, 448
van der Waals equation of states, 449
van der Waals interactions, 247
variational method, 267
velocity vector (momentum) probability distribution function, 455
vibrational (or vibronic) quantum number, 438
vibrational energy, 438
viscous stress tensor, 160
viscous-flow regime, 474
volumetric thermal expansion coefficient, 160
von Kármán universal constant, 493

wave function, 96
wave packets, 16
wave vector, 97
waves, 16
Wiedemann–Franz law, 349, 389, 391
Wien displacement law, 525
Wigner–Seitz primitive cell, 739

Young modulus, 159, 162

zero-point energy, 103